10TH ANNIVERSARY
2015 - 2025

International Journal of BIOPRINTING



ISSN: 2424-7723 (Print)
ISSN: 2424-8002 (Online)
Volume 11·Issue 6
December 2025

ACCSCIENCE PUBLISHING

ACCSCIENCE PUBLISHING

International Journal of Bioprinting

Print ISSN: 2424-7723

Online ISSN: 2424-8002

International Journal of Bioprinting is an international journal covering the technology, science and clinical application of the broadly defined field of Bioprinting. Bioprinting is defined as the use of 3D printing technology with materials that incorporate viable living cells or biological elements to produce tissue or biotechnological products. We are interested in the scientific topics spanning all stages of bioprinting process from concept creation to fabrication and beyond.



Scan to access website:

Scan to submit papers:

About the Publisher

AccScience Publishing is a publishing company based in Singapore. We publish a range of high-quality, open-access, peer-reviewed journals and books from a broad spectrum of disciplines.

Contact Us

Managing Editor
ijb.office@accscience.sg

AccScience Publishing
9 Raffles Place, Republic Plaza 1 #06-00 Singapore 048619.

Volume 11 • Issue 6 • December 2025
ISSN 2424-7723 (print) ISSN 2424-8002 (online)

INTERNATIONAL JOURNAL OF BIOPRINTING

Editor-in-Chief

Chee Kai Chua

Singapore University of Technology and Design, Singapore

ACCSCIENCE PUBLISHING

Access Science Without Barriers

Full issue copyright © 2025 AccScience Publishing
All rights reserved. Without permission in writing from the publisher, this full issue publication in its entirety may not be reproduced or transmitted for commercial purposes in any form or by any means, electronic or mechanical, including photocopying, recording, or any information storage and retrieval system. Permissions may be sought from ijb.office@accscience.sg.

Article copyright © Respective Author(s)
See articles for copyright year. All articles in this full issue publication are open-access. There are no restrictions in the distribution and reproduction of individual articles, provided the original work is properly cited. However, permission to reuse copyrighted materials of an article for commercial purposes is applicable if the article is licensed under Creative Commons Attribution-NonCommercial License. Check the specific license before reusing.

INTERNATIONAL JOURNAL OF BIOPRINTING

ISSN: 2424-7723 (print)
ISSN: 2424-8002 (online)



Editorial and Production Credits

Publisher: AccScience Publishing
Managing Editor: Ivanna Gao
Editorial Assistants: Puva Ramakrishnan, Flora Kang
Production Editor: Puva Ramakrishnan
Special Issue Commissioning Editors: Shirley Song, Terra Shi
Article Layout and Typeset: Bsmart Publishing (India)

For all advertising queries, contact ijb.office@accscience.sg.

Supplementary file

Supplementary files of articles can be obtained at https://accscience.com/journal/IJB/11/6.

Disclaimer

AccScience Publishing is not liable to the statements, perspectives, and opinions contained in the publications. The appearance of advertisements in the journal shall not be construed as a warranty, endorsement, or approval of the products or services advertised and/or the safety thereof. AccScience Publishing disclaims responsibility for any injury to persons or property resulting from any ideas or products referred to in the publications or advertisements. AccScience Publishing remains neutral with regard to jurisdictional claims in published maps and institutional affiliations.

International Journal of Bioprinting

Editorial Board

Editor-in-Chief

Chee Kai Chua
Singapore University of Technology and Design, Singapore

Associate Editors

Wai Yee Yeong
Nanyang Technological University, Singapore

Jiankang He
Xi'an Jiaotong University, China

Amit Bandyopadhyay
Washington State University, USA

Liliang Ouyang
Tsinghua University, China

Maling Gou
Sichuan University, China

Yongqiang Hao (Clinician)
Shanghai Jiao Tong University School of Medicine, China

Xiaoxiao Han
Hunan University, China

Editorial Board Members*

Jason A. Burdick, *USA*
Shweta Agarwala, *Denmark*
Eben Alsberg, *USA*
Anthony Atala, *USA*
Douglas B. Chrisey, *USA*
Andrea Barbetta, *Italy*
Mikhael Bechelany, *France*
Martin Birchall, *UK*
Mohd Fauzi Mh Busra, *Malaysia*
Paulo J.D.S. Bártolo, *Singapore*
Christian Celia, *Italy*
Elisabetta Ceretti, *Italy*
Ming-Wei Chang, *UK*
Maria Chatzinikolaidou, *Greece*
Jun Chen, *Australia*
Daniel Chen, *Canada*
Boris Chichkov, *Germany*
Dong-Woo Cho, *Korea*
Gianluca Ciardelli, *Italy*
Jeremy Crook, *Australia*
Cédric Delattre, *France*
Rui Domingues, *Portugal*
Dennis Douroumis, *UK*
Nileshkumar Dubey, *USA*
Tal Dvir, *Israel*
Eleonora Ferraris, *Belgium*
Sanjay Garg, *Australia*
Antonio Gloria, *Italy*
Manuela Gomes, *Portugal*
Brunella Grigolo, *Italy*
Michinao Hashimoto, *Singapore*
Charlotte A. E. Hauser, *Saudi Arabia*
Dong Nyoung Heo, *Korea*
Raymund E. Horch, *Germany*
Geun Hyung Kim, *Korea*
Richard James Bibb, *UK*
Jinah Jang, *South Korea*
Jingchao Jiang, *China*
Qing Jiang, *China*
Hyun-Do Jung, *Korea*
Lifeng Kang, *Australia*
Ali Khademhosseini, *USA*
Moon Suk Kim, *South Korea*
Jangho Kim, *South Korea*
Bahattin Koç, *Turkey*
Dimitrios A. Lamprou, *UK*
Junmin Lee, *South Korea*
Jin Woo Lee, *South Korea*
Shulamit Levenberg, *Israel*
Khoon Lim, *Australia*
Ki-Taek Lim, *South Korea*
Fengyuan Liu, *UK*
Xiao Liu, *Australia*
Veronica MacChi, *Italy*
Carmelo De Maria, *Italy*
Elena Martínez Fraiz, *Spain*
Laurence Meagher, *Australia*
Ferry Melchels, *Australia*
Nikolaos Michailidis, *Greece*
David K. Mills, *USA*
Vladimir Mironov, *Russia*
Mario Moisés Alvarez, *Mexico*
Maurice N Collins, *Ireland*

Makoto Nakamura, *Japan*
Seung Yun Nam, *Korea*
Roger Narayan, *USA*
Insup Noh, *Korea*
Ali Nokhodchi, *UK*
J.M.A.C. de Oliveira, *Portugal*
Aleksandr Ovsianikov, *Austria*
Sang-Hyug Park, *Korea*
Sungsu Park, *South Korea*
Alokesh Pramanik, *Australia*
Aldo R. Boccaccini, *Germany*
Michael Raghunath, *Switzerland*
Anabela Raymundo, *Portugal*
Shinji Sakai, *Japan*
Thomas Scheibel, *Germany*
Cijun Shuai, *China*
Swee Leong Sing, *Singapore*
Kedong Song, *China*
Jie Sun, *China*
Zhonghua Sun, *Australia*
Ergün Süleyman, *Germany*
Ibrahim Tarik Ozbolat, *USA*
Savas Tasoglu, *Turkey*
S. Vijayavenkataraman, *UAE*
Giovanni Vozzi, *Italy*
Liqiang Wang, *China*
Yin Xiao, *Australia*
Seung-Schik Yoo, *USA*
Barbara Zavan, *Italy*
Ioanna Zergioti, *Greece*
Yu Shrike Zhang, *USA*
Yi Zhang, *China*
Wei Zhu, *China*
Hala Zreiqat, *Australia*

Assistant Editor

Jia An, *Singapore*

Youth Editorial Board Members

Tanveer Ahmad, *Saudi Arabia*
Shivesh Anand, *USA*
Gokhan Bahcecioglu, *USA*
Gianluca Cidonio, *Italy*
Wangwang Ding, *China*
Giovanni Falcone, *Italy*
Ruben Foresti, *Italy*
Gabriele Maria Fortunato, *Italy*
Farnaz Ghorbani, *UK*
Paola Serena Ginestra, *Italy*
Xulin Hu, *China*
Anna Jezierski, *Canada*
Yiting Lei, *China*
Lan Li, *China*
Huixin Liang, *China*
Elena Marcello, *Italy*
Wei Long Ng, *Singapore*
Egor Osidak, *Russia*
Chenxi Peng, *Australia*
Rúben Pereira, *Portugal*
Mohammadmajid Sepantafar, *USA*
João Carlos Silva, *Portugal*
Yogendra Pratap Singh, *India*
Thiago Domingues Stocco, *Brazil*
Binbin Sun, *China*
Aitor Tejo-Otero, *Spain*
Danlei Zhao, *China*
Hui Zhu, *China*

*Editorial Board Members as of December 15, 2025

ACCSCIENCE PUBLISHING

Volume 11 | Issue 6 | December 2025 | Page 1 – 550 |

International Journal of Bioprinting

https://accscience.com/journal/IJB

CONTENTS

REVIEW ARTICLES

1 **Artificial intelligence-augmented bioprinting systems: Data-driven optimization and future applications in pharmacological research**
Yangyang Wang, Haotian Bai, Yufei Ren, Yanning Yang, Jihan Wang

23 **3D bioprinting–microfluidics technology: Pioneering advances in tumor microenvironment modeling, cancer treatment optimization, and diagnostic biomarker discovery**
Wang Wang, Zhicheng Zhang, Yang Yu, Yikang Wang, Kai Ni

51 **Biomimetic and personalized optimization of additively manufactured metallic bone implants: Design, simulation, and clinical outcomes**
Lamiae Jaouher, Abdelwahed Barkaoui, Khalil Aouadi, Haifa Sallem

83 **3D printing-driven evolution in lung surgery: From precision resection to biomaterial-based functional reconstruction**
Zhenghao Dong, Wenjing Jiang, Xiang Lin, Yu Tong, Beinuo Wang, Jian Zhou, Hu Liao

107 **3D-printed hydrogels for treating diabetic wounds: Recent developments**
Mengdi Yin, Yutong Wang, Yuhang Wei, Changjia Li, Yiqiao Yin, Tiantang Fan, Peixin Wang

130 **Skin bioprinting for burn reconstruction: From stem cell integration to smart in situ regenerative systems**
Aline Yen Ling Wang, Ana Elena Aviña, Yen-Yu Liu, Huang-Kai Kao

PERSPECTIVE ARTICLE

197 **AI-enhanced magnetically controlled 4D printing: Reshaping the future of medical robotics**
Jinrun Liu, Qi Wang, Ke Xu, Zhenkun Li, Juan Liu

RESEARCH ARTICLES

205 **Suspended 3D printing of polycaprolactone/hydroxyapatite composites for the fabrication of complex bone scaffolds**
Juhyun Kang, Masoud Shirzad, Priya Ranganathan, Dageon Oh, Sudip Mondal, Junghwan Oh, Hae Gyun Lim, Mahdi Bodaghi, Seung Yun Nam

220 **3D-bioprinted osteochondral model based on hierarchical polymeric microarchitectures for *in vitro* osteoarthritis drug screening**
Yi-Cheng Wang, Xiao-Jie Song, Xiao-Chang Lu, Zhou-Jiang Chen, Yue-Wei Li, Ranjith Kumar Kankala, Ai-Zheng Chen, Shi-Bin Wang, Chao-Ping Fu

238 **A 3D-bioprinted alginate-MgP scaffold for superior regeneration of calvarial bone defects in a rat model**
Shaimaa ElShebiney, Sara A. M. El-Sayed, Mduduzi N. Sithole, Mashudu T. Mphaphuli, Hanan H. Beherei, Pradeep Kumar, Mostafa Mabrouk, Yahya E. Choonara

260 **3D-printed perfusable tumor model for evaluating perfusion and chemotherapeutic response in ovarian cancer cells**
Md Shahriar, Marielena Molinares, Ganesh Acharya, Komaraiah Palle, Changxue Xu

279 **Bioprinting vascularized human islet tissue models via aggregate-based co-culture and self-assembly**
Yijun Su, Supeng Ding, Tiankun Liu, Yongyong Zhou, Yinying Lu, Feng Lin, Mingen Xu, Rui Yao

298 **A mobile drop-on-demand laser-assisted printing head integrated with a robotic arm and a target tracking system**

Ahad Mohammadi, Shakiba Davani, Christos Boutopoulos

311 Evaluation of biomechanical properties and early osseointegration of biomimetic bone trabecular Ti6Al4V scaffolds based on Voronoi design

Jinghong Yang, Zi Wang, Lujun Jiang, Zhong Li, Linlin Liu, Juncai Liu

327 Integrating machine learning and finite element simulation for interpretable prediction of 3D-printed bone scaffold mechanics

Rixiang Quan, Fengyuan Liu, Sergio Cantero Chinchilla

349 3D-bioprinted kartogenin-laden hydrogel promotes cartilage regeneration via Smad1/5/9-mediated chondrogenesis of bone marrow stromal cells

Chenhui Yang, Changshun Chen, Rongjin Cheng, Fei Yang, Hefang Xiao, Bin Geng, Yayi Xia

374 Hyaluronic acid-based self-healing hydrogels with enhanced hydrolytic stability for 3D bioprinting in tissue engineering

Minhyung Kong, Hyun Seung Kim, Jiwon Hwang, Joon Seo Park, In Young Lee, Kuen Yong Lee

390 Synergistic bone regeneration by surface modified 3D-printed PCL/β-TCP scaffolds in various animal defect models

Yulin Jiang, Guanghui Xi, Chen Zhou, Haisong Xu, Xi Yang, Dongxu Ke

407 Three-dimensional-printed collagen scaffold with limbal stem cells derived from adipose derived mesenchymal stem cells for the treatment of limbal stem cell deficiency

Martha Stokking, Marta Cadenas-Martín, Ana I. Martín-González, Alba Fernández-Ferrer, Francisco Arnalich-Montiel, Maria P. De Miguel

430 Development and evaluation of dual-controlled release antibiotic-loaded bone scaffolds

Peijie Zhao, Liangguo Si, Huan He, Huanhuan Sun, Zhipeng Yang, Mei Tian, Haiqiang Ma, Xu Ma, Huanxiang Guan, Yaodong Wang, Zewen Qiao

451 Optimal structural characteristics of bone tissue engineering scaffolds from bionics and PSO-BPNSGA III integrated algorithm

Yuxi Liu, Aihua Li, Hong Sun, Shuge Li, Song Chen

472 Mixed ultrashort peptide bioinks for improved 3D bioprinting of self-healing trachea-like constructs

Alexander U. Valle-Pérez, Dana Alhattab, Rui Ge, Eter Othman, Panayiotis Bilalis, Abdulelah Alrashoudi, Antonio Cárdenas-Calvario, Alan Eduardo Avila Ramírez, Zainab N. Khan, Manola Moretti, Christian Baumgartner, Charlotte A. E. Hauser

499 Enhancing osteogenesis using 3D-printed porous tantalum scaffolds: A biomechanical, *in vivo*, and *in vitro* study

Mengxiao Tantai, Yi Zhang, Chengbin Wang, Tongwei Du, Sihao Yu, Zhihai Zhang, Hui Ma, Junliang Song, Dong Qu, Gangning Feng, Zhidong Lu

515 Design and performance of 3D-printed cross-scale metamaterial porous structures for orthopedic implants

Guoqing Zhang, Junxin Li, Congcong Shangguan, Juanjuan Xie, Yongsheng Zhou, Aibing Huang, Yuchao Bai

531 Personalized 3D-printed TDM/ZrO_2 scaffolds laden with iPSC-derived SOX9+ sclerotomal progenitors for functional osteochondral regeneration

Yuqing Dong, Zhijun Zhang, Fengxiao Zhao, Weihua Guo, Jingfei Xiong, Zhonghan Li, Yuming Zhao

ACCSCIENCE PUBLISHING

International Journal of Bioprinting

REVIEW ARTICLE

Artificial intelligence-augmented bioprinting systems: Data-driven optimization and future applications in pharmacological research

Yangyang Wang[1], Haotian Bai[1], Yufei Ren[1], Yanning Yang[1], and Jihan Wang[2]*

[1]Department of Automation, School of Physics and Electronic Information, Yan'an University, Yan'an, Shaanxi, China

[2]Department of Basic Medicine, Yan'an Medical College, Yan'an University, Yan'an, Shaanxi, China

(This article belongs to the *Special Issue*: *AI-Driven Bioprinting Workflows or Bioprinting for Disease Modeling and Drug Screening*)

Abstract

The high attrition rate of drug candidates in clinical trials is often attributed to the use of conventional two-dimensional cell cultures and animal models that fail to accurately recapitulate human physiology. Three-dimensional (3D) bioprinting has emerged as a transformative technology for creating sophisticated, patient-relevant tissue models for drug screening and toxicity assessment. Concurrently, machine learning (ML) offers a powerful paradigm for extracting insights from complex, multi-modal data and optimizing intricate processes. This review presents a comprehensive and critical overview of the convergence of 3D bioprinting and ML, with a focus on their integrated applications in drug development. We critically and comprehensively analyze the various data types generated throughout the bioprinting workflow, from process parameters and material properties to biological and "omics" data. We then discuss the application of diverse ML approaches, from statistical methods to deep learning, for optimizing bioprinting processes and enhancing the predictive accuracy of drug screening. By including specific quantitative outcomes and comparative analyses from recent studies, we provide an evidence-based perspective on the state of the field and highlight its potential to accelerate the drug discovery pipeline.

Keywords: 3D bioprinting; Deep learning; Drug discovery; Machine learning; Predictive modeling

***Corresponding author:**
Jihan Wang
(jihanwang@yau.edu.cn)

Citation: Wang Y, Bai H, Ren Y, Yang Y, Wang J. Artificial intelligence-augmented bioprinting systems: Data-driven optimization and future applications in pharmacological research. *Int J Bioprint*. 2025;11(6):1-22. doi: 10.36922/IJB025350349

Received: August 25, 2025
1st revised: September 15, 2025
2nd revised: September 24, 2025
Accepted: September 30, 2025
Published online: October 6, 2025

Copyright: © 2025 Author(s). This is an Open Access article distributed under the terms of the Creative Commons Attribution License, permitting distribution and reproduction in any medium, provided the original work is properly cited.

Publisher's Note: AccScience Publishing remains neutral with regard to jurisdictional claims in published maps and institutional affiliations.

1. Introduction

Drug discovery and development remain lengthy, costly, and high-risk processes, with an average timeline exceeding a decade and costs reaching billions of dollars per approved drug.[1,2] A major bottleneck lies in the translation of preclinical findings into successful clinical outcomes, as conventional two-dimensional (2D) cell cultures and animal models often fail to replicate the complexity of human physiology.[3-5] This mismatch contributes to high attrition rates in late-stage clinical trials, particularly due to unforeseen toxicity or insufficient efficacy.[6-8]

Bioprinting has emerged as a transformative platform to address these challenges.[9-11] By enabling the automated fabrication of three-dimensional (3D) tissue constructs with

precise control over architecture, cell composition, and microenvironment,[12–14] bioprinting offers physiologically relevant models for drug screening and toxicity testing.[15] These 3D models can more accurately mimic human tissue function, improving predictive power for pharmacological and toxicological assessments.[16–18] Furthermore, the scalability and reproducibility of bioprinting make it well-suited for experimental pipelines requiring standardized and reproducible tissue models.[13]

However, the full potential of bioprinting is hindered by the complexity of its workflows and the vast amount of heterogeneous data it generates.[19] Variations in bioprinting parameters, biomaterial properties, and biological responses create multidimensional datasets that are challenging to interpret using traditional statistical approaches.[20,21] Herein, machine learning (ML) offers powerful solutions.[22,23] By identifying hidden patterns, learning from complex datasets, and enabling predictive modeling, ML can be integrated into bioprinting systems to optimize printing parameters, automate quality control, and predict drug responses with higher accuracy.[24–26]

The integration of ML with bioprinting represents a paradigm shift toward more intelligent and automated biomedical research workflows.[12,23] In such systems, ML algorithms continuously process data from bioprinted constructs—ranging from imaging and viability assays to omics-based readouts—and feed back into the printing process in real time.[27] This closed-loop approach not only accelerates experimental cycles but also enhances the reproducibility, scalability, and predictive reliability of preclinical studies.[23] As a result, the convergence of ML and bioprinting holds significant promise for drug development, including potential benefits for shortening timelines, reducing costs, and improving patient safety.[26,28]

Despite this promise, direct research integrating ML and bioprinting specifically for drug discovery and pharmacological testing remains scarce. Most current efforts focus on print process optimization and quality assessment rather than end-to-end applications in drug pipelines. Addressing this gap is crucial for unlocking the full translational potential of ML-driven bioprinting. The organizational framework of this review is presented in Figure 1. It first provides foundational principles of bioprinting and the current applications of ML in biomedical research. The review then explores strategies for leveraging artificial intelligence (AI) to achieve the data-driven optimization of bioprinting workflows and create predictive models for drug screening and toxicity testing. It highlights recent advances in developing advanced models for disease and therapeutic screening before concluding with a discussion on the future outlook and translational roadmap for intelligent, data-driven drug discovery platforms.

2. Fundamentals of bioprinting

Bioprinting refers to the automated, layer-by-layer fabrication of 3D biological structures using living cells, biomaterials, and supporting factors.[14] This technology enables precise spatial control over cell placement and scaffold architecture, allowing researchers to recreate complex tissue microenvironments with high fidelity.[29] Unlike traditional tissue engineering approaches, bioprinting offers improved reproducibility, customization, and scalability, making it a powerful tool for building functional biological systems for a wide range of biomedical applications.

2.1. Core principles and workflow

The bioprinting workflow typically begins with the preparation of bioinks, which are biomaterial formulations designed for both printability and biological compatibility. These formulations may include cell-laden hydrogels, microparticles, and other components.[30–33] Automated bioprinting platforms then deposit these bioinks in a layer-by-layer fashion with precise spatial control, guided by computer-aided design models.[34] Post-printing, the constructs undergo processes such as crosslinking, maturation, and culture under controlled environmental conditions to achieve functional tissue properties.[35] The entire workflow is integrated with high-content analytical systems—including imaging platforms, viability assays, and biochemical sensors—that enable rapid and consistent data acquisition across large sample sets.[10,36] The core principles and stages of this workflow are illustrated in Figure 2.

2.2. Bioprinting technologies

Various bioprinting modalities have been adapted for high-throughput applications, each with distinct strengths.[37,38] Inkjet bioprinting enables rapid, droplet-based deposition of low-viscosity bioinks, ideal for miniaturized tissue constructs, and cost-efficient screening.[39] Microextrusion systems allow for continuous filament deposition of more viscous bioinks, supporting higher cell densities and better structural stability, though often at the expense of printing speed.[40,41] Light-based methods, such as stereolithography and digital light processing, use photopolymerization to achieve high resolution and complex architectures, making them valuable for creating intricate tissue microenvironments.[42–44] Increasingly, hybrid platforms combine these approaches to balance throughput, resolution, and biomaterial compatibility for different experimental needs.[10,45]

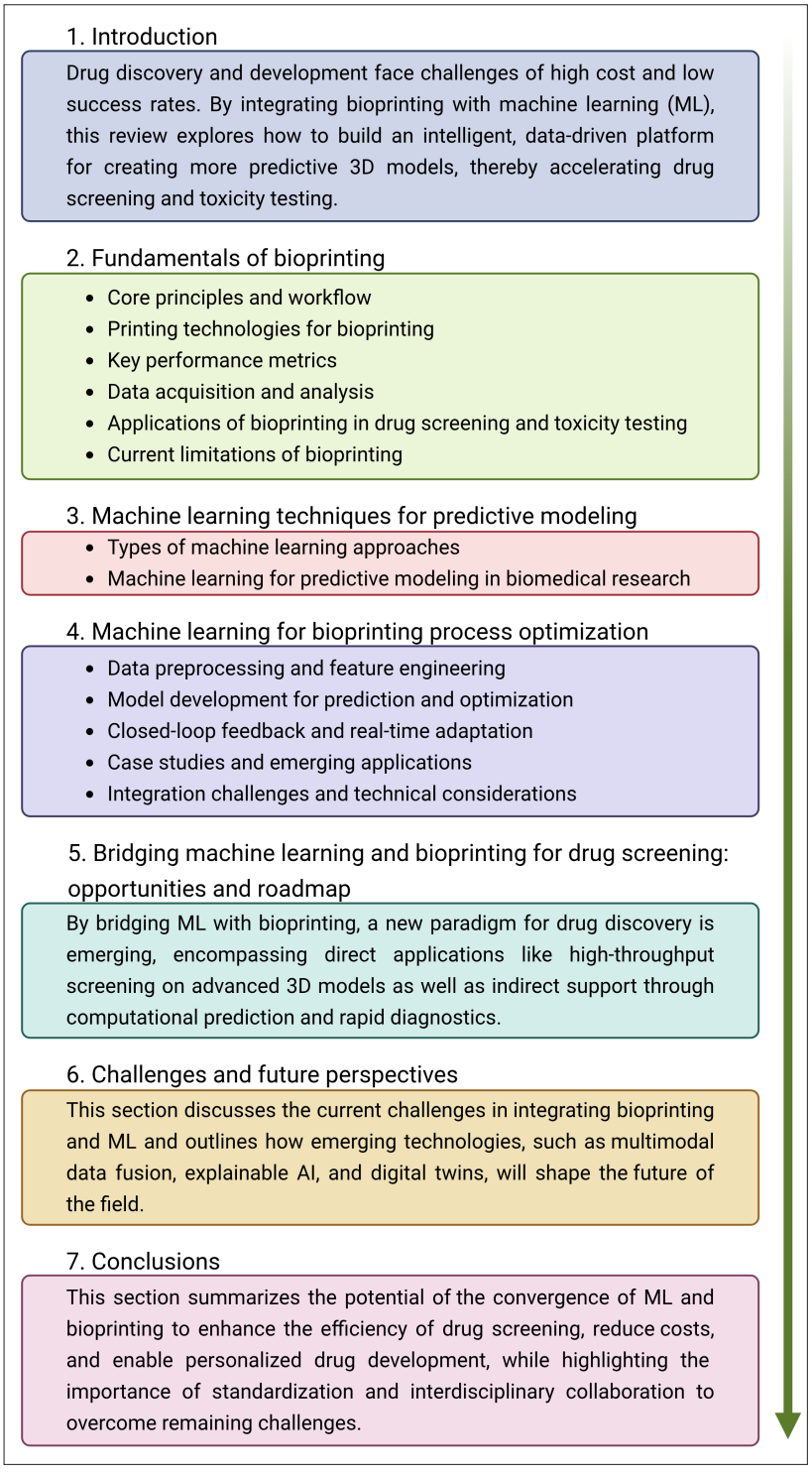

Figure 1. An overview of the organizational framework of this review. The framework first provides foundational principles of bioprinting and machine learning, then explores their synergistic applications in data-driven bioprinting workflows and drug discovery, and finally concludes with a discussion on the future outlook and translational roadmap.

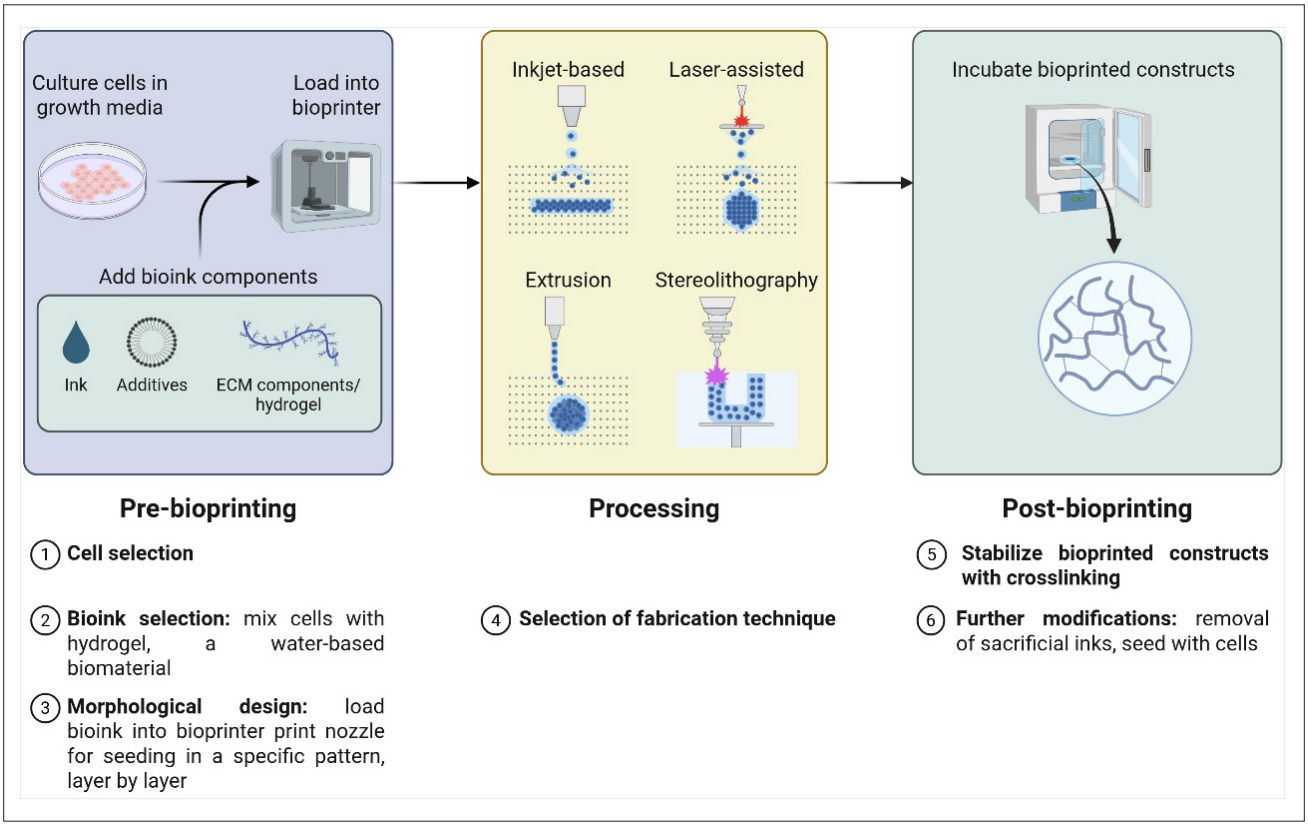

Figure 2. Bioprinting workflow. The process comprises three main stages: pre-bioprinting (cell cultures and bioink preparation, including cell selection and construct design), processing (layer-by-layer deposition of bioinks using different bioprinting technologies), and post-bioprinting (construct stabilization via crosslinking and maturation in controlled environments). Abbreviation: ECM, extracellular matrix.

2.3. Key performance metrics

For bioprinting to be impactful in drug discovery, several performance parameters are critical. Among them, throughput—defined as the number of tissue constructs produced per unit time—determines scalability.[46] Resolution influences how accurately microenvironmental features are reproduced, which can affect cell behaviors and drug responses.[30,47,48] Reproducibility ensures consistency in geometry, cell distribution, and viability across large batches, all of which are essential for generating reliable screening data.[49] Biological fidelity—the ability of printed constructs to replicate relevant *in vivo* functions—directly impacts the predictive value of assays.[47,50] Finally, integration compatibility with automated liquid handling, microfluidic systems, and high-content imaging is essential to streamline workflows in industrial and research settings.[51]

2.4. Data acquisition and analysis

Bioprinting platforms are a foundation for integrating with ML because they generate vast amounts of heterogeneous data. The first critical step is the systematic collection of these high-quality, multi-modal datasets. These data streams, which include those from fluorescence imaging, live–dead staining assays, metabolic activity measurements, and multi-omics profiling, provide critical information about the biological constructs.[46] This is complemented by detailed process parameters such as nozzle pressure, extrusion speed, and bioink rheology collected from embedded sensors.[52,53] The quality, diversity, and completeness of these datasets directly influence the accuracy and generalizability of downstream ML models.[54] Table 1 provides a comprehensive overview of the various data types generated throughout the bioprinting workflow, detailing their common processing methods and the associated ML models and tasks.

2.5. Applications of bioprinting in drug screening and toxicity testing

In practice, bioprinting has been applied to generate a diverse range of tissue models for both efficacy and toxicity studies.[64,65] Examples include liver spheroids for drug metabolism analysis, tumor organoids for cancer drug sensitivity profiling, and cardiac microtissues for cardiotoxicity evaluation.[16,66,67] These 3D constructs can be tailored to represent specific patient populations or

Table 1. Data types generated during bioprinting workflows and their integration with machine learning models

Data type	General data sources	Common processing methods	Associated ML models & tasks	Advantages	Limitations	References
Imaging data (microscopy, high-content screening)	Fluorescence microscopy, confocal imaging, high-content imaging systems in bioprinting setups	Image preprocessing (denoising, normalization), segmentation (cell/nuclei/organoid), feature extraction (morphology, intensity), DL-based classification	DL (especially CNNs) for real-time quality control, defect detection, cell counting, and morphological analysis; unsupervised learning for anomaly detection and morphological pattern recognition	Rich spatial and morphological information; enables phenotypic profiling and subcellular resolution	High data volume; requires complex preprocessing and large storage; sensitive to imaging artifacts	[55]
Bioprinter process data (print path, droplet size, temperature, pressure)	Real-time printer logs, embedded sensor arrays, nozzle monitoring systems	Time-series analysis, sensor fusion, anomaly detection, predictive maintenance modeling	Regression models for predicting print quality, cell viability, and mechanical properties; reinforcement learning for real-time parameter optimization and closed-loop control	Enables real-time quality control and process optimization	Requires specialized hardware; complex integration of heterogeneous signals	[56,57]
Mechanical property data (tissue stiffness, viscoelasticity)	Atomic force microscopy, compression testing, and rheology measurements	Curve fitting, stress–strain modeling, statistical comparison across conditions	Regression models for predicting mechanical properties and printability from process parameters	Provides functional readouts relevant to tissue physiology	Destructive testing may limit repeated measures; device calibration is needed	[58,59]
Viability and metabolic activity data	Live/dead staining, ATP-based luminescence assays, resazurin assays	Signal normalization, dose–response curve fitting, statistical analysis	Classification models for predicting toxicity or drug response (live vs. dead); regression models for predicting quantitative cell viability values	Rapid and widely used for cell health monitoring	Limited mechanistic insight; end-point only (non-real time)	[8]
Genomic/transcriptomic/proteomic/metabolomic data	Bulk RNA-seq, LC–MS, GC–MS, NMR profiling from printed constructs or culture supernatants	Quality control, normalization, differential expression, pathway enrichment, peptide/metabolite identification	Clustering and classification models for predicting tissue states, cell phenotypes, or drug response	Comprehensive, systems-level view; detects complex relationships; non-invasive monitoring	High cost and complexity; requires specialized tools; challenging data integration	[60,61]
Bioink composition data	Rheological measurements, spectroscopic analysis of bioinks	Composition profiling, crosslinking efficiency testing, viscosity analysis	Regression models for predicting printability and viscosity; clustering models for grouping similar bioink formulations	Critical for reproducible printing; affects cell viability and construct integrity	Bioink variability between batches; sensitive to storage/handling	[58,62,63]

Abbreviations: CNN, convolutional neural network; DL, deep learning; GC, gas chromatography; LC, liquid chromatography; ML, machine learning; MS, mass spectrometry; NMR, nuclear magnetic resonance.

doi: 10.36922/IJB025350349

disease states, offering valuable platforms for personalized medicine research.[68,69] By enabling large-scale, physiologically relevant testing, bioprinting holds promise for improving early-stage decision-making and reducing the rate of costly late-stage clinical trial failures.[70] Table 2 provides a summary of relevant studies (since 2020) that highlight the application of bioprinting in drug screening and toxicity testing.

2.6. Current limitations of bioprinting

Despite its potential, bioprinting still faces challenges. The range of bioinks that combine printability with long-term biological functionality remains limited, constraining the diversity of tissue constructs.[94] Standardized metrics for assessing construct quality and performance are lacking, making it difficult to compare results across laboratories.[95] Biological complexity—such as multi-tissue interactions, immune responses, and long-term maturation—remains difficult to reproduce at scale.[96,97] Additionally, the sheer volume of heterogeneous data generated through bioprinting platforms creates a bottleneck in analysis and interpretation, underscoring the need for advanced computational approaches, including ML, to fully harness the technology's capabilities.

3. Machine learning techniques for predictive modeling

Machine learning, a subset of AI, has emerged as a powerful computational approach for uncovering patterns, making predictions, and optimizing processes in complex biomedical systems.[56,98] In drug discovery and development, ML algorithms are capable of analyzing vast, heterogeneous datasets, including chemical structures, molecular interaction profiles, genomic and proteomic data, imaging outputs, and clinical records.[99,100] Through learning from these diverse inputs, ML can predict compound efficacy, identify potential toxicity, and even suggest novel molecular designs with improved pharmacological properties.[101] This data-driven approach has the potential to accelerate early-stage research, reduce experimental costs, and increase the success rate of clinical translation.[102] The fundamental concepts of ML are illustrated in Figure 3.

3.1. Types of machine learning approaches

Different classes of ML methods are applied to biomedical problems, each suited to particular data types and research objectives.[103,104] Supervised learning methods, such as random forests (RFs)[105] and support vector machines,[106] are trained on labeled datasets to predict specific outcomes, such as drug responses and cell viability. A key subfield of supervised learning is deep learning (DL), which utilizes multi-layered neural networks to learn complex patterns. Deep neural networks and their specialized architectures, such as convolutional neural networks, have proven particularly effective in processing high-dimensional data, including images and time-series signals, enabling rapid, automated analysis of microscopy images and real-time quality control.[107,108] Unsupervised learning methods, including clustering algorithms and dimensionality reduction techniques, are used to reveal hidden structures in unlabeled datasets, for example, the identification of disease subtypes from patient omics profiles.[109] Reinforcement learning methods allow systems to improve decision-making through iterative trial-and-error processes, a strategy increasingly explored in automated experimental design.[110]

3.2. Machine learning for predictive modeling in biomedical research

In drug screening and toxicity testing, ML has been successfully used to predict off-target effects, model dose–response relationships, and stratify compounds based on their predicted therapeutic potential[111–113]. Algorithms trained on large public toxicity datasets can predict the safety profiles of novel molecules.[114,115] Furthermore, ML can optimize experimental workflows by selecting the most informative combinations of parameters to test, thereby reducing the number of experiments required without sacrificing predictive accuracy.[116,117]

While different ML methods can be broadly categorized, their practical application depends on the specific bioprinting data type and research goal.[118] Supervised learning is most suitable for bioprinting datasets with labeled outcomes, such as predicting the final cell viability from process parameters or anticipating drug response from omics data. Its strength lies in its ability to provide clear, quantifiable predictions, though it relies on the availability of large, high-quality labeled datasets. In contrast, unsupervised learning excels at exploring unlabeled data to uncover hidden patterns, making it invaluable for tasks such as identifying new tissue phenotypes or grouping similar bioink formulations without prior knowledge. Meanwhile, DL, the powerful subset of these methods, is particularly effective with high-dimensional data. For example, a standard deep neural network can be used to model complex, non-linear relationships in multi-modal datasets, and convolutional neural networks are the go-to choices for image-based data, enabling automated defect detection and morphological analysis.[119,120] Finally, reinforcement learning is suited for dynamic, real-time optimization, allowing the bioprinting system to learn and autonomously adjust parameters to achieve a desired outcome without direct human intervention.[121] This predictive capability is particularly relevant in bioprinting,

Table 2. Representative studies of bioprinting in drug screening and toxicity testing

Cell type/source	Bioprinting modality	Construct type/model	Main findings	References
Alveolar, bronchial, and intestinal epithelial cells	Inkjet-based bioprinting	Simple epithelial layers (alveolar, bronchial, intestinal)	Developed a protocol for the automated and reproducible printing of simple epithelial layers for respiratory and gastrointestinal models, useful for high-throughput toxicity screening.	[71]
HepaRG liver cells	Extrusion-based bioprinting	3D-bioprinted HepaRG cultures	3D models were more resistant to aflatoxin B1 and viable for longer (up to three weeks) than 2D cultures, providing a better model for chronic hepatotoxicity studies.	[72]
Cryopreserved primary human hepatocytes and hepatic stellate cells	Extrusion-based bioprinting	3D-bioprinted human liver tissues	3D tissue showed improved viability and enhanced drug-metabolism gene expression compared to controls. It can detect the toxicity of compounds undetected using 2D culture and conventional spheroids, offering high sensitivity for hepatotoxicity prediction.	[73]
Multiple cell types	Inkjet-based bioprinting	Stiffness-tunable collagen-alginate microgels	Developed a high-throughput, stiffness-tunable 3D culture platform with consistent reproducibility, which can be used to screen chemotherapeutics and study mechanobiology.	[74]
Human pluripotent stem cells	Extrusion-based bioprinting	Kidney organoids	Bioprinting improves organoid reproducibility, viability, and nephron yield compared to manual methods. It facilitates the generation of uniformly patterned kidney tissue sheets for drug testing and *in vitro*/*in vivo* applications.	[75]
Human liver-derived epithelial organoids	Extrusion-based bioprinting	Bioprinted liver organoids	Bioprinted organoids showed stable viability and increased expression of hepatic markers. They demonstrated the ability to detect toxicity from acetaminophen, indicating their potential for use as toxicology and disease models.	[76]
HepG2 cells	Extrusion-based bioprinting	Hexagonal bioprinted hepatic construct	A spinning culture condition enhanced proliferation and functionality, increasing the susceptibility of the model to acetaminophen-induced hepatotoxicity and better mimicking *in vivo* liver injury.	[77]
Unspecified cells for cartilage model	Extrusion-based bioprinting	Scaffold-free 3D-bioprinted cartilage model	Developed a scalable bioprinting method for creating cartilage constructs suitable for high-efficiency *in vitro* toxicology studies.	[78]
HepG2 cells	Extrusion-based bioprinting	3D HepG2 liver spheroid model in hydrogel constructs	Developed a platform for *in situ* quantitative evaluation of drug toxicity. Spheroids were more resistant to nefazodone-induced toxicity than 2D cells, and fluorescence intensities of markers could be used to determine EC50 values.	[79]
Lung cancer cell line	Extrusion-based bioprinting	3D-bioprinted tumor model with a multicomponent bioink	Developed and validated a novel bioink and a 3D tumor model suitable for anti-cancer drug screening, overcoming limitations of 2D monolayer models.	[80]
Renal epithelial cells	Inkjet-based bioprinting	Bioprinted renal spheroids	3D spheroids showed enhanced sensitivity to cisplatin compared to monolayers. A DL algorithm was developed for automatic toxicity readout from images with 78.7% accuracy.	[81]
SW480 cells, tumor-associated macrophages, and endothelial cells	Extrusion-based bioprinting	3D multicellular colorectal cancer model	The multicellular model showed improved tumor-related gene expression and higher resistance to chemotherapy than single-cell models, demonstrating its improved physiological relevance for drug screening.	[82]

(Continues....)

Table 2. Representative studies of bioprinting in drug screening and toxicity testing

Human pancreatic cancer cells and stromal fibroblasts	Extrusion-based bioprinting	Pancreatic tumor-stroma microtissues (hydrogel beads)	Engineered tumor-stroma microtissues recapitulated native features, demonstrated better resistance to anti-cancer drugs than mono-cultured spheroids, and served as a new drug screening platform.	[83]
Hepatocytes and human umbilical vein endothelial cells	Extrusion-based bioprinting	Endothelialized liver lobule-like constructs	The model successfully recreated liver lobule-like morphology and showed stronger drug resistance to sorafenib compared to other models, demonstrating its potential as a tumor-scale drug screening platform.	[84]
Cervical cancer cells from PDOs	Light-based bioprinting	3D-bioprinted PDOs	Higher expression of NSUN6 promotes radioresistance in the 3D PDOs model by activating a specific molecular pathway, while silencing *NSUN6* increases radiosensitivity.	[85]
Triple-negative breast cancer PDOs	Extrusion-based bioprinting	3D-bioprinted models from PDOs	Identified a new molecular glue (aurovertin B) that promotes the degradation of coronin 1A, resulting in robust antitumor effects in the 3D-bioprinted models.	[86]
HuH-7 cell line	Extrusion-based bioprinting	Xeno-free 3D-bioprinted liver model	Developed the first xeno-free 3D-bioprinted liver model, which showed high cell viability and required three-fold higher concentrations of a biotoxin to induce cytotoxicity compared to 2D cultures.	[87]
Dermal fibroblasts, adipose-derived stem cells, and human epidermal keratinocytes	Extrusion-based bioprinting	3D-bioprinted skin equivalent (tri-layer with an epidermal layer)	Developed a 3D skin model and confirmed permeation and cellular uptake of a drug-loaded nanocapsule. The combined nanocapsule and photodynamic therapy resulted in reduced cytokine levels, suggesting a new therapeutic approach for skin inflammation.	[88]
MCF-7 breast cancer cells	Inkjet-based bioprinting	Single spheroids	Developed a fast-crosslinking bioink for high-throughput and reproducible single spheroid formation, highlighting the importance of ink characterization for future drug screening applications.	[89]
Foregut cells differentiated from human iPSCs	Droplet-based printing	HLOs on a pillar plate platform	Achieved a high-throughput, reproducible generation of HLOs with superior function compared to conventional methods, demonstrating their utility for hepatotoxicity assays.	[90]
Primary hepatocytes	Light-based bioprinting	HCD liver model	An HCD model was fabricated with enhanced cell–cell interactions and metabolic functions. The model was more sensitive to drug treatments than lower-density models, demonstrating the importance of HCD for recapitulating physiological drug responses.	[91]
Neonatal mouse primary testicular cells	Light-based bioprinting	Testicular organoids	Bioprinted organoids recapitulated key testicular features and showed the loss of a tight junction protein and altered gene expression in response to a known toxicant, demonstrating a high-throughput platform for reproductive toxicity assessment.	[92]
E18 mouse fetus epidermal and dermal cells	Inkjet-based bioprinting	Skin organospheres	Developed a high-throughput, reproducible model to assess microplastic-induced skin toxicity, demonstrating a size-dependent uptake rate and increased oxidative stress in response to ultraviolet A-irradiated prevalence of microplastics.	[93]

Abbreviations: DL, deep learning; EC50, half-maximal effective concentration; HCD, high cell density; HLO, human liver organoid; iPSC, induced pluripotent stem cell; NSUN6, NOP2/Sun RNA methyltransferase family member 6; PDO, patient-derived organoid.

doi: 10.36922/IJB025350349

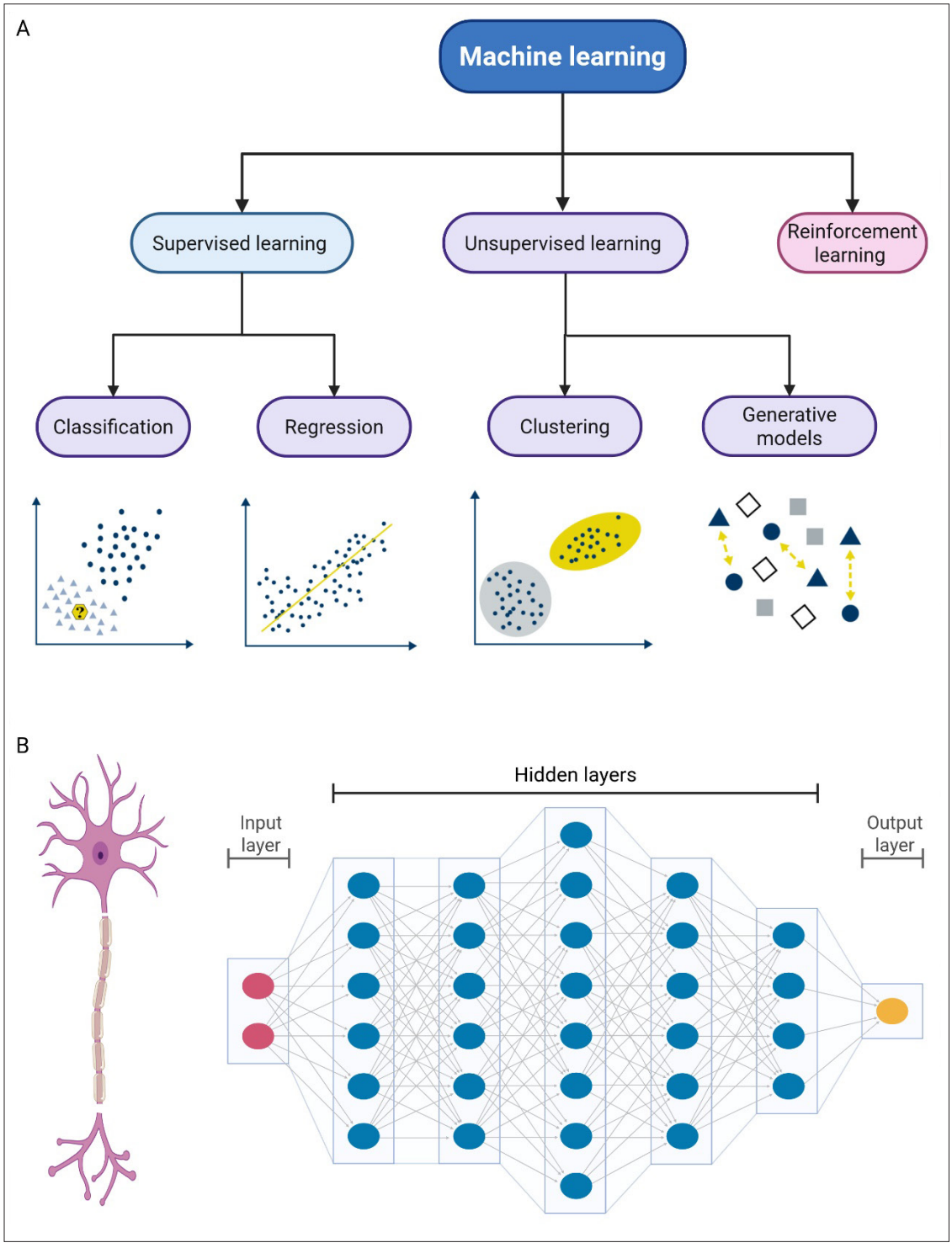

Figure 3. Machine learning (ML) techniques. (A) An overview of the main ML paradigms, illustrating the three primary types of ML: supervised learning, which uses labeled data for tasks such as classification (sorting data points into categories) and regression (predicting a continuous value); unsupervised learning, which discovers hidden structures in unlabeled data, as seen in clustering (grouping similar data points) and generative models (creating new data from learned patterns); and reinforcement learning, where an agent learns to make optimal decisions through a system of rewards and punishments. (B) The architecture of an artificial neural network is the basis of deep learning. It shows how information is processed from an input layer, through multiple hidden layers, to an output layer, mimicking the structure and function of a biological neuron.

where ML-driven approaches have been used to analyze bioprinted structures for drug response profiling[12,60,122] and to predict key biological outcomes, such as cell viability and tissue maturation.[22,23,123] For example, deep convolutional neural networks have been applied to analyze optical coherence tomography data to enable the automated detection and growth tracking of bioprinted organoid clusters.[123,124] This predictive capability extends to optimizing printing parameters to improve throughput and print fidelity in cellular droplet bioprinting.[125,126] These applications demonstrate the direct utility of ML in enhancing the precision of the bioprinting process.

4. Machine learning for bioprinting process optimization

As experimental technologies such as bioprinting continue to evolve, the application of ML becomes increasingly important. Bioprinting platforms generate multidimensional datasets encompassing imaging, viability metrics, molecular readouts, and environmental parameters, all of which can be integrated into ML models for more efficient and adaptive experimentation.[26,127] By enabling automated analysis, real-time feedback, and predictive modeling, ML provides the computational backbone needed to transform high-throughput experimental platforms into intelligent, closed-loop systems capable of continuously improving their performance.[128,129] A conceptual pipeline of how AI-driven multi-modal sensing can achieve comprehensive results in such a system is shown in Figure 4.

4.1. Data preprocessing and feature engineering

Before ML models can be trained, raw bioprinting data require preprocessing to remove noise, standardize formats, and extract relevant features.[12,23] While a summary of common methods has been provided in Table 1, the specific approach is highly dependent on the data type and research objective. For imaging data, which includes microscopy and high-content screening, the process often begins with image preprocessing steps, such as denoising, normalization, and artifact removal, to ensure data quality.[130,131] This is followed by segmentation to isolate biological entities, such as cells, nuclei, and organoids.

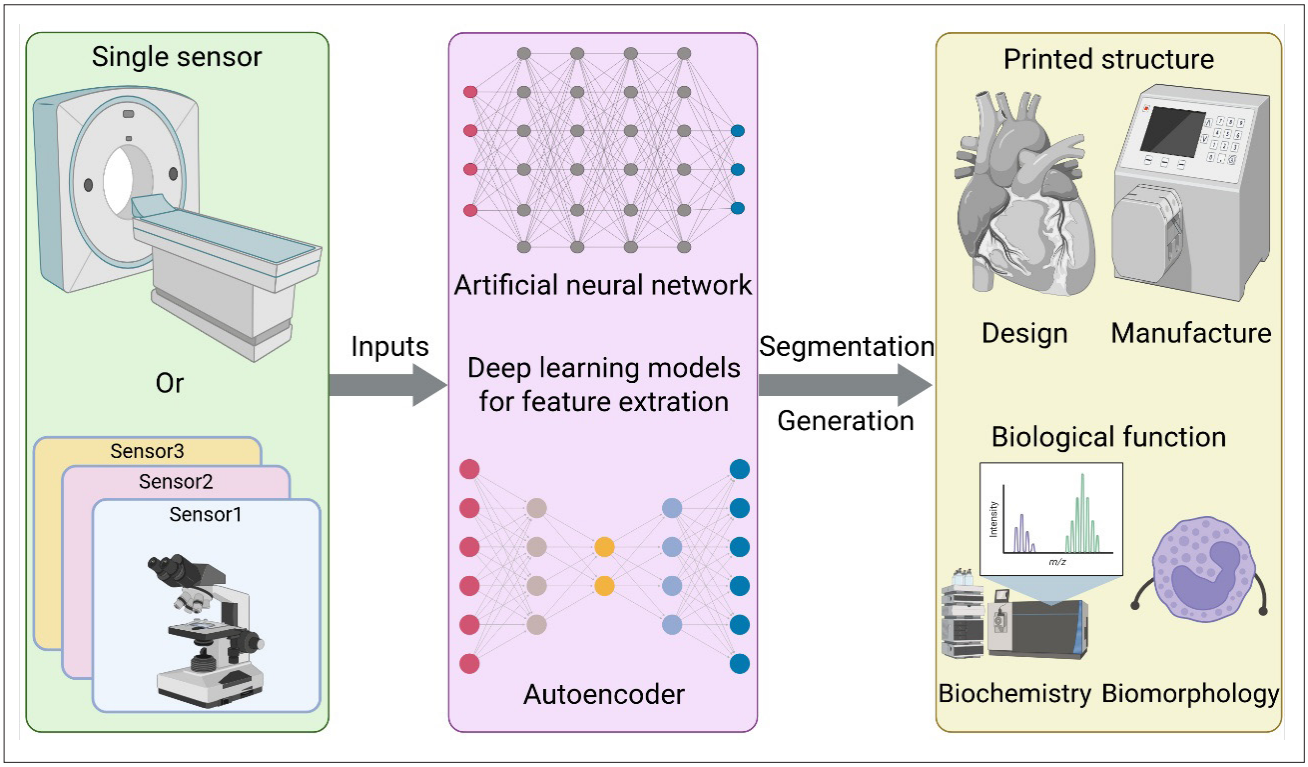

Figure 4. An artificial intelligence-driven multi-modal sensing pipeline for achieving comprehensive results in bioprinting. The workflow starts with data collection from diverse sensors and bioprinter logs. In data preprocessing and feature extraction, these data streams are processed by deep learning models to extract key features. The machine learning modeling step uses these features to predict important outcomes. Finally, in bioprinting process optimization, the model's predictions are used to provide real-time feedback for autonomous adjustments to the bioprinting process, ensuring a closed-loop system for continuous improvement.

Feature engineering then quantifies these elements into morphological descriptors, such as size, shape, porosity, and cellular distribution.

For sensor-based process data, such as time-series readouts of nozzle pressure and temperature, advanced techniques, including sensor fusion and time-series analysis, are used to integrate disparate signals.[132,133] These processed data streams are aligned with experimental metadata to enable the modeling of complex, non-linear relationships, and the detection of anomalies for predictive maintenance. Similarly, with omics datasets, which are often high-dimensional, specialized pipelines are required. After initial quality control and normalization, techniques like dimensionality reduction are crucial to mitigate redundancy and focus on the most informative genes or proteins.[134,135] Feature engineering—whether handcrafted or automatically learned through DL—plays a key role in transforming raw bioprinting data into informative representations that capture both biological and manufacturing variables.[136,137] These refined features form the basis for robust ML models that can accurately predict a wide range of outcomes.

4.2. Model development for prediction and optimization

Machine learning models can serve multiple purposes within bioprinting workflows.[138] Predictive models are trained to forecast biological responses, such as drug efficacy or toxicity, based on construct features and experimental parameters.[139,140] Optimization models, often employing reinforcement learning or Bayesian optimization, can identify optimal combinations of printing parameters, bioink compositions, and culture conditions to achieve desired outcomes.[128,141] In addition, generative models, such as variational autoencoders and generative adversarial networks, can be used to design novel tissue architectures with tailored functional properties.[136,142] The choice of algorithm depends on the prediction target, dataset size, and desired interpretability.

4.3. Closed-loop feedback and real-time adaptation

A defining feature of truly "smart" bioprinting systems is the implementation of closed-loop feedback, where ML models continuously analyze experimental data and adjust bioprinting parameters in real time.[143,144] For example, if imaging data indicate uneven cell distribution or structural collapse, the system can automatically recalibrate nozzle pressure, printing speed, or crosslinking intensity to correct the issue in subsequent prints.[25,145] This adaptive control reduces variability, improves reproducibility, and minimizes material waste. Real-time integration requires seamless communication among ML algorithms, printer control software, and data acquisition systems, supported by low-latency computation.[146]

4.4. Case studies and emerging applications

The integration of ML into bioprinting is moving beyond theoretical concepts and is being applied in concrete research to enhance the entire workflow. For example, ML models are now used to predict optimal printing parameters, such as extrusion pressure and laser power, to minimize trial-and-error and material waste.[147,148] Furthermore, AI-driven image analysis provides real-time feedback on construct fidelity and cell viability, allowing for immediate process adjustments to ensure quality control.[121] These advancements in process optimization are paving the way for fully automated and intelligent biomanufacturing. Table 3 provides a summary of representative studies, detailing the specific bioprinting modalities, constructs, and ML approaches used in these applications.

4.5. Integration challenges and technical considerations

While the potential benefits are substantial, several barriers hinder seamless ML–bioprinting integration. Data heterogeneity across imaging platforms, bioink formulations, and cell sources complicates model training and transferability.[26] The need for large, high-quality labeled datasets can be a bottleneck, particularly for rare disease models and patient-specific constructs. Additionally, ensuring that ML models are interpretable and compliant with regulatory standards is essential for eventual clinical translation.[152] Overcoming these challenges requires not only advances in algorithmic development but also the standardization of bioprinting protocols, improved interoperability between hardware and software, and the adoption of open data sharing practices.

5. Bridging machine learning and bioprinting for drug screening: opportunities and roadmap

The integration of ML with bioprinting offers transformative opportunities for drug screening by enabling data-driven, predictive, and automated experimentation. By combining the precise fabrication capabilities of bioprinting with ML's ability to extract patterns and make predictions from complex datasets, researchers can move beyond conventional trial-and-error approaches and establish more efficient and reproducible workflows. This synergy allows for not only the optimization of tissue construct design and printing parameters but also the anticipation of functional outcomes, such as drug response, toxicity, and phenotypic changes. As a conceptual roadmap for this integrated workflow, Figure 5 highlights the opportunities

Table 3. Representative studies on the integration of machine learning with bioprinting

Dataset source	ML method	Bioprinting modality	Construct type/ model	Main findings	References
A dataset of 48 prints with systematically varied print parameters	HML with LASSO	Extrusion-based bioprinting	3D alginate hydrogel features	Developed an HML framework to predict dominant build parameters for high-fidelity 3D prints, reducing the need for iterative testing and identifying process maps for optimization.	[125]
Data collected from 75 published papers on extrusion-based bioprinting	Supervised regression and classification models	Extrusion-based bioprinting	Cell-laden alginate and gelatin composite filaments	ML models trained on literature data can predict printing outcomes (cell viability, filament diameter, extrusion pressure) and show the potential for optimizing bioprinting experimental design.	[149]
Patient-derived glioblastomas and tumor-associated macrophages bioprinted into 3D models	Multi-algorithm ML, including a weighted ensemble model	Light-based bioprinting	3D-bioprinted patient-derived glioma tissues (complex multicellular models)	Developed an integrated workflow of 3D bioprinting and ML to predict glioma treatment responses, with the ensemble model outperforming individual algorithms and identifying promising compounds.	[60]
A dataset of cellular droplets (over 50 printed simultaneously)	Multilayer perceptron and decision tree	Droplet-based bioprinting	Cellular droplets	Developed an ML-enhanced platform to optimize five key printing parameters and predict cellular droplet size with high accuracy, enabling reproducible and scalable organoid production.	[26]
Experimental data from GelMA and HAMA bioinks	Bayesian optimization	Extrusion-based bioprinting	3D scaffolds from GelMA and HAMA bioinks	Bayesian optimization drastically reduced the number of experiments needed to identify optimal print parameters, enabling the quantitative assessment of printability for reproducible scaffold fabrication.	[27]
Experimental data from the development of a chitosan–gelatin–agarose ink	Bayesian optimization	Extrusion-based bioprinting	3D complex tissue constructs from an optimized chitosan–gelatin–agarose biomaterial ink	Employed ML to assist in developing an optimized biomaterial ink with suitable printability, rheological properties, and biocompatibility for fabricating 3D tissue constructs.	[150]
224 datapoints from 3D printing experiments; 9 CAD images; a self-designed "complexity index"	Gradient boosting regression and eight other ML algorithms	Extrusion-based bioprinting	Single-layer hydrogel filaments and multilayer lattice constructs	GBR achieved the best prediction accuracy for filament morphology; the application of eight ML methods facilitated parameter optimization; combining ML with extrusion printing reduced experimental iterations and improved reproducibility and fidelity.	[147]
Experimental dataset of extrusion-based bioprinting with NIH/3T3 fibroblasts, varying pressure, speed, and nozzle diameter	Support vector regression	Extrusion-based bioprinting	3D-printed objects based on CAD images	Developed an ML-embedded graphical user interface to optimize printing parameters and predict print outcome, reducing trial-and-error and waste.	[151]
High-throughput droplet images and an extensive dataset generated by the bioprinting platform	Supervised ML models, including RF, ANN, and others	Droplet-based bioprinting	Cellular droplets and 3D microtissues	Developed an ML-driven platform to predict and control cellular droplet volume, promising to advance the mass production of organoids and microtissues with precise volume control.	[129]

Abbreviations: ANN, artificial neural network; CAD, computer-aided design; GelMA, gelatin methacryloyl; GBR, gradient boosting regression; HAMA, hyaluronic acid methacrylate; HML, hierarchical machine learning; LASSO, least absolute shrinkage and selection operator; ML, machine learning; RF, random forest.

for combining bioprinting and ML to revolutionize drug screening.

In the short term, ML can be employed to optimize bioprinting experimental designs, improving both efficiency and data utilization. Predictive models, such as random forests, which are trained on historical bioprinting and assay data, can guide the selection of bioink formulations, printing parameters (e.g., pressure,

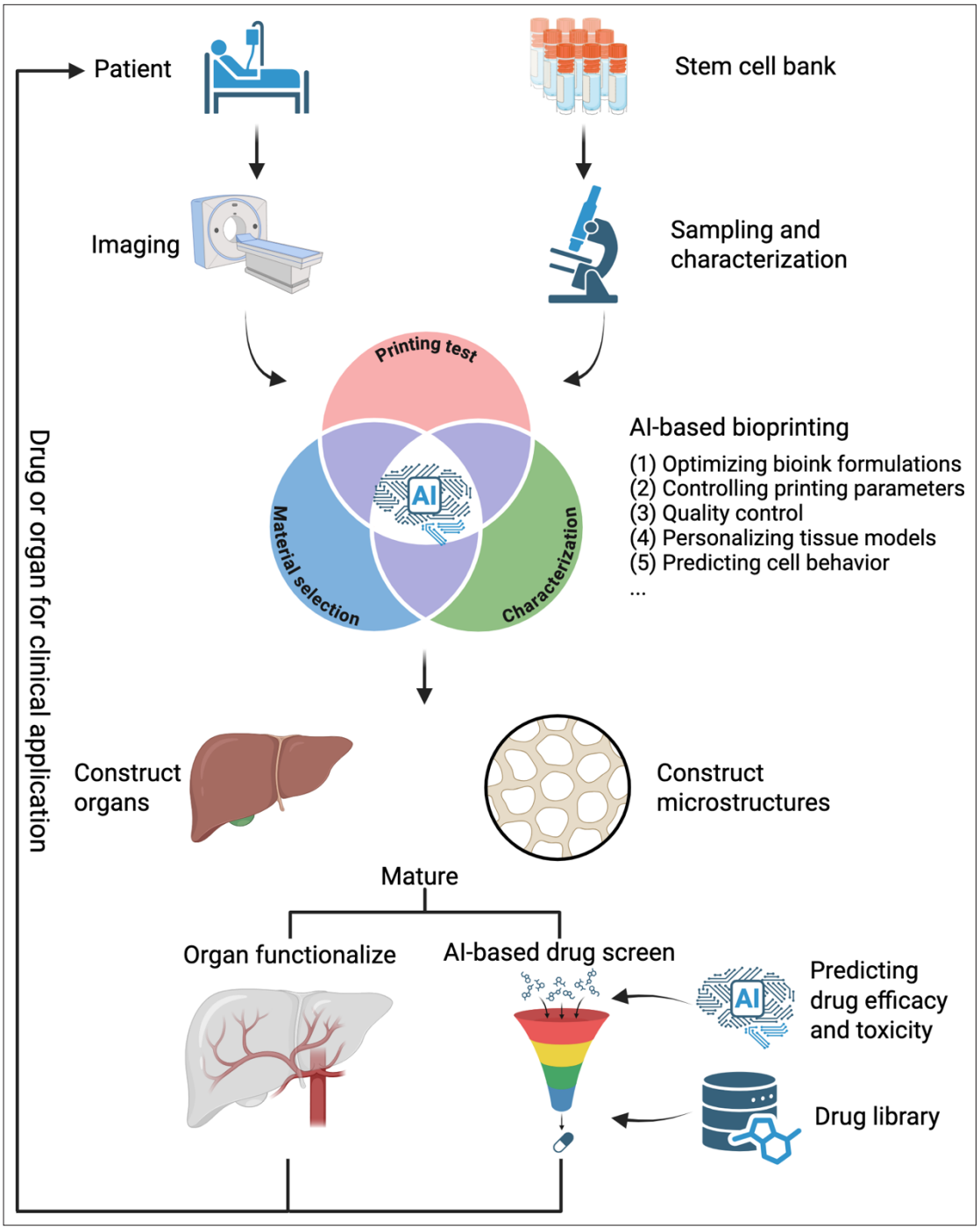

Figure 5. An artificial intelligence (AI)-powered drug screening workflow integrating bioprinting and machine learning (ML). This framework outlines a comprehensive data-driven approach, from generating multi-modal data with 3D bioprinting and high-throughput screening to using AI/ML models for predictive analysis. The workflow includes a feedback loop that informs new experimental designs, enabling efficient and iterative drug discovery.

speed, and nozzle diameter), and culture conditions, reducing the number of iterations needed to achieve high-quality constructs.[21] This approach maximizes the informational content of each experiment and supports the rapid generation of reproducible tissue models suitable for downstream drug screening applications.

In the medium term, closed-loop platforms can be developed in which ML algorithms continuously monitor data from in-line sensors (e.g., cameras for real-time image analysis and embedded pressure sensors), viability assays, and biochemical readouts, and then adjust printing parameters in real time.[150] By integrating predictive models for toxicity or drug response into this feedback system, bioprinting pipelines can be dynamically tuned to produce tissue constructs with consistent properties and functional readouts. Such adaptive systems will enhance reproducibility, enable multi-day experimental runs, and reduce variability in pharmacological testing. Additionally, the development of more interpretable AI models will be crucial to facilitate regulatory approval and clinical translation.

Looking toward the long term, the combination of ML and bioprinting could facilitate the development of truly personalized and disease-specific tissue constructs. Advances in bioink design informed by patient-derived data, along with AI-driven tissue modeling, can allow for the generation of "digital twins" or *in silico* models that recapitulate individual genetic or pathological contexts.[153,154] These approaches will support patient-specific drug testing, the identification of optimal therapeutic regimens, and the exploration of complex multi-tissue interactions. Ultimately, AI-guided bioprinting can enable the *in silico* design and *in vitro* fabrication of highly predictive tissue models, forming a new paradigm for preclinical drug development.

Several recent studies have demonstrated the feasibility of integrating ML into bioprinting workflows for drug screening and toxicity testing. For example, in a study on nephrotoxicity testing, researchers used bioprinted renal spheroids and a DL approach to automatically analyze microscopic images. The study found that the bioprinted spheroids showed enhanced sensitivity to cisplatin, with an inhibitory concentration leading to 50% cell death (IC_{50}) of 9 ± 3 μM compared to 17 ± 2 μM for conventional monolayers. Furthermore, the DL algorithm was able to distinguish between no, mild, and severe treatment effects with a balanced accuracy of 78.7%.[81] Similarly, in a study on glioma, researchers integrated 3D bioprinting and multi-algorithm ML to assess treatment responses. The bioprinted patient-derived glioma tissues successfully mimicked the molecular properties and drug responses of native tumors, with the GlioML ensemble model achieving a median R^2 value of 0.83 for World Health Organization grade IV gliomas, significantly outperforming individual algorithms. This model also showed high predictive accuracy for recurrent glioblastoma, with an R^2 value as high as 0.94, validating the use of bioprinted models and computational predictors for robust, gene-expression-based drug screening.[60] Another study showcased how to leverage bioprinting and ML for drug screening at the single-organoid level,[8] successfully identifying organoids that were transiently or persistently sensitive or resistant to specific therapies. The study's XGBoost classifier, used to filter organoid data, achieved a high cross-validation score of 93.1 ± 1.3% with an area under the curve of 0.966 ± 0.020. This approach successfully quantified drug responses, revealing, for example, that when treated with 10 μM neratinib, only 4.5% of MCF-7 cell clusters grew, while in another cell line (BT-474) treated with 10 μM lapatinib, 73.7% of cell clusters lost mass. This ability to quantify intra-sample heterogeneity highlights the platform's potential for robust drug screening.

Beyond these direct drug screening applications, the convergence of bioprinting and AI technology also enables other critical biomedical functions that indirectly support therapeutic development. In the early stages of drug discovery, AI plays a crucial role in predicting the absorption, distribution, metabolism, excretion, and toxicity (ADMET) properties of drugs. For example, a study developed AI-based ADMET models that can rapidly and efficiently predict the properties of molecules using computational methods rather than physical bioprinting.[155] Moreover, this synergy opens up new avenues for diagnostics that inform therapeutic decisions. One study combined acoustic bioprinting with AI-assisted spectroscopy for the high-throughput identification of bacteria in blood.[156] This platform is indirectly linked to drug therapy by enabling rapid pathogen identification—a critical first step in guiding the selection of appropriate antimicrobial drugs and combating antibiotic resistance. This highlights the potential for this synergistic technology to streamline not only drug development but also the targeted application of existing treatments.

6. Challenges and future perspectives

Integrating ML with bioprinting offers significant promise for drug screening and toxicity testing, but several barriers remain. Data heterogeneity—arising from differences in imaging systems, bioink formulations, and cell sources—limits model generalizability, while the scarcity of large, high-quality labeled datasets hinders robust algorithm training. Technical integration requires custom interfaces and real-time processing pipelines, while biological

complexity means that even advanced models struggle to replicate multi-tissue interactions or long-term drug effects.[14,157] Concerns over interpretability, reproducibility, and regulatory compliance further slow adoption. Notably, despite the conceptual synergy, there is still a lack of direct, systematic research focusing on the integration of ML with bioprinting specifically for drug discovery and preclinical testing; most studies remain either proof-of-concept or focused separately on each field.

Future advances can address these limitations. Multi-modal data fusion will allow the integration of imaging, omics, biomechanical, and environmental datasets into unified predictive frameworks, while explainable AI can enhance trust and regulatory acceptance. Edge computing and embedded AI may enable real-time, on-device analysis, improving closed-loop bioprinting control. Meanwhile, digital twin models can simulate and optimize experiments before printing, saving time and resources. Standardized protocols, shared databases, and interoperable software will be critical for scalability. Through sustained interdisciplinary collaboration, ML-enhanced bioprinting platforms can revolutionize preclinical testing by accelerating discovery, reducing costs, and enabling personalized predictive drug evaluation.

7. Conclusion

In conclusion, the convergence of ML and 3D bioprinting presents a transformative paradigm for drug discovery and toxicology testing. By enabling data-driven optimization of bioprinting processes and providing a powerful framework for analyzing complex biological readouts, ML-augmented bioprinting systems are poised to address key limitations of conventional preclinical models. This review has demonstrated how diverse ML methods can be applied across the entire bioprinting workflow, from predicting material printability and optimizing process parameters to enhancing the predictive accuracy of drug response in physiologically relevant 3D tissue models. The inclusion of specific quantitative results from recent case studies underscores the tangible benefits of this integration, moving the field beyond conceptual discussions and towards verifiable, evidence-based applications. While significant challenges remain, particularly in the standardization of data collection and the development of more robust, universal models, the rapid advancement in both fields points to a promising future. The continued synergy between ML and bioprinting holds the potential to accelerate the development of personalized, effective, and safer therapeutics, ultimately bridging the gap between preclinical research and clinical success.

Acknowledgment

None.

Funding

This work was supported by the National Natural Science Foundation of China (No. 82560411) and the Research Project of Yan'an University (No. YAU202512552).

Conflict of interest

The authors declare that they have no conflicts of interest.

Author contributions

Conceptualization: Yangyang Wang, Jihan Wang
Funding acquisition: Jihan Wang
Project administration: Yangyang Wang
Supervision: Jihan Wang
Visualization: Yangyang Wang, Haotian Bai, Yufei Ren, Yanning Yang
Writing–original draft: Yangyang Wang, Haotian Bai, Yufei Ren, Yanning Yang
Writing–review & editing: Jihan Wang

Ethics approval and consent to participate

Not applicable.

Consent for publication

Not applicable.

Availability of data

Not applicable.

References

1. Schlander M, Hernandez-Villafuerte K, Cheng CY, Mestre-Ferrandiz J, Baumann M. How much does it cost to research and develop a new drug? A systematic review and assessment. *Pharmacoeconomics*. 2021;39(11):1243-1269.
doi: 10.1007/s40273-021-01065-y

2. Rennane S, Baker L, Mulcahy A. Estimating the cost of industry investment in drug research and development: a review of methods and results. *Inquiry*. 2021;58:00469580211059731.
doi: 10.1177/00469580211059731

3. Esposito A, Ferraresi A, Vallino L, Garavaglia B, Dhanasekaran DN, Isidoro C. Three-dimensional *in vitro* cell cultures as a feasible and promising alternative to two-dimensional and animal models in cancer research. *Int J Biol Sci*. 2024;20(13):5293-5311.

doi: 10.7150/ijbs.96469

4. Urzì O, Gasparro R, Costanzo E, *et al*. Three-dimensional cell cultures: the bridge between *in vitro* and *in vivo* models. *IJMS*. 2023;24(15):12046. doi: 10.3390/ijms241512046
5. Kreutzer FP, Meinecke A, Schmidt K, Fiedler J, Thum T. Alternative strategies in cardiac preclinical research and new clinical trial formats. *Cardiovasc Res*. 2022;118(3):746-762. doi: 10.1093/cvr/cvab075
6. Han X, Cai C, Deng W, *et al*. Landscape of human organoids: ideal model in clinics and research. *Innovation (Camb)*. 2024;5(3):100620. doi: 10.1016/j.xinn.2024.100620
7. Cacciamali A, Villa R, Dotti S. 3D cell cultures: evolution of an ancient tool for new applications. *Front Physiol*. 2022;13:836480. doi: 10.3389/fphys.2022.836480
8. Tebon PJ, Wang B, Markowitz AL, *et al*. Drug screening at single-organoid resolution via bioprinting and interferometry. *Nat Commun*. 2023;14(1):3168. doi: 10.1038/s41467-023-38832-8
9. Soheilmoghaddam F, Rumble M, Cooper-White J. High-throughput routes to biomaterials discovery. *Chem Rev*. 2021;121(18):10792-10864. doi: 10.1021/acs.chemrev.0c01026
10. Engel M, Belfiore L, Aghaei B, Sutija M. Enabling high throughput drug discovery in 3D cell cultures through a novel bioprinting workflow. *SLAS Technol*. 2022;27(1):32-38. doi: 10.1016/j.slast.2021.10.002
11. Johnson PA, Menegatti S, Chambers AC, *et al*. A rapid high throughput bioprinted colorectal cancer spheroid platform for in vitro drug- and radiation-response. *Biofabrication*. 2023;15(1):014103. doi: 10.1088/1758-5090/ac999f
12. Da Silva VA, Sharma R, Shteinberg E, *et al*. Machine learning approaches to 3D models for drug screening. *Biomedi Mater Dev*. 2024;2(2):695-720. doi: 10.1007/s44174-023-00142-4
13. Kim MH, Singh YP, Celik N, *et al*. High-throughput bioprinting of spheroids for scalable tissue fabrication. *Nat Commun*. 2024;15(1):10083. doi: 10.1038/s41467-024-54504-7
14. Mazzocchi A, Soker S, Skardal A. 3D bioprinting for high-throughput screening: drug screening, disease modeling, and precision medicine applications. *Appl Phys Rev*. 2019;6(1):011302. doi: 10.1063/1.5056188
15. Huskin G, Chen J, Davis T, Jun HW. Tissue-engineered 3D in vitro disease models for high-throughput drug screening. *Tissue Eng Regen Med*. 2023;20(4):523-538. doi: 10.1007/s13770-023-00522-3
16. Wang X, Luo Y, Ma Y, Wang P, Yao R. Converging bioprinting and organoids to better recapitulate the tumor microenvironment. *Trends Biotechnol*. 2024;42(5):648-663. doi: 10.1016/j.tibtech.2023.11.006
17. Tofani LB, Avelino TM, De Azevedo RJ, *et al*. Biofabricated 3D intestinal models as an alternative to animal-based approaches for drug toxicity assays. *Tissue Eng Regen Med*. 2025;22(2):181-194. doi: 10.1007/s13770-024-00694-6
18. Kesti M, Fisch P, Pensalfini M, Mazza E, Zenobi-Wong M. Guidelines for standardization of bioprinting: a systematic study of process parameters and their effect on bioprinted structures. *BioNanoMaterials*. 2016;17(3-4):193-204. doi: 10.1515/bnm-2016-0004
19. Putrama IM, Martinek P. Heterogeneous data integration: challenges and opportunities. *Data Brief*. 2024;56:110853. doi: 10.1016/j.dib.2024.110853
20. Rickert CA, Lieleg O. Machine learning approaches for biomolecular, biophysical, and biomaterials research. *Biophys Rev*. 2022;3(2):021306. doi: 10.1063/5.0082179
21. Yu J, Yao D, Wang L, Xu M. Machine learning in predicting and optimizing polymer printability for 3D bioprinting. *Polymers (Basel)*. 2025;17(13):1873. doi: 10.3390/polym17131873
22. Rafieyan S, Ansari E, Vasheghani-Farahani E. A practical machine learning approach for predicting the quality of 3D (bio)printed scaffolds. *Biofabrication*. 2024;16(4):045014. doi: 10.1088/1758-5090/ad6374
23. Sun J, Yao K, An J, Jing L, Huang K, Huang D. Machine learning and 3D bioprinting. *IJB*. 2024;9(4):717. doi: 10.18063/ijb.717
24. Ahmed E, Mulay P, Ramirez C, Tirado-Mansilla G, Cheong E, Gormley AJ. Mapping biomaterial complexity by machine learning. *Tissue Eng Part A*. 2024;30(19-20):662-680. doi: 10.1089/ten.tea.2024.0067
25. Freeman S, Calabro S, Williams R, Jin S, Ye K. Bioink formulation and machine learning-empowered bioprinting optimization. *Front Bioeng Biotechnol*. 2022;10:913579. doi: 10.3389/fbioe.2022.913579
26. Shin J, Kang R, Hyun K, *et al*. Machine learning-enhanced optimization for high-throughput precision in cellular droplet bioprinting. *Adv Sci*. 2025;12(20):2412831. doi: 10.1002/advs.202412831
27. Ruberu K, Senadeera M, Rana S, *et al*. Coupling machine learning with 3D bioprinting to fast track optimisation of extrusion printing. *Appl Mater Today*. 2021;22:100914. doi: 10.1016/j.apmt.2020.100914
28. Vitacolonna M, Bruch R, Schneider R, *et al*. A spheroid whole mount drug testing pipeline with machine-learning based image analysis identifies cell-type specific differences

in drug efficacy on a single-cell level. *BMC Cancer*. 2024;24(1):1542.
doi: 10.1186/s12885-024-13329-9

29. Fritschen A, Lindner N, Scholpp S, *et al*. High-scale 3D-bioprinting platform for the automated production of vascularized organs-on-a-chip. *Adv Healthc Mater*. 2024;13(17):2304028.
doi: 10.1002/adhm.202304028

30. Gu Z, Fu J, Lin H, He Y. Development of 3D bioprinting: from printing methods to biomedical applications. *Asian J Pharma Sci*. 2020;15(5):529-557.
doi: 10.1016/j.ajps.2019.11.003

31. Santoni S, Gugliandolo SG, Sponchioni M, Moscatelli D, Colosimo BM. 3D bioprinting: current status and trends—a guide to the literature and industrial practice. *Bio-des Manuf*. 2022;5(1):14-42.
doi: 10.1007/s42242-021-00165-0

32. Ramiah P, Du Toit LC, Choonara YE, Kondiah PPD, Pillay V. Hydrogel-based bioinks for 3D bioprinting in tissue regeneration. *Front Mater*. 2020;7:76.
doi: 10.3389/fmats.2020.00076

33. Chen XB, Fazel Anvari-Yazdi A, Duan X, *et al*. Biomaterials / bioinks and extrusion bioprinting. *Bioact Mater*. 2023;28:511-536.
doi: 10.1016/j.bioactmat.2023.06.006

34. Ng WL, Lee JM, Yeong WY, Win Naing M. Microvalve-based bioprinting – process, bio-inks and applications. *Biomater Sci*. 2017;5(4):632-647.
doi: 10.1039/C6BM00861E

35. Zhang J, Wehrle E, Rubert M, Müller R. 3D Bioprinting of Human Tissues: Biofabrication, Bioinks, and Bioreactors. *IJMS*. 2021;22(8):3971.
doi: 10.3390/ijms22083971

36. Datta P, Barui A, Wu Y, Ozbolat V, Moncal KK, Ozbolat IT. Essential steps in bioprinting: from pre- to post-bioprinting. *Biotechnol Adv*. 2018;36(5):1481-1504.
doi: 10.1016/j.biotechadv.2018.06.003

37. Choi JW, Kang SJ, Choi JI, Kwack K, Kim M. Role of Nuclear-receptor-related 1 in the synergistic neuroprotective effect of umbilical cord blood and erythropoietin combination therapy in hypoxic ischemic encephalopathy. *IJMS*. 2022;23(5):2900.
doi: 10.3390/ijms23052900

38. Murphy SV, De Coppi P, Atala A. Opportunities and challenges of translational 3D bioprinting. *Nat Biomed Eng*. 2020;4(4):370-380.
doi: 10.1038/s41551-019-0471-7

39. Tarassoli SP, Jessop ZM, Jovic T, Hawkins K, Whitaker IS. Candidate bioinks for extrusion 3D bioprinting—a systematic review of the literature. *Front Bioeng Biotechnol*. 2021;9:616753.
doi: 10.3389/fbioe.2021.616753

40. Yu J, Park SA, Kim WD, *et al*. Current advances in 3D bioprinting technology and its applications for tissue engineering. *Polymers*. 2020;12(12):2958.
doi: 10.3390/polym12122958

41. Panwar A, Tan LP. Current status of bioinks for micro-extrusion-based 3D bioprinting. *Molecules*. 2016;21(6):685.
doi: 10.3390/molecules21060685

42. Kong Z, Wang X. Bioprinting technologies and bioinks for vascular model establishment. *IJMS*. 2023;24(1):891.
doi: 10.3390/ijms24010891

43. Yu C, Schimelman J, Wang P, *et al*. Photopolymerizable biomaterials and light-based 3D printing strategies for biomedical applications. *Chem Rev*. 2020;120(19):10695-10743.
doi: 10.1021/acs.chemrev.9b00810

44. Li W, Wang M, Ma H, Chapa-Villarreal FA, Lobo AO, Zhang YS. Stereolithography apparatus and digital light processing-based 3D bioprinting for tissue fabrication. *iScience*. 2023;26(2):106039.
doi: 10.1016/j.isci.2023.106039

45. Wang Z, Abdulla R, Parker B, Samanipour R, Ghosh S, Kim K. A simple and high-resolution stereolithography-based 3D bioprinting system using visible light crosslinkable bioinks. *Biofabrication*. 2015;7(4):045009.
doi: 10.1088/1758-5090/7/4/045009

46. Strauß S, Schroth B, Hubbuch J. Evaluation of the reproducibility and robustness of extrusion-based bioprinting processes applying a flow sensor. *Front Bioeng Biotechnol*. 2022;10:831350.
doi: 10.3389/fbioe.2022.831350

47. Pössl A, Hartzke D, Schlupp P, Runkel FE. Optimized cell mixing facilitates the reproducible bioprinting of constructs with high cell viability. *Appl Sci*. 2021;12(1):326.
doi: 10.3390/app12010326

48. Grijalva Garces D, Strauß S, Gretzinger S, *et al*. On the reproducibility of extrusion-based bioprinting: round robin study on standardization in the field. *Biofabrication*. 2023;16(1):015002.
doi: 10.1088/1758-5090/acfe3b

49. Strauß S, Grijalva Garces D, Hubbuch J. Analytics in extrusion-based bioprinting: standardized methods improving quantification and comparability of the performance of bioinks. *Polymers*. 2023;15(8):1829.
doi: 10.3390/polym15081829

50. Schwab A, Levato R, D'Este M, Piluso S, Eglin D, Malda J. Printability and shape fidelity of bioinks in 3D bioprinting. *Chem Rev*. 2020;120(19):11028-11055.
doi: 10.1021/acs.chemrev.0c00084

51. Upton A, Mylona A, Zimbitas G. Utilising design of experiment to design an optimised bioink for 3D bioprinting. *J Mater Sci*. 2025;60(25):10467-10477.
doi: 10.1007/s10853-025-11076-1

52. Chen H, Liu Y, Balabani S, Hirayama R, Huang J. Machine learning in predicting printable biomaterial formulations for direct ink writing. *Research*. 2023;6:0197. doi: 10.34133/research.0197

53. Yang Y, Jia Y, Yang Q, Xu F. Engineering bio-inks for 3D bioprinting cell mechanical microenvironment. *IJB*. 2022;9(1):632. doi: 10.18063/ijb.v9i1.632

54. An J, Chua CK, Mironov V. Application of machine learning in 3D bioprinting: focus on development of big data and digital twin. *IJB*. 2024;7(1):342. doi: 10.18063/ijb.v7i1.342

55. Maharjan S, Ma C, Singh B, *et al*. Advanced 3D imaging and organoid bioprinting for biomedical research and therapeutic applications. *Adv Drug Deliv Rev*. 2024;208:115237. doi: 10.1016/j.addr.2024.115237

56. Shin J, Lee Y, Li Z, Hu J, Park SS, Kim K. Optimized 3D bioprinting technology based on machine learning: a review of recent trends and advances. *Micromachines*. 2022;13(3):363. doi: 10.3390/mi13030363

57. Wu D, Xu C. Predictive modeling of droplet formation processes in inkjet-based bioprinting. *J Manuf Sci Eng*. 2018;140(10):101007. doi: 10.1115/1.4040619

58. Sarah R, Rohauer R, Schimmelpfennig K, Limon SM, Lewis CL, Habib A. Data-driven optimization of bioink formulations for extrusion-based bioprinting: a predictive modeling approach. *J Manuf Sci Eng*. 2025;147(10):101001. doi: 10.1115/1.4069041

59. Nadernezhad A, Groll J. Machine learning to explain printability induced by rheology additives. ChemRxiv. 2021. doi: 10.26434/chemrxiv-2021-41mn8

60. Tang M, Jiang S, Huang X, *et al*. Integration of 3D bioprinting and multi-algorithm machine learning identified glioma susceptibilities and microenvironment characteristics. *Cell Discov*. 2024;10(1):39. doi: 10.1038/s41421-024-00650-7

61. Choi YM, Na D, Yoon G, *et al*. Prediction of patient drug response via 3D bioprinted gastric cancer model utilized patient-derived tissue laden tissue-specific bioink. *Adv Sci (Weinh)*. 2025;12(10):e2411769. doi: 10.1002/advs.202411769

62. Sarah R, Schimmelpfennig K, Rohauer R, Lewis CL, Limon SM, Habib A. Characterization and machine learning-driven property prediction of a novel hybrid hydrogel bioink considering extrusion-based 3D bioprinting. *Gels*. 2025;11(1):45. doi: 10.3390/gels11010045

63. Habib A, Sarah R, Tuladhar S, Khoda B, Limon SM. Modulating rheological characteristics of bio-ink with component weight and shear rate for enhanced bioprinted scaffold fidelity. *Bioprinting*. 2024;38:e00332. doi: 10.1016/j.bprint.2024.e00332

64. Janani G, Priya S, Dey S, Mandal BB. Mimicking native liver lobule microarchitecture in vitro with parenchymal and non-parenchymal cells using 3D bioprinting for drug toxicity and drug screening applications. *ACS Appl Mater Interfaces*. 2022;14(8):10167-10186. doi: 10.1021/acsami.2c00312

65. Szűcs D, Fekete Z, Guba M, *et al*. Toward better drug development: three-dimensional bioprinting in toxicological research. *IJB*. 2023;9(2):663. doi: 10.18063/ijb.v9i2.663

66. Royo F, Garcia-Vallicrosa C, Azparren-Angulo M, Bordanaba-Florit G, Lopez-Sarrio S, Falcon-Perez JM. Three-dimensional hepatocyte spheroids: model for assessing chemotherapy in hepatocellular carcinoma. *Biomedicines*. 2024;12(6):1200. doi: 10.3390/biomedicines12061200

67. Maloney E, Clark C, Sivakumar H, *et al*. Immersion bioprinting of tumor organoids in multi-well plates for increasing chemotherapy screening throughput. *Micromachines*. 2020;11(2):208. doi: 10.3390/mi11020208

68. Parodi I, Di Lisa D, Pastorino L, Scaglione S, Fato MM. 3D bioprinting as a powerful technique for recreating the tumor microenvironment. *Gels*. 2023;9(6):482. doi: 10.3390/gels9060482

69. Ma Y, Deng B, He R, Huang P. Advancements of 3D bioprinting in regenerative medicine: exploring cell sources for organ fabrication. *Heliyon*. 2024;10(3):e24593. doi: 10.1016/j.heliyon.2024.e24593

70. Langer EM, Allen-Petersen BL, King SM, *et al*. Modeling tumor phenotypes in vitro with three-dimensional bioprinting. *Cell Rep*. 2019;26(3):608-623.e6. doi: 10.1016/j.celrep.2018.12.090

71. Estermann M, Bisig C, Septiadi D, Petri-Fink A, Rothen-Rutishauser B. Bioprinting for human respiratory and gastrointestinal in vitro models. *Methods Mol Biol*. 2020;2140:199-215. doi: 10.1007/978-1-0716-0520-2_13

72. Schmidt K, Berg J, Roehrs V, Kurreck J, Al-Zeer MA. 3D-bioprinted HepaRG cultures as a model for testing long term aflatoxin B1 toxicity in vitro. *Toxicol Rep*. 2020;7:1578-1587. doi: 10.1016/j.toxrep.2020.11.003

73. Ide I, Nagao E, Kajiyama S, Mizoguchi N. A novel evaluation method for determining drug-induced hepatotoxicity using 3D bio-printed human liver tissue. *Toxicol Mech Methods*. 2020;30(3):189-196. doi: 10.1080/15376516.2019.1686795

74. Ort C, Chen Y, Ghagre A, Ehrlicher A, Moraes C. Bioprintable, stiffness-tunable collagen-alginate microgels for increased throughput 3D cell culture studies. *ACS Biomater Sci Eng*. 2021;7(6):2814-2822. doi: 10.1021/acsbiomaterials.1c00129

75. Lawlor KT, Vanslambrouck JM, Higgins JW, *et al*. Cellular extrusion bioprinting improves kidney organoid reproducibility and conformation. *Nat Mater*. 2021;20(2):260-271. doi: 10.1038/s41563-020-00853-9

76. Bouwmeester MC, Bernal PN, Oosterhoff LA, *et al*. Bioprinting of human liver-derived epithelial organoids for toxicity studies. *Macromol Biosci*. 2021;21(12):e2100327. doi: 10.1002/mabi.202100327

77. Kang HK, Sarsenova M, Kim DH, *et al*. Establishing a 3D *in vitro* hepatic model mimicking physiologically relevant to *in vivo* state. *Cells*. 2021;10(5):1268. doi: 10.3390/cells10051268

78. Datta P, Wu Y, Yu Y, Moncal KK, Ozbolat IT. A scaffold free 3D bioprinted cartilage model for in vitro toxicology. *Methods Mol Biol*. 2021;2147:175-183. doi: 10.1007/978-1-0716-0611-7_15

79. Hong S, Song JM. A 3D cell printing-fabricated HepG2 liver spheroid model for high-content in situ quantification of drug-induced liver toxicity. *Biomater Sci*. 2021;9(17):5939-5950. doi: 10.1039/d1bm00749a

80. Geevarghese R, Somasekharan LT, Bhatt A, Kasoju N, Nair RP. Development and evaluation of a multicomponent bioink consisting of alginate, gelatin, diethylaminoethyl cellulose and collagen peptide for 3D bioprinting of tissue construct for drug screening application. *Int J Biol Macromol*. 2022;207:278-288. doi: 10.1016/j.ijbiomac.2022.02.191

81. Tröndle K, Miotto G, Rizzo L, *et al*. Deep learning-assisted nephrotoxicity testing with bioprinted renal spheroids. *Int J Bioprint*. 2022;8(2):528. doi: 10.18063/ijb.v8i2.528

82. Wang P, Sun L, Li C, *et al*. Study on drug screening multicellular model for colorectal cancer constructed by three-dimensional bioprinting technology. *Int J Bioprint*. 2023;9(3):694. doi: 10.18063/ijb.694

83. Huang B, Wei X, Chen K, Wang L, Xu M. Bioprinting of hydrogel beads to engineer pancreatic tumor-stroma microtissues for drug screening. *Int J Bioprint*. 2023; 9(3):676. doi: 10.18063/ijb.676

84. Fan Z, Wei X, Chen K, Wang L, Xu M. 3D bioprinting of an endothelialized liver lobule-like construct as a tumor-scale drug screening platform. *Micromachines (Basel)*. 2023;14(4):878. doi: 10.3390/mi14040878

85. Yu M, Ni M, Xu F, *et al*. NSUN6-mediated 5-methylcytosine modification of NDRG1 mRNA promotes radioresistance in cervical cancer. *Mol Cancer*. 2024; 23(1):139. doi: 10.1186/s12943-024-02055-2

86. Gu WJ, Liu XX, Shen YW, *et al*. TRIM4 enhances small-molecule-induced neddylated-degradation of CORO1A for triple negative breast cancer therapy. *Theranostics*. 2024;14(18):7023-7041. doi: 10.7150/thno.97662

87. Ali ASM, Berg J, Roehrs V, *et al*. Xeno-free 3D bioprinted liver model for hepatotoxicity assessment. *Int J Mol Sci*. 2024;25(3):1811. doi: 10.3390/ijms25031811

88. do Amaral SR, Amantino CF, Atanasov A, *et al*. Photodynamic therapy as a novel therapeutic modality applying quinizarin-loaded nanocapsules and 3D bioprinting skin permeation for inflammation treatment. *Pharmaceuticals (Basel)*. 2024;17(9):1169. doi: 10.3390/ph17091169

89. Suwannakot P, Zhu L, Tolentino MAK, *et al*. Electrostatically cross-linked bioinks for jetting-based bioprinting of 3D cell cultures. *ACS Appl Bio Mater*. 2024;7(1):269-283. doi: 10.1021/acsabm.3c00849

90. Shrestha S, Lekkala VKR, Acharya P, Kang SY, Vanga MG, Lee MY. Reproducible generation of human liver organoids (HLOs) on a pillar plate platform via microarray 3D bioprinting. *Lab Chip*. 2024;24(10):2747-2761. doi: 10.1039/d4lc00149d

91. Lu TY, Ji Y, Lyu C, *et al*. Bioprinted high cell density liver model with improved hepatic metabolic functions. *Biomaterials*. 2025;320:123256. doi: 10.1016/j.biomaterials.2025.123256

92. Feng T, Wei L, Zhou C, *et al*. Light-based 3D bioprinting of testicular organoid as an in vitro model for reproductive toxicity assessment. *ACS Biomater Sci Eng*. 2025;11(7):4357-4367. doi: 10.1021/acsbiomaterials.5c00414

93. Hu Y, Nicolas GM, Cai Y, Dai X, Ma S. Epidermal and dermal cell-composed organospheres to assess microplastic-induced skin toxicity. *Biomaterials*. 2026;324:123513. doi: 10.1016/j.biomaterials.2025.123513

94. Chandarana C, Sane D, Mishra S, Chaubey A, Gohil U, Prajapati B. Recent advances in bioink research for biomedical applications. *Biomed Mater Dev*. 2025. doi: 10.1007/s44174-025-00478-z

95. Alonzo M, Dominguez E, Alvarez-Primo F, *et al*. A comparative study in the printability of a bioink and 3D models across two bioprinting platforms. *Mater Lett*. 2020;264:127382. doi: 10.1016/j.matlet.2020.127382

96. Mandrycky C, Wang Z, Kim K, Kim DH. 3D bioprinting for engineering complex tissues. *Biotechnol Adv*. 2016;34(4):422-434. doi: 10.1016/j.biotechadv.2015.12.011

97. Murphy SV, Atala A. 3D bioprinting of tissues and organs. *Nat Biotechnol*. 2014;32(8):773-785. doi: 10.1038/nbt.2958

98. Yu C, Jiang J. A perspective on using machine learning in 3D bioprinting. *IJB*. 2020;6(1):253. doi: 10.18063/ijb.v6i1.253

99. Elbadawi M, McCoubrey LE, Gavins FKH, *et al*. Disrupting 3D printing of medicines with machine learning. *Trends Pharmacol Sci*. 2021;42(9):745-757. doi: 10.1016/j.tips.2021.06.002

100. Visan AI, Negut I. Integrating artificial intelligence for drug discovery in the context of revolutionizing drug delivery. *Life*. 2024;14(2):233. doi: 10.3390/life14020233

101. Elbadawi M, Muñiz Castro B, Gavins FKH, *et al*. M3DISEEN: a novel machine learning approach for predicting the 3D printability of medicines. *Int J Pharma*. 2020;590: 119837. doi: 10.1016/j.ijpharm.2020.119837

102. Ong JJ, Castro BM, Gaisford S, *et al*. Accelerating 3D printing of pharmaceutical products using machine learning. *Int J Pharma: X*. 2022;4:100120. doi: 10.1016/j.ijpx.2022.100120

103. Rahmani AM, Yousefpoor E, Yousefpoor MS, *et al*. Machine learning (ML) in medicine: review, applications, and challenges. *Mathematics*. 2021;9(22):2970. doi: 10.3390/math9222970

104. Jovel J, Greiner R. An introduction to machine learning approaches for biomedical research. *Front Med*. 2021;8:771607. doi: 10.3389/fmed.2021.771607

105. Cano G, Garcia-Rodriguez J, Garcia-Garcia A, *et al*. Automatic selection of molecular descriptors using random forest: application to drug discovery. *Expert Syst Appl*. 2017;72:151-159. doi: 10.1016/j.eswa.2016.12.008

106. Rodríguez-Pérez R, Bajorath J. Evolution of support vector machine and regression modeling in chemoinformatics and drug discovery. *J Comput Aided Mol Des*. 2022;36(5):355-362. doi: 10.1007/s10822-022-00442-9

107. Gupta R, Srivastava D, Sahu M, Tiwari S, Ambasta RK, Kumar P. Artificial intelligence to deep learning: machine intelligence approach for drug discovery. *Mol Divers*. 2021;25(3):1315-1360. doi: 10.1007/s11030-021-10217-3

108. Tsuneki M. Deep learning models in medical image analysis. *J Oral Biosci*. 2022;64(3):312-320. doi: 10.1016/j.job.2022.03.003

109. Chen W, Liu X, Zhang S, Chen S. Artificial intelligence for drug discovery: resources, methods, and applications. *Mol Ther Nucleic Acids*. 2023;31:691-702. doi: 10.1016/j.omtn.2023.02.019

110. Ravindra Padalkar G, Dinkar Patil S, Mallikarjun Hegadi M, Kailash Jaybhaye N. Drug discovery using generative adversarial network with reinforcement learning. In: *2021 International Conference on Computer Communication and Informatics (ICCCI)*. IEEE; 2021:1-3. doi: 10.1109/ICCCI50826.2021.9402449

111. Wang J, He R, Wang X, Li H, Lu Y. MCF-DTI: multi-scale convolutional local–global feature fusion for drug–target interaction prediction. *Molecules*. 2025;30(2):274. doi: 10.3390/molecules30020274

112. Zhang L, Zhang H, Ai H, *et al*. Applications of machine learning methods in drug toxicity prediction. *CTMC*. 2018;18(12):987-997. doi: 10.2174/1568026618666180727152557

113. Vo AH, Van Vleet TR, Gupta RR, Liguori MJ, Rao MS. An overview of machine learning and big data for drug toxicity evaluation. *Chem Res Toxicol*. 2020;33(1):20-37. doi: 10.1021/acs.chemrestox.9b00227

114. Parvatikar PP, Patil S, Khaparkhuntikar K, *et al*. Artificial intelligence: machine learning approach for screening large database and drug discovery. *Antiviral Res*. 2023;220:105740. doi: 10.1016/j.antiviral.2023.105740

115. Judson R, Elloumi F, Setzer RW, Li Z, Shah I. A comparison of machine learning algorithms for chemical toxicity classification using a simulated multi-scale data model. *BMC Bioinformatics*. 2008;9(1):241. doi: 10.1186/1471-2105-9-241

116. Pu L, Naderi M, Liu T, Wu HC, Mukhopadhyay S, Brylinski M. eToxPred: a machine learning-based approach to estimate the toxicity of drug candidates. *BMC Pharmacol Toxicol*. 2019;20(1):2. doi: 10.1186/s40360-018-0282-6

117. Yang H, Sun L, Li W, Liu G, Tang Y. In silico prediction of chemical toxicity for drug design using machine learning methods and structural alerts. *Front Chem*. 2018;6:30. doi: 10.3389/fchem.2018.00030

118. Fu R, Chen Z, Tian H, *et al*. A review on the applications of machine learning in biomaterials, biomechanics, and biomanufacturing for tissue engineering. *Smart Mater Med*. 2025;6(2):171-204. doi: 10.1016/j.smaim.2025.06.003

119. Tuna C, Ouzir N, Dubois D, *et al*. Automated defect classification in aerospace x-ray images using CNNs. *eJNDT*. 2025;30(8). doi: 10.58286/31418

120. Cumbajin E, Rodrigues N, Costa P, *et al*. A systematic review on deep learning with CNNs applied to surface defect detection. *J Imaging*. 2023;9(10):193.

doi: 10.3390/jimaging9100193

121. Zhang Z, Zhou X, Fang Y, Xiong Z, & Zhang T. AI-driven 3D bioprinting for regenerative medicine: from bench to bedside. *Bioact Mater*. 2025;45:201-230. doi: 10.1016/j.bioactmat.2024.11.021

122. Wang J, Heshmati Aghda N, Jiang J, Mridula Habib A, Ouyang D, Maniruzzaman M. 3D bioprinted microparticles: Optimizing loading efficiency using advanced DoE technique and machine learning modeling. *Int J Pharma*. 2022;628:122302. doi: 10.1016/j.ijpharm.2022.122302

123. Ng WL, Chan A, Ong YS, Chua CK. Deep learning for fabrication and maturation of 3D bioprinted tissues and organs. *Virtual Phys Prototyping*. 2020;15(3):340-358. doi: 10.1080/17452759.2020.1771741

124. Bao D, Wang L, Zhou X, Yang S, He K, Xu M. Automated detection and growth tracking of 3D bio-printed organoid clusters using optical coherence tomography with deep convolutional neural networks. *Front Bioeng Biotechnol*. 2023;11:1133090. doi: 10.3389/fbioe.2023.1133090

125. Bone JM, Childs CM, Menon A, *et al*. Hierarchical machine learning for high-fidelity 3D printed biopolymers. *ACS Biomater Sci Eng*. 2020;6(12):7021-7031. doi: 10.1021/acsbiomaterials.0c00755

126. Lee J, Oh SJ, An SH, Kim WD, Kim SH. Machine learning-based design strategy for 3D printable bioink: elastic modulus and yield stress determine printability. *Biofabrication*. 2020;12(3):035018. doi: 10.1088/1758-5090/ab8707

127. Chen H, Zhang B, Huang J. Recent advances and applications of artificial intelligence in 3D bioprinting. *Biophys Rev*. 2024;5(3):031301. doi: 10.1063/5.0190208

128. Xu Y, Sarah R, Habib A, Liu Y, Khoda B. Constraint based Bayesian optimization of bioink precursor: a machine learning framework. *Biofabrication*. 2024;16(4):045031. doi: 10.1088/1758-5090/ad716e

129. Shin J, Kang M, Hyun K, *et al*. Machine learning driven optimization for high precision cellular droplet bioprinting. BioRxiv. 2024:2024;611131. doi: 10.1101/2024.09.04.611131

130. Rezvani A, Bigverdi M, Rohban MH. Image-based cell profiling enhancement via data cleaning methods. *PLoS One*. 2022;17(5):e0267280. doi: 10.1371/journal.pone.0267280

131. Dehbozorgi P, Ryabchykov O, Bocklitz T. A systematic investigation of image pre-processing on image classification. *IEEE Access*. 2024;12:64913-64926. doi: 10.1109/ACCESS.2024.3395063

132. Asachi M, Alonso Camargo-Valero M. Multi-sensors data fusion for monitoring of powdered and granule products: Current status and future perspectives. *Adv Powder Technol*. 2023;34(7):104055. doi: 10.1016/j.apt.2023.104055

133. Kush JC. Integrating sensor technologies with conversational AI: enhancing context-sensitive interaction through real-time data fusion. *Sensors*. 2025;25(1):249. doi: 10.3390/s25010249

134. Yetgin A. Revolutionizing multi-omics analysis with artificial intelligence and data processing. *Quant Biol*. 2025;13(3):e70002. doi: 10.1002/qub2.70002

135. Zhang J, Che Y, Liu R, Wang Z, Liu W. Deep learning-driven multi-omics analysis: enhancing cancer diagnostics and therapeutics. *Brief Bioinform*. 2025;26(4):bbaf440. doi: 10.1093/bib/bbaf440

136. You S, Fan Y, Chen Y, *et al*. Advancements and prospects of deep learning in biomaterials evolution. *CR-PHYS-SC*. 2024;5(9):102116. doi: 10.1016/j.xcrp.2024.102116

137. Tripathi S, Mandal SS, Bauri S, Maiti P. 3D bioprinting and its innovative approach for biomedical applications. *MedComm (2020)*. 2023;4(1):e194. doi: 10.1002/mco2.194

138. Ning H, Zhou T, Joo SW. Machine learning boosts three-dimensional bioprinting. *IJB*. 2023;9(4):739. doi: 10.18063/ijb.739

139. Bonatti AF, Vozzi G, De Maria C. Enhancing quality control in bioprinting through machine learning. *Biofabrication*. 2024;16(2):022001. doi: 10.1088/1758-5090/ad2189

140. Al-Kharusi G, Dunne NJ, Little S, Levingstone TJ. The role of machine learning and design of experiments in the advancement of biomaterial and tissue engineering research. *Bioengineering*. 2022;9(10):561. doi: 10.3390/bioengineering9100561

141. Setiya A, Jani V, Sonavane U, Joshi R. MolToxPred: small molecule toxicity prediction using machine learning approach. *RSC Adv*. 2024;14(6):4201-4220. doi: 10.1039/D3RA07322J

142. Kamble SD, Singh SC, Ashwani Kumar, Dwivedi G, eds. *Tissue Engineering and Regenerative Medicine: Advances and Applications*. 1st edition. CRC Press, Taylor & Francis Group; 2025. doi: 10.1201/9781003536352

143. Bonatti AF, Vozzi G, Chua CK, Maria CD. A deep learning quality control loop of the extrusion-based bioprinting process. *Int J Bioprint*. 2022;8(4):620. doi: 10.18063/ijb.v8i4.620

144. Arduengo J, Hascoet N, Chinesta F, Hascoet JY. Open-loop control system for high precision extrusion-based bioprinting through machine learning modeling. *J Mach Eng*. 2024;24(1):103-117.

doi: 10.36897/jme/186044

145. Sani AR, Zolfagharian A, Kouzani AZ. Artificial intelligence-augmented additive manufacturing: insights on closed-loop 3D printing. *Adv Intell Syst*. 2024;6(10):2400102. doi: 10.1002/aisy.202400102

146. Arduengo J, Hascoët N, Chinesta F, Hascoet JY. Closed-loop control of extrusion-based bioprinting through real-time computer vision. *J Mach Eng*. 2025;25(2):28-42. doi: 10.36897/jme/205422

147. Rahmani Dabbagh S, Ozcan O, Tasoglu S. Machine learning-enabled optimization of extrusion-based 3D printing. *Methods*. 2022;206:27-40. doi: 10.1016/j.ymeth.2022.08.002

148. Inayathullah S, Buddala R. Review of machine learning applications in additive manufacturing. *Results Eng*. 2025;25:103676. doi: 10.1016/j.rineng.2024.103676

149. Tian S, Stevens R, McInnes BT, Lewinski NA. Machine assisted experimentation of extrusion-based bioprinting systems. *Micromachines (Basel)*. 2021;12(7):780. doi: 10.3390/mi12070780

150. Hashemi A, Ezati M, Zumberg I, *et al*. Characterization and optimization of a biomaterial ink aided by machine learning-assisted parameter suggestion. *Mater Today Commun*. 2024;40:109777. doi: 10.1016/j.mtcomm.2024.109777

151. Zhang C, Elvitigala KCML, Mubarok W, Okano Y, Sakai S. Machine learning-based prediction and optimisation framework for as-extruded cell viability in extrusion-based 3D bioprinting. *Virtual Phys Prototyping*. 2024;19(1):e2400330. doi: 10.1080/17452759.2024.2400330

152. Ronzetti M, Simeonov A. A comprehensive update on the application of high-throughput fluorescence imaging for novel drug discovery. *Expert Opin Drug Discov*. 2025;20(6):785-797. doi: 10.1080/17460441.2025.2499123

153. Vinken M, Grimm D, Baatout S, *et al*. Taking the 3Rs to a higher level: replacement and reduction of animal testing in life sciences in space research. *Biotechnol Adv*. 2025;81:108574. doi: 10.1016/j.biotechadv.2025.108574

154. Ayad A. Bioinspired NeuroPods: AI-Enhanced 4D Composite Bioprinting Revolutionizing Brain-on-Chip and Neural Regeneration; 2025. doi: 10.20944/preprints202507.1943.v1

155. Biehn SE, Goncalves LM, Lehmann J, *et al*. BioPrint meets the AI age: development of artificial intelligence-based ADMET models for the drug-discovery platform SAFIRE. *Future Med Chem*. 2024;16(7):587-599. doi: 10.4155/fmc-2024-0007

156. Safir F, Vu N, Tadesse LF, *et al*. Combining acoustic bioprinting with AI-assisted raman spectroscopy for high-throughput identification of bacteria in blood. *Nano Lett*. 2023;23(6):2065-2073. doi: 10.1021/acs.nanolett.2c03015

157. Satpathy A, Datta P, Wu Y, Ayan B, Bayram E, Ozbolat IT. Developments with 3D bioprinting for novel drug discovery. *Expert Opin Drug Discov*. 2018;13(12):1115-1129. doi: 10.1080/17460441.2018.1542427

ACCSCIENCE PUBLISHING

International Journal of Bioprinting

REVIEW ARTICLE

3D bioprinting–microfluidics technology: Pioneering advances in tumor microenvironment modeling, cancer treatment optimization, and diagnostic biomarker discovery

Wang Wang†, Zhicheng Zhang†, Yang Yu†, Yikang Wang†, and Kai Ni*

Department of Urology, Shanghai Sixth People's Hospital Affiliated to Shanghai Jiao Tong University School of Medicine, Shanghai, China.

(This article belongs to the *Special Issue*: *3D-Printed Biomedical Devices*)

Abstract

Conventional tumor models have historically failed to fully recapitulate the intricate pathophysiological complexity and dynamic microenvironment of human malignancies, significantly limiting their translational potential. The recent convergence of microfluidic technology and 3D bioprinting has ushered in a paradigm shift in oncology research, enabling more physiologically relevant models. This review provides a comprehensive analysis of the limitations inherent in traditional tumor modeling platforms and elaborates on the fundamental principles underlying microfluidics and additive manufacturing. It systematically explores the integrated applications of 3D-bioprinting–microfluidics systems across three core domains: engineering pathomimetic tumor models, advancing therapeutic screening platforms, and developing high-sensitivity diagnostic tools. This interdisciplinary synergy allows for unprecedented spatiotemporal control over the tumor microenvironment, precise biochemical gradient formation, and seamless integration of functional biosensors. The review further discusses persistent challenges—such as material biocompatibility, fabrication scalability, and the need for standardized validation—and proposes future directions—including the development of multiorgan-on-chip systems, stimuli-responsive biomaterials, and artificial intelligence-enhanced analytical frameworks. The continued integration of 3D bioprinting and microfluidics holds transformative potential for accelerating precision oncology and improving clinical outcomes.

Keywords: 3D printing; Cancer treatment optimization; Diagnostic biomarker discovery; Microfluidic technology; Tumor microenvironment model

1. Introduction

Contemporary oncology research has undergone transformative advancement through increasingly sophisticated tumor modeling platforms. While conventional two-dimensional (2D) monolayer cultures facilitate high-throughput compound screening, they fundamentally lack the multidimensional complexity of native tissue ecosystems—failing to recapitulate critical physiological features, such as oxygen/nutrient gradients, metabolic crosstalk, and spatially organized cell–cell communication[1–3] (Figure 1). Three-

†These authors contributed equally to this work.

***Corresponding author:**
Kai Ni (kai.ni@shsmu.edu.cn)

Citation: Wang W, Zhang Z, Yu Y, Wang Y, Ni K. 3D bioprinting–microfluidics technology: Pioneering advances in tumor microenvironment modeling, cancer treatment optimization, and diagnostic biomarker discovery. *Int J Bioprint*. 2025;11(6):23-50. doi: 10.36922/IJB025320314

Received: August 6, 2025
Revised: September 3, 2025
Accepted: September 12, 2025
Published Online: September 17, 2025

Copyright: © 2025 Author(s). This is an Open Access article distributed under the terms of the Creative Commons Attribution License, permitting distribution and reproduction in any medium, provided the original work is properly cited.

Publisher's Note: AccScience Publishing remains neutral with regard to jurisdictional claims in published maps and institutional affiliations.

dimensional (3D) models address critical limitations by preserving key architectural features, such as extracellular matrix (ECM)–cell crosstalk and the niche architecture of human malignancies.[4] Nevertheless, standard 3D systems remain inadequate for capturing dynamic tumor microenvironment (TME) remodeling or essential mechanical stimuli (e.g., interstitial fluid pressure, vascular shear stress) that drive tumor progression[5] (Figure 1).

Genetically engineered mouse models (GEMMs) and patient-derived xenografts (PDXs) partially overcome these shortcomings. GEMMs recapitulate tumor initiation and progression within native microenvironments, closely modeling molecular and systemic interactions across tumorigenesis, metastasis, and therapeutic response while preserving human cancer characteristics.[6] On the other hand, PDX models, established by engrafting patient-derived tumor fragments into immunodeficient mice, retain TME architecture and replicate the pathological, histological, and genomic profiles of original tumors while maintaining drug response fidelity.[7,8] Nevertheless, both models face significant scalability, time, and cost constraints, hindering clinical translation.[9] Furthermore, these static systems particularly fail to recapitulate hemodynamic parameters (e.g., blood/interstitial flow) essential for studying metastasis, immune recruitment, and drug pharmacokinetics[10] (Figure 1), highlighting the unmet need for dynamically perfusable platforms.

Conventional tumor models, while valuable for foundational insights, are increasingly superseded by microfluidic-integrated tumor-on-a-chip platforms that overcome their limitations through interdisciplinary innovation (Figure 1):

(i) Organoid-on-a-chip: Organoids are generated by isolating normal or cancer stem cells from human epithelial tissues and culturing them within an ECM gel.[11] Under optimized conditions, these cells self-assemble into 3D organoid microstructures, which recapitulate key architectural and functional elements of the human TME.[12–14] The integration of organoid culture with microfluidic technology has created a transformative "organoid-on-a-chip" platform that significantly advances *in vitro* modeling.[15] By enabling precise spatiotemporal control over the cellular microenvironment through dynamic perfusion and regulation of oxygen, nutrients, and mechanical forces, this combined approach overcomes limitations of traditional 3D cultures while better replicating *in vivo* complexity.[16,17] Microfluidic systems facilitate high-throughput parallel culturing of organoids with automated monitoring, revolutionizing drug screening and personalized medicine applications through patient-derived models. The technology allows reconstruction of sophisticated tissue interfaces by incorporating vascular networks, immune cells, and stromal components, thereby closely mimicking TMEs and tissue barriers.[18–20] With capabilities for gradient-based drug testing and enhanced physiological relevance, this next-generation platform shows tremendous potential for cancer research, regenerative medicine, and toxicology. Future developments in 3D bioprinting, vascularization, and artificial intelligence (AI)-assisted analysis promise to further refine these models, potentially reducing the need for animal

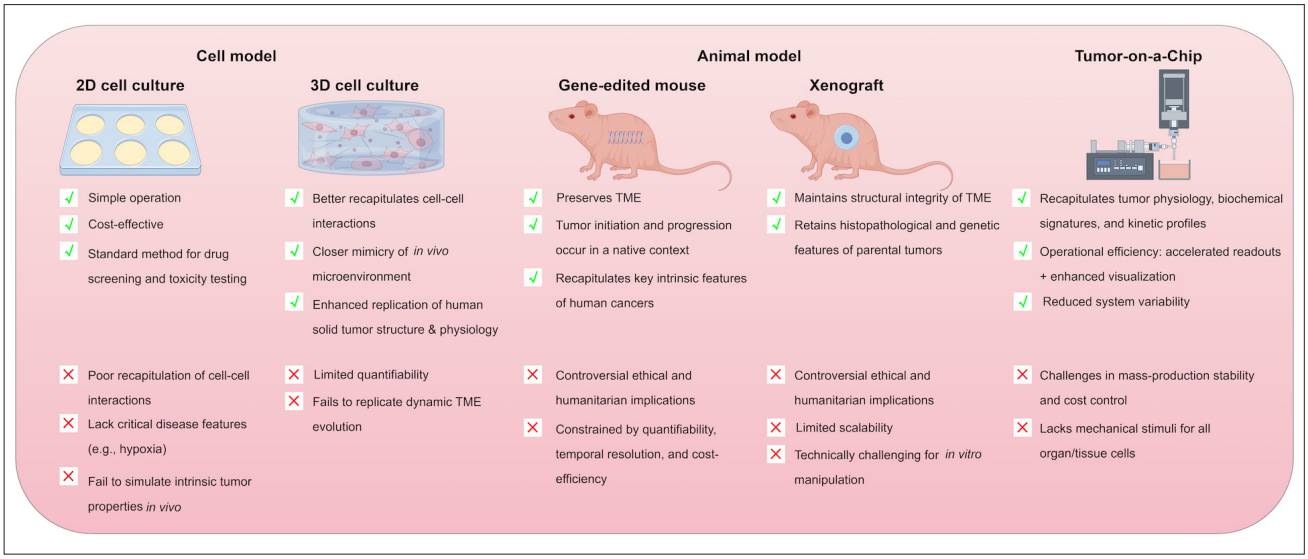

Figure 1. Advantages and limitations of different tumor models.

testing while accelerating translational research with unprecedented precision.

(ii) Organ-on-a-chip: Micro-engineered systems that replicate human organ functions and disease states under controlled conditions. This platform enables precise regulation of cellular microenvironment, closely mimicking *in vivo* tissue architectures and dynamic physiological processes.[21,22] Compared to traditional animal models, organ-on-a-chip platforms provide superior experimental simplicity and cost-efficiency—requiring significantly less infrastructure, reducing ethical constraints, and enabling parallelized experimentation—while achieving unprecedented fidelity in recapitulating human TME dynamics.[23] These micro-engineered systems facilitate precise modeling of multistep carcinogenesis: from initial tumor–stroma interactions and angiogenesis to metastatic intravasation/extravasation, all under physiologically relevant mechanical stimuli. Simultaneously, they support high-throughput drug efficacy screening with real-time resolution of pharmacokinetic/pharmacodynamic relationships.[24] Despite these advantages over animal models, organ-on-a-chip technology faces persistent challenges, including fabrication scalability limitations, material biocompatibility constraints, and the need for advanced sensor integration—all requiring further optimization to achieve clinical predictive validity.[25,26]

(iii) Tumor spheroids: Uniform, high-throughput multicellular spheroids permit drug screening under physiologically relevant conditions. The development of tumor spheroids can be precisely controlled in terms of size and composition through continuous perfusion using microfluidic technology.[27–29] Additionally, integrating 3D-printed scaffolds with microfluidic control enables the precise generation of tumor stem-like spheroids with enhanced physiological relevance.[30] These spheroids simulate a solid tumor 3D structure while retaining cancer stem cell characteristics. They exhibit *in vivo*-like cellular complexity, critical cell–cell interactions, ECM deposition, and chemical gradients that restrict drug diffusion to levels comparable to human tissues.[27,31] Spheroids also serve as models for evaluating drug sensitivity and resistance, typically displaying heightened resistance to chemotherapy and radiotherapy versus 2D monolayers.[32] They enable analysis of growth constraints, such as oxygen tension, nutrient deficiency, radiation effects, and angiogenesis.[33,34] Therefore, convergent advances in 3D bioprinting and tumor-on-a-chip technologies are yielding biomimetic tumor models with unprecedented clinical relevance.[35] 3D printing facilitates personalized manufacturing, complex structure construction, and cost reduction.[36,37] Microfluidics dynamically simulates the TME, enables high-throughput drug screening, and precisely controls physicochemical conditions.[10] Integrating these technologies enhances tumor model humanization and clinical translation, evidenced by successes in tumor-on-a-chip and drug delivery applications[38] (summarized in Table 1).

Existing reviews typically examine microfluidics or 3D printing in isolation, lacking a systematic analysis of their synergistic convergence for oncology applications. Therefore, this review comprehensively elucidates advancements and prospects in integrated microfluidics–3D printing technologies through mechanistic analysis

Table 1. Summary of advanced tumor modeling platforms

Platforms	Principle	Applications	Advantages	Limits
Organoid-on-a-chip	Patient-derived stem cells self-organized in an extracellular matrix gel integrated with microfluidic perfusion control	Personalized therapy development through patient-specific mutation modeling	Reconstructs the human tumor microenvironment's complexity through vascular/immune integration in dynamic microenvironments	Limited replication of native mechanical forces despite perfusion control
Organ-on-a-chip	Micro-engineered systems replicating human organ-level physiology and disease dynamics	High-throughput drug efficacy studies with real-time pharmacokinetic/pharmacodynamic analysis	Models multistep metastasis processes, including intravasation or extravasation, under mechanical stimuli	Faces fabrication scalability challenges and material biocompatibility constraints
Tumor spheroids	Self-assembled 3D cell aggregates enabling high-throughput drug screening under physiological gradients	Initial assessment of chemoradiation resistance and drug toxicity profiles	Recapitulates solid tumor architecture with hypoxic cores and drug diffusion gradients	Lacks vascularization and stromal components, resulting in poor clinical correlation

of core principles and developmental trajectories. Distinctively, this review adopts a deliberately clinical lens—evaluating how these platforms directly address oncology practice gaps, including generating patient-specific tumor models for personalized therapy and liquid biopsy diagnostics at clinically actionable thresholds. Moreover, it uniquely focuses on 3D-printed microfluidic systems engineered explicitly for tumor pathophysiology, dissecting cancer-tailored architectures, such as perfusable vascular networks and metastasis models with tumor-derived bioinks. The review specifically maps applications across physiologically relevant tumor modeling, therapeutic screening, and high-sensitivity biomarker diagnostics using 3D-printed microfluidic platforms. Finally, it provides a forward-looking perspective addressing current technical constraints and emerging frontiers, including transformative four-dimensional/five-dimensional (4D/5D) bioprinting paradigms.

Fundamental principles of microfluidic and 3D bioprinting technologies

2.1. Characteristics of microfluidic technology

Microfluidics manipulates minute fluid volumes (10^{-9} to 10^{-18} L) through microscale channels (tens to hundreds of micrometers).[39] Commercial devices primarily utilize glass, polydimethylsiloxane (PDMS), and thermoplastics for their mechanical stability, chemical inertness, and biocompatibility.[40,41] Three principal fabrication techniques are summarized as follows, and in Table 2[42]:

(i) Micromolding: The most accessible method, requiring minimal equipment, ideal for phase-transition biomaterials such as hydrogels.[43]

(ii) Photolithography: Employing photochemical processes (e.g., photo-degradation/polymerization) to achieve geometrically complex quasi-planar networks with superior design flexibility.[44]

(iii) 3D printing: Offering unparalleled material diversity and spatial freedom through unrestricted nozzle movement, enabling biomimetic vascular networks and organ-on-a-chip architectures unattainable via conventional techniques.[45]

As previously established, microfluidics involves studying and manipulating fluids at submillimeter scales. Unlike macroscale systems, where gravity dominates fluid behavior, surface tension and capillary forces govern fluid dynamics at the microfluidic level. In fluid dynamics, the Reynolds number (R_e) quantifies the ratio of inertial to viscous forces within a fluid, defining its flow regime.[46] It is expressed as:

$$R_e = \frac{ul}{v} \quad (I)$$

where u is fluid velocity, L is characteristic length (e.g., channel hydraulic diameter), and v is kinematic viscosity. Submillimeter microfluidic channels yield low Reynolds numbers ($R_e << 2300$), indicating laminar flow. Under these conditions, flow properties (e.g., velocity and pressure) remain temporally stable and exhibit gradual spatial transitions. These force-dominated characteristics enable key passive functions: microchannel fluid pumping, analyte filtration, selective capture, and droplet generation without external energy.[41] Microfluidic devices are classified by actuation:

Table 2. Summary of preparation methods for microfluidic devices

Microfluidic fabrication techniques	Principle	Materials	Advantages	Limits
Micro-molding	Microfluidic channels are formed by molding biomaterials onto pre-patterned templates, followed by template removal	Biomaterials (e.g., hydrogels) undergoing liquid-to-solid phase transition	Low technical requirements Excellent for prototyping elementary microphysiological scaffolds Requires only basic laboratory equipment	Geometric limitations Mold cost constraints
Photolithography	Light-directed microchannel fabrication via photodegradation or photopolymerization patterning	Optically transparent materials (e.g., hydrogels)	Enables fabrication of arbitrary, complex microfluidic architectures Pattern formation is no longer restricted to material surfaces	Requires a trade-off between patterning resolution and fabrication speed
3D printing	Direct fabrication of microfluidic channels via 3D printing	Universal, suitable for a wide range of materials	Spatial multifunctionality (enabled by unconstrained 3D nozzle mobility)	3D printing technologies exhibit inferior resolution compared to micro-molding or photolithography techniques

(i) Passive devices: Utilize engineered geometries to harness intrinsic forces (e.g., interfacial effects, diffusion, and secondary flows) for fluid mixing and particle control.

(ii) Active devices: Employ external energy sources (e.g., magnetic/acoustic fields) to enhance fluid manipulation.[47]

2.2. Characteristics of 3D printing technology

Additive manufacturing, or 3D printing, constructs 3D objects from computer-aided design/digital models by depositing, connecting, or curing materials layer-by-layer under computer control (e.g., fusing plastic, liquids, or powders).[48,49] Recent advances in 3D printing have revolutionized the fabrication of microfluidic devices, offering unparalleled flexibility in design, material selection, and functional integration. Among the most widely adopted techniques are inkjet 3D printing (i3DP), stereolithography (SLA), two-photon polymerization (2PP), and fused deposition modeling (FDM), each with distinct operational principles, strengths, and limitations.[50]

The I3DP technique excels in multimaterial deposition, enabling the fabrication of heterogeneous tissue constructs with spatially controlled biochemical cues.[51] This capability is particularly valuable for tumor models requiring graded stiffness or embedded vasculature. However, i3DP is limited by moderate resolution (~50–100 μm) and challenges in maintaining droplet uniformity with viscous bioink.[52] SLA leverages photopolymerization to achieve high resolution (<20 μm),[51] critical for replicating intricate microchannel architectures that mimic *in vivo* vascular networks. Despite its precision, SLA is constrained by material brittleness and limited compatibility with cell-laden hydrogels unless modified for biocompatibility. Meanwhile, 2PP stands out for its sub-200 nm feature resolution, enabled by nonlinear optical absorption. This technique is ideal for creating nanoscale topographies that influence cell migration or drug diffusion in cancer models.[51] However, 2PP's slow throughput and high operational costs restrict its use to specialized applications. FDM remains the most cost-effective (<$0.50/cm^3) option for rapid prototyping, using thermoplastics such as polyactic acid or acrylonitrile butadiene styrene. While FDM is accessible and scalable, its resolution (~100–300 μm) and surface roughness often necessitate post-processing for microfluidic applications.

The selection of an optimal 3D printing modality for tumor modeling demands a systematic evaluation of three critical, interdependent parameters: spatial resolution, which governs the precision of microchannel geometries and cellular-scale features; biomaterial compatibility, determining suitability for cell encapsulation, ECM mimicry, and long-term culture viability[53]; and economic feasibility, ensuring a balance among fabrication precision, functional performance, and budget constraints—particularly crucial for large-scale studies. A comprehensive comparative analysis of these factors (summarized in Table 3) is vital to align fabrication strategies with specific research objectives, such as replicating hypoxia gradients, vascular networks, or metastatic microenvironments. Emerging innovations, including hybrid printing techniques (e.g., integrating SLA with i3DP) and advanced bioresins,[54] hold promises for bridging current limitations in resolution, biocompatibility, and cost efficiency, thereby expanding the potential of 3D-printed tumor models.

Table 3. Summary of comparative advantages and limitations of different 3D printing types

3D printing type	Principle	Advantages	Limitations
Inkjet 3D printing	Droplet-by-droplet deposition of liquid materials	Multi-material capability High-speed printing Commercial viability Complex device fabrication	Limited material selection Challenges in droplet optimization Resolution-speed tradeoff
Stereolithography	UV laser sequentially solidifies the photopolymer resin layer-by-layer through point-by-point scanning	Balanced resolution, cost, and performance Superior surface finish Rapid innovation in materials and equipment	Resolution constrained by optical hardware and resin properties Challenges in uncured resin removal Single-material limitation per print
Two-photon polymerization	Nonlinear absorption of femtosecond near-infrared laser enables 3D voxel patterning	Sub-micron resolution (<1 μm) True 3D structuring capability Diverse material options	Extremely slow process High equipment costs Cleanroom requirements Difficult for enclosed microfluidics
Fused deposition modeling	Molten thermoplastic extrusion through a heated nozzle with XY motion control	Low-cost and user-friendly Wide material compatibility Minimal post-processing	Poor surface finish Poor *Z*-axis mechanical strength Low dimensional accuracy (200–500 μm features) Slow printing speed

Compared to traditional manufacturing, 3D printing provides exceptional design freedom and enables personalized, decentralized production. It produces complex geometries with high precision; its additive nature minimizes material waste, reducing costs and environmental impact.[37,55] However, there are still numerous challenges 3D printing technology faces in the biomedical manufacturing field (Table 3): adhesive selection, suboptimal product mechanical properties, limited dimensional accuracy, powder agglomeration, nozzle/distribution size constraints, material limitations, texture/color variations, material longevity, fit/design customization, layer height issues, and construction failures. Product management areas, such as employee training, pricing, cybersecurity, and intellectual property, also require attention.[56]

Cost-effectiveness and personalization drive 3D printing's adoption in traditional manufacturing, healthcare, and biological research. Particularly, SLA—characterized by layer-by-layer UV patterning in photopolymer resins—has gained considerable traction for its cost-effectiveness, high resolution, and ease of use.[57,58] For example, Shafique *et al.*[59] demonstrated that low-cost liquid crystal display 3D printing achieves 50 μm resolution at faster build rates than conventional methods, enabling scalable production of organ-on-a-chip devices. In summary, the integration of 3D printing with tumor microfluidics substantially reduces manufacturing costs and compresses design-to-validation cycles from months to weeks while reducing material waste by 40–60% compared to traditional fabrication.[36] Despite these advances, limitations remain: current 3D printing struggles with microstructures <100 μm, and restricted manufacturing precision[60,61] and insufficient transparency[62] impede sample visualization[63] (Figure 2).

3. Advanced tumor modeling: integrating 3D bioprinting and microfluidic technologies

Conventional static culture systems often inadequately capture the intricate complexity and dynamic nature of TME.[5] Although microfluidic technology has emerged as a promising solution through the development of tumor-on-chip platforms that overcome these limitations, challenges remain regarding cost-effectiveness and scalable production. The integration of 3D printing with microfluidics has consequently become crucial for engineering biomimetic tumor models.[64,65] This synergistic approach offers distinct advantages: microfluidic systems enable continuous perfusion of nutrients and therapeutic agents[5] while recapitulating both 3D tissue architecture and pathophysiological conditions.[66,67]

A notable example is the work by Ayuso *et al.*,[68] who engineered a tumor-lymphatic microfluidic model that closely mimics the 3D organization and functional characteristics, including endothelial barrier properties and lymphangiogenic potential, of *in vivo* lymphatic vessels. This innovative platform was employed to study breast cancer-associated lymphatic dysfunction through the analysis of altered gene expression patterns in lymphatic endothelial cells. As next-generation experimental tools, these tumor-on-chip systems provide physiologically relevant platforms that are transforming cancer research paradigms.

The application of microfluidics has yielded significant insights into fundamental cancer mechanisms, such as collective cancer cell migration/invasion processes (Figure 3A)[69] and hypoxia-inducible factor pathways,[70] substantially advancing both diagnostic and therapeutic development. For example, Ao *et al.*[71] demonstrated the clinical potential of this technology by developing a "mini tumor chip" through tumor cell injection into microwell arrays, enabling prediction of immunotherapy responses in just 24 hours—a dramatic reduction compared to conventional *in vitro* culture durations. Similarly, Ruzycka *et al.*[72] employed microfluidic platforms to model TMEs for metastatic lung cancer investigation, establishing that these systems provide more physiologically accurate assessment of nanomaterial toxicity and therapeutic efficacy while reducing reliance on animal models (Figure 3B).

The integration of 3D printing with microfluidic technology has significantly accelerated the development of tumor-on-chip systems with enhanced physiological relevance. For example, Behroodi *et al.*[73] demonstrated this synergy by combining projected micro-SLA 3D printing with computer-numerical-control micromachining to fabricate large-scale microfluidic molds, streamlining the production of high-resolution devices (Figure 3C). Meanwhile, Steinberg *et al.*[60] engineered fully 3D-printed microfluidic platforms capable of maintaining patient-derived multicellular spheroids for prolonged high-throughput drug screening, thereby facilitating personalized medicine and improving the prediction of optimal therapeutic regimens.

Beyond conventional applications, this combined approach has unlocked unique capabilities in specialized tumor research. For example, in microgravity biology, 3D-printed microfluidic systems overcome critical limitations of traditional culture flasks and plates—such as medium leakage and bubble formation—while offering superior biocompatibility and experimental control. Leveraging this advantage, Silvani *et al.*[74] employed such a platform to subject glioblastoma and endothelial cells to simulated microgravity for 24 hours, enabling

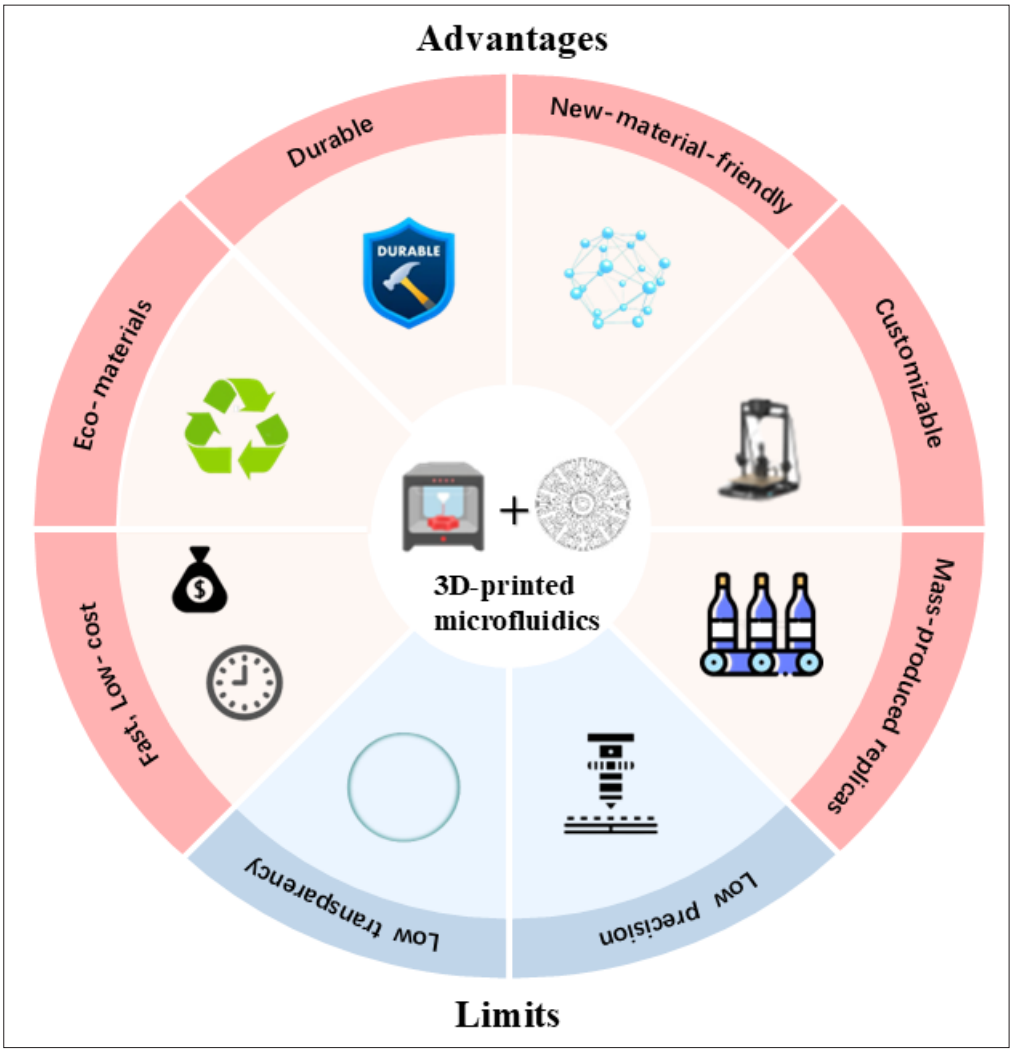

Figure 2. Advantages and limitations of 3D printing combined with microfluidic technology.

mechanistic investigation of cellular adaptation and mechanical signaling pathways in response to altered gravitational forces.

4. Applications in drug screening and therapeutic development

Preclinical development of cancer therapies typically involves testing potential anticancer drugs in tumor cell cultures.[1] The lack of suitable models hinders the development of therapeutic strategies. Researchers have developed diverse *in vitro* cancer models—transwell-based 2D platforms, 3D organoids, hybrid platforms, and microfluidic systems—to simulate tumor tissue and serve as drug research platforms.[75–78] As understanding of cancer biology deepens and microtechnologies advance, microfluidic technology is increasingly utilized in the detection, diagnosis, and treatment of cancer. Its inherent advantages—e.g., minimal sample volume, high sensitivity, and rapid processing—overcome limitations of traditional tumor cultures, such as the lack of dynamic conditions, tissue–tissue interfaces, organ-level structures, and fluid flow.[79,80] These advancements overcome critical limitations of conventional models while positioning microfluidics at the forefront of cancer diagnostics and therapeutic development.

The comparative advantages and disadvantages of leading technologies—PDMS microfluidics versus 3D bioprinting—for tumor therapy applications are systematically evaluated in Table 4, highlighting their distinct application strategies, drug testing scenarios,

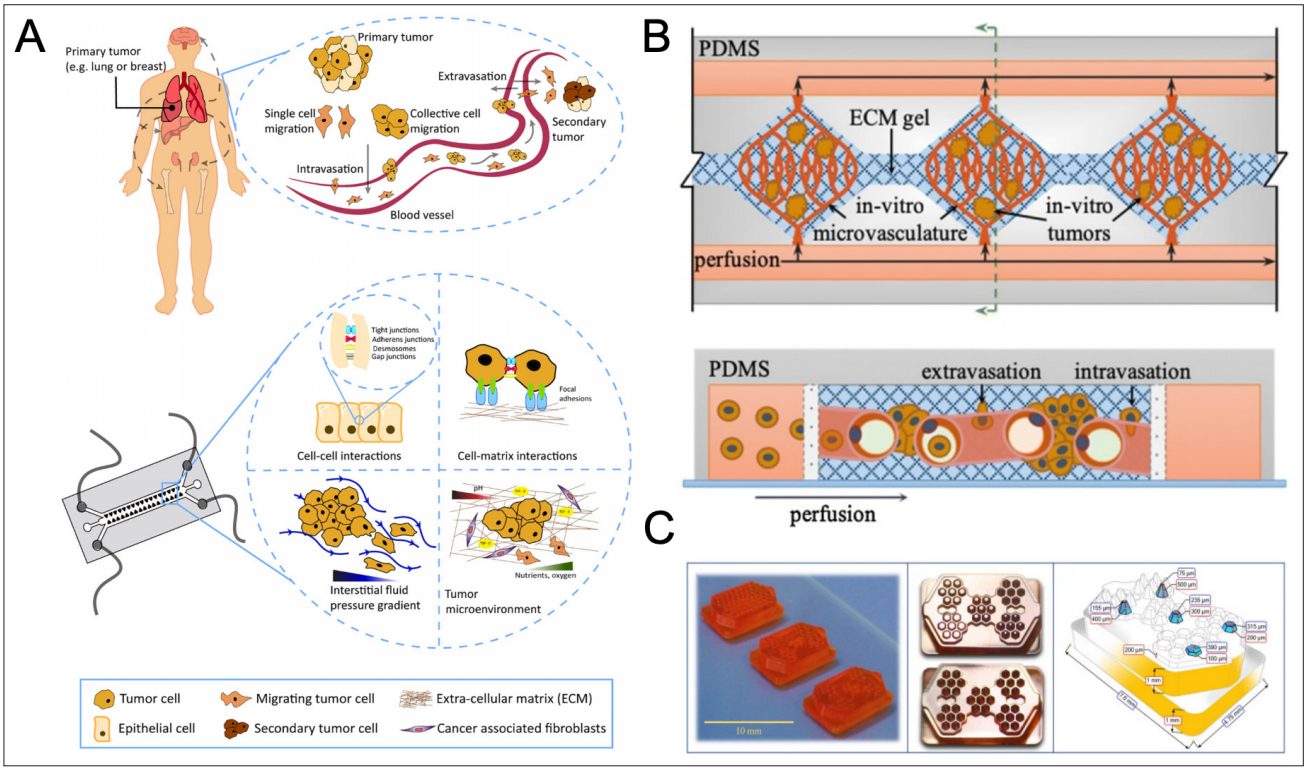

Figure 3. Different tumor models based on 3D printing microfluidic technology. (A) (top) Schematic diagram of the migration behavior of aggressive cancer cells. (Bottom) Application of microfluidics technology in the study of tumor invasion, including real-time imaging of cell–ECM interactions and biophysical changes, controlled application of promigratory factors, pathomimetic tumor microenvironment construction, and organ-specific metastasis modeling. Adapted from Mehta *et al.*[69] (B) Biomimetic microvascular network-on-chip for studying lung cancer metastasis. A diamond-shaped central chamber harbors co-cultured endothelial cells, fibroblasts, and smooth muscle cells within ECM gel, forming a perfusable 3D vasculature. Flanking perfusion channels deliver nutrients or cancer cells. Adapted from Ruzycka *et al.*[72] (C) Different types of 3D-printed molds for the production of 3D tumor spheroid models demonstrate the flexibility of 3D printing to produce microfluidic devices. Adapted from Behroodi *et al.*[73] Abbreviations: PDMS, polydimethylsiloxane; ECM, extracellular matrix.

advantages, and limitations. PDMS microfluidics excel in constructing TME components,[81] enabling spatiotemporal drug delivery control, and culturing spheroids with concentration gradient generation[82] to simulate nutrient and drug transport. However, it faces challenges in scalability. Tumor slice cultivation systems integrate biosensors and mechanical stimuli, but require complex operations,[83] while tumor cell invasion models facilitate high-throughput screening with minimal sample volumes,[84] albeit with contamination risks. PDMS-based *in vitro* cell extravasation models incorporate microvascular networks for real-time imaging, but involve laborious chip fabrication.[85] In addition, Sano *et al.*[86] also mentioned the high absorptivity of hydrophobic small-molecule drugs, leading to significant alterations in effective drug concentration and pharmacokinetic profiles. Key strengths of PDMS include high biomimicry for precise microenvironment replication, excellent reproducibility,[71] and multifunctional integration for real-time monitoring. Its limitations include restricted utility for large tissue specimens, time-consuming fabrication processes (e.g., photolithography), and contamination susceptibility during open operations.[84]

3D printing technologies offer innovative solutions for tumor modeling. For example, Gallegos-Martínez *et al.*[36] and Rahimifard *et al.*[87] developed devices for multicellular and hydrogel-embedded cultures, streamlining prototyping and reducing costs, though SLA resin limitations (e.g., biocompatibility and optical transparency) were noted. Similarly, Ong *et al.*[61] highlighted the user- and eco-friendly nature of 3D printing for spheroid formation assessment. However, resolution limitations at the cellular level, as well as limited optical transparency and biocompatibility concerns with certain materials, remain critical challenges. Li *et al.*[88] employed 3D bioprinting to generate liver cancer cell clusters, reducing preparation workload but facing precision issues that require bioink perfusion. Additionally, Moroni *et al.*[89] stated that most extruded bioprints have

Table 4. Summary of polydimethylsiloxane (PDMS) microfluidics and 3D printing technology in tumor therapy research

Fabrication	Strategy	Drugs	Advantages	Disadvantages	Reference
PDMS	Constructing tumor microenvironment components	Nanoparticles	Precise spatial and temporal control for microenvironment Precise simulation of the in vivo microenvironment Good transport and concentration gradients of nutrients and drugs by fluid flow Ability to integrate with various biosensors and mechanical stimuli Possible for high-throughput screening (low sample volume requirement) Adaptable for real-time imaging and measurements High experimental reproducibility Processing and routine analysis of multicellular spheroids Cost-effective Visualization of in vitro complex phenomena with high resolution Short in vitro culture time	Difficult to scale up No standardized protocol More complex in operation Require external equipment High chance of contamination Laborious process of chip fabrication Closed-system design of CoC devices restricted the utility for culturing larger tissue specimens High absorptivity of hydrophobic small-molecule drugs, leading to significant alterations in effective drug concentration and pharmacokinetic profiles	Oh *et al.*[81]
	Culturing spheroids integrated with a concentration gradient generation	Irinotecan			Lim and Park[82]
	Establishing a tumor slice cultivation system	Cisplatin			Komar *et al.*[83]
	Establishing a tumor cell invasion model	Paclitaxel			Du *et al.*[84]
	Creating an in vitro cell extravasation model with a microvascular network	Engineered T-cells			Pavesi *et al.*[85]
	Uniformly infusing dissociated tumor cells	Anti-PD1 therapeutic agents			Ao *et al.*[71]
	Simulate liver function and evaluate drug metabolism and toxicity	Coumarin			Sano *et al.*[86]
		Midazolam			
		Bufuralol			
3D printing	Using 3D bioprinting to fabricate liver cancer cell clusters and microfluidic chips for cellular maintenance	Metuzumab	Reduced model preparation workload Higher cell proliferation efficiency Streamlining the cycle of designing, prototyping, and testing new microfluidic devices Significant reduction in post-processing time and cost User-friendly Environmentally friendly (compared to polymethyl methacrylate)	Insufficient precision in 3D cell printing (still requires bioink-assisted perfusion), limiting the physiological accuracy of vascularized models Inadequate biocompatibility (SLA resin) Limited optical transparency (SLA resin)	Li *et al.*[88]
	Developing a device to sustain patient-derived multicellular spheroids	Different chemotherapies			Steinberg *et al.*[60]
	Using a device to culture cancer cells or spheroids embedded in hydrogels	Doxorubicin			Gallegos-Martínez *et al.*[36]
	Assessing tumor spheroid formation ability	New pyrazino (1,2-a) benzimidazole derivatives			Rahimifard *et al.*[87]
	Fabricating a perfusion cell culture device	Various drug			Ong *et al.*[61]

Abbreviations: PD1, programmed cell death protein 1; SLA, stereolithography.

a resolution of 50–200 μm, while human capillaries are only 5–10 μm in diameter. This directly leads to the fact that the bioprinted vascular network cannot truly mimic physiological capillaries at scale, and can only produce large "vasculatures" rather than real "capillaries."

In summary, PDMS excels in precision and reproducibility but struggles with scalability, while 3D printing offers rapid prototyping and reduced costs but faces material-related limitations. In clinical practice and scientific research, this review recommends:

(i) For studying nanoparticle transport and vascular permeability: PDMS-based devices are recommended, as they currently offer superior optical clarity for real-time imaging, despite inherent drug absorption issues.

(ii) For generating patient-specific avascular tumor models for high-throughput drug screening:

3D-bioprinted spheroid/organoid arrays present an ideal solution.

(iii) For constructing integrated multitissue models with perfusable vasculature: A hybrid approach utilizing high-resolution 3D-printed molds for PDMS device fabrication currently represents the most viable strategy.

4.1 Precision drug screening using microfluidic device arrays

3D tumor models overcome monolayer limitations by facilitating spatially relevant cell–cell and cell–matrix interactions.[90] Tumor spheroids, well-characterized early-stage cancer models, are widely used in research and drug development due to their simplicity and structural similarity to *in vivo* conditions. Constructed from cancer cells alone or co-cultured with stromal cells (scaffolded or scaffold-free), microfluidics simulates tumor tissue/organs via *in vitro* models and spheroid culture systems, establishing drug screening platforms.[91]

4.1.1. Microfluidic modeling of the tumor microenvironment

Researchers have developed microfluidic 3D tumor models with organ-specific characteristics or varying tumor progression by controlling ECM properties and cellular compositions for applications such as drug screening (Figure 4A).[92] Furthermore, microfluidic devices have been demonstrated to effectively deliver nutrients and/or drugs to tumor tissues through microchannels, thereby sustaining their physiological activities (Figure 4B).[93] The TME comprises heterogeneous ECM components, neighboring cells (e.g., fibroblasts, pericytes, and astrocytes), immune cells, adipocytes, stem cells, vasculature, lymphatics, and physical conditions governing convection/diffusion.[94,95]

Introducing TME components into microfluidic devices allows for the development of tumor models that replicate the *in vivo* environment, while enabling real-time high-resolution imaging for drug testing.[96] For example, Xiong *et al.*[97] developed a customized bladder-shaped microfluidic device with biomimetic guides and triangular markers. This platform enabled long-term culture (more than 4 weeks) of patient-derived spheroids while preserving histopathological and genetic signatures. By optimizing drug diffusion kinetics (uniform distribution within 6 s) and hydrodynamic conditions, the system achieved high-fidelity drug susceptibility testing across eight patients. Each microfluidic device was seeded with 5–15 tumor spheroids, serving as a preclinical model to predict drug response by assessing the effects of different chemotherapeutic agents and their concentrations on the spheroids. Results correlated closely with PDX models and clinical responses, demonstrating their capacity to recapitulate the *in vivo* TME. Crucially, the device overcame limitations of traditional methods (e.g., spheroid loss in ultra-low attachment plates), providing a clinically translatable tool for rapid personalized chemotherapy screening (Figure 4C & D).

Meanwhile, Skubal *et al.*[98] utilized a microfluidic platform to capture the vascularization process during the development of renal cell carcinoma spheroids in real time. They successfully obtained high-resolution images of the tumor-on-a-chip model before and after treatment with bevacizumab to evaluate the efficacy of the vascular-targeting therapy (Figure 4E). Similarly, Oh *et al.*[81] constructed a TME with spatiotemporal control by integrating components (e.g., ECM, vasculature, stromal cells, and interstitial fluid) on-chip, monitoring nanoparticle accumulation/uptake in target cells to address nanomedicine translation challenges. Du *et al.*[84] developed a microfluidic platform simulating/controlling multiple TME factors, evaluating 3D tumor invasion into stroma, and investigating paclitaxel (PTX) effects on cancer cell migration, survival, and morphology. Likewise, Pavesi *et al.*[85] designed a platform reconstructing human umbilical vein endothelial cell microvascular networks to observe cancer cell extravasation and capture T cell movement spatiotemporal data/cytotoxic efficiency, validating T cell therapy.

4.1.2. High-throughput drug screening enabled by the hybrid 3D printing–microfluidics system

Recent advances leverage 3D printing to fabricate microfluidic devices, offering a cost-effective and physiologically relevant strategy that streamlines production, reduces costs, and enables customization. Building on this concept, Steinberg *et al.*[60] engineered a fully 3D-printed microphysiological system capable of maintaining patient-derived tumor spheroids under long-term culture conditions, enabling comprehensive evaluation of drug combination therapies (Figure 4F). Gallegos-Martínez *et al.*[36] introduced a user-friendly, flexible 3D-printed device for culturing cancer cells or organoid spheroids in hydrogels within controlled environments.

Beyond device fabrication, 3D printing can directly generate tumor cell clusters; bioprinting potentially reduces culture cycles and simplifies experimental preparation. For example, Li *et al.*[88] prepared liver cancer cell clusters via 3D cell printing, with the microfluidic chip providing a biomimetic microenvironment, validating the feasibility as a novel *in vitro* drug screening model. What's more, Rahimifard *et al.*[87] used a 3D-printed microfluidic device to evaluate glioblastoma spheroid formation after exposure to novel pyrazinyl [1,2-a] benzimidazole derivatives, assessing

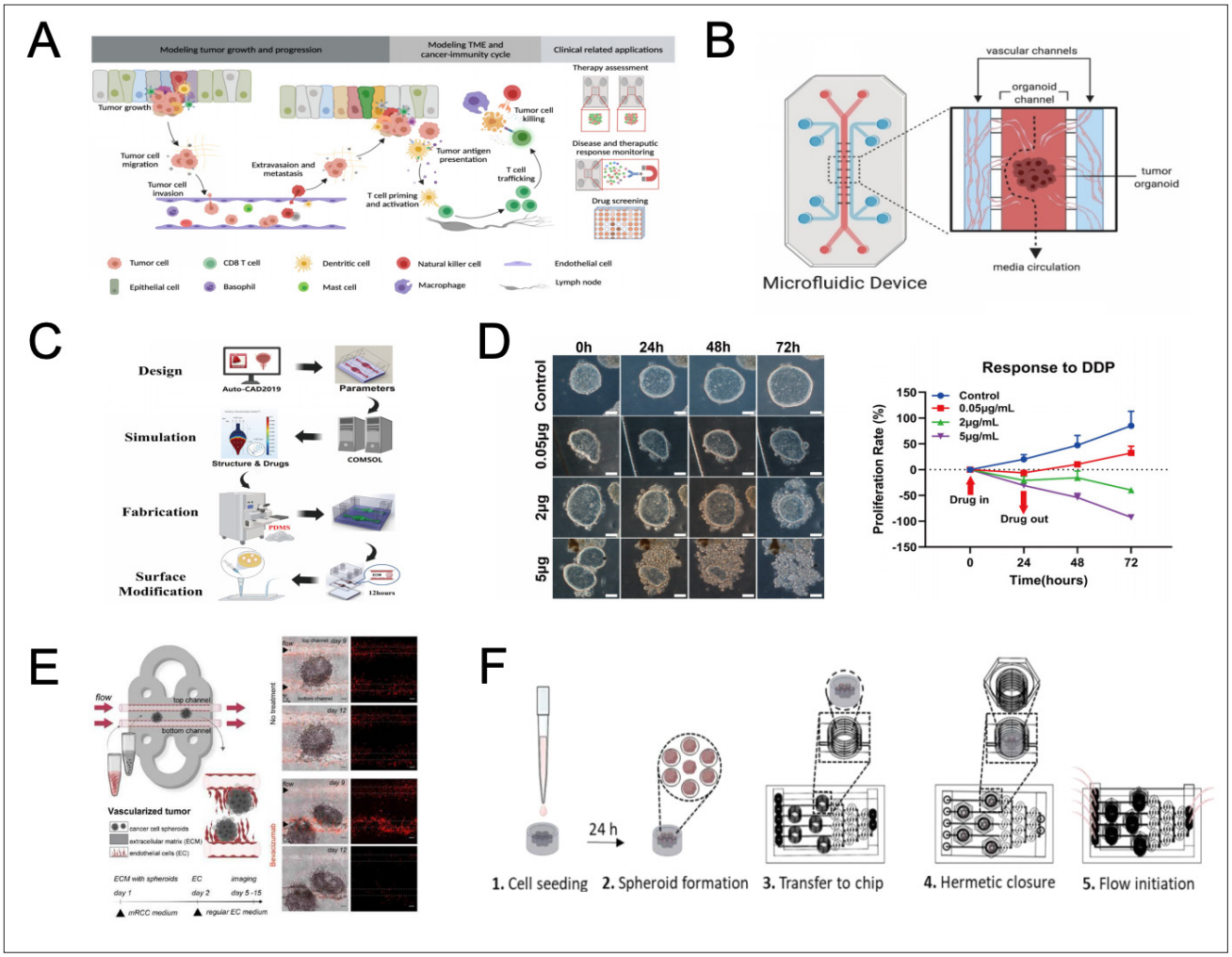

Figure 4. Advanced 3D-printed microfluidic platforms for anticancer drug development. (A) By integrating microfluidic technology with 3D culture systems, it is possible to precisely control matrix structure, cellular composition and ratios, flow velocity, and other characteristics to meet the demands of cancer modeling—such as tumor growth, cancer cell extravasation, and angiogenesis—clinically applied for efficacy evaluation, treatment response monitoring, and drug screening. Adapted from Xie *et al.*[92] (B) A schematic diagram of a tumor-on-a-chip model. Tumor organoids are cultured within the organoid channel, and nutrients and/or drugs are efficiently delivered to the tumor tissue through the vascular channels, enabling the long-term maintenance of the physiological activity of the tumor-like organoids and establishing a media circulation. Adapted from Gunti *et al.*[93] (C) Schematic diagram of the workflow for designing and constructing a microfluidic device for culturing tumor spheroids and drug susceptibility assays. Adapted from Xiong *et al.*[97] (D) Morphological changes of tumor spheroids following treatment with varying concentrations of cisplatin (DDP) (scale bar: 50 μm). Adapted from Xiong *et al.*[97] (E) Schematic illustration of the microfluidic chip setup with an integrated vascularized tumor model and confocal microscopy images of the chips before (Day 9) and after (Day 12) bevacizumab treatment. Left panels show mRCC spheroids (non-fluorescent) co-cultured with endothelial cells (red fluorescence). The right panels show endothelial cells only (red fluorescence). Adapted from Skubal *et al.*[98] (F) Illustration of the operating steps for using the 3D-printed versatile tumor-on-a-chip for spheroid culture. Adapted from Steinberg *et al.*[60]

their inhibitory effects. The application of 3D-printed microfluidics in the establishment of drug screening platforms has streamlined the cycle of designing, fabricating, and testing new devices, reducing the workload for model construction and improving reproducibility. Moreover, these devices demonstrate enhanced biocompatibility in many applications and are more environmentally friendly compared to traditional materials.

4.2 Enhancing cancer therapy using microfluidic drug delivery systems and biomimetic scaffolds

Recent advances in microfluidic technologies have enabled precise control over nanoparticle fabrication, offering significant advantages in reproducibility, scalability, and tunability compared to conventional bulk methods. Current microfluidic device designs, including droplet-based, continuous-flow, and hybrid systems, have been engineered to optimize nanoparticle synthesis through

fine-tuned manipulation of fluid dynamics, mixing efficiency, and interfacial phenomena. These platforms have facilitated the development of diverse nanodelivery systems, such as lipid nanoparticles, polymeric nanocarriers, and inorganic hybrids, tailored for applications in drug delivery, diagnostics, and theranostics (Figure 5A).[99] However, challenges persist in achieving large-scale production, ensuring long-term stability, and addressing biocompatibility concerns. Furthermore, the integration of smart materials, AI-driven optimization,

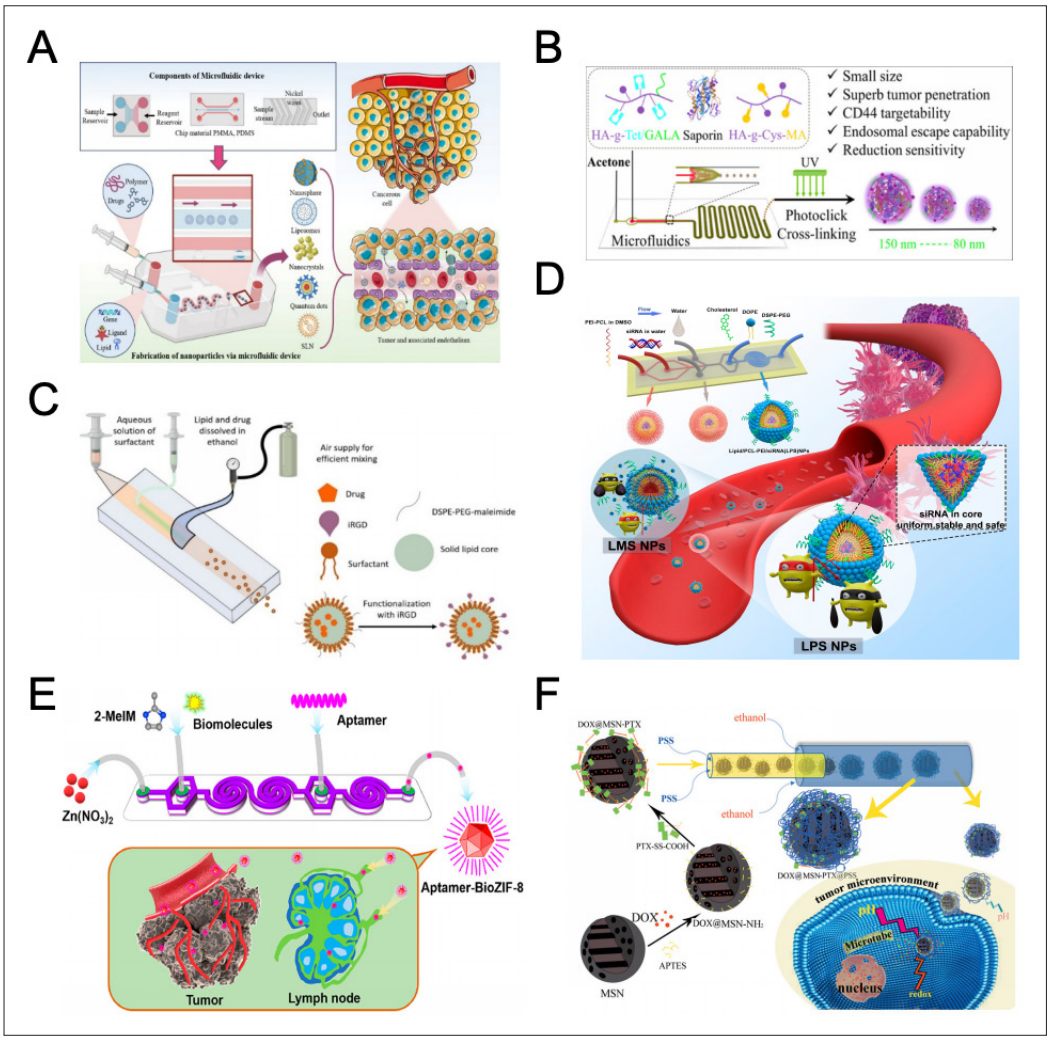

Figure 5. Therapeutic applications of 3D-printed microfluidics in oncology. (A) The fabrication of microfluidic devices and their application in formulating various nanodelivery systems, such as nanospheres, liposomes, nanocrystals, quantum dots, and solid lipid nanoparticles, enhances the efficacy and homogeneity of nanomedicines for tumor therapy. Adapted with permission from G *et al.*[99] Copyright © 2025 American Chemical Society. (B) Microfluidics-fabricated small-sized (with a kinetic diameter of 80–150 nm), tumor-penetrable, endosome-escaping, and bioresponsive hyaluronic acid nanogels (HA-NGs) were developed for cluster of differentiation (CD)44-targeted intracellular delivery of therapeutic proteins. Adapted with permission from Huang *et al.*[103] Copyright © 2019 American Chemical Society. (C) Paclitaxel (PTX)-solid lipid nanoparticles were produced using microfluidic technology by mixing an aqueous surfactant solution with lipids and drug dissolved in ethanol, followed by functionalization with iRGD peptide. Adapted with permission from G *et al.*[99] Copyright © 2025 American Chemical Society. (D) A microfluidic platform facilitates the precise fabrication of core–shell lipid–polymer nanoparticles (LPS NPs) for efficient small interfering RNA (siRNA) delivery. The process initiates with siRNA complexation using low-molecular-weight poly(ethylene imine) (LMW PEI) within reverse micelles, followed by interfacial assembly of a lipid membrane (DOPE/cholesterol/DSPE-PEG) to form monodisperse, anionic nanoparticles. Adapted with permission from Wei *et al.*[105] Copyright © 2020 American Chemical Society. (E) The microfluidic chip enables rapid, one-step synthesis of aptamer-modified biozeolitic imidazolate framework (BioZIF-8) nanoparticles for targeted delivery to lymph nodes and tumors. In the first stage, ZIF-8 nanoparticles encapsulating biomolecules are formed; in the second stage, their surfaces are functionalized with aptamers. Adapted with permission from Balachandran *et al.*[106] Copyright © 2021 American Chemical Society. (F) Schematic illustration of DOX@MSN-PTX synthesis and microfluidic preparation of DOX@MSN-PTX@PSS. The PSS layer swells in the acidic tumor microenvironment, conferring a positive surface charge on the DOX@MSN-PTX@PSS nanoparticles. This facilitates their internalization into tumor cells via endocytosis. Subsequently, the pH and redox conditions within tumor cells trigger the release of doxorubicin and PTX. Adapted from Yan *et al.*[107]

and modular microfluidic architecture presents promising avenues to overcome these limitations and advance next-generation nanomedicine.

Bevacizumab, a humanized anti-vascular endothelial growth factor monoclonal antibody, inhibits malignant cell proliferation/metastasis by suppressing tumor vasculature formation and is clinically approved for angiogenesis inhibition and cancer treatment.[100] However, poor biodistribution and pharmacokinetics limit its bioavailability at tumor sites, reducing efficacy.[101] Microfluidics addresses this by generating size-uniform microgels encapsulating proteins as effective drug carriers. For example, Chen *et al.*[102] developed microgels with tumor adhesive properties and pH-dependent degradability via microfluidics and photopolymerization for sustained local delivery of bevacizumab/docetaxel. This approach normalized tumor vasculature, enabling uniform drug distribution and deeper penetration, thereby improving chemotherapy outcomes and offering a platform for treating recurrent/metastatic cancers. Similarly, Huang *et al.*[103] prepared small, traceable, endosome-disrupting, and bioresponsive nanogels via microfluidics for the cluster of differentiation (CD) 44-targeted cytoplasmic delivery of therapeutic proteins (Figure 5B). Arduino *et al.*[104] developed a biomimetic liposome system based on microfluidic technology and 3D printing, overcoming blood–brain barrier penetration and immune clearance challenges in glioblastoma treatment, enhancing PTX/carboplatin targeting and efficacy. This system offers precise control over nanoparticle synthesis, enabling the development of tailored nanocarriers for targeted central nervous system malignancies therapeutics. Building on this, they developed internalizing Arg-Gly-Asp motif (iRGD)-functionalized PTX-loaded solid lipid nanoparticles via microfluidic technology, enhancing their anticancer potential through selective drug delivery to cancer cells and increased accumulation and penetration at tumor sites. The study also demonstrated that iRGD functionalization improved cellular uptake and cytotoxicity (Figure 5C). Meanwhile, Wei *et al.*[105] utilized microfluidics to synthesize a novel core–shell hybrid nanoparticle with a small interfering RNA (siRNA) core, exhibiting strong siRNA protection and loading capacity, improved *in vivo* stability and biosafety, as well as effective antitumor efficacy (Figure 5D). Balachandran *et al.*[106] developed an integrated microfluidic chip to synthesize aptamer-modified biozeolitic imidazolate frameworks for targeting lymph nodes and tumors (Figure 5E). Yan *et al.*[107] fabricated a pH/redox-triggered mesoporous silica nanoparticle nanoplatform for the co-delivery of doxorubicin/PTX (Figure 5F).

Microfluidics also shows significant potential in tumor immunotherapy. Han *et al.*[108] used commercial devices (Dolomite) for fluoroconjugation of epigallocatechin gallate–ligand–siRNA anti-TOX nanoparticles to regulate tumor cells and exhausted T cells synergistically. Moreover, 3D-printed microfluidic devices show significant promise for advancing drug delivery across the blood–brain barrier. Therefore, by integrating advanced microfluidic platforms for precision nanoparticle synthesis with conventional antitumor drugs, the resulting hybrid drug delivery systems can significantly enhance therapeutic efficacy and targeting specificity. This synergistic approach leverages the tunability of nanocarriers and the proven mechanisms of chemotherapeutic agents, offering a promising strategy to improve cancer treatment outcomes.

Similarly, the integration of 3D printing and microfluidic technologies has led to the development of microfluidic 3D-printed scaffolds, a groundbreaking strategy for addressing post-operative tumor recurrence and facilitating tissue regeneration. A notable example is the work by Zhang *et al.*,[109] who designed a light-responsive platinum (IV) (Pt[IV]) prodrug-loaded scaffold using a microfluidic-assisted 3D printing approach. The scaffold, composed of polymerized gelatin methacryloyl, exploits the photoconversion of low-toxicity Pt(IV) to highly cytotoxic Pt(II) species upon irradiation, enabling localized and controlled drug release. This system demonstrated remarkable tumor-suppressive efficacy, anti-metastatic activity, and pro-regenerative properties in post-surgical applications. Building on this concept, Li *et al.*[110] developed a fish gelatin/berberine composite scaffold for post-operative gastric cancer therapy, exhibiting potent tumor growth inhibition and excellent biocompatibility, further validating the potential of hybrid 3D-printed microfluidic scaffolds in precision oncology and regenerative medicine. These advances highlight the transformative role of convergent biofabrication technologies in developing multifunctional implants for cancer therapy and tissue repair.

While integrated 3D-microfluidic bioprinting platforms have revolutionized preclinical drug development and therapeutic delivery, their clinical impact extends beyond treatment to transformative diagnostic capabilities. The same engineering principles enabling physiologically relevant tumor models and targeted nanotherapeutics—precision fluidic control, biomimetic spatial design, and patient-specific customization—now empower the development of next-generation liquid biopsy platforms. By transitioning focus from therapeutic intervention to early detection and real-time monitoring, these technologies address a critical unmet need in oncology: minimally invasive, longitudinal tracking of tumor dynamics to guide precision therapy adjustments.

5. 3D-printed microfluidic platforms for cancer diagnostics and biomarker detection

While tissue biopsy remains the clinical gold standard for tumor characterization, its invasiveness limits serial disease monitoring, especially when sample volumes are insufficient for diverse molecular testing.[111] Liquid biopsy approaches analyzing circulating tumor-derived components—including circulating tumor cells (CTCs), circulating tumor DNA (ctDNA), exosomes, and proteomic signatures—provide minimally invasive access to real-time tumor dynamics.[112,113] State-of-the-art 3D-printed microfluidic systems have achieved unprecedented precision in tumor biomarker isolation through bioinspired architectures that recapitulate key features of *in vivo* capture microenvironments.[114,115] As comprehensively documented in Table 5, these engineered platforms demonstrate remarkable specificity and efficiency in isolating three critical classes of oncological biomarkers: CTCs, exosomes, and protein markers. Contemporary technological advances have yielded microfluidic designs that incorporate (i) biomimetic surface topographies for enhanced cellular interactions, (ii) tunable fluidic parameters for size-based exosome sorting, and (iii) nanostructured interfaces for ultrasensitive protein detection—collectively representing a paradigm shift in liquid biopsy technologies.[116]

5.1. Microfluidic isolation and detection of circulating tumor cells

CTCs are found in circulation, shed from malignancies to enter the bloodstream and migrate to distant organs, forming metastases.[117] Dissemination from primary tumors initiates metastasis and is a major cause of cancer mortality. CTCs are extremely rare compared to blood cells, making their separation from circulation—or of tumor cells from

Table 5. Summary of studies on 3D-printed microfluidic systems to capture tumor markers

Biomarkers	Microfluidic technology	Results	Advantages	Reference
CTCs	RUBYchip™	The average capture efficiency of renal cell carcinoma is 74.9%, significantly higher than other methods.	Efficiently captures CTCs and remains unaffected by epithelial–mesenchymal transition.	Leitão *et al.*[125]
	Sorting by interfacial tension (SIFT)	Effectively isolates cancer cell subpopulations with high glycolytic activity.	Adjusts the pH selection threshold by altering fluid conditions.	Zielke *et al.*[162]
	A 3D-nanostructured substrate coated with anti-EpCAM	The synergistic effect enhances CTC capture performance observed in blood samples.	The micro-mixer function enhances the interaction between cells and the substrate's local topography.	Wang *et al.*[122,123]
	The Parsortix® PR1 system	Using various downstream analyses to enrich breast cancer cells in a small volume of blood from healthy donors.	Various labeled tumor cell lines can be captured from the blood without being restricted by surface antigens.	Cohen *et al.*[124]
	Hyaluronic acid-functionalized electrospun chitosan nanofiber-integrated microfluidic platform	Specifically captured cluster of differentiation 44-overexpressing cancer cells with an efficiency of up to 91% and achieved 90% complete cell release through treatment with glutathione.	Enables non-destructive release of the captured cells, facilitating subsequent cell analysis.	Wang *et al.*[163]
	V-BioChip	Detecting CTCs in patients with cervical cancer and endometrial cancer; the expression of HER2 and GATA3 in CTCs is highly associated with early recurrence.	Allows for genomic amplification and mutation analysis of individual CTCs, offering potential for personalized treatment.	Law *et al.*[126]
Exosomes	Microfluidic chip	Efficiently and specifically isolates exosomes with high purity and superior yield.	Isolates exosomes from small sample volumes, with the isolated exosomes exhibiting high purity and integrity.	Dorayappan *et al.*[141]
Protein markers	A microfluidic microarray made using 3D printing	Successfully detected the metastatic marker desmoglein 3 and other accompanying biomarkers for head and neck squamous cell carcinoma.	The first microfluidic device with sub-fg level sensitivity for single-cell protein measurements and cancer metastasis.	Sharafeldin *et al.*[144]

Abbreviations: CTC, circulating tumor cell; EpCAM, epithelial cell adhesion molecule; GATA3, GATA binding protein 3; HER2, human epidermal growth factor receptor 2.

body fluids—significant for diagnosis, disease monitoring, and metastasis understanding. In metastatic patients, the peripheral blood CTC concentration is typically extremely low (<10 cells/mL). Efficient recovery of highly pure, viable single CTC or clusters from large blood volumes (>5 mL) poses a core technological challenge. Early strategies relied on CTC-specific surface markers, such as epithelial cell adhesion molecule (EpCAM), exemplified by the antibody-based "CTC-chip". However, affinity-based capture applicability is limited for non-epithelial tumors (e.g., melanoma) and CTCs undergoing epithelial–mesenchymal transition with downregulated EpCAM.[118] Sorting technologies based on physical properties (e.g., size, density, deformability, electrical impedance, and acoustics) have advanced rapidly to address this. Notably, Fachin *et al.*[119] developed a microfluidic device called CTC-iChip to separate CTCs based on cell size and EpCAM expression heterogeneity, overcoming CTC heterogeneity challenges (Figure 6A).

5.2. Integrated microfluidic systems for circulating tumor cells capture and molecular profiling

Leveraging the capabilities of microfluidic devices for microchannel fluid pumping, analyte filtration, and selective capture, alongside the high design flexibility and material versatility offered by 3D printing technology in the fabrication of such devices, researchers have developed diverse and efficient strategies for capturing CTCs.

5.2.1. Optimized microfluidic geometries for improved separation purity and throughput

Leveraging additive manufacturing, Chen *et al.*[62] employed 3D printing to fabricate microfluidic devices featuring tailored microchannel geometries and specialized surface modifications. This innovative approach significantly enhanced CTC capture efficiency by optimizing cell-surface interactions. Stiefel *et al.*[120] integrated immunomagnetic bead enrichment, microfluidic fluorescence activation sorting, and single-cell droplet distribution modules, and designed a multifunctional microfluidic chip including sample storage area, hydrodynamic focusing channel, optical detection area, and cell dispensing nozzle to achieve efficient separation of rare cells, and successfully isolated CTC subsets of head and neck squamous cell carcinoma patients, showing good clinical translation potential and providing real-time monitoring tools for personalized treatment (Figure 6B).

Building on geometric innovation, Tan *et al.*[121] engineered microchannels integrated with crescent-shaped isolation well arrays. These structures incorporated precisely calibrated 5-μm gaps that selectively expelled smaller blood components while retaining target cells, achieving both high-purity capture and efficient background depletion. Further advancing structural design, Wang *et al.*[122,123] systematically compared 3D anti-EpCAM antibody-coated micropillar arrays against conventional planar substrates. Their results confirmed that the 3D-printed nanostructured substrates dramatically increased capture efficiency, attributed to their expanded surface area for ligand binding and optimized local hydrodynamics (Figure 6C & D). For broader clinical applicability, Cohen *et al.*[124] utilized the commercial Parsortix® PR1 system, which exploits serpentine microchannels to perform label-free, size-based CTC separation and enrichment. This method demonstrated robust broad-spectrum capture across diverse tumor lines, irrespective of variable antigen expression profiles.

5.2.2. From lab to clinic: validating 3D-printed microfluidic systems for ultra-sensitive diagnostic applications

Advancing clinical translation, Leitão *et al.*[125] engineered the RUBYchip™, a 3D-printed microfluidic platform that demonstrates superior capture efficiency for renal cell carcinoma compared to conventional methods. Critically, their work established a robust association between CTC enumeration and patient prognosis, highlighting its clinical utility for disease monitoring. Complementing this, Law *et al.*[126] developed a vertically structured 3D-printed biosensor (V-BioChip) for high-efficiency enrichment and detection of CTCs in gynecological malignancies (e.g., cervical/endometrial cancers). Their analysis revealed novel prognostic relationships: expression levels of transcription factors human epidermal growth factor receptor 2/GATA binding protein 3 and surface markers CD13 in captured CTCs showed significant correlations with early cancer recurrence. Collectively, these 3D-printed innovations—through optimized capture performance and biomarker discovery—substantially accelerate the integration of CTC diagnostics into clinical practice (Figure 6E).

5.3. Detection of circulating nucleic acids, exosomes, and protein biomarkers

Over the past decade, microfluidic devices for molecular analysis have made remarkable progress, evolving from proof-of-concept demonstrations to sophisticated platforms capable of performing complex analytical workflows. These miniaturized systems now offer distinct advantages over conventional techniques, including reduced sample/reagent consumption, faster analysis times, improved sensitivity through enhanced mass transport, and the ability to integrate multiple processing steps on a single chip. With demonstrated success in applications ranging from point-of-care diagnostics to high-throughput omics analysis, microfluidics has reached a technological

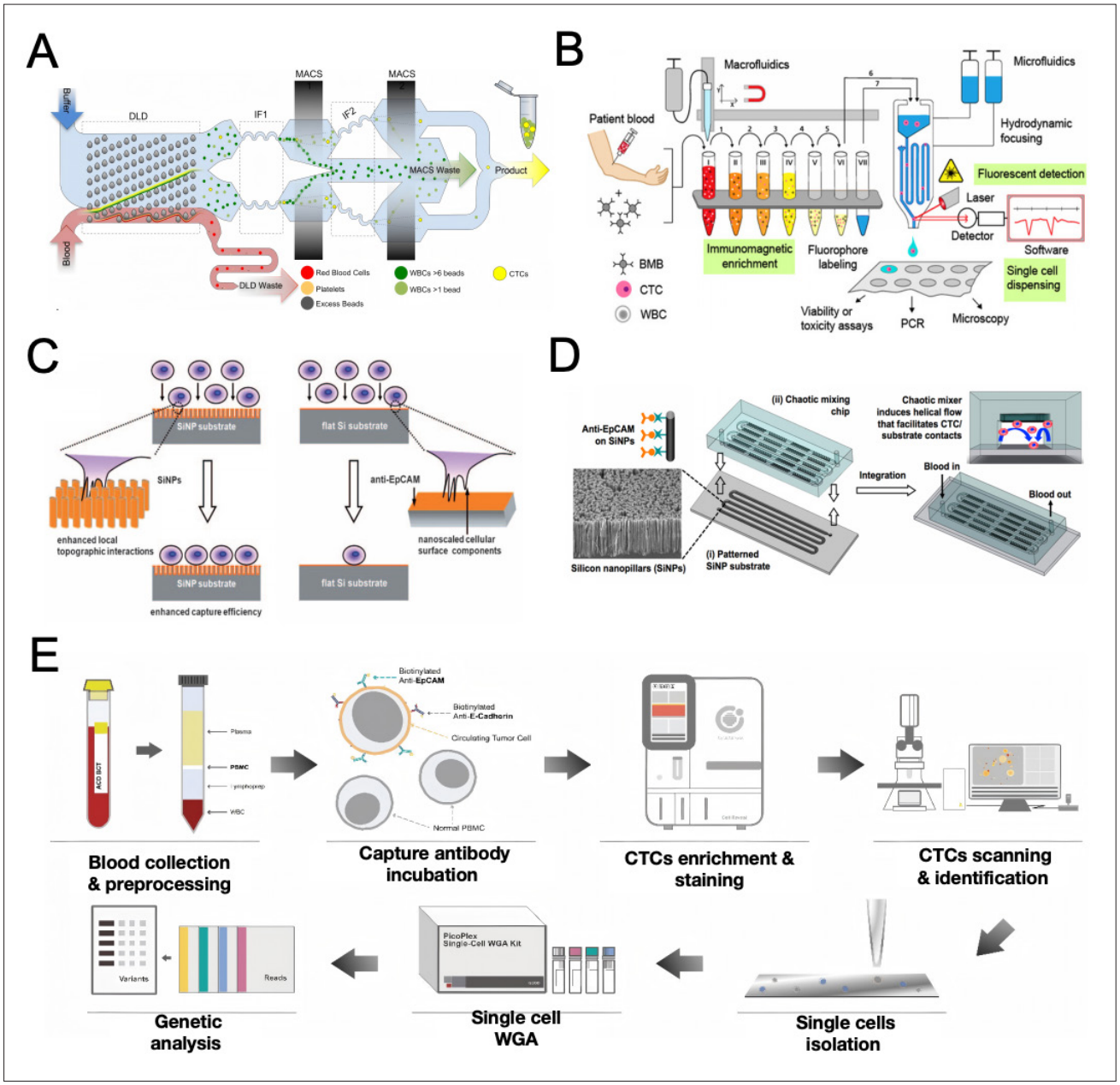

Figure 6. Advanced circulating tumor cell (CTC) isolation platforms using 3D-printed microfluidics. (A) Schematic of a rapid CTC processing chip featuring deterministic lateral displacement for size-based enrichment, coupled with integrated cell handling modules for downstream molecular analysis. Adapted from Fachin *et al.*[119] (B) CTCelect automated workflow for single-cell isolation. Positive selection of tumor cells and subsequent white blood cell (WBC) consumption and fluorophore-conjugated labeling were performed in the enrichment module of the device. The enriched sample is then transferred to the cell sorting subunit into a microfluidic chip for cell sorting and dispensing of single cells in microliter droplets. Adapted from Stiefel *et al.*[120] (C) A new CTC capture platform consisting of patterned SiNP substrates with high CTC affinity and serpentine chaotic mixing channels with anti-EpCAM coatings. The platform enables efficient CTC capture through the synergistic effect of high CTC/substrate affinity and increased contact frequency. Adapted with permission from Wang *et al.*[122] Copyright © 2011 WILEY-VCH Verlag GmbH & Co. KGaA. (D) 3D SiNP architecture coated with anti-EpCAM antibodies demonstrating significantly enhanced capture efficiency (>90%) for cancer cells in whole blood, attributed to increased surface area and biomimetic nanotopography. Adapted with permission from Wang *et al.*[123] Copyright © 2009 WILEY-VCH Verlag GmbH & Co. KGaA. (E) Schematic of the 3D-printed V-BioChip biosensor for gynecological cancers (cervical/endometrial), featuring CTC enrichment via size-based filtration, immunoaffinity-based capture, and on-chip HER2/GATA3 biomarker detection for recurrence risk stratification. Adapted from Law *et al.*[126]

maturity where it can legitimately compete with, and in some cases surpass, traditional analytical methods, including enzyme-linked immunosorbent assay (ELISA), polymerase chain reaction (PCR), and mass spectrometry. Particularly in scenarios requiring portability, automation, or multiplexed detection, microfluidic platforms are increasingly becoming the preferred choice, suggesting they are ready to transition from research laboratories to widespread clinical and industrial adoption. Microfluidic models for molecular diagnostics have emerged as powerful platforms for comprehensive biomarker analysis, particularly through innovative device designs enabling back-to-back processing of CTCs, cell-free DNA (cfDNA), tumor-derived exosomes, and protein biomarker isolation from minimally processed whole blood (Figure 7A).[127]

5.3.1. Circulating nucleic acid separation

Circulating cfDNA, primarily released by apoptotic or necrotic cells, includes tumor-derived mutant fragments termed ctDNA.[128,129] CtDNA is a highly tumor-specific biomarker (Figure 7B).[130–132] However, elevated cfDNA levels also occur in benign conditions or tissue injury, overlapping with early-stage cancer concentrations.[133] Detection systems must therefore discriminate and quantify mutant allele frequencies.[134] Compared to CTC isolation, integrated microfluidic devices for direct quantitative cfDNA isolation from whole blood remain scarce, largely due to extraction challenges from minute volumes and complex preprocessing. Recent advances include nanostructured microelectrode electrochemical sensors enabling amplification-free, direct detection of mutant ctDNA in serum.[135–137]

5.3.2. Tumor-derived exosome enrichment

Exosomes are extracellular vesicles actively secreted by cells, including tumor cells.[138] They carry molecular cargo (e.g., DNA, RNA, proteins, and lipids), harboring rich tumor information. Highly abundant in body fluids and more stable than ctDNA, exosomes enable detection in early-stage cancers, making them promising biomarkers (Figure 7C).[139] Traditional isolation techniques (e.g., ultracentrifugation, precipitation, and filtration) are laborious and time-consuming, as well as yield suboptimal purity. Microfluidic techniques primarily use immunoaffinity capture. The ^{EV}HB-chip, with a Y-configuration, processes milliliters of serum; its nanostructured surface captures vesicles across size ranges, outperforming ultracentrifugation/magnetic bead methods.[140] Dorayappan *et al.*[141] developed a microfluidic device combining anti-CD63 and anti-EpCAM antibodies for high-purity, high-yield specific exosome isolation from culture media/patient serum.

6. Low-abundance protein biomarker isolation

Detection of proteins and their metabolites in microfluidics is among the most mature and commercialized microfluidics applications.[142] Breakthroughs exist in integration, multiplexing, sensitivity, and throughput. Integrated devices perform plasma separation from a blood drop while quantifying multiple proteins, matching conventional ELISA efficiency. Emde *et al.*[143] used 3D printing to develop a chip that detects acute promyelocytic leukemia-specific biomarkers (promyelocytic leukemia-retinoic acid receptor α [PML::RARA] fusion protein), significantly shortening development cycles for rapid prototyping/personalized diagnostics (Figure 7D). Sharafeldin *et al.*[144] designed and 3D-printed a low-cost microfluidic immunoarray for on-chip cell lysis and quantitative protein analysis. Antibodies captured in chambers coated with swellable 3D chitosan hydrogel films enabled sandwich immunosorbent assays, successfully detecting metastatic head and neck squamous cell carcinoma markers, such as desmoglein 3, and co-biomarkers.

Overall, these integrated systems utilize continuous perfusion of whole blood through cascaded microchambers and microchannels that sequentially apply multiple microscale separation principles, including deterministic lateral displacement, inertial focusing, affinity capture, and size-exclusion filtration, to achieve high-purity isolation of diverse blood components, such as leukocytes, CTCs, ctDNA, proteins, and exosomes. Following separation, the captured cells and biomolecules can either be extracted for downstream genomic/proteomic analysis (e.g., single-cell RNA sequencing or digital PCR) or directly analyzed on-chip through integrated detection modules (e.g., impedance cytometry for cellular characterization or surface-enhanced Raman spectroscopy for protein profiling). This "sample-in-answer-out" capability positions microfluidic systems as transformative tools for liquid biopsy applications, offering advantages in automation, multiplexing, and analytical sensitivity compared to conventional centrifugation-based and immunoaffinity-based workflows.

7. Outlook

3D microfluidic tumor models surpass traditional 2D cultures in biological fidelity by closely replicating essential *in vivo* features, such as (i) 3D tissue architecture, (ii) physiologically accurate cell–cell and cell–matrix interactions, and (iii) dynamic nutrient and oxygen gradients. The advent of 3D printing has further revolutionized these systems, enabling rapid prototyping of intricate microstructures while drastically reducing costs and operational complexity compared to animal models.

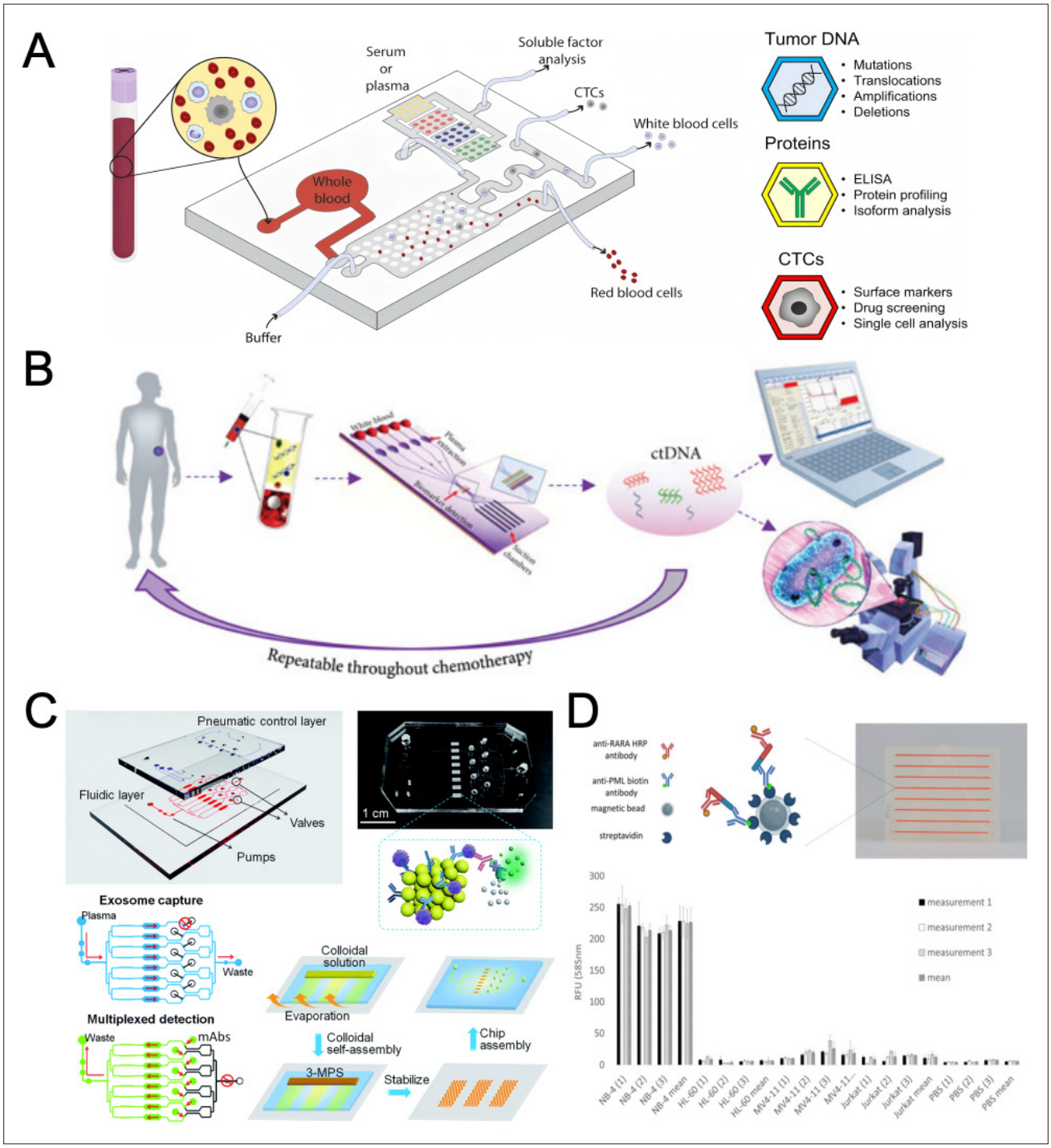

Figure 7. Separation of circulating tumor biomarkers using the 3D printing–microfluidic technology. (A) Theoretical device design for the analysis of circulating tumor cells (CTCs), circulating proteins, and DNA from whole blood. Whole blood is perfused through a series of microchambers and microchannels that leverage several microscale-based separation techniques to isolate multiple components such as immune cells, CTCs, circulating tumor DNA (ctDNA), proteins, and exosomes. Adapted from Ayuso *et al.*[127] (B) Clinical microfluidic devices have revolutionized noninvasive liquid biopsy for ctDNA detection and analysis by enabling rapid, cost-effective, and simple workflows that allow repeatable molecular analysis anytime and anywhere. Adapted from Gauri and Ahmad.[132] (C) An integrated multichannel platform for multiplexed, sensitive, and high-throughput immunophenotyping of circulating exosomes. Adapted from Wang *et al.*[139] (D) 3D-printed microfluidic enzyme-linked immunosorbent assay implementing magnetic bead-based sandwich immunoassay for the ultrasensitive detection of promyelocytic leukemia-retinoic acid receptor α oncoproteins in acute promyelocytic leukemia. Adapted from Emde *et al.*[143]

Beyond tumor modeling, the convergence of microfluidics and 3D printing has driven significant innovations in therapeutic delivery,[145,146] including (i) precision-engineered drug-loaded microcarriers with programmable release kinetics, (ii) patient-specific implantable scaffolds for targeted therapy, and (iii) microphysiological systems for personalized drug screening.

It must be acknowledged that although 3D-printed microfluidics holds considerable promise, it still faces multiple challenges. There exists a fundamental trade-off between resolution and printing speed, where high-precision printing is often time-consuming and requires costly equipment, thereby limiting the fabrication of complex structures and large-scale implementation.[147] Furthermore, existing 3D-printing materials, such as photopolymer resins, exhibit insufficient biocompatibility, optical transparency, and mechanical properties,[148] along with difficulties in achieving multimaterial printing. These limitations make it challenging to meet the stringent requirements of applications such as biological detection and chemical synthesis. Additionally, the lack of standardization in 3D-printed microfluidic devices and competition with conventional microfabrication techniques further hinder their translation from laboratory research to commercial and clinical adoption. Beyond current applications, this review explores how integration with novel biosensing modalities and computational analytics could revolutionize personalized cancer diagnostics and treatment development.

3D-printed microfluidics demonstrates transformative potential in tumor research. Building upon 3D printing, 4D printing introduces a temporal dimension through stimulus–response systems activated by pressure, light, or heat, enabling dynamic modulation of flow dynamics. The reversible shape-changing behavior of soft materials enhances the flexibility and complexity of the microfluidic actuator.[149–151] Utilizing shape-memory polymers' phase-change capability to dynamically tune microchannel geometries via thermal/optical stimuli,[152] next-generation tumor-on-chip models will precisely mimic patient-specific biology and enable real-time drug delivery optimization, advancing precision therapy.

However, 4D printing still faces considerable technical challenges, such as the biocompatibility and long-term stability of shape-memory polymers, precise control over stimulus application, and reproducible dynamic responses under physiological conditions.[153] Moreover, clinical translation is hampered by significant hurdles, including chip-to-human physiological discrepancies, a lack of standardization in fabrication and operational protocols, and the inherent complexity of integrating dynamic materials into biomedical devices.[154,155]

Building on 3D/4D printing, Lai and Wang[156] conceptualized 5D printing: embedded information (e.g., growth factors, nanoparticles, genetic/cellular data) as the fifth dimension. 5D printing yields structures with shape-changing and information-embedding capabilities that actively interact with their environment, unlike passive 3D/4D objects. 5D-printed scaffolds represent a transformative advancement in biofabrication, integrating spatially encoded structural information with dynamic, stimuli-responsive properties that actively interface with native biological microenvironments. These sophisticated constructs achieve two paradigm-shifting capabilities: (i) spatiotemporal control of therapeutic agent release through shape-morphing architectures that respond to physiological cues (e.g., pH, enzymes, and temperature),[34] significantly enhancing treatment precision and efficacy; and (ii) fabrication of organ-level constructs with unprecedented biological fidelity—incorporating vascular networks, heterogeneous cell distributions, and ECM gradients that more accurately recapitulate *in vivo* conditions than conventional 3D models.[157]

Despite these promising advances, 5D printing encounters substantial barriers to clinical adoption. Challenges include scalability, biocompatibility of embedded synthetic components, full recapitulation of human tissue complexity, and regulatory obstacles associated with multicomponent implantable devices. A critical and balanced assessment of these limitations—including safety, manufacturing reproducibility, and validation under clinically relevant conditions—is essential to translate this technology into viable clinical solutions.[156]

The convergence of microfluidics with 5D printing technology is particularly promising for oncology applications,[158] enabling: (a) tumor-on-a-chip platforms with physiologically relevant drug response profiles, (b) biomimetic drug delivery systems that adapt their release kinetics to TME dynamics, and (c) patient-specific tumor models that evolve post-implantation to match disease progression.[159] Recent studies demonstrate 5D-printed scaffolds achieving 92% shape fidelity upon environmental triggering and sustaining three-week drug release profiles with 89% bioactivity retention.[156] This technological synergy addresses critical limitations in conventional drug screening by providing dynamic, vascularized tumor models that better predict clinical outcomes while reducing animal testing requirements (Figure 8).

While 3D-printed microfluidics currently represents an emerging technology still in its developmental phase, it has already demonstrated transformative potential in revolutionizing our understanding of tumor biology. These advanced systems enable researchers to recreate

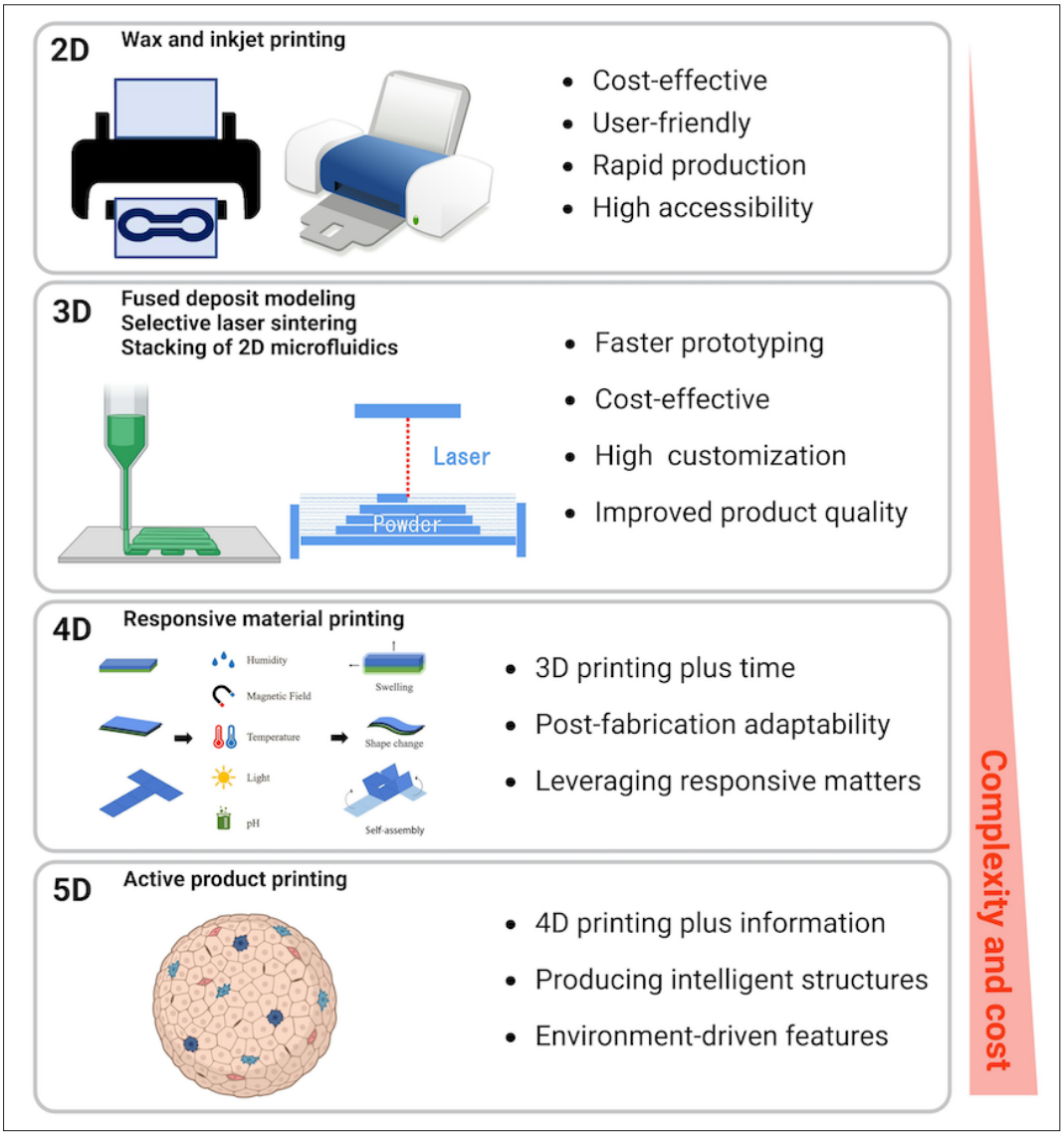

Figure 8. Comparison of 2D, 3D, 4D, and 5D printing technologies. Created in BioRender. Zhicheng, Z. (2025) https://BioRender.com/yq3p4vc.

complex TMEs with unprecedented spatial and temporal precision,[157] facilitating investigations into critical oncological processes such as angiogenesis, metastasis, and drug resistance mechanisms.[160] Technology's unique capability to incorporate multiple cell types, ECM components, and vascular networks within precisely controlled microarchitectures[161] offers a powerful platform for studying tumor–stroma interactions and cellular crosstalk under physiologically relevant conditions.[79]

8. Conclusion

This review provides a systematic examination of the transformative role of conventional and 3D-printed microfluidic technologies in three pivotal areas of cancer research: tumor modeling, therapeutic development, and clinical diagnostics. By comparing these platforms with traditional methodologies, the review underscores their ability to overcome key limitations of conventional approaches.

Looking toward the future, the integration of microfluidics with next-generation 4D and 5D printing technologies promises to usher in a new era of intelligent, adaptive systems for precision oncology. These sophisticated platforms will feature dynamic, stimuli-responsive materials capable of morphological or functional changes in response to specific biological cues, effectively blurring the boundaries between engineered systems and living tissues. Such biologically

integrated engineering solutions are poised to create a seamless continuum from tumor modeling to therapeutic intervention, enabling real-time monitoring of treatment responses, autonomous adjustment of drug release profiles, and continuous optimization of therapeutic strategies based on evolving tumor dynamics. This convergence of technologies represents a paradigm shift in cancer research and treatment, potentially enabling truly personalized medicine approaches that adapt to each patient's unique disease progression.

Acknowledgments

None.

Fundings

This work was supported by the National Natural Science Foundation of China (grant number: 82103260 to K.N.); the Shanghai Rising-Star Program (grant number: 22QA1407100 to K.N.); the Excellent Youth Cultivation Program of Shanghai Sixth People's Hospital (grant number: ynyq202204 to K.N.); and the Fundamental Research Funds for the Shanghai Sixth People's Hospital (grant number: X-2490 to K.N.).

Conflict of interest

The authors declare no conflict of interest.

Author contributions

Conceptualization: Kai Ni
Writing–original draft: Wang Wang, Zhicheng Zhang, Yang Yu, Yikang Wang
Writing–review & editing: Kai Ni
All authors approved the final manuscript for publication.

Ethics approval and consent to participate

Not applicable.

Consent for publication

Not applicable.

Availability of data

Not applicable.

References

1. Day CP, Merlino G, Van Dyke T. Preclinical mouse cancer models: a maze of opportunities and challenges. *Cell*. 2015;163(1):39-53.
doi: 10.1016/j.cell.2015.08.068

2. Kim JW, Ho WJ, Wu BM. The role of the 3D environment in hypoxia-induced drug and apoptosis resistance. *Anticancer Res*. 2011;31(10):3237-3245.

3. Loessner D, Stok KS, Lutolf MP, Hutmacher DW, Clements JA, Rizzi SC. Bioengineered 3D platform to explore cell–ECM interactions and drug resistance of epithelial ovarian cancer cells. *Biomaterials*. 2010;31(32):8494-8506.
doi: 10.1016/j.biomaterials.2010.07.064

4. Katt ME, Placone AL, Wong AD, Xu ZS, Searson PC. In vitro tumor models: advantages, disadvantages, variables, and selecting the right platform. *Front Bioeng Biotechnol*. 2016;4:12.
doi: 10.3389/fbioe.2016.00012

5. Trujillo-de Santiago G, Flores-Garza BG, Tavares-Negrete JA, *et al*. The tumor-on-chip: recent advances in the development of microfluidic systems to recapitulate the physiology of solid tumors. *Materials*. 2019;12(18):2945.
doi: 10.3390/ma12182945

6. Winters IP, Murray CW, Winslow MM. Towards quantitative and multiplexed in vivo functional cancer genomics. *Nat Rev Genet*. 2018;19(12):741-755.
doi: 10.1038/s41576-018-0053-7

7. Yoshida GJ. Applications of patient-derived tumor xenograft models and tumor organoids. *J Hematol Oncol*. 2020; 13(1):4.
doi: 10.1186/s13045-019-0829-z

8. Abdolahi S, Ghazvinian Z, Muhammadnejad S, Saleh M, Asadzadeh Aghdaei H, Baghaei K. Patient-derived xenograft (PDX) models, applications and challenges in cancer research. *J Transl Med*. 2022;20(1):206.
doi: 10.1186/s12967-022-03405-8

9. James Kirkpatrick C, Fuchs S, Iris Hermanns M, Peters K, Unger RE. Cell culture models of higher complexity in tissue engineering and regenerative medicine. *Biomaterials*. 2007;28(34):5193-5198.
doi: 10.1016/j.biomaterials.2007.08.012

10. Nolan J, Pearce OMT, Screen HRC, Knight MM, Verbruggen SW. Organ-on-a-chip and microfluidic platforms for oncology in the UK. *Cancers*. 2023;15(3):635.
doi: 10.3390/cancers15030635

11. Li Z, Li Q, Zhou C, *et al*. Organoid-on-a-chip: current challenges, trends, and future scope toward medicine. *Biomicrofluidics*. 2023;17(5):51505.
doi: 10.1063/5.0171350

12. Drost J, Clevers H. Organoids in cancer research. *Nat Rev Cancer*. 2018;18(7):407-418.
doi: 10.1038/s41568-018-0007-6

13. Xu R, Zhou X, Wang S, Trinkle C. Tumor organoid models in precision medicine and investigating cancer-stromal interactions. *Pharmacol Ther*. 2021;218:107668.
doi: 10.1016/j.pharmthera.2020.107668

14. Quintard C, Tubbs E, Jonsson G, *et al*. A microfluidic platform integrating functional vascularized organoids-on-chip. *Nat Commun*. 2024;15(1):1452. doi: 10.1038/s41467-024-45710-4

15. Yu F, Hunziker W, Choudhury D. Engineering microfluidic organoid-on-a-chip platforms. *Micromachines*. 2019;10(3):165. doi: 10.3390/mi10030165

16. Zhang J, Tavakoli H, Ma L, Li X, Han L, Li X. Immunotherapy discovery on tumor organoid-on-a-chip platforms that recapitulate the tumor microenvironment. *Adv Drug Deliv Rev*. 2022;187:114365. doi: 10.1016/j.addr.2022.114365

17. Li C, Holman JB, Shi Z, Qiu B, Ding W. On-chip modeling of tumor evolution: advances, challenges and opportunities. *Mater Today Bio*. 2023;21:100724. doi: 10.1016/j.mtbio.2023.100724

18. Shirure VS, Hughes CCW, George SC. Engineering vascularized organoid-on-a-chip models. *Annu Rev Biomed Eng*. 2021;23:141-167. doi: 10.1146/annurev-bioeng-090120-094330

19. Zou Z, Lin Z, Wu C, *et al*. Micro-engineered organoid-on-a-chip based on mesenchymal stromal cells to predict immunotherapy responses of HCC patients. *Adv Sci (Weinh)*. 2023;10(27):e2302640. doi: 10.1002/advs.202302640

20. Du Y, Wang YR, Bao QY, *et al*. Personalized vascularized tumor organoid-on-a-chip for tumor metastasis and therapeutic targeting assessment. *Adv Mater*. 2025;37(6):e2412815. doi: 10.1002/adma.202412815

21. Ayuso JM, Rehman S, Virumbrales-Munoz M, *et al*. Microfluidic tumor-on-a-chip model to evaluate the role of tumor environmental stress on NK cell exhaustion. *Sci Adv*. 2021;7(8):eabc2331. doi: 10.1126/sciadv.abc2331

22. Gil JF, Moura CS, Silverio V, Gonçalves G, Santos HA. Cancer models on chip: paving the way to large-scale trial applications. *Adv Mater*. 2023;35(35):e2300692. doi: 10.1002/adma.202300692

23. Ju M, Jin Z, Yu X, *et al*. Gastric cancer models developed via GelMA 3D bioprinting accurately mimic cancer hallmarks, tumor microenvironment features, and drug responses. *Small*. 2025;21(8):e2409321. doi: 10.1002/smll.202409321

24. R N, Aggarwal A, Sravani AB, Mallya P, Lewis S. Organ-on-a-chip: an emerging research platform. *Organogenesis*. 2023;19(1):2278236. doi: 10.1080/15476278.2023.2278236

25. Ko J, Park D, Lee S, Gumuscu B, Jeon NL. Engineering organ-on-a-chip to accelerate translational research. *Micromachines*. 2022;13(8):1200. doi: 10.3390/mi13081200

26. Kimura H, Sakai Y, Fujii T. Organ/body-on-a-chip based on microfluidic technology for drug discovery. *Drug Metab Pharmacokinet*. 2018;33(1):43-48. doi: 10.1016/j.dmpk.2017.11.003

27. Mehta G, Hsiao AY, Ingram M, Luker GD, Takayama S. Opportunities and challenges for use of tumor spheroids as models to test drug delivery and efficacy. *J Control Release*. 2012;164(2):192-204. doi: 10.1016/j.jconrel.2012.04.045

28. El Harane S, Zidi B, El Harane N, Krause KH, Matthes T, Preynat-Seauve O. Cancer spheroids and organoids as novel tools for research and therapy: state of the art and challenges to guide precision medicine. *Cells*. 2023;12(7):1001. doi: 10.3390/cells12071001

29. Li W, Zhou Z, Zhou X, *et al*. 3D biomimetic models to reconstitute tumor microenvironment In vitro: spheroids, organoids, and tumor-on-a-chip. *Adv Healthc Mater*. 2023;12(18):e2202609. doi: 10.1002/adhm.202202609

30. Mehta V, Vilikkathala Sudhakaran S, Nellore V, Madduri S, Rath SN. 3D stem-like spheroids-on-a-chip for personalized combinatorial drug testing in oral cancer. *J Nanobiotechnology*. 2024;22(1):344. doi: 10.1186/s12951-024-02625-y

31. Nayak P, Bentivoglio V, Varani M, Signore A. Three-dimensional in vitro tumor spheroid models for evaluation of anticancer therapy: recent updates. *Cancers*. 2023;15(19):4846. doi: 10.3390/cancers15194846

32. Torisawa YS, Takagi A, Shiku H, Yasukawa T, Matsue T. A multicellular spheroid-based drug sensitivity test by scanning electrochemical microscopy. *Oncol Rep*. 2005;13(6):1107-1112. doi: 10.3892/or.13.6.1107

33. Kelm JM, Fussenegger M. Microscale tissue engineering using gravity-enforced cell assembly. *Trends Biotechnol*. 2004;22(4):195-202. doi: 10.1016/j.tibtech.2004.02.002

34. Banerjee D, Singh YP, Datta P, *et al*. Strategies for 3D bioprinting of spheroids: a comprehensive review. *Biomaterials*. 2022;291:121881. doi: 10.1016/j.biomaterials.2022.121881

35. O'Neill PF, Ben Azouz A, Vázquez M, *et al*. Advances in three-dimensional rapid prototyping of microfluidic devices for biological applications. *Biomicrofluidics*. 2014;8(5):52112. doi: 10.1063/1.4898632

36. Gallegos-Martínez S, Choy-Buentello D, Pérez-Álvarez KA, *et al*. A 3D-printed tumor-on-chip: user-friendly platform for the culture of breast cancer spheroids and the evaluation of anti-cancer drugs. *Biofabrication*. 2024;16(4). doi: 10.1088/1758-5090/ad5765

37. Auricchio F. The magic world of 3D printing. In: *2017 IEEE MTT-S International Microwave Workshop Series on Advanced Materials and Processes for RF and Thz Applications (IMWS-AMP)*. 2017:1-1.
doi: 10.1109/IMWS-AMP.2017.8247328

38. Dong T, Hu J, Dong Y, *et al*. Advanced biomedical and electronic dual-function skin patch created through microfluidic-regulated 3D bioprinting. *Bioact Mater*. 2024;40:261-274.
doi: 10.1016/j.bioactmat.2024.06.015

39. Joseph A, Rajendran A, Karthikeyan A, Nair BG. Implantable microfluidic device: an epoch of technology. *Curr Pharm Des*. 2022;28(9):679-689.
doi: 10.2174/1381612827666210825114403

40. Whitesides GM. The origins and the future of microfluidics. *Nature*. 2006;442(7101):368-373.
doi: 10.1038/nature05058

41. Sackmann EK, Fulton AL, Beebe DJ. The present and future role of microfluidics in biomedical research. *Nature*. 2014;507(7491):181-189.
doi: 10.1038/nature13118

42. Tien J, Dance YW. Microfluidic biomaterials. *Adv Healthc Mater*. 2021;10(4):e2001028.
doi: 10.1002/adhm.202001028

43. Bischel LL, Lee SH, Beebe DJ. A practical method for patterning lumens through ECM hydrogels via viscous finger patterning. *J Lab Autom*. 2012;17(2):96.
doi: 10.1177/2211068211426694

44. Zhang AP, Qu X, Soman P, *et al*. Rapid fabrication of complex 3D extracellular microenvironments by dynamic optical projection stereolithography. *Adv Mater*. 2012;24(31):4266-4270.
doi: 10.1002/adma.201202024

45. Wu W, DeConinck A, Lewis JA. Omnidirectional printing of 3D microvascular networks. *Adv Mater*. 2011;23(24):H178-183.
doi: 10.1002/adma.201004625

46. Gong L, Cretella A, Lin Y. Microfluidic systems for particle capture and release: a review. *Biosens Bioelectron*. 2023;236:115426.
doi: 10.1016/j.bios.2023.115426

47. Gharib G, Bütün İ, Muganlı Z, *et al*. Biomedical applications of microfluidic devices: a review. *Biosensors*. 2022;12(11):1023.
doi: 10.3390/bios12111023

48. Waheed S, Cabot JM, Macdonald NP, *et al*. 3D printed microfluidic devices: enablers and barriers. *Lab Chip*. 2016;16(11):1993-2013.
doi: 10.1039/c6lc00284f

49. Zhang N, Wang Z, Zhao Z, *et al*. 3D printing of micro-nano devices and their applications. *Microsyst Nanoeng*. 2025;11(1):35.
doi: 10.1038/s41378-024-00812-3

50. Logunov L, Ulesov A, Khramenkova V, *et al*. 3D and inkjet printing by colored mie-resonant silicon nanoparticles produced by laser ablation in liquid. *Nanomaterials*. 2023;13(6):965.
doi: 10.3390/nano13060965

51. Sagot M, Derkenne T, Giunchi P, *et al*. Functionality integration in stereolithography 3D printed microfluidics using a "print-pause-print" strategy. *Lab Chip*. 2024;24(14):3508-3520.
doi: 10.1039/D4LC00147H

52. Su R, Wang F, McAlpine MC. 3D printed microfluidics: advances in strategies, integration, and applications. *Lab Chip*. 2023;23(5):1279-1299.
doi: 10.1039/D2LC01177H

53. Groll J, Burdick JA, Cho DW, *et al*. A definition of bioinks and their distinction from biomaterial inks. *Biofabrication*. 2018;11(1):13001.
doi: 10.1088/1758-5090/aaec52

54. Coates IA, Pan W, Saccone MA, *et al*. High-resolution stereolithography: negative spaces enabled by control of fluid mechanics. *Proc Natl Acad Sci U S A*. 2024;121(37):e2405382121.
doi: 10.1073/pnas.2405382121

55. Randhawa A, Dutta SD, Ganguly K, Patel DK, Patil TV, Lim KT. Recent advances in 3D printing of photocurable polymers: types, mechanism, and tissue engineering application. *Macromol Biosci*. 2023;23(1):e2200278.
doi: 10.1002/mabi.202200278

56. Shahrubudin N, Koshy P, Alipal J, Kadir MHA, Lee TC. Challenges of 3D printing technology for manufacturing biomedical products: a case study of Malaysian manufacturing firms. *Heliyon*. 2020;6(4):e03734.
doi: 10.1016/j.heliyon.2020.e03734

57. Naderi A, Bhattacharjee N, Folch A. Digital manufacturing for microfluidics. *Annu Rev Biomed Eng*. 2019;21:325-364.
doi: 10.1146/annurev-bioeng-092618-020341

58. Karamzadeh V, Sohrabi-Kashani A, Shen M, Juncker D. Digital manufacturing of functional ready-to-use microfluidic systems. *Adv Mater*. 2023;35(47):2303867.
doi: 10.1002/adma.202303867

59. Shafique H, Karamzadeh V, Kim G, *et al*. High-resolution low-cost LCD 3D printing for microfluidics and organ-on-a-chip devices. *Lab Chip*. 2024;24(10):2774-2790.
doi: 10.1039/D3LC01125A

60. Steinberg E, Friedman R, Goldstein Y, *et al*. A fully 3D-printed versatile tumor-on-a-chip allows multi-drug screening and correlation with clinical outcomes for personalized medicine. *Commun Biol*. 2023;6(1):1-14.
doi: 10.1038/s42003-023-05531-5

61. Ong LJY, Islam A, DasGupta R, Iyer NG, Leo HL, Toh YC. A 3D printed microfluidic perfusion device for multicellular spheroid cultures. *Biofabrication*. 2017;9(4):045005. doi: 10.1088/1758-5090/aa8858

62. Chen J, Liu CY, Wang X, *et al*. 3D printed microfluidic devices for circulating tumor cells (CTCs) isolation. *Biosens Bioelectron*. 2020;150:111900. doi: 10.1016/j.bios.2019.111900

63. Wang S, Chen X, Han X, *et al*. A review of 3D printing technology in pharmaceutics: technology and applications, now and future. *Pharmaceutics*. 2023;15(2):416. doi: 10.3390/pharmaceutics15020416

64. Han C, Zhang R, He X, *et al*. A digital manufactured microfluidic platform for flexible construction of 3D co-culture tumor model with spatiotemporal resolution. *Biofabrication*. 2024;17(1). doi: 10.1088/1758-5090/ad9636

65. Moghimi N, Hosseini SA, Dalan AB, Mohammadrezaei D, Goldman A, Kohandel M. Controlled tumor heterogeneity in a co-culture system by 3D bio-printed tumor-on-chip model. *Sci Rep*. 2023;13:13648. doi: 10.1038/s41598-023-40680-x

66. Schuster B, Junkin M, Kashaf SS, *et al*. Automated microfluidic platform for dynamic and combinatorial drug screening of tumor organoids. *Nat Commun*. 2020;11(1):5271. doi: 10.1038/s41467-020-19058-4

67. Prince E, Kheiri S, Wang Y, *et al*. Microfluidic arrays of breast tumor spheroids for drug screening and personalized cancer therapies. *Adv Healthc Mater*. 2022;11(1):e2101085. doi: 10.1002/adhm.202101085

68. Ayuso JM, Gong MM, Skala MC, Harari PM, Beebe DJ. Human tumor-lymphatic microfluidic model reveals differential conditioning of lymphatic vessels by breast cancer cells. *Adv Healthc Mater*. 2020;9(3):1900925. doi: 10.1002/adhm.201900925

69. Mehta P, Rahman Z, Ten Dijke P, Boukany PE. Microfluidics meets 3D cancer cell migration. *Trends Cancer*. 2022;8(8):683-697. doi: 10.1016/j.trecan.2022.03.006

70. Morshed A, Dutta P. Hypoxic behavior in cells under controlled microfluidic environment. *Biochim Biophys Acta Gen Subj*. 2017;1861(4):759-771. doi: 10.1016/j.bbagen.2017.01.017

71. Ao Z, Cai H, Wu Z, *et al*. Evaluation of cancer immunotherapy using mini-tumor chips. *Theranostics*. 2022;12(8):3628-3636. doi: 10.7150/thno.71761

72. Ruzycka M, Cimpan MR, Rios-Mondragon I, Grudzinski IP. Microfluidics for studying metastatic patterns of lung cancer. *J Nanobiotechnology*. 2019;17(1):71. doi: 10.1186/s12951-019-0492-0

73. Behroodi E, Latifi H, Bagheri Z, Ermis E, Roshani S, Salehi Moghaddam M. A combined 3D printing/CNC micro-milling method to fabricate a large-scale microfluidic device with the small size 3D architectures: an application for tumor spheroid production. *Sci Rep*. 2020;10(1):22171. doi: 10.1038/s41598-020-79015-5

74. Silvani G, Bradbury P, Basirun C, *et al*. Testing 3D printed biological platform for advancing simulated microgravity and space mechanobiology research. *NPJ Microgravity*. 2022;8(1):19. doi: 10.1038/s41526-022-00207-6

75. Jubelin C, Muñoz-Garcia J, Griscom L, *et al*. Three-dimensional in vitro culture models in oncology research. *Cell Biosci*. 2022;12(1):155. doi: 10.1186/s13578-022-00887-3

76. Vitale S, Calapà F, Colonna F, *et al*. Advancements in 3D in vitro models for colorectal cancer. *Adv Sci*. 2024;11(32):2405084. doi: 10.1002/advs.202405084

77. Yi HG. Introduction to bioprinting of in vitro cancer models. *Essays Biochem*. 2021;65(3):603-610. doi: 10.1042/EBC20200104

78. Yang R, Zhan M, Shen S, *et al*. Microfluidic synthesis of carrier-free full-active metal-phenolic nanocapsules for tumor chemo-chemodynamic-immune therapy. *Adv Funct Mater*. 2025;35(11):2417070. doi: 10.1002/adfm.202417070

79. Sontheimer-Phelps A, Hassell BA, Ingber DE. Modelling cancer in microfluidic human organs-on-chips. *Nat Rev Cancer*. 2019;19(2):65-81. doi: 10.1038/s41568-018-0104-6

80. Yang R, Ouyang Z, Guo H, *et al*. Microfluidic synthesis of intelligent nanoclusters of ultrasmall iron oxide nanoparticles with improved tumor microenvironment regulation for dynamic MR imaging-guided tumor photothermo-chemo-chemodynamic therapy. *Nano Today*. 2022;46:101615. doi: 10.1016/j.nantod.2022.101615

81. Oh HJ, Kim J, Kim H, Choi N, Chung S. Microfluidic reconstitution of tumor microenvironment for nanomedical applications. *Adv Healthc Mater*. 2021;10(9):2002122. doi: 10.1002/adhm.202002122

82. Lim W, Park S. A microfluidic spheroid culture device with a concentration gradient generator for high-throughput screening of drug efficacy. *Molecules*. 2018;23(12):3355. doi: 10.3390/molecules23123355

83. Komar ZM, van Gent DC, Chakrabarty S. Establishing a microfluidic tumor slice culture platform to study drug response. *Curr Protoc*. 2023;3(3):e693. doi: 10.1002/cpz1.693

84. Du Z, Mi S, Yi X, Xu Y, Sun W. Microfluidic system for modelling 3D tumour invasion into surrounding stroma and drug screening. *Biofabrication*. 2018;10(3):034102. doi: 10.1088/1758-5090/aac70c

85. Pavesi A, Tan AT, Chen MB, Adriani G, Bertoletti A, Kamm RD. Using microfluidics to investigate tumor cell extravasation and T-cell immunotherapies. In: *2015 37th Annual International Conference of the IEEE Engineering in Medicine and Biology Society (EMBC)*. 2015: 1853-1856. doi: 10.1109/EMBC.2015.7318742

86. Sano E, Deguchi S, Matsuoka N, *et al*. Generation of tetrafluoroethylene-propylene elastomer-based microfluidic devices for drug toxicity and metabolism studies. *ACS Omega*. 2021;6(38):24859-24865. doi: 10.1021/acsomega.1c03719

87. Rahimifard M, Bagheri Z, Hadjighassem M, *et al*. Investigation of anti-cancer effects of new pyrazino[1,2-*a*] benzimidazole derivatives on human glioblastoma cells through 2D in vitro model and 3D-printed microfluidic device. *Life Sci*. 2022;302:120505. doi: 10.1016/j.lfs.2022.120505

88. Li Y, Zhang T, Pang Y, Li L, Chen ZN, Sun W. 3D bioprinting of hepatoma cells and application with microfluidics for pharmacodynamic test of Metuzumab. *Biofabrication*. 2019;11(3):034102. doi: 10.1088/1758-5090/ab256c

89. Moroni L, Boland T, Burdick JA, *et al*. Biofabrication: a guide to technology and terminology. *Trends Biotechnol*. 2018;36(4):384-402. doi: 10.1016/j.tibtech.2017.10.015

90. Benien P, Swami A. 3D tumor models: history, advances and future perspectives. *Future Oncol*. 2014;10(7): 1311-1327. doi: 10.2217/fon.13.274

91. Jaiswal C, Dey S, Prasad J, Gupta R, Agarwala M, Mandal BB. 3D bioprinted microfluidic based osteosarcoma-on-a chip model as a physiomimetic pre-clinical drug testing platform for anti-cancer drugs. *Biomaterials*. 2025;320:123267. doi: 10.1016/j.biomaterials.2025.123267

92. Xie H, Appelt JW, Jenkins RW. Going with the flow: modeling the tumor microenvironment using microfluidic technology. *Cancers*. 2021;13(23):6052. doi: 10.3390/cancers13236052

93. Gunti S, Hoke ATK, Vu KP, London NR. Organoid and spheroid tumor models: techniques and applications. *Cancers*. 2021;13(4):874. doi: 10.3390/cancers13040874

94. Swartz MA, Iida N, Roberts EW, *et al*. Tumor microenvironment complexity: emerging roles in cancer therapy. *Cancer Res*. 2012;72(10):2473-2480. doi: 10.1158/0008-5472.CAN-12-0122

95. Han J, Jeong HJ, Choi J, *et al*. Bioprinted patient-derived organoid arrays capture intrinsic and extrinsic tumor features for advanced personalized medicine. *Adv Sci (Weinh)*. 2025;12(20):e2407871. doi: 10.1002/advs.202407871

96. Xu K, Huang Y, Wu M, Yin J, Wei P. 3D bioprinting of multi-cellular tumor microenvironment for prostate cancer metastasis. *Biofabrication*. 2023;15(3). doi: 10.1088/1758-5090/acd960

97. Xiong Q, Liu T, Ying Y, *et al*. Establishment of bladder cancer spheroids and cultured in microfluidic platform for predicting drug response. *Bioeng Transl Med*. 2024;9(2):e10624. doi: 10.1002/btm2.10624

98. Skubal M, Larney BM, Phung NB, *et al*. Vascularized tumor on a microfluidic chip to study mechanisms promoting tumor neovascularization and vascular targeted therapies. *Theranostics*. 2025;15(3):766-783. doi: 10.7150/thno.95334

99. G P, Singh M, Gupta PK, Shukla R. Synergy of microfluidics and nanomaterials: a revolutionary approach for cancer management. *ACS Appl Bio Mater*. 2025;8(4):2716-2734. doi: 10.1021/acsabm.5c00123

100. Goel HL, Mercurio AM. VEGF targets the tumour cell. *Nat Rev Cancer*. 2013;13(12):871-882. doi: 10.1038/nrc3627

101. Abdalla AME, Xiao L, Ullah MW, Yu M, Ouyang C, Yang G. Current challenges of cancer anti-angiogenic therapy and the promise of nanotherapeutics. *Theranostics*. 2018;8(2):533-548. doi: 10.7150/thno.21674

102. Chen X, Qian H, Qiao H, *et al*. Tumor-adhesive and pH-degradable microgels by microfluidics and photo-cross-linking for efficient antiangiogenesis and enhanced cancer chemotherapy. *Biomacromolecules*. 2020;21(3):1285-1294. doi: 10.1021/acs.biomac.0c00049

103. Huang K, He Y, Zhu Z, *et al*. Small, traceable, endosome-disrupting, and bioresponsive click nanogels fabricated via microfluidics for CD44-targeted cytoplasmic delivery of therapeutic proteins. *ACS Appl Mater Interfaces*. 2019;11(25):22171-22180. doi: 10.1021/acsami.9b05827

104. Arduino I, Di Fonte R, Sommonte F, *et al*. Fabrication of biomimetic hybrid liposomes via microfluidic technology: homotypic targeting and antitumor efficacy studies in glioma cells. *Int J Nanomedicine*. 2024;19:13217-13233. doi: 10.2147/IJN.S489872

105. Wei W, Sun J, Guo XY, *et al*. Microfluidic-based holonomic constraints of siRNA in the kernel of lipid/polymer hybrid nanoassemblies for improving stable and safe in vivo delivery. *ACS Appl Mater Interfaces*. 2020;12(13):14839-14854. doi: 10.1021/acsami.9b22781

106. Balachandran YL, Li X, Jiang X. Integrated microfluidic synthesis of aptamer functionalized biozeolitic imidazolate framework (BioZIF-8) targeting lymph node and tumor. *Nano Lett*. 2021;21(3):1335-1344.
doi: 10.1021/acs.nanolett.0c04053

107. Yan J, Xu X, Zhou J, *et al*. Fabrication of a pH/redox-triggered mesoporous silica-based nanoparticle with microfluidics for anticancer drugs doxorubicin and paclitaxel codelivery. *ACS Appl Bio Mater*. 2020;3(2):1216-1225.
doi: 10.1021/acsabm.9b01111

108. Han X, Zhang G, Wu X, *et al*. Microfluidics-enabled fluorinated assembly of EGCG-ligands-siTOX nanoparticles for synergetic tumor cells and exhausted t cells regulation in cancer immunotherapy. *J Nanobiotechnology*. 2024;22(1):90.
doi: 10.1186/s12951-024-02328-4

109. Zhang Q, Wang X, Kuang G, Yu Y, Zhao Y. Photopolymerized 3D printing scaffolds with Pt(IV) prodrug initiator for postsurgical tumor treatment. *Research (Wash DC)*. 2022;2022:9784510.
doi: 10.34133/2022/9784510

110. Li J, Zhu T, Jiang Y, Zhang Q, Zu Y, Shen X. Microfluidic printed 3D bioactive scaffolds for postoperative treatment of gastric cancer. *Mater Today Bio*. 2024;24:100911.
doi: 10.1016/j.mtbio.2023.100911

111. Xu Y, Zhu S, Xia C, *et al*. Liquid biopsy-based multi-cancer early detection: an exploration road from evidence to implementation. *Sci Bull*. 2025;70(17):2852-2867.
doi: 10.1016/j.scib.2025.06.030

112. Sun H, Yao X, Jiao Y, *et al*. DNA remnants in red blood cells enable early detection of cancer. *Cell Res*. 2025;35(8):568-587.
doi: 10.1038/s41422-025-01122-7

113. Abusara OH, Agha ASAA, Bardaweel SK. Advancements and innovations in liquid biopsy through microfluidic technology for cancer diagnosis. *Analyst*. 2025;150(9):1711-1725.
doi: 10.1039/d5an00105f

114. Xie Y, Xu X, Wang J, Lin J, Ren Y, Wu A. Latest advances and perspectives of liquid biopsy for cancer diagnostics driven by microfluidic on-chip assays. *Lab Chip*. 2023;23(13):2922-2941.
doi: 10.1039/d2lc00837h

115. Marassi V, Giordani S, Placci A, *et al*. Emerging microfluidic tools for simultaneous exosomes and cargo biosensing in liquid biopsy: new integrated miniaturized FFF-assisted approach for colon cancer diagnosis. *Sensors*. 2023;23(23):9432.
doi: 10.3390/s23239432

116. Asleh K, Dery V, Taylor C, Davey M, Djeungoue-Petga MA, Ouellette RJ. Extracellular vesicle-based liquid biopsy biomarkers and their application in precision immuno-oncology. *Biomark Res*. 2023;11(1):99.
doi: 10.1186/s40364-023-00540-2

117. Hou Y, Lin J, Yao H, Wu Z, Lin Y, Lin JM. Linking metastatic behavior and metabolic heterogeneity of circulating tumor cells at single-cell level using an integrative microfluidic system. *Adv Sci (Weinh)*. 2025;12(14):e2413978.
doi: 10.1002/advs.202413978

118. Sollier E, Go DE, Che J, *et al*. Size-selective collection of circulating tumor cells using Vortex technology. *Lab Chip*. 2013;14(1):63-77.
doi: 10.1039/C3LC50689D

119. Fachin F, Spuhler P, Martel-Foley JM, *et al*. Monolithic chip for high-throughput blood cell depletion to sort rare circulating tumor cells. *Sci Rep*. 2017;7(1):10936.
doi: 10.1038/s41598-017-11119-x

120. Stiefel J, Freese C, Sriram A, *et al*. Characterization of a novel microfluidic platform for the isolation of rare single cells to enable CTC analysis from head and neck squamous cell carcinoma patients. *Eng Life Sci*. 2022;22(5):391-406.
doi: 10.1002/elsc.202100133

121. Tan SJ, Yobas L, Lee GYH, Ong CN, Lim CT. Microdevice for the isolation and enumeration of cancer cells from blood. *Biomed Microdevices*. 2009;11(4):883-892.
doi: 10.1007/s10544-009-9305-9

122. Wang S, Liu K, Liu J, *et al*. Highly efficient capture of circulating tumor cells using nanostructured silicon substrates with integrated chaotic micromixers. *Angew Chem Int Ed Engl*. 2011;50(13):3084-3088.
doi: 10.1002/anie.201005853

123. Wang S, Wang H, Jiao J, *et al*. Three-dimensional nanostructured substrates toward efficient capture of circulating tumor cells. *Angew Chem Int Ed Engl*. 2009;48(47):8970-8973.
doi: 10.1002/anie.200901668

124. Cohen EN, Jayachandran G, Hardy MR, Venkata Subramanian AM, Meng X, Reuben JM. Antigen-agnostic microfluidics-based circulating tumor cell enrichment and downstream molecular characterization. *PLoS One*. 2020;15(10):e0241123.
doi: 10.1371/journal.pone.0241123

125. Leitão TP, Corredeira P, Kucharczak S, *et al*. Clinical validation of a size-based microfluidic device for circulating tumor cell isolation and analysis in renal cell carcinoma. *Int J Mol Sci*. 2023;24(9):8404.
doi: 10.3390/ijms24098404

126. Law KS, Huang CE, Chen SW. Detection of circulating tumor cell-related markers in gynecologic cancer using microfluidic devices: a pilot study. *Int J Mol Sci*. 2023;24(3):2300.
doi: 10.3390/ijms24032300

127. Ayuso JM, Virumbrales-Muñoz M, Lang JM, Beebe DJ. A role for microfluidic systems in precision medicine. *Nat Commun*. 2022;13:3086.
doi: 10.1038/s41467-022-30384-7

128. Xu J, Wan R, Cai Y, *et al*. Circulating tumor DNA-based stratification strategy for chemotherapy plus PD-1 inhibitor in advanced non-small-cell lung cancer. *Cancer Cell*. 2024;42(9):1598-1613.e4.
doi: 10.1016/j.ccell.2024.08.013

129. Jamshidi A, Liu MC, Klein EA, *et al*. Evaluation of cell-free DNA approaches for multi-cancer early detection. *Cancer Cell*. 2022;40(12):1537-1549.e12.
doi: 10.1016/j.ccell.2022.10.022

130. Pantel K, Alix-Panabières C. Liquid biopsy and minimal residual disease — latest advances and implications for cure. *Nat Rev Clin Oncol*. 2019;16(7): 409-424.
doi: 10.1038/s41571-019-0187-3

131. Chen H, Zhou Q. Detecting liquid remnants of solid tumors treated with curative intent: circulating tumor DNA as a biomarker of minimal residual disease (review). *Oncol Rep*. 2023;49(5):1-13.
doi: 10.3892/or.2023.8543

132. Gauri S, Ahmad MR. ctDNA detection in microfluidic platform: a promising biomarker for personalized cancer chemotherapy. *J Sens*. 2020;2020(1):8353674.
doi: 10.1155/2020/8353674

133. Wan JCM, Massie C, Garcia-Corbacho J, *et al*. Liquid biopsies come of age: towards implementation of circulating tumour DNA. *Nat Rev Cancer*. 2017;17(4):223-238.
doi: 10.1038/nrc.2017.7

134. Pekin D, Skhiri Y, Baret JC, *et al*. Quantitative and sensitive detection of rare mutations using droplet-based microfluidics. *Lab Chip*. 2011;11(13):2156-2166.
doi: 10.1039/C1LC20128J

135. He M, Crow J, Roth M, Zeng Y, Godwin AK. Integrated immunoisolation and protein analysis of circulating exosomes using microfluidic technology. *Lab Chip*. 2014;14(19):3773-3780.
doi: 10.1039/C4LC00662C

136. Das J, Ivanov I, Sargent EH, Kelley SO. DNA clutch probes for circulating tumor DNA analysis. *J Am Chem Soc*. 2016;138(34):11009-11016.
doi: 10.1021/jacs.6b05679

137. Im YR, Tsui DWY, Diaz LA, Wan JCM. Next-generation liquid biopsies: embracing data science in oncology. *Trends Cancer*. 2021;7(4):283-292.
doi: 10.1016/j.trecan.2020.11.001

138. Simpson RJ, Lim JW, Moritz RL, Mathivanan S. Exosomes: proteomic insights and diagnostic potential. *Expert Rev Proteomics*. 2009;6(3):267-283.
doi: 10.1586/epr.09.17

139. Wang Y, Wang S, Li L, Zou Y, Liu B, Fang X. Microfluidics-based molecular profiling of tumor-derived exosomes for liquid biopsy. *View*. 2023;4(2):20220048.
doi: 10.1002/VIW.20220048

140. Reátegui E, van der Vos KE, Lai CP, *et al*. Engineered nanointerfaces for microfluidic isolation and molecular profiling of tumor-specific extracellular vesicles. *Nat Commun*. 2018;9(1):175.
doi: 10.1038/s41467-017-02261-1

141. Dorayappan KDP, Gardner ML, Hisey CL, *et al*. A microfluidic chip enables isolation of exosomes and establishment of their protein profiles and associated signaling pathways in ovarian cancer. *Cancer Res*. 2019;79(13):3503-3513.
doi: 10.1158/0008-5472.CAN-18-3538

142. Barbosa AI, Reis NM. A critical insight into the development pipeline of microfluidic immunoassay devices for the sensitive quantitation of protein biomarkers at the point of care. *Analyst*. 2017;142(6):858-882.
doi: 10.1039/C6AN02445A

143. Emde B, Niehaus K, Tickenbrock L. Evaluation of 3D-printed microfluidic structures for use in AML-specific biomarker detection of PML::RARA. *Int J Mol Sci*. 2025; 26(2):497.
doi: 10.3390/ijms26020497

144. Sharafeldin M, Chen T, Ozkaya GU, *et al*. Detecting cancer metastasis and accompanying protein biomarkers at single cell levels using a 3D-printed microfluidic immunoarray. *Biosens Bioelectron*. 2021;171:112681.
doi: 10.1016/j.bios.2020.112681

145. Chen C, Ran B, Liu B, *et al*. Development of a novel microfluidic biosensing platform integrating micropillar array electrode and acoustic microstreaming techniques. *Biosens Bioelectron*. 2023;223:114703.
doi: 10.1016/j.bios.2022.114703

146. Lee D, Tran HQ, Sharma NS, *et al*. 3D-printed microfluidic platform for creating porous nanofibrous microspheres to regulate cell response and enhance tissue regeneration. *Small*. 2025:e2502033.
doi: 10.1002/smll.202502033

147. Nielsen AV, Beauchamp MJ, Nordin GP, Woolley AT. 3D printed microfluidics. *Annu Rev Anal Chem (Palo Alto Calif)*. 2020;13(1):45-65.
doi: 10.1146/annurev-anchem-091619-102649

148. Barbosa F, Coutinho P, Ribeiro MP, Moreira AF, Lourenço LM, Miguel SP. Advancements and challenges in SLA-based microfluidic devices for organ-on-chip applications. *Mater Des*. 2025;256:114254.
doi: 10.1016/j.matdes.2025.114254

149. Lui YS, Sow WT, Tan LP, Wu Y, Lai Y, Li H. 4D printing and stimuli-responsive materials in biomedical aspects. *Acta Biomater*. 2019;92:19-36.
doi: 10.1016/j.actbio.2019.05.005

150. Loo JFC, Ho AHP, Turner APF, Mak WC. Integrated printed microfluidic biosensors. *Trends Biotechnol*. 2019;37(10):1104-1120.
doi: 10.1016/j.tibtech.2019.03.009

151. Ding A, Tang F, Alsberg E. 4D printing: a comprehensive review of technologies, materials, stimuli, design, and emerging applications. *Chem Rev*. 2025;125(7):3663-3771. doi: 10.1021/acs.chemrev.4c00070

152. Zhang C, Cai D, Liao P, *et al*. 4D printing of shape-memory polymeric scaffolds for adaptive biomedical implantation. *Acta Biomater*. 2021;122:101-110. doi: 10.1016/j.actbio.2020.12.042

153. Gara DK, Gujjala R, Prasad PS, Madaboosi N, Ojha S. 4D bioprinting: a review on smart bio-adaptable technology to print stimuli-responsive materials. *Prog Addit Manuf*. 2024;10:4375-4417. doi: 10.1007/s40964-024-00876-7

154. Kalogeropoulou M, Diaz-Payno PJ, Mirzaali MJ, van Osch GJVM, Fratila-Apachitei LE, Zadpoor AA. 4D printed shape-shifting biomaterials for tissue engineering and regenerative medicine applications. *Biofabrication*. 2024;16(2):22002. doi: 10.1088/1758-5090/ad1e6f

155. Maidin S, Wee KJ, Sharum MA, Rajendran TK, Ali LM, Ismail S. A review on 4d additive manufacturing the applications, smart materials & effect of various stimuli on 4d printed objects. *J Teknol Sci Eng*. 2023;85(5): 63-71. doi: 10.11113/jurnalteknologi.v85.19889

156. Lai J, Wang M. Developments of additive manufacturing and 5D printing in tissue engineering. *J Mater Res*. 2023;38(21):4692-4725. doi: 10.1557/s43578-023-01193-5

157. Cheng YJ, Wu TH, Tseng YS, Chen WF. Development of hybrid 3D printing approach for fabrication of high-strength hydroxyapatite bioscaffold using FDM and DLP techniques. *Biofabrication*. 2024;16(2). doi: 10.1088/1758-5090/ad1b20

158. Han X, Saiding Q, Cai X, *et al*. Intelligent vascularized 3D/4D/5D/6D-printed tissue scaffolds. *Nano Micro Lett*. 2023;15(1):239. doi: 10.1007/s40820-023-01187-2

159. Peng S, Yan Y, Ogino K, Ma G, Xia Y. Spatiotemporal coordination of antigen presentation and co-stimulatory signal for enhanced anti-tumor vaccination. *J Control Release*. 2024;374:312-324. doi: 10.1016/j.jconrel.2024.08.025

160. Boussommier-Calleja A, Li R, Chen MB, Wong SC, Kamm RD. Microfluidics: a new tool for modeling cancer-immune interactions. *Trends Cancer*. 2016;2(1):6-19. doi: 10.1016/j.trecan.2015.12.003

161. Kolesky DB, Homan KA, Skylar-Scott MA, Lewis JA. Three-dimensional bioprinting of thick vascularized tissues. *Proc Natl Acad Sci U S A*. 2016;113(12):3179-3184. doi: 10.1073/pnas.1521342113

162. Zielke C, Pan CW, Gutierrez Ramirez AJ, *et al*. Microfluidic platform for the isolation of cancer-cell subpopulations based on single-cell glycolysis. *Anal Chem*. 2020;92(10):6949-6957. doi: 10.1021/acs.analchem.9b05738

163. Wang M, Xiao Y, Lin L, Zhu X, Du L, Shi X. A microfluidic chip integrated with hyaluronic acid-functionalized electrospun chitosan nanofibers for specific capture and nondestructive release of CD44-overexpressing circulating tumor cells. *Bioconjug Chem*. 2018;29(4):1081-1090. doi: 10.1021/acs.bioconjchem.7b00747

ACCSCIENCE PUBLISHING

International Journal of Bioprinting

REVIEW ARTICLE

Biomimetic and personalized optimization of additively manufactured metallic bone implants: Design, simulation, and clinical outcomes

Lamiae Jaouher[1], Abdelwahed Barkaoui[1,2]*, Khalil Aouadi[3], and Haifa Sallem[4]

[1]LERMA Lab, International University of Rabat, Parc Technopolis, Rocade de Rabat-Sale, Morocco

[2]LMAI Lab, Ecole Nationale d'Ingénieurs de Tunis, Université de Tunis El Manar, Tunisia

[3]Engineering and Durability of Materials Center, Moroccan Foundation for Advanced Science, Innovation & Research (MAScIR), Mohammed VI Polytechnic University, Hay Moulay Rachid, Ben Guerir, Morocco

[4]Institute of Systems Engineering (HEI), HES-SO Valais-Wallis, University of Applied Sciences and Arts Western Switzerland (HES-SO), Sion, Switzerland

(This article belongs to the *Special Issue: 3D Printing for Advancing Orthopedic Applications*)

Abstract

Additive manufacturing (AM) has transformed the field of metallic bone implants by enabling the production of patient-specific, biomimetic, and high-performance devices. This review focuses on the personalized design of bone implants using AM technologies, particularly selective laser melting and electron beam melting, which allow the fabrication of complex lattice structures that replicate the trabecular architecture of native bone. These architectures enhance load transfer, reduce stress shielding, and promote osseointegration. The review also explores current strategies and digital tools for biomimetic design, as well as numerical simulation methods—including finite element analysis, computational fluid dynamics, and multi-field coupling models—used to optimize implant geometry, porosity, and mechanical performance. Furthermore, recent clinical and preclinical data on *in vivo* functionality and biological integration are synthesized, with emphasis on the latest advancements to enhance functional outcomes. Altogether, the work provides a comprehensive roadmap for researchers and clinicians seeking to advance implant innovation and improve skeletal tissue repair.

Keywords: Additive manufacturing; Biomimetic implants; Electron beam melting; Lattice structures; Numerical simulation; Personalized bone implants; Selective laser melting

***Corresponding author:**

Abdelwahed Barkaoui (abdelwahed.barkaoui@uir.ac.ma)

Citation: Jaouher L, Barkaoui A, Aouadi K, Sallem H. Biomimetic and personalized optimization of additively manufactured metallic bone implants: Design, simulation, and clinical outcomes. *Int J Bioprint*. 2025;11(6):51-82. doi: 10.36922/IJB025270261

Received: July 1, 2025
Revised: August 3, 2025
Accepted: August 6, 2025
Published online: August 19, 2025

Copyright: © 2025 Author(s). This is an Open Access article distributed under the terms of the Creative Commons Attribution License, permitting distribution, and reproduction in any medium, provided the original work is properly cited.

Publisher's Note: AccScience Publishing remains neutral with regard to jurisdictional claims in published maps and institutional affiliations.

1. Introduction

Musculoskeletal disorders are among the most prevalent global health conditions, affecting more than 1.7 billion people worldwide, according to the World Health Organization.[1] Chronic conditions such as osteoarthritis, osteoporosis, and trauma-induced fractures often result in significant pain, loss of mobility, and reduced independence. As global populations age, the incidence of these disorders continues to

rise, contributing to an increasing demand for bone repair and replacement procedures. According to *The Lancet*, over 2.86 million knee and 1.32 million hip replacements are performed each year,[2] a number expected to increase with longer life expectancy and the rising burden of degenerative joint diseases. This growing clinical need has led to major innovations in implant technology, particularly the development of metallic implants capable of enduring high mechanical loads while promoting biological integration. However, conventional manufacturing processes are often limited in their ability to produce geometrically complex, anatomically tailored, and functionally graded structures. These constraints have accelerated the adoption of additive manufacturing (AM). The biomedical AM market is experiencing unprecedented growth, projected to reach USD 4.7 billion by 2027, with metallic implants comprising more than 45% of this market.[3] Unlike subtractive techniques, AM offers unprecedented design freedom, paving the way for the development of patient-specific implants with precise control over geometry, porosity, and internal architecture. This capability is particularly valuable for creating lightweight structures with mechanical properties that closely mimic natural bone.[4] Since its inception in the 1980s with stereolithography (SLA), AM has evolved from a rapid prototyping tool to a robust platform for fabricating end-use medical devices. Notable milestones include the first fully 3D-printed prosthetic leg in 2008 and the first mandibular implant in 2012.[5] According to classifications by the International Organization for Standardization and the American Society for Testing and Materials, AM comprises a wide range of processes, including powder bed fusion (PBF), SLA, directed energy deposition (DED), material extrusion fused deposition modeling/fused filament fabrication, and vat photopolymerization digital light processing.[6] Among these, PBF technologies have emerged as the leading methods for metallic implant fabrication due to their precision, microstructural control, and ability to produce highly complex designs. Concurrently, polymer-based AM techniques remain widely used for anatomical models, surgical guides, and bioresorbable scaffolds, particularly in regenerative medicine.[7,8]

Importantly, AM is no longer regarded merely as a fabrication technique, but rather as a central component of an integrated digital workflow. This ecosystem encompasses medical imaging for anatomical data acquisition, image segmentation, biomimetic lattice design, computer-aided design (CAD) modeling, and advanced numerical simulations. Within this context, biomimetic design strategies are increasingly adopted to replicate the hierarchical structure and mechanical behavior of native bone, thereby improving implant functionality and integration.

This review focuses on the personalized design of bone implants using AM technologies, the implementation and outcomes of numerical simulation models, and the clinical performance of additively manufactured metallic implants. As illustrated in **Figure 1**, the paper begins with an overview of AM technologies, comparing selective laser melting and electron beam melting (EBM) in terms of process parameters and suitability for biomedical applications. It then critically analyzes mechanical properties and material selection, emphasizing the clinical relevance of Ti–6Al–4V and cobalt–chromium (Co–Cr) alloys for their strength, biocompatibility, and long-term reliability. A dedicated section discusses *in vivo* performance and clinical validation of AM implants. Subsequently, the review presents key digital tools and strategies for biomimetic implant design, including porous and lattice architectures and the latest advancements in personalized bone implant optimization. Finally, an in-depth analysis is provided on numerical simulation techniques—including finite element analysis (FEA), computational fluid dynamics (CFD), and multi-field coupling models—employed to predict mechanical behavior, assess stress distribution, and optimize implant geometry and functionality.

2. Applications for additive manufacturing in metallic bone implants

AM has rapidly gained prominence in the biomedical field, especially in the development of bone implants. As shown in **Figure 2**, the exponential rise in AM-related publications between 2007 and 2024 highlights its growing integration into disciplines such as materials science and orthopedic surgery. AM constructs components layer by layer from CAD models, offering exceptional geometric flexibility and personalization. The general digital workflow is illustrated in **Figure 3**, enabling the fabrication of implants directly adapted to patient anatomy using medical imaging data.

In orthopedic surgery, AM is increasingly used to produce load-bearing implants such as femoral stems, femoral heads, acetabular cups, and tibial trays. These components benefit from precise anatomical fit, reduced intraoperative adjustments, and design freedom that supports functional optimization.[9,10] Similarly, in spinal applications, AM enables the creation of intervertebral fusion cages and vertebral body replacements with tailored mechanical behavior and surface structures to support spinal stability and biological integration.[11,12] In maxillofacial and craniofacial reconstruction, AM is widely used to fabricate custom implants for the mandible, zygomatic arch, and orbital floor, particularly in trauma or

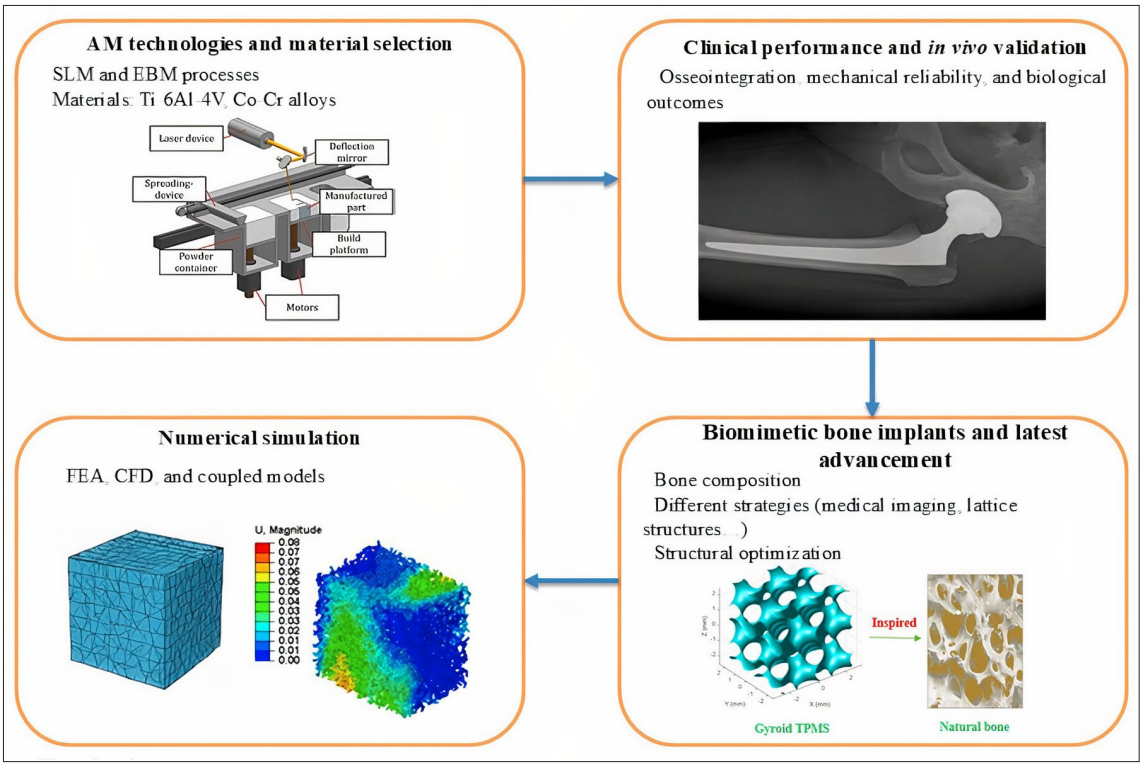

Figure 1. Graphical summary of the review paper. Abbreviations: AM:, additive manufacturing; EBM, electron beam melting; CFD, computational fluid dynamics; FEA, finite element analysis; SLM, selective laser melting; Ti–6Al–4V, titanium alloy with 6% aluminum and 4% vanadium.

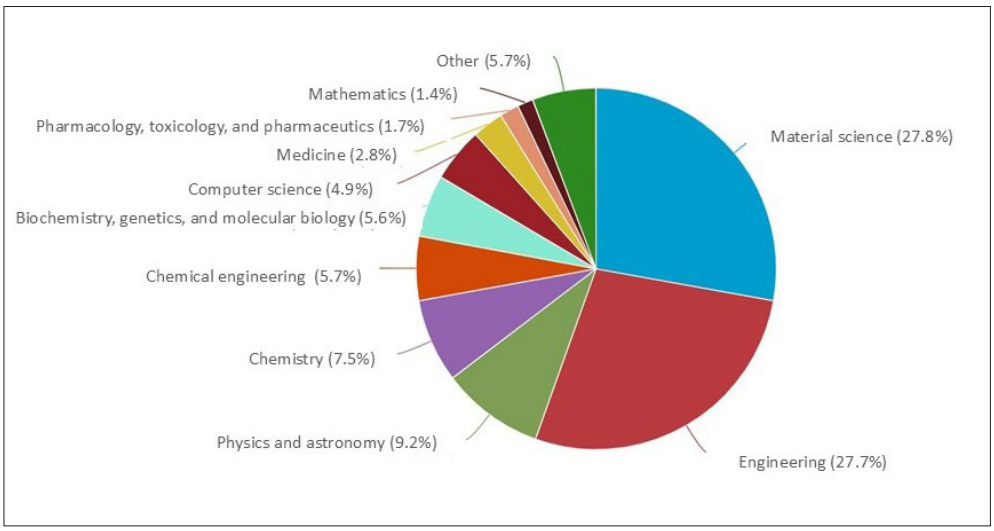

Figure 2. Distribution of publications on AM in biomedicine. Source: SCOPUS. Abbreviation: AM, additive manufacturing.

tumor resection cases. The ability to reproduce complex bone contours and integrate functional elements, such as fixation holes, contributes to improved surgical outcomes.[13] Another critical application is in revision surgeries and the management of large bone defects, particularly in the pelvis or proximal femur, where standard implants are insufficient due to irregular or deficient bone structures. AM allows for the rapid production of customized implants with integrated design features, thereby improving fixation and long-term clinical stability.[14] An overview of these metallic AM applications across various anatomical regions is presented in **Figure 4**.

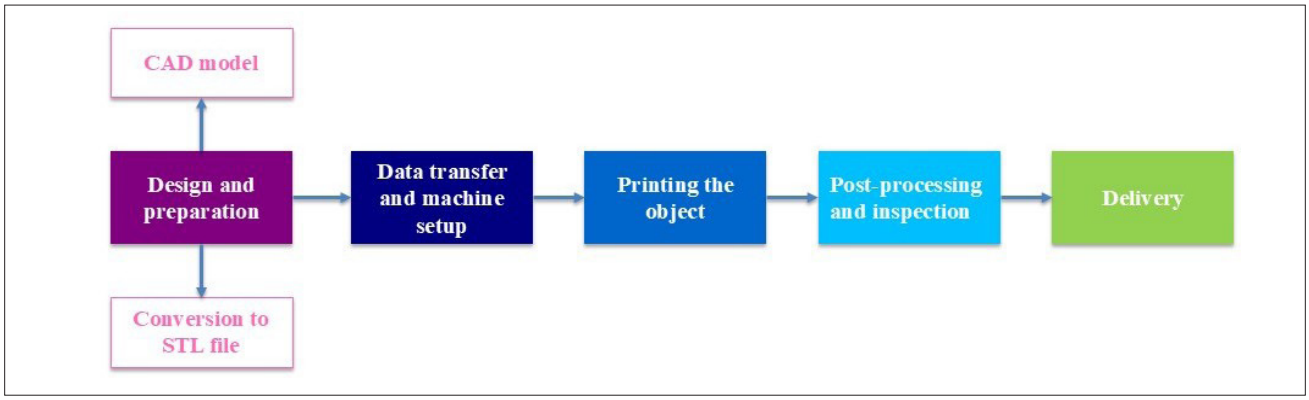

Figure 3. General steps of AM. Abbreviations: AM, additive manufacturing; CAD, computer-aided design; STL, standard tessellation language.



Figure 4. Examples of metallic implants using AM. (A) Knee implant. (B) Craniofacial implant. (C) Spinal implant. (D) Hip implant. Adapted from ref. [13] Abbreviation: AM, additive manufacturing.

Building on these diverse anatomical applications, recent advancements have introduced new paradigms in AM—such as 4D, 5D, and 6D printing—considered evolutionary extensions of conventional 3D printing aimed at further enhancing implant functionality, adaptability, and patient-specific integration. For example, 4D printing incorporates smart materials, such as shape-memory alloys or stimuli-responsive polymers, allowing implants to adapt dynamically to physiological changes. This opens the door to self-adjusting orthopedic devices capable of improving fit or functionality post-implantation.[15,16] Similarly, 5D printing utilizes multi-axis deposition of curved layers,

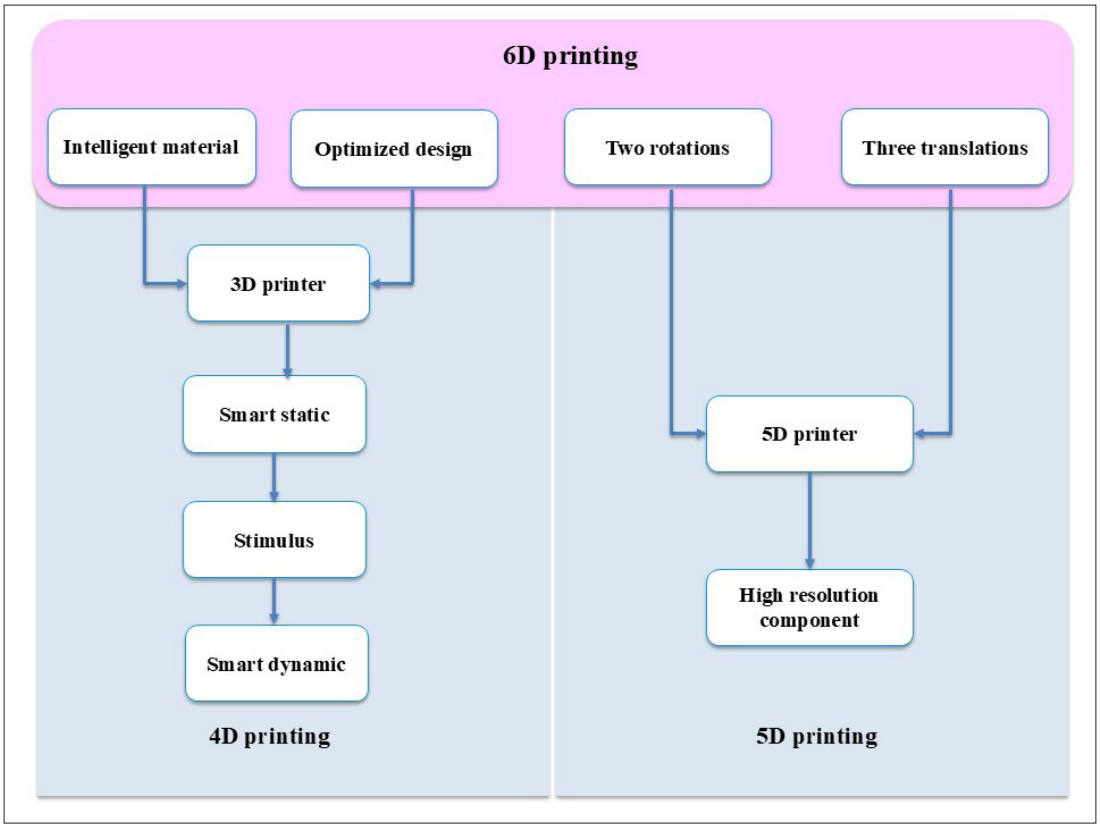

Figure 5. The 6D printing method as a combination of 4D and 5D printing.

resulting in enhanced mechanical performance, improved fatigue resistance, and optimized load distribution in anatomically complex implants like acetabular cups or spinal cages.[17,18] As illustrated in **Figure 5**, 6D printing combines both structural adaptability and responsive behavior, potentially enabling real-time adaptation of implants to patient-specific biomechanical environments. Although still in early development, these advances hold great promise for the future of smart, personalized bone repair solutions.[19,20]

3. Additive manufacturing of metallic bone implants: properties, processes, and clinical performance

3.1. Additive manufacturing processes for metallic implants

3.1.1. Selective laser melting

SLM has established itself as a leading technology in the manufacture of metallic implants due to its unique ability to create complex, optimized, and biocompatible structures with unmatched precision. Direct fabrication of biocompatible alloys like Ti–6Al–4V has been reported using SLM, allowing customization of architecture and mechanical properties to match patients' physiological conditions.[11] As shown in **Figure 6**, the principle of SLM involves the use of a high-power laser beam to selectively fuse fine layers of metal powder inside an inert atmosphere chamber, ensuring full and homogeneous melting of material.[21]

The robustness and quality of SLM-fabricated implants highly depend on processing parameters, including laser power (P), scanning speed (v), layer thickness (t), and hatch spacing (h), all of which directly influence the final density, residual porosity, and internal stresses of the implant.[22] A key parameter used to optimize these settings is the volumetric energy density (E_v), defined by **Equation I**.

$$Ev = \frac{P}{h \times v \times t} \quad (1)$$

Precise calibration of E_v helps prevent typical defects associated with SLM, such as thermal cracking, gas porosity, and residual deformation, which may compromise implant reliability.[23] Optimized implant designs fabricated by SLM have demonstrated relative densities greater than 99.5%, providing excellent mechanical properties and durability.[12]

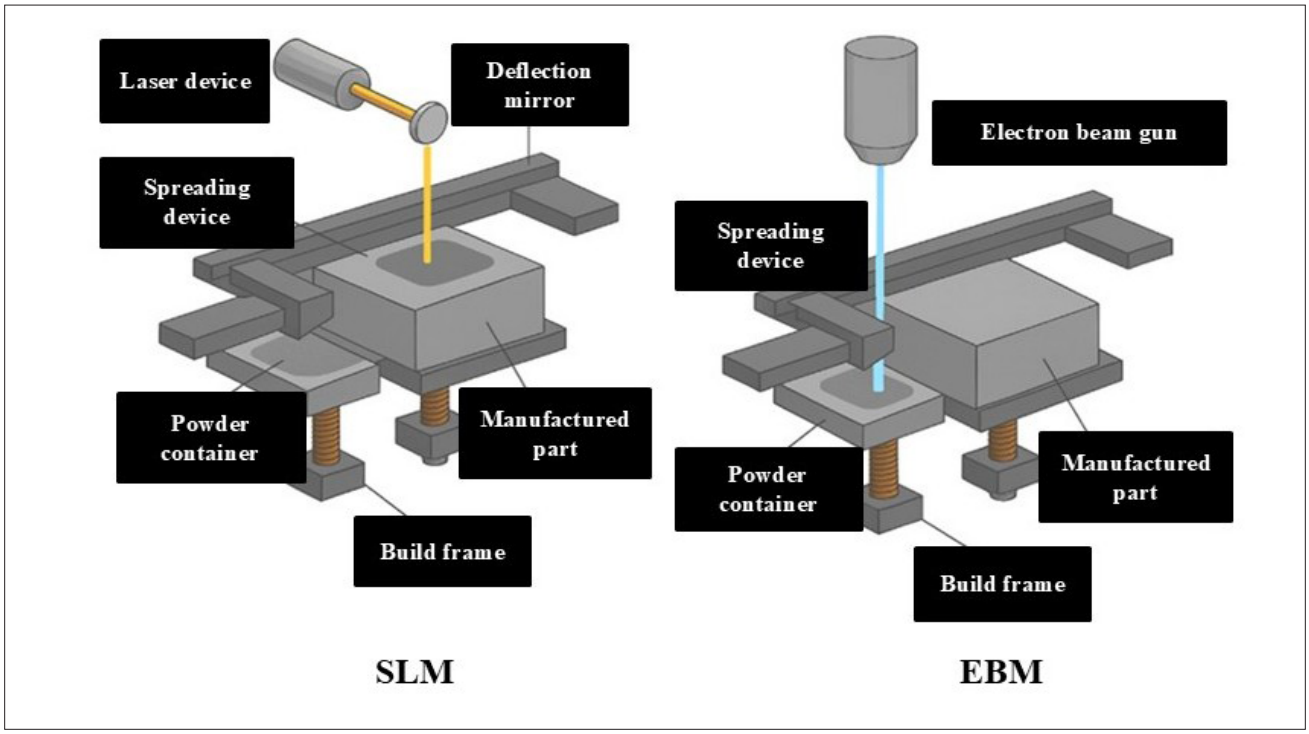

Figure 6. SLM and EBM processes. Abbreviations: EBM, electron beam melting; SLM, selective laser melting.

Additional advantages of SLM include post-processing treatments, such as heat treatment for residual stress relief and improved corrosion resistance.[22]

From a technical standpoint, the success of SLM fabrication relies on an optimized scanning strategy. Different scanning strategies—including hatch, stripes, chess, and spiral patterns—have been analyzed to minimize thermal distortion and maintain homogeneous fusion of material.[21] For example, offset contour scanning reduces residual stress by adjusting the laser direction and angle for each layer, while the partition scanning divides the build area into several subregions to homogenize temperature distribution and limit deformation.[24]

Despite its numerous advantages, challenges remain. The high cost of metal powders and laser equipment restricts wider adoption in clinical settings. Manufacturing precision can also be affected layer accumulation, leading to deviations between the CAD model and the final implant. However, advancement in artificial intelligence and numerical simulations are expected to enable real-time optimization of manufacturing parameters, potentially reducing defects and improving the consistency of implant fabrication.[6,25]

3.1.2. Electron beam melting

EBM is another advanced AM technology that has gained significant traction in the production of biomedical devices, particularly metallic bone implants.[26] Similar to selective laser sintering (SLS) and SLM, EBM uses a high-energy electron beam to selectively melt layers of metal powder in a vacuum environment (**Figure 6**). The controlled atmosphere prevents oxidation of the materials and improves the mechanical properties of the produced components. The process starts with the deposition of a thin metal powder layer onto the building platform. A precisely controlled electron beam then scans the layer according to a 3D CAD model, selectively melting the material. Upon solidification of the layer, the platform is lowered, and a new layer of powder is added. This cycle repeats until the final part is completed.[27,28]

EBM offers several advantages for implant fabrication, including the ability to produce dense, homogeneous structures with reduced deformation and higher energy efficiency compared to laser-based technologies. The controlled scanning system based on the magnetic coil of the electron beam allows for faster and more accurate beam positioning. However, EBM is limited by lower resolution compared to SLM, as the larger electron beam diameter

reduces the ability to reproduce fine details and results in higher surface roughness. Additionally, processing parameters such as beam current, scanning speed, acceleration voltage, and powder layer thickness directly influence density, porosity, and mechanical strength.[29]

Current research on EBM optimization focuses on surface modification and defect minimization, with special emphasis on post-processing treatments like hot isostatic pressing (HIP). HIP effectively reduces residual porosity and strengthens the fatigue resistance of implants. Despite the high costs of metal powders and equipment, increasing interest in metallic AM for biomedical applications has driven investments and research efforts toward improving efficiency and lowering costs. This progress is expected to accelerate the clinical adoption of EBM for next-generation metallic implants.[30] A comparative analysis of SLM and EBM technologies is provided in **Table 1**.

3.2. Mechanical properties and material selection for additive manufacturing metallic bone implants

3.2.1. Material selection and classification

In the manufacturing and development of metallic bone implants, choosing the ideal metal is important because the material choice greatly impacts the characteristics of the manufactured implants.[31] The ideal material for metallic bone implants must satisfy four fundamental criteria: biomechanical compatibility, biocompatibility, corrosion and wear resistance, and osseointegration. Biomechanical compatibility ensures that the material's elastic modulus is as close as possible to cortical bone (10–30 GPa), thereby reducing stress shielding. Biocompatibility is crucial to minimize inflammatory responses, hypersensitivity reactions, and toxicity risks, ensuring a stable and long-lasting implant. Corrosion and wear resistance are essential for implant durability, preventing material degradation in physiological environments and the release of metallic ions that could induce osteolysis and implant failure. Finally, osseointegration is vital for direct bone-implant bonding, reducing the risk of fibrous encapsulation and enhancing long-term fixation.[32]

In addition to biological and mechanical requirements, materials should be compatible with AM processes. For instance, titanium alloys are highly compatible with SLM.[33] Cost-effectiveness is also an important consideration, as balancing material expense with performance determines the economic viability and accessibility of implants.[34] In this review, we classified the metallic biomaterials into two categories: the commonly used and less commonly used materials (**Tables 2** and **3**).

Among metallic biomaterials, titanium alloys—particularly Ti–6Al–4V—are the most widely used owing to their high strength-to-weight ratio, excellent corrosion resistance, and superior biocompatibility. These characteristics contribute to their long-term clinical success. Clinical studies have reported survival rates of up to 99% over 10 years for titanium-based implants, with consistent osseointegration and minimal biological complications, making them a reliable option for both dental and orthopedic applications.[41] Furthermore, surface modifications of titanium alloys have been shown to enhance bone bonding and cellular responses, thereby improving clinical outcomes.[42] However, the relatively high elastic modulus of Ti–6Al–4V compared to cortical bone can lead to stress shielding, and concerns over the cytotoxicity of vanadium have prompted the development of β-type titanium alloys. These newer alloys, incorporating elements such as niobium, zirconium, or tantalum, demonstrate improved biomechanical compatibility and enhanced bioactivity.[43,44]

Beyond titanium, Co–Cr alloys are widely used for orthopedic applications due to their exceptional wear resistance, mechanical strength, and corrosion stability. They are especially suitable for load-bearing prostheses such as hip and knee joints. Clinically, Co–Cr alloys have

Table 1. Comparative analysis of SLM and EBM for metallic implants

Criteria	SLM	EBM
Energy source	Laser beam melting	Electron beam melting
Processing environment	Inert gas (argon, nitrogen)	Vacuum (no oxidation)
Material suitability	Ti–6Al–4V, Co–Cr, stainless steel	Ti–6Al–4V, Co–Cr–Mo
Surface quality and resolution	High resolution, smoother surfaces	Lower resolution, rougher surfaces
Microstructure and mechanical properties	Fine-grained, strong	Coarser grains, lower residual stress
Build speed and energy efficiency	Slower, less energy-efficient	Faster, more energy-efficient
Post-processing requirements	Heat treatment to relieve stress	HIP required to reduce porosity

Abbreviations: Co–Cr, cobalt–chromium; Co–Cr–Mo, cobalt–chromium–molybdenum; EBM, electron beam melting; HIP, hot isostatic pressing; SLM, selective laser melting; Ti–6Al–4V, titanium alloy with 6% aluminum and 4% vanadium.

Table 2. The most used metals in bone metallic implants

Materials	Young's modulus (GPa)	Yield strength (MPa)	Tensile strength (MPa)	Properties	Applications	References
Titanium	105	695	785	Lightweight, corrosion-resistant, biocompatible	Hip and knee implants; spinal implants; bone plates	[35]
Ti–6Al–4V	110	850–900	960–970	Versatile alloy, high mechanical strength, biocompatible	Hip and knee implants; spinal implants; bone plates	[35]
Tantalum	186	140–350	200–520	Highly biocompatible, excellent osseointegration	Acetabular cups; bone augmentations	[36]
Stainless steel (316L)	190	290	580	Corrosion-resistant; mainly used for temporary implants	Bone plates; bone screws; joint implants	[37,38]
Co–Cr–Mo	230	200–800	430–1000	High wear resistance, high strength	Hip and knee implants; dental implants	[38]
Magnesium	45	160	250	Biocompatible, biodegradable, low density	Orthopedic implants	[38,39]
Zirconium alloys	100	200–500	400–800	Biocompatibility, corrosion resistance	Spinal applications	[32]
Cortical bone	10–30	30–70	70–150	Natural reference material	–	[38]

Abbreviations: Co–Cr–Mo, cobalt–chromium–molybdenum; Ti–6Al–4V, titanium alloy with 6% aluminum and 4% vanadium.

Table 3. Less commonly used metals in bone metallic implants

Materials	Young's modulus (GPa)	Yield strength (MPa)	Tensile strength (MPa)	Properties	References
Iron	200	50	540	High mechanical strength, potentially biodegradable	[38]
Zinc	83–108	30	37	Biocompatible, biodegradable	[38]
Silver	80	30	150	Antibacterial, biocompatible	[40]
Palladium	110–120	50	150–200	Corrosion-resistant; alloyed	[40]
Platinum	150	150	240	Corrosion-resistant, biocompatible	[40]
Gold	79	25	130	Biocompatible, highly corrosion-resistant	[40]

demonstrated excellent durability and low revision rates, particularly in young and active patients.[45] Their use in femoral heads and articulating components has shown reliable long-term performance. Studies report that even after 18 years of implantation, systemic metal ion levels remain below clinically accepted thresholds, with no evidence of adverse immune responses.[46] Nevertheless, their high stiffness can contribute to stress shielding and bone resorption, while the release of metal wear debris remains a concern in some cases.[47]

Several other metallic biomaterials have also been investigated. For example, stainless steel (316L) is widely used for temporary metallic implants such as bone plates and screws due to its good mechanical strength and cost-effectiveness. However, its relatively low corrosion resistance in physiological environments and limited biocompatibility restrict its long-term use.[44,48] Tantalum, by contrast, is highly biocompatible and exhibits excellent osteoconductivity, making it particularly suitable for bone augmentation and porous implants; yet, its high cost remains a significant barrier to widespread clinical

adoption.[49,50] Magnesium alloys have emerged as promising biodegradable materials capable of providing temporary mechanical support before gradually resorbing *in vivo*. Despite their bioresorbable nature and potential for reducing secondary surgery, their rapid degradation and poor mechanical stability under physiological conditions remain major limitations for long-term structural applications.[51,52]

3.2.2. Microstructure and mechanical properties

Compared to traditionally manufactured implants, metallic AM implants often exhibit distinct microstructural characteristics. The rapid cooling and solidification inherent to AM processes can result in finer grain structures, potentially enhancing mechanical properties such as fatigue resistance.[31] However, microstructural defects—including incomplete melting, unmelted particles, and non-equilibrium phases—may compromise mechanical performance.[31] Therefore, the study of morphology in AM biomaterials is crucial, as both surface characteristics and microstructure directly influence mechanical and biological performance. Key morphological factors such as surface roughness, porosity, pore interconnectivity, and overall structural integrity play a vital role in implant–tissue integration and the ability to endure physiological loads. In orthopedic and dental applications, surface morphology significantly impacts osseointegration, the process by which bone cells adhere to and grow on an implant surface. Rough, micro-textured surfaces have been shown to promote better cell attachment and accelerate tissue integration.[53] Additionally, strategic design of porosity and pore architecture enhances vascularization, nutrient diffusion, and tissue ingrowth, all of which are essential for long-term implant stability.

The mechanical strength of metallic AM implants—including their tensile, yield, and ultimate strengths—may differ from that of traditionally manufactured implants. Some studies report that AM implants, particularly those made from Ti–6Al–4V, exhibit comparable or superior mechanical strength.[31] However, variations in porosity and density, often process-dependent, can negatively influence mechanical behavior.

Fatigue resistance (**Figure 7**) is a critical consideration, as implants are subject to cyclic loading *in vivo*. To ensure long-term functionality, implants must withstand high durability demands and resist fatigue failure. However, the fatigue behavior of AM implants remains inconsistent across studies.[54] While some studies indicate improved fatigue performance compared to conventional manufacturing, others point to process-induced defects as causes of failure. These defects include lack of fusion, gas porosity, and incomplete melting, which act as stress concentrators, initiating cracks under physiological loads and reducing fatigue life.[55]

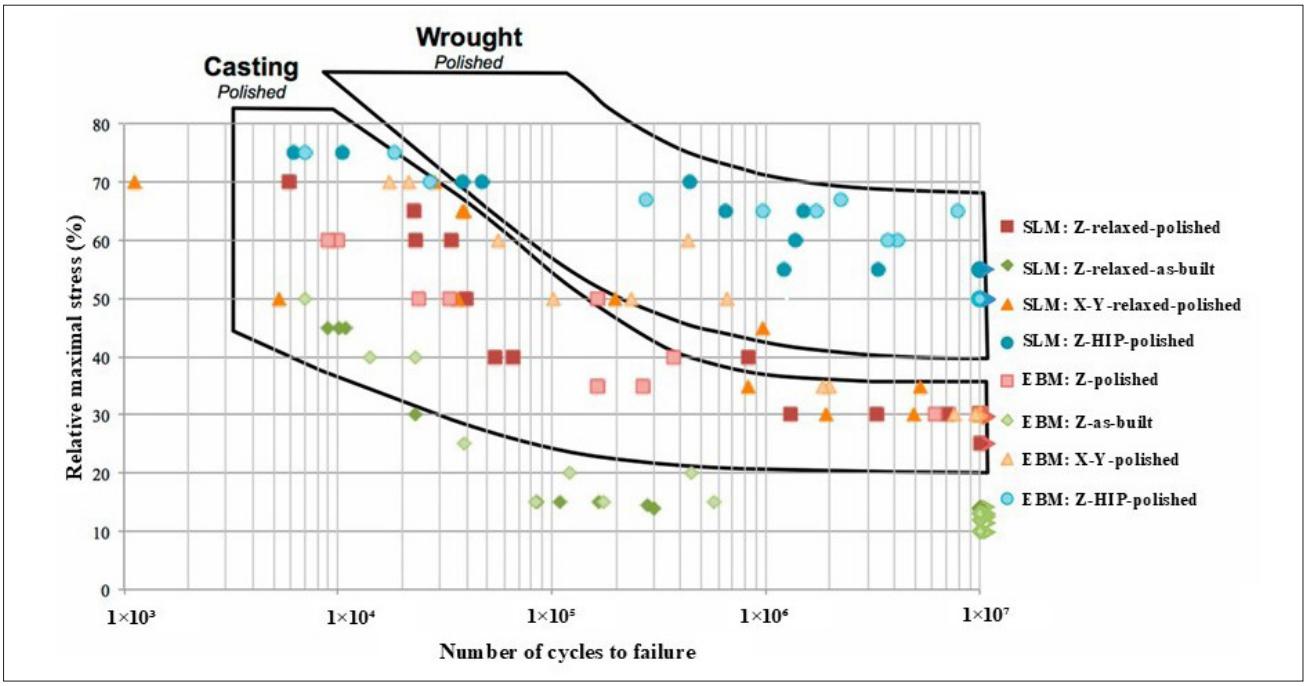

Figure 7. Comparison of fatigue resistance of metallic materials produced by SLM, EBM, casting, and wrought processing. Adapted from ref.[56]. Abbreviations: EBM, electron beam melting; HIP, hot isostatic pressing; SLM, selective laser melting.

Moreover, the thermal cycles and directional solidification intrinsic to AM create heterogeneous grain structures and residual stresses, leading to mechanical anisotropy and variability across orientations. These inconsistencies raise concerns about structural reliability, patient safety, and regulatory approval. Several studies confirm that AM parts may have lower fatigue performance without post-processing treatments, such as HIP, precision surface machining, or laser shock peening.[57] These treatments significantly improve outcomes by minimizing internal porosity, homogenizing microstructure, and enhancing fatigue resistance.[58] Without these measures, the risk of premature failure or poor osseointegration remains high, especially in load-bearing orthopedic implants. Thus, ensuring clinical reliability requires a comprehensive defect-control strategy throughout the AM process chain.

3.3. Long-term *in vivo* performance and clinical reliability of additive manufacturing implants

While mechanical properties, material selection, and manufacturing parameters are fundamental to the development of high-performance metallic implants, these factors must ultimately translate into reliable and durable clinical outcomes. AM has enabled the production of metallic implants—including titanium and its alloys—with complex geometries and tunable surface features that promote osseointegration and long-term biological integration. Clinical data remain limited, but available evidence is encouraging. In a 3-year multicenter study, Tunchel *et al.*[59] reported a survival rate of 94.5% and a crown success rate of 94.3% for 3D-printed titanium dental implants, with minimal marginal bone loss, suggesting high potential for sustained clinical performance. Similarly, Shu *et al.*[60] demonstrated that SLM-fabricated titanium implants exhibited significantly higher removal torque and early bone interlocking, confirming improved biomechanical anchorage compared to conventionally manufactured implants.

Preclinical investigations support these findings. Gu *et al.*[61] reviewed 46 animal studies and reported that Ti–6Al–4V porous scaffolds with 500–600 μm pore sizes and 60–70% porosity achieved bone area fractions up to 59.3% within 8–10 weeks, highlighting the importance of microarchitectural optimization for bone ingrowth. From a broader perspective, Gao *et al.*[33] emphasized that metallic AM scaffolds can reduce stress shielding, improve bone–implant mechanical compatibility, and allow bone ingrowth without the need for additional coating—provided that pore architecture and surface roughness are well controlled. Park *et al.*[62] further advanced this approach by embedding Ti–6Al–4V implants with biogenic hydroxyapatite (HAp), resulting in enhanced osseointegration and reduced inflammatory response *in vitro* and *in vivo*. Collectively, these findings illustrate how AM can enable not only geometric precision but also surface-level functionalization, producing implants that are both structurally robust and biologically responsive.

Nonetheless, as noted by Matsko and França,[63] the current clinical reports are constrained by small patient cohorts and short follow-up durations—often less than 3 years—thereby limiting our ability to assess the long-term safety and functional durability. Extending beyond conventional intraosseous applications, Onică *et al.*[64] reported the longest follow-up to date for 3D-printed subperiosteal titanium implants, with 6 years of monitoring. Despite complications in over half the cases—such as metal frame exposure and late-stage mobility—some implants maintained stable integration and satisfactory outcomes. These findings highlight the potential of customized AM implants, particularly for patients with severe anatomical deficits where careful design and precise surgical planning are critical. **Figure 8** shows the intraoral clinical appearance of AM implants at different time points. The images reveal peri-implant mucosal changes ranging from stable conditions to inflammation and late complications, underlining the need for long-term monitoring. **Table 4** summarizes the clinical studies reviewed, with the findings collectively emphasizing that long-term clinical reliability depends not only on material performance but also on patient-specific anatomical factors, surgical technique, and post-operative care.

Altogether, the current body of evidence supports the clinical viability of metallic AM implants, particularly regarding biological integration, stress transfer optimization, and short- to mid-term reliability. Yet, the durability of these implants under long-term mechanical and biological loads—especially in weight-bearing skeletal regions—remains insufficiently documented. To transition from promising prototypes to clinically validated solutions, future studies should prioritize large-scale, multicenter longitudinal trials with standardized outcome measures and detailed failure mode analyses. Such efforts are essential to securing regulatory approval, ensuring patient safety, and establishing AM as a reliable option for the long-term treatment of musculoskeletal disorders.

4. Biomimetic bone implants

The purpose of this paper is to highlight the importance of AM, supported advanced design and tools, in the manufacturing of biomimetic implants that address the limitations of conventional counterparts. Biomimicry is key to this approach, drawing inspiration from the structural and functional features of natural bone. The



Figure 8. Intraoral views at different follow-up intervals. (A) 24 months. (B) 42 months. (C) 72 months. Adapted from ref.[64].

Table 4. Key preclinical and clinical studies on AM metallic implants

Study	Implant type	Key outcome	Remarks	References
Tunchel *et al.*	3D-printed titanium dental implants	94.5% survival in 3 years; minimal bone loss	Multicenter; limited to dental applications	[59]
Shu *et al.*	SLM titanium implants	Higher removal torque and improved early bone interlocking	Superior to conventional implants	[60]
Gu *et al.*	Porous Ti–6Al–4V scaffolds (animal model)	59.3% bone area at 8–10 weeks (500–600 μm pores; 60–70% porosity)	Emphasizes the importance of pore design	[61]
Gao *et al.*	Metallic AM scaffolds	Effective osseointegration without coating if porosity and surface roughness are optimized	General review; supports design strategies	[33]
Park *et al.*	Ti–6Al–4V with biogenic HAp	Enhanced osseointegration and reduced inflammation (*in vitro* & *in vivo*)	Promising material–biology synergy	[62]
Matsko and França	Clinical review	Limited data (<3 years follow-up; small cohorts)	Stresses the need for large-scale longitudinal trials	[63]
Onică *et al.*	3D-printed subperiosteal implants	6-year follow-up; >50% complications, though some stable outcomes observed	Custom designs are useful in severe bone loss cases	[64]

Abbreviations: AM, additive manufacturing; Hap, hydroxyapatite; SLM, selective laser melting; Ti–6Al–4V, titanium alloy with 6% aluminum and 4% vanadium.

ultimate objective is to reconstruct artificial bones rather than to simply replace damaged or fractured natural bones with conventional implants. To achieve this, a deep understanding and mastery of the bone's composition is essential.

4.1. Bone composition

Bone is a hierarchically organized composite, consisting of a mixture of organic and inorganic phases. The organic phase represents 30–40% of the bone's dry weight and is dominated by collagen type I, which contributes about 90% of the organic fraction. This fibrillar protein forms the extracellular matrix (ECM), imparting phase flexibility and resilience against deformations.[65] The remaining 10% is composed of non-collagenous proteins such as osteocalcin, which regulates calcium ion binding during mineralization; osteopontin (OSP), associated with *osteopontin (OSP),* which is associated with cell adhesion; and osteonectin, which is involved in the regulation of mineralization; and osteonectin, which is involved in cell adhesion and regulation of mineralization.[66]

The inorganic phase, on the other hand, accounts for 60–70% of the bone's dry weight and is dominated by nanometric HAp crystals [$Ca_{10}(PO_4)_6(OH)_2$]. These crystals are integrated within collagen fibrils, forming a fiber–mineral composite. The bone mineral is not a pure stoichiometry HAp but incorporates ionic substitutions including carbonate (CO_3^{2-}), magnesium (Mg^{2+}), sodium (Na^+), potassium (K^+), and silicon (Si). These ionic variations critically influence bioactivity, crystallinity, and chemical resistance of the bone matrix systems.[67] These

ions can partially substitute OH^{-} or PO_4^{3-} groups in the crystals, enabling bone to adapt its composition according to physiological requirements and anatomical location.[68]

In addition, water content accounts for approximately 15–25% of the total bone matrix, distributed within the matrix intercrystalline spaces. This water is fundamental in nutrient diffusion, mechanical force transmission, and hydration of organic proteins, thus contributing to the viscoelastic properties of the bone.[66]

Structurally, bone exists in two primary forms: cortical (compact) bone and trabecular (spongy) bone, as illustrated in **Figure 9**. Cortical bone is dense and rigid, composed of osteons—cylindrical units of concentric lamellae surrounding Haversian canals that house blood vessels and nerves. In contrast, trabecular bone has a porous, interconnected architecture of thin trabeculae, providing sites for vascularization, bone marrow storage, and rapid remodeling.[67,68] The relative proportion of cortical and trabecular bone varies across skeletal sites, reflecting the specific functional and mechanical demands of each bone type.

4.2. Types and properties of bone implants

Bone implants, including prostheses, screws, and plates, are essential in the treatment of different orthopedic diseases and traumatic injuries. These implants enhance the patient's quality of life, provide structural support, and improve damaged bones, thereby improving and ameliorating mobility. The main advantage of these devices lies in their ability to treat fractures and degenerative bone diseases while accelerating recovery and reducing pain.[70] This section explores the different types of bone implants (**Figure 10**), their classifications, properties, and specific applications in orthopedic surgery.

4.2.1. Craniofacial and dental implants

Craniofacial and dental implants are specialized medical devices designed to reconstruct lost or damaged bone structures in the craniofacial region and oral cavity caused by trauma, congenital anomalies, or surgical resections such as tumor removal.[13] These implants serve both functional and aesthetic purposes, significantly enhancing patients' quality of life.[71] Craniofacial implants play a crucial role in multiple procedures: orbital reconstructions to restore the integrity of the eye socket; maxillofacial surgeries to realign the jaws and support dental prostheses; and mandibular reconstructions to stabilize bone structure following tumor removal or trauma.[72,73] The anatomical integration of these implants is essential, requiring advanced customization to ensure a perfect fit with the patient's unique cranial and facial structure.[72] Dental implants replace missing teeth by integrating a metallic anchor directly into the jawbone, providing stability and functionality comparable to natural teeth.

These implants come in various types to meet different clinical needs. Endosteal implants, in the form of screws, cylinders, or blades, are the most common and are inserted directly into the bone.[74] Subperiosteal implants are placed beneath the gum but above the bone and are used when bone height is insufficient. Transosteal implants are fixed at the base of the mandible using metal plates, while

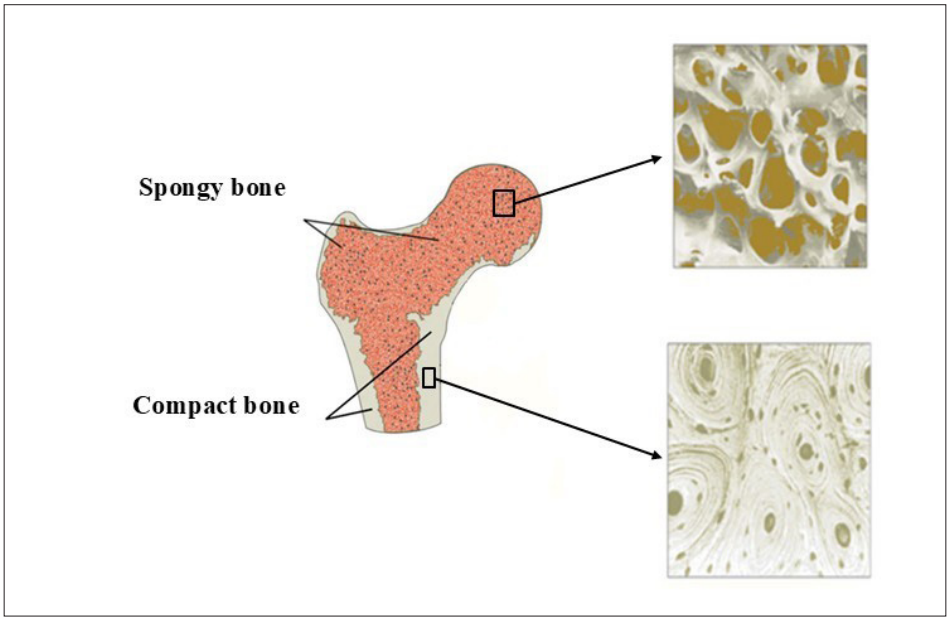

Figure 9. Structural organization of bone, illustrating the microarchitecture of trabecular and cortical bone

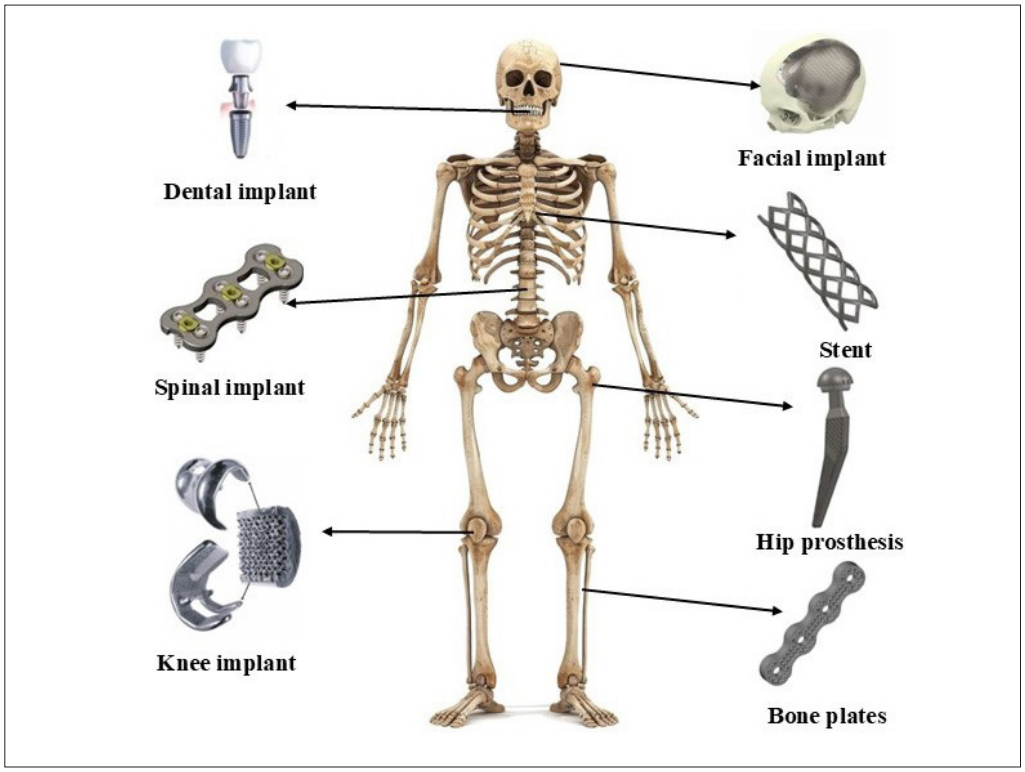

Figure 10. Types of bone implants

zygomatic implants—anchored in the zygomatic bone—provide an alternative to bone grafts for patients with severe bone loss.[75] The commonly used materials for these implants include titanium and its alloys.

4.2.2. Spinal implants

Spinal implants are essential orthopedic devices used to treat disorders affecting the vertebral column and spinal cord, playing a fundamental role in stabilizing and protecting the spine. They are commonly employed to address vertebral fractures, scoliosis, and spinal instability. The implantation of the first titanium intervertebral fusion cage by C.D. Ray and J.W. Brantigan in 1989 marked a significant milestone in spinal surgery.[13] Since then, spinal implants have evolved into multiple categories based on specific clinical needs. Pedicle screws—often made of titanium or stainless steel—enhance stability and facilitate bone fusion, particularly in cases of spinal deformities or fractures. Stabilizing rods are attached to these screws to align the spine and restrict unnecessary movements. Intervertebral cages—inserted between two vertebrae—promote bone growth and reinforce spinal stability. Artificial discs represent a major advancement, preserving spinal mobility and preventing the degeneration of adjacent segments.[76,77] Commonly used materials for these implants include titanium and its alloys, 316L stainless steel, and Co–Cr alloys, known for their high wear resistance. 3D printing techniques such as SLM and EBM have revolutionized spinal implant design by fabricating porous, biomimetic structures that improve osseointegration and reduce stress shielding.[13,78]

4.2.3. Joint implants

Joint implants are designed to restore mobility and relieve pain in patients suffering from degenerative diseases such as osteoarthritis, joint trauma, or inflammatory disorders. Hip and knee prostheses are the most widely used implants in orthopedic surgery. A hip implant consists of several key components, including the femoral head, femoral stem, neck, and acetabular cup, which together mimic the natural mechanics of the joint. During surgery, the acetabular cup replaces the damaged hip socket while the femoral stem is securely anchored in the femur, ensuring optimal stability and functional movement. Knee implants are composed of essential components such as the femoral component, tibial component, patellar component, and a polyethylene articulating surface.[13] These structures are specifically designed to support mechanical loads and provide smooth, stable articulation. Titanium and its alloys are widely favored as the implant material for their lightweight nature and high mechanical strength, while Co–Cr alloys are employed for their robustness and wear resistance.[79]

4.3. Essential tools and strategies for biomimetic implant development

AM plays a central role in designing bone implants that are tailored to patients' biomechanical and anatomical needs. One of the key benefits of AM in implant fabrication is personalization. The use of medical imaging, such as computed tomography (CT) scans and magnetic resonance imaging (MRI), allows for precise anatomical data acquisition, ensuring that the fabricated prosthesis matches the patient's skeletal structure. This high level of customization reduces surgical complications and enhances patient outcomes.[80]

A second major contribution of AM is the ability to design porous structures that mimic the natural trabecular architecture of bone. These porous architectures promote osseointegration, thereby reducing the risk of implant loosening and mitigating stress shielding by adjusting the elastic modulus of the implant. Widely used designs include regular, random, gradient, and topologically optimized lattice structures, which can be tailored to exhibit graded porosity in denser bone regions. These approaches significantly improve the mechanical compatibility between implant and host bone, ensuring long-term stability.[81] Furthermore, AM facilitates the development of implants with optimized surface properties, making them suitable for bioactive coatings such as Hap.[82]

In addition to material selection and structural optimization, several advanced tools and methodologies contribute to the success of AM-fabricated implants. High-quality 3D modeling, enabled by software such as nTop, SolidWorks, and AutoCAD, ensures precise control over implant geometry and internal architecture. Numerical simulations, including FEA and CFD, further optimize implant performance before fabrication, reducing failure risks and improving patient outcomes.[81] The overall workflow of biomimetic implant fabrication using AM is illustrated in **Figure 11**.

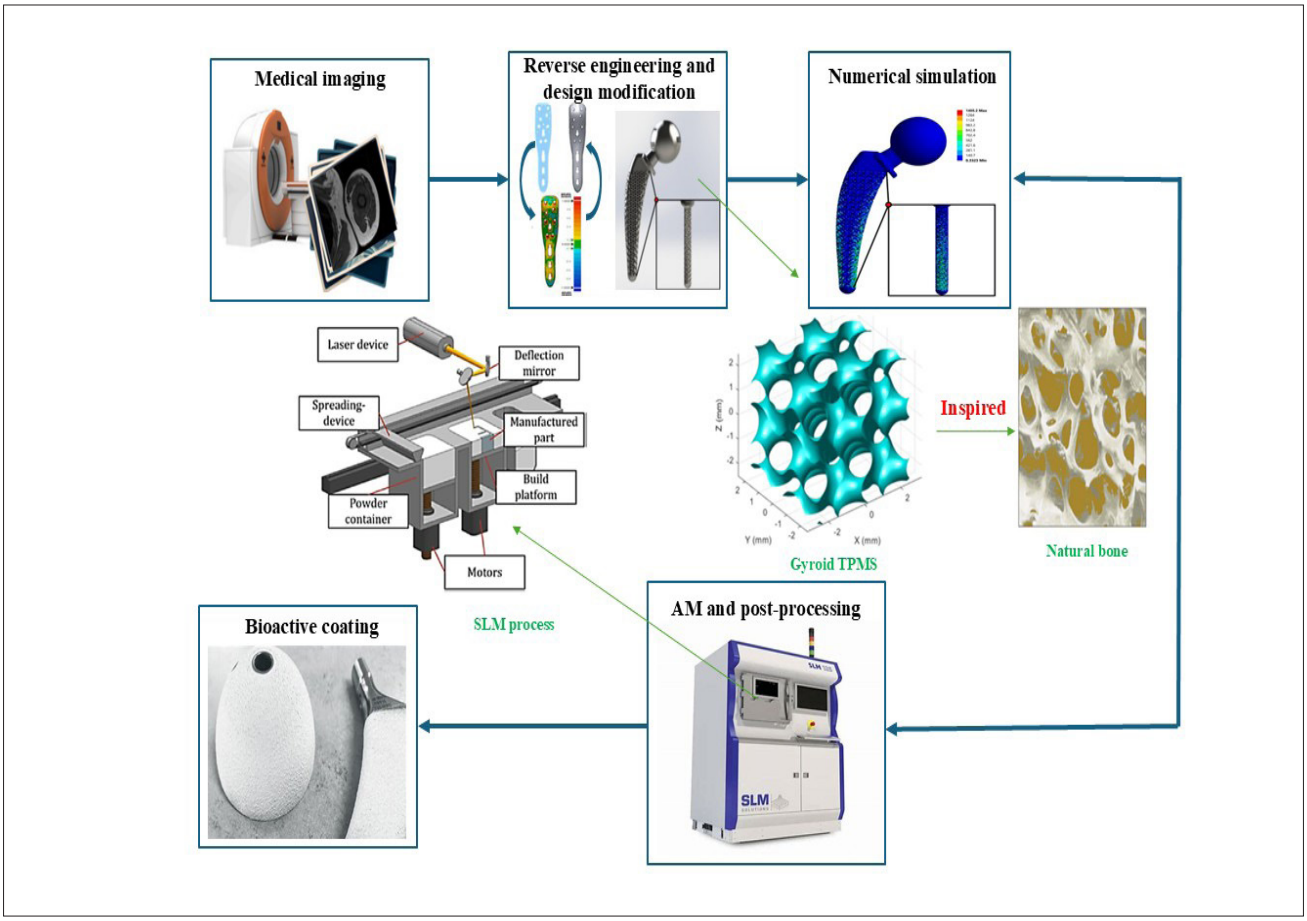

Figure 11. Workflow of biomimetic implant fabrication using AM. Abbreviations: AM, additive manufacturing; SLM, selective laser melting; TPMS, triply periodic minimal surfaces.

4.3.1. Importance of biocompatibility and osseointegration

Biocompatibility refers to the ability of a material to function effectively within a biological environment without triggering adverse reactions such as inflammation, immune rejection, or toxicity, while simultaneously supporting tissue repair and regeneration.[83] It is crucial for the long-term success of implants, as the material must not only integrate harmoniously with the surrounding tissues but also promote healing and functional restoration. The choice of biomaterials plays a pivotal role in ensuring biocompatibility. Titanium alloys, for instance, are highly valued for their exceptional strength-to-weight ratio, corrosion resistance, and low elastic modulus, which helps minimize mechanical mismatch with surrounding tissues. Their surface chemistry further enhances biocompatibility by forming a stable oxide layer that promotes cellular adhesion and proliferation, while reducing inflammation.[84]

Equally critical is osseointegration, a complex biological process that ensures stable and functional integration of an implant with living bone. This process is facilitated by surface modifications, such as bioactive coatings of HAp or titanium oxide, which enhance protein adsorption, cellular adhesion, and subsequent bone-implant bonding.[85,86] The dynamic interplay between biocompatibility and osseointegration ultimately determines an implant's stability, durability, and functional performance. Neglecting these factors can lead to complications such as implant loosening, inflammatory responses, and mechanical failure. Poor biocompatibility may trigger immune reactions that inhibit osseointegration, while insufficient osseointegration can weaken bone–implant bonding, elevating stress at the interface and jeopardizing structural integrity. Therefore, optimizing both biocompatibility and osseointegration is essential for ensuring the longevity and clinical success of orthopedic and dental implants.[13]

4.3.2. Patient-specific implants and customization

The shift toward patient-specific implants has revolutionized biomedical engineering, moving beyond standardized "one-size-fits-all" solutions to highly individualized devices. This approach relies heavily on advanced medical imaging techniques such as CT scans and MRIs, which generate high-resolution digital imaging and communications in medicine (DICOM) data used to reconstruct digital models of patient anatomy. These models serve as the foundation for CAD modeling, enabling precise digital reconstruction of patient-specific anatomical structures.[87] Furthermore, specialized software like nTop utilizes these medical imaging outputs to generate highly optimized lattice structures for AM. The integration of AM with computational modeling facilitates the creation of complex, patient-specific implants, improving biomechanical compatibility, enhancing load distribution, and reducing postoperative complications. Conversely, neglecting patient-specific considerations in implant design can lead to misalignment, instability, and discomfort, potentially compromising biomechanical function and necessitating additional surgical interventions for the associated complications.[13] **Table 5** provides an overview of the commonly used software for the design, simulation, and manufacturing of AM-based metal orthopedic implants.

4.3.3. Lattice structures

Lattice structures in metallic bone implants represent a transformative approach in biomedical engineering, enabling implants to better mimic natural bone properties, enhance osseointegration, and fulfill the mechanical demands of load-bearing applications. These structures can be categorized into four types—regular, random, gradient, and topological distribution structures—each offering unique features that enhance biomimetic capabilities.

Regular lattice structures, such as cubic, diamond, and octet-truss, offer uniform mechanical properties and favorable strength-to-weight ratios, making them suitable for implants requiring even load distribution.[88] However, their simple geometry limits their ability to mimic the complex, irregular architecture of natural bone, which adapts to mechanical stimuli. This mismatch can cause stress shielding. Cubic lattices are easy to manufacture and ensure isotropic mechanical performance. Diamond lattices provide better deformation resistance and strength—ideal for high-load applications like hip prostheses. Octet-truss structures perform well under dynamic loading, thereby improving clinical outcomes.[89]

Random lattice structures, exemplified by Voronoi-based designs, incorporate irregular, heterogeneous patterns that more accurately reflect the trabecular structure of natural bones. This variability enhances load transfer while fostering a favorable microenvironment for cellular proliferation, vascularization, and nutrient diffusion—processes essential for bone regeneration and integration with host tissue.[90,91]

Moreover, they can reduce the likelihood of implant failure by distributing stress more effectively during mobilization and daily activities.

Gradient lattice structures further elevate the biomimetic capabilities of implants through the incorporation of spatial variations in porosity and strut thickness. Such designs allow implants to replicate the mechanical behaviors of both cortical and cancellous bone, ensuring site-specific functionality. This capability not only enhances compatibility but also provides a

Table 5. Key software tools for additive manufacturing of metal bone implants

Software package	Company	Primary application	Use in metal orthopedic implants	Advantages	Limitations
SolidWorks	Dassault Systèmes	CAD design	Design of orthopedic implants and prosthetics	User-friendly, parametric modeling; integrates with simulation tools	Limited advanced simulation capabilities
nTopology	nTopology Inc.	Generative design	Lattice structures for porous implants, topology optimization	Advanced lattice and topology optimization, ideal for AM	Steep learning curve; may need additional simulation software
Abaqus	Dassault Systèmes	FEA	Structural and biomechanical simulation of implants	Advanced material models, excellent for stress–strain analysis	Requires expertise; high computational cost
ANSYS	ANSYS Inc.	FEA and multiphysics simulation	Fatigue and mechanical performance analysis	Industry-leading multiphysics supports	Expensive licenses; requires powerful hardware
COMSOL Multiphysics	COMSOL Inc.	Multiphysics simulation	Bone–implant interaction modeling; heat transfer in AM	Versatile for biomechanical and thermal studies	Computationally intensive; requires deep expertise
Materialise Mimics	Materialise NV	Medical image processing	3D reconstruction from CT/MRI for patient-specific implants	Precise anatomical modeling; ideal for personalized implants	Limited CAD capabilities, focused on image processing
Materialise Magics	Materialise NV	3D printing preparation	Mesh editing and STL preparation for metal AM	Advanced AM preparation tools	High cost; lacks FEA capabilities
3D Slicer	Open Source	Medical image processing	Patient-specific implant design and preoperative planning	Open-source; strong imaging and segmentation tools	Not designed for CAD or FEA
Fusion 360	Autodesk	CAD and CAM	Design and manufacturing optimization of implants	Cloud-based; integrates CAD and CAM	Limited advanced FEA features
HyperMesh	Altair Engineering	Mesh preprocessing for FEA	High-quality meshing for implant simulations	Optimized meshing; supports multiple solvers	Steep learning curve; complex interface
nTop Platform	nTopology Inc.	Computational design	Advanced lattice structures for implants	Optimized for metal AM	Requires high computational power
Optistruct	Altair Engineering	Structural optimization	Lightweight, topology-optimized implants	Advanced simulation and optimization	Limited multiphysics coverage
Simpleware	Synopsys	Image processing and FEA meshing	Converting CT/MRI data to FEA-ready models	Excellent segmentation and meshing	Expensive; requires additional FEA software
Morpheus	Biovia (Dassault Systèmes)	Computational materials science	Material behavior and surface coating analysis	Good for metal biomaterials and coatings research	Not a full CAD or meshing tool

Abbreviations: AM, additive manufacturing; CAD, computer-aided design; CAM, computer-aided manufacturing; CT, computed tomography; FEA, finite element analysis; MRI, magnetic resonance imaging; STL, standard tessellation language.

smooth transition between stiff and compliant areas, thereby mitigating mismatch in elasticity and lowering the likelihood of implant failure under typical loading conditions.[92] Recent studies have confirmed that graded porosity can significantly improve the overall performance of bone implants by enhancing their mechanical strength and reducing the risk of periprosthetic fractures.[92]

Topological distribution structures utilize advanced optimization algorithms to strategically allocate

material based on loading conditions and performance requirements. This innovative design process produces highly efficient geometries that balance mechanical strength with lightweight characteristics, thereby enhancing the structural integrity and fatigue resistance of bone implants.[93] A notable example involves the use of triply periodic minimal surfaces (TPMS), such as gyroid, diamond, Neovius, and primitive structures.[94] These periodic surfaces facilitate effective stress distribution and adaptability to physiological loads, while their high degree of interconnected porosity supports fluid transport and cellular anchorage.[95] Such advancements are critical not only for mechanical performance but also for promoting effective osseointegration, which is fundamental to the bone healing process.

An overview of the four major categories of lattice structures used in metallic bone implants—regular, random, gradient, and topological—is provided in **Figure 12**, illustrating their distinct geometrical designs. Their implications for biomimetics are profound: by closely mimicking the micro-architectural characteristics of natural bone, these designs significantly enhance biological compatibility and functional efficiency. With ongoing progress in AM, the ability to fabricate highly intricate porous metallic lattices holds great promise for patient-specific, optimized implants that promote rapid recovery, seamless osseointegration, and improved long-term clinical outcomes.[96]

4.4. Recent advancements in the optimization of personalized bone implant design

Recent advancements in the optimization of personalized metallic bone implant design (**Table 6**) mark a major shift away from standardized solutions in favor of intelligently engineered, highly individualized, and biologically integrated devices. This transformation is enabled by the convergence of AM, bioinspired architectures, multiscale modeling, advanced surface treatments, and AI. Together, these technologies allow for the design of metallic

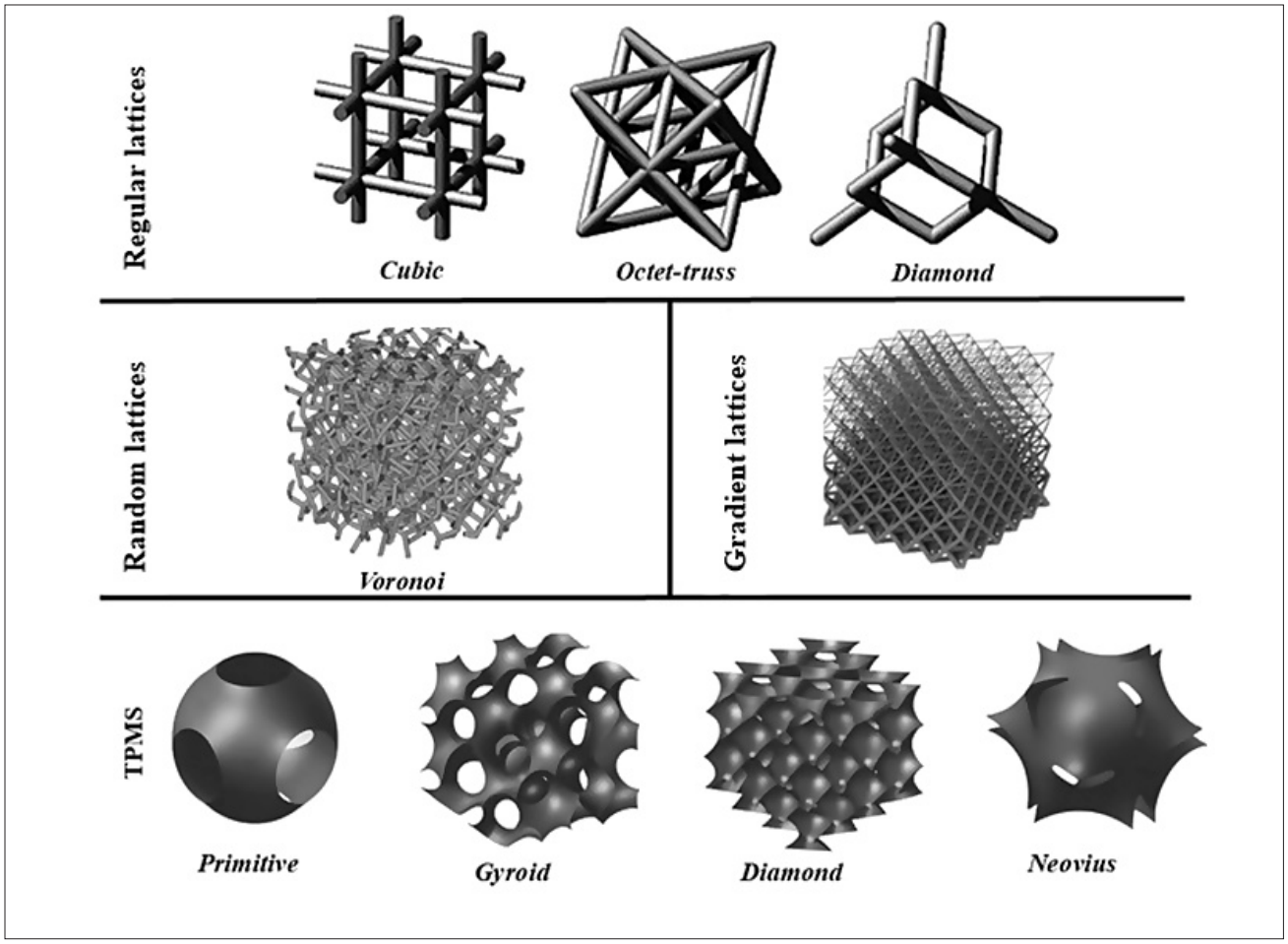

Figure 12. Types of lattice structures for metallic bone implants. Adapted from ref.[89]. Abbreviation: TPMS, triply periodic minimal surfaces.

Table 6. Recent advances in personalized metallic bone implant design

References	Innovation area	Key contribution
[97–99]	Anatomical personalization	Patient-specific implants based on imaging data, enabling improved biomechanical restoration
[100,101]	Multiscale architecture and surface design	Integration of macro–micro–nano porosity and optimized surface topography to enhance osseointegration
[93,102,103]	Biomimetic structures	Elastic modulus adaptation to reduce stress shielding and enhance implant fixation
[104,105]	AI-driven geometric optimization	Application of machine learning and genetic algorithms for automated implant design
[106,107]	Personalized surgical techniques	Patient-specific osseodensification protocols to improve primary stability
[108,109]	Targeted clinical validation	Customized implants shown to restore joint mechanics more accurately than standard models

Abbreviation: AI, artificial intelligence.

implants optimized in terms of geometry, porosity, surface roughness, and mechanical properties, to better match the biological and mechanical complexity of the patient. The central driver of this personalization is the direct use of medical imaging data to generate 3D digital models tailored to individual anatomy. For example, Caiti *et al.*[97] showed that the use of patient-specific metallic fixation plates in osteotomy procedures leads to better biomechanical restoration. Similarly, Milovanović *et al.*[98] demonstrated the clinical effectiveness of personalized titanium mandibular implants, while Wang *et al.*[99] emphasized the relevance of modular hemipelvic endoprostheses for reconstructing complex bone defects. These examples illustrate how morphological conformity, intraoperative adaptability, and modularity have become key decisive factors in clinical success.

At the microstructural level, the work of Martinez-Marquez *et al.*[100] and Deng *et al.*[110] demonstrated that metallic implants with multiscale architectures—combining macro-, micro-, and nanoporosity—promote cell adhesion, vascularization, and osseointegration, even without bioactive coatings. These advances reinforce the concept that internal architecture alone, if properly controlled, can induce a favorable biological response. Furthermore, Wähnert *et al.*[101] highlighted the role of surface topography in peri-implant bone remodeling, ultimately influencing long-term secondary stability. Bioinspired metallic lattice structures, such as trabecular-like networks or TPMS, play a central role in this strategy. Chao *et al.*[93] and Maietta *et al.*[102] showed how such architectures reduce stress shielding by locally adjusting the implant's elastic modulus while maintaining mechanical robustness. Rogala *et al.*[103] also proposed a multi-spiked endoprosthesis that mimics trabecular interdigitation, enhancing primary fixation in complex joint reconstruction. These architectures, further enhanced by graded porosity, facilitate smoother mechanical continuity between implant and host bone.

AI actively contributes to this evolution. Two studies used machine learning techniques and genetic algorithms to automate the design and optimization of metallic implants, particularly lattice geometries, based on biomechanical and biological criteria.[104,105] These tools allow for the rapid exploration of thousands of geometric configurations, while simultaneously considering clinical and manufacturing constraints. On the surgical side, personalized techniques extend into intraoperative protocols. Mello-Machado *et al.*[106] and Olmedo-Gaya *et al.*[107] demonstrated that patient-specific osseodensification protocols enhance bone compaction around the implant, improving primary stability. Additional clinical studies by Dong *et al.*[108] and Kim *et al.*[111] confirmed that customized implants, such as tibial components or femoral head prostheses, restore joint mechanics more physiologically than standard models, reducing misalignments and supporting functional rehabilitation. Kang *et al.*[109] further demonstrated the benefits of topological optimization in improving postoperative outcomes for talar implants.

Despite these remarkable advances, several challenges remain. Long-term validation of these personalized implants is still limited to small patient cohorts, and the lack of interoperability between medical imaging, modeling, mechanical simulation, and 3D printing software hinders the full automation of the design workflow. Additionally, the high cost of metallic materials, advanced fabrication equipment, and post-processing treatments continues to restrict large-scale clinical adoption. The absence of standardized biological and mechanical evaluation protocols, both *in vitro* and *in vivo*, also limits the ability to reliably compare outcomes across different studies. Overcoming these barriers requires long-term multicenter

clinical trials with standardized assessment criteria, development of integrated software platforms for seamless workflow management, and deeper incorporation of AI tools into the modeling, simulation, and quality assurance. The future of personalized metallic implantology thus lies in the development of smart implants equipped with sensors for real-time physiological monitoring, the deployment of 5D and 6D printing technologies for enhanced fatigue resistance and geometric fidelity, the integration of gradient mechanical structures for localized stiffness tuning, and fully AI-guided surgical planning synchronized with design and manufacturing. By closing the loop between design, production, implantation, and clinical monitoring, these innovations aim to significantly improve patient outcomes and usher orthopedic and dental implantology into the era of precision medicine.

5. Advanced numerical simulation of biomimetic metallic bone implants: from classical tools to multiphysics coupling

5.1. Finite element analysis

FEA is an essential approach in the design and evaluation of metallic biomimetic implants, enabling the prediction of mechanical behavior under different physiological loads before manufacturing. This technique optimizes the internal structure of implants, improves osseointegration, and reduces the risk of long-term complications. However, simulation outcomes still require experimental validation. The modeling process typically proceeds from mesh generation to the application of boundary conditions and physiological loads. Digital models, often derived from medical imaging, are segmented using Mimics and then further processed with software such as ANSYS, ABAQUS, nTopology, and SolidWorks. Accurate meshing is essential to avoid prediction errors and inefficiencies in numerical calculations. Equally important is the correct assignment of material properties: Ti–6Al–4V remains the benchmark alloy for metallic implants, while composites such as HAp-reinforced polyether ether ketone (PEEK) are increasingly investigated to improve bone integration and reduce excessive stiffness. FEA simulations evaluate parameters such as von Mises stresses, displacement, stiffness, safety factor, and fatigue behavior.[112] A key determinant in implant biomechanics is porosity, as natural bone is inherently porous and heterogeneous. Comparative analyses of lattice structures provide valuable insights into stress distribution, stress-shielding mitigation, and overall implant performance.

Caouette *et al.*[113] demonstrated that a biomimetic carbon fiber femoral stem coated with HAp considerably reduced stress shielding compared with a Ti–6Al–4V titanium stem, while maintaining micromovements below the threshold critical for osseointegration. Similarly, Ceddia *et al.*[114] explored the benefits of carbon fiber composites in femoral stem design through topology optimization and FEA. The study revealed that a carbon-fiber-reinforced femoral stem exhibited a significant stress reduction from 987 to 509 MPa, along with a 30% weight reduction, contributing to a more homogeneous load transfer and decreased risk of bone resorption (**Figure 13**). Rezapourian *et al.*[115] studied different biomimetic topologies using FEA, revealing that the structure inspired by haversian canals (model D9) achieved an elastic modulus of 20.18 GPa and a porosity of 37.26%, favoring homogeneous stress distribution. A comparative study by Munteanu *et al.*[116] evaluated a femoral stem topologically optimized by AM against conventional Ti–6Al–4V implants. Their results show a 15% reduction in mass, a decrease in maximum stress to 349.1 MPa, and improved osseointegration due to controlled porosity, all of which reduces stress shielding while maintaining the required mechanical strength.

The study by Zhang *et al.*[80] showed that incorporating porosities ranging from 66.1 to 79.5% in Ti–6Al–4V implants provides an optimal compromise between mechanical strength and biological performance, with compressive strengths of between 36 and 140 MPa, values consistent with both trabecular and cortical bone. These results align with Alemayehu *et al.*,[117] who analyzed the influence of pore size on the stress distribution and mechanical stability of biomimetic dental implants made from Voronoi structures, with porosity ranging from 70 to 95%. Using nTopology and Creo Parametric, this study revealed that increasing pore size reduces mechanical stress, with von Mises values dropping from 305.93 MPa for a 1 mm pore to 161.16 MPa for a 2.5 mm pore (**Figure 14**). However, the micromotion increased to 17 μm for 2.5 mm pores, which could compromise the initial stability of the implant (**Figure 15**). An optimal pore size of 2 mm was thus identified as a good compromise between mechanical strength and biomimetic integration. In the same context, Simoneau *et al.*[118] and Mehboob *et al.*[119] studied the effect of porosity on orthopedic implants and confirmed the importance of striking a balance between strength and flexibility. Mehboob *et al.*[119] specifically analyzed cubic, diamond, and body-centered cubic (BCC) structures, with porosities ranging from 20 to 90%, using ABAQUS 6.17. Their simulations showed that porosity has a direct influence on implant stiffness and strength, with an optimal porosity of 47.3% replicating the mechanical properties of cortical bone. Taken together, these studies demonstrate that porosity plays a decisive role in the design of biomimetic implants, where a balance between mechanical strength, flexibility, and osseointegration

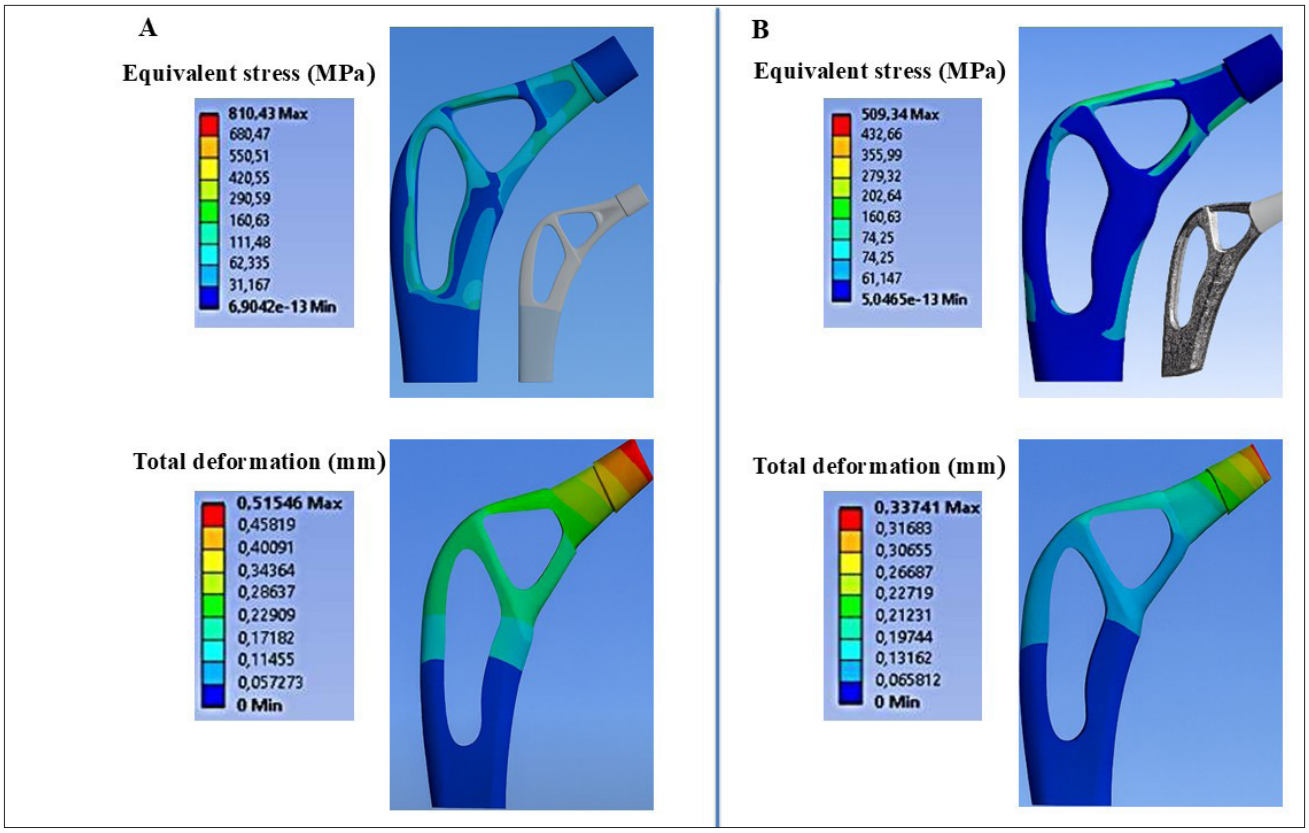

Figure 13. Results of Von Mises stress and total deformation for the topologically optimized stem: (A) titanium and (B) composite material. Adapted from ref.[114]. Abbreviation: FEA, finite element analysis.

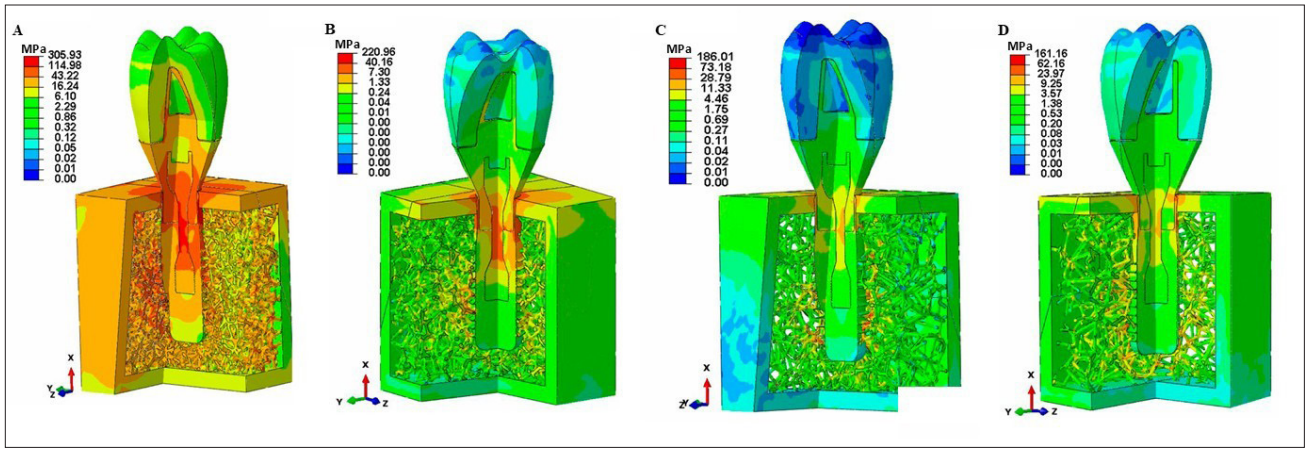

Figure 14. Maximum von Mises stress distribution in double-sliced assembled implant sections for four biomimetic VTB models. (A) VTB10. (B) VTB15. (C) VTB20. (D) VTB25. Adapted from ref.[117]. Abbreviation: VTB, voronoi trabecular bone.

is essential to improve bone compatibility and reduce undesirable effects such as stress shielding.

Pei *et al.*[120] explored homogeneous, quasi-homogeneous, and heterogeneous Ti–6Al–4V implants fabricated by SLM. FEA demonstrated superior stress distribution in the quasi-homogeneous implants compared with the other models (**Figure 16**). Li *et al.*[121] compared biomimetic implants made of PEEK/n-HAp/Carbon fibers, PEEK/HAp, and Ti–6Al–4V for mandibular reconstruction. Their study showed that Ti–6Al–4V, although more rigid, offers more stable fixation and improved osseointegration, while PEEK-based implants absorb loads better but present an increased risk of deformation and micromovements, which can compromise their stability and promote bone

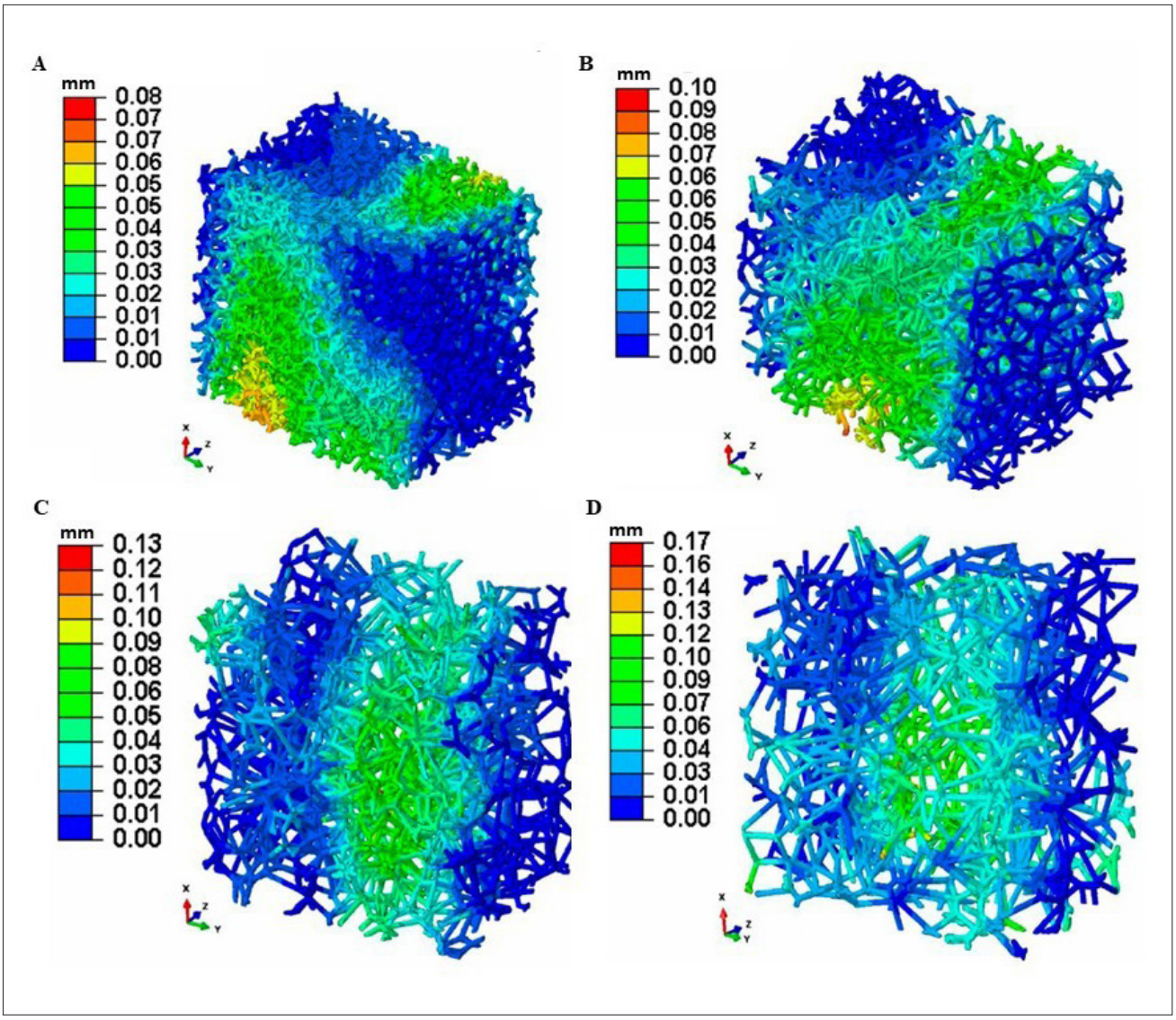

Figure 15. Displacement magnitude contour plots for biomimetic VTB structures with different pore sizes. (A) VTB10. (B) VTB15. (C) VTB20. (D) VTB25. Adapted from ref.[117]. Abbreviation: VTB, voronoi trabecular bone.

resorption. Despite their lightweight and biological compatibility, PEEK implants need further optimization to improve their osseointegration.

FEA has also been widely used to compare different biomimetic structures and architectures in the design of orthopedic implants. Mehboob *et al.*[119] analyzed several geometries of lattice structures and showed that cubic structures offer high compressive strength but anisotropic behavior, while diamond structures have lower stiffness. BCC structures, on the other hand, represent an optimal compromise between rigidity and flexibility, ensuring better biomechanical adaptation and a more even distribution of physiological stresses. Chatzigeorgiou *et al.*[122] studied the impact of TPMS structures on stress distribution and the reduction of stress shielding in the context of partial femur replacement. Their multiscale approach—incorporating a global model and a local model based on bone anatomy—demonstrated that primitive structures significantly improved stress distribution, while gyroid structures reduced stress concentration zones (**Figure 17**). Soro *et al.*[123] also used FEA further showed that gyroid TPMS in Ti-25Ta implants effectively reduced stress shielding, ensuring better mechanical adaptation to physiological conditions. In addition, Salaha *et al.*[124] compared gyroid and Voronoi structures applied to hip implants and found that the Voronoi implant provided better stress dissipation and reduced mass while maintaining even load distribution on the bone. This study also highlighted titanium alloy

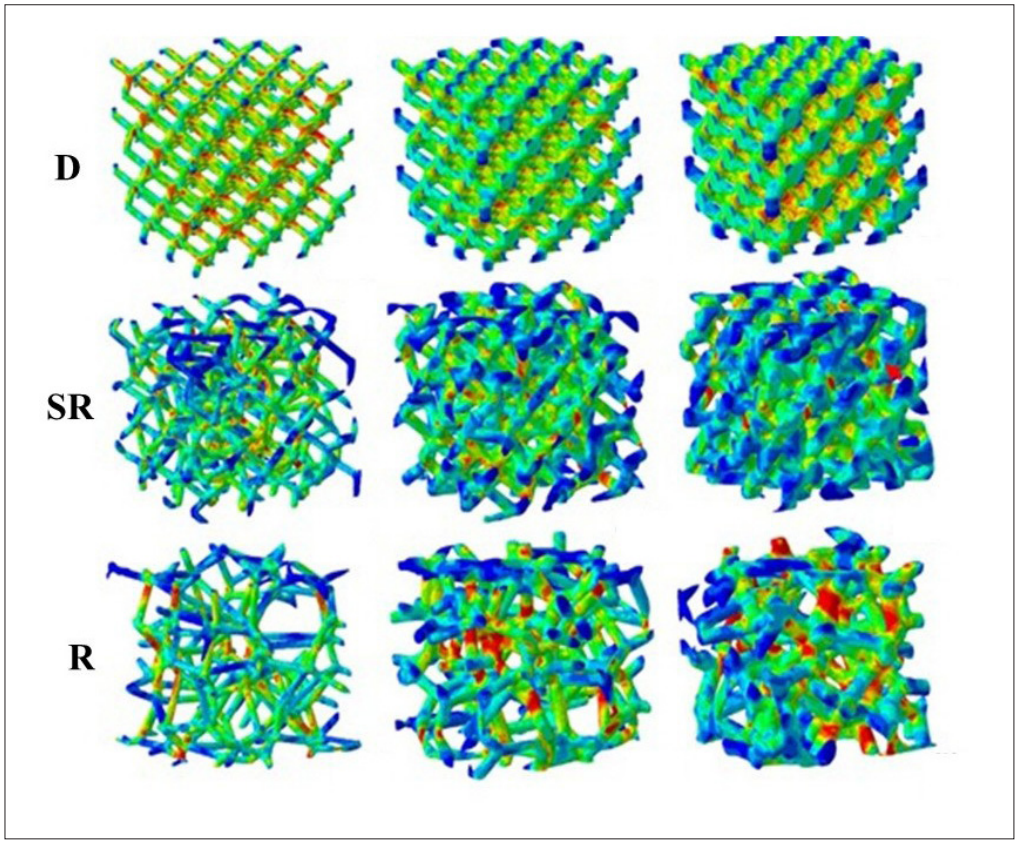

Figure 16. Compressive mechanical testing and FEA simulation results of three structural designs: D = Deterministic regular lattice structures, SR = Semi-random lattice structures, and R = Random lattice structures. Each category includes three parametric variations (different pore sizes and relative densities) to illustrate the effect of structural variation on stress distribution. Adapted from Pei *et al.*[120] Abbreviation: FEA, finite element analysis.

Ti–6Al–4V as the most suitable material due to its high strength and biomechanical compatibility, although magnesium alloys may offer lightweight alternatives for minimizing bone stresses.

5.2. Computational fluid dynamics

CFD has emerged as a powerful numerical tool for investigating the biological performance of lattice-based metallic implants, particularly in the context of osseointegration. Unlike purely mechanical simulations, CFD enables the modeling of interstitial fluid flow, wall shear stress (WSS), and nutrient transport through complex porous architectures. These parameters are critical for regulating cellular behaviors such as adhesion, proliferation, osteogenic differentiation, and vascularization, all of which are essential for successful implant integration.

Numerous studies have highlighted the strong influence of internal geometry, especially TPMS structures, on local fluid dynamics and permeability. Ali *et al.*[125] demonstrated that gyroid and diamond architectures produce more homogeneous WSS distributions and greater permeability than conventional topologies, thereby enhancing the osteogenic response. Karuna *et al.*[126] further showed that introducing a porosity gradient within TPMS implants improves nutrient transport and reduces regions of low shear stress, a key factor in preventing cellular stagnation and hypoxia. Similarly, Lai *et al.*[127] emphasized the role of curvature and geometric connectivity in shaping both local flow behavior and internal stress gradients within porous implants. Pei *et al.*[120] used CFD to compare the permeability of three types of Ti–6Al–4V lattice structures (homogeneous, quasi-homogeneous, and heterogeneous), demonstrating that the quasi-homogeneous configuration offers an optimal trade-off between mechanical integrity and fluid diffusion, thus promoting a more favorable environment for bone ingrowth and long-term osseointegration. These findings underline the importance of designing implants with fluid-conductive architectures that not only meet mechanical requirements but also create microenvironments conducive to tissue regeneration and angiogenesis. CFD results are thus becoming key design

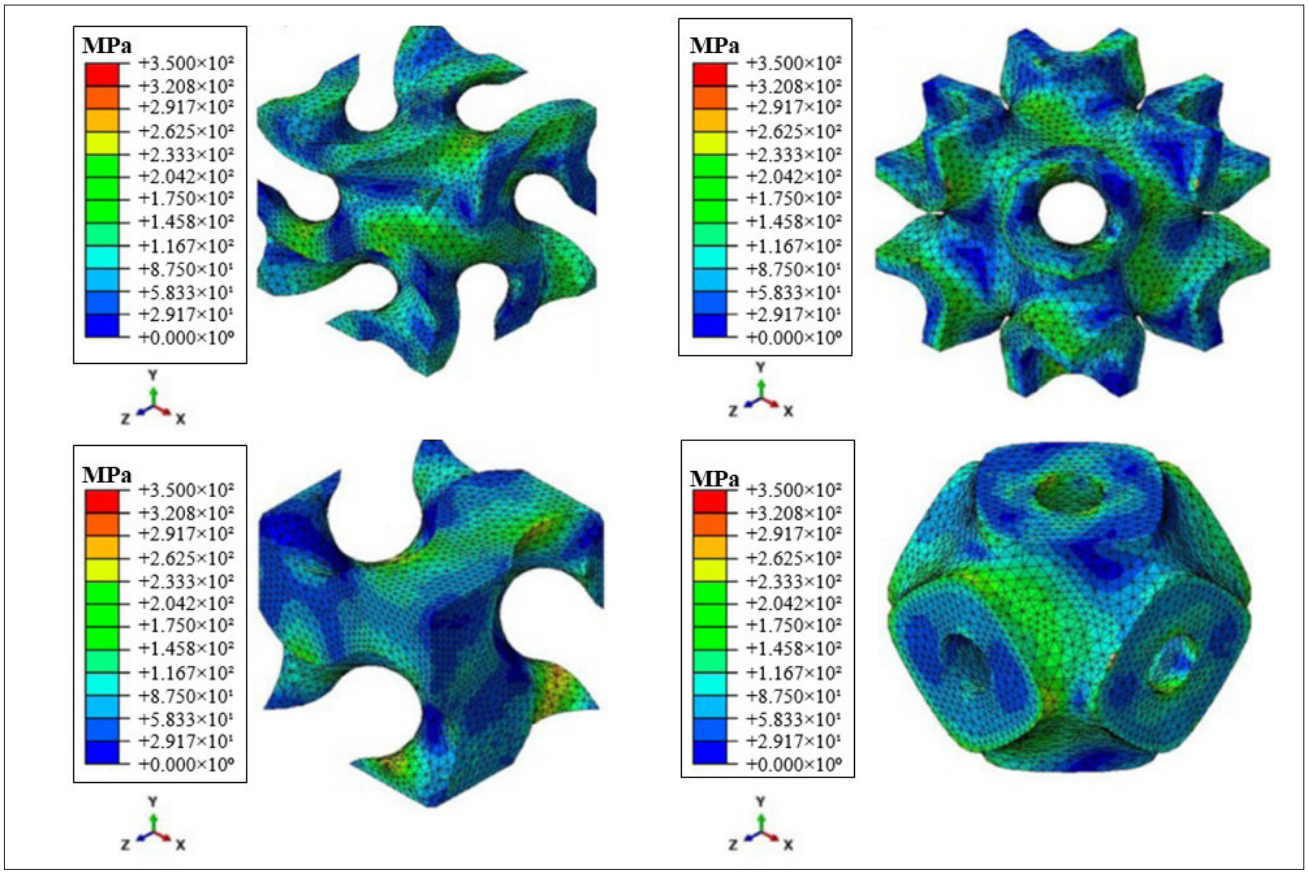

Figure 17. Von Mises stress contours for gyroid sheet, IWP sheet, gyroid skeletal, and primitive sheet unit cells. Adapted from ref.[122].

parameters, integrated early into the digital workflow of next-generation biomimetic implants.

5.3. Integration of multi-field coupling models for physiological accuracy

To better reproduce the complex physiological environment surrounding metallic bone implants, recent studies have adopted multiphysics simulation models that couple several physical domains—mechanical, thermal, chemical, biological, and electromagnetic—within a single computational framework. These models are particularly relevant for porous or lattice implants fabricated by AM, where multiple physical phenomena interact simultaneously and influence implant performance. **Figure 18** illustrates a typical multiphysics workflow, combining structural analysis, fluid dynamics, and topology optimization with additional coupled processes such as thermal conduction, chemical degradation, ion transport, and electromagnetic behavior under MRI exposure.

A pioneering example is provided by Ma *et al.*,[128] who developed a triply coupled framework integrating FEA, CFD, and topology optimization. Their model simultaneously assessed mechanical stability and interstitial fluid transport in TPMS-based implants. The results revealed optimal pore arrangements that improved both structural strength and permeability—key prerequisites for osseointegration, nutrient delivery, and cellular proliferation. In another domain, Jin *et al.*[129] investigated the mechanical-chemical degradation of biodegradable magnesium-based implants. Using time-dependent FEA, they modeled progressive implant resorption and its impact on local stress redistribution and bone remodeling, showing how degradation rates affect stress shielding and peri-implant bone health. Such models are critical for tailoring degradation kinetics to the natural healing timeline.

From the manufacturing perspective, Medina-Gálvez *et al.*[130] introduced a thermo-mechanical simulation to predict microstructural transformations in Ti-6Al-4V implants during SLM. Their study highlighted the influence of thermal gradients, cooling rates, and energy input on the formation of martensitic α′ phases and residual stresses, both of which have a major impact on implant fatigue resistance and biological response.

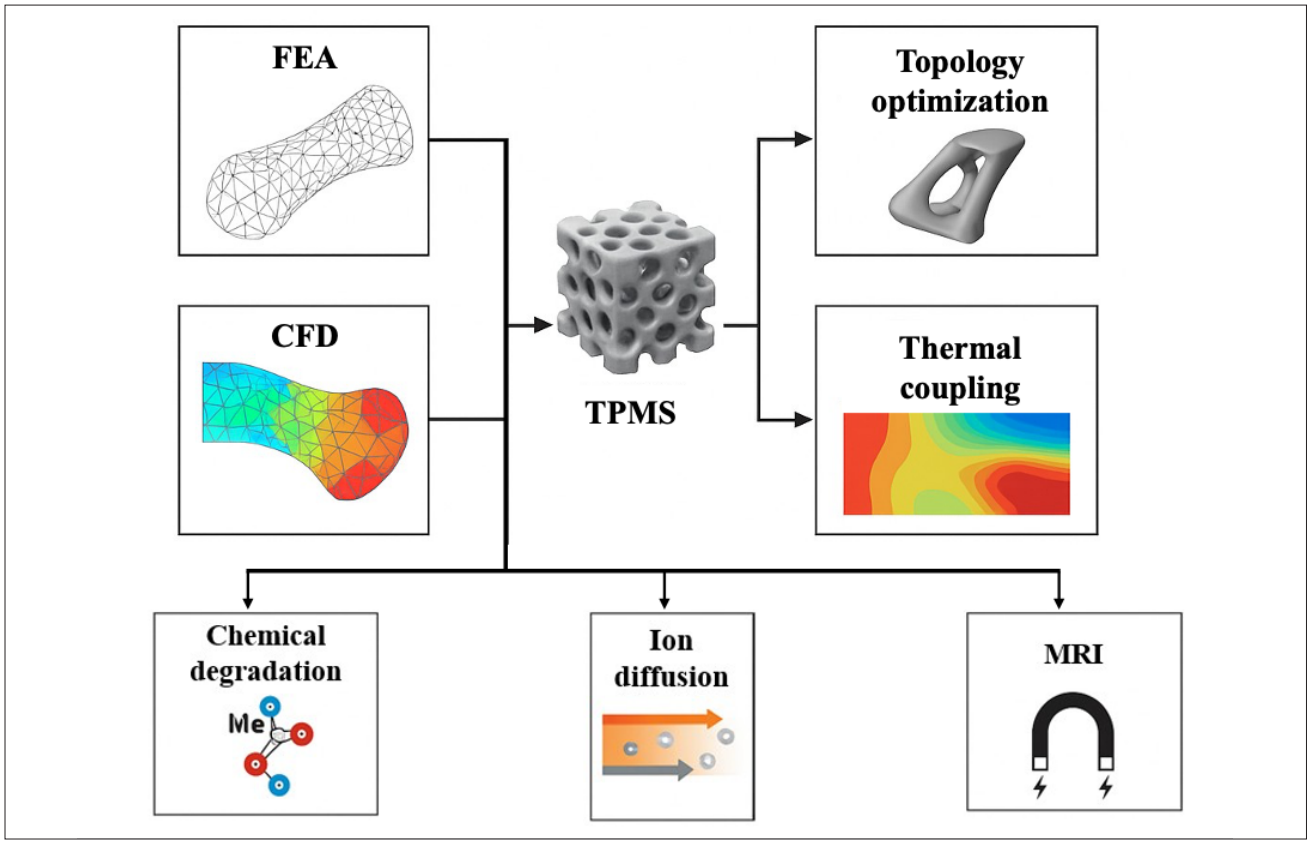

Figure 18. Schematic of a multiphysics simulation workflow for metallic bone implants. Abbreviations: CFD, computational fluid dynamics; FEA, finite element analysis; MRI, magnetic resonance imaging; TPMS, triply periodic minimal surfaces.

At the interface level, Ogawa *et al.*[131] and Rappe *et al.*[132] proposed chemical–mechanical–diffusive models to simulate metallic ion release through corrosion and subsequent tissue diffusion. These simulations revealed potential local inflammatory responses, linking surface degradation mechanisms to implant biocompatibility and safety. By including variables such as pH, oxide film behavior, and stress-assisted corrosion, these models offer a predictive understanding of long-term performance. For experimental validation, Hafidz *et al.*[133] integrated surface acoustic wave sensors into AM implants to measure real-time thermal and mechanical conditions during loading. The data validated predictions from a thermomechanical simulation, confirming temperature distributions and stress fields within the implant. This work demonstrates the synergy between *in silico* modeling and sensor-based monitoring for implant reliability. Lastly, Makarov *et al.*[134] employed an electromagnetic–thermal model to simulate radiofrequency-induced heating of metallic implants during MRI exposure. Their results identified hotspots and temperature elevations near implant surfaces, which are crucial for ensuring patient safety and adherence to MRI standards.

Altogether, these studies exemplify the transition from simplified, single-physics models to integrated, multiphysics computational tools that are not only more physiologically realistic but also vital for optimizing implant design, function, durability, and clinical safety under patient-specific conditions. They pave the way for next-generation, smart biomedical implants with predictive, personalized, and feedback-enabled capabilities. Considering this growing body of research, it becomes increasingly clear that the adoption of multiphysics coupling in numerical simulations is not merely an enhancement but a necessity for the rational design of metallic bone implants. These models enable researchers and clinicians to bridge the gap between mechanical reliability, biological integration, and patient-specific variability. In our view, the integration of such advanced computational strategies, especially when validated by real-time experimental data, will play a pivotal role in the future of implant development. They not only allow for predictive insight into failure modes and biological outcomes but also facilitate regulatory compliance and clinical translation. Ultimately, multiphysics modeling should become the gold standard in the simulation pipeline

for next-generation implants, particularly those leveraging the full potential of AM and biofunctionalization.

6. Conclusion and future perspectives

AM has fundamentally transformed the landscape of bone implantology by enabling the fabrication of personalized, structurally optimized, and biomimetic metallic implants that closely replicate the complex architecture and mechanical behavior of native bone. This review has systematically explored the current technological, clinical, and biological advances that support the emergence of AM-based implants, focusing on key manufacturing processes such as SLM and EBM, the selection and optimization of advanced biocompatible materials like Ti-6Al-4V and cobalt-chromium alloys, and the compelling *in vivo* and clinical data highlighting their mid-term reliability and success in orthopedic applications.

Biomimetic design strategies—including the incorporation of graded porosity and topologically optimized lattice architectures—have demonstrated significant benefits in enhancing osseointegration, reducing stress shielding, and promoting a favorable biomechanical environment at the bone–implant interface. Simultaneously, patient-specific customization, enabled by high-resolution CT and MRI imaging, DICOM segmentation, and advanced CAD modeling, allows implants to be anatomically tailored while integrating bioinspired mechanical behavior. Numerical simulation tools, such as FEA and CFD, play an essential role in preclinical evaluation, offering predictive insights into stress distribution, fluid flow, fatigue performance, and structural stability under physiological loads. Emerging multiphysics coupling models that integrate mechanical, thermal, chemical, and biological domains have further revolutionized the predictive design pipeline, offering highly realistic simulations of *in vivo* conditions, including degradation kinetics, nutrient diffusion, corrosion, and remodeling dynamics. Despite these breakthroughs, several barriers continue to limit widespread clinical translation: the high cost of metal powders and AM equipment, the lack of universal standards for testing and validation, fragmented digital workflows, limited clinician training in AM technologies, and insufficient long-term clinical evidence, particularly for weight-bearing applications in younger and active patients.

Looking forward, the future of AM metallic bone implants lies in the convergence of multiple innovations: the integration of AI and digital twin technologies for real-time process optimization and automated implant design; the development of smart, sensor-integrated implants capable of postoperatively monitor strain, temperature, and biological markers; and the adoption of advanced manufacturing paradigms such as 5D and 6D printing, which combine multi-axis deposition, smart materials, and biofunctional gradients to produce next-generation adaptive implants. Furthermore, sustainable approaches must be prioritized, including the use of recyclable metal powders, streamlined post-processing protocols, and scalable manufacturing workflows to make these advanced solutions accessible to broader healthcare systems. In conclusion, AM—when synergized with biomimetic architecture, patient-specific customization, predictive multiphysics simulation, and intelligent clinical feedback systems—holds the potential to redefine the standard of care in skeletal reconstruction. It offers not only a path toward superior mechanical performance and biological integration but also ushers in a new era of intelligent, regenerative, and truly personalized orthopedic and dental implantology, where the implant becomes a dynamic interface between engineered precision and living biology.

Acknowledgments

The authors express their sincere gratitude to the Ministry of Higher Education, Scientific Research and Innovation of the Kingdom of Morocco and the State Secretariat for Education, Research and Innovation of the Swiss Confederation for their support through the Morocco–Switzerland bilateral program. The authors also warmly thank the participating research teams and the doctoral students whose commitment and collaboration were instrumental to the success of this project.

Funding

This work was supported by the Morocco–Switzerland bilateral program within the framework of the Memorandum of Understanding between the Ministry of Higher Education, Scientific Research and Innovation of the Kingdom of Morocco and the State Secretariat for Education, Research and Innovation of the Swiss Confederation.

Conflict of interest

The authors declare no competing interests.

Author contributions

Conceptualization: Lamiae Jaouher, Abdelwahed Barkaoui
Supervision: Abdelwahed Barkaoui, Khalil Aouadi, Haifa Sallem
Visualization: Lamiae Jaouher
Writing–original draft: Lamiae Jaouher
Writing–review & editing: All authors

Ethics approval and consent to participate

Not applicable.

Consent for publication

Not applicable.

Availability of data

Not applicable.

References

1. Musculoskeletal health. https://www.who.int/news-room/fact-sheets/detail/musculoskeletal-conditions. Accessed December 24, 2024.
2. Fortune Business Insights. *Orthopedic Implants Market Size, Share & Industry Analysis, by Product (Joint Reconstruction, Spinal Implants, Trauma Implants, and Others), by End-user (Hospitals & Ambulatory Surgery Centers, Orthopedic Clinics & Others), and Regional Forecas*t, 2024-2032. Fortune Business Insights; 2025. Accessed May 10, 2025. https://www.fortunebusinessinsights.com/industry-reports/orthopedic-implants-market-101659
3. Healthcare Additive Manufacturing Market Size Report, 2030. https://www.grandviewresearch.com/industry-analysis/healthcare-additive-manufacturing-market. Accessed December 24, 2024.
4. Kumar R, Kumar M, Chohan JS. The role of additive manufacturing for biomedical applications: a critical review. *J Manuf Process*. 2021;64:828-850. doi: 10.1016/j.jmapro.2021.02.022
5. Hull CW, Gabriel S. National Center for Biotechnology Information. PubChem Patent Summary for US-6027324-A, Apparatus for production of three dimensional objects by stereolithography. https://pubchem.ncbi.nlm.nih.gov/patent/US-6027324-A. Accessed June 3, 2025.
6. Zhou L, Miller J, Vezza J, *et al.* Additive manufacturing: a comprehensive review. *Sensors*. 2024;24(9):2668. doi: 10.3390/s24092668
7. Amaya-Rivas JL, Perero BS, Helguero CG, *et al.* Future trends of additive manufacturing in medical applications: an overview. *Heliyon*. 2024;10(5):e26641. doi: 10.1016/j.heliyon.2024.e26641
8. Li W, Li J, Pan C, Lee JS, Kim BS, Gao G. Light-based 3D bioprinting techniques for illuminating the advances of vascular tissue engineering. *Mater Today Bio*. 2024;29:101286. doi: 10.1016/j.mtbio.2024.101286
9. Hajare DM, Gajbhiye TS. Additive manufacturing (3D printing): recent progress on advancement of materials and challenges. *Mater Today Proc*. 2022;58(Part 2):736-743. doi: 10.1016/j.matpr.2022.02.391
10. Ngo TD, Kashani A, Imbalzano G, Nguyen KTQ, Hui D. Additive manufacturing (3D printing): a review of materials, methods, applications and challenges. *Compos B Eng*. 2018;143:172-196. doi: 10.1016/j.compositesb.2018.02.012
11. Aufa AN, Hassan MZ, Ismail Z, *et al.* Current trends in additive manufacturing of selective laser melting for biomedical implant applications. *J Mater Res Technol*. 2024;31:213-243. doi: 10.1016/j.jmrt.2024.06.041
12. Zhao L, Wang Y, Wang Q, Zhang Y, Yang G. Optimization design and SLM manufacturing of porous titanium alloy femoral stem. *Materials*. 2024;17(19):4896. doi: 10.3390/ma17194896
13. Razzaq MH, Zaheer MU, Asghar H, Aktas OC, Aycan MF, Mishra YK. Additive manufacturing for biomedical bone implants: shaping the future of bones. *Mater Sci Eng R Rep*. 2025;163:100931. doi: 10.1016/j.mser.2025.100931
14. Osipovich K, Kalashnikov K, Chumaevskii A, *et al.* Wire-feed electron beam additive manufacturing: a review. *Metals*. 2023;13(2):279. doi: 10.3390/met13020279
15. Javaid M, Haleem A. 4D printing applications in medical field: a brief review. *Clin Epidemiol Glob Health*. 2019;7(3):317-321. doi: 10.1016/j.cegh.2018.09.007
16. Amukarimi S, Mozafari M. 4D bioprinting of tissues and organs. *Bioprinting*. 2021;23:e00161. doi: 10.1016/j.bprint.2021.e00161
17. Haleem A, Javaid M, Vaishya R. 5D printing and its expected applications in orthopaedics. *J Clin Orthop Trauma*. 2019;10(4):809-810. doi: 10.1016/j.jcot.2018.11.014
18. Cheng Y, Fu Y, Ma L, *et al.* Rheology of edible food inks from 2D/3D/4D printing, and its role in future 5D/6D printing. *Food Hydrocoll*. 2022;132:107855. doi: 10.1016/j.foodhyd.2022.107855
19. Vasiliadis AV, Koukoulias N, Katakalos K. From three-dimensional (3D)- to 6D-printing technology in orthopedics: science fiction or scientific reality? *JFB*. 2022;13(3):101. doi: 10.3390/jfb13030101
20. Georgantzinos SK, Giannopoulos GI, Bakalis PA. Additive manufacturing for effective smart structures: the idea of 6D printing. *J Compos Sci*. 2021;5(5):119. doi: 10.3390/jcs5050119
21. Gao B, Zhao H, Peng L, Sun Z. A review of research progress in selective laser melting (SLM). *Micromachines*. 2022;14(1):57. doi: 10.3390/mi14010057
22. Bandyopadhyay A, Ghosh S, Boccaccini AR, Bose S. 3D printing of biomedical materials and devices. *J Mater Res*. 2021;36(19):3713-3724.

doi: 10.1557/s43578-021-00407-y

23. Salem H, Carter LN, Attallah MM, Salem HG. Influence of processing parameters on internal porosity and types of defects formed in Ti-6Al-4V lattice structure fabricated by selective laser melting. *Mater Sci Eng A*. 2019;767:138387. doi: 10.1016/j.msea.2019.138387

24. Zhai Y, Zhang H, Wang J, Zhao D. Research progress of metal-based additive manufacturing in medical implants. *Rev Adv Mater Sci*. 2023;62(1):20230148. doi: 10.1515/rams-2023-0148

25. Xiong W, Hao L, Li Y, *et al.* Effect of selective laser melting parameters on morphology, microstructure, densification and mechanical properties of supersaturated silver alloy. *Mater Des*. 2019;170:107697. doi: 10.1016/j.matdes.2019.107697

26. Eldesouky I, Harrysson O, West H, Elhofy H. Electron beam melted scaffolds for orthopedic applications. *Addit Manuf*. 2017;17:169-175. doi: 10.1016/j.addma.2017.08.005

27. Wu Y, Wang Y, Liu M, Shi D, Hu N, Feng W. Mechanical properties and in vivo assessment of electron beam melted porous structures for orthopedic applications. *Metals*. 2023;13(6):1034. doi: 10.3390/met13061034

28. Herzog D, Seyda V, Wycisk E, Emmelmann C. Additive manufacturing of metals. *Acta Mater*. 2016;117:371-392. doi: 10.1016/j.actamat.2016.07.019

29. Amato KN, Gaytan SM, Murr LE, *et al.* Microstructures and mechanical behavior of Inconel 718 fabricated by selective laser melting. *Acta Mater*. 2012;60(5):2229-2239. doi: 10.1016/j.actamat.2011.12.032

30. Ni J, Ling H, Zhang S, *et al.* Three-dimensional printing of metals for biomedical applications. *Mater Today Bio*. 2019;3:100024. doi: 10.1016/j.mtbio.2019.100024

31. Kennedy SM, A V, K A. Exploring the frontiers of metal additive manufacturing in orthopaedic implant development. *MethodsX*. 2024;13:103056. doi: 10.1016/j.mex.2024.103056

32. Pei X, Wu L, Lei H, *et al.* Fabrication of customized Ti6AI4V heterogeneous scaffolds with selective laser melting: optimization of the architecture for orthopedic implant applications. *Acta Biomater*. 2021;126:485-495. doi: 10.1016/j.actbio.2021.03.040

33. Gao C, Wang C, Jin H, *et al.* Additive manufacturing technique-designed metallic porous implants for clinical application in orthopedics. *RSC Adv*. 2018;8(44):25210-25227. doi: 10.1039/C8RA04815K

34. Tan XP, Tan YJ, Chow CSL, Tor SB, Yeong WY. Metallic powder-bed based 3D printing of cellular scaffolds for orthopaedic implants: a state-of-the-art review on manufacturing, topological design, mechanical properties and biocompatibility. *Mater Sci Eng C*. 2017;76:1328-1343. doi: 10.1016/j.msec.2017.02.094

35. Liu X, Chu P, Ding C. Surface modification of titanium, titanium alloys, and related materials for biomedical applications. *Mater Sci Eng R Rep*. 2004;47(3-4):49-121. doi: 10.1016/j.mser.2004.11.001

36. Wauthle R, Van Der Stok J, Amin Yavari S, *et al.* Additively manufactured porous tantalum implants. *Acta Biomater*. 2015;14:217-225. doi: 10.1016/j.actbio.2014.12.003

37. Dewidar MM, Khalil KA, Lim JK. Processing and mechanical properties of porous 316L stainless steel for biomedical applications. *Trans Nonferrous Met Soc China*. 2007;17(3):468-473. doi: 10.1016/S1003-6326(07)60117-4

38. Bai L, Gong C, Chen X, *et al.* Additive manufacturing of customized metallic orthopedic implants: materials, structures, and surface modifications. *Metals*. 2019;9(9):1004. doi: 10.3390/met9091004

39. Jin W, Wu G, Gao A, Feng H, Peng X, Chu PK. Hafnium implanted WE43 magnesium alloy for enhanced corrosion protection and biocompatibility. *Surf Coat Technol*. 2016;306 (Part A):11-15. doi: 10.1016/j.surfcoat.2016.02.055

40. Wataha JC. Alloys for prosthodontic restorations. *J Prosthet Dent*. 2002;87(4):351-363. doi: 10.1067/mpr.2002.123817

41. Nicholson JW. Titanium alloys for dental implants: a review. *Prosthesis*. 2020;2(2):100-116. doi: 10.3390/prosthesis2020011

42. Zhou K, Wang M, Zhang S, *et al.* Titanium alloys for orthopedic applications: a review on the osteointegration induced by physicomechanical stimuli. *J Mater Res Technol*. 2024;30:8260-8276. doi: 10.1016/j.jmrt.2024.05.207

43. Combres Y. *Properties of Titanium and Its Alloys [in French]. In: Study and Properties of Metals* (Dossier M4780). Techniques de l'Ingénieur; Published online March 2010. Accessed May 24, 2025 https://www.techniques-ingenieur.fr/base-documentaire/materiaux-th11/metaux-et-alliages-non-ferreux-42357210/proprietes-du-titane-et-de-ses-alliages-m4780/

44. Aherwar A, Singh AK, Patnaik A. Current and future biocompatibility aspects of biomaterials for hip prosthesis. *AIMS Bioeng*. 2015;3(1):23-43. doi: 10.3934/bioeng.2016.1.23

45. Morano C, Garofalo S, Bertuccio P, Sposato A, Zappone I, Pagnotta L. A comprehensive literature review of total hip arthroplasty (THA): part 1—biomaterials. *JFB*. 2025;16(5):179. doi: 10.3390/jfb16050179

46. Brüggemann A, Hailer NP. Concentrations of cobalt, chromium and titanium and immunological changes after primary total knee arthroplasty—a cohort study with an 18-year follow-up. *JCM*. 2024;13(4):951.
doi: 10.3390/jcm13040951

47. Kurtz PW, Aslani S, Kurtz MA, *et al.* Cobalt-chromium-molybdenum femoral knee implant damage correlates with elevated periprosthetic metal concentrations. *J Arthroplasty*. 2025;40(7):S315-S323.
doi: 10.1016/j.arth.2025.02.075

48. Wang N, Meenashisundaram GK, Chang S, Fuh JYH, Dheen ST, Senthil Kumar A. A comparative investigation on the mechanical properties and cytotoxicity of Cubic, Octet, and TPMS gyroid structures fabricated by selective laser melting of stainless steel 316L. *J Mech Behav Biomed Mater*. 2022;129:105151.
doi: 10.1016/j.jmbbm.2022.105151

49. Han Q, Wang C, Chen H, Zhao X, Wang J. Porous tantalum and titanium in orthopedics: a review. *ACS Biomater Sci Eng*. 2019;5(11):5798-5824.
doi: 10.1021/acsbiomaterials.9b00493

50. Guo Y, Xie K, Jiang W, *et al.* In vitro and in vivo study of 3D-printed porous tantalum scaffolds for repairing bone defects. *ACS Biomater Sci Eng*. 2019;5(2):1123-1133.
doi: 10.1021/acsbiomaterials.8b01094

51. Qu X, Yang H, Jia B, *et al.* Zinc alloy-based bone internal fixation screw with antibacterial and anti-osteolytic properties. *Bioact Mater*. 2021;6(12):4607-4624.
doi: 10.1016/j.bioactmat.2021.05.023

52. Salama M, Vaz MF, Colaço R, Santos C, Carmezim M. Biodegradable iron and porous iron: mechanical properties, degradation behaviour, manufacturing routes and biomedical applications. *JFB*. 2022;13(2):72.
doi: 10.3390/jfb13020072

53. Moura De Souza Soares F, Barbosa DM, Reis Corado HP, De Carvalho Santana AI, Elias CN. Surface morphology, roughness, and corrosion resistance of dental implants produced by additive manufacturing. *J Mater Res Technol*. 2022;21:3844-3855.
doi: 10.1016/j.jmrt.2022.10.114

54. Bandyopadhyay A, Ciliveri S, Guariento S, Zuckschwerdt N, Hogg WW. Fatigue behavior of additively manufactured Ti3Al2V alloy. *MSAM*. 2023;2(3):1705.
doi: 10.36922/msam.1705

55. Ednie L, Antonysamy AA, Parimi L, Mani M, Thomas M, Lancaster RJ. Understanding the fatigue behaviour of Ti–6Al–4V manufactured via various additive processes. *J Mater Res Technol*. 2024;31:1337-1354.
doi: 10.1016/j.jmrt.2024.06.168

56. Charkaluk E, Chastand V. Fatigue of additive manufacturing specimens: a comparison with casting processes. In: *The 18th International Conference on Experimental Mechanics*. MDPI; 2018:474.
doi: 10.3390/ICEM18-05352

57. Zarei MA, Shabestari MG, Shabestari SG, Abedi H. Microstructural heterogeneity and anisotropic mechanical propertiers of titanium alloys manufactured by wire arc additive manufacturing: a review. *J Mater Res Technol*. 2025;36:8381-8409.
doi: 10.1016/j.jmrt.2025.05.106

58. Ge MZ, Tang Y, Zhang YK, Wang Y. Enhancement in fatigue property of Ti-6Al-4V alloy remanufactured by combined laser cladding and laser shock peening processes. *Surf Coat Technol*. 2022;444:128671.
doi: 10.1016/j.surfcoat.2022.128671

59. Tunchel S, Blay A, Kolerman R, Mijiritsky E, Shibli JA. 3D printing/additive manufacturing single titanium dental implants: a prospective multicenter study with 3 years of follow-up. *Int J Dent*. 2016;2016:8590971.
doi: 10.1155/2016/8590971

60. Shu T, Shi H, Li M, Lin YC, Li A, Pei D. Microscale bone interlocking enhances osseointegration strength on the rough surface of 3D-printed titanium implants: experimental and finite element analysis. *BMC Oral Health*. 2025;25(1):208.
doi: 10.1186/s12903-025-05586-2

61. Gu Y, Sun Y, Shujaat S, Braem A, Politis C, Jacobs R. 3D-printed porous Ti-6Al-4V scaffolds for long bone repair in animal models: a systematic review. *J Orthop Surg Res*. 2022;17(1):68.
doi: 10.1186/s13018-022-02960-6

62. Park S, Lee J, Kim JJ, *et al.* Osseointegrative and immunomodulative 3D-Printing Ti-6Al-4V-based implants embedded with biogenic hydroxyapatite. *Mater Des*. 2024;240:112822.
doi: 10.1016/j.matdes.2024.112822

63. Matsko A, França R. Design, manufacturing and clinical outcomes for additively manufactured titanium dental implants: a systematic review. *Dent Rev*. 2022;2(1):100041.
doi: 10.1016/j.dentre.2022.100041

64. Onică N, Budală DG, Baciu ER, *et al.* Long-term clinical outcomes of 3D-printed subperiosteal titanium implants: a 6-year follow-up. *JPM*. 2024;14(5):541.
doi: 10.3390/jpm14050541

65. Raisz LG. Physiology and pathophysiology of bone remodeling. *Clin Chem*. 1999;45(8Pt2):1353-1358. Erratum in: *Clin Chem*. 1999;45(10):1885
doi: 10.1093/clinchem/45.8.1353

66. Anselme K. Osteoblast adhesion on biomaterials. *Biomaterials*. 2000;21(7):667-681.
doi: 10.1016/S0142-9612(99)00242-2

67. Barkaoui A, Chamekh A, Merzouki T, Hambli R, Mkaddem A. Multiscale approach including microfibril scale to assess

elastic constants of cortical bone based on neural network computation and homogenization method. Int J Numer *Method Biomed Eng*. 2014;30(3):318-338. Epub 2013. doi: 10.1002/cnm.2604

68. Germaini MM, Belhabib S, Guessasma S, Deterre R, Corre P, Weiss P. Additive manufacturing of biomaterials for bone tissue engineering – a critical review of the state of the art and new concepts. *Prog Mater Sci*. 2022;130:100963. doi: 10.1016/j.pmatsci.2022.100963

69. Bigi A, Cojazzi G, Panzavolta S, *et al.* Chemical and structural characterization of the mineral phase from cortical and trabecular bone. *J Inorg Biochem*. 1997;68(1): 45-51. doi: 10.1016/S0162-0134(97)00007-X

70. Curtis DA, Sharma AB, Finzen FC. The use of dental implants to improve quality of life for edentulous patients. *J Calif Dent Assoc*. 2008;36(4):275-280. doi: 10.1080/19424396.2008.12221490

71. Hierl T, Wollny G, Schulze FP, *et al.* CAD-CAM implants in esthetic and reconstructive craniofacial surgery. *CIT*. 2006;14(1):65. doi: 10.2498/cit.2006.01.07

72. Mishchenko O, Kopchak A, Chernohorskyi D, *et al.* Craniofacial reconstruction using 3D personalized implants with enhanced surface properties: technological and clinical aspects. *Appl Surf Sci Adv*. 2023;16:100437. doi: 10.1016/j.apsadv.2023.100437

73. Ackland DC, Robinson D, Redhead M, Lee PVS, Moskaljuk A, Dimitroulis G. A personalized 3D-printed prosthetic joint replacement for the human temporomandibular joint: from implant design to implantation. *J Mech Behav Biomed Mater*. 2017;69:404-411. doi: 10.1016/j.jmbbm.2017.01.048

74. Lee CC, Lin SC, Kang MJ, Wu SW, Fu PY. Effects of implant threads on the contact area and stress distribution of marginal bone. *J Dent Sci*. 2010;5(3):156-165. doi: 10.1016/S1991-7902(10)60023-2

75. Marcián P, Borák L, Valášek J, Kaiser J, Florian Z, Wolff J. Finite element analysis of dental implant loading on atrophic and non-atrophic cancellous and cortical mandibular bone – a feasibility study. *J Biomech*. 2014;47(16):3830-3836. doi: 10.1016/j.jbiomech.2014.10.019

76. Meena VK, Kumar P, Kalra P, Sinha RK. Additive manufacturing for metallic spinal implants: A systematic review. *Ann 3D Print Med*. 2021;3:100021. doi: 10.1016/j.stlm.2021.100021

77. Silva-Correia J, Correia SI, Oliveira JM, Reis RL. Tissue engineering strategies applied in the regeneration of the human intervertebral disk. *Biotechnol Adv*. 2013;31(8):1514-1531. doi: 10.1016/j.biotechadv.2013.07.010

78. Saini A, Elhattab K, Gummadi SK, Nadkarni GR, Sikder P. Fused filament fabrication-3D printing of poly-ether-ether-ketone (PEEK) spinal fusion cages. *Mater Lett*. 2022;328:133206. doi: 10.1016/j.matlet.2022.133206

79. Bandyopadhyay A, Traxel KD, Bose S. Nature-inspired materials and structures using 3D printing. *Mater Sci Eng R Rep*. 2021;145:100609. doi: 10.1016/j.mser.2021.100609

80. Zhang B, Pei X, Zhou C, *et al.* The biomimetic design and 3D printing of customized mechanical properties porous Ti-6Al-4V scaffold for load-bearing bone reconstruction. *Mater Des*. 2018;152:30-39. doi: 10.1016/j.matdes.2018.04.065

81. Kladovasilakis N, Tsongas K, Tzetzis D. Finite element analysis of orthopedic hip implant with functionally graded bioinspired lattice structures. *Biomimetics*. 2020;5(3):44. doi: 10.3390/biomimetics5030044

82. Zhang B, Myers D, Wallace G, Brandt M, Choong P. Bioactive coatings for orthopaedic implants—recent trends in development of implant coatings. *IJMS*. 2014;15(7): 11878-11921. doi: 10.3390/ijms150711878

83. Fadzil AFBA, Pramanik A, Basak AK, Prakash C, Shankar S. Role of surface quality on biocompatibility of implants—a review. *Ann 3D Print Med*. 2022;8:100082. doi: 10.1016/j.stlm.2022.100082

84. Apostu D, Lucaciu O, Berce C, Lucaciu D, Cosma D. Current methods of preventing aseptic loosening and improving osseointegration of titanium implants in cementless total hip arthroplasty: a review. *J Int Med Res*. 2018;46(6):2104-2119. doi: 10.1177/0300060517732697

85. Shah FA, Thomsen P, Palmquist A. Osseointegration and current interpretations of the bone-implant interface. *Acta Biomater*. 2019;84:1-15. doi: 10.1016/j.actbio.2018.11.018

86. Parithimarkalaignan S, Padmanabhan TV. Osseointegration: an update. *J Indian Prosthodont Soc*. 2013;13(1):2-6. doi: 10.1007/s13191-013-0252-z

87. Koppunur R, Dama KK, Rokkala U, Thirupathi B, Sagar NVSS, Gugulothu B. Design and fabrication of patient-specific implant for maxillofacial surgery using additive manufacturing. *Adv Mater Sci Eng*. 2022;2022:1-7. doi: 10.1155/2022/7145732

88. Khan N, Riccio A. A systematic review of design for additive manufacturing of aerospace lattice structures: Current trends and future directions. *Prog Aerosp Sci*. 2024;149:101021. doi: 10.1016/j.paerosci.2024.101021

89. Korkmaz ME, Gupta MK, Robak G, Moj K, Krolczyk GM, Kuntoğlu M. Development of lattice structure with selective

laser melting process: a state of the art on properties, future trends and challenges. *J Manuf Process*. 2022;81:1040-1063. doi: 10.1016/j.jmapro.2022.07.051

90. Skrzat A, Eremeyev VA. On the effective properties of foams in the framework of the couple stress theory. *Continuum Mech Thermodyn*. 2020;32(6):1779-1801. doi: 10.1007/s00161-020-00880-6

91. Li Z, Lu M, Zhang Y, *et al.* 3D-printed personalized lattice implant as an innovative strategy to reconstruct geographic defects in load-bearing bones. *Orthop Surg*. 2024;16(4): 821-829. doi: 10.1111/os.14003

92. Sienkiewicz J, Płatek P, Jiang F, Sun X, Rusinek A. Investigations on the mechanical response of gradient lattice structures manufactured via SLM. *Metals*. 2020;10(2):213. doi: 10.3390/met10020213

93. Chao L, Jiao C, Liang H, Xie D, Shen L, Liu Z. Analysis of mechanical properties and permeability of trabecular-like porous scaffold by additive manufacturing. *Front Bioeng Biotechnol*. 2021;9:779854. doi: 10.3389/fbioe.2021.779854

94. Huang X, Tang H, Wang L. Effect of residual stress on mechanical properties of triply periodic minimal surface lattice structures in additive manufacturing. *Comput Mater Sci*. 2024;245:113318. doi: 10.1016/j.commatsci.2024.113318

95. Malekan M, Sigurjónsson B. On the mechanical behavior of polymeric lattice structures fabricated by stereolithography 3D printing. *Eng Rep*. 2024;6(12):e13003. doi: 10.1002/eng2.13003

96. Park JW, Seo E, Park H, *et al.* Hybrid solid mesh structure for electron beam melting customized implant to treat bone cancer. *IJB*. 2024;9(4):716. doi: 10.18063/ijb.716

97. Caiti G, Dobbe JGG, Bervoets E, *et al.* Biomechanical considerations in the design of patient-specific fixation plates for the distal radius. *Med Biol Eng Comput*. 2019; 57(5):1099-1107. doi: 10.1007/s11517-018-1945-6

98. Milovanovic JR, Stojkovic MS, Husain KN, Korunovic ND, Arandjelovic J. Holistic approach in designing the personalized bone scaffold: the case of reconstruction of large missing piece of mandible caused by congenital anatomic anomaly. *J Healthc Eng*. 2020;2020:1-13. doi: 10.1155/2020/6689961

99. Wang J, Min L, Lu M, *et al.* Three-dimensional-printed custom-made hemipelvic endoprosthesis for primary malignancies involving acetabulum: the design solution and surgical techniques. *J Orthop Surg Res*. 2019;14(1):389. doi: 10.1186/s13018-019-1455-8

100. Martinez-Marquez D, Mirnajafizadeh A, Carty CP, Stewart RA. Application of quality by design for 3D printed bone prostheses and scaffolds. *PLoS One*. 2018;13(4):e0195291. doi: 10.1371/journal.pone.0195291

101. Wähnert D, Greiner J, Brianza S, Kaltschmidt C, Vordemvenne T, Kaltschmidt B. Strategies to improve bone healing: innovative surgical implants meet nano-/ micro-topography of bone scaffolds. *Biomedicines*. 2021; 9(7):746. doi: 10.3390/biomedicines9070746

102. Maietta S, Gloria A, Improta G, Richetta M, De Santis R, Martorelli M. A further analysis on Ti-6Al-4V lattice structures manufactured by selective laser melting. *J Healthc Eng*. 2019;2019:3212594. doi: 10.1155/2019/3212594

103. Rogala P, Uklejewski R, Winiecki M, Dąbrowski M, Gołańczyk J, Patalas A. First biomimetic fixation for resurfacing arthroplasty: investigation in swine of a prototype partial knee endoprosthesis. *Biomed Res Int*. 2019;2019:6952649. doi: 10.1155/2019/6952649

104. Omigbodun FT, Oladapo BI. AI-optimized lattice structures for biomechanics scaffold design. *Biomimetics*. 2025;10(2):88. doi: 10.3390/biomimetics10020088

105. Xu M, Zhang Y, Wang S, Jiang G. Genetic-based optimization of 3D Burch–Schneider cage with functionally graded lattice material. *Front Bioeng Biotechnol*. 2022;10:819005. doi: 10.3389/fbioe.2022.819005

106. Mello-Machado RC, Sartoretto SC, Granjeiro JM, *et al.* Osseodensification enables bone healing chambers with improved low-density bone site primary stability: an in vivo study. *Sci Rep*. 2021;11(1):15436. doi: 10.1038/s41598-021-94886-y

107. Olmedo-Gaya MV, Romero-Olid MN, Ocaña-Peinado FM, Vallecillo-Rivas M, Vallecillo C, Reyes-Botella C. Influence of different surgical techniques on primary implant stability in the posterior maxilla: a randomized controlled clinical trial. *Clin Oral Invest*. 2023;27(7):3499-3508. doi: 10.1007/s00784-023-04962-y

108. Dong Y, Zhang Z, Dong W, Hu G, Wang B, Mou Z. An optimization method for implantation parameters of individualized TKA tibial prosthesis based on finite element analysis and orthogonal experimental design. *BMC Musculoskelet Disord*. 2020;21(1):165. doi: 10.1186/s12891-020-3189-5

109. Kang Y, Kim S, Kim J, Lee JW, Park JC. Evaluating the validity of lightweight talar replacement designs: rational models and topologically optimized models. *Biomater Res*. 2022;26(1):10. doi: 10.1186/s40824-022-00256-8

110. Deng J, Cohen DJ, Berger MB, *et al.* Osseointegration of titanium implants in a botox-induced muscle paralysis rat model is sensitive to surface topography and semaphorin 3A treatment. *Biomimetics*. 2023;8(1):93. doi: 10.3390/biomimetics8010093

111. Kim DH, Byun JY, Kim D, Kim B, Lim W. Geometric evaluation of biomimetic 3D printed rat femur. *J Hard Tissue Biol*. 2023;32(2):133-138.
doi: 10.2485/jhtb.32.133

112. Verma A, Jain A, Sekhar Sethy S, *et al.* Finite element analysis and its application in orthopaedics: a narrative review. *J Clin Orthop Trauma*. 2024;58:102803.
doi: 10.1016/j.jcot.2024.102803

113. Caouette C, Yahia L, Bureau MN. Reduced stress shielding with limited micromotions using a carbon fibre composite biomimetic hip stem: a finite element model. *Proc Inst Mech Eng H*. 2011;225(9):907-919.
doi: 10.1177/0954411911412465

114. Ceddia M, Trentadue B, De Giosa G, Solarino G. Topology optimization of a femoral stem in titanium and carbon to reduce stress shielding with the FEM method. *J Compos Sci*. 2023;7(7):298.
doi: 10.3390/jcs7070298

115. Rezapourian M, Kamboj N, Jasiuk I, Hussainova I. Biomimetic design of implants for long bone critical-sized defects. *J Mech Behav Biomed Mater*. 2022;134:105370.
doi: 10.1016/j.jmbbm.2022.105370

116. Munteanu S, Munteanu D, Gheorghiu B, et al. Additively manufactured femoral stem topology optimization: case study. *Materials Today: Proceedings*. 2019;19(Part 3): 1019-1025.
doi: 10.1016/j.matpr.2019.08.016

117. Alemayehu DB, Todoh M, Huang SJ. Advancing 3D dental implant finite element analysis: incorporating biomimetic trabecular bone with varied pore sizes in voronoi lattices. *JFB*. 2024;15(4):94.
doi: 10.3390/jfb15040094

118. Simoneau C, Terriault P, Jetté B, Dumas M, Brailovski V. Development of a porous metallic femoral stem: Design, manufacturing, simulation and mechanical testing. *Mater Des*. 2017;114:546-556.
doi: 10.1016/j.matdes.2016.10.064

119. Mehboob H, Tarlochan F, Mehboob A, Chang SH. Finite element modelling and characterization of 3D cellular microstructures for the design of a cementless biomimetic porous hip stem. *Mater Des*. 2018;149:101-112.
doi: 10.1016/j.matdes.2018.04.002

120. Pei X, Wang L, Zhou C, *et al.* Ti-6Al-4V orthopedic implant with biomimetic heterogeneous structure via 3D printing for improving osteogenesis. *Mater Des*. 2022;221:110964.
doi: 10.1016/j.matdes.2022.110964

121. Li Y, Hu Y, Chen H, *et al.* A novel conceptual design of a biomimetic oral implant and its biomechanical effect on the repairment of a large mandibular defect. *Med Nov Technol Dev*. 2022;15:100147.
doi: 10.1016/j.medntd.2022.100147

122. Chatzigeorgiou C, Piotrowski B, Meraghni F, Chemisky Y. Multiscale mechanical analysis for biomimetic implant design based on triply periodic minimal surfaces (TPMS) lattices: application to partial replacement of femoral bone. *Res Eng*. 2025;25:103984.
doi: 10.1016/j.rineng.2025.103984

123. Soro N, Brodie EG, Abdal-hay A, Alali AQ, Kent D, Dargusch MS. Additive manufacturing of biomimetic Titanium-Tantalum lattices for biomedical implant applications. *Mater Des*. 2022;218:110688.
doi: 10.1016/j.matdes.2022.110688

124. Salaha ZFM, Ammarullah MI, Abdullah NNAA, *et al.* Biomechanical effects of the porous structure of gyroid and voronoi hip implants: a finite element analysis using an experimentally validated model. *Materials*. 2023;16(9):3298.
doi: 10.3390/ma16093298

125. Ali D, Ozalp M, Blanquer SBG, Onel S. Permeability and fluid flow-induced wall shear stress in bone scaffolds with TPMS and lattice architectures: a CFD analysis. *Eur J Mech B Fluids*. 2020;79:376-385.
doi: 10.1016/j.euromechflu.2019.09.015

125. Karuna C, Poltue T, Khrueaduangkham S, Promoppatum P. Mechanical and fluid characteristics of triply periodic minimal surface bone scaffolds under various functionally graded strategies. *J Comput Des Eng*. 2022;9(4):1258-1278.
doi: 10.1093/jcde/qwac052

127. Lai R, Jiang J, Huo Y, *et al.* Design of novel graded bone scaffolds based on triply periodic minimal surfaces with multi-functional pores. *Front Bioeng Biotechnol*. 2025;13:1503582.
doi: 10.3389/fbioe.2025.1503582

128. Ma X, Diao X, Li Z, *et al.* Simulation analysis of impact damage to the bone tissue surrounding a dental implant. *Sci Rep*. 2020;10(1):6927.
doi: 10.1038/s41598-020-63666-5

129. Jin ZH, Peng MD, Li Q. The effect of implant neck microthread design on stress distribution of peri-implant bone with different level: a finite element analysis. *J Dent Sci*. 2020;15(4):466-471.
doi: 10.1016/j.jds.2019.12.003

130. Medina-Galvez R, Cantó-Navés O, Marimon X, Cerrolaza M, Ferrer M, Cabratosa-Termes J. Bone stress evaluation with and without cortical bone using several dental restorative materials subjected to impact load: a fully 3D transient finite-element study. *Materials*. 2021;14(19):5801.
doi: 10.3390/ma14195801

131. Ogawa M, Tohma Y, Ohgushi H, Takakura Y, Tanaka Y. Early fixation of cobalt-chromium based alloy surgical implants to bone using a tissue-engineering approach. *IJMS*. 2012;13(5):5528-5541.
doi: 10.3390/ijms13055528

132. Rappe KS, Ortiz-Hernandez M, Punset M, *et al.* On-growth and in-growth osseointegration enhancement in PM porous Ti-scaffolds by two different bioactivation strategies: alkali thermochemical treatment and RGD peptide coating. *IJMS*. 2022;23(3):1750.
doi: 10.3390/ijms23031750

133. Hafizh M, Soliman M, Qiblawey Y, *et al.* Surface acoustic wave (SAW) sensors for hip implant: a numerical and computational feasibility investigation using finite element methods. *Biosensors*. 2023;13(1):79.
doi: 10.3390/bios13010079

134. Makarov S, Noetscher G, Nummenmaa A, eds. *Brain and Human Body Modelling 2021: Selected Papers Presented at 2021 BHBM Conference at Athinoula A. Martinos Center for Biomedical Imaging, Massachusetts General Hospital.* Cham, Switzerland: Springer International Publishing; 2023.
doi: 10.1007/978-3-031-15451-5

ACCSCIENCE PUBLISHING

International Journal of Bioprinting

REVIEW ARTICLE

3D printing-driven evolution in lung surgery: From precision resection to biomaterial-based functional reconstruction

Zhenghao Dong[1†], Wenjing Jiang[2†], Xiang Lin[1], Yu Tong[1], Beinuo Wang[1], Jian Zhou[1*], and Hu Liao[1*]

[1]Department of Thoracic Surgery, West China Hospital, Sichuan University, Chengdu, Sichuan, China

[2]West China School of Medicine, Sichuan University, Chengdu, Sichuan, China

(This article belongs to the *Special Issue*: *3D-Printed Biomedical Devices*)

Abstract

The complexity and variability of lung anatomy, together with the difficulty of repairing lung tissue defects, have long constrained the progress of lung surgery in the era of precision and individualized treatment. In recent years, three-dimensional (3D) printing, deeply integrated with biomedical materials, has emerged as a transformative innovation in regenerative medicine and tissue engineering, offering new strategies to overcome these technical bottlenecks. This review summarizes the current status and clinical applications of 3D printing in lung surgery. By enabling the accurate reproduction of patient-specific anatomical models and the fabrication of functional tissue substitutes in combination with bioactive materials, 3D printing provides unprecedented opportunities to address major challenges such as complex lung nodule resection and bronchial repair and reconstruction. Initially confined to the generation of static anatomical models for surgical planning, teaching, and training, the technology has now advanced, especially with the integration of artificial intelligence, toward the development of real-time intraoperative navigation guides and customized implants. Collectively, these advances have transformed 3D printing from an auxiliary adjunct into a pivotal driver of personalized approaches in lung surgery, with the potential to reshape surgical paradigms and expand future therapeutic frontiers.

Keywords: 3D printing; Artificial intelligence; Bronchial reconstruction; Lung surgery; Preoperative planning

†These authors contributed equally to this work.

***Corresponding authors:**
Hu Liao
(liaohu202504@163.com)

Jian Zhou
(jian_zhou@wchscu.cn)

Citation: Dong Z, Jiang W, Lin X, *et al.* 3D printing-driven evolution in lung surgery: From precision resection to biomaterial-based functional reconstruction. *Int J Bioprint.* 2025;11(6):83-106. doi: 10.36922/IJB025350357

Received: August 30, 2025
1st revised: September 25, 2025
2nd revised: October 1, 2025
Accepted: October 2, 2022
Published online: October 23, 2025

Copyright: © 2025 Author(s). This is an Open Access article distributed under the terms of the Creative Commons Attribution License, permitting distribution and reproduction in any medium, provided the original work is properly cited.

Publisher's Note: AccScience Publishing remains neutral with regard to jurisdictional claims in published maps and institutional affiliations.

1. Introduction

Since Chuck Hull invented the stereolithography machine and proposed the layer-by-layer forming theory in 1983, 3D printing technology has undergone rapid development and has been widely applied in industrial and manufacturing fields.[1] With the popularization of personalized medicine, 3D printing has been integrated into medicine and biology and has emerged as a valuable tool in healthcare, particularly in surgery. Currently, 3D printing has achieved clinical translation and large-scale application in multiple subspecialties, including orthopedics,[2] oral and maxillofacial surgery,[3] and

cardiac surgery,[4] demonstrating satisfactory effects in educational training, preoperative simulation, tissue and organ repair and reconstruction, and personalized implant customization.[5–7] The development of 3D printing has fundamentally transformed the current paradigms and methods of surgical practice, holding significant potential for the future of surgery.[8]

Pulmonary diseases, particularly malignant tumors and end-stage lung diseases, continue to pose a major threat to human health.[9,10] Among these, lung cancer, one of the most common malignant tumors in terms of incidence and mortality, has shown a significant increase in early diagnosis rates due to the widespread adoption of low-dose chest computed tomography (CT) screening, leading to a substantial rise in the detection rate of pulmonary nodules.[11] This trend has not only created opportunities for early intervention but also imposed higher demands on preoperative precise localization and minimally invasive resection. Nevertheless, due to the complexity of lung anatomy and the limitations of two-dimensional (2D) image spatial information, accurate localization of pulmonary nodules, especially those that are volumetrically small and distant from the pleura, remains difficult and often relies on imaging markers, preoperative biopsy, or surgeon experience.[12] The risks of localization errors and complications cannot be ignored. On the other hand, complex tracheal diseases, such as primary or metastatic tracheal tumors, bronchial fistulas, long-segment tracheal stenosis, and tracheal softening, often lack suitable repair materials or personalized substitutes, resulting in most patients requiring repeated surgeries, severely impacting their quality of life.[13] Moreover, lung transplantation, the only effective curative treatment for patients with end-stage lung diseases, is limited by the severe shortage of qualified donors and high treatment costs, thereby depriving many patients of treatment opportunities.[14] Therefore, these limitations underscore the urgent need in current lung surgery for precise preoperative lesion localization, accurate identification of patient-specific organ and tissue anatomy, development of optimal surgical plans to minimize surgical risks, and advancement of functional reconstruction and repair techniques.

Due to its unique advantages in constructing personalized 3D structures and integrating bioactive materials, enhanced by synergistic advances in artificial intelligence (AI), 3D printing has provided revolutionary prospects for overcoming the bottlenecks in lung surgery. Currently, 3D printing is widely used for personalized treatment of thoracic diseases, including thoracic wall tumor resection and post-traumatic repair and reconstruction,[15–17] and correction of thoracic deformities, such as pectus carinatum and pectus excavatum.[18] Recent studies have reported the application of 3D printing to assist in the precise localization of pulmonary nodules and local reconstruction of bronchi,[19,20] preliminarily demonstrating the potential advantages of this technology in addressing the current challenges in lung surgery. This review examines recent advances in 3D printing for lung surgery, explores its potential and direction in preoperative planning and personalized reconstruction, and looks ahead to the future of this technology in advancing precision medicine.

2. Principles and methods of 3D printing

Three-dimensional printing, also known as additive manufacturing, is an advanced manufacturing technology that employs computer-controlled processes to layer materials in a precise manner, sequentially stacking multiple 2D digital slices to ultimately fabricate a solid structure with an accurate 3D form.[21] Beyond conventional 3D printing, which primarily produces static objects, the following two advanced forms have emerged: four-dimensional (4D) printing and 3D bioprinting. 4D printing refers to the fabrication of structures using smart materials that can change their shape, property, or function over time in response to external stimuli (e.g., temperature, humidity, pH, and light), enabling dynamic adaptation and functionality post-production.[22,23] Meanwhile, 3D bioprinting, a specialized subset of 3D printing, involves the layer-by-layer deposition of bioinks—often containing living cells, biomolecules, and biocompatible materials—to construct biologically functional tissues and organ analogs.[24,25] While standard 3D printing is widely used for fabricating anatomical models, surgical guides, and custom implants, bioprinting aims to replicate the architectural and functional complexity of native tissues for regenerative medicine and drug screening applications.

The application of 3D printing in surgery involves multiple steps rather than a single process. It encompasses medical imaging data acquisition, 3D digital model construction, selection of materials and printing methods, and subsequent processing and verification. By following these steps, surgeons can obtain personalized 3D structures that accurately replicate patient anatomy, thereby providing a solid foundation for subsequent treatment.

2.1. Construction and processing of 3D models

During the design phase, the first step is to generate accurate 3D models from medical imaging data. Common data sources include CT or magnetic resonance imaging (MRI) images, with imaging data stored in the Digital Imaging and Communications in Medicine (DICOM) format. Clinically, physicians identify and segment regions of interest in DICOM data, which are then processed by

engineers using computer-aided design (CAD) software for 3D reconstruction—specifically, volume rendering—to generate high-resolution digital anatomical models.[26] However, DICOM image files cannot be directly recognized by 3D printers and must therefore be converted into the Standard Tessellation Language (STL) format. This format discretizes complex anatomical surfaces into a large number of interconnected triangular meshes, precisely assembled like a 3D puzzle, thereby enabling printability.

Prior to 3D printing, STL models must undergo appropriate post-processing to ensure printability and structural accuracy.[27] During the conversion of DICOM to STL format, surface defects such as gaps, overlaps, or deformities may occur as a result of imaging artifacts, metal interference, reverberations, or echo effects. These defects must be corrected through a fixing process to ensure the structural integrity and geometric accuracy of the model. After repair, the STL model typically enters the design phase, where it is modified based on specific clinical requirements, such as removing irrelevant structures to highlight the lesion area or customizing the implant shape. Additionally, the surgical plane can be generated, and the implant can be matched preoperatively during this phase. The completed STL model can be converted into an interactive 3D file for preoperative discussion and surgical planning prior to final printing.

2.2. 3D printing materials and methods

The successful implementation of 3D bioprinting depends on advanced printing technology and functionalized bioinks. Printing technology determines the precision, speed, and cell survival rate of the manufacturing process, whereas bioinks provide the microenvironment required for cell survival and function. With ongoing advancements in 3D printing technology, the range of available printing methods and materials has become increasingly diverse. Notably, the recent progress in bioactive materials has shifted surgical applications from simple anatomical replication to functional tissue simulation.[28] Currently, common medical 3D printing technologies include fused deposition modeling, stereolithography, selective laser sintering, and extrusion printing, each offering distinct advantages in printing principles, material compatibility, forming precision, and mechanical properties.[21] Fused deposition modeling and stereolithography are primarily employed for prototyping and surgical guides, while selective laser sintering and extrusion printing are more suitable for tissue engineering and implant manufacturing.[29–31] Common 3D printing materials include thermoplastic polymers (e.g., polylactic acid and polyether ether ketone), metals (e.g., titanium alloys), and natural or synthetic polymers (e.g., gelatin and alginate). These materials provide biocompatibility, mechanical support, biodegradability, or high-precision molding capabilities.[32] Clinicians can flexibly combine printing methods and materials according to surgical objectives and tissue characteristics. A summary of common 3D printing methods, materials, and their respective advantages and disadvantages is provided in Table 1.[32–49]

3. Application of 3D printing in lung surgery

With its unique advantages in personalization, precision, and biomimicry, 3D printing is reshaping lung surgery, progressing from preoperative planning models to intraoperative navigation templates and customized implants for tissue reconstruction. Clinical integration of 3D printing has significantly enhanced surgical accuracy and safety while broadening the therapeutic scope of thoracic surgery.

3.1. Preoperative planning, positioning, and intraoperative navigation

With the widespread application of low-dose chest thin-section CT in physical examinations, an increasing number of early-stage lung cancers characterized primarily by ground-glass nodules have been detected. Previous studies have demonstrated that for early-stage lung cancers with tumors directly measuring less than 2 cm, segmentectomy can achieve almost the same short-term and long-term results as standard lobectomy while retaining more lung tissue.[50–52]

Pulmonary segmentectomy requires higher professional skills from surgeons compared to traditional lobectomy, with the main challenges focusing on familiarity with the anatomical structure of the lung segment and precise localization of lesions. The anatomical structure of the lung segment is extremely complex, with significant individual variations in arteries, veins, and bronchi. Failure to clearly identify the anatomy during surgery increases the risk of intraoperative bleeding or injury to nerves and bronchi.[53] Previous studies confirmed that during segmentectomy, vascular injury caused by anatomical variations in segmental vessels is an independent risk factor for conversion to open surgery or lobectomy in video-assisted thoracoscopic surgery (VATS).[54,55] Moreover, due to the limited scope of segmentectomy, precise localization of the nodule is essential to achieve complete resection of the lesion and ensure negative margins, thereby avoiding unnecessary extended resection or even secondary surgery due to incorrect or missed resection. However, segmentectomy is typically used for small, non-solid nodules, which present significant challenges in terms of precise localization. It is evident that the correct assessment of anatomical variations

Table 1. Characteristics of 3D printing technologies used in the medical field

Printing methods	Suitable materials	Medical applications	Advantages	Limitations	References
FDM	PLA, ABS, PMMA, nylon	Cranial implants, bone models, prosthetics	Low cost, easy operation, fast prototyping	Low resolution, limited sterilization, poor mechanical strength	[33–36,49]
SLA	Photopolymers, light-curable resin	Surgical guides, sinus/neurovascular cavity models	High resolution, excellent surface finish	Toxic ultraviolet rays exposure, long print times, fragile structures	[37–39]
SLS	Polyamide, metals (e.g.titanium), ceramics	Bone scaffolds, maxillofacial implants, orthopedic devices	Strong parts, broad material choice	High cost, slow process, large equipment needed	[39–41,48]
Extrusion-based printing	Alginate, gelatin, collagen, PEG, chitosan	Aortic valves, muscle and neural tissues, bone constructs	Long cell viability, low cost, dense printing possible	May damage cells with pressure, limited in complex tissue reproduction	[32,33]
EBM	Titanium, magnesium, CP-Ti, nickel alloys	Porous implants for bone integration	Strong, stable, ideal for porous structures	Expensive setup, high vacuum required	[42,43]
DED	Metal alloys	Implant repair, surface modification, structural augmentation	Repair capability, strong metallurgical bonds	Lower resolution and efficiency than EBM/SLM	[42,44,45]
Inkjet printing	PEG, hydroxyapatite, PVA, TCP	Protein/nucleic acid printing, cartilage and soft tissue models	High resolution, fast, multicolor capability	Nozzle clogging, low mechanical strength	[42,46,47]
Laminated object manufacturing	Paper, plastic, metals	Simple anatomical prototypes	Low cost, fast, simple setup	Difficult to model complex tissue structures	[32,33]

Abbreviations: ABS: Acrylonitrile butadiene styrene; CP-Ti: Commercially pure titanium; EBM: Electron beam melting; DED: Directed energy deposition; FDM: Fused deposition modeling; PEG: Polyethylene glycol; PLA: Polylactic acid; PMMA: Polymethyl methacrylate; PVA: Polyvinyl alcohol; SLA: Stereolithography; SLM: Selective laser melting; SLS: Selective laser sintering; TCP: Tricalcium phosphate.

in the lung and precise localization of the lesion are critical to the success of lung surgery.[56] Therefore, comprehensive preoperative planning and reliable auxiliary localization methods are required.

Currently, surgeons typically plan the surgical paths and resection ranges based on preoperative CT imaging markers. This process requires surgeons to be highly familiar with specific markers, such as bony structures, pulmonary vessels, and the trachea, which can be challenging for less-experienced surgeons. Compared with 2D-CT, 3D-CT effectively reconstructs 3D images of the target lung lobe's vessels, bronchi, and tumors, and is widely used for preoperative planning and modeling. Studies have shown that patients undergoing preoperative 3D-CT-assisted imaging have lower rates of postoperative complications, shorter surgical times, and higher surgical safety.[57,58] However, displaying 3D images on a 2D monitor still limits surgeons' judgment of the relative positions of the target lung segment and structures, such as blood vessels and the trachea. 3D printing technology can effectively address this limitation.

The primary advantage of 3D printing in preoperative planning for lung surgery involves converting 2D imaging data into precise, tactile 3D material models, thereby clearly illustrating each patient's lung lobe development, the direction of accompanying blood vessels and bronchi, as well as adjacent and individual anatomical variations (Figure 1).[59,60] Surgeons can observe from multiple angles and use tactile feedback to more intuitively assess the anatomical relationships of the lungs at their actual size. This combination of 3D perception and tactile feedback significantly improves the accuracy of preoperative planning and greatly shortens the learning curve for junior surgeons.[61] Studies by Chen *et al.*[60] and Qiu *et al.*[62] demonstrated that 3D printing outperforms 3D-CT reconstruction in preoperative planning for segmental lung resection. Patients in the 3D printing group had more precise surgical paths, shorter operative times, and reduced intraoperative bleeding and postoperative drainage volumes.

Additionally, the advantages of 3D printing for preoperative planning are more pronounced in clinically complex pulmonary segmentectomy. A retrospective analysis of 298 patients undergoing segmental resection found that 3D-printed models assisted in planning to effectively reduce the duration and bleeding of complex segmentectomy, thereby enhancing the safety and efficiency

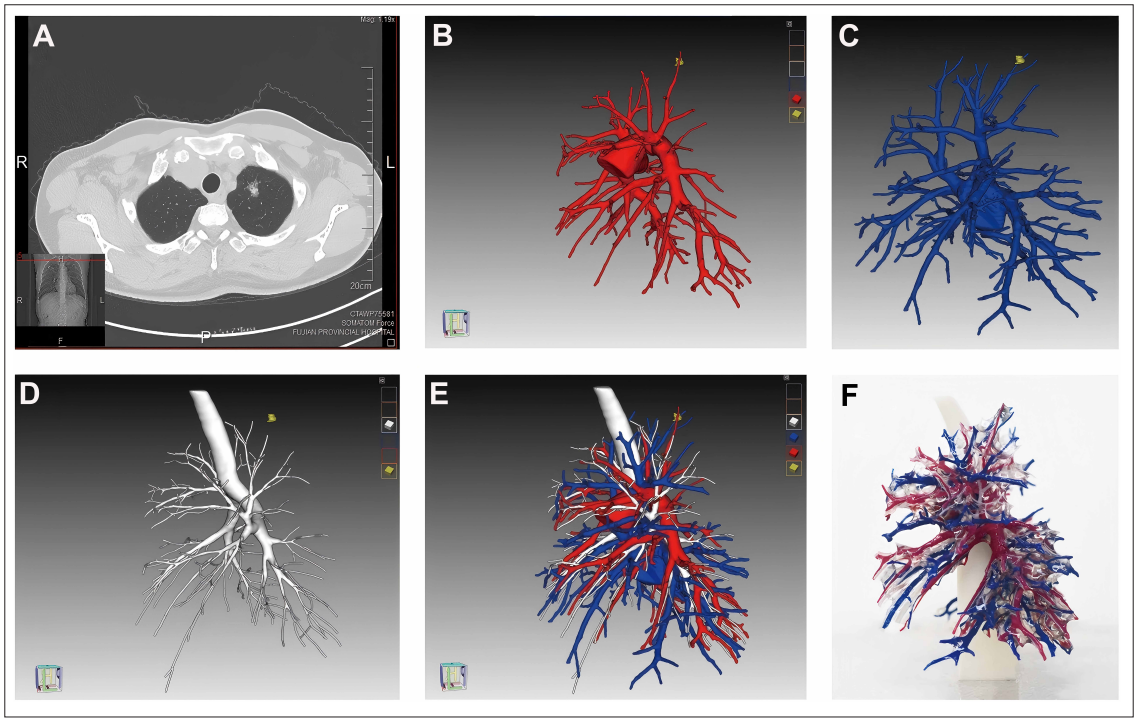

Figure 1. Computed tomography (CT) scan, 3D reconstruction, and printed model of the same patient. (A) Axial CT image showing a part-ground glass nodule in the left upper lobe. (B–E) 3D reconstruction highlighting pulmonary vessels and bronchi for clearer anatomical visualization. (F) Patient-specific 3D-printed lung model enabling anatomical assessment, lesion localization, and preoperative planning of precise resection. Reproduced from Chen *et al.*[60]

of such procedures.[62] Akiba *et al.*[63] utilized 3D printing technology to reconstruct lung models for two patients with pulmonary cleft hypoplasia, providing surgeons with an accurate anatomical understanding of the surgical field and achieving favorable surgical outcomes.

Besides carefully identifying the anatomical structures of the lungs, accurate lesion localization is another key determinant of successful lung surgery. Traditional localization methods include preoperative CT-guided percutaneous needle localization, electromagnetic navigation bronchoscopy localization, and intraoperative palpation.[64,65] However, these methods are often invasive, time-consuming, associated with potential complications, and highly dependent on operator experience.[64–66] They also fail to provide reliable localization for multiple target lesions in patients with multiple primary pulmonary nodules.

Customized patient-specific models or templates generated with 3D printing can mitigate these risks, enabling non-invasive lesion localization and efficient intraoperative navigation, thereby enhancing surgical safety and precision.[67] In one study, 3D reconstruction was performed to determine the location of multiple pulmonary nodules, followed by 3D printing of patient-specific lung models to facilitate intraoperative localization.[68] Using this approach, a total of 12 lesions were successfully resected (Figure 2). 3D surgical templates can be precisely designed based on preoperative CT images, with shapes that conform exactly to the patient's thoracic surface. Surgeons can directly indicate the surface projection location of the underlying nodule using the pre-set guide holes or marked points on the template, guiding resection or biopsy (Figure 3).[69] Most studies indicate that this novel localization method demonstrates excellent safety, feasibility, and accuracy.[70–72]

The integration of AI with 3D visualization technology is expected to bring about another paradigm shift in lung surgery.[73] During the conversion from 2D images to 3D models, AI-driven advanced algorithms can automatically or semi-automatically perform complex tasks such as image segmentation, tissue recognition, and model construction, significantly improving the efficiency and accuracy of 3D reconstruction. This enhances the rapid and accurate identification of microstructures, such as lung nodules, blood vessels, and trachea, providing the technical foundation and data support for printing more realistic individualized 3D anatomical models.[74,75] Advances in digital surgical technologies have enabled the integration of 3D printed models with augmented reality (AR) and

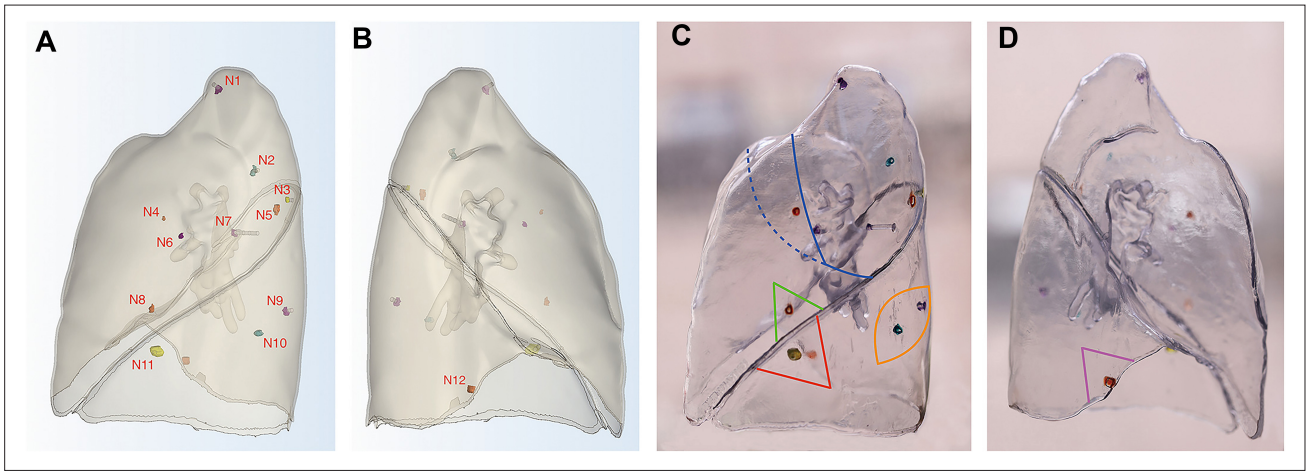

Figure 2. Digitally reconstructed (A and B) and 3D-printed pulmonary nodule localization models (C and D) shown from lateral (A and C) and medial (B and D) perspectives. Colored lines represent the surgical strategy derived from the printed model: the blue line outlines resection of segments (S)1+2 to include nodules 1, 2, 3, 5, and 7, while the dashed blue line indicates extended S1+2 resection toward S3 to remove nodules 4 and 6. Green, red, orange, and purple lines correspond to wedge resections in S4+5 (nodule 8), S7+8 (nodule 11), S9 (nodules 9 and 10), and S10 (nodule 12), respectively. Modified from Li *et al.*[68] Copyright © 2022 The Authors.

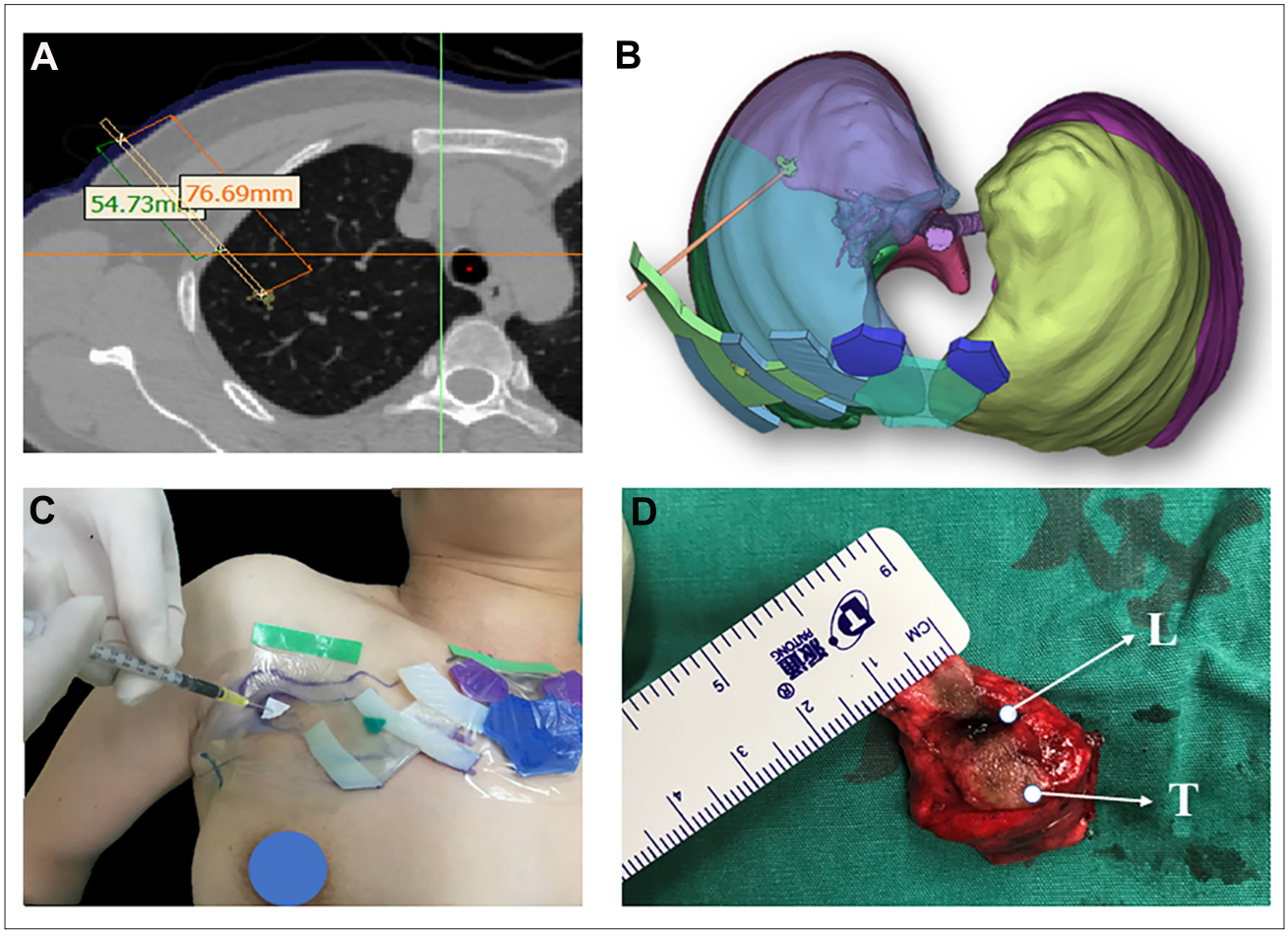

Figure 3. Workflow of 3D-printed localization strategy. (A) Determination of puncture depth. (B) Thoracic structure reconstruction. (C) Localization process. (D) Resected specimen. Modified from Fu *et al.*[69] Copyright © 2020 The Authors. Abbreviations: L, localization site; T, tumor site.

mixed reality (MR), elevating intraoperative navigation to unprecedented levels.[74,76]

While traditional 3D-printed models are intuitive, surgeons still need to mentally align them with the actual surgical field of view. AR and MR technologies, however, use specialized head-mounted displays to overlay preoperative 3D virtual models, including key structures such as tumors, blood vessels, and bronchi, in real time and with high precision onto the patient's actual anatomical structures, achieving a navigation mode that combines virtual and real elements.[77] Studies have shown that integrating 3D-printed navigation templates with MR technology allows surgeons to synchronously compare virtual models with physical templates, further enhancing nodule localization accuracy.[78] Furthermore, combining 3D-printed models with AR assistance significantly reduces lung surgery duration, minimizes intraoperative bleeding, and shortens postoperative hospital stays.[77]

3.2. Customized application of bronchial and airway stents

The core significance of 3D printed personalized stents lies in achieving "precision customization" of medical implants. These stents achieve precise anatomical conformity, thereby significantly enhancing surgical accuracy and efficiency. Their porous architecture facilitates mucosal integration with airway tissues, optimizes biomechanical performance, accelerates postoperative recovery, and can be functionalized with drug loading for targeted therapy.[22,23,79,80] Personalized stents provide improved efficacy, reduced trauma, and faster recovery by virtue of their superior anatomical conformity, functional design, and biocompatibility.

Currently, research on 3D-printed bronchial and airway soft-material stents is shifting from a rigid-support paradigm toward a flexible, regenerative approach. Recent advances focus on the use of high-precision light-curing technologies (e.g., digital light processing) to fabricate biodegradable materials such as polycaprolactone, thereby enabling customization and seamless airway integration. Cutting-edge research increasingly emphasizes functionalization, including localized therapy through drug loading (e.g., anti-proliferative and antitumor agents) and the exploration of 4D-printed smart stents and bioactive inks. The ultimate objective is the development of bioactive stents capable of promoting tissue regeneration and self-degradation, thereby eliminating the need for secondary surgeries. As demonstrated by Krivitsky *et al.*,[79] the incorporation of drugs such as nintedanib and levofloxacin into customized bioabsorbable 3D-printed airway stents provides dual therapeutic benefits of mechanical support and controlled drug release.

The primary clinical indication for airway stent implantation is malignant or benign luminal stenosis. Although both conditions result in airway obstruction and dyspnea, they differ substantially in pathological basis, disease progression, and therapeutic objectives. Malignant stenosis typically progresses rapidly and requires combined antitumor therapy with urgent luminal reconstruction. In contrast, management of benign stenosis emphasizes long-term airway patency, tissue compatibility, and the reduction of complications.

Malignant central airway obstruction is most often caused by primary lung cancer or metastatic tumors.[81] Conventional standardized stents frequently fail to conform to complex airway anatomy, leading to complications such as migration (13–32%), granulation tissue hyperplasia (19–52%), and mucus plugging.[82–84] 3D printing technology improves stent compatibility and therapeutic efficacy through precise anatomical modeling, patient-specific design, and functionalized fabrication. Patient-specific 3D airway models reconstructed from CT/MRI data accurately simulate stenotic morphology and adjacent anatomy. For example, Guibert *et al.*[85] utilized a 3D-printed model to modify stent branch angles and lengths, achieving precise matching to complex bronchial anastomotic stenosis following lung transplantation and improving postoperative airway patency rates by 40%. Similarly, for tortuous stenoses secondary to tumor compression, 3D models can replicate post-decompression airway configuration, guiding stent shape optimization, such as adjusting Y-stent arm length (Figure 4).[86] Guibert *et al.*[85] indicated that this approach reduced intraoperative stent adjustment attempts and shortened procedure time. 3D-printed metal-coated or silicone stents can incorporate personalized aperture designs that counteract extrinsic compression while inhibiting tumor ingrowth, thereby enabling precise intervention in malignant airway stenosis. Ayub *et al.*[82] reported a 93% technical success rate with significant improvement in dyspnea scores (Borg score reduction ≥ 2 points) among advanced-stage patients.

Beyond structural support, 3D-printed stents may be functionalized with antitumor or anti-fibrotic drugs for controlled local release, serving as multidrug delivery platforms with synergistic therapeutic effects.[79,84] In a canine model, Wang *et al.*[88] demonstrated that paclitaxel-eluting stents reduced granulation tissue formation by 70% over 5 months while maintaining undetectable serum drug concentrations. Additionally, in a rabbit model, Krivitsky *et al.*[79] demonstrated that stents co-loaded with levofloxacin (2 wt%) and nintedanib (1.5 wt%) inhibited bacterial colonization (80% reduction in *Staphylococcus* detection) and downregulated interleukin 8 expression (50% reduction in inflammatory markers), thereby

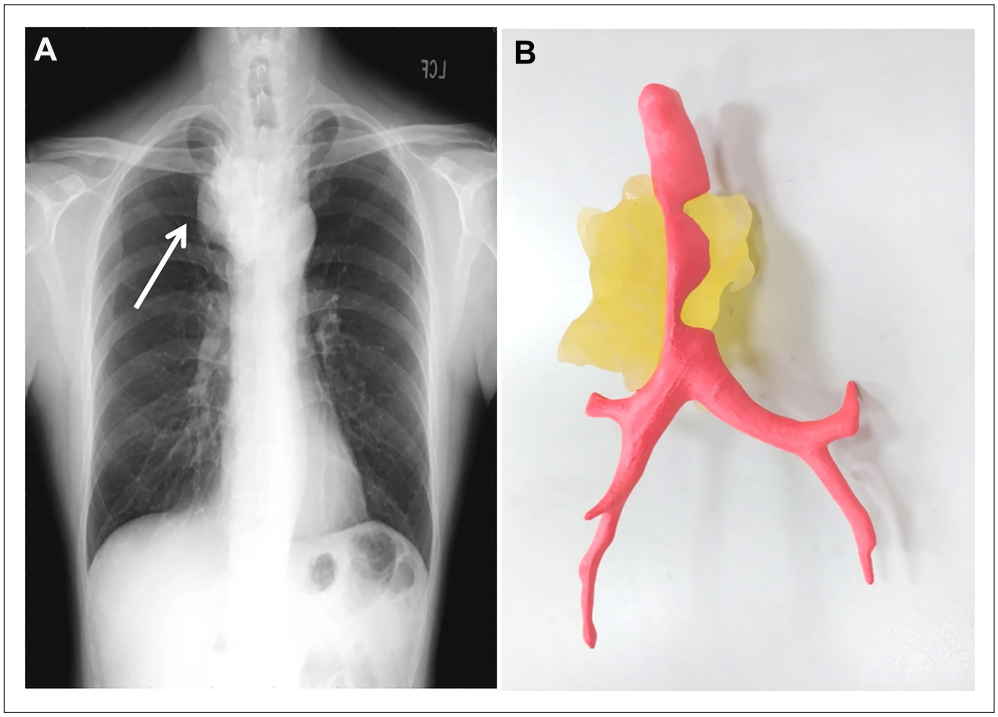

Figure 4. Preoperative planning for complex airway stenosis using a 3D-printed model. **(A)** Chest X-ray and corresponding (B) 3D-printed model of the trachea and a large mediastinal chondrosarcoma (white arrow) causing significant airway compression. The model aided in preoperative simulation and stent design optimization. Modified from Shai *et al.*[86]

reducing infection risk and granulation hyperplasia. In 2024, Jin *et al.*[87] integrated personalized, bionic structure, high-drug-loading 3D printing with local chemotherapy to develop a dual-functional tracheal stent that effectively addresses both mechanical stenosis and tumor growth. This innovative approach was validated in an orthotopic rabbit tumor model, demonstrating its excellent anti-stenotic efficacy, potent antitumor effects, and no significant systemic toxicity (Figures 5 and 6).

Patients with benign lesions, such as post-tuberculosis stenosis, tracheobronchomalacia, post-traumatic stenosis, and post-intubation injury, typically have a long life expectancy. Permanent metal stents are associated with long-term complications, including granulomatous hyperplasia, difficulty in removal, and impaired ciliary function. Additionally, rigid stents may cause discomfort due to their inability to conform to the dynamic movements of respiration. Therefore, the application of 3D-printed stents in benign lesions emphasizes their advantages of fewer complications, effective management of the condition, and biodegradability (Figure 7).[23,83,88–90] 3D-printed customized stents achieve a high degree of morphological matching with the patient's airway, resulting in fewer complications and a significant reduction in the frequency of stent replacement. This results in a significant reduction in migration rate to 4–7%, compared to 25–39% for traditional silicone stents. Furthermore, the enhanced stent-airway fit mitigates localized high-pressure points, reducing the granulation tissue formation rate from 22% with conventional stents to 11%.[22,83] In two cases of complex bronchial stenosis reported by Gildea *et al.*,[88] the frequency of stent replacement decreased from a preoperative average of every 39–52 days to 135–537 days following the implantation of 3D-printed Y-shaped stents. Moreover, 3D models enable preoperative simulation of stent placement, shortening surgical time by approximately 30%[89] and allowing precise positioning of the stent relative to the vocal cords to prevent laryngeal injury.[91] Long-term follow-up suggests that customized stents may promote remodeling of stenotic regions through sustained support. Ntiamoah *et al.*[22] implanted nine patient-specific airway stents in one patient over 4 years, and gradual airway dilation was observed. Subsequent stents required sizing approximately 20% larger to accommodate morphological changes, indicating "airway plasticity."

The major advantage of 3D-printed airway stents over traditional non-degradable stents is their biodegradability. Although conventional silicone stents provide immediate airway support, they are prone to migration and often require secondary surgical removal, which may cause tissue

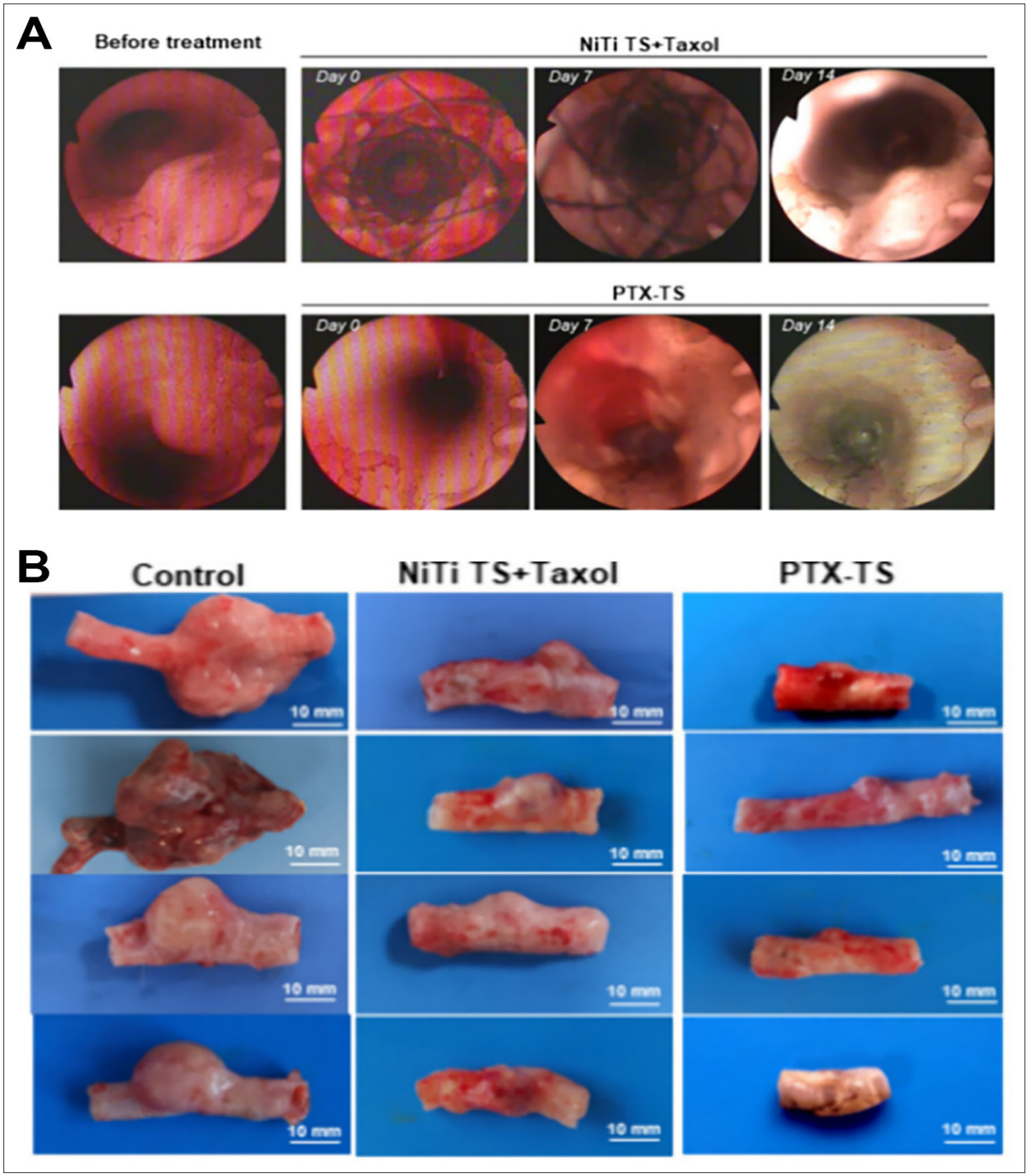

Figure 5. *In vivo* efficacy of the paclitaxel-eluting tracheal stent (PTX-TS). (A) Representative bronchoscopic images of rabbit airways before and after treatment with Niti TS + Taxol or PTX-TS, demonstrating the antistenotic effect of PTX-TS. (B) Anatomical views of tracheal tumors in each group on Day 14 post-treatment, illustrating the antitumor efficacy of PTX-TS. Scale bar: 10 mm. Data are presented as mean ± SD (n = 4). Modified with permission from Jin *et al.*[87] Copyright © 2024 American Chemical Society.

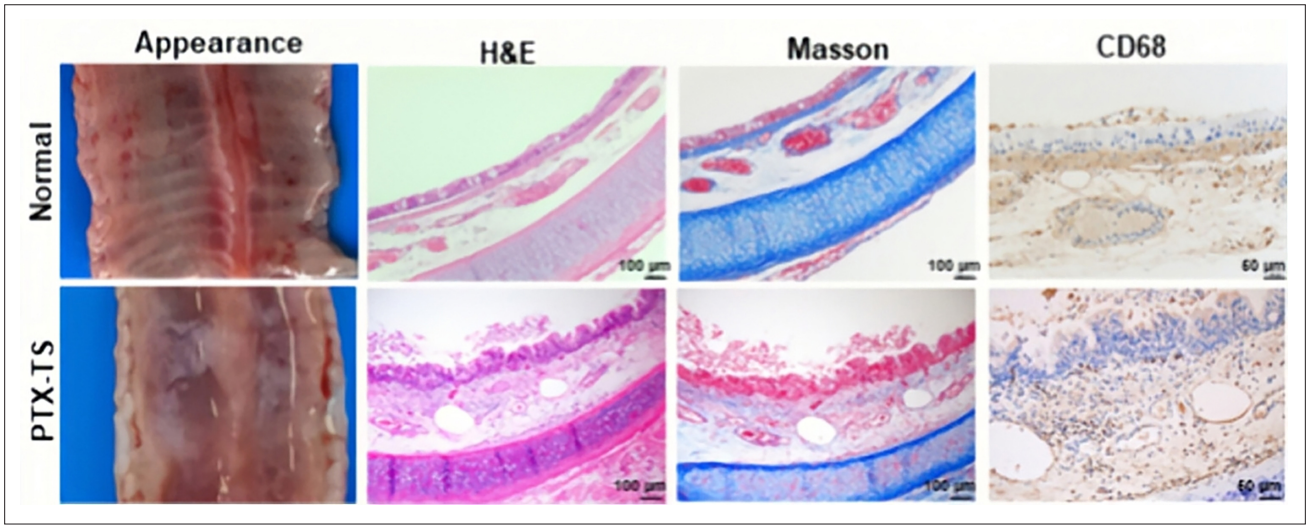

Figure 6. Systemic toxicity and local tissue response to paclitaxel-eluting tracheal stent (PTX-TS) implantation. Representative histological sections (hematoxylin and eosin [H&E], Masson's trichrome, and CD68 staining) of normal trachea and trachea in contact with PTX-TS on Day 30 post-implantation. Images show anatomical and pathological changes, as well as the degree of inflammation. Scale bars: 100 μm (50 μm for CD68); magnifications: 100 and 50 μm for CD68. Modified with permission from Jin *et al.*[87] Copyright © 2024 American Chemical Society.

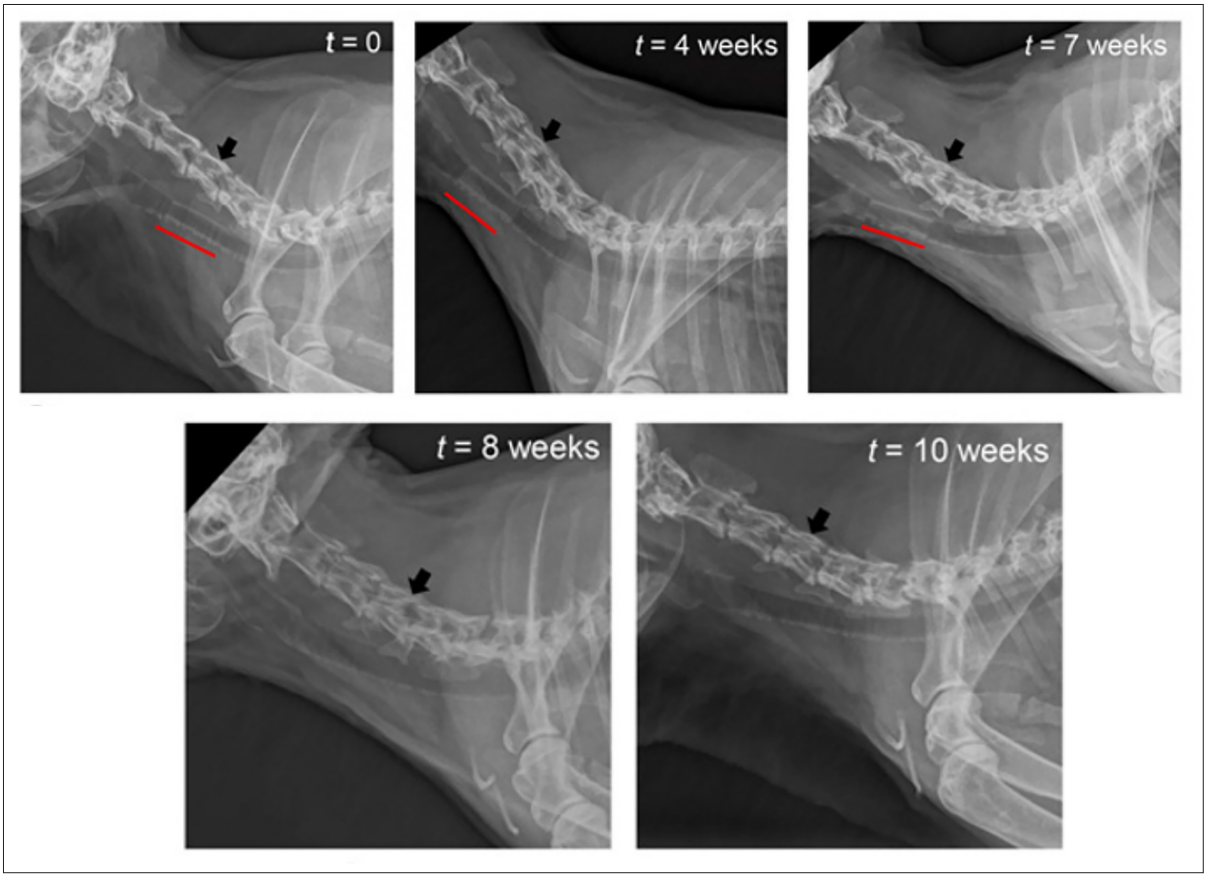

Figure 7. *In vivo* evaluation of a radiopaque, customizable 3D-printed biodegradable stent. Serial radiographs of a rabbit implanted with a 3D-printed stent incorporating 1 wt% gold for radiopacity, tracked over 10 weeks. The stent position is marked by a red line. Black arrows indicate the C4 vertebrae for anatomical reference, demonstrating stent position stability. Reproduced from Paunovic *et al.*[23]

damage—particularly problematic in pediatric patients. Paunovic *et al.*[23] developed a dual-polymer bioink based on poly(ω-lactide-co-ε-caprolactone) and successfully fabricated biodegradable stents with elastomeric mechanical properties. Both *in vitro* degradation experiments and animal studies demonstrated that 3D-printed biodegradable stents provided personalized mechanical support while avoiding secondary surgeries through controlled degradation. These characteristics make them particularly suitable for pediatric and elderly patients and indicate substantial potential for clinical translation.

3.3. Biomaterial-based functional reconstruction

Beyond generating anatomical models and inert implants, the most transformative application of 3D printing in lung surgery lies in the use of advanced biomaterials for functional tissue reconstruction. This strategy aims not only to repair structural defects but also to restore the physiological functions of the lung—such as gas exchange, mechanical compliance, and the underlying biochemical signalings—through the construction of bioactive engineered tissues.[24,92–97]

The core of achieving this goal is 3D bioprinting technology, which fabricates tissue-like constructs by encapsulating living cells and bioactive molecules within bioinks.[24,25,95,98] The selection of biomaterials must balance multiple requirements: excellent biocompatibility to avoid immune rejection, mechanical properties matching lung parenchyma to support ventilation, controllable biodegradability to synchronize with tissue regeneration, and suitable printability to ensure structural precision.

Current research focuses on developing multi-material composite bioinks that mimic the lung's extracellular matrix.[98] Natural polymers, such as alginate, gelatin, collagen, and hyaluronic acid, promote cell adhesion and growth but often lack sufficient mechanical strength.[99] In contrast, synthetic materials, including polycaprolactone, polylactic acid, and polyethylene glycol, offer tunable mechanical properties and degradation rates but often require surface modification to improve cell compatibility.[100] Composite bioinks combine the advantages of both; for example, polycaprolactone–gelatin systems can form scaffolds with both mechanical strength and bioactivity, promoting cell survival and differentiation.[101,102] A recent study reported the development of a multi-tissue integrated tissue-engineered trachea that more closely mimics native tracheal architecture and functions using 3D-printed bioelastomer scaffolds, highlighting a promising direction for advancing functional alveolar reconstruction (Figure 8).[20]

To construct functional alveolar-capillary units, studies have successfully bioprinted simplified alveolar models *in vitro*, achieving preliminary gas exchange functions.[96,103,104] These models typically use porous biodegradable membranes as a base to co-culture lung epithelial cells (such as A549 and primary alveolar cells) and human pulmonary microvascular endothelial cells, simulating the air–blood barrier. These structures not only provide platforms for disease modeling and drug screening but also form the foundation for future construction of large transplantable tissues.

Furthermore, 3D-printed scaffolds can be used for localized drug delivery. By incorporating bioactive molecules, such as vascular endothelial growth factor, fibroblast growth factor, cytokines, and antibiotics, these scaffolds can guide tissue regeneration, reduce inflammation, prevent infection, and promote targeted repair.[79,105,106] This technology holds particular potential for defect repair after tumor resection or tissue reconstruction in contaminated environments.

In summary, 3D bioprinting based on advanced biomaterials is driving lung surgery from passive structural replacement toward active functional regeneration. By precisely integrating cells, materials, and biological factors into 3D structures, this technology holds promise for truly restoring lung function, marking the dawn of a new era in reconstructive lung surgery.

3.4. Application of 3D printing for teaching and training

The 3D printing technology has significantly advanced simulation training for VATS by producing high-fidelity, customizable, and reusable anatomical models, thereby supporting surgeons of varying experience levels in skill development. These models replicate complex anatomical structures and provide realistic haptic feedback, addressing limitations of traditional training methods, including cadaver shortages, ethical concerns with animal models, and limited spatial awareness in 2D imaging. 3D-printed models clearly depict lung segment boundaries, vascular branching, and tumor resection margins, thereby assisting trainees in comprehending spatial relationships. Yang *et al.*[107] developed a transparent 3D-printed lung model that displayed segmental boundaries and vascular spatial relationships, resulting in significantly better test performance in segmentectomy training compared with traditional 3D visualization groups ($p < 0.05$), particularly regarding vascular spatial comprehension (Figures 9 and 10). Similarly, Meershoek *et al.*[108] reported that 3D-printed bronchopulmonary tree models increased trainees' accuracy in anatomical questions from 26.6% to 70.0% ($p = 0.001$) and shortened operative time (207 s vs. 122 s).

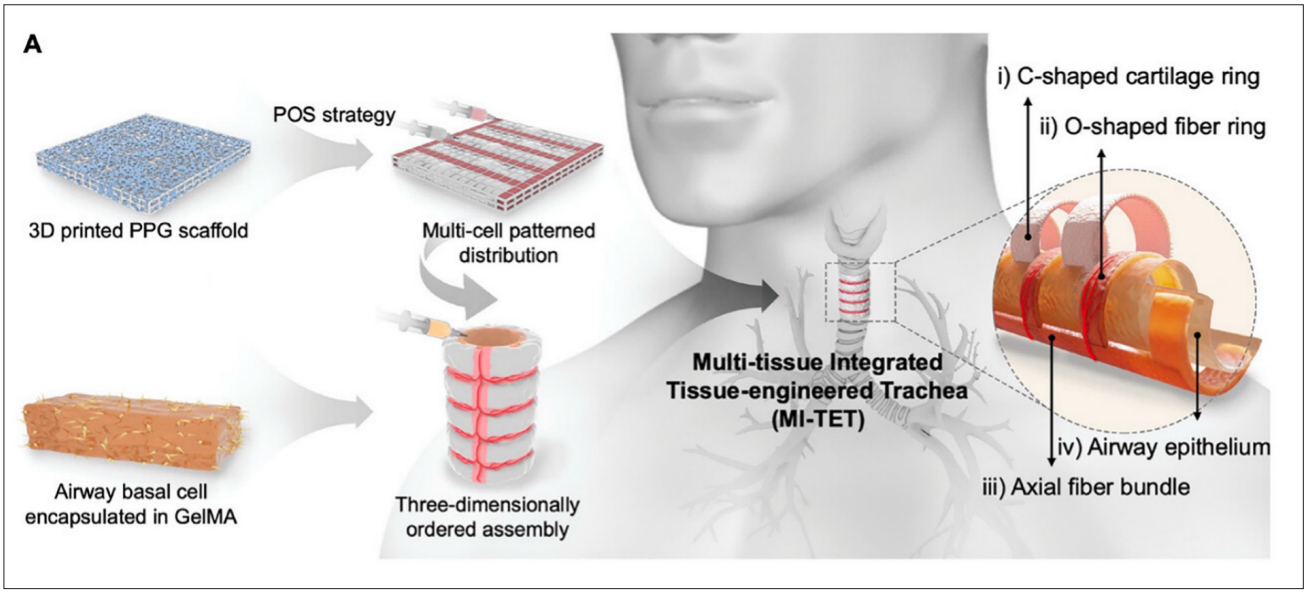

Figure 8. Schematic of tracheal reconstruction using 3D-printed polyglycerol sebacate–gelatin (PPG) scaffolds and a post-occupancy sacrifice (POS) strategy to spatially organize chondrocytes and fibroblasts, followed by 3D assembly to regenerate alternating C-ring/F-ring structures and fiber bundles. A photo-crosslinked gelatin methacryloyl hydrogel is further applied to seed airway basal cells on the luminal surface, generating a biomimetic epithelial layer. Adapted from Song *et al.*[20]

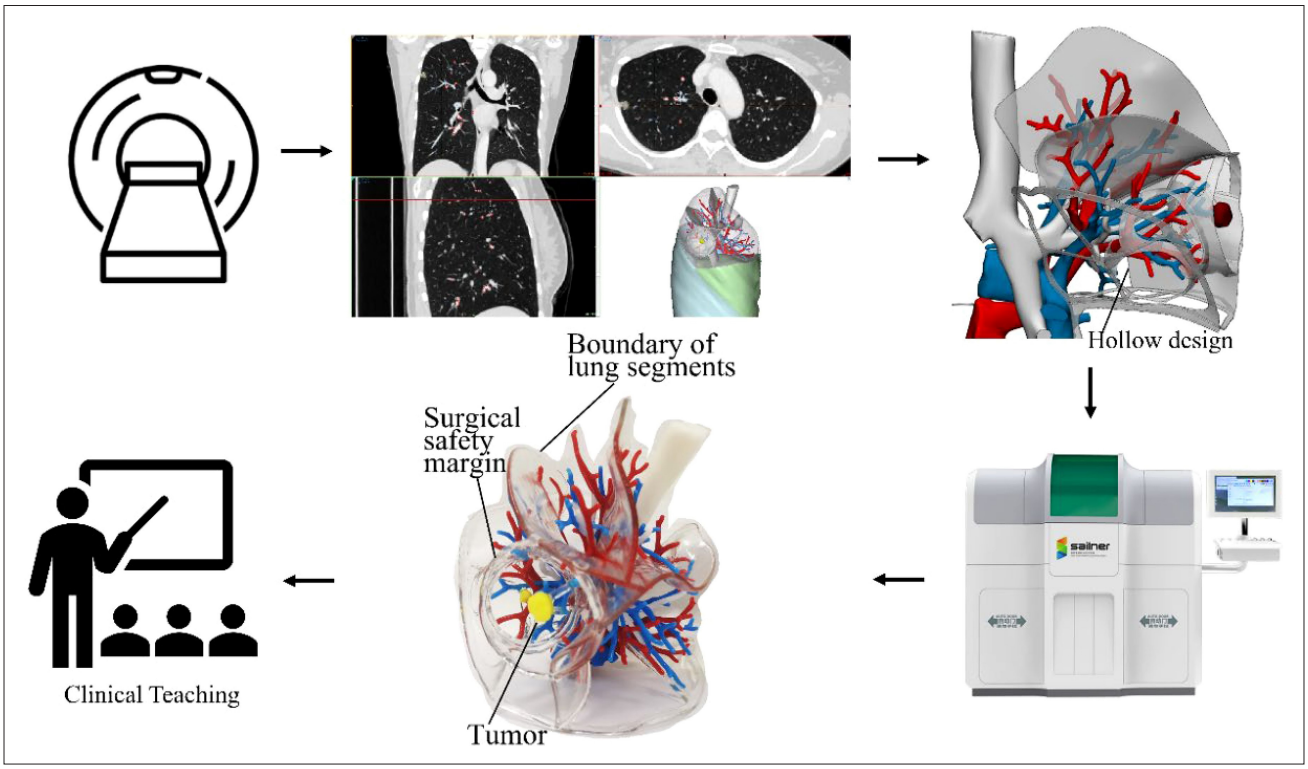

Figure 9. Workflow for generating and applying a 3D-printed hollow lung model in surgical education. The flowchart outlines the process from acquiring computed tomography images of a right upper lobe lung cancer case, through 3D reconstruction, to the printing of a physical, transparent model with hollowed segmental boundaries and safety margins. This model was subsequently used for clinical teaching of thoracoscopic sublobar resection. Reproduced from Yang *et al.*[107]

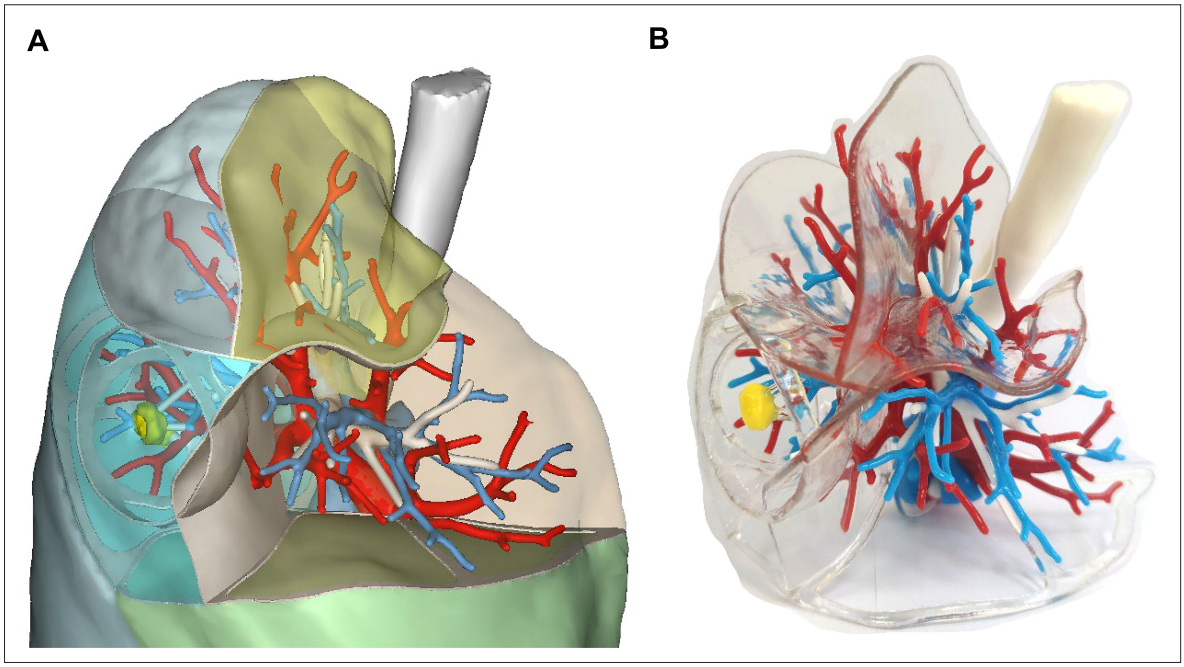

Figure 10. Comparison of 3D-visualized (3DV) and 3D-printed (3DP) models for surgical planning. (A) 3DV model of early-stage lung cancer in the right upper lobe. (B) The corresponding transparent 3DP model, which clearly displays segmental boundaries (without lung parenchyma) and safe resection margins. Notes: Color code: trachea (white), veins (red), arteries (blue), tumor (yellow). Modified from Yang *et al.*[107]

Functional wet-tissue models, such as the Fasolab lung simulator (developed by FASOTEC Co., Ltd., Japan, featuring realistic lung-lobe texture, bronchovascular anatomy, vessel networks, and lymph node positions), allow realistic surgical maneuvers—including cutting, suturing, and stapling—thereby offering hands-on training for complex VATS procedures. Tanaka *et al.*[109] employed 3D-printed biotexture wet-lung models for lobectomy simulation and found that experienced surgeons (>100 VATS cases) achieved significantly shorter operative times than novices (30 min vs. 64.9 min; $p < 0.001$). The model was widely acknowledged as beneficial for novice skill development. Morikawa's third-generation thoracic model, fabricated with foamed polyvinyl alcohol, simulated tissue cutting and energy-device application, thereby enabling realistic thoracoscopic lobectomy practice.[110] Moreover, 3D-printed models establish standardized platforms for critical procedures such as diaphragmatic defect measurement. The Paediatric Surgical Trainees Research Network team developed a congenital diaphragmatic hernia model, accessible through laparoscopic and thoracoscopic approaches, which demonstrated no significant differences in measurement errors among surgeons of varying experience levels ($p > 0.05$), thereby confirming its reliability for technique standardization.[111] For rare or complex conditions such as esophageal atresia with tracheoesophageal fistula (EA/TEF), 3D printing enables patient-specific surgical training. Choi *et al.*[112] developed a neonatal EA/TEF model that integrated motion tracking to quantify instrument path length, revealing significantly shorter paths in experts than in novices (right instrument: 0.68 m vs. 1.86 m; $p < 0.05$), thereby providing objective metrics for skill assessment. A study developed the first full-process thoracoscopic EA-TEF simulator using patient CT-derived 3D printing, achieving high-fidelity simulation ideal for overcoming the learning curve among junior surgeons.[113] Hong *et al.*[114] further enhanced model versatility by incorporating replaceable silicone components (e.g., trachea and esophagus) of varying stiffness to simulate diverse pathologies (Figure 11).

By enabling high-precision replication of patient-specific airway anatomy, 3D printing technology is transforming bronchoscopy skills training. It enhances the tracheobronchoscopic skills of beginners safely and efficiently while significantly reducing training costs. Researchers employ composite materials to replicate the hardness, elasticity, and color of airway tissues, thereby ensuring model realism. Weatherall *et al.*[115] replicated pediatric airway mucosal elasticity and cartilaginous rigidity by combining 3D-printed molds with silicone casting. Likewise, Liu *et al.*[116] used flexible resin to fabricate bronchial trees, achieving tactile feedback comparable to that of real tissue. Ho *et al.*[117] employed material jetting

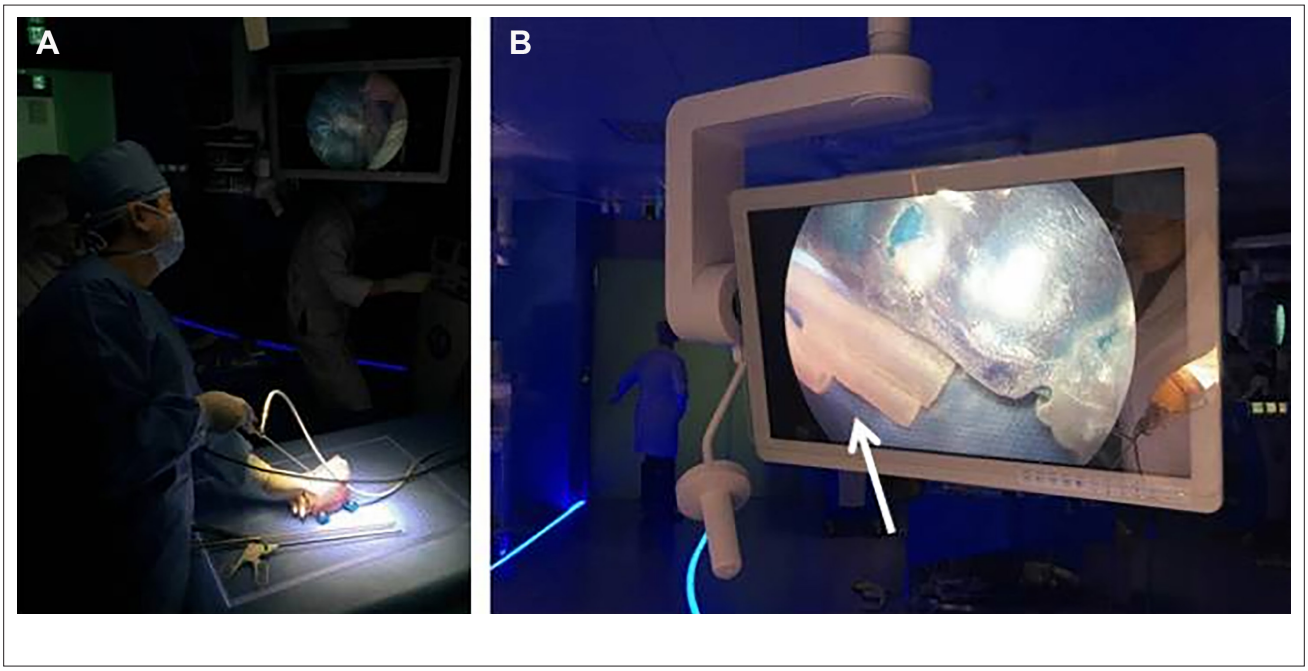

Figure 11. Simulation of thoracoscopic surgery for esophageal atresia with tracheoesophageal fistula (EA/TEF) using a 3D-printed phantom. (A) A surgeon performing a simulated video-assisted thoracoscopic surgery procedure on the patient-specific 3D-printed model. (B) The corresponding view on the thoracoscopic video screen, with the thick white arrow indicating the EA/TEF anatomy. Reproduced from Hong *et al.*[114]

and polymer fusion techniques, utilizing real CT data to create pathological human airway models. This low-cost approach supports the development of customized pathology libraries (e.g., anatomical variations and tumor compression), addressing the limitations of commercial simulators.

Furthermore, dynamic models enable precise simulation of physiological processes, thereby providing a more realistic training environment. Maier *et al.*[118] developed a vacuum pump-connected dynamic model that simulated pediatric airway changes, including expansion during inspiration and collapse during expiration. This design accurately reproduced the dynamic environment encountered during real procedures (Figure 12). Parotto *et al.*'s[119] study demonstrated that after four practice sessions with 3D models, trainees' bronchoscopy operation times decreased from 152.9 to 98.7 s ($p = 0.03$), while their operation scores improved from 8.3 to 18.2 ($p < 0.001$). Ghazy *et al.*[120] showed that after only 15 min of training with 3D models, inexperienced individuals achieved performance comparable to that of experienced practitioners. Both groups also demonstrated significant reductions in the time required to retrieve foreign bodies from the tracheobronchial system after training ($p < 0.001$), thereby validating the model's efficiency.

From an economic standpoint, traditional commercial simulators are costly. For example, the AirSim Combo Bronchi X is priced at approximately USD 3000. In contrast, 3D-printed models markedly reduce expenses. Parotto *et al.*'s[119] bronchial tree model required only USD 5 in materials, and Shaylor *et al.*'s[121] hybrid model (Laerdal upper airway + 3D-printed lower airway) cost less than USD 50. These low-cost models substantially decrease the expense of tracheobronchoscopy skills training, making it particularly suitable for resource-limited settings.

4. Artificial intelligence-driven 3D printing

The convergence of AI and 3D printing is revolutionizing the workflow of personalized lung surgery, transforming it from a manual, experience-dependent process into an intelligent, data-driven, and predictive paradigm. AI enhances every stage, from image segmentation and model optimization to real-time printing control and outcome simulation, enabling a level of precision, efficiency, and personalization previously unattainable.

4.1. Artificial intelligence-enhanced image segmentation and model reconstruction

The traditional conversion of medical images into printable 3D models often involves manual or semi-automated segmentation—a process that is not only time-consuming but also highly operator-dependent. The integration of AI, particularly deep learning, has revolutionized this step by enabling fully automated segmentation with remarkable

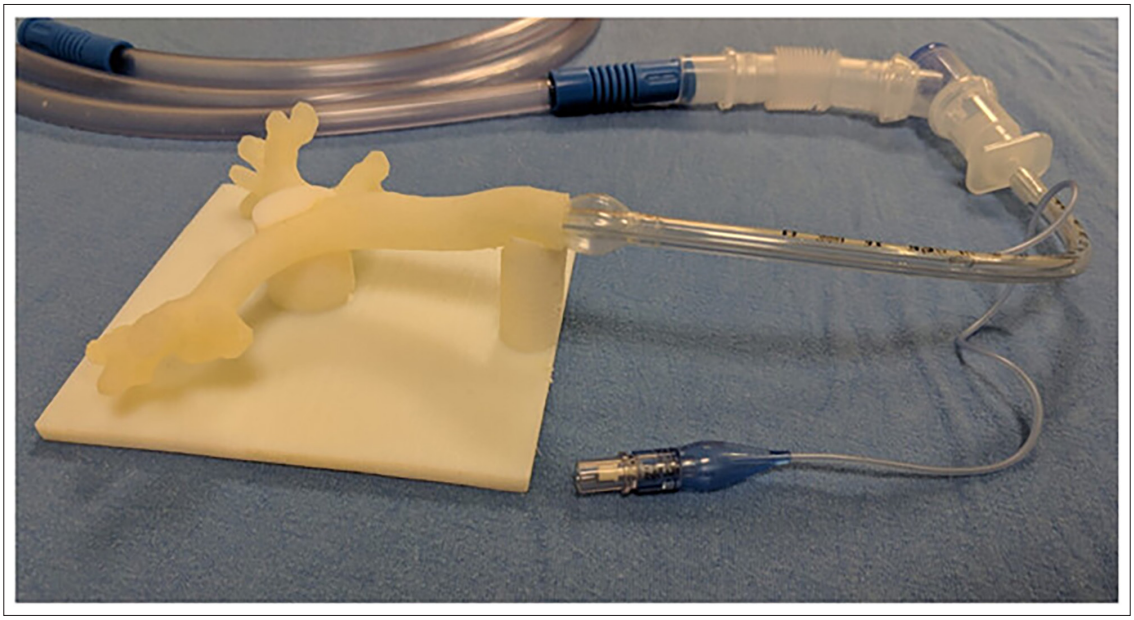

Figure 12. A dynamic 3D-printed airway model for realistic bronchoscopy training. The model, connected to a suction pump via an endotracheal tube (with inflated balloon), simulates physiological breathing movements—expansion during inspiration and collapse during expiration—providing a highly realistic training environment for procedural practice. Reproduced with permission from Maier *et al.*[118] Copyright © 2021 Wiley.

speed and accuracy. Convolutional neural networks, trained on extensive annotated CT or MRI datasets, can automatically and precisely delineate complex pulmonary structures—including vessels, airways, and nodules—even in cases with pathological alterations or low imaging contrast.[122–125]

For example, Ekman *et al.*[122] developed a generalizable deep learning framework that performs robust 3D lung segmentation with limited training data, drastically reducing preprocessing time without compromising anatomical accuracy (Figure 13). Similarly, Im *et al.*[124] used patient-specific "PixelPrint" phantoms to train AI models for improved CT reconstruction, thereby enhancing input data quality for subsequent 3D printing. These AI-powered tools not only expedite model generation but also reduce inter-observer variability, ensuring reproducible patient-specific anatomical models.

Beyond automation, AI facilitates intelligent design optimization. By analyzing geometric, biomechanical, and functional data, AI algorithms can propose design modifications to stents or implants to optimize anatomical fit, mechanical properties, and tissue integration.[126,127] Yilmaz and Kara,[126] for example, applied AI-optimized mathematical surface functions to design airway stents that better conform to patient-specific anatomy while preserving physiological airflow dynamics.

4.2. Intelligent printing process monitoring and control

Artificial intelligence further enhances 3D printing reliability through real-time process monitoring. Machine learning (ML) algorithms utilize visual or sensor feedback to compare each printed layer against its digital blueprint, instantly detecting anomalies such as layer shifting or extrusion defects.[128,129] For example, Rahmani Dabbagh *et al.*[125] pioneered an ML-driven system that dynamically adjusts printing parameters (e.g., nozzle temperature and speed) based on real-time feedback, significantly improving the structural integrity of complex biological scaffolds. Such closed-loop control is vital for fabricating functional tissues and implants, where microstructural precision dictates biological performance.

4.3. Predictive modeling and functionalized design

The most transformative impact of AI may lie in its predictive capabilities. Using patient-specific clinical, genetic, and imaging data, AI models can simulate the biomechanical behavior of 3D-printed implants before they are ever manufactured.[130] For example, computational models can predict stent deformation under respiratory motion, assess stress distribution at the tissue-implant interface, and optimize drug release profiles from bioactive stents.[127,130] Additionally, AI also facilitates functionalized design. For example, in cases of malignant airway stenosis, AI can recommend personalized drug combinations and

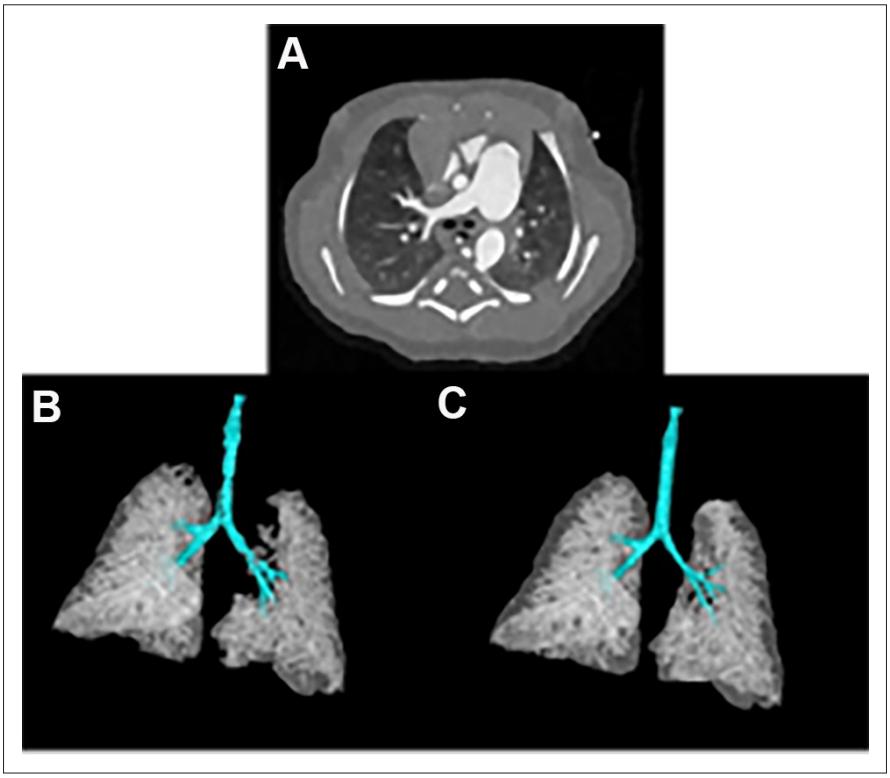

Figure 13. Artificial intelligence-driven segmentation of lung structures. (A) A representative DICOM slice. (B) Automated segmentation results, including post-processing. (C) Manual segmentation. Reproduced from Ekman *et al.*[122]

release kinetics for drug-eluting stents based on tumor genotype and patient physiology.[79,106] This approach was exemplified by Krivitsky *et al.*,[79] who used computational modeling to optimize the co-loading of antibiotics and anti-fibrotic agents into 3D-printed stents, achieving synergistic therapeutic effects in preclinical models.

The integration of AI throughout the 3D printing pipeline enables a closed-loop intelligent ecosystem, seamlessly linking image preprocessing, design optimization, real-time printing control, and outcome prediction with minimal human input. This end-to-end automation not only boosts efficiency but also provides clinicians with powerful decision-support tools, enhancing surgical planning and enabling highly personalized therapeutic strategies.

5. Challenges and prospects

Lung tissue is among the most complex to engineer, combining delicate, highly vascular alveolar structures with the cyclic expansion and contraction of breathing. Replicating this intricate architecture poses significant technical challenges.[131] Current 3D printing methods struggle to achieve high resolution, sufficient mechanical strength, and rapid fabrication simultaneously. For example, printing a personalized airway stent with fine microchannels (such as drug-eluting designs) often forces a trade-off between printing speed and precision, delaying the timely production of patient-specific devices.[22,79,80,132] Moreover, matching a printed scaffold's properties to those of native lung tissue is difficult. Many biomaterials (e.g., poly[lactic-co-caprolactone] and other biodegradable polymers) either degrade faster or slower than the rate of tissue healing. If a scaffold loses structural integrity prematurely, there is a risk of airway collapse or restenosis during degradation, whereas persistent materials may provoke chronic inflammation or infection. The biocompatibility and long-term fate of degradation byproducts also require careful investigation.[23] In addition, replicating the lung's heterogeneous composition—from the cartilage and smooth muscle of bronchi to the thin, elastic alveolar septa with dense capillary networks—would require advanced multi-material printing beyond current capabilities. Furthermore, from a clinical practice perspective, highly personalized stent designs currently lack standardized guidelines and robust long-term, large-scale clinical evidence. Key aspects such as safety, efficacy, and interactions with the complex airway environment

(e.g., effects on mucociliary clearance) remain insufficiently understood.[22,23,79,80] Finally, regulatory approval pathways and manufacturing costs continue to pose major obstacles. The approval process for personalized products is complex, and the individualized workflow—from medical imaging through digital design to final printing—remains costly, thereby limiting widespread adoption.[126,127] In summary, despite their promise, substantial advances in materials science, manufacturing methods, clinical validation, and regulatory frameworks are required before 3D-printed stents can become routine in pulmonary surgery.

In the future, emerging integrations of advanced computational power and imaging techniques offer a viable path to address the challenge of balancing model accuracy with time constraints. AI and ML enable the optimization of both scaffold designs and printing parameters for complex lung geometries, thereby enhancing the efficiency of the entire 3D modeling and printing process.[130,133] Furthermore, deep convergence of AI, VR, AR, and MR with 3D bioprinting represents a transformative trend aimed at overcoming critical challenges in complex surgical intervention.[74,77,130,134] This integration addresses the following two fundamental limitations: the need for greater precision in planning and the gap between planning and execution. AI and ML algorithms address the first challenge,[77,135] while VR, AR, and MR offer solutions to the second. VR facilitates immersive surgical rehearsal, and more significantly, AR/MR systems provide direct intraoperative guidance. Here, AI-processed bioprinting data are superimposed onto the patient's anatomy, effectively granting the surgeon "X-ray vision" and enhancing navigation accuracy during lung surgery. This closed-loop system from digital planning to physical model to augmented execution marks a significant leap forward in personalized medicine. As the technology advances, multi-center clinical trials should be conducted to support widespread implementation in lung surgery. At the frontier is the goal of bioprinting fully functional lung tissues or even whole organs. Nevertheless, this goal remains hindered by challenges in vascularization, neurogenesis, immune compatibility, and scalable manufacturing. Integration of organ-on-a-chip technology with gene editing techniques offers potential solutions.[106,136] Utilizing bioink loaded with cells, researchers are constructing tissue-engineered trachea, alveolar models, and lung tissue, opening possibilities for organ repair and regeneration.[20,137,138] Researchers have begun exploring the construction of *in vitro* lung cancer models for drug screening and the printing of tissue-engineered trachea for lung function restoration.[138,139] Overall, 3D bioprinting is at the forefront of advancing precision medicine in lung surgery. Ongoing innovation and clinical translation are expected to markedly improve therapeutic outcomes, quality of life, and prognosis for patients with lung diseases.

6. Conclusion

In conclusion, 3D printing has advanced from a planning aid into a versatile platform for patient-specific implants and functional simulations. To translate these capabilities into routine clinical practice, coordinated advances in biomaterials, scalable manufacturing, regulatory frameworks, and AI-assisted design are required. Future multi-center clinical trials and standardized workflows are essential to harness the full potential of 3D printing in lung surgery.

Acknowledgments

None.

Funding

None.

Conflict of interest

The authors declare they have no competing interests.

Author contributions

Conceptualization: Zhenghao Dong, Jian Zhou
Funding acquisition: Hu Liao
Investigation: Zhenghao Dong, Wenjing Jiang, Xiang Lin, Beinuo Wang
Project administration: Jian Zhou, Hu Liao
Supervision: Hu Liao, Jian Zhou,
Writing–original draft: Zhenghao Dong, Wenjing Jiang
Writing–review & editing: Jian Zhou, Hu Liao, Yu Tong

Ethics approval and consent to participate

Not applicable.

Consent for publication

Not applicable.

Availability of data

Not applicable.

References

1. Kroll E, Artzi D. Enhancing aerospace engineering students' learning with 3D printing wind-tunnel models. *Rapid Prototyp J*. 2011;17(5):393-402.
doi: 10.1108/13552541111156522

2. Meng M, Wang J, Huang H, Liu X, Zhang J, Li Z. 3D printing metal implants in orthopedic surgery: Methods, applications and future prospects. *J Orthop Translat*. 2023;42:94-112. doi: 10.1016/j.jot.2023.08.004

3. Khorsandi D, Fahimipour A, Abasian P, *et al*. 3D and 4D printing in dentistry and maxillofacial surgery: printing techniques, materials, and applications. *Acta Biomater*. 2021;122:26-49. doi: 10.1016/j.actbio.2020.12.044

4. Bartel T, Rivard A, Jimenez A, Mestres CA, Müller S. Medical three-dimensional printing opens up new opportunities in cardiology and cardiac surgery. *Eur Heart J*. 2018;39(15):1246-1254. doi: 10.1093/eurheartj/ehx016

5. Tack P, Victor J, Gemmel P, Annemans L. 3D-printing techniques in a medical setting: a systematic literature review. *Biomed Eng Online*. 2016;15(1):115. doi: 10.1186/s12938-016-0236-4

6. Grunert R, Winkler D, Frank F, *et al*. 3D-printing of the elbow in complex posttraumatic elbow-stiffness for preoperative planning, surgery-simulation and postoperative control. *3D Print Med*. 2023;9(1):28. doi: 10.1186/s41205-023-00191-x

7. Lam EHY, Yu F, Zhu S, Wang Z. 3D bioprinting for next-generation personalized medicine. *Int J Mol Sci*. 2023;24(7):6357. doi: 10.3390/ijms24076357

8. Jovic TH, Combellack EJ, Jessop ZM, Whitaker IS. 3D bioprinting and the future of surgery. *Front Surg*. 2020;7:609836. doi: 10.3389/fsurg.2020.609836

9. Leiter A, Veluswamy RR, Wisnivesky JP. The global burden of lung cancer: current status and future trends. *Nat Rev Clin Oncol*. 2023;20(9):624-639. doi: 10.1038/s41571-023-00798-3

10. GBD 2019 Chronic Respiratory Diseases Collaborators. Global burden of chronic respiratory diseases and risk factors, 1990-2019: an update from the Global Burden of Disease Study 2019. *EClinicalMedicine*. 2023;59:101936. doi: 10.1016/j.eclinm.2023.101936

11. Choi HK, Mazzone PJ. Lung cancer screening. *Med Clin North Am*. 2022;106(6):1041-1053. doi: 10.1016/j.mcna.2022.07.007

12. McDermott S, Fintelmann FJ, Bierhals AJ, *et al*. Image-guided preoperative localization of pulmonary nodules for video-assisted and robotically assisted surgery. *Radiographics*. 2019;39(5):1264-1279. doi: 10.1148/rg.2019180183

13. Ch'ng S, Wong GL, Clark JR. Reconstruction of the trachea. *J Reconstr Microsurg*. 2014;30(3):153-162. doi: 10.1055/s-0033-1358786

14. Siddiqui FM, Diamond JM. Lung transplantation for chronic obstructive pulmonary disease: past, present, and future directions. *Curr Opin Pulm Med*. 2018;24(2):199-204. doi: 10.1097/MCP.0000000000000452

15. Aranda JL, Jiménez MF, Rodríguez M, Varela G. Tridimensional titanium-printed custom-made prosthesis for sternocostal reconstruction. *Eur J Cardiothorac Surg*. 2015;48(4):e92-e94. doi: 10.1093/ejcts/ezv265

16. Jacob S, Pooley RA, Thomas M. Three-dimensional-printed model as a template for chest wall reconstruction. *Heart Lung Circ*. 2020;29(10):1566-1570. doi: 10.1016/j.hlc.2020.02.004

17. Pontiki AA, Natarajan S, Parker FNH, *et al*. Chest wall reconstruction using 3-dimensional printing: functional and mechanical results. *Ann Thorac Surg*. 2022;114(3):979-988. doi: 10.1016/j.athoracsur.2021.07.103

18. Lin K-H, Huang Y-J, Hsu H-H, *et al*. The role of three-dimensional printing in the nuss procedure: three-dimensional printed model-assisted Nuss procedure. *Ann Thorac Surg*. 2018;105(2):413-417. doi: 10.1016/j.athoracsur.2017.09.031

19. Grigoroiu M, Paul J-F, Brian E, *et al*. 3D printing in anatomical lung segmentectomies: a randomized pilot trial. *Heliyon*. 2024;10(11):e31842. doi: 10.1016/j.heliyon.2024.e31842

20. Song X, Zhang P, Luo B, *et al*. Multi-tissue integrated tissue-engineered trachea regeneration based on 3D printed bioelastomer scaffolds. *Adv Sci (Weinh)*. 2024;11(39):e2405420. doi: 10.1002/advs.202405420

21. Malik HH, Darwood ARJ, Shaunak S, *et al*. Three-dimensional printing in surgery: a review of current surgical applications. *J Surg Res*. 2015;199(2):512-522. doi: 10.1016/j.jss.2015.06.051

22. Ntiamoah P, Gildea TR, Baiera A. Determination of patient-specific airway stent fit using novel 3D reconstruction measurement techniques: a 4-year follow-up of a patient. *Ther Adv Respir Dis*. 2023;17:17534666221137999. doi: 10.1177/17534666221137999

23. Paunovic N, Bao YY, Coulter FB, *et al*. Digital light 3D printing of customized bioresorbable airway stents with elastomeric properties. *Sci Adv*. 2021;7(6):eabe9499. doi: 10.1126/sciadv.abe9499

24. Matai I, Kaur G, Seyedsalehi A, McClinton A, Laurencin CT. Progress in 3D bioprinting technology for tissue/organ regenerative engineering. *Biomaterials*. 2020;226:119536. doi: 10.1016/j.biomaterials.2019.119536

25. Kim W, Lee Y, Kang D, Kwak T, Lee H-R, Jung S. 3D inkjet-bioprinted lung-on-a-chip. *ACS Biomater Sci Eng*. 2023;9(5):2806-2815. doi: 10.1021/acsbiomaterials.3c00089

26. Cornejo J, Cornejo-Aguilar JA, Vargas M, *et al*. Anatomical engineering and 3D printing for surgery and medical devices: international review and future exponential innovations. *BioMed Res Int*. 2022;2022:6797745. doi: 10.1155/2022/6797745

27. Mitsouras D, Liacouras P, Imanzadeh A, *et al*. Medical 3D printing for the radiologist. *Radiographics*. 2015;35(7):1965-1988. doi: 10.1148/rg.2015140320

28. Ma ZY, Wang J, Qin LG, Chortos A. 3D printing in biofabrication: from surface textures to biological engineering. *Chem Eng J*. 2024;500:156477. doi: 10.1016/j.cej.2024.156477

29. Ciocca L, Fantini M, De Crescenzio F, Persiani F, Scotti R. Computer-aided design and manufacturing construction of a surgical template for craniofacial implant positioning to support a definitive nasal prosthesis. *Clin Oral Implants Res*. 2011;22(8):850-856. doi: 10.1111/j.1600-0501.2010.02066.x

30. Liu Y-f, Xu L-w, Zhu H-y, Liu SS-Y. Technical procedures for template-guided surgery for mandibular reconstruction based on digital design and manufacturing. *Biomed Eng Online*. 2014;13:63. doi: 10.1186/1475-925X-13-63

31. Niikura T, Sugimoto M, Lee SY, *et al*. Tactile surgical navigation system for complex acetabular fracture surgery. *Orthopedics*. 2014;37(4):237-242. doi: 10.3928/01477447-20140401-05

32. Sachdev A, Acharya S, Gadodia T, *et al*. A review on techniques and biomaterials used in 3D bioprinting. *Cureus*. 2022;14(8):e28463. doi: 10.7759/cureus.28463

33. Tappa K, Jammalamadaka U. Novel biomaterials used in medical 3D printing techniques. *J Funct Biomater*. 2018;9(1):17. doi: 10.3390/jfb9010017

34. Chia HN, Wu BM. Recent advances in 3D printing of biomaterials. *J Biol Eng*. 2015;9:4. doi: 10.1186/s13036-015-0001-4

35. Mohan N, Senthil P, Vinodh S, Jayanth N. A review on composite materials and process parameters optimisation for the fused deposition modelling process. *Virtual Phys Prototyp*. 2017;12(1):47-59. doi: 10.1080/17452759.2016.1274490

36. Velu R, Calais T, Jayakumar A, Raspall F. A comprehensive review on bio-nanomaterials for medical implants and feasibility studies on fabrication of such implants by additive manufacturing technique. *Materials (Basel)*. 2019;13(1):92. doi: 10.3390/ma13010092

37. Zaharin HA, Rani AMA, Ginta TL, Azam FI. Additive manufacturing technology for biomedical components: a review. *IOP Conf Ser: Mater Sci Eng*. 2017;328:012003. doi: 10.1088/1757-899x/328/1/012003

38. Melchels FPW, Feijen J, Grijpma DW. A review on stereolithography and its applications in biomedical engineering. *Biomaterials*. 2010;31(24):6121-6130. doi: 10.1016/j.biomaterials.2010.04.050

39. Wong TM, Jin J, Lau TW, *et al*. The use of three-dimensional printing technology in orthopaedic surgery. *J Orthop Surg (Hong Kong)*. 2017;25(1):2309499016684077. doi: 10.1177/2309499016684077

40. Mazzoli A. Selective laser sintering in biomedical engineering. *Med Biol Eng Comput*. 2013;51(3):245-256. doi: 10.1007/s11517-012-1001-x

41. Williams JM, Adewunmi A, Schek RM, *et al*. Bone tissue engineering using polycaprolactone scaffolds fabricated via selective laser sintering. *Biomaterials*. 2005;26(23):4817-4827. doi: 10.1016/j.biomaterials.2004.11.057

42. Gao C, Wang C, Jin H, *et al*. Additive manufacturing technique-designed metallic porous implants for clinical application in orthopedics. *RSC Adv*. 2018;8(44):25210-25227. doi: 10.1039/c8ra04815k

43. Grover T, Pandey A, Kumari ST, *et al*. Role of titanium in bio implants and additive manufacturing: an overview. *Mater Today: Proc*. 2020;26:3071-3080. doi: 10.1016/j.matpr.2020.02.636

44. Thompson SM, Bian LK, Shamsaei N, Yadollahi A. An overview of Direct Laser Deposition for additive manufacturing; Part I: Transport phenomena, modeling and diagnostics. *Addit Manuf*. 2015;8:36-62. doi: 10.1016/j.addma.2015.07.001

45. Li YZ, Hu YB, Cong WL, Zhi L, Guo ZN. Additive manufacturing of alumina using laser engineered net shaping: effects of deposition variables. *Ceram Int*. 2017;43(10):7768-7775. doi: 10.1016/j.ceramint.2017.03.085

46. Wang Y, Wang K, Li X, *et al*. 3D fabrication and characterization of phosphoric acid scaffold with a HA/β-TCP weight ratio of 60:40 for bone tissue engineering applications. *PLoS One*. 2017;12(4):e0174870. doi: 10.1371/journal.pone.0174870

47. Burmeister DM, Stone R, Wrice N, *et al*. Delivery of allogeneic adipose stem cells in polyethylene glycol-fibrin hydrogels as an adjunct to meshed autografts after sharp debridement of deep partial thickness burns. *Stem Cells Transl Med*. 2018;7(4):360-372. doi: 10.1002/sctm.17-0160

48. Attarilar S, Ebrahimi M, Djavanroodi F, Fu Y, Wang L, Yang J. 3D printing technologies in metallic implants: a thematic review on the techniques and procedures. *Int J Bioprint*. 2021;7(1):306. doi: 10.18063/ijb.v7i1.306

49. Jang EJ, Patel R, Sankpal NV, Bouchard LS, Patel M. Alginate, hyaluronic acid, and chitosan-based 3D printing hydrogel for cartilage tissue regeneration. *Eur Polym J*. 2024;202:112651.
doi: 10.1016/j.eurpolymj.2023.112651

50. Schuchert MJ, Abbas G, Awais O, *et al*. Anatomic segmentectomy for the solitary pulmonary nodule and early-stage lung cancer. *Ann Thorac Surg*. 2012;93(6):1780-1785.
doi: 10.1016/j.athoracsur.2011.11.074

51. Fan J, Wang L, Jiang GN, Gao W. Sublobectomy versus lobectomy for Stage I non-small-cell lung cancer, a meta-analysis of published studies. *Ann Surg Oncol*. 2012;19(2):661-668.
doi: 10.1245/s10434-011-1931-9

52. Hwang Y, Kang CH, Kim H-S, Jeon JH, Park IK, Kim YT. Comparison of thoracoscopic segmentectomy and thoracoscopic lobectomy on the patients with non-small cell lung cancer: a propensity score matching study. *Eur J Cardiothorac Surg*.2015;48(2):273-278.
doi: 10.1093/ejcts/ezu422

53. Fourdrain A, De Dominicis F, Blanchard C, *et al*. Three-dimensional CT angiography of anatomic variations in the pulmonary arterial tree. *Surg Radiol Anat*. 2018;40(1):45-53.
doi: 10.1007/s00276-017-1914-z

54. Decaluwe H, Petersen RH, Hansen H, *et al*. Major intraoperative complications during video-assisted thoracoscopic anatomical lung resections: an intention-to-treat analysis. *Eur J Cardiothorac Surg*. 2015;48(4):588-598.
doi: 10.1093/ejcts/ezv287

55. Gossot D, Lutz JA, Grigoroiu M, Brian E, Seguin-Givelet A. Unplanned procedures during thoracoscopic segmentectomies. *Ann Thorac Surg*. 2017;104(5):1710-1717.
doi: 10.1016/j.athoracsur.2017.05.081

56. Akiba T, Marushima H, Harada J, Kobayashi S, Morikawa T. Importance of preoperative imaging with 64-row three-dimensional multidetector computed tomography for safer video-assisted thoracic surgery in lung cancer. *Surg Today*. 2009;39(10):844-847.
doi: 10.1007/s00595-009-3965-1

57. Hagiwara M, Shimada Y, Kato Y, *et al*. High-quality 3-dimensional image simulation for pulmonary lobectomy and segmentectomy: results of preoperative assessment of pulmonary vessels and short-term surgical outcomes in consecutive patients undergoing video-assisted thoracic surgery†. *Eur J Cardiothorac Surg*. 2014;46(6): e120-e126.
doi: 10.1093/ejcts/ezu375

58. Oizumi H, Kanauchi N, Kato H, *et al*. Anatomic thoracoscopic pulmonary segmentectomy under 3-dimensional multidetector computed tomography simulation: a report of 52 consecutive cases. *J Thorac Cardiovasc Surg*. 2011;141(3):678-682.
doi: 10.1016/j.jtcvs.2010.08.027

59. Sun Z, Wong YH, Yeong CH. Patient-specific 3D-printed low-cost models in medical education and clinical practice. *Micromachines*. 2023;14(2):464.
doi: 10.3390/mi14020464

60. Chen Y, Zhang J, Chen Q, *et al*. Three-dimensional printing technology for localised thoracoscopic segmental resection for lung cancer: a quasi-randomised clinical trial. *World J Surg Oncol*. 2020;18(1):223.
doi: 10.1186/s12957-020-01998-2

61. Zheng Y-x, Yu D-f, Zhao J-g, Wu Y-l, Zheng B. 3D printout models vs. 3D-rendered images: which is better for preoperative planning? *J Surg Educ*. 2016;73(3):518-523.
doi: 10.1016/j.jsurg.2016.01.003

62. Qiu B, Ji Y, He H, Zhao J, Xue Q, Gao S. Three-dimensional reconstruction/personalized three-dimensional printed model for thoracoscopic anatomical partial-lobectomy in stage I lung cancer: a retrospective study. *Transl Lung Cancer Res*. 2020;9(4):1235-1246.
doi: 10.21037/tlcr-20-571

63. Akiba T, Nakada T, Inagaki T. Simulation of the fissureless technique for thoracoscopic segmentectomy using rapid prototyping. *Ann Thorac Cardiovasc Surg*. 2015;21(1):84-86.
doi: 10.5761/atcs.nm.13-00322

64. Nardini M, Dunning J. Pulmonary nodules precision localization techniques. *Future Oncol*. 2020;16(16s):15-19.
doi: 10.2217/fon-2019-0069

65. Hou Y-L, Wang Y-D, Guo H-Q, Zhang Y, Guo Y, Han H. Ultrasound location of pulmonary nodules in video-assisted thoracoscopic surgery for precise sublobectomy. *Thorac Cancer*. 2020;11(5):1354-1360.
doi: 10.1111/1759-7714.13384

66. Cornella KN, Repper DC, Palafox BA, *et al*. A surgeon's guide for various lung nodule localization techniques and the newest technologies. *Innovations (Phila)*. 2021; 16(1):26-33.
doi: 10.1177/1556984520966999

67. Suffo M, Quiroga-De Castro M, Galán-Romero L, Andrés-Cano P. Intra-hospital patient-specific 3D printed surgical guide for patients with thoracic scoliotic deformities, the collaboration between engineer and surgeon. *3D Print Med*. 2025;11(1):40.
doi: 10.1186/s41205-025-00279-6

68. Li K, Ding N, Xu Y, *et al*. Synchronous resection of 12 small pulmonary nodules guided by a noninvasive 3D printed emulation model: a case report. *Thorac Cancer*. 2022;13(15):2260-2263.
doi: 10.1111/1759-7714.14546

69. Fu R, Chai Y-F, Zhang J-T, *et al*. Three-dimensional printed navigational template for localizing small pulmonary nodules: a case-controlled study. *Thorac Cancer*. 2020;11(9):2690-2697.
doi: 10.1111/1759-7714.13550

70. Tang H, Yue P, Wei N, *et al*. Three-dimensional printing template for intraoperative localization of pulmonary nodules in the pleural cavity. *JTCVS Tech*. 2022;16:139-148. doi: 10.1016/j.xjtc.2022.10.003

71. Zhang L, Li M, Li Z, *et al*. Three-dimensional printing of navigational template in localization of pulmonary nodule: a pilot study. *J Thorac Cardiovasc Surg*. 2017;154(6):2113-2119.e7. doi: 10.1016/j.jtcvs.2017.08.065

72. E H, Chen J, Sun W, *et al*. Three-dimensionally printed navigational template: a promising guiding approach for lung biopsy. *Transl Lung Cancer Res*. 2022;11(3):393-403. doi: 10.21037/tlcr-22-172

73. Thacharodi A, Singh P, Meenatchi R, *et al*. Revolutionizing healthcare and medicine: the impact of modern technologies for a healthier future-a comprehensive review. *Health Care Sci*. 2024;3(5):329-349. doi: 10.1002/hcs2.115

74. Chen Z, Zhang Y, Yan Z, *et al*. Artificial intelligence assisted display in thoracic surgery: development and possibilities. *J Thorac Dis*. 2021;13(12):6994-7005. doi: 10.21037/jtd-21-1240

75. Huang H, Wu Y. A deep learning-based method for rapid 3D whole-heart modeling in congenital heart disease. *Cardiology*. 2025;150(3):243-258. doi: 10.1159/000541980

76. Isikay I, Cekic E, Baylarov B, Tunc O, Hanalioglu S. Narrative review of patient-specific 3D visualization and reality technologies in skull base neurosurgery: enhancements in surgical training, planning, and navigation. *Front Surg*. 2024;11:1427844. doi: 10.3389/fsurg.2024.1427844

77. Fu R, Zhang C, Zhang T, *et al*. A three-dimensional printing navigational template combined with mixed reality technique for localizing pulmonary nodules. *Interact Cardiovasc Thorac Surg*. 2021;32(4):552-559. doi: 10.1093/icvts/ivaa300

78. Li C, Zheng B, Yu Q, Yang B, Liang C, Liu Y. Augmented reality and 3-dimensional printing technologies for guiding complex thoracoscopic surgery. *Ann Thorac Surg*. 2021;112(5):1624-1631. doi: 10.1016/j.athoracsur.2020.10.037

79. Krivitsky A, Paunović N, Klein K, *et al*. 3D printed drug-eluting stents: toward personalized therapy for airway stenosis. *J Control Release*. 2025;377:553-562. doi: 10.1016/j.jconrel.2024.11.031

80. Chen S, Du T, Zhang H, Zhang Y, Qiao A. Advances in studies on tracheal stent design addressing the related complications. *Mater Today Bio*. 2024;29:101263. doi: 10.1016/j.mtbio.2024.101263

81. Sabath BF, Ost DE. Update on airway stents. *Curr Opin Pulm Med*. 2018;24(4):343-349. doi: 10.1097/MCP.0000000000000486

82. Ayub A, Al-Ayoubi AM, Bhora FY. Stents for airway strictures: selection and results. *J Thorac Dis*. 2017;9(S2):S116-S121. doi: 10.21037/jtd.2017.01.56

83. Alraiyes AH, Avasarala SK, Machuzak MS, Gildea TR. 3D printing for airway disease. *AME Med J*. 2019;4:14. doi: 10.21037/amj.2019.01.05

84. Xu J, Ong HX, Traini D, Byrom M, Williamson J, Young PM. The utility of 3D-printed airway stents to improve treatment strategies for central airway obstructions. *Drug Dev Ind Pharm*. 2019;45(1):1-10. doi: 10.1080/03639045.2018.1522325

85. Guibert N, Moreno B, Plat G, Didier A, Mazieres J, Hermant C. Stenting of complex malignant central-airway obstruction guided by a three-dimensional printed model of the airways. *Ann Thorac Surg*. 2017;103(4):e357-e359. doi: 10.1016/j.athoracsur.2016.09.082

86. Shai S-E, Lai Y-L, Li H-N, Hung S-C. 3-D printing model used to streamline surgical procedures for an intricate condition of airway compression caused by devastating mediastinal chondrosarcoma: a case report. *J Med Case Rep*. 2020;14(1):14. doi: 10.1186/s13256-019-2312-4

87. Jin Z, Fu Y, Zhang Y, Guo S. Lesion-adaptative bionic tracheal stent with local paclitaxel release for enhanced therapy of tracheal tumor and stenosis. *ACS Biomater Sci Eng*. 2024;10(10):6677-6689. doi: 10.1021/acsbiomaterials.4c01523

88. Gildea TR, Young BP, Machuzak MS. Application of 3D printing for patient-specific silicone stents: 1-year follow-up on 2 patients. *Respiration*. 2018;96(5):488-494. doi: 10.1159/000489669

89. Fiorelli A, Scaramuzzi R, Minerva I, *et al*. Three-dimensional (3D) printed model to plan the endoscopic treatment of upper airway stenosis. *J Bronchol Intervent Pulmonol*. 2018;25(4):349-354. doi: 10.1097/LBR.0000000000000504

90. Schleich S, Kronen P, Krivitsky A, *et al*. Effects of shape and structure of a new 3D-printed personalized bioresorbable tracheal stent on fit and biocompatibility in a rabbit model. *PLoS One*. 2024;19(6):e0300847. doi: 10.1371/journal.pone.0300847

91. Natale G, Reginelli A, Testa D, *et al*. The use of 3D printing model as tool for planning endoscopic treatment of benign airway stenosis. *Transl Cancer Res*. 2020;9(3):2117-2122. doi: 10.21037/tcr.2020.01.22

92. Tan B, Gan S, Wang X, Liu W, Li X. Applications of 3D bioprinting in tissue engineering: advantages, deficiencies, improvements, and future perspectives. *J Mater Chem B*. 2021;9(27):5385-5413. doi: 10.1039/d1tb00172h

93. Shiwarski DJ, Hudson AR, Tashman JW, *et al*. 3D bioprinting of collagen-based high-resolution internally perfusable scaffolds for engineering fully biologic tissue systems. *Sci Adv*. 2025;11(17):eadu5905.
doi: 10.1126/sciadv.adu5905

94. Erben A, Hörning M, Hartmann B, *et al*. Precision 3D-printed cell scaffolds mimicking native tissue composition and mechanics. *Adv Healthc Mater*. 2020;9(24):e2000918.
doi: 10.1002/adhm.202000918

95. Huo Y, Xu Y, Wu X, *et al*. Functional trachea reconstruction using 3D-bioprinted native-like tissue architecture based on designable tissue-specific bioinks. *Adv Sci (Weinh)*. 2022;9(29):e2202181.
doi: 10.1002/advs.202202181

96. Zhang Y, Liu Y, Shu C, *et al*. 3D bioprinting of the airways and lungs for applications in tissue engineering and in vitro models. *J Tissue Eng*. 2024;15:20417314241309183.
doi: 10.1177/20417314241309183

97. Dabaghi M, Carpio MB, Moran-Mirabal JM, Hirota JA. 3D (bio)printing of lungs: past, present, and future. *Eur Respir J*. 2023;61(1):2200417.
doi: 10.1183/13993003.00417-2022

98. De Santis MM, Alsafadi HN, Tas S, *et al*. Extracellular-matrix-reinforced bioinks for 3d bioprinting human tissue. *Adv Mater*. 2021;33(3):e2005476.
doi: 10.1002/adma.202005476

99. Echave MC, Saenz del Burgo L, Pedraz JL, Orive G. Gelatin as biomaterial for tissue engineering. *Curr Pharm Des*. 2017;23(24):3567-3584.
doi: 10.2174/1381612823666170511123101

100. Izgordu MS, Uzgur EI, Ulag S, *et al*. Investigation of 3D-printed polycaprolactone-/polyvinylpyrrolidone-based constructs. *Cartilage*. 2021;13(2_suppl):626S-635S.
doi: 10.1177/1947603519897302

101. Ren P, Wei D, Liang M, Xu L, Zhang T, Zhang Q. Alginate/gelatin-based hybrid hydrogels with function of injecting and encapsulating cells in situ. *Int J Biol Macromol*. 2022;212:67-84.
doi: 10.1016/j.ijbiomac.2022.05.058

102. Wang N, Yu K-K, Li K, Yu X-Q. A biocompatible polyethylene glycol/alginate composite hydrogel with significant reactive oxygen species consumption for promoting wound healing. *J Mater Chem B*. 2023;11(29):6934-6942.
doi: 10.1039/d3tb00771e

103. Ng WL, Ayi TC, Liu Y-C, Sing SL, Yeong WY, Tan B-H. Fabrication and characterization of 3d bioprinted triple-layered human alveolar lung models. *Int J Bioprint*. 2021;7(2):332.
doi: 10.18063/ijb.v7i2.332

104. da Rosa NN, Appel JM, Irioda AC, *et al*. Three-dimensional bioprinting of an in vitro lung model. *Int J Mol Sci*. 2023;24(6):5852.
doi: 10.3390/ijms24065852

105. Frankowski J, Kurzątkowska M, Sobczak M, Piotrowska U. Utilization of 3D bioprinting technology in creating human tissue and organoid models for preclinical drug research - state-of-the-art. *Int J Pharm*. 2023;644:123313.
doi: 10.1016/j.ijpharm.2023.123313

106. Liu C, Shi C, Wang S, *et al*. Bridging the gap: how patient-derived lung cancer organoids are transforming personalized medicine. *Front Cell Dev Biol*. 2025;13:1554268.
doi: 10.3389/fcell.2025.1554268

107. Yang D, Miao Y, Li L, *et al*. From virtual to reality: application of a novel 3D printing hollow model for early-stage lung cancer in the clinical teaching of thoracoscopic sublobar resection. *Front Oncol*. 2025;15:1526592.
doi: 10.3389/fonc.2025.1526592

108. Meershoek AJA, Loonen TGJ, Maal TJJ, Hekma EJ, Hugen N. Three dimensional printing as a tool for anatomical training in lung surgery. *Med Sci Educ*. 2023;33(4):873-878.
doi: 10.1007/s40670-023-01807-x

109. Tanaka T, Shimada Y, Furumoto H, *et al*. Comparative analysis of the results of video-assisted thoracic surgery lobectomy simulation using the three-dimensional-printed biotexture wet-lung model and surgeons' experience. *Interact Cardiovasc Thorac Surg*. 2021;32(2):284-290.
doi: 10.1093/icvts/ivaa240

110. Morikawa T, Yamashita M, Odaka M, *et al*. A step-by-step development of real-size chest model for simulation of thoracoscopic surgery. *Interact Cardiovasc Thorac Surg*. 2017;25(2):173-176.
doi: 10.1093/icvts/ivx110

111. PSTRN PSTRNPS. Development of a 3D-printed neonatal congenital diaphragmatic hernia model and standardisation of intra-operative measurement. *Pediatr Surg Int*. 2023;40(1):28.
doi: 10.1007/s00383-023-05600-0

112. Choi C, Wells J, Luenenschloss N, *et al*. The role of motion tracking in assessing technical skill acquisition using a neonatal 3D-printed thoracoscopic esophageal atresia/tracheo-esophageal fistula simulator. *J Pediatr Surg*. 2022;57(6):1087-1091.
doi: 10.1016/j.jpedsurg.2022.01.029

113. Youn JK, Ko D, Yang H-B, Kim H-Y. A 3D printed esophageal atresia-tracheoesophageal fistula thorascopy simulator for young surgeons. *Sci Rep*. 2024;14(1):11489.
doi: 10.1038/s41598-024-62154-4

114. Hong D, Kim H, Kim T, Kim Y-H, Kim N. Development of patient specific, realistic, and reusable video assisted thoracoscopic surgery simulator using 3D printing and pediatric computed tomography images. *Sci Rep*. 2021;11(1):6191.
doi: 10.1038/s41598-021-85738-w

115. Weatherall AD, Rogerson MD, Quayle MR, Cooper MG, McMenamin PG, Adams JW. A novel 3-dimensional printing fabrication approach for the production of pediatric airway models. *Anesth Analg*. 2021;133(5): 1251-1259.
doi: 10.1213/ANE.0000000000005260

116. Liu W-L, Lee IH, Lee L-N, Yang S-H, Chao K-Y. A 3D-printed high-fidelity bronchial tree for bronchoscopy. *Respir Care*. 2023;68(4):527-530.
doi: 10.4187/respcare.10671

117. Ho BHK, Chen CJ, Tan GJS, *et al*. Multi-material three dimensional printed models for simulation of bronchoscopy. *BMC Med Educ*. 2019;19(1):236.
doi: 10.1186/s12909-019-1677-9

118. Maier P, Silvestro E, Goldfarb SB, Piccione J, Phinizy PA, Andronikou S. Three-dimensional printed realistic pediatric static and dynamic airway models for bronchoscopy and foreign body removal training. *Pediatr Pulmonol*. 2021;56(8):2654-2659.
doi: 10.1002/ppul.25516

119. Parotto M, Jiansen JQ, AboTaiban A, *et al*. Evaluation of a low-cost, 3D-printed model for bronchoscopy training. *Anaesthesiol Intensive Ther*. 2017;49(3):189-197.
doi: 10.5603/AIT.a2017.0035

120. Ghazy A, Chaban R, Vahl C-F, Dorweiler B. Development and evaluation of 3-dimensional printed models of the human tracheobronchial system for training in flexible bronchoscopy. *Interact Cardiovasc Thorac Surg*. 2019;28(1):137-143.
doi: 10.1093/icvts/ivy215

121. Shaylor R, Golden E, Goren O, Verenkin V, Cohen B. Development and validation of a hybrid bronchoscopy trainer using three-dimensional printing. *Simul Healthc*. 2024;19(1):52-55.
doi: 10.1097/SIH.0000000000000687

122. Ekman T, Barakat A, Heiberg E. Generalizable deep learning framework for 3D medical image segmentation using limited training data. *3D Print Med*. 2025;11(1):9.
doi: 10.1186/s41205-025-00254-1

123. Zhang Z, Wang Y, Wang W. Machine learning in gel-based additive manufacturing: from material design to process optimization. *Gels*. 2025;11(8):582.
doi: 10.3390/gels11080582

124. Im JY, Halliburton SS, Mei K, *et al*. Patient-derived PixelPrint phantoms for evaluating clinical imaging performance of a deep learning CT reconstruction algorithm. *Phys Med Biol*. 2024;69(11):115009.
doi: 10.1088/1361-6560/ad3dba

125. Rahmani Dabbagh S, Ozcan O, Tasoglu S. Machine learning-enabled optimization of extrusion-based 3D printing. *Methods*. 2022;206:27-40.
doi: 10.1016/j.ymeth.2022.08.002

126. Yilmaz B, Kara BY. Mathematical surface function-based design and 3D printing of airway stents. *3D Print Med*. 2022;8(1):24.
doi: 10.1186/s41205-022-00154-8

127. Ayechu-Abendaño A, Pérez-Jiménez A, Sánchez-Matás C, *et al*. Computational analysis of polymeric biodegradable and customizable airway stent designs. *Polymers*. 2024;16(12):1691.
doi: 10.3390/polym16121691

128. Rezapour Sarabi M, Alseed MM, Karagoz AA, Tasoglu S. Machine learning-enabled prediction of 3D-printed microneedle features. *Biosensors (Basel)*. 2022;12(7):491.
doi: 10.3390/bios12070491

129. Rojek I, Dostatni E, Kopowski J, Macko M, Mikołajewski D. AI-based support system for monitoring the quality of a product within industry 4.0 paradigm. *Sensors (Basel)*. 2022;22(21):8107.
doi: 10.3390/s22218107

130. Pradhan A, Pattnaik G, Das S, Acharya B, Patra CN. Advancements in lung cancer: molecular insights, innovative therapies, and future prospects. *Med Oncol*. 2025; 42(9):383.
doi: 10.1007/s12032-025-02725-1

131. Hrubovčák J, Tulinský L, Pieš M, *et al*. The utilization of 3D printing in surgery as an innovative approach to preoperative planning. *Rozhl Chir*. 2024;103(8):305-312.
doi: 10.48095/ccrvch2024305

132. Wang T, Zhang J, Wang J, Pei YH, Qiu XJ, Wang YL. Paclitaxel drug-eluting tracheal stent could reduce granulation tissue formation in a canine model. *Chin Med J*. 2016;129(22):2708-2713.
doi: 10.4103/0366-6999.193461

133. Liang Y, Wei S, Zhang A. Bioengineered tracheal graft with enhanced vascularization and mechanical stability for functional airway reconstruction. *Regen Ther*. 2025;29:364-380.
doi: 10.1016/j.reth.2025.03.016

134. Pelizzo G, Costanzo S, Roveri M, *et al*. Developing virtual reality head mounted display (HMD) set-up for thoracoscopic surgery of complex congenital lung malformations in children. *Children (Basel)*. 2022;9(1):50.
doi: 10.3390/children9010050

135. Cen J, Liufu R, Wen S, *et al*. Three-dimensional printing, virtual reality and mixed reality for pulmonary atresia: early surgical outcomes evaluation. *Heart Lung Circ*. 2021;30(2):296-302.
doi: 10.1016/j.hlc.2020.03.017

136. Pun S, Haney LC, Barrile R. Modelling human physiology on-chip: historical perspectives and future directions. *Micromachines*. 2021;12(10):1250.
doi: 10.3390/mi12101250

137. Hua W, Zhang C, Raymond L, *et al*. Embedded 3D printing of engineered lung cancer model for assisting fine-needle aspiration biopsy. *Biofabrication*. 2024. doi: 10.1088/1758-5090/ad9fe0

138. Kwok JKS, Lau RWH, Zhao Z-R, *et al*. Multi-dimensional printing in thoracic surgery: current and future applications. *J Thorac Dis*. 2018;10(Suppl 6):S756-S763. doi: 10.21037/jtd.2018.02.91

139. Harun A, Bendele N, Khalil MI, *et al*. 3D tumor-mimicking phantom models for assessing NIR I/II nanoparticles in fluorescence-guided surgical interventions. *ACS Nano*. 2025;19(21):19757-19776. doi: 10.1021/acsnano.5c01919

ACCSCIENCE PUBLISHING

International Journal of Bioprinting

REVIEW ARTICLE

3D-printed hydrogels for treating diabetic wounds: Recent developments

Mengdi Yin[1†], Yutong Wang[2†], Yuhang Wei[2†], Changjia Li[3], Yiqiao Yin[2], Tiantang Fan[2], and Peixin Wang[1*]

[1]Qingdao Hospital, University of Health and Rehabilitation Sciences (Qingdao Municipal Hospital), Qingdao, Shandong, China

[2] College of Medical Engineering, Jining Medical University, Jining, Shandong, China

[3]Department of Colorectal and Anal Surgery, Qingdao Central Hospital, University of Health and Rehabilitation Sciences, Qingdao, Shandong, China

Abstract

Diabetic wound healing disorder is one of the common complications in diabetic patients, characterized by chronic inflammation, impaired angiogenesis, abnormal extracellular matrix (ECM) remodeling, and markedly elevated oxidative stress. Although traditional treatment models have achieved some success, they still face challenges such as prolonged wound healing duration, increased risk of infection, and continuous formation of scar tissue, particularly in gastrointestinal surgical incisions, breast surgery incisions, orthopedic surgical incisions, and neurosurgical incisions. In recent years, the integration of biomaterials and advanced manufacturing technologies has brought new opportunities for diabetic wound healing. Hydrogels have gained increasing attention due to their excellent biocompatibility, degradability, and significant wound healing ability. As an emerging advanced manufacturing method, 3D printing technology could accurately fabricate hydrogels according to the shape and size of the wound, providing an ideal microenvironment for wound healing. This work systematically reviewed the latest research on 3D-printed hydrogels in diabetic wound healing in the past 5 years. It also thoroughly discussed the preparation methods, including physical, chemical, and biological cross-linking methods, and the specific mechanisms of promoting wound healing, such as regulating inflammatory response, promoting angiogenesis, and guiding the normal remodeling of ECM. This review aimed to provide a solid theoretical and experimental basis for the continued development and eventual clinical application of 3D-printed hydrogels for diabetic wounds.

Keywords: 3D-printed hydrogel; Diabetic wound; Mechanism; Preparation method; Surgical incision

1. Introduction

Diabetes mellitus (DM), as a typical metabolic disorder, is characterized by persistently abnormally elevated blood glucose levels. Its pathological basis is closely related to insufficient insulin secretion or functional defects, causing multiple organ damage and a series of serious complications, such as renal impairment, visual impairment,

†These authors contributed equally to this work.

***Corresponding author:**
Peixin Wang
(qddxwpx@163.com)

Citation: Yin M, Wang Y, Wei Y, *et al.* Recent development of 3D printed hydrogels for treating of diabetic wound. *Int J Bioprint*. 2025;11(6):107-129. doi: 10.36922/IJB025320322

Received: August 10, 2025
Revised: September 11, 2025
Accepted: September 15, 2025
Published online: September 18, 2025

Copyright: © 2025 Author(s). This is an Open Access article distributed under the terms of the Creative Commons Attribution License, permitting distribution and reproduction in any medium, provided the original work is properly cited.

Publisher's Note: AccScience Publishing remains neutral with regard to jurisdictional claims in published maps and institutional affiliations.

neuropathy, and cardiovascular diseases.[1,2] According to epidemiological data and the Diabetes Atlas of the International Diabetes Federation, the global prevalence of diabetes rose dramatically to 536 million patients by 2021 and is projected to reach 783 million by 2025.[3–5] It is noteworthy that China ranked first worldwide in terms of the diabetic patient population, with the number of adult diabetics reaching a staggering 148 million in 2022, representing approximately 18% of the global total. This situation significantly impacted patients' lives and imposed a considerable strain on the healthcare system.[6]

During normal wound healing, superoxide anion (O^{2-}) and hydrogen peroxide (H_2O_2) are essential to prevent infection. Small amounts of reactive oxygen species (ROS) can promote collagen and fibronectin production, neovascularization, fibroblast proliferation and migration, and epithelial tissue regeneration. However, in diabetic patients, hyperglycemia not only provides a favorable environment for bacterial proliferation but also leads to a significant increase in ROS levels in the body by activating polyol pathways and accumulating advanced glycation end products. These cause changes in skin structure and function, damaging the mechanical integrity of the skin, and weakening its self-healing ability. Eventually, chronic wounds form.[7] From the molecular mechanism perspective, hyperglycemia persistently exerts negative impacts on cell functions, vascular endothelial growth factor (VEGF) expression, and inflammatory responses. For example, it inhibits the proliferation and migration of fibroblasts, down-regulates the expression of VEGF, induces neovascularization dysfunction, leads to insufficient blood supply in local tissues, and excessive expression of pro-inflammatory factors, further aggravating the complexity of wound healing.[8]

Diabetic wound healing is a complex and dynamic process; the chronic inflammation, oxidative stress, and cellular dysfunction caused by hyperglycemia significantly delay the healing process and often fail to complete normal healing.[9–12] Research hotspots for different stages are emerging, including new hemostatic material development, macrophage polarization regulation,[13,14] ROS clearance,[15] angiogenesis and nerve regeneration, collagen deposition, and scar regulation. Nevertheless, the current traditional treatment methods, such as dressing coverage, debridement, and antibiotic therapy, have obvious limitations. For example, it is difficult to precisely regulate the wound microenvironment, cope with complex pathophysiological changes, adapt to the diversification of wound morphology, and treat deep ulcers or complex infections.[16] Besides, antibiotic therapy is also facing the risk of drug resistance, and there exists a notable shortage of individualized treatment strategies. An ideal modern wound dressing should possess excellent moisturizing ability, air permeability, and exudation management capabilities to establish a suitable humid environment while effectively preventing the accumulation of effusion and subsequent infections.[15] At the same time, it is imperative for the dressing to exhibit excellent antibacterial capabilities, mechanical strength, and biocompatibility, enabling it to effectively repel external bacterial intrusion, safeguard the wound against external trauma, and minimize the likelihood of rejection.[17,18] Furthermore, the design of the wound dressing should prioritize ease of clinical handling, ensuring that medical staff can effortlessly perform essential operations.

Recently, the field of wound dressings for healing prolonged diabetic wounds has witnessed remarkable progress, achieving a leap from traditional dressings to a variety of new material systems. Among them, hydrogel dressings can mimic a natural moist environment due to their high water content, thereby fostering cell migration and proliferation.[19] Additionally, the 3D network structure allows the free exchange of oxygen and nutrients while blocking the invasion of pathogens.[20] Moreover, certain hydrogels can be engineered to incorporate bioactive ingredients, such as antibacterial agents and growth factors, enabling precise regulation of biological activity and thereby expediting the wound healing process.[21–24] However, traditional hydrogels still exhibit limitations, including insufficient mechanical strength, uncontrollable pore structures, and the uneven release of antibacterial components.[25]

As bio-manufacturing technology advances rapidly, 3D printing has broken through traditional hydrogel preparation limits, achieving an upgrade from structural biomimicry to functional integration and providing smarter, personalized solutions for diabetic wound healing. For example, through precise adjustment of printing parameters and material composition, it is possible to optimize the moisturizing and breathable characteristics of the dressing, while also enabling the accurate incorporation of antibacterial agents. Its layer-by-layer manufacturing ability enables the construction of biomimetic gradient structures to mimic the mechanical properties of natural tissues, further improving the adaptability of dressings to wounds. Thus, this modern dressing, with its multifunctional and optimized design, is of great significance in addressing the limitations of traditional dressings, accelerating wound healing, improving patient prognosis, and shortening the rehabilitation cycle.

In view of the unique advantages and great potential of 3D-printed hydrogels in diabetic wound healing, it is of scientific and clinical significance to explore their preparation methods and mechanisms of action. This review systematically summarizes the research progress

in 3D-printed hydrogels over the past 5 years, aiming to provide a solid theoretical basis and technical support for the development of a new generation of smart wound dressings for diabetic wound healing.

2. Preparation methods for 3D-printed hydrogels

As a cutting-edge technology, 3D printing is deeply integrated with hydrogels, opening up a new path for the biomedical field and effectively overcoming the limitations of traditional cross-linking methods. Currently, the preparation methods for 3D-printed hydrogels primarily include physical cross-linking, chemical cross-linking, and biological cross-linking methods (Figure 1 and Table 1).

2.1. Physical cross-linking method

The physical cross-linking method is one of the primary methods in the preparation of 3D-printed hydrogels. The core principle of this method is the use of non-covalent bond interactions, including hydrogen bonds, electrostatic attraction, and hydrophobic effects, to build a 3D porous network structure of hydrogels.[26] This method preserves the natural structure and biological activity of the raw materials—benefits that are of great significance for tissue engineering, drug delivery, diabetic wound repair, and the treatment of gastrointestinal surgical incisions.[27] However, hydrogels generated through a physical cross-linking method have shortcomings, such as relatively poor uniformity, mechanical strength, and long-term stability. The introduction of 3D printing technology has led to significant breakthroughs in this area, playing an important role in the development of improved materials for diabetic wound healing.

The temperature-induced cross-linking method is an important type of physical cross-linking. It regulates the non-covalent interactions between molecules to

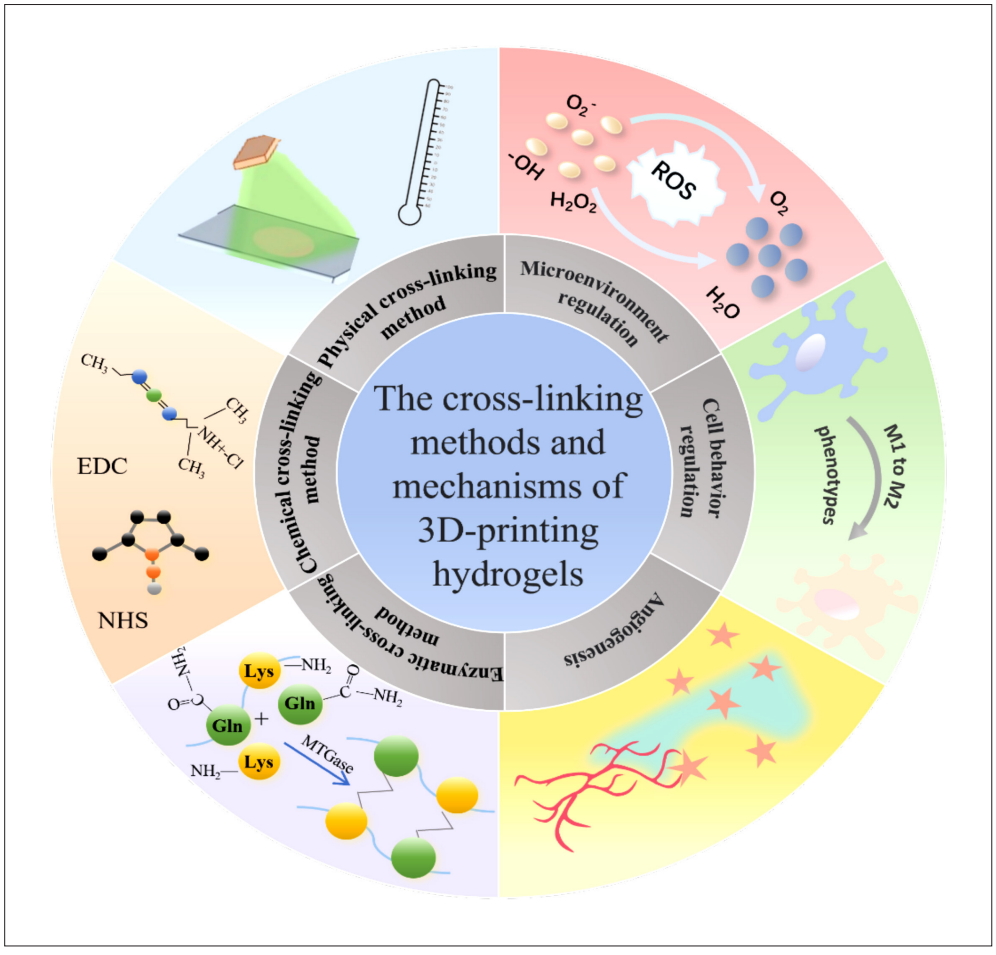

Figure 1. The cross-linking methods and mechanisms of 3D-printed hydrogels. Abbreviations: EDC, 1-Ethyl-3-(3-dimethylaminopropyl)carbodiimide; Gln, glutamine; Lys, lysine; MTGase, microbial transglutaminase; NHS, N-Hydroxysuccinimide; ROS, reactive oxygen species.

achieve gelation through temperature changes. At low temperatures, raw materials remain stably in a soluble state; when the temperature rises to physiological range, they spontaneously assemble to form fiber networks through non-covalent forces. For example, Drzewiecki *et al.*[28] used microbiota-modified collagen to generate collagen methacrylamide (CMA). This hydrogel retained the self-assemblability, biodegradability, and natural biological activity of collagen. Under the physiological temperature and pH conditions, CMA exhibited rapid and temperature-dependent reversible self-assembly. Rombouts *et al.*[29] prepared a silk fibroin–collagen hydrogel that achieved reversible state changes through temperature switching (Figure 2A). When the temperature was increased to 40°C, the silk proteins self-assembled, whereas upon cooling to 20°C, the self-assembly process became synchronized with the formation of triple helix structures. Moreover, the introduction of anionic polypeptide poly(γ-glutamic acid) into the CMA hydrogel effectively enhanced the temperature-dependent phase transition behavior of collagen, resulting in a low-viscosity solution at room temperature and a non-flowing gel at approximately 37°C.[30] However, it is still challenging to precisely control the gelation time, porosity, and mechanical properties of collagen hydrogels.

Through the integration of computer-aided design (CAD) and precise temperature gradient control, 3D printing technology enables the realization of structural precision and functional customization in hydrogel fabrication. Studies have shown that bovine serum albumin demonstrates a concentration-dependent gelation when heated at or above its melting point at a pH far from its isoelectric point. Naik *et al.*[31] incorporated aloe vera into bovine serum albumin and prepared a hydrogel using 3D printing technology. The results revealed that the local application of this hydrogel effectively stimulated collagen deposition, thereby promoting wound healing in diabetic patients, increasing VEGF expression, and improving the delivery of nutrients required for angiogenesis and collagen synthesis. Based on a template replication and 3D printing strategy, Zhang *et al.*[32] developed a novel type of biomimetic adaptive indwelling microneedles, which consisted of adjustable polyvinyl-alcohol-hydrogel needle tips encapsulating mesenchymal stem cell-derived exosomes, along with a removable 3M medical tape serving as the supporting substrate. The results showed clinical values in the treatment of diabetic complications. Likewise, Xia *et al.*[33] used 3D printing technology to construct scaffolds by mixing gelatin methacrylate (GelMA) with adipose-derived stem cells (ADSCs) and incorporating the anti-inflammatory antioxidant curcumin, achieving 85% porosity and a cell survival rate of 92%. The temperature-induced cross-linking method rapidly fabricated the scaffold at 37°C, while the interlayer bond strength was improved by optimizing the temperature gradient (gradually increasing from 20 to 37°C) to two times that of the traditional method, thereby significantly enhancing the mechanical stability.

Wound-site bioelectrical stimulation can accelerate wound healing processes by supporting regular collagen deposition and proper extracellular matrix (ECM) remodeling. Kumi *et al.*[34] used 3D printing technology to develop a customized antibacterial porous flexible electrode (APFE) hydrogel dressing that combined the antibacterial properties of modified chitosan (CS) derivatives with the conductivity of poly(3,4-ethylenedioxythiophene):polystyrene sulfonic acid (PEDOT:PSS). This electrical stimulation dressing enabled the delivery of targeted treatment to promote the healing of infected diabetic wounds.

In addition, Metwally *et al.*[35] fabricated a bilayer hydrogel scaffold via hyaluronic acid/CS (HA/CS) inks (Figure 2B). The scaffold consisted of an upper dense planar hydrogel layer and an antibacterial/regenerative nanofiber layer integrated with poly (lactic acid) nanofiber microspheres. Compared with traditional hydrogels, this hydrogel represents a transition from passive dressings to actively regulated, precision treatment platforms through digital extrusion printing. It not only replicates the bionic bilayer structure of the skin but also generates a customizable multi-level pore network through the incorporation of drug-loaded nanofiber microspheres, thus structurally surpassing the uniform random pores of traditional hydrogels. Furthermore, this design enables the efficient loading, uniform distribution, and sustained release of ZnO nanoparticles and didecyldimethylammonium bromide, ultimately producing a synergistic effect of strong antibacterial properties, modulation of the inflammatory microenvironment, and significant acceleration of tissue regeneration. In diabetic wound infection models, it achieved an ultra-high healing rate of 95%, a level difficult to attain with traditional hydrogels.

Although the physical cross-linking method offers unique advantages, it also presents notable drawbacks. For example, inadequate control over cross-linking uniformity can produce hydrogels with compromised mechanical properties, reduced strength, and diminished stability. During *in vivo* applications, the rapid degradation rate of certain materials may render them unsuitable for scenarios demanding high mechanical strength or prolonged implantation periods. This accelerated degradation can compromise the hydrogel's structural integrity over time, thereby adversely affecting the overall therapeutic outcome.

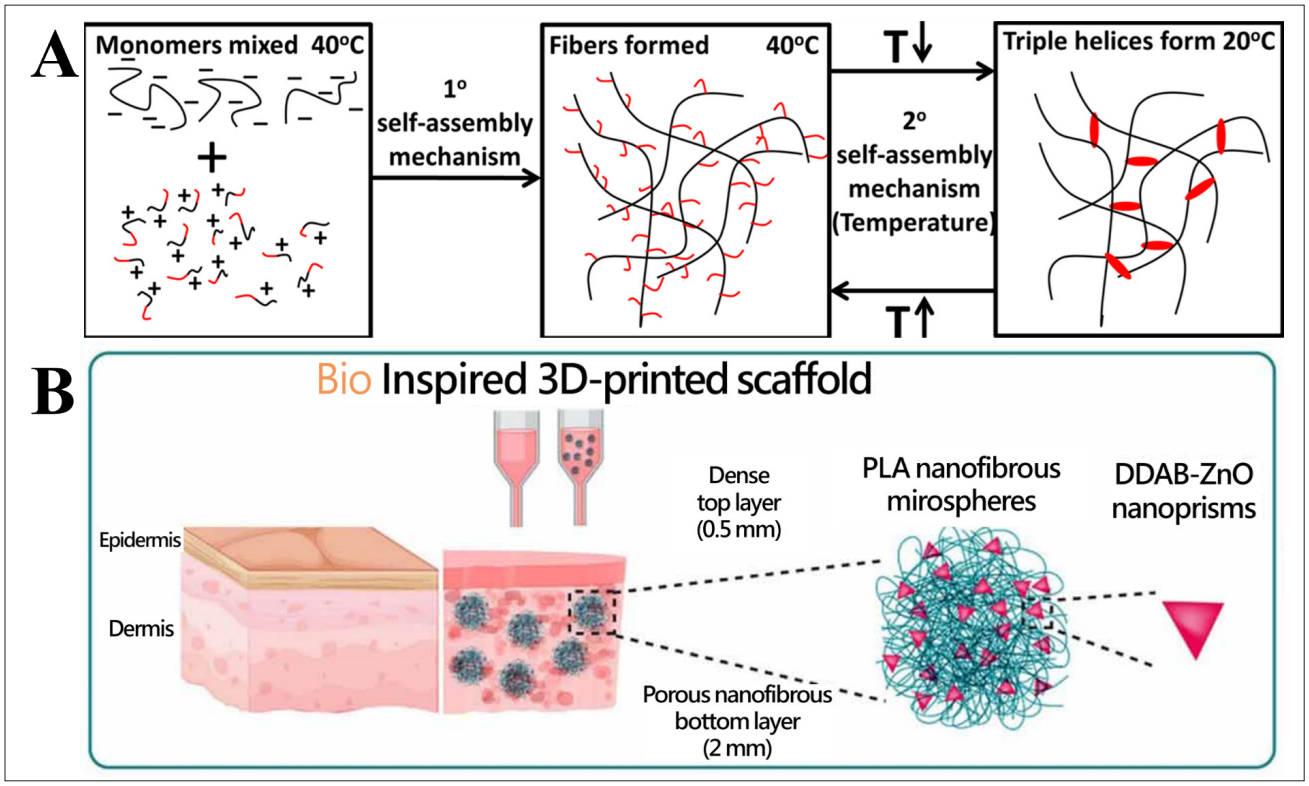

Figure 2. Schematic diagram of the preparation of physical cross-linked hydrogels. (A) The states of collagen hydrogel at different temperatures. Adapted with permission from Rombouts *et al.*[29] Copyright © 2015 American Chemical Society. (B) Schematic process for the developed, bioinspired composite DZ-MS@scaffold. Adapted from Metwally *et al.*[35] Abbreviations: DDAB, didecyldimethylammonium bromide; DZ, DDAB-treated ZnO nanoparticle; MS, microsphere; PLA, poly (lactic acid).

2.2. Chemical cross-linking method

Due to the unique mechanism of action and significant advantages, the chemical cross-linking method has become a research hotspot in the field of biomaterials. The method can precisely control the degradation rate of hydrogels by precisely regulating the types and concentrations of cross-linking agents, meeting the varied requirements of different treatment scenarios. The key factor in preparing hydrogels via the chemical cross-linking method lies in selecting appropriate cross-linking agents, which significantly influence a hydrogel's properties, degradation rate, and overall performance. With the directional modification of key functional groups, such as –CHO and $–NH_2$, within a molecular structure, specific chemical reactions are triggered to facilitate the formation of cross-linking between molecular chains. This tailored approach enables the fabrication of hydrogel structures that are precisely engineered to meet distinct functional requirements for targeted applications.[36] 3D-printed hydrogels obtained through the chemical cross-linking method are an ideal solution for solving personalized medical requirements, particularly in the treatment of diabetic wounds.

2.2.1. Photo–cross-linking method

The photo–cross-linking method represents a pivotal approach in chemical cross-linking. It utilizes photosensitizers, such as riboflavin and methacrylic anhydride, to initiate free radical reactions under specific wavelengths of light sources. This process leads to the formation of covalent bonds or dynamic coordination bonds, ultimately constructing a 3D network structure within the hydrogel.[37] Besides, the photo–cross-linking method exhibits rapid gelation, with gelation times reaching the sub-second range under optimal conditions. This property aligns well with the immediate molding requirements of 3D printing technology and is particularly suitable for rapid wound closure in diabetic wound healing. Chen *et al.*[38] fabricated a 3D-printed dual-network hydrogel incorporating ceria-based metal–organic framework (MOF) nanoenzymes, consisting of a cerium–cross-linked sodium alginate network and a polyacrylamide network. During the printing process, 365 nm ultraviolet light was used to promote the polymerization of acrylamide. After printing, the sample was further cured under ultraviolet light for 10 min to achieve rapid cross-linking. Owing to the anti-inflammatory and hypoglycemic effects of the

nanoenzyme hydrogel, wounds of 1 cm^2 in size in diabetic rats were completely healed within 21 days. Similarly, Cao *et al.*[39] addressed excessive ROS and the imbalance between pro-inflammatory and anti-inflammatory cells/factors by preparing a wound dressing consisting of doxycycline hydrochloride-loaded, ROS-responsive polyurethane membranes combined with 3D-printed hydrogel strips using the photoinitiator lithium phenyl-2,4,6-trimethylbenzoylphosphinate (LAP). This multifunctional dressing significantly accelerated the healing of chronic wounds, exhibiting enhanced epithelialization, angiogenesis, and collagen deposition.

Li *et al.*[40] developed a highly self-supporting CS-based hydrogel ink using the photoinitiator Irgacure 2959 for the *in situ* 3D printing of diabetic wound dressings. The ink formed a reversible, physically cross-linked structure through multiple electrostatic interactions and hydrogen-bond networks between carboxymethyl CS and clay nanoparticles. Even after autoclaving, the ink retained its ability to undergo ultraviolet cross-linking, and the photoinitiator remained intact, non-toxic, and biocompatible. The resulting 3D-printed dressings exhibited both antibacterial and pro-angiogenic properties, significantly accelerating wound healing, achieving complete healing within 17 days, accompanied by hair follicle regeneration and angiogenesis. This work not only provides a new strategy for developing highly self-supporting biopolymer inks but also paves the way for advanced, personalized wound dressings.

Ding *et al.*[41] fabricated a multifunctional hydrogel dressing via digital light processing (DLP) technology, inspired by the ECM properties of *Acomys* (African spiny mouse) during wound healing. They introduced methylacryloyl groups into GelMA and HA methacrylate (HAMA), endowing the molecular chains with photosensitive groups capable of undergoing free radical polymerization under ultraviolet light in the presence of photoinitiators, thereby forming a covalently cross-linked network. The precise control over the structural, mechanical, and biological properties of hydrogels was achieved through the photosensitivity of GelMA/HAMA and DLP-based light-curing printing.

Hu *et al.*[42] fabricated an ECM-based 3D-printed dermal hydrogel scaffold loaded with Cu–epigallocatechin gallate capsules. They reacted decellularized ECM (dECM) derived from pigskin with glycidyl methacrylate anhydride, introducing photo–cross-linkable methacrylate groups to form a methacrylated decellularized extracellular matrix (EM). Then it was mixed with the photoinitiator LAP to prepare the bio-ink. Upon ultraviolet (350 nm) irradiation, the double bonds in EM underwent photo-initiated free radical polymerization, forming covalently cross-linked hydrogels. Notably, the EM hydrogel also exhibited temperature-sensitive properties, remaining in a gel state at low temperatures and transitioning into a gel state near body temperature. This combination of physical and chemical cross-linking not only facilitated printing and shaping but also endowed the scaffold with excellent mechanical properties and biological activity. Furthermore, the hydrogel scaffold inhibited excessive inflammation by promoting macrophage polarization from M1 to M2, while supporting the organization of endothelial cells into stable tubular structures essential for neovascularization.

Xia *et al.*[33] used the same method, simultaneously loading curcumin into a 3D-bioprinting hydrogel to create a suitable microenvironment for ADSCs. They demonstrated that curcumin enhanced the reparative effects of ADSCs on diabetic wounds by targeting the advanced glycation end product (AGE)/AGE receptor/p65 signaling pathway. Likewise, Wan *et al.*[43] synthesized modified Has, including maleinated sodium hyaluronate (MHA) and thiolated sodium hyaluronate (SHHA), with highly substituted acrylate groups. MHA/SHHA hydrogels were prepared by blending the modified HA with mercaptoacrylate via Michael addition pre-cross-linking, followed by covalent cross-linking through thiol–acrylate and acrylate–acrylate photopolymerization. These hydrogels represented promising hydrogel scaffold candidates for diabetic wound healing.

2.2.2. Schiff base reaction

The Schiff base reaction, a mild and efficient condensation reaction between –CHO and $–NH_2$ groups forming an imine bond (C=N), plays a crucial role in hydrogel preparation. It allows adjusting the proportion of reactants and precisely controlling the reaction conditions, such as temperature, pH value, and reaction time.[44] The introduction of 3D printing technology enables the precise fabrication of hydrogels through layer-by-layer stacking based on pre-designed models. By precisely controlling printing parameters and the conditions of the Schiff base reaction, hydrogel scaffolds with complex 3D structures can be directly fabricated. Moreover, adjusting the degree of Schiff base cross-linking allows the optimization of the mechanical properties and pore structure of the 3D-printed hydrogels to better match the specific requirements of different tissue engineering applications.

Common cross-linkers used in Schiff base reactions include genipin, dialdehyde cholesterol-modified starch, and oxidized konjac glucomannan. They can react with different polymer matrices to tailor the properties of 3D-printed hydrogels. Fu *et al.*[45] used multi-cross-linking strategies, including free radical polymerization,

Michael addition, Schiff base reaction, and hydrogen bonding, to fabricate a cell-loaded collagen-based bio-ink consisting of CMA and dihydromyricetin. Following oxidation, dihydromyricetin generates aldehyde groups that participate in Schiff base formation, while unreacted phenolic hydroxyl groups retain ROS-scavenging ability. This multiple cross-linking strategy accelerated gelation by 375%, increased stiffness by 161%, enhanced mechanical elasticity by 231%, and improved biodegradability by 208%.

Yang *et al.*[46] prepared 3D-printed grid-like hydrogels loaded with deferoxamine, cross-linked via Schiff base bonds between –CHO from oxidized mannan oligosaccharides and $–NH_2$ from hyaluronic acrylamide. These hydrogels not only exhibited antioxidant effects and regulated inflammatory responses but also promoted wound angiogenesis, providing a novel strategy for diabetic wound healing. Lin *et al.*[47] utilized Schiff base reactions between the aldehyde group of oxidized sodium alginate and the amino group of gelatins to prepare bio-inks containing sodium alginate, oxidized sodium alginate, gelatin, and $CaCO_3$ microspheres, thereby enhancing their printability. The resulting porous 3D-printed hydrogel scaffolds featured a stable structure (pore area: 4.43 ± 0.14 μm^2; wire diameter: 184 ± 25 μm), providing a potential solution for improving diabetic wound healing.

While dynamic hydrogels are valuable for tissue healing, improving their adaptability to complex chronic wounds without additional active substances remains a major challenge. To address this, Ding *et al.*[48] developed a 3D-printed hydrogel scaffold from aldehyde-modified dextran and benzaldehyde (DEX-BA) and MoS_2 nanosheets. This hydrogel scaffold formed dynamic Schiff base bonds with tissue protein $–NH_2$ on the surface of wounds through –CHO provided by DEX-BA, achieving strong adhesion to the wound surfaces. Application of 3D printing of the scaffolds into chronic diabetic wounds accelerated wound healing, promoted wound closure, mitigated oxidative stress, and eradicated bacterial infections, highlighting its potential as a multifunctional *in-situ* 3D-printed hydrogel scaffold for diabetic wound healing and other tissue engineering applications.

2.2.3. Click chemical cross-linking reaction

The click chemical cross-linking method is another common method to prepare 3D-printed hydrogels. It enables rapid and site-specific cross-linking through bio-orthogonal reactions to construct highly uniform 3D network structures. Hydrogels prepared via click chemistry typically exhibit exceptional hyperelasticity, shear-thinning behaviors, self-healing properties, and extremely low swelling ratios. Besides, the click chemical cross-linking process effectively avoids the generation of toxic by-products, significantly improving cell survival rates and ensuring long-term encapsulation stability.[49] Common reactions include copper-catalyzed azo-alkynyl cycloaddition, copper-free click reactions, strain-enhanced azo-alkynyl cycloaddition, and sulfyl-Michael addition.[50]

The combination of click chemical cross-linking and 3D printing technology represents a novel approach for fabricating hydrogels with precise structures and superior functional properties, thereby offering promising opportunities in biomedical applications. The structure and shape of 3D-printed hydrogels can be accurately designed according to specific requirements, while click chemical cross-linking ensures the formation of stable 3D network structures during the printing process, facilitating the fabrication of complex structures with sub-micron precision.

However, limited research has been reported on the preparation of 3D-printed hydrogels via the click chemical cross-linking strategy, limiting their broader adoption and advancement in the field. Huang *et al.*[51] developed a full-peptide 3D-printed hydrogel platform using a one-step thiol-ene click chemistry method, enabling the encapsulation of VEGF165-overexpressing cells under physiological temperatures (Figure 3). Through DLP technology, they fabricated hydrogel scaffolds with high resolution (up to 10 μm) and intricate structures such as branching vascular networks, providing a novel strategy for constructing advanced bioactive scaffolds.

2.3. Enzymatic cross-linking method

The enzymatic cross-linking method refers to an efficient cross-linking process under mild reaction conditions, leveraging the specific catalytic activity of enzymes to facilitate rapid and biocompatible material modification. This method effectively preserves the native structure and bioactivity of collagen and other biomolecules by circumventing damage caused by harsh conditions, such as high temperature, extreme pH (strong acid/alkali), and ultraviolet radiation, thereby maintaining their biological integrity to the greatest possible extent.[52] Moreover, enzymatic cross-linking eliminates the need for toxic chemical cross-linking agents, enhancing the biocompatibility of the final products, thus making it particularly well-suited for *in vivo* applications or the development of advanced biomedical materials. In addition, enzymatic reactions exhibit high substrate specificity, enabling the accurate identification and targeting of specific cross-linking sites, thereby achieving precise regulation of the cross-linking process. This precise regulation not only preserves the functional activity of biomaterials but also significantly reduces potential side effects, providing a strong guarantee for the preparation

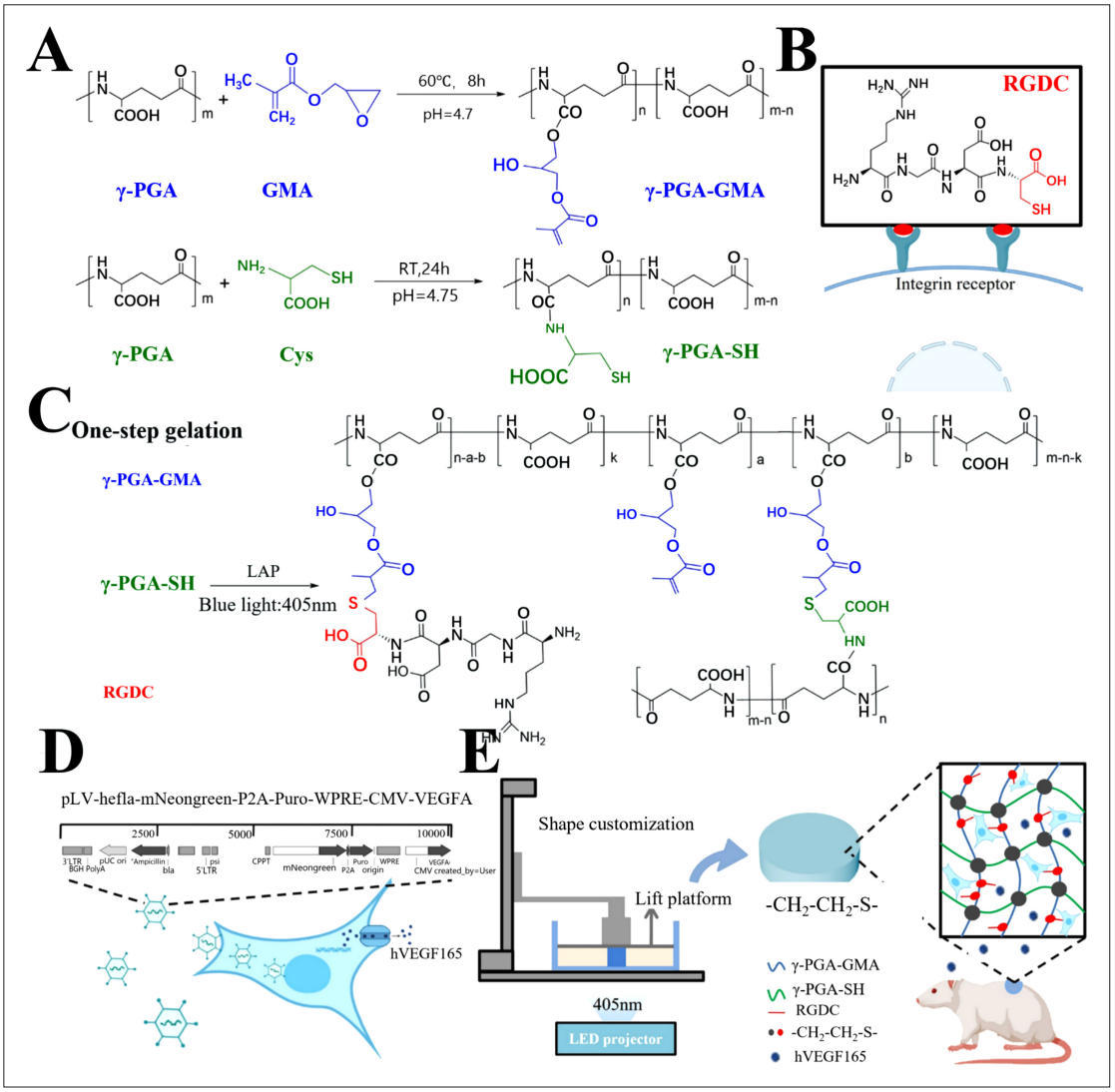

Figure 3. Design of cell-printable peptide hydrogel platform to produce self-renewable VEGF165 for diabetic wound healing. (A) Synthetic routes of γ-PGA-GMA and γ-PGA-SH. (B) Chemical structure of RGDC, which presents additional thiol groups compared to RGD. (C) One-step generation of all-peptide hydrogels using the thiol-ene click reaction of γ-PGA-GMA with γ-PGA-SH and RGDC. LAP is a type of photoinitiator that is stimulated by blue light. (D) Transfection of VEGF165 transcript-carried lentivirus in HUVECs for overexpressing VEGF165. (E) Printing the HUVEC$^{vegf165+}$-laden peptide hydrogels for diabetic wound healing using sustained-release VEGF165. Adapted from Huang *et al.*[51] Abbreviations: γ-PGA-GMA, glycidyl methacrylate-conjugated γ-polyglutamic acid; γ-PGA-SH, thiolated γ-polyglutamic acid; HUVEC, human umbilical vein endothelial cell; LAP, lithium phenyl-2,4,6-trimethylbenzoylphosphinate; RGDC, thiolated arginine-glycine-aspartate; RT, room temperature; VEGF, vascular endothelial growth factor.

of high-performance biomaterials. With the use of 3D printing technology, the 3D structure of hydrogels can be accurately designed, while the enzymatic cross-linking method enables rapid and mild stabilization of structures during the printing process, ensuring optimal mechanical properties and biocompatibility in the final hydrogel constructs.

Zhang *et al.*[53] prepared an injectable hydrogel system that contained type collagen tyramine (Col-TA) and HA tyramine (HA-TA) using horseradish peroxidase (HRP) and H_2O_2. HRP rapidly catalyzes the oxidation of phenolic hydroxyl groups in Col-TA and HA-TA to generate ROS intermediates within 10 s under physiological conditions, and promotes the formation of covalent diamine cross-links between tyramine molecules. Likewise, Mahran *et al.*[54] prepared a 3D-printed biocatalytic scaffold consisting of mesoporous SiO_2 hydrogels suitable for the immobilization of enzymes with different properties (Figure 4). Sakai *et al.*[55] prepared 3D-printed hydrogel wound dressings

using a precursor ink containing phenolated CS and CS nanofibers, which underwent HRP-mediated gelation. By adjusting the content of phenolated CS and CS nanofibers, the viscosity of the ink, the gelation time, and the mechanical performance of the 3D-printed hydrogels could be precisely controlled. While this process enabled the fabrication of hydrogels with enhanced mechanical robustness, its reliance on H_2O_2 as an oxidizing agent introduced oxidative by-products that may compromise biocompatibility and pose cytotoxicity risks.

Huang *et al.*[56] utilized transglutaminase, an enzyme with broad substrate specificity and high catalytic efficiency, to covalently cross-link gel with recombinant human type III collagen. This enzymatic approach facilitated the formation of ε-(γ-glutamyl)lysine isopeptide bonds between protein molecules under mild reaction conditions, thereby circumventing the cytotoxicity associated with chemical cross-linking agents. Meanwhile, this approach also preserved both the biocompatibility and 3D printability, offering an efficient strategy for fabricating whole-protein hydrogel scaffolds with excellent mechanical stability and cell-adhesive properties.

Jafari *et al.*[57] fabricated biocompatible Gel-chito-oligosaccharides (COS) hydrogels through a dual cross-linking strategy, including co-enzyme-mediated cross-linking via glucose oxidase (GOx)/HRP and a phenolated polyelectrolyte complex. The cross-linking was initiated through spontaneous electrostatic interaction between positively charged CS and COS and negatively charged phenolated alginate, followed by mild co-enzymatic cross-linking triggered by H_2O_2 gradually released from the GOx reaction. This hydrogel showed strong potential in treating diabetic foot and venous leg ulcers through its combined protective, healing, and antimicrobial properties. Zhou *et al.*[58] developed a 3D-printed GelMA hydrogel with adjustable flow properties, shear-thinning behavior, and dual-stage cross-linking. The hydrogel maintained cell viability while providing long-lasting structures for tissue engineering applications.

2.4. Optimization of 3D printing parameters

In addition to cross-linking methods, the optimization of 3D printing parameters is also crucial for the performance of hydrogels. In recent years, artificial intelligence (AI) technology has been introduced to efficiently optimize the printing process. Optimization of 3D bioprinting parameters, including temperature, extrusion pressure, and cross-linking kinetics, is essential for fabricating hydrogel scaffolds with high structural fidelity and uniform material properties.[59] Traditional parameter optimization in 3D bioprinting depends heavily on operators' experience and numerous time-consuming experiments, resulting in inefficient processes that are challenging to standardize.

Mohammad *et al.*[60] accurately predicted the rheological properties of 3D-printed polyacrylamide hydrogels using

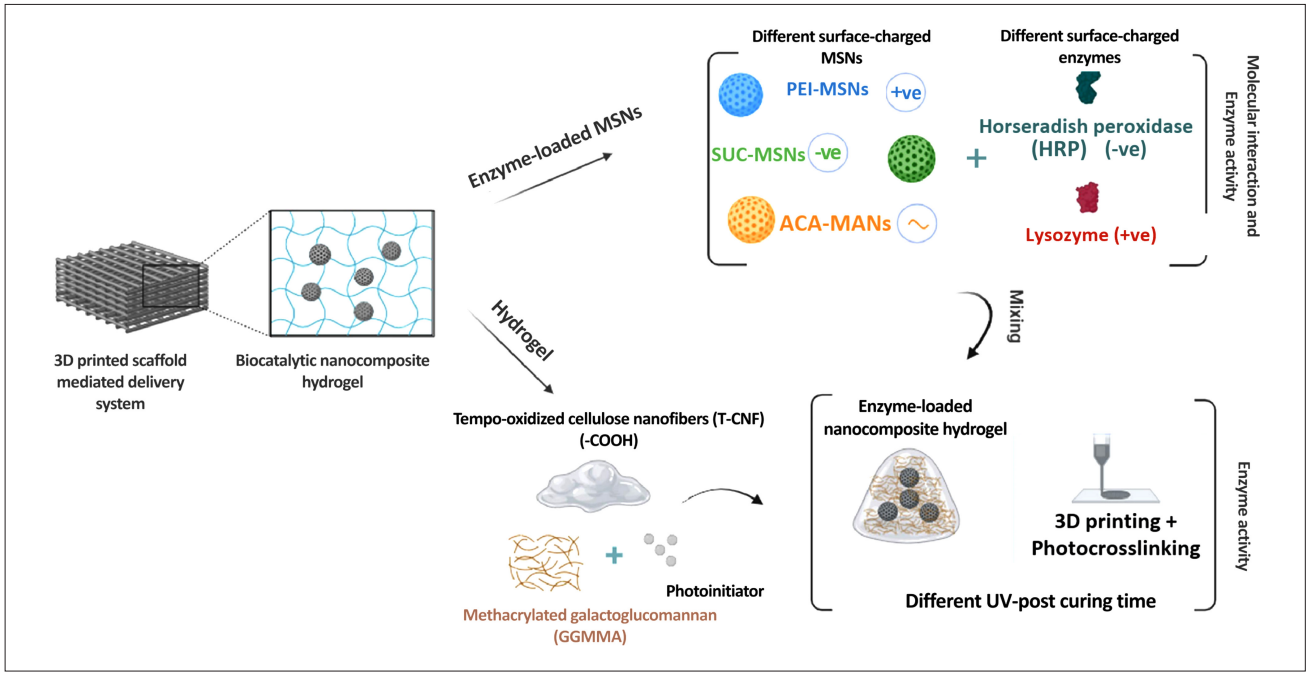

Figure 4. Schematic process of the biocatalytic mesoporous silica nanocomposite hydrogels. Adapted from Mahran *et al.*[54] Abbreviations: ACA, acetic anhydride; MSN, mesoporous silica nanoparticle; PEI, polyethylene imine; SUC, succinic anhydride.

Table 1. Comparative analysis of cross-linking methods for 3D-bioprinted hydrogels

Cross-linking method	Cross-linking agent/ condition	Printability and gelation kinetics	Advantages	Limitations	References
Physical cross-linking	Temperature	Moderate; requires precise environmental control; reversible gelation	Biocompatible, avoids chemical cross-linkers and potential cytotoxicity, allows for reversible sol–gel transitions	Poor mechanical strength, weak structural stability, rapid degradation, high sensitivity to environmental conditions	[24,27]
Chemical cross-linking	Photoinitiators, Schiff base reaction, click chemical reaction	High; rapid, irreversible curing; enables high-resolution printing and complex architectures	Excellent mechanical properties, high structural fidelity and stability, tunable degradation profiles	Risk of cytotoxicity from unreacted photoinitiators/ cross-linkers, potential for damaging biomolecules/ cells (UV light), irreversible process	[36,37,44,49]
Enzymatic cross-linking	Horseradish peroxidase, microbial transglutaminase	Low to moderate; slower gelation kinetics; requires careful optimization to prevent nozzle clogging	High bio-orthogonality and specificity, occurs under physiological conditions (e.g., mild pH and temperature), and excellent cytocompatibility	Enzyme activity can be sensitive to printing parameters (e.g., shear stress and temperature), high cost of enzymes, and potential for immunogenicity	[52]

deep learning models and inferred multiple feasible material composition and printing parameter combinations from the target modulus values through generative AI models. These AI methods have significantly reduced the cost of experimental trial-and-error, achieving a forward mapping from material formulation to performance prediction and a reverse design from performance requirements to formula generation.

Furthermore, the advancement in 3D printing and AI technologies has enhanced material precision and adaptability, suggesting that traditional diabetes treatment strategies may soon become insufficient to meet emerging therapeutic demands. Chen *et al.*[61] developed an AI-assisted high-throughput system combining a pneumatic extrusion 3D bioprinter with AI-based image analysis to rapidly optimize 3D printing parameters for tissue engineering applications. Based on the system, the printing conditions of the hydrogel architecture with uniform structures are screened in a high-throughput manner. Similarly, Kim *et al.*[62] developed a functional 3D printing ink composed of salmon sperm DNA and sponge-inspired DNA-induced biosilica for the machine learning-based 3D printing of wound dressings (Figure 5). These biomimetic 3D-printed hydrogels provided excellent functional platforms in diabetic wound healing, demonstrating the broad prospects of the combination of 3D printing and AI in the field of diabetic wound healing.

3. Mechanisms of 3D-printed hydrogel in diabetic wound healing

Diabetic wound healing is hindered by a pathological microenvironment characterized by persistent hyperglycemia, chronic inflammation, and cellular dysfunction. The inherent design flexibility of 3D printing technology enables hydrogels to combine multifunctional components with spatially controlled structures, thereby simultaneously addressing interrelated pathological barriers at the molecular, cellular, and tissue levels. 3D-printed hydrogels can overcome these obstacles through multi-level mechanism interventions:

(i) Dynamic microenvironment regulation achieved by modulating water and oxygen permeability, promoting ROS clearance, and preventing infection.

(ii) Targeted cell behavior regulation to restore fibroblast migration, macrophage polarization, and ECM remodeling.

(iii) Accelerated angiogenesis and tissue regeneration through continuous growth factor delivery and dynamic ECM remodeling.

3.1. Regulation of microenvironment

The microenvironment is important for the biological behavior of cells, affecting cellular adhesion, migration, differentiation, proliferation, and intercellular

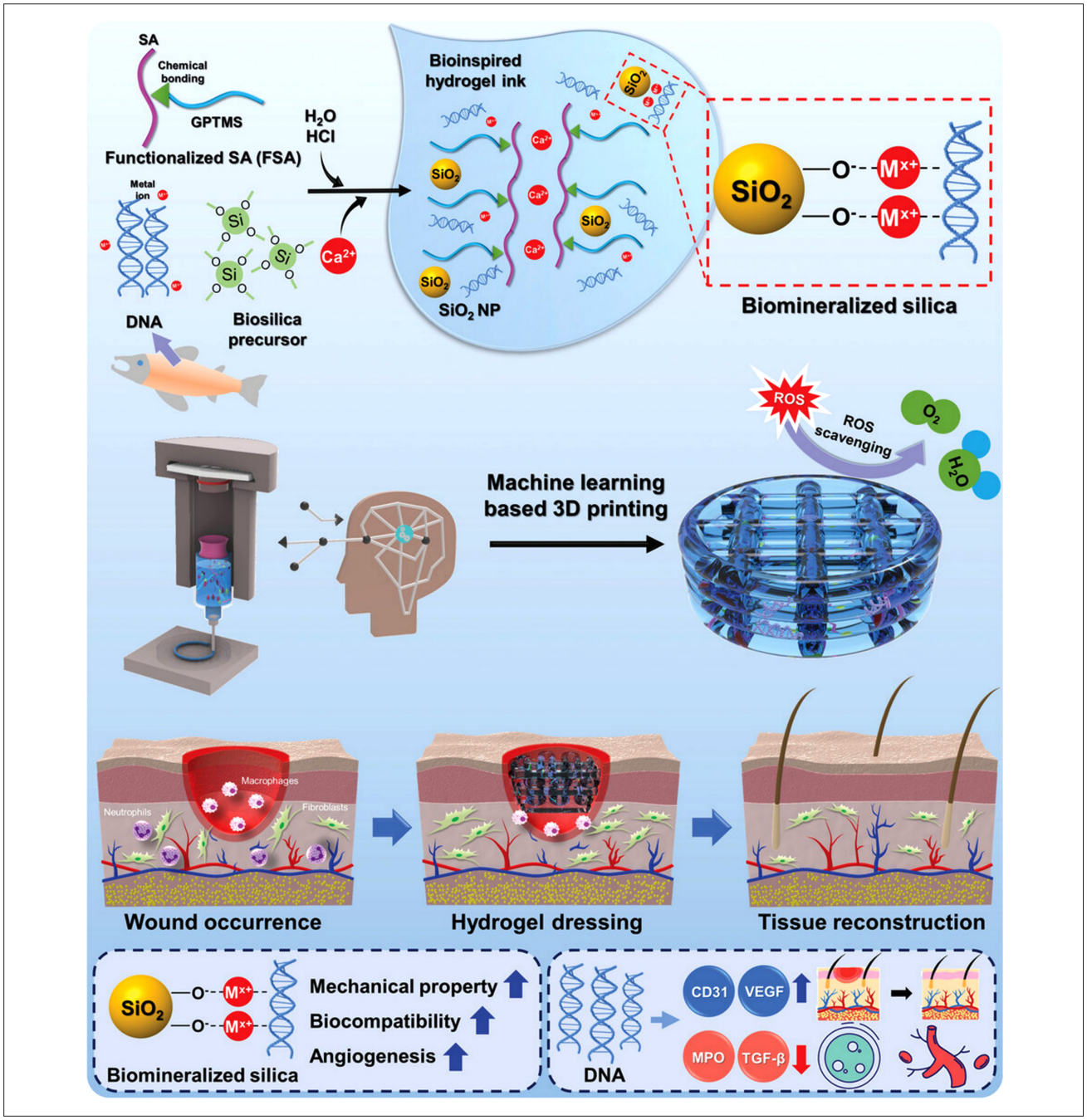

Figure 5. Schematic process of 3D-printed hydrogels by DNA-induced biomineralization. Adapted from Kim *et al.*[62] Abbreviations: CD31, cluster of differentiation 31; GPTMS, 3-Glycidoxypropyl trimethoxysilane; MPO, myeloperoxidase; NP, nanoparticle; ROS, reactive oxygen species; SA, sodium alginate; TGF-β, transforming growth factor-beta; VEGF, vascular endothelial growth factor.

communication between cells and the ECM or biomaterial surfaces. As a finely regulated "command center," the microenvironment guides cells to complete a series of life activities through a variety of signaling molecules, as well as physical and chemical factors. In addition, chemical composition, sizes, biomaterial microstructures, and cellular geometries also influence the microenvironment.[63] In diabetic wound healing, hydrogels regulate the water content of wounds, promote O_2 permeability, facilitate ROS clearance, and reduce oxidative stress responses, representing a new therapeutic strategy.

Hydrogels for diabetic wound healing must be able to absorb a large amount of wound exudates and maintain a moist microenvironment.[64] A moist wound microenvironment enhances cell survival rates, sustains growth factor release, and significantly accelerates wound healing by optimizing key healing processes, including re-epithelialization, angiogenesis, and ECM remodeling.[65] 3D printing technology, especially the extruding-based bioprinting strategy, has achieved multi-level precise control of the macroscopic structure and microscopic pores of hydrogel scaffolds by programming the rheological properties, printing parameters, and the model structure of hydrogel inks.[66] This control ability enables researchers to design and fabricate complex 3D porous architectures with customized pore size, porosity, connectivity, and spatial gradient distribution, thereby significantly optimizing the mechanical properties, swelling behaviors, and material transport characteristics of hydrogels.[67] More importantly, through multi-print head systems or functionalized inks, it is possible to achieve on-demand distribution and targeted release of bioactive molecules.[68] This synergistic regulation ability of physical structure and chemical microenvironment has greatly enhanced the comprehensive performance of hydrogel scaffolds in managing exudate at wound sites, maintaining appropriate moisture, promoting oxygen exchange, guiding directional cell migration and infiltration, and sequentially releasing bioactive factors. Thus, it creates a controlled, dynamic, and tissue regenerative microenvironment for the healing of diabetic wounds.

Kim *et al.*[62] developed a 3D-printed hydrogel by integrating marine-derived and marine-inspired materials, and found that this material rapidly absorbed wound exudates while maintaining mechanical stability during AI-assisted printing, protecting healing tissues from deformation and promoting vascularized regeneration. Likewise, Jin *et al.*[69] developed a lemon-derived GelMA/dialdehyde starch/exosome hydrogel dressing targeting the diabetic wound microenvironment and demonstrated that this hydrogel participated in immunomodulation and promoted the regeneration of vascular and fibrous tissues on macrophages. Li *et al.*[65] developed a 3D nanofiber/hydrogel core-shell scaffold that promoted diabetic wound healing by enhancing angiogenesis (Figure 6). Compared to 2D poly(*D*,*L*-lactic acid) nanofiber scaffolds, the 3D scaffold showed 1.6-times higher porosity, 21-times longer water retention, and 1.9-times greater water vapor permeability, significantly improving wound healing conditions. *In vivo* results showed that the 3D scaffold not only effectively managed wound exudates but also significantly promoted the formation of 3D capillary networks. Meanwhile, Huang *et al.*[70] loaded epinecidin-1–chitosan nanoparticles into electrospun poly(lactid acid-co-trimethylene carbonate) nanofibers and GelMa hydrogel to fabricate a thermoresponsive self-shrinking nanofiber/hydrogel composite dressing. The dressing regulated the microenvironment of diabetic wounds by enhancing collagen deposition, promoting angiogenesis, and reducing inflammation, thereby accelerating chronic wound healing.

The hyperglycemic microenvironment of diabetic wounds induces inhibitory angiogenesis and excessive ROS, leading to oxidative stress damage of biomolecules, such as lipids, nucleic acids, and proteins, and cells, such as endothelial cells, keratinocytes, and fibroblasts, thereby impeding wound healing.[71,72] Therefore, there is an urgent need to develop a novel strategy that provides continuous O_2 supply while controlling excessive ROS accumulation. At present, the primary strategy is to load bioactive compounds, such as antioxidants and enzymes, into hydrogels, thereby eliminating ROS and alleviating oxidative stress.

The combination of 3D printing technology and hydrogels provides customizable services for diabetic wound patients. Wei *et al.*[73] grafted gallic acid and methacrylic acid onto gelatin, respectively, endowing the hydrogel with ROS scavenging and ultraviolet polymerization properties. More importantly, the addition of gallic acid significantly improved the rheological properties of GelGA–GelMA bio-inks, ensuring the printability of customizable hydrogel scaffolds. Likewise, Fellin *et al.*[74] employed a high-precision 3D printing through DLP technology to construct complex bionic structures. Tannic acid (TA) treatment post-printing provided efficient ROS scavenging capacity through phenolic hydroxyl groups and significantly enhanced the mechanical properties of the hydrogel, offering a scaffold solution that combines antioxidant protection and customizable shapes for diabetic wound healing.

Studies have shown that excessive ROS accumulation disrupts macrophage polarization by transforming M1 into M2 macrophages while inducing oxidative stress, collectively leading to impaired phagocytosis and tissue necrosis. To address this issue, researchers have explored enzyme-based ROS scavenging strategies and nanoenzymatic catalysts, such as manganese dioxide,[75] Prussian blue,[76] manganese–cobalt oxide,[77] and black phosphorus,[78,79] as well as catalases that degrade H_2O_2 while simultaneously generating oxygen. Meanwhile, black phosphorus, MOFs, and DNA-based nanostructures can enhance the spatiotemporal control of 3D-printed hydrogels in therapeutic release and microenvironment regulation, improve their mechanical properties, ROS

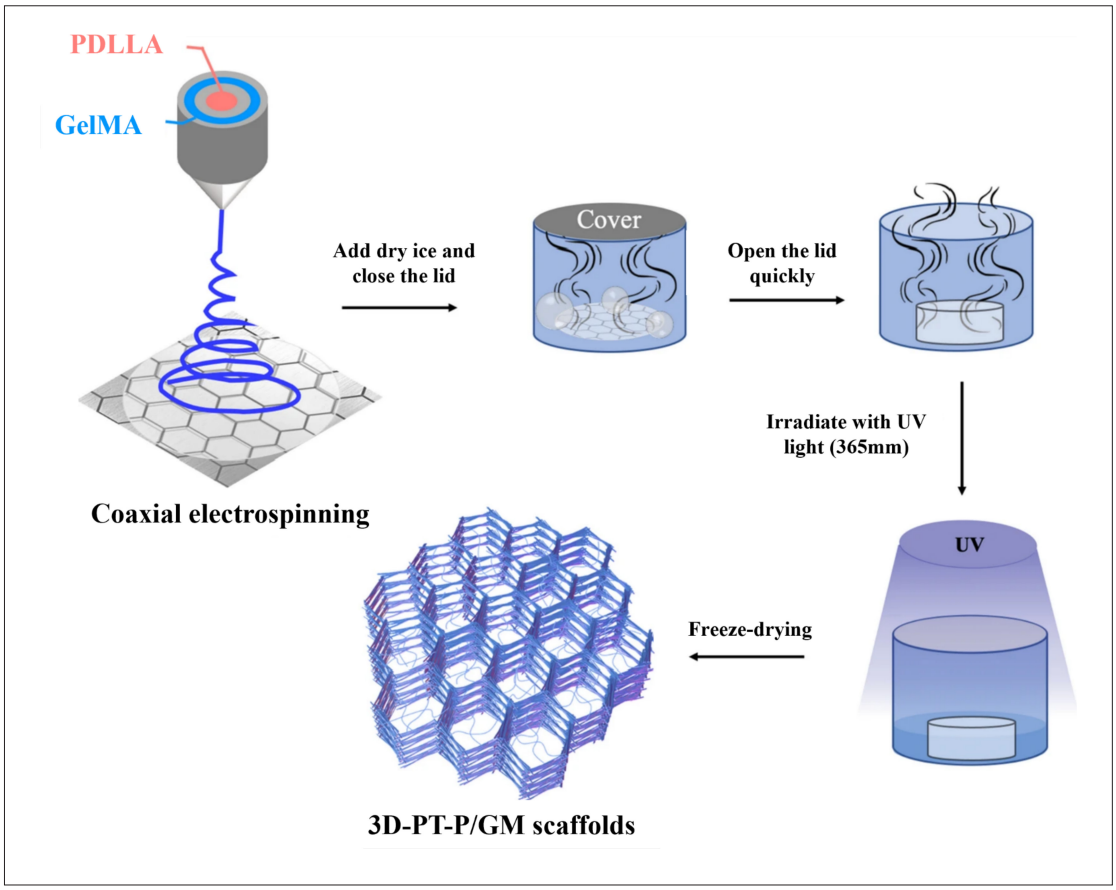

Figure 6. Fabrication illustration of a nanofiber/hydrogel core–shell scaffold with 3D multilayer patterned structure (3D-PT-P/GM) scaffolds. Adapted from Li *et al.*[65] Abbreviations: GelMA, gelatin methacrylate; PDLLA: poly(*D*,*L*-lactic acid).

scavenging capacity, and antibacterial activity, and further expand the functions of 3D-printed hydrogels.[80]

The healing of large-scale bone defects and incisions from gastrointestinal surgeries remains a clinical challenge. Chen *et al.*[81] innovatively developed a 3D-bioprinted, antioxidant M–Mn_3O_4@Gel by integrating M–Mn_3O_4 nanozyme into photo–cross-linked GelMA. The incorporation of M–Mn_3O_4 enhanced the mechanical properties of the nanocomposite hydrogels, with a compressive modulus 141.79% higher than that of pure GelMA. The hydrogels maintained excellent 3D printing adaptability and exhibited an efficient function of ROS clearance.

Similarly, gastrointestinal surgical incisions often face an acidic environment-induced ROS burst. Muñoz *et al.*[82] proposed a new idea for alleviating oxidative stress in diabetic wounds by blocking 95% of protease permeation through modified polyethylene imine with buffering capacity and a micelle-dense structure. The damage to skin barriers and poor vascularization in diabetic patients increases the risk of bacterial infection, while local hyperglycemia also creates a fertile environment for bacterial proliferation.[83,84] This interplay between hypoxia and infection transforms diabetic wounds into a complex inflammatory state that impedes the healing process.[85,86] Recent advances in hydrogel wound dressings have yielded improved mechanical barrier function, histocompatibility, and antimicrobial properties, making them a promising option for diabetic wound care. This microenvironment regulation strategy can avoid direct interference with host cell behaviors, especially in the high-risk environment of chronic wound infection. Liu *et al.*[87] designed a lichen-inspired, 3D-bioprinted bioderived hydrogel with a customizable structure to accelerate the healing of chronic diabetic wounds. These hydrogels exhibited superior performance both *in vitro* and *in vivo*, including enhanced dissolved oxygen production by microalgae and effective probiotic anti-infection activity. Similarly, Kumi *et al.*[34] proposed a 3D-printable APFE that combined electrical stimulation therapy targeting infected diabetic wound healing. APFE demonstrated excellent cell activity, with

antibacterial rates of 85.71% against methicillin-resistant *Staphylococcus aureus* and 93.65% against *Escherichia coli*.

Collectively, these innovative strategies orchestrate a multifaceted therapeutic outcome in diabetic wound healing, concurrently addressing oxidative stress via ROS scavenging, inhibiting inflammation, and promoting tissue healing through macrophage phenotype modulation.

3.2. Regulation of cellular behavior

Three-dimensional printing technology plays a significant role in regulating cell behavior. It can guide the directional migration, proliferation, and differentiation of cells by constructing scaffolds with bionic multi-level channels, customized mechanical properties, and heterogeneous structures.[88] The multi-nozzle system can precisely target immunomodulatory and growth factors to different regions of the scaffold, collaboratively regulating the polarization of macrophages to the M2 type to alleviate chronic inflammation, promote ECM secretion by fibroblasts, and stimulate neovascularization by vascular endothelial cells.[89] Not only that, 3D printing supports direct loading of mesenchymal stem cells and the construction of bionic co-culture systems, continuously releasing nutrient factors and further optimizing the microenvironment.[90]

Guo *et al.*[91] loaded the inherent bioactive components of egg white into hydrogels, thereby providing cell recognition sites, simulating the ECM environment, promoting cell adhesion, proliferation, and migration. At the same time, with the help of 3D printing technology, they constructed the porous structure of hydrogels, enhancing the ability of nutrient penetration and the regulation of cell spatial distribution. Ultimately, this scaffold significantly accelerated the recovery of cellular function and tissue regeneration in diabetic wounds. Similarly, Rybak *et al.*[92] embedded electrowoven short fibers loaded with gold nanorods and dexamethasone into GelMA/sodium alginate hydrogels and constructed photothermal responsive scaffolds through 3D printing. These scaffolds can locally heat up and trigger drug-controlled release under near-infrared irradiation, significantly enhancing the antibacterial and anti-inflammatory effects, and promoting the adhesion, extension, and proliferation of L929 fibroblasts.

The promoting effects of hydrogel on diabetic wound healing have multidimensional biological mechanisms. Its core advantages are reflected not only in the precise regulation of the wound microenvironment but also in the synergistic healing effects by targeting the key behaviors of cells.[87,93,94] In the healing process of normal skin injury, fibroblasts, as the core effector cells, rapidly respond to the injury signal and migrate to the wound site to construct a temporary repair hydrogel scaffold by synthesizing and secreting type I collagen and other ECM components. In this process, the balance between dynamic synthesis and the degradation of collagen is the key to drive orderly tissue healing: matrix metalloproteinases (MMPs) secreted by fibroblasts and tissue inhibitors cooperate to regulate collagen turnover, ensuring that newly generated tissues have sufficient mechanical strength and providing space for subsequent cell infiltration and angiogenesis.[95,96]

However, chronic hyperglycemia in diabetic patients directly damages the functions of fibroblasts by activating the polyol pathway and accumulating advanced glycation end products, characterized by a significant decrease in migration ability, VEGF secretion, and hypoxia-inducible factor 1α (HIF-1α) stability, leading to angiogenesis disorders. Moreover, reactive aldehydes produced by lipid peroxidation can covalently modify collagen molecules to form cross-linked structures, not only reducing the bioavailability of collagen but also disrupting ECM homeostasis by activating the overexpression of MMPs. This double hit further impairs the migration ability of keratinocytes and delays the re-epithelialization process.[97]

Liang *et al.*[98] used recombinant human collagen methacrylate and HA to construct a 3D network using ultraviolet light cross-linking and loaded with gold nanoparticles. The porous structure of the network mimicked the ECM, promoting fibroblast adhesion and migration, while collagen components directly induced collagen deposition. Together with its antibacterial properties, this hydrogel established a healing-conducive microenvironment and accelerated wound healing. Similarly, Huang *et al.*[99] constructed a bovine dermal type I collagen bionic scaffold loaded with overexpressed fibroblast growth factor (bFGF). This biomimetic scaffold activated the HIF-1 signaling pathway through continuous release of bFGF, promoting endothelial tube formation and fibroblast migration, and accelerating diabetic wound healing by enhancing protein kinase B phosphorylation and collagen deposition. The scaffolds were similar to hydrogels in terms of their porous structure, biocompatibility, and controllable release characteristics.

Gastrointestinal surgical incisions are often affected by an acidic environment, which delays the formation of blood clots and granulation tissues. Therefore, fibroblast growth factor can be added to hydrogels to address this issue.[100] Wang *et al.*[101] used the chemical ligation method of Spy to efficiently integrate interferon-alpha (IFN-α) into hydrogels, preserving its biological activity. This design enhanced fibroblast migration and upregulated the

expression of ECM proteins, such as type I collagen alpha chain and α-smooth muscle actin.

Macrophages are tissue-resident immune cells with dual roles: M1 subtype addresses infections via ROS and pro-inflammatory cytokines, while M2 subtype promotes tissue healing through anti-inflammatory factors and ECM remodeling, making them key targets for treating chronic inflammation and cancers.[102] In diabetic wounds, the abnormal polarization of macrophages has become an important barrier to wound healing. This issue arises from the chronic inflammatory environment induced by hyperglycemia and obesity, perpetuating the activation of M1 macrophages and hindering tissue regeneration.[103] Reduced expressions of macrophage-secreted growth factors (e.g., transforming growth factor-β1 and platelet-derived growth factor-BB) and pro-inflammatory cytokines (e.g., interleukin-6 and tumor necrosis factor-α) create an optimal healing environment: keratinocytes differentiate properly, fibroblasts deposit balanced collagen, and new blood vessels form without leakage, resulting in faster wound closure with minimal scarring.

Macrophages are highly heterogeneous and exhibit a variety of functions and phenotypes.[104–107] Diabetic wounds are characterized by a prolonged inflammatory phase and difficulty in healing due to the accumulation of M1 macrophages in the wound. Therefore, dressings with macrophage heterogeneity regulation ability have great potential in treating diabetic wound healing. However, the conversion of M1 into M2 macrophages through simple and biosafe methods remains a significant challenge. Chen *et al.*[108] developed an ROS/glucose-responsive hydrogel coupled to a chemokine aptamer encapsulating mannose-modified lipid nanoparticles (mLNPs) loaded with ADAM17 small interfering RNA (siRNA). This hydrogel enhanced macrophage recruitment by enriching endogenous chemokines. In addition, it was responsive to the pathological microenvironment with dynamic release of mLNPs to deliver targeted siRNAs to macrophages. ADAM17 siR@mLNPs treatment significantly enhanced hyperphagia through the tyrosine kinase Mer–Ras-related C3 botulinum toxin substrate 1 pathway and glycolytic reprogramming, thereby initiating the resolution of inflammation and tissue healing. Likewise, Fu *et al.*[109] developed a natural hydrogel capable of modulating macrophage heterogeneity to promote angiogenesis and diabetic wound healing. This hydrogel exhibited excellent bio-adhesion, antibacterial performance, and ROS scavenging ability. Notably, the hydrogel could transform M1 macrophages into M2 macrophages without any additional components.

Hypoxic bone marrow mesenchymal stem cell-derived exosomes are important in regulating cellular functions through their microRNAs. Shi *et al.*[110] developed a multifunctional hydrogel based on gallic acid-coupled CS and partially oxidized HA. The hydrogels significantly promoted diabetic wound healing by modulating macrophage polarization to the M2 phase. It can be ascribed to the fact that the extracellular vesicle miR-4645-5p and the antioxidant properties of the hydrogel work together to inhibit the activity of sterol regulatory element-binding protein 2 in macrophages. Shu *et al.*[111] designed a GelMA hydrogel for sustained release at the wound site and evaluated its potential for promoting wound healing in diabetic patients. Mechanistic studies showed that the wound liner regulated macrophage heterogeneity through the adenosine A2b receptor/signal transducer and activator of transcription/peroxisome proliferator-activated receptor gamma signaling pathway and promoted endothelial cell function, thereby accelerating wound healing in diabetic patients. Similarly, Wang *et al.*[112] developed a silk fibroin/gelatin (SG) hydrogel for chronic diabetic wounds and incorporated mitochondrial division inhibitor-1 (SG/M). Compared with the pure SG hydrogel, the SG/M hydrogel significantly accelerated wound healing in diabetic patients. The therapeutic effect of mitochondrial division inhibitor-1 was attributed to its ability to enhance macrophage polarization toward the M2 phenotype and to alleviate high glucose-induced mitochondrial dysfunction in both macrophages and human umbilical vein endothelial cells (HUVECs). Su *et al.*[113] prepared an asymmetric bilayer hydrogel through ultraviolet polymerization of chemically modified CS (TA@CS) combined with a deamidated and pyrogallol-derivatized form of marine collagen. The resulting asymmetric hydrogel exhibited unique directional adhesion properties, which are critical for healing diabetic and gastrointestinal wounds. This feature simplifies surgical application by reducing handling complexity and minimizing associated risk.[114]

3.3. Promotion of angiogenesis and tissue regeneration

In diabetic wound healing, angiogenesis and tissue regeneration are the key biological links that determine the healing effects. They complement each other and jointly affect the quality and speed of wound healing. Studies have shown that the expression of VEGF in diabetic wounds is significantly lower than that in normal wounds. This reduction impairs the migration ability of endothelial cells and the formation of tubular structures, thereby blocking angiogenesis. As a result, blood supply to the wound becomes insufficient, limiting the delivery of nutrients and oxygen while hindering the discharge of metabolic waste, thereby delaying the healing process.[115,116]

Three-dimensional printing technology primarily builds hydrogel scaffolds with bionic multi-level channels and fully interconnected micro-networks. This is achieved by manipulating the spatial structure of biomaterials to simulate the structural and functional characteristics of the natural vascular system from both physical topology and cellular microenvironment levels, thereby promoting angiogenesis and tissue regeneration. Luo *et al.*[117] utilized 3D printing technology to construct a hydrogel scaffold with a fully interconnected microchannel network that mimics the structure of natural blood vessels, guiding the directional arrangement of endothelial cells and angiogenesis. This approach enabled the integrated and precise manufacturing of macropores and microchannels, enhancing nutrient transport and cell survival capabilities. The hydrogel scaffold promoted blood vessel growth toward the central region both *in vivo* and *in vitro*, addressing the challenge of insufficient vascularization in traditional tissue engineering. The 3D-printed hydrogel prepared by Mujawar *et al.*[118] represented an ideal physical scaffold for cell migration and vascular growth through its precisely fabricated interconnected porous structure. The incorporation of aloe vera extract enabled sustained release of bioactive factors, which promoted angiogenesis, effectively reduced inflammation and oxidative stress, and synergistically optimized the wound microenvironment. Ultimately, it efficiently enhanced vascularization and facilitated high-quality tissue healing by accelerating granulation tissue formation, collagen deposition, and epithelial regeneration while reducing scar formation.

Hydrogels can provide physical topological guidance and support for endothelial cell migration and tubular structure formation by simulating the 3D porous structure and mechanical properties of ECM. Their high-water content characteristic can maintain the moisture of the wound surface and provide a favorable pathway for cell metabolism and communication.[119] Han *et al.*[120] constructed an injectable self-healing HA hydrogel via a Schiff base cross-linking method and incorporated GOx–MnO_2 nanoenzymes, synthesized through condensation reactions, and VEGF nanobubbles produced prepared through double emulsification. This design established a novel US@GOx@VEGF (UGV) hydrogel system for diagnosis and treatment. The results showed that VEGF could be precisely released through *ex vivo* ultrasound to enhance the vascularization and accelerate diabetic wound healing. Huang *et al.*[121] prepared VEGF plasmid-loaded macrophage exosomes and encapsulated them in injectable self-healing hydrogels prepared through dynamic Schiff base cross-linking. This system enhanced VEGF binding to VEGF receptor 2 through VEGF production and release from exosomes, secretion by M2 macrophages, and the high affinity of the 2-N,6-O-sulfated chitosan (SCS) hydrogel, creating an intrinsic immunomodulatory environment that effectively promoted angiogenesis. Kim *et al.*[122] prepared an anisotropic nanofiber hydrogel using fibrin electrospinning and self-assembling peptide modification. By leveraging the triangular synergy of the immuno-angiogenic neurogenesis microenvironment, this hydrogel exhibited an ideal directional arrangement of nanoscale fibers and significant pro-angiogenic bioactivity, thereby improving diabetic wound healing.

The abnormal expression of MMPs in diabetic wounds is also an important factor affecting wound healing. Overexpression of MMPs disrupts the dynamic balance of the ECM, leading to excessive degradation of key ECM components, such as collagen and fibronectin. This degradation compromises tissue integrity and impairs the formation of stable granulation tissue, further delaying the wound healing process.[123] Specifically, overexpression of MMP-9 is involved in this process. Therefore, wound dressings that validly inhibit the expression of MMP-9 have significant translational potential in clinical practice. Lan *et al.*[124] developed a composite hydrogel dressing for the locally sustained delivery of MMP-9 siRNA (siMMP9). After forming a complex with glycogen–triethylenetetramine, siMMP-9 was loaded into a thermosensitive hydrogel based on Pluronic F-127 and hydroxypropyl methylcellulose. The hydrogel released the encapsulated GT/siMMP9 into wound tissues through heat-sensitive controlled release over seven days, inhibiting MMP-9 expression and significantly accelerating diabetic wound healing. Similarly, Lei and Fan[125] prepared TA-siRNA nanogels for the first time, based on the self-assembled interaction between TA and siRNA. This highly efficient and biodegradable nanogel was incorporated into polyvinyl alcohol–human-like collagen–TA–borax hydrogels. Electrical stimulation improved the *in vivo* release of the hydrogels and the endocytosis of the nanogels. Combination therapy using electrical stimulation and TA-siRNA hydrogels accelerated diabetic wound healing by lowering ROS and MMP-9 levels, as well as promoting macrophage polarization, collagen production, and angiogenesis. Meanwhile, Wu *et al.*[126] developed a supramolecular peptide hydrogel doped with nanoparticles for the local delivery of siMMP9. siMMP9 was encapsulated within nanoparticles fabricated from amphiphilic cationic lipid-like compounds, subsequently embedded within a supramolecular peptide hydrogel formed through the self-assembly of amphiphilic peptides. The hydrogels significantly prolonged the retention time of siMMP9-loaded nanoparticles in wound tissues and their porous networks gradually released

these nanoparticles to enhance siMMP9 uptake by keratinocytes, thereby achieving efficient MMP9 silencing and markedly accelerating diabetic wound healing. Zheng *et al.*[127] highlighted the critical role of m6A methylation in regulating MMP-9 expression during diabetic wound healing. They combined enhanced mRNA m6A modification with a ROS scavenging strategy by loading an FTO inhibitor into a nanocolloidal hydrogel, which showed excellent wound-healing effects in a diabetic model.

Diabetic wounds represent a complex pathological condition driven by the interplay of multiple systemic and local factors, where any single factor may exacerbate the healing process. Consequently, multifunctional hydrogels that simultaneously address infection, inflammation, and impaired angiogenesis are crucial for clinical efficacy.[128] For example, Huang *et al.*[51] developed a click chemistry-based all-peptide hydrogel platform, as discussed in the click chemical cross-linking section. Constructed through a one-step photo-curing reaction, this hydrogel featured high-precision 3D printing capabilities and was loaded with HUVECs overexpressing VEGF165, enabling the self-continuous release of growth factors. The hydrogel not only promoted cell adhesion and migration through the RGDS sequence but also significantly enhanced angiogenesis through continuous VEGF165 secretion. Meanwhile, it protected endothelial cells from high glucose-induced damage by inhibiting Bax-mediated mitochondrial membrane perforation, thereby reducing oxidative stress and inflammation levels. Moreover, this material demonstrated excellent biocompatibility and degradability both *in vivo* and *in vitro*, and can be customized to different wound morphologies through DLP printing technology.

4. Conclusion

Diabetic wound healing remains a major challenge in clinical medicine, as its complex pathological microenvironment imposes multidimensional functional requirements on treatment strategies. With precise structural control enabled by CAD and additive manufacturing, combined with strong biocompatibility and dynamic microenvironment regulation, 3D-printed hydrogels have demonstrated significant advantages for diabetic wound healing. However, current studies often rely on single functional modules, exhibit imperfect dynamic response mechanisms, and face major barriers to clinical translation. The long-term biocompatibility and potential immunogenicity of synthetic polymers and cross-linking agents remain insufficiently explored. In addition, sterilization methods, such as those using gamma radiation and ethylene oxide, may alter hydrogel structure and biological activity, while the high cost of bio-inks and specialized 3D printers limits widespread adoption. Future research should focus on multifunctional and synergistic intelligent 3D-printed hydrogel systems that integrate treatment strategies across three stages: infection control, inflammation regulation, and tissue remodeling. Incorporating living cells, extracellular vesicles, or gene editing technologies into hydrogel design could enable targeted cell differentiation and on-demand synthesis of ECM components, creating a "material–cell–gene" trinity treatment system. Meanwhile, AI-assisted material platforms could accelerate hydrogel optimization by analyzing high-throughput experimental data with machine learning algorithms, guiding the formulation of bio-inks and printing parameters to speed up the development of personalized hydrogel dressings. It is also worth noting that while gastrointestinal surgical incisions and diabetic wounds share pathological characteristics, their microenvironments differ and require tailored design. For example, multifunctional 3D-printed hydrogels could adopt modular strategies, such as coating gastrointestinal wound scaffolds with acid-resistant layers, to establish cross-indication treatment strategies.

Acknowledgments

None.

Funding

This work was supported by the Research Fund for Academician Lin He New Medicine.

Conflict of interest

The authors declare they have no competing interests.

Author contributions

Conceptualization: Tiantang Fan, Peixin Wang
Funding: Tiantang Fan
Supervision: Tiantang Fan, Peixin Wang
Writing–original draft: Mengdi Yin, Yutong Wang, Yuhang Wei, Changjia Li, Yiqiao Yin
Writing–review & editing: Tiantang Fan, Peixin Wang

Ethics approval and consent to participate

Not applicable.

Consent for publication

Not applicable.

Availability of data

Not applicable.

References

1. Chung WK, Erion K, Florez JC, *et al.* Precision medicine in diabetes: A consensus report from the American Diabetes Association (ADA) and the European Association for the Study of Diabetes (EASD). *Diabetes Care.* 2020;43(7):1617-1635. doi: 10.2337/dci20-0022
2. Zhang J, Lin C, Jin S, *et al.* The pharmacology and therapeutic role of cannabidiol in diabetes. *Exploration.* 2023;3(5):20230047. doi: 10.1002/EXP.20230047
3. Ogurtsova K, Guariguata L, Barengo NC, *et al.* IDF diabetes atlas: Global estimates of undiagnosed diabetes in adults for 2021. *Diabetes Res Clin Pract.* 2022;183:109118. doi: 10.1016/j.diabres.2021.109118
4. Saeedi P, Petersohn I, Salpea P, *et al.* Global and regional diabetes prevalence estimates for 2019 and projections for 2030 and 2045: Results from the International Diabetes Federation Diabetes Atlas, 9th edition. *Diabetes Res Clin Pract.* 2019;157:107843. doi: 10.1016/j.diabres.2019.107843
5. Cho NH, Shaw JE, Karuranga S, *et al.* IDF diabetes atlas: Global estimates of diabetes prevalence for 2017 and projections for 2045. *Diabetes Res Clin Pract.* 2018;138:271-281. doi: 10.1016/j.diabres.2018.02.023
6. Verma AK, Goyal Y, Bhatt D, *et al.* A compendium of perspectives on diabetes: A challenge for sustainable health in the modern era. *Diabetes Metab Syndr Obes.* 2021;14:2775-2787. doi: 10.2147/DMSO.S304751
7. Sharma S, Kishen A. Dysfunctional crosstalk between macrophages and fibroblasts under LPS-infected and hyperglycemic environment in diabetic wounds. *Sci Rep.* 2025;15(1). doi: 10.1038/s41598-025-00673-4
8. Kartika RW, Alwi I, Suyatna FD, *et al.* The role of VEGF, PDGF and IL-6 on diabetic foot ulcer after platelet rich fibrin + hyaluronic therapy. *Heliyon.* 2021;7(9):e07934. doi: 10.1016/j.heliyon.2021.e07934
9. Sharifiaghdam M, Shaabani E, Faridi-Majidi R, *et al.* Macrophages as a therapeutic target to promote diabetic wound healing. *Mol Ther.* 2022;30(9):2891-2908. doi: 10.1016/j.ymthe.2022.07.016
10. Kamal R, Awasthi A, Pundir M, *et al.* Healing the diabetic wound: Unlocking the secrets of genes and pathways. *Eur J Pharmacol.* 2024;975:176645. doi: 10.1016/j.ejphar.2024.176645
11. Prema D, Balashanmugam P, Kumar JS, *et al.* Fabrication of GO/ZnO nanocomposite incorporated patch for enhanced wound healing in streptozotocin (STZ) induced diabetic rats. *Colloid Surface A.* 2022;649:129331. doi: 10.1016/j.colsurfa.2022.129331
12. Talebi M, Ghale RA, Asl RM, *et al.* Advancements in characterization and preclinical applications of hyaluronic acid-based biomaterials for wound healing: A review. *Carbohydr Polym Tech.* 2025;9:100706. doi: 10.1016/j.carpta.2025.100706
13. Yong SK, Meera G. Macrophages in wound healing: Activation and plasticity. *Immunol Cell Biol.* 2019;97(3):258-267. doi: 10.1111/imcb.12236
14. Wang X, Ding J, Chen X, *et al.* Light-activated nanoclusters with tunable ROS for wound infection treatment. *Bioact Mater.* 2024;41:385-399. doi: 10.1016/j.bioactmat.2024.07.009
15. Nguyen HM, Le TTN, Nguyen AT, *et al.* Biomedical materials for wound dressing: Recent advances and applications. *RSC Adv.* 2023;13(8):5509-5528. doi: 10.1039/d2ra07673j
16. Kim JH, Ruegger PR, Lebig EG, *et al.* High levels of oxidative stress create a microenvironment that significantly decreases the diversity of the microbiota in diabetic chronic wounds and promotes biofilm formation. *Front Cell Infect Microbiol.* 2020;10:259. doi: 10.3389/fcimb.2020.00259
17. Li M, Xia W, Khoong YM, *et al.* Smart and versatile biomaterials for cutaneous wound healing. *Biomater Res.* 2023;27(1):87. doi: 10.1186/s40824-023-00426-2
18. Shi S, Wang L, Song C, *et al.* Recent progresses of collagen dressings for chronic skin wound healing. *Collagen Leather.* 2023;5(1):31. doi: 10.1186/s42825-023-00136-4
19. Zhou C, Sheng C, Gao L, *et al.* Engineering poly(ionic liquid) semi-IPN hydrogels with fast antibacterial and anti-inflammatory properties for wound healing. *Chem Eng J.* 2021;413:127429. doi: 10.1016/j.cej.2020.127429
20. Zhao X, Xue W, Ding W, *et al.* A novel injectable sodium alginate/chitosan/sulfated bacterial cellulose hydrogel as biohybrid artificial pancreas for real-time glycaemic regulation. *Carbohydr Polym.* 2025;354:123323. doi: 10.1016/j.carbpol.2025.123323
21. Chen J, He J, Yang Y, *et al.* Antibacterial adhesive self-healing hydrogels to promote diabetic wound healing. *Acta Biomater.* 2022;146:119-130. doi: 10.1016/j.actbio.2022.04.041
22. Miao L, Lu X, Wei Y, *et al.* Near-infrared light-responsive nanocomposite hydrogels loaded with epidermal growth factor for diabetic wound healing. *Mater Today Bio.* 2025;31:101578. doi: 10.1016/j.mtbio.2025.101578
23. Zhang L, Nasar NKA, Huang X, *et al.* Light-assisted 3D-printed hydrogels for antibacterial applications. *Small Sci.* 2024;4(8):2400097. doi: 10.1002/smsc.202400097

24. Li J, Wang Y, Fan L, *et al.* Liquid metal hybrid antibacterial hydrogel scaffolds from 3D printing for wound healing. *Chem Eng J.* 2024;496:153805. doi: 10.1016/j.cej.2024.153805

25. Ma R, Xu L, Li Z, *et al.* NIR-responsive tissue-adaptive hydrogel for accelerating healing of seawater-immersed wounds. *Mater Today Bio.* 2025;32:101915. doi: 10.1016/j.mtbio.2025.101915

26. Ribeiro MM, Simões M, Vitorino C, *et al.* Physical crosslinking of hydrogels: The potential of dynamic and reversible bonds in burn care. *Coord Chem Rev.* 2025;542:216868. doi: 10.1016/j.ccr.2025.216868

27. Yang J, Chen Y, Zhao L, *et al.* Constructions and properties of physically cross-linked hydrogels based on natural polymers. *Polym Rev.* 2022;63(3):574-612. doi: 10.1080/15583724.2022.2137525

28. Drzewiecki KE, Parmar AS, Gaudet ID, *et al.* Methacrylation induces rapid, temperature-dependent, reversible self-assembly of type-I collagen. *Langmuir.* 2014;30:11204-11211. doi: 10.1021/la502418s

29. Rombouts HW, Kort DWD, Pham TTH, *et al.* Reversible temperature-switching of hydrogel stiffness of coassembled, silk-collagen-like hydrogels. *Biomacromolecules.* 2015;16(8):2506-2513. doi: 10.1021/acs.biomac.5b00766

30. Sun-Hee C, Ahreum K, Woojung S, *et al.* Photothermo-modulated drug delivery and magnetic relaxation based on collagen/poly(γ-glutamic acid) hydrogel. *Int J Nanomedicine.* 2017;12:2607-2620. doi: 10.2147/ijn.s133078

31. Naik K, Singh P, Yadav M, *et al.* 3D printable, injectable amyloid-based composite hydrogel of bovine serum albumin and aloe vera for rapid diabetic wound healing. *J Mater Chem B.* 2023;11(34):8142-8158. doi: 10.1039/D3TB01151H

32. Zhang X, Gan J, Fan L, *et al.* Bioinspired adaptable indwelling microneedles for treatment of diabetic ulcers. *Adv Mater.* 2023;35(23):2210903. doi: 10.1002/adma.202210903

33. Xia S, Weng T, Jin R, *et al.* Curcumin-incorporated 3D bioprinting gelatin methacryloyl hydrogel reduces reactive oxygen species-induced adipose-derived stem cell apoptosis and improves implanting survival in diabetic wounds. *Burns Trauma.* 2022;10:tkac001. doi: 10.1093/burnst/tkac001

34. Kumi M, Hou Z, Zhang Y, *et al.* 3D printed chitosan-based flexible electrode with antimicrobial properties for electrical stimulation therapy in wound healing. *Supramol Mater.* 2025;4:100110. doi: 10.1016/j.supmat.2025.100110

35. Metwally WM, El-Habashy SE, El-Hosseiny LS, *et al.* Bioinspired 3D-printed scaffold embedding DDAB-nano ZnO/nanofibrous microspheres for regenerative diabetic wound healing. *Biofabrication.* 2023;16(1):015001. doi: 10.1088/1758-5090/acfd60

36. Xue X, Hu Y, Wang S, *et al.* Fabrication of physical and chemical crosslinked hydrogels for bone tissue engineering. *Bioact Mater.* 2022;12:327-339. doi: 10.1016/j.bioactmat.2021.10.029

37. Zhang Q, Yan K, Zheng X, *et al.* Research progress of photo-crosslink hydrogels in ophthalmology: A comprehensive review focus on the applications. *Mater Today Bio.* 2024;26:101082. doi: 10.1016/j.mtbio.2024.101082

38. Chen Z, Song S, Zeng H, *et al.* 3D printing MOF nanozyme hydrogel with dual enzymatic activities and visualized glucose monitoring for diabetic wound healing. *Chem Eng J.* 2023;471:144649. doi: 10.1016/j.cej.2023.144649

39. Cao W, Peng S, Yao Y, *et al.* A nanofibrous membrane loaded with doxycycline and printed with conductive hydrogel strips promotes diabetic wound healing in vivo. *Acta Biomater.* 2022;152:60-73. doi: 10.1016/j.actbio.2022.08.048

40. Li S, Xu Y, Zheng L, *et al.* High self-supporting chitosan-based hydrogel ink for in situ 3D printed diabetic wound dressing. *Adv Funct Mater.* 2024;35(5):2414625. doi: 10.1002/adfm.202414625

41. Ding N, Fu X, Gui Q, *et al.* Biomimetic structure hydrogel loaded with long-term storage platelet-rich plasma in diabetic wound repair. *Adv Healthc Mater.* 2023;13(10):2303192. doi: 10.1002/adhm.202303192

42. Hu Y, Xiong Y, Zhu Y, *et al.* Copper-epigallocatechin gallate enhances therapeutic effects of 3D-printed dermal scaffolds in mitigating diabetic wound scarring. *ACS Appl Mater Interfaces.* 2023;15(32):38230-38246. doi: 10.1021/acsami.3c04733

43. Wan T, Fan P, Zhang M, *et al.* Multiple crosslinking hyaluronic acid hydrogels with improved strength and 3D printability. *ACS Appl Bio Mater.* 2021; 5(1):334-343. doi: 10.1021/acsabm.1c01141

44. Nezhad-Mokhtari P, Ghorbani M, Roshangar L, Rad JS. A review on the construction of hydrogel scaffolds by various chemically techniques for tissue engineering. *Eur Polym J.* 2019;117:64-76. doi: 10.1016/j.eurpolymj.2019.05.004

45. Fu C, Liu G, Fan Y, *et al.* Highly printable and multifunctional cell-laden collagen-based bioinks for precise DLP bioprinting and rapid diabetic wound regeneration. *Mater Today Bio.* 2025;32:101908. doi: 10.1016/j.mtbio.2025.101908

46. Yang H, Wang Y, Li R, *et al.* A 3D-printed grid-like hyaluronic acid-based hydrogel loaded with deferoxamine

as wound dressing promotes diabetic wound healing. *Int J Biol Macromol.* 2025;303:140598.
doi: 10.1016/j.ijbiomac.2025.140598

47. Lin Z, Xie W, Cui Z, Huang J, Cao H, Li Y. 3D printed alginate/gelatin-based porous hydrogel scaffolds to improve diabetic wound healing. *Giant.* 2023;16:100185.
doi: 10.1016/j.giant.2023.100185

48. Ding X, Yu Y, Li W, Zhao Y. In situ 3D-bioprinting MoS2 accelerated gelling hydrogel scaffold for promoting chronic diabetic wound healing. *Matter.* 2023;6(3):1000-1014.
doi: 10.1016/j.matt.2023.01.001

49. Finetti C, Sola L, Elliott J, Chiari M. Synthesis of hydrogel via click chemistry for DNA electrophoresis. *J Chromatogr A.* 2017;1513:226-234.
doi: 10.1016/j.chroma.2017.07.042

50. Li Y, Wang X, Han Y, Sun HY, Hilborn J, Shi L. Click chemistry-based biopolymeric hydrogels for regenerative medicine. *Biomed Mater.* 2021;16(2):022003.
doi: 10.1088/1748-605X/abc0b3

51. Huang J, Yang R, Jiao J, *et al.* A click chemistry-mediated all-peptide cell printing hydrogel platform for diabetic wound healing. *Nat Commun.* 2023;14(1):7856.
doi: 10.1038/s41467-023-43364-2

52. Moreira TLS, Feijen J, van Be CA, Dijkstra PJ, Karperien M. Enzyme-catalyzed crosslinkable hydrogels: emerging strategies for tissue engineering. *Biomaterials.* 2012;33(5):1281-1290.
doi: 10.1016/j.biomaterials.2011.10.067

53. Zhang Y, Cao Y, Zhao H, *et al.* An injectable BMSC-laden enzyme-catalyzed crosslinking collagen-hyaluronic acid hydrogel for cartilage repair and regeneration. *J Mater Chem B.* 2020;8(19):4237-4244.
doi: 10.1039/d0tb00291g

54. Mahran A, Howaili F, Bhadane R, *et al.* Functional enzyme delivery via surface-modified mesoporous silica nanoparticles in 3D printed nanocomposite hydrogels. *Eur J Pharm Sci.* 2025;211:107132.
doi: 10.1016/j.ejps.2025.107132

55. Sakai S, Yamamoto S, Hirami R, Hidaka M, Elvitigala KCML. Enzymatically gellable chitosan inks with enhanced printability by chitosan nanofibers for 3D printing of wound dressings. *Eur Polym J.* 2024;210:112960.
doi: 10.1016/j.eurpolymj.2024.112960

56. Huang J, Lei X, Huang Z, *et al.* Bioprinted gelatin-recombinant type III collagen hydrogel promotes wound healing. *Int J Bioprinting.* 2022;8(2):517.
doi: 10.18063/ijb.v8i2.517

57. Jafari H, Alimoradi H, Delporte C, *et al.* An injectable, self-healing, 3D printable, double network co-enzymatically crosslinked hydrogel using marine poly- and oligo-saccharides for wound healing application. *Appl Mater Today.* 2022;29:101581.
doi: 10.1016/j.apmt.2022.101581

58. Zhou M, Lee BH, Tan YJ, Tan LP. Microbial transglutaminase induced controlled crosslinking of gelatin methacryloyl to tailor rheological properties for 3D printing. *Biofabrication.* 2019;11(2):025011.
doi: 10.1088/1758-5090/ab063f

59. Hassan M, Misra M, Taylor GW, Mohanty AK. A review of AI for optimization of 3D printing of sustainable polymers and composites. *Compos Part C Open Access.* 2024;15:100513.
doi: 10.1016/j.jcomc.2024.100513

60. Mohammad S, Akand R, Cook KM, Nilufar S, Chowdhury F. Leveraging deep learning and generative AI for predicting rheological properties and material compositions of 3D printed polyacrylamide hydrogels. *Gels.* 2024;10(10):660.
doi: 10.3390/gels10100660

61. Chen B, Dong J, Ruelas M, *et al.* Artificial intelligence-assisted high-throughput screening of printing conditions of hydrogel architectures for accelerated diabetic wound healing. *Adv Funct Mater.* 2022;32(38):2201843.
doi: 10.1002/adfm.202201843

62. Kim N, Lee H, Han G, *et al.* 3D-printed functional hydrogel by DNA-induced biomineralization for accelerated diabetic wound healing. *Adv Sci.* 2023;10(17):2300816.
doi: 10.1002/advs.202300816

63. Gao J, Yu X, Wang X, He Y, Ding J. Biomaterial-related cell microenvironment in tissue engineering and regenerative medicine. *Engineering.* 2022;13:31-45.
doi: 10.1016/j.eng.2021.11.025

64. Lin X, Mao Y, Li P, *et al.* Ultra-conformable ionic skin with multi-modal sensing, broad-spectrum antimicrobial and regenerative capabilities for smart and expedited wound care. *Adv Sci.* 2021;8(9):2004627.
doi: 10.1002/advs.202004627

65. Li J, Zhang T, Pan M, *et al.* Nanofiber/hydrogel core-shell scaffolds with three-dimensional multilayer patterned structure for accelerating diabetic wound healing. *J Nanobiotechnol.* 2022;20(1):28.
doi: 10.1186/s12951-021-01208-5

66. Sun Z, Zhao Q, Ma S, Wu J. DLP 3D printed hydrogels with hierarchical structures post-programmed by lyophilization and ionic locking. *Mater Horiz.* 2023;10(1):179-186.
doi: 10.1039/d2mh00962e

67. Zhou X, Yu X, You T, *et al.* 3D printing-based hydrogel dressings for wound healing. *Adv Sci.* 2024;11(47):2404580.
doi: 10.1002/advs.202404580

68. Xu C, Dai G, Hong Y. Recent advances in high-strength and elastic hydrogels for 3D printing in biomedical applications. *Acta Biomater.* 2019;95:50-59.
doi: 10.1016/j.actbio.2019.05.032

69. Jin E, Yang Y, Cong S, *et al.* Lemon-derived nanoparticle-functionalized hydrogels regulate macrophage

reprogramming to promote diabetic wound healing. *J Nanobiotechnol.* 2025;23(1):68.
doi: 10.1186/s12951-025-03138-y

70. Huang Y, Song M, Li X, *et al.* Temperature-responsive self-contraction nanofiber/hydrogel composite dressing facilitates the healing of diabetic-infected wounds. *Mater Today Bio.* 2024;28:101214.
doi: 10.1016/j.mtbio.2024.101214

71. Schäfer M, Werner S. Oxidative stress in normal and impaired wound repair. *Pharmacol Res.* 2008;58(2):165-171.
doi: 10.1016/j.phrs.2008.06.004

72. Falanga V. Wound healing and its impairment in the diabetic foot. *Lancet.* 2005;366(9498):1736-1743.
doi: 10.1016/S0140-6736(05)67700-8

73. Wei H, Zhang H, Yan S, *et al.* 3D-printed ROS-scavenging, proangiogenic, and biodegradable hydrogel for enhancing burn wound healing. *ACS Appl Mater Interfaces.* 2025;17(28):39955-39966.
doi: 10.1021/acsami.5c04216

74. Fellin C, Steiner R, Yuan X, Jariwala S. A collagen-based biomaterial ink for the digital light processing 3D printing of tough, dual-crosslinked hydrogels via post-print tannic acid treatment. *Bioprinting.* 2025;50:e0042.
doi: 10.2139/ssrn.5164808

75. Tu C, Lu H, Zhou T, *et al.* Promoting the healing of infected diabetic wound by an anti-bacterial and nano-enzyme-containing hydrogel with inflammation-suppressing, ROS-scavenging, oxygen and nitric oxide-generating properties. *Biomaterials.* 2022;286:121597.
doi: 10.1016/j.biomaterials.2022.121597

76. Guo Y, Li Y, Fan R, *et al.* Silver@prussian blue core-satellite nanostructures as multimetal ions switch for potent zero-background SERS bioimaging-guided chronic wound healing. *Nano Lett.* 2023;23(18):8761-8769.
doi: 10.1021/acs.nanolett.3c02857

77. Li Z, Zhao Y, Huang H, *et al.* A nanozyme-immobilized hydrogel with endogenous ROS-scavenging and oxygen generation abilities for significantly promoting oxidative diabetic wound healing. *Adv Healthc Mater.* 2022;11(22):2201524.
doi: 10.1002/adhm.202201524

78. Cano SM, Lancel S, Boulanger E, Neviere R. Targeting oxidative stress and mitochondrial dysfunction in the treatment of impaired wound healing: a systematic review. *Antioxidants.* 2018;7(8):98.
doi: 10.3390/antiox7080098

79. Ding Q, Sun T, Su W, *et al.* Bioinspired multifunctional black phosphorus hydrogel with antibacterial and antioxidant properties: a stepwise countermeasure for diabetic skin wound healing. *Adv Healthc Mater.* 2022; 11(12):2102791.
doi: 10.1002/adhm.202102791

80. Lee H, Kim KS, Zare I, *et al.* Smart nanomaterials for multimodal theranostics and tissue regeneration. *Coord Chem Rev.* 2025;541:216801.
doi: 10.1016/j.ccr.2025.216801

81. Chen Y, Han H, Liu L, *et al.* 3D bioprinted nanozyme-enhanced GelMA hydrogel with antioxidant/anti-inflammatory potential for bone repair. *Nano Res.* 2025;18:94907979.
doi: 10.26599/nr.2025.94907979

82. Muñoz TG, Dahis D, Dosta P, Edelman E, Artzi N. Sprayable hydrogel sealant for gastrointestinal wound shielding. *Adv Mater.* 2024;36(24):2311798.
doi: 10.1002/adma.202311798

83. Lu Z, Cui J, Liu F, *et al.* A 4D printed adhesive, thermo-contractile, and degradable hydrogel for diabetic wound healing. *Adv Healthc Mater.* 2024;13(10):2303499.
doi: 10.1002/adhm.202303499

84. Maschalidi S, Mehrotra P, Keçeli BN, *et al.* Targeting SLC7A11 improves efferocytosis by dendritic cells and wound healing in diabetes. *Nature.* 2022;606(7915):776-784.
doi: 10.1038/s41586-022-04754-6

85. Theocharidis G, Yuk H, Roh H, *et al.* A strain-programmed patch for the healing of diabetic wounds. *Nat Biomed Eng.* 2022;6(10):1118-1133.
doi: 10.1038/s41551-022-00905-2

86. Xiong Y, Feng Q, Lu L, *et al.* Metal–organic frameworks and their composites for chronic wound healing: from bench to bedside. *Adv Mater.* 2024;36(2):2302587.
doi: 10.1002/adma.202302587

87. Liu H, Mei H, Jiang H, *et al.* Bioprinted symbiotic dressings: a lichen-inspired approach to diabetic wound healing with enhanced bioactivity and structural integrity. *Small.* 2025;21(4):2407105.
doi: 10.1002/smll.202407105

88. Wang Z, Lao A, Huang X, Zhou Y, Shen SG, Lin D. Apt-19s-functionalized 3D-printed mesoporous bioactive glass scaffold promotes BMSC recruitment in bone regeneration via SDF-1α/CXCR4 axis and MAPK signaling. *Adv Funct Mater.* 2024;34(27):2316675.
doi: 10.1002/adfm.202316675

89. Li L, Wang Z, Wang K, *et al.* Paintable bioactive extracellular vesicle ink for wound healing. *ACS Appl Mater Interfaces.* 2023;15(21):25427-25436.
doi: 10.1021/acsami.3c03630

90. Yu Q, Wang Q, Zhang L, *et al.* The applications of 3D printing in wound healing: the external delivery of stem cells and antibiosis. *Adv Drug Deliv Rev.* 2023;197:114823.
doi: 10.1016/j.addr.2023.114823

91. Guo L, Niu X, Chen X, Lu F, Gao J, Chang Q. 3D direct writing egg white hydrogel promotes diabetic chronic wound healing via self-relied bioactive property. *Biomaterials.* 2022;282:121406.
doi: 10.1016/j.biomaterials.2022.121406

92. Rybak D, Du J, Nakielski P, *et al.* NIR-light activable 3D printed platform nanoarchitectured with electrospun plasmonic filaments for on demand treatment of infected wounds. *Adv Healthc Mater.* 2025;14(6):2404274. doi: 10.1002/adhm.202404274

93. Zhang S, Huang D, Lin H, Xiao Y, Zhang X. Cellulose nanocrystal reinforced collagen-based nanocomposite hydrogel with self-healing and stress-relaxation properties for cell delivery. *Biomacromolecules.* 2020;21(6): 2400-2408. doi: 10.1021/acs.biomac.0c00345

94. Li X, Teng Y, Liu J, Lin H, Fan Y, Zhang X. Chondrogenic differentiation of BMSCs encapsulated in chondroinductive polysaccharide/collagen hybrid hydrogels. *J Mater Chem B.* 2017;5(26):5109-5119. doi: 10.1039/c7tb01020f

95. Yang J, Tang Z, Liu Y, Luo Z, Xiao Y, Zhang X. Comparison of chondro-inductivity between collagen and hyaluronic acid hydrogel based on chemical/physical microenvironment. *Int J Biol Macromol.* 2021;182:1941-1952. doi: 10.1016/j.ijbiomac.2021.05.188

96. Moura FBR, Ferreira BA, Muniz EH, *et al.* Antioxidant, anti-inflammatory, and wound healing effects of topical silver-doped zinc oxide and silver oxide nanocomposites. *Int J Pharm.* 2022;617:121620. doi: 10.1016/j.ijpharm.2022.121620

97. Kong X, Fu J, Shao K, Wang L, Lan X, Shi J. Biomimetic hydrogel for rapid and scar-free healing of skin wounds inspired by the healing process of oral mucosa. *Acta Biomater.* 2019;100:255-269. doi: 10.1016/j.actbio.2019.10.011

98. Liang M, Dong L, Guo Z, *et al.* Collagen-hyaluronic acid composite hydrogels with applications for chronic diabetic wound repair. *ACS Biomater Sci Eng.* 2023;9(9): 5376-5388. doi: 10.1021/acsbiomaterials.3c00695

99. Huang F, Gao T, Feng Y, *et al.* Bioinspired collagen scaffold loaded with bFGF-overexpressing human mesenchymal stromal cells accelerating diabetic skin wound healing via HIF-1 signal pathway regulated neovascularization. *ACS Appl Mater Interfaces.* 2024;16(14):17072-17085. doi: 10.1021/acsami.4c08174

100. Liu S, Luan Z, Wang T, *et al.* Endoscopy deliverable and mushroom-cap-inspired hyperboloid-shaped drug-laden bioadhesive hydrogel for stomach perforation repair. *ACS Nano.* 2023;17(1):111-126. doi: 10.1021/acsnano.2c05247

101. Wang J, Li J, Sun Y, *et al.* Genetically encoded incorporation of IFN-α into collagen-like protein-hyaluronic acid hydrogels for diabetic chronic wound healing. *ACS Mater Lett.* 2024;6(9):4133-4141. doi: 10.1021/acsmaterialslett.4c01170

102. Jiang J, Wang F, Huang W, *et al.* Mobile mechanical signal generator for macrophage polarization. *Explor.* 2023;3(2):20220147. doi: 10.1002/exp.20220147

103. Louiselle AE, Niemiec SM, Zgheib C, Liechty KW. Macrophage polarization and diabetic wound healing. *Transl Res.* 2021;236:109-116. doi: 10.1093/burnst/tkac051

104. Kong L, Wu Z, Zhao H, *et al.* Bioactive injectable hydrogels containing desferrioxamine and bioglass for diabetic wound healing. *ACS Appl Mater Interfaces.* 2018;10(36):30103-30114. doi: 10.1021/acsami.8b09191

105. Choi SM, Lee KM, Kim HJ, *et al.* Effects of structurally stabilized EGF and bFGF on wound healing in type I and type II diabetic mice. *Acta Biomater.* 2017;66:325-334. doi: 10.1016/j.actbio.2017.11.045

106. Bonito V, Smits AIPM, Goor OJGM, *et al.* Modulation of macrophage phenotype and protein secretion via heparin-IL-4 functionalized supramolecular elastomers. *Acta Biomater.* 2018;71:247-260. doi: 10.1016/j.actbio.2018.02.032

107. Koria P, Yagi H, Kitagawa Y, *et al.* Self-assembling elastin-like peptides growth factor chimeric nanoparticles for the treatment of chronic wounds. *Proc Natl Acad Sci U S A.* 2011;108(3):1034-1039. doi: 10.1073/pnas.1009881108

108. Chen Y, Chen W, Ren Y, *et al.* Macrophage-targeted efferocytosis therapy promotes diabetic wound healing via cellular level debridement. *Adv Funct Mater.* 2025;2503035. doi: 10.1002/adfm.202503035

109. Fu YJ, Shi YF, Wang LY, *et al.* All-natural immunomodulatory bioadhesive hydrogel promotes angiogenesis and diabetic wound healing by regulating macrophage heterogeneity. *Adv Sci.* 2023;10(13):2206771. doi: 10.1002/advs.202206771

110. Shi Y, Wang S, Wang K, *et al.* Relieving macrophage dysfunction by inhibiting SREBP2 activity: a hypoxic mesenchymal stem cells-derived exosomes loaded multifunctional hydrogel for accelerated diabetic wound healing. *Small.* 2024;20(25):2309276. doi: 10.1002/smll.202309276

111. Shu F, Huang H, Xiao S, Xia Z, Zheng Y. Netrin-1 co-cross-linked hydrogel accelerates diabetic wound healing in situ by modulating macrophage heterogeneity and promoting angiogenesis. *Bioact Mater.* 2024;39:302-316. doi: 10.1016/j.bioactmat.2024.04.019

112. Wang H, Zhou M, Ruan Y, *et al.* 2A-biohydrogels accelerate diabetic wound healing by promoting M2 macrophage polarization and functionalized mitochondrial transfer to endothelial cells. *Chem Eng J.* 2025;514:163130. doi: 10.1016/j.cej.2025.163130

113. Su Z, Zhang W, Mo Z, *et al.* Novel asymmetrical double-layer structural adhesive hydrogels with synergetic neuroprotection and angiogenesis effect for diabetic wound healing. *Chem Eng J.* 2024;492:159081. doi: 10.1016/j.cej.2024.159081

114. Wang Z, Xu J, Wu X, *et al.* A sprayable Janus hydrogel as an effective bioadhesive for gastrointestinal perforation repair. *Adv Funct Mater.* 2024;34(48):2408479. doi: 10.1002/adfm.202408479

115. Liu C, Yalavarthi S, Tambralli A, *et al.* Inhibition of neutrophil extracellular trap formation alleviates vascular dysfunction in type 1 diabetic mice. *Sci Adv.* 2023;9(43):eadj1019. doi: 10.1126/sciadv.adj1019

116. Okonkwo UA, Chen L, Ma D, *et al.* Compromised angiogenesis and vascular integrity in impaired diabetic wound healing. *PLoS One.* 2020;15(4):e0231962. doi: 10.1371/journal.pone.0231962

117. Luo Y, Zhang T, Lin X. 3D printed hydrogel scaffolds with macro pores and interconnected microchannel networks for tissue engineering vascularization. *Chem Eng J.* 2022;430:132926. doi: 10.1016/j.cej.2021.132926

118. Mujawar SS, Arbade GK, Bisht N, *et al.* 3D printed Aloe barbadensis loaded alginate-gelatin hydrogel for wound healing and scar reduction: in vitro and in vivo study. *Int J Biol Macromol.* 2025;296:139745. doi: 10.1016/j.ijbiomac.2025.139745

119. Shao Z, Yin T, Jiang J, He Y, Xiang T, Zhou S. Wound microenvironment self-adaptive hydrogel with efficient angiogenesis for promoting diabetic wound healing. *Bioact Mater.* 2023;20:561-573. doi: 10.1016/j.bioactmat.2022.06.018

120. Han X, Chen S, Cai Z, *et al.* A diagnostic and therapeutic hydrogel to promote vascularization via blood sugar reduction for wound healing. *Adv Funct Mater.* 2023;33(14):2213008. doi: 10.1002/adfm.202213008

121. Huang W, Guo Q, Wu H, Zheng Y, Xiang T, Zhou S. Engineered exosomes loaded in intrinsic immunomodulatory hydrogels with promoting angiogenesis for programmed therapy of diabetic wounds. *ACS Nano.* 2025;19(14):14467-14483. doi: 10.1021/acsnano.5c02896

122. Kim K, Yang J, Li C, *et al.* Anisotropic structure of nanofiber hydrogel accelerates diabetic wound healing via triadic synergy of immune-angiogenic-neurogenic microenvironments. *Bioact Mater.* 2025;47:64-82. doi: 10.1016/j.bioactmat.2025.01.004

123. Chen J, Qin S, Liu S, *et al.* Targeting matrix metalloproteases in diabetic wound healing. *Front Immunol.* 2023;14:1089001. doi: 10.3389/fimmu.2023.1089001

124. Lan B, Zhang L, Yang L, *et al.* Sustained delivery of MMP-9 siRNA via thermosensitive hydrogel accelerates diabetic wound healing. *J Nanobiotechnol.* 2021;19(1):130. doi: 10.1186/s12951-021-00869-6

125. Lei H, Fan D. A combination therapy using electrical stimulation and adaptive, conductive hydrogels loaded with self-assembled nanogels incorporating short interfering RNA promotes the repair of diabetic chronic wounds. *Adv Sci.* 2022;9(30):2201425. doi: 10.1002/advs.202201425

126. Wu L, Chen Y, Zeng G, *et al.* Supramolecular peptide hydrogel doped with nanoparticles for local siRNA delivery and diabetic wound healing. *Chem Eng J.* 2023;457:141244. doi: 10.1016/j.cej.2022.141244

127. Zheng X, Deng S, Li Y, *et al.* Targeting m6A demethylase FTO to heal diabetic wounds with ROS-scavenging nanocolloidal hydrogels. *Biomaterials.* 2025;317:123065. doi: 10.1016/j.biomaterials.2024.123065

128. Shi S, Hu L, Hu D, Ou X, Huang Y. Emerging nanotherapeutic approaches for diabetic wound healing. *Int J Nanomed.* 2024;19:8815-8830. doi: 10.2147/ijn.s476006

ACCSCIENCE PUBLISHING

International Journal of Bioprinting

REVIEW ARTICLE

Skin bioprinting for burn reconstruction: From stem cell integration to smart in situ regenerative systems

Aline Yen Ling Wang[1]*, Ana Elena Aviña[1,2], Yen-Yu Liu[1], and Huang-Kai Kao[3,4]

[1]Center for Vascularized Composite Allotransplantation, Chang Gung Memorial Hospital, Taoyuan, Taiwan

[2]College of Medicine, Taipei Medical University, Taipei, Taiwan

[3]Department of Plastic and Reconstructive Surgery, Chang Gung Memorial Hospital, Taoyuan, Taiwan

[4]College of Medicine, Chang Gung University, Taoyuan, Taiwan

(This article belongs to the *Special Issue*: *Next-Gen Biofabrication: Innovations in 3D & 4D Bioprinting for Future-Ready Applications*)

Abstract

Bioprinting of smart skin structures is emerging as a versatile platform not only for wound coverage but also for potential sensory regeneration, real-time monitoring of structures, and tissue repair. This review presents a comprehensive roadmap to bridge the gap between biofabrication science and clinical translation. We explore investigations related to piezoelectric scaffolds, conductive polymers, and stimuli-responsive inks in preclinical environments to produce functional features such as thermal and tactile sensing. Early clinical case reports have demonstrated the feasibility of *in vitro* skin bioprinting strategies, such as skin patches printed for patient-specific applications using minimally manipulated autologous extracellular matrix and umbilical cord mesenchymal stem cell-laden hydrogels for the management of chronic wounds. In parallel, several preclinical *in situ* bioprinting studies using handheld or microfluidic-assisted devices have shown promising results in full-thickness diabetic and burn wound models in terms of enhanced re-epithelization and neovascularization. We also present inherent differences between *in vitro* bioprinting of autologous dermo-epithelial substitutions and *in situ* strategies based on artificial intelligence-guided print path generation and wound topography mapping. Although sensor-equipped bioprinted grafts have shown promising results, they are still in the early stages of development and require validation in large-scale clinical trials. Nevertheless, integration of stem cell technologies, smart biomaterials, and bio-intelligent control systems may eventually be used to support bioprinted skin constructs not only as replacement tissue, but also as potential living, sensing interfaces. This broad multidisciplinary convergence may be beneficial in redefining skin repair by enabling dynamic interactions between engineered skin grafts and host tissue physiology.

Keywords: Bioinks; Burn wound reconstruction; *In situ* bioprinting; Skin bioprinting; Skin substitutes; Smart skin; Stem cells; Vascularization

***Corresponding author:**
Aline Yen Ling Wang
(aline@cgmh.org.tw)

Citation: Wang AYL, Aviña AE, Liu YY, Kao HK. Skin bioprinting for burn reconstruction: From stem cell integration to smart *in situ* regenerative systems. *Int J Bioprint*. 2025;11(6):130-196. doi: 10.36922/IJB025360364

Received: September 3, 2025
Revised: September 28, 2025
Accepted: September 29, 2025
Published Online: September 29, 2025

Copyright: © 2025 Author(s). This is an Open Access article distributed under the terms of the Creative Commons Attribution License, permitting distribution, and reproduction in any medium, provided the original work is properly cited.

Publisher's Note: AccScience Publishing remains neutral with regard to jurisdictional claims in published maps and institutional affiliations.

1. Introduction

Burn injuries are more than just skin injuries—they present a global health burden across various populations.[1,2] Each year, millions of people experience burn injuries caused by heat, chemicals, electricity, or radiation. Although high-income countries have specialized burn centers, the burden of burn injuries is overwhelming in low- and middle-income countries where resources are scarce.[2,3] In severe cases, the injury is not simply a patch of damaged tissue, but a precipitant of systemic dysregulation, characterized by uncontrolled inflammation, immune suppression, metabolic imbalance, and increased susceptibility to infection.[2,4] Advances in acute care have significantly improved survival rates, even for burns covering more than 90% of the total body surface area.[5,6] However, survival is accompanied by additional problems, such as slow healing, hypertrophic scarring in up to 70% of patients, contractures, chronic pain, and severe psychosocial impact.[1,6]

Clinically, it is not often easy to repair the skin after a significant burn. The loss of the epidermis and dermis eliminates the natural barrier of the body, causing fluid loss, invasion of organisms, and temperature imbalances.[4,7] In the absence of swift coverage, patients can be exposed to a great danger of dehydration, electrolyte disturbance, and systemic sepsis.[7] Skin grafts or skin substitutes are therefore essential not only to restore a physical barrier but also to provide a provisional matrix for cellular migration and tissue remodeling until native skin regenerates.[1,8] Early closure is critical to prevent organ failure; however, in extensive burns, healthy donor sites are scarce, limiting the feasibility of autologous grafts.[5,7,8] Although coverage is successful, the lack of vascularization in most engineered grafts undermines the integration of these grafts, causing slough and dysfunction.[5] Preventing infections is an ongoing challenge, and effective healing requires not only wound closure but also scar reduction, preservation of mobility, and restoration of appearance to facilitate social reintegration.[1,6]

Although split-thickness skin grafting (STSG) is still considered the gold standard in covering deep burns, its limitations are becoming more apparent.[9–12] Autologous graft success depends on the availability of donor skin, which is often insufficient in extensive injuries.[9,10] The secondary wounds that form as a result of harvesting the donor tissue expose the area to the risks of infections, hyperpigmentation, chronic pain, and esthetics.[10] Clinicians have responded by employing various skin substitutes: from allogenic and xenogeneic grafts to synthetic and tissue-engineered tissue substitutes. Allograft skin is a short-term substitute but is sensitive to immune rejection and disease spread. Xenografts are readily available but immunogenic with a short lifespan, while synthetic scaffolds are completely biologically risk-free for humans but unable to mimic the biomechanical and physiological behavior of native skin.[13]

Over the last 20 years, the therapeutic repertoire has expanded with the development of bioengineered skin substitutes. Human acellular amniotic membrane, a type of acellular scaffold, serves as a biocompatible scaffold with anti-inflammatory and anti-scarring potential; however, it presents challenges related to mechanical strength, vascular integration, and scalable production.[13] Commercial bilayered constructs and cultured autologous cell sheets have demonstrated clinical benefits, including reduced hospital stays and improved scar quality; however, prolonged culture times, Good Manufacturing Practice (GMP) facility requirements, and high costs often delay intervention during critical acute phases.[9,10,14–16] Even modern treatment protocols cannot achieve a compromise between speed, functional recovery, and esthetics, e.g., in wounds with uneven topography, high microbial load, and/or low vascularization.

It is within this context that *in situ* bioprinting has become a paradigm shift in the reconstruction of burns. In contrast to conventional skin substitute fabrication, which takes a few days or weeks to process in sterile facilities, *in situ* bioprinting localizes the processing in the wound bed and accomplishes it with patient-specific, real-time printing of cells, bioinks, and biomaterial deposition.[17,18] This is very beneficial for burn injuries, as the wounds must be covered immediately to save life and avoid infections. By combining imaging, robotics, and custom bioinks, clinicians are able to create scaffolds that are not only capable of closing wounds but also provide regenerative signals, including growth factors, antimicrobials, or vascularization-inducing factors.[19–21] Preclinical studies have shown accelerated re-epithelialization, improved dermal architecture, reduced hypertrophic scarring, and better integration.[22,23]

The key to fully utilizing material potential *in situ* bioprinting is the inclusion of stem cells or stem cell-differentiated skin cells.[17] As opposed to terminally differentiated keratinocytes or fibroblasts, stem cells—mesenchymal, induced pluripotent stem cells (iPSCs)-based, or epidermal progenitors—provide self-renewal, multi-lineage differentiation, and a rich paracrine profile capable of modulating inflammation, promoting angiogenesis, and remodeling the extracellular environment.[24] In preclinical wound models, stem cell-derived constructs have enhanced epithelial coverage, dermal thickness, and vascular infiltration.[25,26] Scalable GMP-compliant systems now enable production of clinically relevant cell numbers within days, and iPSC-derived cells offer a theoretically

limitless source from a minimal patient biopsy—amenable to banking, cryopreservation, and integration into portable bioprinting workflows.[27,28]

Looking into the future, the idea of "smart" bioengineered skin has come into focus, conceptualized as a dynamic structure that could sense, respond, and adapt itself during the healing process. Exploration in preclinical models currently exists, including the use of novel biomaterials with embedded biosensors and microfluidic channels, and proof-of-concept studies are exploring flexible electronics as a means of wireless monitoring.[29–33] Though these approaches have primarily been pursued at the experimental or early case-report stage in the clinic, sensor-integrated grafts have yet to be validated through large-scale trials. Nevertheless, the combination of regenerative medicine, digital health, and tissue engineering describes a forward-looking vision, where bioprinted skin may one day evolve from a replacement tissue to a living interface that senses its environment.[30,34]

2. Clinical translation challenges in skin bioprinting

2.1. Animal skin bioprinting models

Animal models are now inevitable in the fast-emerging field of skin bioprinting, not only as a proof-of-concept model, but as evidence of clinical potential. To capture relevant literature related to studies on bioprinting of skin along with *in vivo* applications, a structured search was conducted in the primary database PubMed (last updated August 2025). We used the basic search terms "bioprinting" and "skin" to obtain a broad pool of references. In this initial stage, no language filters were applied. Titles and abstracts were then manually searched for studies involving *in vivo* testing, particularly those using models of burn wounds or chronic ulcers. Studies in which only *in vitro* experiments, reviews, conference abstracts, or unrelated dermatologic applications were excluded. Screening and data extraction were performed independently by two reviewers, and a consensus was reached if there was disagreement. Details of the search and selection process are presented in the Preferred Reporting Items for Systematic Reviews and Meta-Analyses diagram (Figure 1).

Initially, we identified 634 papers. After excluding 231 review articles, a total of 403 original research papers remained. We further narrowed down this pool to studies that are specifically associated with skin bioprinting and *in vivo* applications, resulting in a total of 29 relevant articles. Notably, all these chosen studies employed *in vitro* bioprinting with *in vivo t*esting; for example, the skin constructs were initially printed in a controlled laboratory environment and then applied to animal models or human wounds. Among these, two studies reported human clinical trials, detailed in Table 5. The majority of the remaining literature involved animal experiments (27 papers), with 15 studies focusing on mouse wound models (Table 1), and eight studies using rat or porcine models (Table 2). In addition, four studies explored functional restoration, such as glandular or sensory recovery, and are summarized in Table 3. Our analysis of recent preclinical studies, summarized in Tables 1–3, highlights not only the diversity of animal models but also a clear evolution in both bioprinting strategies and regenerative outcomes. Starting with diabetic wounds in mice and progressing to functional sweat gland (SG) regeneration in complex models, the field is advancing beyond simple wound healing toward actual functional tissue replacement. To facilitate standardized comparison between studies, we extracted common healing outcome metrics, including the percentage of wound closure at Days 7 and 14, $CD31^+$ vascular density, re-epithelialization scores, and sample sizes, as shown in Tables S1–S3, Supporting Information. To facilitate readability, we also included trend indicators for wound healing, angiogenesis, and re-epithelialization in each table. Given that the percentage of wound closure was the most consistently reported and comprehensive outcome across studies, we created summary tables showing the median, interquartile range, and a full range of wound closure percentages for studies in Tables 1 and 2 (Table 4). However, for the four studies in Table 3, which emphasized skin appendage functional differentiation and rarely reported wound closure percentages, such summary statistics were not compiled.

The most widely used models are mouse models (Table 1), as they are accessible, cheap, and genetically manipulable. A key trend evident in recent studies is the emergence of these models as a testing ground for bioink innovation. For instance, a photocrosslinkable methacrylated hyaluronic acid-based bioink, when crosslinked with ultraviolet (UV) light, has been used to fabricate three-dimensional (3D)-printed patches that can sustainably release small extracellular vesicles and facilitate wound integration.[35] Although only single-mode photo-crosslinking was used, the system exhibited a strong print fidelity and supported epithelial, vascular, and neural regeneration in diabetic ulcer models. In one notable paper, a thermosensitive double cross-linked gelatin-alginate bioink was developed, allowing *in situ* printing with high structural fidelity and excellent biocompatibility.[36] In addition to significantly enhancing the deposition accuracy and mechanical stability, the coaxial photo-ionic crosslinking formulation also contributed to tissue repair. The printed constructs, when tested *in vivo*, showed very rapid wound healing, lower inflammatory response, and

collagen deposition, indicating that the bioink itself, and not just the scaffold, can serve as a bioactive agent.

Notably, more recently, studies have also started to consider more functionally stratified reconstruction. Integrated tissue-organ printing systems have made it possible to print tri-layered skin grafts that contain not only epidermal and dermal layers, but also hypodermis-like structures and follicle-inductive cells, such as dermal papillae, extending the limits to true skin analogs.[37] These constructs demonstrated basket-weave collagen remodeling and a tiered cellular structure, with the potential for future full-thickness functional reconstruction.

Furthermore, efforts to mimic native mechanical heterogeneity have led to the development of bioinks with gradient stiffness, as demonstrated in the study by Ma *et al*.,[38] which utilized urine models to test the zonal mechanical tuning of dermal equivalents. To reinforce the structure and better adapt to local cell behavior, multiple linear or non-linear gradients were used. Although resolution and complexity tend to be given priority, speed and scale are also important, particularly in trauma care. An early study from Cubo *et al*.[39] featured a bioprinting platform for skin printing that could produce large (100 cm^2) constructs within <35 min and, as such, demonstrated a proof-of-concept for rapid production of clinically relevant skin substitutes on a small animal scale.

Additionally, these constructs also involved the integration of stem cells, human adipose-derived stem cells, and human umbilical cord mesenchymal stem cells (MSCs), widely used for their regenerative capacity and paracrine effects: immune regulation, angiogenesis, and re-epithelialization.[36,40,41] Other studies have gone a step further to add extracellular vesicles or decellularized extracellular matrix (ECM) to form a more natural-like microenvironment.[35,40,41] One group used a xeno-free bioink formulation with four human cell types (fibroblasts, endothelial cells, pericytes, and keratinocytes) to successfully engineer vascularized bilayer skin with rete ridge-like structures—a level of anatomical fidelity that is rarely achieved in small animal models.[42]

Although extrusion-based bioprinting still prevails in murine research, in recent years, the significance of alternative approaches, including laser-assisted and droplet-based bioprinting, is on the rise. As an example, laser-assisted bioprinting (LAB) facilitated the formation of entire cellularized, multi-layered skin constructs with accurate 3D architecture that implanted murine full-thickness wounds.[43] On the same note, bioprinting using droplets, i.e., using bioinks with low viscosity to deposit them with high efficiency, is an effective way to create skin equivalents capable of inducing collagen remodeling and angiogenesis after implantation.[44] These observations imply that bioprinting methods other than extrusion can offer superior control, resolution, and biocompatibility for *in vivo* skin regeneration. Among the most interesting methods is the modified inkjet bioprinting on vascular layer engineering.[45] A modified inkjet bioprinting system was used to fabricate bilayered skin grafts with spatially defined endothelial compartments. The inkjet unit enabled accurate deposition of human microvascular endothelial cells in the dermal layer to promote the formation of prevascular networks. After implantation into full-thickness murine wounds, these grafts led to significant increases in perfusion and revascularization and decreased wound contraction, demonstrating the importance of vascular integration for graft survival. In contrast to the traditional extrusion-based processes, inkjet processes provide increased resolution and droplet control, and therefore, are particularly suited to the patterning of delicate vascular forms. Taken together, the studies described in Table 1 highlight that murine models are not only useful for screening new bioinks but also for modeling complex healing processes (such as angiogenesis, innervation, and full-thickness regeneration), as evidenced by over 60% of high functional outcomes.

Large animal models (Table 2) are not as numerous, but are of vital importance to bridging the translational gap. This is where innovation becomes cellular novelty to scaffold architecture, vascular integration, and immune compatibility. Multiple studies reported the use of fish- or porcine-derived gelatin methacrylate (GelMA) hydrogels enriched with human platelet lysate or recombinant human collagen to enhance bioactivity.[46–49] One group produced a core/shell nanocomposite scaffold system containing antibacterial copper carbon dots and rosmarinic acid, which would provide both antimicrobial and regenerative effects, important for infectious burn wounds.[50] The use of hybrid methods for fabrication, such as a combination of extrusion with electrospinning or digital light processing (DLP) printing, is particularly promising.[48,51] These allow for the building of multi-layered skin analogues, with separated epidermal and dermal compartments and embedded microchannels for nutrient diffusion. A DLP-printed construct tested on pigs demonstrated neovascularization, skin appendage differentiation, and long-term dermal stability, indicating real-world durability.[48] As presented in Table 2, large animal models are instrumental in determining biomechanical durability, vascular maturation, and immune acceptance, and thus serve as a last-stage preclinical validation step before human application.

While much of the attention in the past has been on wound closure metrics such as re-epithelialization rates

and collagen deposition, there is a well-defined evolution toward functional regeneration (Table 3). Several original studies have extended the boundaries by reconstructing appendages such as SG and hair follicles.[52–55] One group bioprinted a construct consisting of stem cell-derived SG cells and dermal microvascular endothelial cells in a matrix with high content of plantar ECM that could restore sweat function in a mouse paw model, a notoriously complex niche.[52] Another study has utilized 3D-printed molds to engineer hair follicle microenvironments, demonstrating functional hair growth after transplantation, including vascularity.[55] These studies, as summarized in Table 3, indicate that functional constructs are not merely theoretical—they are feasible and are already demonstrating restoration of specific skin functions in preclinical studies.

This trend in functional complexity is also driving the need for more precise control of cell position and architecture. Whether by replicating the geometry of the follicle as a 3D-printed microwell or recreating the tri-layered anatomy of native skin, these efforts constitute a paradigm shift from scar minimization to function restoration. Across these models, three broad trends emerge:

(i) Smart bioink design: Bioinks are no longer passive matrices. Whether it is through dual crosslinking, integration with the ECM, or even cell-derived exosomes, they are being designed to interact with the wound microenvironment in a biologically meaningful way.

(ii) Multicellular, vascularized constructs: Grafts composed of a mix of fibroblasts, keratinocytes, endothelial cells, and now pericytes have resulted in constructs that not only survive post-transplantation but also inosculate with host vasculature.

(iii) Functional, not just structural, regeneration: The field is moving definitively away from wound coverage to restoring specialized cutaneous functions: sweat secretion, hair growth, pigmentation, and even sensory reinnervation.

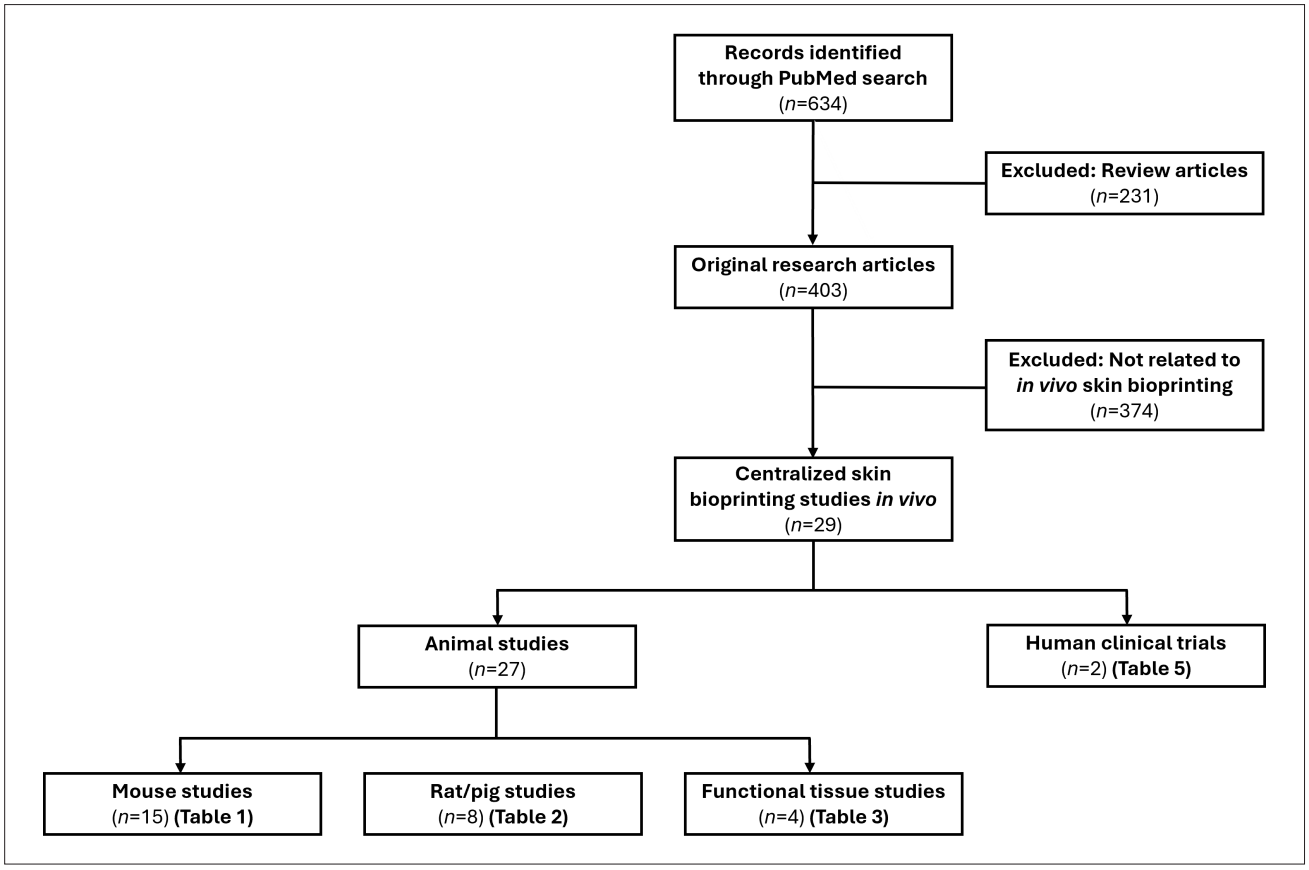

Figure 1. The Preferred Reporting Items for Systematic Reviews and Meta-Analyses flow diagram of study selection for centralized skin bioprinting studies conducted *in vivo*. Flowchart illustrating the identification, screening, and inclusion of original research articles on *in vivo* applications of skin bioprinting in wound healing, encompassing studies on both animals and humans.

Tables 1–3 reflect an emerging consensus opinion: successful skin regeneration is not about copying form, but restoring function. This ambition is mirrored in the selection of animal models. Mice provide a platform for rapid iteration and mechanism. Larger models, such as pigs, provide skin anatomy and immune profiles closer to humans. Functional regeneration models are increasingly designed to answer the question: can we bring skin back to life, not just back to the surface? As the advent of skin bioprinting moves forward toward clinical application, these studies in animals inspire future work. By understanding how these constructs function in living organisms—with real vascular challenges, immune responses, and function demands—we are one step closer to skin substitutes that do not just heal, but also regenerate.

2.2. Clinical skin bioprinting trials

Skin bioprinting is still in its infancy as a clinical tool, yet initial trials are encouraging and already hint at the possibilities of translating engineered constructs from bench to bedside. As highlighted in Table 5, three main clinical strategies have been implemented to date; each of these addresses real-life problems in chronic or complex wounds through highly personalized bioprinting strategies.

An interesting trend is the move toward therapies that are patient-specific and minimally manipulated. Kesavan *et al*.[62] used extrusion-based printing to produce customized patches using minimally manipulated autologous ECM, which was obtained from the patient herself (from adipose tissue). In contrast to isolating stem cells, this protocol maintained native cellular constituents within the ECM, simplifying the workflow while bypassing regulatory considerations of cell expansion. The approach enabled re-epithelialization to be completed in under a month, along with vascular improvement, making it a compelling strategy for personalized, off-the-shelf tissue.

Another evolution is from Zhang *et al*.,[63] who used a hydrogel of gelatin-alginate and human umbilical cord-derived MSCs to treat a chronic wound associated with non-healing after chemical injection treatment. The bioprinted construct could be completely closed in 20 days, and the treated area showed immediate relief from pain and did not recur even a year after treatment. The novelty lay not only in the choice of cell type but also in the spatial programming of cell deposition, which adapts the shape and structure of the cell patch to the precise topography of the wound. This is an example of the potential of imaging, biomaterials, and regenerative biology as a truly integrated clinical workflow.

However, these promising case studies also highlight key limitations. First, sample size and standardization remain significant gaps; more often, published trials are single-patient studies or are not validated in a long-term multicenter study. It is also essential to highlight the limitations of comparability between current trials from the clinical point of view. First, follow-up periods are widely varied, from 4 weeks to >12 months, making it difficult to consistently compare recurrence and long-term outcomes. Second, many studies are not powered or designed for examinations of comparative effectiveness or safety. We have consequently included a concise summary of the risk of bias in Table 5 according to the case report evaluation criteria, providing insight into the current evidence strength. Third, GMP compliance and scalability of cell manufacturing are challenges that must not be ignored. One ongoing trial (NCT04925323) is addressing this by focusing not on the wound itself, but on validating a GMP-compatible pipeline for producing autologous dermo-epidermal grafts. While this trial is still ongoing, its emphasis on regulatory readiness is a vital step toward clinical integration.

Collectively, the studies summarized in Table 5 comprise a transition from experimentally covering wounds to clinically integrated, image-guided, and cell-informed wound repair. These clinical applications place a particular focus on precision medicine and how bioprinting can be used to generate bespoke constructs to treat skin in a patient-specific way consistent with their pathology and anatomy. The clinical space is evolving with a cautious but calculated pace. Instead of mass-producing generic grafts, the focus has shifted to precision bioprinting, customizing bioinks, cell sources, and architectures to cater to each patient's biology and wound profile. Achieving scale, quality, consistency, and cost-effectiveness in deploying these systems remains a significant challenge. For now, bioprinting is transitioning from concept to clinic, one custom patch at a time.

2.3. Regulatory and manufacturing challenge

If skin bioprinting is to translate from concept to clinic, it must first navigate one of the most complex terrains in biomedical translation—regulatory approval and scalable manufacturing.[64–66] The challenge is heightened by the fact that bioprinted skin does not fit neatly within existing regulatory categories. It often sits at the intersection of biologics, medical devices, and gene or cell therapies, depending on its composition and intended use.[67,68] This hybrid nature creates uncertainty at almost every step, including classification, approval, and post-market surveillance.

The first and most significant challenge is product classification. In the United States, the way a product is classified into one of several categories can be a key determinant of the path to market: 361HCT/P (minimally

Table 1. Summary of three-dimensional *in vitro* bioprinting approaches for skin and wound repair in mouse models

Wound category	Specific wound/ Animal species	Bioprinting modality	Bioink material	Cell type used	Healing outcome	Key technical innovation	Reference
Diabetic wound/ extrusion	Diabetic pressure ulcer; diabetic db/ db mice	Extrusion-based 3D bioprinting (Rokit Invivo 4D2)	MeHA (4% w/v) with Irgacure 2959 (0.1% w/v), used as a photocrosslinkable hydrogel	Human adipose-derived mesenchymal stem cells-derived small extracellular vesicles (1.2 mg/mL)	Improved wound epithelialization, angiogenesis, and innervation	Extrusion-based 3D bioprinting combined with *in situ* UV photocrosslinking for mechanically stable, porous patches	[35]
Excisional wound/ extrusion	Full-thickness skin wound; Institute of Cancer Research mice	Extrusion-based 3D bioprinting (temperature-controlled, coaxial photo/ionic double-crosslinking)	GH/AT hydrogel gel-HPA (10% w/v) + alginate-tyramine (1.5% w/v) with ruthenium/ sodium persulfate initiators (0.5 mM ruthenium and 10 mM sodium persulfate); photo/ionic crosslinking (0.18 M $CaCl_2$/450 nm blue light irradiation)	NIH 3T3 mouse FBs (3×10^6 cells/mL) and human umbilical cord mesenchymal stem cells (3×10^6 cells/mL)	Accelerated wound closure, improved re-epithelialization, enhanced collagen deposition, and reduced inflammation	Development of a thermosensitive, double-crosslinked GH/AT bioink enabling *in situ* printing with high structural fidelity and biocompatibility	[36]
	Full-thickness skin wound; C57BL/6 mice	Extrusion-based 3D bioprinting (single-syringe, monolayer FB-laden patch printing)	GelSilMA (G-S) hydrogel: GelMA (3–5% w/v) + SilMA (4–12% w/v) dissolved in LAP (0.25% w/v) photo-crosslinking	Primary mouse dermal FBs (20×10^6 cells/mL)	Faster wound closure, enhanced collagen deposition, and improved angiogenesis	Customized single-syringe printing of cell-laden GelMA/SilMA composite hydrogel patches with tunable mechanical and degradation properties for skin repair	[56]
	Full-thickness skin wound; BALB/c mice	Extrusion-based 3D bioprinting (layer-by-layer with dual thermosensitive + photocrosslinking)	Composite hydrogel of decellularized adipose tissue ECM (dECM, 1.125% w/v) + GelMA (7.5% w/v) + HAMA (1% w/v), with LAP (0.25% v/v) photo-crosslinking	hADSCs (1×10^7 cells/ mL)	Enhanced wound closure, improved collagen deposition, increased angiogenesis, and blood perfusion	Integration of patient-derived adipose dECM with GelMA/HAMA in a UV-crosslinked, hADSC-laden 3D-printed skin substitute for improved vascularized wound healing	[40]
	Full-thickness skin wound; BALB/c nude mice	Extrusion-based 3D bioprinting (layer-by-layer with dual thermosensitive + photocrosslinking)	Composite hydrogel of dECM (1.125% w/v) + GelMA (7.5% w/v) + HAMA (1% w/v), with LAP (0.25% v/v) photo-crosslinking	hADSCs (1×10^7 cells/ mL)	Accelerated wound closure, enhanced neovascularization, increased collagen secretion, and remodeling	Integration of patient-derived adipose dECM and ADSCs into a dual-crosslinkable GelMA–HAMA scaffold for high bioactivity, better cytocompatibility, and improved *in vivo* regenerative performance	[41]

Continue...

Table 1. *Continue...*

Wound category	Specific wound/ Animal species	Bioprinting modality	Bioink material	Cell type used	Healing outcome	Key technical innovation	Reference
	Full-thickness skin wound; C.B-17 SCID/bg immunodeficient mice	Extrusion-based 3D bioprinting (layer-by-layer dermis + epidermis)	Xeno-free dermal bioink: human collagen type I (0.6% w/v), human fibronectin (0.1% w/v), VitroGel; Xeno-free epidermal bioink: KC medium with KGF (5 ng/mL), $CaCl_2$ (1.64 mM), ascorbic acid (50 μg/mL)	Xeno-free dermal bioink formulated with 4.5×10^6/mL human FBs, 4.5×10^6/mL human ECs, and 5.5×10^5/mL human placental PCs; xeno-free epidermal bioink formulated with 2×10^6/mL human KCs	Formation of mature stratified epidermis with rete ridge-like structures; perfused human EC-lined vessels within 2 weeks; prevention of graft necrosis; host angiogenic vessel integration	First demonstration of fully xeno-free bioprinted vascularized bilayer human skin graft using four primary human cell types and xeno-free matrix components, showing *in vivo* vascularization and integration	[42]
	Full-thickness skin graft over integrated cartilage construct; BALB/c nude mice	Extrusion-based 3D bioprinting (INKREDIBLE)	Nanofibrillated cellulose/alginate (NFC/Alg); crosslinked with $CaCl_2$ (100 mM)	Human nasal chondrocytes (20%), human bone marrow-derived mesenchymal stem cells (80%)	Skin grafts integrated well with 3D-bioprinted constructs; a tight connection between the fibrous vascularized capsule and the skin graft; no necrosis observed; the skin survived environmental exposure	Demonstrated that *in vivo*-integrated 3D-bioprinted cartilage can serve as a sufficient base for full-thickness skin grafts, enabling potential auricular reconstruction applications	[57]
	Full-thickness skin wound; mouse	Extrusion-based 3D bioprinting	Gelatin–alginate hydrogel with gradient stiffness; cross-linked via calcium substrate	Adipose-derived stem cells	Enhanced angiogenesis and wound healing via improved paracrine secretion and scaffold stability	Gradient stiffness hydrogel mimicking dermal stiffness microenvironment via calcium-mediated secondary cross-linking during printing	[38]
	Full-thickness skin wound; athymic nude mice	Integrated tissue and organ printing, extrusion bioprinting with CAD	Fibrinogen (3% w/v)-based bioink with gelatin (3.5% w/v), glycerol (100 μL/mL), hyaluronic acid (0.3% w/v), aprotinin (40 μg/mL); crosslinked with thrombin (20 IU/mL)	Epidermis: human KCs + melanocytes (9:1); dermis: human FBs, follicle dermal papilla cells, dermal microvascular ECs (6:1:1); hypodermis: human preadipocytes	By Day 21, all bioprinted skin wounds closed via epithelialization (not contraction); restored basket-weave collagen organization; stratified epidermis; dermal maturation; vascularization; human cell integration	First quantification of collagen remodeling in bioprinted skin-treated wounds; demonstrated phenotypically normal skin regeneration with layered tri-cellular architecture, including hypodermis, dermis, and epidermis	[37]

Continue...

Wound category	Specific wound/ Animal species	Bioprinting modality	Bioink material	Cell type used	Healing outcome	Key technical innovation	Reference
	Full-thickness skin wound on face-shaped dorsal skin structure; athymic nude mice	Extrusion-based 3D bioprinting using the in-house integrated tissue-organ printing system	Composite hydrogel: hyaluronic acid (0.3% w/v), glycerol (10% v/v), gelatin (3% w/v), fibrinogen (2% w/v); porous polyurethane (PU) support layer; crosslinked with thrombin (20 U/mL)	Epidermis: human epidermal KCs (1×10^7 cells/mL); dermis: human dermal FBs (5×10^6 cells/mL)	Accelerated wound closure, regeneration of epidermis and dermis, improved integration with surrounding tissue	Patient-specific, computer tomography image-based BioMask design; triple-layer construct (PU dressing, KC hydrogel, FB hydrogel) fitting complex facial contours	[58]
	Full-thickness skin wound; immunodeficient mice	Extrusion-based 3D bioprinting	Human plasma-based bioink with fibrin	Primary human FBs and KCs from skin biopsies	Generated skin structurally and functionally similar to human skin, indistinguishable from handmade bilayered equivalents	Rapid fabrication of 100 cm^2 bilayered human skin in <35 min, automated process, reduced production time from weeks to minutes	[39]
	Full-thickness skin wound; C.B-17 SCID/bg immunodeficient mice	Extrusion-based bioprinting (Bio X, CELLINK)	Dermal bioink: rat tail type I collagen (0.35% w/v) + FBS + HAM-F12 + foreskin dermal FBs, ECs, ±placental PCs; Epidermal bioink: KC growth medium + differentiation supplements + KCs; crosslinked with nebulized $NaHCO_3$ (2.2% w/v)	Dermal bioink formulated with 7.0×10^5/mL human FBs and 7.0×10^5/mL human ECs, with/without 3.5×10^5/mL human PCs; epidermal bioink formulated with 2×10^6/mL human KCs	Formation of multilayered epidermis; EC-lined vascular structures inosculated with mouse microvessels and became perfused within four weeks; PCs enhanced host vessel invasion and epidermal rete formation	Inclusion of PCs in dermal bioink to improve both dermal vascularization and epidermal maturation; optimization of KC: FB and PC: FB: EC ratios to mimic native skin structure; pre-vascularized construct enabling inosculation with host vasculature	[59]
Excisional wound/ inkjet	Full-thickness skin wound; Athymic nude mice (homozygous nude *Foxn1*^{nu}/*Foxn1*^{nu}; strain name: J:NU)	Modified inkjet bioprinting (for vascular layer)	Collagen type I gel (0.32% w/v) with neonatal human dermal FBs, fibrin gel with human microvascular ECs, and collagen gel with neonatal human epidermal KCs	Human dermal FBs (2×10^6 cell/mL); human microvascular ECs (2×10^6 cell/mL.); human epidermal KCs (2×10^6 cell/mL)	Improved wound contraction (~10% better than controls), regenerated neoskin with dermis and epidermis resembling normal skin, and survival of implanted cells	Bilayer skin graft with printed endothelial microvasculature integrated with FBs and KCs for enhanced graft survival and vascularization	[45]
	Full-thickness skin wound; mouse	Inkjet droplet-based 3D bioprinting/ nebulization	Collagen-based bioink	Human dermal FBs, human epidermal KCs	Promoted skin regeneration with improved collagen deposition and vascularization	Use of low-viscosity droplet-based bioprinting/ nebulization for high-viability deposition and systematic construction of human skin equivalents with morphologically native-like dermis and epidermis	[44]

Continue...

Table 1. ***Continue...***

Wound category	Specific wound/ Animal species	Bioprinting modality	Bioink material	Cell type used	Healing outcome	Key technical innovation	Reference
Excisional wound/ laser	Full-thickness wound in the dorsal skin fold chamber; BALB/c nude mice	Laser-assisted bioprinting	Collagen type I (rat tail) on Matriderm® scaffold	NIH3T3 FBs (1.5×10^6 cells/mL), HaCaT KCs (1.5×10^6 cells/mL)	Multi-layered epidermis with beginning differentiation, stratum corneum formation, FB collagen production, vascular ingrowth from the wound bed	Precise spatial placement of different cell types in a 3D pattern onto a stabilizing matrix, enabling complex skin tissue formation	[43]

Abbreviations: 3D, three-dimensional; CAD, computer-aided designing; ECs, endothelial cells; ECM, extracellular matrix; FB, fibroblast; GelMA, gelatin methacryloyl; GH/AT, gelatin-alginate; HAMA, hyaluronic acid methacryloyl; hADSCs, human adipose-derived stem cells; KCs, keratinocytes; LAP, photo-initiator lithium phenyl-2,4,6-trimethylbenzoylphosphinate; MeHA, methacrylated hyaluronic acid; PCs, pericytes; SilMA, silk fibroin methacrylate.

manipulated, homologous use) or under the more stringent 351 pathway, which requires an investigational new drug application and a complete Biological License Application.[69] Constructs that contain allogeneic cells, genetic manipulation, or more than minimal manipulation (combining stem cells with synthetic scaffolds) will almost always fall into 351, requiring extensive pre-clinical and clinical requirements. The "Same Surgical Procedure Exception" in 21 CFR 1271.15(b) can be applied to certain autologous, intraoperative uses, but bioprinting workflows are often outside these very narrow confines in terms of multiple procedural manipulations, storage steps, or incorporated bioactive components.[70]

In Europe, the European Medicines Agency (EMA) considers bioprinted products under the umbrella of advanced therapy medicinal products (ATMPs).[71–73] While the "hospital exemption" clause allows for limited flexibility in terms of custom, non-commercial uses, products still require high bars for GMP compliance, traceability, and defined mechanisms of action.[74,75] The absence of global consistency between the Food and Drug Administration (FDA) and EMA requirements is an additional component in the burden of regulatory requirements, particularly for developers who aim to conduct multinational trials or eventually commercialize their therapies.[76] Due to the regulatory uncertainty, we listed the existing types of dossiers as well as the current classification pathways for bioprinted skin in the FDA and EMA systems (Tables 6 and 7). Table 6 summarizes the types of regulatory dossiers and product characteristics that trigger each, and Table 7 groups classification into four regulatory pathways to help present the regulatory route and dossier requirements for each scenario in the FDA and EMA guidance. These summaries are used to help delineate the different regulatory expectations for products based on their cellular content and structural characteristics, as well as when drugs or electronics are incorporated into the product. For example, entirely acellular scaffolds could follow a medical device pathway. In contrast, scaffolds that contain live cells, growth factors, or a great deal of manipulation would follow the more rigorous biologics or combination product route. The tables not only detail the applicable areas and approval pathways, but also the documentation that is needed, from GMP compliance to device technical files, biodiversity and biocompatibility reports, and clinical trial applications. These differences can be significant for developers to recognize their regulatory responsibilities up-front to prevent misclassification and optimize clinical translation between jurisdictions.

Meanwhile, GMP manufacturing remains a significant bottleneck.[74,75,77,78] Bioprinting is not merely about stacking cells; one must stack cells in a controllable,

Table 2. Summary of three-dimensional *in vitro* bioprinting approaches for skin and wound repair in large animal models

Wound category	Specific wound/ Animal species	Bioprinting modality	Bioink material	Cell type used	Healing outcome	Key technical innovation	Reference
Diabetic wound	Full-thickness skin wound in a diabetic model (50 mg/kg streptozotocin-induced); Wistar rat	Extrusion-based 3D printing (low-temperature manufacturing system)	Chitosan (6% w/v) in acetic acid (2% v/v) with D-(+)-raffinose pentahydrate	Normal dermal human fibroblasts (1×10^5 cells/mL) and human keratinocytes (HaCaT, 1×10^5 cells/mL)	Improved wound closure and better tissue quality vs. commercial patch or no treatment	Low-temperature extrusion-based printing of chitosan scaffolds; optional chitosan film base to retain cells inside the scaffold	[60]
Excisional wound	Critical-sized full-thickness skin wound; Wistar rat	Extrusion-based 3D bioprinting (CELLINK)	Fish skin-derived GelMA (10% w/v) hydrogel supplemented with HPL (5% v/v); crosslinked with 365 nm UV light	Human ASCs, 5×10^6 cells/mL)	Delayed wound contraction, enhanced collagen deposition, and increased neovascularization compared to the untreated and GelMA-only groups	Development of fish skin-based GelMA bio-ink with tunable methacrylation degree and extrusion-printability, enabling ASC + HPL delivery for improved wound healing	[46]
	Full-thickness skin wound; Sprague Dawley rat	Extrusion-based 3D bioprinting (Biomaker 2, SunP Biotech)	GelMA (7.5% w/v, porcine skin) + rhCol3 (0.8–3.2% w/v); cross-linked with 405 nm UV light	HDFs (1×10^6/mL), human epidermal keratinocytes (HaCaTs, 3.3×10^5 cells/mL)	rhCol3 promoted faster epidermal confluence (~100% by Day 3), enhanced dermal and epidermal growth, improved wound closure, and tissue regeneration vs. rhCol3-free	Use of recombinant human type III collagen as a bioactive component in GelMA bioink to accelerate skin cell proliferation, epidermal confluence, and wound healing	[47]
	Full-thickness skin wound; Sprague Dawley rat	3D printing (Tongli micro-nano technology), combining electrospinning and extrusion printing	Outer layer: PLGA nanofiber membrane (15% w/v in HFIP, electrospun) inner layer: alginate hydrogel (crosslinked in 5% $CaCl_2$)	None (acellular scaffold)	Bleomycin scaffold showed the fastest and best skin regeneration, enhanced neovascularization (CD31), increased collagen I/III deposition, and reduced interleukin-1 beta and tumor necrosis factor alpha expression compared to PLGA, alginate, and untreated control	Bilayer design (outer PLGA for antibacterial and moisture retention, inner porous alginate for cell adhesion, and proliferation); integration of electrospinning and 3D printing for skin-mimicking structure; acellular scaffold reduces immune rejection	[51]
	Full-thickness skin wounds; rat	3D-embedded bioprinting	Thermosensitive thiolated Pluronic F127 (PF127-SH) + HAMA hydrogel	Not specified	Enhanced wound healing, promoted re-epithelialization, accelerated collagen deposition, angiogenesis, and modulated inflammation	Stepwise multi-cross-linking bioink strategy: Michael addition at low temperature, hydrophobic self-assembly at body temp, thiolene click photo-cross-linking	[61]

Continue...

Table 2. ***Continue...***

Wound category	Specific wound/ Animal species	Bioprinting modality	Bioink material	Cell type used	Healing outcome	Key technical innovation	Reference
	Full-thickness skin wound; rat	Extrusion-based 3D printing (core/shell scaffold fabrication)	PLA shell; core: hyaluronic acid (HA), chitosan hydrogel, copper carbon dots (Cu-CDs, 0.25–2% w/v), rosmarinic acid	L929 fibroblast stem cells	Significantly improved wound healing after 15 days compared to PLA scaffold alone; enhanced histological regeneration; upregulated PDGF, TGF-β, and MMP-1 expression	Core/shell nanocomposite scaffold integrating antibacterial Cu-CDs with HA/chitosan/rosmarinic acid for combined antimicrobial and regenerative effects	[50]
	Full-thickness skin wound; Sprague Dawley rat; Bama little pig	DLP-based 3D bioprinting	GelMA (5% w/v) + HA-NB (1.25% w/v) + LAP (0.1% v/v) + phenol red (0.04% w/v); cross-linked with 365 nm UV light	HSFs (4×10^5 cells/mL); HUVECs (4×10^5 cells/mL)	Promoted skin regeneration, enhanced neovascularization, formation of skin appendages, and superior dermal regeneration	Bioink with HA-NB for photocrosslinking and tissue adhesion; DLP printing enabling high-resolution microchannels for nutrient transport; rapid fabrication of functional living skin for large-area wounds	[48]
	Not specified; Animal	3D bioprinting (modality not explicitly stated)	GelMA + collagen (Col) doped with tyrosinase (Ty)	Human melanocytes, human keratinocytes (HaCat), HDF	Formation of epidermis and dermis *in vivo*; high (>90%) cell viability; Ty enhanced melanocyte proliferation, inhibited fibroblast overgrowth, and supported balanced skin regeneration	Tyrosinase-doped GelMA/Col bioink; dual crosslinking via enzymatic and photocrosslinking for enhanced mechanical strength; bioactive role of Ty in pigmentation and wound healing	[49]

Abbreviations: 3D, three-dimensional; ASCs, adipose tissue-derived mesenchymal stromal cells; DLP, digital light processing; GelMA, gelatin methacryloyl; HA-NB, N-(2-aminoethyl)-4-(4-(hydroxymethyl)-2-methoxy-5-nitrosophenoxy) butanamide linked hyaluronic acid; HAMA, hyaluronic acid methacrylate; HDFs, human dermal fibroblasts; HFIP, hexafluoroisopropanol; HPL, human platelet lysate; HSFs, human skin fibroblasts; HUVECs, human umbilical vein endothelial cells; LAP, photo-initiator lithium phenyl-2,4,6-trimethylbenzoylphosphinate; MMP-1, matrix metalloproteinase 1; PDGF, platelet-derived growth factor; PLA, poly(lactic acid); PLGA, poly(lactic-co-glycolic) acid; rhCol3, recombinant human type III collagen; TGF-β, transforming growth factor beta; UV, ultraviolet.

doi: 10.36922/IJB025360364

Table 3. Summary of three-dimensional *in vitro* bioprinting approaches for skin functional tissue regeneration

Wound category	Specific wound/ Animal species	Bioprinting modality	Bioink material	Cell type used	Healing outcome	Key technical innovation	Reference
Functional tissue regeneration	Sweat gland injury/ regeneration model (including thermal injury in mouse paw pad); C57BL/6 mice, CAG-tdTomato mice, Sprague Dawley rats	Extrusion-based 3D bioprinting (Regenovo)	Sodium alginate (1% w/v) + gelatin (3% w/v) + plantar dermis ECM (58 μg/mL); crosslinked with $CaCl_2$ (2.5% w/v)	ADSCs (1×10^7 cells/mL) differentiated into SGCs (4.8×10^2 spheroids/mL), co-cultured with DMECs (4.8×10^5cells/mL)	Promoted physiologically relevant vascularized sweat gland morphogenesis, restored sweat secretion, enhanced vascularization *in vitro* and *in vivo*	Creation of a vascularized sweat gland regeneration model combining 3D-bioprinted SGC spheroids and prevascularized ECM scaffolds to mimic SG-vascular niche reciprocal interactions	[52]
	Burn injury on paw pad; C57BL/6 mice	Extrusion-based 3D bioprinting (Bio-Architect PRO, Regenovo)	Gelatin (10% w/v) + alginate (2% w/v) hydrogel with paw pad dermal homogenates (PD, 58 μg/mL); crosslinked with $CaCl_2$ (100 mM)	MSCs (1×10^6 cells/mL)	Regeneration of functional sweat glands confirmed by acetylcholine-induced sweat test; restoration of glandular morphology; enhanced sweat gland gene expression	Identification of *CTHRC1* (biochemical cue) and *Hmox1* (structural cue-responsive factor) as synergistic regulators directing MSC differentiation into SGCs; integration of biochemical (ECM proteins) and structural (3D microarchitecture) cues in printed constructs	[53]
	Burn injury on paw pad; C57BL/6 mice	Extrusion-based 3D bioprinting (Bio-Architect PRO, Regenovo)	Composite hydrogel of gelatin (20% w/v) and sodium alginate (4% w/v) with paw pad dermal homogenates and EGF (15 ng/mL); crosslinked with $CaCl_2$ (10% w/v)	Epidermal progenitor cells (from mouse dorsal skin)	Functional restoration of sweat glands *in vivo*	Creation of a 3D ECM mimic providing spatial inductive cues to direct epidermal progenitors into sweat gland lineage, enabling regeneration in injured tissue	[54]

Continue...

Table 3. ***Continue...***

	Full-thickness dorsal midline excision with silicone chamber implantation; Immunodeficient nude mice (*athymic nude, Crl:NU(NCr)-Foxn1nu*)	3D-printed molds (Objet24, UV-curable material VeroWhite) to create hair follicle microwells	Type I collagen gel for the dermal layer embedded with 3D-printed mold structures	Human dermal fibroblasts (1.25×10^5 cells/mL), dermal papilla cells (*LEF1*-transfected to enhance hair follicle induction), neonatal keratinocytes, GFP-tagged human umbilical vein endothelial cells (HUVECs for vascularization, 2×10^6 cells/mL)	Formation of human hair follicles within engineered skin constructs; vascularized grafts grew hair effectively after transplantation into mice	Biomimetic developmental approach: 3D-printed mold to recapitulate human fibroblast microenvironment geometry; *LEF1* overexpression restores dermal papilla cell inductive capacity; pre-vascularization improves survival and function	[55]

Abbreviations: 3D, three-dimensional; ADSC, adipose-derived mesenchymal stem cell; DMECs, dermal microvascular endothelial cells; ECM, extracellular matrix; GFP, green fluorescent protein; MSCs, mesenchymal stem cells; SGCs, sweat gland cells; UV, ultraviolet.

sterile, and reproducible manner. Unlike traditional biologic manufacturing, which is conducted in centralized manufacturing facilities, the focus of many bioprinting applications (especially *in situ* systems) is real-time deposition at the bedside. This raises challenging questions about process validation, bioprinter calibration, sterility assurance, and documentation. Even centralized workflows (whereby derivatives are printed and matured before implantation) have challenges with batch-to-batch consistency, long lead times, and GMP-compliant facilities. Quality systems for traditional drugs rarely translate into dynamically growing, patient-specific constructs produced on demand.

Despite the scientific maturation of 3D-bioprinted skin, the regulatory landscape remains fragmented and unprepared to address the complexity of this technology.[65] In essence, bioprinted constructs are hybrid products (a complex of cellular, structural, and sometimes genetic components), leading to overlapping regulatory spaces between the laws and regulations related to biologics, devices, and tissue controls.[72,79,80] Such products have been categorized in various ways, on a case-by-case basis, depending on the level of manipulation, cell source, and clinical purpose. As the regulatory agencies, such as the FDA and EMA, have yet to unambiguously define the bioprinted constructs, there is a level of ambiguity in the regulatory pathway and risk categorization for the bioprinted constructs.[81]

To deal with the operational complexity of hybrid constructs—characterized by cellular, structural, and device elements—regulatory authorities have begun to provide pathway-specific guidance. The FDA's Office of Combination Products offers the Request for Designation mechanism to resolve the primary mode of action and whether a hybrid construct should be regulated as a biologic, device, or combination product. In the European Union, developers will need to engage early on with both EMA and notified bodies to determine whether the construct is covered by either ATMP or device directives. In Japan, the Pharmaceuticals and Medical Devices Agency permits conditional approvals for regenerative products with minimal efficacy requirements, a structured path for iterative development of regenerative products. However, these tools are underutilized in bioprinting, making formalized hybrid construct classifications frameworks necessary. Without such tools, developers are left dependent on ad hoc consultation, which can slow translational clinical development, as well as complicate global coordination processes.

Additionally, the materials implemented in bioinks make it more complex.[82,83] Most are still in an experimental

Table 4. Summary statistics of percentage wound closure in animal models of skin bioprinting

Model type	Timepoint	Median (%)	Interquartile range (%)	Range (%)
Mouse	Day 7	79.67	59.5–84.8	50.0–91.0
	Day 14	99.2	90.0–100.0	72.0–100.0
Rat	Day 7	78.0	72.2–85.0	50.0–90.0
	Day 14	100.0	100.0–100.0	94.0–100.0

Note: Among the mouse data from the 15 studies listed in **Table 1**, three lacked full-text access and were therefore excluded. This resulted in 12 studies being included in **Table S1, Supporting Information**. Among these, five did not report quantitative wound closure data and were excluded from the final analysis. Summary statistics were calculated from the remaining seven studies and are presented as medians, interquartile ranges, and full ranges. Among the rat data from the eight studies listed in **Table 2**, two lacked full-text access and were, therefore, excluded. This resulted in six studies being included in **Table S2, Supporting Information**. Among these, one did not report quantitative wound closure data and was excluded from the final analysis. Summary statistics were calculated from the remaining five studies and presented as medians and full ranges.

stage, with pure and stability profiles still not clearly defined and often containing animal-derived or xenogenic materials. This raises concerns about safety and sterility, especially since conventional sterilization methods (e.g., radiation or ethylene oxide) may compromise the functionality of bioink or harm embedded cells.[84–87] Additionally, no bioinks currently on the market are approved for human use, and well-developed criteria for biocompatibility testing for living, patient-specific constructs are presently not available.

Risk profiles are also challenging to assess. Most hazard analyses for conventional devices fall short when applied to dynamic, on-demand constructs involving live cells. Other features of these grafts, such as immune response, tumorigenicity, or variability of vascular integration, have not been sufficiently characterized. This is further compounded by the decentralization of manufacturing. Many bioprinting systems perform *in situ* bioprinting by the bedside, a marked difference from centralized GMP-certified facilities. This trend of re-distributed manufacturing challenges traditional notions of quality control, traceability, and liability.[88]

Additionally, product shelf-life remains a regulatory blind spot.[89] Viable cell-laden components are time-sensitive, yet protocols for expiration dating, packaging, and transport remain underdeveloped. In parallel, standardization of testing, particularly regarding print fidelity, structural integrity, and functional outcome, is still evolving. Only a few American Society for Testing and Materials (ASTM) standards have been proposed, and most are restricted to extrusion-based bioprinting.

Post-market surveillance is another critical gap.[90] Authorities lack data on the real-world performance and adverse events, with limited clinical data and long-term follow-up. Few trials have progressed beyond feasibility or safety endpoints, such that long-term integration, remodeling, and regeneration outcomes are unknown. This is further complicated by living autologous cells, whose heterogeneity across patients makes outcome prediction difficult.

Complicating things is the fragility of the bioprinting supply chain. Clinical-grade bioinks, or especially those with recombinant collagen, growth factors, or decellularized ECM, are difficult to obtain in a GMP-certified fashion.[74] Batch-to-batch variation, cold-chain logistics, and a short shelf life put a product at risk of delay or failure. Moreover, devices such as cryopreserved, stem cell-laden cartridges—designed to support portable or point-of-care printing—are still in early development and have yet to be commercially scalable.

There is an international push toward regulatory harmonization; however, considerable confusion exists regarding the classification of bioprinted skin constructs. Although the key principles in the International Council for Harmonisation (ICH) Q8–Q11 guidance documents on drug development, quality risk management, and quality systems are increasingly being discussed for emerging therapies such as tissue-engineered products, bioprinted or tissue-engineered constructions remain outside their scope, underscoring the need for dedicated regulatory guidance in this area.[91–94] Similarly, the World Health Organization has published international standards through the Expert Committee on Biological Standardization, but actual conformity is not well enforced.[95] For instance, the FDA regulates complex autologous grafts under the HCT/P framework (361 or 351 pathways), whereas the EMA classifies them as ATMP under Regulation (EC) No 1394/2007, requiring centralized marketing authorization.[96,97] In contrast, Japan's Pharmaceuticals and Medical Devices Agency has placed a conditional time-limited approval system in place for regenerative therapies, speeding up access but requiring post-marketing surveillance.[98,99] The International Medical Device Regulators Forum has developed harmonized definitions and regulatory pathways for personalized medical devices (custom-made, patient-matched, and modular devices)

Table 5. Clinical summary of three-dimensional *in vitro* bioprinting approaches for skin and wound repair

Wound type	Design/Sample size	Bioprinting modality	Bioink material	Cell type used	Follow-up/ Bias risk	Healing outcome	Key technical innovation	Reference
Diabetic foot ulcer (chronic, neuropathic, located below the malleoli)	Randomized controlled trial/17 (test group); 16 (control group)	Extrusion-based 3D bioprinting (ROKIT Dr INVIVO)	Minimally manipulated autologous extracellular matrix (MA-ECM) from adipose tissue	Native adipose-derived cellular components within MA-ECM (no ADSC isolation)	24 weeks/ low-moderate (no blinding)	Complete re-epithelialization in ~4 weeks; accelerated wound closure; improved vascularization	Custom patient-specific wound patch bioprinted from autologous MA-ECM; integration of imaging-to-G-code workflow	[62]
Chronic non-healing wound caused by bleomycin A5 intralesional injection for plantar warts (with infection, superficial phlebitis)	Case report/1	Extrusion-based 3D bioprinting (Regenovo Biotechnology)	Alginate (1% w/v) + gelatin (3% w/v); crosslinked with $CaCl_2$	Human umbilical cord-derived mesenchymal stem cells (hUCMSCs, 1×10^6 cells/mL)	One year/ Moderate (no comparator)	Complete wound closure in 20 days after first application; improved vascularity; pain reduction within 3 days; no recurrence at 1-year follow-up	Patient-specific wound-shaped skin substitute with hUCMSCs; precise spatial arrangement of cells; customization of bioink and print pattern for individual wounds	[63]
Surgical wound tissue (from plastic/ reconstructive surgery)— used for generating dermo-epidermal autologous skin substitute	GMP validation/25	Not specified	Not specified	Keratinocytes, fibroblasts (isolated and expanded from healthy patient surgical waste tissue)	Not applicable	Trial focuses on GMP validation and *in vitro* product generation, not clinical wound healing	GMP-compliant automated bioprinting process for dermo-epidermal skin substitute; integration of keratinocyte and fibroblast expansion with bioprinting workflow	ClinicalTrials.gov Identifier: NCT04925323; status: recruiting (as of last update June 14, 2021)

Abbreviations: 3D, three-dimensional; ADSC, adipose-derived mesenchymal stem cell; GMP, good manufacturing practice.

doi: 10.36922/IJB025360364

Table 6. Overview of regulatory dossier types and their applicability in bioprinting

Dossier type	Investigational new drug	Biologics license application	Device technical file	Good manufacturing practice
Applicable region	U.S. FDA	U.S. FDA	U.S./EU	Global
Application type	Clinical trial approval	Marketing authorization (biologics)	Medical device	Manufacturing
Purpose	Required for products containing drugs or biological components (e.g., stem cells or tissues). Must submit to the FDA before the clinical trial begins	If the product passes clinical trials and seeks marketing, a biologics license application must be submitted to the FDA	For acellular or scaffold-based products, such as ECM or electronic sensor components, a technical file must be submitted to a notified body (EU) or the FDA (U.S.)	Required for biological products and some medical devices to ensure consistency, safety, and traceability
Evaluation documents	• Animal toxicology and preclinical safety • CMC (chemistry, manufacturing, control) • Clinical trial protocol	• Clinical trial data (efficacy and safety) • GMP compliance • Risk management system	• Design documentation and engineering validation reports • Safety and performance data • Biocompatibility data • User instructions	• Aseptic processing • Batch record • Equipment calibration and maintenance • Raw material control • Quality control
When required	For products containing allogeneic cells, drug components, growth factors, or extensively manipulated autologous cells	For products containing live cells or therapeutic components (e.g., autologous or allogeneic stem cell skin substitutes, or gene-modified constructs)	For device-classified products such as acellular ECM, three-dimensional-printed scaffolds, and devices with electronic components (but no live cells)	Almost all products intended for human application involving biologics require GMP, e.g., harvested tissues, expanded stem cells, or cell-laden printed constructs

Abbreviations: ECM, extracellular matrix; EU, European Union; FDA, Food and Drug Administration; GMP, good manufacturing practice; U.S.: United States.

that are especially relevant to *in situ* bioprinting platforms where the bioprinter and printed tissue or structure are an inseparable combination product.[100] Australia's Therapeutic Goods Administration has, in line with the International Medical Device Regulators Forum guidance, amended its regulatory framework to specifically cover 3D-printed devices intended for personalized medicine, including devices produced using new technologies such as bioprinting, in acknowledgement of their increasing presence in the clinic and the inherent risks in combining biological material with devices.[101] Despite these advances, there is a constant regulatory delay due to the absence of standardized technical guidelines specific to bioprinting processes. However, in comparison to the more mature standards used to guide traditional biologics and medical devices, bioprinting-specific standards are sparse and narrow in scope. For instance, to date, only extrusion-based bioprinting has seen proposed technical standards, such as ASTM WK65680 (New Test Methods for Printability of Bioinks and Biomaterial Inks) and ASTM WK72274 (Printability of Bioinks for Extrusion-based Bioprinting).[64] Additionally, ASTM F2900-11, a guideline for characterization of hydrogels for their use in regenerative medicine, is often used, but does not cover the full range of new applications of bioprinting. Existing standards are not able to cope with new modalities such as embedded bioprinting (e.g., freeform reversible embedding of suspended hydrogels) or light-based bioprinting, such as stereolithography and volumetric photopatterning, that are becoming increasingly popular due to their high resolution and structural complexity.[102] In addition, existing frameworks are primarily focused on centralized manufacturing and are therefore inadequate for point-of-care bioprinting, where ensuring quality control, sterility assurance, and traceability is crucial in dynamic clinical settings. Thus, parallel to international regulatory harmonization, technical specifications must be revised and expanded for future safety, consistency, and cross-border interoperability of bioprinted therapies.

Good Manufacturing Practice compliance of bioprinted products is a unique task due to the dynamic, personalized, and often decentralized nature of production. In Europe, ATMPs are subjected to EudraLex Volume 4, Annexes 1 (Manufacture of Sterile Medicinal Products) and 2 (Manufacture of Biologically Active Substances and Medicinal Products for Human Use), which emphasize aseptic processing, validated cleaning procedures, and risk-based environmental monitoring. The additional requirements of Grade A/B clean areas during bioink deposition increase implementation challenges, especially on *in situ* platforms. In the United States, traceability, donor screening, and adverse event reporting are required for

Table 7. Regulatory pathways and dossier requirements for bioprinted skin products under the Food and Drug Administration and the European Medicines Agency frameworks

Pathway	Condition	Regulatory route	Dossier required
Path A (Simplest and least stringent regulatory route)	Autologous, minimal manipulation, *in situ*, no drug/electronics e.g., point-of-care use with autologous ECM directly printed onto the wound	FDA: 361 HCT/P (21 CFR Part 1271)	• GMP-lite • Traceability
		EMA: Hospital Exemption (Regulation (EC) No 1394/2007)	• National authority approval • Hospital-grade GMP • IRB/Ethics oversight
Path B (Full regulatory pathway for biologics)	Allogeneic or more-than-minimal manipulation (culture or gene modification) e.g., centralized bioprinting using expanded cells or allogeneic stem cells	FDA: IND → BLA (351 Biologic, regulated under Section 351 of the Public Health Service Act)	• IND • BLA • GMP-full
		EMA: ATMP Central Route	• CTA • ATMP • EU-GMP
Path C (Combination product with drug or electronic components)	Any path + Drug delivery or Electronics e.g., smart skin bioprinting with sensors, growth factors, or antibiotic gels	FDA: Combination product (Biologic + Medical device)	• IND • BLA • Device technical file • GMP (21 CFR 210/211 + 21 CFR Part 4) • QSR (21 CFR 820)
		EMA: ATMP + Medical Device Regulation (EU 2017/745)	• CTA • ATMP • Device technical file • EU-GMP (EudraLex Vol 4, Annex 13) • MDR QMS (ISO 13485)
Path D (acellular, device-based product)	Acellular products or decellularized matrix only e.g., scaffold-based skin substitutes without live cells	FDA: 510(k) or De Novo	• Device dossier (510(k) or De Novo) • Biocompatibility report (ISO 10993) • QSR (21 CFR 820)
		EMA: CE-marked device under MDR (EU 2017/745)	• Technical file (Annex II of MDR) • CER • CE mark under MDR • QMS/ISO 13485

Abbreviations: ATMP, advanced therapy medicinal product; BLA, biologics license application; CE, Conformité Européenne; CER, clinical evaluation report; CFR, Code of Federal Regulations; CTA, clinical trial application; EC, Ethics Committee; ECM, extracellular matrix; EMA, European Medicines Agency; EU, European Union; FDA, Food and Drug Administration; GMP, good manufacturing practice; HCT/P, human cells, tissues, and cellular and tissue-based products; IND, investigational new drug; IRB, Institutional review board; ISO, International Organization for Standardization; MDR, Medical Device Regulation; QMS, quality management system; QSR, quality system regulation.

both 21 CFR Part 210/211 (biologics) and Part 1271 (HCT/Ps), and innovative solutions such as closed-cartridge systems, single-use sterile nozzles, and real-time particle counters are helping to ensure asepsis in the operating room.[69,103] Some institutions are considering GMP-in-a-box models—cleanroom-grade modules rolling in next to surgical theatres. Furthermore, quality by design and process analytical technology are currently being explored to track print fidelity, nozzle temperature, and shear stress, all of which affect cell viability.[104,105] As regulators start acknowledging decentralized constructions for point-of-care applications, it is necessary to develop clearer GMP pathways for mobile bioprinters.

Ethical oversight in bioprinting will need to consider the dual complexity of the cellular content and dynamic manufacturing. Products that are autologous and minimally manipulated might qualify for expedited Institutional Review Board review, particularly if processed within the same surgical session (per FDA's 21 CFR 1271.15).[69,70] Most bioprinted skin constructs are beyond the threshold structure, where expanded cell culture, allogeneic components, or artificial intelligence (AI)-guided wound modeling are used, thereby requiring full Institutional Review Board or Ethics Committee scrutiny. There are also new issues of digital accountability, as patient imaging data for wound modeling must be General Data Protection Regulation or Health Insurance

Portability and Accountability Act compliant, especially as it may be stored in cloud-based planning systems.[106,107] Additionally, algorithmic bias in wound shape mapping or bioink distribution creates new dynamics of ethical accountability, where transparent validation and oversight of the operator(s) is needed. Informed consent becomes complicated when constructs include donor-derived or gene-edited elements or when devices are applied in an emergency, where it is challenging to give preoperative counseling. These types of scenarios require strong ethical protocols, as well as interdisciplinary oversight to ensure patients' safety, data security, and equitable access.

Ultimately, what is needed is not only better technology but also stronger infrastructure. This hybrid nature of bioprinted skin creates a need for regulatory frameworks to adapt to the unique circumstances.[108] Manufacturing platforms need to be designed with compliance and scalability in mind.[109,110] Cooperation across disciplines between engineers, cell biologists, regulators, and clinicians must be implemented. Until these challenges are resolved, even the most scientifically promising constructs may remain stuck in the pre-clinical pipeline. Bioprinting has demonstrated to us what is possible; the task now is to make it viable and legally accessible to the patients who need it the most.

2.4. Patient stratification and wound complexity

Not all wounds are the same, and neither should be treatment. In skin bioprinting, patient stratification is more than clinical categorization; it is a roadmap for tailoring biofabrication strategies to real-world complexity. Whether it is an extensive, third-degree burn wound or a diabetic ulcer that is healing slowly, each type of wound presents its own biological, mechanical, and logistical challenges.

Consider, for example, extensive burn injuries. These are not only large in surface area but often involve volatile wound environments—acidic pH, high protease activity, dehydration, and thermal stress.[111,112] That is why ink stability becomes the main technical bottleneck. Unlike standard inks, which are stored in a laboratory environment, bioinks used in this process must withstand printing times, high ambient temperatures, and biochemical chaos, while still maintaining cell viability and structure.[113] If the ink breaks apart in the middle, then the entire treatment is compromised.

Chronic ulcers, such as diabetic foot wounds, present a different type of challenge. These wounds are typically irregular in shape, poorly perfused, often infected, and surrounded by fibrotic tissue.[114,115] Precision is of paramount importance, but the execution of *in situ* printing becomes difficult in such non-ideal microenvironments. Any minor deviation of the nozzle traveling or deposition speed will lead to uneven or cell loss. The inflammatory milieu that is constantly present may negate any regenerative advantages, making these wounds not only challenging to treat but also difficult to heal.

In battlefield or field-trauma settings, portability is paramount. But most current bioprinters are not built for dusty, humid, and temperature-variable environments. Their dependence on stable electricity, controlled sterile conditions, and vibration-free operation means that they are not suitable for real-life trauma zones.[116] The technical bottleneck here lies in ruggedizing the system—creating compact, pre-calibrated devices that can be plugged in and print even on a moving vehicle or field hospital. It is not only about miniaturizing the technology, but also about making it more resilient.

Esthetic dermal repair, such as scar revisions and cosmetic skin restoration, presents a different challenge.[117,118] Here, the urgency is not the driving factor; rather, it is the demand for perfection. If there are minor discrepancies in print resolution, texture, or pigmentation, then the results are less than ideal. Adding to that, the regulatory bar is higher for non-life-threatening indications, especially when long-term cosmetic effects are involved. The cost–benefit ratio becomes a critical issue, confronting companies with difficult questions about insurance coverage, patient out-of-pocket costs, and whether the investment can ultimately be justified.

2.5. Clinical and emergency integration

Regardless of its technological novelty, a solution that cannot be integrated into established clinical workflows is unlikely to find adoption in the operating room. One of the biggest hurdles for skin bioprinting is not the bioinks or the cells—it is the system-wide integration of how this technology fits into surgical routines, trauma protocols, and emergency timeframes.

In elective or scheduled surgeries, there is at least time to plan, prepare the printer, run sterility checks, and align the construct design with imaging. However, such cases remain the exception rather than the rule. Burn care is a race against time—early wound coverage within 48–72 hours can make a difference between survival and sepsis.[4,119,120] In battlefield trauma scenarios, clinicians must contend with chaotic environments, limited sterility, unreliable power sources, and the necessity of operating within minutes. In these situations, even the slightest delay in operating a bioprinter or calibrating a nozzle is clinically unacceptable.

Additionally, surgical teams also possess limitations. Bioprinting cannot require numerous additional steps or reliance on specialized personnel beyond those already

available within the hospital. Seamless integration requires that the device be intuitive, fast, and readily deployable in a plug-and-play manner.[121,122] If the printer cannot be used by a trained operating room staff with minimal training (and without halting/slowing the flow of the surgery), then it is not ready to be integrated in the operating room. Most current systems are too fragile, bulky, or slow for such applications.

Moreover, logistics is also a key challenge. Sterile packaging, cell storage, power management, and digital design transmission must be standardized before bioprinting can be routinely used in trauma bays or burn units. Workability alone is insufficient as the printer must be able to survive transport, sterilization cycles, and sudden deployment on a 24/7 clinical clock.

Additionally, if complications arise during printing—such as a printer jam, construct delamination, or bioink batch failure—the question of accountability becomes critical.[123] Hospitals will not purchase systems without clear standard operating procedures, contingency plans, and regulatory coverage. In many jurisdictions, this remains a regulatory grey area. Ultimately, successful clinical integration depends less on continuous innovation and more on effective simplification. Skin bioprinting does not need to revolutionize the operating room; it needs to integrate into it seamlessly. Until then, even the most advanced bioprinted skin may never leave the benchtop.

2.6. Technological readiness and operative integration

In the case of skin bioprinting, being technology-ready entails not only that the device functions properly, but also that the entire system can be implemented seamlessly within existing clinical workflows. Most existing bioprinting systems work well in controlled lab settings, but as they move into real-world surgery, challenges rapidly accrue.

First, there is the issue of real-time scanning and printing.[124] In actual surgical scenarios, everything happens on the clock. Patients are anesthetized, and there is minimal time to scan the wound, model the defect, plan the print path, and begin printing. This entire process needs to be seamless and fast. However, most currently available imaging devices are not geared toward high resolution, low latency, scanning in dynamic wound sets that might be actively bleeding or changing. Any delay or data error can throw the whole workflow off balance.

Subsequently, there is the printing itself. Technical accuracy alone is not enough, as the printer must be compact, modular, and foolproof.[125,126] Operative teams cannot afford to take time out to manually calibrate the print head, resolve temperature drift, or change materials mid-surgery. The system needs to be smart enough to auto-adjust parameters and simple enough to be operated by trained surgical staff—not engineers—in a high-pressure setting. If it cannot be handled like any other surgical tool, it will not be adopted.

Another huge challenge is integration with the current operating room infrastructure. This is more than installing a printer in the sterile field. Printers must be synced with hospital information technology systems, extracting imaging data from picture archiving and communication systems, complying with sterile packaging protocols, and powering up on standard operating room outlets without risk of voltage sags or overheating.[124]

Another often-overlooked challenge is post-operative data capture and traceability. Bioprinted grafts are not a one-and-done treatment—they require follow-up, performance monitoring, and digital documentation.[124,127] The opportunity of iterative improvement and regulation compliance is lost if there are no integrated data logging, cloud synchronization, and feedback integration systems in place. In short, every print should have a digital footprint.

From scanning and modeling to printing and intraoperative execution, every part of the bioprinting workflow must reach a level of operational simplicity before it can truly enter the operating room. Skin bioprinting does not need to reinvent the surgical process—it needs to fit into it, quietly and efficiently. The point at which it is no longer treated as a centerpiece but instead functions as a routine tool on the operating room tray will signify its readiness for clinical integration.

2.7. Cost-benefit considerations and reimbursement barriers

Regardless of how advanced skin bioprinting becomes, it will not achieve mainstream adoption unless it is economically viable—for hospitals, payers, and patients. Right now, one of the biggest challenges is cost. Bioprinters are not cheap, whereas bioinks are specialty products, and cell expansion under GMP is resource-intensive.[128] Additionally, the requirement for trained personnel, validated cleanroom protocols, and potentially downtime for calibration or quality control measurements increases the overall cost.

Compared to the gold standard—autologous STSG—STSG has a low material cost and decades of clinical familiarity.[129–131] It does not need sophisticated hardware or involve much regulatory navigation. However, it possesses several limitations, such as donor site morbidity, limited availability of grafts in extensive burns, recurrent surgery, increased length of hospital stay, and often less than optimal esthetic or functional outcomes. With additional rehabilitation time, wound care supplies, and

complications, such as infection or hypertrophic scarring, the cost of STSG increases.

Skin bioprinting, by contrast, offers the promise of one-and-done treatments.[121,122,132] Personalized constructs could decrease the number of surgeries, accelerate epithelialization, decrease the risk of infection, and potentially shorten Intensive Care Unit time. For complex or pediatric cases, this could equate to significant long-term savings. However, currently, these advantages are just theoretical in the absence of extensive clinical data.

Reimbursement presents another challenge. Currently, no standardized coding or payment structure exists for bioprinted grafts, leaving payers uncertain whether to classify them as tissue grafts, medical devices, or cellular therapies. Unclear costs associated with implementing bioprinting, even if hospitals are willing to take on the investment, they cannot be assured of recouping expenses. In the absence of reimbursement, patients are left to pay the cost (not viable for the majority of people, particularly in low-resource environments).

Cosmetic and elective uses—such as scar revision or pigment correction—face an even steeper hill,[117,118] which are often not covered by insurance. In spite of the ability of the technology to provide outstanding esthetic outcomes, the market for such applications is limited unless the cost decreases or value can be demonstrated.

To move forward, bioprinting needs a better value proposition: not just faster healing, but measurable cost offsets.[133] Reduced length of stay or fewer complications, or an earlier return to work, may help to justify reimbursement. A key part of building this case will be through collaboration with payers, health economists, and real-world data studies. In the end, bioprinting will succeed not merely by producing superior skin, but by demonstrating that the value of the skin justifies its cost. Until this threshold is met, even the most elegant constructs will falter in their justification for employment in a cost-sensitive health care system.

3. *In situ* bioprinting in wound medicine: Opportunities for burn care translation

Bioprinting technologies have evolved rapidly in recent years, and their clinical relevance is no longer confined to laboratory benchtops. The field has traditionally been dominated by *in vitro* bioprinting (constructing skin equivalents under controlled conditions before implantation).[134] These approaches provide unprecedented control over structural fidelity, cell positioning, and maturation conditions. Layered bilayered grafts, vascularized skin equivalents, and pigmented or hair follicle-containing constructs have all been achieved through *ex vivo* fabrication, using extrusion-based, inkjet, or laser-assisted techniques. In this context, recent advancements in 3D bioprinting have led to a vast expansion of the field of engineered skin constructs by embedding complex cell lineages, vascularization techniques, and functional appendages. Baltazar *et al.*[59] demonstrated a multilayered, vascularized skin graft composed of keratinocytes, fibroblasts, endothelial cells, and pericytes, which achieved perfusion and host integration *in vivo*, marking a significant step toward clinically relevant skin substitutes. de Bengy *et al.*[135] developed a 3D *ex vivo* sebaceous gland model that preserved sebocyte lipid metabolism and function for over 6 weeks, opening new directions for studying glandular skin physiology and drug screening. In a biomimetic approach to recreating dermal papilla cells and spatial follicular organization, Abaci *et al.*[55] were able to recover the *de novo* hair follicle formation in human skin constructs. Min *et al.*[136] demonstrated the *in vitro* bioprinting of a biomimetic skin model containing melanocytes that successfully recapitulated UV-independent pigmentation patterning—a crucial step forward in modeling skin color and its associated diseases. In the same line, Yamauchi *et al.*[137] used muse cells to construct pigmented 3D human skin, in which endogenous adult stem cells were able to regenerate melanocytes, keratinocytes, and fibroblasts in an integrated scaffold. Kolesky *et al.*[138] recently presented a paradigm change in thick tissue engineering by co-printing multiple cell types together with perfusable vasculature and keeping tissues thicker than 1 cm viable and functional beyond 6 weeks. Huang *et al.*[54] designed a 3D-printed ECM that mimicked the glandular niche and enabled epithelial progenitor cells to differentiate into SG lineages both *in vitro* and *in vivo*—demonstrating how spatially defined biochemical cues can dictate lineage-specific outcomes. These advances are visually summarized in Figure 2, in which the central panel highlights the multilayered vascularized graft by Baltazar *et al.*[59]. The insets around it illustrate specialized constructs, such as biomimetic pigmentation models,[136,137] sebaceous gland analogs,[135] *de novo* hair follicle formation,[55] perfusable thick tissue,[138] and spatially guided sweat gland differentiation.[54] Clinically, this figure highlights the increasing potential of *in vitro* 3D bioprinting for the recreation of functional skin constituents with a growing level of fidelity and complexity. However, as visually compelling as these developments are, they are limited by factors such as scalability, sterility requirements, and the way that static constructs can be adapted to dynamic environments such as a patient's wound.

In vitro constructs are frequently subject to complex culture requirements, bioreactors, prolonged

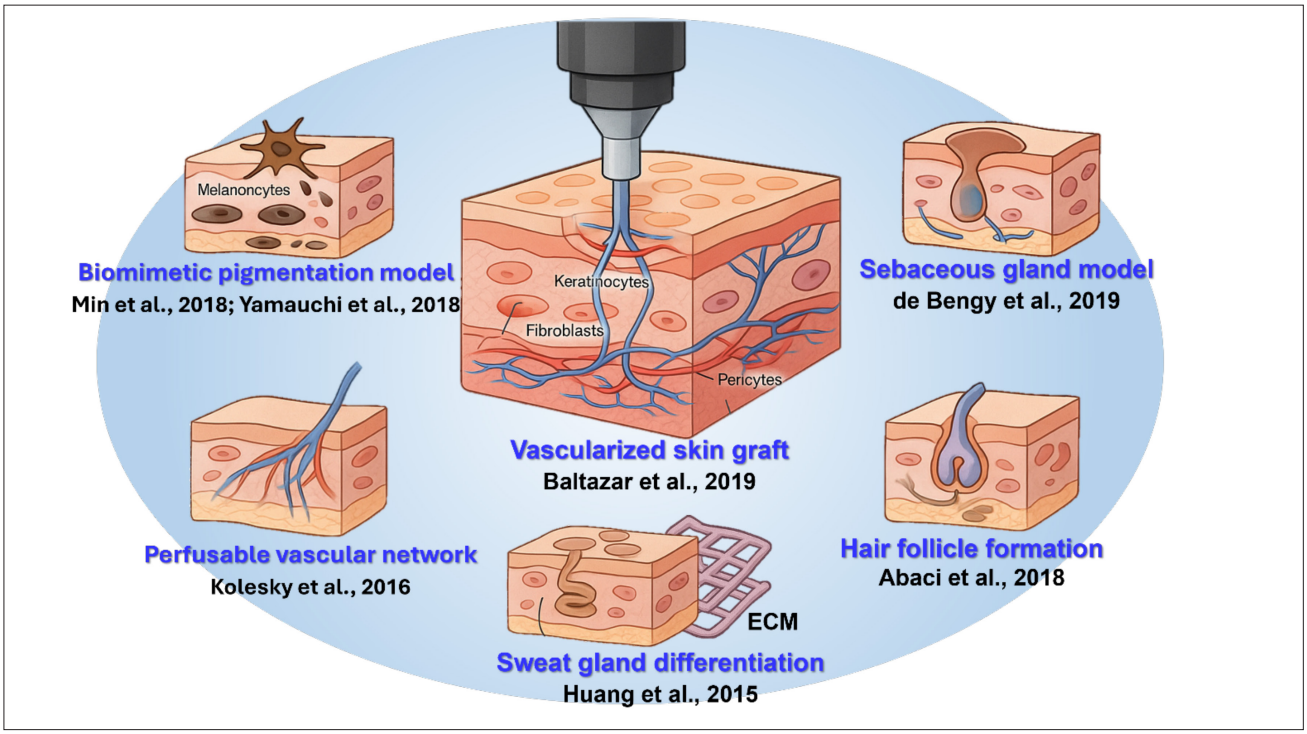

Figure 2. Recent advances in three-dimensional (3D) bioprinting for engineered skin constructs. This illustration highlights key breakthroughs in 3D bioprinting of human skin tissue. The middle panel shows the multilayered, vascularized skin graft grown by Baltazar *et al.*,[59] incorporating keratinocytes, fibroblasts, endothelial cells, and pericytes, and showing successful *in vivo* perfusion and host integration, a key milestone toward clinical skin substitutes. Surrounding insets depict complementary advances: biomimetic pigmentation models using melanocytes,[136,137] an *ex vivo* sebaceous gland model maintaining sebocyte function,[135] hair follicle formation via dermal papilla restoration,[55] perfusable vascular networks in thick tissues,[138] and spatially guided sweat gland differentiation via engineered extracellular matrices (ECM).[54] Figure created using illustrations generated via ChatGPT (OpenAI image tools), with final layout and annotations edited in Microsoft PowerPoint.

preconditioning, and cryopreservation, which are factors slowing down the delivery to the clinical setting.[139] In addition, scaling up to large surface areas (e.g., for extensive burns) is logistically, sterility, and storage challenging. More importantly, the static geometry of *in vitro* grafts cannot accommodate the dynamic irregularities of wound beds in the real world.

A number of bioprinting modalities have recently been revolutionized *in vitro*, including extrusion-based, inkjet, and laser-based bioprinting, all of which feature different advantages in terms of printing accuracy, resolution, and bioink compatibility.[140–142] Extrusion-based bioprinting, for example, enables printing of high-viscosity bioinks and multicellular structures, which makes it suitable for dermal-epidermal layering. Inkjet printing is fast, and viable cells can be deposited, but only over a limited viscosity range and vertically. LAB provides high precision with low shear stress induced by a nozzle, which is appropriate for spatially delicate structures such as melanocyte patterning or microvascular network bioconstruction.

However, *in vitro* bioprinting is still limited by being static and pre-manufactured.[143–145] Models are created in perfect laboratory conditions that are optimized for sterility, nutrient supply, scaffold support—but rarely mimic the complex, heterogeneous nature of real wound environments. Additionally, the time of bioreactor conditioning, vascularization, and post-print maturation, as well as the infrastructure the processes demand, creates delays that are incompatible with acute clinical situations such as burn trauma, where time is of the essence. These limitations show the increasing demand for bioprinting platforms that can function beyond the walls of the controlled laboratory.

This is the paradigm that *in situ* bioprinting redefined, not by replacing the *in vitro* strategy, but by translating bioprinting to an on-demand, in-theater therapeutic device. It allows printing of bioactive materials, cells, or matrix-mimicking hydrogels directly on the wound bed without the need for pre-cultured grafts. This shift from construct fabrication to real-time tissue reconstruction offers distinct advantages for burn care.

3.1. The potential of *in situ* bioprinting in burn medicine

Speed matters when treating burn injuries. Severe burns need early coverage of wounds (preferably within 48–72 h) to avoid fluid loss, infection, and systemic complications.[2,120,146] Traditional grafting procedures often have several delays, such as donor site harvest, graft preparation, and transfer.[120] In contrast, *in situ* bioprinting enables on-site, direct deposition of cells and biomaterial without lengthy preparation and enables real-time tissue fabrication directly onto the wound bed.[124,147]

The other key strength is customization. Burn wounds are rarely uniform—they are large, irregularly shaped, and biologically hostile. *In situ* systems can digitally scan wound topography and print constructs that match the wound's exact shape, depth, and geometry, layer-by-layer.[140] Not only does this customized fit aid in graft integration, but it also minimizes material wastage and handling errors.

This method is also minimally invasive and repeatable. Unlike autografting, which involves sacrificing healthy skin, *in situ* printing avoids donor site morbidity, a significant advantage for patients with large total body surface area burns.[140] Moreover, the process is inherently modular, allowing for repeated applications as the wound evolves.

To better contextualize the clinical advantages of *in situ* bioprinting in burn care, it is essential to contrast it with the more traditional *in vitro* bioprinting approach. While both are focused on fabricating functional tissue constructs, their operational workflows, clinical readiness, and applications are very different. *In vitro* bioprinting is often performed by building up tissue constructs *in vitro* before implantation, while *in situ* bioprinting could directly fabricate tissue constructs in real time on wound beds. As described in Table 8, significant differences are (i) printing location: sterile lab versus operating room, (ii) personalization level: scaffold is predefined versus real-time 3D scan-based structure, (iii) cell viability: decreased *in vitro* due

Table 8. Comparative overview of *in vitro* and *in situ* bioprinting approaches

Aspect	*In vitro* bioprinting	*In situ* bioprinting
Definition	Fabrication of tissue constructs in a controlled lab environment before implantation	Direct printing of biomaterials and cells onto or within the defect site in the body
Environment	Sterile, static, and tightly controlled laboratory or cleanroom settings	Dynamic, often irregular, and biologically active surgical or wound site
Application timing	Construct is printed first, then implanted later	Printing occurs intraoperatively or immediately at the point of care
Surface stability	Stable, flat substrates (e.g., glass slides, petri dishes)	Soft, curved, moving tissues (e.g., breathing lung, beating heart, bleeding wounds)
Workflow	Computer-aided design modeling → Print → Mature in incubator → Implant	Scan → Model → Print → Crosslink (real-time, on-site)
Time to treatment	Requires time for pre-fabrication and post-printing maturation	Enables rapid or immediate wound coverage
Precision and resolution	High precision is possible due to a stable environment	Moderate to high; depends on scanner accuracy and motion compensation
Device complexity	Often complex and large-scale bioprinters	Ranges from simple handheld tools to advanced robotic platforms
Surgeon control	Surgeon performs implantation, but not fabrication	A surgeon may guide printing directly (handheld) or through a robotic interface
Customization	Generic constructs may not match patient-specific anatomy	Fully personalized constructs based on real-time wound geometry
Use case examples	Organ-on-chip, tissue graft production, lab-grown cartilage or skin	Burn wound repair, bone defect filling, corneal repair, and muscle regeneration
Crosslinking method	Performed post-printing using light (ultraviolet/visible), thermal, ionic, or enzymatic methods in a controlled environment such as an incubator or ultraviolet chamber	Requires integrated, real-time crosslinking using on-site UV/blue light, thermal control, ionic co-axial extrusion, or enzymatic triggers
Portability	Low; equipment is lab-bound	High (handheld) to moderate (robotic); designed for intraoperative use
Scalability	Suitable for mass production of constructs	Tailored for individualized therapy
Challenges	Vascularization, maturation before implantation	Bioink retention on wet/moving surfaces, sterilization, and accuracy under surgical conditions
Clinical readiness	More mature in terms of regulatory pathways and manufacturing	Rapidly evolving, promising for point-of-care regenerative therapies

to time/storage versus increased *in situ* by immediate use, and (iv) integration pathway: separate implantation versus seamless deposition. These differences are shown in **Table 8**, demonstrating the differences between these two modalities that play important but separate yet complementary roles in translational skin medicine. *In vitro* printing is still suitable for engineered grafts with complex stratification and maturation, and long-term maturation; *in situ* bioprinting, in contrast, provides a handy, portable, on-demand system in the closed wound environment.

A clear example of the translational potential of *in situ* skin bioprinting was shown by Cheng *et al.*,[25] who used a porcine full-thickness burn model to demonstrate a handheld bioprinting instrument for depositing wound-conformal skin precursor sheets directly onto sites of injury. This hand-held platform combined 3D scanning with precise deposition of dermal and epidermal cell-laden biomaterials, fitting snugly to the complex geometries of deep burns. Re-epithelialization, vascularization, and wound contraction returned at a quicker pace in treated wounds versus control groups. Notably, the device was suitable for point-of-care use, obviated traditional graft fabrication workflows, and was feasible in clinically relevant, large animal models.

3.2. Technical architecture of *in situ* bioprinting

In situ bioprinting systems can be classified by deployment modality (robotic-assisted vs. handheld) and printing mechanism (extrusion-based, inkjet, or laser-assisted).[18,19,147] Most current *in situ* systems, whether robotic or handheld, rely on extrusion-based techniques due to their robustness and compatibility with cell-laden bioinks. Inkjet and laser-assisted deposition techniques are still in their clinical translation, but they offer promise for smaller diameter applications such as fine pattern deposition or vascular microstructure.

3.2.1. Deployment modality

In situ bioprinting is emerging as a paradigm-shifting approach in regenerative medicine, where biomaterials and cell-laden constructs can be fabricated and functionalized in real time and customized for specific wounds or tissue defects. Within this broad field, two key classes of systems have been established based on the interface, level of automation, and clinical applicability, namely hand-held bioprinting devices and robotic-assisted systems.[18,19,147] These categories embody two philosophies of surgical integration: one predicated upon precision through automation, the other simple portability.

3.2.1.1. Robotic-assisted in situ bioprinting

Robotic-assisted systems represent the high-tech frontier of *in situ* bioprinting.[148–150] Typically, these configurations have a robotic arm of multiple degrees of freedom (DOF) attached to modular print heads capable of extrusion, inkjet, or even LAB. The high precision positioning and controlled movement of the robotic arm in 3D space are relevant to complex and irregular wound geometry.

In the robotic-assisted modality, the standard workflow starts with 3D scanning of the defect site by structured light, stereo vision, or light detection and ranging (LiDAR).[151] The resulting digital mesh is then read into a computer-aided design (CAD) software and translated into G-code, which generates a layer-by-layer printing path.[152] This automation allows high reproducibility and spatial accuracy, which is especially useful for microsurgical applications such as corneal, cartilage, and even neurosurgeonic bioprinting.[148,153]

An example of such robotic-assisted *in situ* bioprinting was recently demonstrated by Zhao *et al.*,[23] who have designed a custom extrusion-based robotic arm platform with dual-nozzle bioprinting and real-time 3D scanning. This system enabled platelet-rich plasma augmented bioinks to be deposited one layer at a time directly onto the full-thickness wounds of rats. The automated path planning and nozzle switching enabled fast multilayer building, leading to enhanced wound closure, vascularization, and less inflammation.

However, robotic systems have major caveats.[148] These devices are expensive, time-consuming to learn, and must be sterilized, while requiring operating room space, which are barriers to clinical implementation. These systems often need a team of engineers and clinicians to tune them and make them work properly. Furthermore, deformation of tissue, wet surfaces, and varying intraoperative conditions can impact fidelity unless adaptive compensation schemes are available.

To effectively tackle these issues, adaptive printing frameworks have been suggested in which the feedback from the scanning system can be used to adapt the deposition trajectory in real-time. This dynamic correction allows the robotic printer to track along the contours of living tissue, even when there is a small motion artifact. Additionally, incorporation of magnetic or electric field-assisted crosslinking to improve scaffold alignment and mechanical robustness during deposition is being investigated.[154]

Taken together, robotic-assisted bioprinting has excellent potential for complex tissues with multiple layers, especially in deep tissue or high-resolution reconstruction applications. Its long-term potential is the integration into minimally invasive robotic surgery platforms, in which the

internal bioprinting is carried out through the laparoscopy or endoscopy.[155,156]

3.2.1.2. Handheld in situ bioprinting

Handheld bioprinting is an easier-to-use and more accessible technology that foregoes automation for portability and intuitive control. These devices are typically pen-like or pistol-grip tools containing motorized or pneumatic extrusion systems, small cartridge reservoirs, and sometimes integrated light-based crosslinking.[157–159]

Typically, the device is positioned by the operator, usually a surgeon, and its deposition is directed across the target site to provide direct-write fabrication in real time. This makes the use of handheld printers especially appropriate for non-uniform wounds, anatomically challenging areas, or a field setting where it would be impractical to use complete robotic setups.[160–162]

A well-known example of handheld *in situ* bioprinting was shown by Cheng *et al.*,[25] who designed a modified handheld extrusion-like delivery system that can be used with a microfluidic printhead and a compliant silicone wheel. This system allowed the precise deposition of a fibrinogen/thrombin/hyaluronic acid bioink containing MSCs derived from cord tissue (1×10^6 cells/mL) directly on top of full-thickness burn wounds in a porcine model. The device was capable of deposition control, even on inclined surfaces up to 45°, and proved to greatly improve re-epithelialization, neovascularization, and dermal cell repopulation. This study confirmed the potential of wound conformal delivery systems to improve outcomes of healing for complex burn wounds. Importantly, the ease of operation and the small footprint and sterilization capability of the tool also made the tool suitable for point-of-care and on-site use, even in low-resource settings.

The benefits of handheld systems are numerous, including low cost, ease of sterilization, minimal training requirements, and flexibility for a wide variety of clinical settings.[160] They are beneficial in the field of military or disaster response applications, where portability and speed are more critical than micrometer-quality accuracy. Further, these instruments allow on-the-spot manipulation by clinicians in response to dynamic changes in wound contour due to bleeding, swelling, or debridement.

However, handheld printing is not without challenges.[163] Without automated control, variable cut of uniformity across constructs is possible, particularly with larger wounds. Operator fatigue, variable speeds, and no feedback loops can reduce reproducibility. To compensate for this, some teams have incorporated planar guide rails or rotating wheels that help to keep the nozzle stable and the filament thickness consistent over large surfaces.

Furthermore, the resolution of handheld systems is mostly determined by nozzle diameter and extrusion rate, which might not be comparable with the ultra-fine control available from the robotic platforms.[158] However, ongoing advancements—such as multi-material planar nozzles and modular handheld print heads—are progressively narrowing this gap.

3.2.1.3. Toward a hybrid future

Despite the distinctions between robotic-assisted and handheld modalities, each holds an important and complementary place in the growing ecosystem of *in situ* bioprinting. While robotic platforms are great for complex multi-tissue reconstructions, handheld tools are ideal for single-tissue reconstructions and in situations that need a rapid response time.

It is conceivable that, in the future, these systems will converge, bringing together technological advances into more unified and clinically deployable platforms. For instance, semi-automated robotic-assisted handheld devices could integrate surgeon-controlled motion with real-time stabilization algorithms.[164,165] Meanwhile, both AI-based path correction and smart bioinks and tactile feedback may further endow handheld printing with machine-like accuracy.[166–168]

Ultimately, robotic versus handheld *in situ* bioprinting should be dictated clinically through wound complexity, anatomical location, surgical logistics, and desired resolution. As these technologies mature, they are poised to expand the surgeon's repertoire—from mobile, pen-like printers to fully autonomous bioprinting stations—each designed with the specific challenges of regenerative care in mind.

3.2.2. Printing mechanism

In addition to deployment modality, *in situ* bioprinting systems are also defined by the underlying printing mechanism. Each method, extrusion-based, inkjet, and laser-assisted, has its own advantages and limitations with respect to resolution, bioink compatibility, mechanical stability, and clinical adaptability.[19] While extrusion-based bioprinting is still the most mature and widespread technique with regard to *in situ* applications, other mechanisms like inkjet and laser-assisted printing are in constant development, especially for niche or high-precision applications. As summarized in Figure 3, the broad bioink compatibility and simplicity of operation in extrusion-based bioprinting make it ideal for deep wound reconstruction, with associated trade-offs in resolution and cell shear stress. Inkjet printing, in contrast, has a high resolution and minimal cell damage and will therefore be well-suited for patterning of epidermis

or printing of appendages, yet is hindered by the low viscosity requirement and risk of clogging. In contrast, LAB provides unsurpassed precision at the microscale, which is suitable for a vascular or neural construct but is restricted due to bulky optics and potential damage to cells from elevated temperatures. The combination of modality-specific features (resolution, viscosity compatibility, cell viability, and clinical adaptability) reported in Figure 3 is graphically summarized as a functional scheme of their involvement in different conditions of wound healing. This comparative framework not only facilitates technology choice for specific wound types but also suggests practical

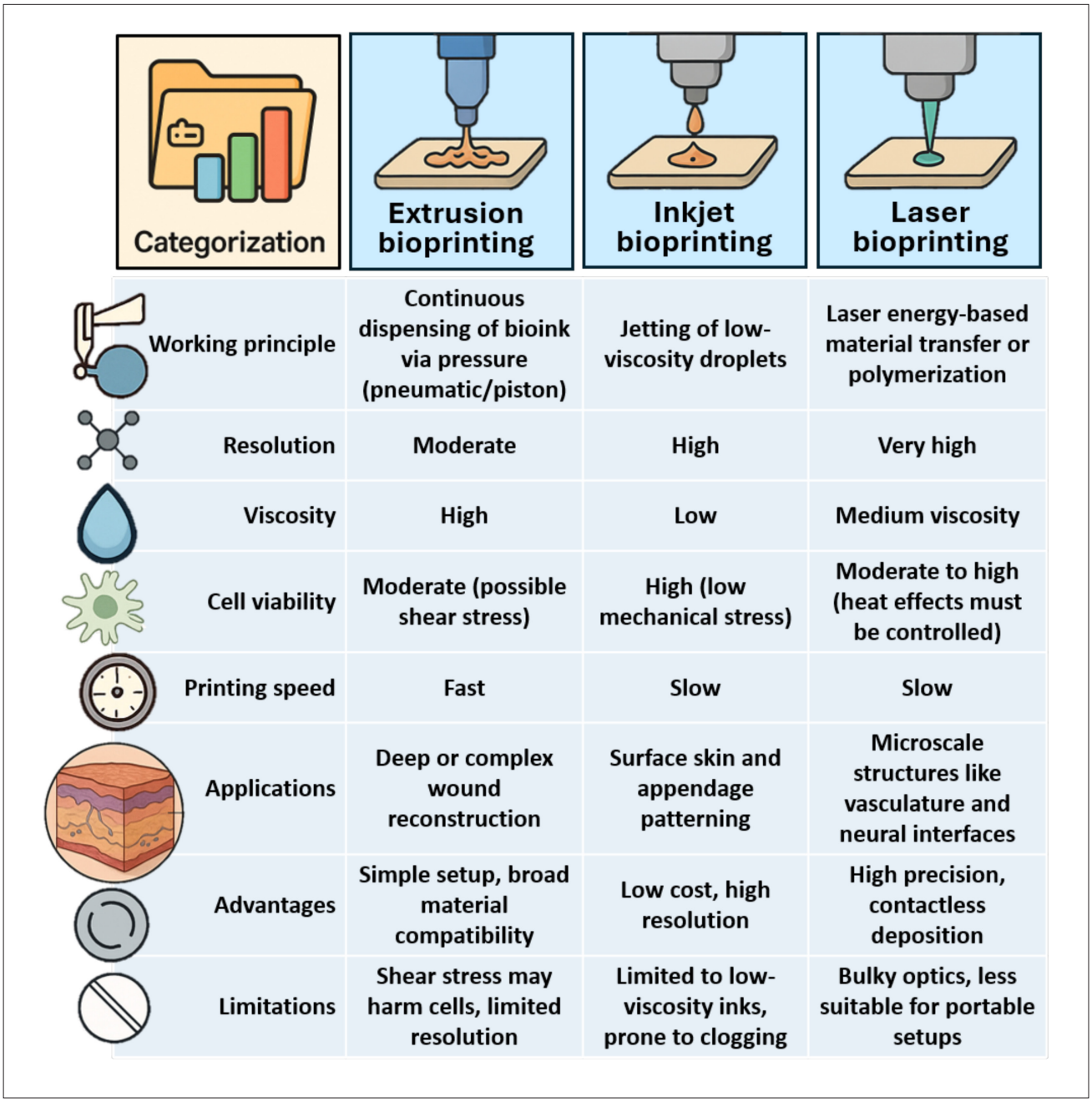

Figure 3. Comparison of bioprinting techniques: extrusion, inkjet, and laser-assisted methods. This figure summarizes the main differences in operating principles, material handling, print resolution, scalability, and limitations of the three main bioprinting approaches currently used in tissue engineering and *in situ* applications. Figure created using illustrations generated via ChatGPT (OpenAI image tools), with final layout and annotations edited in Microsoft PowerPoint.

limitations that require attention for clinical translation of *in situ* bioprinting systems.

3.2.2.1. Extrusion-based bioprinting

Extrusion-based bioprinting is the prevailing technology for *in situ* applications due to its robustness, versatility, and ability to process high-viscosity biomaterials, such as bioinks.[169] This method consists of the continuous dispensing of cell-loaded materials from nozzles moved by pneumatic, mechanical (piston or screw), or solenoid-based extrusion systems.[170] In particular, it has proven to be optimal for printing hydrogels like GelMA, alginate, or decellularized ECM that can encapsulate cells and maintain their viability during printing.[113,171]

One of the significant benefits of extrusion-based bioprinting is its ability to supply multiple bioinks at a time through multi-nozzle geometries, allowing for heterogeneous tissue constructs with spatially controlled cell distribution. Its mechanical simplicity and ability to print directly onto deforming and irregular wound beds make it ideal for use with both robotic and handheld *in situ* platforms. Furthermore, its past clinical use in arthroscopic cartilage repair procedures provides clinical analogy and regulatory familiarity that is favorable for translational development.[172,173]

However, the extrusion rate of extrusion-based bioprinting is usually restricted by nozzle diameter, while high extrusion pressure may cause shear stress on encapsulated cells. Despite this, considerable progress in nozzle design, pressure control, and bioink rheology has contributed to improved cell viability and construct fidelity in recent studies.[174–176]

3.2.2.2. Inkjet bioprinting

Inkjet bioprinting entails driving bioink droplets onto a substrate in a controlled delivery, either in a continuous stream or on a drop-on-demand (thermal, piezoelectric, and electrostatic actuation).[177] This method is based on conventional inkjet technology and, as such, benefits from a high number of commercially available components and is thus cost-effective and relatively easy to implement.[178]

High-resolution inkjet-based systems are better suited for patterning low viscosity bioinks in thin coatings. They are beneficial for deposition of growth factors, small molecules, or single-cell suspensions, and have proven potential for the fabrication of epidermal layers and skin appendages. Their low force for deposition reduces shear stress, thereby increasing cell viability.[179]

However, inkjet bioprinting is restricted by strict viscosity requirements of the bioinks, nozzle clogging, and relatively low volumetric throughput.[180] The limitations of this application tend to constrain its use in deeper wounds or high-volume constructs. As a result, inkjet bioprinting is currently more suited to surface-level tissue repairs or adjunctive patterning in combination with other techniques.

3.2.2.3. Laser-assisted bioprinting

Laser-assisted bioprinting utilizes laser energy to print bioink with ultra-high spatial resolution.[181] Typically, laser-induced forward transfer or stereolithography techniques are used to propel or polymerize bioink onto a target substrate.[182] These techniques provide the possibility of microscale patterning where cell placement and tissue architecture can be fine-controlled.[183]

Applications in which laser bioprinting has been particularly successful are those that require high-precision microfabrication, such as vascular microchannels or neural tissue interfaces.[182,184,185] It is suitable for various materials, including photocrosslinkable hydrogels, and has the potential for contactless, non-invasive deposition, an attractive feature in sterile surgical settings.

However, laser bioprinting still has a few challenges to overcome for *in situ* deployment. Laser power or exposure to high-intensity UV light produces heat that can be deleterious to the viability of the cell.[182] In addition, many of the optical systems necessary for laser bioprinting are bulky and not particularly suitable for handheld or portable systems. In future systems, the miniaturization of stereolithographic heads or fiber-optic-based light delivery may be integrated to mitigate these limitations.

3.3. Operational components and workflow integration in *in situ* bioprinting

Beyond hardware classification and printing mechanisms, the performance of *in situ* bioprinting systems depends heavily on the seamless integration of scanning, modeling, printing, and stabilization.[17,143,147,186] This whole pipeline includes scanner modules, printheads, trajectory planning, crosslinking strategies, and ultimately, each of these must operate in real time, and often under unpredictable surgical circumstances. This section describes the fundamental working design framework of how the *in situ* bioprinters move from digital design to biological reality to provide precision tissue reconstruction at the point of care.

3.3.1. From scan to stabilization: A four-step operational pipeline

Nearly every *in situ* bioprinting workflow follows a familiar path: scan, model, print, and crosslink, as depicted in Figure 4. The algorithm begins with the acquisition of the actual topography of the wound in real time. Surface contours, depth, and curvature are obtained by structured light, stereo cameras, or even LiDAR sensors in irregular

and fluid-exposed environments.[187,188] This step is crucial to creating a site-specific framework that informs the remaining steps in the process. The scanned geometry is converted to a printable geometry in 3D printing technology. Using CAD software, the platform creates a path that takes into account material type, layer height, and target tissue areas (spatial map) for multi-material deposition.[189–191] During the printing stage, the printing head (handheld, robotic) moves along the intended pathway layer-by-layer while depositing bioinks laden with cells or acellular scaffolds with millimeter-scale accuracy. Finally, crosslinking or curing the printed structure by light, heat, or ion interaction stabilizes the printed structure and ensures functionality.[192–194] This simplified pipeline allows *in situ* bioprinting to provide precision in high-stakes surgical conditions under real-world limitations. Each of these steps is graphically summarized in Figure 4 and highlights the clinical importance of the presented pipeline: real-time, patient-specific tissue reconstruction is possible at the point-of-care and despite evolving surgical conditions. This modularity and adaptability are further promoted by the visual loop between imaging, biofabrication, and functional stabilization.

3.3.2. Scanner modules: Visualizing before printing

Accurate printing begins with precise visualization. Therefore, the use of scanner modules is necessary for mapping the defect geometry in real time.[195] Most systems today use structured light or infrared depth sensors to generate point clouds of the wound surface.[196,197] For example, a robot-guided 3D scanning platform was presented to enable computer-controlled sub-millimeter wound reconstruction, utilizing a structured-light scanner attached to a 7-DOF arm, which is capable of accurately modeling complex wound geometries such as those caused by chronic ulcers and burn injuries.[198,199] These scanners enable the system to adapt to asymmetric or evolving geometries and develop a wound-conformal deposition plan.

Some higher-end platforms include thermal imaging or multispectral imaging sensors to scan tissue viability before printing.[200,201] More recent systems are using AI-based depth reconstruction to compensate for movement or challenging lighting conditions, producing more accurate surface models for irregular and dynamic wounds.[202,203]

3.3.3. Printhead configurations: Tailoring the tool for the task

The printhead is the interface between the design and the biological delivery of a bioprinting system.[143] Most *in situ* printheads use extrusion-based mechanisms, driven by pneumatic or mechanical pistons to dispense viscous, cell-laden hydrogels.[204–206] While early systems were based on just simple single-nozzle print heads, modern systems include coaxial, multi-nozzle, or modular printheads.[207,208]

Coaxial structures can be used for simultaneous deposition of a bioink core and a shell containing crosslinkers (essential for structure maintenance during extrusion).[209–211] Modular heads take it one step further,

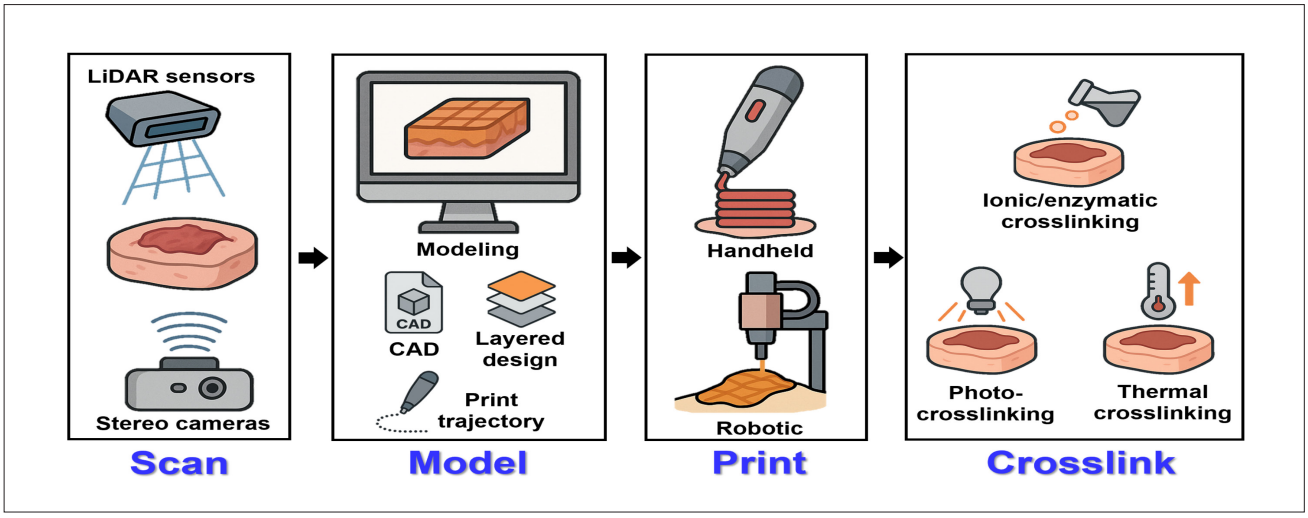

Figure 4. Four-step operational pipeline of *in situ* bioprinting. Schematic representation of the combined workflow of *in situ* bioprinting. The process starts with a scan, during which the geometry of the wound is recorded by light detection and ranging (LiDAR) sensors or stereo cameras. Next, the print trajectory for each wound, modeled according to its topology, is created in the model phase using layered design and computer-aided design (CAD) tools. The print step involves the deposition of bioink using handheld extrusion or robotic extrusion systems. Finally, in the crosslink stage, the printed materials are stabilized using ionic, enzymatic, photo, or thermal crosslinking methods. This four-stage loop allows individual, patient-specific, point-of-care tissue reconstruction in evolving surgical settings. Figure created using illustrations generated via ChatGPT (OpenAI image tools), with final layout and annotations edited in Microsoft PowerPoint.

providing a plug-and-play functionality for various types of materials or cell types, depending on different crosslinking modes. Multi-material ink developments now enable the modulation of the mechanical properties and biological cues of the bioink in real time during printing, providing improved control over tissue architecture, particularly for reconstructing multilayered or mechanically heterogeneous defects.[212]

3.3.4. Trajectory planning: Printing on a living, moving canvas

In vitro bioprinting is typically performed on a static surface, whereas *in situ* bioprinting occurs directly within the dynamic environment of the wound or tissue site. Human tissue is soft, irregular, and frequently in motion due to breathing, a heartbeat, or involuntary muscle contractions. That makes trajectory planning one of the most challenging and distinctive aspects of *in situ* platforms.[213]

Advanced systems now feature adaptive slicing algorithms, which dynamically adjust the print path based on the amount of material available to the printer, providing real-time feedback from the scanner.[214–216] A system that can adapt to variations in tissue topology in real-time and optimize the position, velocity, and angle of the nozzle for consistent print quality, even when used on curved or moving surfaces, has been developed. It relies on sensor readings and feedback control based on machine learning.[217] This *in situ* adaptation is of utmost importance for both the safety and preservation of the structural integrity of the material being worked on, especially when working in proximity to any sensitive structures such as nerves or blood vessels.

Some systems also include predictive compensation by incorporating deformation models to predict motion and pre-adjust trajectories (similar to a global positioning system that reroutes before you encounter traffic).[218] In robotic systems, this is typically associated with closed-loop control that utilizes visual or force feedback for micrometer-scale corrections.

3.3.5. Crosslinking and stabilization: Securing the print

Once bioink is laid down, it must be stabilized immediately—especially in the moist, dynamic environment of living tissue. Crosslinking of the biomaterial ensures that the construct maintains its mechanical structural integrity until cellular integration occurs.

Currently employed methods include photocrosslinking, in which photo-sensitive hydrogels, such as GelMA, undergo polymerization upon UV or blue light exposure.[219–221] Some platforms incorporate light sources into the nozzle tip, allowing for pointwise curing.[185] Another approach, based on the phenomenon of thermal gelation, involved using heated nozzles or cooled wound surfaces to induce gelation in temperature-sensitive bioinks.[206,222]

A common approach in the development of coaxial extrusion architectural designs is to incorporate crosslinkers, such as calcium ions or transglutaminase, into the sheath to facilitate ionic or enzymatic gelation through contact.[211,223,224] A more recent method is stimulus-assisted crosslinking. Recent *in situ* applications have shown that using electric and magnetic fields during deposition can also accelerate crosslink formation, trigger cell orientation alignment, or modulate cell fate decisions without compromising print fidelity.[20] These multimodal strategies go beyond making the material stick; they provide a new level of control over tissue programming at the point of care.

There is no one-size-fits-all implementation for *in situ* bioprinting. Some wounds require robotic precision, while others require quick, handheld agility. What makes next-generation systems powerful is their integration, which combines high-resolution scanning with intelligent path planning, modular printheads, and multimodal crosslinking onto a single, cohesive platform. As these technologies are honed, we are closer to the vision of *in situ* bioprinters that are not simply machines but instead deployed as intelligent surgical instruments to enable real-time tissue engineering at the bedside with patient-specific tissue engineering properties.

3.4. Bioink engineering for on-site applications

While the spotlight in *in situ* bioprinting often falls on the robotics or handheld hardware, the reality is that even the most advanced system is only as good as the material it prints.[17,225,226] Not all bioinks are the same, especially in the clinical or operatorial setting where time is limited, conditions are not well controlled, and the safety of patients is a significant concern. More than just a good bioink, what was needed was a clinically ready, fast-acting, biologically compatible, and truly bedside-operable material. Figure 5 describes six fundamental design principles that are key to the success of *in situ* bioprinting, especially under clinical limitations. These metrics—from *in vitro* performance to biological function—serve as a basis for translating bioinks developed in the lab to a functional therapeutic device.

3.4.1. Ready-to-use and operational stability

In a surgical setting, clinicians do not have time to conduct powder weighing or make last-minute decisions about polymer concentrations. Bioinks, which can be used for *in situ* printing, must be ready-to-use straight out of the package or require minimal preparation, such as gentle warming

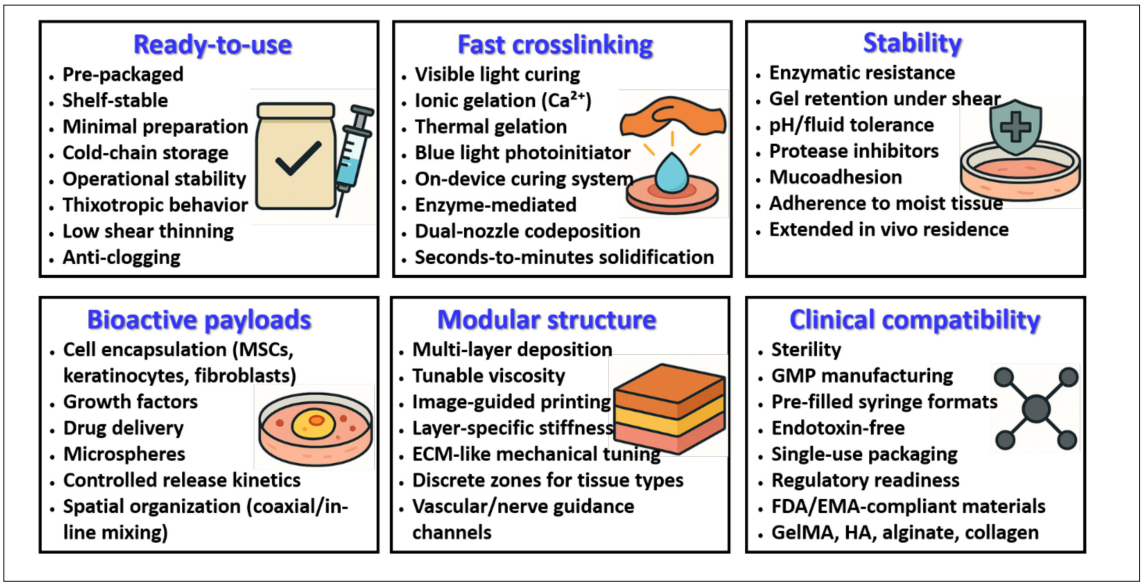

Figure 5. Core design criteria for bioinks in on-site *in situ* bioprinting. The figure maps out the six critical features needed for bioinks as scaffolds *in situ* bioprinting: (i) off-the-shelf ready for immediate clinical use, (ii) rapid crosslinking for dynamic surgical settings, (iii) physical and biochemical stability on inflamed or exuding beds, (iv) adaptability with bioactive payloads such as cells or therapeutics, (v) compatibility with modular and layered tissues, and (vi) clinical-grade safety, sterility, and regulatory compliance. Figure created using illustrations generated via ChatGPT (OpenAI image tools), with final layout and annotations edited in Microsoft PowerPoint. Abbreviations: ECM, extracellular matrix; EMA, European Medicines Agency; FDA, Food and Drug Administration; GelMA, gelatin methacryloyl; GMP, good manufacturing practice; HA, hyaluronic acid.

or a quick vortex following refrigeration. Embodiments that can be stored for an extended time on a shelf without losing functionality, and that can be stored in a cold chain without losing functionality, are desirable, particularly for use in mobile or resource-limited environments.

Of equal importance is the rheological stability of the ink in the printing process. The viscosity should stay consistent, with minimal risk of nozzle clogging or material backflow.[227] Slight variances in temperature or humidity—common in operating rooms—would not affect flow rates. For this reason, pre-tested low-shear-thinning bioinks with high thixotropy are favorites under these circumstances. Such ease of use has a direct impact on emergency burn care situations, where it is crucial to be able to deploy biomaterials quickly.

3.4.2. Fast and field-compatible crosslinking

In situ bioprinting does not take place in the controlled sterility of a laboratory—it unfolds in the complexity and messiness of real wounds. That means bioinks need to solidify fast, ideally within seconds to a few minutes.[228,229] Any longer, and the material risks deforming, sliding, or mixing with exudates on the wound bed. Crosslinking techniques such as visible-light curing, ionic gelation (e.g., Ca^{2+}), thermal gelation, or enzyme-mediated systems are widely used due to their speed, safety, and simplicity.[230-232]

Importantly, these crosslinking mechanisms must be non-toxic and compatible with living tissues.[233] For example, although glutaraldehyde exhibits good bonding strength, it is not suitable for use on live wounds due to its toxicity.[234] Alternatively, new systems use photoinitiators that are activated by low-intensity blue light, allowing rapid crosslinking without heating or damaging surrounding cells.[235]

Handheld platforms usually incorporate on-device light sources or two-nozzle systems that co-deposit crosslinking agents on the fly.[236,237] Regardless of the delivery format, the ink must react quickly and consistently to the trigger without complex timing, guarding, or external gearing.

3.4.3. Stability in challenging wound environments

Burn wounds and other complex defects are biologically hostile environments characterized by inflammation, changes in pH, enzymatic breakdown, and rapid fluid turnover.[2] This means that a bioink must gel and stay gelled even when exposed to proteases, wound exudate, or mechanical shear from dressing changes. Selected examples, showing their strengths in clinical settings and existing limitations that have to be optimized, are summarized in Table 9.

Natural hydrogels, such as alginate, off-the-shelf gelatin derivatives (e.g., GelMA), and hyaluronic acid-based combinations, have proven to be good candidates

due to their ability to preserve their structure under harsh environments.[238,239] Crosslinked hydrogels that remain in a hydrated, semi-solid form despite enzymatic attack are particularly useful. In more advanced formulations, protease inhibitors or enzyme-resistant backbones have been incorporated to increase the residence time of the compound in the body.[240]

Another factor to consider is surface adherence. Bioinks must remain in intimate contact with tissue, even if the substrate is moist or bleeding. Mucoadhesive properties or secondary bonding mechanisms (e.g., fibrin integration) can help keep printed constructs exactly where they are needed.[222,241,242] Several bioinks have been developed with *in situ* usability in mind, designing for fast gelation, printability, and bioactivity. Bioinks that can persist and function in hostile environments within the wound extend the treatment window and reduce the frequency of repeat treatments. Interestingly, a common theme is the trade-off between bioactivity and resilience: bioinks not only have to carry therapeutic agents or cells, but also must stay attached and intact in the dynamic proteolytic environment of chronic wounds.

3.4.4. Bioactive payload compatibility

Beyond serving as a scaffold, bioinks are often expected to carry living cells or therapeutic agents.[128,243,244] More complex than this is the fact that the material must not only be suitable in terms of printing mechanics but also maintain and protect the biological activity.[245,246] Common types of cells include keratinocytes, fibroblasts, MSCs, and even endothelial progenitors for vascularization. The ink must be physiologically isosmotic, facilitate nutrient transport, and protect against the shear injury caused by extrusion.

Additionally, controlled release kinetics, rather than an initial burst release, are essential for bioinks carrying drugs, growth factors, or antimicrobial peptides.[247] Delivery systems or particle encapsulation (e.g., with microspheres) can allow phased bioactivity, particularly for wounds that heal in a stepwise manner.[248–250] Recent work has also investigated the concept of coaxial printing or inline mixing to provide spatial control of bioactive cues, enabling the deposition of epidermal, dermal, and vascular components in specific layers or zones within the same construct.[209]

3.4.5. Modular and multi-layer printing capability

In wound repair, especially in burn wounds, multi-layered tissue structures are often required.[251,252] A single uniform gel is not enough. Instead, bioinks must be formulated to be suitable for modular deposition, i.e., with tunable viscosity, gelation kinetics, and mechanical stiffness to accommodate different tissue strata.[253–255]

For example, a softer hydrogel with nutrients that support epidermal regeneration can be used, whereas a stiffer hydrogel that mimics the ECM supports dermal fibroblasts and vessel ingrowth.[256,257] In more complex reconstructions, separate channels can be printed to guide vascularization or support nerve regrowth.[258,259] For this to work, the ink must remain printable across a range of viscosities, without interfering with the downstream stability of the other layers. In addition, inks for use with image-guided printing systems, where the geometry of a scanned plane determines the nozzle path, must be able to maintain a constant width and fidelity of the filament over increasingly complex paths.[168,260]

3.4.6. Clinical compatibility and regulatory readiness

Ultimately, no bioink—regardless of its level of advancement—can enter clinical usage without meeting the basic standards for sterility, traceability, and safety.[64,82,83] Materials have to be either FDA/EMA compliant for clinical use or at least be made from components of a known regulatory track record.[76,81] That often limits the usage of *in situ*-compatible bioinks to well-studied materials like collagen, gelatin (including GelMA), hyaluronic acid, alginate, or their combinations. Sterilization procedures used (gamma irradiation or filtration) should not affect the functionality of the ink.[82,83] Packaging should be hermetic, single-use, and easy to use, e.g., in pre-filled syringes or cartridges that connect to standard printers. The ability to perform GMP-compliant manufacturing and quality control testing—including endotoxin levels and batch consistency—remains a significant determinant of translational success.[74,75]

In situ bioprinting is as much a materials problem as it is a robotics one. Bioinks for bedside fabrication must strike the right balance between biological performance, physical reliability, and clinical feasibility. As research opens the doors to what can be printed, the challenge is no longer about finding new materials—it is about ensuring they function under pressure, in real time, and in real patients. At their best, the ideal bioinks are not only printable-they are surgical-grade tools, designed to be equally at home on an operating table as they are on the lab bench. Figure 5 is therefore not only a visual checklist to guide ink developers, but also a translational roadmap of steps to ensure that printed materials are effective, safe, and functionally competent at the point of care.

3.5. Preclinical validation: *In vivo* applications of *in situ* skin bioprinting

To translate *in situ* bioprinting from laboratory benches to living tissues, rigorous preclinical validation is necessary. Animal models, particularly full-thickness skin wounds in rodents and pigs, have become crucial platforms for testing the technical feasibility, healing outcomes, and limitations

Table 9. Representative bioinks for *in situ* skin bioprinting: advantages and limitations

Bioink	Advantage	Limitation	Reference
Gelatin methacryloyl + LAP (visible light cured)	Rapid photopolymerization; high cell compatibility	Requires a light source; limited penetration in deep or irregular wounds	[236,261–263]
Alginate + Ca^{2+} (ionic crosslink)	Instant gelation; good stability; low toxicity	Poor cell adhesion; mechanical strength is often insufficient alone	[160,261,264,265]
Gelatin-alginate dual-crosslink bioink	Dual crosslinking (ionic + photonic); tunable mechanical properties	Requires precise crosslinking control; more complex formulation	[36]
Methacrylated hyaluronic acid + stem cells	Suitable for slow-release; good for chronic wound healing	Mechanical integrity is often weak and sensitive to enzymatic degradation	[35]
Fibrinogen + thrombin	Blood-derived; naturally biocompatible; rapid clot-like gelation	Short *in vivo* stability; rapid degradation limits structural support	[22,25,160,266–268]

Abbreviation: LAP, photo-initiator lithium phenyl-2,4,6-trimethylbenzoylphosphinate.

of such systems under relevant biological constraints. To identify relevant studies, we performed a dedicated search in the PubMed database using the keywords "in situ bioprinting" and "skin," which provided a curated set of studies for screening. The search was conducted without date and language restrictions and was updated in August 2025. Titles and abstracts were manually screened by two independent reviewers, and disagreements were resolved through discussion. In particular, we included original research articles reporting on *in vivo* applications of *in situ* bioprinting to the skin, including burns, diabetic wounds, and full-thickness excisions. Studies were excluded if they only included *in vitro* experiments, were performed on non-cutaneous tissues, or did not use a bioprinting method. The selection process is detailed in the Preferred Reporting Items for Systematic Reviews and Meta-Analyses flow diagram (Figure 6). A total of 49 search results were identified, 18 of which were excluded as review articles, leaving us with 31 original research papers. After further screening for relevance to *in situ* skin bioprinting, 29 studies were retained. Of these, eight papers were limited to *in vitro*-only experiments and were therefore excluded from further analysis. The remaining 21 *in vivo* studies form the basis of the summary presented in Table 10. In Table 10, we present a curated summary of *in vivo* studies by different wound types and bioprinting modalities.

3.5.1. Burn wound applications: Conformal delivery and topographic adaptation

The work of Cheng *et al*., which dealt with the technical complexity of treating full-thickness burns in pigs using a handheld extrusion-based device, is an excellent example.[25] The system was a combination of a microfluidic printhead and a silicone wheel, which can conformally deposit bioink sheets on inclined or irregular surfaces—a huge difference from rigid, flat-layer printing. The bioink mixture (fibrinogen, thrombin, and hyaluronic acid) was enzymatically crosslinked at the site of delivery, allowing the rapid gelling of the ink on live wound beds.

Notably, the microfluidic architecture was capable of consistent sheet extrusion, and the roller provided gentle and consistent contact with the skin, even at a 45° angle. The system was capable of controlling deposition in real time and improving re-epithelialization and vascularization outcomes. However, it is a bespoke non-commercial product, and its deposition requires surface contact, which poses challenges when applied to moving or highly contoured anatomical areas. Additionally, multi-layer or heterogeneous tissue constructs might not necessarily fit into a sheet-based delivery device.

3.5.2. Chronic wounds: Addressing hypoxia and complex microenvironments

In the models of chronic diabetic wounds, Wang *et al*.[261] used a coaxial microfluidic-assisted extrusion system for the direct delivery of living photosynthetic scaffolds into ischemic wound sites. Their solution inspired a new concept of incorporating *Chlorella* microalgae in a bilayer hydrogel, which could enable *in situ* autotrophic oxygen generation. The two layers were crosslinked with dual triggers (ionic and UV) to create a hollow oxygenating structure after deposition of the layer containing GelMA and alginate on the outside and gelatin and $CaCl_2$ on the inside. This setting improved hypoxia at the local level, as well as collagen deposition and angiogenesis. The tubular printing at the wound site was realized using a custom coaxial chip, which substituted the conventional printer nozzle for a bi-layer tubular printing method. However, due to the complexity of the fabrication process and the use of non-standard biological elements (e.g., microalgae), this system poses challenges for translation into a clinical setting, primarily due to regulatory approval and sterility issues.

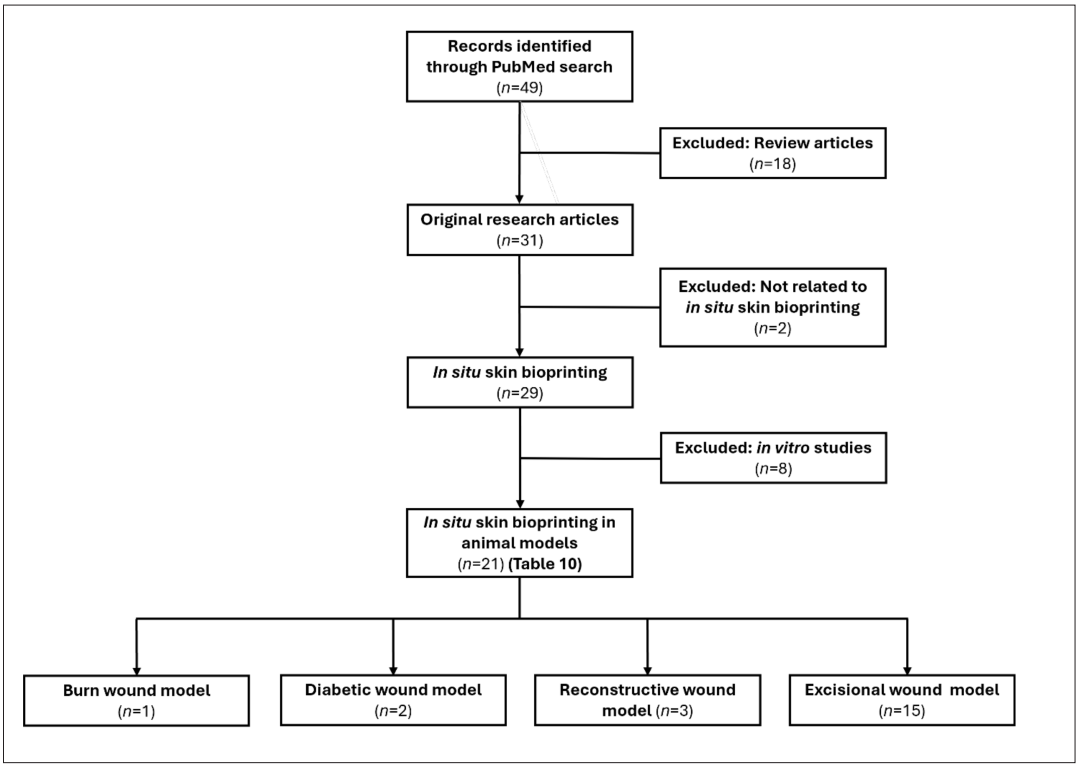

Figure 6. Preferred Reporting Items for Systematic Reviews and Meta-Analyses (PRISMA) flow diagram of study selection for *in vivo* applications of *in situ* skin bioprinting in preclinical animal models. The diagram illustrates the systematic selection of original research articles sourced from the literature, reporting on *in vivo* applications of *in situ* skin bioprinting in animal models. After screening 49 PubMed entries, 21 papers were found to use *in situ* bioprinting in preclinical wound models (burn, diabetic, reconstructive wound, excisional wound).

In a separate study, Zhou *et al.*[262] developed the "SkinPen," a handheld bioprinter integrating ultrasound and UV systems for real-time crosslinking. It produced a bioadhesion and antibacterial activity-enhanced GelMA/copper-doped bioactive glass nanoparticle bioink. The composite energy-based method (ultrasound cavitation and UV curing) provided fast solidification and increased adherence to moist, irregular wound beds.

3.5.3. Reconstructive applications: Extending beyond skin to craniofacial and osseous repair

In situ bioprinting has been extended beyond skin to craniomaxillofacial regeneration, where reconstruction of soft and hard tissues is required. Keriquel *et al.*[156,163] used LAB systems to deliver nano-hydroxyapatite and collagen inks, with or without stromal cells, onto calvarial defects in mice.They demonstrated laser-directed *in situ* delivery of a five-ink carousel system with high resolution using LAB. These studies showed restoration of bone volume and histologic evidence of osteogenesis; however, the results were variable. Laboratory experiments still involve technically challenging tasks, where the laser beam must be aimed accurately, optical components must be capable of withstanding demanding conditions, and laser safety procedures are stringent.

Moncal *et al.*[266] took this a step further by demonstrating hybrid *in situ* bioprinting using extrusion-based hard tissue ink and inkjet-based soft tissue bioinks in a rat craniofacial defect model. Their multi-arm robotic platform enabled the spatially precise co-deposition of dermal and osseous components, mimicking the native architecture. The bioprinted constructs showed bone regeneration of ~50% and skin closure of ~80% after 6 weeks and 10 days, respectively. A key emphasis of this study is on modular deposition through multi-ink integration. However, the operation complexity and absence of commercially available counterparts prevent its widespread adoption at the present level.

3.5.4. Excisional wounds: Dominant model for feasibility and versatility testing

Full-thickness excisional wounds in rodent and swine have been used as gold standard test beds for *in situ* systems. Among the most technically advanced is the work of Zhao *et al.*,[23,269] who developed a 6-DOF motion-controlled robotic arm-assisted dual-nozzle bioprinting system coupled with real-time 3D scanning. Their platform could

Table 10. Summary of preclinical *in situ* skin bioprinting studies on wound models, printing modalities, and healing outcomes

Wound category	Specific wound/ Animal species	Bioprinting modality	Bioink material	Cell type used	Healing outcome	Key technical innovation	Reference
Burn wound/ extrusion	Full-thickness skin burn (thermal injury with a 200°C aluminum plate for 20 s); Pig	Handheld extrusion-like device with microfluidic printhead and silicon wheel (not a commercial printer; customized system)	Fibrinogen (2% w/v) + thrombin (500 IU/mL) + hyaluronic acid (0.5–2% w/v); crosslinked via thrombin	Umbilical cord-derived MSCs at 1×10^6 cells/mL	Improved re-epithelialization, neovascularization, and dermal cell repopulation	Handheld wound-conformal printer with compliant wheel and microfluidic sheet delivery; deposition on inclined surfaces (up to 45°); real-time deposition control	[25]
Diabetic wound/ extrusion	Full-thickness skin diabetic wound induced by STZ (50 mg/kg); C57BL/6 mice	Microfluidic-assisted extrusion bioprinting (custom-made coaxial capillary microfluidic chip with 3D printer platform)	Microalgae-laden hollow fibers: outer phase (GelMA 5% w/v, sodium alginate 2.5% w/v), and LAP 0.1% v/v); inner phase (gelatin 5% w/v and $CaCl_2$ 0~2% w/v); crosslinked by $CaCl_2$ (0–2% w/v) and UV (365 nm)	Microalgae (*Chlorella pyrenoidosa*, 1×10^6 cells/mL)	Faster wound closure, enhanced angiogenesis (CD31), reduced hypoxia (hypoxia-inducible factor 1 alpha), and higher collagen deposition (51.6%)	*In situ* microfluidic-assisted bioprinting with photosynthetic microalgae for autotrophic oxygenation; custom coaxial capillary chip replacing printer nozzle	[261]
	Diabetic wound (full-thickness, chronic infected wound); Rat	Extrusion-based handheld bioprinter ("SkinPen") with integrated US and UV system	GelMA and copper-containing bioactive glass nanoparticles (Cu-BGn); UV crosslinking + US-induced cavitation	Not mentioned	Promoted blood clotting, normalized vascularization, accelerated wound closure, improved bioadhesion (≥3× shear strength)	Portable handheld "SkinPen" uses combined US and UV for instant *in situ* gelation and enhanced bioadhesion; designed for field or clinical use	[262]
Reconstructive wound	Calvarial critical-size bone defect; OF-1 mice	Laser-assisted bioprinting; automated workstation	Nano-HA	Not mentioned	Preliminary bone regeneration observed; heterogeneous results	Laser-based bioprinting platform designed for high-throughput and computer-assisted surgery	[156]
	Calvarial critical-size bone defect; BALB/c mice	LAB, automated laser workstation (Nd:YAG laser, 1,064 nm)	Type I collagen (0.2% w/v) + nano-HA (1.2% w/v); collagen crosslinks thermally	Mouse bone marrow stromal precursor cells (D1 line); 120×10^6 cells/mL; 693 or 796 cells/mm^2	Enhanced bone regeneration; bone volume and mineral density assessed by micro-computed tomography and histology	High-resolution LAB platform with 5-ink carousel; *in situ* laser printing onto exposed dura mater	[183]

Continue...

Wound category	Specific wound/ Animal species	Bioprinting modality	Bioink material	Cell type used	Healing outcome	Key technical innovation	Reference
	Craniomaxillofacial defect model; F344 rat	Hard bone bioprinting: extrusion-based multi-arm bioprinter for hard-tissue ink (HT-ink); skin composite bioprinting: custom-designed inkjet droplet-based bioprinter (jetlab® 4, MicroFab Technologies Inc.) for soft-tissue ink (ST-ink)	ST-ink: collagen (0.2% w/v) + fibrinogen (2% w/v) + thrombin crosslinker; HT-ink: chitosan (2% w/v) + collagen (0.9% w/v) + nano-HA	Extrusion-based bone bioprinting: rat bone marrow MSCs (rBMSCs)-laden HT-ink (5 × 10^6 cells/mL); droplet-based skin bioprinting: rat primary dermal fibroblasts (rDFs)-laden ST-ink (1.33 × 10^5 cells/mL)	~80% bone regeneration in six weeks; ~60% skin closure in six days; ~80% skin + 50% bone closure in 10 days (composite)	Hybrid IOB using extrusion and droplet-based modes for layered hard/soft tissue reconstruction; stratified deposition of multiple inks for composite tissue reconstruction; real-time, spatially controlled bioprinting	[266]
Excisional wound/robotic extrusion	Full-thickness skin wound; BALB/c nude mice	Extrusion-based and robot-assisted *in situ* 3D bioprinting (NORM series)	GelMA (2.5%, 5%, & 10% w/v), with LAP (0.1% v/v); photocrosslinked by 405 nm UV	Epidermal stem cells: 5×10^7/mL skin-derived precursors: 1×10^8/mL	Full skin regeneration, including epidermis, dermis, hair follicles, blood vessels, and sebaceous glands	Robot-assisted bioprinting system with *in situ* precision delivery and crosslinking; use of dual stem cells for regeneration	[263]
	Full-thickness skin wound; BALB/c nude mice	Extrusion-based robotic bioprinting with 6-DOF manipulator and closed-loop visual tracking system	Matrigel (no added crosslinker); shear-thinning; gelation at 22–37°C	Epidermal stem cells: 5×10^7 cells/mL; skin-derived precursors: 1×10^8 cells/mL	Complete wound healing in four weeks; regeneration of epidermis, dermis, blood vessels, sebaceous glands, and hair follicles; hair retention up to 10 months	Adaptive multi-degree-of-freedom (6-DOF) *in situ* bioprinting robot; closed-loop 3D scanning and visual tracking; eye-in-hand camera setup; automatic conformal path planning	[269]
	Full-thickness skin wound; Sprague-Dawley rat	Extrusion-based robotic arm bioprinting (6-DOF; with dual-jet system and *in situ* scanning; custom-built)	PRP-integrated alginate-gelatin composite hydrogel bioink: Alginate + gelatin + PRP (0%, 2%, 5%, 10% v/v) crosslinked with transglutaminase (1 % w/v); gelatin: dissolved in PBS; alginate: magnetically stirred at 37°C overnight	Human primary dermal fibroblasts (1×10^6/mL) and rat epidermal stem cells (1×10^7/mL); dual-layer bioprinting	Accelerated high-quality wound closure; promoted vascularization (CD31, α-SMA), re-epithelialization (hematoxylin & eosin staining), reduced inflammation (CD68, CD3, myeloperoxidase)	Custom robotic *in situ* printer with real-time 3D scanning (binocular), dual-nozzle, bilayer printing; point cloud-based path planning (ΔL = 0.2 mm; planning time ~3 s); automated layer switch	[23]
	Circular full-thickness skin wound; Wistar rat and Wiesenau minipig	Extrusion-based articulated robotic arm (KUKA); automatic with real-time skin movement tracking	Viscoll sterile porcine collagen (8% w/v), + platelet lysate (10%); crosslinking by temperature-sensitive polymerization	Fibroblasts: 1×10^6 cells/mL (rat & pig primary)	Enhanced adhesion, angiogenesis, reduced inflammation; improved histological regeneration in both models	First commercial articulated bioprinter; KUKA robot + end-effector with cooling (Peltier) + breathing sensor; real-time adaptive extrusion software	[264]

Continue...

Table 10. *Continue...*

Wound category	Specific wound/ Animal species	Bioprinting modality	Bioink material	Cell type used	Healing outcome	Key technical innovation	Reference
	Full-thickness skin wound; nude mice	Extrusion-based; Automatic; Livprint 3D bioprinter (NORM series)	Matrigel with embedded cells; no explicit crosslinking (physical gelation)	Epidermal stem cells: 5×10^7 cells/mL; skin-derived precursors: 1×10^8 cells/mL	Hair follicle regeneration (4 weeks); other appendages also regenerated; histology confirmed regeneration	Customized *in situ* printing workflow based on wound dimensions; computer-aided design modeling + automatic dispensing via Livprint NORM bioprinter; nozzle control at 2 mm height	[270]
	Full-thickness skin wound; Athymic nude mice	Pressure-driven extrusion-based system; automated three-axis in-house bioprinting platform	Heparin-conjugated HA (1% w/v) + Gelin-S (thiolated gelatin, 1% w/v), with PEGDA crosslinker (2% w/v); UV (365 nm) photopolymerization	Human amniotic fluid-derived stem cells (5×10^6 cells in 500 µL hydrogel)	Improved wound closure, re-epithelialization, increased vascularization, and ECM production; histological evidence up to 14 days	Custom-developed three-axis bioprinter with dual-nozzle printhead for cell/hydrogel + crosslinker; *in situ* photocuring via integrated UV	[26]
	Full-thickness skin wound; Athymic nude mice	Pressure-driven extrusion-based system; automated three-axis in-house bioprinting platform	Fibrinogen (5% w/v) + type I collagen (0.22% w/v); crosslinked via thrombin (20 IU/mL)	Human amniotic fluid-derived stem cells, human bone marrow-derived MSCs, both 16.6×10^6 cells/mL	Enhanced wound closure, increased re-epithelialization, elevated microvessel density and capillary diameter (Days 0, 7, 14); temporary cell integration	Custom-built automated extrusion bioprinter; multilayer gel/cell printing; green fluorescent protein-based cell tracking; proteomic analysis of secretome	[267]
Excisional wound/handheld extrusion	Full-thickness skin wound; mouse and pig	Handheld, extrusion-based, pressure-driven; manually operated	Alginate-collagen sheet: Alginate (2% w/v), collagen type I (0.25% w/v); dermal bioink: 1.25% (w/v) fibrinogen, HA (0.25% w/v) and collagen (0.25% w/v); epidermal bioink: Fibrinogen (2.5% w/v) and HA (0.25% w/v); crosslinking: ionic ($CaCl_2$), enzymatic (thrombin), thermal (collagen)	Dermal: 4×10^5 human fibroblasts/mL; epidermal: 1.25×10^6 human keratinocytes/mL	Demonstrated *in situ* sheet deposition; compatibility with inclined/moving surfaces	Lightweight handheld skin printer with microfluidic cartridge, active roller-based motion control, and onboard syringe pumps	[160]
	Full-thickness skin wound; Yorkshire pig	Extrusion-based handheld bioprinter (custom-built syringe-pump with motorized plunger, UV LED for crosslinking, gauge 22 conical nozzle)	GelMA (9% w/v), crosslinked with LAP (0.067% v/v) using 395 nm blue light LED; VEGF added at 400 ng/mL	No cells printed	Reduced contraction (18±4%), increased epithelial thickness (165±28 µm), higher rete ridges (9.32/mm), lower scar elevation index (1.09±0.01), increased vascularization (vWF staining), and lower inflammation	Handheld partially automated printer with integrated UV light; adjustable flow rate (4–18 µL/s); designed for *in situ* curved surface printing	[236]

Continue...

Wound category	Specific wound/ Animal species	Bioprinting modality	Bioink material	Cell type used	Healing outcome	Key technical innovation	Reference
	Full-thickness skin wound; Sprague-Dawley rat	Extrusion-based, handheld, programmable, smartphone-controlled	Granular hydrogel: Component A + Component B; Crosslinking via 405 nm blue light; component A: PEGDA (5% w/v), HA (0.5 % w/v), and LAP (0.5 % v/v), UV light pre-crosslinking; component B: PEGDA (10% w/v) and LAP (0.5 % v/v), UV light pre-crosslinking	HUVECs (2.5×10^6 cells/mL) + rat PRP mixture	Wound closure, PRP hydrogel integration, histological hematoxylin and eosin staining for healing observation	Handheld programmable printer; pneumatic and mechanical extrusion modes; smartphone web app control; multi-ink switching; microchannel nozzles	[237]
	Full-thickness skin wound; C57BL/6J mice	Extrusion-based (Regenovo Bio-architect SR), desktop bioprinter, not handheld or robotic	Hemostatic alginate-based bioink (AL@FM): AlgMA (4% w/v) + LAP + PVP + CMC + glycerol + ε-PL; crosslinking via 405 nm light LED	No cells printed	Wound closure rate, angiogenesis (CD31), fibroblast activation (vimentin, fibronectin 1), immune regulation (F4/80, LY6G/C, CD86, arginase 1) at day 7 and 14	Photocrosslinkable alginate-based bioink with rapid hemostasis, antibacterial, and injectable properties	[265]
Excisional wound/inkjet	Full-thickness skin wound; Athymic nude mice	Inkjet-based *in situ* bioprinting; likely handheld/manual device (device not explicitly specified)	N/A (bioink unspecified)	Human keratinocytes and fibroblasts; concentration N/A	Wound closure by three weeks; organized dermal collagen and fully formed epidermis; human cells incorporated into skin appendages	Novel *in situ* bioprinting device for direct wound delivery of cells in full-thickness skin injuries	[271]
	Full-thickness skin wound; Athymic nude mice and Yorkshire pigs	Drop-on-demand inkjet bioprinting (custom mobile *in situ* skin bioprinter with integrated imaging)	Fibrinogen (2.5% w/v) + collagen I (0.11% w/v); crosslinked with thrombin (20 IU/mL)	Human dermal fibroblasts (1.875×10^6/0.5 mL) and human keratinocytes (3.75×10^6/0.5 mL); ratio 1:2 (dermal:epidermal)	Accelerated wound closure, reduced contraction, enhanced re-epithelialization, organized collagen fibers, mature vascularization, proliferating keratinocytes (CD31, α-SMA, Ki67)	Mobile handheld bioprinter with integrated imaging for layered *in situ* autologous/allogeneic cell delivery	[22]
	Full-thickness skin wound, craniomaxillofacial zone; Rowett Nude Rat immunodeficient nude rat	Inkjet droplet-based bioprinting using Jetlab® 4 (MicroFab Technologies), micro-valve dispensing device (INKX0517500A)	Fibrin-based bioink: fibrinogen (0.5% w/v) + human adipose-derived ECM (1–2% w/v); crosslinked via thrombin + Factor XIII 2 U/mL thrombin + coagulation Factor XIII (0.1% w/v) in $CaCl_2$ (10 mM)	Human adipose-derived MSCs (1×10^6 cells/mL)	~91–93% wound closure by Day 14; faster re-epithelialization (~70% by Day 7); enhanced adipogenesis; hair follicle-like downgrowths; increased vascularization (CD31 expression); collagen deposition	IOB directly on the surgical wound; micro-solenoid valve system for precise droplet control; stratified dermis/hypodermis structure; Jetlab® 4 bioprinter; smart use of patient-derived materials	[268]

Continue...

Table 10. ***Continue...***

Wound category	Specific wound/ Animal species	Bioprinting modality	Bioink material	Cell type used	Healing outcome	Key technical innovation	Reference
Excisional wound/laser	Not mentioned (but applied to dermis, muscle, brain tissue); Mouse	Laser-assisted (Two-photon, intravital; automated via multiphoton microscope)	Photosensitive polymer hydrogel; crosslinked via two-photon bio-orthogonal cycloaddition (>850 nm)	Donor muscle-derived stem cells	*De novo* formation of myofibres in skeletal muscle	*In vivo* 3D bioprinting using multiphoton microscopy for accurate positioning inside live tissue	[272]

Abbreviations: 3D, Three-dimensional; AlgMA, methacrylate alginate; α-SMA, alpha smooth muscle actin; CMC, carboxymethyl cellulose; DOF, degrees of freedom; ECM, extracellular matrix; ε-PL, epsilon-polylysine; GelMA, methacrylate gelatin; HA, sodium hyaluronate; HUVECs, human umbilical vein endothelial cells; IOB, intraoperative bioprinting; LAB, laser-assisted bioprinting; LAP, photo-initiator lithium phenyl-2,4,6-trimethylbenzoylphosphinate; LED, light emitting diode; MSCs, mesenchymal stem cells; PEGDA, polyethylene glycol diacrylate; PRP, platelet-rich plasma; PVP, polyvinylpyrrolidone; rDFs, rat primary dermal fibroblasts; STZ, streptozotocin; UV, ultraviolet; VEGF, vascular endothelial growth factor; vWF, von Willebrand factor.

automatically generate a point-cloud map of the wound and plan bi-layered deposition paths in seconds. The group found that the use of platelet-rich plasma-enriched bioink resulted in increased vascularization and reduced inflammation and dermal repair in rats.

Alternatively, Chen *et al.*[263,270] produced more efficient automated platforms (NORM series) for Matrigel-based hydrogels embedded with epidermal stem cells and dermal precursors. It consistently regenerated full skin structures, including hair follicles and glands, as confirmed with histological analyses. Simultaneous dual cell population and robotic precision directed nearly native skin regeneration.

Other investigations, e.g., Albanna *et al.*[22] and Hakimi *et al.*,[160] applied a manual held extrusion printer or drop-on-demand inkjet printer to deliver stratified layers of keratinocytes and fibroblasts directly to wound beds. These platforms highlighted the benefit of simplicity and flexibility, but typically lacked closed-loop control or robotic precision. These findings represent an increasing maturity in preclinical validation pipelines, and Table 10 can be considered as both a reference map and a benchmark summary for the state-of-the-art in *in vivo* testing of *in situ* bioprinting systems.

4. Stem cells in skin bioprinting: Applications and potentials

Stem cells are not only now seen as sources of cell agents for replacement, but also as performing bio-units with the ability to form dynamic regenerative environments, characterized by plasticity and the secretome, as well as interactive behavior within printed constructs. When applied to skin bioprinting in the context of burn healing, stem cells, including MSCs and iPSCs, provide cellular plasticity and paracrine signaling that stimulate tissue repair, immunomodulation, and vascularization.[251,273] This section reviews the current applications and future potential of various types of stem cells for skin bioprinting, comparing their functional potential, differentiation status, and translational possibilities.

4.1. Stem cells as functional units in biofabricated skin

Stem cells in skin bioprinting are no longer a passive building block; instead, they are becoming an active mechanism in the regeneration process. Compared to conventional somatic cells, iPSCs and MSCs exhibit distinct combinations of expandability, plasticity, and biological responsiveness, making them ideally suited for biofabrication.[274,275] These cells are not simply printed to fill out space; they play an active role within the post-printing tissue microenvironment, secreting trophic factors, altering

immune responses, and stimulating neovascularization via paracrine signaling.[276–280] That qualifies them to be especially helpful in complex wound healing in burned or damaged skin.

Stem cells are additionally more easily expanded and standardized in batches than primary patient-derived cells, which often suffer from limited proliferative potential and donor variability. Immortalized cell lines, such as HaCaT, are easy to expand and provide a convenient model for experimental systems; however, they suffer from genetic abnormalities and a lack of clinical translatability.[43,47,49,60] Stem cells, on the other hand, strike a balance between biological functionality and their potential for production. Another significant advantage is their immunological profile: autologous iPSCs can be tailored to the individual patient, and ongoing efforts to develop universal donor lines will help resolve the present limitations associated with immune rejection.[264,281]

However, these come with caveats. One of the remaining technical challenges, especially with iPSCs, is differentiation consistency. While MSCs show high paracrine activity and are relatively easy to handle, their lineage-specific functionality in forming complete skin structures is limited.[282,283] Furthermore, the regulatory and manufacturing requirements for stem cell-derived bioprinted constructs are significantly higher than those for standard cell types, making clinical translation particularly challenging.[69,72,73,76,78]

Nevertheless, stem cells continue to enjoy momentum as the basic building blocks of engineered skin. Their potential to be structure-forming and function-regulating agents distinguishes them in the emerging field of regenerative medicine. As bioprinting technologies mature, stem cells are increasingly positioned not just as a superior alternative to other cell sources, but as indispensable agents of tissue-specific regeneration. Table 11 provides a comparative overview of stem cells, primary cells, and immortalized cell lines in relation to skin bioprinting applications. Some of the differences between these cell types are outlined in terms of expandability, immunocompatibility, technical requirements, and clinical potential. As shown in Table 11, stem cells have superior clinical translatability and maintenance properties in comparison to immortalized lines, but are still inferior with regard to the reproducibility of directed differentiation to primary keratinocytes or fibroblasts. Despite the regulatory complexity that sometimes makes stem cells a more challenging choice, this table provides a clear, side-by-side overview that will help demystify stem cell sourcing and selection in pre-clinical and clinical settings. Stem cells are now increasingly placed not simply as a better alternative to other cell sources, but as critical agents of tissue-specific regeneration. This is visually summarized in Figure 7, which illustrates the multifaceted role of stem cells, specifically, MSCs and iPSCs, in bioprinted skin applications. The figure schematically shows how stem cells contribute not only to wound healing and craniofacial reconstruction, but also to the regeneration of complex skin appendages such as sweat glands. Notably, their double functional character is illustrated in Figure 7: as structural (through differentiation) and as biological mediators (through the secretion of trophic factors and modulation of the immune system). Additionally, the figure illustrates the integration of both robotic and handheld bioprinting strategies (ST-ink for soft tissue and HT-ink for hard tissue), demonstrating their technical versatility in creating stratified tissue architecture. However, Figure 7 also identifies some key challenges, such as lineage selectivity, reproducibility of differentiation, and regulatory challenges, reaffirming that stem cells remain powerful yet imperfect tools in regenerative bioprinting.

4.2. Comparative overview of stem cell sources in skin bioprinting

Not every stem cell is made equal in the growing area of skin bioprinting. While the umbrella term stem cell tends to imply flexibility and regenerative potential, different sources—such as iPSCs, MSCs, amniotic fluid stem cells (AFSs), and endothelial progenitor cells—carry distinct biological traits and limitations that make them more or less suitable for skin fabrication applications.[274,288] When selecting an appropriate cell type, it is essential to trade off several aspects: scalability, differentiation potential, immunogenicity, and, more recently, paracrine signaling potential.

The unmatched plasticity of iPSCs is outstanding. Their ability to differentiate into essentially any cell lineage makes them theoretically ideal for reconstructing complex, layered skin.[289] They can be expanded indefinitely, providing a steady and renewable source of cells. Nevertheless, iPSCs present practical challenges, particularly in terms of consistency of differentiation, genomic instability, and the high cost of production. So far, their use has been primarily confined to *in vitro* systems or preclinical modeling, with clinical translation still on the horizon.[290–297]

Mesenchymal stem cells, by contrast, are far more mature in their therapeutic development. Though their differentiation potential is more limited—especially when it comes to generating fully functional epidermal structures—they are well-regarded for their paracrine activity. MSCs can actively direct the wound environment by secreting cytokines, growth factors, and extracellular vesicles that promote angiogenesis, alter inflammation,

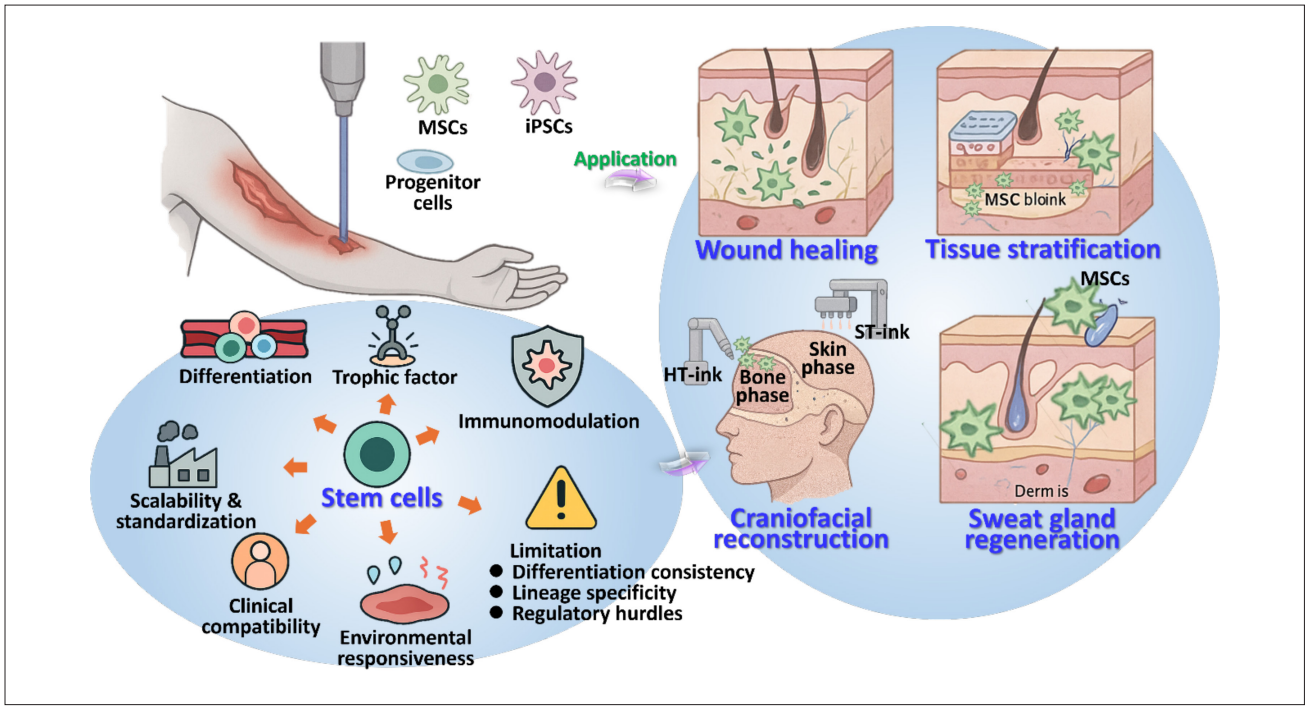

Figure 7. Multifaceted roles and applications of stem cells in skin bioprinting. Schematic representation of stem cells as active biological agents in skin bioprinting. Stem cells, such as mesenchymal stem cells (MSCs), induced pluripotent stem cells (iPSCs), and progenitor cells, are used through bioprinting platforms for wound healing, stratification, craniofacial reconstruction, and functional regeneration of skin appendages, including sweat glands. They are not only differentiated but also secrete trophic factors, modulate the immune system, and respond to changes in their environment. However, issues remain, such as lineage selectivity, reproducibility of differentiation, and pathway control. As shown, both handheld and robotic printing approaches can spatially control the delivery of different cell-laden bioinks (e.g., ST-ink for soft tissue and HT-ink for hard tissue), underscoring their versatility and translational potential in regenerative applications. Figure created using illustrations generated via ChatGPT (OpenAI image tools), with final layout and annotations edited in Microsoft PowerPoint.

Table 11. Comparison of stem cells, primary cells, and immortalized cell lines for use in skin bioprinting

Cell type	Expandability	Immunocompatibility	Cost and technical demand	Differentiation consistency	Clinical feasibility	Bioprinting performance	Reference
Stem cells (e.g., mesenchymal stem cells)	High	Personalizable (autologous)	High	Challenging	Emerging	Promising (requires further validation)	[25,26,36,52,53,63,266,267]
Primary cells (Patient-derived)	Limited	High (autologous)	Moderate	Stable	Already used	Most commonly used	[23,39,42,56,264,266]
Immortalized cell lines (e.g., HaCaT)	High	Poor	Low	Stable	Research use only	Low (due to genetic abnormalities)	[0,47,49,22,284–287]

and promote epithelial regeneration.[298,299] These secretory effects are increasingly viewed as an independent therapeutic mechanism, valuable even in the absence of complete lineage commitment.

On the other hand, AFSs offer a favorable compromise. They are relatively easy to expand, show a preference for skin-related lineages, and also possess notable paracrine effects.[300] They are considered moderate in their immunogenicity and may be manageable through immunosuppression methods or by matching the donor. Preclinical work suggests they may soon enter broader translational pipelines, particularly for pediatric or congenital skin disorders.[26,267,301]

Endothelial progenitor cells bring a narrower functional profile but fill an essential niche in vascular bioengineering.[302] They are dedicated to endothelial

Table 12. Comparative features of different cell types relevant to skin bioprinting

Cell type	Expandability	Differentiation	Paracrine	Immunogenicity	Status
Induced pluripotent stem cell	High	Versatile	Moderate	Customizable	Preclinical [290]
Mesenchymal stem cell	Moderate	Limited	High	Low	Clinical[63]; preclinical [25,36,52,53,266,267]
Amniotic fluid stem cell	High	Skin lineage	High	Moderate	Preclinical [26,267]
Endothelial progenitor cell	Moderate	Endothelial only	Medium	Variable	Preclinical [302–304]

lineages, making them highly applicable in promoting neovascularization in printed scaffolds. However, their *in vivo* data are sparse, and their immunogenicity behavior is not yet well characterized; thus, they are less predictable in clinical situations.

Comprehensively, the choice of stem cell source should be based on the targeted therapeutic objectives: is the proposed therapy focused on developing full-thickness skin equivalents, promoting vascular integration, or utilizing the secretome to regulate tissue? As summarized in Table 12, each stem cell type offers a distinct constellation of strengths and trade-offs that must be carefully matched to both technical capabilities and clinical strategies. Importantly, paracrine signaling is now recognized as an independent regenerative mechanism—beyond cell differentiation—that plays a central role in immune modulation, angiogenesis, and epithelial repair.

4.3. Applications of mesenchymal stem cells in skin bioprinting

Among all stem cell types explored for skin regeneration, MSCs have arguably garnered the most clinical and experimental attention—particularly in the context of burn and wound healing.[283,305–307] MSCs are considered multipotential (stromal) cells that can develop into different mesodermal lineages, including fibroblasts, osteoblasts, and adipocytes. However, their actual usefulness in regenerative medicine may be a lot more than their ability to differentiate. The strength of MSCs for skin bioprinting lies in their high paracrine activity, which is characterized by the secretion of a vast range of cytokines, growth factors, and extracellular vesicles that influence the wound microenvironment. These secreted factors have the potential to increase angiogenesis, reduce inflammation, and stimulate re-epithelialization, effectively transforming MSCs into potent cellular pharmacies that dynamically regulate the repair process. Numerous preclinical and clinical studies have confirmed these therapeutic benefits. For instance, recent reviews have reported MSC-mediated enhancement of burn wound closure, decreases in scar appearance, and increases in vascular density.[251] A recent *in vivo* study in 2024 further showed that bone marrow MSC transplantation (1×10^6 cells/wound) not only accelerated re-epithelialization in burn injuries but also regulated inflammatory cytokines such as interleukin 6 and transforming growth factor beta, promoting a more regenerative and less fibrotic healing environment.[308] These findings strengthen the hypothesis that MSCs actively and multi-dimensionally coordinate tissue regeneration not only through cellular replacement.

Zhang *et al.*[63] have provided a rare clinical perspective on MSC-based bioprinting by treating a chronic, therapy-refractory wound with a 3D bioprinted skin substitute containing human umbilical cord MSCs (1×10^6 cells/mL). In this case, the patient had a wound due to intralesional injections of bleomycin to treat plantar warts that were not responding to standard treatments such as platelet-rich plasma and autologous skin grafting, and hyperbaric oxygen therapy. The bioprinted construct—composed of alginate-gelatin bioink and loaded with human umbilical cord MSCs—was directly applied to the wound and resulted in rapid re-epithelialization, granulation tissue formation, and no observed adverse effects. The novelty in this case lies in the ability of MSC bioprinting to be translated from the bench to the bedside, addressing an actual wound with structural complexity and a high microbial burden. Nevertheless, the study has a limitation in that it is a one-case, open-label study, and no wider clinical validation has been conducted yet.

In an earlier and widely cited preclinical effort, Cheng *et al.*[25] introduced a handheld *in situ* bioprinting device capable of delivering umbilical cord-derived MSCs (1×10^6 cells/mL) directly into full-thickness burn wounds in a porcine model. These MSCs were not mere fillers, as they actively contributed to improved re-epithelialization, neovascularization, and re-population of dermal cells, resulting in considerably improved wound healing relative to the controls. The development of a microfluidic printhead capable of depositing conformal skin precursor sheets on wound surfaces, both in oblique and irregular shapes, with real-time deposition control, represents a

significant advance in this study and can be ascribed great clinical importance for acute burn care. However, there were still some limitations: long-term functional records on after-healing skin regeneration were still lacking.

Using craniofacial tissue, Moncal *et al.*[266] demonstrated in a large animal model a hybrid intraoperative bioprinting strategy for craniomaxillofacial reconstruction. They developed a bioprinting system that involves extrusion-based bioprinting (hard tissue, HT-ink) and inkjet droplet-based bioprinting (soft tissue, ST-ink), allowing the deposition of bone and skin components in a single surgical operation. More specifically, MSCs isolated from rat bone marrow (5×10^6 cells/mL) were encapsulated within a chitosan–collagen matrix and printed as the bone phase. In contrast, primary rat dermal fibroblasts (1.33×10^5 cells/mL) were encapsulated in a gelatin-collagen ink for the skin layer. These dual-ink approaches raised 60–68% skin closure and 80% bone regeneration within 10 days and 6 weeks, respectively, with layer-specific and spatially controlled healing. Compartmentalized regeneration of hard and soft tissues was possible through this stratified cell-ink combination. However, the use of fibroblasts—rather than MSCs—in the skin compartment meant the soft tissue lacked regenerative signaling typical of MSCs, and no skin appendages were observed. This restricts skin functional recovery and emphasizes the importance of MSC-based soft tissue optimization in subsequent versions.

From a foundational perspective, Skardal *et al.*[267] demonstrated that bioprinted AFS could significantly enhance healing in large skin defects in mice. Their automated, pressure-driven 3D extrusion platform printed a fibrinogen-collagen hydrogel loaded with human AFS and human bone marrow-derived MSCs, each at a density of 16.6×10^6 cells/mL. The printed constructs applied to the full-thickness skin wounds of immunodeficient mice enhanced wound closure, re-epithelialization, and microvascular density. Interestingly, their proteomic study on the cell secretome highlighted that therapeutic efficacy was primarily a result of paracrine signaling, rather than direct tissue regeneration. However, cell integration remained temporary, and long-term stability or skin organoid formation was not achieved.

More recently, Hao *et al.*[36] presented a temperature-sensitive gelatin-alginate hydrogel bioink that was crosslinked using a photo- and ionic approach, and customized for extrusion printing in a 3D format for wound healing applications. The bioink consisted of a co-culture of NIH 3T3 mouse fibroblasts (3×10^6 cells/mL) and human umbilical cord MSCs (3×10^6 cells/mL). When applied to excisional wounds in Institute of Cancer Research mice, the combination significantly promoted wound contraction, re-epithelialization, collagen deposition, and reduced inflammation. Importantly, this work highlighted the capacity of an appropriately engineered matrix to synergistically combine with MSC activity, achieving not just a scaffold but a truly active partner in tissue repair. Despite promising outcomes, the lack of comparative *in vivo* control groups using MSCs alone limits our understanding of how much benefit was material-driven versus cell-mediated.

In a remarkable effort of functional skin appendage regeneration, Yao *et al.*[53] utilized mouse MSCs (1×10^6 cells/mL) wrapped in a 3D-bioprinted hydrogel composed of gelatin and alginate, further supplemented with paw pad homogenates of the dermis. Their bioprinting concept, using an extrusion-based approach, developed a matrix that could direct MSCs into lineages of an SG. Notably, the biochemical cues (collagen triple helix repeat containing 1) and structural cues (heme oxygenase-1) were introduced into the construct to drive differentiation. Exciting results were obtained for SG's structural and functional restoration through re-exposure to acetylcholine-induced sweat-mediated responses and the expression of SG-specific genes. Based on this paradigm, Yuan *et al.*[52] further extended the regeneration of SG by establishing a vascularized SG regeneration model (SVIM). In the study, adipose-derived mesenchymal stem cells (1×10^7 cells/mL) were first differentiated into SG cells (100 pcs/cm^2), then bioprinted together with dermal microvascular endothelial cells (1×10^5 cells/cm^2) into a composite hydrogel composed of sodium alginate, gelatin, and plantar dermal ECM. This co-culture approach allowed the printed constructs not only to resume glandular architecture and secretory function but also to develop physiologically applicable vascularization. The research demonstrated how the reciprocal interactions between the SG niche and its vasculature could be modeled, showing the ability to achieve a new level of bioprinting of integrated tissue systems. But even based on the technical novelty, an unresolved issue was the scalability of the model and the long-term functional follow-up in systems other than the murine model.

Collectively, these studies paint a picture of MSCs as a highly versatile addition to the bioprinting toolkit, not only in the successful closure of wounds, but also in modulating the wound niche itself, tissue compartmentalization, and even initiating specialized tissue regeneration. However, some constraints remain as follows: cell fate after printing is challenging to monitor, and lineage commitment is not yet at high levels, especially in the reconstruction of complex appendages or stratified tissues of the skin. With the advancement of bioinks and the improvement of knowledge on how MSCs interact with the ECM, there is

a strong possibility that MSCs will still hold a prominent place in the second generation of clinically applicable skin substitutes.

5. Smart bioengineered skin

Skincare reconstruction has not only moved beyond the classic notion of a passive barrier in the changing setting of the regenerative medical industry. The development of bio-engineered skin as a smart functional interface with sensory perception, dynamic monitoring, and adaptive response remains primarily at the proof-of-concept stage in preclinical and early clinical settings.[309–311] With deep burns and chronic wounds persisting to defy the norms of skin grafting, the emergence of electronic skin (e-skin) technologies, piezoelectric scaffolds, and biocompatible materials has created alternative directions for regaining the sense of touch and temperature.[312–314] Current prototypes not only restore physiological function but also have the potential for two-way communication between engineered tissues and external devices (such as sensor-integrated grafts, which are currently conceptual or in very early stages of development). In parallel, developments in the field of wearable biosensing wound dressings allow for a more immediate proof of concept; for example, Kalasin *et al.*[315] demonstrated the FLEX-AI bandage system, a combination of a pH-sensitive hydrogel with a radio frequency sensor and neural network that achieved a near 95% accuracy in predicting chronic wound healing trajectories.

In parallel with this shift, a concept of smart bioinks has emerged, which involves formulations incorporating conducting polymers, piezoelectric composites, and stimuli-responsive compounds, thereby enabling a certain level of structural fidelity as well as functional integration with the bioprinting process.[316–318] Furthermore, artificial skin can be equipped with smart sensors and wireless modules to monitor wound healing, pH values, and possible infection continuously to assist decision-making in clinics.[311,319,320]

The overall integration of AI and Internet of Things (IoT) technologies also has potential applications in bioengineered skin.[321,322] The next generation of skin substitutes will fundamentally change treatment paradigms due to their ability to assess wounds with data, provide self-reporting solutions, and utilize cloud-based systems, allowing therapy to become adaptive and autonomous.[168,323,324] This section discusses the interdisciplinary approaches that support this change—materials science to digital health—and describes the new blueprints of creating genuinely intelligent skin systems. This system-level transformation is summarized in Figure 8, which schematically depicts the integration of 3D bioprinting, electronic skin, intelligent inks, and AI/IoT monitoring into next-generation smart skin grafts. As shown in the diagram, the grafting of different types of wounds can be applied to burns, diabetic ulcers, and excision wounds, and may include sensor inks, thermal/pH response units, and cloud-based data loops for real-time monitoring. The figure further highlights the clinical paradigm shift from conventional passive dressings to actively sensing and adaptive wound platforms, which enable personalized and data-driven therapy at the point of care. This graphical design suggests that smart skin constructs are not only about structure anymore, but may also become diagnostic and therapeutic devices that open up new and exciting directions for the field of wound care through smart responsiveness and digital health.

5.1. Strategies for tactile and thermal sensory restoration

Restoring the ability to feel—whether it is the warmth of sunlight or the gentle pressure of contact—is a key milestone in making bioengineered skin feel alive again. Conventional grafts can close a wound, but they fail to communicate with the nervous system. This is where tactile and thermal sensory restoration takes center stage, advancing beyond reconstruction to focus on reconnection—rebuilding skin that not only covers, but feels.[325]

The e-skin, also known as electronic skin, is at the center of this transformation. Designed to emulate the stretchability and sensitivity of native skin, e-skin platforms are now integrating soft, flexible circuits and embedded sensors that respond to temperature changes, mechanical strain, or pressure.[326–328] To provide better adhesion and biocompatibility when transferred into the clinical setting, these systems are increasingly printed on hydrogel-based substrates to closely mimic the hydration and softness of native tissue.[329–331] For example, e-skin sheets can now detect minor temperature differences using flexible thermistors and resistive sensors, allowing for thermal feedback to be achieved.[332–334]

Piezoelectric scaffolds represent one of these promising technologies, complementary to e-skin, that can convert mechanical deformation into electrical signals.[335–337] These bionic platforms are typically constructed from materials such as polyvinylidene fluoride or synthetic proteins like silk fibroin, which creates an interface between motion and perception.[338,339] When incorporated into engineered dermal structures, they can provide localized electromechanical feedback, which may in the future be connected directly to peripheral nerves or read by wearable processing units.

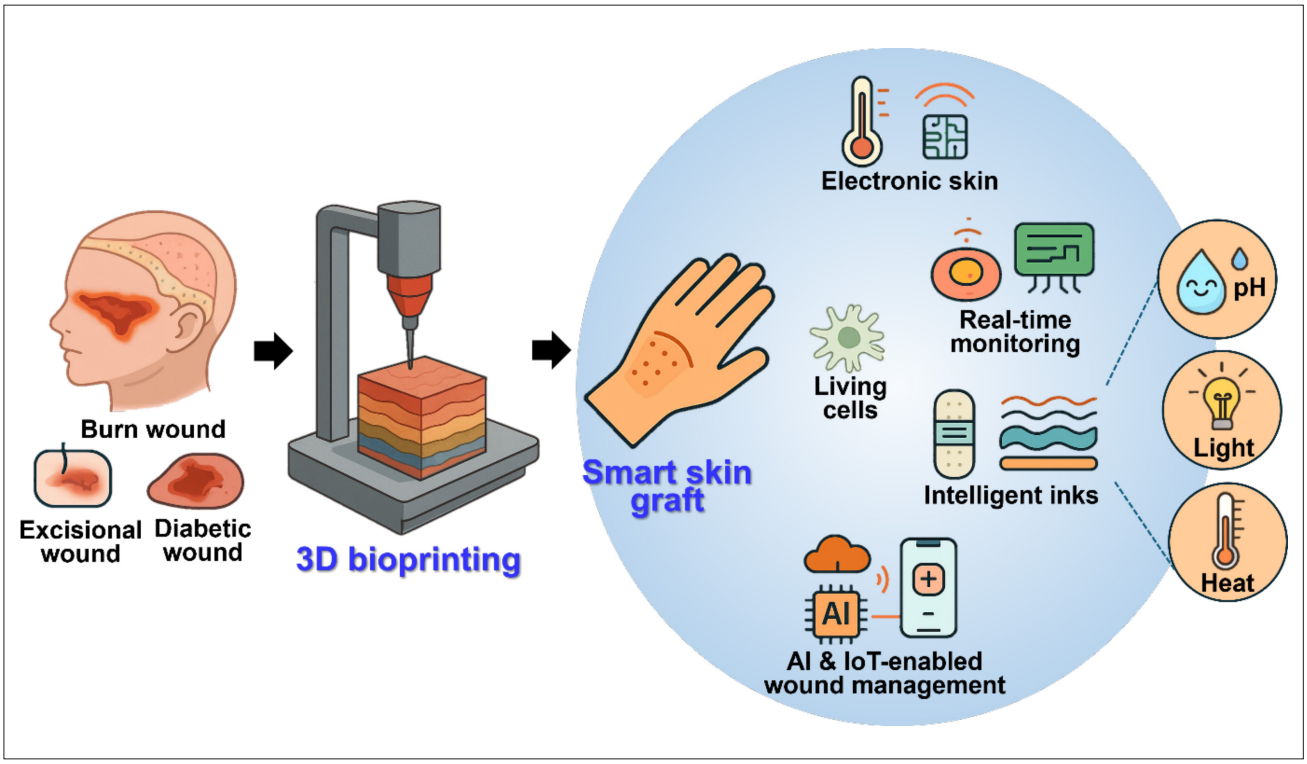

Figure 8. Smart skin grafts integrating three-dimensional (3D) bioprinting with intelligent sensing and digital health technologies. Development of smart skin grafts using 3D bioprinting technologies for different types of wounds (burn, diabetic, and excisional). The next generation of intelligent systems is a hybrid of living cells and smart materials, including electronic skin, intelligent inks, and responsive hydrogels, which facilitate the real-time tracking of physiological signals (e.g., pH, light, and heat). The combination of artificial intelligence (AI) and Internet of Things (IoT) technologies enables continuous wound monitoring, autonomous data analysis, and cloud-based reporting. Collectively, these are a step away from passive wound dressings to active therapeutic surfaces that can sense, adapt, and facilitate individualized care. Figure created using illustrations generated via ChatGPT (OpenAI image tools), with final layout and annotations edited in Microsoft PowerPoint.

In the meantime, bio-conductive materials establish the fundamental connection between the structure and the signal. Without electrical conductivity, none of these technologies could communicate.[340,341] Conductive poly(3,4-ethylenedioxythiophene) (PEDOT): polystyrene sulfonate (PSS), graphene derivatives, or carbon nanotube-laced hydrogels have been refined to be highly conductive and cell-compatible.[342–344] Such smart substrates can be used not only to transmit signals but also to facilitate cell adhesion and differentiation, including those of neural and epidermal lineages. Moreover, they can be co-printed with living cells through multi-ink bioprinting, allowing for a match between functionality and regenerative capability.

Together, these technologies present a vision for skin substitutes of the future that could someday lead to closing wounds, while also restoring sensory functions; however, validation to date has been limited to animal tests and early feasibility reports. This is not merely to replace lost tissue, but to renew communication between the skin and brain, injury and response, using engineered, living, and sensing interfaces.

5.2. Design and applications of intelligent inks

When printing skin, the ink applied should not only retain its shape; it must also think, react, and even feel. This is where intelligent inks can play a role. Compared to traditional bioinks, which are designed to ensure cell viability and print fidelity, intelligent inks are triggered by their surroundings and take an active role in functional regeneration.[345,346]

One of the most explored families in this space is conductive polymers. Materials like PEDOT:PSS, polyaniline, and polypyrrole introduce electrical conductivity into the bioprinting world, enabling printed constructs to support cells and transmit signals.[347–349] These polymers are advantageous when an individual wants to construct skin that can detect temperature, touch, or even subtle ionic variations. Their conductivity can be tuned through doping, and their compatibility with the body can be enhanced without sacrificing performance by embedding them in hydrogels.[350–352] For instance, it has recently been demonstrated that a straightforward mixture of PEDOT: PSS and GelMA or silk fibroin can produce

printable and functional inks that bridge the gap between electrical response and biological incorporation.[353]

Piezoelectric composites are materials that physically produce voltage as they are bent or stretched. These are not inert fillers but active ingredients that mimic natural skin behavior in response to movement and deformation.[354,355] Polyvinylidene fluoride-based blends, barium titanate nanoparticles, or silk-based matrices with piezoelectric components are often used.[356] When incorporated into printed dermal layers, these composites enable the conversion of mechanical input, such as pressure or stretch, into usable electrical signals.[357,358] This opens up the possibility of establishing feedback loops in skin interfaces or even training AI models that have been learned on motion-based data.

The last example is the stimulus-sensitive inks—the bioprinting chameleons. Such materials respond to external stimuli, such as light, heat, or pH, by changing color, stiffness, or conductivity.[359,360] For example, hydrogels loaded with photochromic molecules or temperature-sensitive polymers, such as poly(N-isopropylacrylamide), can shift their properties in real time, giving researchers control over how skin constructs behave after printing.[361,362] This responsiveness can be highly beneficial in the wound care field, such as a printed patch that stiffens upon an increase in temperature around the wound due to infection, or one that releases drugs in a clinical environment upon exposure to light.

Smart inks help fine-tune the line between material and functionality. Instead of merely anchoring cells, these inks are also involved in the healing process, including sensing, responding, and even communicating. The implication of this, in the context of bioprinted skin, is that the constructs are not only capable of surviving after implantation but also actively promote recovery. The design space of smart inks will continue to expand as printer heads become more accurate and multi-material systems become available. What was once merely a support material has now become an essential co-therapist—printing not just tissue, but function.

5.3. Integration of real-time monitoring systems

While the fabrication of skin constructs is crucial, monitoring their post-printing performance is equally vital, as wound healing is a dynamic and patient-specific process rather than a fixed event. They swell, fluctuate, become infected, or suddenly close rapidly.[363] Next-generation skin constructs must be capable of more than sitting quietly on a wound to detect these shifts in real time. They need to observe, record, and sometimes respond.[364] This is precisely the functionality now being integrated into bioengineered skin through real-time monitoring systems.[314,365]

An example would be pH-responsive patches. Changes in local pH are often the first signs that something is going wrong. A decrease in pH might represent an inflammation or bacterial growth, while an increase could signal tissue necrosis.[366] The concept of a color-changing smart patch is no longer a far-fetched idea, and it has already demonstrated its potential in preclinical applications. These visualization materials, commonly involving phenol red or bromothymol blue trapped in hydrogel matrices, can be visualized immediately.[367–369] Even more advanced iterations can convert pH fluctuations into electrical signals that are captured and analyzed, providing clinicians or caregivers with more than just a color indication.[370,371]

However, passive sensing is not enough. Embedded biosensors are miniaturized systems implanted directly into the skin.[372,373] Built using materials such as stretchable gold nanowires, conductive ink, or soft silicone microfluidics, embedded sensors can monitor oxygen saturation, hydration levels, or inflammatory cytokines, depending on their specific tuning.[374–376] Importantly, many of these sensors are now thin and flexible enough to conform to the skin, thereby avoiding the stiffness mismatch that once made implantation difficult.[377–379]

The final component in this framework involves wireless data transmission modules. Detecting physiological signals represents only part of the process; effective translation requires that this information be accurately transmitted and analyzed in real time. Whether it is a phone application, a cloud database, or an AI model that examines wound development patterns, the wireless transmission of sensor data is central to making bioengineered skin truly smart.[380,381] Low-energy Bluetooth, near-field communication, and even energy-harvesting radio systems are being adapted for skin-level interfaces.[382–384] This permits continuous, non-invasive monitoring, without requiring any additional wires, external readers, or hospital-only systems. A healing patch can now silently send updates to a connected device, alerting clinicians only when it detects a deviation from expected healing patterns.

When these factors combine, pH-sensitive materials enable the establishment of an early warning, an embedded sensor provides more information, and wireless technology ensures the data flow, all of which make printed skin more than just a scaffold. It becomes an intelligent collaborator in care. No longer just a surface covering, but a networked, communicative, diagnostic platform that watches the wound in real time and evolves with it. Such responsiveness

may mean the difference between regular healing and early intervention that prevents complications.

5.4. Artificial intelligence and Internet of Things-enabled wound management platforms

Information must become action, and in wound care, time is of the essence. The actual magic lies in the fact that skin constructs cease to be mere passive data recorders and become active participants in the healing process. This is where AI and the IoT come into play, turning real-time monitoring into something smarter: predictive, autonomous, and connected.[385–387]

Predictive healing analytics are a good starting point. Consider a printed skin patch that not only monitors pH or hydration levels but also learns from that information over time. By using machine learning models trained on thousands of wound cases, these systems can begin to identify patterns—what healing looks like, what early infection signals resemble, and when a wound is deviating from its expected course.[388,389] Rather than waiting till the symptoms escalate, clinicians can receive early alarms before anything becomes visibly wrong. These models are not just general-purpose; with enough data, predictions can be personalized to the patient's age, comorbidities, and wound type. This is preventative care rather than reactive treatment.

Next, autonomous wound reporting closes the feedback loop.[390] Under the traditional system, the information must be manually examined and interpreted, and undergo a series of steps before a decision is reached. But what if the system could flag an issue itself? Or auto-record daily healing data. It is now not inconceivable that we will see platforms where the printed skin, with its embedded sensors, raises alerts—e.g., through a smartphone notification or a clinician dashboard—when healing does not follow the expected patterns. They can operate around the clock, gathering data even in the absence of human observation, and can be used in home care and outpatient settings.

The backbone of all this is cloud-based data integration. Without seamless, secure data storage and accessibility, these systems may not be able to function.[391] Cloud platforms enable the centralized collection, cleaning, and analysis of biosensor data from printed patches, often in real-time. They also enable the passive construction of cross-patient comparisons and research-grade datasets. That means better models, better diagnostics, and even remote consultations without requiring the patient to travel. This becomes even more key for rural or resource-scarce areas where experts may not always be available, but smart infrastructure can bridge the gap.

Artificial intelligence and IoT, together, not only add layers of technology but also bring a completely different approach to wound management. Healing can be observed, comprehended, and even anticipated before complications occur. To patients, it means fewer trips to the hospital, quicker interventions, and greater assurance of healing. To clinicians, it presents an opportunity to shift their practices of relying on charts to make guesses to data-based decision-making. And for the printed skin itself? Although currently proof-of-concept platforms are far from being clinically validated treatments, in principle, such constructs could function as intelligent interfaces between biological and electronic components.

6. Future perspectives

6.1. Technological bottlenecks and future directions in skin bioprinting

Although skin bioprinting efforts to date are promising, technical bottlenecks still need to be overcome before it can be fully realized clinically. Focusing on new bioinks and smart systems receives a lot of attention, but from a systems perspective, deeper systemic challenges, from materials to machine interfaces to regulatory ecosystems, must be addressed holistically. This section outlines the primary limitations and provides realistic future directions, drawing on the current literature and trends in translational bioprinting.

6.1.1. Bioink stability and functional limitations

Modern-day bioinks still struggle under the conditions of actual wound environments, including extreme pH levels, inflammation, thermal damage, and oxidative stress.[111,112] Despite exhibiting good performance *in vitro*, many formulations fail to maintain their integrity under *in vivo* conditions, either in terms of physical stability or bioactivity. Cell viability during deposition, especially when using shear-sensitive stem cells, remains a significant concern.[392,393] Moreover, most clinically explored bioinks (like alginate or GelMA) offer limited bioresponsiveness and mechanical tunability.[171] Irregularities in viscosity make the printability and resolution difficult, whereas crosslinking kinetics remain either too sluggish or inconsistent to permit steady intraoperative use.[44,180,227,255]

For future strategic directions, bioinks that are xeno-free, GMP-compliant, and that can react dynamically to real-time stimuli such as wound pH, enzymes, or even wireless stimuli are needed. This includes the exploration of ECM-derived smart hydrogels, as well as thermo- and light-curable, and multi-phase co-axial constructs capable of adjusting themselves after deposition. Inks with integrated sensing and feedback loops will, in addition,

have the potential to fill a gap between passive grafts and responsive, living tissues.

6.1.2. Hardware: Portability, precision, and adaptability

Large bioprinters, however, are bulky, consume a significant amount of power, and are too complicated to print quickly in an emergency or surgical environment. Even handheld bioprinters experience nozzle clogging/or uneven print speeds, and poor resolutions when printing on uneven wound surfaces.[124,147]

A new generation of rugged, handheld bioprinters that can automatically scan, model, and print with little human input. To minimize operator error, these systems should incorporate smart material recognition, lidar surface mapping, and dynamic calibration systems, be haptics aware, and allow printing in irregular, moist, and bleeding wounds. Robotic surgical arms with wound-specific motion prediction are also worth exploring.

6.1.3. Clinical workflow integration

Although bioprinting has excellent potential, it can be challenging to integrate it into the real-world operating room. Existing workflows are associated with a significant amount of setup, validation of biocompatibility, and qualified operators—factors that are not always available in high-speed trauma or burn units. [90,186]

Thus, there is a need to critically advance toward the development of true plug-and-play platforms. Consider, for example, prefillable single-use cartridges, on-device image processing, and cloud-connected design pipelines that enable surgeons to upload wound images and receive a ready-to-print file in minutes.[90,186,196,197,380,391,394] Automated nozzle cleaning, wireless feedback from biosensors, and instant printing presets should be built into smart systems, ensuring that just-in-time grafting does not impede operating room schedules.[29,174,207,310,311,313,316,319,332–334,355]

6.1.4. Cell source and differentiation challenges

One of the most significant biological barriers is the unreliability of stem cell-derived constructs. For example, primary cells exhibit unpredictable differentiation and senescence, while iPSCs raise concerns regarding tumorigenicity and epigenetic drift.[27,28,53,60] Scale-up cell expansion remains slow, costly, and difficult to effect.

Induced progenitor cells with lineage biases (i.e., epidermal, glandular, or neural) could be a potential strategy to overcome this challenge.[52–54,135,184,224,258,259,284,291,293,340] Such *in situ* differentiation using spatially guided biochemical gradients combined with feedback loops driven by machine learning can help control cell fate after cell implantation. The integration of biosensors, monitoring gene expression or secretion profiles, provides dynamic control of regeneration.

6.1.5. Vascularization and functional appendage integration

While vascular grafts have significantly evolved to this point, the prospect of making fully perfusable, anastomosis-ready constructs that exhibit appendage integration (sweat glands, sebaceous units, pigmentation, sensation) is still an uphill effort.[52–54,135,137,313,332,334] Constructs frequently have issues with necrosis or fail to reconstitute sensory-motor functions.

Technologies such as microfluidic vascular scaffold, coaxial printing for channels resembling vessels, and growth factor gradients for controlling angiogenesis show promise.[42,45,59,71,145,161,175,185,260,279,290,302,303] Neural regeneration is also gaining popularity, with piezoelectric or conductive scaffolds demonstrating their potential to direct axon growth.[395,396] Efforts should now be directed toward imitating the appendage-specific architecture, as shown in recent skin models, which exhibit rudimentary gland formation.[52–54,135]

6.1.6. Manufacturing, regulation, and standardization

A less widely discussed problem is regulatory uncertainty. Depending on the jurisdiction, bioprinted skin can be classified as a "biologic," "medical device," or "ATMP" product.[64,66,68,71,72] Without standard manufacturing pipelines and testing criteria, even the most innovative of technologies risk being locked up in preclinical limbo.

There have been increasing demands for additional global harmonization of regulatory pathways, particularly between the FDA and the EMA. Establishing consistent quality control standards for sterility, degradation kinetics, and bioactivity is necessary. Companies should also advocate for pre-qualified clinical-grade bioinks, off-the-shelf sterile GMP cartridges, and point-of-care manufacturing units with real-time traceability over the cloud.

6.1.7. Cost, reimbursement, and ethics

Lastly, cost remains a significant barrier. In the absence of established reimbursement codes and scant long-term outcome data, bioprinting currently exists on the periphery of the health insurance system.[123,129,130] Furthermore, the ethical issues that accompany gene-edited cells or AI-directed surgical interventions are not extensively discussed.

As bioprinting moves closer to clinical reality, subsequent trials should incorporate economic outcomes measures, including shorter hospital stays, fewer graft revisions, and improved functional recovery. Collaborations

involving health economists, payer advisory boards, and ethics panels should be started early on. This field is still in its early stages, and, as it develops, new ethical guidelines will be needed to ensure cross-border data sharing and informed consent procedures.

6.2. Emerging directions in smart skin bioprinting: From concept to early translation

While current advances have primarily focused on resolving specific technological barriers, several conceptual and translational trends are beginning to redefine the long-term vision for skin bioprinting. Although many are in preclinical or early explorative stages, they represent important directions for further development. The skin we print today is smarter than it was 5 years ago—but it is nowhere near reaching its full potential. This is only the first chapter of a far larger narrative, in which tissue regeneration, biosensing, and smart feedback loops converge to form living systems that not only correct damage but also evolve to become responsive to it.[7,29,391,397] In the future, the most radical growth in this area may not be in the materials themselves, but in the way systems communicate, acquire knowledge as they process data, and evolve. These conceptual trends, which range from autonomous *in situ* printing to regulatory integration, are summarized in Figure 9, providing a system-level roadmap of how these innovations can converge in future smart skin platforms.

One of the most exciting directions lies in fully autonomous *in situ* bioprinting platforms.[140] Although it is still heavily reliant on manual control today, future systems may behave more like robotic surgeons, scanning wounds in real-time, deciding on the ideal cell and ink mix, adjusting print parameters on the fly, and embedding sensors during a single automated pass. Solutions based on real-time image and route planning using AI would significantly reduce the guesswork and variation in wound reconstruction. The structure that we are heading to is that the printer reacts to the wound as a living, evolving environment—not just a surface to be covered but a dynamic interface to be interpreted.

We shall also see a dramatic growth in multi-functional ink formulations, particularly those integrating regenerative, sensory, and therapeutic purposes. Instead of layering different materials for structure, signal, and drug delivery, future inks may be able to do all three simultaneously. Imagine a single extrusion containing cells, a responsive polymer that stiffens with temperature, and a time-release antibiotic triggered by infection markers.[29,34,398] These inks will be more complex and will require increased effort in formulation science and printer hardware, but the reward will be skin-like constructs that act more like the skin, which is flexible, interactive, and self-assembling.

Predictive models trained on large datasets of healthcare data will come to the forefront of digital innovation. All printed patches, embedded sensors, and uploaded wound logs contribute to an expanding knowledge graph. This data can then be used to predict healing schedules, prescribe interventions, or optimize print plans in real-time using machine learning models.[217,389] Smart skin, combined with smart software, enables personalized wound care that was once an elusive dream.[168,202] Connectivity with hospital networks and wearable health ecosystems will both push these systems into daily clinical operations, quietly gathering data behind the scenes, only intervening when there is something to be addressed.

Of course, regulatory pathways and ethical frameworks must evolve in parallel.[64–66,76] As we proceed with autonomous wound management and AI-powered diagnostics, issues regarding data security, clinical accountability, and long-term monitoring will need to be addressed directly. Who owns the data from a sensing patch? In what situations is it appropriate to assist human judgment with an AI in critical care situations? They are not only technical challenges, but also social ones, as they will determine the way in which these technologies are incorporated and adopted.

Lastly, the horizon is not restricted to wound care. The principles developed here—adaptive bioprinting, intelligent sensing, and cloud-integrated healing—will eventually spill into broader applications, including soft robotics, brain–machine interfaces, and artificial organs.[166,309,324,399] The starting point might be smart skin, but the ultimate goal is to create a generation of biohybrid systems that push the boundary between biology and engineered intelligence.

In brief, it is not merely a better graft that is the future of smart bioengineered skin. It is about designing systems that think, feel, and respond—skin that listens to the body, learns from it, and helps it heal faster, smarter, and more completely.[166,168,327] Figure 9 is a strategic synthesis of this vision, not as a visual synopsis of the vision, but as a framework to interconnect technological innovation and translational readiness. As a whole, it sketches out a systemic convergence: autonomous robotic platforms, real-time wound interpretation and adaptive printing behavior, multi-functional materials for single-step formulations, machine learning systems, cumulative sensors for personalized and predictive wound care plans, and regulatory and ethical realms as co-requisites for clinical translation. Taken together, these pieces serve to highlight a paradigm change—one from printing skin to

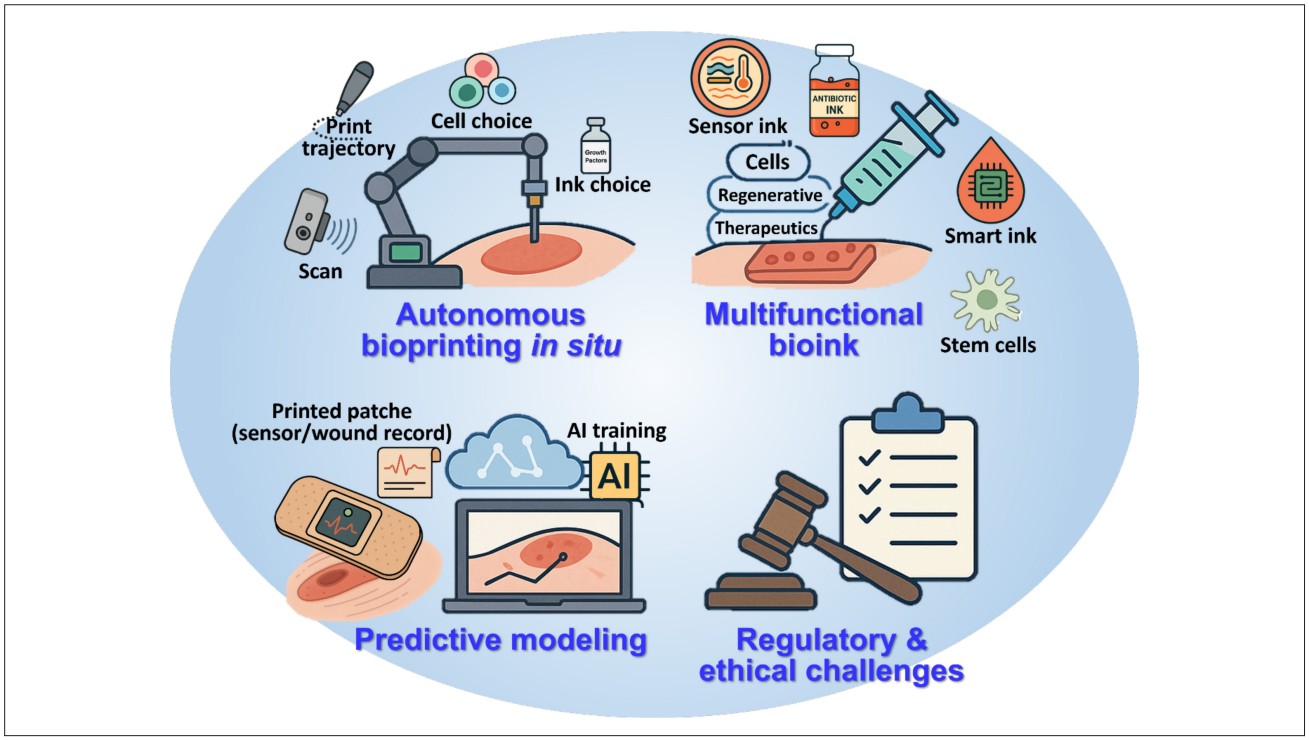

Figure 9. Future roadmap of smart skin bioprinting: Autonomous systems, multifunctional inks, predictive modeling, and ethical integration. Map of the future bioprinting landscape of smart skin. The top-left portion of the figure shows an entirely autonomous *in situ* bioprinting system, enabled by real-time imaging, intelligent print path planning driven by artificial intelligence (AI), and intelligent material selection. The top right shows the advancement of integrated bioinks containing living cells, smart therapeutics, and responsive sensors (e.g., the release of antibiotics, heat-cleaving polymers, and signaling light-emitting ink). The bottom-left corner reflects the rise of AI-enhanced wound care platforms, where printed patches are embedded with sensors, linked to cloud databases, and capable of performing predictive modeling through deep learning. Finally, the bottom-right refers to those regulatory and ethical challenges related to data ownership, clinical accountability, and authorization pathways that must be developed in tandem with the technology. This skin becomes an active system—communicating and intelligent—and this technology represents a novel paradigm in regenerative medicine where skin substitutes become active systems. Figure created using illustrations generated via ChatGPT (OpenAI image tools), with final layout and annotations edited in Microsoft PowerPoint.

creating responsive healing systems. Such a visual roadmap is critical to understanding not only where we are, but where we need to be to make regenerative skin truly smart.

7. Conclusion

Skin is no longer just something we aim to replace—it is something we now seek to upgrade. With the convergence of bioprinting, smart materials, and digital health technologies, bioengineered skin has begun to evolve into not only a structural replacement but also a living, sensing, and responsive system. This transformation represents a paradigm shift in our approach to wound care and tissue repair, transitioning from a passive, data-driven, and functionally disjointed process to an active, data-driven, and functionally unified one.

Here, we discussed the key factors driving this shift, including both tactile and thermal restoration approaches, the development of smart inks that enable sensing and reaction, and real-time biosensing networks, as well as wound management platforms utilizing AI. All these combine to create a blueprint of the new generation of skin constructs: biocompatible systems, as well as communicative, adaptable, and intelligent.

The challenges that await, in optimization of materials, unification of devices, and regulation, are significant, and so is the potential. Smart skin bioprinting is no longer confined to the lab bench. It is stepping into the clinic, into homes, and eventually, into a broader vision of human–machine symbiosis. What we print today will determine how the body heals tomorrow—and perhaps, how it relates to the world in ways it has never dreamed of.

Abbreviations

ASCs	adipose tissue-derived mesenchymal stromal cells
ATMPs	advanced therapy medicinal products

CAD	computer-aided designing
DOF	degrees of freedom
ECs	endothelial cells
EMA	European Medicines Agency
EU	European Union
FDA	Food and Drug Administration (United States)
GelMA	gelatin methacryloyl
HCT/P	human cells, tissues, and cellular and tissue-based products
ICH	International Council for Harmonisation
IND	investigational new drug
IoT	Internet of Things
iPSCs	induced pluripotent stem cells
ISO	International Organization for Standardization
LAB	laser-assisted bioprinting
LAP	photo-initiator lithium phenyl-2,4,6- trimethylbenzoylphosphinate
MSCs	mesenchymal stem cells
PEGDA	polyethylene glycol diacrylate
PLGA	poly(lactic-co-glycolic) acid
SG	Sweat gland
STSG	split-thickness skin grafting

Acknowledgments

None.

Funding

This research was funded by grants from the National Science and Technology Council, Taiwan (NSTC 112-2314-B-182A-045-MY3), and the Chang Gung Medical Foundation, Chang Gung Memorial Hospital, Taiwan (CMRPG3M0283).

Conflict of interest

The authors declare they have no competing interests.

Author contributions

Conceptualization: Aline Yen Ling Wang
Formal analysis: Ana Elena Aviña, Yen-Yu Liu
Investigation: Aline Yen Ling Wang, Ana Elena Aviña, Yen-Yu Liu, Huang-Kai Kao
Methodology: Ana Elena Aviña, Yen-Yu Liu
Writing – original draft: Aline Yen Ling Wang
Writing – review & editing: Huang-Kai Kao

Ethics approval and consent to participate

Not applicable.

Consent for publication

Not applicable.

Availability of data

Not applicable

References

1. Wang Y, Beekman J, Hew J, *et al*. Burn injury: challenges and advances in burn wound healing, infection, pain and scarring. *Adv Drug Deliv Rev*. 2018;123:3-17. doi: 10.1016/j.addr.2017.09.018
2. Jeschke MG, van Baar ME, Choudhry MA, Chung KK, Gibran NS, Logsetty S. Burn injury. *Nat Rev Dis Primers*. 2020;6(1):11. doi: 10.1038/s41572-020-0145-5
3. Goh M, Du M, Peng WR, Saw PE, Chen Z. Advancing burn wound treatment: exploring hydrogel as a transdermal drug delivery system. *Drug Deliv*. 2024;31(1):2300945. doi: 10.1080/10717544.2023.2300945
4. Rowan MP, Cancio LC, Elster EA, *et al*. Burn wound healing and treatment: review and advancements. *Crit Care*. 2015;19:243. doi: 10.1186/s13054-015-0961-2
5. Shahin H, Elmasry M, Steinvall I, Soberg F, El-Serafi A. Vascularization is the next challenge for skin tissue engineering as a solution for burn management. *Burns Trauma*. 2020;8:tkaa022. doi: 10.1093/burnst/tkaa022
6. Finnerty CC, Jeschke MG, Branski LK, Barret JP, Dziewulski P, Herndon DN. Hypertrophic scarring: the greatest unmet challenge after burn injury. *Lancet*. 2016;388(10052):1427-1436. doi: 10.1016/S0140-6736(16)31406-4
7. Shpichka A, Butnaru D, Bezrukov EA, *et al*. Skin tissue regeneration for burn injury. *Stem Cell Res Ther*. 2019;10(1):94. doi: 10.1186/s13287-019-1203-3
8. Luze H, Nischwitz SP, Smolle C, Zrim R, Kamolz LP. The use of acellular fish skin grafts in burn wound management-a systematic review. *Medicina (Kaunas)*. 2022;58(7):912. doi: 10.3390/medicina58070912

9. Dagher J, Arcand C, Auger FA, Germain L, Moulin VJ. The self-assembled skin substitute history: successes, challenges, and current treatment indications. *J Burn Care Res*. 2023;44(Suppl_1):S57-S64. doi: 10.1093/jbcr/irac074
10. Seet WT, Mat Afandi MA, Ishak MF, *et al*. Quality management overview for the production of a tissue-engineered human skin substitute in Malaysia. *Stem Cell Res Ther*. 2023;14(1):298. doi: 10.1186/s13287-023-03536-9
11. Paggiaro AO, Bastianelli R, Carvalho VF, Isaac C, Gemperli R. Is allograft skin, the gold-standard for burn skin substitute? A systematic literature review and meta-analysis. *J Plast Reconstr Aesthet Surg*. 2019;72(8):1245-1253. doi: 10.1016/j.bjps.2019.04.013
12. Seth AK, Friedstat JS, Orgill DP, Pribaz JJ, Halvorson EG. Microsurgical burn reconstruction. *Clin Plast Surg*. 2017;44(4):823-832. doi: 10.1016/j.cps.2017.05.014
13. Li Y, An S, Deng C, Xiao S. Human acellular amniotic membrane as skin substitute and biological scaffold: a review of its preparation, preclinical research, and clinical application. *Pharmaceutics*. 2023;15(9):2249. doi: 10.3390/pharmaceutics15092249
14. Barbachowska A, Korzeniowski T, Surowiecka A, Struzyna J. Alloplastic epidermal skin substitute in the treatment of burns. *Life (Basel)*. 2023;14(1):43. doi: 10.3390/life14010043
15. Bartkova J, Horalkova E, Barcinova V, Hrusovska R. Summary of the skin substitute revolution - skin coverings in the modern era of healthcare. *Rozhl Chir*. 2024;103(6):202-207. Revoluce koznich nahrad - kozni kryty v moderni ere zdravotnictvi. doi: 10.33699/PIS.2024.103.6.202-207
16. Widgerow AD. Bioengineered skin substitute considerations in the diabetic foot ulcer. *Ann Plast Surg*. 2014;73(2):239-244. doi: 10.1097/SAP.0b013e31826eac22
17. MacAdam A, Chaudry E, McTiernan CD, Cortes D, Suuronen EJ, Alarcon EI. Development of in situ bioprinting: a mini review. *Front Bioeng Biotechnol*. 2022;10:940896. doi: 10.3389/fbioe.2022.940896
18. Singh S, Choudhury D, Yu F, Mironov V, Naing MW. In situ bioprinting - bioprinting from benchside to bedside? *Acta Biomater*. 2020;101:14-25. doi: 10.1016/j.actbio.2019.08.045
19. Dong H, Hu B, Zhang W, *et al*. Robotic-assisted automated in situ bioprinting. *Int J Bioprint*. 2023;9(1):629. doi: 10.18063/ijb.v9i1.629
20. Hwangbo H, Koo Y, Nacionales F, Kim J, Chae S, Kim GH. Stimulus-assisted in situ bioprinting: advancing direct bench-to-bedside delivery. *Trends Biotechnol*. 2025;43(5):1015-1030. doi: 10.1016/j.tibtech.2024.11.001
21. Jain P, Kathuria H, Ramakrishna S, Parab S, Pandey MM, Dubey N. In situ bioprinting: process, bioinks, and applications. *ACS Appl Bio Mater*. 2024;7(12):7987-8007. doi: 10.1021/acsabm.3c01303
22. Albanna M, Binder KW, Murphy SV, *et al*. In situ bioprinting of autologous skin cells accelerates wound healing of extensive excisional full-thickness wounds. *Sci Rep*. 2019;9(1):1856. doi: 10.1038/s41598-018-38366-w
23. Zhao M, Wang J, Zhang J, *et al*. Functionalizing multi-component bioink with platelet-rich plasma for customized in-situ bilayer bioprinting for wound healing. *Mater Today Bio*. 2022;16:100334. doi: 10.1016/j.mtbio.2022.100334
24. Li R, Zhao Y, Zheng Z, *et al*. Bioinks adapted for in situ bioprinting scenarios of defect sites: a review. *RSC Adv*. 2023;13(11):7153-7167. doi: 10.1039/d2ra07037e
25. Cheng RY, Eylert G, Gariepy JM, *et al*. Handheld instrument for wound-conformal delivery of skin precursor sheets improves healing in full-thickness burns. *Biofabrication*. 2020;12(2):025002. doi: 10.1088/1758-5090/ab6413
26. Skardal A, Murphy SV, Crowell K, Mack D, Atala A, Soker S. A tunable hydrogel system for long-term release of cell-secreted cytokines and bioprinted in situ wound cell delivery. *J Biomed Mater Res B Appl Biomater*. 2017;105(7):1986-2000. doi: 10.1002/jbm.b.33736
27. Kim B, Kim J, Lee S. Unleashing the power of undifferentiated induced pluripotent stem cell bioprinting: current progress and future prospects. *Int J Stem Cells*. 2024;17(1):38-50. doi: 10.15283/ijsc23146
28. Shukla AK, Gao G, Kim BS. Applications of 3D bioprinting technology in induced pluripotent stem cells-based tissue engineering. *Micromachines (Basel)*. 2022;13(2):155. doi: 10.3390/mi13020155
29. Derman ID, Rivera T, Garriga Cerda L, *et al*. Advancements in 3D skin bioprinting: processes, bioinks, applications and sensor integration. *Int J Extrem Manuf*. 2025;7(1):012009. doi: 10.1088/2631-7990/ad878c
30. Santhamoorthy M, Kim SC. A review of the development of biopolymer hydrogel-based scaffold materials for drug delivery and tissue engineering applications. *Gels*. 2025;11(3):178. doi: 10.3390/gels11030178
31. Marimuthu T, Kumar P, Choonara YE. Visible light-curable water-soluble chitosan derivative, chitosan hydrogel, and preparation method: a patent evaluation of US2019202998A1. *Expert Opin Ther Pat*. 2021;31(5):351-360. doi: 10.1080/13543776.2021.1903433
32. Euti EM, Wolfel A, Picchio ML, *et al*. Controlled thermoreversible formation of supramolecular

hydrogels based on poly(vinyl alcohol) and natural phenolic compounds. *Macromol Rapid Commun*. 2019;40(18):e1900217.
doi: 10.1002/marc.201900217

33. Das S, Das D. Rational design of peptide-based smart hydrogels for therapeutic applications. *Front Chem*. 2021;9:770102.
doi: 10.3389/fchem.2021.770102

34. Ding K, Liao M, Wang Y, Lu JR. Advances in composite stimuli-responsive hydrogels for wound healing: mechanisms and applications. *Gels*. 2025;11(6):420.
doi: 10.3390/gels11060420

35. Ferroni L, D'Amora U, Gardin C, *et al*. Stem cell-derived small extracellular vesicles embedded into methacrylated hyaluronic acid wound dressings accelerate wound repair in a pressure model of diabetic ulcer. *J Nanobiotechnology*. 2023;21(1):469.
doi: 10.1186/s12951-023-02202-9

36. Hao L, Zhao S, Hao S, *et al*. Functionalized gelatin-alginate based bioink with enhanced manufacturability and biomimicry for accelerating wound healing. *Int J Biol Macromol*. 2023;240:124364.
doi: 10.1016/j.ijbiomac.2023.124364

37. Jorgensen AM, Varkey M, Gorkun A, *et al*. Bioprinted skin recapitulates normal collagen remodeling in full-thickness wounds. *Tissue Eng Part A*. 2020;26(9-10):512-526.
doi: 10.1089/ten.TEA.2019.0319

38. Ma Y, Wang Y, Chen D, *et al*. 3D bioprinting of a gradient stiffened gelatin-alginate hydrogel with adipose-derived stem cells for full-thickness skin regeneration. *J Mater Chem B*. 2023;11(13):2989-3000.
doi: 10.1039/d2tb02200a

39. Cubo N, Garcia M, Del Canizo JF, Velasco D, Jorcano JL. 3D bioprinting of functional human skin: production and in vivo analysis. *Biofabrication*. 2016;9(1):015006.
doi: 10.1088/1758-5090/9/1/015006

40. Fu H, Zhang D, Zeng J, *et al*. Application of 3D-printed tissue-engineered skin substitute using innovative biomaterial loaded with human adipose-derived stem cells in wound healing. *Int J Bioprint*. 2023;9(2):674.
doi: 10.18063/ijb.v9i2.674

41. Zhang D, Fu Q, Fu H, Zeng J, Jia L, Chen M. 3D-bioprinted human lipoaspirate-derived cell-laden skin constructs for healing of full-thickness skin defects. *Int J Bioprint*. 2023;9(4):718.
doi: 10.18063/ijb.718

42. Baltazar T, Jiang B, Moncayo A, *et al*. 3D bioprinting of an implantable xeno-free vascularized human skin graft. *Bioeng Transl Med*. 2023;8(1):e10324.
doi: 10.1002/btm2.10324

43. Michael S, Sorg H, Peck CT, *et al*. Tissue engineered skin substitutes created by laser-assisted bioprinting form skin-like structures in the dorsal skin fold chamber in mice. *PLoS One*. 2013;8(3):e57741.
doi: 10.1371/journal.pone.0057741

44. Lee S-G, Lee S, Bae H-K, *et al*. Evaluation of the therapeutic efficacy of human skin equivalents manufactured through droplet-based bioprinting/nebulization technology. *Mol Cell Toxicol*. 2023;20(1):129-138.
doi: 10.1007/s13273-023-00330-9

45. Yanez M, Rincon J, Dones A, De Maria C, Gonzales R, Boland T. In vivo assessment of printed microvasculature in a bilayer skin graft to treat full-thickness wounds. *Tissue Eng Part A*. 2015;21(1-2):224-233.
doi: 10.1089/ten.TEA.2013.0561

46. Tanadchangsaeng N, Pasanaphong K, Tawonsawatruk T, *et al*. 3D bioprinting of fish skin-based gelatin methacryloyl (GelMA) bio-ink for use as a potential skin substitute. *Sci Rep*. 2024;14(1):23240.
doi: 10.1038/s41598-024-73774-1

47. Yang Y, Xu R, Wang C, Guo Y, Sun W, Ouyang L. Recombinant human collagen-based bioinks for the 3D bioprinting of full-thickness human skin equivalent. *Int J Bioprint*. 2022;8(4):611.
doi: 10.18063/ijb.v8i4.611

48. Zhou F, Hong Y, Liang R, *et al*. Rapid printing of bio-inspired 3D tissue constructs for skin regeneration. *Biomaterials*. 2020;258:120287.
doi: 10.1016/j.biomaterials.2020.120287

49. Shi Y, Xing TL, Zhang HB, *et al*. Tyrosinase-doped bioink for 3D bioprinting of living skin constructs. *Biomed Mater*. 2018;13(3):035008.
doi: 10.1088/1748-605X/aaa5b6

50. Azadmanesh F, Pourmadadi M, Zavar Reza J, Yazdian F, Omidi M, Haghirosadat BF. Synthesis of a novel nanocomposite containing chitosan as a three-dimensional printed wound dressing technique: emphasis on gene expression. *Biotechnol Prog*. 2021;37(4):e3132.
doi: 10.1002/btpr.3132

51. Wang S, Xiong Y, Chen J, *et al*. Three dimensional printing bilayer membrane scaffold promotes wound healing. *Front Bioeng Biotechnol*. 2019;7:348.
doi: 10.3389/fbioe.2019.00348

52. Yuan X, Duan X, Enhejirigala, *et al*. Reciprocal interaction between vascular niche and sweat gland promotes sweat gland regeneration. *Bioact Mater*. 2023;21:340-357.
doi: 10.1016/j.bioactmat.2022.08.021

53. Yao B, Wang R, Wang Y, *et al*. Biochemical and structural cues of 3D-printed matrix synergistically direct MSC differentiation for functional sweat gland regeneration. *Sci Adv*. 2020;6(10):eaaz1094.
doi: 10.1126/sciadv.aaz1094

54. Huang S, Yao B, Xie J, Fu X. 3D bioprinted extracellular matrix mimics facilitate directed differentiation of epithelial

progenitors for sweat gland regeneration. *Acta Biomater*. 2016;32:170-177.
doi: 10.1016/j.actbio.2015.12.039

55. Abaci HE, Coffman A, Doucet Y, *et al*. Tissue engineering of human hair follicles using a biomimetic developmental approach. *Nat Commun*. 2018;9(1):5301.
doi: 10.1038/s41467-018-07579-y

56. Xu L, Zhang Z, Jorgensen AM, *et al*. Bioprinting a skin patch with dual-crosslinked gelatin (GelMA) and silk fibroin (SilMA): an approach to accelerating cutaneous wound healing. *Mater Today Bio*. 2023;18:100550.
doi: 10.1016/j.mtbio.2023.100550

57. Apelgren P, Amoroso M, Saljo K, *et al*. Skin grafting on 3D bioprinted cartilage constructs in vivo. *Plast Reconstr Surg Glob Open*. 2018;6(9):e1930.
doi: 10.1097/GOX.0000000000001930

58. Seol YJ, Lee H, Copus JS, *et al*. 3D bioprinted biomask for facial skin reconstruction. *Bioprinting*. 2018;10:e00028.
doi: 10.1016/j.bprint.2018.e00028

59. Baltazar T, Merola J, Catarino C, *et al*. Three dimensional bioprinting of a vascularized and perfusable skin graft using human keratinocytes, fibroblasts, pericytes, and endothelial cells. *Tissue Eng Part A*. 2020;26(5-6):227-238.
doi: 10.1089/ten.TEA.2019.0201

60. Intini C, Elviri L, Cabral J, *et al*. 3D-printed chitosan-based scaffolds: an in vitro study of human skin cell growth and an in-vivo wound healing evaluation in experimental diabetes in rats. *Carbohydr Polym*. 2018;199:593-602.
doi: 10.1016/j.carbpol.2018.07.057

61. Hao L, Tao X, leeeng M, *et al*. Stepwise multi-cross-linking bioink for 3D embedded bioprinting to promote full-thickness wound healing. *ACS Appl Mater Interfaces*. 2023;15(20):24034-24046.
doi: 10.1021/acsami.3c00688

62. Kesavan R, Sheela Sasikumar C, Narayanamurthy VB, Rajagopalan A, Kim J. Management of diabetic foot ulcer with MA-ECM (minimally manipulated autologous extracellular matrix) using 3D bioprinting technology - an innovative approach. *Int J Low Extrem Wounds*. 2024;23(1):161-168.
doi: 10.1177/15347346211045625

63. Zhang M, Li Z, Yang R, *et al*. Revolutionizing chronic wound treatment: treating bleomycin intralesional injection-related chronic wounds with 3-dimensional bioprinted skin substitutes. *J Invest Dermatol*. 2025;145(8):2111-2114 e7.
doi: 10.1016/j.jid.2024.12.018

64. Mladenovska T, Choong PF, Wallace GG, O'Connell CD. The regulatory challenge of 3D bioprinting. *Regen Med*. 2023;18(8):659-674.
doi: 10.2217/rme-2022-0194

65. Gilbert F, O'Connell CD, Mladenovska T, Dodds S. Print Me an Organ? Ethical and regulatory issues emerging from 3D bioprinting in medicine. *Sci Eng Ethics*. 2018;24(1):73-91.
doi: 10.1007/s11948-017-9874-6

66. Ricles LM, Coburn JC, Di Prima M, Oh SS. Regulating 3D-printed medical products. *Sci Transl Med*. 2018;10(461):eaan6521.
doi: 10.1126/scitranslmed.aan6521

67. Considerations for the Design of Early-Phase Clinical Trials of Cellular and Gene Therapy Products, Guidance for Industry. Food and Drug Administration. U.S.; 2015.

68. Evaluation of Devices Used with Regenerative Medicine Advanced Therapies, Guidance for Industry. U.S.: Food and Drug Administration; 2019.

69. Regulatory Considerations for Human Cells, Tissues, and Cellular and Tissue-Based Products: Minimal Manipulation and Homologous Use, Guidance for Industry. U.S.: Food and Drug Administration; 2020.

70. Same Surgical Procedure Exception under 21 CFR 1271.15(b): Questions and Answers Regarding the Scope of the Exception, Guidance for Industry. U.S.: Food and Drug Administration; 2017.

71. Bibb R, Nottrodt N, Gillner A. Artificial vascularized scaffolds for 3D-tissue regeneration — a report of the ArtiVasc 3D Project. *Int J Bioprint*. 2016;2(1):93-102.
doi: 10.18063/ijb.2016.01.004

72. Li P, Faulkner A. 3D bioprinting regulations: a UK/EU perspective. *Eur J Risk Regul*. 2017;8(2):441-447.
doi: 10.1017/err.2017.19

73. Bicudo E, Brass I, Carmichael P, Farid S. The UK's emerging regulatory framework for point-of-care manufacture: insights from a workshop on advanced therapies. *Cell Gene Ther Insights*. 2021;7(9):1005-1015.
doi: 10.18609/cgti.2021.133

74. Guidelines on Good Manufacturing Practice for Advanced Therapy Medicinal Products. European Medicines Agency, European Commission; 2017.

75. Guidelines on Good Clinical Practice specific to Advanced Therapy Medicinal Products. European Medicines Agency, European Commission; 2019.

76. Iglesias-Lopez C, Obach M, Vallano A, Agusti A. Comparison of regulatory pathways for the approval of advanced therapies in the European Union and the United States. *Cytotherapy*. 2021;23(3):261-274.
doi: 10.1016/j.jcyt.2020.11.008

77. Potency Tests for Cellular and Gene Therapy Products, Guidance for Industry. U.S.: Food and Drug Administration; 2011.

78. Manufacturing Changes and Comparability for Human Cellular and Gene Therapy Products, Draft Guidance for Industry. U.S.: Food and Drug Administration; 2023.

79. International Organization for Standardization. ISO 13485:

2016 Medical Devices — Quality Management Systems – Requirements for Regulatory Purposes; 2016.

80. International Organization for Standardization. ISO 14155: 2020 Clinical Investigation of Medical Devices for Human Subjects — Good Clinical Practice; 2020.

81. Nissan AM. Regulating the three-dimensional future: how the FDA should structure a regulatory mechanism for additive manufacturing (3d printing). *Bost. Univ. J. Sci. Technol.* Law. 2016; 22: 267–97.

82. O'Connell CD, Onofrillo C, Duchi S, *et al*. Evaluation of sterilisation methods for bio-ink components: gelatin, gelatin methacryloyl, hyaluronic acid and hyaluronic acid methacryloyl. *Biofabrication*. 2019;11(3):035003. doi: 10.1088/1758-5090/ab0b7c

83. Lorson T, Ruopp M, Nadernezhad A, *et al*. Sterilization methods and their influence on physicochemical properties and bioprinting of alginate as a bioink component. *ACS Omega*. 2020;5(12):6481-6486. doi: 10.1021/acsomega.9b04096

84. Rynio P, Galant K, Wojcik L, *et al*. Effects of sterilization methods on different 3D printable materials for templates of physician-modified aortic stent grafts used in vascular surgery-a preliminary study. *Int J Mol Sci*. 2022;23(7):3539. doi: 10.3390/ijms23073539

85. International Organization for Standardization. ISO 17665: 2006 Sterilization of Health Care Products – Moist Heat; 2006.

86. International Organization for Standardization. ISO 11137: 2017 Sterilization of Health Care Products – Radiation; 2017.

87. International Organization for Standardization. ISO 11135: 2014: Sterilization of Health-Care Products — Ethylene Oxide — Requirements for the Development, Validation and Routine Control of a Sterilization Process for Medical Devices; 2014.

88. Nielsen J, Kaldor J, Irwin A, Stewart C, Nicol D. Bespoke regulation for bespoke medicine? A comparative analysis of bioprinting regulation in Europe, the USA and Australia. *J 3D Print Med*. 2021;5(3):155-167. doi: 10.2217/3dp-2021-0011

89. International Organization for Standardization. ISO 10993-1:2018 Biological Evaluation of Medical Devices – Part 1: Evaluation and Testing Within a Risk Management Process; 2018.

90. Guttridge C, Shannon A, O'Sullivan A, O'Sullivan KJ, O'Sullivan LW. Biocompatible 3D printing resins for medical applications: a review of marketed intended use, biocompatibility certification, and post-processing guidance. *Ann 3D Printed Med*. 2022;5: 100044. doi: 10.1016/j.stlm.2021.100044

91. Q8(R2) Pharmaceutical Development. International Council for Harmonisation of Technical Requirements for Pharmaceuticals for Human Use (ICH); 2009.

92. Q9(R1) Quality Risk Management. International Council for Harmonisation of Technical Requirements for Pharmaceuticals for Human Use (ICH); 2023.

93. Q10 Pharmaceutical Quality System. International Council for Harmonisation of Technical Requirements for Pharmaceuticals for Human Use (ICH); 2009.

94. Q11 Development and Manufacture of Drug Substances. International Council for Harmonisation of Technical Requirements for Pharmaceuticals for Human Use (ICH); 2012.

95. WHO Expert Committee on Biological Standardization: Sixty-Eighth Report (WHO Technical Report Series No. 1011). *World Health Organization*; 2018.

96. Yano K, Watanabe N, Tsuyuki K, Ikawa T, Kasanuki H, Yamato M. Regulatory approval for autologous human cells and tissue products in the United States, the European Union, and Japan. *Regen Ther*. 2015;1:45–56. doi: 10.1016/j.reth.2014.10.001

97. Detela G, Lodge A. EU regulatory pathways for ATMPs: standard, accelerated and adaptive pathways to marketing authorisation. *Mol Ther Methods Clin Dev*. 2019;13:205-232. doi: 10.1016/j.omtm.2019.01.010

98. Cyranoski D, Sipp D, Mallik S, Rasko JEJ. Too little, too soon: Japan's experiment in regenerative medicine deregulation. *Cell Stem Cell*. 2023;30(7):913-916. doi: 10.1016/j.stem.2023.06.005

99. Hakariya H, Ozaki A, Kaneda Y, Tanimoto T. Japan's conditional/time-limited early approval system in regenerative medicine: a case study of rise and falls of autologous skeletal myoblast sheets. *Clin Pharmacol Ther*. 2025;117(5):1171-1174. doi: 10.1002/cpt.3562

100. Horst A, McDonald F. Uncertain but not unregulated: medical product regulation in the light of three-dimensional printed medical products. *3D Print Addit Manuf*. 2020;7(5):248-257. doi: 10.1089/3dp.2020.0076

101. Regulation Impact Statement: Proposed Regulatory Scheme For Personalised Medical Devices, Including 3d-Printed Devices. Therapeutic Goods Administration, Department of Health, Australian; 2019.

102. Lee A, Hudson AR, Shiwarski DJ, *et al*. 3D bioprinting of collagen to rebuild components of the human heart. *Science*. 2019;365(6452):482-487. doi: 10.1126/science.aav9051

103. Investigating and Reporting Adverse Reactions Related to Human Cells, Tissues, and Cellular and Tissue-Based Products (HCT/Ps) Regulated Solely under Section 361 of the Public Health Service Act and 21 CFR Part 1271, Guidance for Industry. U.S.: Food and Drug Administration; 2016.

104. Calhan SD, Eker ED, Sahin NO. Quality by design (QbD) and process analytical technology (PAT) applications

in pharmaceutical industry. *Eur J Chem*. 2017;8(4): 430-433.
doi: 10.5155/eurjchem.8.4.430-433.1667

105. Wu H, White M, Khan MA. Quality-by-design (QbD): an integrated process analytical technology (PAT) approach for a dynamic pharmaceutical co-precipitation process characterization and process design space development. *Int J Pharm*. 2011;405(1-2):63-78.
doi: 10.1016/j.ijpharm.2010.11.045

106. Shojaei P, Vlahu-Gjorgievska E, Chow Y-W. Security and privacy of technologies in health information systems: a systematic literature review. *Computers*. 2024;13(2):41.
doi: 10.3390/computers13020041

107. Diaz O, Kushibar K, Osuala R, *et al*. Data preparation for artificial intelligence in medical imaging: a comprehensive guide to open-access platforms and tools. *Phys Med*. 2021;83:25-37.
doi: 10.1016/j.ejmp.2021.02.007

108. Expedited Programs for Regenerative Medicine Therapies for Serious Conditions, Guidance for Industry. U.S.: Food and Drug Administration; 2019.

109. Morrison RJ, Kashlan KN, Flanangan CL, *et al*. Regulatory considerations in the design and manufacturing of implantable 3D-printed medical devices. *Clin Transl Sci*. 2015;8(5):594-600.
doi: 10.1111/cts.12315

110. Carl AK, Hochmann D. Comparison of the regulatory requirements for custom-made medical devices using 3D printing in Europe, the United States, and Australia. *Biomed Tech (Berl)*. 2022;67(2):61-69.
doi: 10.1515/bmt-2021-0266

111. Spruijt NE, Hoogbergen MM, Buijs SJE, Grosveld MJW, Buth J. Stratification of chronic and complex wounds according to healing characteristics: a retrospective study. *J Wound Care*. 2019;28(7):446-452.
doi: 10.12968/jowc.2019.28.7.446

112. Millan-Reyes MJ, Afanador-Restrepo DF, Carcelen-Fraile MDC, *et al*. Reducing infections and improving healing in complex wounds: a systematic review and meta-analysis. *J Clin Med*. 2025;14(9):3237.
doi: 10.3390/jcm14093237

113. Chu H, Zhang K, Rao Z, *et al*. Harnessing decellularised extracellular matrix microgels into modular bioinks for extrusion-based bioprinting with good printability and high post-printing cell viability. *Biomater Transl*. 2023;4(2):115-127.
doi: 10.12336/biomatertransl.2023.02.006

114. Boulton AJM, Whitehouse RW. *The Diabetic Foot*. Endotext; 2000.

115. Falanga V, Isseroff RR, Soulika AM, *et al*. Chronic wounds. *Nat Rev Dis Primers*. 2022;8(1):50.
doi: 10.1038/s41572-022-00377-3

116. Matamoros M, Gomez-Blanco JC, Sanchez AJ, *et al*. Temperature and humidity PID controller for a bioprinter atmospheric enclosure system. *Micromachines (Basel)*. 2020;11(11):999.
doi: 10.3390/mi11110999

117. Torres A, Rego L, Martins MS, *et al*. How to promote skin repair? In-depth look at pharmaceutical and cosmetic strategies. *Pharmaceuticals (Basel)*. 2023;16(4):573.
doi: 10.3390/ph16040573

118. Garg S, Dahiya N, Gupta S. Surgical scar revision: an overview. *J Cutan Aesthet Surg*. 2014;7(1):3–13.
doi: 10.4103/0974-2077.129959

119. Boehm D, Menke H. Sepsis in burns-lessons learnt from developments in the management of septic shock. *Medicina (Kaunas)*. 2021;58(1):26.
doi: 10.3390/medicina58010026

120. Jeschke MG, Shahrokhi S, Finnerty CC, *et al*. Wound coverage technologies in burn care: established techniques. *J Burn Care Res* 2018;39(3):313-318.
doi: 10.1097/BCR.0b013e3182920d29

121. Zhang J, Wehrle E, Rubert M, Muller R. 3D bioprinting of human tissues: biofabrication, bioinks, and bioreactors. *Int J Mol Sci*. 2021;22(8):3971.
doi: 10.3390/ijms22083971

122. Pazhouhnia Z, Beheshtizadeh N, Namini MS, Lotfibakhshaiesh N. Portable hand-held bioprinters promote in situ tissue regeneration. *Bioeng Transl Med*. 2022;7(3):e10307.
doi: 10.1002/btm2.10307

123. James M. Beck MDJ. 3D printing: what could happen to products liability when users (and everyone else in between) become manufactur one else in between) become manufacturers. *MJLST*. 2017;18(1):143.

124. Zhao W, Hu C, Xu T. In vivo bioprinting: Broadening the therapeutic horizon for tissue injuries. *Bioact Mater*. 2023;25:201-222.
doi: 10.1016/j.bioactmat.2023.01.018

125. Leberfinger AN, Dinda S, Wu Y, *et al*. Bioprinting functional tissues. *Acta Biomater*. 2019;95:32-49.
doi: 10.1016/j.actbio.2019.01.009

126. Sodupe-Ortega E, Sanz-Garcia A, Pernia-Espinoza A, Escobedo-Lucea C. Accurate calibration in multi-material 3D bioprinting for tissue engineering. *Materials (Basel)*. 2018;11(8):1402.
doi: 10.3390/ma11081402

127. Gil CJ, Evans CJ, Li L, *et al*. Leveraging 3D bioprinting and photon-counting computed tomography to enable noninvasive quantitative tracking of multifunctional tissue engineered constructs. *Adv Healthc Mater*. 2023;12(31):e2302271.
doi: 10.1002/adhm.202302271

128. Mathur V, Agarwal P, Kasturi M, Srinivasan V, Seetharam RN, Vasanthan KS. Innovative bioinks for 3D bioprinting:

exploring technological potential and regulatory challenges. *J Tissue Eng*. 2025;16:20417314241308022. doi: 10.1177/20417314241308022

129. Carson JS, Carter JE, Hickerson WL, *et al*. Analysis of real-world length of stay data and costs associated with use of autologous skin cell suspension for the treatment of small burns in U.S. centers. *Burns*. 2023;49(3):607-614. doi: 10.1016/j.burns.2022.11.007

130. Carter JE, Carson JS, Hickerson WL, *et al*. Length of stay and costs with autologous skin cell suspension versus split-thickness skin grafts: burn care data from US Centers. *Adv Ther*. 2022;39(11):5191-5202. doi: 10.1007/s12325-022-02306-y

131. Braza ME, Marietta M, Fahrenkopf MP. Split-Thickness Skin Grafts. StatPearls; 2025.

132. Weng T, Zhang W, Xia Y, *et al*. 3D bioprinting for skin tissue engineering: current status and perspectives. *J Tissue Eng*. 2021;12:20417314211028574. doi: 10.1177/20417314211028574

133. Liu S, Kilian D, Bernhardt A, *et al*. Novel protein-rich bioactive bioink stimulates cellular proliferation and response in 3D bioprinted volumetric constructs. *Adv Healthc Mater*. 2025;14(10):e2404470. doi: 10.1002/adhm.202404470

134. Xiang Y, Miller K, Guan J, Kiratitanaporn W, Tang M, Chen S. 3D bioprinting of complex tissues in vitro: state-of-the-art and future perspectives. *Arch Toxicol*. 2022;96(3):691-710. doi: 10.1007/s00204-021-03212-y

135. de Bengy AF, Forraz N, Danoux L, *et al*. Development of new 3D human ex vivo models to study sebaceous gland lipid metabolism and modulations. *Cell Prolif*. 2019;52(1):e12524. doi: 10.1111/cpr.12524

136. Min D, Lee W, Bae IH, Lee TR, Croce P, Yoo SS. Bioprinting of biomimetic skin containing melanocytes. *Exp Dermatol*. 2018;27(5):453-459. doi: 10.1111/exd.13376

137. Yamauchi T, Yamasaki K, Tsuchiyama K, Aiba S. Artificial pigmented human skin created by muse cells. *Adv Exp Med Biol*. 2018;1103:255-271. doi: 10.1007/978-4-431-56847-6_14

138. Kolesky DB, Homan KA, Skylar-Scott MA, Lewis JA. Three-dimensional bioprinting of thick vascularized tissues. *Proc Natl Acad Sci U S A*. 2016;113(12):3179-3184. doi: 10.1073/pnas.1521342113

139. Mitra D, Whitehead J, Yasui OW, Leach JK. Bioreactor culture duration of engineered constructs influences bone formation by mesenchymal stem cells. *Biomaterials*. 2017;146:29-39. doi: 10.1016/j.biomaterials.2017.08.044

140. Varkey M, Visscher DO, van Zuijlen PPM, Atala A, Yoo JJ. Skin bioprinting: the future of burn wound reconstruction? *Burns Trauma*. 2019;7:4. doi: 10.1186/s41038-019-0142-7

141. Yu J, Park SA, Kim WD, *et al*. Current advances in 3D bioprinting technology and its applications for tissue engineering. *Polymers (Basel)*. 2020;12(12):2958. doi: 10.3390/polym12122958

142. Chiticaru EA, Ionita M. Commercially available bioinks and state-of-the-art lab-made formulations for bone tissue engineering: a comprehensive review. *Mater Today Bio*. 2024;29:101341. doi: 10.1016/j.mtbio.2024.101341

143. Mirshafiei M, Rashedi H, Yazdian F, Rahdar A, Baino F. Advancements in tissue and organ 3D bioprinting: current techniques, applications, and future perspectives. *Mater Design*. 2024;240:112853. doi: 10.1016/j.matdes.2024.112853

144. Mota C, Camarero-Espinosa S, Baker MB, Wieringa P, Moroni L. Bioprinting: from tissue and organ development to in vitro models. *Chem Rev*. 2020;120(19):10547-10607. doi: 10.1021/acs.chemrev.9b00789

145. Chen EP, Toksoy Z, Davis BA, Geibel JP. 3D bioprinting of vascularized tissues for in vitro and in vivo applications. *Front Bioeng Biotechnol*. 2021;9:664188. doi: 10.3389/fbioe.2021.664188

146. Merchant M, Hu SB, Miller C, Ahmadi T, Garcia E, Smith MI. Comprehensive management of severe burn injuries: a multidisciplinary approach from resuscitation to rehabilitation. *Emerg Care Med*. 2025;2(2):26. doi: 10.3390/ecm2020026

147. Samandari M, Mostafavi A, Quint J, Memic A, Tamayol A. In situ bioprinting: intraoperative implementation of regenerative medicine. *Trends Biotechnol*. 2022;40(10):1229-1247. doi: 10.1016/j.tibtech.2022.03.009

148. Li L, Shi J, Ma K, *et al*. Robotic in situ 3D bio-printing technology for repairing large segmental bone defects. *J Adv Res*. 2021;30:75-84. doi: 10.1016/j.jare.2020.11.011

149. Ma K, Zhao T, Yang L, *et al*. Application of robotic-assisted in situ 3D printing in cartilage regeneration with HAMA hydrogel: an in vivo study. *J Adv Res*. 2020;23:123-132. doi: 10.1016/j.jare.2020.01.010

150. Li X, Lian Q, Li D, Xin H, Jia S. Development of a robotic arm based hydrogel additive manufacturing system for in-situ printing. *Appl Sci*. 2017;7(1):73. doi: 10.3390/app7010073

151. Li L, Yu F, Shi J, *et al*. In situ repair of bone and cartilage defects using 3D scanning and 3D printing. *Sci Rep*. 2017;7(1):9416. doi: 10.1038/s41598-017-10060-3

152. Yao Y, Zhang Y, Aburaia M, Lackner M. 3D printing of objects with continuous spatial paths by a multi-axis robotic FFF platform. *Appl Sci*. 2021;11(11):4825. doi: 10.3390/app11114825

153. Romanelli P, Conti A, Bianchi L, Bergantin A, Martinotti A, Beltramo G. Image-guided robotic radiosurgery for trigeminal neuralgia. *Neurosurgery*. 2018;83(5):1023-1030. doi: 10.1093/neuros/nyx571

154. Zhou C, Yang Y, Wang J, Wu Q, Gu Z, Zhou Y, *et al*. Ferromagnetic soft catheter robots for minimally invasive bioprinting. *Nat Commun*. 2021;12(1):5072. doi: 10.1038/s41467-021-25386-w

155. Zhao W, Xu T. Preliminary engineering for in situ in vivo bioprinting: a novel micro bioprinting platform for in situ in vivo bioprinting at a gastric wound site. *Biofabrication*. 2020;12(4):045020. doi: 10.1088/1758-5090/aba4ff

156. Keriquel V, Guillemot F, Arnault I, *et al*. In vivo bioprinting for computer- and robotic-assisted medical intervention: preliminary study in mice. *Biofabrication*. 2010;2(1):014101. doi: 10.1088/1758-5082/2/1/014101

157. O'Connell CD, Di Bella C, Thompson F, *et al*. Development of the Biopen: a handheld device for surgical printing of adipose stem cells at a chondral wound site. *Biofabrication*. 2016;8(1):015019. doi: 10.1088/1758-5090/8/1/015019

158. Ying G, Manriquez J, Wu D, *et al*. An open-source handheld extruder loaded with pore-forming bioink for in situ wound dressing. *Mater Today Bio*. 2020;8:100074. doi: 10.1016/j.mtbio.2020.100074

159. Bhattacharyya A, Ham HW, Sonh J, *et al*. 3D bioprinting of complex tissue scaffolds with in situ homogeneously mixed alginate-chitosan-kaolin bioink using advanced portable biopen. *Carbohydr Polym*. 2023;317:121046. doi: 10.1016/j.carbpol.2023.121046

160. Hakimi N, Cheng R, Leng L, *et al*. Handheld skin printer: in situ formation of planar biomaterials and tissues. *Lab Chip*. 2018;18(10):1440-1451. doi: 10.1039/c7lc01236e

161. Duarte Campos DF, Zhang S, Kreimendahl F, *et al*. Hand-held bioprinting for de novo vascular formation applicable to dental pulp regeneration. *Connect Tissue Res*. 2020;61(2):205-215. doi: 10.1080/03008207.2019.1640217

162. Duchi S, Onofrillo C, O'Connell CD, *et al*. Handheld co-axial bioprinting: application to in situ surgical cartilage repair. *Sci Rep*. 2017;7(1):5837. doi: 10.1038/s41598-017-05699-x

163. Wang M, He J, Liu Y, Li M, Li D, Jin Z. The trend towards in vivo bioprinting. *Int J Bioprint*. 2024;1(1):15-26. doi: 10.18063/ijb.2015.01.001

164. Knudsen JE, Ghaffar U, Ma R, Hung AJ. Clinical applications of artificial intelligence in robotic surgery. *J Robot Surg*. 2024;18(1):102. doi: 10.1007/s11701-024-01867-0

165. Vossel M, Muller M, Niesche A, Theisgen L, Radermacher K, de la Fuente M. MINARO HD: control and evaluation of a handheld, highly dynamic surgical robot. *Int J Comput Assist Radiol Surg*. 2021;16(3):467-474. doi: 10.1007/s11548-020-02306-9

166. Pugliese R, Regondi S. Artificial intelligence-empowered 3D and 4D printing technologies toward smarter biomedical materials and approaches. *Polymers (Basel)*. 2022;14(14):2794. doi: 10.3390/polym14142794

167. Chen H, Zhang B, Huang J. Recent advances and applications of artificial intelligence in 3D bioprinting. *Biophys Rev (Melville)*. 2024;5(3):031301. doi: 10.1063/5.0190208

168. Zhang Z, Zhou X, Fang Y, Xiong Z, Zhang T. AI-driven 3D bioprinting for regenerative medicine: from bench to bedside. *Bioact Mater*. 2025;45:201-230. doi: 10.1016/j.bioactmat.2024.11.021

169. Ozbolat IT, Hospodiuk M. Current advances and future perspectives in extrusion-based bioprinting. *Biomaterials*. 2016;76:321-343. doi: 10.1016/j.biomaterials.2015.10.076

170. Pati F, Gantelius J, Svahn HA. 3D bioprinting of tissue/organ models. *Angew Chem Int Ed Engl*. 2016;55(15):4650-4665. doi: 10.1002/anie.201505062

171. Adib AA, Sheikhi A, Shahhosseini M, *et al*. Direct-write 3D printing and characterization of a GelMA-based biomaterial for intracorporeal tissue. *Biofabrication*. 2020;12(4):045006. doi: 10.1088/1758-5090/ab97a1

172. Di Bella C, Duchi S, O'Connell CD, *et al*. In situ handheld three-dimensional bioprinting for cartilage regeneration. *J Tissue Eng Regen Med*. 2018;12(3):611-621. doi: 10.1002/term.2476

173. Cohen DL, Lipton JI, Bonassar LJ, Lipson H. Additive manufacturing for in situ repair of osteochondral defects. *Biofabrication*. 2010;2(3):035004. doi: 10.1088/1758-5082/2/3/035004

174. Jentsch S, Nasehi R, Kuckelkorn C, Gundert B, Aveic S, Fischer H. Multiscale 3D bioprinting by nozzle-free acoustic droplet ejection. *Small Methods*. 2021;5(6):e2000971. doi: 10.1002/smtd.202000971

175. Sun H, Jia Y, Dong H, Dong D, Zheng J. Combining additive manufacturing with microfluidics: an emerging method for developing novel organs-on-chips. *Curr Opin Chem Eng*. 2020;28:1-9. doi: 10.1016/j.coche.2019.10.006

176. Darwish LR, El-Wakad MT, Farag MM. Towards an ultra-affordable three-dimensional bioprinter: a heated inductive-enabled syringe pump extrusion multifunction module for open-source fused deposition modeling three-dimensional printers. *J Manuf Sci Eng*. 2021;143(12):125001. doi: 10.1115/1.4050824

177. Campbell PG, Weiss LE. Tissue engineering with the aid of inkjet printers. *Expert Opin Biol Ther*. 2007;7(8):1123-1127. doi: 10.1517/14712598.7.8.1123

178. Salehi MM, Ataeefard M. Micro powder poly lactic acid/carbon black composite as a bio printing ink. *J Compos Mater*. 2019;53(17):2407-2414. doi: 10.1177/0021998319828154

179. Masaeli E, Marquette C. Direct-write bioprinting approach to construct multilayer cellular tissues. *Front Bioeng Biotechnol*. 2019;7:478. doi: 10.3389/fbioe.2019.00478

180. Russell CS, Mostafavi A, Quint JP, *et al*. In situ printing of adhesive hydrogel scaffolds for the treatment of skeletal muscle injuries. *ACS Appl Bio Mater*. 2020;3(3):1568-1579. doi: 10.1021/acsabm.9b01176

181. Dou C, Perez V, Qu J, Tsin A, Xu B, Li J. A State-of-the-art review of laser-assisted bioprinting and its future research trends. *ChemBioEng Rev*. 2021;8(5):517-534. doi: 10.1002/cben.202000037

182. Chang J, Sun X. Laser-induced forward transfer based laser bioprinting in biomedical applications. *Front Bioeng Biotechnol*. 2023;11:1255782. doi: 10.3389/fbioe.2023.1255782

183. Keriquel V, Oliveira H, Remy M, *et al*. In situ printing of mesenchymal stromal cells, by laser-assisted bioprinting, for in vivo bone regeneration applications. *Sci Rep*. 2017;7(1):1778. doi: 10.1038/s41598-017-01914-x

184. Curley JL, Sklare SC, Bowser DA, Saksena J, Moore MJ, Chrisey DB. Isolated node engineering of neuronal systems using laser direct write. *Biofabrication*. 2016;8(1):015013. doi: 10.1088/1758-5090/8/1/015013

185. Budharaju H, Sundaramurthi D, Sethuraman S. Embedded 3D bioprinting – an emerging strategy to fabricate biomimetic & large vascularized tissue constructs. *Bioact Mater*. 2024;32:356-384. doi: 10.1016/j.bioactmat.2023.10.012

186. Fortunato GM, Sigismondi S, Nicoletta M, *et al*. Analysis of the robotic-based in situ bioprinting workflow for the regeneration of damaged tissues through a case study. *Bioengineering (Basel)*. 2023;10(5):560. doi: 10.3390/bioengineering10050560

187. Gu F, Song Z, Zhao Z. Single-shot structured light sensor for 3D dense and dynamic reconstruction. *Sensors (Basel)*. 2020;20(4):1094. doi: 10.3390/s20041094

188. Sten G, Feng L, Moller B. Enhancing off-road topography estimation by fusing LIDAR and stereo camera data with interpolated ground plane. *Sensors (Basel)*. 2025;25(2):509. doi: 10.3390/s25020509

189. Yang S, Chen Q, Wang L, Xu M. In situ defect detection and feedback control with three-dimensional extrusion-based bioprinter-associated optical coherence tomography. *Int J Bioprint*. 2023;9(1):624. doi: 10.18063/ijb.v9i1.624

190. Chakraborty D, Aneesh Reddy B, Roy Choudhury A. Extruder path generation for curved layer fused deposition modeling. *Computer-Aided Design*. 2008;40(2):235-243. doi: 10.1016/j.cad.2007.10.014

191. Ezair B, Fuhrmann S, Elber G. Volumetric covering print-paths for additive manufacturing of 3D models. *Computer-Aided Design*. 2018;100:1-13. doi: 10.1016/j.cad.2018.02.006

192. Brunel LG, Hull SM, Heilshorn SC. Engineered assistive materials for 3D bioprinting: support baths and sacrificial inks. *Biofabrication*. 2022;14(3): 10.1088/1758-5090/ac6bbe. doi: 10.1088/1758-5090/ac6bbe

193. Sola A, Trinchi A, Hill AJ. Self-assembly meets additive manufacturing: bridging the gap between nanoscale arrangement of matter and macroscale fabrication. *Smart Mater Manuf*. 2023;1:100013. doi: 10.1016/j.smmf.2022.100013

194. Mierke CT. Bioprinting of cells, organoids and organs-on-a-chip together with hydrogels improves structural and mechanical cues. *Cells*. 2024;13(19):1638. doi: 10.3390/cells13191638

195. Ye B, Kim K-J, Sacks EP. Global and local defect detection for 3D printout surface based on geometric shape comparison. *Precision Eng*. 2023;82:324-337. doi: 10.1016/j.precisioneng.2023.04.005

196. Huang X, Wu C, Xu X, *et al*. Polarization structured light 3D depth image sensor for scenes with reflective surfaces. *Nat Commun*. 2023;14(1):6855. doi: 10.1038/s41467-023-42678-5

197. Sansoni G, Trebeschi M, Docchio F. State-of-the-art and applications of 3d imaging sensors in industry, cultural heritage, medicine, and criminal investigation. *Sensors (Basel)*. 2009;9(1):568-601. doi: 10.3390/s90100568

198. Filko D, Marijanovic D, Nyarko EK. Automatic robot-driven 3d reconstruction system for chronic wounds. *Sensors (Basel)*. 2021;21(24):8308. doi: 10.3390/s21248308

199. Filko D, Nyarko EK. Autonomous robot-driven chronic wound 3D reconstruction and analysis system. *Robotics*. 2025;14(3):30. doi: 10.3390/robotics14030030

200. Nowakowski AZ, Kaczmarek M. Artificial intelligence in IR thermal imaging and sensing for medical applications. *Sensors (Basel)*. 2025;25(3):891. doi: 10.3390/s25030891

201. Lucas Y, Niri R, Treuillet S, Douzi H, Castaneda B. Wound size imaging: ready for smart assessment and monitoring. *Adv Wound Care (New Rochelle)*. 2021;10(11):641-661. doi: 10.1089/wound.2018.0937

202. Liu H, Sun W, Cai W, *et al*. Current status, challenges, and prospects of artificial intelligence applications in wound repair theranostics. *Theranostics*. 2025;15(5):1662-1688. doi: 10.7150/thno.105109

203. Chang CW, Ho CY, Lai F, *et al*. Application of multiple deep learning models for automatic burn wound assessment. *Burns*. 2023;49(5):1039-1051. doi: 10.1016/j.burns.2022.07.006

204. Rossi A, Pescara T, Gambelli AM, *et al*. Biomaterials for extrusion-based bioprinting and biomedical applications. *Front Bioeng Biotechnol*. 2024;12:1393641. doi: 10.3389/fbioe.2024.1393641

205. Gu Z, Fu J, Lin H, He Y. Development of 3D bioprinting: from printing methods to biomedical applications. *Asian J Pharm Sci*. 2020;15(5):529-557. doi: 10.1016/j.ajps.2019.11.003

206. Chen XB, Fazel Anvari-Yazdi A, Duan X, *et al*. Biomaterials / bioinks and extrusion bioprinting. *Bioact Mater*. 2023;28:511-536. doi: 10.1016/j.bioactmat.2023.06.006

207. Zhang B, Li J, Yang X, Yin Z. Advances in multimodal electrohydrodynamic printing for high-resolution sensor fabrication: mechanisms, materials, and applications. *Nanoscale*. 2025;17(25):15132-15174. doi: 10.1039/d5nr01375e

208. Hansen CJ, Saksena R, Kolesky DB, *et al*. High-throughput printing via microvascular multinozzle arrays. *Adv Mater*. 2013;25(1):96-102. doi: 10.1002/adma.201203321

209. Kjar A, McFarland B, Mecham K, Harward N, Huang Y. Engineering of tissue constructs using coaxial bioprinting. *Bioact Mater*. 2021;6(2):460-471. doi: 10.1016/j.bioactmat.2020.08.020

210. Mohan TS, Datta P, Nesaei S, Ozbolat V, Ozbolat IT. 3D coaxial bioprinting: process mechanisms, bioinks and applications. *Prog Biomed Eng (Bristol)*. 2022;4(2):022003. doi: 10.1088/2516-1091/ac631c

211. Liu W, Zhong Z, Hu N, *et al*. Coaxial extrusion bioprinting of 3D microfibrous constructs with cell-favorable gelatin methacryloyl microenvironments. *Biofabrication*. 2018;10(2):024102. doi: 10.1088/1758-5090/aa9d44

212. Chimene D, Kaunas R, Gaharwar AK. Hydrogel bioink reinforcement for additive manufacturing: a focused review of emerging strategies. *Adv Mater*. 2020;32(1):e1902026. doi: 10.1002/adma.201902026

213. Fortunato GM, Rossi G, Bonatti AF, *et al*. Robotic platform and path planning algorithm for in situ bioprinting. *Bioprinting*. 2021;22:e00139. doi: 10.1016/j.bprint.2021.e00139

214. Pandey PM, Reddy NV, Dhande SG. Real time adaptive slicing for fused deposition modelling. *Int J Mach Tools Manuf*. 2003;43(1):61-71. doi: 10.1016/s0890-6955(02)00164-5

215. Ma L, Yu S, Xu X, Moses Amadi S, Zhang J, Wang Z. Application of artificial intelligence in 3D printing physical organ models. *Mater Today Bio*. 2023;23:100792. doi: 10.1016/j.mtbio.2023.100792

216. Fianko SK, Dzogbewu TC, Agbamava E, de Beer DJ. Mass customisation strategies in additive manufacturing: a systematic review and implementation framework. *Processes*. 2025;13(6):1855. doi: 10.3390/pr13061855

217. Gerdes S, Gaikwad A, Ramesh S, Rivero IV, Tamayol A, Rao P. Monitoring and control of biological additive manufacturing using machine learning. *J Intell Manuf*. 2023;35(3):1055-1077. doi: 10.1007/s10845-023-02092-6

218. Ngoc HV, Mayer JRR, Bitar-Nehme E. Deep learning to directly predict compensation values of thermally induced volumetric errors. *Machines*. 2023;11(4):496. doi: 10.3390/machines11040496

219. Zhang Q, Yan K, Zheng X, Liu Q, Han Y, Liu Z. Research progress of photo-crosslink hydrogels in ophthalmology: a comprehensive review focus on the applications. *Mater Today Bio*. 2024;26:101082. doi: 10.1016/j.mtbio.2024.101082

220. Huang L, Guo Z, Yang X, *et al*. Advancements in GelMA bioactive hydrogels: strategies for infection control and bone tissue regeneration. *Theranostics*. 2025;15(2):460-493. doi: 10.7150/thno.103725

221. Wang Y, Zhang S, Wang J. Photo-crosslinkable hydrogel and its biological applications. *Chinese Chem Lett*. 2021;32(5):1603-1614. doi: 10.1016/j.cclet.2020.11.073

222. Schwab A, Levato R, D'Este M, Piluso S, Eglin D, Malda J. Printability and shape fidelity of bioinks in 3D bioprinting. *Chem Rev*. 2020;120(19):11028-11055. doi: 10.1021/acs.chemrev.0c00084

223. Cai B, Kilian D, Ramos Mejia D, Rios RJ, Ali A, Heilshorn SC. Diffusion-based 3D bioprinting strategies. *Adv Sci*. 2023;11(8):2306470. doi: 10.1002/advs.202306470

224. Orr A, Kalantarnia F, Nazir S, *et al*. Recent advances in 3D bioprinted neural models: a systematic review on the applications to drug discovery. *Adv Drug Deliv Rev*. 2025;218:115524. doi: 10.1016/j.addr.2025.115524

225. Kumar MS, Varma P, Kandasubramanian B. From lab to life: advances in in-situ bioprinting and bioink technology. *Biomed Mater*. 2024;20(1):1391259. doi: 10.1088/1748-605X/ad9dd0

226. Hu C, Wang C, Bian S, *et al*. In situ bioprinting: tailored printing strategies for regenerative medicine. *Int J Bioprint*. 2024;10(5):3366. doi: 10.36922/ijb.3366

227. Wu J, Wu C, Zou S, *et al*. Investigation of biomaterial ink viscosity properties and optimization of the printing process based on pattern path planning. *Bioengineering (Basel)*. 2023;10(12):1358.
doi: 10.3390/bioengineering10121358

228. Gungor-Ozkerim PS, Inci I, Zhang YS, Khademhosseini A, Dokmeci MR. Bioinks for 3D bioprinting: an overview. *Biomater Sci*. 2018;6(5):915-946.
doi: 10.1039/c7bm00765e

229. Li L, Wu W, Zhu Q, *et al*. Advanced cell-adaptable hydrogels for bioprinting. *Bioact Mater*. 2025;53:831-854.
doi: 10.1016/j.bioactmat.2025.07.044

230. Noshadi I, Hong S, Sullivan KE, *et al*. In vitro and in vivo analysis of visible light crosslinkable gelatin methacryloyl (GelMA) hydrogels. *Biomater Sci*. 2017;5(10):2093-2105.
doi: 10.1039/c7bm00110j

231. Gadzinski P, Froelich A, Jadach B, *et al*. Ionotropic gelation and chemical crosslinking as methods for fabrication of modified-release gellan gum-based drug delivery systems. *Pharmaceutics*. 2022;15(1):108.
doi: 10.3390/pharmaceutics15010108

232. Senturk E, Bilici C, Afghah F, *et al*. 3D bioprinting of tyramine modified hydrogels under visible light for osteochondral interface. *Biofabrication*. 2023;15(3).
doi: 10.1088/1758-5090/acd6bf

233. Bhattacharjee P, Ahearne M. Significance of crosslinking approaches in the development of next generation hydrogels for corneal tissue engineering. *Pharmaceutics*. 2021;13(3):319.
doi: 10.3390/pharmaceutics13030319

234. Baldino L, Concilio S, Cardea S, De Marco I, Reverchon E. Complete glutaraldehyde elimination during chitosan hydrogel drying by SC-CO2 processing. *J Supercrit Fluids*. 2015;103:70-76.
doi: 10.1016/j.supflu.2015.04.020

235. Rizzo R, Barber DM, Wilt JK, Ainscough AJ, Lewis JA. Photoinitiator-free light-mediated crosslinking of dynamic polymer and pristine protein networks. *Biomater Sci*. 2024;13(1):210-222.
doi: 10.1039/d4bm00849a

236. Nuutila K, Samandari M, Endo Y, *et al*. In vivo printing of growth factor-eluting adhesive scaffolds improves wound healing. *Bioact Mater*. 2022;8:296-308.
doi: 10.1016/j.bioactmat.2021.06.030

237. Wang C, Hu C, Cheng H, *et al*. A programmable handheld extrusion-based bioprinting platform for in situ skin wounds dressing: balance mobility and customizability. *Adv Sci (Weinh)*. 2024;11(46):e2405823.
doi: 10.1002/advs.202405823

238. Rotaru-Zavaleanu AD, Bica M, Dinescu SN, Ruscu MA, Vasile RC, Zavate AC, *et al*. Bioactive hydrogels for spinal cord injury repair: emphasis on gelatin and its derivatives. *Gels*. 2025;11(7):497.
doi: 10.3390/gels11070497

239. Dong Z, Yuan Q, Huang K, Xu W, Liu G, Gu Z. Gelatin methacryloyl (GelMA)-based biomaterials for bone regeneration. *RSC Adv*. 2019;9(31):17737-17744.
doi: 10.1039/c9ra02695a

240. Wei Y, Huang M, Jiang L. Advancements in serine protease inhibitors: from mechanistic insights to clinical applications. *Catalysts*. 2024;14(11):787.
doi: 10.3390/catal14110787

241. de Melo BAG, Jodat YA, Cruz EM, Benincasa JC, Shin SR, Porcionatto MA. Strategies to use fibrinogen as bioink for 3D bioprinting fibrin-based soft and hard tissues. *Acta Biomater*. 2020;117:60-76.
doi: 10.1016/j.actbio.2020.09.024

242. Shpichka A, Osipova D, Efremov Y, *et al*. Fibrin-based bioinks: new tricks from an old dog. *Int J Bioprint*. 2020;6(3):269.
doi: 10.18063/ijb.v6i3.269

243. Chen H, Xue H, Zeng H, Dai M, Tang C, Liu L. 3D printed scaffolds based on hyaluronic acid bioinks for tissue engineering: a review. *Biomater Res*. 2023;27(1):137.
doi: 10.1186/s40824-023-00460-0

244. Persaud A, Maus A, Strait L, Zhu D. 3D bioprinting with live cells. *Eng Regenerat*. 2022;3(3):292-309.
doi: 10.1016/j.engreg.2022.07.002

245. Nikolova MP, Chavali MS. Recent advances in biomaterials for 3D scaffolds: a review. *Bioact Mater*. 2019;4:271-292.
doi: 10.1016/j.bioactmat.2019.10.005

246. Wang Z, Sun Y, Li C. Advances in 3D printing technology for preparing bone tissue engineering scaffolds from biodegradable materials. *Front Bioeng Biotechnol*. 2024;12:1483547.
doi: 10.3389/fbioe.2024.1483547

247. Faramarzi N, Yazdi IK, Nabavinia M, *et al*. Patient-specific bioinks for 3D bioprinting of tissue engineering scaffolds. *Adv Healthc Mater*. 2018;7(11):e1701347.
doi: 10.1002/adhm.201701347

248. Zeng Y, Hoque J, Varghese S. Biomaterial-assisted local and systemic delivery of bioactive agents for bone repair. *Acta Biomater*. 2019;93:152-168.
doi: 10.1016/j.actbio.2019.01.060

249. Yoon MS, Lee JM, Jo MJ, *et al*. Dual-drug delivery systems using hydrogel-nanoparticle composites: recent advances and key applications. *Gels*. 2025;11(7):520.
doi: 10.3390/gels11070520

250. Guo Z, Zhang Yn, Zhao M, *et al*. Intelligent transdermal nanoparticles as synergizing advanced delivery systems for precision therapeutics. *Mater Today Bio*. 2025;34:102220.
doi: 10.1016/j.mtbio.2025.102220

251. Lukomskyj AO, Rao N, Yan L, *et al*. Stem cell-based tissue engineering for the treatment of burn wounds: a

systematic review of preclinical studies. *Stem Cell Rev Rep*. 2022;18(6):1926-1955.
doi: 10.1007/s12015-022-10341-z

252. Suca H, Coma M, Tomsu J, *et al*. Current approaches to wound repair in burns: how far have we come from cover to close? A narrative review. *J Surg Res*. 2024;296:383-403.
doi: 10.1016/j.jss.2023.12.043

253. Karvinen J, Kellomäki M. Design aspects and characterization of hydrogel-based bioinks for extrusion-based bioprinting. *Bioprinting*. 2023;32:e00274.
doi: 10.1016/j.bprint.2023.e00274

254. Ashammakhi N, Ahadian S, Xu C, *et al*. Bioinks and bioprinting technologies to make heterogeneous and biomimetic tissue constructs. *Mater Today Bio*. 2019;1:100008.
doi: 10.1016/j.mtbio.2019.100008

255. Du Plessis LH, Gouws C, Nieto D. The influence of viscosity of hydrogels on the spreading and migration of cells in 3D bioprinted skin cancer models. *Front Cell Dev Biol*. 2024;12:1391259.vv
doi: 10.3389/fcell.2024.1391259

256. Xu F, Dawson C, Lamb M, *et al*. Hydrogels for tissue engineering: addressing key design needs toward clinical translation. *Front Bioeng Biotechnol*. 2022;10:849831.
doi: 10.3389/fbioe.2022.849831

257. Barajaa MA, Ghosh D, Laurencin CT. Decellularized extracellular matrix-derived hydrogels: a powerful class of biomaterials for skeletal muscle regenerative engineering applications. *Regen Eng Transl Med*. 2025;11(1):39-63.
doi: 10.1007/s40883-023-00328-8

258. Huang Y, Wu W, Liu H, *et al*. 3D printing of functional nerve guide conduits. *Burns Trauma*. 2021;9:tkab011.
doi: 10.1093/burnst/tkab011

259. Schimelman J, Berry DB, Johnson S, *et al*. 3D printed nerve guidance conduit for biologics-free nerve regeneration and vascular integration. *bioRxiv*. 2025: 2025.04.30.651603.
doi: 10.1101/2025.04.30.651603

260. Lee H, Jang TS, Han G, Kim HW, Jung HD. Freeform 3D printing of vascularized tissues: Challenges and strategies. *J Tissue Eng*. 2021;12:20417314211057236.s
doi: 10.1177/20417314211057236

261. Wang X, Yang C, Yu Y, Zhao Y. In Situ 3D bioprinting living photosynthetic scaffolds for autotrophic wound healing. *Research (Wash D C)*. 2022;2022:9794745.
doi: 10.34133/2022/9794745

262. Zhou F, Xin L, Wang S, *et al*. Portable handheld "SkinPen" loaded with biomaterial ink for in situ wound healing. *ACS Appl Mater Interfaces*. 2023;15(23):27568-27585.
doi: 10.1021/acsami.3c02825

263. Chen H, Ma X, Gao T, Zhao W, Xu T, Liu Z. Robot-assisted in situ bioprinting of gelatin methacrylate hydrogels with stem cells induces hair follicle-inclusive skin regeneration. *Biomed Pharmacother*. 2023;158:114140.
doi: 10.1016/j.biopha.2022.114140

264. Levin AA, Karalkin PA, Koudan EV, *et al*. Commercial articulated collaborative in situ 3D bioprinter for skin wound healing. *Int J Bioprint*. 2023;9(2):675.
doi: 10.18063/ijb.v9i2.675

265. Zhang M, Hou L, Song W, *et al*. Development of an alginate-based bioink with enhanced hemostatic and antibacterial properties. *Int J Biol Macromol*. 2025;302:140549.
doi: 10.1016/j.ijbiomac.2025.140549

266. Moncal KK, Gudapati H, Godzik KP, *et al*. Intra-operative bioprinting of hard, soft, and hard/soft composite tissues for craniomaxillofacial reconstruction. *Adv Funct Mater*. 2021;31(29):2010858.
doi: 10.1002/adfm.202010858

267. Skardal A, Mack D, Kapetanovic E, *et al*. Bioprinted amniotic fluid-derived stem cells accelerate healing of large skin wounds. *Stem Cells Transl Med*. 2012;1(11):792-802.
doi: 10.5966/sctm.2012-0088

268. Kang Y, Yeo M, Derman ID, *et al*. Intraoperative bioprinting of human adipose-derived stem cells and extra-cellular matrix induces hair follicle-like downgrowths and adipose tissue formation during full-thickness craniomaxillofacial skin reconstruction. *bioRxiv*. 2023.
doi: 10.1101/2023.10.03.560695

269. Zhao W, Chen H, Zhang Y, *et al*. Adaptive multi-degree-of-freedom in situ bioprinting robot for hair-follicle-inclusive skin repair: a preliminary study conducted in mice. *Bioeng Transl Med*. 2022;7(3):e10303.
doi: 10.1002/btm2.10303

270. Chen H, Zhang Y, Zhou D, Ma X, Yang S, Xu T. Mechanical engineering of hair follicle regeneration by in situ bioprinting. *Biomater Adv*. 2022;142:213127.
doi: 10.1016/j.bioadv.2022.213127

271. Binder KW, Zhao W, Aboushwareb T, Dice D, Atala A, Yoo JJ. In situ bioprinting of the skin for burns. *J Am Coll Surg*. 2010;211(3):S76.
doi: 10.1016/j.jamcollsurg.2010.06.198

272. Urciuolo A, Poli I, Brandolino L, Raffa P, Scattolini V, Laterza C, *et al*. Intravital three-dimensional bioprinting. *Nat Biomed Eng*. 2020;4(9):901-915.
doi: 10.1038/s41551-020-0568-z

273. Wang AYL, Avina AE, Liu YY, Kao HK. Pluripotent stem cells: recent advances and emerging trends. *Biomedicines*. 2025;13(4):765.
doi: 10.3390/biomedicines13040765

274. Thanaskody K, Jusop AS, Tye GJ, Wan Kamarul Zaman WS, Dass SA, Nordin F. MSCs vs. iPSCs: potential in therapeutic applications. *Front Cell Dev Biol*. 2022;10:1005926.
doi: 10.3389/fcell.2022.1005926

275. Wang AYL, Loh CYY. Episomal induced pluripotent stem cells: functional and potential therapeutic applications. *Cell Transplant*. 2019;28(1_suppl):112S-131S.

doi: 10.1177/0963689719886534

276. Wang AYL, Kao HK, Liu YY, Loh CYY. Engineered extracellular vesicles derived from pluripotent stem cells: a cell-free approach to regenerative medicine. *Burns Trauma*. 2025;13:tkaf013. doi: 10.1093/burnst/tkaf013

277. Hsu HH, Wang AYL, Loh CYY, Pai AA, Kao HK. Therapeutic potential of exosomes derived from diabetic adipose stem cells in cutaneous wound healing of db/db mice. *Pharmaceutics*. 2022;14(6):1206. doi: 10.3390/pharmaceutics14061206

278. Wang AYL. Human induced pluripotent stem cell-derived exosomes as a new therapeutic strategy for various diseases. *Int J Mol Sci*. 2021;22(4):1769. doi: 10.3390/ijms22041769

279. Ngo MT, Harley BAC. Angiogenic biomaterials to promote therapeutic regeneration and investigate disease progression. *Biomaterials*. 2020;255:120207. doi: 10.1016/j.biomaterials.2020.120207

280. Nadine S, Correia CR, Mano JF. Engineering immunomodulatory hydrogels and cell-laden systems towards bone regeneration. *Biomater Adv*. 2022;140:213058. doi: 10.1016/j.bioadv.2022.213058

281. Simpson A, Hewitt AW, Fairfax KA. Universal cell donor lines: A review of the current research. *Stem Cell Rep*. 2023;18(11):2038-2046. doi: 10.1016/j.stemcr.2023.09.010

282. Bagno LL, Salerno AG, Balkan W, Hare JM. Mechanism of action of mesenchymal stem cells (MSCs): impact of delivery method. *Expert Opin Biol Ther*. 2022;22:449-463. doi: 10.1080/14712598.2022.2016695

283. Bian D, Wu Y, Song G, Azizi R, Zamani A. The application of mesenchymal stromal cells (MSCs) and their derivative exosome in skin wound healing: a comprehensive review. *Stem Cell Res Ther*. 2022;13(1):24. doi: 10.1186/s13287-021-02697-9

284. Jin S, Oh YN, Son YR, *et al*. Three-dimensional skin tissue printing with human skin cell lines and mouse skin-derived epidermal and dermal cells. *J Microbiol Biotechnol*. 2022;32(2):238-247. doi: 10.4014/jmb.2111.11042

285. Carvalho JPF, Teixeira MC, Lameirinhas NS, *et al*. Hydrogel bioinks of alginate and curcumin-loaded cellulose ester-based particles for the biofabrication of drug-releasing living tissue analogs. *ACS Appl Mater Interfaces*. 2023;15(34):40898-40912. doi: 10.1021/acsami.3c07077

286. Lameirinhas NS, Carvalho JPF, Teixeira MC, *et al*. Nanocomposite hydrogel-based bioinks composed of a fucose-rich polysaccharide and nanocellulose fibers for 3D-bioprinting applications. *Bioprinting*. 2025;45: e00382. doi: 10.1016/j.bprint.2024.e00382

287. Chastagnier L, Essayan L, Thomann C, *et al*. 3D bioprinting of bioproduction cell lines. *Bioprinting*. 2025;50:e00423. doi: 10.1016/j.bprint.2025.e00423

288. Panferov E, Dodina M, Reshetnikov V, *et al*. Induced pluripotent (iPSC) and mesenchymal (MSC) stem cells for in vitro disease modeling and regenerative medicine. *Int J Mol Sci*. 2025;26(12):5617. doi: 10.3390/ijms26125617

289. Aboul-Soud MAM, Alzahrani AJ, Mahmoud A. Induced pluripotent stem cells (iPSCs)-roles in regenerative therapies, disease modelling and drug screening. *Cells*. 2021;10(9):2319. doi: 10.3390/cells10092319

290. Liu X, Michael S, Bharti K, Ferrer M, Song MJ. A biofabricated vascularized skin model of atopic dermatitis for preclinical studies. *Biofabrication*. 2020;12(3):035002. doi: 10.1088/1758-5090/ab76a1

291. Moreau M, Capallere C, Chavatte L, *et al*. Reconstruction of functional human epidermis equivalent containing 5%IPS-derived keratinocytes treated with mitochondrial stimulating plant extracts. *Sci Rep*. 2022;12(1):9073. doi: 10.1038/s41598-022-13191-4

292. Itoh M, Umegaki-Arao N, Guo Z, Liu L, Higgins CA, Christiano AM. Generation of 3D skin equivalents fully reconstituted from human induced pluripotent stem cells (iPSCs). *PLoS One*. 2013;8(10):e77673. doi: 10.1371/journal.pone.0077673

293. Xie T, Qiao W, Jia T, Kaku K. Human induced pluripotent stem cells-derived reconstructed epidermal skin model as an alternative model for skin irritation. *Cosmetics*. 2025;12(2):75. doi: 10.3390/cosmetics12020075

294. Smith L, Bunton D, Finch M, Przyborski S. Bioengineering a human dermal equivalent using induced pluripotent stem cell-derived fibroblasts to support the formation of a full-thickness skin construct. *Cells*. 2025;14(14):1044. doi: 10.3390/cells14141044

295. Dubau M, Tripetchr T, Mahmoud L, Schumacher F, Kleuser B. Development of an iPSC-derived immunocompetent skin model for identification of skin sensitizing substances. *J Tissue Eng*. 2025;16:20417314251336296. doi: 10.1177/20417314251336296

296. Dubau M, Tripetchr T, Mahmoud L, Kral V, Kleuser B. Advancing skin model development: a focus on a self-assembled, induced pluripotent stem cell-derived, xeno-free approach. *J Tissue Eng*. 2024;15:20417314241291848. doi: 10.1177/20417314241291848

297. Zhou H, Wang L, Zhang C, *et al*. Feasibility of repairing full-thickness skin defects by iPSC-derived epithelial stem cells seeded on a human acellular amniotic membrane. *Stem Cell Res Ther*. 2019;10(1):155. doi: 10.1186/s13287-019-1234-9

298. Han Y, Yang J, Fang J, *et al*. The secretion profile of mesenchymal stem cells and potential applications in treating human diseases. *Signal Transduct Target Ther*. 2022;7(1):92.
doi: 10.1038/s41392-022-00932-0

299. Riedl J, Popp C, Eide C, Ebens C, Tolar J. Mesenchymal stromal cells in wound healing applications: role of the secretome, targeted delivery and impact on recessive dystrophic epidermolysis bullosa treatment. *Cytotherapy*. 2021;23(11):961-973.
doi: 10.1016/j.jcyt.2021.06.004

300. Loukogeorgakis SP, De Coppi P. Concise review: amniotic fluid stem cells: the known, the unknown, and potential regenerative medicine applications. *Stem Cells*. 2017;35(7):1663-1673.
doi: 10.1002/stem.2553

301. Buckland KF, Bobby Gaspar H. Gene and cell therapy for children--new medicines, new challenges? *Adv Drug Deliv Rev*. 2014;73(100):162-169.
doi: 10.1016/j.addr.2014.02.010

302. Dai L-G, Dai N-T, Chen T-Y, Kang L-Y, Hsu S-h. A bioprinted vascularized skin substitute with fibroblasts, keratinocytes, and endothelial progenitor cells for skin wound healing. *Bioprinting*. 2022;28: e00237.
doi: 10.1016/j.bprint.2022.e00237

303. Mazari-Arrighi E, Lepine M, Ayollo D, *et al*. Self-Organization of Long-Lasting Human endothelial capillary-like networks guided by DLP bioprinting. *Adv Healthc Mater*. 2024;13(14):e2302830.
doi: 10.1002/adhm.202302830

304. Beerens M, Aranguren XL, Hendrickx B, *et al*. Multipotent adult progenitor cells support lymphatic regeneration at multiple anatomical levels during wound healing and lymphedema. *Sci Rep*. 2018;8(1):3852.
doi: 10.1038/s41598-018-21610-8

305. Wang M, Xu X, Lei X, Tan J, Xie H. Mesenchymal stem cell-based therapy for burn wound healing. *Burns Trauma*. 2021;9:tkab002.
doi: 10.1093/burnst/tkab002

306. Surowiecka A, Chrapusta A, Klimeczek-Chrapusta M, Korzeniowski T, Drukała J, Strużyna J. Mesenchymal stem cells in burn wound management. *Int J Mol Sci*. 2022;23(23):15339.
doi: 10.3390/ijms232315339

307. Guillamat-Prats R. The role of MSC in wound healing, scarring and regeneration. *Cells*. 2021;10(7):1729.
doi: 10.3390/cells10071729

308. El-Sayed ME, Atwa A, Sofy AR, *et al*. Mesenchymal stem cell transplantation in burn wound healing: uncovering the mechanisms of local regeneration and tissue repair. *Histochem Cell Biol*. 2024;161(2):165-181.
doi: 10.1007/s00418-023-02244-y

309. Zhu Y, Li J, Kim J, *et al*. Skin-interfaced electronics: a promising and intelligent paradigm for personalized healthcare. *Biomaterials*. 2023;296:122075.
doi: 10.1016/j.biomaterials.2023.122075

310. Short WD, Olutoye OO, 2nd, Padon BW, *et al*. Advances in non-invasive biosensing measures to monitor wound healing progression. *Front Bioeng Biotechnol*. 2022;10:952198.
doi: 10.3389/fbioe.2022.952198

311. Vo DK, Trinh KTL. Advances in wearable biosensors for wound healing and infection monitoring. *Biosensors (Basel)*. 2025;15(3):139.
doi: 10.3390/bios15030139

312. Zhu Y, Chen B, Liu Y, *et al*. Recent advances in conductive hydrogels for electronic skin and healthcare monitoring. *Biosensors (Basel)*. 2025;15(7):463.
doi: 10.3390/bios15070463

313. Liu J, Zhao W, Ma Z, Zhao H, Ren L. Self-powered flexible electronic skin tactile sensor with 3D force detection. *Materials Today*. 2024;81:84-94.
doi: 10.1016/j.mattod.2024.10.011

314. Youn S, Ki MR, Abdelhamid MAA, Pack SP. Biomimetic materials for skin tissue regeneration and electronic skin. *Biomimetics (Basel)*. 2024;9(5):278.
doi: 10.3390/biomimetics9050278

315. Kalasin S, Sangnuang P, Surareungchai W. Intelligent wearable sensors interconnected with advanced wound dressing bandages for contactless chronic skin monitoring: artificial intelligence for predicting tissue regeneration. *Anal Chem*. 2022;94(18):6842-6852.
doi: 10.1021/acs.analchem.2c00782

316. Byrne R, Carrico A, Lettieri M, Rajan AK, Forster RJ, Cumba LR. Bioinks and biofabrication techniques for biosensors development: a review. *Mater Today Bio*. 2024;28:101185.
doi: 10.1016/j.mtbio.2024.101185

317. Aizarna-Lopetegui U, Bittinger SC, Alvarez N, Henriksen-Lacey M, Jimenez de Aberasturi D. Stimuli-responsive hybrid materials for 4D in vitro tissue models. *Mater Today Bio*. 2025;33:102035.
doi: 10.1016/j.mtbio.2025.102035

318. Elango J, Zamora-Ledezma C. Rheological, structural, and biological trade-offs in bioink design for 3D bioprinting. *Gels*. 2025;11(8):659.
doi: 10.3390/gels11080659

319. Lu S-H, Samandari M, Li C, *et al*. Multimodal sensing and therapeutic systems for wound healing and management: a review. *Sens Actuat Rep*. 2022;4:100075.
doi: 10.1016/j.snr.2022.100075

320. Patel S, Ershad F, Zhao M, *et al*. Wearable electronics for skin wound monitoring and healing. *Soft Sci*. 2022;2:9.
doi: 10.20517/ss.2022.13

321. Shankhwar N, Verma AK, Noumani A, *et al*. Integrating advanced synthesis techniques and AI-driven approaches

with nanofiber technology: a state-of-the-art approach to wound care management. *Next Nanotechnol*. 2025;8:100147. doi: 10.1016/j.nxnano.2025.100147

322. Manickam P, Mariappan SA, Murugesan SM, *et al*. Artificial Intelligence (AI) and Internet of Medical Things (IoMT) assisted biomedical systems for intelligent healthcare. *Biosensors (Basel)*. 2022;12(8):562. doi: 10.3390/bios12080562

323. Abhinav V, Basu P, Verma SS, *et al*. Advancements in wearable and implantable BioMEMS devices: transforming healthcare through technology. *Micromachines (Basel)*. 2025;16(5):522. doi: 10.3390/mi16050522

324. Pang Q, Yang F, Jiang Z, Wu K, Hou R, Zhu Y. Smart wound dressing for advanced wound management: Real-time monitoring and on-demand treatment. *Mater Design*. 2023;229: 111917. doi: 10.1016/j.matdes.2023.111917

325. Shlomy I, Divald S, Tadmor K, Leichtmann-Bardoogo Y, Arami A, Maoz BM. Restoring tactile sensation using a triboelectric nanogenerator. *ACS Nano*. 2021;15(7):11087-11098. doi: 10.1021/acsnano.0c10141

326. Sun X, Guo X, Gao J, *et al*. E-Skin and its advanced applications in ubiquitous health monitoring. *Biomedicines*. 2024;12(10):2307. doi: 10.3390/biomedicines12102307

327. Yang JC, Mun J, Kwon SY, Park S, Bao Z, Park S. Electronic skin: recent progress and future prospects for skin-attachable devices for health monitoring, robotics, and prosthetics. *Adv Mater*. 2019;31(48):e1904765. doi: 10.1002/adma.201904765

328. Bunea AC, Dediu V, Laszlo EA, *et al*. E-skin: the dawn of a new era of on-body monitoring systems. *Micromachines (Basel)*. Sep 10 2021;12(9):1091. doi: 10.3390/mi12091091

329. Parvin N, Kumar V, Joo SW, Mandal TK. Cutting-edge hydrogel technologies in tissue engineering and biosensing: an updated review. *Materials (Basel)*. 2024;17(19):4792. doi: 10.3390/ma17194792

330. Gogoi D, Kumar M, Singh J. A comprehensive review on hydrogel-based bio-ink development for tissue engineering scaffolds using 3D printing. *Annals 3D Printed Med*. 2024;15:100159. doi: 10.1016/j.stlm.2024.100159

331. Lu P, Ruan D, Huang M, *et al*. Harnessing the potential of hydrogels for advanced therapeutic applications: current achievements and future directions. *Signal Transduct Target Ther*. 2024;9(1):166. doi: 10.1038/s41392-024-01852-x

332. Su Y, Ma C, Chen J, *et al*. Printable, highly sensitive flexible temperature sensors for human body temperature monitoring: a review. *Nanoscale Res Lett*. 2020;15(1):200. doi: 10.1186/s11671-020-03428-4

333. Li Z, Mi B, Ma X, *et al*. Review of thin-film resistor sensors: Exploring materials, classification, and preparation techniques. *Chem Eng J*. 2023;477:147029. doi: 10.1016/j.cej.2023.147029

334. Liu L, Dou Y, Wang J, *et al*. Recent advances in flexible temperature sensors: materials, mechanism, fabrication, and applications. *Adv Sci (Weinh)*. 2024;11(36):e2405003. doi: 10.1002/advs.202405003

335. Wang X, Stefanello ST, Shahin V, Qian Y. From mechanoelectric conversion to tissue regeneration: translational progress in piezoelectric materials. *Adv Mater*. 2025;37(33):e2417564. doi: 10.1002/adma.202417564

336. Liu L, Li Z, Zhu T, Sun Y, Xu J. Advances in applications of low-dimensional piezoelectric materials in musculoskeletal system. *Mater Today Bio*. 2025;33:102065. doi: 10.1016/j.mtbio.2025.102065

337. Ganeson K, Tan Xue May C, Abdullah AAA, Ramakrishna S, Vigneswari S. Advantages and prospective implications of smart materials in tissue engineering: piezoelectric, shape memory, and hydrogels. *Pharmaceutics*. 2023;15(9):2356. doi: 10.3390/pharmaceutics15092356

338. Lee JC, Suh IW, Park CH, Kim CS. Polyvinylidene fluoride/silk fibroin-based bio-piezoelectric nanofibrous scaffolds for biomedical application. *J Tissue Eng Regen Med*. 2021;15(10):869-877. doi: 10.1002/term.3232

339. De Giorgio G, Matera B, Vurro D, *et al*. Silk fibroin materials: biomedical applications and perspectives. *Bioengineering*. 2024;11(2):167. doi: 10.3390/bioengineering11020167

340. Bierman-Duquette RD, Safarians G, Huang J, *et al*. Engineering tissues of the central nervous system: interfacing conductive biomaterials with neural stem/progenitor cells. *Adv Healthc Mater*. 2022;11(7):e2101577. doi: 10.1002/adhm.202101577

341. Wei L, Wang S, Shan M, *et al*. Conductive fibers for biomedical applications. *Bioact Mater*. 2023;22:343-364. doi: 10.1016/j.bioactmat.2022.10.014

342. Tang H, Li Y, Liao S, Liu H, Qiao Y, Zhou J. Multifunctional conductive hydrogel interface for bioelectronic recording and stimulation. *Adv Healthc Mater*. 2024;13(22):e2400562. doi: 10.1002/adhm.202400562

343. Brooke R, Lay M, Jain K, *et al*. Nanocellulose and PEDOT:PSS composites and their applications. *Polymer Rev*. 2022;63(2):437-477. doi: 10.1080/15583724.2022.2106491

344. Liu X, Miller Ii AL, Park S, *et al*. Covalent crosslinking of graphene oxide and carbon nanotube into hydrogels

enhances nerve cell responses. *J Mater Chem B*. 2016;4(43):6930-6941.
doi: 10.1039/c6tb01722c

345. Pourmokhtari M, Mohammad-Namazi A, Mohseni N, Imani R, Kianfar P. Advances in bioprinting with a focus on self-healing hydrogels bio-inks for soft tissue regeneration: innovations, applications, and future perspectives. *Mater Today Commun*. 2025;44:112094.
doi: 10.1016/j.mtcomm.2025.112094

346. Keshavarz M, Jahanshahi M, Hasany M, *et al*. Smart alginate inks for tissue engineering applications. *Mater Today Bio*. 2023;23:100829.
doi: 10.1016/j.mtbio.2023.100829

347. Criado-Gonzalez M, Dominguez-Alfaro A, Lopez-Larrea N, Alegret N, Mecerreyes D. Additive manufacturing of conducting polymers: recent advances, challenges, and opportunities. *ACS Appl Polym Mater*. 2021;3(6): 2865-2883.
doi: 10.1021/acsapm.1c00252

348. Serafin A, Casanova CR, Chandel AKS, Reis RL, Oliveira JM, Collins MN. Conductive biological materials for in vitro models: properties and sustainability implications. *In Vitro Model*. 2025;4(2):89-110.
doi: 10.1007/s44164-025-00088-5

349. Jiang Y, Zhou Y, Tian Y, *et al*. Conductive polymers in smart wound healing: from bioelectric stimulation to regenerative therapies. *Mater Today Bio*. 2025;34:102114.
doi: 10.1016/j.mtbio.2025.102114

350. Imani KBC, Dodda JM, Yoon J, *et al*. Seamless integration of conducting hydrogels in daily life: from preparation to wearable application. *Adv Sci (Weinh)*. 2024;11(13):e2306784.
doi: 10.1002/advs.202306784

351. Li Y, Tan S, Zhang X, Li Z, Cai J, Liu Y. Design strategies and emerging applications of conductive hydrogels in wearable sensing. *Gels*. 2025;11(4):258.
doi: 10.3390/gels11040258

352. Li C. Towards conductive hydrogels in e-skins: a review on rational design and recent developments. *RSC Adv*. 2021;11(54):33835-33848.
doi: 10.1039/d1ra04573c

353. Spencer AR, Shirzaei Sani E, Soucy JR, *et al*. Bioprinting of a cell-laden conductive hydrogel composite. *ACS Appl Mater Interfaces*. 2019;11(34):30518-30533.
doi: 10.1021/acsami.9b07353

354. Ali M, Bathaei MJ, Istif E, Karimi SNH, Beker L. Biodegradable piezoelectric polymers: recent advancements in materials and applications. *Adv Healthc Mater*. 2023;12(23):e2300318.
doi: 10.1002/adhm.202300318

355. Zhang J, Wang J, Zhong C, Zhang Y, Qiu Y, Qin L. Flexible electronics: advancements and applications of flexible piezoelectric composites in modern sensing technologies. *Micromachines (Basel)*. 2024;15(8):982.
doi: 10.3390/mi15080982

356. Su YP, Sim LN, Coster HGL, Chong TH. Incorporation of barium titanate nanoparticles in piezoelectric PVDF membrane. *J Membr Sci*. 640 (2021):119861.
doi: 10.1016/j.memsci.2021.119861

357. Ying B, Liu X. Skin-like hydrogel devices for wearable sensing, soft robotics and beyond. *iScience*. 2021;24(11):103174.
doi: 10.1016/j.isci.2021.103174

358. Razack RK, Sadasivuni KK. Advancing nanogenerators: the role of 3d-printed nanocomposites in energy harvesting. *Polymers (Basel)*. 2025;17(10):1367.
doi: 10.3390/polym17101367

359. Morouço P, Azimi B, Milazzo M, *et al*. Four-dimensional (Bio-)printing: a review on stimuli-responsive mechanisms and their biomedical suitability. *Appl Sci*. 2020;10(24):9143.
doi: 10.3390/app10249143

360. Gao Q, Lee JS, Kim BS, Gao G. Three-dimensional printing of smart constructs using stimuli-responsive biomaterials: a future direction of precision medicine. *Int J Bioprint*. 2023;9(1):638.
doi: 10.18063/ijb.v9i1.638

361. Wu J, Xue W, Yun Z, Liu Q, Sun X. Biomedical applications of stimuli-responsive "smart" interpenetrating polymer network hydrogels. *Mater Today Bio*. 2024;25:100998.
doi: 10.1016/j.mtbio.2024.100998

362. El-Husseiny HM, Mady EA, Hamabe L, *et al*. Smart/stimuli-responsive hydrogels: Cutting-edge platforms for tissue engineering and other biomedical applications. *Mater Today Bio*. 2022;13:100186.
doi: 10.1016/j.mtbio.2021.100186

363. Guo S, Dipietro LA. Factors affecting wound healing. *J Dent Res*. 2010;89(3):219-229.
doi: 10.1177/0022034509359125

364. Hossain MI, Zahid MS, Chowdhury MA, *et al*. Smart bandage: a device for wound monitoring and targeted treatment. *Results Chem*. 2024;7:101292.
doi: 10.1016/j.rechem.2023.101292

365. Wang Z, Xiao C, Roy M, *et al*. Bioinspired skin towards next-generation rehabilitation medicine. *Front Bioeng Biotechnol*. 2023;11:1196174.
doi: 10.3389/fbioe.2023.1196174

366. Hajjar S, Zhou X. pH sensing at the intersection of tissue homeostasis and inflammation. *Trends Immunol*. 2023;44(10):807-825.
doi: 10.1016/j.it.2023.08.008

367. Herrmann A, Haag R, Schedler U. Hydrogels and their role in biosensing applications. *Adv Healthc Mater*. 2021;10(11):e2100062.
doi: 10.1002/adhm.202100062

368. He X, Wei Y, Xu K. Hydrogel-based treatment of diabetic wounds: from smart responsive to smart monitoring. *Gels*. 2025;11(8):647. doi: 10.3390/gels11080647

369. Revathi D, Panda S, Deshmukh K, Khotele N, Murthy VRK, Pasha SKK. Smart hydrogels for sensing and biosensing – preparation, smart behaviours, and emerging applications – a comprehensive review. *Polymer Test*. 2025;150:108912. doi: 10.1016/j.polymertesting.2025.108912

370. Liu Y, Liu X, Wang X, Jiang H. AI-empowered electrochemical sensors for biomedical applications: technological advances and future challenges. *Biosensors (Basel)*. 2025;15(8):487. doi: 10.3390/bios15080487

371. Pullanchery S, Kulik S, Schonfeldova T, *et al*. pH drives electron density fluctuations that enhance electric field-induced liquid flow. *Nat Commun*. 2024;15(1):5951. doi: 10.1038/s41467-024-50030-8

372. Rodrigues D, Barbosa AI, Rebelo R, Kwon IK, Reis RL, Correlo VM. Skin-integrated wearable systems and implantable biosensors: a comprehensive review. *Biosensors (Basel)*. 2020;10(7):79. doi: 10.3390/bios10070079

373. Ferrari E, Palma C, Vesentini S, Occhetta P, Rasponi M. Integrating biosensors in organs-on-chip devices: a perspective on current strategies to monitor microphysiological systems. *Biosensors (Basel)*. 2020;10(9):110. doi: 10.3390/bios10090110

374. An T, Anaya DV, Gong S, *et al*. Self-powered gold nanowire tattoo triboelectric sensors for soft wearable human-machine interface. *Nano Energy*. 2020;77:105295. doi: 10.1016/j.nanoen.2020.105295

375. Azimzadeh M, Khashayar P, Amereh M, Tasnim N, Hoorfar M, Akbari M. Microfluidic-based oxygen (O(2)) sensors for on-chip monitoring of cell, tissue and organ metabolism. *Biosensors (Basel)*. 2021;12(1):6. doi: 10.3390/bios12010006

376. Gu J, Shen Y, Tian S, Xue Z, Meng X. Recent advances in nanowire-based wearable physical sensors. *Biosensors (Basel)*. 2023;13(12):1025. doi: 10.3390/bios13121025

377. Lin R, Lei M, Ding S, *et al*. Applications of flexible electronics related to cardiocerebral vascular system. *Mater Today Bio*. 2023;23:100787. doi: 10.1016/j.mtbio.2023.100787

378. Luo Y, Abidian MR, Ahn JH, *et al*. Technology roadmap for flexible sensors. *ACS Nano*. 2023;17(6):5211-5295. doi: 10.1021/acsnano.2c12606

379. Carnicer-Lombarte A, Chen ST, Malliaras GG, Barone DG. Foreign body reaction to implanted biomaterials and its impact in nerve neuroprosthetics. *Front Bioeng Biotechnol*. 2021;9:622524. doi: 10.3389/fbioe.2021.622524

380. Mohammed SA, Murad SS, Albeyboni HJ, *et al*. Supporting global communications of 6G networks using AI, digital twin, hybrid and integrated networks, and cloud: features, challenges, and recommendations. *Telecom*. 2025;6(2):35. doi: 10.3390/telecom6020035

381. Xiong Z, Achavananthadith S, Lian S, *et al*. A wireless and battery-free wound infection sensor based on DNA hydrogel. *Sci Adv*. 2021;7(47):eabj1617. doi: 10.1126/sciadv.abj1617

382. Kang SG, Song MS, Kim JW, Lee JW, Kim J. Near-field communication in biomedical applications. *Sensors (Basel)*. 2021;21(3):703. doi: 10.3390/s21030703

383. Lazaro A, Villarino R, Lazaro M, Canellas N, Prieto-Simon B, Girbau D. Recent advances in batteryless NFC sensors for chemical sensing and biosensing. *Biosensors (Basel)*. Jul 31 2023;13(8):775. doi: 10.3390/bios13080775

384. Chai T, Kim D, Shin S. Efficient internet of things communication system based on near-field communication and long range radio. *Sensors (Basel)*. 2025;25(8):2509. doi: 10.3390/s25082509

385. Khadam U, Davidsson P, Spalazzese R. Exploring the role of artificial intelligence in internet of things systems: a systematic mapping study. *Sensors (Basel)*. 2024;24(20):6511. doi: 10.3390/s24206511

386. Ullah I, Adhikari D, Su X, Palmieri F, Wu C, Choi C. Integration of data science with the intelligent IoT (IIoT): current challenges and future perspectives. *Digital Commun Netw*. 2025;11(2):280-298. doi: 10.1016/j.dcan.2024.02.007

387. Kodumuru R, Sarkar S, Parepally V, Chandarana J. Artificial intelligence and internet of things integration in pharmaceutical manufacturing: a smart synergy. *Pharmaceutics*. 2025;17(3):290. doi: 10.3390/pharmaceutics17030290

388. Griffa D, Natale A, Merli Y, *et al*. Artificial intelligence in wound care: a narrative review of the currently available mobile apps for automatic ulcer segmentation. *BioMedInformatics*. 2024;4(4):2321-2337. doi: 10.3390/biomedinformatics4040126

389. Berezo M, Budman J, Deutscher D, Hess CT, Smith K, Hayes D. Predicting chronic wound healing time using machine learning. *Adv Wound Care*. 2022;11(6):281-296. doi: 10.1089/wound.2021.0073

390. Schmidt K, Lerm D, Schmidt A, *et al*. Automated high-throughput live cell monitoring of scratch wound closure. *Biomed Eng Comput Biol*. 2024;15:11795972241295619. doi: 10.1177/11795972241295619

391. Samon Daniel SB, Joseph Oluwaseyi. Cloud-Based Big Data Analytics (Aws, Azure, Google Cloud). Seraphina Brightwood; 2024.

392. Espina JA, Cordeiro MH, Milivojevic M, Pajic-Lijakovic I, Barriga EH. Response of cells and tissues to shear stress. *J Cell Sci*. 2023;136(18):jcs.260985.
doi: 10.1242/jcs.260985

393. Xu HQ, Liu JC, Zhang ZY, Xu CX. A review on cell damage, viability, and functionality during 3D bioprinting. *Mil Med Res*. 2022;9(1):70.
doi: 10.1186/s40779-022-00429-5

394. Hagemann C, Bailey MCD, Carraro E, *et al*. Low-cost, versatile, and highly reproducible microfabrication pipeline to generate 3D-printed customised cell culture devices with complex designs. *PLoS Biol*. 2024;22(3):e3002503.
doi: 10.1371/journal.pbio.3002503

395. Sirkkunan D, Pingguan-Murphy B, Muhamad F. Directing axonal growth: a review on the fabrication of fibrous scaffolds that promotes the orientation of axons. *Gels*. 2021;8(1):25.
doi: 10.3390/gels8010025

396. Shlapakova LE, Surmeneva MA, Kholkin AL, Surmenev RA. Revealing an important role of piezoelectric polymers in nervous-tissue regeneration: a review. *Mater Today Bio*. 2024;25:100950.
doi: 10.1016/j.mtbio.2024.100950

397. Wang Z, Liang X, Wang G, Wang X, Chen Y. Emerging bioprinting for wound healing. *Adv Mater*. 2025;37(31):e2304738.
doi: 10.1002/adma.202304738

398. Rahimnejad M, Jahangiri S, Zirak Hassan Kiadeh S, *et al*. Stimuli-responsive biomaterials: smart avenue toward 4D bioprinting. *Crit Rev Biotechnol*. 2024;44(5):860-891.
doi: 10.1080/07388551.2023.2213398

399. Ma W, Lu H, Xiao Y, Wu C. Advancing organoid development with 3D bioprinting. *Organoid Res*. 2025;1(1):025040004.
doi: 10.36922/or025040004

ACCSCIENCE PUBLISHING

International Journal of Bioprinting

PERSPECTIVE ARTICLE

AI-enhanced magnetically controlled 4D printing: Reshaping the future of medical robotics

Jinrun Liu[1,2†], Qi Wang[2†], Ke Xu[3,4*], Zhenkun Li[5,6*], and Juan Liu[2*]

[1]The Institute of Translational Medicine, Jiangxi Province Key Laboratory of Precision Cell Therapy, The Second Affiliated Hospital of Nanchang University, Jiangxi Medical College, Nanchang University, Nanchang, Jiangxi, China.

[2]Beijing Tsinghua Changgung Hospital, School of Clinical Medicine, Tsinghua Medicine, Tsinghua University, Beijing, China

[3]Department of Hand Microsurgery and Plastic Reconstructive Surgery, Ningbo No. 6 Hospital, Ningbo, Zhejiang, China

[4]Ningbo Clinical Research Center for Orthopedics, Sports Medicine & Rehabilitation, Ningbo, Zhejiang, China

[5]School of Mechanical, Electronic and Control Engineering, Beijing Jiaotong University, Beijing, China

[6]Rheobot Laboratory, Beijing Jiaotong University, Beijing, China

Abstract

As a frontier interdisciplinary breakthrough, magnetically controlled 4D printing integrates smart materials, additive manufacturing, and magnetic actuation, and is contributing considerably to healthcare practices. By introducing time as the fourth dimension, magnetic 4D-printed devices can dynamically transform their structure and function in response to physiological or external magnetic stimuli, enabling minimally invasive interventions with enhanced adaptability and precision. Integrating artificial intelligence (AI) into magnetically controlled 4D printing accelerates material discovery, optimizes design and manufacturing, and enables intelligent navigation and control in complex *in vivo* environments. Recent advances highlight promising applications in interventional therapy, targeted drug delivery, and tissue repair, yet challenges remain in achieving biocompatible multifunctional materials, scalable fabrication, and safe clinical translation. Looking ahead, synergistic integration of AI with multimodal actuation, digital twins, and biomimetic systems may unlock unprecedented opportunities for personalized, adaptive, and intelligent medical robots. This perspective outlines current progress, key challenges, and future directions of AI-enhanced magnetically controlled 4D printing, underscoring its transformative potential in redefining next-generation medical robotics.

Keywords: AI-enhanced 4D printing; Magnetic actuation; Medical robotics

†These authors contributed equally to this work.

***Corresponding authors:**
Ke Xu (godxu1987@163.com)

Zhenkun Li (zhkli@bjtu.edu.cn)

Juan Liu (lja02720@btch.edu.cn)

Citation: Liu J, Wang Q, Xu K, Li Z, Liu J. AI-enhanced magnetically controlled 4D printing: Reshaping the future of medical robotics. *Int J Bioprint*. 2025;11(6):197-204. doi: 10.36922/IJB025420427

Received: October 17, 2025
Revised: November 5, 2025
Accepted: November 6, 2025
Published online: November 6, 2025

Copyright: © 2025 Author(s). This is an Open Access article distributed under the terms of the Creative Commons Attribution License, permitting distribution, and reproduction in any medium, provided the original work is properly cited.

Publisher's Note: AccScience Publishing remains neutral with regard to jurisdictional claims in published maps and institutional affiliations.

1. Introduction

The advent of 4D printing represents a significant evolution and expansion of 3D printing technology.[1] By introducing time as the fourth dimension, 4D-printed robotics possess the

capability to dynamically modify their shapes, functions, or properties in response to external stimuli, including temperature, light, pH, as well as electric and magnetic fields.[2] Magnetically 4D-printed magnetic robotics emerges as a revolutionary interdisciplinary technology at the intersection of smart materials, additive manufacturing, magnetic actuation, and machine learning.[3] Compared with other 4D printing approaches driven by stimuli such as heat, light, or humidity, magnetic 4D printing offers distinct advantages for medical applications. First, magnetic fields enable non-contact, remote, and tissue-penetrating control of device deformation, overcoming the limited penetration depth of light or thermal stimuli. Second, the strength and orientation of magnetic fields can be precisely adjusted, allowing rapid, reversible, and high-accuracy responses even in complex *in vivo* environments. Third, magnetic actuation avoids excessive local heating or chemical triggers, thereby ensuring superior safety and biocompatibility. These features make magnetic 4D printing particularly well suited for minimally invasive surgical tools, targeted drug delivery, and deep-tissue repair.[4] However, magnetic 4D printing still faces challenges in material optimization and functional integration, making the introduction of artificial intelligence (AI) essential to enhance efficiency in design, manufacturing, and control. In recent years, the rapidly advancing AI technology has demonstrated remarkable capabilities in significantly enhancing material functionalities, optimizing manufacturing processes, efficiently integrating medical imaging data, enabling path planning, and supporting dynamic control.[5] From our perspective, the true paradigm shift lies not merely in integrating AI into 4D printing workflows, but in rethinking the design–manufacture–control cycle as an intelligent, data-driven ecosystem. We posit that future magnetic 4D-printed medical robots will evolve from passive, material-based devices to adaptive, self-learning systems capable of closed-loop interaction with the human body. This viewpoint forms the conceptual foundation of this perspective. As shown in Figure 1, by enabling the development of AI, magnetically 4D-printed minimally invasive medical devices can adapt dynamically to complex physiological environments, reshaping the future of medical robotics.

In this perspective, our goal is not simply to review existing progress in magnetic 4D printing and medical microrobotics, but also to articulate a forward-looking framework for the intelligent, data-driven design–manufacture–control cycle. Rather than treating materials, fabrication, and actuation as isolated technological components, we advocate for their integration with AI to form closed-loop, adaptive, and clinically responsive robotic systems. This perspective thus aims to provide a conceptual roadmap that guides the field from device-centric innovation toward unified, intelligent, and clinically translational robotic ecosystems.

2. Materials, printing techniques, and core principles of magnetic 4D printing

2.1. Matrix materials and magnetic composites for 4D printing

Magnetically controlled 4D printing integrates magnetically responsive composites—consisting of matrix materials (*e.g.*, silicone, hydrogels, shape memory polymers) and magnetic fillers (superparamagnetic nanoparticles, soft/hard magnetic particles), with time as the fourth dimension. These materials undergo programmable shape transformations under magnetic stimulation, offering advantages like remote control, rapid response, and high biocompatibility, which align with biomedical demands for non-invasiveness and precision.[6] Ge *et al.* demonstrated one of the earliest practical implementations of 4D printing using shape-memory polymers, establishing the foundation for active materials capable of complex shape morphing under external stimuli.[7] More typical materials used in magnetically controlled 4D printing are summarized in Table 1.

2.2. Printing techniques and magnetization programming

Magnetic 4D printing currently relies on several additive manufacturing techniques, including stereolithography, fused deposition modeling, direct ink writing, and selective laser sintering. These processes utilize composites of magnetic particles with photosensitive resins, thermoplastic polymers, magnetic hydrogels, or powder-based systems to fabricate structures with different scales and properties. After printing, an external magnetic field is typically applied to orient the particles, thereby endowing the devices with programmable responsive behaviors.[8]

More specifically, the core principle can be summarized as follows: During printing or post-processing, magnetic particles are given specific orientations or magnetization patterns. When an external magnetic field is applied, the magnetic components inside the material generate torques and stresses that drive the entire structure to deform according to the pre-programmed design. Soft magnetic particles can flexibly respond to changing fields to achieve gripping or locomotion, whereas hard magnetic particles maintain stable magnetization, enabling complex yet predictable deformations even under uniform fields. Through time-sequenced magnetic control, devices manifest dynamic, controllable, and personalized functions along the "fourth dimension."[9] Building on these unique features, the feasibility of applying magnetic 4D printing

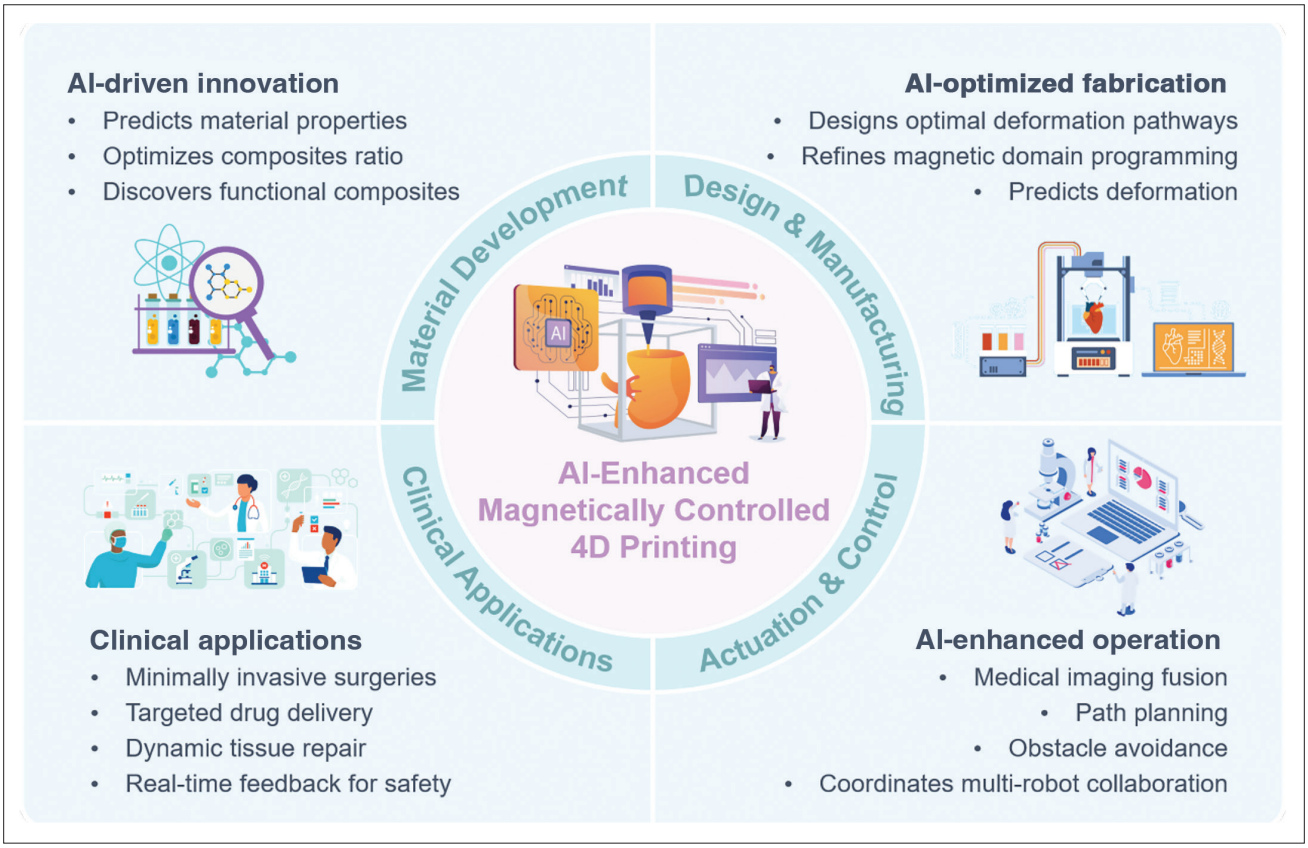

Figure 1. Future prospects of AI-enhanced magnetically controlled 4D printing in medical robotics. Schematic created with BioRender. Yu, L. (2025) https://BioRender.com/j5t9ayd (Agreement No. PQ28YQY00U).

in clinical settings becomes increasingly clear, naturally leading to its translational potential in medical robotics.

2.3. Function-driven material design guidelines for biomedical translation

Although magnetically responsive materials have shown impressive shape-morphing and actuation, translating them into biomedical use calls for function-driven design rather than material-driven selection. Different clinical scenarios impose distinct targets for mechanical compliance, magnetic actuation efficiency, *in vivo* stability, and biodegradation kinetics: short-term therapeutic implants should match soft-tissue elasticity—approximately 10 to several tens of kilopascals to minimize inflammatory mechanical mismatch[10]—and undergo controlled biodegradation within about 2–16 weeks to align with wound healing[11,12]; tissue-regeneration and load-transferring scaffolds require higher stiffness, on the order of 0.5–20 GPa to sustain structural support, with degradation profiles tuned to the indication, and many such applications benefit from moderate timelines of roughly 3–6 months to track tissue remodeling[13]; for long-term or permanent interventional devices intended to function for years to decades, the prevailing strategy is to eliminate biodegradation entirely or reduce it to a rate that is effectively negligible within the patient's lifetime. Together, these criteria establish a material–clinical function matching framework that guides the selection and engineering of magnetic 4D-printing materials according to therapeutic goals.

3. Translational advances of magnetic 4D printing in medical robotics for clinical therapy

Magnetic 4D printing's clinical potential spans critical areas. In interventional therapy, 4D-printed devices such as bioabsorbable left atrial appendage occluders and tracheal stents overcome limitations of traditional rigid instruments by adapting to anatomical structures via magnetic actuation, reducing tissue damage and enabling controlled degradation.[22] Targeted drug delivery systems, including magnetically guided soft robots and hydrogel-based carriers, navigate complex luminal environments (*e.g.*, gastrointestinal tract, blood vessels) to release therapeutics precisely at lesion sites, minimizing systemic

Table 1. Typical materials for magnetically controlled 4D printing

	Materials	Magnetic properties	Actuation mechanisms	Mechanical properties/Printability	Biocompatibility/biodegradability	Examples	Ref.
Matrix	Shape memory polymer	Non-magnetic	Light, water, magnetism, electricity, and heat-induced actuation	Good elasticity	Biodegradable	Polyolefin elastomers	[14,15]
	Silicone	Non-magnetic	Magnetically induced passive deformation	Good elasticity	Non-degradable but compatible	SE1700, Ecoflex	[16]
	Hydrogel	Non-magnetic	Magnetically induced passive deformation	Low mechanical strength	Highly biodegradable	PEG, PEGDA	[17]
	Liquid crystal elastomer	Non-magnetic	Magnetically induced passive deformation	Good elasticity	Customizable degradation properties	RM82	[18]
Magnetic fillers	Hard magnetic particle	High remanence, high coercivity	Permanent magnetic domains suitable for complex programmed magnetic fields	Easy to sedimentation	Toxic	NdFeB	[19]
	Soft magnetic particles	High remanence, low coercivity	No pre-programmed magnetic domain, complex trajectories typically require time-varying/gradient fields	Better dispersion	Biodegradable	Fe, Ni	[20]
	Superparamagnetic nanoparticles	No remanence, no coercivity	No residual magnetization (reduces aggregation after actuation), but needs strong gradients or higher volume fraction for noticeable forces	Easily for mix in matrix precursors, and suitable for printing	Biodegradable	SPIOs	[21]

Abbreviations: PEG, poly(ethylene glycol); PEGDA, poly(ethylene glycol) diacrylate; SPIOs, superparamagnetic iron oxide nanoparticles.

side effects.[23] For tissue repair, smart scaffolds and patches achieve on-demand adhesion, controlled release of growth factors, and biodegradation, accelerating wound healing and regeneration.[24] However, to enable these functions to operate efficiently in complex *in vivo* environments, more intelligent design and control strategies are required—this is precisely where AI emerges as a pivotal enabler.

4. AI as a pivotal enabler across the lifecycle of magnetic 4D-printed medical robotics

In magnetically controlled 4D printing, the dominant AI paradigms are machine-learning and deep-learning frameworks. Supervised regression models—random forests and support vector machines foremost among them—map composition, filler dispersion, and field strength to macroscopic deformation with prediction accuracies consistently exceeding 90%, outperforming traditional finite element analyses by orders of magnitude in computational speed. For 3D morphing patterns that obey Maxwell–Cauchy constraints, convolutional neural networks and physics-informed neural networks encode spatial–temporal features while explicitly embedding conservation laws, thereby guaranteeing generalizability beyond the training manifold. Reinforcement learning agents and model predictive control (MPC) schemes close the loop *in vivo*: a reinforcement learning policy learns optimal actuation sequences through interaction with a hemodynamic simulator, and the MPC layer refines magnetic field vectors in real time using stereoscopic imaging feedback, ensuring robust path-planning and attitude regulation despite physiological variability. Collectively, these algorithms endow the entire magnetically controlled 4D-printing pipeline—from inverse design of particulate composites to closed-loop navigation in deep tissue—with quantifiable predictability and deterministic controllability.[25,26]

The integration of AI with magnetic 4D printing fundamentally lies in translating "desired functions" into "actionable designs and controls." While magnetic 4D printing uses external fields to deform flexible composites embedded with magnetic particles, AI enables rapid prediction and inverse identification of the optimal structures and field inputs needed to achieve a given function. In this way, AI acts as a "bridge," translating the desired clinical function into specific printing parameters and magnetic control strategies, and continuously refining them with feedback during operation, thereby enabling more intelligent and controllable medical applications.[27] Building on this principle, the role of AI extends far beyond conceptual modeling, permeating material development, structural design, manufacturing, and real-time navigation and control throughout the entire lifecycle of magnetic

4D-printed medical robotics. In material development, machine learning and deep learning algorithms predict material properties (magnetic responsiveness, mechanical strength, biocompatibility) from compositional data, accelerating the discovery of multifunctional composites. For example, AI models optimize magnetic filler concentration and surface functionalization to balance performance and safety.[28] In design and manufacturing, generative AI autonomously creates robotic architectures with optimal deformation pathways, while reinforcement learning refines magnetic domain programming, ensuring structures bend, twist, or contract as intended under magnetic fields. AI also enhances deformation prediction, replacing cumbersome physical simulations with efficient data-driven models. Intelligent control systems, powered by AI, address critical challenges in *in vivo* navigation. By fusing medical imaging (MRI, CT, ultrasound) with real-time feedback, AI enables precise path planning, obstacle avoidance, and adaptive motion control in dynamic environments like blood flow.[29] Reinforcement learning and MPC algorithms allow robots to learn and adapt to physiological variations, ensuring stable performance in unpredictable conditions.[30] Moreover, advanced learning strategies support swarm intelligence, allowing multiple magnetic microrobots to coordinate complex tasks *in vivo*, such as collective transport or parallel drug delivery.[31] By integrating patient-specific imaging and physiological data into the design pipeline of magnetic 4D printing, AI enables the creation of digital twins that simulate how magnetically actuated devices deform and navigate *in vivo*. This allows personalized device optimization and preoperative rehearsal, while also supporting real-time surgeon–robot interaction through adaptive trajectory correction during minimally invasive procedures.[4,32] When combined with magnetically actuated deformation models, AI-driven predictive algorithms can evaluate therapeutic responses—such as drug release profiles or tissue remodeling—and dynamically tune magnetic field sequences. In this way, the printed devices operate under a closed-loop control framework that enhances clinical outcomes.[29] In the translational pathway, AI enhances the safety of magnetic 4D-printed systems by continuously monitoring their actuation parameters and simulating worst-case scenarios, such as overheating or excessive field exposure. This predictive capability supports regulatory approval and ensures reliable and ethical deployment of these devices in clinical settings.[5]

Although the integration of AI has significantly expanded the capabilities of magnetic 4D printing, numerous challenges remain in material development, manufacturing processes, and clinical applications. These challenges not only determine whether the technology can be successfully translated but also highlight the pressing issues that future research and cross-disciplinary collaboration must address.

5. Discussion and conclusion

Despite progress, key challenges remain in magnetic 4D printing. Material development faces hurdles in balancing magnetic responsiveness, mechanical robustness, and biocompatibility, particularly for long-term *in vivo* applications, and high-precision magnetic domain programming and scalable manufacturing of micro/nano-scale structures demand advances in printing hardware and process control. In clinical translation, issues like real-time deep-tissue imaging, force feedback, and regulatory approval for "actively intelligent" devices require interdisciplinary collaboration. Ethical concerns, including data privacy for AI-driven systems and liability for autonomous decisions, also need addressing**.**

Future directions should focus on multimodal integration, combining magnetic actuation with other stimuli (light, heat) for enhanced functionality; personalized medicine, leveraging patient-specific data to design tailored devices via AI digital twins; and biomimetic systems that integrate 4D-printed scaffolds with live cells for organ repair. Miniaturization toward micro/nano-robots will enable cellular-level interventions, while AI-driven closed-loop systems (design-simulation-manufacturing-feedback) will accelerate clinical translation.[33–35]

While recent studies have demonstrated proof-of-concept devices, we posit that the field is approaching a critical bottleneck. The majority of current works remain proof-of-concept demonstrations in *ex vivo* or small-animal models, with limited scalability, reproducibility, or clinical relevance. Three fundamental gaps persist:

(i) *Material gap:* There is no standardized biomaterial platform that simultaneously satisfies magnetic responsiveness, mechanical resilience, biodegradability, and cytocompatibility. Most studies optimize for one property at the expense of others, leading to fragile trade-offs that hinder translational potential.

(ii) *AI gap:* Although widely promoted, AI remains underutilized in achieving closed-loop feedback and control. Most AI models are trained offline on synthetic or idealized datasets and therefore fail to generalize to intra-patient variability, including bleeding, peristalsis, and inflammation. We lack real-time, adaptive AI systems that can learn *in vivo*, not just simulate *ex vivo*. Furthermore, AI systems face challenges of data dependency and limited generalizability, as large, high-quality training

datasets are still scarce in biomedical magnetic 4D printing, restricting the ability of these models to perform reliably in complex *in vivo* environments.[25]

To move beyond the current AI gap, we emphasize that progress requires not only more powerful model architectures, but more importantly, large-scale, standardized, and shareable datasets that reflect real spatiotemporal complexity in both *in vitro* and *in vivo* environments. To this end, we propose two concrete and field-scalable strategies:

- *Data reporting protocol for magnetic 4D printing experiments:* We recommend establishing a unified data reporting framework that standardizes how magnetic 4D printing studies document experimental conditions and outcomes. Key elements include: (a) Magnetic field inputs: strength, gradient, waveform, temporal sequencing. (b) Magnetization programming: magnetic domain orientation patterns, encoding method, spatial resolution. (c) Quantitative motion outputs: deformation amplitude, actuation efficiency, kinematic trajectories, and dynamic response profiles in both *in vitro* and *in vivo* environments. Standardizing these parameters will enable reproducible benchmarking across laboratories, reduce irreproducibility artifacts, and facilitate data-driven comparison of magnetic actuation strategies.
- *Open-source data repository for medical microrobotics and 4D bioprinting:* We advocate for the establishment of a shared, continuously expanding data repository to house raw and processed kinematic datasets, magnetic field control sequences, imaging data from studies, and annotated clinical translational case prototypes. Such a repository would support collaborative model training, foster transparent comparison of AI control systems, and accelerate the development of generalizable, adaptive navigation and actuation intelligence for real-world biomedical applications.

Taken together, these initiatives outline a practical roadmap toward overcoming the AI Gap, transforming AI from offline, static prediction tools into clinically robust, closed-loop intelligent control systems capable of operating reliably in patient-specific physiological environments.

(iii) *Clinical gap:* Regulatory pathways for actively intelligent implants remain largely undefined. Unlike passive implants, AI-enhanced magnetic robots exhibit dynamic, adaptive, and partially autonomous behaviors, often with decision-making processes that are not fully transparent. Although the regulatory landscape for intelligent and adaptive medical devices is still evolving, several frameworks offer useful precedents. The U.S. Food and Drug Administration has introduced the Software as a Medical Device framework and the Good Machine Learning Practice principles, emphasizing transparency, traceability, and post-market monitoring of AI-enabled systems. Similarly, the European Medicines Agency released its Guideline on Artificial Intelligence and Machine Learning in the Development of Human Medicines (2023), which outlines requirements for data governance, algorithm validation, and clinical performance evaluation under the Medical Device Regulation (MDR 2017/745). For biohybrid or degradable materials, international standards such as ISO 10993 (biocompatibility) and ISO/TR 20416 (post-market surveillance) remain applicable. These developments highlight persistent ethical and legal uncertainties surrounding accountability, data protection, and patient safety. Major barriers to clinical translation and regulatory approval remain, as AI-driven magnetic systems have yet to achieve full compliance with established clinical standards of safety, robustness, and ethical governance. Addressing issues such as excessive magnetic exposure, real-time control reliability, and data privacy will require coordinated efforts across materials science, robotics, clinical medicine, and bioethics.[4] Bridging these three gaps—material, AI, and clinical—will be essential for transforming magnetic 4D printing from a proof-of-concept technology into a clinically deployable platform.

In conclusion, AI-enhanced magnetically controlled 4D printing holds transformative potential for medical robotics, enabling safer, more precise, and personalized therapies. By overcoming current technical and regulatory barriers through cross-disciplinary innovation, magnetically controlled 4D printing is poised to redefine minimally invasive interventions, drug delivery, and tissue engineering, ultimately improving patient outcomes.

Acknowledgments

We would like to extend our heartfelt gratitude to the Beijing Association for Science and Technology for their strong support of this project. We thank all the lab members for their critical reading and comments on the manuscript. The authors also acknowledge the BioRender platform (biorender.com) for figure illustrations.

Funding

This work was partially supported by grants from the following sources: Beijing Natural Science Foundation (No.7254466), the National Natural Science Foundation

of China (No. 32371477, 82572451), the Ningbo Clinical Research Center for Orthopedics, Sports Medicine & Rehabilitation (2024L004), the Fundamental Research Funds for the Central Universities (No. 2024JBMC011), the Aeronautical Science Foundation of China (No. 2024Z0560M5001), the Natural Science Projects funded by Hebei Province (No. E2024105049), the National Natural Science Foundation of China (No. 92359301), the Ningbo Top Medical and Health Research Program (No. 2022020506), and Jiangxi Province Key Laboratory of Precision Cell Therapy (2024SSY06241).

Conflict of interest

The authors declare that they have no competing interests.

Author contributions

Conceptualization: Jinrun Liu, Ke Xu, and Juan Liu
Visualization: Qi Wang, Jinrun Liu, and Juan Liu
Writing–original draft: Jinrun Liu, Qi Wang, Zhenkun Li
Writing–review & editing: Ke Xu, Zhenkun Li, and Juan Liu

Ethics approval and consent to participate

Not applicable.

Consent for publication

Not applicable.

Availability of data

Not applicable.

References

1. Tibbits S. 4D printing: multi-material shape change. *Archit Des.* 2014;84(1):116-121.
doi: 10.1002/ad.1710

2. Chen S, Li J, Zheng L, Huang J, Wang M. Biomimicking trilayer scaffolds with controlled estradiol release for uterine tissue regeneration. *Exploration.* 2024;4(5): 20230141.
doi: 10.1002/EXP.20230141

3. Su L, Jin D, Wang Y, *et al*. Modularized microrobot with lock-and-detachable modules for targeted cell delivery in bile duct. *Sci Adv.* 2023;9(50):eadj0883.
doi: 10.1126/sciadv.adj0883

4. Iacovacci V, Diller E, Ahmed D, Menciassi A. Medical microrobots. *Annu Rev Biomed Eng.* 2024;26(1):561-591.
doi: 10.1146/annurev-bioeng-081523-033131

5. Pugliese R, Regondi S. Artificial intelligence-empowered 3D and 4D printing technologies toward smarter biomedical materials and approaches. *Polymers.* 2022;14(14):2794.
doi: 10.3390/POLYM14142794

6. Zhang L, Huang X, Cole T, *et al*. 3D-printed liquid metal polymer composites as NIR-responsive 4D printing soft robot. *Nat Commun.* 2023;14(1):7815.
doi: 10.1038/s41467-023-43667-4

7. Ge Q, Qi HJ, Dunn ML. Active materials by four-dimension printing. *Appl Phys Lett.* 2013;103(13):131901.
doi: 10.1063/1.4819837

8. Bai Y, Zhu S, Liang J, Xing R, Kong J. 4D printing of magnetically responsive materials and their applications. *Research.* 2025;8:0847.
doi: 10.34133/research.0847

9. Bao X, Wang F, Zhang J, *et al*. Real-time in situ magnetization reprogramming for soft robotics. *Nature.* 2025;645(8080):375-384.
doi: 10.1038/s41586-025-09459-0

10. Engler AJ, Sen S, Sweeney HL, Discher DE. Matrix elasticity directs stem cell lineage specification. *Cell* 2006;126(4):677-689.
doi: 10.1016/j.cell.2006.06.044

11. Smith AN, Ulsh JB, Gupta R, *et al*. Characterization of degradation kinetics of additively manufactured PLGA under variable mechanical loading paradigms. *J Mech Behav Biomed Mater.* 2024;153:106457.
doi: 10.1016/j.jmbbm.2024.106457

12. Yue K, Trujillo-de Santiago G, Alvarez MM, Tamayol A, Annabi N, Khademhosseini A. Synthesis, properties, and biomedical applications of gelatin methacryloyl (GelMA) hydrogels. *Biomaterials.* 2015;73:254-271.
doi: 10.1016/j.biomaterials.2015.08.045

13. Bose S, Roy M, Bandyopadhyay A. Recent advances in bone tissue engineering scaffolds. *Trends Biotechnol.* 2012;30(10):546-554.
doi: 10.1016/j.tibtech.2012.07.005

14. Gao Y, Liu W, Zhu S. Thermoplastic polyolefin elastomer blends for multiple and reversible shape memory polymers. *Ind Eng Chem Res.* 2019;58(42):19495-19502.
doi: 10.1021/acs.iecr.9b03979

15. Xia Y, He Y, Zhang F, Liu Y, Leng J. A review of shape memory polymers and composites: mechanisms, materials, and applications. *Adv Mater.* 2021;33(6): 2000713.
doi: 10.1002/adma.202000713

16. Kim Y, Yuk H, Zhao R, Chester SA, Zhao X. Printing ferromagnetic domains for untethered fast-transforming soft materials. *Nature.* 2018;558(7709):274-279.
doi: 10.1038/s41586-018-0185-0

17. Deng C, Qu J, Dong J, *et al*. 4D printing of magnetic smart structures based on light-cured magnetic hydrogel. *Chem Eng J.* 2024;494:152992.
doi: 10.1016/j.cej.2024.152992

18. Espíndola-Pérez ER, Campo J, Sánchez-Somolinos C. Multimodal and multistimuli 4D-printed magnetic composite liquid crystal elastomer actuators. *ACS Appl Mater Interfaces.* 2024;16(2):2704-2715. doi: 10.1021/acsami.3c14607

19. Zhao R, Kim Y, Chester SA, Sharma P, Zhao X. Mechanics of hard-magnetic soft materials. *J Mech Phys Solids.* 2019;124:244-263. doi: 10.1016/j.jmps.2018.10.008

20. Silveyra JM, Ferrara E, Huber DL, Monson TC. Soft magnetic materials for a sustainable and electrified world. *Science.* 2018;362(6413):eaao0195. doi: 10.1126/science.aao0195

21. Liu J, Yu S, Xu B, *et al*. Magnetically propelled soft microrobot navigating through constricted microchannels. *Appl Mater Today.* 2021;25:101237. doi: 10.1016/j.apmt.2021.101237

22. Lin C, Liu L, Liu Y, Leng J. 4D printing of bioinspired absorbable left atrial appendage occluders: a proof-of-concept study. *ACS Appl Mater Interfaces.* 2021;13(11):12668-12678. doi: 10.1021/acsami.0c17192

23. Wang H, Yue M, Sun X, Zhao X. Cooperative formation control strategy for multi-robot system based on APF algorithm and sliding mode estimator. *Robot Auton Syst.* 2025;193:105075. doi: 10.1016/j.robot.2025.105075

24. Wei T, Hu Y, Yang M, Shi C, Hu C. A magnetic patch robot with photothermal-activated multi-modality for targeted anti-postoperative adhesion. *Int J Extreme Manuf.* 2025;7(5):055502. doi: 10.1088/2631-7990/add2de

25. Sun X, Yue L, Yu L, *et al*. Machine learning-enabled forward prediction and inverse design of 4D-printed active plates. *Nat Commun.* 2024;15(1):5509. doi: 10.1038/s41467-024-49775-z

26. Salehi A, Hosseinpour S, Tabatabaei N, Soltani Firouz M, Yu T. Intelligent navigation of a magnetic microrobot with model-free deep reinforcement learning in a real-world environment. *Micromachines.* 2024;15(1):112. doi: 10.3390/mi15010112

27. Meng X, Li S, Shen X, Tian C, Mao L, Xie H. Programmable spatial magnetization stereolithographic printing of biomimetic soft machines with thin-walled structures. *Nat Commun.* 2024;15(1):10442. doi: 10.1038/s41467-024-54773-2

28. Huang X, Wong YX, Goh GL, Gao X, Lee JM, Yeong WY. Machine learning-driven prediction of gel fraction in conductive gelatin methacryloyl hydrogels. *Int J AI Mater Des.* 2024;1(2):61-75. doi: 10.36922/ijamd.3807

29. Abbasi SA, Ahmed A, Noh S, *et al*. Autonomous 3D positional control of a magnetic microrobot using reinforcement learning. *Nat Mach Intell.* 2024;6(1):92-105. doi: 10.1038/s42256-023-00779-2

30. Yang Y, Bevan MA, Li B. Efficient navigation of colloidal robots in an unknown environment via deep reinforcement learning. *Adv Intell Syst.* 2020;2(1):1900106. doi: 10.1002/aisy.201900106

31. Heuthe V-L, Panizon E, Gu H, Bechinger C. Counterfactual rewards promote collective transport using individually controlled swarm microrobots. *Sci Robot.* 2024;9(97):eado5888. doi: 10.1126/scirobotics.ado5888

32. Acosta JN, Falcone GJ, Rajpurkar P, Topol EJ. Multimodal biomedical AI. *Nat Med.* 2022;28(9):1773-1784. doi: 10.1038/s41591-022-01981-2

33. Katsoulakis E, Wang Q, Wu H, *et al*. Digital twins for health: a scoping review. *NPJ Digit Med.* 2024;7(1):77. doi: 10.1038/s41746-024-01073-0

34. Lai J, Liu Y, Lu G, *et al*. 4D bioprinting of programmed dynamic tissues. *Bioact Mater.* 2024;37:348-377. doi: 10.1016/j.bioactmat.2024.03.033

35. Zhu Y-X, Jia H-R, Jiang Y-W, *et al*. A red blood cell-derived bionic microrobot capable of hierarchically adapting to five critical stages in systemic drug delivery. *Exploration.* 2024;4(2):20230105. doi: 10.1002/EXP.20230105

ACCSCIENCE PUBLISHING

International Journal of Bioprinting

RESEARCH ARTICLE

Suspended 3D printing of polycaprolactone/hydroxyapatite composites for the fabrication of complex bone scaffolds

Juhyun Kang[1†], Masoud Shirzad[2†], Priya Ranganathan[2], Dageon Oh[2], Sudip Mondal[3], Junghwan Oh[1,2,4], Hae Gyun Lim[1,2,4], Mahdi Bodaghi[5*], and Seung Yun Nam[1,2,4*]

[1]Department of Biomedical Engineering, Pukyong National University, Busan, Republic of Korea

[2]Industry 4.0 Convergence Bionics Engineering, Pukyong National University, Busan, Republic of Korea

[3]Digital Healthcare Research Center, Institute of Information Technology and Convergence, Pukyong National University, Busan, Republic of Korea

[4]Major of Biomedical Engineering, Division of Smart Healthcare, College of Information Technology and Convergence, Pukyong National University, Busan, Republic of Korea

[5]Department of Engineering, School of Science and Technology, Nottingham Trent University, Nottingham, UK

[†]These authors contributed equally to this work.

***Corresponding authors:**
Seung Yun Nam
(synam@pknu.ac.kr)

Mahdi Bodaghi
(mahdi.bodaghi@ntu.ac.uk)

Citation: Kang J, Shirzad M, Ranganathan P, *et al*. Suspended 3D printing of polycaprolactone/hydroxyapatite composites for the fabrication of complex bone scaffolds. *Int J Bioprint*. 2025;11(6):205-219. doi: 10.36922/IJB025320319

Received: August 8, 2025
1st revised: August 25, 2025
2nd revised: August 29, 2025
Accepted: September 1, 2025
Published Online: September 2, 2025

Copyright: © 2025 Author(s). This is an Open Access article distributed under the terms of the Creative Commons Attribution License, permitting distribution, and reproduction in any medium, provided the original work is properly cited.

Publisher's Note: AccScience Publishing remains neutral with regard to jurisdictional claims in published maps and institutional affiliations.

Abstract

Extrusion-based three-dimensional (3D) printing has been rapidly advancing as a key technique for fabricating tissue-engineering scaffolds. However, printing complex structures with appropriate mechanical strength and biocompatibility remains a challenge. Suspended 3D printing is an emerging fabrication strategy that enables the generation of tissues or organs within a support medium that provides a stable printing environment without the need for additional support structures. This study presents a novel strategy for fabricating intricate scaffolds using suspended 3D printing of bioinks incorporating dissolved polycaprolactone (dPCL) and hydroxyapatite (HA). The optimized dPCL/HA bioink demonstrated up to an 85% reduction in print errors compared to conventional methods, significantly enhancing 3D printability. Moreover, mechanical assessments revealed a compressive Young's modulus approximately 50 MPa higher in dPCL/HA scaffolds compared to dPCL scaffolds. Furthermore, dPCL/HA scaffolds outperformed both PCL and dPCL scaffolds in cell proliferation tests. Complex 3D shapes, including helices, saddles, multi-curvature structures, hollow hemispheres, and zygomatic bones, were successfully fabricated, demonstrating the ability to mimic natural and intricate anatomical structures of the human body. These approaches pave the way for 3D printing patient-specific and structurally robust bone constructs with enhanced mechanical and biological properties.

Keywords: Bone tissue engineering; Biomimetic scaffolds; Composites; Extrusion-based three-dimensional printing; Suspended three-dimensional printing

1. Introduction

Complex bone defects resulting from fractures, osteoporosis, and infections pose significant challenges to the healing process due to the intricate biomechanical and biological demands of bone tissue.[1-3] Addressing these critical requirements necessitates advanced strategies to accelerate healing. The implementation of biocompatible scaffolds represents one such strategy, offering appropriate mechanical and biological properties to support the growth of host tissue.[4] Over the past few years, both conventional and advanced methods have been developed for the fabrication of tissue-engineering scaffolds. Among these methods, extrusion-based three-dimensional (3D) printing has emerged as a promising approach, enabling the construction of scaffolds through the repetitive, layer-by-layer deposition of biomaterials while offering a wide range of material choices.[5–7] However, conventional extrusion-based printing methods face significant limitations, particularly in fabricating complex 3D geometries. These structures often require additional support, making the process time-consuming and less efficient.[8,9]

To overcome these limitations, suspended 3D printing was introduced as an advanced technique, enhancing extrusion-based 3D printing by allowing the fabrication of detailed structures without the need for additional supports.[10-12] This method utilizes a support medium, such as a gel or viscous liquid, to facilitate freeform construction in multiple directions, enabling the creation of complex structures. Moreover, compared with conventional extrusion-based 3D printing, suspended 3D printing offers greater flexibility in material selection, which is particularly advantageous for fabricating functional tissue-engineered constructs.[13–15] This method also promotes the formation of perfusable vascular channels and supports the integration of native tissue components by maintaining the spatial fidelity of soft hydrogels. Despite these advancements, the application of suspended 3D printing in bone tissue engineering remains limited, primarily due to the insufficient mechanical properties of conventional hydrogel-based bioinks, which are often inadequate for load-bearing environments.[16,17] More importantly, most studies employing room-temperature suspended printing have predominantly focused on hydrogel inks rather than thermoplastic polymers.[14,15]

In the fabrication of bone scaffolds, polycaprolactone (PCL) is widely used due to its excellent biocompatibility and favorable mechanical properties. In addition, combining PCL with hydroxyapatite (HA), which constitutes approximately 70% of bone composition, has been extensively investigated, as HA enhances the biofunctionality and compressive modulus of bone scaffolds.[18–22] However, PCL, which is generally printed at 60°C or higher, is unsuitable for suspended printing in gel with high moisture content at room temperature.[23] Notably, one previous study attempted melt-printing of PCL within a thermally stable support matrix. However, this approach required printing at elevated temperatures above 65°C, limiting its applicability under biologically or thermally sensitive conditions.[24]

To address these challenges, this study aims to overcome the limitations associated with conventional 3D printing methods for fabricating complex bone scaffolds by utilizing suspended 3D printing with PCL/HA composites at room temperature. Accordingly, the physicochemical properties of the dissolved PCL (dPCL) integrated with HA were evaluated using Fourier transform infrared spectroscopy (FTIR), X-ray diffraction (XRD), thermogravimetric analysis (TGA), contact angle analysis, scanning electron microscopy (SEM), and field emission SEM (FESEM). Additionally, the printability and rheological properties of the suspended 3D printing process were quantitatively analyzed. The rheological properties were assessed for both the polymer and the composites. Mechanical performance was evaluated under tensile and compressive loads, and cell proliferation was examined using the alamarBlue assay to assess the biological effects of the proposed strategy. A schematic overview of the study design is illustrated in Figure 1. Furthermore, Table 1 provides a comparative summary between the present study and previously published work, highlighting the novelty of this study and demonstrating its advantages over prior studies.

Table 1. Comparison of printing methods for bone scaffold fabrication

Method	Temperature	High viscosity/ mechanical properties	Support printing	Complexity of post-processing	Reference
Suspended	Low	Available	Available	Low	Current study
Suspended	Moderate	N/A	Available	Low	3,6,10–15,24,40,41,52
Conventional	High	Variable	N/A	High	4,5,7,8,20,25,30,34,35,39,42,44,45,49,50,51,53,55–57
Photo-polymerization	Low	Available	N/A	High	8,43

Abbreviation: N/A, not available.

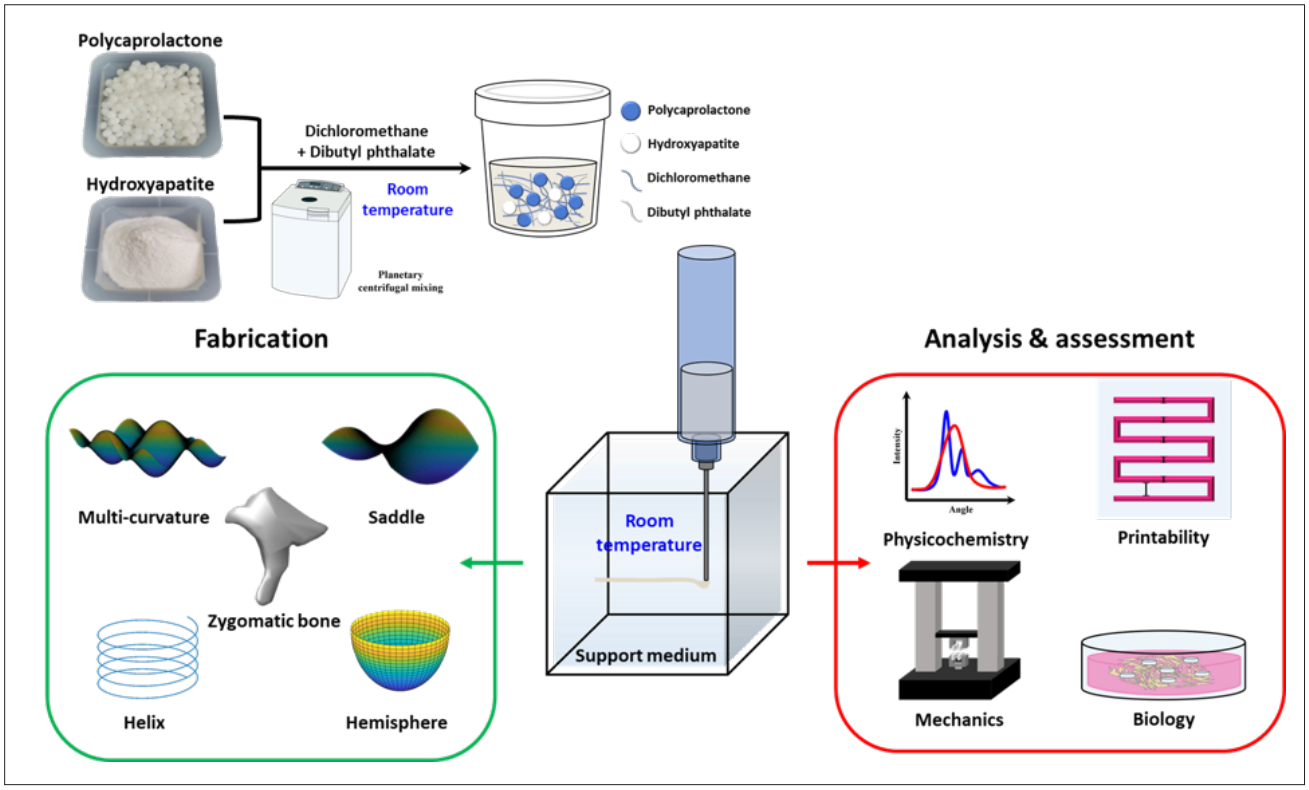

Figure 1. Schematic illustration of the suspended three-dimensional printing process for fabricating complex structures using dissolved polycaprolactone–hydroxyapatite composites.

2. Materials and methods

2.1. Hydroxyapatite synthesis

HA powder was synthesized via a wet precipitation method using calcium nitrate tetrahydrate ($Ca(NO_3)_2{\cdot}4H_2O$; Sigma-Aldrich, USA) and diammonium hydrogen phosphate (Supelco, USA). In this method, ammonium hydroxide solution (28%–30%) (Sigma-Aldrich, USA) was used as the precipitating agent. A 0.24 M solution of $Ca(NO_3)_2{\cdot}4H_2O$ was stirred vigorously at room temperature. Subsequently, a 0.29 M solution of diammonium hydrogen phosphate was slowly added to the $Ca(NO_3)_2{\cdot}4H_2O$ solution. The pH of the final mixture was adjusted to 11 by adding an ammonium hydroxide solution. After a reaction period of 6 hours and an aging period of over 12 hours, the precipitate was filtered from the reaction solution until a neutral pH was reached. The filtered precipitate was dried overnight at 90°C and subsequently calcined at 600°C for one hour in air to remove residual volatiles and ensure crystallinity of the apatite phase prior to compounding.[18]

2.2. Bioink and support medium preparation

A suspended bioink was prepared by dissolving PCL (molecular weight: 50,000; Polysciences, USA) in a binary solvent system consisting of dichloromethane (DCM; Sigma-Aldrich, USA) and dibutyl phthalate (Sigma-Aldrich, USA) mixed at a 10:1 (v/v) ratio relative to the total weight of PCL and HA. This solvent system facilitated extrusion printing at room temperature. The resulting dPCL was combined with HA in a 7:3 (w/w) ratio, yielding a dPCL/HA composite in which HA was uniformly dispersed. Homogenization was achieved using a planetary centrifugal mixer (AR-100, THINKY Corporation, Japan). For comparison, PCL scaffolds were also fabricated by extrusion at 120°C using a customized extrusion-based printer. The Laponite RD-based support medium (BYK, Germany) was prepared at different concentrations by homogeneous mixing with distilled water under magnetic stirring at 500 rpm for 10 minutes. Subsequently, the mixture was transferred to a cubic-shaped container ($40 \times 40 \times 40$ mm^3) and allowed to gel over 24 hours at room temperature.

2.3. Physicochemical analysis

FTIR was conducted using an FTIR instrument (FT-4100, JASCO, Japan) in the scan range of 4000–650 cm^{-1}. XRD analysis (Ultima IV, Rigaku, Japan) was performed using copper Kα radiation (λ = 1.5406 Å) at 40 kV and 30 mA.

The diffraction angles (2θ) were scanned with a step size of 0.02° per second over a range of 10°–70°. The HA powder and fabricated scaffolds were compared with the standard HA diffraction pattern (JCPDS card no. 72-1243). TGA (Discovery TGA 55, TA Instruments, USA) was performed under a nitrogen atmosphere with a heating rate of 10°C/min up to 700°C. Contact angle analysis was performed using a contact angle analyzer (Phoenix-MT, Surface and Electro Optics, South Korea). Morphological analysis was conducted using FESEM operated at 15 kV (MIRA3, Tescan, Czech Republic) and SEM operated at 10 kV (Vega2, Tescan, Czech Republic). Surface roughness (Ra) and structural features were further characterized using a 3D optical profiler (VR-5200, Keyence, Japan), which scans samples vertically on a measurement platform.

2.4. Printability assessment

The rheological properties of the PCL/HA composites were assessed using a rheometer (HR-2, TA Instruments, USA) with a 20 mm parallel plate and a gap of 1000 μm. A solvent trap was used in all assessments to prevent drying. The frequency sweep test of the bioink was performed by varying the angular frequency from 0.1 to 100 rad/s at 25°C with a strain of 0.1%. The recovery test of the support medium involved three steps: the first and third steps were performed at a shear rate of 0.1/s for 60 seconds, and the second step was conducted at a shear rate of 100/s for 10 seconds. All steps were conducted at 25°C.

Additionally, the following printing parameters were used: a pressure of 450 kPa and a 21-gauge (0.52 mm) nozzle. These parameters were applied to assess three factors in two different printing directions: vertical thickness (side), axial position error (side), and horizontal thickness (bottom) at nozzle speeds ranging from 1 to 6 mm/s (Figure 3A).

To measure the thickness of the printed strands, a MATLAB code was implemented to calculate the number of pixels, which was then multiplied by the pixel resolution and converted into millimeters. Any single-line section of the strand that did not match the expected color was excluded to minimize potential errors. Subsequently, the mean and standard deviation values were calculated.

This study focused on the central section to assess the printed strand thickness. The strand step was set to 2 mm for thickness measurement. Thickness was evaluated using **Equation I**:

$$Strand\,thickness\left(mm\right)=\frac{\sum\left(P_N\times P_R\right)}{N} \qquad (I)$$

where P_N is the number of pixels per line, P_R is the pixel resolution (pixels per millimeter), and N is the total number of pixels counted.

Repeated layering was performed after the standard strand with a 2 mm step to assess axial position error. Axial position error was evaluated by using **Equation II**:

$$Axial\,position\,error\left(\%\right)=\frac{H_O-H_D}{H_O}\times 100 \qquad (II)$$

where H_O denotes the original height of the feature, and H_D is the deformed height of the feature.

2.5. Mechanical assessment

The mechanical properties of conventionally printed and suspended 3D-printed scaffolds were evaluated using a universal testing machine (LR5K Plus, LLOYD Instruments, United Kingdom). Compressive specimens were prepared as cubes (5 × 5 × 5 mm^3), and tensile specimens were fabricated as rectangular plates (0.5 × 5 × 30 mm^3). All compression and tensile tests were conducted at a constant crosshead speed.

2.6. Biological analysis

The scaffolds were fabricated as sheets and then punched into discs with a 5 mm biopsy punch. After sterilization with 70% ethanol followed by immersion in phosphate-buffered saline for seven days, the scaffolds were preconditioned in Dulbecco's modified Eagle's medium at 37°C in a humidified atmosphere of 5% CO_2 for 24 hours before cell seeding. Rat adipose-derived mesenchymal stem cells (rADSCs, Cyagen, USA) at passage 5 were seeded onto the scaffolds at a density of 2.0×10^5 cells per scaffold. The cells were then cultured in Dulbecco's modified Eagle's medium supplemented with 10% fetal bovine serum and 1% penicillin–streptomycin at 37°C with 5% CO_2. After one day of cultivation, cell proliferation was determined using alamarBlue reagent (alamarBlue™, Invitrogen, USA) by incubating the scaffolds for four hours with 10% alamarBlue reagent at 37°C. The alamarBlue assay was quantified using a ultraviolet-visible spectrophotometer (Epoch, BioTek, USA) at absorbance wavelengths of 570 nm and 600 nm.

3. Results and discussion

A comprehensive physicochemical analysis was performed to verify the preservation of the chemical and structural properties of PCL and HA, confirming stable synthesis and efficient mixing of the materials. Figure 2A shows the FTIR spectra of the HA, PCL, and PCL-based composites. The synthesized HA exhibited characteristic peaks at 962,

1024, and 1088 cm^{-1}, attributed to P–O bending vibrations, along with a peak at 3573 cm^{-1}, corresponding to O–H stretching from hydroxyl groups. The spectra of PCL and dPCL showed peaks at 1164 and 1238 cm^{-1} for C–O–C, 1721 cm^{-1} for C=O stretching of ester groups, and 2866 and 2942 cm^{-1} for C–H stretching. Notably, the spectra of dPCL closely resembled those of PCL, indicating that dissolution and processing of PCL did not significantly alter its chemical structure. In the dPCL/HA composite, a reduction in transmittance was observed at the C=O and C–H bonds compared with pure PCL and HA. However, the retention of most characteristic peaks from both PCL and HA confirmed that the chemical properties of these materials were preserved during synthesis and mixing. This finding indicates successful integration of HA into PCL without significant chemical degradation.

Figure 2B shows the XRD patterns of PCL, HA, and dPCL/HA, providing insights into their crystalline structures. The dPCL exhibited characteristic peaks at 2θ values of 21.5° and 23.8°, corresponding to the crystalline structures of PCL. These peaks were also prominent in the dPCL/HA composite, indicating that incorporation of HA did not disrupt the crystalline structure of PCL. The HA peaks at 2θ values of 25.87°, 31.74°, and 32.86° corresponded to the reference data (JCPDS card no. 72-1243). In the dPCL/HA composite, weaker HA peaks were observed, suggesting partial crystallization of HA within the composite. Importantly, despite this partial crystallization, the primary crystalline features of PCL were preserved, as confirmed by the consistent peaks.

As illustrated in Figure 2G, TGA analysis was conducted to evaluate the thermal stability of the composite. HA demonstrated high thermal stability up to 700°C. In contrast,

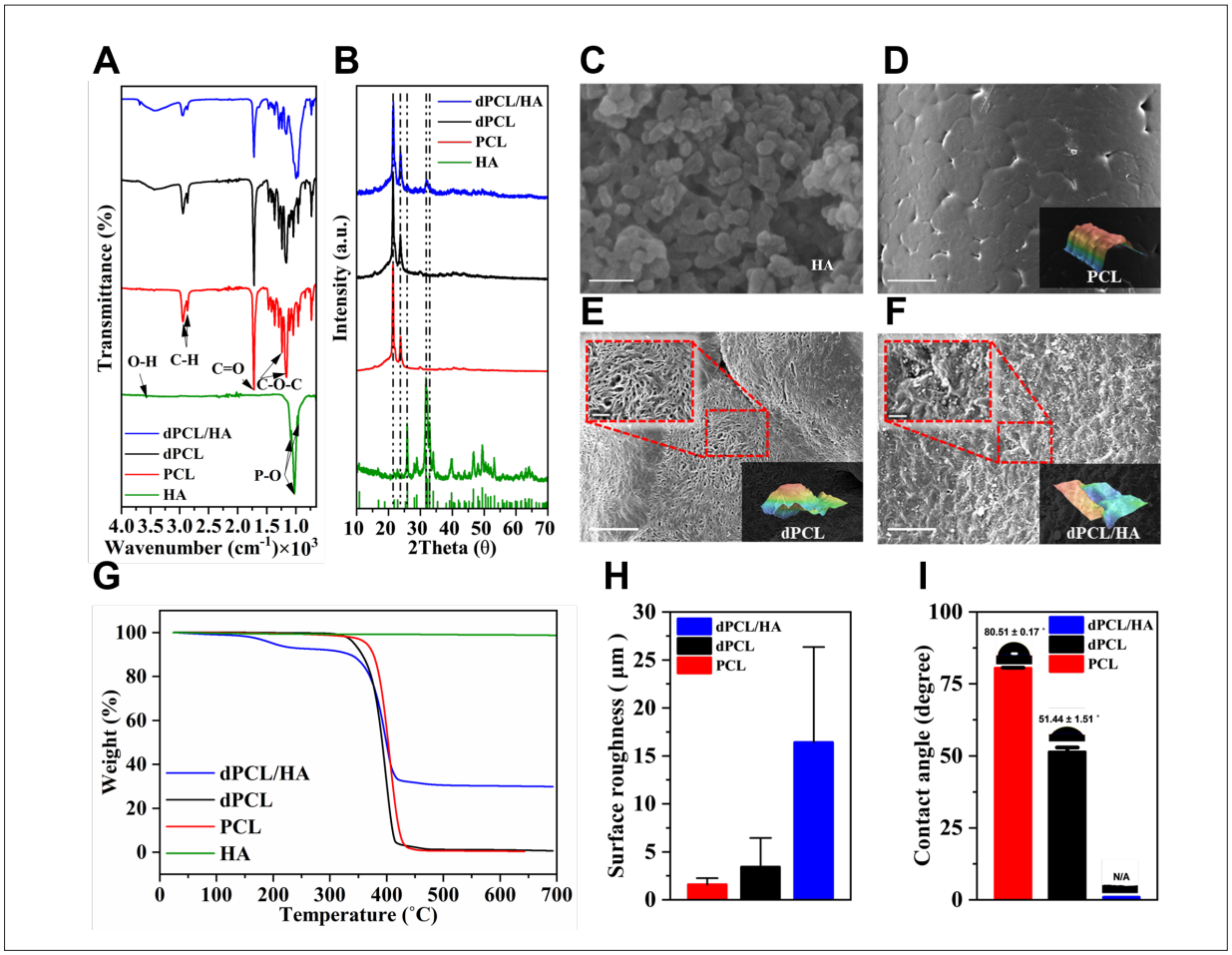

Figure 2. Characterization of PCL, dPCL, HA, and dPCL/HA scaffolds. (A) Fourier transform infrared spectra. (B) X-ray diffraction patterns. (C) Field emission scanning electron microscopy image of HA particles (scale bar: 100 nm; magnification: 400×). (D–F) Scanning electron microscopy images of (D) PCL, (E) dPCL, and (F) dPCL/HA scaffolds (scale bar: 50 μm; magnification: 1×; insets in E and F: 10 μm; magnification: 5×). (G) Thermogravimetric analysis curves. (H) Surface roughness profiles. (I) Contact angle values. Abbreviations: dPCL, dissolved polycaprolactone; HA, hydroxyapatite; N/A, not available; PCL, polycaprolactone.

both dPCL and dPCL/HA exhibited significant weight loss beginning at approximately 400°C, corresponding to the thermal decomposition of PCL. Interestingly, dPCL/HA retained approximately 30% residual mass at elevated temperatures, which was attributed to the incorporation of non-combustible HA within the composite. Furthermore, this value was consistent with the intended 7:3 (w/w) composition, serving as an indirect indicator of batch-level compositional uniformity. Although the thermal degradation rates of both dPCL and dPCL/HA were slightly accelerated compared to pure PCL, the differences remained within acceptable limits, indicating that the composite materials possessed sufficient thermal stability for practical applications. This stability is essential for ensuring reliable material performance in bone tissue engineering applications.

The HA particles were synthesized using the wet method, with a size of approximately 50 nm (Figure 2C). Figure 2D and E shows the SEM images of PCL and dPCL, respectively. Although inter-pore connectivity was not clearly visible, micropores were distributed across the dPCL surface (Figure 2E). Notably, these micropores were not observed in pure PCL, suggesting that solvent evaporation induced surface porosity in dPCL. The microstructures observed in these samples were comparable to the morphological properties of specimens prepared via a gas foaming process.[25] These findings supported the assumption that the microporous structure in dPCL formed as a direct result of DCM volatilization. However, in Figure 2F, dPCL/HA did not exhibit a pattern similar to dPCL, instead displaying irregular topography with HA particles and crater-like features. These findings confirmed that HA could fill the voids created by DCM.

As depicted in Figure 2H, dPCL/HA (16.4 ± 9.9 μm) exhibited significantly higher surface roughness compared to dPCL (3.4 ± 3.0 μm) and PCL (1.6 ± 0.7 μm). This increased surface roughness may provide a more suitable biocompatible environment. Interestingly, a notable difference in contact angle was observed between dPCL (51.44 ± 1.51°) and PCL (80.51 ± 0.17°) (Figure 2I). The contact angle of dPCL/HA could not be accurately determined, as water was fully absorbed at the initial stage of the assessment, possibly due to the vaporization of DCM and the strong hydrophilic properties of HA.[26,27] Consequently, the microporosity induced by DCM in dPCL significantly improved surface roughness and reduced the contact angle, while HA incorporation further enhanced these properties. These modifications are particularly beneficial for enhancing the bioactivity of the composite, as both increased surface roughness and hydrophilicity are strongly correlated with improved cellular attachment and tissue integration.[28] Overall, these findings suggest that the dPCL/HA composite possesses favorable physicochemical and surface properties, making it highly promising for biomaterial applications, particularly in applications requiring enhanced biocompatibility and cell–material interactions. Such enhancements significantly increase the potential of dPCL/HA composites in biomaterial applications.[29,30]

Moreover, the rheological properties of the prepared dPCL and dPCL/HA were assessed using a frequency sweep test. As shown in Figure 3B and C, the PCL-based ink demonstrated highly consistent viscosity. Both the storage modulus (G') and the loss modulus (G") exhibited a consistent, nearly linear increase with angular frequency ranging from 0.1 to 100 rad/s. However, the crossover phenomenon, typically defined as the point where G' and G" intersect in hydrogel-based inks, was not observed.[31,32] The absence of a crossover point indicates that the solid-like viscoelastic behavior of dPCL maintains stable rheological properties even as the frequency increases.[33–35]

The complex viscosity of both dPCL and dPCL/HA inks was consistently maintained at approximately 190 Pa·s across the entire frequency range (0.1–100 rad/s). This stable viscosity facilitated uniform extrusion flow under varying shear conditions, making it particularly suitable for suspended 3D printing. Consequently, PCL-based inks exhibited stable elastic behavior even at elevated frequencies, indicating minimal changes in their network structure. These rheological properties render dPCL and dPCL/HA inks particularly advantageous compared to hydrogel-based inks, which frequently show lower viscosity and reduced structural stability at higher shear rates.[33,36]

The Laponite RD-based support medium provides a stable suspended 3D printing environment for dPCL and dPCL/HA inks. Thixotropic behavior, defined as a reversible decrease in viscosity under applied stress followed by recovery upon stress removal, is a key factor influencing the recovery performance of Laponite RD. This recovery behavior strongly depends on both the strength of the particle network structure and the concentration of Laponite RD (Figure 3D).[37] At concentrations of 3% and 4%, a noticeable gap was observed between the pre- and post-stress viscosities, indicating incomplete recovery due to insufficient network density. In contrast, the 5% and 6% concentrations exhibited nearly identical pre- and post-stress viscosities, reflecting a denser particle network that facilitates faster recovery. However, this rapid recovery can hinder strand formation, as the support medium stabilizes quickly and prevents sufficient spreading of the extruded bioink to fill cracks or voids generated by nozzle movement.[15]

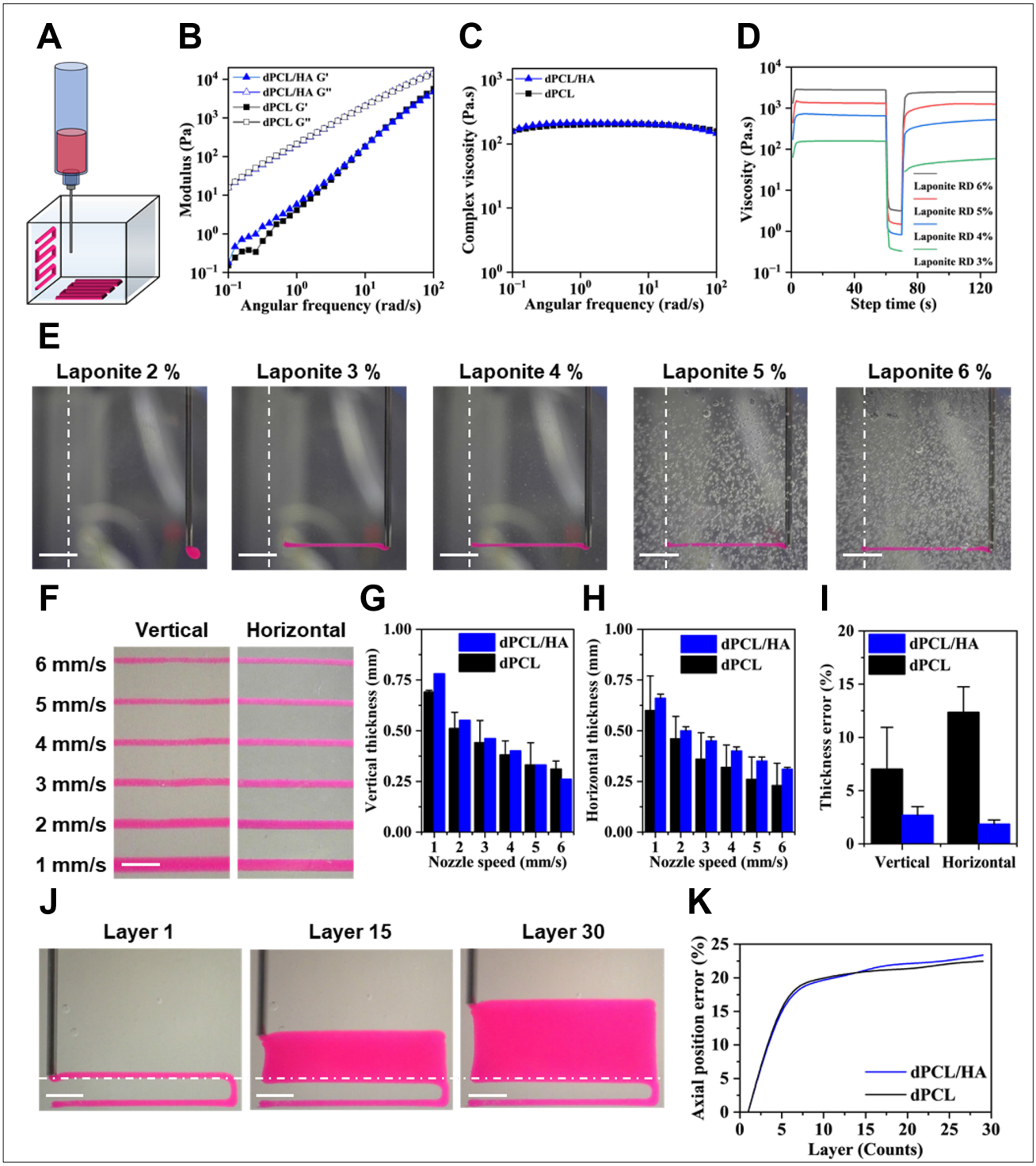

Figure 3. Comprehensive evaluation of rheological properties and print performance of dPCL and dPCL/HA. (A) Schematic illustration of the printability assessment. (B) Storage modulus (G'), loss modulus (G"), and (C) complex viscosity from frequency sweep tests of dPCL and dPCL/HA. (D) Flow peak–hold test of the support media with different concentrations. (E) Printing test of the support media (scale bar: 5 mm). (F) Strand thickness tests at varying nozzle speeds (scale bar: 2 mm). Strand thickness measurements in the (G) vertical and (H) horizontal directions. (I) Strand thickness errors for both vertical and horizontal directions. (J) Images of axial position error tests (scale bar: 2 mm). (K) Numerical evaluation of error rate with increasing layers. Abbreviations: dPCL, dissolved polycaprolactone; HA, hydroxyapatite; PCL, polycaprolactone.

In the next step, the fixation and stability of printed strands were evaluated at various concentrations of the support medium (Figure 3E). The results showed that strands printed in 3%–6% Laponite solutions remained fixed, while the 2% concentration produced unstable shapes, forming irregular bioink bumps rather than defined structures. Although 5% and 6% concentrations provided sufficient fixation, the support medium trapped bubbles and developed crevices during the printing process. These structural instabilities compromised print quality by affecting the medium's uniformity and consistency. Based on these findings, the 4% concentration was identified as the most reliable condition for stable suspended printing.

As shown in Figure 3F, the variation in strand thickness at different nozzle speeds was assessed. At a nozzle speed of 1 mm/s, the strand thickness exceeded the nozzle diameter (21 G, 0.51 mm) in both orientations. However, as nozzle speed increased, strand thickness decreased steadily, ultimately dropping below the nozzle diameter. Among all tested speeds, a nozzle speed of 2 mm/s produced the most consistent and accurate strand thickness, closely matching the nozzle diameter in both vertical (dPCL: 0.51 ± 0.08 mm; dPCL/HA: 0.55 ± 0.02 mm) and horizontal (dPCL: 0.46 ± 0.11 mm; dPCL/HA: 0.50 ± 0.02 mm) orientations (Figure 3G and H). Accordingly, 2 mm/s was determined to be the optimal printing speed for achieving uniform extrusion with minimal thickness deviation.

Subsequently, strand thickness error was assessed in both vertical and horizontal orientations, as shown in Figure 3I. The results revealed that strand thickness errors varied between orientations, with vertical strands showing lower error than horizontal strands, indicating superior control and stability in the vertical direction. Compared to dPCL alone, the dPCL/HA composite showed a 70% enhancement in printability in the vertical direction and an 85% enhancement in the horizontal direction. This improvement is attributed to the presence of HA particles, which act as physical reinforcements within the bioink. These particles contributed to maintaining printed shape fidelity by reducing spreading and deformation following extrusion, thereby increasing consistency in line thickness and improving overall printing accuracy.[23,38,39] This study also investigated axial position error, a key parameter in 3D printing. This improvement effectively reduced thickness errors in both vertical and horizontal orientations. However, the first ten layers exhibited increased deposition errors, with positional error values reaching approximately 20%–25% (Figure 3K). This phenomenon is attributed to the unique environment of suspended 3D printing, where the nozzle is positioned within the support medium.[12,15] During this phase, gaps temporarily form and are subsequently refilled as the support medium recovers. During initial layer deposition, the nozzle displaces the previously recovered support medium surrounding the printed strands, significantly reducing the accuracy of initial deposition.

In contrast to conventional 3D printing methods, suspended 3D printing necessitated a narrower vertical printing step size to achieve stable layering, which contributed to higher positional errors in the initial layers. Beyond the tenth layer, the positional error decreased significantly and stabilized at a value below 1%. This stabilization likely resulted from the support medium and nozzle reaching equilibrium, mitigating the effects of temporary pressure differences.[15,40] Both dPCL and dPCL/HA inks showed nearly identical outcomes, with no significant differences in positional error (Figure 3I). The observed stabilization is crucial for achieving reliable and precise structures in suspended 3D printing, particularly for ensuring consistent accuracy in subsequent layers. These findings underscore the robustness and reliability of the printing process.

Based on these findings, suspended 3D printing offers a significant advantage in fabricating intricate, unsupported geometries that are challenging for conventional extrusion-based methods. As exemplified by the helical structure in Figure 4, this technique enabled the creation of continuous, linear curved forms.[41] However, conventional extrusion techniques inherently struggle to fabricate complex geometries without relying on additional support structures.[42,43] The hemisphere, saddle, and multi-curvature structures further demonstrated the distinct capabilities of suspended 3D printing for fabricating complex geometries without the need for internal infill or support structures. The hemisphere confirmed the feasibility of producing hollow forms in both horizontal and vertical orientations, thereby enhancing material efficiency and reducing processing time. Concurrently, the saddle and multi-curvature structures—defined by continuous topographical variation—expanded the applicability of suspended printing to geometries with higher structural complexity than flat planes.[44,45] This capability to reliably deposit materials on surfaces with varying curvature radii highlights the potential of suspended 3D printing for freeform shape fabrication.

A more advanced and practical structure was fabricated to further demonstrate the feasibility of this method compared to conventional extrusion-based techniques. A natural zygomatic bone was selected for fabrication using the suspended 3D printing method, as its continuous curvature variations and multi-layered configurations pose technical challenges for support-free printing.[46-49] The zygomatic bone is a critical component of the facial

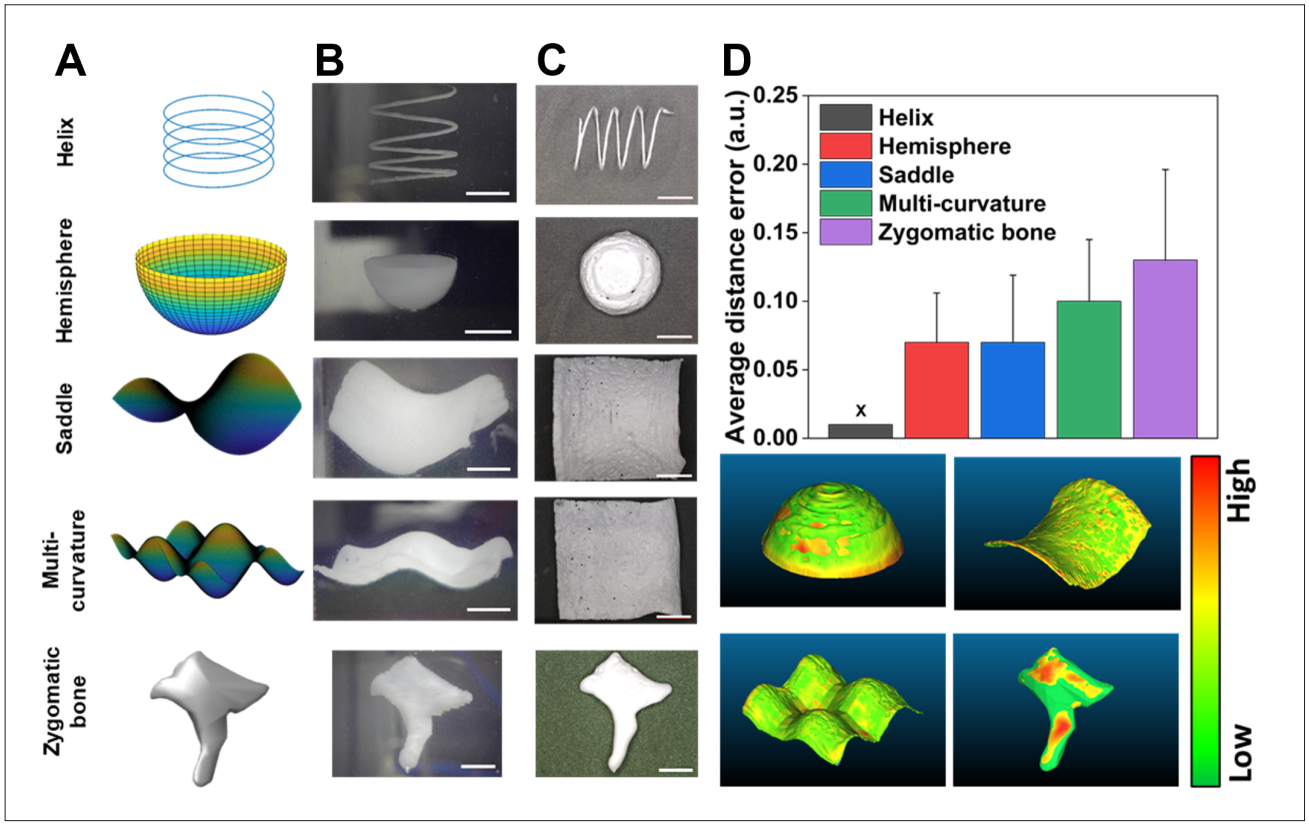

Figure 4. Suspended 3D printing of complex structures, including a helix, saddle, multi-curvature, hemisphere, and zygomatic bone. (A) Structure designs, (B) suspended 3D-printed structures within the support medium (scale bar: 5 mm), (C) structures after removal of the support medium (scale bar: 5 mm), and (D) shape fidelity analysis: average distance error (a.u.) between the reference STL and the scanned printed STL for each geometry, computed in CloudCompare. Abbreviation: 3D, three-dimensional.

skeleton, playing an essential role in maintaining facial structure and protecting the ocular region. However, its complex, curved surface architecture renders it particularly vulnerable to deformation caused by gravity when fabricated using conventional extrusion-based 3D printing techniques.[47,49,50]

As shown in Figure 4D, structural comparisons were performed using a 3D optical profiler. The printed zygomatic bone was vertically scanned, and deviations from the reference model were subsequently analyzed. The geometric discrepancies were quantified using CloudCompare software (Telecom Paris Tech and EDF R&D, France) and represented through a color map, with red indicating larger deviations and green representing smaller errors. The findings confirmed consistent printing precision across a wide range of geometries, with minimal substantial deviations. A comparative analysis between the designed STL format model and the scanned suspended structure revealed that increasing geometric complexity led to a gradual increase in average distance error, reaching over 0.1 mm.[51,52] As shown in Figure 5, the structures fabricated using the suspended 3D printing method exhibited superior and more consistent print quality in all four directions (front, back, left, and right) compared to those produced by conventional fused deposition modeling techniques.[8,9,53]

In this study, the mechanical and biological properties of the scaffolds were experimentally investigated. As depicted in Figure 6B–E, the compressive moduli were measured for dPCL/HA (105.06 ± 24.87 MPa), dPCL (58.22 ± 0.73 MPa), and PCL (136.83 ± 22.37 MPa). Among all materials, dPCL had the lowest compressive modulus, possibly due to its morphology, as observed in the structural analysis, which showed higher porosity, potentially leading to a reduction in mechanical properties (see Figure 2C–F). The compressive stress–strain curve of dPCL/HA exhibited a significant increase after 20% strain, reflecting enhanced resistance to deformation under compressive loads. Additionally, dPCL showed a steady increase in stress but with lower compressive strength compared to dPCL/HA. The enhancement in compressive modulus is attributed to the conversion of porous regions

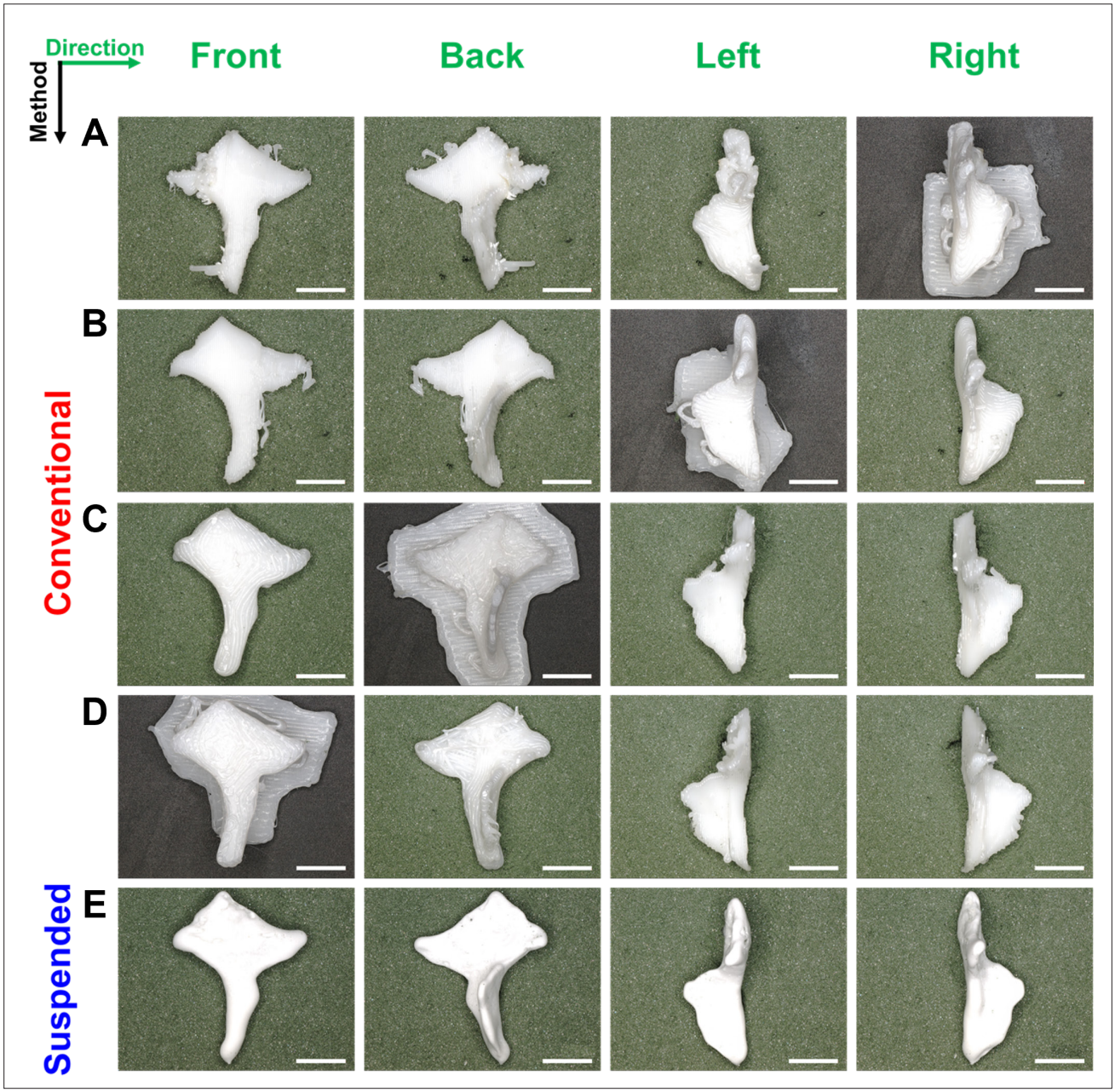

Figure 5. Comparison of zygomatic bone structures fabricated using suspended and conventional extrusion-based three-dimensional printing. (A–D) Structures printed using the conventional method in the (A) rightward, (B) leftward, (C) backward, and (D) forward directions. (E) Structures fabricated using suspended three-dimensional printing, shown from the front, back, left, and right views (scale bar: 5 mm).

within the scaffold into denser, non-porous structures. The generation of microscale voids during solvent evaporation was found to compromise the structural integrity of the material. While dPCL exhibited superior tensile strength, its compressive strength was reduced due to the presence of voids. Conversely, in the dPCL/HA composite, HA particles embedded within the dPCL matrix served as structural reinforcements, effectively compensating for this limitation. This enhanced mechanical support suggests that dPCL/HA is more suitable than dPCL alone for load-bearing bone applications.[26] Consequently, the addition of HA enhanced the compressive properties, consistent with previous studies highlighting the beneficial effects of HA in composite materials.[20,22,54]

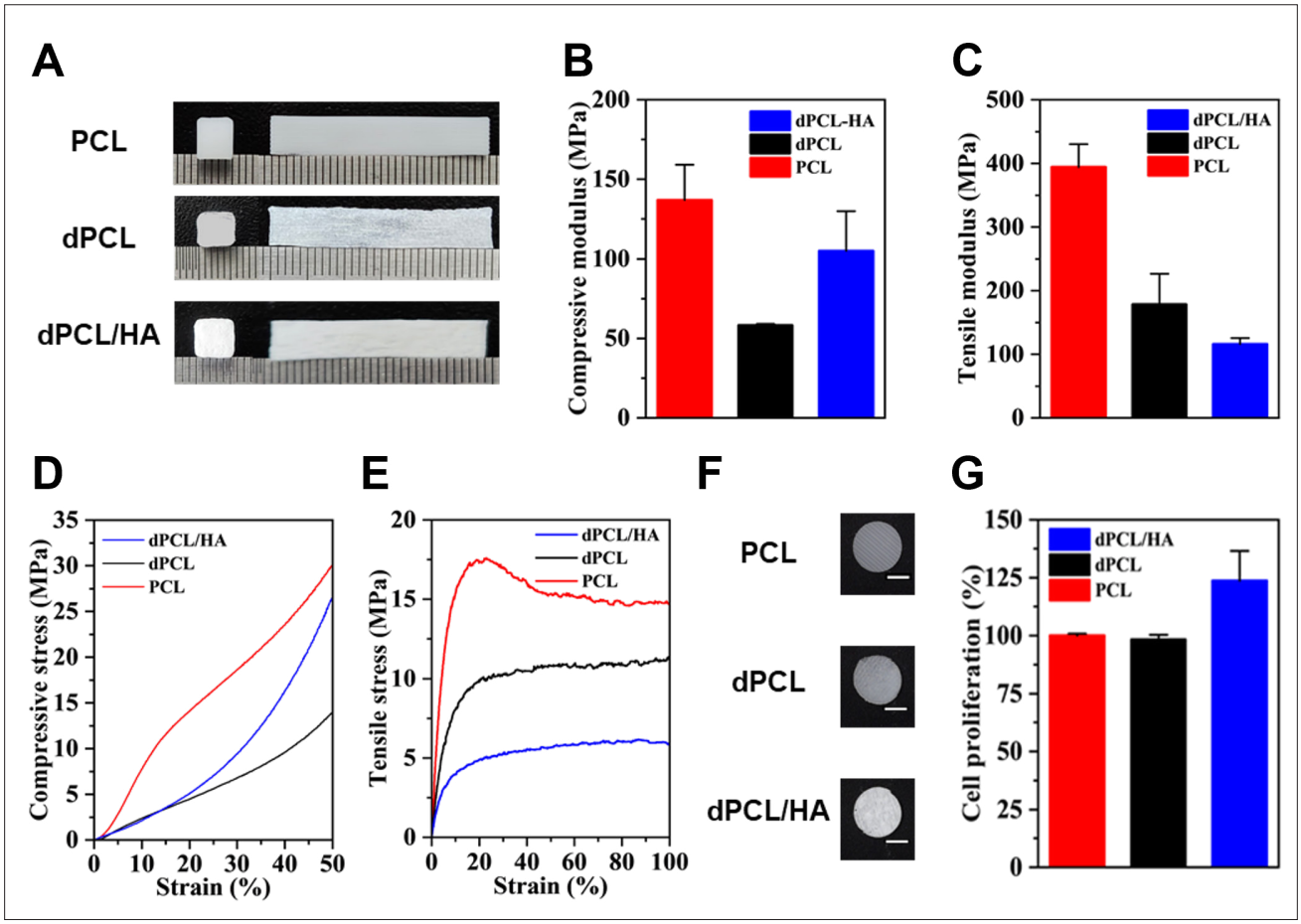

Figure 6. Mechanical and biological properties of PCL, dPCL, and dPCL/HA scaffolds. (A) Fabricated specimens used for mechanical assessment. (B) Compressive modulus and (C) tensile modulus of PCL, dPCL, and dPCL/HA. (D) Compressive modulus and (E) tensile stress–strain curves. (F) Specimens used for biological analysis (scale bar: 2 mm). (G) Cell proliferation of rat adipose-derived mesenchymal stem cells on various scaffolds. Abbreviations: dPCL, dissolved polycaprolactone; HA, hydroxyapatite; PCL, polycaprolactone.

In the tensile test, the results revealed the tensile moduli for dPCL/HA (116.10 ± 9.39 MPa), dPCL (178.37 ± 47.86 MPa), and PCL (394.05 ± 36.35 MPa). Contrary to the compressive test, dPCL showed a higher tensile modulus than dPCL/HA. All three bioinks exhibited a significant increase in stress up to 20% strain; however, their trends diverged thereafter depending on the material composition. For PCL, stress decreased after 20% strain until approximately 50%, after which it stabilized. In contrast, both dPCL/HA and dPCL maintained relatively stable stress profiles beyond 20% strain. Furthermore, dPCL/HA and dPCL demonstrated lower tensile performance overall, with dPCL/HA exhibiting even lower values than dPCL. This reduction is attributed to the presence of HA interfering with the intermolecular bonding of PCL, consistent with previous studies.[1,54] Notably, the mechanical properties of dPCL/HA fall within the range of tensile properties of cancellous bone, suggesting its potential suitability for applications in load-bearing bone scaffolds.[55,56]

The cell proliferation of rADSCs on both PCL and PCL-based composite scaffolds was assessed using the alamarBlue assay (Figure 6G). The results showed comparable cell proliferation for PCL (100%) and dPCL (98.28%), while dPCL/HA (123.72%) exhibited higher cell proliferation than both control (PCL) and dPCL. The comparative analysis yielded equivalent biocompatibility for rADSCs cultured on both PCL and dPCL scaffolds, implying that dPCL did not adversely affect cellular viability after fabrication. However, no significant difference in cell proliferation was observed between PCL and dPCL, despite their morphological differences.[30,57] In contrast, dPCL/HA demonstrated a marked improvement in cell proliferation, surpassing that of both PCL and dPCL. This enhancement suggests a pivotal role for HA

in promoting biocompatibility, supported by both the morphological characteristics observed in this study and previous findings.[26] These results highlight the potential of dPCL/HA scaffolds for improved cell compatibility in bone tissue engineering applications.

4. Conclusion

In conclusion, dPCL/HA scaffolds were systematically evaluated using suspended 3D printing to assess both material and structural performance. To fabricate precisely controlled scaffolds, a comprehensive printability assessment was conducted to optimize the key printing parameters. The incorporation of HA into dPCL significantly enhanced printability, improving resolution by up to 85% in the horizontal direction compared to pure dPCL. This advancement enabled the fabrication of complex geometries without the need for additional support structures. In addition, the dPCL/HA scaffolds showed improved mechanical performance, with compressive strengths approximately 50 MPa higher than dPCL alone. In contrast to conventional printing methods, the proposed support-free suspended printing strategy demonstrated the capability to produce structurally intricate constructs. These findings suggest that the developed room-temperature, dPCL-based suspended printing approach holds significant promise for fabricating geometrically complex and biocompatible scaffolds in bone tissue engineering applications.

Acknowledgments

None.

Funding

This research was supported by a National Research Foundation of Korea grant (NRF-2021R1I1A3040459) funded by the Ministry of Education, Republic of Korea, and by a Korea Health Technology R&D Project grant through the Korea Health Industry Development Institute, funded by the Ministry of Health and Welfare, Republic of Korea (HI22C1323).

Conflict of interest

Seung Yun Nam serves as the Editorial Board Member of the journal, but did not in any way involve in the editorial and peer-review process conducted for this paper, directly or indirectly. Other authors declare they have no competing interests.

Author contributions

Conceptualization: Juhyun Kang, Masoud Shirzad, Seung Yun Nam
Data curation: Juhyun Kang, Masoud Shirzad
Formal analysis: Juhyun Kang
Funding acquisition: Seung Yun Nam
Investigation: Juhyun Kang, Masoud Shirzad, Mahdi Bodaghi, Sudip Mondal, Hae Gyun Lim, Junghwan Oh
Methodology: Juhyun Kang, Masoud Shirzad, Priya Ranganathan, Dageon Oh, Sudip Mondal
Project administration: Seung Yun Nam
Resource: Seung Yun Nam
Software: Juhyun Kang
Supervision: Seung Yun Nam
Validation: Juhyun Kang
Visualization: Juhyun Kang, Masoud Shirzad
Writing–original draft: Juhyun Kang, Masoud Shirzad
Writing–review & editing: All authors

Ethics approval and consent to participate

Not applicable.

Consent for publication

Not applicable.

Availability of data

The data that support the findings of this study are available from the corresponding author upon reasonable request.

References

1. Deng X, Yu C, Zhang X, *et al*. A chitosan-coated PCL/nano-hydroxyapatite aerogel integrated with a nanofiber membrane for providing antibacterial activity and guiding bone regeneration. *Nanoscale*. 2024;16(20):9861-9874. doi: 10.1039/d4nr00563e
2. Song T, Zhou J, Shi M, *et al*. Osteon-mimetic 3D nanofibrous scaffold enhances stem cell proliferation and osteogenic differentiation for bone regeneration. *Biomater Sci*. 2022;10(4):1090-1103. doi: 10.1039/d1bm01489g
3. Romanazzo S, Hudson AR, Shiwarski DJ, *et al*. Synthetic bone-like structures through omnidirectional ceramic bioprinting in cell suspensions. *Adv Funct Mater*. 2021;31(13):2008216. doi: 10.1002/adfm.202008216
4. Kim MH, Chalisserry EP, Mondal S, Oh J, Nam SY. Silicon-substituted hydroxyapatite reinforced 3D printed gelatin membrane for guided bone regeneration. *Mater Lett*. 2021;304:130670. doi: 10.1016/j.matlet.2021.130670
5. Lee H, Yoo JM, Ponnusamy NK, Nam SY. 3D-printed hydroxyapatite/gelatin bone scaffolds reinforced with graphene oxide: optimized fabrication and mechanical characterization. *Ceram Int*. 2022;48(7):10155-10163. doi: 10.1016/j.ceramint.2021.12.227

6. Montalbano G, Molino G, Fiorilli S, Vitale-Brovarone C. Synthesis and incorporation of rod-like nano-hydroxyapatite into type I collagen matrix: a hybrid formulation for 3D printing of bone scaffolds. *J Eur Ceram Soc*. 2020;40(11):3689-3697.
doi: 10.1016/j.jeurceramsoc.2020.02.018

7. Shirzad M, Kang J, Kim G, Bodaghi M, Nam SY. Bioinspired 3D-printed auxetic structures with enhanced fatigue behavior. *Adv Eng Mater*. 2024;26(20):2302036.
doi: 10.1002/adem.202302036

8. Hu K, Jin S, Wang CC. Support slimming for single material based additive manufacturing. *Comput Aided Des*. 2015;65:1-10.
doi: 10.1016/j.cad.2015.03.001

9. Jiang J, Xu X, Stringer J. Support structures for additive manufacturing: a review. *J Manuf Mater Process*. 2018;2(4):64.
doi: 10.3390/jmmp2040064

10. Alioglu MA, Yilmaz YO, Singh YP, *et al*. Nested biofabrication: matryoshka-inspired intra-embedded bioprinting. *Small Methods*. 2023;8(8):e2301325.
doi: 10.1002/smtd.202301325

11. Song KH, Highley CB, Rouff A, Burdick JA. Complex 3D-printed microchannels within cell-degradable hydrogels. *Adv Funct Mater*. 2018;28(31).
doi: 10.1002/adfm.201801331

12. Bhattacharjee T, Zehnder SM, Rowe KG, *et al*. Writing in the granular gel medium. *Sci Adv*. 2015;1(8):e1500655.
doi: 10.1126/sciadv.1500655

13. Wu W, DeConinck A, Lewis JA. Omnidirectional printing of 3D microvascular networks. *Adv Mater*. 2011;23(24):H178-H183.
doi: 10.1002/adma.201004625

14. Jin Y, Compaan A, Chai W, Huang Y. Functional nanoclay suspension for printing-then-solidification of liquid materials. *ACS Appl Mater Interfaces*. 2017;9(23):20057-20066.
doi: 10.1021/acsami.7b02398

15. Lee A, Hudson A, Shiwarski D, *et al*. 3D bioprinting of collagen to rebuild components of the human heart. *Science*. 2019;365(6452):482-487.
doi: 10.1126/science.aav9051

16. Gao C, Sow WT, Wang Y, *et al*. Hydrogel composite scaffolds with an attenuated immunogenicity component for bone tissue engineering applications. *J Mater Chem B*. 2021;9(8):2033-2041.
doi: 10.1039/d0tb02588g

17. Liu L, Yang B, Wang LQ, *et al*. Biomimetic bone tissue engineering hydrogel scaffolds constructed using ordered CNTs and HA induce the proliferation and differentiation of BMSCs. *J Mater Chem B*. 2020;8(3):558-567.
doi: 10.1039/c9tb01804b

18. Mondal S, Dey A, Pal U. Low temperature wet-chemical synthesis of spherical hydroxyapatite nanoparticles and their in situ cytotoxicity study. *Adv Nano Res*. 2016;4(4):295-307.
doi: 10.12989/anr.2016.4.4.295

19. Shi Y, Wang L, Sun L, *et al*. Melt electrospinning writing PCL scaffolds after alkaline modification with outstanding cytocompatibility and osteoinduction. *Int J Bioprint*. 2023;9(6):1071.
doi: 10.36922/ijb.1071

20. Biscaia S, Branquinho MV, Alvites RD, *et al*. 3D printed poly(ε-caprolactone)/hydroxyapatite scaffolds for bone tissue engineering: a comparative study on a composite preparation by melt blending or solvent casting techniques and the influence of bioceramic content on scaffold properties. *Int J Mol Sci*. 2022;23(4):2318.
doi: 10.3390/ijms23042318

21. Rezaei A, Mohammadi MR. Development of hydroxyapatite nanorods-polycaprolactone composites and scaffolds derived from a novel in-situ sol-gel process. *Tissue Eng Regen Med*. 2012;9(6):295-303.
doi: 10.1007/s13770-012-0002-z

22. Wang Y, Liu L, Guo S. Characterization of biodegradable and cytocompatible nano-hydroxyapatite/polycaprolactone porous scaffolds in degradation in vitro. *Polym Degrad Stabil*. 2010;95(2):207-213.
doi: 10.1016/j.polymdegradstab.2009.11.023

23. Cestari F, Petretta M, Yang Y, Motta A, Grigolo B, Sglavo VM. 3D printing of PCL/nano-hydroxyapatite scaffolds derived from biogenic sources for bone tissue engineering. *Sustain Mater Technol*. 2021;29:e00318.
doi: 10.1016/j.susmat.2021.e00318

24. Zeng X, Meng Z, Qiu Z, He J, Fan J, Li D. Melt-based embedded printing for freeform fabrication of overhanging and flexible polycaprolactone scaffolds. *Virt Phys Prototyp*. 2023;18(1).
doi: 10.1080/17452759.2023.2209778

25. Jakus AE, Rutz AL, Jordan SW, *et al*. Hyperelastic "bone": a highly versatile, growth factor-free, osteoregenerative, scalable, and surgically friendly biomaterial. *Sci Transl Med*. 2016;8(358):358ra127.
doi: 10.1126/scitranslmed.aaf7704

26. Moghadam MZ, Hassanajili S, Esmaeilzadeh F, Ayatollahi M, Ahmadi M. Formation of porous HPCL/LPCL/HA scaffolds with supercritical CO2 gas foaming method. *J Mech Behav Biomed Mater*. 2017;69:115-127.
doi: 10.1016/j.jmbbm.2016.12.014

27. Lee H-U, Jeong Y-S, Jeong S-Y, *et al*. Role of reactive gas in atmospheric plasma for cell attachment and proliferation on biocompatible poly ε-caprolactone film. *Appl Surf Sci*. 2008;254(18):5700-5705.
doi: 10.1016/j.apsusc.2008.03.049

28. Liu Z, Liu X, Ramakrishna S. Surface engineering of biomaterials in orthopedic and dental implants: strategies to improve osteointegration, bacteriostatic and bactericidal activities. *Biotechnol J*. 2021;16(7):2000116. doi: 10.1002/biot.20200011

29. Wang L, Wang C, Zhou L, *et al*. Fabrication of a novel three-dimensional porous PCL/PLA tissue engineering scaffold with high connectivity for endothelial cell migration. *Eur Polym J*. 2021;161:110834. doi: 10.1016/j.eurpolymj.2021.110834

30. Ma J, Lin L, Zuo Y, *et al*. Modification of 3D printed PCL scaffolds by PVAc and HA to enhance cytocompatibility and osteogenesis. *RSC Adv*. 2019;9(10):5338-5346. doi: 10.1039/c8ra06652c

31. Oh D, Shirzad M, Kim MC, Chung E-J, Nam SY. Rheology-informed hierarchical machine learning model for the prediction of printing resolution in extrusion-based bioprinting. *Int J Bioprint*. 2023;9(6):1280. doi: 10.36922/ijb.1280

32. Kim MH, Lee YW, Jung WK, Oh J, Nam SY. Enhanced rheological behaviors of alginate hydrogels with carrageenan for extrusion-based bioprinting. *J Mech Behav Biomed Mater*. 2019;98:187-194. doi: 10.1016/j.jmbbm.2019.06.014

33. Huang B, Bártolo PJ. Rheological characterization of polymer/ceramic blends for 3D printing of bone scaffolds. *Polym Test*. 2018;68:365-378. doi: 10.1016/j.polymertesting.2018.04.033

34. He M, Zhang F, Li C, *et al*. Mechanical properties and oral restoration applications of 3D printed aliphatic polyester-calcium composite materials. *Alex Eng J*. 2024;88:245-252. doi: 10.1016/j.aej.2024.01.042

35. Motloung MP, Mofokeng TG, Ray SS. Viscoelastic, thermal, and mechanical properties of melt-processed poly (epsilon-caprolactone) (PCL)/hydroxyapatite (HAP) composites. *Materials (Basel)*. 2021;15(1):104. doi: 10.3390/ma15010104

36. Daskalakis E, Hassan MH, Omar AM, Cooper G, Weightman A, Bartolo P. Rheological behaviour of different composite materials for additive manufacturing of 3D bone scaffolds. *J Mater Res Technol*. 2023;24:3670-3682. doi: 10.1016/j.jmrt.2023.03.231

37. Waters R, Alam P, Pacelli S, Chakravarti AR, Ahmed RP, Paul A. Stem cell-inspired secretome-rich injectable hydrogel to repair injured cardiac tissue. *Acta Biomater*. 2018;69:95-106. doi: 10.1016/j.actbio.2017.12.025

38. Guo C, Wu J, Zeng Y, Li H. Construction of 3D bioprinting of HAP/collagen scaffold in gelation bath for bone tissue engineering. *Regen Biomater*. 2023;10:rbad067. doi: 10.1093/rb/rbad067

39. Milazzo M, Fitzpatrick V, Owens CE, *et al*. 3D printability of silk/hydroxyapatite composites for microprosthetic applications. *ACS Biomater Sci Eng*. 2023;9(3):1285-1295. doi: 10.1021/acsbiomaterials.2c01357

40. Hinton TJ, Jallerat Q, Palchesko RN, *et al*. Three-dimensional printing of complex biological structures by freeform reversible embedding of suspended hydrogels. *Sci Adv*. 2015;1(9):e1500758. doi: 10.1126/sciadv.1500758

41. Wu Q, Zhu F, Wu Z, *et al*. Suspension printing of liquid metal in yield-stress fluid for resilient 3D constructs with electromagnetic functions. *NPJ Flex Electron*. 2022;6(1):50. doi: 10.1038/s41528-022-00184-6

42. Enea S, Moon SK. Guidelines for 3D printed springs using material extrusion. *Rapid Prototyp J*. 2022;28(3):409-427. doi: 10.1108/RPJ-04-2020-0078

43. Okutani C, Yokota T, Miyazako H, Someya T. 3D printed spring-type electronics with liquid metals for highly stretchable conductors and inductive strain/pressure sensors. *Adv Mater Technol*. 2022;7(7):2101657. doi: 10.1002/admt.202101657

44. Rodriguez-Padilla C, Cuan-Urquizo E, Roman-Flores A, Gordillo JL, Vázquez-Hurtado C. Algorithm for the conformal 3D printing on non-planar tessellated surfaces: applicability in patterns and lattices. *Appl Sci*. 2021;11(16):7509. doi: 10.3390/app11167509

45. Abdullah AM, Dunn ML, Yu K. Robotic 3D printing of continuous fiber reinforced thermoset composites. *Adv Mater Technol*. 2024;9(24):2400839. doi: 10.1002/admt.202400839

46. Murali A, Parameswaran R. Extrusion 3D printing advances for craniomaxillofacial bone tissue engineering. *Polym Plast Technol Mater*. 2024;63(7):889-912. doi: 10.1080/25740881.2024.2307351

47. Tao O, Kort-Mascort J, Lin Y, *et al*. The applications of 3D printing for craniofacial tissue engineering. *Micromachines*. 2019;10(7):480. doi: 10.3390/mi10070480

48. Meglioli M, Naveau A, Macaluso GM, Catros S. 3D printed bone models in oral and cranio-maxillofacial surgery: a systematic review. *3D Print Med*. 2020;6(1):30. doi: 10.1186/s41205-020-00082-5.

49. Nyberg E, O'Sullivan A, Grayson W. scafSLICR: a MATLAB-based slicing algorithm to enable 3D-printing of tissue engineering scaffolds with heterogeneous porous microarchitecture. *PLoS One*. 2019;14(11):e0225007. doi: 10.1371/journal.pone.0225007

50. Moiduddin K, Mian SH, Umer U, Alkhalefah H, Ahmed F, Hashmi FH. Design, analysis, and 3D printing of a patient-specific polyetheretherketone implant for the reconstruction of zygomatic deformities. *Polymers*. 2023;15(4):886. doi: 10.3390/polym15040886

51. Van Belleghem S, Torres Jr L, Santoro M, *et al*. Hybrid 3D printing of synthetic and cell-laden bioinks for shape retaining soft tissue grafts. *Adv Funct Mater*. 2020;30(3):1907145.
doi: 10.1002/adfm.201907145

52. Shiwarski DJ, Hudson AR, Tashman JW, *et al*. 3D bioprinting of collagen-based high-resolution internally perfusable scaffolds for engineering fully biologic tissue systems. *Sci Adv*. 2025;11(17):eadu5905.
doi: 10.1126/sciadv.adu5905

53. Guerrero-de-Mier A, Espinosa M, Domínguez M. Bricking: a new slicing method to reduce warping. *Proc Eng*. 2015;132:126-131.
doi: 10.1016/j.proeng.2015.12.488

54. Moeini S, Mohammadi MR, Simchi A. In-situ solvothermal processing of polycaprolactone/hydroxyapatite nanocomposites with enhanced mechanical and biological performance for bone tissue engineering. *Bioact Mater*. 2017;2(3):146-155.
doi: 10.1016/j.bioactmat.2017.04.004

55. Shirzad M, Bodaghi M, Oh D, Yi M, Nam SY. Design and optimization of bioinspired auxetic structure for biomedical applications. *Eur J Mech A Solids*. 2024;103:105139.
doi: 10.1016/j.euromechsol.2023.105139

56. Almela T, Brook IM, Khoshroo K, *et al*. Simulation of cortico-cancellous bone structure by 3D printing of bilayer calcium phosphate-based scaffolds. *Bioprinting*. 2017;6:1-7.
doi: 10.1016/j.bprint.2017.04.001

57. Huang B, Caetano G, Vyas C, Blaker JJ, Diver C, Bartolo P. Polymer-ceramic composite scaffolds: the effect of hydroxyapatite and beta-tri-calcium phosphate. *Materials (Basel)*. 2018;11(1):129.
doi: 10.3390/ma11010129

ACCSCIENCE PUBLISHING

International Journal of Bioprinting

RESEARCH ARTICLE

3D-bioprinted osteochondral model based on hierarchical polymeric microarchitectures for *in vitro* osteoarthritis drug screening

Yi-Cheng Wang[1†], Xiao-Jie Song[1†], Xiao-Chang Lu[1], Zhou-Jiang Chen[2], Yue-Wei Li[1], Ranjith Kumar Kankala[1], Ai-Zheng Chen[1], Shi-Bin Wang[1*], and Chao-Ping Fu[1*]

[1]Institute of Biomaterials and Tissue Engineering & Fujian Provincial Key Laboratory of Biochemical Technology, Huaqiao University, Xiamen, Fujian, China

[2]Engineering Research Center for Pharmaceuticals and Equipment of Sichuan Province, Sichuan Industrial Institute of Antibiotics, School of Pharmacy, Chengdu University, Chengdu, Sichuan, China

(This article belongs to the *Special Issue*: *Advanced Strategies in 3D Bioprinting for Disease Modelling*)

Abstract

Compared to conventional two-dimensional (2D) or scaffold-free three-dimensional (3D) drug screening models, biomimetic osteochondral constructs offer superior physiological relevance for studying osteoarthritis (OA) and accelerating therapeutic discovery. This study reports the development of a polymeric microarchitecture (PM)-based 3D osteochondral model for drug screening applications. Microfluidics-assisted fabrication enabled the generation of cartilage-like and osteogenic microtissues by encapsulating chondrocytes and endothelial/osteoblast cells within PMs. These multicellular aggregates were embedded in gelatin methacryloyl and assembled via 3D bioprinting into a stratified osteochondral construct. The model exhibited favorable cell viability, high proliferation, and organized microtissue formation, validating its biological functionality. An OA-like microenvironment was induced using lipopolysaccharide, significantly elevating pro-inflammatory cytokines. Treatment with diclofenac, dexamethasone, or curcumin markedly attenuated this response, reducing tumor necrosis factor-alpha, interleukin (IL)-1β, and IL-6 to 42.1, 193.5, and 193.5 pg/mL, respectively, while elevating the anti-inflammatory cytokine IL-10 to 90.2 pg/mL. Overall, this PM-based 3D osteochondral platform reproduces key features of native joint tissue and holds promise for OA research, drug screening, and regenerative medicine.

***Keywords*:** 3D osteochondral model; Curcumin; Drug screening; Microfluidics; Porous microspheres

†These authors contributed equally to this work.

***Corresponding authors:**
Shi-Bin Wang (sbwang@hqu.edu.cn)

Chao-Ping Fu (fuchp@hqu.edu.cn)

Citation: Wang YC, Song XJ, Lu XC, *et al.* 3D-bioprinted osteochondral model based on hierarchical polymeric microarchitectures for *in vitro* osteoarthritis drug screening. *Int J Bioprint*. 2025;11(6):220-237. doi: 10.36922/IJB025290288

Received: July 14, 2025
Revised: August 31, 2025
Accepted: September 10, 2025
Published online: September 10, 2025

Copyright: © 2025 Author(s). This is an Open Access article distributed under the terms of the Creative Commons Attribution License, permitting distribution and reproduction in any medium, provided the original work is properly cited.

Publisher's Note: AccScience Publishing remains neutral with regard to jurisdictional claims in published maps and institutional affiliations.

1. Introduction

Body articulation or joint-related diseases often lead to difficulties in mobility and even paralysis in some instances, seriously affecting the quality of life in patients. Among various joint-related diseases, osteoarthritis (OA) is one of the most common

degenerative diseases of the skeletal system, affecting around 85 million people globally every year.[1,2]

Articular cartilage plays a crucial role in the lubrication and protection of the joint. The development of OA is manifested by the gradual loss of the articular cartilage and the densification of the underlying subchondral bone, leading to osteophyte formation and subchondral sclerosis, or even chondrocyte apoptosis and synovial effusion.[3–6] Several treatment strategies, including the most common joint replacement surgical procedure, are sophisticated and complicated and often suggested at the advanced pathophysiological stage. In addition, chemotherapeutic assistance is provided by prescribing steroids and non-steroidal anti-inflammatory drugs (NSAIDs) for OA patients. However, the prescribed medication provides merely symptomatic pain relief, which is short-lived and transient, thereby requiring long-term therapeutic strategies for OA.[7,8] Moreover, it should be noted that most of the currently available drug candidates are still having limited efficiency. Therefore, extensive research has been conducted to develop highly efficient, cost-effective, and non-invasive strategies for OA therapy.[9,10]

The establishment of screening models is essential for the rapid development of chemotherapeutic drugs. In this vein, highly efficient preclinical models are required to achieve high-throughput drug screening and enable precise and accurate investigation of OA pathology.[11–13] Several *in vivo* models replicate OA with clinically relevant features. However, these models suffer from several limitations, such as high cost, long development periods, and handling challenges.

Numerous *in vitro* models have been developed to address these shortcomings for the efficient initial screening of therapeutic agents towards OA therapy.[14,15] Typically, the two-dimensional (2D) cell culture of chondrocytes is considered a "model cell" for investigating OA *in vitro*. Comparatively, the three-dimensional (3D) models based on chondrocytes are more reliable than the conventional 2D monolayers to investigate OA due to their simulations of cell–cell and cell–extracellular matrix (ECM) interactions. Further advancements include developing the scaffold-based 3D models as the screening platforms, enabling controlled matrix elasticity for the co-culturing of multiple cell types (including bone cells) and investigations of cell fate. Moreover, the encapsulated chondrocytes in 3D scaffolds could better maintain their physiological phenotype and thus enhance the regeneration capacity of articular cartilage compared to the 2D culture models.[16,17]

Among the joint tissues, the subchondral bone cells play a significant role in maintaining the proper cartilage matrix and the articular physiology by interacting with each other.[18,19] In a previous study, Maihemuti *et al.*[20] proposed a 3D-printed porous multilayer scaffold based on cold-water fish skin gelatin for osteoarticular cartilage regeneration of damaged cartilage after arthritis. It was demonstrated that the simulation of the physiological microstructure of articular cartilage and subchondral bone was essential to construct a 3D scaffold-based OA model. In another study, Korpayev *et al.*[21] designed a multilayer scaffold embedding chondrocytes and preosteoblastic cells as a biomimetic osteochondral model. The close simulation and construction of bone joint structure and composition would benefit the investigation of OA pathology and drug screening.[22–24]

Polymeric microarchitecture (PM)-based scaffolds have attracted enormous attention from researchers owing to their outstanding biocompatibility, excellent cell carrying capacity, and ability to facilitate ECM-like environments for cell growth.[25–27] These PMs with exceptional porosity and interconnecting windows substantially encapsulate cells and enable their infiltration into the interiors. This ensures cell survival and proliferation by enabling the passage of required nutrients for cells to survive at the PMs core. Among various polymers from natural and synthetic sources, poly(lactic-co-glycolic) acid (PLGA), a synthetic polymer approved by the United States (US) Food and Drug Administration, has garnered enormous interest in the field of biomaterials due to the favorable mechanical properties, low toxicity, and low immunogenicity.[28,29] It has been demonstrated that cells are attached more rapidly to PLGA-based PMs with a significantly enhanced growth rate compared to commercially available porcine gelatin microcarriers.[27,30–32]

Notably, these PMs can be applied for drug delivery towards joint diseases. In a study, Dhanabalan *et al.*[33] designed a rapamycin-encapsulated PLGA-based PM, demonstrating high residence time and co-localization with various joint tissues when administered in the mouse knee via intra-articular injections. Such biomaterial-based delivery of rapamycin offers great potential for testing in animal models and clinical translation as a patient-compliant treatment. The controllable spatial distribution of microsphere-based scaffolds could mimic the native tissues and thus form bone-like and cartilage-like macro-sized architectures.[34–36]

Gelatin methacryloyl (GelMA) hydrogel has emerged as an ideal biomaterial for 3D bioprinting owing to its photo-crosslinkability, excellent biocompatibility, and tunable mechanical properties. Studies have demonstrated that the density of the molecular network (DMN) of GelMA can be precisely modulated by optimizing the

degree of substitution and solid content, enabling its compressive modulus to span a wide pressure range of 3–123 kPa.[37] This versatility allows GelMA to match the mechanical characteristics of various soft tissues, such as the liver, brain, and kidney. Furthermore, by incorporating reinforcing materials, GelMA-based composites can approach the mechanical requirements of stiffer tissues, including cartilage and bone. The innate arginyl–glycyl–aspartic acid sequences in GelMA support cell adhesion and migration. Low-DMN formulations facilitate cell spreading and proliferation, supporting high cell viability (>95%), while high-DMN versions offer enhanced shape fidelity and mechanical stability, making them suitable for printing complex architectures. These attributes collectively enable GelMA to mimic the native cellular microenvironment *in vitro*, thereby reducing the need for repetitive preliminary experiments and providing a standardized platform for applications such as tissue engineering and organ-on-a-chip systems.

Lipopolysaccharide (LPS) is the most abundant component within the cell membrane of Gram-negative bacteria. It can stimulate the release of inflammatory cytokines in various cell types, leading to an acute inflammatory response toward pathogens. OA is a low-grade inflammatory condition, and the elevation of the LPS levels in obesity and metabolic syndrome could contribute to OA.[38,39]

Motivated by these considerations, we demonstrated the fabrication of an *in vitro* OA model composed of hierarchical osteochondral tissue architectures using a combinatorial approach of microfluidic technique and 3D bioprinting.[40] Initially, PMs were prepared using the microfluidic technique. Mouse embryonic chondrocytes (C518) were then embedded into the PMs to construct cartilaginous cellular microtissues (C-MTs). In addition, mouse embryonic osteoblasts (MC3T3-E1) and mouse aorta endothelial cells (MAEC) were simultaneously encapsulated in a separate batch of PMs to construct endothelial osteoblastic microtissues (EO-MTs). Then, the C-MTs and EO-MTs were mixed with GelMA as a bioink for building a hierarchical osteochondral architecture using the 3D bioprinting approach (Figure 1). OA condition was finally induced in the designed hierarchical architectures by exposing the osteochondral model to LPS.

Curcumin (Cur) is a natural anti-inflammatory agent used in treating medical conditions for many years. Several reports indicated its potency to target multiple inflammatory diseases, including OA, rheumatoid arthritis, and other inflammatory arthritic conditions.[41–43] Similarly, the synthetic glucocorticoid dexamethasone (Dex) has been widely employed in intra-articular therapy for OA due to its potent anti-inflammatory effects, effectively inhibiting pro-inflammatory cytokines, such as interleukin (IL)-6, tumor necrosis factor-alpha (TNF-α), and matrix

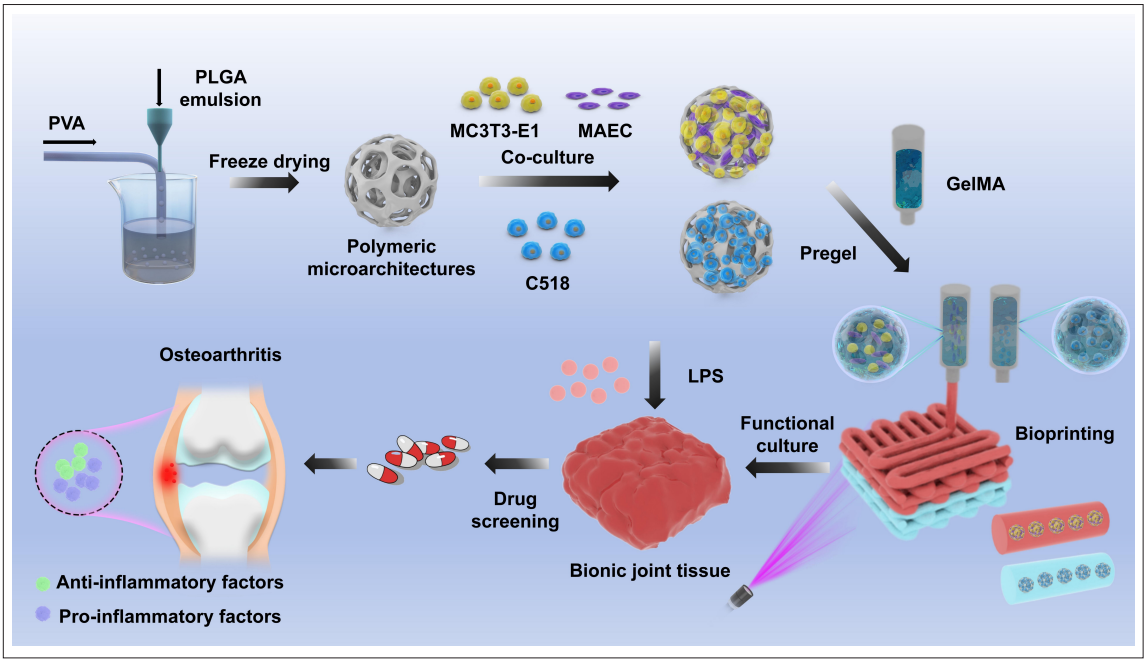

Figure 1. Schematic illustrating the preparation of hierarchical osteochondral architectures based on PLGA-based polymeric microarchitectures, fabricated through a combination of microfluidics and bioprinting technologies for drug screening. Abbreviations: GelMA, gelatin methacryloyl; LPS, lipopolysaccharide; MAEC, mouse aorta endothelial cell; PLGA, poly(lactic-co-glycolic) acid; PVA, polyvinyl alcohol.

metalloproteinases, through nuclear factor kappa-light-chain-enhancer of activated B cells pathway suppression.[44] Additionally, diclofenac (Dic), an NSAID, is commonly administered topically or orally to alleviate OA pain and inflammation by inhibiting cyclooxygenase activity.[45] Therefore, in this study, Cur, Dex, and Dic were employed as drug models for proof-of-concept to investigate the drug screening efficacy of the constructed osteochondral unit.

2. Materials and methods

2.1. Materials

Polyvinyl alcohol (PVA), PLGA (lactide:glycolide = 75:25, 66–107 kDa), gelatin, Dic, Dex, ascorbic acid, and β-glycerophosphate sodium were obtained from Sigma-Aldrich (US). Cur (99.7%) and dichloromethane were purchased from Sinopharm Group Chemical Reagent Co., Ltd. (China). Cell Counting Kit-8 (CCK-8) and 4',6-diamidino-2-phenylindole (DAPI) were purchased from Nanjing Keygen Biotech Co., Ltd. (China). The Bradford assay kit was purchased from Bio-Rad (US). Qtracker®525 and 655 Cell Labeling Kits were obtained from Thermo Fisher Scientific (US). Penicillin–streptomycin, fetal bovine serum (FBS), and Dulbecco's modified Eagle medium (DMEM) were purchased from Gibco (US).

2.2. Preparation and characterization of polymeric microarchitectures

Initially, PLGA-based PMs were prepared using a microfluidic technique, as previously reported.[30] Briefly, a customized coaxial microfluidic system was prepared using plastic tubes (inner diameter: 1 mm), a glass capillary (outer diameter: 1 mm), and a needle (27G, inner diameter: 210 μm, outer diameter: 400 μm). PLGA (180 mg) was dissolved in dichloromethane (4.5 mL), and the aqueous gelatin (6% w/v) was then added to form a water-in-oil emulsion. The initial emulsion was stabilized by ultrasonication and then introduced into the microfluidic device as the discontinuous phase, while PVA solution (1% w/v) was used as the continuous dispersion phase. The flow rates of the discontinuous and the dispersion phases were set at 0.05 and 2 mL/min, respectively. The PLGA-based PMs were subsequently collected in a pre-cooled PVA solution (1% w/v). After stabilization, the PMs were washed with deionized water at 40°C to eliminate gelatin and achieve a porous structure. Finally, the PMs were lyophilized and stored until further use.

The morphology of PMs was observed using field emission-scanning electron microscopy (FE-SEM; S-4800, HITACHI, Japan) after sputter-coating with gold. Fourier transform infrared (FTIR) spectra were obtained using a Nicolet iS50 model FTIR spectrophotometer (Thermo Nicolet Corporation, US) at a 4 cm^{-1} resolution using KBr pellets. The degradation of PMs was investigated by exposing the PMs to phosphate-buffered saline (PBS; pH 7.4) at 37°C, and the changes in the morphology of PMs at different predetermined time intervals were observed using FESEM. Furthermore, the protein adsorption efficacy of PMs was investigated using a standard Bradford assay kit. Briefly, PMs were placed in 96-well plates, and then 200 μL of 10% FBS-containing DMEM was added to each well, and the medium was replaced at predetermined time intervals. After washing with PBS, the PMs were immersed in 200 μL of protein eluent for 30 min, and the protein content was determined using the Bradford assay kit.

2.3. Preparation and characterization of cartilaginous cellular microtissues and endothelial osteoblastic microtissues

Cell lines MC3T3-E1, C518, and MAECs (Beina Biotechnology Research Institute, China) were cultured in complete medium (basal medium supplemented with 10% [v/v] FBS, 1% [v/v] penicillin–streptomycin) at 37°C in 5% CO_2 and 95% relative humidity. Firstly, PM suspension with different concentrations (0.25, 0.5, and 1 mg/mL) was prepared in DMEM and added to the cells for different incubation times. Cell viability was detected through the CCK-8 assay. C-MTs and EO-MTs were developed by encapsulating the cells in PMs separately.[32,46] For the construction of C-MTs, microspheres were placed in each well of a 96-well plate after sterilization. Then, 200 μL of C518 cell suspension at a concentration of 1.6×10^4 cells/mL was added for culturing modes. The PMs were placed in an incubator for static culture, or placed at 37°C and 110 rpm for dynamic culture under the condition of ensuring nutrition and oxygen supply. Similarly, EO-MTs were constructed by co-culturing MAECs and MC3T3-E1 cells together with PMs. After 3, 9, and 24 h of culture, non-adherent cells were removed by washing three times with PBS after removing the medium, and PMs were collected and digested with trypsin and counted. Adhesion and proliferation assays were performed using triplicate cultures, and the data were representative. The cell adhesion rate was calculated using **Equation I**, as previously reported[30]:

$$\text{Cell adhesion rate (\%)} = \text{Cell adhesion/Cell inoculation number} \times 100 \quad \text{(I)}$$

The MAECs and MC3T3-E1 cells were labeled with Qtracker®655 and Qtracker®525, respectively, and the distribution of cells in EO-MTs was observed through Leica TCS SP8 confocal laser scanning microscopy (CLSM) (Leica Microsystems GmbH, Germany). Immunofluorescence staining was used to observe

the expression of aggrecan, collagen I, and collagen II in C-MTs. The CCK-8 method was used to detect the proliferation of cells in the MTs under static and dynamic culture. The MTs were fixed with paraformaldehyde and stained with DAPI for CLSM imaging. Other MTs were embedded in paraffin and sectioned for hematoxylin and eosin (HE) staining. After dehydration with gradient ethanol solutions, the fixed sealing plates were observed using a light microscope (Nikon Eclipse Ts2, Japan). Assays were performed with triplicate cultures, and data are representative of three experiments.

Next, MAECs and MC3T3-E1 cells were co-cultured using the method described in Section 2.3. After 5 days of co-culture, the cells were transferred to 24-well plates. Half of the wells were maintained in regular complete medium, while the other half were switched to osteogenic induction medium (complete medium supplemented with 1 mM Dex, 10 mM ascorbic acid, and 1 M β-glycerophosphate sodium). On day 7, alkaline phosphatase (ALP) activity was detected using the BCIP/NBT ALP detection kit (Beyotime, China). On day 14, calcium deposition on EO-MTs was stained with Alizarin Red S (ARS). After thorough staining, the staining solution was washed off, and the ARS-stained calcium deposits were dissolved in 10% w/v cetylpyridinium chloride. The absorbance was then measured at a wavelength of 562 nm.

For C518 cells of the same passage, cells were harvested by trypsinization and seeded into six-well plates. Half of the wells were cultured under normal conditions, while the other half were supplemented with additional PMs. The plates were then incubated on an orbital shaker. On day 4, culture supernatants were collected, and the secreted glycosaminoglycan (GAG) content was measured using an enzyme-linked immunosorbent assay (ELISA) kit. For C-MTs, at different time points (days 1, 4, and 7) of co-culture, 2 mL aliquots were collected from the co-culture system under mixed conditions. Of these aliquots, 1 mL was used for GAG content detection, while the remaining 1 mL was used for DNA content assay. GAG content was then normalized to DNA content.

2.4. Preparation and characterization of microtissue–gelatin methacryloyl composite bioink

For the modification of gelatin with methacrylic anhydride and subsequent processing, gelatin was added to carbonate buffer (0.25 M, pH = 9.0) and heated at 50°C to facilitate dissolution. Once the solution became clear with no visible undissolved gelatin particles, methacrylic anhydride was slowly added, and the reaction was allowed to proceed under continuous stirring in the dark. During the reaction, the pH was maintained using 1 M NaOH. Following the reaction, the solution was immediately transferred to a preheated dialysis membrane (molecular weight cutoff: 8–14 kDa) while still hot for dialysis. Dialysis was performed with water changes three times daily for one week. After dialysis, the solution was frozen overnight in a −80°C freezer and subsequently lyophilized for 48 h, yielding a spongy sample. The sample was then stored dry at −20°C.

An Avance III 500 MHz spectrometer (Bruker, Switzerland) was used to acquire ^{1}H nuclear magnetic resonance (NMR) spectra at room temperature. Samples were dissolved in D_2O (10 mg/mL) and measured in a 5 mm NMR tube. GelMA was dissolved in PBS buffer at 50°C under gentle stirring to prepare a 10% w/v solution. Then, 0.25% w/v lithium phenyl-2,4,6-trimethylbenzoylphosphinate was incorporated to form the GelMA bioink. For FESEM observation, 1 mL of bioink was crosslinked under blue light for 30 s in a mold. The resulting hydrogel was frozen in liquid nitrogen, lyophilized for 48 h, snap-fractured in liquid nitrogen, and sputter-coated with gold before imaging. To assess swelling behavior, PMs were blended into the GelMA bioink and crosslinked. After demolding, samples were rinsed with PBS (pH 7.4) and blotted to remove excess liquid. The initial dry weight was recorded. Samples were immersed in 20 mL PBS at 37°C under shaking (50 rpm). At specified intervals (1–24 h), samples were removed, blotted, and weighed. Swelling equilibrium was defined as a weight change ≤5% between two consecutive points. The swelling ratio and moisture ratio were calculated accordingly. Rheological properties were characterized using a dynamic shear rheometer Discovery HR-1 (TA Instruments, US) with a 50 mm parallel-plate geometry (1 mm gap). Both uncrosslinked (PM/GelMA mixture with photoinitiator, degassed) and crosslinked (1-mm-thick discs, photocured) samples were tested. Shear viscosity was measured at room temperature from 0 to 1000 s^{-1}. Temperature-dependent viscosity and moduli (G' and G") were recorded during cooling from 40°C to 0°C at 5°C/min.

2.5. Construction of biomimetic osteochondral tissue model

The mixture of C-MTs or EO-MTs and GelMA hydrogel was layer-printed by an extruded 3D bioprinter to construct a biomimetic osteochondral tissue model. First, EO-MT–GelMA hydrogel composite (50 microtissue/mL) was printed in six-well plates and cured using blue light irradiation for 10 s. The C-MT–hydrogel composite (50 microtissue/mL) was then printed on the EO-MT layer and cured using blue light irradiation. Then, 1 mL of the complete medium was added and placed in an incubator. Meanwhile, MT/GelMA bioink was directly added into sterilized silicone molds, photocrosslinked with blue light,

demolded, and then transferred to six-well plates for culture as the casting group. On days 1, 4, and 7, cell viability of both the casting group and the scaffold group was assessed using the CCK-8 assay. On day 14, the scaffolds were retrieved, washed with PBS to remove residual medium, and their structural integrity was observed. Additionally, on day 14, the scaffolds were stained using the BCIP/NBT ALP chromogenic kit; on day 21, calcium deposition on the scaffolds was stained with ARS.

For cellular tracking, C-MTs and EO-MTs were labeled with Qtracker®655 and Qtracker®525, respectively. The labeled MTs were then mixed with GelMA hydrogel and printed under light-protected conditions, followed by blue light-induced photocrosslinking. The constructs were transferred to a cell culture incubator for subsequent culture, and all subsequent procedures were performed under dark conditions. On days 7 and 14, the interface region between the osseous layer and cartilaginous layer was observed using CLSM.

2.6. Lipopolysaccharide-induced osteoarthritis model

Medium containing LPS at different concentrations (0, 0.01, 0.5, 1, and 10 μg/mL) was added to cultured chondrocytes for 48 h, and the cell viability was investigated using the CCK-8 assay. After the biomimetic osteochondral tissue model was constructed, LPS (0.5 μg/mL) was added to the culture medium for 6, 24, and 48 h to induce OA. At various time points, the supernatants were collected, and the levels of TNF-α and IL-1β were then detected using respective ELISA assay kits (LunChangShuoBiotech, China). In addition, Dic, Dex, and Cur were used as the drug model to treat OA. Different concentrations of Dic (75, 100, and 125 μM), Dex (1.5, 3, and 4.5 μM), and Cur (30, 40, and 50 μM) were added to the culture medium. After 48 h of incubation, cell viability was assessed using the CCK-8 assay. Cur was labeled with FITC, added to the cells, and incubated for a certain period of time. Then, the cells were fixed with 4% paraformaldehyde, nuclear stained with DAPI, and observed using CLSM imaging. The designed biomimetic joint tissue was treated with LPS for 48 h, and was then added Dic, Dex, or Cur solution for incubation over 48 h. The contents of inflammatory cytokines TNF-α, IL-1β, IL-6, and IL-10 in the supernatant were measured using ELISA kits. All the assays were performed in triplicate, and the data were representative of three experiments.

2.7. Statistical analysis

Data were analyzed using Origin 2021 (Origin Lab, US). All experimental data displayed as mean ± standard deviation (SD) were assessed using the unpaired Student's *t*-test and analysis of variance with post hoc test using Tukey's honestly significant difference (HSD) method, and $p < 0.05$ was considered statistically significant.

3. Results and discussion

3.1. Characterization of polymeric microarchitectures

This study employed the microfluidic technique to fabricate PLGA-based porous PMs. The gelatin was distributed in the PLGA droplets as a porogen and then corroded using hot water. Notably, the FESEM images (Figure 2A & B) showed that the microfluidic techniques resulted in monodisperse PMs with a uniform diameter of 450–550 μm and a pore size distribution in the range of 20–50 μm (Figure 2D & E). In addition, the cross-sectional view of the PMs presented interconnected windows (Figure 2C), which could substantially facilitate the transportation of nutrients and oxygen. These results were in agreement with the reported literature, in which PMs with a diameter of 250–700 μm could retain the viability of cells cultured for 3–14 days due to their significant proliferation ability, attributing to the interconnected pores of 20–70 μm.[47,48]

The designed PMs were further systematically characterized using various techniques and compared with the raw PLGA material (Figure S1). The results showed that no structural changes occurred during the preparation process. The PMs exhibited a uniform size with porous structure and good physicochemical characteristics—potentially an optimal platform for cell growth.

Notably, the degradability attribute of the biomaterials is equally important to exploring the characterization and performance efficacy. To this end, PMs were placed in PBS and incubated for seven weeks to investigate their degradation properties. As presented in Figure S2, although PLGA was gradually degraded, the porous structure of the PMs remained intact for several weeks, suggesting them as the most suitable carrier for cells, while the slow degradation of PMs favored biomaterial absorption and tissue formation.[49–51] In addition, protein adsorption effects were used to explore cell adhesion effects on the surface of the PMs by exposing the PMs to serum proteins and evaluating them using the Bradford protein assay following the manufacturer's instructions. The results showed that the adsorption kinetics of the proteins were approximately 1.40×10^{-2} mg/PM for 30 min, followed by equilibrium (Figure S3). Collectively, the characterizations, degradability, and protein adsorption efficacy could substantially reflect the cell adhesion ability of the designed PMs, indicating their potential ability for tissue regeneration.[50,52]

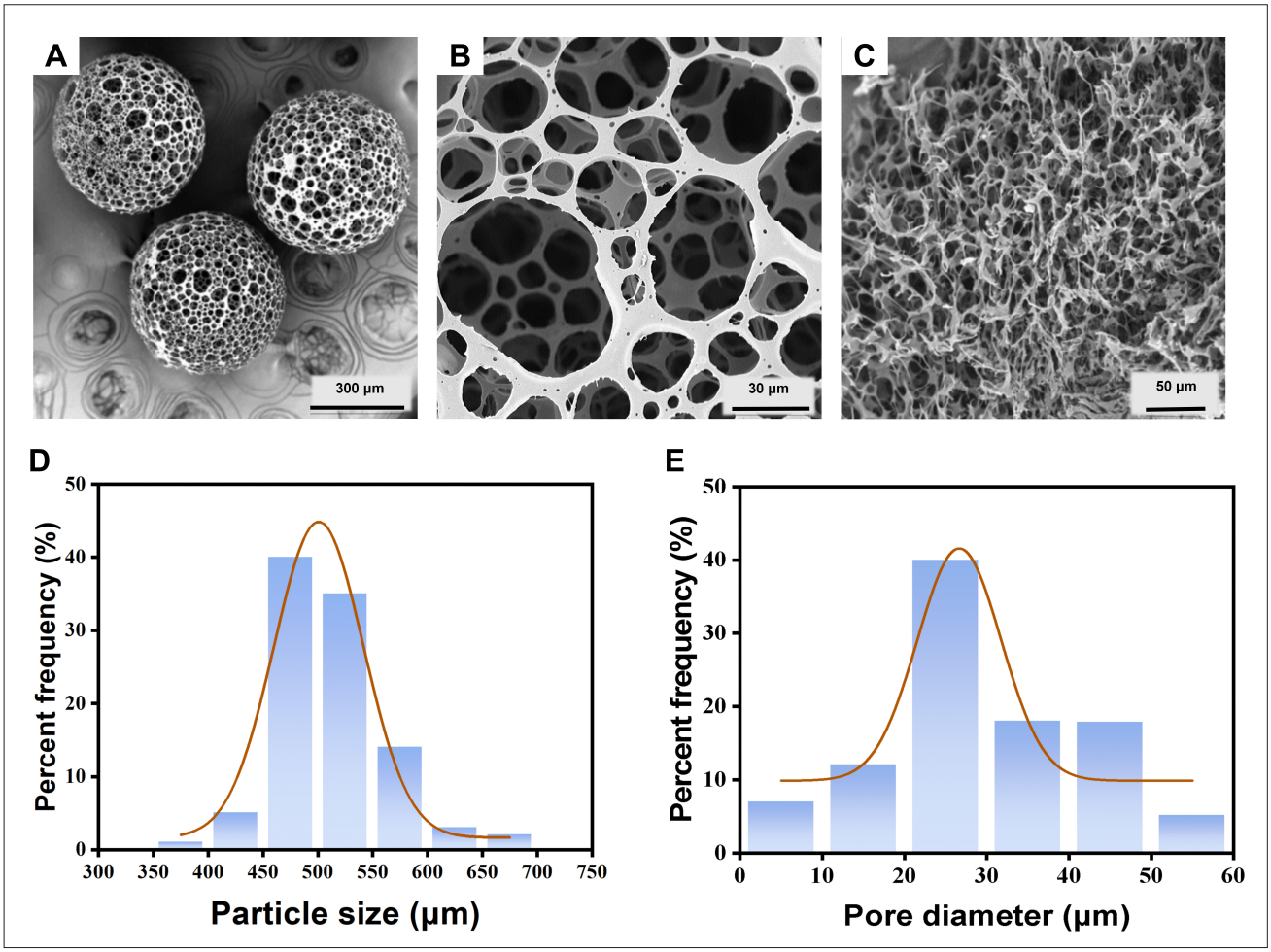

Figure 2. Characterizations of the polymeric microarchitectures. (A & B) Scanning electron microscopy images of the particles. Scale bars: (A) 300 μm, (B) 30 μm; magnification: (A) 200×, (B) 700×. (C) Cross-sectional view. Scale bar: 50 μm; magnification: 900×. (D) Particle size distribution. (E) Pore diameter distribution.

3.2. Preparation and characterization of cartilaginous cellular microtissues and endothelial osteoblastic microtissues

Among several constituents, chondrocytes and subchondral osteoblasts are key components of articular joints. Within these joints, blood vessels are distributed in the subchondral bone, where endothelial cells play a pivotal role in bone development and in the repair of articular body joints.[53] Considering these aspects, MC3T3-E1 cells and MAECs were co-cultured in the PMs to simulate subchondral bone tissues. Different concentrations of PM suspension were prepared to treat the cells. The live and dead staining fluorescence images at 24 h showed that almost no dead cells existed, with a high cell survival rate, indicating that the PM suspensions had no obvious toxicity to the cells at this time (Figure 3A). Furthermore, the CCK-8 assay was used to detect the cytotoxicity of the PM suspension, and the results showed that high cell viability was still observed at the concentration of 1 mg/mL for 72 h (Figure 3B & C).

C-MTs and EO-MTs, both static and dynamic cultivation methods were employed. The adhesion and growth of cells on the PMs were determined through nuclear staining and the measurement of cell proliferation, respectively. It was evident that the MC3T3-E1 cells and MAECs presented excellent proliferation efficacy with the increased cell numbers in the initial 5 days, potentially attributing to the biocompatibility of the PMs (Figure 4A). Additionally, the highly open and porous microstructure facilitates cellular penetration into the PMs while enabling efficient substance exchange to meet the nutritional requirements of cells within the PMs, thereby promoting cell filling within its interior. Similarly, C-MTs also presented excellent proliferation efficacy of chondrocytes in the PMs (Figure 4A), demonstrating that all three cell

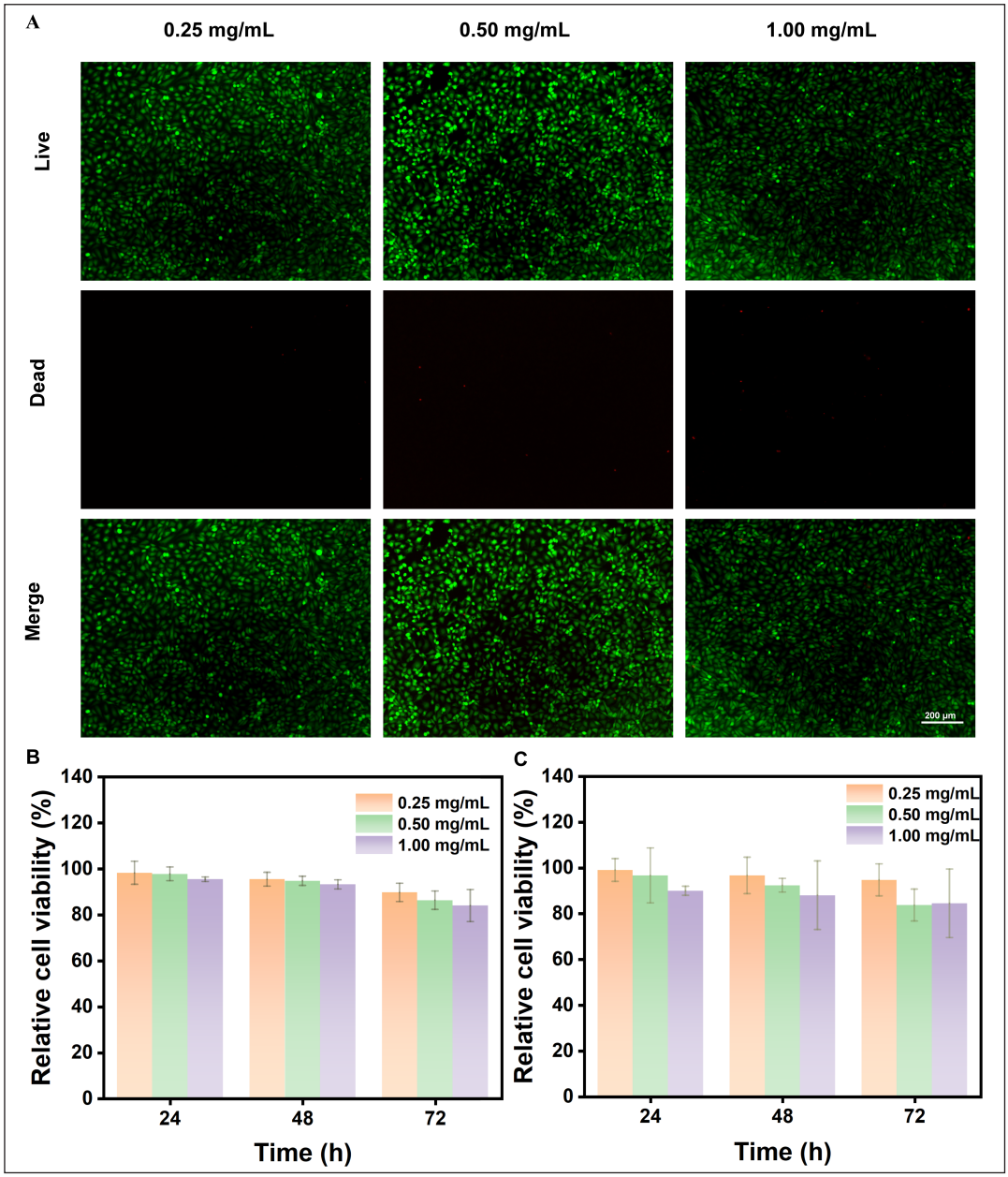

Figure 3. The biocompatibility of polymeric-microarchitecture suspensions. (A) Fluorescence images of the live and dead staining of cells treated with different concentrations of suspensions for 24 h (green: live; red: dead). Scale bar: 200 μm; magnification: 40×. Cell cytotoxicity of (B) MC3T3-E1 (n = 3) and (C) C518 (n = 3) under different suspension concentrations and exposure times was analyzed using the cell counting kit-8 assay.

types could grow well in the PMs. Notably, comparative analysis revealed that cells in MTs prepared under dynamic culture exhibited slightly higher proliferation than those in static culture, attributable to enhanced nutrient, oxygen, and waste transport.[33]

In addition, the adhesion and proliferation efficiencies of cells in PMs were measured quantitatively using the cell counting and CCK-8 analyses, respectively. The results showed that the PMs possessed excellent cell adhesion ability. In EO-MTs under static culture, the average adhesion rate of MC3T3-E1 cells and MAECs was 6.0% at 3 h compared to the inoculated cell numbers, which subsequently increased to 10.5% at 9 h and 28.6% at 24 h (Figure 4B). Interestingly, the cell adhesion rate in the dynamic culture method was 33.1% at 24 h, markedly higher than that of the static culturing method. Although there exists a slight difference, both cell culturing modes

presented excellent adhesion efficacies. Meanwhile, cell proliferation in EO-MTs showed that the relative viability rate of harbored cells nearly doubled from day 1 to day 7 under static culture, indicating that the 3D microenvironment of PMs was optimal for cell growth (Figure 4C). Similarly, CLSM observations (Figure 4A) showed a significant increase in dynamically cultured C518 chondrocytes after initial adhesion within the polymer structure, with cells maintaining a steady growth state in PMs (Figure 4D & E). Notably, C518 chondrocytes showed proliferation and infiltration patterns similar to those of MAECs and MC3T3-E1 cells, with a 24 h adhesion rate of 58.2% under dynamic culture, exceeding that achieved under static culture.

In normal subchondral bone, endothelial cells are essential for intercellular signaling, angiogenesis, and osteogenesis. Hence, the strategy to prepare EO-MTs apparently mimics subchondral tissues. Co-culturing endothelial cells with osteocytes is the most direct approach to establishing the vascular function of supplying nutrients and metabolite excretion for constructing bone tissue models. Accordingly, MAECs were co-cultured with MC3T3-E1 cells in PMs, mimicking native vascularized bone tissues. To investigate cell distribution in EO-MTs, the osteoblasts and the endothelial cells were fluorescently labeled using Qtracker®655 and Qtracker®525, respectively. Although angiogenic sprouting and vascular lumen formation were rarely seen, CLSM imaging confirmed that both MAECs and MC3T3-E1 cells were distributed in the MTs and maintained high viability (Figure 5A). Together, the co-culture of MC3T3-E1/MAEC in PMs produced complex tissues with considerable cell–cell communications, indicating the establishment of a vascularized bone-like microenvironment. In the cultured C-MTs, cartilage-specific proteins, including aggrecan, collagen I, and collagen II, were detected (Figure 5B), indicating robust chondrocyte proliferation within the carriers. In addition, HE staining was performed to better visualize cell distributions on the PMs. It was evident that the tissues with dense cell density and orderly arrangement were formed, while prolonged culture induced scaffold morphology changes due to the aggregation of individual PM architectures (Figure 5C). Furthermore, in our previous study,[30] the bioefficacy of MTs constructed using cell-laden PLGA-based PMs was demonstrated, as cells released significantly higher levels of essential proteins, including albumin and multidrug resistance proteins, compared to 2D static culture. Taken together, these findings suggest that the designed PMs provide abundant adhesion sites, support high cell viability, and sustain essential cell functions.

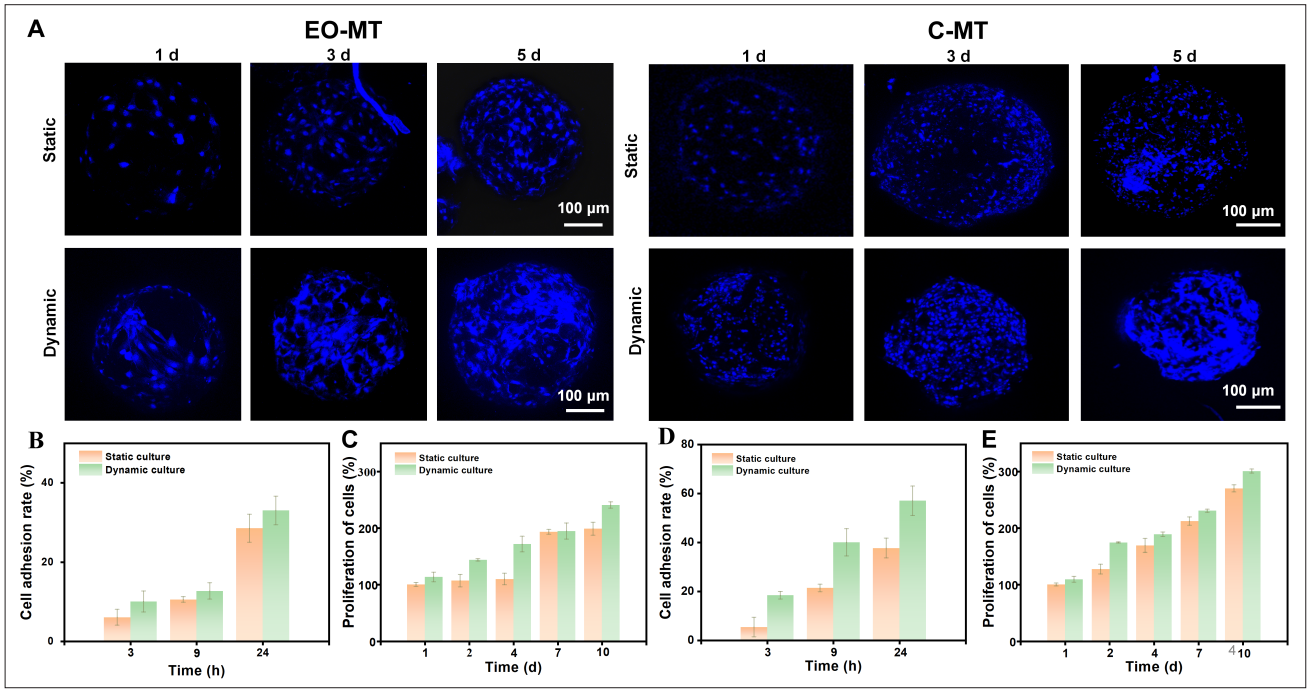

Figure 4. Co-culture of polymeric microarchitectures and endothelial osteoblastic microtissues (EO-MTs) or cartilaginous cellular microtissues (C-MTs). (A) Confocal laser scanning microscopy images of EO-MTs and C-MTs cultured for different times (blue: DAPI). Scale bar: 100 μm; magnification: 40×. Quantification of cell adhesion and proliferation in (B & C) EO-MTs and (D & E) C-MTs under static or dynamic culture modes (n = 3).

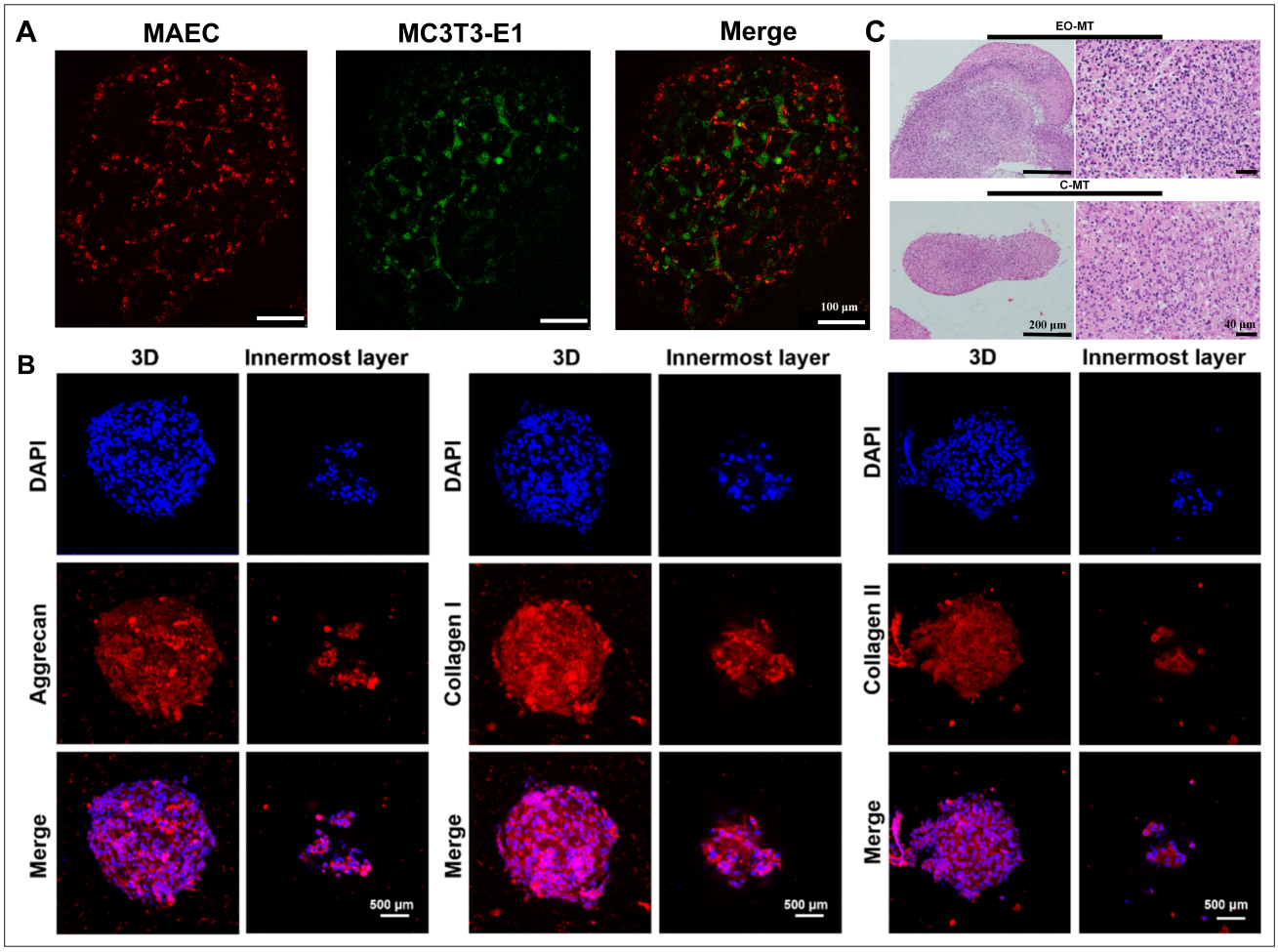

Figure 5. CLSM imaging. (A) CLSM of MAECs and MC3T3-E1 cells in EO-MTs. Scale bar: 100 μm; magnification: 20×. (B) CLSM of aggrecan, collagen I, and collagen II in C-MTs. Scale bar: 500 μm; magnification: 10×. (C) Hematoxylin and eosin staining of EO-MTs and C-MTs. Scale bar: 200 or 40 μm; magnification: 40× and 100× Abbreviations: C-MT, cartilaginous cellular microtissue; EO-MT, endothelial osteoblastic microtissue; MAEC, mouse aorta endothelial cell; CLSM, confocal laser scanning microscopy.

To better recapitulate native cartilage and subchondral bone microenvironments, the functionalized culture of the prepared EO-MTs and C-MTs was performed. For EO-MTs, osteogenic induction medium was formulated by supplementing complete medium with osteogenic growth factors, including Dex, ascorbic acid, and β-glycerophosphate sodium, followed by long-term culture. ALP, a key and classical biomarker for osteoblast activity and bone formation, directly reflects osteoblast maturation and functional status. It plays a crucial role in bone matrix mineralization; its expression is significantly upregulated when osteoblasts transition from the proliferative phase to the mature differentiation phase. On day 7, quantitative analysis of ALP activity in EO-MTs using an ALP assay kit revealed that the osteogenic induction group exhibited significantly higher activity (0.141 μM) compared to the non-induced blank group (0.107 μM), indicating that osteoblasts adhering to and proliferating on EO-MTs had entered an active bone-forming phase (Figure 6A). Notably, increased ALP activity does not necessarily indicate extensive mineralized bone formation; thus, on day 14, ARS staining was performed to visualize calcium nodules on EO-MTs (Figure S4), followed by quantitative analysis via dissolution with 10% w/v cetylpyridinium chloride (Figure 6B). The results showed significantly higher calcium deposition in the osteogenic induction group than in the blank group, confirming calcium salt deposition and indicating mineralized bone formation. Through ALP and ARS stainings, markers of early and late osteogenesis, respectively, mutually validate the successful osteogenic functionalization of EO-MTs. These findings align with the regulatory role of Runt-related transcription factor 2 (RunX2), the master transcription factor of osteogenesis, where ALP upregulation and ARS-positive

mineralization represent the terminal events of RunX2-mediated signaling cascade activation.

For C-MTs, GAG, a critical component of chondrocyte ECM, serves as a direct indicator of chondrogenic MT maturity and quality. On day 4 of co-culture, GAG content in supernatants (Figure 6C) showed that 2D-cultured cells exhibited higher GAG levels (106.8 μg/mL) than 3D-co-cultured cells on PMs (49.5 μg/mL). This can be attributed to the fact that 3D PMs provide abundant attachment sites for secreted GAG, which gradually deposit on the scaffold to form ECM, whereas 2D-cultured GAG diffuses freely into the medium. Additionally, for 3D-co-cultured C-MTs, deposited GAG was detected at different time points and normalized to DNA content (Figure 6D), revealing that chondrocytes gradually adapted to the microenvironment, activated the synthetic phenotype, and initiated GAG and proteoglycan synthesis over time, indicating MT formation and favorable cellular functionality. This progressive GAG accumulation corresponds to the terminal output of the SOX-9 signaling cascade, as SOX-9, the central transcription factor for chondrogenesis, directly regulates the expression of GAG-synthesizing enzymes and proteoglycan core proteins. In summary, the functionalized culture of MTs enables improved recapitulation of native cartilage and subchondral bone microenvironments.

3.3. Characterization of microtissue–gelatin-methacryloyl-hydrogel composite bioink

GelMA hydrogels were synthesized via amidation of gelatin amino groups with methacrylic anhydride, as confirmed by ^{1}H NMR analysis. The spectrum showed characteristic peaks of methacrylate vinyl protons (δ = 5.31 and 5.55 ppm) and the attenuation of the amide-associated signal (δ = 2.88 ppm), indicating effective double-bond modification (Figure 7A). GelMA hydrogels exhibited an interconnected porous structure after lyophilization (Figure 7B), favorable for nutrient diffusion and cell infiltration. Subsequently, PM–GelMA composite hydrogels were prepared, and swelling ratio and moisture ratio tests were performed (Figure 7C & D). The results showed that the addition of PMs had no significant effect on the bioink, potentially because the added PMs were already in an equilibrium state; the slight increase observed in the composite group may be attributed to the added MTs increasing the internal space of the overall structure. Mechanical property test results (Figure 7E & F) demonstrated that increasing MT concentration from 0 to 20 mg/mL enhanced hydrogel stiffness, as evidenced by steeper stress–strain curves and a higher compressive modulus. This enhancement can be attributed to PMs acting as rigid fillers that facilitate stress transfer within the gel network. Since matrix stiffness is known to effectively regulate cell behavior—higher stiffness promotes osteogenic differentiation while moderate or lower stiffness favors chondrogenesis[54,55]—these results suggest that adjusting PM incorporation offers a practical strategy for modulating hydrogel stiffness in future studies.

Rheological analysis further confirmed that PMs improved the printability of GelMA bioinks. Both GelMA and PMs/GelMA displayed thermo-responsive gelation, with G' surpassing G" near 15°C (Figure 7G), indicating sol–gel transition unaffected by PM addition. Temperature–viscosity curves further demonstrated the thermal responsiveness of GelMA and PMs/GelMA; however, the initial viscosity of PM-containing inks was significantly higher than that of pure GelMA (Figure 7H). This may be due to the increased internal friction of particle–polymer interactions and the complexity of the microstructure. This property is advantageous for 3D bioprinting, as higher static viscosity enhances shape fidelity. Importantly, shear-thinning behavior was preserved (Figure 7I), satisfying the extrusion printing requirement of high viscosity at rest and low viscosity under shear. In conclusion, the incorporation of PMs not only achieves effective regulation of the swelling behavior and mechanical strength of GelMA hydrogels but

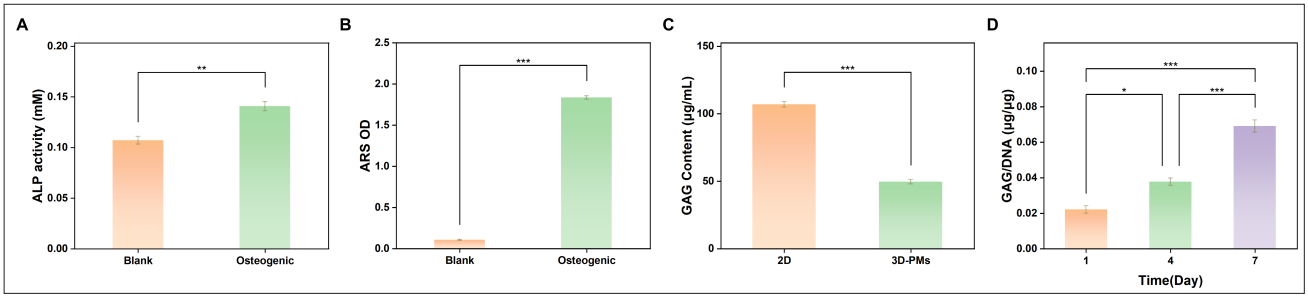

Figure 6. Functional characterization of microtissues during culture. (A) ALP activity of EO-MTs at day 7 of osteogenic induction culture (n = 3). (B) Quantitative analysis of ARS staining for calcium deposition in EO-MTs at day 14 of osteogenic induction (n = 3). (C) GAG content in the supernatants of C518 cells cultured for 4 days under different conditions (n = 3). (D) Changes in GAG content of C-MTs at different culture time points (n = 3). Notes: *p < 0.05, **p < 0.01, ***p < 0.001. Abbreviations: ALP, alkaline phosphatase; ARS: Alizarin Red S; C-MT, cartilaginous cellular microtissue; EO-MT, endothelial osteoblastic microtissue; GAG, glycosaminoglycan; OD, optical density; PM, polymeric microarchitecture.

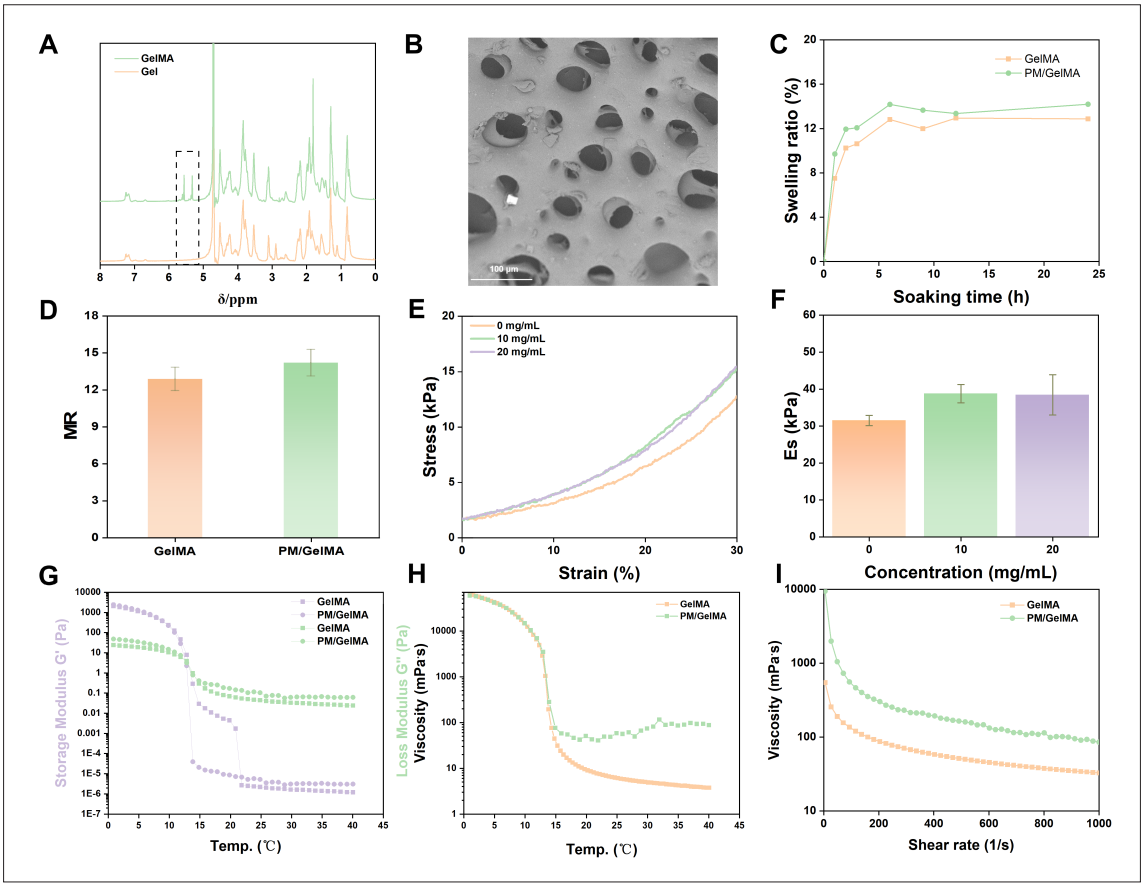

Figure 7. Physicochemical characterization of bioink. (A) ^{1}H NMR spectra of gelatin and GelMA. (B) Scanning electron microscopy image of photocrosslinked GelMA. Scale bar: 100 μm; magnification: 600×. (C) Swelling ratio. (D) MR. (E) Stress–strain curves. (F) Compressive modulus (Es). (G) Storage modulus (G') and loss modulus (G"). (H) Temperature–viscosity curves. (I) Shear rate–viscosity curves of PM/GelMA composite bioink. Abbreviations: GelMA, gelatin methacryloyl; NMR, nuclear magnetic resonance; PM, polymeric microarchitecture; MR, moisture ratio.

also endows them with good printability by optimizing rheological properties, laying the experimental foundation for the application of this composite bioink in the field of bone/cartilage tissue engineering.

PMs were co-cultured with different cell types to generate corresponding MTs, which were then subjected to functionalized culture. Subsequently, the MTs were uniformly mixed with GelMA for 3D bioprinting. To intuitively demonstrate the advantages of 3D printing, mold-cast and 3D-printed MT/GelMA constructs were prepared separately (Figure 8A). After culturing for different time periods, cell viability was assessed using the CCK-8 assay (Figure 8B). The results showed that the 3D-bioprinted scaffold group exhibited significantly enhanced cell proliferation capacity compared to the mold-cast group. This could be attributed to the fact that mold-cast solid cylindrical hydrogels typically have a dense structure (or rely solely on the material's intrinsic microporosity), whereas 3D-printed scaffolds can form regular and interconnected macroporous channel networks through parameter design (e.g., layer height, pore size, and porosity), thereby providing superior mass transfer capacity, including the transport of oxygen and nutrients as well as the removal of metabolic waste. Furthermore, the mechanical microenvironment of 3D-printed scaffolds is better suited for cell proliferation. Mold-cast solid cylindrical hydrogels generally have high and uniformly distributed overall mechanical strength, while the porous structure of 3D-printed scaffolds allows the regulation of local stiffness through design, more closely mimicking the mechanical heterogeneity of native tissues. The channel structure of the scaffold permits local elastic deformation, avoiding "mechanical compression" of cells caused by excessive overall rigidity of solid cylinders, while providing moderate mechanical stimulation. Meanwhile, the porous network of 3D-printed scaffolds facilitates cells to secrete their own ECM components (e.g., collagen and fibronectin) and undergo matrix remodeling, forming a "cell–matrix"

positive feedback loop that further supports proliferation. In contrast, the dense structure of solid cylinders limits the active-matrix remodeling capacity of cells.

To better recapitulate the osteochondral model, the scaffolds were continuously subjected to functionalized culture. After one week of culture, the scaffold maintained good structural integrity (Figure 8Ci). On day 14, ALP activity in the bone layer of the scaffold was characterized using an ALP chromogenic kit (Figure 8Cii), and on day 21, the mineralization level of the bone layer was characterized via ARS staining (Figure 8Ciii). The results indicate that the scaffold exhibited favorable osteogenic capacity.

Subsequently, EO-MTs and C-MTs were fluorescently labeled separately and then subjected to bioprinting. After culturing for different time periods, the scaffolds were observed via CLSM. The primary focus was on the interface region between the EO-MT layer and the C-MT layer. On day 7 of culture (Figure 8Di), distinct upper and lower cell layers were observed. In addition, faint red fluorescence was detected at the bottom of the green-fluorescent C-MT layer. On day 14 (Figure 8Dii), significant overlap between red and green fluorescence was observed. These results indicate that with the extension of culture time, the bone layer represented by EO-MTs and the cartilage layer represented by C-MTs exhibit gradually enhanced crosstalk, suggesting that the cartilage and bone layers may eventually achieve functional integration.

3.4. Biological performance of osteoarthritis model

In recent times, 3D bioprinting technology has garnered enormous attention to fabricate engineered living systems for better health.[56] By applying this innovative technology, a microarchitecture-based hierarchical osteochondral model was fabricated, mimicking the osteochondral microenvironment *in vivo*. The 3D model was constructed using the MT–GelMA composite bioink (Figure 8A). GelMA was selected as it provides a bionic interface for

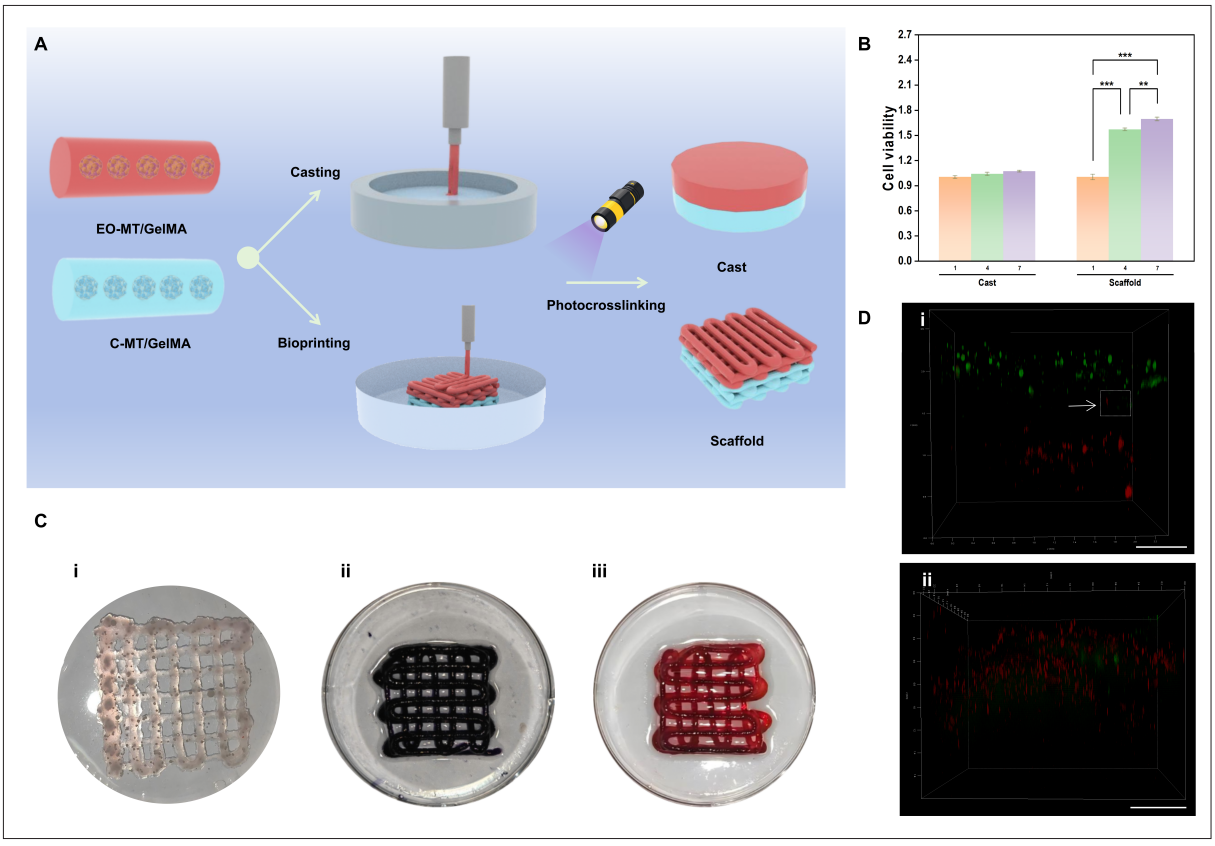

Figure 8. Bioprinting and characterization of MT/GelMA composite bioink. (A) Schematic representation of the osteochondral model constructed by 3D bioprinting and direct casting. (B) Cell viability of the casting group and scaffold group at different time points ($n = 3$). (C) Macroscopic images of the scaffold: (i) Macroscopic morphology after one week of culture; (ii) ALP staining image after 14 days of culture; and (iii) ARS staining image after 21 days of culture. (D) Confocal laser scanning microscopy images of the scaffold at different culture time points: (i) Day 7 and (ii) Day 14 (green: C-MTs, red: EO-MTs). Scale bar: 500 μm; magnification: 10×. Notes: $^{**}p < 0.01$, $^{***}p < 0.001$. Abbreviations: ALP, alkaline phosphatase; ARS: Alizarin Red S; C-MT, cartilaginous cellular microtissue; EO-MT, endothelial osteoblastic microtissue; GelMA, gelatin methacryloyl; MT, microtissue.

cartilages and bone tissues, facilitating the transportation of nutrients due to the porosity of hydrogel networks. The 3D model was completely immersed in the medium for continuous culture, and then LPS was added to induce OA. Dic, Dex, and Cur were selected for drug screening, and the production and improvement of inflammation were verified by detecting the levels of anti-inflammatory and pro-inflammatory factors (Figure 9A).

To elucidate the drug screening efficacy of the designed 3D osteochondral model, herein, LPS-induced inflammation was further applied to the pre-designed 3D chondrocyte model *in vitro*. LPS, a component of bacterial membrane, has been extensively used to establish an inflammatory model as it stimulates the release of inflammatory cytokines, including IL-8, IL-6, and IL-1β.[57] The *in vitro* chondrocyte model of LPS-induced

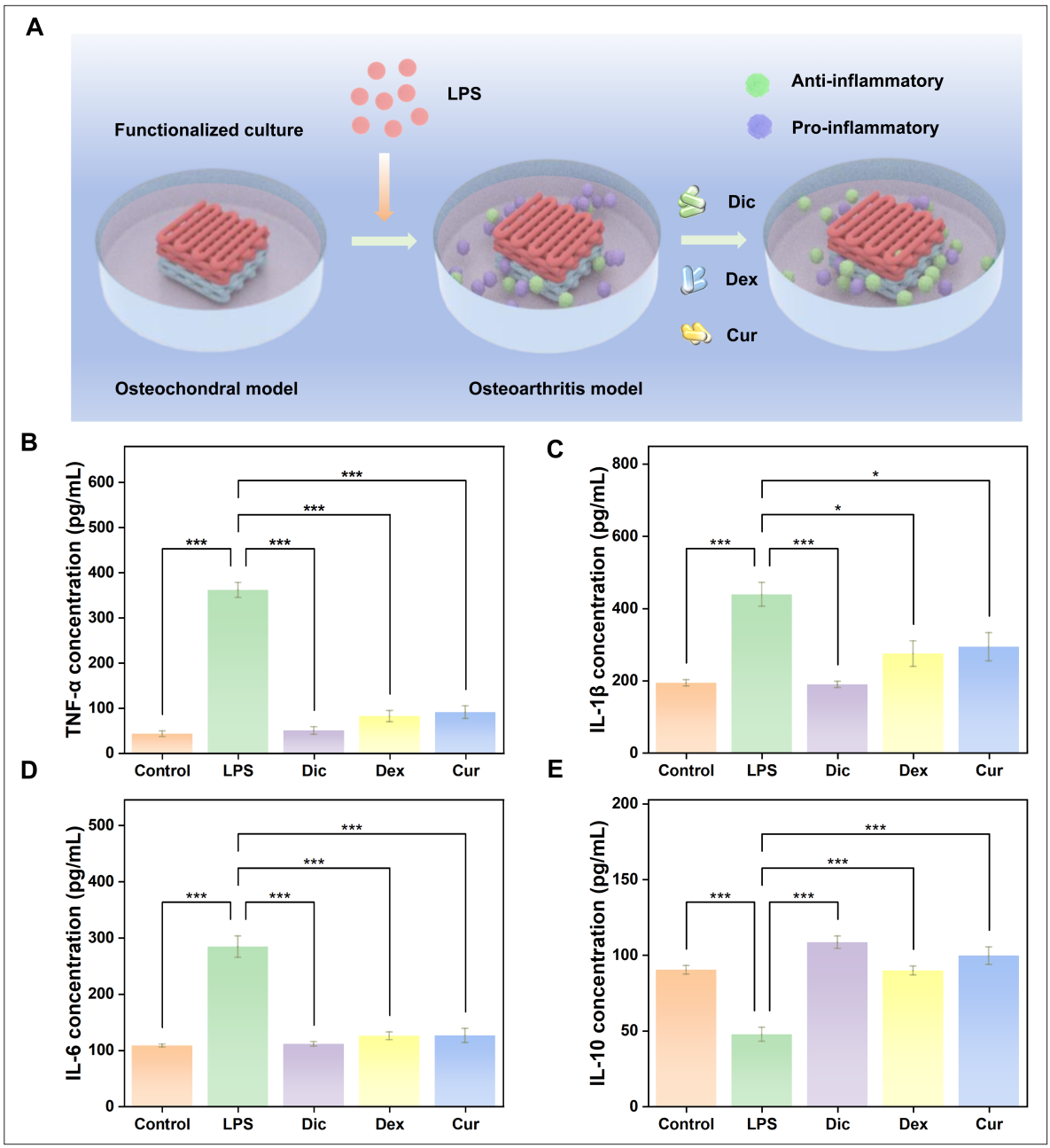

Figure 9. Bioprinting of microtissue bioinks. (A) Schematic diagram of the OA model constructed for drug screening. The effects of drug treatment on (B) TNF-α, (C) IL-1β, (D) IL-6, and (E) IL-10 concentrations ($n = 3$). Notes: $^{*}p < 0.05$, $^{***}p < 0.001$). Abbreviations: Cur, curcumin; Dex, dexamethasone; Dic, diclofenac; LPS, lipopolysaccharide; TNF-α, tumor necrosis factor-alpha; IL, interleukin; OA, osteoarthritis.

inflammation has been widely reported, showing that the LPS treatment could promote the production of IL-1β and TNF-α in chondrocytes.[58–60] No significant effect on cell viability was detected even when the concentration of LPS reached 1 μg/mL (Figure S5). The next step involved the utilization of LPS to induce the secretion of pro-inflammatory cytokines IL-1β and TNF-α in the OA model for a duration exceeding 48 h. Subsequently, ELISA was employed to measure the levels of LPS-induced IL-1β and TNF-α in the supernatant of the biomimetic osteochondral model (Figure S6). LPS treatment resulted in a 25.1% increase in IL-1β released in the OA model after exposure to 0.5 μg/mL LPS for 48 h, compared to that from the saline-treated group. Similarly, the TNF-α expression was also markedly increased by 29.9% at 48 h following LPS treatment. The secretion of inflammatory cytokines appeared to increase over time, likely due to the interaction between osteochondral cells and LPS, which stimulated further cytokine release. These inflammatory markers are implicated in cartilage inflammation and chondrocyte apoptosis during the development and progression of OA.[60]

To further investigate the performance of the OA model, Dic, Dex, and Cur were tested in the LPS-induced OA model. Dic is an NSAID, Dex is a glucocorticoid, and Cur is a natural polyphenolic compound, each exerting distinct therapeutic mechanisms in OA treatment.[43–45] The CCK-8 assay was used to evaluate the effects of different concentrations of Dic, Dex, or Cur on cell viability over 48 h. Cellular uptake experiments showed that Cur completely entered the cell interior within 4 h (Figure S7). Dic, Dex, or Cur treatment significantly reduced the expression levels of TNF-α, IL-1β, and IL-6 in the LPS-induced model, restoring them to levels close to those in the untreated control group. In parallel, IL-10 expression increased significantly compared to the LPS group, approaching levels in the untreated control group (Figure 9B–D). These findings indicate that the three drugs regulate OA inflammation through a dual mechanism: suppressing pro-inflammatory factors (e.g., TNF-α, IL-1β, and IL-6) while enhancing the anti-inflammatory factor IL-10 via the improvement of the inflammatory microenvironment and immunomodulation. Collectively, these actions restore the balance of the pro-inflammatory–anti-inflammatory cytokine network, approaching the physiological state of the untreated group and demonstrating the effective regulatory effect of the drugs on OA inflammation. Considering the biocompatibility, biodegradability, and performance efficacy of the system against LPS-induced OA, the osteochondral model developed using microfluidics and bioprinting technologies represents a promising platform for screening OA therapeutics.

4. Conclusion

This study established a biomimetic osteochondral model by integrating microfluidics-generated PMs with 3D bioprinting. The PMs provide a biocompatible, microporous framework that supports chondrocyte and endothelial/osteoblast MT formation while preserving cell phenotype and function. Incorporation of PMs into GelMA enables tunable matrix stiffness without compromising printability, facilitating the fabrication of stratified osteochondral constructs. The resulting 3D model sustains long-term cell viability, recapitulates key features of the osteochondral microenvironment, and mimics OA-like inflammation under LPS stimulation by upregulating both pro- and anti-inflammatory cytokines. Importantly, treatment with Dic, Dex, and Cur effectively attenuated the induced inflammatory response, underscoring the platform's translational potential for anti-inflammatory drug screening. Taken together, this biomimetic osteochondral system represents a versatile and physiologically relevant platform for investigating OA pathology, evaluating therapeutic candidates, and advancing osteochondral tissue engineering.

Acknowledgments

None.

Funding

This work was funded by the National Natural Science Foundation of China (grant numbers: 32271410), the Science and Technology Projects in Fujian Province (grant numbers: 2022FX1 and 2023Y4008), the Natural Science Foundation of Fujian Province (grant number: 2022J01297), the Fundamental Research Funds for the Central Universities (grant number: ZQN-1107), and the Program for Innovative Research Team in Science and Technology in Fujian Province, Scientific Research Funds of Huaqiao University (grant number: 24BS132).

Conflict of interest

The authors declare that they have no known competing financial interests or personal relationships that could have influenced the work reported in this paper.

Author contributions

Conceptualization: Yi-Cheng Wang, Xiao-Jie Song, ChaoPing Fu

Funding acquisition: Shi-Bin Wang, Ai-Zheng Chen, Chao-Ping Fu

Investigation: Yi-Cheng Wang, Xiao-Jie Song, Xiao-Chang Lu

Methodology: Yi-Cheng Wang, Xiao-Jie Song
Project administration: Shi-Bin Wang, Ai-Zheng Chen, Chao-Ping Fu
Supervision: Chao-Ping Fu
Visualization: Yi-Cheng Wang, Xiao-Jie Song
Writing–original draft: Yi-Cheng Wang, Xiao-Jie Song
Writing–review & editing: Yue-Wei Li, Zhou-Jiang Chen, Ranjith Kumar Kankala, Chao-Ping Fu

Ethics approval and consent to participate

Not applicable.

Consent for publication

Not applicable.

Availability of data

Additional data and materials not included in the manuscript or supplementary materials are available from the corresponding authors upon reasonable request.

References

1. Bhardwaj N, Singh YP, Mandal BB. Silk fibroin scaffold-based 3D co-culture model formodulation of chondrogenesis without hypertrophy via reciprocal cross-talk and paracrine signaling. *ACS Biomater Sci Eng.* 2019;5(10):5240-5254. doi: 10.1021/acsbiomaterials.9b00573
2. Wang D, Liu W, Venkatesan JK, Madry H, Cucchiarini M. Therapeutic controlled release strategies for human osteoarthritis. *Adv Healthc Mater.* 2024;14(2):e2402737. doi: 10.1002/adhm.202402737
3. Samvelyan HJ, Hughes D, Stevens C, Staines KA. Models of osteoarthritis: relevance and new insights. *Calcif Tissue Int.* 2021;109(3):243-256. doi: 10.1007/s00223-020-00670-x
4. Yessica Eduviges ZC, Martínez-Nava G, Reyes-Hinojosa D, *et al*. Impact of cadmium toxicity on cartilage loss in a 3D in vitro model. *Environ Toxicol Pharmacol*. 2020;74:103307. doi: 10.1016/j.etap.2019.103307
5. Jones G, Winzenberg T. Osteoarthritis: a new short-term treatment option? *Lancet*. 2019;394(10213):1967-1968. doi: 10.1016/s0140-6736(19)32729-1
6. Yang D, Xu J, Xu K, Xu P. Skeletal interoception in osteoarthritis. *Bone Res.* 2024;12(22). doi: 10.1038/s41413-024-00328-6
7. Cowan KJ, Kleinschmidt-Dörr K, Gigout A, *et al*. Translational strategies in drug development for knee osteoarthritis. *Drug Discov Today*. 2020;25(6): 1054-1064. doi: 10.1016/j.drudis.2020.03.015
8. Assi R, Quintiens J, Monteagudo S, Lories RJ. Innovation in targeted intra-articular therapies for osteoarthritis. *Drugs*. 2023;83(8):649-663. doi: 10.1007/s40265-023-01863-y
9. Cao H, Deng S, Chen X, *et al*. An injectable cartilage-coating composite with long-term protection, effective lubrication and chondrocyte nourishment for osteoarthritis treatment. *Acta Biomater.* 2024;179:95-105. doi: 10.1016/j.actbio.2024.03.015
10. Wu M, Zheng K, Li W, *et al*. Nature-inspired strategies for the treatment of osteoarthritis. *Adv Funct Mater.* 2023;34(4):2305603. doi: 10.1002/adfm.202305603
11. Yeung P, Cheng KH, Yan CH, Chan BP. Collagen microsphere based 3D culture system for human osteoarthritis chondrocytes (hOACs). *Sci Rep.* 2019;9(1):12453. doi: 10.1038/s41598-019-47946-3
12. Zou Z, Luo X, Chen Z, Zhang YS, Wen C. Emerging microfluidics-enabled platforms for osteoarthritis management: from benchtop to bedside. *Theranostics*. 2022;12(2):891-909. doi: 10.7150/thno.62685
13. Liu H, Wu X, Liu R, Wang W, Zhang D, Jiang Q. Cartilage-on-a-chip with magneto-mechanical transformation for osteoarthritis recruitment. *Bioact Mater.* 2024; 33:61-68. doi: 10.1016/j.bioactmat.2023.10.030
14. Chapman JH, Ghosh D, Attari S, Ude CC, Laurencin CT. Animal models of osteoarthritis: updated models and outcome measures 2016–2023. *Regen Eng Transl Med.* 2023;10(2):127-146. doi: 10.1007/s40883-023-00309-x
15. Singh YP, Moses JC, Bhardwaj N, Mandal BB. Overcoming the dependence on animal models for osteoarthritis therapeutics – the promises and prospects of in vitro models. *Adv Healthc Mater.* 2021;10(20):2100961. doi: 10.1002/adhm.202100961
16. Zhou M, Lozano N, Wychowaniec JK, *et al*. Graphene oxide: a growth factor delivery carrier to enhance chondrogenic differentiation of human mesenchymal stem cells in 3D hydrogels. *Acta Biomater.* 2019;96:271-280. doi: 10.1016/j.actbio.2019.07.027
17. Ding SL, Zhao XY, Xiong W, *et al*. Cartilage lacuna-inspired microcarriers drive hyaline neocartilage regeneration. *Adv Mater.* 2023;35(30):e2212114. doi: 10.1002/adma.202212114
18. Hwang HS, Kim HA. Chondrocyte apoptosis in the pathogenesis of osteoarthritis. *In. J Mol Sci.* 2015;16(11):26035-26054. doi: 10.3390/ijms161125943
19. Ebata T, Terkawi MA, Kitahara K, *et al*. Noncanonical pyroptosis triggered by macrophage-derived extracellular

vesicles in chondrocytes leading to cartilage catabolism in osteoarthritis. *Arthritis Rheumatol*. 2023;75(8):1358-1369. doi: 10.1002/art.42505

20. Maihemuti A, Zhang H, Lin X, *et al*. 3D-printed fish gelatin scaffolds for cartilage tissue engineering. *Bioact. Mater.* 2023;26:77-87. doi: 10.1016/j.bioactmat.2023.02.007
21. Korpayev S, Kaygusuz G, Şen M, Orhan K, Oto Ç, Karakeçili A. Chitosan/collagen based biomimetic osteochondral tissue constructs: A growth factor-free approach. *Int J Biol Macromol.* 2020;156:681-690. doi: 10.1016/j.ijbiomac.2020.04.109
22. Singh YP, Moses JC, Bandyopadhyay A, Mandal BB. 3D bioprinted silk-based in vitro osteochondral model for osteoarthritis therapeutics. *Adv Healthc Mater.* 2022;11(24):200209. doi: 10.1002/adhm.202200209
23. Salehi S, Brambilla S, Rasponi M, Lopa S, Moretti M. Development of a microfluidic vascularized osteochondral model as a drug testing platform for osteoarthritis. *Adv Healthc Mater.* 2024;13(31):e2402350. doi: 10.1002/adhm.202402350
24. Ong LJY, Sun AR, Wang Z, Lee J, Prasadam I, Toh YC. Localized oxygen control in a microfluidic osteochondral interface model recapitulates bone–cartilage crosstalk during osteoarthritis. *Adv Funct Mater.* 2024;34(28):2315608. doi: 10.1002/adfm.202315608
25. Wei Y, Deng Y, Ma S, *et al*. Local drug delivery systems as therapeutic strategies against periodontitis: a systematic review. *J Control Release*. 2021;333:269-282. doi: 10.1016/j.jconrel.2021.03.041
26. Jo YK, Lee D. Biopolymer microparticles prepared by microfluidics for biomedical applications. *Small*. 2020;16(9):1903736. doi: 10.1002/smll.201903736
27. Jin Z, Zhai Y, Zhou Y, *et al*. Regulation of mesenchymal stem cell osteogenic potential via microfluidic manipulation of microcarrier surface curvature. *Chem Eng J.* 2022;448:137739. doi: 10.1016/j.cej.2022.137739
28. He Q, Zhang J, Liao Y, *et al*. Current advances in microsphere based cell culture and tissue engineering. *Biotechnol Adv.* 2020;39:107459. doi: 10.1016/j.biotechadv.2019.107459
29. Hendow EK, Iacoviello F, Casajuana Ester M, Pellet-Many C, Day RM. Hierarchically structured biodegradable microspheres promote therapeutic angiogenesis. *Adv Healthc Mater.* 2024;13(31):e2401832. doi: 10.1002/adhm.202401832
30. Wang Y, Kankala RK, Zhang J, *et al*. Modeling endothelialized hepatic tumor microtissues for drug screening. *Adv Sci.* 2020;7(21):2002002. doi: 10.1002/advs.202002002
31. Zhang Y, Ma C, Xie J, Ågren H, Zhang H. Black phosphorus/polymers: status and challenges. *Adv Mater.* 2021;37(33):2100113. doi: 10.1002/adma.202100113
32. Bai L, Han Q, Han Z, *et al*. Stem cells expansion vector via bioadhesive porous microspheres for accelerating articular cartilage regeneration. *Adv Healthc Mater.* 2023;13(3):2302327. doi: 10.1002/adhm.202302327
33. Dhanabalan KM, Gupta VK, Agarwal R. Rapamycin–PLGA microparticles prevent senescence, sustain cartilage matrix production under stress and exhibit prolonged retention in mouse joints. *Biomater Sci.* 2020;8(15):4308-4321. doi: 10.1039/D0BM00596G
34. Wang Y, Yuan X, Yu K, *et al*. Fabrication of nanofibrous microcarriers mimicking extracellular matrix for functional microtissue formation and cartilage regeneration. *Biomaterials*. 2018;171:118-132. doi: 10.1016/j.biomaterials.2018.04.033
35. Hu Z, Lin H, Wang Z, *et al*. 3D printing hierarchical porous nanofibrous scaffold for bone regeneration. *Small*. 2024; 21(2):2405406. doi: 10.1002/smll.202405406
36. Dai W, Li S, Jia H, *et al*. Indirect 3D printing CDHA scaffolds with hierarchical porous structure to promote osteoinductivity and bone regeneration. *J Mater Sci Technol*. 2025;207:295-307. doi: 10.1016/j.jmst.2024.04.032
37. He J, Sun Y, Gao Q, *et al*. Gelatin methacryloyl hydrogel, from standardization, performance, to biomedical application. *Adv Healthc Mater.* 2023;12(23):2300395. doi: 10.1002/adhm.202300395
38. Huang Z, Kraus VB. Does lipopolysaccharide-mediated inflammation have a role in OA? *Nat Rev Rheumatol.* 2016;12(2):123-129. doi: 10.1038/nrrheum.2015.158
39. Xue C, Tian J, Cui Z, *et al*. Reactive oxygen species (ROS)-mediated M1 macrophage-dependent nanomedicine remodels inflammatory microenvironment for osteoarthritis recession. *Bioact Mater.* 2024;33:545-561. doi: 10.1016/j.bioactmat.2023.10.032
40. Yu X, Gholipourmalekabadi M, Wang X, Yuan C, Lin K. Three-dimensional bioprinting biphasic multicellular living scaffold facilitates osteochondral defect regeneration. *Interdiscip Mater.* 2024;3(5):738-756. doi: 10.1002/idm2.12181
41. Jhun J, Min H-K, Na HS, *et al*. Combinatmarion treatment with *Lactobacillus acidophilus* LA-1, vitamin B, and curcumin ameliorates the progression of osteoarthritis by inhibiting the pro-inflammatory mediators. *Immunol Lett.* 2020;228:112-121.

doi: 10.1016/j.imlet.2020.10.008

42. Luo W, Bai L, Zhang J, *et al*. Polysaccharides-based nanocarriers enhance the anti-inflammatory effect of curcumin. *Carbohydr Polym*. 2023;311:120718. doi: 10.1016/j.carbpol.2023.120718

43. Liu X, Chen B, Chen J, *et al*. A cardiac-targeted nanozyme interrupts the inflammation-free radical cycle in myocardial infarction. *Adv Mater*. 2023;36(2):2308477. doi: 10.1002/adma.202308477

44. Yao Q, Yang Y, Hu M, Qiu Y, Shi Y, Kou L. Liposomal dexamethasone for intra-articular therapy: Functional strategies and clinical progress. *J Control Release*. 2025;385:114040. doi: 10.1016/j.jconrel.2025.114040

45. da Costa BR, Pereira TV, Saadat P, *et al*. Effectiveness and safety of non-steroidal anti-inflammatory drugs and opioid treatment for knee and hip osteoarthritis: network meta-analysis. *BMJ*. 2021;375:n2321. doi: 10.1136/bmj.n2321

46. Chen Y, Chen L-F, Wang Y, *et al*. Engineered dECM-based microsystem promotes cartilage regeneration in osteoarthritis by synergistically enhancing chondrogenesis of BMSCs and anti-inflammatory effect. *Compos B*. 2025;290:111974. doi: 10.1016/j.compositesb.2024.111974

47. Wu D, Yu Y, Zhao C, *et al*. NK cell-encapsulated porous microspheres via microfluidic electrospray for tumor immunotherapy. *ACS Appl Mater Interfaces*. 2019;11(37):33716-33724. doi: 10.1021/acsami.9b12816

48. Chen X, Zhang D, Wang X, *et al*. Preparation of porous GelMA microcarriers by microfluidic technology for stem-cell culture. *Chem Eng J*. 2023;477:146444. doi: 10.1016/j.cej.2023.146444

49. Long J, Yao Z, Zhang W, *et al*. Regulation of osteoimmune microenvironment and osteogenesis by 3D-printed PLAG/black phosphorus scaffolds for bone regeneration. *Adv Sci*. 2023;10(28):2302539. doi: 10.1002/advs.202302539

50. Wei J, Xia X, Xiao S, *et al*. Sequential dual-biofactor release from the scaffold of mesoporous HA microspheres and PLGA matrix for boosting endogenous bone regeneration. *Adv Healthc Mater*. 2023;12(20):2300624. doi: 10.1002/adhm.202300624

51. Dong R, Kang M, Qu Y, Hou T, Zhao J, Cheng X. Incorporating hydrogel (with low polymeric content) into 3D-printed PLGA scaffolds for local and sustained release of BMP2 in repairing large segmental bone defects. *Adv Healthc Mater*. 2024;14(2):2403613. doi: 10.1002/adhm.202403613

52. Kamboj N, Kazantseva J, Rahmani R, Rodríguez MA, Hussainova I. Selective laser sintered bio-inspired silicon-wollastonite scaffolds for bone tissue engineering. *Mater Sci Eng C*. 2020;116:111223. doi: 10.1016/j.msec.2020.111223

53. Zhu S, Bennett S, Kuek V, *et al*. Endothelial cells produce angiocrine factors to regulate bone and cartilage via versatile mechanisms. *Theranostics*. 2020;10(13):5957-5965. doi: 10.7150/thno.45422

54. Sun T, Feng Z, He W, *et al*. Novel 3D-printing bilayer GelMA-based hydrogel containing BP, β-TCP and exosomes for cartilage–bone integrated repair. *Biofabrication*. 2023;16(1):015008. doi: 10.1088/1758-5090/ad04fe

55. Liu S, Chen G, Chen Z, Wang F, Lv Y. Research progress on stiffness controllable scaffolds based on gelatin methacryloyl hydrogels for tissue repair and reconstruction. *Int J Biol Macromol*. 2025;321(Pt 3):146485. doi: 10.1016/j.ijbiomac.2025.146485

56. Matai I, Kaur G, Seyedsalehi A, McClinton A, Laurencin CT. Progress in 3D bioprinting technology for tissue/organ regenerative engineering. *Biomaterials*. 2020;226:119536. doi: 10.1016/j.biomaterials.2019.119536

57. Tong W, Chen X, Song X, *et al*. Resveratrol inhibits LPS-induced inflammation through suppressing the signaling cascades of TLR4-NF-κB/MAPKs/IRF3. *Exp Ther Med*. 2020;19(3):1824-1834. doi: 10.3892/etm.2019.8396

58. Lei J, Fu Y, Zhuang Y, Zhang K. Sema4D aggravated LPS-Induced injury via activation of the MAPK signaling pathway in ATDC5 chondrocytes. *Biomed Res Int*. 2020;2020:8691534. doi: 10.1155/2020/8691534

59. Peng K, Li Y, Lu C, Hu S. ABIN-1 protects chondrocytes from lipopolysaccharide-induced inflammatory injury through the inactivation of NF-κB signalling. *Clin Exp Pharmacol Physiol*. 2020;47(7):1212-1220. doi: 10.1111/1440-1681.13291

60. Yan F, Li H, Zhong Z, *et al*. Co-delivery of prednisolone and curcumin in human serum albumin nanoparticles for effective treatment of rheumatoid arthritis. *Int J Nanomedicine*. 2019;14:9113-9125. doi: 10.2147/ijn.S219413

ACCSCIENCE PUBLISHING

International Journal of Bioprinting

RESEARCH ARTICLE

A 3D-bioprinted alginate-MgP scaffold for superior regeneration of calvarial bone defects in a rat model

Shaimaa ElShebiney[1], Sara A. M. El-Sayed[2], Mduduzi N. Sithole[3], Mashudu T. Mphaphuli[3], Hanan H. Beherei[2], Pradeep Kumar[3], Mostafa Mabrouk[2]*, and Yahya E. Choonara[3]*

[1]Narcotics, Ergogenics, and Poisons Department, Medical Research and Clinical Studies Institute, National Research Centre (NRC), Giza, Egypt

[2]Refractories, Ceramics and Building Materials Department, National Research Centre, Dokki, Cairo, Egypt

[3]Wits Advanced Drug Delivery Platform Research Unit, Department of Pharmacy and Pharmacology, School of Therapeutic Sciences, Faculty of Health Sciences, University of the Witwatersrand, Johannesburg, South Africa

(This article belongs to the *Special Issue*: *Multifunctional Bioprinting for Tissue/Organ Engineering*)

Abstract

While autologous transplants are the traditional standard intervention for non-healing bone defect regeneration, they carry many risks and limitations. Regenerative composite biomaterials are promising alternatives to conventional autograft and allograft implants. This study aimed to overcome these challenges by creating a novel biodegradable 3D biomaterial scaffold that mimics the structural and physiological properties of native bone. Scaffolds composed of magnesium phosphate (MgP) doped with copper oxide (CuO) in specific proportions (3, 5, or 7% [w/w]) were homogenously distributed in an alginate polymer matrix for the repair of calvarial bone defects in a rat model. The scaffolds were fabricated using a 3D bioprinting technique, and their physical properties were characterized through X-ray diffraction, Fourier transform infrared spectroscopy, and mechanical strength assessments. The bioactivity of the scaffolds was evaluated *in vitro* for biomineralization and cytotoxicity, revealing high biomineralization and cell viability. Female rats were used for the *in vivo* experiments, and the defects were examined using microscopic and histological analysis, computed tomography imaging, as well as serum markers including osteocalcin and procollagen III. The *in vivo* results demonstrated high efficacy of the scaffolds in promoting bone regeneration and enhanced healing in the calvarial defect model. The incorporation of CuO not only improved the scaffolds' mechanical properties but also exhibited angiogenic effects, fostering an environment conducive to bone healing. Our results indicated that the Alg–MgP–CuO scaffolds have great promise for bone tissue engineering applications and repair, especially with 7% (w/w) CuO doping.

***Keywords*:** 3D bioprinting; Alginate; Bone regeneration; Copper oxide doping; Magnesium phosphate.

***Corresponding authors:**
Yahya Choonara
(yahya.choonara@wits.ac.za)

Mostafa Mabrouk
(mostafamabrouk.nrc@gmail.com)

Citation: ElShebiney S, El-Sayed SAM, Sithole MN, *et al*. A 3D-bioprinted alginate-MgP scaffold for superior regeneration of calvarial bone defects in a rat model. *Int J Bioprint*. 2025;11(6):238-259. doi: 10.36922/IJB025190188

Received: May 9, 2025
1st revised: June 10, 2025
2nd revised: June 27, 2025
Accepted: July 2, 2025
Published online: July 2, 2025

Copyright: © 2025 Author(s). This is an Open Access article distributed under the terms of the Creative Commons Attribution License, permitting distribution and reproduction in any medium, provided the original work is properly cited.

Publisher's Note: AccScience Publishing remains neutral with regard to jurisdictional claims in published maps and institutional affiliations.

1. Introduction

Bone defects or fractures, including congenital defects and osteoporosis, are common disability-linked health problems that impact the well-being of the population and standard of living. Traditional interventions—such as autograft, allograft, and xenograft—have demonstrated clinical success in many cases. However, several limitations remain, such as insufficient donor sites, risk of disease transmission,[1] high cost that may be unaffordable to many patients, and potential site morbidity or rejection.[2] Consequently, considerable research efforts have been directed toward developing artificial bone matrix using various materials—such as polymers, ceramics, metals—as well as mesenchymal cells and growth factors, to restore damaged osseous tissue. More recently, degradable metals, particularly iron (Fe)-based alloys, have received great attention as load-bearing scaffold substrates. For example, chloride-mediated dissolution and intrusion products have been demonstrated to persistently accelerate the degradation of Fe-based implants, and the preferential corrosion of secondary manganese-sulfide (Mn-S) phases markedly enhances the biodegradation of Fe–Mn-S biocomposites.[3,4] As bone defect issues become increasingly prevalent due to various factors—such as aging and lifestyle choices—there is an urgent need to innovate and improve biomaterials for effective and rapid bone repair.

There has been a marked increase in interest in employing 3D printing technologies for the fabrication of biomaterial scaffolds. Conventional engineering methods often fall short of addressing the complexities involved in bone regeneration, prompting extensive research into bioinspired materials that mimic natural bone. Bone scaffolds are biodegradable materials that are used to fill bone defects and act as an artificial extracellular matrix, supporting the proliferation and differentiation of host osteogenic cells until the native bone tissue and its biomechanical properties are fully restored.[5] An efficient 3D scaffold should be able to produce a similar composite to bone tissue, which is naturally built as a mesh of collagen fibers and hydroxyapatite crystals. The designers of these advanced 3D scaffolds aim to replicate the mechanical and osteoconductive properties that are crucial for effective bone healing.[6] Despite the progress, identifying and developing suitable composite biomaterials that can provide the necessary performance for bone tissue engineering (BTE) applications remains a significant challenge. The development of novel inks for 3D bioprinting is crucial, as it holds the potential to generate constructs that not only facilitate cell growth but also improve the overall regenerative capacity for treating large bone defects.

Various materials, including bioglass, hydroxyapatite,[7] tri-calcium phosphate,[8] polycaprolactone,[9] and polylactide-co-glycolide,[10,11] have demonstrated notable osteoinductive properties. Recently, magnesium phosphate (MgP) has gained significant attention due to its high *in vivo* solubility, which allows it to transform into calcium phosphate (CaP) phases under physiological conditions.[5]

The economic, safe, natural polymer alginate (Alg) is a perfect material for hosting cell regeneration, as it can serve as an extracellular matrix. The relative stability and biocompatibility of Alg make it suitable for use as a biomaterial.[12,13] Alg can produce stable hydrogels by interacting with bivalent ions (e.g., Mg) through its cation and carboxyl functional group. This crosslinking process renders the Alg hydrophobic, allowing it to be used for the fabrication of 3D scaffolds.[14,15]

From another perspective, the presence of antimicrobial agents such as copper (Cu) is essential for preventing secondary infections. Cu, a fundamental trace element associated with several physiological processes, is particularly valuable for hard tissue replacements and displays antibacterial and angiogenic capabilities, which favor osteogenesis.[16] This study proposes the development of a novel injectable ink for 3D bioprinting technology, which involves creating 3D biomaterial scaffolds from Alg–MgP-based composites with trace CuO doping through *in situ* conjugation using polyelectrolyte complexation. The ink could produce a 3D-printed composite scaffold that promotes bone growth with exceptional efficacy, building on previously established technologies. The prepared 3D scaffold was characterized using physicochemical, mechanical, and biomineralization assessments. Given the challenges associated with repairing large or irregular bone defects,[17] this study employed the rat calvarial critical-size defect model[17] to evaluate the *in vivo* bone-regenerative capacity of the 3D-printed scaffold.

2. Materials and methods

2.1. Materials

Ammonium dihydrogen phosphate ($NH_4H_2PO_4$; molecular weight: 115.03 g/mol) and magnesium nitrate hexahydrate ($Mg(NO_3)_2{\cdot}6H_2O$; molecular weight: 256.41 g/mol) were sourced from MERCk, Germany. Copper (II) nitrate trihydrate ($Cu(NO_3)_2{\cdot}3H_2O$; molecular weight: 241.60 g/mol) was sourced from QualiKems, India. Sodium Alg (molecular weight: 500,000 g/mol) was obtained from Kibun Food Chemipha, Japan Aldrich Chemical Co., Japan. Poly(ethyleneimine) solution (PEI; 50% [w/v] in water; molecular weight: 575,000) was acquired from Sigma-Aldrich (USA).

2.2. Preparation of CuO-doped MgP

We prepared a pure MgP sample at a ratio of 1:1 as previously reported.[17] Ammonium dihydrogen phosphate and magnesium nitrate hexahydrate were both dissolved in 400 mL of distilled water. The solution was then stirred for 1 h at room temperature with a magnetic stirrer and subsequently kept in the dryer at 80°C until gelation. The resulting hard gel was calcined at 600°C for 2 h. CuO-doped MgP samples were prepared using the same procedure, with copper (II) nitrate trihydrate incorporated in place of a corresponding proportion of magnesium. Three doping copper concentrations were prepared: 3, 5, and 7% (w/w) CuO. Comprehensive validation analyses of the obtained MgP nanopowders, both before and after CuO doping, have been previously reported.[17]

2.3. Bioprinted composite scaffold preparation

Sodium Alg (200 mg/mL) was dissolved in ultra-purified deionized water to form a bioink, which was then combined with pure MgP and CuO-doped MgP (200 mg/mL). Separately, 29% (v/v) PEI solution was prepared, with ethanol serving as the solvent. Using 3D Bioplotter® (EnvisionTEC, GmbH, Germany), Alg–MgP–CuO-doped scaffolds were constructed. The process was facilitated by computer-aided design software; 3D Bioplotter® software for scaffold construction and Visual Machine software for material and machine control. The printing parameters in this study were similar to those previously established by Sithole *et al.*[18] Prior to printing the 3D scaffolds, the viscosities of Alg solutions—in the presence and absence of different fillers— were measured using a digital viscometer (DAIHAN Scientific, South Korea). The device was calibrated according to the manufacturer's instructions prior to use. Samples were measured using spindle 4 at 6 rpm and at a constant temperature of 23°C to ensure accurate and consistent viscosity readings. The viscometer spindle was immersed in the sample to the required depth, and measurements were taken once the instrument reading stabilized to record the viscosity value. The scaffolds were fabricated at 37°C utilizing Alg–MgP–CuO-doped bioink supplied from a 30 cm^3 cartridge and extruded through a plastic nozzle (diameter: 0.41 mm) under a pressure of 0.5 bar, at a deposition rate of 8 mm/s, onto a Petri dish containing a solidifying solution of PEI dissolved in ethanol. The layers were deposited perpendicularly to the underlying layer, which was kept in PEI solution overnight to harden.

2.4. Scaffold characterization

2.4.1. X-ray diffraction

The crystallinity and amorphous characteristics of the Alg–MgP–CuO-doped 3D-bioprinted composite scaffolds were assessed using an X-ray diffractometer (RIGAKU, INC., Japan). The system was equipped with Cu-kα radiation (λ = 1.54056 Å). The samples were scanned over a 2θ range of 2–70° at 2°/min under ambient conditions.

2.4.2. Fourier transform infrared spectroscopy

Fourier transform infrared (FTIR) spectra of the 3D-printed scaffolds were obtained using an FTIR spectrophotometer (Perkin-Elmer, UK). High-resolution analysis was conducted over a wavelength range of 4000–650 cm^{-1}. The evaluation focused on determining the presence or absence of functional moieties in a 1–3 mg sample.

2.4.3. Texture analyzer for compressive strength measurement

The mechanical properties of the scaffolds were investigated using a texture analyzer (TA.XTplusStable Microsystems, UK). The tests were conducted on the 3D-printed scaffolds with dimensions of 10 × 10 × 10 mm^3. After the test, the scaffolds were allowed to return to their initial dimension.

2.4.4. Brunauer–Emmett–Teller surface area analysis

To evaluate the microstructural properties of the 3D-printed scaffolds, an N_2 adsorption/desorption analysis (ASAP 2000, Micromeritics Inc., USA) was performed. Samples were degassed under vacuum for 24 h at 40°C prior to measurements. The specific surface area of the 3D-printed scaffolds was assessed using the Brunauer–Emmett–Teller (BET) method.

2.5. Bioactivity of 3D-printed composite scaffolds

The 3D-printed scaffolds were submerged in 100 mL of simulated body fluid (SBF) for 14 days. At specific time intervals (1, 3, 7, and 14 days), 5 mL of the SBF was extracted to quantify ion release using a UV spectrophotometer, and the removed volume was replaced with fresh SBF. After 14 days, the 3D scaffolds were removed from the SBF solution, washed, and dried. The surface layer formed on the 3D scaffolds was then examined using scanning electron microscopy (SEM) combined with energy-dispersive X-ray spectroscopy (EDX; TESCAN, USA). The pH levels of the SBF solutions were measured at specified intervals during the incubation period. Additionally, the swelling capacity of 3D-printed scaffolds developed using Alg-based bioink was assessed.

2.6. Cell viability

Cell viability on 3D-printed scaffolds was evaluated using the human MG-63 cell line (PromoLab (Pty) T/A Separations, South Africa). The cells were cultured in Dulbecco's Modified Eagle Medium (Thermo Fisher Scientific, South Africa), supplemented with 10% fetal bovine serum, 2 mM L-glutamine, 1% penicillin G sodium, 1% streptomycin sulfate, and 250 ng/mL amphotericin B,

with the medium replaced every 3 days. The cytotoxicity of the scaffolds was assessed using an MTT assay. Briefly, the MG-63 cells were seeded in 48-well tissue culture plates at 1×10^5 cells per well in the presence of the 3D-printed scaffolds and incubated at 37°C in a humidified atmosphere with 5% CO_2. Evaluations were conducted at 24- and 48-h post-seeding. At the end of the incubation period, MTT solution (80 µL) was added to each well, and the cells were incubated for 4 h at 37°C. The formazan crystals were solubilized, and after 1 h, the absorbance at 570 nm was measured using a Victor™ X3 plate reader (PerkinElmer, Germany).

2.7. Mode of cell death

MG-63 cells were detected using fluorescent staining and incubated with the different scaffold composites (1 mg ± 10%) added to wells in duplicates for 24 and 48 h, as previously described.[19] A dual stain of acridine orange (100 µg/mL) and ethidium bromide (100 µg/mL) dissolved in phosphate buffer saline (PBS; Merck KGaA, Germany) was used, and the cells were evaluated under a fluorescence microscope (AxioImager Z2, Zeiss, Germany).

2.8. Alkaline phosphatase activity

To evaluate the effect of MgP within the Alg 3D-printed scaffolds on cell differentiation, alkaline phosphatase (ALP) activity was measured. Saos-2 cells were cultured in a serum-free media with 0.1% bovine serum albumin at a density of 5×10^4 cells per well and maintained at 37°C for 4 and 7 days. After incubation, the plate was washed with Hanks' balanced salt solution (HBSS, Sigma-Aldrich, USA). To lyse the cells, 80 mL of Triton® X-100 (0.5% in PBS) was added to each well. A 40 µL aliquot of lysate was collected from each well to evaluate ALP, and a 10 µL sample was used to determine protein concentration utilizing the BCA protein assay. ALP was quantified using p-nitrophenol,[5] and data were presented as µg of ALP per mg of total protein.

2.9. *In vivo* bone regeneration in rats with critical-size calvarial defects

2.9.1. Animals and surgical procedure

The study involved a total of 36 adult National Research Centre, Egypt (NRC)-inbred female Wistar rats, aged 12 weeks. The animals were kept in standard polyacrylic boxes and left to acclimatize for 1 week in the experimental room under controlled environmental conditions. All rats were randomly divided into six groups, including control, Alg, Alg–MgP, Alg–MgP–CuO3%, Alg–MgP–CuO5%, and Alg–MgP–CuO7%, according to the filling scaffold. The animals used as controls did not get any bone filler (3D scaffolds). The study was conducted in line with the Declaration of Helsinki and obtained approval from the Animal Care and Use Committee of the National Research Centre (approval no. 1311102022).

Rats were anesthetized with a ketamine/xylazine cocktail at doses of 70 and 7 mg/kg. The head was shaved and disinfected with alternative swabs of 70% ethanol and betadine. To expose the periosteum, a sagittal skin incision was performed, followed by a blunt dissection of the soft tissues. A circular bone defect was created using a 5-mm trephine drill under continuous irrigation with 0.9% saline to prevent local overheating. Scaffolds were then implanted into the defect region, either with Alg, Alg–MgP, Alg–MgP–CuO3%, Alg–MgP–CuO5%, or Alg–MgP–CuO7% scaffolds, or left unfilled for the control. The incision was sutured with nylon 10/0 sutures after the operation, followed by sanitization with betadine. Analgesic and 3 mL of saline were administered subcutaneously. A prophylactic intraperitoneal injection of antibiotics was delivered for 3 days following the surgical procedure. Computed tomography (CT) scans were performed in week 8. Blood samples were collected, and sera were separated. The animals were sacrificed, and the skulls containing the lesion were surgically removed and preserved in 15% formalin (formalin saline) for subsequent analysis.

2.9.2. Macroscopic evaluation

The skulls were defleshed after sacrifice, and the repaired defects were exposed and observed. The regenerative capacity was assessed utilizing an assessment scale established by Badawi *et al.*,[20] with scores ranging from 4 (minimal healing) to 11 (optimal recovery).

2.9.3. Computed tomography scan of rat calvaria

The samples were examined with a CT scanner (MRCE, Egypt). Specialized software was utilized to generate the volume of interest from the acquired 2D projections. Bone mineral density (BMD) was quantified as a metric for bone mineralization and was expressed in mg/cm³.

2.9.4. Histological examination and analysis

The specimens were decalcified with 10% ethylenediaminetetraacetic acid solution for 2 weeks, subsequently dehydrated by serial alcohol dilutions, and fixed in paraffin. The specimens were cut into 5 µm-thick sections and stained with haematoxylin and eosin. The prepared specimens were observed under light microscopy and recorded with a digital slide scanner. The resulting images were analyzed digitally using ImageJ 1.53e (National Institutes of Health, USA).

2.9.5. Bone turnover markers

Finally, sera were analyzed with ELISA commercial kits for procollagen-III (PIIINP) and osteocalcin, which are

markers of bone turnover. The results of these analyses were compared between the different groups.

2.10. Statistical analysis

In vitro data were statistically analyzed using two-way analysis of variance (ANOVA) with multiple comparisons. No statistically significant differences were observed between the samples at different time points when $p > 0.05$. Data from *in vivo* investigations are presented as mean ± standard deviation. Statistical analysis using one-way ANOVA was conducted for cell studies, with significance indicated at $p < 0.05$. The sample size was calculated using power analysis, allocating six animals to each group. All statistical analyses were performed using GraphPad Prism Version 10.2.0 (Graphstats Technologies, USA).

3. Results

3.1. Bioprinted composite scaffold development and characterization

Based on the viscosity measurements (Table 1), all scaffold solutions appear to fall within a range (0.3–600,000 P) suitable for extrusion-based 3D printing.[21]

3.2. XRD and FTIR analyses of the 3D-printed scaffolds

The X-ray diffraction (XRD) results (Figure 1) indicate several important findings regarding the scaffolds developed from MgP and CuO-doped nanopowders in the sodium Alg matrix. Firstly, the XRD curves of the composite scaffolds closely resemble those of pure MgP, and CuO-doping had minimal effect, suggesting that the crystalline structure of the nanopowders is preserved within the 3D-printed scaffolds. The structure of the MgP and CuO-doped MgP nanopowders appears to overlap over that of the Alg polymer. This indicates that the properties imparted by the nanopowders are more significant than those provided by the polymer alone, which is a common observation in similar studies involving bioactive materials. This behavior was commonly observed when bioactive semi-crystalline nanopowders were included in the polymeric matrix of 3D scaffolds.[22]

Table 1. Viscosities of scaffold solutions before 3D printing

Sample	Viscosity (P)
Alg	20.8 ± 0.6
Alg–MgP	25.9 ± 0.8
Alg–MgP–CuO3%	26.7 ± 0.5
Alg–MgP–CuO5%	29.5 ± 0.8
Alg–MgP–CuO7%	30.0 ± 0.7

The FTIR analysis of the developed scaffolds provides important insights into the chemical composition and interactions of the components involved. The spectra revealed several key functional groups that contribute to the overall properties of the scaffolds, which are critical for their application in tissue engineering. The presence of characteristic functional groups in the MgP nanopowders, such as the O–H groups, phosphate (PO_4^{3-}), and Mg–O bonds, is indicative of the materials' bioactive nature.[23,24] Broad absorption bands around 3448 cm^{-1} indicate water molecules essential for hydration and biological interactions (Figure 2A and B),[25] while a strong 1050 cm^{-1} P–O stretching band suggests potential for cell adhesion and proliferation.[26]

The FTIR spectra of MgP–CuO-doped scaffolds exhibited similar features to CuO-free MgP, indicating that doping did not significantly alter the material's fundamental structure (Figure 2B–D). However, a reduction in O–H bond intensity suggests the formation of Cu–O bonds, potentially affecting hydration and ion release. Peaks between 623–625 cm^{-1} corresponded to phosphate ion vibrations,[27] while Mg–O stretching bands (578–587 cm^{-1}) confirmed the presence of Mg.[28]

Sodium Alg was identified by a broad 3500–3000 cm^{-1} stretch, with 1595 and 1397 cm^{-1} peaks linked to carboxylate groups. PEI was confirmed by NH_2 stretching peaks at 3345 and 3287 cm^{-1} and CH_2 vibrations at 2945 and 2844 cm^{-1}, highlighting its role in mechanical stability and biocompatibility.[29,30] The interaction between MgP and the polymer matrix likely improves scaffold performance by preventing direct nanopowder-tissue contact, which may regulate ion release and minimize cytotoxicity.[31]

The incorporation of Cu ions into the MgP framework is anticipated to enhance the biological activity of the scaffolds. Cu is known to play a vital role in angiogenesis by stabilizing hypoxia-inducible factor, thereby promoting blood vessel formation crucial for tissue regeneration. The expectation that Cu ions will be released into the extracellular environment is significant, as it could facilitate enhanced angiogenic responses.

3.3. Compressive strength of the 3D-printed scaffolds

The mechanical resilience of the 3D-printed cubic scaffolds was determined using a texture analyzer. As displayed in Figure 3, the inclusion of MgP nanopowders with and without Cu significantly enhanced the mechanical stability of the engineered scaffolds. Specifically, nanopowder-free polymeric scaffolds exhibited a lower mechanical strength (11.82 MPa), while the presence of

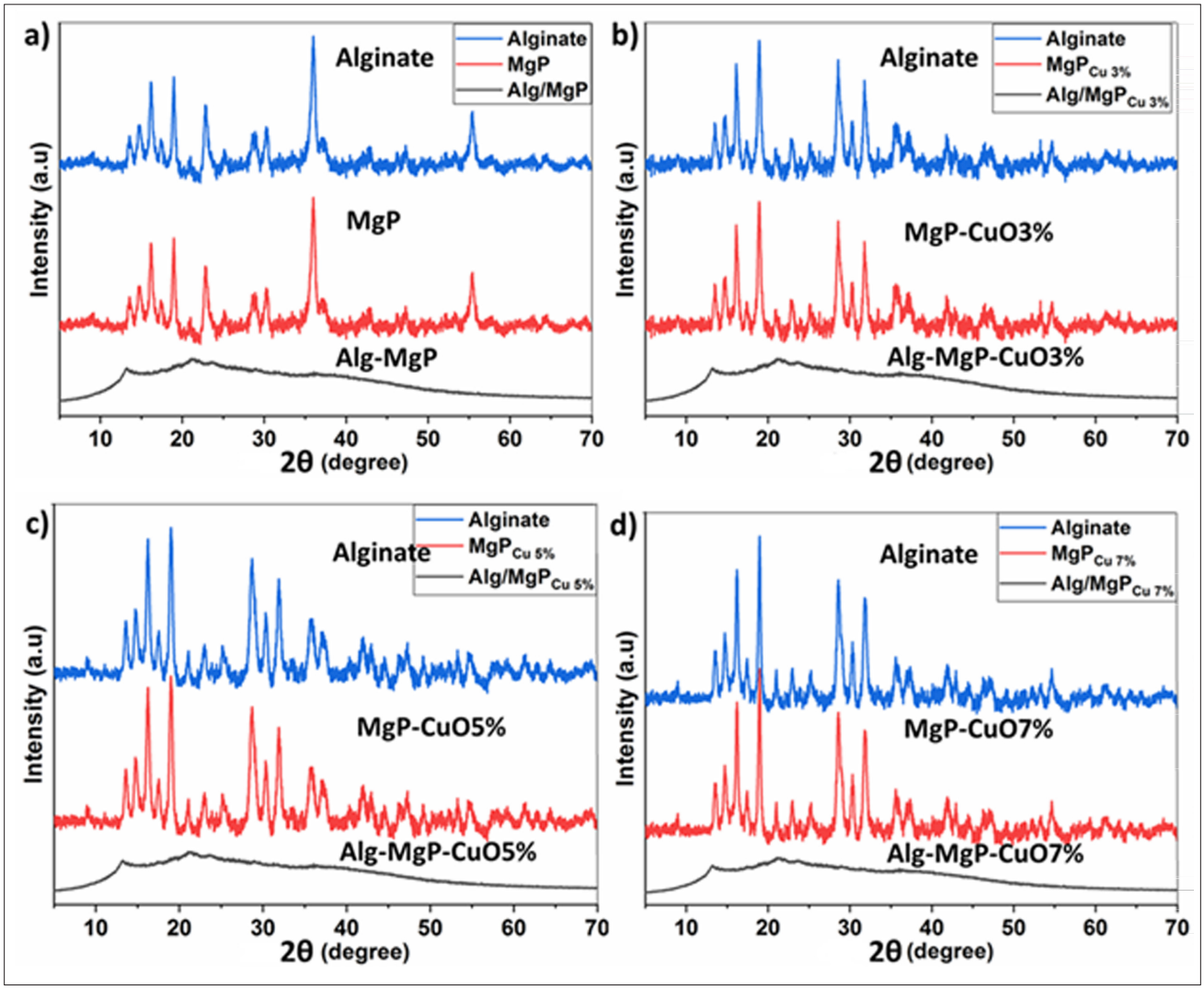

Figure 1. X-rays diffraction (XRD) curves of the 3D-printed composite (Alg–MgP–CuO-doped) scaffolds: Alg–MgP (a), Alg–MgP–CuO3% (b), Alg–MgP–CuO5% (c), and Alg–MgP–CuO7% (d).

MgP nanopowders increased the mechanical strength (30.27 MPa). Doping with Cu resulted in a notable increase in compressive strength (47.45 MPa). Previous studies have highlighted that the presence of transition metals in nanopowders contributes to the enhancement of mechanical properties.[30–33] However, the inclusion of inorganic nanopowders within the matrix of polymeric scaffolds facilitates the development of suitable implants for the repair of damaged hard tissues.[34]

3.4. Surface area of the 3D-printed scaffolds

Surface area and porosity analyses provided structural insights into the fabricated scaffolds, which can be correlated with potential biological applications. The porosity ratio—ratio between pore volume and solid volume—is critical for preserving the integrity of the scaffold after implantation and promoting nutrient diffusion and cell infiltration into the scaffold, both of which are essential for tissue regeneration.[35,36] Results demonstrated that the presence of MgP or CuO-doped nanopowders in the Alg matrix enhanced scaffold porosity, consistent with the observed increase in BET surface area across different compositions.

Figure 4 illustrates the adsorption isotherm of the fabricated scaffolds, comparing their behavior before and after the incorporation of MgP nanopowders into the Alg polymer matrix. Generally, the isotherm curves of all the scaffolds exhibited type IV and V classes. The presence of hysteresis loops (H3-type) as shown in Figure 4A and C, indicates loosely packed, plate-like particle aggregates, likely due to the MgP nanopowders.[37] This classification

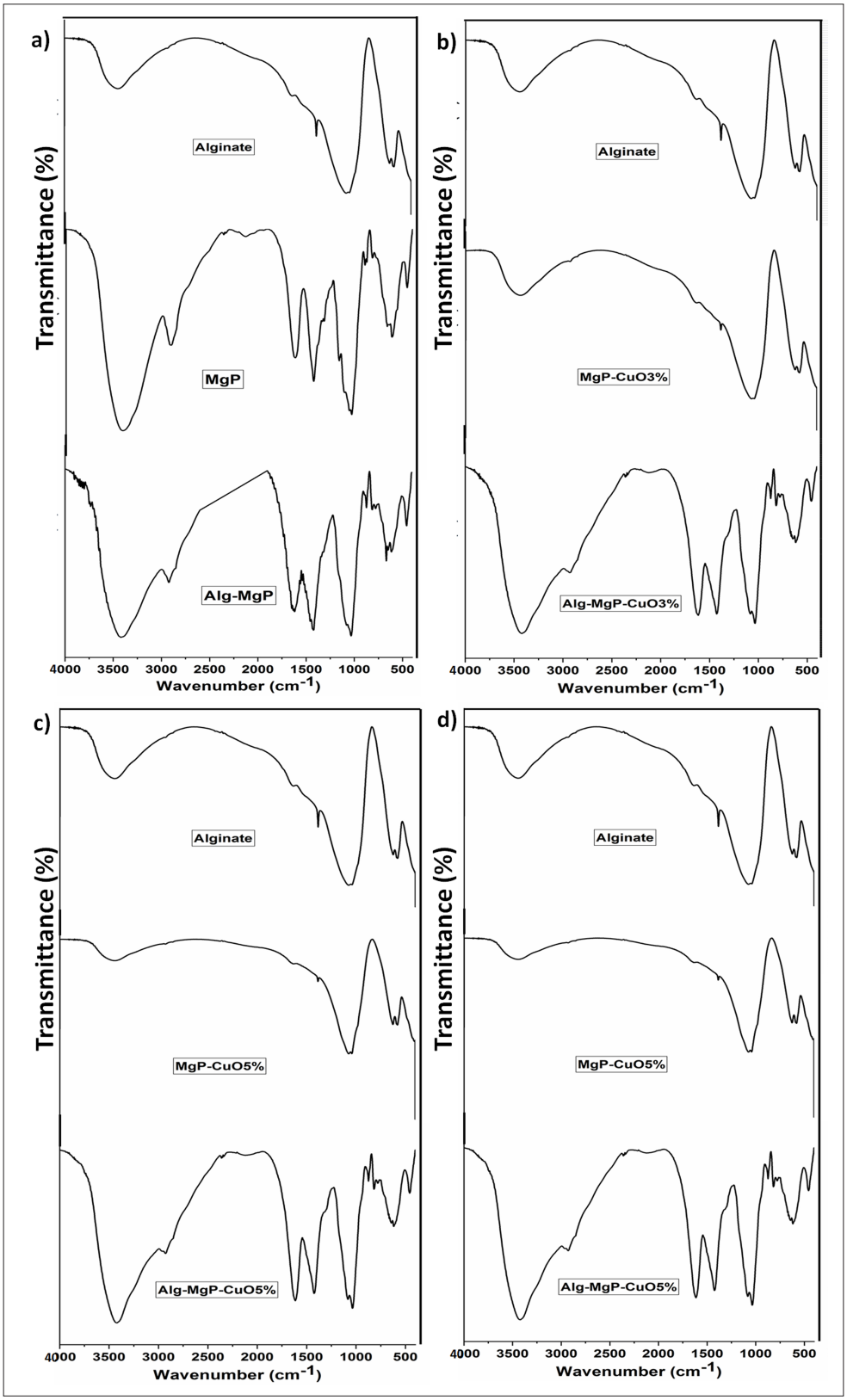

Figure 2. Fourier transform infrared spectroscopy (FTIR) spectra of the 3D-printed composite (Alg–MgP–CuO-doped) scaffolds: Alg–MgP (a), Alg–MgP–CuO3% (b), Alg–MgP–CuO5% (c), and Alg–MgP–CuO7% (d).

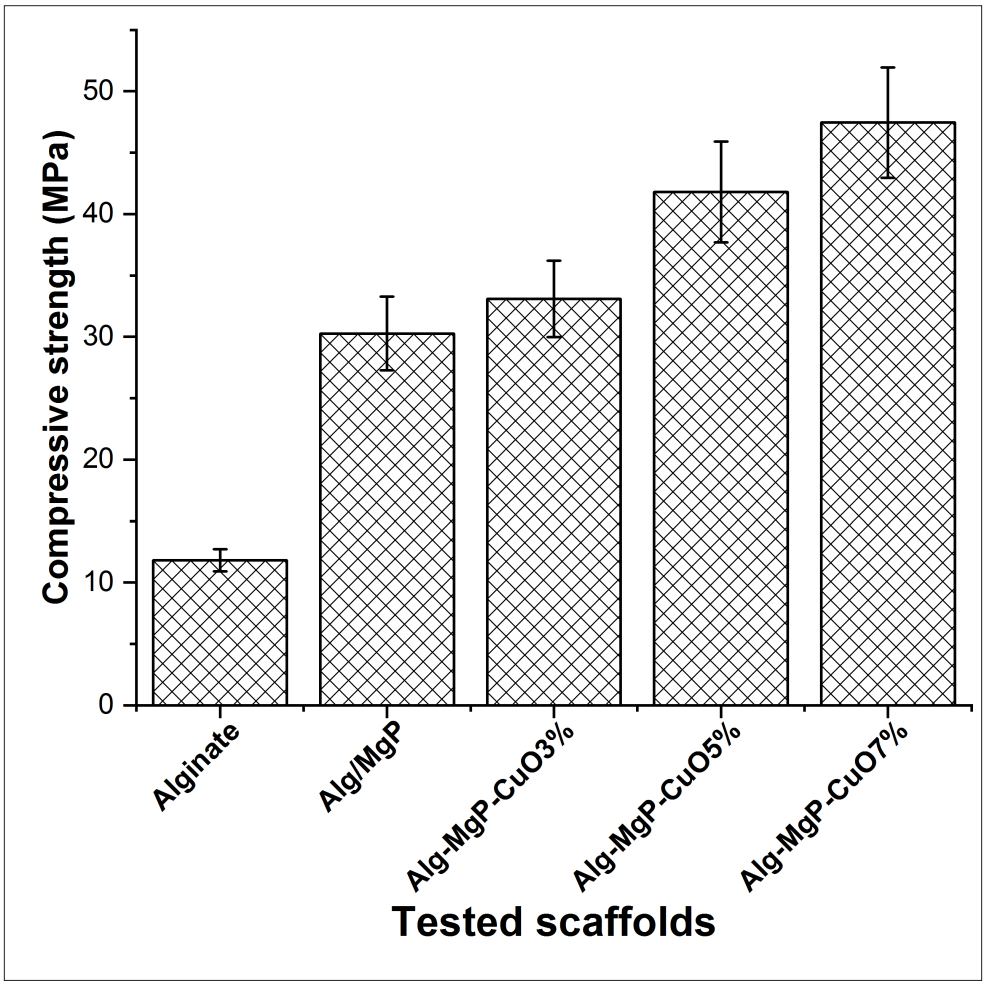

Figure 3. Compressive strength of the 3D-printed scaffolds ($n = 3$).

aligns with the expected behavior of scaffolds designed to mimic the extracellular matrix, as mesoporous structures are known to support cell adhesion and growth by providing a conducive microenvironment. The occurrence of non-closed desorption isotherms (Figure 4B and D), which is linked to the physical properties of the adsorbate rather than pore size, highlights the complexity of gas interactions within the scaffold's porous structure.[35,38]

The adsorption phase cavitations in the pores are responsible for the complexity of gas interactions within the scaffold's porous structure. Due to cavitation pressure effects, the pore size distribution is derived from the adsorption isotherm. While this peak is observed, it is important to note that it may not accurately reflect the functional pore sizes relevant for biological applications because it arises from cavitation phenomena associated with N_2 desorption at 77K. The findings demonstrate that the concentration of Cu ions in MgP-doped nanopowders increases the porous interface of the scaffolds. The measured surface area of the pure Alg, Alg–MgP–CuO3%, Alg–MgP–CuO5%, and Alg–MgP–CuO7% scaffolds were 0.379 ± 0.17, 1.635 ± 0.16, 3.369 ± 0.12, and 3.8 ± 0.13 m^2/g, respectively. This enhancement in porosity and surface area is significant, as a higher surface area can facilitate greater adsorption of biological molecules and improve the scaffolds' interaction with surrounding tissues. The increased surface area suggests that the scaffolds may provide more active sites for cellular attachment and growth, thereby enhancing their bioactivity.

3.5. Surface morphological changes of the 3D-printed scaffolds

Figure 5 displays the SEM images used to evaluate the effect of Cu on the formation of CaP layers on the surface of the 3D-printed scaffolds. The concentration of Cu was found to affect the quantity, size, and shape of the CaP layer. The EDX analysis revealed that the 5% CuO-doped

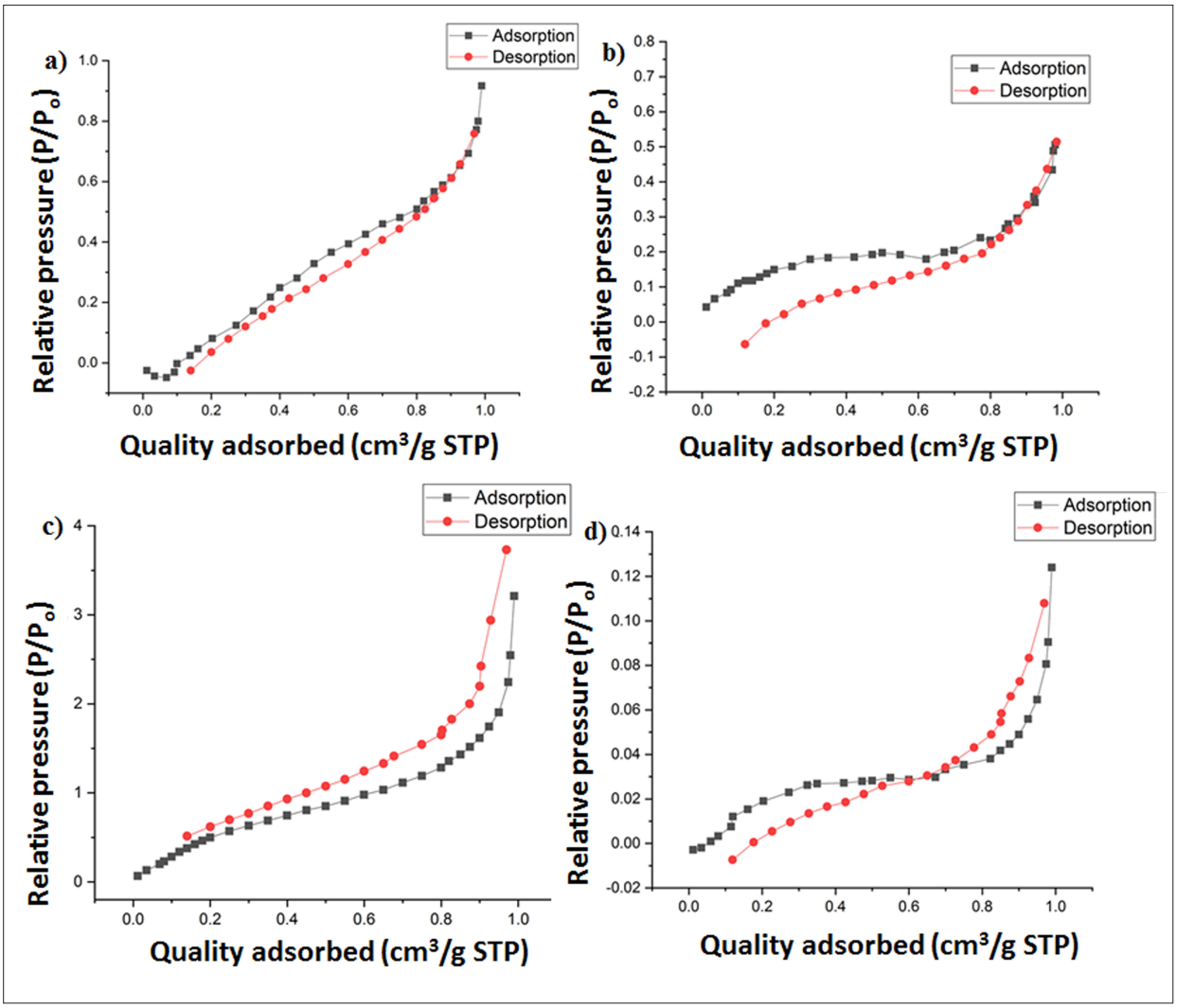

Figure 4. Isotherm curves of the fabricated scaffolds obtained by BET surface area measurements: (a) Alg–MgP, (b) Alg–MgP–CuO3%, (c) Alg–MgP–CuO5% and (d) Alg–MgP–CuO7%. Abbreviations: BET, Brunauer–Emmett–Teller; STP, standard temperature and pressure.

scaffold exhibited the highest calcium-to-phosphorus ratio, closely resembling that of hydroxyapatite. This observation is consistent with previous research that highlighted the positive impact of Cu presence on hydroxyapatite formation.[17,39–41]

3.6. Bioactivity of the 3D-printed scaffolds

Ion release from the 3D-printed scaffolds in the SBF (P, Ca, and Mg) and pH changes were measured over 14 and 28 days, respectively (Figure 6). The release of P ions decreased in the first 3 days of immersion due to swelling of the 3D scaffolds; the incorporation of MgP initiated the release of P ions, thereby restoring the original concentration. In contrast, Ca ions increased in the initial phase, especially in CuO-doped scaffold solutions; Ca ion release increased gradually until day 5, then decreased until day 14. The decrease in P and Ca ion concentrations at these time points suggests a correlation to the deposition of a mineralized layer on the scaffold surface.

On day 1, the Mg ion concentration in the SBF containing the 3D scaffolds decreased due to water absorption or the uptake of the solution by the MgP bioactive glass. From day 2, Mg ion concentration gradually increased until day 14, and this can be attributed to their release from the MgP scaffold. However, the concentration of Mg ions after 14 days was relatively low compared to its initial concentration in the SBF. Variations in pH of the SBF throughout the immersion period are parallel to the release and deposition of Ca and P ions (Figure 6D). Due to the alkaline nature of Ca ions and the acidic nature of

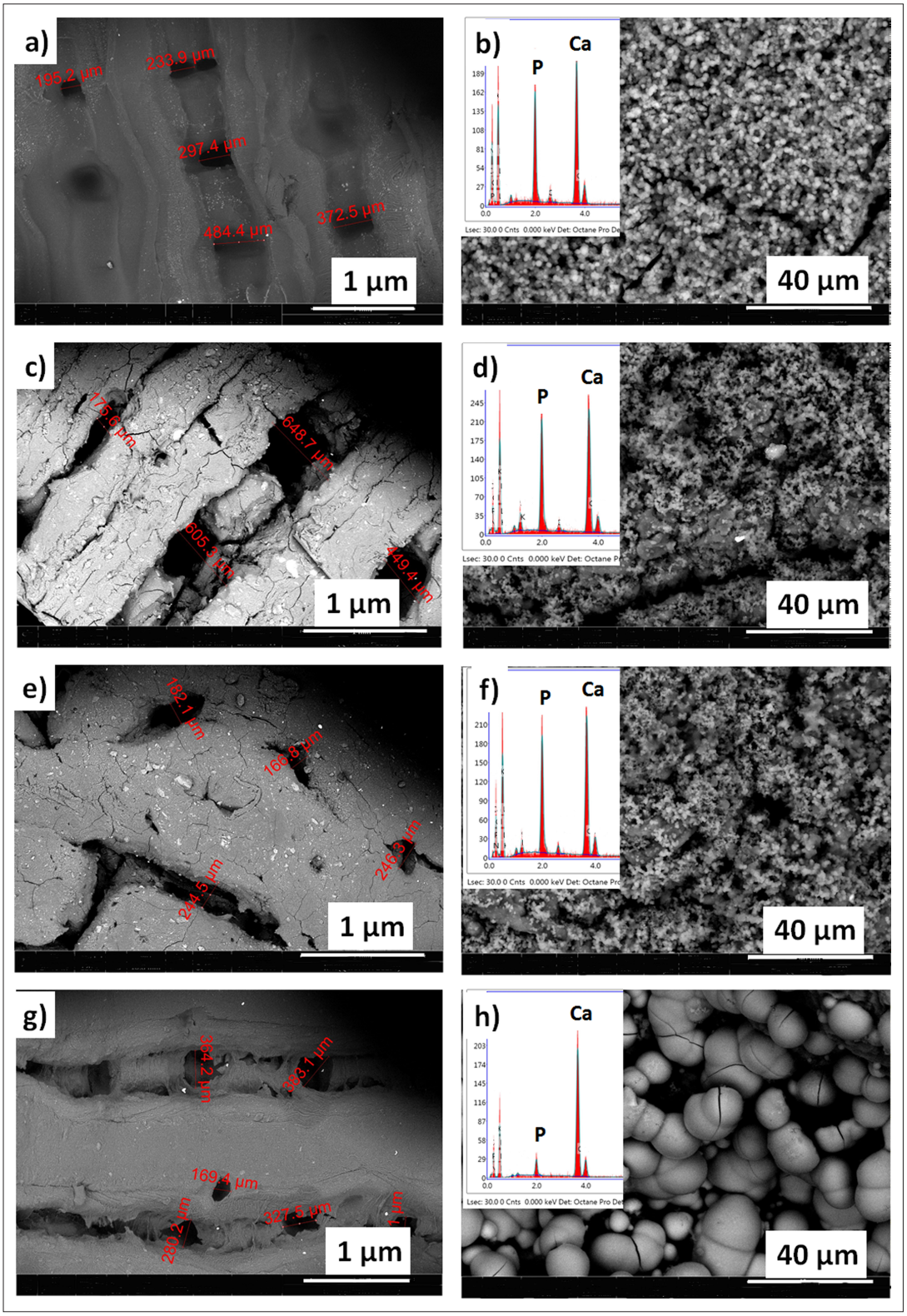

Figure 5. Scanning electron microscopy (SEM) images of the 3D-printed scaffolds. SEM images (a, c, e, and g) of the 3D-printed scaffolds before soaking in SBF: (a) alginate, (c) Alg–MgP, (e) Alg–MgP–CuO3%, and (g) Alg–MgP–CuO7%. SEM images (b, d, f, and h) and energy dispersive X-rays (EDX) analyses (inset) of the 3D-printed scaffolds after immersion in SBF: (b) alginate, (d) Alg–MgP, (f) Alg–MgP–CuO3%, and (h) Alg–MgP–CuO7%. Scale bars: 1 µm (a, c, e and g); 40 µm (b, d, f and h). Abbreviations: P, phosphorus; Ca, calcium; Lsec: Low secondary electrons; Det: Detector.

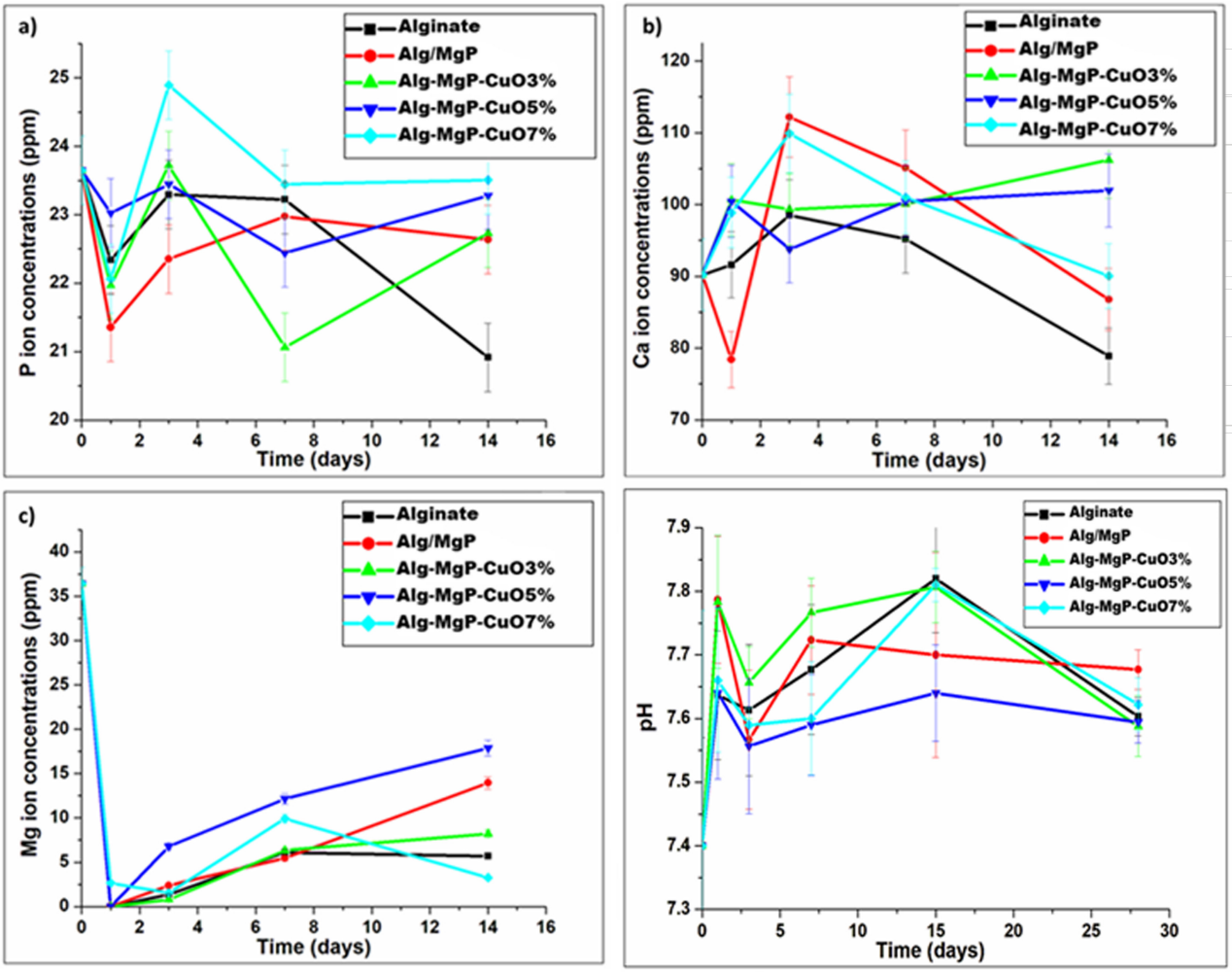

Figure 6. Ion release from the 3D-printed scaffolds and pH changes in the simulated body fluid (SBF). Concentrations of ions in the SBF over 14 days: (a) P, (b) Ca, and (c) Mg ($n = 3$). (d) Changes in pH over 28 days ($n = 3$). Abbreviations: P, phosphorus; Ca, calcium; Mg, magnesium; ppm: particle per million.

P ions, the pH value increased during the first 3 days as the concentration of Ca ions increased while that of P ions decreased. However, as the P ions increased after 5 days, the pH value subsequently decreased.

Figure 7 displays the percentage of swelling that occurred in the 3D-printed scaffolds over 28 days. The swelling percentage progressively increased for 3 days, followed by a decline. This was caused by potential interactions between the scaffolds and the SBF, such as ion release from the scaffolds into the SBF solution. The results highlighted distinct behaviors at specific time points: Alg (5% at day 1, peaking at 20% on day 15, 18% at day 28); Alg/MgP (10% on day 1, peaking at 45% on day 15, 40% at day 28); Alg–MgP–CuO3% (8–35%); Alg–MgP–CuO5% (7–30%); and Alg–MgP–CuO7% (6–28%). The high solubility of MgP led to the Alg/MgP scaffold exhibiting the greatest swelling, whereas the CuO-doped scaffolds displayed lower swelling percentages, presumably due to the increased mechanical strength and stability imparted by CuO-doping. At day 28, all scaffolds exhibited a decline in swelling, suggesting a stabilization of their structure. Nonetheless, the Alg/MgP scaffold exhibited the highest swelling percentage (i.e., 40%). These swelling behaviors can be attributed to the unique properties of the scaffold materials, particularly the high solubility of MgP and the mechanical enhancements imparted by Cu. Due to the high solubility of MgP, the Alg/MgP scaffold exhibited the highest swelling percentage.[41] However, the incorporation of Cu enhanced the mechanical strength and chemical stability of MgP, resulting in reduced swelling in the Cu-doped scaffolds.[42]

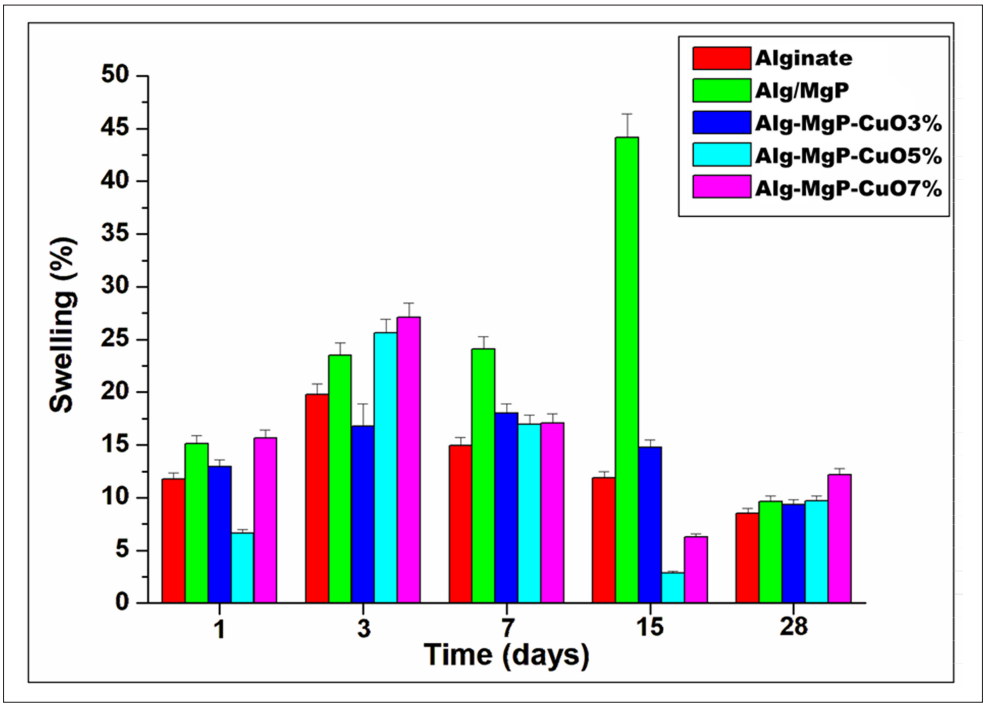

Figure 7. Swelling percentage of the 3D-printed scaffolds (n = 3).

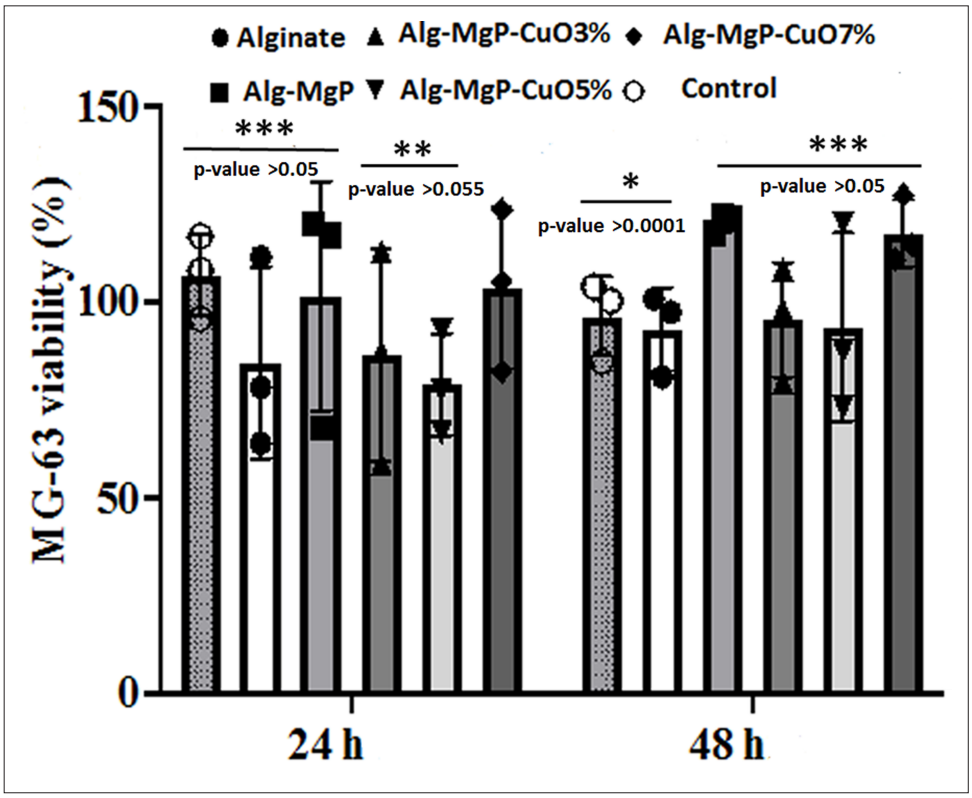

Figure 8. Cell viability of the different scaffolds (n = 3). Two-way analysis of variance (ANOVA) with multiple comparisons displayed no significant differences between samples at different time points ($p > 0.05$). * represents groups that are statistically similar to each other. ** indicates a different statistical grouping from *. *** further differentiates another set of groups that might show significant differences in cell viability compared to both * and **.

The significant increase in swelling for the Alg–MgP scaffold can be attributed to its interaction with the SBF. The high solubility of MgP facilitates the release of ions into the SBF, contributing to the initial increase in swelling by promoting osmotic pressure within the scaffold. Consequently, the Alg–MgP scaffold exhibited the highest swelling percentage among the scaffolds tested. However, after 3 days, a decline in swelling was observed, suggesting that while the initial hydration promotes swelling, the mechanical integrity of the scaffold is crucial in limiting excessive expansion.[6,13,15] The incorporation of Cu into the scaffolds mitigates this excessive swelling due to its role in enhancing mechanical strength and chemical stability, which is vital for maintaining scaffold shape and function during tissue engineering applications.[16,42] Notably, the swelling behavior of the Alg–MgP scaffold illustrates the significance of material composition in regulating hydration and stability.

3.7. Cytotoxicity of the 3D-printed scaffolds

The cell viability of MG-63 cells cultured on the 3D-printed scaffolds was evaluated (Figures 8 and 9). The scaffolds demonstrated cell viability comparable to the control (unexposed cells). However, 7% CuO-doped scaffolds displayed a relative increase in cell viability, likely due to the leaching of alkaline particles in the culture media, which has a positive effect on cell viability. These results were also confirmed by ALP activity analysis (Figure 10),

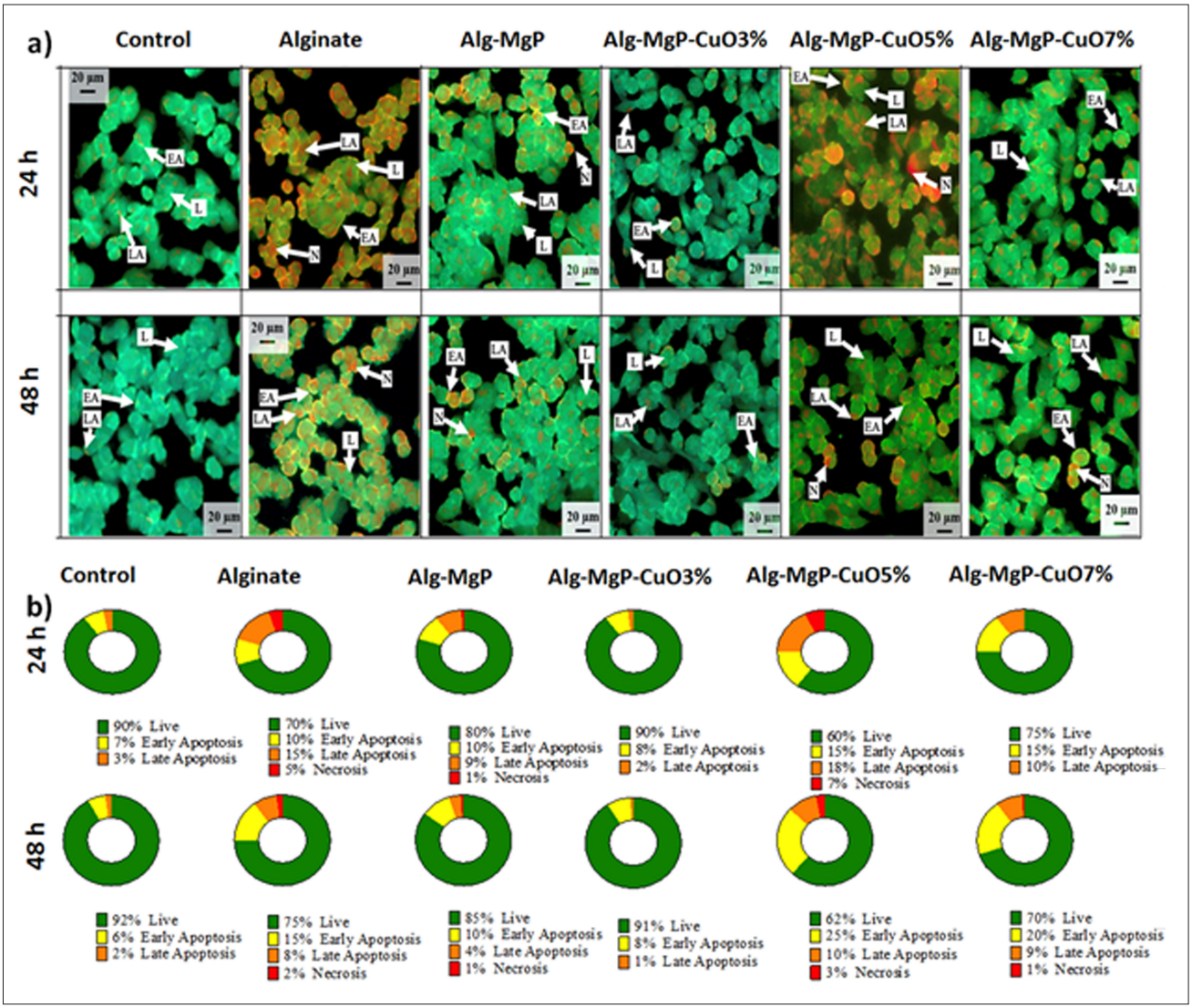

Figure 9. Cell viability of MG-63 cells cultured on the 3D-printed scaffolds. (a) Fluorescent microscopy images depicting live and apoptotic cells in the control and experimental groups at 24 and 48 h. Magnification: 20×. Scale bars: 20 µm. (b) Percentage of live, early apoptotic, and necrotic cells, illustrating the effects of different treatments on cell viability. Abbreviations: EA, early apoptosis; L, live; LA, late apoptosis; N, necrosis.

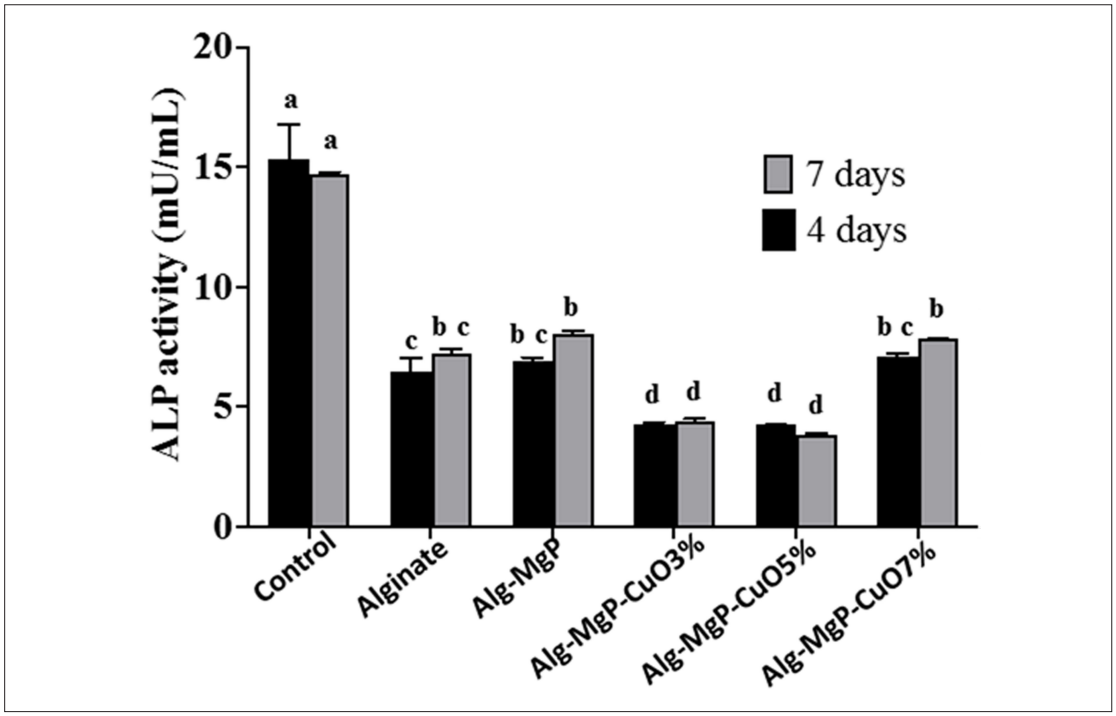

Figure 10. Alkaline phosphatase (ALP) activity in all scaffolds on days 4 and 7. Bars denoted with the same letters indicate no significant difference. Two-way analysis of variance (ANOVA) with multiple comparisons displayed no significant differences between samples at different time points ($p > 0.05$). "a" represents groups that are statistically similar to each other ($p > 0.005$). "b" indicates a different statistical grouping from "a" ($p > 0.01$). "c" further differentiates another set of groups that might have significant differences in ALP activity compared to both "a" and "b" ($p > 0.05$). "d" represents groups that are distinct from those labeled "a," "b," and "c" ($p > 0.001$).

where all scaffolds reported significantly lower ALP activity compared to the control ($p < 0.001$). For each scaffold type, no significant difference in ALP activity was observed between days 4 and 7 ($p > 0.05$). ALP activities of Alg–MgP–CuO3% and Alg–MgP–CuO5% were significantly lower compared to the other scaffolds ($p < 0.001$).

3.8. *In vivo* evaluation using a rat calvarial critical-size defect

3.8.1. Macroscopic evaluation

The calvarial defect model is commonly used to evaluate the bone regeneration potential of biomaterials.[21] This model is suitable for studying fractures in flat bones, such as those of the skull, ribs, and pelvis. The results revealed that all defect sites healed adequately, with no notable indications of infection or inflammation. The data demonstrated the distinct efficacy of CuO-doped MgP in promoting calvarial defect repair in the animal model. The median scores were: 4.5 (coefficient of variation [CV]: 17%) for the control group, 4.0 (CV: 9.8%) for Alg scaffolds, 5.5 (CV: 14%) for Alg–MgP scaffolds, 8.0 (CV: 16%) for Alg–MgP–CuO3% scaffolds, 9.5 (CV: 8.4%) for Alg–MgP–CuO5% scaffolds, and 12 (CV: 4.4%) for Alg–MgP–CuO7% scaffolds. The scores for both Alg–MgP–CuO5% and Alg–MgP–CuO7% scaffolds were significantly higher compared to the control group ($p < 0.05$).

3.8.2. CT scan of the calvarial defect

The CT scan displayed complete ossification of the defects in rats filled with Alg–MgP–CuO7%, while the control rats had an exposed defect (Figure 12). Alg and Alg–MgP scaffolds revealed narrowing of the defect by 20%, whereas Alg–MgP–CuO3% and Alg–MgP–CuO5% displayed over 50% defect filling, consistent with previous reported outcomes for bone implants.[27,43,44,45] There was no significant difference in BMD between defects filled with Alg or Alg–MgP and the control group ($p > 0.05$). Incorporation of CuO significantly increased the BMD ($p < 0.05$). Alg–MgPCu–O7% defect filling was significantly higher compared to Alg–MgP–CuO3% and Alg–MgP–CuO5% ($p < 0.05$) (Figure 12).

3.8.3. Serum procollagen-III and osteocalcin levels

Osteocalcin level was significantly higher after implantation with Alg–MgP–CuO5% and Alg–MgP–CuO7% compared to the control and Alg scaffolds ($p < 0.05$) (Figure 13A). Likewise, the serum PIIINP level significantly increased in the Alg–MgP–CuO7% scaffold group compared to the

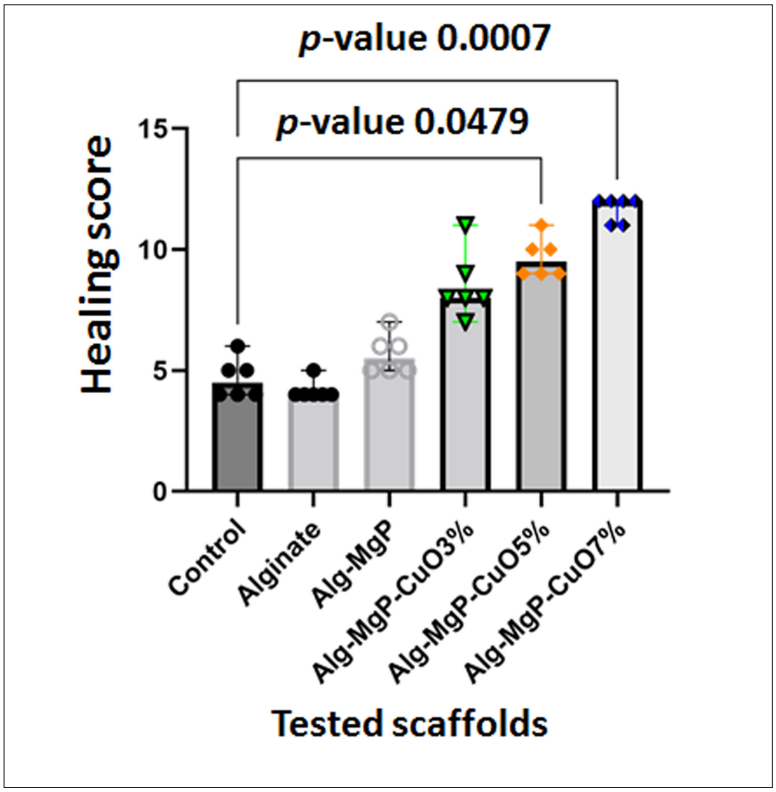

Figure 11. Healing score of the implanted 3D scaffolds (n = 3).

other scaffold and control groups (Figure 13B), consistent with the healing scores presented in Figure 11.

3.8.4. Histological assessment

Control animals with unfilled defects revealed granulation tissue, new blood vessels, and fibrous tissue, while Alg scaffold-filled defects displayed regenerated bone at the boundary of the defect with some scattered blood vessels. Alg–MgP-filled scaffold revealed fibrous tissue and scattered cartilage. CuO-doped scaffolds exhibited enhanced angiogenesis. Bone defects treated with 3% CuO revealed regeneration at the defect boundary and within the defect area, along with multiple scattered blood vessels. The 5% CuO scaffold yielded comparable results to the 3% CuO scaffold. In contrast, bone defects treated with 7% CuO scaffold demonstrated regeneration around the defect perimeter, characterized by fibrous tissue and highly vascular tissue (Figure 14).

4. Discussion

In this study, we developed a bioink for 3D printing bone grafts composed of Alg and MgP composites. This study is the first to utilize MgP-based bioink containing CuO as a dopant in BTE. The viscosity of a bioink is a critical factor in determining its printability, as it influences flow through the nozzle, layer adhesion, and the shape fidelity of the final structure. The ideal viscosity range depends on the specific 3D printing technique used, with extrusion-based printing accommodating a broader range compared to droplet-based methods.[21] Results from the XRD and FTIR analyses provide important insights into the structural integrity and chemical composition of the developed 3D scaffolds. Despite the presence of CuO, the XRD patterns indicate that the crystal structure of MgP remains unchanged.[22–30] CuO doping was confirmed to enhance the mechanical properties and biocompatibility of the 3D-printed scaffolds. The increased compressive strength reflects improved structural integrity and facilitates the transfer of the nanopowder's properties to the final scaffold structure, surpassing those of the Alg matrix alone. However, the complete incorporation of MgP and CuO-doped MgP nanopowders into the Alg matrix highlights the crucial role of polymers as support materials. FTIR analysis supports these findings by revealing key chemical groups associated with the scaffold's bioactivity. The characteristic O–H and P–O bonds suggest that the scaffold can facilitate cell adhesion and spreading,[35–38] which are essential for successful tissue engineering. The presence of CuO within

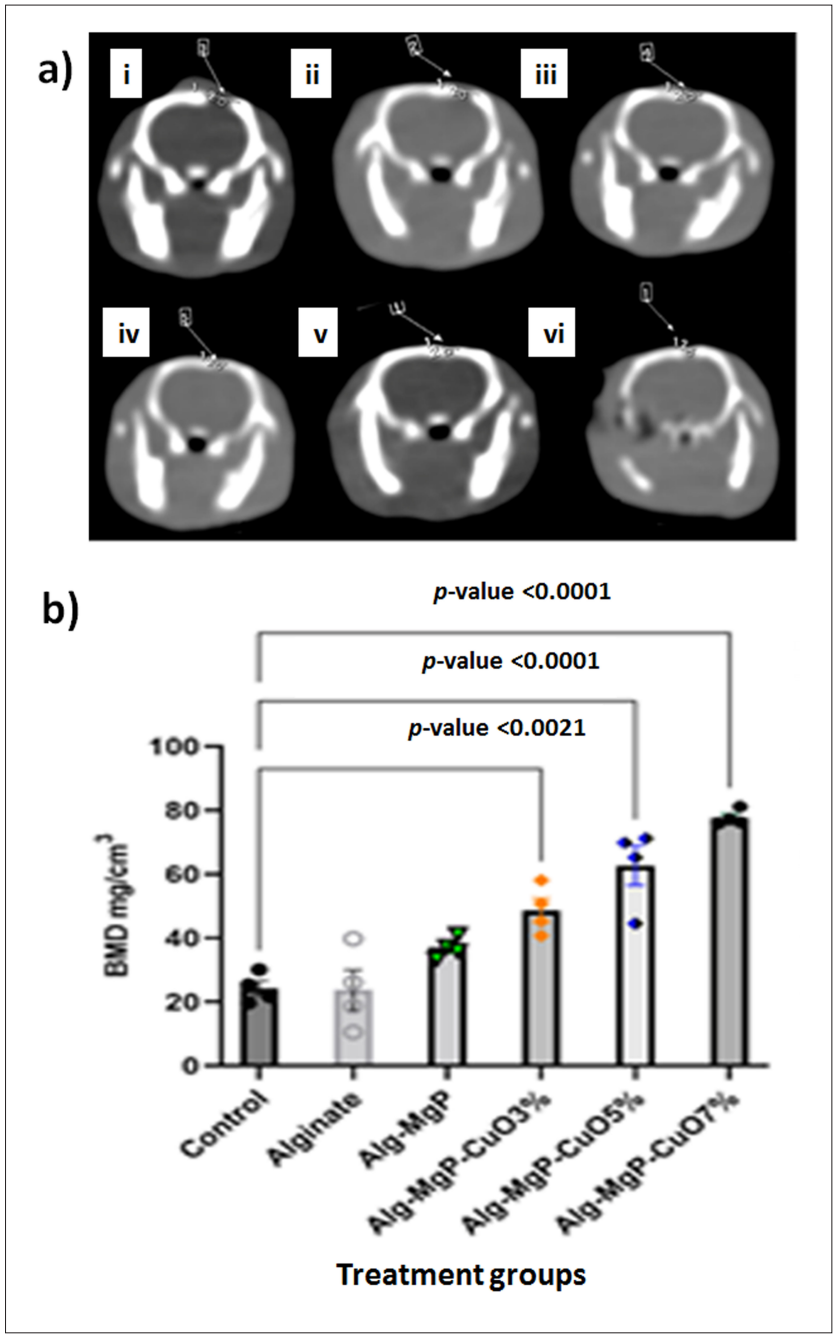

Figure 12. Effect of the implanted 3D scaffolds on ossification in rats suffering from calvarial bone defect. (a) Computed tomography (CT) images of the calvarial bone defect in different groups: (i) control, (ii) alginate, (iii) Alg–MgP, (iv) Alg–MgP–CuO3%, (v) Alg–MgP–CuO5%, and (vi) Alg–MgP–CuO7%. (b) Bone mineral density (BMD) of the implanted 3D scaffolds ($n = 3$). Data is presented as the mean ± standard deviation; data were analyzed using one-way analysis of variance (ANOVA), with statistical significance set at $p < 0.05$.

the 3D scaffold matrix decreases the vibrational intensity of the O–H groups, suggesting the formation of Cu–O bonds. These bonds may alter the hydration dynamics and ion release behavior, potentially enhancing the biological activity of the scaffolds.[38–42]

Commercial synthetic bone grafts primarily rely on CaP or other minerals. Moreover, most available commercial products, including Bioresorb, Chronos, Norian SRS, Ostim, and Vitos, are not produced in a 3D format; instead, they are either available in the form of granules or injectable

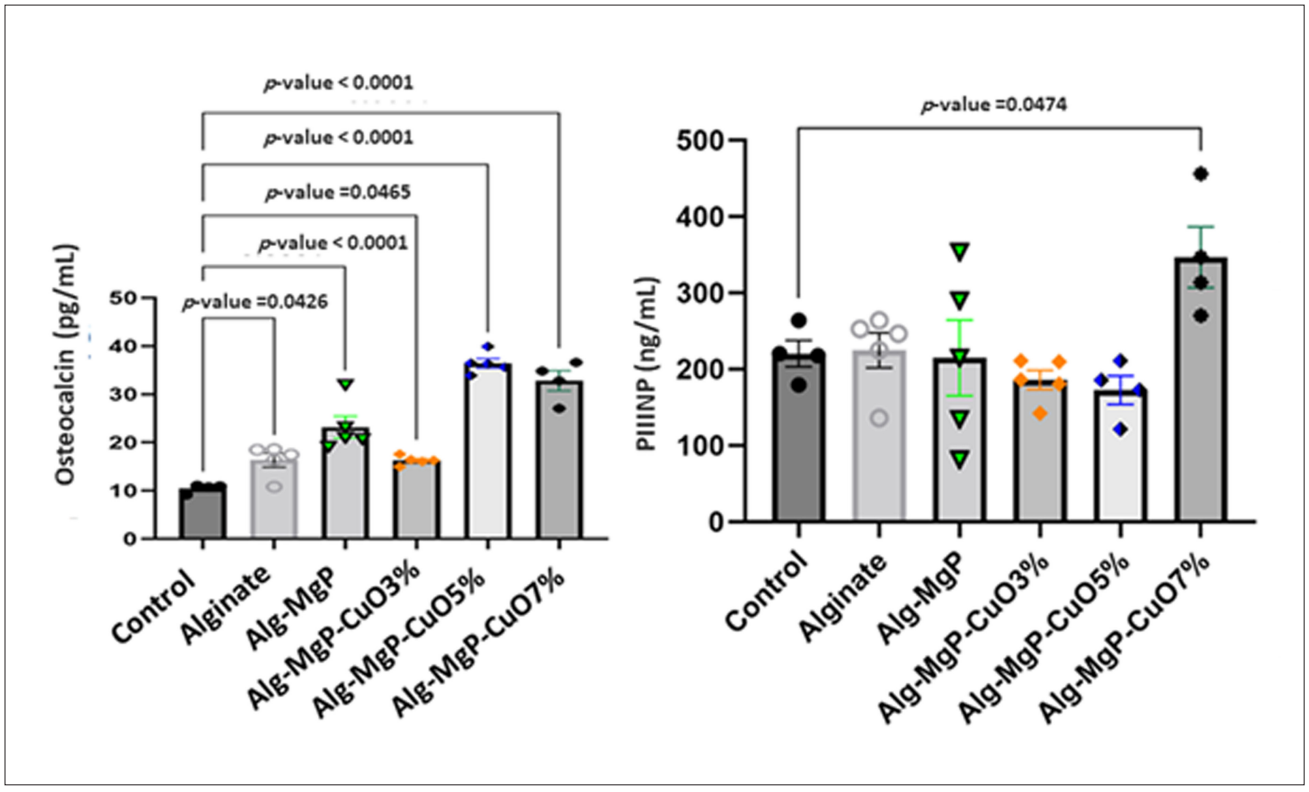

Figure 13. Serum osteocalcin (a) and procollagen III (PIIINP) (b) levels after filling the calvarial defects with the respective 3D scaffolds (n = 3).

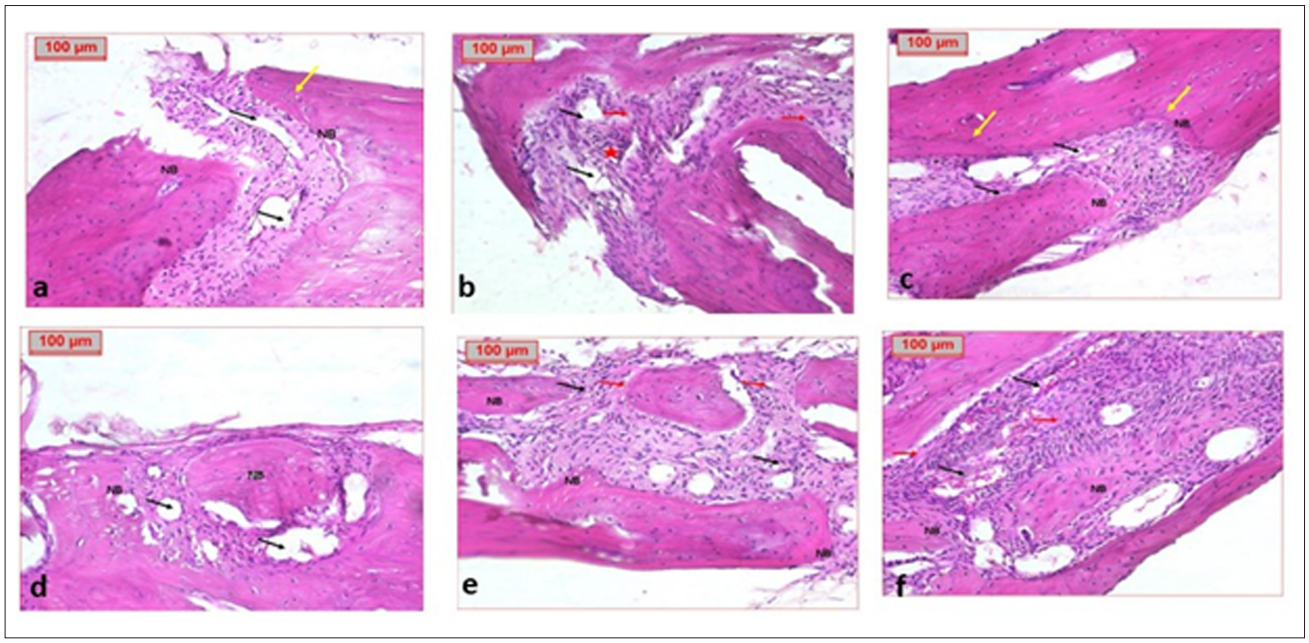

Figure 14. Hematoxylin and eosin (H&E) staining of XXX. (a) New bone formation and disconnected defect edges in control animals. (b) Granulation tissue (*), new blood vessels (black arrows), and fibrous tissue (red arrow) after Alg scaffold filling of the defect. (c) Defect treated with Alg–MgP scaffold revealed new bone formation at the defect edge (NB), a connected defect line (yellow arrows), and scattered blood vessels (black arrows). (d) Scaffold doped with 3% CuO induced regeneration at the boundary and within the defect area (NB), along with multiple scattered blood vessels (black arrows). (e) The 5% CuO scaffold displayed regeneration at the defect perimeter, fibrous tissue (red arrows), and scattered blood vessels (black arrows). (f) Scaffold doped with 7% CuO induced regeneration at the boundary of the defect (NB), and the tissue appeared highly vascular (black arrows). Magnification: 100×. Scale bars: 100 µm.

solutions. These materials possess low mechanical stability and only moderate biodegradability.[46,47] Although Ostim contains nanoscale apatite particles, its mechanical strength remains limited.[48,49,50] Bio-Oss Collagen® is a widely utilized bone graft that consists of a porous scaffold made of calcium and phosphorus. While it possesses the capacity for bone conduction, its capacity for promoting bone tissue regeneration is relatively poor.

Our 3D-printed scaffold demonstrated good mechanical strength due to the CuO dopant, consistent with previous studies incorporating inorganic metal oxides.[32,33,40] Additionally, the successful incorporation of MgP nanopowders into the Alg matrix enabled modulation of pore size and surface area, leading to enhanced porosity and surface area as indicated by adsorption isotherms. This tunability allows for customization of the scaffolds to meet optimal biological requirements.

Generally, materials that contain calcium or MgP are non-toxic, biocompatible, and bioresorbable. Magnesium offers an added advantage due to its ability to chelate various natural substances, supporting several metabolic processes.[43] This property can eliminate the need for additional surgical interventions to remove implants.[23] Additionally, Miner-Oss/Collagen® demonstrated significant regenerative capabilities in a 6-mm rabbit calvaria critical-sized defect model. Maxresorb, a synthetic bioceramic containing calcium, demonstrated enhanced osteogenic effects and the formation of well-structured and vascularized bone tissue matrix after 16 weeks.[51,52]

In this study, a complete bone tissue with vascularization and a filled defect area was observed through tomographical and histological examinations after 8 weeks of grafting. Based on our findings, our matrix demonstrates a unique capacity to support the regeneration of bone tissue with superior structural and vascular characteristics within a shorter timeframe.[53,54] Furthermore, our bioink fully degraded upon neo-tissue formation—a significant improvement over other existing products, such as Norian SRS, a CaP-based granule. Norian SRS gradually degrades from the outermost to the innermost layers, which can lead to the persistence of residual material and the potential need for surgical removal after tissue regrowth.

Inorganic metal oxides, such as CuO, have been observed to facilitate endothelial cell proliferation and differentiation. It can promote angiogenesis through hypoxia and vascularization in newly formed tissue, thus accelerating the bone regeneration process.[22] Previous studies have highlighted the vital role of Cu in the regulation of the vascular endothelial growth factor, fibronectin, and fibroblastic growth factors,[54] all of which play fundamental roles in bone healing and vascularization.[55,58] Lin *et al.*[41] demonstrated that small amounts of $Cu_3(PO_4)_2$ positively impact osteogenesis and angiogenesis in bone marrow-derived mesenchymal stem cells. This finding aligns with our histological and tomographical analyses, which indicated that the scaffold containing 7% CuO exhibited the most enhanced bone filling and highest vascular tissue density. Furthermore, Cu particles possess antimicrobial characteristics that can help to combat early-stage localized infections,[16,59] as bacterial colonization is a common complication in surgical procedures.[60]

Bone defects treated with the 3D-bioprinted scaffolds demonstrated enhanced osteogenesis and vascularized tissue, especially when using the Alg–MgP–CuO7% scaffold. The formation of blood vessels that provide adequate blood supply is crucial for improving the nutrition of bone tissue, thereby promoting the survival of tissue-engineered bone and protecting it from ischaemia.[15,49,54] Osteocalcin is an integral part of the bone formation process; it is secreted within the bone microenvironment and facilitates hydroxyapatite crystal formation, bone mineralization, and calcium ion homeostasis.[61] Serum osteocalcin levels have been correlated with increases in BMD during treatment.[62,63] Our study revealed that plasma osteocalcin concentration correlated with the percentage of CuO in the scaffolds. Osteocalcin is synthesized through the carboxylation of glutamic acid residues in an aerobic process requiring a reducing agent. It is plausible that an optimal percentage of CuO acts as a catalyst in the reaction, enhancing the reduction process and facilitating osteocalcin formation. This hypothesis aligns with the observed early release patterns in our *in vitro* assays.

The repair and regeneration of bone injuries require the interaction between multiple growth factors and cytokines that facilitate extracellular matrix production. Initially composed of type I collagen, the extracellular matrix forms in the callus. This temporary cartilaginous structure is later remodeled into calcified bone through tightly regulated intercellular and intracellular signaling pathways.[61] The early expression of collagen is indicated through the PIIINP biomarker. In the present study, increased PIIINP levels were observed after scaffold implantation, peaking in animals treated with the 7% CuO-doped scaffolds, and corresponded with osteocalcin levels.

The observed increments in osteocalcin and PIIINP levels correlated with histological findings and improvements in BMD at skull defect sites, particularly following grafting with Alg–MgP–CuO5% and Alg–MgP–CuO7% scaffolds. Furthermore, the scaffold's surface topography facilitated the diffusion of nutrients and growth factors through surface pores, as confirmed by

SEM analysis and consistent with previous reports.[64–66] Structural analysis validated the effective integration of MgP and CuO-doped MgP nanopowders within the Alg/PEI matrix, highlighting the scaffolds' potential for tissue engineering applications. The presence of bioactive functional groups and the release of Cu ions were likely responsible for the enhanced cell growth and angiogenesis after scaffold grafting. Overall, the *in vivo* performance in a critical-sized cranial defect model in rats demonstrated promising therapeutic outcomes. Future studies should focus on quantitatively assessing the release kinetics of Cu ions and evaluating their long-term biological effects to fully understand the scaffolds' therapeutic potential.

5. Conclusion

This study represents a significant advancement in BTE through the development of a novel 3D scaffold composed of MgP, CuO, and Alg to treat calvarial bone defects in a Wistar rat model. The successful fabrication of Alg–MgP–CuO scaffolds via 3D bioprinting demonstrates the potential for designing customizable and precise scaffolds. The characterization results indicate that CuO doping enhances mechanical strength, biological activity, and angiogenic properties of the scaffold. At a doping concentration of 7% (w/w), *in vitro* analyses demonstrated high cell viability, indicating excellent biocompatibility and osteoinductive properties. In vivo evaluation further validated the scaffold's therapeutic efficacy, with significant improvements in bone regeneration and healing observed in the calvarial defect model. Microscopic and histological analyses provided extensive evidence of improved healing and bone growth. The study also emphasized the synergistic effect of MgP and CuO in promoting an environment conducive to bone healing and regeneration. These findings highlight the promising application of Alg–MgP–CuO scaffolds in BTE, offering a foundation for future studies and potential clinical applications. Overall, this study reinforces the significance of innovative biomaterials in overcoming the challenges of bone defect repair, ultimately contributing to improved therapeutic outcomes.

Acknowledgments

None.

Funding

This research was funded by the project "Composite Bioinks for 3D Bioprinting and Their Application in Bone Tissue Engineering," supported by the Academy of Scientific Research and Technology (ASRT) in Egypt. The authors acknowledge the financial support of the National Research Foundation (NRF) of South Africa under the SARChI Chair program (grant no. PPNT230823145247) awarded to Prof. Yahya Choonara.

Conflict of interest

The authors declare no conflict of interest.

Author contributions

Conceptualization: Mostafa Mabrouk, Pradeep Kumar, Yahya Choonara

Formal analysis: Shaimaa El-Shebiney, Sara A. M. El-Sayed, Mduduzi N. Sithole, Mashudu T. Mphaphuli

Funding acquisition: Mostafa Mabrouk, Yahya Choonara

Investigation: Shaimaa El-Shebiney, Sara A. M. El-Sayed, Mduduzi N. Sithole, Mashudu T. Mphaphuli

Methodology: Shaimaa El-Shebiney, Sara A. M. El-Sayed, Mduduzi N. Sithole, Mashudu T. Mphaphuli

Project administration: Mostafa Mabrouk, Yahya Choonara

Supervision: Mostafa Mabrouk, Pradeep Kumar, Yahya Choonara

Writing—original draft: Shaimaa El-Shebiney, Sara A. M. El-Sayed, Mduduzi N. Sithole, Mashudu T. Mphaphuli

Writing—review & editing: Mostafa Mabrouk, Pradeep Kumar, Yahya Choonara, Hanan H. Beherei

All authors have read and agreed to the published version of the manuscript.

Ethics approval and consent to participate

The study was conducted in line with the Declaration of Helsinki and approval was obtained from the Animal Care and Use Committee of the National Research Centre (approval no. 1311102022).

Consent for publication

Not applicable.

Availability of data

Data is available from the corresponding author upon reasonable request.

References

1. Allison DC, McIntyre JA, Ferro A, Brien E, Menendez LR. Bone grafting alternatives for cavitary defects in children. *Curr Orthop Pract*. 2013;24(3):267. doi: 10.1097/BCO.0b013e3182910f94.

2. Chinnasami H, Dey MK, Devireddy R. Three-dimensional scaffolds for bone tissue engineering. *Bioengineering*. 2023;10(7):759. doi: 10.3390/bioengineering10070759.

3. Ren J, Jiang Y, Jin X, *et al*. Dissolution and intrusion of chloride disrupted biodegradation products to persistently accelerate biodegradation of Fe-based implants. *Corros Sci*. 2024;240:112461. ISSN 0010-938X. doi: 10.1016/j.corsci.2024.112461.

4. Jiang Y, Ren J, Jin X, *et al*. Accelerated biodegradation of Fe-30Mn-S biocomposite via preferential corrosion of secondary phase. *Intermetallics*. 2024;175:108539. ISSN 0966-9795. doi: 10.1016/j.intermet.2024.108539.

5. Micic M, Antonijevic D, Milutinovic-Smiljanic S, *et al*. Developing a novel resorptive hydroxyapatite-based bone substitute for over-critical size defect reconstruction: physicochemical and biological characterization and proof of concept in segmental rabbit's ulna reconstruction. *Biomed Eng Biomed Technol*. 2020;65(4):491-505. doi: 10.1515/bmt-2019-0218.

6. Liu L, Shi G, Cui Y, *et al*. Individual construction of freeform-fabricated polycaprolactone scaffolds for osteogenesis. *Biomed Eng Biomed Techol*. 2017;62(5):467-479. doi: 10.1515/bmt-2016-0005.

7. Tohamy KM, Soliman IE, Mabrouk M, *et al*. Novel polysaccharide hybrid scaffold loaded with hydroxyapatite: fabrication, bioactivity, and in vivo study. *Mater Sci Eng C*. 2018;93:1-11. doi: 10.1016/j.msec.2018.07.054

8. Ke D, Bose S. Effects of pore distribution and chemistry on physical, mechanical, and biological properties of tricalcium phosphate scaffolds by binder-jet 3D printing. *Addit Manuf*. 2018;22:111-117. doi: 10.1016/j.addma.2018.04.020.

9. Mabrouk M, Beherei HH, ElShebiney S, Tanaka M. Newly developed controlled release subcutaneous formulation for tramadol hydrochloride. *Saudi Pharm J*. 2018; 26(4):585-592. doi: 10.1016/j.jsps.2018.01.014.

10. Rakovsky A, Gotman I, Rabkin E, Gutmanas EY. β-TCP–polylactide composite scaffolds with high strength and enhanced permeability prepared by a modified salt leaching method. *J Mech Behav Biomed Mater*. 2014;32:89-98. doi: 10.1016/j.jmbbm.2013.12.022.

11. Błaszczyk B., Kaspera W., Ficek K., *et al*., Effects of polylactide copolymer implants and platelet-rich plasma on bone regeneration within a large calvarial defect in sheep. *BioMed Res Int*. 2018;2018(1):1-11. doi: 10.1155/2018/4120471.

12. Hasnain MS, Nayak AK. Alginates: *Versatile Polymers in Biomedical Applications and Therapeutics*. CRC Press; 2019.

13. Abbas HA, Mabrouk M, Soliman AA, Beherei HH. Dual-function membranes based on alginate/methyl cellulose composite for control drug release and proliferation enhancement of fibroblast cells. *Int J Biol Macromol*. 2020;164:2831-2841. doi: 10.1016/j.ijbiomac.2020.08.171

14. Tomić SL, Babić Radić MM, Vuković JS, Filipović VV, Nikodinovic-Runic J, Vukomanović M. Alginate-based hydrogels and scaffolds for biomedical applications. *Mar Drugs*. 2023;21(3):177. doi: 10.3390/md21030177.

15. Tohamy KM, Mabrouk M, Soliman IE, Beherei HH, Aboelnasr MA. Novel alginate/hydroxyethyl cellulose/hydroxyapatite composite scaffold for bone regeneration: In vitro cell viability and proliferation of human mesenchymal stem cells. *Int J Biol Macromol*. 2018;112:448-460. doi: 10.1016/j.ijbiomac.2018.01.181

16. Gutierrez E, Burdiles PA, Quero F, Palma P, Olate-Moya F, Palza H. 3D printing of antimicrobial alginate/bacterial-cellulose composite hydrogels by incorporating copper nanostructures. *ACS Biomater Sci Eng*. 2019;5(11):6290-6299. doi: 10.1021/acsbiomaterials.9b01048.

17. El-Sayed SAM, ElShebiney S, Beherei HH, Kumar P, Choonara YE, Mabrouk M. Copper-doped magnesium phosphate nanopowders for critical size calvarial bone defect intervention. *J Biomed Mater Res B Appl Biomater*. 2024;112(2):e35376. doi: 10.1002/jbm.b.35376.

18. Sithole MN, Kumar P, Du Toit LC, Erlwanger KH, Ubanako PN, Choonara YE. A 3D-printed biomaterial scaffold reinforced with inorganic fillers for bone tissue engineering: in vitro assessment and in vivo animal studies. *Int J Mol Sci*. 2023;24(8):7611. doi: 10.3390/ijms24087611

19. Mabrouk M, Mousa SM, ElGhany WAA, Abo-elfadl MT, El-Bassyouni GT. Bioactivity and cell viability of Ag+- and Zr4+-co-doped biphasic calcium phosphate. *Appl Phys A*. 2021;127(12):948. doi: 10.1007/s00339-021-05051-1.

20. Khalef L, Lydia R, Filicia K, Moussa B. Cell viability and cytotoxicity assays: biochemical elements and cellular compartments. *Cell Biochem Funct*. 2024;42(3):e4007. doi: 10.1002/cbf.4007

21. Tajik S, Garcia CN, Gillooley S, Tayebi L. 3D printing of hybrid-hydrogel materials for tissue engineering: a critical review. *Regen Eng Transl Med*. 2023;9(1):29-41. doi: 10.1007/s40883-022-00267-w. Epub 2022 Aug 1. PMID: 37193257; PMCID: PMC10181842.

22. Badawi MS, Elfayomy S, Zaki BM, Sayed AM, Abuzahra F. Assessment of healing in calvarial bone defect by allogenic demineralized bone matrix and adipose derived stem cells. *Egypt J Plast Reconstr Surg*. 2018;42(2):353-362. doi: 10.21608/ejprs.2018.80752.

23. Hohenbild F, Arango Ospina M, Schmitz SI, Moghaddam A, Boccaccini AR, Westhauser F. An in vitro evaluation of the biological and osteogenic properties of magnesium-doped bioactive glasses for application in bone tissue engineering. *Int J Mol Sci*. 2021;22(23):12703. doi: 10.3390/ijms222312703.

24. Dong J, Ding H, Wang Q, Wang L. A 3D-printed scaffold for repairing bone defects. *Polymers*. 2024;16(5):706. doi: 10.3390/polym16050706.

25. Dong Q, Zhang M, Zhou X, *et al*. 3D-printed Mg-incorporated PCL-based scaffolds: a promising approach for bone healing. *Mater Sci Eng C*. 2021;129:112372. doi: 10.1016/j.msec.2021.112372.

26. Mácová P, Viani A. Investigation of setting reaction in magnesium potassium phosphate ceramics with time resolved infrared spectroscopy. *Mater Lett*. 2017;205:62-66. doi: 10.1016/j.matlet.2017.06.063.

27. Stefov V, Šoptrajanov B, Kuzmanovski I, Lutz HD, Engelen B. Infrared and Raman spectra of magnesium ammonium phosphate hexahydrate (struvite) and its isomorphous analogues. III. Spectra of protiated and partially deuterated magnesium ammonium phosphate hexahydrate. *J Mol Struct*. 2005;752(1-3):60-67. doi: 10.1016/j.molstruc.2005.05.040.

28. Aramendía MA, Borau V, Jiménez C, Marinas JM, Romero FJ. Synthesis and characterization of magnesium phosphates and their catalytic properties in the conversion of 2-hexanol. *J Colloid Interface Sci*. 1999;217(2):288-298. doi: 10.1006/jcis.1999.6380.

29. Kanellopoulos A, Qureshi TS, Al-Tabbaa A. Glass encapsulated minerals for self-healing in cement based composites. *Constr Build Mater*. 2015;98:780-791. doi: 10.1016/j.conbuildmat.2015.08.127.

30. Zhao M, Du J, Lei H, *et al*. Enhanced electrocatalytic activity of FeNi alloy quantum dot-decorated cobalt carbonate hydroxide nanosword arrays for effective overall water splitting. *Nanoscale*. 2022;14(8):3191-3199. doi: 10.1039/D1NR08035K.

31. Fais G, Sidorowicz A, Perra G, *et al*., Cytotoxic effects of ZnO and Ag nanoparticles synthesized in microalgae extracts on PC12 cells. *Mar Drugs*. 2024;22(12):549. doi: 10.3390/md22120549.

32. Shen J-N, Yu C-C, Zeng G-N, Van der Bruggen B. Preparation of a facilitated transport membrane composed of carboxymethyl chitosan and polyethylenimine for CO2/N2 separation. *Int J Mol Sci*. 2013;14(2):3621-3638. doi: 10.3390/ijms14023621.

33. Pascual-González C, de la Vega J, Thompson C, *et al*. Processing and mechanical properties of novel biodegradable poly-lactic acid/Zn 3D printed scaffolds for application in tissue regeneration. *J Mech Behav Biomed Mater*. 2022;132:105290. doi: 10.1016/j.jmbbm.2022.105290.

34. Radhakrishnan S, Nagarajan S, Belaid H, *et al*. Fabrication of 3D printed antimicrobial polycaprolactone scaffolds for tissue engineering applications. *Mater Sci Eng C*. 2021;118:111525. doi: 10.1016/j.msec.2020.111525.

35. Liao M, Zhu S, Guo A, *et al*. 3D printed bioactive glasses porous scaffolds with high strength for the repair of long-bone segmental defects. *Compos B Eng*. 2023;254:110582. doi: 10.1016/j.compositesb.2023.110582.

36. Lei B, Gao X, Zhang R, Yi X, Zhou Q. In situ magnesium phosphate/polycaprolactone 3D-printed scaffold induce bone regeneration in rabbit maxillofacial bone defect model. *Mater Des*. 2022;215:110477. doi: 10.1016/j.matdes.2022.110477.

37. Sing KSW. Reporting physisorption data for gas/solid systems with special reference to the determination of surface area and porosity (Recommendations 1984). *Pure Appl Chem*. 1985;57(4):603-619. doi: 10.1351/pac198557040603.

38. Lowell S, Shields JE, Thomas MA, Thommes M. *Characterization of Porous Solids and Powders: Surface Area, Pore Size and Density*. Springer Science & Business Media; 2012.

39. Zhao XS, Lu GQ (Max), Millar GJ. Advances in mesoporous molecular sieve MCM-41. *Ind Eng Chem Res*. 1996;35(7):2075-2090. doi: 10.1021/ie950702a.

40. Broekhoff JCP. Mesopore determination from nitrogen sorption isotherms: fundamentals, scope, limitations. In: *Studies in Surface Science and Catalysis*. Elsevier; 1979;3:663-684. https://www.sciencedirect.com/science/article/pii/S0167299109602433. Accessed December 25, 2024.

41. Lin Z, Cao Y, Zou J, *et al*. Improved osteogenesis and angiogenesis of a novel copper ions doped calcium phosphate cement. *Mater Sci Eng C*. 2020;114:111032. doi: 10.1016/j.msec.2020.111032.

42. Yu W, Sun T-W, Ding Z, *et al*. Copper-doped mesoporous hydroxyapatite microspheres synthesized by a microwave-hydrothermal method using creatine phosphate as an organic phosphorus source: application in drug delivery and enhanced bone regeneration. *J Mater Chem B*. 2017;5(5):1039-1052. doi: 10.1039/C6TB02747D.

43. Noori A, Hoseinpour M, Kolivand S, *et al*. Exploring the various effects of Cu doping in hydroxyapatite nanoparticle. *Sci Rep*. 2024;14(1):3421. doi: 10.1038/s41598-024-53704-x.

44. Chen C-Y, Shie M-Y, Lee AK-X, Chou Y-T, Chiang C, Lin C-P. 3D-printed ginsenoside Rb1-loaded mesoporous calcium silicate/calcium sulfate scaffolds for inflammation inhibition and bone regeneration. *Biomedicines*. 2021;9(8):907. doi: 10.3390/biomedicines9080907

45. Jakus AE, Rutz AL, Jordan SW, *et al*. Hyperelastic "bone": a highly versatile, growth factor–free, osteoregenerative, scalable, and surgically friendly biomaterial. *Sci Transl Med*. 2016;8(358):358ra127-358ra127.

doi: 10.1126/scitranslmed.aaf7704.

46. Reginster J-Y, Seeman E, De Vernejoul MC, *et al*. Strontium ranelate reduces the risk of nonvertebral fractures in postmenopausal women with osteoporosis: treatment of peripheral osteoporosis (TROPOS) study. *J Clin Endocrinol Metab*. 2005;90(5):2816-2822.
doi: 10.1210/jc.2004-1774

47. Kazakova G, Safronova T, Golubchikov D, Shevtsova O, Rau JV. Resorbable Mg2+-containing phosphates for bone tissue repair. *Materials*. 2021;14(17):4857.
doi: 10.3390/ma14174857.

48. Patel H, Bonde M, Srinivasan G. Biodegradable polymer scaffold for tissue engineering. *Trends Biomater Artif Organs*. 2011;25(1):20-29.

49. Wu Z, Meng Z, Wu Q, *et al*. Biomimetic and osteogenic 3D silk fibroin composite scaffolds with nano MgO and mineralized hydroxyapatite for bone regeneration. *J Tissue Eng*. 2020;11:2041731420967791.
doi: 10.1177/2041731420967791.

50. Huber F-X, Belyaev O, Hillmeier J, *et al*. First histological observations on the incorporation of a novel nanocrystalline hydroxyapatite paste OSTIM® in human cancellous bone. *BMC Musculoskelet Disord*. 2006;7(1):50.
doi: 10.1186/1471-2474-7-50.

51. Garcia C, Orozco Y, Betancur A, *et al*. Fabrication of polycaprolactone/calcium phosphates hybrid scaffolds impregnated with plant extracts using 3D printing for potential bone regeneration. *Heliyon*. 2023;9(2):e13176.
doi: 10.1016/j.heliyon.2023.e13176.

52. Cheon E, Kim S-H, Lee D-K, *et al*. Osteostimulating ability of β-tricalcium phosphate/collagen composite as a practical bone-grafting substitute: in vitro and in vivo comparison study with commercial one. *Biotechnol Bioprocess Eng*. 2021;26(6):923-932.
doi: 10.1007/s12257-021-0059-4.

53. Kamal M, Andersson L, Tolba R, *et al*. Bone regeneration using composite non-demineralized xenogenic dentin with beta-tricalcium phosphate in experimental alveolar cleft repair in a rabbit model. *J Transl Med*. 2017;15(1):263.
doi: 10.1186/s12967-017-1369-3.

54. Potres Z, Deshpande S, Klöeppel H, Voss K, Klineberg I. Assisted wound healing and vertical bone regeneration with simultaneous implant placement: a histologic pilot study. *Int J Oral Maxillofac Implants* 2016;31(1):45-54.
doi: 10.11607/jomi.3951.

55. Luo R, Huang Y, Yuan X, *et al*. Controlled co-delivery system of magnesium and lanthanum ions for vascularized bone regeneration. *Biomed Mater*. 2021;16(6):065024.
doi: 10.1088/1748-605X/ac2886.

56. Wang Z, Zheng B, Yu X, *et al*. Promoting neurovascularized bone regeneration with a novel 3D printed inorganic-organic magnesium silicate/PLA composite scaffold. *Int J Biol Macromol*. 2024;277:134185.
doi: 10.1016/j.ijbiomac.2024.134185.

57. Stein GS, Lian JB. Molecular mechanisms mediating proliferation/differentiation interrelationships during progressive development of the osteoblast phenotype. *Endocr Rev*. 1993;14(4):424-442.
doi: 10.1210/edrv-14-4-424

58. Sousa CP, Dias IR, Lopez-Peña M, *et al*. Bone turnover markers for early detection of fracture healing disturbances: a review of the scientific literature. *An Acad Bras Ciênc*. 2015;87:1049-1061.
doi: 10.1590/0001-3765201520150008

59. Barralet J, Gbureck U, Habibovic P, Vorndran E, Gerard C, Doillon CJ. Angiogenesis in calcium phosphate scaffolds by inorganic copper ion release. *Tissue Eng Part A*. 2009;15(7):1601-1609.
doi: 10.1089/ten.tea.2007.0370.

60. Liu Y, Xu Z, Qiao M, Cai H, Zhu Z. Metal-based nano-delivery platform for treating bone disease and regeneration. *Front Chem*. 2022;10:955993.
doi: 10.3389/fchem.2022.955993.

61. Mostofi M, Mostofi F, Hosseini S, *et al*. Efficient three-dimensional (3D) human bone differentiation on quercetin-functionalized isotropic nano-architecture chitinous patterns of cockroach wings. *Int J Biol Macromol.* 2024;258(2):129155.
doi: 10.1016/j.ijbiomac.2023.129155

62. Hajduga MB, Bobiński R, Dutka M, *et al*. Analysis of the antibacterial properties of polycaprolactone modified with graphene, bioglass and zinc-doped bioglass. *Acta Bioeng Biomech*. 2021;23(10.37190):131-138.
doi: 10.37190/abb-01766-2020-03.

63. Zoch ML, Clemens TL, Riddle RC. New insights into the biology of osteocalcin. *Bone*. 2016;82:42-49.
doi: 10.1016/j.bone.2015.05.046.

64. Alarcin E, Akguner ZP, Ozturk AB, *et al*. Biomimetic 3D bioprinted bilayer GelMA scaffolds for the delivery of BMP-2 and VEGF exogenous growth factors to promote vascularized bone regeneration in a calvarial defect model in vivo. *Int J Biol Macromol*. 2025; 306(2):141440.
doi: 10.1016/j.ijbiomac.2025.141440

65. Dirckx N, Moorer MC, Clemens TL, Riddle RC. The role of osteoblasts in energy homeostasis. *Nat Rev Endocrinol*. 2019;15(11):651-665.
doi: 10.1038/s41574-019-0246-y

66. Kurdy NMG. Serology of abnormal fracture healing: the role of PIIINP, PICP, and BsALP. *J Orthop Trauma*. 2000;14(1):48-53.
doi: 10.1097/00005131-200001000-00010

ACCSCIENCE PUBLISHING

International Journal of Bioprinting

RESEARCH ARTICLE

3D-printed perfusable tumor model for evaluating perfusion and chemotherapeutic response in ovarian cancer cells

Md Shahriar[1], Marielena Molinares[1], Ganesh Acharya[2], Komaraiah Palle[2], and Changxue Xu[1]*

[1]Department of Industrial, Manufacturing, and Systems Engineering, Edward E. Whitacre Jr. College of Engineering, Texas Tech University, Lubbock, Texas, USA

[2]Department of Cell Biology and Biochemistry, School of Medicine, Texas Tech University Health Sciences Center, Lubbock, Texas, USA

Abstract

Understanding the role of perfusion and chemotherapeutic response in solid tumors requires advanced *in vitro* models that closely recapitulate the tumor microenvironment. Addressing this need, we developed a perfusable three-dimensional (3D) gelatin methacrylate (GelMA)-based tumor model embedded with a hollow microchannel to investigate spatial variations in SKOV3 ovarian cancer cell behavior and their response to carboplatin. This study aims to overcome the limitations of conventional two-dimensional and non-perfused 3D cultures by introducing controlled perfusion and directional drug delivery, thereby providing a more physiologically relevant platform for cancer research and drug testing. Using extrusion- and inkjet-based bioprinting, SKOV3 cells were cultured within the GelMA matrix and exposed to continuous medium flow. We observed that cell behavior varied significantly with distance from the perfusion channel. Cells closer to the channel (0–300 μm) showed increased elongation (aspect ratio: 3.5), faster migration (28.98 μm/day), higher viability (96%), and elevated proliferation (index: 3.8), which progressively declined with increasing distance. Upon carboplatin exposure (0–50 μM), SKOV3 cells exhibited dose-dependent reductions in viability, proliferation, migration, and elongation, with the aspect ratio dropping to 1.17 and the viability to 5% at 50 μM. Matrix degradation analysis revealed increased pore enlargement under perfusion (87–190 μm), suggesting higher matrix metalloproteinase activity. This perfused 3D model enables precise evaluation of chemotherapeutic efficacy and tumor cell heterogeneity, offering a powerful tool for preclinical drug screening, tumor biology research, and future integration of vascular and immune components.

Keywords: Carboplatin chemotherapy; Cell migration; Drug resistance; Drug screening platform; Ovarian cancer cell; Perfusable three-dimensional tumor model; Three-dimensional bioprinting

***Corresponding author:**
Changxue Xu
(changxue.xu@ttu.edu)

Citation: Shahriar M, Molinares M, Acharya G, Palle K, Xu C. 3D bioprinting of a perfusable tumor microenvironment model to investigate perfusion and chemotherapeutic responses in ovarian cancer cells. *Int J Bioprint*. 2025;11(6):260-278. doi: 10.36922/IJB025320316

Received: August 7, 2025
1st revised: September 3, 2025
2nd revised: September 19, 2025
Accepted: September 22, 2025
Published online: September 23, 2025

Copyright: © 2025 Author(s). This is an Open Access article distributed under the terms of the Creative Commons Attribution License, permitting distribution, and reproduction in any medium, provided the original work is properly cited.

Publisher's Note: AccScience Publishing remains neutral with regard to jurisdictional claims in published maps and institutional affiliations.

1. Introduction

Metastasis remains the leading cause of cancer-related mortality, accounting for approximately 90% of cancer deaths across various tumor types.[1] This complex,

multifactorial process involves the detachment of malignant cells from the primary tumor, local invasion of adjacent tissues, and dissemination through the vasculature to distant organs.[2] The tumor microenvironment (TME), comprising extracellular matrix (ECM) components, stromal cells, biochemical gradients, and mechanical cues, plays a pivotal role in promoting tumor heterogeneity, invasion, and therapeutic resistance.[3] Understanding these intricate cellular behaviors requires model systems that recapitulate the three-dimensional (3D) architecture, biochemical gradients, and dynamic fluidic conditions found *in vivo*.[4]

Although widely used in cancer research, conventional two-dimensional monolayer cultures fail to replicate key physiological characteristics of the native TME. These systems lack the structural complexity, mechanical cues, and spatial organization that influence cell polarity, differentiation, and intercellular communication.[5] They also do not account for critical factors such as interstitial flow, oxygen and nutrient gradients, and shear stress, which play essential roles in tumor progression and treatment response. As a result, drug testing in two-dimensional models often overestimates therapeutic efficacy due to uniform drug exposure and the absence of diffusion barriers and ECM-mediated signaling found *in vivo*.[6] The simplified environment masks important mechanisms of drug resistance, including variable cell–matrix interactions and regional heterogeneity in drug penetration. To overcome these limitations, 3D culture systems have been developed to mimic the TME more accurately. Recent advancements in 3D tumor modeling have introduced diverse platforms, including multicellular tumor spheroids, patient-derived organoids, microfluidic systems, and bioprinted constructs. While multicellular tumor spheroids offer scalability for drug screening and patient-derived organoids preserve patient-specific tumor characteristics, both lack integrated perfusion, limiting nutrient and oxygen delivery, and resulting in necrotic cores and incomplete TME mimicry.[7] Microfluidic devices address this by introducing dynamic flow but offer limited spatial complexity. In contrast, 3D bioprinting enables precise spatial control and the fabrication of perfusable vascular structures, closely replicating *in vivo* physiological gradients and shear stress.[8] This enhances cancer cell proliferation, drug response, and metastasis modeling. Among hydrogel scaffolds used, gelatin and its methacrylated derivative, gelatin methacrylate (GelMA), are particularly advantageous. Derived from collagen, they mimic key characteristics of the ECM, including cell-binding motifs (i.e., Arg-Gly-Asp sequences) and matrix metalloproteinase (MMP)-sensitive degradation sites, both of which originate from the parent collagen and inherently support cell adhesion and proliferation.[9] Furthermore, GelMA's tunable stiffness and photo-crosslinkability make it suitable for constructing biomimetic, perfusable TMEs with high fidelity, and translational relevance. While gelatin alone can form hydrogels (often enzymatically crosslinked with microbial transglutaminase [TG]), this process takes hours for bulk models.[10] Such a long curing time would greatly prolong fabrication, leaving cells suspended in a liquid environment and potentially disrupting the 3D tumor architecture before solidification. Moreover, prolonged ultraviolet crosslinking time for GelMA can significantly decrease cell viability in a time-dependent manner.[9] Therefore, we adopted an innovative two-step crosslinking approach in which gelatin supplementation and a secondary TG crosslink enabled shorter ultraviolet curing of the GelMA–gelatin construct, thereby enhancing cell viability. Furthermore, we fabricated the hollow perfusable channel via sacrificial bioprinting of Pluronic F-127, enabling precise lumen positioning and clean removal within the 3D construct, yielding smooth, patent conduits suitable for reliable perfusion.

Several researchers have investigated the behavior of cancer cells using 3D perfusable tumor models to understand mechanisms of drug response and resistance. For instance, Wang *et al.*[11] developed a perfusable 3D brain tumor co-culture model using polyethylene glycol hydrogels and alginate microfibers with patient-derived glioblastoma cells, enhancing tumor cell proliferation. Ertekin *et al.*[12] utilized alginate–gelatin scaffolds containing breast cancer aggregates and established cell morphology as a malignancy indicator within 3D models. Their findings suggest that confinement and mechanical stress, rather than hypoxia, drive the formation of multinucleated cells, potentially contributing to drug resistance within the artificial TME.[12] More recently, a 3D-bioprinted tumor mimic by Maggiotto *et al.*[13] used GelMA and Pluronic F-127 with neuroblastoma cells to achieve a perfusable TME model, showing enhanced cell viability and metastatic mimicry. Moreover, a key focus on current 3D cancer modeling involves investigating drug resistance and diverse cellular responses to chemotherapy. Hong *et al.*[14] utilized 3D-bioprinted spheroids of HeLa, HepG2, and A549 cells to model multidrug resistance against doxorubicin, revealing that 3D cultures exhibited greater resistance proportional to their transporter protein levels. Similarly, a study from Fang *et al.*[15] employed a microarray device for 3D patient-derived breast cancer organoids to examine adriamycin resistance, noting significant heterogeneity in drug response between naïve and resistant organoid groups. While these studies have advanced our understanding of drug sensitivity in cancer

cells, accurately replicated functional perfusable structures that closely resemble the native TME are still lacking.

This study presents a perfusable 3D GelMA–gelatin tumor model to investigate spatial gradients and chemotherapeutic response in SKOV3 ovarian cancer cells. A sacrificially patterned microchannel enabled continuous medium flow, mimicking physiological perfusion, and nutrient delivery. The model revealed distinct differences in drug sensitivity and adaptive behavior, influenced by proximity to the perfusion channel. By integrating ECM-mimetic scaffolds with dynamic flow, this platform offers a physiologically relevant system for studying tumor progression, drug resistance, and microenvironmental regulation *in vitro*.

2. Materials and methods

2.1. Ink preparation

In this study, a mixture of GelMA and gelatin was selected as the bioink formulation to replicate the ECM environment and serve as a cell carrier, as they contain cell-binding motifs (i.e., Arg-Gly-Asp sequences) and MMP-sensitive degradation sites from the parent collagen, which inherently support cell adhesion and proliferation.[9] GelMA was synthesized according to a previously published method.[16] For bioink preparation, lyophilized GelMA was dissolved in Dulbecco's phosphate-buffered saline (DPBS; 6% w/v) at 37 °C with 0.3% (w/v) lithium phenyl-2,4,6-trimethylbenzoylphosphinate (Sigma-Aldrich, USA), then stored at 4 °C until further use. A 6% (w/v) gelatin solution was prepared separately by dissolving gelatin powder in DPBS at 37 °C for 30 min and stored at 4 °C. Gelatin can be enzymatically crosslinked using TG, as reported by Ren *et al.*[17] To prepare the TG solution, 20% (w/v) TG was made by dissolving lyophilized TG powder (Moo Glue; Modernist Pantry, USA) in DPBS at 37 °C for 30 min, followed by storage at 4 °C.

To generate a sacrificial template for hollow perfusable channels within the hydrogel matrix, Pluronic F-127 (poloxamer 407), a synthetic biocompatible thermoresponsive hydrogel, was utilized. Its gelation is reversible and temperature-dependent.[18] A 40% (w/v) Pluronic F-127 ink was prepared by dissolving Pluronic F-127 powder (Sigma-Aldrich, USA) in deionized water at 4 °C with continuous stirring for 1 h. The resultant ink was stored at 4 °C until use.

2.2. Perfusable tumor model fabrication

The fabrication of the perfusable 3D hydrogel-based TME model is schematically illustrated in Figure 1. A 3D-printed polylactic acid (PLA) block (15 × 10 × 2 mm^3) was centrally placed in a 35 mm Petri dish. Polydimethylsiloxane (10:1 base-to-curing agent ratio; Sylgard 184, USA) was poured to embed the block and cured at 70 °C overnight. The PLA block was removed, creating a polydimethylsiloxane mold with a central cavity.

A hydrogel mixture comprising 6% (w/v) GelMA and 6% gelatin in a 1:1 ratio was prepared at 37 °C, followed by the addition of TG at a 19:1 hydrogel-to-enzyme ratio. This solution was cast into the polydimethylsiloxane mold to form a thin bottom layer of 1 mm thickness. This layer was cooled at 4 °C to induce rapid gelation. Following this, Pluronic F-127 was printed onto the GelMA–gelatin layer using an extrusion-based 3D bioprinter (TissueStart, Tissuelabs, Switzerland) equipped with a 27G needle. A straight channel (500 μm width) was deposited at a 30 μL/min flow rate. Subsequently, an inkjet-based bioprinting system (PH-47, MicroFab Technologies, USA) was employed to deposit cell-laden GelMA adjacent to the Pluronic channel. The cell-laden droplets (1×10^6 cells/mL) were printed in a single layer with a nominal line spacing of ~100 μm to ensure proximity between the cell-laden region and the channel. Inkjet printing was performed as described in a previous study.[19–21]

After printing, a 1-mm-thick top layer of the GelMA–gelatin mixture was deposited, and the construct was crosslinked under ultraviolet light (10 mW/cm^2, 20 s). The construct was then incubated at 37 °C for 3 h to enable enzymatic crosslinking via TG. To form the perfusable channel, Pluronic F-127 was liquefied at 4 °C and removed with a syringe. A pair of 27G needles was inserted at both ends and connected to a peristaltic pump with a 0.5 mm perfusion tube for medium perfusion. The final tumor model was maintained at 37 °C with continuous medium flow (16 μL/min) for subsequent experiments. This flow rate was selected to generate physiologically relevant shear stress (~0.22 dyn/cm^2), within the reported range for peritoneal organs (0.02–1 dyn/cm^2).[22] In both perfused and non-perfused models, 5 mL of culture medium was used per construct. The medium was refreshed every 48 h during normal culture, and every 24 h during carboplatin treatment to ensure consistent nutrients and drug exposure.

2.3. Shear stress measurement

The wall shear stress (τ) in the perfusion channel was calculated using the following Hagen–Poiseuille equation (**Equation I**) for the 500 μm diameter cylindrical channel[23]:

$$\tau = \frac{4\mu Q}{\pi r^3} \quad \text{(I)}$$

where μ is the dynamic viscosity of the medium, Q is the volumetric flow rate, and r is the channel radius.

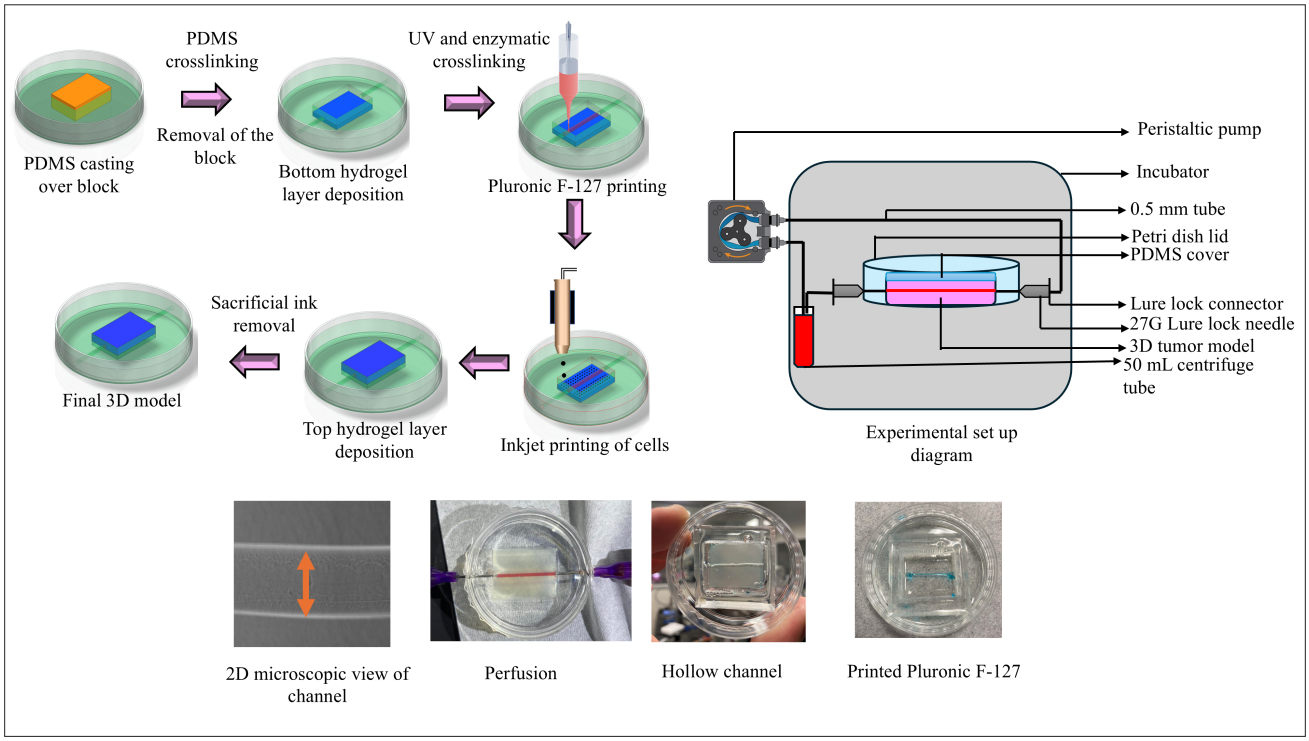

Figure 1. Schematic of the perfusable three-dimensional tumor model fabrication workflow. Abbreviations: 2D, two-dimensional; 3D, three-dimensional; PDMS, polydimethylsiloxane; UV, ultraviolet.

2.4. Hydrogel degradation measurement

Conventional methods have evaluated hydrogel degradation by exposing specimens to collagenase.[24,25] However, monitoring cell-mediated enzymatic breakdown in encapsulated samples provides a more realistic readout of *in situ* remodeling.[26] In this study, enzymatic degradation was evaluated as a percentage mass loss of the hydrogel over 5 days of SKOV3 culture. Immediately after fabrication, cell-laden hydrogels were lyophilized at −50 °C for 12 h, and their initial dry weight (W_0) was recorded. Parallel sets were cultured under perfused and non-perfused conditions and, at Days 1, 3, and 5, were lyophilized under the same conditions to obtain the timepoint dry weight (W_t). The degradation percentage was calculated using **Equation (II):**[26]

$$Degradation(\%) = \left(\frac{W_0 - W_t}{W_0} \right) \times 100 \quad \text{(II)}$$

where W_0 is the dry weight of the specimen immediately after fabrication, and W_t is the dry weight of the specimen after a specific incubation time with SKOV3 cells.

2.5. Cell culture

Human ovarian cancer cell line SKOV3 was purchased from ATCC (United States). Cells were cultured in Dulbecco's Modified Eagle Medium (Sigma-Aldrich, USA), supplemented with 10% fetal bovine serum (Invitrogen, USA) and 1% penicillin–streptomycin (50 U/mL penicillin, 50 µg/mL streptomycin; Invitrogen, USA) at 37 °C and 5% carbon dioxide. Before bioprinting, cells were detached using 0.25% trypsin-ethylenediaminetetraacetic acid (Corning, USA), centrifuged, and resuspended in 6% (w/v) GelMA at 1×10^6 cells/mL for bioink preparation.

2.6. Cell morphology, migration, proliferation, and viability analysis

Cell morphology was quantified using aspect ratio and circularity, extracted from live-cell images via ImageJ (version 2.14.0). A high aspect ratio indicates an elongated, spindle-like shape associated with increased motility and epithelial-to-mesenchymal transition. In contrast, low values and high circularity reflect rounded, less migratory, or apoptotic phenotypes.[27,28] Morphology was assessed using fluorescence microscopy (AMF4300, EVOS FL, USA). Constructs were perfused with DPBS, fixed with 4% formaldehyde, and permeabilized using Triton X-100. Staining was performed with phalloidin (F-actin, green;

Santa Cruz Biotechnology Inc., USA) and 4',6-diamidino-2-phenylindole (nuclei, blue; Santa Cruz Biotechnology Inc., USA), followed by incubation in the dark at room temperature for imaging.

To assess cell migration, live-cell fluorescence images were acquired at 2-h intervals over 3 days. The displacement of individual cell nuclei was tracked relative to their initial positions at time zero. Migration speed was determined by calculating the total distance traveled by each nucleus and dividing it by the corresponding time interval. The global turning angle was used to evaluate directional changes in cell migration trajectories. The normalized cell proliferation index was calculated by dividing the total cell count on Day 7 by the initial seeding density within the tumor construct. A standard live/dead assay was used to assess cell viability, as previously reported.[29] Cell viability was quantified as the percentage of live cells relative to the total number of cells in each sample.

2.7. Scanning electron microscopy imaging of the hydrogel

To evaluate the microstructure of the hydrogels before and after experimentation, the samples were perfused with DPBS for 3 h to remove residual culture medium and cellular waste. Subsequently, the hydrogels were frozen at −80 °C overnight and lyophilized using a freeze dryer (Labconco, USA) for 3 days. Prior to the scanning electron microscopy (SEM) imaging, the dried samples were gold-coated using a sputter coater (Ted Pella Inc., USA) at 0.1 mA/mbar for 30 s at room temperature. The microstructures were then imaged using a scanning electron microscope (Phenom Pharos, Thermo Fisher Scientific, USA), and the images were analyzed using the ImageJ software.[28]

2.8. Experimental design and data analysis

In both perfused and non-perfused models, a central hollow channel was embedded during fabrication to ensure consistency in spatial geometry and to enable direct comparisons between groups. While only the perfused model received continuous medium flow through this channel, the non-perfused model retained the same channel structure for distance mapping and spatial sampling, but no dynamic perfusion was applied. To evaluate the influence of perfusion and spatial proximity to the perfusion channel on cellular behavior, the tumor constructs were segmented into three distinct regions based on radial distance from the channel: 0–300, 300–600, and 600–900 μm. These zones were selected based on the known diffusion limit of oxygen (~200 μm) and prior studies showing reduced viability beyond 500–600 μm, with 900 μm representing an extreme diffusion-limited condition.[30,31] The 0–300 μm zone was expected to represent a well-perfused region with optimal access to nutrients and oxygen, thereby supporting higher viability, proliferation, and motility. In contrast, the 600–900 μm zone was expected to model diffusion-limited, quasi-anoxic regions, leading to suppressed cellular activity and survival, closely mimicking necrotic tumor cores. The flow rate of 16 μL/min was chosen to achieve low interstitial shear stress (~0.22 dyn/cm^2), within the physiological range observed in tumors, and was expected to induce mechanotransductive responses that enhance cellular elongation and directional migration.[22] Cells were cultured in the tumor model for 7 days, where Day 1 was the initial day of cell encapsulation and Day 7 was the final day of cell culture. Cell morphology, proliferation, and viability were measured on Day 1 and Day 7 of these experiments. To assess cell migration, SKOV3 cells were cultured for 4 days to enable matrix degradation, remodeling, and tumor-like tissue establishment. Migration speed was then quantified over the subsequent 3 days, with the first day of tracking designated as Day 1 and the final day as Day 3. Quantitative parameters from cells within each region were extracted using the ImageJ software, based on live-cell fluorescence images acquired at 2-h intervals. To evaluate the effect of the chemotherapeutic drug, following an initial 4-day culture period enabling cellular adaptation and tumor establishment, carboplatin with varying concentrations (0–30 μM) was introduced into the perfusion channel and maintained for 3 consecutive days. This concentration range was chosen to investigate the dose-dependent suppression of cellular response. For consistency, the day of initial drug introduction was designated as Day 1, and the final day of perfusion as Day 3. All analyses were focused on the perivascular region of the tumor model, specifically the area located 0–300 μm from the perfusion channel, where nutrient and drug diffusion are presumed to be most effective. All experiments were independently repeated at least three times under identical conditions. Statistical analysis was performed using the analysis of variance and Tukey's post hoc test (Python, version 3.11), and differences were considered statistically significant at $p < 0.05$.

3. Results

3.1. Effect of perfusion and spatial gradients on cell behavior

3.1.1. Effect on cell morphology

To evaluate the impact of perfusion on cell morphology, aspect ratio and circularity were quantified from bright-field images of SKOV3 cells after 7 days of culture under perfused and non-perfused conditions at distances of 300, 600, and 900 μm from the channel (Figure 2A). In the perfused model, the aspect ratio significantly ($p < 0.05$) decreased (3.50–2.65) and circularity increased

(0.23–0.34) with distance, indicating reduced elongation. In the non-perfused model, the lack of convective flow eliminated nutrient/oxygen gradients, resulting in uniform hypoxia and metabolic stress across all regions. This led to statistically insignificant morphological changes (aspect ratio 1.98–2.02, circularity 0.39–0.41, $p > 0.05$), with slight variations attributed to stochastic cellular responses rather than mechanistic differences. Qualitative observation of cell morphology supports these quantitative findings (Figure 2B). On Day 1, both models showed similar cell shapes; by Day 7, the perfused model developed a polarized, spindle-like morphology typical of invasive phenotypes, while the non-perfused model retained rounded forms. These images illustrate the development of a polarized cell morphology over time in perfused 3D tumors, versus the retention of a rounded morphology in non-perfused tumors.

Fluid shear stress from perfused media is a key regulator of cell morphology in 3D tumor models. Even low interstitial shear levels provide mechanical cues that influence cell behavior via mechanoreceptors. Prior studies have shown that shear exposure enhances cell spreading and reduces circularity, indicating a transition to a motile, polarized phenotype.[32] In our model, cells near the perfusion channel were exposed to higher shear, which exhibited elongated morphologies with higher aspect ratios. This spatial variation also reflects differences in nutrient and oxygen availability; cells proximal to the channel were well-nourished, while those farther away faced diffusion limitations and metabolic waste accumulation.[33] In non-perfused conditions, the absence of convective flow led to disorganized actin structures, reduced focal adhesions, and spherical cell shapes due to stress-induced adaptation.[34] These findings underscore the role of perfusion in maintaining physiological morphology and preventing stress-driven rounding in 3D tumor environments.

3.1.2. Effect on cell migration

Figure 3A presents the average migration speed of SKOV3 cells over 3 days in both perfused and non-perfused 3D tumor models. In the perfused condition, average cell migration speed decreased significantly with increasing distance from the channel: 28.98 μm/day at 0–300 μm, 26.57 μm/day at 300–600 μm, and 21.27 μm/day at 600–900 μm ($p < 0.05$). In contrast, cells in the non-perfused model exhibited consistently lower migration speeds, ranging from 13.05 to 13.57 μm/day and 13.57–12.71 μm/day across the same spatial zones. The representative bright field images demonstrate typical 3-day single cell migration in the 0–300 μm region in both models (Figure 3B). Figure 3C and D illustrates representative migration trajectories and angular orientation plots of cells in both conditions. In the perfused model, with increasing distance from the perfusion channel (0–300, 300–600, 600–900 μm), the 3-day mean net displacement decreased significantly from 82.5 to 58.5 μm and from 58.5 to 39.1 μm ($p < 0.05$). Furthermore, cells in the 0–300

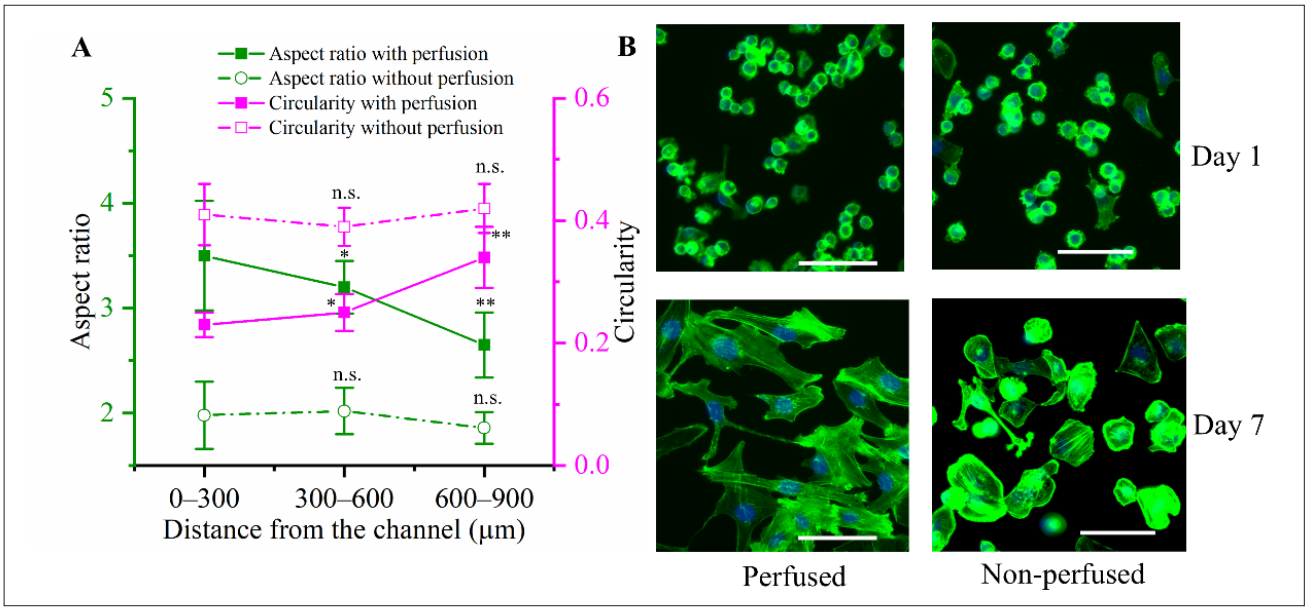

Figure 2. Effect of perfusion on cellular morphology. (A) Comparison of cellular aspect ratio and circularity of SKOV3 cells at Day 7, depending on the distance from the perfusion channel, grown in perfused and non-perfused conditions. (B) Representative fluorescence images of cell morphology at Day 1 and Day 7 within the 0–300 μm region in both models. Green fluorescence shows cytoskeletal staining of F-actin with phalloidin, and blue fluorescence shows nuclear counterstain. Scale bar: 100 μm; magnification: 40×. Notes: $n = 3$, n.s. = not significant, $^{*}p < 0.05$, $^{**}p < 0.01$, $^{***}p < 0.001$.

μm region displayed directed movement aligned with or toward the flow direction of the medium. However, as the distance increased, cell trajectories became progressively more random. Quantitative analysis showed that 63% of cells within 0–300 μm oriented along the flow direction, decreasing to 45% in the 300–600 μm zone and 40% in the 600–900 μm region ($p < 0.05$). In the non-perfused model, migration paths remained random across all regions. This spatial trend suggests that interstitial flow provides directional cues that guide cell orientation near the perfusion channel.

Oxygen gradients can serve as directional cues for cancer cell migration. In hydrogel systems, sarcoma cells have been shown to move toward more oxygenated regions, mimicking vessel-directed migration.[35] In our model, cells within ~300 μm of the perfusion channel had sufficient

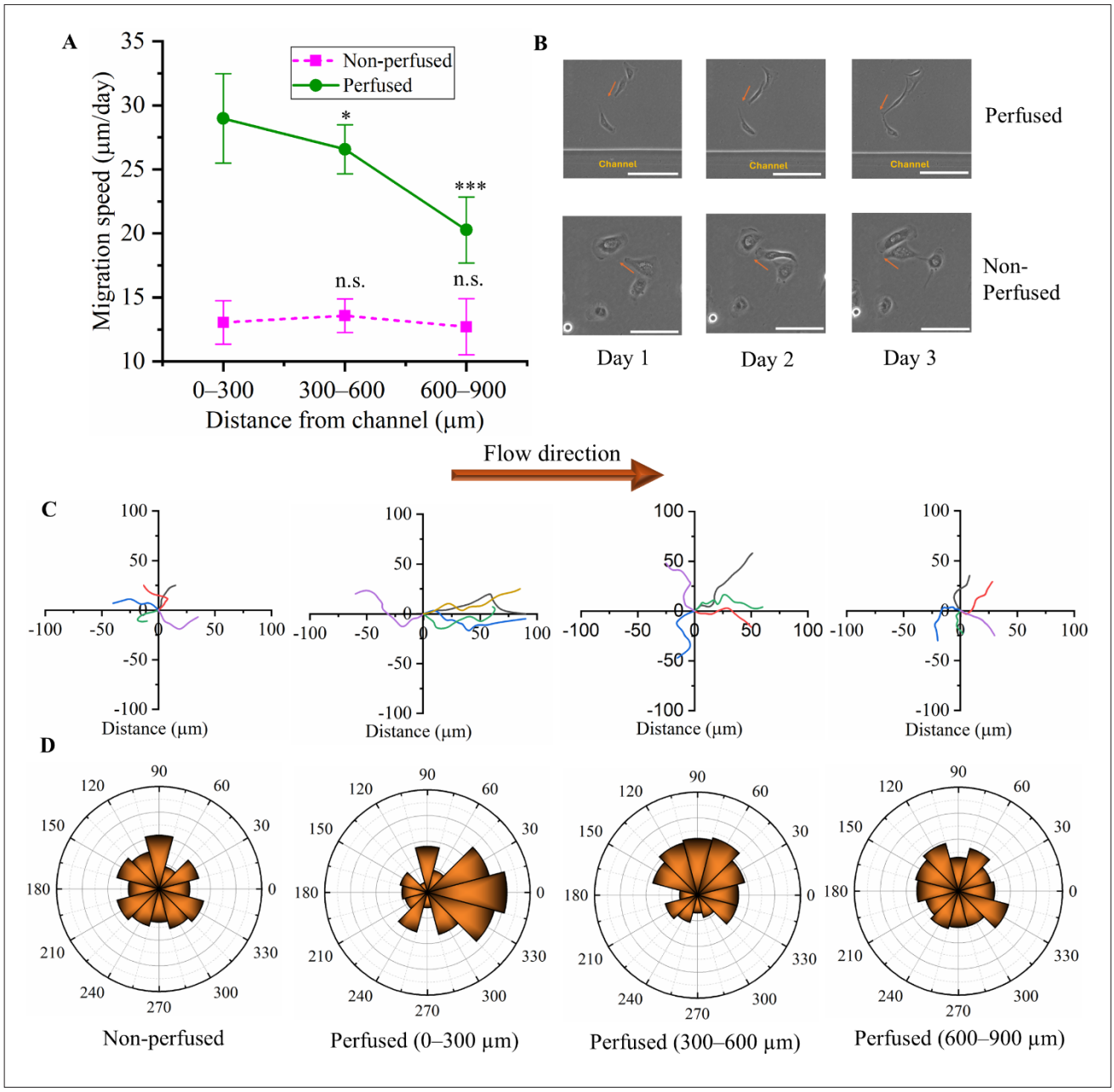

Figure 3. Effect of perfusion on cell migration. (A) Effect of perfusion on cell migration speed. (B) A typical cell migration representation from Day 1 to Day 3 within the 0–300 μm region in the perfused and non-perfused model (arrow indicates cell migration trajectory). Scale bar: 100 μm; magnification: 40×. (C) Representative typical cell migration trajectories. (D) Angular orientation distributions as a function of distance from the perfusion channel under perfused and non-perfused culture conditions. Notes: $n = 3$, n.s. = not significant, $^{*}p < 0.05$, $^{**}p < 0.01$, $^{***}p < 0.001$.

oxygen to support migration and may have sensed and followed the gradient. Cells further from the channel had reduced oxygen and nutrients, which impaired motility. Additionally, interstitial flow near the channel provides mechanotactic signals and fluid shear that guide migration by creating intracellular tension gradients. This has been linked to β1-integrin and focal adhesion kinase polarization, promoting protrusion along the flow direction.[36] Similarly, OVCAR-3 cells exposed to moderate shear stress showed elongated morphologies and aligned migration.[37] Thus, in our perfused model, combined oxygen availability and fluid-induced mechanical cues near the perfusion channel likely promoted directional migration, underscoring the importance of perfusion gradients in regulating tumor cell motility.

3.1.3. Effect on cell proliferation

Figure 4A illustrates the cell proliferation index as a function of distance from the perfused channel after 7 days, comparing conditions with and without perfusion. The data reveal a decline in the proliferation index with increasing distance from the channel under perfused conditions, decreasing from 3.8 at 0–300 μm to 3.2 at 300–600 μm, and further to 2.9 at 600–900 μm. In contrast, under non-perfused conditions, the overall proliferation index was significantly lower ($p < 0.05$) and showed minimal variation with distance. Specifically, the proliferation indices across the same regions were 2.1, 2.3, and 2.0, respectively. The representative bright field images demonstrated a substantial increase in cell density over time in the perfused model, highlighting the positive effect of continuous medium flow on cell growth (Figure 4B). In contrast, the non-perfused model exhibited minimal changes in cell density, underscoring the critical role of perfusion in supporting cell proliferation within the GelMA–gelatin tumor model.

In the 3D tumor model, the perfusion channel mimics a blood vessel, continuously delivering oxygen and nutrients to support cell metabolism and proliferation. Cells near the channel benefit from normoxic conditions and show enhanced growth, as observed by Gilmore *et al.*[38] in perfused 3D breast tumor models. However, increasing distance from the channel leads to diffusion-limited gradients of oxygen and glucose, resulting in hypoxia and reduced proliferation.[39] While perfusion improves nutrient delivery via convection, spatial limitations persist, making proximity to the channel a key determinant of cellular behavior.[40] In non-perfused models, uniform hypoxia and accumulation of metabolic waste, such as lactic acid and carbon dioxide, create an acidic environment that induces cell cycle arrest and inhibits proliferation.[41]

3.1.4. Effect on cell viability

Figure 5A illustrates the cell viability percentages in perfused and non-perfused tumor models after 7 days of culture, as a function of distance from the perfusion channel. In the perfused tumor model, cell viability progressively decreased with increasing distance from the perfusion channel, from 96% at 0–300 μm to 93% at 300–600 μm and

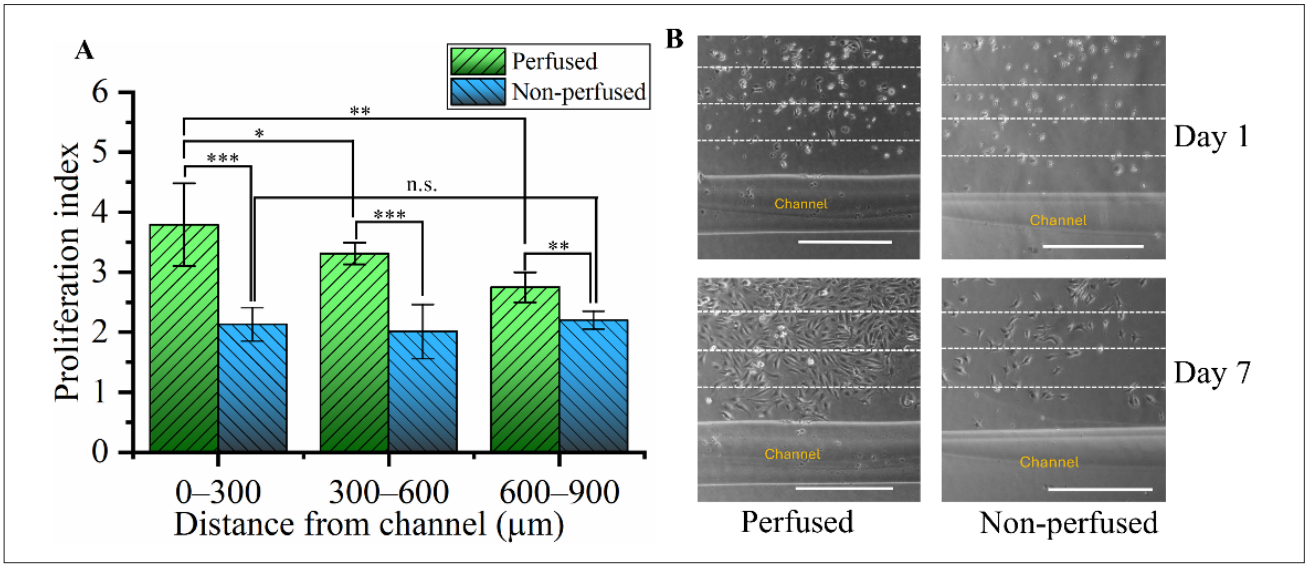

Figure 4. Effect of perfusion on cell proliferation. (A) Comparison of cell proliferation index as a function of distance from the perfusion channel. (B) Representative bright field images at Day 1 and Day 7 under perfused and non-perfused culture conditions. White dashed lines show three regions (0–300, 300–600, and 300–600 μm) adjacent to the channel. Scale bar: 1000 μm; magnification: 4×. Notes: $n = 3$, n.s. = not significant, $^{*}p < 0.05$, $^{**}p < 0.01$, $^{***}p < 0.001$.

88% at 600–900 μm. In contrast, the cell viability in the non-perfused tumor model remained significantly lower, ranging from 69% to 71% across all distances measured ($p < 0.05$). Qualitative observation of cell viability supports these quantitative findings (Figure 5B).

In perfused 3D tumor models, cells near the channel receive sufficient oxygen and nutrients, supporting high viability. However, as the distance increases, reliance on diffusion becomes inadequate beyond ~200 μm, leading to hypoxia and reduced survival.[42] Perfusion also facilitates waste removal, but in distal regions, limited diffusion causes accumulation of carbon dioxide and lactate, further compromising cell viability. In contrast, non-perfused models lack convective flow, resulting in widespread nutrient depletion and toxic buildup. By culturing HCT-116 colon carcinoma cells around a perfused microfluidic lumen, Ayuso *et al.*[43] observed minimal cell death near perfused lumens, with necrosis increasing toward the construct core. Similarly, using a breast cancer microfluidic model, Pasini *et al.*[40] reported uniform viability under perfusion, while non-perfused systems showed extensive nutrient-starved zones. These findings highlight that distance-dependent gradients in oxygen and metabolites are major drivers of cell loss in 3D models, and perfusion is essential for sustaining viability, particularly in deeper tissue regions where diffusion alone is insufficient.

3.2. Effect of perfusion of carboplatin on cell behavior

In this section, we examined the effect of the chemotherapeutic agent carboplatin on the behavior of SKOV3 ovarian cancer cells within a perfused 3D tumor model. Following an initial 4-day culture period to allow cellular adaptation and tumor establishment, carboplatin was introduced into the perfusion channel at varying concentrations and maintained for 3 consecutive days. Cellular responses, including morphology, migration, proliferation, and viability, were assessed during this drug exposure period. For consistency, the day of initial drug introduction was designated as Day 1, and the final day of perfusion as Day 3. All analyses were focused on the perivascular region of the tumor model, specifically the area located 0–300 μm from the perfusion channel, where nutrient and drug diffusion are presumed to be most effective.

3.2.1. Effect on cell morphology

Figure 6A illustrates the effect of increasing carboplatin concentration on cellular morphology after 3 days of drug exposure. As the drug concentration increased from 0 to 10, 20, and 30 μM, a marked decrease in cellular aspect ratio was observed, from 3.15 to 2.88, 2.20, and 1.17, respectively ($p < 0.05$). Concurrently, cell circularity increased from 0.25 to 0.31, 0.43, and 0.70. Representative images of cell morphology confirm that SKOV3 cells initially exhibited an elongated shape in the absence of the drug (Figure 6B). Following exposure to increasing concentrations of carboplatin, cells progressively adopted a more rounded morphology by Day 3, indicative of cytoskeletal remodeling and loss of polarity. In the control group (0 μM), such morphological changes were not observed, consistent with the absence of drug exposure.

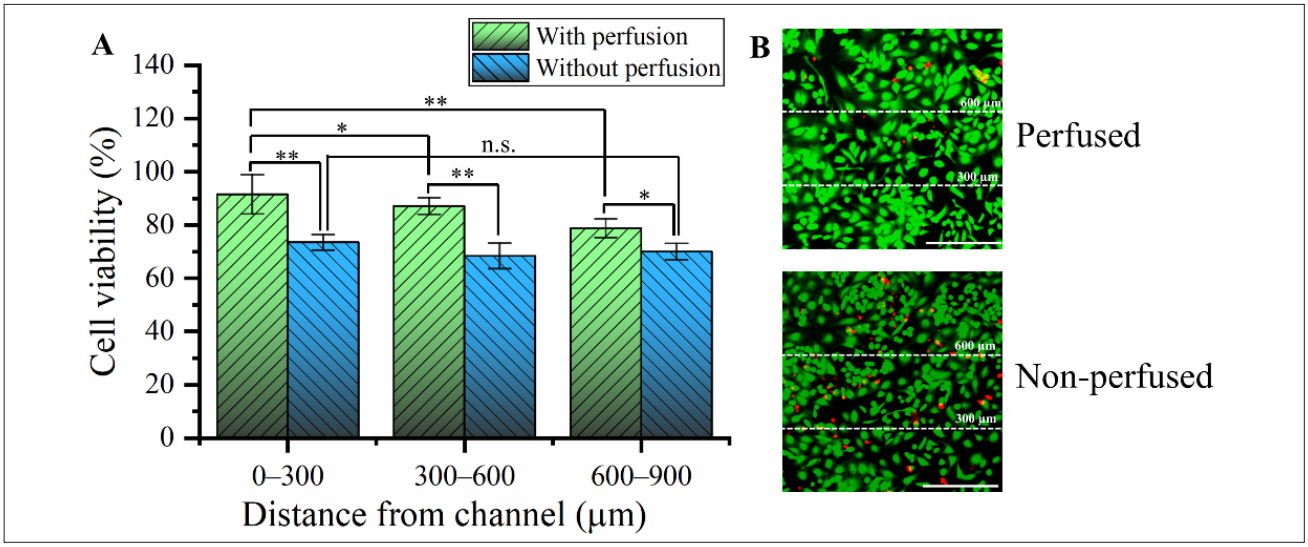

Figure 5. Effect of perfusion on cell viability. (A) Comparison of cell viability as a function of the distance from the perfusion channel. (B) Representative cell viability in perfused and non-perfused conditions after 7 days of cell culture. White dashed lines showing three regions (0–300, 300–600, 300–600 μm) adjacent to the channel, green and red fluorescence show the live and dead cells, respectively. Scale bar: 400 μm; magnification: 10×. Notes: $n = 3$, n.s. = not significant, $^{*}p < 0.05$, $^{**}p < 0.01$, $^{***}p < 0.001$.

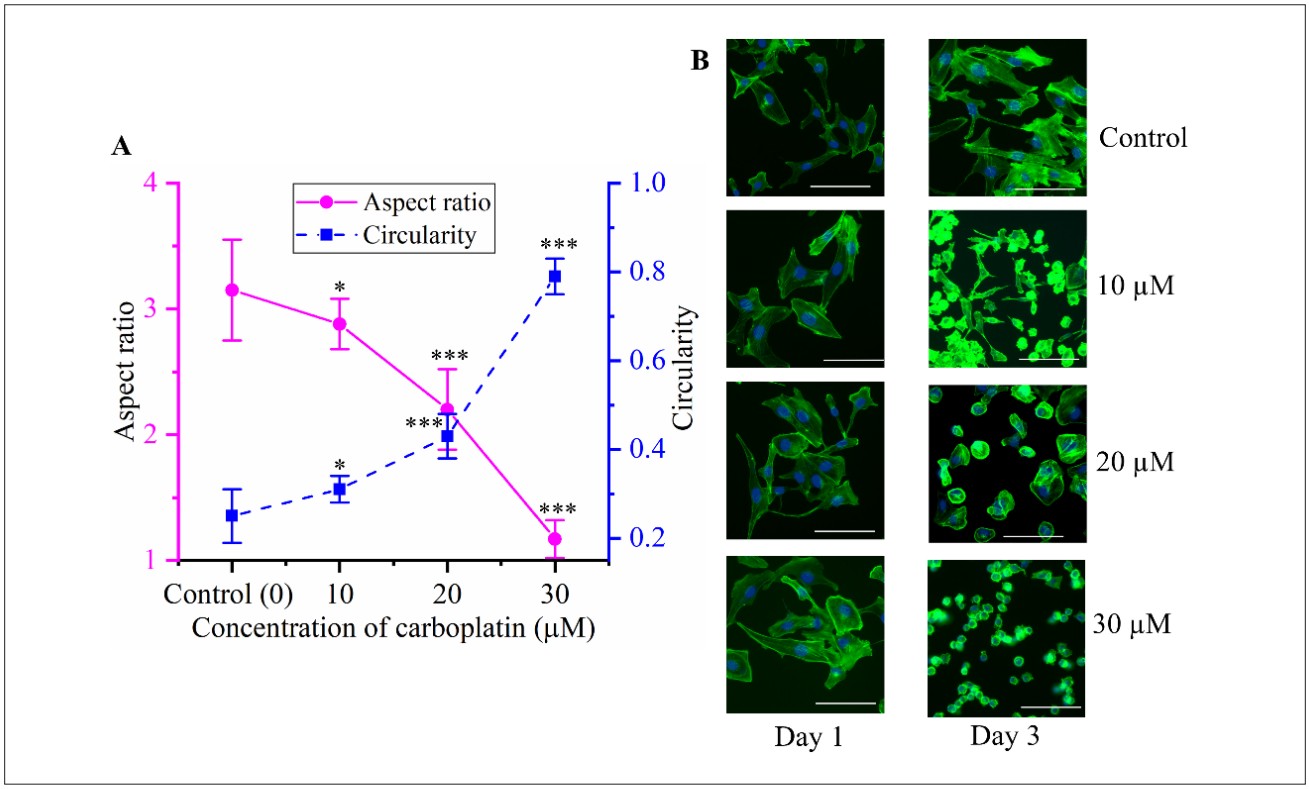

Figure 6. Effect of carboplatin on cellular morphology. (A) Effect of carboplatin drug concentration on cellular morphology after 7 days of cell culture. (B) Representative of cell morphology with an increase in concentration of drug on Day 1 and Day 3 within the 0–300 μm region in the perfused model. Green fluorescence shows cytoskeletal staining of F-actin with phalloidin, and blue fluorescence shows nuclear counterstain. Scale bar: 100 μm; magnification: 40×. Notes: $n = 3$, $^{*}p < 0.05$, $^{**}p < 0.01$, $^{***}p < 0.001$.

Carboplatin, like other platinum-based chemotherapeutics, induces extensive DNA crosslinking that activates the DNA damage response. This typically forces cells into cell-cycle arrest and triggers apoptosis.[44] One key reason for the rounding of cells under carboplatin is the cytoskeleton disruption and loss of cell structural integrity during drug-induced stress. Prior studies showed that chemotherapeutic agents altered the organization of actin filaments and microtubules, leading to changes in cancer cell stiffness, shape, and attachment.[45] In our experiment, the decreased aspect ratio with higher carboplatin doses reflects such depolymerization of F-actin stress fibers and alterations in microtubule networks. Furthermore, early-stage apoptosis involves the disassembly of focal adhesions and detachment from the matrix, coinciding with cells turning from an elongated, spread morphology to a contracted, round shape.[46] Thus, the observed increase in cellular circularity with rising carboplatin concentration in our experiment reflects apoptosis-associated morphological changes and reduced cell–matrix adhesion.

3.2.2. Effect on cell migration

Figure 7A illustrates the quantitative effect of increasing carboplatin concentrations on SKOV3 cell migration speed and visual representations of individual cell movement. As the drug concentration increased from 0 to 10, 20, and 30 μM, the average migration speed significantly declined from 28.98 to 23.12, 12.42, and 4.68 μm/day, respectively ($p < 0.05$). Figure 7B presents representative migration trajectories and angular orientation plots of cells under varying drug exposures. In the control group (0 μM), cells exhibited elongated morphology with a polarized cytoskeleton, enabling persistent and directed migration toward the perfusion channel, largely following the medium flow direction. In contrast, cells exposed to higher carboplatin concentrations lost their polarized morphology, adopted a rounded, amoeboid shape, and exhibited random, non-directional movement. The average net displacement over 3 days significantly decreased from 82.5–30.9 to 22.3–14.5 μm with an increase in drug concentration from 0 to 30 μM ($p < 0.05$). Moreover, quantitative analysis revealed that approximately 63%

of cells in the control condition aligned with the flow direction, which was significantly reduced to 41% at 30 μM carboplatin ($p < 0.05$). These findings suggest that carboplatin disrupts cytoskeletal organization and impairs the ability of cancer cells to sense and respond to directional cues, thereby inhibiting directed migration.

A primary reason for the slowed migration with the increase in drug concentration is the cytotoxic action of carboplatin on the cancer cells. In HN-3 carcinoma cells, carboplatin triggered an accumulation of reactive oxygen species that promoted apoptosis, correlating with a marked suppression of migration *in vitro*.[47] Beyond outright cell death, sublethal exposure to carboplatin can disrupt the cellular machinery of migration. Studies showed that carboplatin exposure led to lower expression of MMP2 and MMP9 in lung cancer cells, two MMPs crucial for degrading the ECM during cell invasion.[48] This reduction in MMP2/9 suggests that carboplatin not only physically slows cells by harming them but also diminishes their invasive machinery at the molecular level, reinforcing the decrease in migratory capacity. Furthermore, in our control condition, SKOV3 cells clearly adopted a polarized,

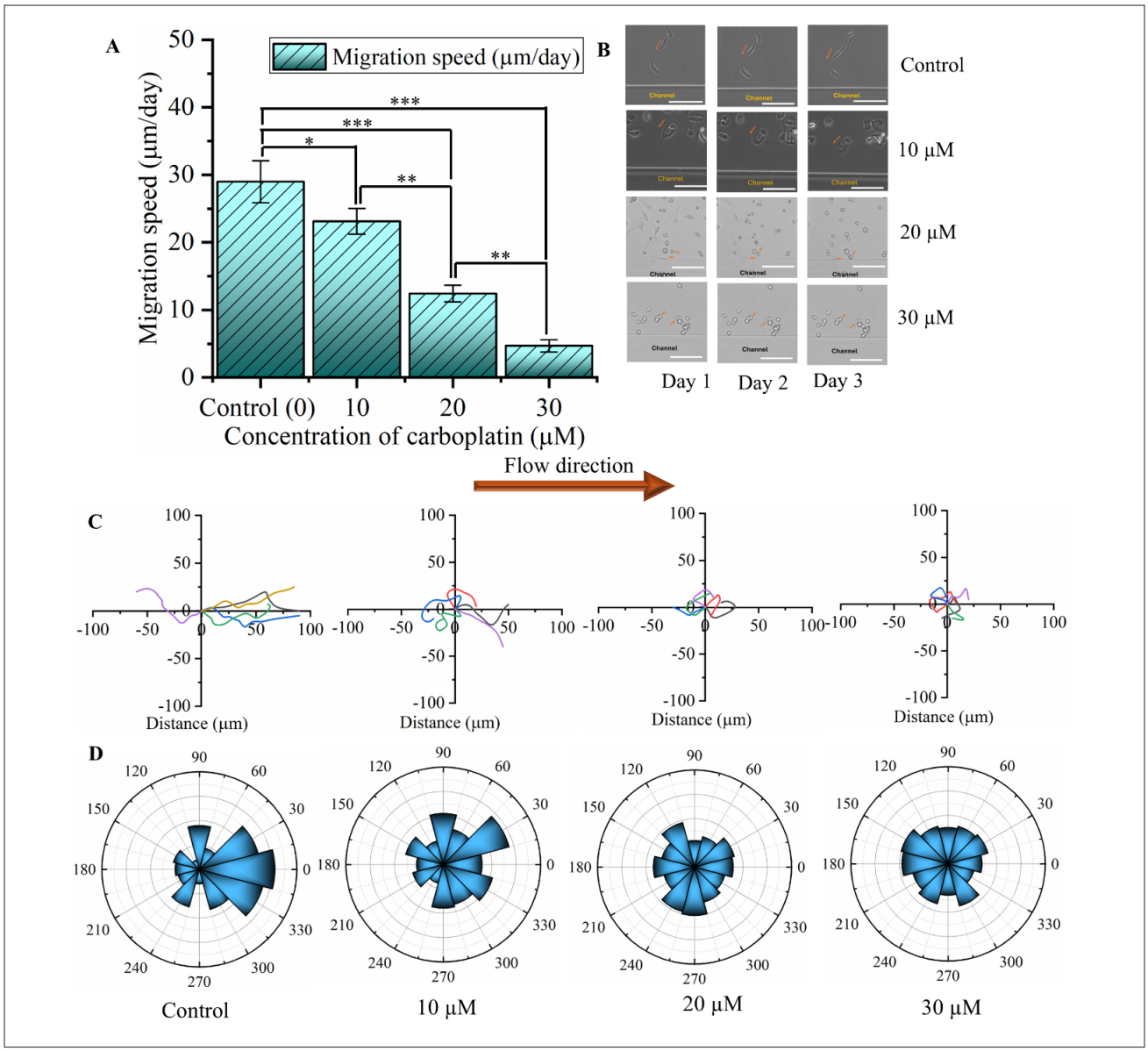

Figure 7. Effect of carboplatin on cell migration. (A) Effect of carboplatin concentration on SKOV3 cell migration speed. (B) A typical cell migration representation from Day 1 to Day 3 within the 0–300 μm region. Scale bar: 100 μm; magnification: 40×. (C) Representative migration trajectories. (D) Angular orientation distributions within the 0–300 μm region as a function of different carboplatin concentrations. Notes: $n = 3$, $^{*}p < 0.05$, $^{**}p < 0.01$, $^{***}p < 0.001$.

mesenchymal-like shape, enabling them to move *en masse* toward the channel. However, carboplatin-treated cells could no longer maintain a polarized cytoskeleton. The high drug concentrations likely cause actin cytoskeleton disassembly and loss of focal adhesions, resulting in cells that round up and lose their front-back orientation. Consistent with our observations, the literature reports that non-polarized cells extend multiple small protrusions and barely move in any one direction.[49] This mirrors the random migration observed under carboplatin: cells protrude and retract in different directions without sustained movement, leading to a random walk rather than a persistent path. Specifically, our high-dose observations (30 μM) showed many cells in a nearly ameboid, round state, unable to form stable lamellipodia, resulting in a loss of persistent, directional migration. Another intriguing aspect of our results is the interplay between fluid flow cues and drug effects. In the control condition, cells migrated toward the perfused channel, aligning their trajectories with the medium flow direction. This suggests that flow-mediated guidance was at work in our tumor model. Prior studies have shown that cancer cells frequently respond to interstitial fluid flow by migrating toward fluid movement.[50] Carboplatin treatment, however, disrupted this directed migration, likely by impairing the molecular pathways responsible for flow sensing and directional guidance.[51]

3.2.3. Effect on cell proliferation

Figure 8A shows the dose-dependent suppression of cancer cell proliferation over 3 days. In the control (0 μM carboplatin), SKOV3 ovarian carcinoma cells proliferated robustly over 3 days (proliferation index 2.3), indicating more than a twofold increase in cell population. However, with increasing carboplatin concentration, the net cell growth significantly ($p < 0.05$) declined: 10 μM yielded a lower proliferation index of 1.85, 20 μM was near-growth arrest (1.1), and at 30 μM the index dropped to 0.46, indicating the cell count after treatment was less than the initial seeding (net cell loss). Qualitative observation of cell proliferation supports these quantitative findings (Figure 8B).

This inverse relationship between drug dose and proliferation is consistent with extensive evidence that higher carboplatin doses induce greater cytotoxicity in cancer cells.[52] The reduction in proliferation index with higher carboplatin concentrations can be explained by the drug's well-characterized mechanisms of action.

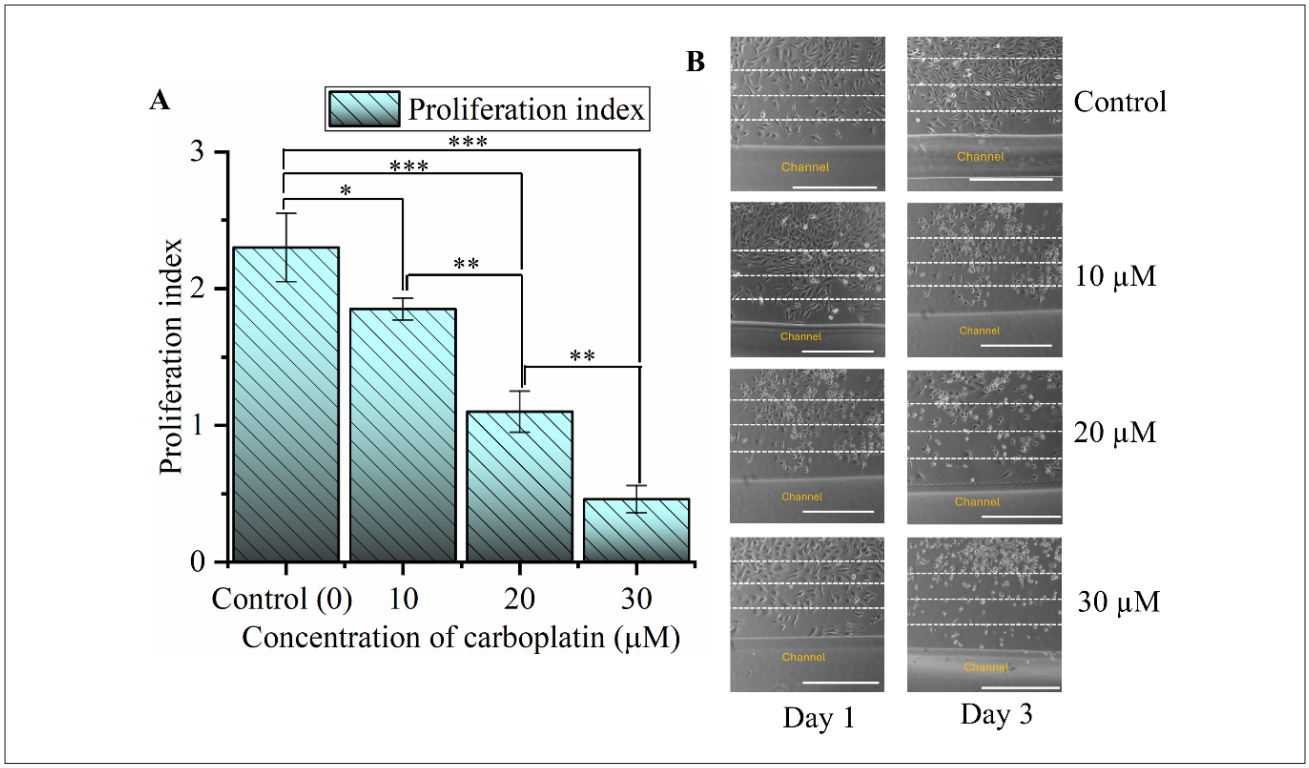

Figure 8. Effect of carboplatin on cell proliferation. (A) Effect of carboplatin concentration on SKOV3 cell proliferation index. (B) Representative bright field images of cell proliferation for 3 days of carboplatin exposure. White dashed lines showing three regions (0–300, 300–600, and 300–600 μm) adjacent to the channel. Scale bar: 1000 μm; magnification: 4×. Notes: $n = 3$, $^{*}p < 0.05$, $^{**}p < 0.01$, $^{***}p < 0.001$.

Carboplatin covalently binds DNA, forming intra- and interstrand DNA crosslinks, and bulky adducts, causing cell cycle arrest. The arrest allows time for DNA repair, but if the damage is too severe or irreparable, cells undergo programmed cell death (apoptosis).[44] At lower drug doses, some cancer cells may manage to repair sub-lethal DNA damage or enter temporary cell-cycle arrest. Hence, a fraction of cells continue dividing; this explains why we still observed modest net growth at 10–20 μM. In contrast, higher doses like 30 μM produce a greater accumulation of DNA adducts and overwhelming DNA damage.[52] Consequently, a large portion of the cell population either remains permanently growth-arrested or undergoes apoptosis. The proliferation index <1 at 30 μM reflects this outcome: cell death and permanent cell-cycle exit outpace any residual cell divisions, leading to a net decrease in viable cell number.

3.2.4. Effect on cell viability

In this section, we investigated the differential response of SKOV3 cells to different concentrations (0–50 μM) of carboplatin exposure using our 3D perfused tumor model. Figure 9A demonstrates how carboplatin affected cell viability. SKOV3 cells showed a classic dose-dependent cytotoxic response: viability dropped from 95% (no drug) to 82% at 10 μM, 65% at 20 μM, 41% at 30 μM, and down to only 5% at 50 μM. Increasing carboplatin exposure caused a statistically significant ($p < 0.05$) loss of viable cells in the sensitive population. This trend is consistent with typical carboplatin sensitivity ranges reported for ovarian cancer lines. It was reported that SKOV3 cells had a carboplatin half-maximal inhibitory concentration of around 12.4 μM,[53] indicating that doses above 20 μM overwhelm their ability to survive. Qualitative observation of cell viability supports these quantitative findings (Figure 9B).

The primary mechanism of carboplatin involves direct damage to cellular DNA.[54] The sharp decline in viability we observed for the SKOV3 cells with rising carboplatin dose is a direct consequence of this mechanism: as more platinum DNA adducts accumulate, a larger fraction of cells undergo irreversible cell-cycle arrest, lethal DNA damage, and apoptosis.[54] *In vitro* studies consistently showed that escalating carboplatin concentrations caused a dose-dependent decline in cancer cell viability, even in 3D tumor models. Ovarian cancer spheroids exposed to increasing carboplatin doses exhibited progressively lower viable cell fractions compared to untreated controls.[55] Notably, in SKOV3 ovarian cancer cells, carboplatin monotherapy significantly suppressed cell growth in a concentration-dependent manner, confirming that viability drops as the dose rises.

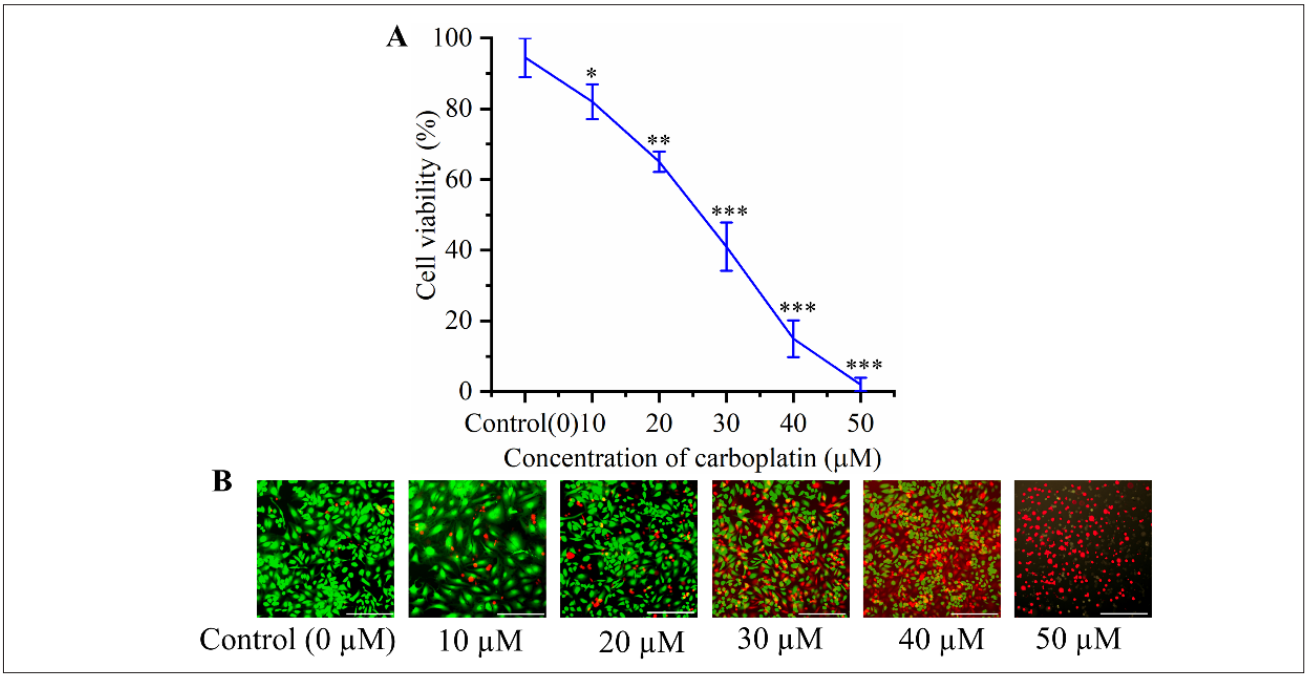

Figure 9. Effect of carboplatin on cell viability. (A) Effect of carboplatin concentrations on SKOV3 cell viability. (B) Representative cell viability after 3 days of carboplatin exposure within the 0–300 μm region. Green and red fluorescence show the live and dead cells, respectively. Scale bar: 400 μm; magnification: 10×. Notes: $n = 3$, $^{*}p < 0.05$, $^{**}p < 0.01$, $^{***}p < 0.001$.

4. Discussion

In this study, we developed a perfusable 3D tumor model with SKOV3 ovarian cancer cells to investigate the effects of spatial gradients and chemotherapeutic exposure on cell behavior. A central hollow channel enabled continuous medium flow, generating nutrient and oxygen gradients across the construct. Prior studies have demonstrated that perfusable channels significantly enhance mass transport in 3D hydrogels. Lieberthal *et al.*[56] perfused red dye and fluorescent tracers through a 3D-printed liver hydrogel and observed rapid radial diffusion into the surrounding matrix.[56] Similar diffusion-enhancing effects of perfusable microchannels have been shown using dye penetration in engineered scaffolds and vascular-like synthetic microfluidic, supporting our zone-based interpretation of spatial gradients in cell behavior.[57,58] Cells within 0–300 μm of the channel accessed abundant oxygen and nutrients, supporting high viability, metabolism, and proliferation. In contrast, cells at 600–900 μm relied on diffusion alone, leading to hypoxia and nutrient deprivation, conditions known to impair cell function beyond ~200 μm in hydrogels.[59] These gradients significantly influenced cellular responses: cells near the channel exhibited an elongated, spindle-like morphology and higher motility, consistent with an active, mesenchymal phenotype. This behavior is driven by improved metabolic conditions and cytoskeletal remodeling. Additionally, shear stress from the interstitial flow near the channel may serve as a mechanical cue, further enhancing cell elongation and directed migration. These findings highlight how perfusion critically shapes tumor cell behavior in 3D environments.

Gelatin methacrylate hydrogels are designed to mimic the ECM and can be enzymatically degraded by cells. GelMA and gelatin contain peptide motifs (derived from collagen) that are cleavable by MMPs.[60] When cells are embedded in the matrix, they secrete MMPs and other proteases that break down the surrounding hydrogel network. Figure 10 quantifies the hydrogel degradation rate by SKOV3 cells over 5 days of cell culture in perfused versus non-perfused conditions. Under continuous perfusion, 6% GelMA–gelatin hydrogel degraded from 9.39% (Day 1) to 26.87% (Day 3) and 68.0% (Day 5), with each interval showing a significant increase ($p < 0.05$). By contrast, static (non-perfused) constructs showed substantially lower degradation, rising from 2.50% (Day 1) to 11.8% (Day 3) and 31.5% (Day 5). At each time point, perfused samples exhibited greater mass loss than non-perfused counterparts ($p < 0.05$), indicating accelerated matrix degradation and remodeling under flow. Furthermore, this cell-mediated degradation effectively enlarges void spaces or "pores" within the hydrogel.[61] In our tumor model, the

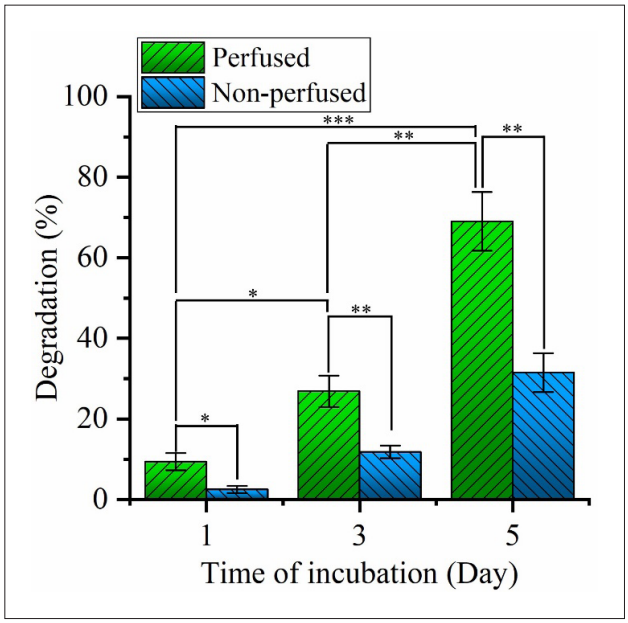

Figure 10. Degradation with increased incubation time for the cell-encapsulated gelatin methacrylate–gelatin hydrogel. Notes: $n = 3$, $^{*}p < 0.05$, $^{**}p < 0.01$, $^{***}p < 0.001$.

initial pore diameter before cell culture was 87 ± 5 μm. After 7 days of culture, the pore diameter increased to 190 ± 8 μm under perfusion, whereas in a non-perfused culture, it reached only 120 ± 4 μm. The greater expansion in the perfused model indicates significantly more extensive matrix degradation, directly attributable to differences in culture conditions. Figure 11 shows the SEM images of the perfusion channel and the microstructure of the hydrogel before and after cell culture. Dynamic medium perfusion through the GelMA–gelatin construct creates a more favorable environment for aggressive tumor cell behavior and ECM remodeling. Studies have shown that perfusion flow led to a several-fold increase in active MMP2 secretion, an enzyme strongly linked to collagen/gelatin degradation and cell migration. This enhanced MMP production accelerates hydrogel breakdown, explaining the large pore enlargement observed after 7 days in our perfused tumor model.[62] Furthermore, the flow of medium imposes fluid shear stress on cells and the matrix, which can serve as a mechanical cue. Tumor cells sense shear forces and often respond by upregulating MMP expression and other remodeling enzymes.[63] In our perfused tumor model, the gentle shear stress from continuous perfusion likely stimulated the cancer cells to secrete more MMPs, accelerating matrix breakdown. This mechanotransduction effect is supported by prior findings that perfusion flow can improve the migratory/invasive phenotype of cancer cells.[40] The robust mass loss and pore enlargement under

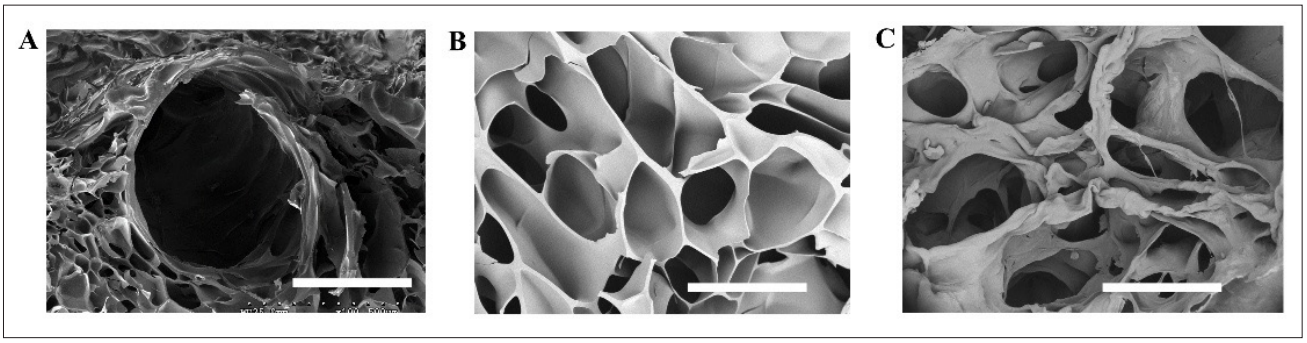

Figure 11. SEM images of the perfusion channel and hydrogel microstruture. (A) Hollow perfusion channel. (B) Hydrogel microstructure before cell culture and (C) degraded hydrogel after cell culture. Scale bar: 300 μm; magnification: 100× for (A) and 180× for (B) and (C).

perfusion demonstrate that our tumor model successfully recapitulates cell-driven ECM degradation, a hallmark of TME remodeling. Moreover, the rapid yet controllable degradation underlines that the GelMA–gelatin system strikes an optimal balance of biocompatibility, enzymatic degradability, and structural support, which is well-suited for simulating the dynamic remodeling processes characteristic of the TME.

We utilized our perfusable 3D tumor model to recapitulate key features of the native TME and investigated the response of SKOV3 ovarian cancer cells to varying concentrations of carboplatin, highlighting the model's utility for chemotherapeutic drug screening. Using a perfusion channel in the tumor construct ensured that it mimicked chemotherapy delivery by a blood vessel in tissues. In less optimized models, gradients in drug penetration can cause variability in cell killing. For instance, in larger static spheroids or hydrogel cultures, cells in the core might evade drug exposure and appear "resistant" due to diffusion limits.[64] By using a flow-through/perfused setup, we minimized those confounding factors, thereby attributing the observed viability differences squarely to cellular phenotypes.

5. Conclusion

This work establishes a perfusable 3D GelMA–gelatin tumor model with a hollow microchannel to interrogate how flow and vascular proximity regulate SKOV3 ovarian cancer cell behavior and chemotherapeutic response. Addressing a key gap in current platforms, our system couples a physiologically scaled, 500 μm perfusable channel with precise, inkjet deposition of tumor cells adjacent to the channel wall, controlled flow (16 μL/min), low shear (0.22 dyn/cm^2), and spatially resolved readouts across concentric regions (0–300, 300–600, and 600–900 μm). Using this integrated design, we quantified distance-dependent changes in morphology, migration, viability, and proliferation under continuous perfusion and contrasted them with static culture.

We found that perfusion significantly enhanced overall cellular function compared to the non-perfused model. After 7 days, cell viability reached 96% in the perfused construct compared to only 71% in the non-perfused counterpart, and the proliferation index was 3.8 in perfused conditions versus 2.2 in non-perfused culture. By dividing the tumor matrix into concentric regions (0–300, 300–600, and 600–900 μm from the channel), we observed a spatial gradient in cell behavior. As the distance from the perfusion channel increased, the cell aspect ratio decreased from 3.5 to 2.45, indicating reduced elongation; migration speed dropped from 28.98 to 21.27 μm/day; and the proliferation index fell from 3.8 to 3.0, highlighting the impact of nutrient and oxygen diffusion limits.

Upon continuous perfusion of carboplatin for 3 days at increasing concentrations (0, 10, 20, and 30 μM), we observed a dose-dependent suppression of cell behavior. Migration speed declined from 28.98 to 4.68 μm/day, proliferation index dropped sharply from 2.3 to 0.46, and cells shifted from elongated to round morphology, with aspect ratio decreasing from 3.15 to 1.17 and circularity increasing from 0.25 to 0.79. Additionally, the perfused model exhibited greater matrix degradation (68% after 5 days of cell culture), with average pore diameter expanding from 87 μm initially to 190 μm after 7 days, compared to only 130 μm in the non-perfused model, suggesting enhanced MMP activity.

Looking ahead, this platform can be further advanced by incorporating endothelial cells to mimic vascular barriers, comparing phenotypic and drug response differences between chemo-naïve and chemo-resistant ovarian cancer subtypes, and investigating synergistic effects of combination chemotherapies within the perfused tumor model. Future studies may include two-dimensional and 3D (perfused and non-perfused) tumor model comparisons, matrix degradation, and molecular

analyses, such as apoptosis and hypoxic markers for deeper mechanistic insights.

Acknowledgments

None.

Funding

None.

Conflict of interest

The authors declare they have no competing interests.

Author contribution

Conceptualization: Md Shahriar, Komaraiah Palle, Changxue Xu
Formal analysis: Md Shahriar, Marielena Molinares, Changxue Xu
Investigation: Md Shahriar, Marielena Molinares
Methodology: Md Shahriar, Komaraiah Palle, Changxue Xu
Writing–original draft: Md Shahriar, Marielena Molinares
Writing–review and editing: Md Shahriar, Ganesh Acharya, Komaraiah Palle, Changxue Xu

Ethics approval and consent to participate

Not applicable.

Consent for publication

Not applicable.

Availability of data

Data is available from the corresponding author upon reasonable request.

References

1. Shi X, Wang X, Yao W, *et al.* Mechanism insights and therapeutic intervention of tumor metastasis: latest developments and perspectives. *Signal Transduct Target Ther*. 2024;9(1):192. doi: 10.1038/s41392-024-01885-2
2. Molinares M, Wolpert N, Gollahon L, Xu C. Effect of micropillar density on morphology and migration of low and high metastatic potential breast cancer cells. *Colloids Surf B Biointerfaces*. 2025;245:114214. doi: 10.1016/j.colsurfb.2024.114214
3. Ge R, Wang Z, Cheng L. Tumor microenvironment heterogeneity an important mediator of prostate cancer progression and therapeutic resistance. *NPJ Precis Oncol*. 2022;6(1):31. doi: 10.1038/s41698-022-00272-w
4. Herrmann D, Conway JR, Vennin C, *et al.* Three-dimensional cancer models mimic cell–matrix interactions in the tumour microenvironment. *Carcinogenesis*. 2014;35(8):1671-1679. doi: 10.1093/carcin/bgu108
5. Cordeiro S, Oliveira BB, Valente R, *et al.* Breaking the mold: 3D cell cultures reshaping the future of cancer research. *Front Cell Dev Biol*. 2024;12:1507388. doi: 10.3389/fcell.2024.1507388
6. Shukla P, Yeleswarapu S, Heinrich MA, Prakash J, Pati F. Mimicking tumor microenvironment by 3D bioprinting: 3D cancer modeling. *Biofabrication*. 2022;14(3):032002. doi: 10.1088/1758-5090/ac6d11
7. Datta P, Dey M, Ataie Z, Unutmaz D, Ozbolat IT. 3D bioprinting for reconstituting the cancer microenvironment. *NPJ Precis Oncol*. 2020;4(1):18. doi: 10.1038/s41698-020-0121-2
8. Gupta D, Derman ID, Xu C, Huang Y, Ozbolat IT. Droplet-based bioprinting. *Nat Rev Methods Primers*. 2025;5(1):25. doi: 10.1038/s43586-025-00394-y
9. Sharifi S, Sharifi H, Akbari A, Chodosh J. Systematic optimization of visible light-induced crosslinking conditions of gelatin methacryloyl (GelMA). *Sci Rep*. 2021; 11(1):23276. doi: 10.1038/s41598-021-02830-x
10. Zhou M, Lee BH, Tan LP. A dual crosslinking strategy to tailor rheological properties of gelatin methacryloyl. *Int J Bioprint*. 2017;3(2):003. doi: 10.18063/IJB.2017.02.003
11. Wang C, Li J, Sinha S, Peterson A, Grant GA, Yang F. Mimicking brain tumor-vasculature microanatomical architecture via co-culture of brain tumor and endothelial cells in 3D hydrogels. *Biomaterials*. 2019;202:35-44. doi: 10.1016/j.biomaterials.2019.02.024
12. Ertekin Ö, Monavari M, Krueger R, *et al.* 3D hydrogel-based microcapsules as an in vitro model to study tumorigenicity, cell migration and drug resistance. *Acta Biomater*. 2022;142:208-220. doi: 10.1016/j.actbio.2022.02.010
13. Maggiotto F, Bova L, Micheli S, *et al.* 3D bioprinting for the production of a perfusable vascularized model of a cancer niche. *Front Bioeng Biotechnol*. 2025;13:1484738. doi: 10.3389/fbioe.2025.1484738
14. Hong M, Hong S, Song JM. 3D bioprinted multidrug resistance (MDR)-dependent tumor spheroids. *ACS Appl Mater Interfaces*. 2025;17(5):7377-7394. doi: 10.1021/acsami.4c19291
15. Fang T, Xie X, Lu W, *et al.* Patient-derived organoids on a microarray for drug resistance study in breast cancer. *Anal Chem*. 2024;96(46):18384-18391. doi: 10.1021/acs.analchem.4c02691
16. Krishnamoorthy S, Wadnap S, Noorani B, Xu H, Xu C. Investigation of gelatin methacrylate working curves in

dynamic optical projection stereolithography of vascular-like constructs. *Eur Polym J*. 2020;124:109487.
doi: 10.1016/j.eurpolymj.2020.109487

17. Ren B, Song K, Sanikommu AR, *et al.* Study of sacrificial ink-assisted embedded printing for 3D perfusable channel creation for biomedical applications. *Appl Phys Rev*. 2022;9(1):011408.
doi: 10.1063/5.0068329

18. Schmolka IR. Artificial skin I. Preparation and properties of pluronic F-127 gels for treatment of burns. *J Biomed Mater Res*. 1972;6(6):571-582.
doi: 10.1002/jbm.820060609

19. Liu J, Xu C. Improving uniformity of cell distribution in post-inkjet-based bioprinting. *J Manuf Sci Eng*. 2024;146(1):014501.
doi: 10.1115/1.4063134

20. Liu J, Xu H, Shahriar M, Xu C. Modeling of cell distribution dynamics in cell-laden bioink with active circulation. *Addit Manuf*. 2023;73:103669.
doi: 10.1016/j.addma.2023.103669

21. Xu H, Liu J, Shahriar M, and Xu C. Investigation of cell aggregation on the printing performance in inkjet-based bioprinting of cell-laden bioink. *Langmuir*. 2022;39(1):545-555.
doi: 10.1021/acs.langmuir.2c02817

22. Hyler AR, Baudoin NC, Brown MS, *et al.* Fluid shear stress impacts ovarian cancer cell viability, subcellular organization, and promotes genomic instability. *PLoS One*. 2018;13(3):e0194170.
doi: 10.1371/journal.pone.0194170.

23. Galpayage Dona KNU, Hale JF, Salako T, *et al.* The use of tissue engineering to fabricate perfusable 3D brain microvessels in vitro. *Front Physiol*. 2021;12:715431.
doi: 10.3389/fphys.2021.715431.

24. Nichol JW, Koshy ST, Bae H, Hwang CM, Yamanlar S, Khademhosseini A. Cell-laden microengineered gelatin methacrylate hydrogels. *Biomaterials*. 2010;31(21):5536-5544.
doi: 10.1016/j.biomaterials.2010.03.064.

25. Zhao X, Lang Q, Yildirimer L, *et al.* Photocrosslinkable gelatin hydrogel for epidermal tissue engineering. *Adv Healthc Mater*. 2016;5(1):108-118.
doi: 10.1002/adhm.201500005.

26. Krishnamoorthy S, Noorani B, Xu C. Effects of encapsulated cells on the physical–mechanical properties and microstructure of gelatin methacrylate hydrogels. *Int J Mol Sci*. 2019;20(20):5061.
doi: 10.3390/ijms20205061.

27. Friedl P, Wolf K. Tumour-cell invasion and migration: diversity and escape mechanisms. *Nat Rev Cancer*. 2003;3(5):362-374.
doi: 10.1038/nrc1075.

28. Helmy IM, AbdelAzim AM. Efficacy of ImageJ in the assessment of apoptosis. *Diagn Pathol*. 2012;7(1):15.
doi: 10.1186/1746-1596-7-15.

29. Liu J, Xu C. Spatial distribution of encapsulated cells dramatically alters biomechanical properties and microstructure of 3D printed cellular structures. *J Manuf Processes*. 2024;120:1203-1212.
doi: 10.1016/j.jmapro.2024.05.029.

30. Figueiredo L, Leisage C, Weiss P, Yang J. Quantifying oxygen levels in 3D bioprinted cell-laden thick constructs with perfusable microchannel networks. *Polymers*. 2020;12(6):1260.
doi: 10.3390/polym12061260.

31. Radisic M, Malda J, Epping E, Geng W, Langer R, Vunjak-Novakovic G. Oxygen gradients correlate with cell density and cell viability in engineered cardiac tissue. *Biotechnol Bioeng*. 2006;93(2):332-343.
doi: 10.1002/bit.20722.

32. Novak CM, Horst EN, Taylor CC, Liu CZ, Mehta G. Fluid shear stress stimulates breast cancer cells to display invasive and chemoresistant phenotypes while upregulating PLAU in a 3D bioreactor. *Biotechnol Bioeng*. 2019; 116(11):3084-3097.
doi: 10.1002/bit.27119.

33. Helmlinger G, Yuan F, Dellian M, Jain RK. Interstitial pH and pO2 gradients in solid tumors in vivo: high-resolution measurements reveal a lack of correlation. *Nat Med*. 1997;3(2):177-182.
doi: 10.1038/nm0297-177.

34. Liverani C, De Vita A, Minardi S, *et al.* A biomimetic 3D model of hypoxia-driven cancer progression. *Sci Rep*. 2019;9(1):12263.
doi: 10.1038/s41598-019-48701-4.

35. Lewis DM, Park KM, Tang V, *et al.* Intratumoral oxygen gradients mediate sarcoma cell invasion. *Proc Natl Acad Sci USA*. 2016;113(33):9292-9297.
doi: 10.1073/pnas.1605317113.

36. Polacheck WJ, German AE, Mammoto A, Ingber DE, Kamm RD. Mechanotransduction of fluid stresses governs 3D cell migration. *Proc Natl Acad Sci USA*. 2014;111(7):2447-2452.
doi: 10.1073/pnas.1316848111.

37. Avraham-Chakim L, Elad D, Zaretsky U, Kloog Y, Jaffa A, Grisaru D. Fluid-flow induced wall shear stress and epithelial ovarian cancer peritoneal spreading. *PLoS One*. 2013;8(4):e60965.
doi: 10.1371/journal.pone.0060965.

38. Gilmore AC, Flaherty SJ, Somasundaram V, *et al.* An in vitro tumorigenesis model based on live-cell-generated oxygen and nutrient gradients. *Commun Biol*. 2021;4(1):477.
doi: 10.1038/s42003-021-01954-0.

39. Chen Z, Han F, Du Y, Shi H, Zhou W. Hypoxic microenvironment in cancer: molecular mechanisms

and therapeutic interventions. *Signal Trans Targeted Ther.* 2023;8(1):70.
doi: 10.1038/s41392-023-01332-8.

40. Pasini A, Lovecchio J, Cortesi M, *et al.* Perfusion flow enhances viability and migratory phenotype in 3D-cultured breast cancer cells. *Ann Biomed Eng.* 2021;49(9):2103-2113.
doi: 10.1007/s10439-021-02727-w.

41. Worsley CM, Veale RB, Mayne ES. The acidic tumour microenvironment: manipulating the immune response to elicit escape. *Hum Immunol.* 2022;83(5):399-408.
doi: 10.1016/j.humimm.2022.01.014.

42. Tannock IF. Oxygen diffusion and the distribution of cellular radiosensitivity in tumours. *Br J Radiol.* 1972;45(535):515-524.
doi: 10.1259/0007-1285-45-535-515.

43. Ayuso JM, Virumbrales-Munoz M, McMinn PH, *et al.* Tumor-on-a-chip: a microfluidic model to study cell response to environmental gradients. *Lab Chip.* 2019;19(20):3461-3471.
doi: 10.1039/c9lc00270g.

44. Lee D, Jeong HS, Hwang SY, Lee YG, Kang YJ. ABCB1 confers resistance to carboplatin by accumulating stem-like cells in the G2/M phase of the cell cycle in p53null ovarian cancer. *Cell Death Discov.* 2025;11(1):132.
doi: 10.1038/s41420-025-02435-7.

45. Alhalhooly L, Mamnoon B, Kim J, Mallik S, Choi Y. Dynamic cellular biomechanics in responses to chemotherapeutic drug in hypoxia probed by atomic force spectroscopy. *Oncotarget.* 2021;12(12):1165.
doi: 10.18632/oncotarget.27974.

46. Povea-Cabello S, Oropesa-Ávila M, De la Cruz-Ojeda P, *et al.* Dynamic reorganization of the cytoskeleton during apoptosis: the two coffins hypothesis. *Int J Mol Sci.* 2017;18(11):2393.
doi: 10.3390/ijms18112393.

47. He PJ, Ge RF, Mao WJ, *et al.* Oxidative stress induced by carboplatin promotes apoptosis and inhibits migration of HN-3 cells. *Oncol Lett.* 2018;16(6):7131-7138.
doi: 10.3892/ol.2018.9563.

48. Alamdari SG, Mohammadzadeh R, Amini M, *et al.* Improvement of carboplatin chemosensitivity in lung cancer cells by siRNA-mediated downregulation of DLGAP1-AS2 expression. *Sci Rep.* 2025; 15(1):7971.
doi: 10.1038/s41598-025-87649-6.

49. Vaidžiulytė K, Macé AS, Battistella A, Beng W, Schauer K, Coppey M. Persistent cell migration emerges from a coupling between protrusion dynamics and polarized trafficking. *Elife.* 2022;11:e69229.
doi: 10.7554/eLife.69229.

50. Shields JD, Fleury ME, Yong C, *et al.* Autologous chemotaxis as a mechanism of tumor cell homing to lymphatics via interstitial flow and autocrine CCR7 signaling. *Cancer Cell.* 2007;11(6):526-538.
doi: 10.1016/j.ccr.2007.04.020.

51. Waldeland JO, Evje S. Competing tumor cell migration mechanisms caused by interstitial fluid flow. *J Biomech.* 2018;81:22-35.
doi: 10.1016/j.jbiomech.2018.09.011.

52. Nath S, Pigula M, Khan AP, *et al.* Flow-induced shear stress confers resistance to carboplatin in an adherent three-dimensional model for ovarian cancer: a role for EGFR-targeted photoimmunotherapy informed by physical stress. *J Clin Med.* 2020;9(4):924.
doi: 10.3390/jcm9040924.

53. Banerji U, Sain N, Sharp SY, *et al.* An in vitro and in vivo study of the combination of the heat shock protein inhibitor 17-allylamino-17-demethoxygeldanamycin and carboplatin in human ovarian cancer models. *Cancer Chemother Pharmacol.* 2008;62(5):769-778.
doi: 10.1007/s00280-007-0662-x.

54. Sousa GFD, Wlodarczyk SR, Monteiro G. Carboplatin: molecular mechanisms of action associated with chemoresistance. *Braz J Pharm Sci.* 2014;50(4):693-701.
doi: 10.1590/S1984-82502014000400004.

55. Patra B, Lateef MA, Brodeur MN, *et al.* Carboplatin sensitivity in epithelial ovarian cancer cell lines: the impact of model systems. *PLoS One.* 2020;15(12):e0244549.
doi: 10.1371/journal.pone.0244549.

56. Lieberthal TJ, Sahakyants T, Szabo-Wexler NR, *et al.* Implantable 3D printed hydrogels with intrinsic channels for liver tissue engineering. *Proc Natl Acad Sci U S A.* 2024;121(47):e2403322121.
doi: 10.1073/pnas.2403322121.

57. Zhang N, Qavi I, Halder S, Tan G. Biomimetic hydrogel scaffolds embedded with porous microtubes as perfusion channels. *Manuf Lett.* 2023;35:184-193.
doi: 10.1016/j.mfglet.2023.08.009.

58. Grebenyuk S, Abdel Fattah AR, Kumar M, *et al.* Large-scale perfused tissues via synthetic 3D soft microfluidics. *Nat Commun.* 2023;14(1):193.
doi: 10.1038/s41467-022-35619-1.

59. Blanco-Fernandez B, Gaspar VM, Engel E, Mano JF. Proteinaceous hydrogels for bioengineering advanced 3D tumor models. *Adv Sci (Weinh).* 2021;8(4):2003129.
doi: 10.1002/advs.202003129

60. Zhu M, Wang Y, Ferracci G, Zheng J, Cho NJ, Lee BH. Gelatin methacryloyl and its hydrogels with an exceptional degree of controllability and batch-to-batch consistency. *Sci Rep.* 2019;9(1):6863.
doi: 10.1038/s41598-019-42186-x

61. Didwischus N, Guduru A, Badylak SF, Modo M. In vitro dose-dependent effects of matrix metalloproteinases on ECM hydrogel biodegradation. *Acta Biomater.* 2024;174:104-115.

doi: 10.1016/j.actbio.2023₹.12.003

62. Saggioro M, D'Agostino S, Veltri G, *et al.* A perfusion-based three-dimensional cell culture system to model alveolar rhabdomyosarcoma pathological features. *Sci Rep*. 2023;13(1):9444.
doi: 10.1038/s41598-023-36210-4

63. Huang Q, Hu X, He W, *et al.* Fluid shear stress and tumor metastasis. *Am J Cancer Res*. 2018;8(5):763-775.

64. Marrella A, Varani G, Aiello M, *et al.* 3D fluid-dynamic ovarian cancer model resembling systemic drug administration for efficacy assay. *Altex*. 2021;38(1):82-94.
doi: 10.14573/altex.2003131

ACCSCIENCE PUBLISHING

International Journal of Bioprinting

RESEARCH ARTICLE

Bioprinting vascularized human islet tissue models via aggregate-based co-culture and self-assembly

Yijun Su[1,2†], Supeng Ding[2,3†], Tiankun Liu[2], Yongyong Zhou[2], Yinying Lu[1,2], Feng Lin[1], Mingen Xu[4*], and Rui Yao[1,2,5*]

[1]Biomanufacturing and Rapid Forming Technology Key Laboratory of Beijing, Department of Mechanical Engineering, School of Mechanical Engineering, Tsinghua University, Beijing, China

[2]Human Organ Physiopathology Emulation System, Institute of Zoology, Chinese Academy of Sciences, Beijing, China

[3]Department of Materials Science and Engineering, Institute for Nanobiotechnology, Johns Hopkins University, Baltimore, MD, United States

[4]Key Laboratory of Medical Information and 3D Bioprinting of Zhejiang, School of Automation, Hangzhou Dianzi University, Hangzhou, Zhejiang, China

[5]Beijing Institute for Stem Cell and Regenerative Medicine, Beijing, China

(This article belongs to the *Special Issue: 3D Bioprinting and Stem Cells for Human Tissue Reconstruction*)

Abstract

Diabetes is a significant global metabolic disease. Current treatments, including islet or pancreas transplantation and insulin therapy, are limited by donor shortages and suboptimal glycemic control. Islet organoids, three-dimensional (3D) cell aggregates that mimic pancreatic islets, offer a powerful tool for diabetes research, drug screening, and transplantation therapies. However, challenges remain in engineering methods for the scalable preparation of human islet organoids (hIOs) with homogeneous consistency and controllable incorporation of vascular elements. In this study, we developed a novel bioengineering approach for the stable production of human islet tissue models with vascular elements using a combination of 3D bioprinting-based organoid co-culture and cell self-assembly principles. Human adipose-derived mesenchymal stem cells were differentiated into massive and uniform human islet β-like cell aggregates (hICAs) using an off-the-shelf polydimethylsiloxane user-defined micropatterning platform system. A tri-module thermal-controlled bioprinting process employing a gelatin–alginate–Matrigel bioink was used for the 3D bioprinting of hICAs and human umbilical vein endothelial cells (HUVECs). Compared with bioprinted hICAs alone, co-bioprinted and co-cultured hICAs and HUVECs more effectively recapitulated the morphogenesis of human islet development, significantly upregulated the expression of pancreatic islet- and endothelial cell-related markers, and enhanced islet function, namely glucose-stimulated insulin secretion. Thus, the self-assembly of hICAs and HUVECs to form hIOs with vascular elements mimics natural human pancreatic islets and may promote functional maturity. Our method provides a scalable platform for generating vascularized aggregation-based tissue models, supporting studies of pancreatic development and diabetes therapy.

Keywords: Bioprinting; Human adipose-derived mesenchymal stem cells; Human islet tissue models; Islet β-like cell aggregates

†These authors contributed equally to this work.

***Corresponding authors:**
Rui Yao (yaorui@ioz.ac.cn)

Mingen Xu (xumingen@hdu.edu.cn)

Citation: Su Y, Ding S, Liu T, *et al.* Bioprinting vascularized human islet tissue models via aggregate-based co-culture and self-assembly. *Int J Bioprint*. 2025;11(6):279-297. doi: 10.36922/IJB025360368

Received: September 6, 2025
Revised: October 1, 2025
Accepted: October 2, 2025
Published online: October 7, 2025

Copyright: © 2025 Author(s). This is an Open Access article distributed under the terms of the Creative Commons Attribution License, permitting distribution, and reproduction in any medium, provided the original work is properly cited.

Publisher's Note: AccScience Publishing remains neutral with regard to jurisdictional claims in published maps and institutional affiliations.

1. Introduction

Diabetes is a global health crisis that affects approximately 540 million adults worldwide, posing significant socioeconomic challenges.[1] Current treatments, such as insulin (INS) therapy and islet or pancreas transplantation, offer varying degrees of success but have limitations, including a shortage of donor tissues, the risk of immune rejection, and suboptimal glycemic control.[2] Recently, human islet organoids (hIOs) have emerged as an alternative to address these challenges. Islet organoids are three-dimensional (3D) cell aggregates that closely resemble pancreatic islets, consisting of INS-producing β-cells and stromal cell types.[3] Their advantages include the capacity to model islet development and function *in vitro*, as well as reduced dependence on donor islets for transplantation, making them highly promising for diabetes research, drug screening, and transplantation therapies.[3,4]

Generating hIOs from embryonic stem cells (ESCs) and induced pluripotent stem cells (iPSCs) has shown great promise in mimicking pancreatic islet functions. However, several limitations hinder their large-scale application.[5,6] ESCs raise ethical concerns since they are derived from human embryos, which creates regulatory challenges. Additionally, both ESCs and iPSCs require complex differentiation protocols, which are prone to variability, leading to inconsistent phenotypes and functions, as well as the risk of tumorigenicity due to residual undifferentiated cells. Moreover, the production scale is limited due to the costly, labor-intensive, and time-consuming nature of these differentiation processes, making it challenging to meet research and clinical demands.[7] In contrast, human adipose-derived mesenchymal stem cells (hADSCs) offer a compelling alternative. hADSCs are mesenchymal stem cells derived from adipose tissue. They are abundant, exhibit low immunogenicity, and possess the potential for mesenchymal lineage differentiation, with significant implications for regenerative medicine.[8] Previous studies have shown that hADSCs can differentiate into INS-producing β-like cells under planar culture conditions, positioning them as a viable candidate for producing functional hIOs on a larger scale.[9,10]

The production of human islet tissue models is constrained not only by the cell source but also by the need to create a complex microenvironment that allows adequate mass transfer. Bioprinting has emerged as a promising technique for creating 3D microenvironments in which extracellular matrix-mimicking hydrogels and cellular components, such as cells, cell aggregates, and organoids, can be spatially positioned.[11,12] Previous studies have demonstrated that 3D bioprinting effectively supports cell-aggregate integrity, spatial organization, and the functional maturation of islets derived from various cell sources, including primary human islets[13] and ESC-derived[14] and iPSC-derived[15] islet-like cell aggregates. While these studies enhanced matrix complexity through bioprinting, they typically focused on a single cell type, namely β-cells, and thus lacked the multicellular characteristics of actual islet tissues. This is particularly important because islet tissues are highly vascularized. Recent research has highlighted the importance of endothelial-derived signals in enhancing the viability and function of insulin-producing cells in bioprinted co-culture models.[16,17] However, due to the technical challenges associated with bioprinting multiple cell types and cell aggregates, current co-bioprinting methods are still limited to single-cell-based formats and have not yet succeeded in the scalable preparation of functional human islet tissue models that incorporate vascular elements in a controlled manner.

In this study, we propose a systematic solution that involves the stepwise preparation of large-scale, uniform cell aggregates and the precise regulation of cell-printing technology to create human islet tissue models featuring multicellular crosstalk and islet functionality similar to that of natural islets. To enable large-scale generation of uniform cell aggregates, we developed an off-the-shelf polydimethylsiloxane (PDMS) user-defined micropatterning platform (PUMP). This system incorporates micro-engineered microwells shaped like inverted pyramids, which possess favorable mechanical properties. Upon differentiation of hADSCs, the PUMP system successfully generated large numbers of human islet β-like cell aggregates (hICAs). The hICAs formed in the PUMP system displayed a more uniform size distribution, enhanced expression of pancreatic islet marker genes, and reduced expression of stemness marker genes compared to those generated by planar culture and the AggreWell plate, a commonly used commercial cell-aggregation platform.

To incorporate vascular elements, we propose a tri-module thermally controlled bioprinting method utilizing an optimized ternary gelatin–alginate–Matrigel bioink. This method enables the bioprinting of hICAs alongside human umbilical vein endothelial cells (HUVECs) into co-culture tissue models. After 5 days of culture following bioprinting, HUVECs migrated and enveloped the surface of the hICAs, forming an endothelial layer and resulting in hIOs that included vascular elements, indicating self-assembly and multicellular crosstalk. In comparison to the bioprinted hICAs alone, the co-cultured hIOs exhibited significantly increased expression of islet-marker genes and enhanced islet functionality, including adequate glucose-stimulated INS secretion (GSIS) (Figure 1). This study presents a novel approach for generating large-scale

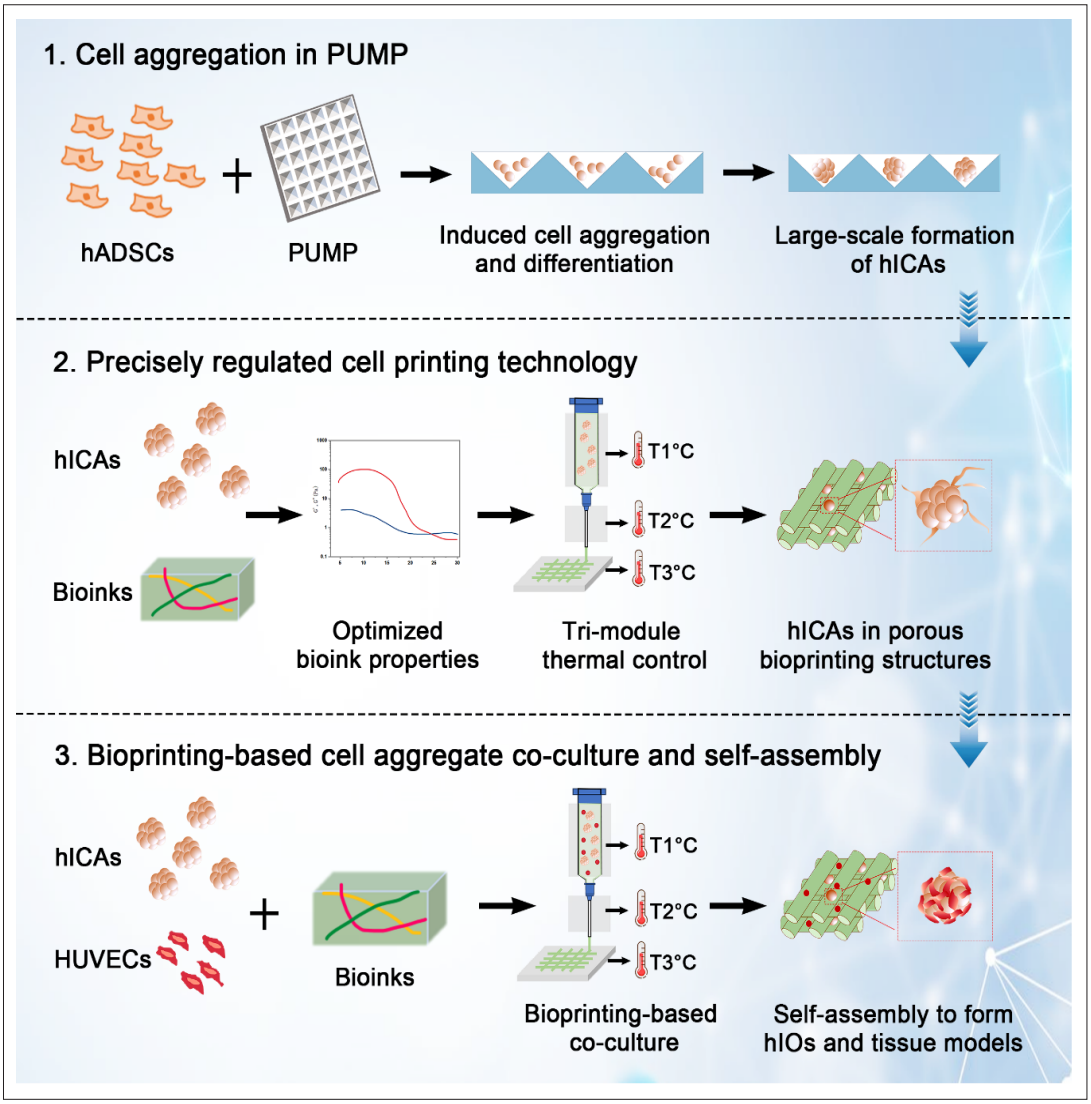

Figure 1. Schematic diagram of the study. Abbreviations: hADSC, human adipose-derived stem cell; hICA, human islet β-like cell aggregate; hIO, human islet organoid; HUVEC, human umbilical vein endothelial cells; PUMP, polydimethylsiloxane user-defined micropatterning platform.

human islet models that facilitate vascular integration and enhanced tissue function, thereby advancing diabetes research and paving the way for engineered therapeutic islet transplants.

2. Materials and methods

2.1. Solution preparation

Human adipose-derived stem cell–islet β-cell differentiation medium, sodium alginate working solution, and gelatin working solution were prepared as follows:

(i) hADSC–islet β-cell differentiation medium: The medium was optimized based on the protocol by Dave *et al.*[10] Briefly, the differentiation medium consisted of Dulbecco's Modified Eagle Medium (DMEM; Gibco, USA) and DMEM/F-12 medium (Gibco, USA) mixed at 1:1 (v/v) ratio, supplemented with 2% B-27 supplement (Gibco, USA), 1% N-2 supplement (Gibco, USA), 10 mM nicotinamide (Sigma-Aldrich, USA), 2 nM human activin A (R&D Systems, USA), 10 nM exendin-4 (Sigma-Aldrich, USA), 10 nM pentagastrin (Sigma-Aldrich, USA), 100 pM human hepatocyte growth factor (R&D Systems, USA), and 1% penicillin–streptomycin (Solarbio, China).

Sodium alginate working solution (4% [w/v]): Sodium alginate powder (Sigma-Aldrich, USA) was dissolved in the 0.9% sodium chloride (NaCl; Sigma-

Aldrich, USA) solution. The solution was heated at 80°C for 3 h, followed by stirring at 750 rpm for 1 h at 37°C on a magnetic stirrer (MS-H340-S4, DLAB, China). The heating and stirring process was repeated three times, with the final stirring conducted overnight. The solution was then filtered through 0.45 μm filter membranes to yield a 4% sodium alginate working solution and stored at 4°C.

(ii) Gelatin working solution (15% [w/v]): Gelatin powder (Sigma-Aldrich, USA) was dissolved in the 0.9% NaCl solution. The solution was heated at 80°C for 3 h, followed by stirring at 750 rpm for 1 h at 37°C on a magnetic stirrer. The heating and stirring process was repeated three times. Then, the 15% gelatin working solution was stored at 4°C.

2.2. Polydimethylsiloxane user-defined micropatterning platform production and characterization

A silicon wafer was constructed with an inverted tetrahedron micropattern array as the original mold by wet-chemical etching. Polymethylmethacrylate (PMMA) hot pressing was performed on the silicon wafer using a hot press machine (WY-30T, Dongguan Weiying Machinery, China). PMMA was preheated at 150°C for 3 min, press-heated at 150°C and 500 psi for 10 min, and annealed while maintaining pressure. Different combinations of pressure (e.g., 300, 500, and 700 psi) and temperature (e.g., 100, 125, 150, and 175°C) were tested to determine the optimal parameters. The PMMA template was demolded mechanically from the silicon wafer. PDMS (DOWSIL, USA) was prepared by mixing the base component with the curing agent at a 10:1 (w/w) ratio. PDMS was cured on the PMMA template at 70°C for 80 min, forming the corresponding micropattern. Different curing times (e.g., 40, 60, 80, and 100 min) and temperatures (e.g., 60, 70, and 80°C) were tested to identify the optimal conditions. The PDMS micropatterns were then cut into circular inserts with a diameter of 1.5 mm and fitted into 24-well plates to form the PUMP system. The PUMP was sterilized before cell culture.

The stiffness of the PDMS was measured using uniaxial compression on a disk-shaped sample (1.3 mm thickness, 6 mm radius) prepared with the same composition as the PUMP, while a polystyrene sample served as a control, representing the AggreWell plate (STEMCELL Technologies, Canada).

The silicon wafer, PMMA stamp, and PDMS insert were coated with gold to enhance their electrical conductivity. Samples were imaged using a field emission scanning electron microscope (FE-SEM; JEOL JSM-7001, JEOL, Japan) with an accelerating voltage of 20.0 kV. The surface microstructure of the PDMS inserts was observed using a LEXT OLS4100 3D laser measuring microscope (Olympus, Japan), and microwell depth was measured.

2.3. Cell culture and differentiation on petri dishes, AggreWell plates, and polydimethylsiloxane user-defined micropatterning platform.

Human adipose-derived stem cell proliferation was performed by culturing hADSCs (Sciencell, USA) in mesenchymal stem cell medium (Sciencell, USA) in T75 culture flasks coated with 0.01 mg/mL poly-L-lysine solution (Sigma-Aldrich, USA) at 37°C in a humidified incubator with 5% CO_2. The medium was changed every 2 days. After the cells reached 90% confluence, the cells were digested using 0.25% trypsin-ethylenediaminetetraacetic acid (EDTA) (Gibco, USA) and passaged at a 1:3 ratio. In this study, hADSCs at passage four were used for subsequent experiments.

HUVEC proliferation was performed by culturing HUVECs (Peking Union Cell Resource Center, China) in endothelial basal medium-2 (EBM-2; LONZA, Switzerland) in T75 culture flasks at 37°C in a humidified incubator with 5% CO_2. The medium was changed daily. After the cells reached 90% confluence, the cells were digested using 0.25% trypsin-EDTA and passaged at a 1:2 ratio. HUVECs at passage four were used for subsequent experiments.

Differentiation of hICAs from hADSCs on petri dishes was performed by culturing hADSCs in hADSC–islet β-cell differentiation medium at a density of 1×10^5 cells/cm^2 for 5 days. The medium was changed every 2 days. PUMP inserts were coated with 1% Pluronic F127 (Sigma-Aldrich, USA), centrifuged at 3000 rpm for 5 min, and treated for 1 h. Then, hADSCs were seeded on treated PUMP inserts at densities of 0.8×10^5, 2.1×10^5, and 4.2×10^5 cells/cm^2 (equivalent to 200, 500, and 1000 cells per microwell, respectively) and centrifuged at 850 rpm for 3 min. Cells were cultured in hADSC–islet β-cell differentiation medium for 5 days, with half-medium changes every 2 days.

A parallel experiment was conducted on AggreWell plates using the same process. Cell densities were 1.2×10^5, 3.0×10^5, and 6.0×10^5 cells/cm^2, equivalent to 200, 500, and 1000 cells per microwell, respectively. The morphology and size of hICAs were monitored during the differentiation process. hICAs seeded at 4×10^5 cells/cm^2 on day 5 were collected for subsequent experiments.

All cells were observed and imaged using an optical microscope (Nikon, Japan). Image analysis was performed using ImageJ Pro 6.0 (National Institute of Health, USA).

2.4. Rheological testing of the bioinks

The bioinks were prepared by mixing gelatin working solution, sodium alginate working solution, Matrigel (Corning, USA), and DMEM to obtain a final concentration of 3.75% gelatin, 1% alginate, and 0.23% Matrigel, unless otherwise specified. The rheological properties were measured using a rotational rheometer (Anton Paar, Austria) with a cone-plate measuring sensor (diameter = 25 mm; cone angle = 1.99°; section = 99 μm). In oscillatory mode, the storage modules (G') and loss modulus (G") of uncrosslinked bioinks were recorded as functions of temperature at a strain of 0.1% and a frequency of 1 Hz. The temperature varied between 4 and 37°C at a rate of 2°C/min to replicate the heating and cooling process.

To further evaluate the rheological properties of crosslinked bioinks, the bioinks were crosslinked with 300 mM calcium chloride ($CaCl_2$; Sigma-Aldrich, USA) for 3 min, and the G' and G" were measured at a strain of 0.1% and a frequency of 1 Hz at 8, 15, and 22°C. In viscosity curve mode, the viscosity of uncrosslinked bioinks was measured over a shear rate scan range of 0.1–1000/s to assess shear-thinning properties.

2.5. Scanning electron microscopy of crosslinked bioinks

The crosslinked bioinks were lyophilized using a vacuum lyophilizer (Beijing Songyuanhuaxing Technology Development, China) for 3 days to maintain the microstructure, and then coated with gold to enhance their electrical conductivity. The samples were imaged using a FE-SEM operated at an accelerating voltage of 20.0 kV.

2.6. Three-dimensional bioprinting

For the 3D bioprinting of hICAs, the following procedure was performed. hICAs at day 5 in PUMP were harvested, centrifuged at 500 rpm for 1 min to collect aggregates, and resuspended in hADSC–islet β-cell differentiation medium at 6000 aggregates/mL (equivalent to 6×10^6 cells/mL). The hICA suspension was first mixed with the sodium alginate working solution at room temperature. The mixture was then combined with Matrigel on ice and incubated at 37°C for 5 min. Subsequently, the hICA–alginate–Matrigel mixture was mixed with the gelatin working solution to achieve a final bioink containing 3.75% gelatin, 1% alginate, and 0.23% Matrigel, with a cell aggregate density of 1200 aggregates/mL (equivalent to 1.2×10^6 cells/mL).

The hICA-laden bioink was printed using a 3D bioprinter (Regenovo Biotechnology Co., Ltd., China) with 25G needles (250 μm) onto 35-mm petri dishes precoated with 0.00125% poly-L-lysine under tri-module or dual-module thermal control. In tri-module bioprinting, the chamber was set to 8, 15, or 22°C, the printing nozzle was set to 1°C lower than the chamber, and the cooling plate was set to 12°C. Dual-module bioprinting used the same chamber and cooling plate temperature settings without nozzle temperature control. The printed six-layer structures were immediately crosslinked by adding 300 mM $CaCl_2$ for 3 min. The printed structures were cultured in hADSC–islet β-cell differentiation medium for 5 days, with the medium changed every 2 days.

For the 3D bioprinting of hICAs and HUVECs, the following steps were performed. HUVECs were harvested and resuspended at 4×10^6 cells/mL in EBM-2 medium. hICAs were harvested and centrifuged as described above, then resuspended at 12,000 aggregates/mL (equivalent to 1.2×10^7 cells/mL) in Hadsc–islet β-cell differentiation medium. After harvesting the hICAs from PUMP, several hICAs were picked and digested into single cells with 0.25% trypsin–EDTA to determine cell numbers. The hICA suspension and HUVEC suspension were then mixed at a 1:1 ratio to prepare the final cell suspension. The cell-laden bioink was prepared using the same method described above, with a final islet-like cell density of 1.2×10^6 cells/mL and HUVEC density of 4×10^5 cells/mL. The bioink was printed at 15°C using the same bioprinting method. The printed structures were cultured in a mixed medium composed of hADSC–islet β-cell differentiation medium and EBM-2 culture medium (1:1) for 5 days, with the medium changed every 2 days.

2.7. Live/dead staining

The live/dead staining solution contained 0.2% calcein–acetoxymethyl ester (Calcein-AM) and 0.3% propidium iodide (PI) (C542, Calcein-AM/PI Double Staining Kit, Donjindo, Japan) in phosphate-buffered saline (PBS). The cell-laden structures after bioprinting were incubated in the live/dead staining solution at room temperature for 10 min, followed by incubation in PBS for 10 min. The stained structures were then imaged using a confocal microscope (Nikon, Japan). As it was difficult to quantify cell numbers in aggregates, cell viability was evaluated by calculating the ratio of dead to live cell signal intensity from three different regions of the structures using the same imaging parameters.

2.8. Immunofluorescence staining

Immunofluorescence staining was performed on cells from planar differentiation, AggreWell plate differentiation, PUMP differentiation, and bioprinted structures on day 5. Primary antibodies included anti-PDX1 antibody (1:500; ab47383, Abcam, UK), anti-PAX6 antibody (1:50; ab5790, Abcam, UK), anti-Islet 1 (ISL1) antibody (1:200; ab86472, Abcam, UK), anti-INS antibody (1:50; ab7842, Abcam, UK), and anti-CD31 antibody (1:200; ab32457, Abcam, UK). The corresponding secondary antibodies

were used at a dilution of 1:1000, including donkey anti-goat IgG (ab150131, Abcam, UK), goat anti-mouse IgG (ab150077, Abcam, UK), goat anti-mouse IgG (ab150115, Abcam, UK), goat anti-guinea pig IgG (ab150185, Abcam, UK), and donkey anti-rabbit IgG (ab150073, Abcam, UK). Nuclei were stained with 4',6-diamidino-2-phenylindole (1 μg/mL; Invitrogen, USA).

The staining procedure was as follows: samples were washed with PBS for 5 min. Then, samples were fixed with 4% paraformaldehyde at 25°C for 30 min, or with 2.5% glutaraldehyde for 4 h if the cells were embedded in the printed structure, followed by washing with PBS for 5 min. Samples were permeabilized with 0.25% Triton X-100 (Sigma-Aldrich, USA) for 20 min, and washed with PBS for 5 min. Samples were then blocked with 10% bovine serum albumin (BSA; Multicell, USA) at 25°C for 1 h, and washed with PBS for 5 min. Subsequently, the samples were incubated with primary antibodies prepared in 0.3% Triton X-100 and 1% BSA overnight at 4°C, and washed with PBS for 5 min. Then, the samples were incubated with the corresponding secondary antibodies for 2 h in the dark and washed with PBS for 5 min. Finally, the samples were stained with 1 μg/mL of 4',6-diamidino-2-phenylindole at room temperature for 15 min in the dark, and washed with PBS for 5 min before imaging using a NIKON Z2 confocal microscope. ImageJ software was used for image processing and quantitative analysis.

2.9. Real-time fluorescence quantitative reverse transcriptase polymerase chain reaction

Quantitative reverse transcriptase polymerase chain reaction assay was performed on cells from planar differentiation, AggreWell plate differentiation, PUMP differentiation, and bioprinted structures on day 5. Samples were washed with PBS for 5 min. Cells in the bioprinted structures were harvested by degrading the construct using a hydration solution (150 mM NaCl, 55 mM sodium citrate, and 20 mM EDTA) for 3 min, followed by termination with culture medium. The cells were lysed using TRIzol (Ambion, USA). For every 1 mL of TRIzol, 0.2 mL trichloromethane was added, the samples were thoroughly mixed, and incubated at room temperature for 10 min. The samples were centrifuged at 13,500 rpm at 4°C for 15 min. The upper aqueous phase was collected and mixed with an equal volume of isopropyl alcohol. The mixture was incubated on ice for 10 min. Then, the samples were centrifuged at 13,500 rpm at 4°C for 8 min, and the supernatant was removed. The RNA pellet was washed with 75% ethanol prepared in RNase-free double-distilled water.

Subsequently, the samples were centrifuged at 10,600 rpm at 4°C for 5 min, and the supernatant was removed. RNase-free double-distilled water was added to dissolve the RNA on ice. RNA concentration was measured using a NanoDrop 2000 spectrophotometer (Thermo Scientific, USA). Based on the RNA concentration and according to the manufacturer's instructions for the FastKing RT Kit (with gDNase) (TIANGEN Biotech, China), RNA reverse transcription was performed using a thermal cycler (T960, Heal Force, China). cDNA amplification was performed according to the manufacturer's instructions for the SuperReal PreMix Plus (SYBR Green) kit (TIANGEN Biotech, China). A real-time fluorescence quantitative polymerase chain reaction system (CFX96, Bio-Rad, USA) was used for signal detection. The primer sequences are listed in Table 1.

2.10. Glucose-stimulated insulin secretion assay

The INS secretion function of hICAs was assessed using a GSIS assay. Bioprinted structures were degraded using a hydration solution, and cell aggregates were harvested. The cell aggregates, hICAs or hIOs, were washed with PBS at least once, and then incubated in Krebs–Ringer bicarbonate buffer without glucose (10 mM 4-(2-hydroxyethyl)piperazine-1-ethanesulfonic acid, 25 mM sodium bicarbonate, 120 mM NaCl, 5 mM potassium chloride, 2.5 mM $CaCl_2$, 1.1 mM magnesium chloride, and 0.1% BSA) for 6 h. Cell aggregates were then incubated with Krebs–Ringer bicarbonate buffer containing 2.8 mM glucose for 1 h, followed by incubation with 16.7 mM glucose for 1 h. The supernatants from these two stages were collected separately. INS concentration was measured using a human INS enzyme-linked immunosorbent assay kit (SEKH-0219, Solarbio, China) according to the manufacturer's instructions. The ratio of INS content secreted at 16.7 mM glucose to that at 2.8 mM glucose was defined as the glucose stimulation index.

2.11. Statistical analysis

Data are presented as mean ± standard deviation or as range for quantitative analyses. The Statistical Package for Social Sciences version 24.0 (IBM, USA) was used to perform two-sided Student's *t*-tests, one-way analysis of variance (ANOVA), and two-way ANOVA with Bonferroni's multiple comparison test. A p-value < 0.05 was considered statistically significant.

3. Results and discussion

3.1. Fabrication and characterization of the polydimethylsiloxane user-defined micropatterning platform system

Pancreatic islets are clusters of cells that function more efficiently under 3D aggregation conditions. The formation of aggregates using micropatterning technology has become

Table 1. Primer sequences of tested genes

Primer	Forward sequence (5'–3')	Reverse sequence (3'–5')
CD31	AAGTGGAGTCCAGCCGCATATC	ATGGAGCAGGACAGGTTCAGTC
CD73	CTGATGATGGGCGGAAGGTT	ATCAATGGGCGACCGGATAC
CDH5	GAAGCCTCTGATTGGCACAGTG	TTTTGTGACTCGGAAGAACTGGC
HES1	GGAAATGACAGTGAAGCACCTCC	GAAGCGGGTCACCTCGTTCATG
INS	ACGAGGCTTCTTCTACACACCC	TCCACAATGCCACGCTTCTGCA
ISL1	GCAGAGTGACATAGATCAGCCTG	GCCTCAATAGGACTGGCTACCA
KDR	GGAACCTCACTATCCGCAGAGT	CCAAGTTCGTCTTTTCCTGGGC
NGN3	CCTAAGAGCGAGTTGGCACTGA	AGTGCCGAGTTGAGGTTGTGCA
NKX6-1	CCTATTCGTTGGGGATGACAGAG	TCTGTCTCCGAGTCCTGCTTCT
NOS3	GAAGGCGACAATCCTGTATGGC	TGTTCGAGGGACACCACGTCAT
PDX1	GAAGTCTACCAAAGCTCACGCG	GGAACTCCTTCTCCAGCTCTAG
SOX9	AGGAAGCTCGCGGACCAGTAC	GGTGGTCCTTCTTGTGCTGCAC
VWF	CCTTGAATCCCAGTGACCCTGA	GGTTCCGAGATGTCCTCCACAT
GAPDH	GTCTCCTCTGACTTCAACAGCG	ACCACCCTGTTGCTGTAGCCAA

Abbreviations: CD31, platelet endothelial cell adhesion molecule 1 gene (*PECAM1*); *CD73*, 5'-nucleotidase Ecto gene (*NT5E)*; *CDH5*, cadherin 5 gene; *GAPDH*, glyceraldehyde-3-phosphate dehydrogenase gene; *HES1*, Hes Family BHLH transcription factor 1 gene; *INS*, insulin gene; *ISL1*, islet 1 gene; *KDR*, kinase insert domain receptor gene; *NGN3*, neurogenin-3 gene; *NKX6-1*, NK6 homeobox 1 gene; *NOS3*, nitric oxide synthase 3 gene; *PDX1*, pancreatic and duodenal homeobox 1 gene; *SOX9*, SRY-box transcription factor 9 gene; *VWF*, von Willebrand factor gene.

a popular method due to its efficiency in producing large quantities of uniform cell aggregates.[18] Previous studies have shown that the geometry of microwells significantly influences the morphology of these aggregates, with V-shaped microwells promoting the formation of more uniform and compact structures.[19] Among the commercially available platforms, the AggreWell plate is a widely recognized V-shaped microwell array. However, it has several limitations, including fixed shapes, excessive substrate stiffness, high costs, and limited reusability. These challenges may hinder its versatility and reduce its appeal for diverse applications.

To address these challenges, we developed the PUMP system, which enables customization of microwell size, shape, and stiffness to meet various cell aggregation requirements. The PUMP fabrication process involved anisotropic wet etching of silicon wafers, hot pressing of PMMA, and curing and insertion of PDMS. This resulted in an inverted pyramid-shaped, V-angled PDMS micropatterning array (Figure 2A).

The dimensions of the micropatterns on the silicon wafer were determined by the mask design and etching parameters. To ensure accurate reproduction of the micropatterns, we assessed the processing conditions for PMMA hot pressing (Figure 2B) and PDMS curing (Figure 2C) to identify the optimal parameter combinations, indicated by gray circles. Using a square mask pattern with a side length of 490 μm and a spacing of 10 μm, we successfully produced densely packed V-shaped microwells with a side length of approximately 485 μm and a depth of about 352 μm, closely matching the intended geometry (Figure 2D & E).

Scanning electron microscopy and laser confocal scanning confirmed that fine structural features were preserved at both the tips and bases of the micropatterns throughout the manufacturing process, with a final tip angle of 70° replicating that of the silicon template (Figure 2D). To facilitate cell seeding and culture, the PDMS micropatterns were punched into cylindrical inserts with diameters of 1.1, 1.5, 2.3, and 3.4 cm, which fit into 48-well, 24-well, 12-well, and 6-well plates, resulting in approximately 400, 740, 1740, and 3810 micropatterns in each well, respectively. This method ensures reproducibility and versatility in the fabrication process, effectively preventing mold adhesion and topographic deformation, which are commonly associated with traditional PDMS casting techniques.[20]

Unlike the AggreWell plate, the PUMP substrate is composed of PDMS, a biocompatible elastomeric material. To evaluate its mechanical compliance, we conducted uniaxial compression tests to measure the Young's modulus of PDMS samples. In contrast to the rigid polystyrene substrate used in AggreWell plates, which has a Young's modulus of approximately 2.6 GPa, the PDMS in the PUMP system exhibited a significantly lower stiffness of approximately 2.0 MPa (Figure 2F). This

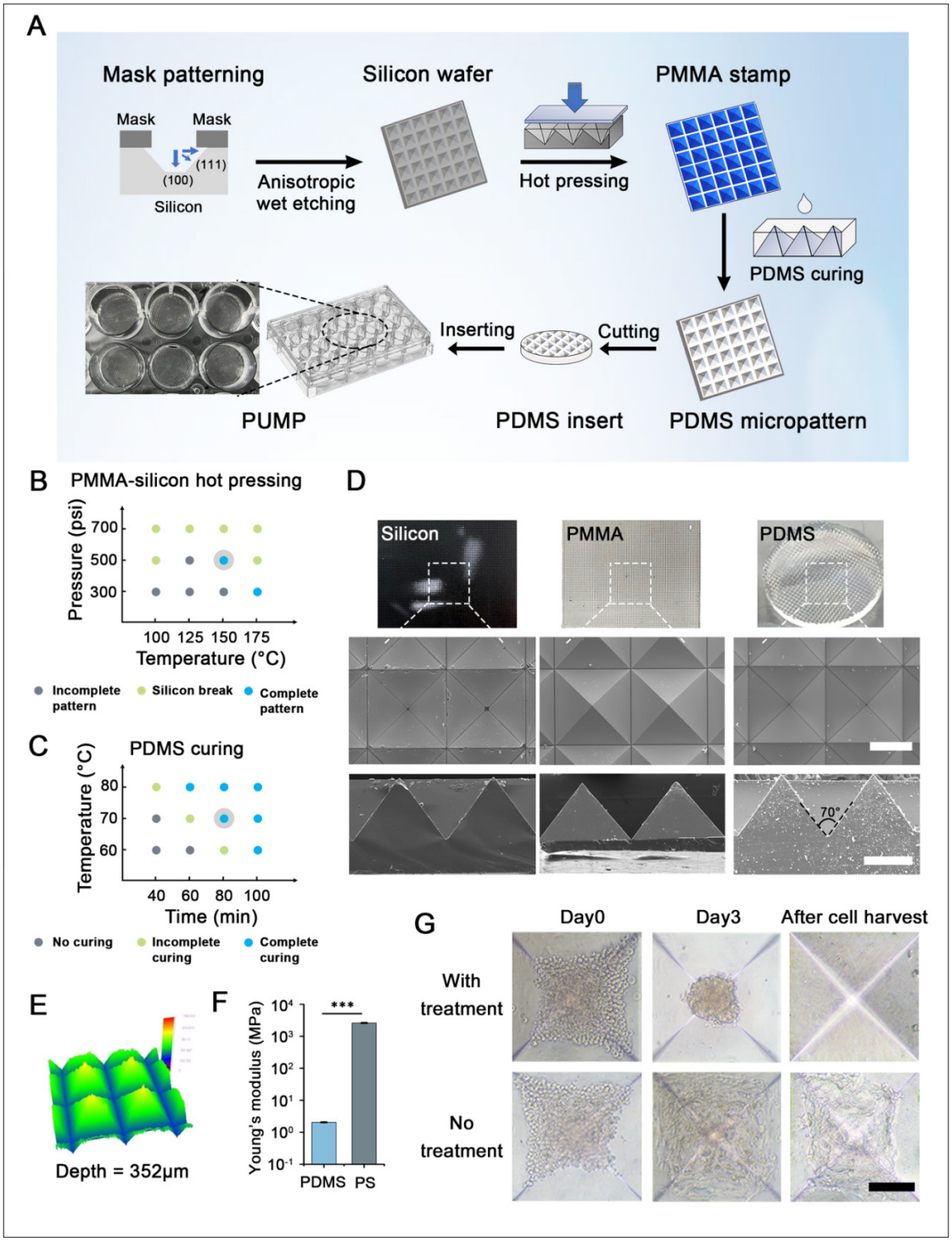

Figure 2. Fabrication and characterization of the PUMP system. (A) Schematic illustration of the fabrication process of the PUMP system. (B, C) Optimization of processing parameters for PMMA hot pressing (B) and PDMS curing (C), with grey circles indicating the optimized conditions used in subsequent experiments. (D) Macroscopic and scanning electron microscopy images of the silicon wafer, PMMA stamp, and PDMS micropattern (scale bar: 250 μm; magnification: 100×). (E) Quantitative analysis of PUMP microwell depth using a laser confocal scanning microscope. (F) Comparison of the Young's modulus of PDMS and PS, representing the substrate materials of the PUMP and AggreWell plates, respectively. (G) Representative images of human adipose-derived mesenchymal stem cells seeded and cultured in PUMP with and without Pluronic F127 treatment (scale bar: 150 μm; magnification: 100×). Statistical analysis was conducted using a two-sided Student's *t*-test. Triple asterisk (***) indicates statistical significance at $p < 0.001$. Abbreviations: PDMS, polydimethylsiloxane; PMMA, polymethylmethacrylate; PUMP, polydimethylsiloxane user-defined micropatterning platform; PS, polystyrene.

substantial reduction in stiffness, by nearly three orders of magnitude, may help minimize stress-induced cellular effects during culture.[21]

To assess cell clustering performance, we cultured hADSCs in the PUMP using a proliferative medium. With proper treatment using Pluronic F127, cell adhesion to the PUMP substrate was effectively prevented, allowing the rapid formation (within 24 h) of cell aggregates with smooth and well-defined contours. These aggregates can be easily harvested through gentle pipetting, leaving no detectable cell residues behind (Figure 2G). Additionally, the PUMP system demonstrated excellent reusability. A PMMA stamp can be reused for at least 50 fabrication cycles, while each PDMS insert can be reused four to five times without compromising cell aggregation efficiency or harvesting performance. This high durability highlights the economic advantages of the PUMP system for repeated applications.

In summary, the PUMP system provides a cost-effective, reusable, and highly customizable platform with user-defined micropatterning geometries and significantly reduced stiffness compared to commercial micropatterning systems. Collectively, these attributes make it a versatile tool for a wide range of cell culture and aggregation applications.

3.2. Large-scale generation of human islet β-like cell aggregates

hADSCs are a type of mesenchymal stem cell derived from human adipose tissue. Previous studies have shown that these cells exhibit strong proliferative capabilities and the potential to differentiate into various cell types, including islet-like cells.[9,22] Due to their accessibility through procedures such as liposuction or surgical fat excision, hADSCs are considered a promising source for autologous tissue engineering and broad clinical applications.

To evaluate the differentiation capacity of hADSCs, we conducted planar differentiation to generate islet β-like cells following an established protocol.[10] Over a 5-day differentiation period, we observed the formation of compact cell clusters with irregular shapes and considerable size variability (Figure 3A). The differentiated hADSCs expressed islet-related marker proteins, including PDX1, PAX6, ISL1, and INS (Figure 3B). Furthermore, the expression levels of islet-related marker genes—*PDX1*, *NGN3*, *ISL1*, *NKX6-1*, and *INS*—were upregulated by 2.8-fold, 6.1-fold, 7.3-fold, 1.8-fold, and 2.8-fold, respectively, with statistically significant differences compared to undifferentiated hADSCs (Figure 3C). These results confirm the ability of hADSCs to differentiate into a pancreatic islet β-cell lineage, consistent with previous studies.[9,22]

Additionally, we conducted islet β-cell differentiation of hADSCs within the PUMP system using the same differentiation cytokines as in planar culture, with AggreWell as a parallel control. To obtain cell aggregates of uniform and appropriate size, different cell seeding densities were tested, including 0.8×10^5, 2.1×10^5, and 4.2×10^5 cells/cm^2 (equivalent to 200, 500, and 1000 cells per microwell). From day 1, cells at all seeding densities rapidly formed tight clusters with smooth contours and showed no adhesion to the substrates in either system (Figure 4A). Throughout the 5-day culture period, both systems maintained relatively stable aggregate sizes, and no significant differences were observed in the aggregates formed from 500 and 1000 cells between the PUMP and AggreWell plates (Figure 4B & C).

Moreover, the size of cell aggregates on day 5 demonstrated a positive correlation with the initial cell seeding density. The cell aggregates had diameters of 92.8 ± 10.5 μm, 114.8 ± 12.6 μm, and 132.8 ± 10.4 μm, at initial cell seeding densities of 200, 500, and 1000 cells per microwell, respectively (Figure 4B). The diameters of hICAs derived from the PUMP system with 1000 cells per microwell were mainly between 120 and 140 μm, closely resembling the average islet diameter *in vivo* (approximately 120 μm). Thus, we selected a seeding density of 1000 cells per microwell, achieving large-scale production of approximately 15,000 hICAs per 24-well plate (Figure 4D). The size uniformity of the PUMP system is comparable to that of the AggreWell plates and is significantly improved compared with planar differentiation (Figure 4E). Furthermore, the aggregates in both the PUMP and AggreWell plates exhibited high viability (Figure 4F).

The findings revealed that hICAs from PUMP expressed islet-related markers, including *PDX1*, *PAX6*, *ISL1*, and *INS* (Figure 4G). The expression of *PDX1*, *NKX6-1*, *INS*, and the hADSC-specific gene *CD73* was quantitatively evaluated (Figure 4H). The expressions of *PDX1*, *NKX6-1*, and *INS* were upregulated by 1.22-fold, 1.23-fold, and 3.05-fold, respectively, with statistical significance compared to planar culture. In contrast, the expression of *CD73* was downregulated to 0.83-fold. When compared with AggreWell plates, the expression of *ISL1* and *NKX6-1* was upregulated by 2.67-fold and 1.33-fold, respectively, with statistical significance. However, the expression of *CD73* was downregulated to 0.72-fold (Figure 4I). These results indicate that the PUMP system facilitated islet β-cell differentiation of hADSCs more effectively than planar culture. This may be due to the PUMP system establishing a physiology-related culture environment compared to planar differentiation, where limited cell–cell interactions lead to proliferation inhibition rather than complex interactions. In addition, the PUMP also exhibited better

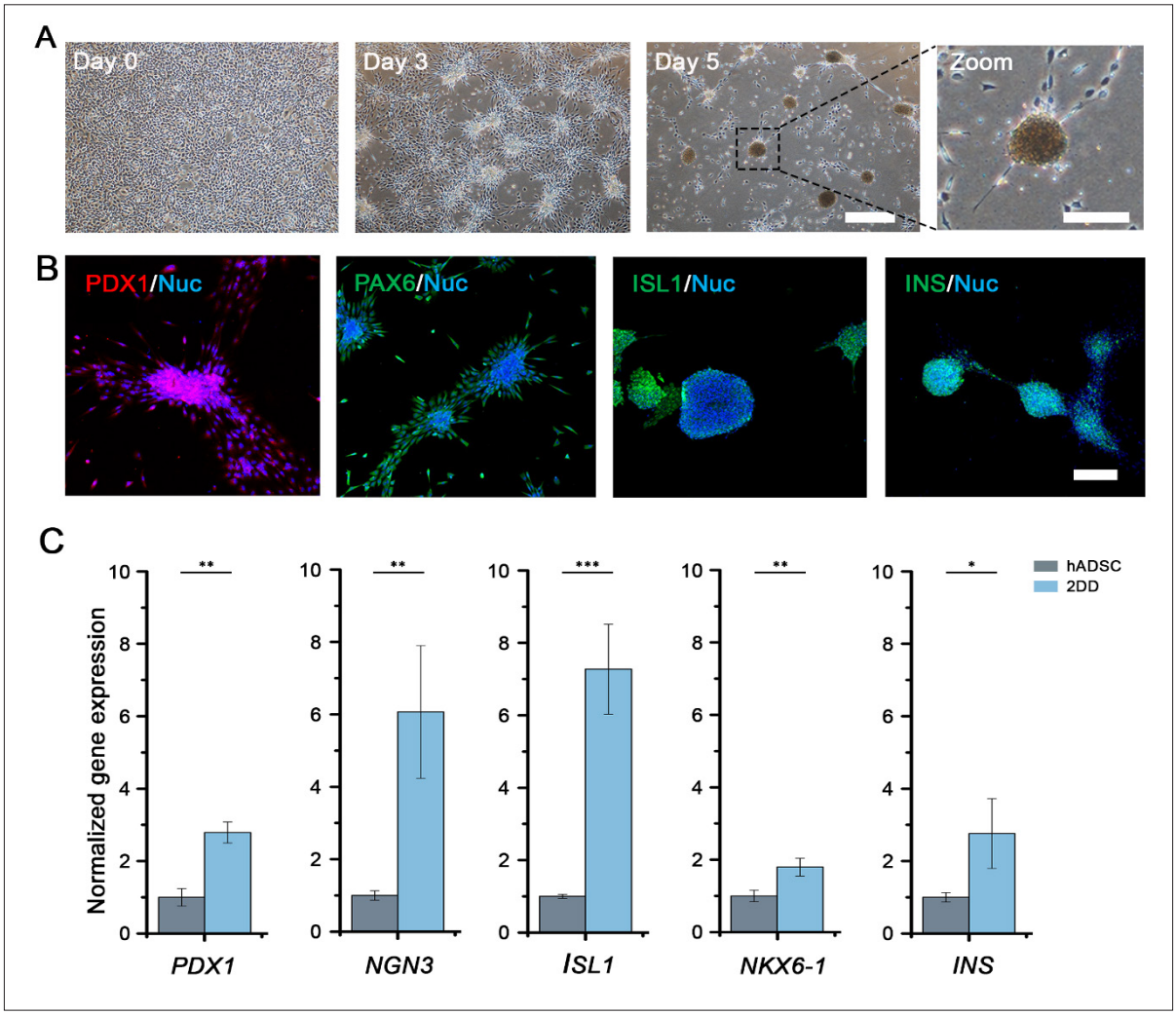

Figure 3. Planar differentiation of hADSCs into islet β-like cells. (A) Phase-contrast microscopy images during the 5-day planar differentiation process (scale bar: 500 μm; magnification:40×). (B) Immunofluorescence images of the cells after 5 days of planar differentiation (scale bar: 200 μm; magnification: 100×). (C) Relative gene expression of cells before (hADSCs) and after planar differentiation (2DD). Gene expression levels were normalized to hADSCs and are represented as $2^{-\Delta\Delta Ct}$ ($n = 3$). Statistical analysis was conducted using a two-sided Student's *t*-test. Single asterisk (*), double asterisk (**), and triple asterisk (***) indicate statistical significance at $p < 0.05$, $p < 0.01$, and $p < 0.001$, respectively. Abbreviations: 2DD, two-dimensional differentiation; hADSC, human adipose-derived mesenchymal stem cell; INS, insulin; ISL1, islet 1; NGN3, neurogenin-3; NKX6-1, NK6 homeobox 1; PAX6, paired box gene 6; PDX1, pancreatic and duodenal homeobox 1.

functionality in differentiating into the islet β-cell lineage compared with commercial AggreWell plates.

Taken together, these results demonstrate that the PUMP system can promote differentiation into hICAs more effectively compared with both planar differentiation and AggreWell plates. Although planar differentiation provides greater exposure of cells to soluble chemical factors, the uniform aggregate structure formed in the PUMP system may contribute to higher expression of islet-related genes. The improvement in hICAs' maturity from PUMP may be partially attributed to the lower stiffness of the culture environment. It has been reported that a high-stiffness environment can reduce *INS* expression,[23] and substrates with stiffness similar to that of the pancreas can help *in vitro* islet-like cells recapitulate the *in vivo* functions of islets.[24] In all, hICAs can be harvested from PUMP with uniform sizes and enhanced differentiation at a large scale, thereby satisfying the requirements for 3D bioprinting and the fabrication of hIOs in subsequent applications.

3.3. Optimization of tri-module bioprinting with ternary bioinks for aggregate bioprinting

A 3D culture environment provides structural, physical, and chemical cues for encapsulated aggregates, which are crucial for further differentiation and maturation.[25,26]

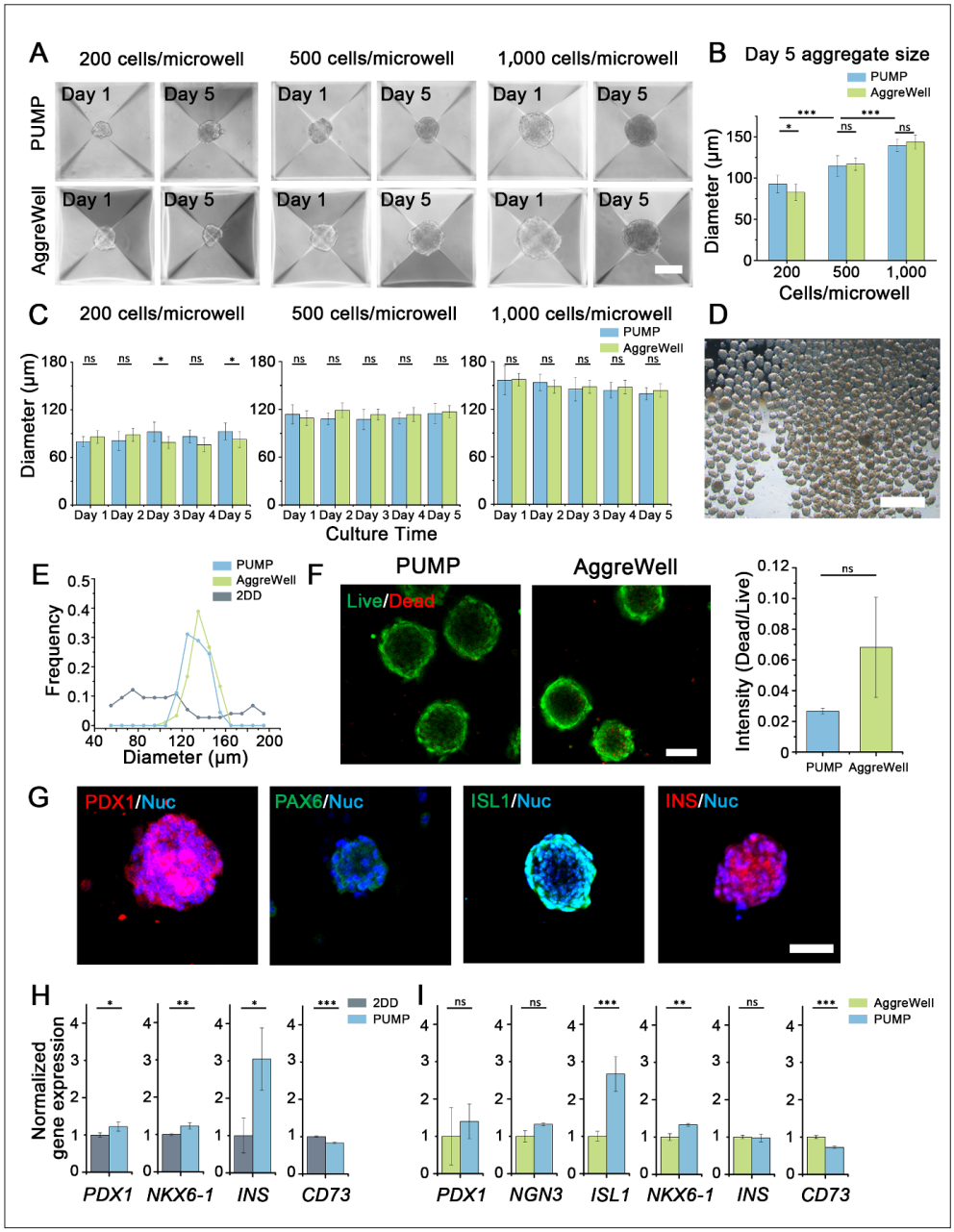

Figure 4. Generation and biological characterization of hICAs in PUMP. (A) Phase-contrast microscopy images of aggregates cultured in PUMP and AggreWell plates with 200, 500, or 1000 cells per microwell (scale bar: 100 μM; magnification: 100×). (B) Aggregate size in PUMP or AggreWell plates with 200, 500, and 1000 cells per microwell on day 5. (C) Changes in aggregate diameter during the 5-day differentiation in PUMP and AggreWell plates at 200, 500, and 1000 cells per microwell. (D) Morphology of hICAs harvested from PUMP on day 5 (scale bar: 500 μM; magnification: 40×). (E) Size distribution of aggregates generated from PUMP, AggreWell plates, and planar differentiation (2DD). (F) Viability assay of aggregates with 1000 cells per microwell on day 5 (scale bar: 50 μM; magnification: 200×). (G) Immunofluorescence images of differentiated cells expressing islet-related markers (PDX1, PAX6, ISL1, and INS) in hICAs derived from PUMP (scale bar: 50 μM; magnification: 200×). (H) Relative gene expression of islet-related markers (*PDX1*, *NKX6-1*, and *INS*) and the hADSC marker (*CD73*) in hICAs differentiated under planar culture (2DD) and PUMP. Gene expression levels were normalized to 2DD and presented as $2^{-\Delta\Delta Ct}$ ($n = 3$). (I) Relative gene expression of islet-related markers (*PDX1*, *NGN3*, *ISL1*, *NKX6-1*, and *INS*) and the hADSC marker (*CD73*) in hICAs differentiated using AggreWell plates and PUMP. Gene expression levels were normalized to AggreWell plates and presented as $2^{-\Delta\Delta Ct}$ ($n = 3$). Statistical analysis was conducted using two-way ANOVA with Bonferroni's multiple comparisons test (B and C) or two-sided Student's *t*-test (F, H, and I). Single asterisk (*), double asterisk (**), and triple asterisk (***) indicate statistical significance at $p < 0.05$, $p < 0.01$, and $p < 0.001$, respectively. "ns" denotes no statistical significance. Abbreviations: 2DD, two-dimensional differentiation; CD73, 5'-nucleotidase Ecto gene (*NT5E*); hADSC, human adipose-derived mesenchymal stem cell; hICA, human islet β-like cell aggregate; INS, insulin; ISL1, islet 1; NGN3, neurogenin-3; NKX6-1, NK6 homeobox 1; PAX6, paired box gene 6; PDX1, pancreatic and duodenal homeobox 1; PUMP, polydimethylsiloxane user-defined micropatterning platform.

However, given the avascular nature of hydrogels and aggregates, nutrient and oxygen diffusion can be a significant issue in supporting cell survival and function.[27] Therefore, we bioprinted hICA-embedded porous bioinks into a mesh structure (Figure 5A), where the spacing between filaments and the micropores within the bioinks may be compatible with long-range and short-range diffusion, respectively.

In addition to printability and biocompatibility, bioinks used for aggregate bioprinting require careful consideration of additional factors, including nozzle clogging, aggregate damage during printing, and the need for appropriate mechanical properties and mass transfer characteristics after printing. In this study, we developed a ternary bioink composed of gelatin, alginate, and Matrigel. In our previous work, a foundational combination of 3.75% gelatin and 1% alginate demonstrated good printability.[28,29] We further introduced Matrigel into the bioinks to mimic the extracellular matrix surrounding pancreatic islets[30] and to enhance the differentiation of pancreatic progenitor cells.[31] However, within the temperature range of 4–37°C, Matrigel accelerates crosslinking as the temperature increases, lacking a precise temperature transition point, which thereby increases the instability of the printing process.

In our preliminary experiment, diluted Matrigel at final concentrations of 0.08% and 0.23% remained uncrosslinked, whereas 0.4% Matrigel showed flocculation and uneven material distribution (Figure 5B). Thus, we adopted a composition of 3.75% gelatin, 1% alginate, and 0.23% Matrigel for the final bioink formulation, ensuring the highest possible biological content. The bioinks exhibited distinct rheological properties during the cooling and heating processes (Figure 5C). The gelling temperatures during cooling and heating were approximately 15 and 25°C, respectively. This indicates that the bioinks are printable with rapid solidification below 15°C, and that the printed structures remain temporarily stable under temperature fluctuations up to 25°C. Bioinks cooled to 8, 15, and 22°C exhibited shear-thinning properties, which is beneficial for bioprinting aggregates due to their reduced viscosity (Figure 5D). With subsequent alginate crosslinking, the bioinks crosslinked at 15°C exhibited a long-term shear storage modulus of 929 Pa and a loss modulus of 259 Pa, values that fall within the range of the healthy human pancreas (Figure 5E).[32] On the other hand, the bioinks crosslinked at 8°C showed a higher storage modulus than pancreatic tissue, while those at 22°C failed to crosslink.

Considering the temperature sensitivity of the bioinks during bioprinting, we developed a tri-module bioprinting strategy that allowed independent control of the printing chamber, printing nozzle, and cooling plate temperatures. At a chamber temperature of 15°C, the printed bioink maintained an intact mesh structure, both with and without cell aggregates. At 8°C, the printed bioink was over-crosslinked, resulting in broken and thinner filaments, whereas at 22°C, it was under-crosslinked and failed to form stable structures (Figure 5F). Therefore, 15°C was selected as the optimal temperature for the chamber. No significant change in filament width was observed after culturing the structures for 7 days, indicating the long-term stability of the bioprinted constructs (Figure 5G). SEM of the crosslinked bioink revealed a pore size of 49.4 μm, sufficient to allow cell migration and promote local mass transfer (Figure 5H). By optimizing both the bioink formulation and the printing parameters, we achieved suitable constructs for aggregate bioprinting, with composition and stiffness comparable to those of native pancreas tissues.

When applied to aggregate bioprinting, we initially observed heterogeneous aggregate distribution across different bioprinted structures (Figure 6A). This is because, before the bioink was extruded, its crosslinking status was not controlled without a well-defined nozzle temperature. As a result, the movement of aggregates was affected. Thus, we developed a tri-module bioprinting strategy with specific nozzle temperature control, achieving homogeneous aggregate distribution and high viability among 20 different structures during a single bioprinting process (Figure 6A & B).

3.4. Maintenance of islet-related marker expression in bioprinted human islet β-like cell aggregates

Based on the optimized ternary bioink composition and tri-module bioprinting strategy, we bioprinted the hICAs and evaluated their morphology and islet-related marker expression (Figure 7A). By day 5, obvious cell spreading was observed from hICAs, in contrast to the compact aggregates present on day 0 (Figure 7B). Immunofluorescence staining showed that hICAs remained positive for islet-related markers after 5 days of culture within the bioprinted structures, including *PDX1*, *PAX6*, *ISL1*, and *INS* (Figure 7C).

These findings suggest that our optimized bioinks provided a biomimetic extracellular matrix that supported the attachment and differentiation of hICA. However, the strong matrix–cell interaction also induced the disassembly of several aggregates, indicating a lack of intercellular signaling necessary to maintain hICA's structural integrity. In this study, hICAs did not include endothelial cells, as differentiation was restricted to the endocrine β-lineage from hADSCs. This highlights the

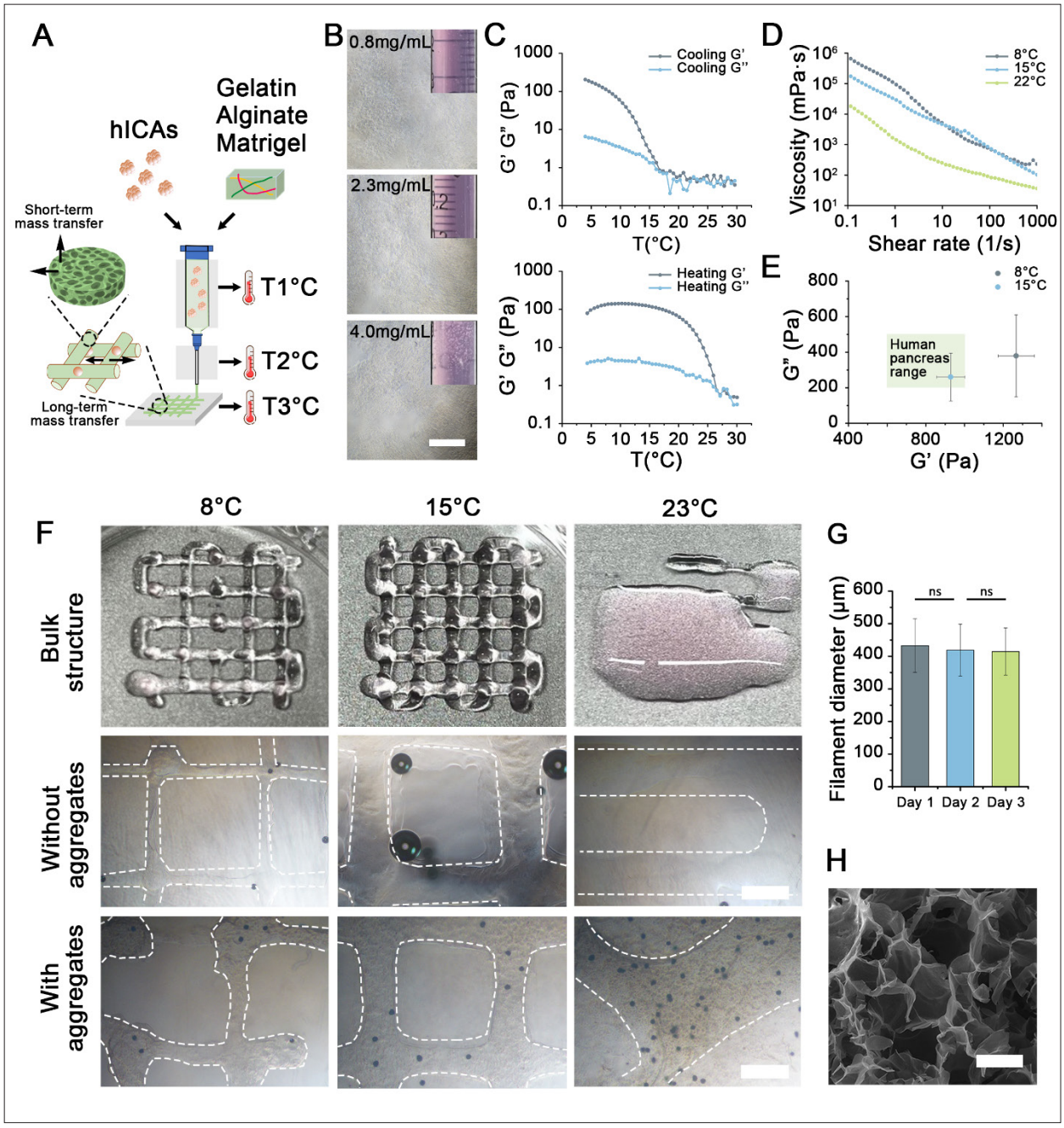

Figure 5. Rheological and structural characterization of bioinks to improve printability. (A) Schematic illustration of the tri-module thermal control strategy for bioprinting, based on the rheological properties of the bioinks. (B) Micro- and macro-scale images (top-right: Matrigel in syringes) of bioinks containing different concentrations of Matrigel (scale bar: 200 μm; magnification: 100×). (C) Shear storage modulus (G') and loss modulus (G") of bioinks measured at 0.1% strain and 1 Hz, during temperature decrease or increase at 2°C/min. (D) Viscosity profiles of bioinks at different temperatures as a function of shear rate. (E) Storage and loss moduli (G' and G") of bioinks after crosslinking with calcium chloride at 8 and 15°C, measured at 0.1% strain and 1 Hz, and compared with those of healthy human pancreatic tissue. (F) Bulk structural images (row 1), microscopic images without cell aggregates (row 2), and microscopic images with cell aggregates (row 3) of printed constructs at 8°C (over-crosslinked), 15°C (properly crosslinked), and 22°C (under-crosslinked) (scale bar: 500 μm; magnification: 40×). (G) Filament diameter changes of printed constructs during 7 days of culture. (H) Scanning electron microscopy images showing internal pore morphology of bioinks after proper crosslinking (scale bar: 50 μm; magnification: 500×). Statistical analysis was performed using one-way analysis of variance with Bonferroni's multiple comparisons test. "ns" denotes no statistical significance. Abbreviations: hICA, human islet β-like cell aggregate; T, temperature.

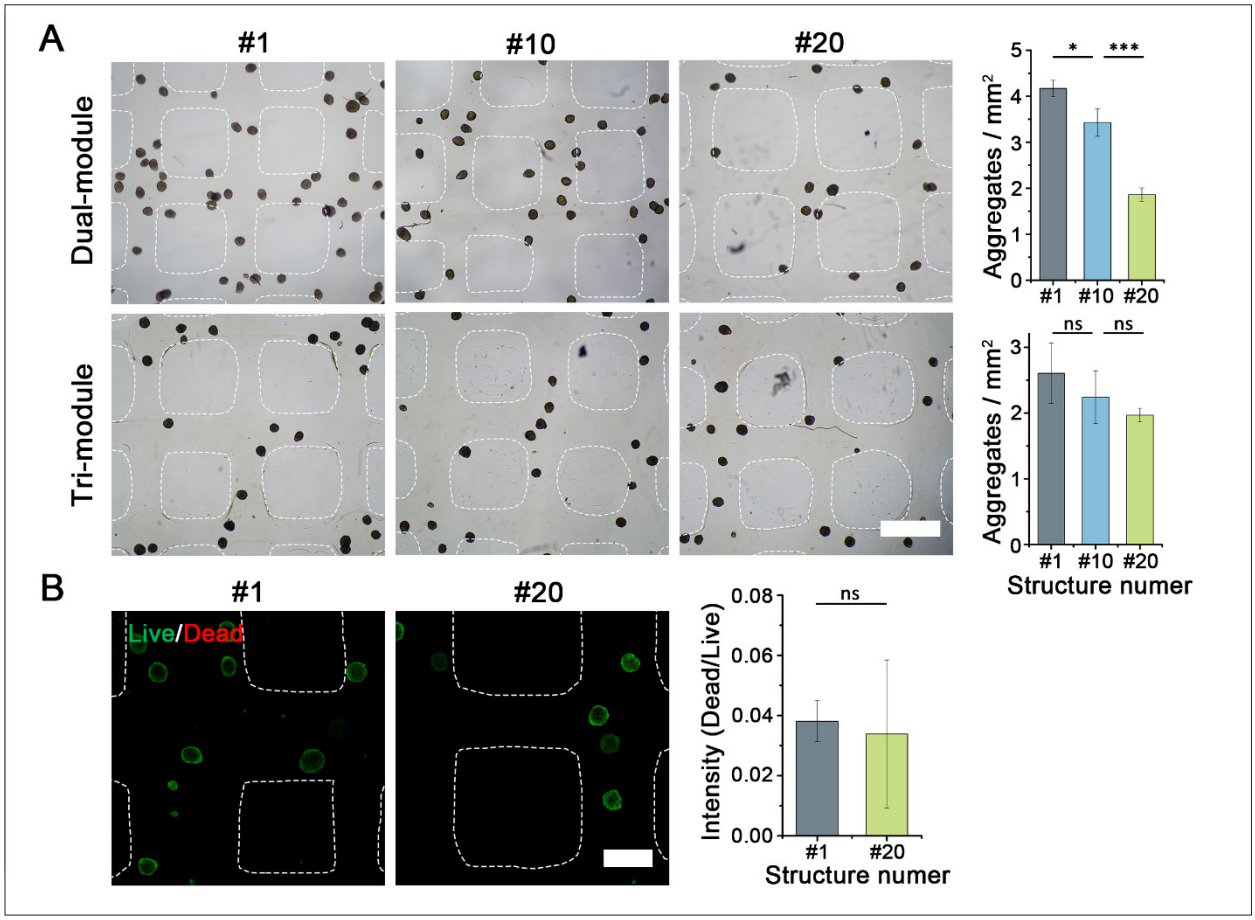

Figure 6. Printing performance of the three-dimensional bioprinting system with dual-module or tri-module thermal control. (A) Aggregate density changes in printed structures from the first sample (#1) to the 20th sample (#20) using traditional dual-module or tri-module thermal control, with quantitative analysis (scale bar: 1 mm; magnification: 20×). (B) Live/dead staining images of aggregates in all bioprinted structures produced under tri-module thermal control, with semi-quantitative analysis (scale bar: 500 μm; magnification: 40×). Statistical analysis was performed using one-way analysis of variance with Bonferroni's multiple comparisons test (A) or two-sided Student's *t*-test (B). Single asterisk (*) and triple asterisk (***) indicate statistical significance at $p < 0.05$ and $p < 0.001$, respectively. "ns" denotes no statistical significance.

potential of incorporating multiple cell types to construct vascularized islet organoids, thereby promoting the further maturation of hICAs.

3.5. Production of vascularized human islet organoid by self-assembly of human islet β-like cell aggregates and human umbilical vein endothelial cells

In vivo, endothelial cells not only form blood vessels,[33] but also promote the differentiation of progenitor cells into endocrine cells and support islet maturation.[34] Recent studies have also shown that endothelial cells play a crucial role in promoting the maturation of pancreatic progenitor cells.[35–37] Therefore, we bioprinted hICAs with HUVECs to further promote the self-assembly of hIOs (Figure 7E).

Both hICAs and HUVECs exhibited viability exceeding 90% after printing (Figure 7D). On day 0, the aggregates (hICAs) and single cells (HUVECs) were separated from each other, as they were homogeneously distributed in the bioinks. By day 3, several single cells appeared around the aggregates, and by day 5, their number further increased. From day 0 to day 5, we observed obvious recruitment of single cells to the surface of the aggregates, suggesting self-assembly driven by intercellular communication through paracrine signaling and HUVEC migration (Figure 7D).

On day 5, immunofluorescence staining further showed that HUVECs formed a tight layer encapsulating individual hICAs, rather than forming vascular connections among aggregates (Figure 7E). The co-culture enhanced the structural integrity of hICAs within the printed hydrogel. The recruitment of HUVECs to the surface of hICAs also mimics the process during pancreatic development, in which endothelial cells migrate to endocrine cell aggregates.[38] The elongated endothelial cell layer structure

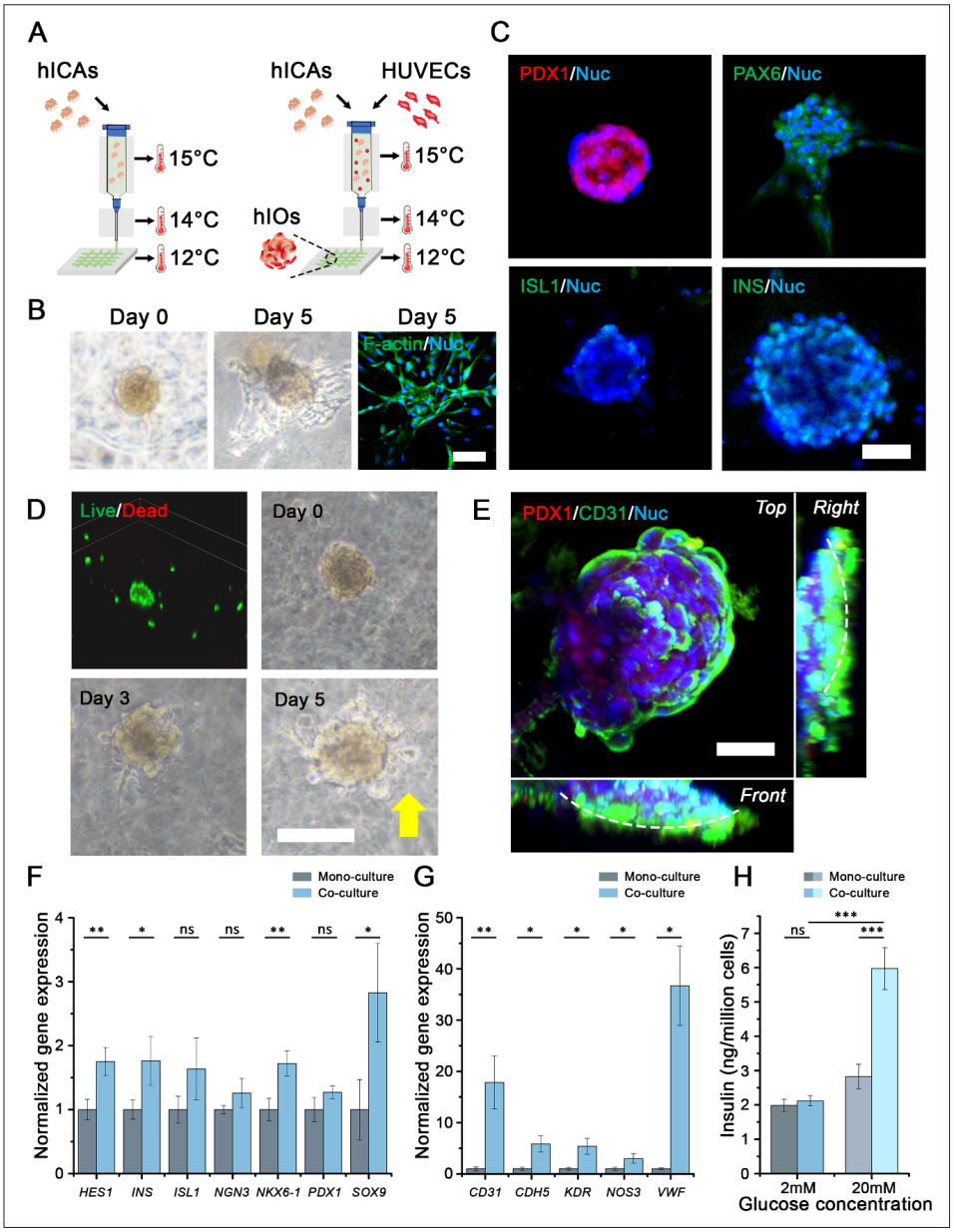

Figure 7. Formation of functional hIOs using 3D bioprinting-based co-culture and cell self-assembly of hICAs and HUVECs. (A) Schematic illustration of 3D bioprinting with hICAs only (left) and 3D bioprinting of hICAs and HUVECs, showing the formation of hIOs (right) under tri-module thermal control. Mono-culture of hICAs: (B) Phase-contrast microscopy images and F-actin staining of printed hICAs during 5 days of culture (scale bar: 50 μm; magnification: 200×). (C) Immunofluorescence images of hICAs in the 3D-bioprinted structure on day 5 showing islet-related proteins (PDX1, PAX6, ISL1, and INS) (scale bar: 50 μm; magnification: 200×). Co-culture of hICAs and HUVECs: (D) Live/dead staining and phase-contrast microscopy images of hICAs (aggregates) and HUVECs (single cells) during culture. The yellow arrow indicates endothelial cells that migrated from the hydrogel and aggregated around hICAs (scale bar: 100 μm; magnification: 200×). (E) 3D projection views of immunofluorescence staining showing the islet marker (PDX1) and HUVEC marker (CD31) on day 5. White dashed curves in the front and right views indicate the aggregate boundary (scale bar: 50 μm; magnification: 200×). (F) Relative gene expression of islet-related markers (*HES1*, *INS*, *ISL1*, *NGN3*, *NKX6-1*, *PDX1*, and *SOX9*) in mono-culture (hICAs only) and co-culture (hICAs and HUVECs). (G) Relative gene expression of endothelial markers (*CD31*, *CDH5*, *KDR*, *NOS3*, and *VWF*) in mono-culture and co-culture. Gene expression levels were normalized to mono-culture and presented as $2^{-\Delta\Delta Ct}$ ($n = 3$). Statistical analysis was performed using the two-sided Student's *t*-test. Single asterisk (*), double asterisk (**), and triple asterisk (***) indicate statistical significance at $p < 0.05$, $p < 0.01$, and $p < 0.001$, respectively. "ns" denotes no statistical significance. Abbreviations: 3D, three-dimensional; CD31, platelet and endothelial cell adhesion molecule 1 gene (*PECAM1*); CDH5, cadherin 5; F-actin, filamentous actin; *HES1*, Hes family BHLH transcription factor 1 gene; hICA, human islet β-like cell aggregate; hIO, human islet organoid; HUVEC, human umbilical vein endothelial cell; INS, insulin; ISL1, islet 1; KDR, kinase insert domain receptor; NGN3, neurogenin-3; NKX6-1, NK6 homeobox 1; NOS3, nitric oxide synthase 3; PAX6, paired box gene 6; PDX1, pancreatic and duodenal homeobox 1; SOX9, SRY-box transcription factor 9; VWF, von Willebrand factor.

in our hIOs resembled an intermediate stage of development between immature and mature islets, when dispersed single cells had aggregated, spread, and enveloped the islet cells, but were still in the early phase of vascular connection and network formation.[39–41] These findings indicate that vascularized islet tissue containing elongated endothelial structures was successfully developed.

We further evaluated the gene expression of islet-related markers and endothelial markers in the hIOs, compared with that of hICAs without HUVECs. The gene expression of mature, INS-producing β-cell markers (*NKX6-1* and *INS*) was upregulated by 1.7-fold and 1.8-fold, respectively, with statistical significance in hIOs. The gene expression of endocrine progenitor markers (*HES1* and *SOX9*) was upregulated by 1.8-fold and 2.8-fold, respectively, and reached statistical significance. Other islet-related markers, including *ISL1*, *NGN3*, and *PDX1*, showed increasing trends in co-cultured hIOs compared with mono-cultured hICAs, although the differences were not significant (Figure 7F). The hIOs demonstrated increased functional maturity, which is beneficial for rapid INS secretion after transplantation. The enhanced expression of endocrine progenitor markers demonstrated the developmental fidelity of the hIOs, supporting their potential to continuously generate islet-like cells after transplantation. The gene expression of endothelial markers, including *CD31*, *CDH5*, *KDR*, *NOS3*, and *VWF*, was upregulated by 17.8-fold, 5.9-fold, 5.4-fold, 3.0-fold, and 36.7-fold, respectively, in hIOs, all with statistical significance, thereby validating the role of HUVECs in promoting islet maturation as supporting cells (Figure 7G). This finding is consistent with a previous report showing that endothelial cells specifically enhance the *INS* gene expression in islet endocrine cells.[38]

Finally, we performed the GSIS assay to evaluate the glucose-responsive insulin secretory function of hIOs (Figure 7H). hIOs showed a significant increase in INS secretion, rising from 2.12 to 5.97 ng/million cells, with a GSIS index of 2.8, whereas mono-cultured hICAs did not show a significant response. The comparison between hIOs and hICAs highlights the importance of endothelial cells in enhancing INS secretion. Although our hIOs exhibited lower levels of INS secretion compared with most ESC- or iPSC-derived β-cells, the GSIS index was comparable.[42–44] This may be attributed to the differentiation strategy and cell purity, as those studies employed more complex differentiation processes from pluripotent stem cells, where only mature β-cells were sorted for use. Our hIOs more closely resembled a complex islet structure *in vivo*, while the INS-producing cells within the hIOs exhibited a similar glucose response to those in other studies, highlighting the importance of endothelial cells in islet functional maturation.

These results indicate that the combination of a printed mesh structure with supporting endothelial cells, appropriate scaffold stiffness, and porous bioactive bioinks established a biomimetic environment that facilitates the formation of hIOs *in vitro*. Using PUMP and bioprint-based co-culture, we can produce these hIOs at a large scale with reduced costs for both research and clinical applications, which represents a significant improvement over traditional methods. The use of hADSCs and HUVECs also potentially reduces immune responses in future transplantation. These hIOs, with a defined structure incorporating vascular elements and glucose-responsive function, hold potential for studies of vascularization, pancreatic development, drug screening, and islet transplantation.

4. Conclusion

In this study, we demonstrated the successful large-scale production of functional vascularized hIOs through a 3D bioprinting-based co-culture and cell self-assembly approach. By employing the PUMP system with optimized stiffness, we generated uniform hICAs from hADSCs. The integration of a tri-module bioprinting process with a ternary gelatin–alginate–Matrigel bioink enabled the bioprinting of hICAs and HUVECs to form hIOs through co-culture and self-assembly. These organoids were structurally and functionally similar to human islets, exhibiting upregulated expression of endocrine progenitor and mature β-cell markers, and demonstrated GSIS. This approach provides a scalable and biologically relevant novel hIO model, advancing applications in vascularization studies, pancreatic development research, drug screening, and islet transplantation for diabetes therapy.

Acknowledgments

None.

Funding

This study was supported by the National Key Research and Development Program of China (2022YFA1104600; 2018YFA0109000).

Conflict of interest

The authors declare that they have no conflict of interest.

Author contributions

Conceptualization: Rui Yao, Yijun Su, Supeng Ding
Formal analysis: Yijun Su, Supeng Ding

Funding acquisition: Rui Yao, Mingen Xu
Investigation: Supeng Ding, Yijun Su, Yinying Lu, Yongyong Zhou
Methodology: Supeng Ding, Yijun Su, Yongyong Zhou
Project administration: Rui Yao, Mingen Xu, Feng Lin
Visualization: Yijun Su, Supeng Ding
Writing–original draft: Yijun Su, Supeng Ding
Writing–review & editing: Rui Yao, Supeng Ding, Yijun Su, Tiankun Liu

Ethics approval and consent to participate

Not applicable.

Consent for publication

Not applicable.

Availability of data

Data is available from the corresponding author upon reasonable request.

References

1. Sun H, Saeedi P, Karuranga S, *et al*. IDF Diabetes Atlas: global, regional and country-level diabetes prevalence estimates for 2021 and projections for 2045. *Diabetes Res Clin Pract*. 2022;183:109119. doi: 10.1016/j.diabres.2021.109119
2. Chhabra P, Brayman KL. Overcoming barriers in clinical islet transplantation: current limitations and future prospects. *Curr Probl Surg*. 2014;51(2):49-86. doi: 10.1067/j.cpsurg.2013.10.002
3. Kim Y, Kim H, Ko UH, *et al*. Islet-like organoids derived from human pluripotent stem cells efficiently function in the glucose responsiveness in vitro and in vivo. *Sci Rep*. 2016;6:35145. doi: 10.1038/srep35145
4. Liang S, Su Y, Yao R. 3D bioprinting of induced pluripotent stem cells and disease modeling. In: Kuehn MH, Zhu W, eds. *Human iPSC-derived Disease Models for Drug Discovery*. Handbook of experimental pharmacology. Springer, Cham. 2023; vol 281: 29-56. doi: 10.1007/164_2023_646
5. Candiello J, Grandhi TSP, Goh SK, *et al*. 3D heterogeneous islet organoid generation from human embryonic stem cells using a novel engineered hydrogel platform. *Biomaterials*. 2018;177:27-39. doi: 10.1016/j.biomaterials.2018.05.031
6. Liang S, Luo Y, Su Y, *et al*. Distinct toxicity of microplastics/TBBPA co-exposure to bioprinted liver organoids derived from hiPSCs of healthy and patient donors. *Int J Bioprint*. 2024;10(3):1403. doi: 10.36922/ijb.1403
7. de Klerk E, Hebrok M. Stem cell-based clinical trials for diabetes mellitus. *Front Endocrinol (Lausanne)*. 2021;12:631463. doi: 10.3389/fendo.2021.631463
8. Panes J, Garcia-Olmo D, Van Assche G, *et al*. Long-term efficacy and safety of stem cell therapy (Cx601) for complex perianal fistulas in patients with Crohn's disease. *Gastroenterology*. 2018;154(5):1334-1342.e4. doi: 10.1053/j.gastro.2017.12.020
9. Hong Y, Park EY, Kim D, Lee H, Jung HS, Jun HS. Glucosamine potentiates the differentiation of adipose-derived stem cells into glucose-responsive insulin-producing cells. *Ann Transl Med*. 2020;8(8):561. doi: 10.21037/atm.2020.03.103
10. Dave SD, Vanikar AV, Trivedi HL. Extrinsic factors promoting in vitro differentiation of insulin-secreting cells from human adipose tissue-derived mesenchymal stem cells. *Appl Biochem Biotechnol*. 2013;170(4):962-71. doi: 10.1007/s12010-013-0250-y
11. Wang X, Luo Y, Ma Y, Wang P, Yao R. Converging bioprinting and organoids to better recapitulate the tumor microenvironment. *Trends Biotechnol*. 2024;42(5):648-663. doi: 10.1016/j.tibtech.2023.11.006
12. Luo Y, Luo L, Wang L, *et al*. Large-scale bioprinting of human epiblast-like models featuring disc-shaped morphogenesis and gastrulation events. *Adv Sci (Weinh)*. 2025;12(33):e05340. doi: 10.1002/advs.202505340
13. Marchioli G, van Gurp L, van Krieken PP, *et al*. Fabrication of three-dimensional bioplotted hydrogel scaffolds for islets of Langerhans transplantation. *Biofabrication*. 2015;7(2):025009. doi: 10.1088/1758-5090/7/2/025009
14. Song J, Millman JR. Economic 3D-printing approach for transplantation of human stem cell-derived beta-like cells. *Biofabrication*. 2016;9(1):015002. doi: 10.1088/1758-5090/9/1/015002
15. Hwang DG, Jo Y, Kim M, *et al*. A 3D bioprinted hybrid encapsulation system for delivery of human pluripotent stem cell-derived pancreatic islet-like aggregates. *Biofabrication*. 2021;14(1). doi: 10.1088/1758-5090/ac23ac
16. Kim J, Shim IK, Hwang DG, *et al*. 3D cell printing of islet-laden pancreatic tissue-derived extracellular matrix bioink constructs for enhancing pancreatic functions. *J Mater Chem B*. 2019;7(10):1773-1781. doi: 10.1039/c8tb02787k
17. Idaszek J, Volpi M, Paradiso A, *et al*. Alginate-based tissue-specific bioinks for multi-material 3D-bioprinting of pancreatic islets and blood vessels: a step towards vascularized pancreas grafts. *Bioprinting*. 2021;24:e00163. doi: 10.1016/j.bprint.2021.e00163

18. Yao R, Wang J, Li X, *et al*. Hepatic differentiation of human embryonic stem cells as microscaled multilayered colonies leading to enhanced homogeneity and maturation. *Small*. 2014;10(21):4311-4323.
doi: 10.1002/smll.201401040

19. Costa EC, de Melo-Diogo D, Moreira AF, Carvalho MP, Correia IJ. Spheroids formation on non-adhesive surfaces by liquid overlay technique: considerations and practical approaches. *Biotechnol J*. 2018;13(1).
doi: 10.1002/biot.201700417

20. Ansari A, Trehan R, Watson C, Senyo S. Increasing silicone mold longevity: a review of surface modification techniques for PDMS-PDMS double casting. *Soft Mater*. 2021; 19(4):388-399.
doi: 10.1080/1539445x.2020.1850476

21. Clark CT, Wang Y, Johnson DC, Lee SC, Smith Q. Effects of PDMS culture on stem cell differentiation towards definitive endoderm and hepatocytes. *Acta Biomater*. 2025; 200:508-519.
doi: 10.1016/j.actbio.2025.05.017

22. Anitha R, Vaikkath D, Shenoy SJ, Nair PD. Tissue-engineered islet-like cell clusters generated from adipose tissue-derived stem cells on three-dimensional electrospun scaffolds can reverse diabetes in an experimental rat model and the role of porosity of scaffolds on cluster differentiation. *J Biomed Mater Res A*. 2020;108(3):749-759.
doi: 10.1002/jbm.a.36854

23. Nyitray CE, Chavez MG, Desai TA. Compliant 3D microenvironment improves β-cell cluster insulin expression through mechanosensing and β-catenin signaling. *Tissue Eng Part A*. 2014;20(13-14):1888-1895.
doi: 10.1089/ten.tea.2013.0692

24. Tran R, Moraes C, Hoesli CA. Developmentally-inspired biomimetic culture models to produce functional islet-like cells from pluripotent precursors. *Front Bioeng Biotechnol*. 2020;8:583970.
doi: 10.3389/fbioe.2020.583970

25. Ding S, Feng L, Wu J, Zhu F, Tan Z, Yao R. Bioprinting of stem cells: interplay of bioprinting process, bioinks, and stem cell properties. *ACS Biomater Sci Eng*. 2018; 4(9):3108-3124.
doi: 10.1021/acsbiomaterials.8b00399

26. Chen R, Su Y, Chen D, *et al*. Bioprinting with superelastic and fatigue-resistant bioinks for large-sized tissue delivery. *Int J Bioprint*. 2024;10(5):3898.
doi: 10.36922/ijb.3898

27. Cahn F. Biomaterials aspects of porous microcarriers for animal cell culture. *Trends Biotechnol*. 1990;8(5):131-136.
doi: 10.1016/0167-7799(90)90154-P

28. Ouyang L, Yao R, Mao S, Chen X, Na J, Sun W. Three-dimensional bioprinting of embryonic stem cells directs highly uniform embryoid body formation. *Biofabrication*. 2015;7(4):044101.
doi: 10.1088/1758-5090/7/4/044101

29. Yao R, Zhang R, Luan J, Lin F. Alginate and alginate/gelatin microspheres for human adipose-derived stem cell encapsulation and differentiation. *Biofabrication*. 2012;4(2):025007.
doi: 10.1088/1758-5082/4/2/025007

30. Townsend SE, Gannon M. Extracellular matrix-associated factors play critical roles in regulating pancreatic beta-cell proliferation and survival. *Endocrinology*. 2019; 160(8):1885-1894.
doi: 10.1210/en.2019-00206

31. Parvaneh S, Kemeny L, Ghaffarinia A, Yarani R, Vereb Z. Three-dimensional bioprinting of functional beta-islet-like constructs. *Int J Bioprint*. 2023;9(2):665.
doi: 10.18063/ijb.v9i2.665

32. Wex C, Frohlich M, Brandstadter K, Bruns C, Stoll A. Experimental analysis of the mechanical behavior of the viscoelastic porcine pancreas and preliminary case study on the human pancreas. *J Mech Behav Biomed Mater*. 2015;41:199-207.
doi: 10.1016/j.jmbbm.2014.10.013

33. Aplin AC, Aghazadeh Y, Mohn OG, Hull-Meichle RL. Role of the pancreatic islet microvasculature in health and disease. *J Histochem Cytochem*. 2024;72(11-12):711-728.
doi: 10.1369/00221554241299862

34. Lammert E, Cleaver O, Melton D. Induction of pancreatic differentiation by signals from blood vessels. *Science*. 2001;294(5542):564-567.
doi: 10.1126/science.1064344 .

35. Wang X, Ye K. Three-dimensional differentiation of embryonic stem cells into islet-like insulin-producing clusters. *Tissue Eng Part A*. 2009;15(8):1941-1952.
doi: 10.1089/ten.tea.2008.0181

36. Aghazadeh Y, Poon F, Sarangi F, *et al*. Microvessels support engraftment and functionality of human islets and hESC-derived pancreatic progenitors in diabetes models. *Cell Stem Cell*. 2021;28(11):1936-1949.e8.
doi: 10.1016/j.stem.2021.08.001

37. Jaramillo M, Mathew S, Mamiya H, Goh SK, Banerjee I. Endothelial cells mediate islet-specific maturation of human embryonic stem cell-derived pancreatic progenitor cells. *Tissue Eng Part A*. 2015;21(1-2):14-25.
doi: 10.1089/ten.tea.2014.0013

38. Zanone MM, Favaro E, Camussi G. From endothelial to beta cells: insights into pancreatic islet microendothelium. *Curr Diabetes Rev*. 2008;4(1):1-9.
doi: 10.2174/157339908783502415

39. Glorieux L, Sapala A, Willnow D, *et al*. Development of a 3D atlas of the embryonic pancreas for topological and quantitative analysis of heterologous cell interactions. *Development*. 2022;149(3):dev199655.
doi: 10.1242/dev.199655

40. Ranjan AK, Joglekar MV, Hardikar AA. Endothelial cells in pancreatic islet development and function. *Islets*. 2009;1(1):2-9.
doi: 10.4161/isl.1.1.9054

41. Mateus Goncalves L, Almaca J. Functional characterization of the human islet microvasculature using living pancreas slices. *Front Endocrinol (Lausanne)*. 2020;11:602519.
doi: 10.3389/fendo.2020.602519

42. Velazco-Cruz L, Song J, Maxwell KG, *et al*. Acquisition of dynamic function in human stem cell-derived beta cells. *Stem Cell Rep*. 2019;12(2):351-365.
doi: 10.1016/j.stemcr.2018.12.012

43. Velazco-Cruz L, Goedegebuure MM, Maxwell KG, Augsornworawat P, Hogrebe NJ, Millman JR. SIX2 regulates human beta cell differentiation from stem cells and functional maturation in vitro. *Cell Rep*. 2020; 31(8):107687.
doi: 10.1016/j.celrep.2020.107687

44. Cardenas-Diaz FL, Osorio-Quintero C, Diaz-Miranda MA, *et al*. Modeling monogenic diabetes using human ESCs reveals developmental and metabolic deficiencies caused by mutations in HNF1A. *Cell Stem Cell*. 2019;25(2):273-289.e5.
doi: 10.1016/j.stem.2019.07.007

ACCSCIENCE PUBLISHING

International Journal of Bioprinting

RESEARCH ARTICLE

A mobile drop-on-demand laser-assisted printing head integrated with a robotic arm and a target tracking system

Ahad Mohammadi[1,2], Shakiba Davani[1,2], and Christos Boutopoulos[1,2,3]*

[1]Institute of Biomedical Engineering, University of Montreal, Montreal, Quebec, Canada

[2]Centre de Recherche Hôpital Maisonneuve-Rosemont, Montreal, Quebec, Canada

[3]Department of Ophthalmology, University of Montreal, Montreal, Quebec, Canada

Abstract

In this work, we present a mobile drop-on-demand (DoD) printing system based on laser-induced side transfer (LIST). By replacing the bulky free-space optics used in previous LIST configurations with a fiber-based laser delivery system, we developed a compact printing head and integrated it as an end-effector onto a robotic arm. Using model inks with viscosities up to 165 cP and time-resolved imaging, we investigated printability, printing dynamics, and the effect of printing head-to-substrate distance on key printing quality metrics. We found that printing quality deteriorates significantly beyond a 3 mm standoff distance. To address motion-induced printing quality loss on dynamic substrates, we integrated a custom-built fiber-optic distance sensor that actively maintains a constant standoff distance in real time. This enabled high-quality printing on moving targets simulating physiological motion. Additionally, we characterized the influence of ink viscosity and laser energy on droplet formation dynamics and ejected volume. Our results demonstrate the feasibility of motion-compensated, laser-assisted DoD printing in dynamic environments, with potential applications in intraoperative tissue engineering.

Keywords: Drop-on-demand; Distance sensor; *In situ* bioprinting; Laser-induced side transfer; Motion compensation; Robotic

***Corresponding author:**
Christos Boutopoulos (christos.boutopoulos@umontreal.ca)

Citation: Mohammadi A, Davani S, Boutopoulos S. A mobile drop-on-demand laser-assisted printing head integrated with a robotic arm and a target tracking system. *Int J Bioprint*. 2025;11(6):298-310. doi: 10.36922/IJB025320321

Received: August 8, 2025
Revised: September 13, 2025
Accepted: September 16, 2025
Published online: September 17, 2025

Copyright: © 2025 Author(s). This is an Open Access article distributed under the terms of the Creative Commons Attribution License, permitting distribution, and reproduction in any medium, provided the original work is properly cited.

Publisher's Note: AccScience Publishing remains neutral with regard to jurisdictional claims in published maps and institutional affiliations.

1. Introduction

Bioprinting involves the deposition of cells and biomaterials to create functional tissues and organ models.[1] It emerged from the broader field of additive manufacturing, which gained momentum in the 1980s. Over time, various bioprinting technologies—such as inkjet, extrusion, and light-based printing—have been developed to address specific needs in printing resolution, speed, and cell viability.[2] Compared to traditional 2D cell cultures, bioprinting enables the fabrication of 3D tissue models that offer more physiologically relevant data for drug testing[3] and may help reduce the reliance on animal experimentation.[4,5] Additionally, bioprinting holds significant promise for advancing regenerative medicine by enabling the creation of patient-specific tissue constructs and reducing dependence on conventional transplantation methods.[6]

Bioprinting is increasingly focused on directly depositing bioinks onto patient tissues, enabling rapid, on-site clinical interventions.[7–10] To support these *in situ* applications, portable and versatile bioprinting systems are needed to navigate the human body—something conventional, bulky benchtop bioprinters cannot achieve. Notably, laser-based bioprinters[11,12] reported for *in situ* applications have been limited to stationary systems without maneuverability. Conversely, handheld bioprinters and robotic arms equipped with extrusion-based depositors have been used to attain the maneuverability required for more complex *in situ* printing applications.[9,13,14]

Achieving reliable *in situ* bioprinting requires the printing head to adapt to physiological movements, as the body may still move under anesthesia due to breathing or involuntary motions.[15] This is critical for maintaining printing resolution and preventing tissue injury. Early *in situ* tissue engineering efforts struggled to maintain print fidelity under dynamic conditions, resulting in low-quality constructs.[16,17] However, with advances in sensor technologies and robotic control, motion compensation has been explored as a solution. By integrating real-time motion compensation, bioprinters can eventually adapt to patient movements, ensuring consistent high-quality prints. Recent studies demonstrate that robotic systems with image-based motion compensation can be used to counteract simulated physiological movements.[14,18]

Among bioprinting techniques, drop-on-demand (DoD) methods—such as inkjet printing,[19] laser-induced forward transfer (LIFT),[20–24] and laser-induced flow focusing[25]—are particularly well suited for applications requiring non-contact biomaterial deposition. Recently, our laboratory introduced a DoD method termed laser-induced side transfer (LIST)[26] for printing low- to moderate-viscosity bioinks. LIST has been successfully tested for printing primary cells, including human umbilical vein endothelial cells and sensory neurons, while maintaining high post-printing viability.[26,27] The latest version of LIST employs continuous bioink perfusion through a glass capillary with a laser-machined hole serving as a nozzle and utilizes focused, low-energy nanosecond laser pulses for droplet ejection.[28] However, all previous implementations of LIST have relied on a bulky free-space beam delivery system, preventing the mobility of the printing head.

Here, we introduced and validated a mobile printing head based on the LIST technique. Central to our approach is the replacement of a bulky free-space beam delivery system with a fiber-based alternative. The mobile printing system was mounted on a robotic arm, and a model ink (with viscosity up to 165 cP), along with a time-resolved imaging setup, was used to study printability and printing dynamics. We investigated how variations in the distance between the printing head and the target substrate affect printing quality. Finally, we developed and validated an automated distance-tracking system based on a fiber-optic sensor to compensate for printing quality degradation when printing on moving substrates that mimic physiological motion in patients.

2. Materials and methods

2.1. Model ink

A water–glycerol mixture was used as a model ink with different mixing ratios, producing a viscosity range from 2.8 to 165 cP.[29] We used a single viscosity (18 cP) to test printability on moving substrates, while the full viscosity range was applied in the second part of the study to investigate the effects of viscosity on bubble formation, jetting dynamics, and printing volume. Due to the transparency of water in the visible range,[30] a biocompatible food dye, Allura Red AC (10 mM) (458848 100G, Sigma-Aldrich), was added to the ink to increase its absorption coefficient at 532 nm.

2.2. Microjet and bubble imaging

We used a time-resolved imaging approach to capture bubble and jet dynamics. The imaging system comprises a high-speed camera (Chronos 1.4; Kron Technologies, Canada), an achromatic lens (AC254-150-A-ML, Thorlabs, USA), an objective lens (RMS4X, Thorlabs), and an LED light source (MCWHL5; Thorlabs). A delay generator (DG535, Stanford Research Systems, USA) and a photodiode (DET10A, Thorlabs) were used to trigger image capturing at the desired time delays with respect to laser firing.

Microscopy images of printed drops were processed using a custom MATLAB script to quantify droplet placement error. The droplet placement error was calculated as the distance between the intended and actual drop landing positions. Droplet circularity, splatter coverage, and area were calculated using ImageJ (NIH, USA) and its built-in image processing tools. Splatter coverage was defined as the ratio of the total satellite drop area to the total main drop area.

2.3. Mobile LIST printing head

The core printing component of the mobile printing head is a glass microcapillary (8250; Vitrocom, USA; inner dimensions: 500 × 500 μm^2; wall thickness: 100 μm) continuously perfused with ink.[28] The capillary features a femtosecond laser-machined 200 μm circular opening on one of its sides, acting as a nozzle.[28] Laser pulses from a pulsed 532 nm Nd:YAG laser (Nano S 60-30; Litron Lasers, UK; 6 ns pulse duration) are used to generate microjets. Unlike our previous work that employed an open beam delivery system,[28] the laser used in this study was coupled

to a 105 μm core optical fiber (FG105LCA; Thorlabs), with the fiber fixed to the glass capillary opposite the laser-machined opening using a 3D-printed holder. This 3D-printed holder also incorporates clamps for the interchange of capillaries and tubing guides, securing both the tubing and fiber, with the entire assembly comprising the mobile printing head. A detailed 3D CAD rendering of the print head can be found in Figure S1, Supplementary File. A syringe pump (NE 1000; New Era Pump Systems Inc., USA) and perfusion tubing (89404-042; VWR, Canada) were used to continuously perfuse ink through the microcapillary at flow rates between 4 and 12 μL/min. The ink does not leak from the nozzle due to surface tension, and microjets are only generated when the delivered laser pulse induces bubble formation and a pressure increase inside the capillary.

2.3. Robotic arm integration and OCT-based distance tracking system

The mobile LIST printing head was mounted on a 5-axis robotic arm (Dorna 2, Dorna Robotics, USA). To simulate the physiological movement of the chest during breathing,[31] microscope slides used as printing substrates were displaced in the Z-axis with a 12 mm amplitude (24 mm peak-to-peak displacement) and a frequency of 0.2 Hz using a translation stage (Z825B, Thorlabs). The printing speed was 5 Hz, and the printing pattern consisted of an array of drops spaced 1.5 mm apart. The pattern was printed in a sequential row-wise pattern, starting with a horizontal line of droplets, followed by a vertical offset to print the next row below, and continuing in this alternating sequence. The z-position of the robotic arm was continuously updated using a distance tracking system to maintain the printing head at a fixed distance from the moving substrate. The distance tracking system automation is based on a homemade spectral-domain common-path optical coherence tomography (OCT) system that has been described in detail elsewhere.[32] For this work, a miniaturized (125 μm in thickness) fiber-based probe was attached to the printing head, emitting light toward the moving substrate. The backscattered light was collected by the same fiber probe and directed to the readout system. A single-mode fiber (SM800-5.6-125, Thorlabs) was used for the probe. To optimize light emission and collection, we spliced a 272-μm GRIN fiber (GIF625, Thorlabs) to the distal end of the single-mode fiber, resulting in a non-diverging light beam emission.[33] The axial resolution of the system was experimentally measured to be 18 μm.

A Python-based algorithm was used to control the entire automation, including processing the tracking system readout and controlling the robotic arm. The entire motion-tracking automation system operated at a frequency of 5 Hz. Real-time Z-axis correction required stepwise movement execution, with all coordinates updated at each step. The X and Y coordinates were predefined to follow the sequential row-wise scanning pattern described above, while the Z coordinate was dynamically calculated. Specifically, at each step, the Z-axis control logic compared the actual printing distance to the target distance (3 mm). If the deviation was less than 50 μm, the Z position remained unchanged; if the deviation exceeded 50 μm, the Z position was adjusted to offset the difference. While the fiber-based sensor operated at 50 Hz, the Python-based control script queried the sensor at 200-ms intervals (5 Hz). This update frequency was chosen as a compromise between minimizing vibrations in the robotic arm and ensuring sufficient sampling to track the substrate movement.

At a fixed standoff distance of 3 mm, droplet arrays were printed at both 2 and 5 Hz to investigate the effect of robotic arm vibrations on printing quality.

2.4. Statistical analysis

All reported values in this work represent the mean and standard deviation from three independent printing experiments. Data in Figure 3 were analyzed by one-way analysis of variance (ANOVA) using Prism 10 software (GraphPad Software, USA).

3. Results

3.1. Mobile LIST implementation

We implemented our mobile LIST printer using a modified version of our latest LIST configuration, which employs continuous ink perfusion through a square glass capillary (500 μm × 500 μm) with a 200 μm circular opening.[28] Our key modification involves replacing the free-space optics with a fiber delivery system (Figure 1), as detailed in the Section 2. The working principle of the printer remains identical to previous LIST implementations,[26–28,34,35] where the interaction of a pulsed laser (pulse duration: 6 ns, wavelength: 532 nm) with the ink within the glass capillary generates an expanding bubble that propels a microjet from the capillary opening (Figure 1A). The microjet eventually detaches from the opening, resulting in the deposition of a nanodroplet onto a receiving substrate. The fiber, connecting tubing, and glass capillary were assembled using a 3D-printed holder. The resulting mobile printing head was attached to a robotic arm as an end-effector (Figure 1B).

3.2. Influence of printing head-to-target distance on printing quality

The printing head-to-target distance is known to affect printing quality in DoD printing systems.[36] Quantifying

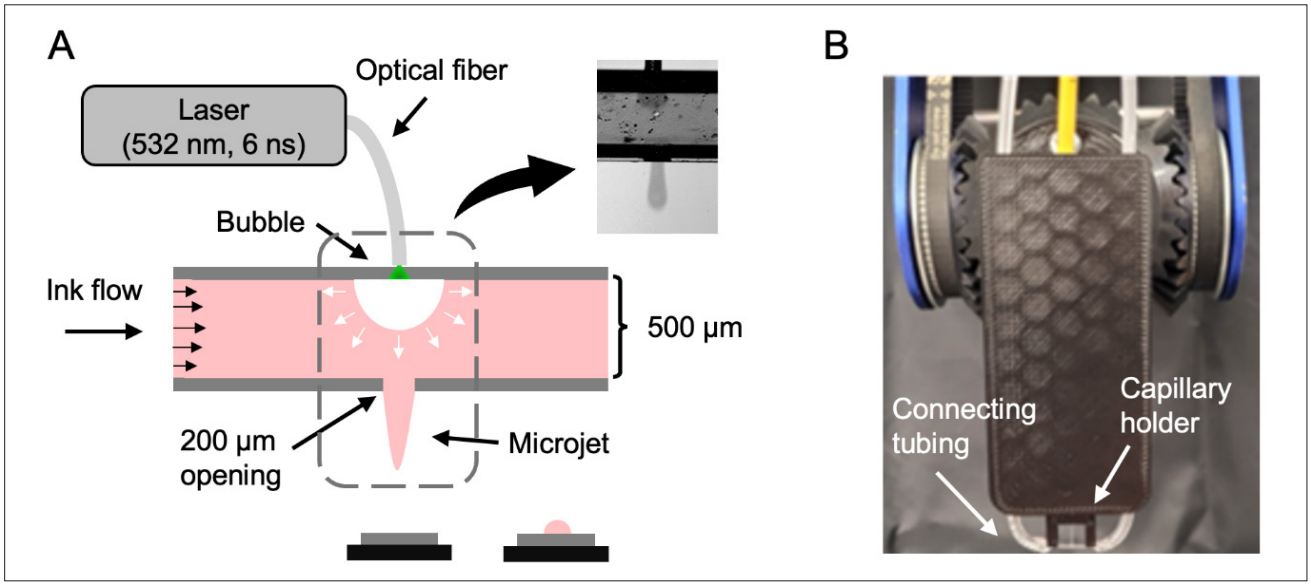

Figure 1. Fiber-based implementation of laser-induced side transfer (LIST) enables a mobile printing head and robotic integration. (A) Schematic overview of the mobile LIST printing head implementation. The inset is a high-speed camera image showing a bubble at the upper part of the capillary, below the fiber–capillary contact point, and a microjet exiting the fiber opening. (B) Photograph of the mobile LIST printing head mounted on a robotic arm as an end-effector.

this effect is important for identifying the operational window in *in situ* printing applications, including the maximum distance limit to maintain a desired level of printing quality. To address this for the mobile LIST printing head, we conducted printing experiments using a model ink (viscosity: 18 cP), varying the distance between the printing head and the target substrate (Figure 2A). Splatter coverage was used as the primary metric to quantify print quality.

Figure 2B shows optical microscopy images of arrays of model ink droplets printed at constant energy per pulse (230 µJ, corresponding to 1.15 times the printing threshold energy) across different printing head-to-target distances. The maximum range at which splatter coverage remained zero was 3 mm. Beyond this point, splatter coverage progressively increased, from 5.11 ± 2.03% at 6 mm to 37.36 ± 13.01% at 24 mm (Figure 2C). Secondary metrics of printing quality, such as drop placement error, drop circularity, and main drop area, followed the same trend. Drop placement error increased from 181 ± 94 µm at 1.5 mm to 383 ± 227 µm at 24 mm (Figure 2D). Drop circularity declined from 0.85 ± 0.12 to 0.69 ± 0.18 (Figure 2E), while the main drop area decreased from 1.29 ± 0.25 to 1.08 ± 0.31 mm^2 (Figure 2F), primarily due to the formation of satellite droplets.

Taken together, these printing quality metrics demonstrate that print quality degrades as the printing head-to-target distance increases. A distance of 3 mm is identified as a practical upper limit, where printing remains splatter-free.

3.3. Preventing printing quality loss in dynamic environments using a distance sensor

For dynamic printing environments where the printing target cannot be fixed (e.g., printing on living animals), the distance between the printing head and the target must be dynamically adjusted to maintain printing quality. We developed an optical fiber-based distance sensor using the OCT principle and integrated it with the mobile printing head and robotic arm to mitigate quality loss when printing on a moving substrate. The working principle of this automation is outlined in Figure 3A and detailed in Section 2.

We employed a dynamic z-position adjustment approach to print our model ink (viscosity: 18 cP) on a moving target that oscillated with a displacement amplitude of 12 mm (24 mm peak-to-peak displacement), representing the average chest expansion due to breathing.[31] Figure 3B shows optical microscopy images of arrays of model ink droplets printed at a constant energy per pulse (230 µJ, corresponding to 1.15-times the printing threshold energy) under three conditions: (i) a constant 3 mm printing head-to-target distance, (ii) target movement without compensation, and (iii) dynamic compensation, where the target moves while the printing head actively maintains a 3 mm distance.

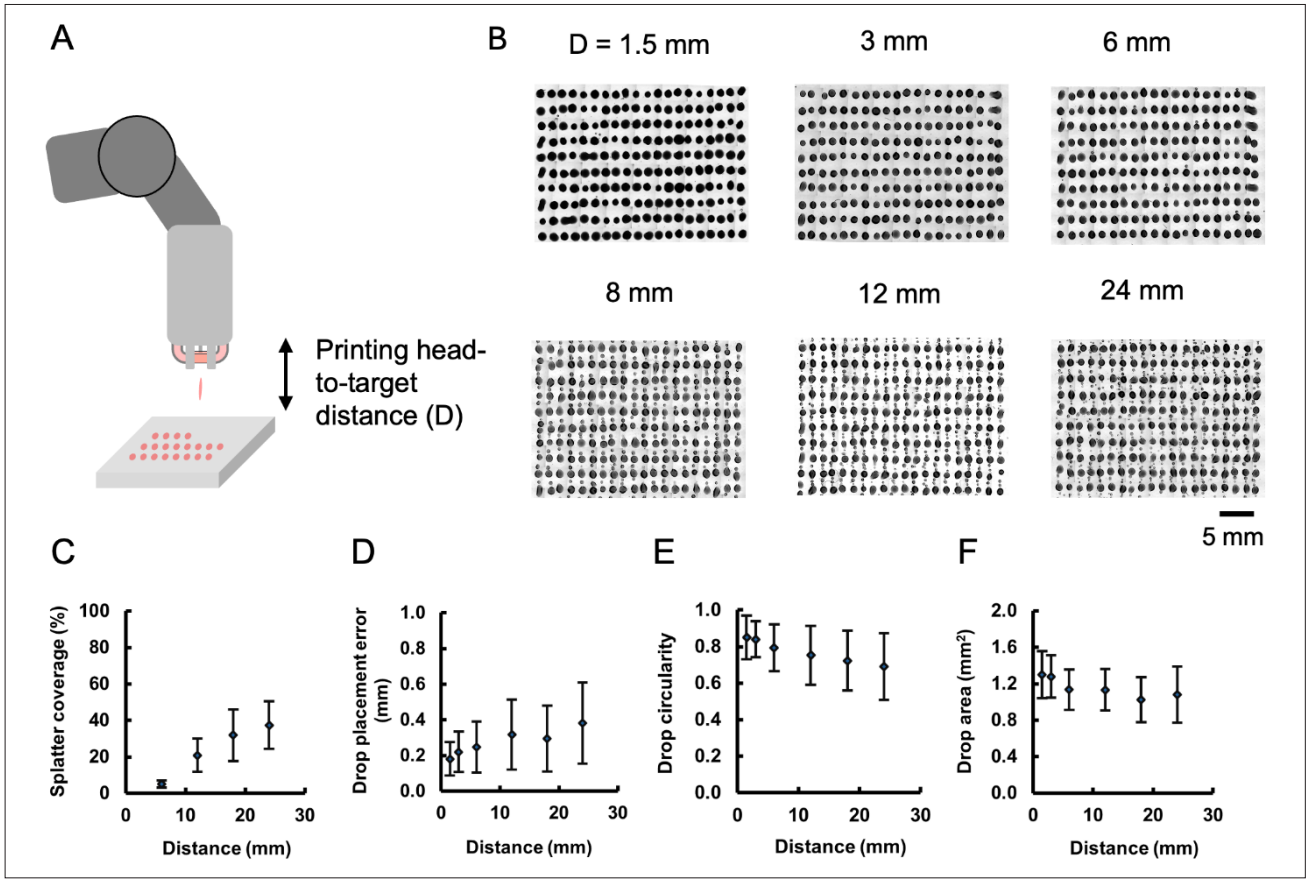

Figure 2. The impact of printing head-to-target distance on print quality. (A) Schematic overview of the approach used to investigate the effect of varying the printing head-to-target distance on print quality. (B) Optical microscope images of model ink arrays printed at different printing head-to-target distance. The effect of varying the printing head-to-target distance on (C) splatter coverage, (D) drop placement error, (E) drop circularity, and (F) drop area. Error bars represent the standard deviation from three independent printing experiments.

Figure 3C–F presents a quantitative analysis of the printing quality metrics under the three conditions. We found that printing on a moving target significantly worsened most printing quality metrics. Splatter coverage increased from 0.00 ± 0.00% to 34.17 ± 5.03% (p = 0.0003), drop circularity decreased from 0.84 ± 0.02 to 0.72 ± 0.05 (p = 0.0016), and the main drop area was reduced from 1.23 ± 0.05 to 1.09 ± 0.10 mm² (p = 0.0360). A similar trend was observed for the drop placement error, which increased from 220 ± 100 to 340 ± 80 μm (p = 0.0576). With dynamic compensation, all printing quality metrics improved, showing no statistically significant difference from printing on a stationary target (Figure 3C–F).

Taken together, these results demonstrate that the fiber-based LIST not only results in a small-footprint mobile system but also enables automation for printing in dynamic environments—something that was impossible with the initial LIST implementation,[28,34,35] which was based on free-space optics and a stationary printing head.

3.4. The effect of the ink viscosity and printing energy on the bubble and jetting dynamics

In DoD printing, the viscosity of the ink plays a crucial role in determining the efficiency and quality of the printing process.[37,38] Here we sought to understand its effect on the bubble and microjet dynamics using the mobile LIST printing head.

Figure 4A shows a microjet ejection from the printing head, with an indicative sequence of images captured using a high-speed camera. A bubble forms below the fiber tip, expands toward the opening, reaches its maximum size, and then collapses. Simultaneously, a microjet forms at the capillary opening, grows, and eventually detaches. Using multiple image sequences, we monitored bubble and jetting dynamics for a range of ink viscosity (2.8–165 cP). We found that the jet generation threshold increased with viscosity, ranging from 180 μJ for 2.8 cP to 260 μJ for

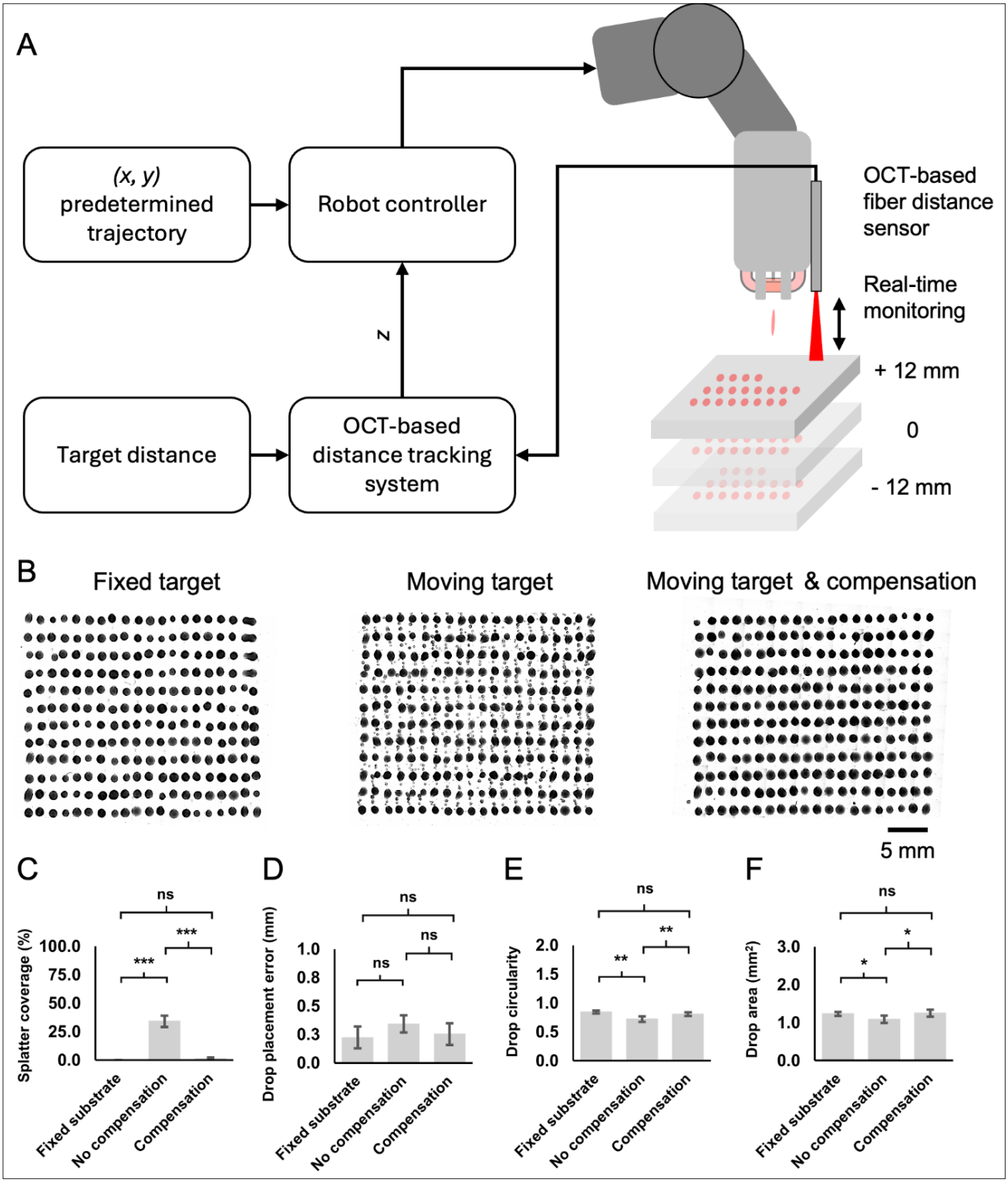

Figure 3. Positioning tracking ensures uncompromised printing quality on a moving target. (A) Flow chart of robot control for printing on a movable target using an optical coherence tomography (OCT) fiber-based distance tracking system. (B) Optical microscope images of model ink arrays printed using: a fixed 3 mm printing head-to-target distance (left), a moving target with a 12 mm amplitude (middle), a moving target with a 12 mm amplitude and dynamic z-position adjustment (right). The effect of the printing mode on: (C) splatter coverage, (D) drop placement error, (E) drop circularity, and (F) drop area at different printing head-to-target distances. Data in graphs (C) to (F) were analyzed using one-way ANOVA. Error bars represent the standard deviation from three independent printing experiments.

165 cP. The jet front position for three selected viscosities (2.8, 75, and 165 cP) is plotted up to the pinch-off time in Figure 4B, while the corresponding plots for all tested viscosities can be found in Figure S2, Supplementary File. Processing the linear part of the jet front allowed for the calculation of jet-ejection velocities for the examined conditions (Figure 4C). The jet velocity increased with the energy for all viscosities, covering the range of 0.78 ± 0.96 to 15.23 ± 0.90 m/s. The corresponding dynamic pressure ($P = \rho v^2/2$) varied from 0.34 ± 0.83 to 127 ± 15.08 kPa (Figure 4D). The jet velocity decreased with increasing viscosity for a given energy. Pinch-off times were observed

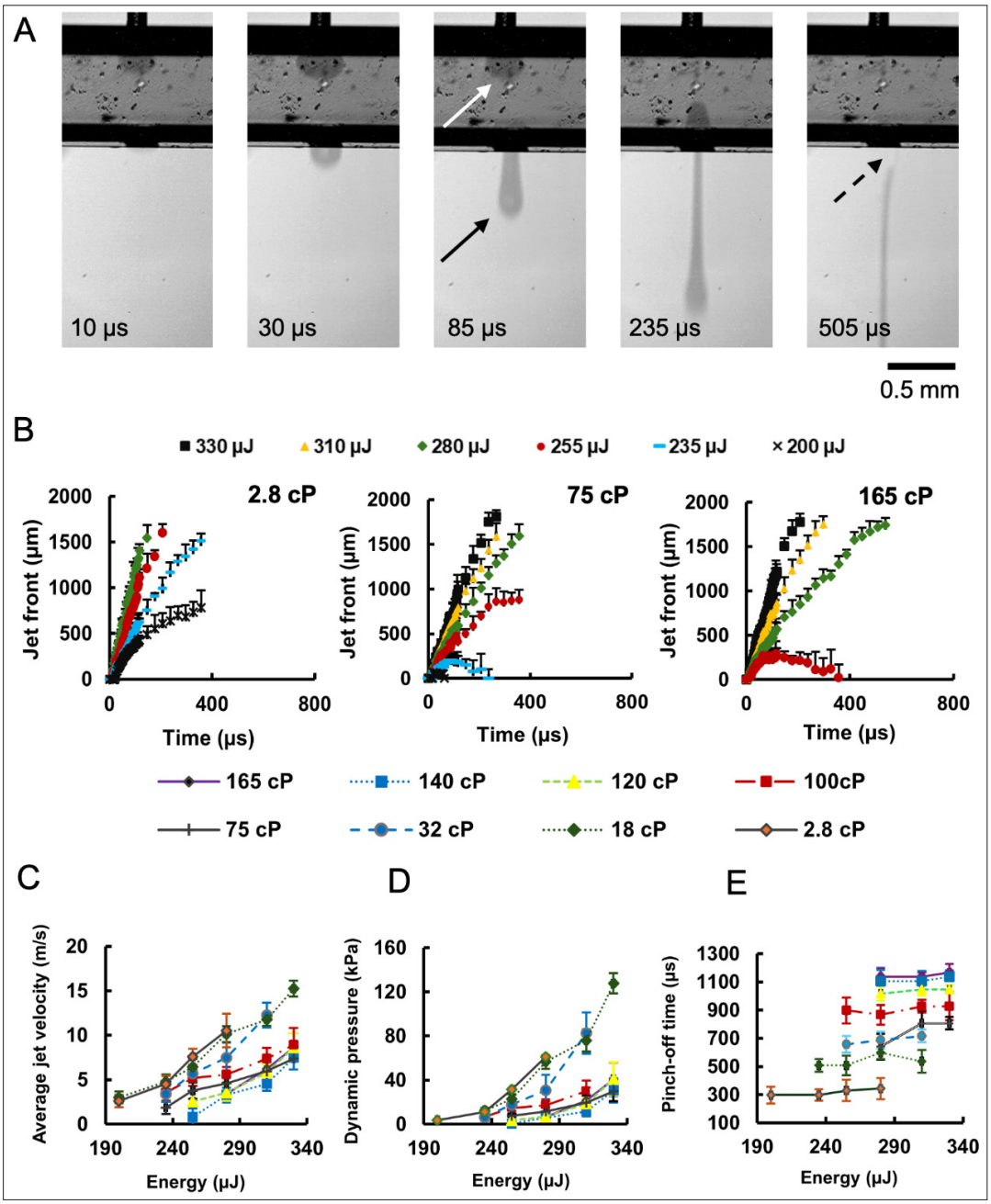

Figure 4. The effect of ink viscosity and laser energy on jetting dynamics. (A) A sequence of images taken with a high-speed camera showing the ejection of a microjet from the glass capillary opening. The solid white arrow indicates the bubble front, the solid black arrow indicates the jet front, and the dashed black arrow indicates the jet pinch-off. (B) The jet front position evolution for three viscosities (2.8 cP—left; 75 cP—middle; 165 cP—right). The dependence of (C) the average jet velocity, (D) dynamic pressure, and (E) pinch-off time on the laser pulse energy for different ink viscosities. Error bars represent the standard deviation from three independent printing experiments.

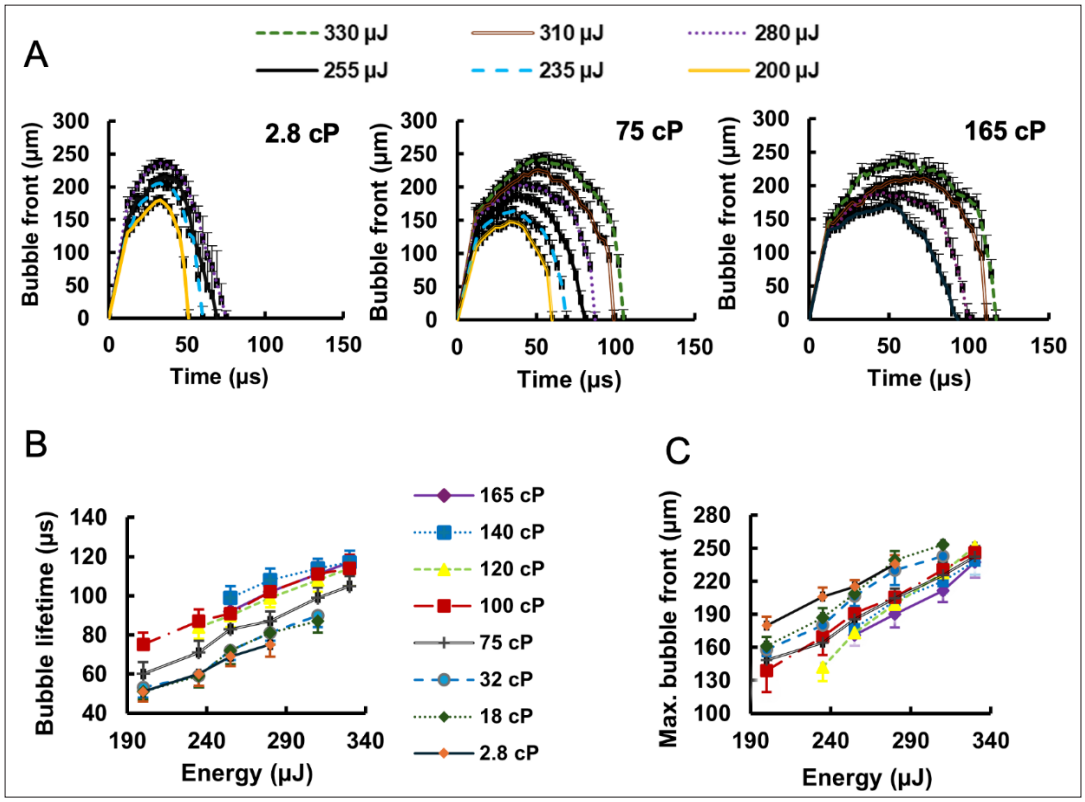

Figure 5. The effect of ink viscosity and laser energy on bubble dynamics. (A) The bubble front evolution for three viscosities (2.8 cP—left; 75 cP—middle; 165 cP—right). The dependence of (B) the bubble lifetime and (C) the maximum bubble front on the laser pulse energy for different ink viscosities. Error bars represent the standard deviation from three independent printing experiments.

to range from 297 ± 60 to 1167 ± 60 μs for the examined conditions, with pinch-off time increasing as viscosity increased for a given laser energy (Figure 4E).

Figure 5A shows the bubble evolution over time for three selected viscosities (2.8, 75, and 165), while the corresponding plots for all tested viscosities can be found in Figure S3, Supplementary File. The bubble lifetime varied from 51 ± 5 to 117 ± 6 μs for the examined conditions (Figure 5B), while the maximum bubble front ranged from 142.13 ± 5.71 to 261.54 ± 14.25 μm (Figure 5C). A clear trend in these graphs is that bubble lifetime increases with the viscosity, whereas the maximum bubble front decreases with increasing viscosity.

Using the images captured by the fast camera (Figure 4A), we calculated the bubble volume and jet volume under the examined conditions. The jet volume

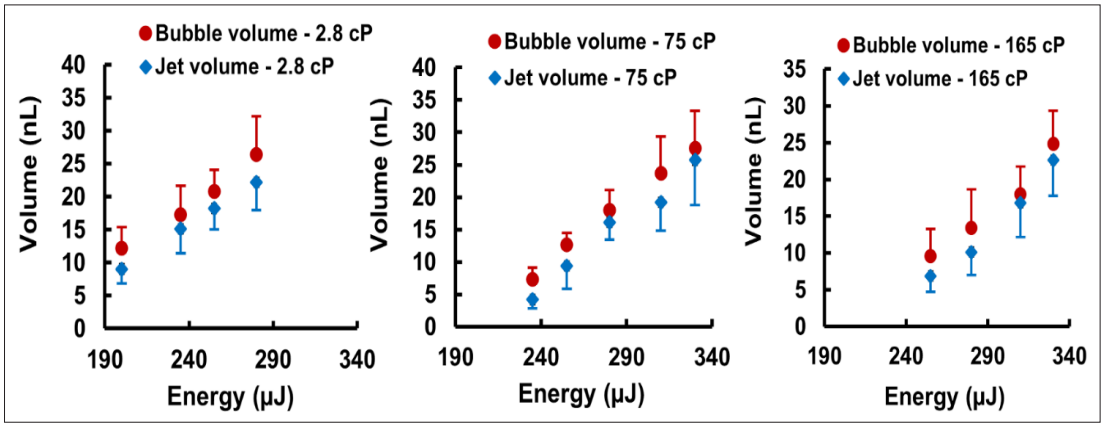

Figure 6. The dependence of the bubble and jet volume on the laser energy for three viscosities (2.8 cP—left; 75 cP—middle; 165 cP—right). Error bars represent the standard deviation from three independent printing experiments.

ranged from 4.17 ± 1.33 to 25.7 ± 6.9 nL and was consistently lower than the bubble volume, which ranged from 7.26 ± 1.83 to 27.56 ± 5.79 nL (Figure 6). Despite this difference, the jet and bubble volumes showed a consistent correlation across the different energies and viscosities.

Taken together, these results highlight the influence of ink viscosity on microjet ejection and bubble dynamics. Higher viscosities require more energy for jet ejection and slow down bubble dynamics, microjet formation, and the detachment process.

4. Discussion

This study aimed to develop and validate a mobile LIST printing platform, with a focus on investigating critical parameters that influence print quality, including head-to-substrate distance, ink viscosity, and motion compensation. Here we discuss the key findings in relation to current limitations and future directions in laser-based DoD printing.

Shape fidelity is crucial in bioprinting because it determines how closely a printed structure matches its intended design. In DoD printing, maintaining high fidelity in printed structures requires precise placement of each droplet on the substrate with minimal deviation or splashing. In this work a printing head-to-target distance of 3 mm was the upper limit for ensuring splatter-free printing. Distances greater than 3 mm resulted in a significant increase in splatter coverage, which reached 37.36 ± 13.01% at 24 mm. This increase can be attributed to the longer flight distance of the droplet, which increases its exposure to aerodynamic forces, causing potential disruptions in its shape or trajectory.[39] These disturbances may lead to droplet breakup into smaller droplets or scattering upon impact. To mitigate this, increasing the droplet ejection speed can reduce flight time and make the process less sensitive to variations in printing head-to-substrate distance, thereby improving positional accuracy.[40] However, caution is needed when increasing jet speed to avoid splashing upon substrate impact or unintended jet penetration, particularly if the target is soft.

Our OCT-based distance sensing approach proved effective in eliminating print quality loss when printing on a moving target, simulating physiological movements. This finding is particularly relevant for *in vivo* bioprinting applications, where the targeted anatomical defect may shift due to breathing, heartbeat, or unpredictable patient motion.[17,41] Previously developed automation systems for compensating target motion in 3D bioprinting are primarily machine vision-based[14,41] and are relatively bulky compared to the miniaturized fiber-based system (0.25 mm in diameter) developed in this work. These existing systems typically offer millimeter-scale precision in position tracking, whereas the OCT system presented here achieves micrometer-level precision. Therefore, this system is well suited for integration with extrusion-based bioprinters, where the required precision in maintaining the nozzle-to-target distance is an order of magnitude higher than in DoD systems.

The central mechanism in the LIST printing process is nanosecond laser-induced thermocavitation—a rapid, localized phenomenon initiated by the interaction of nanosecond laser pulses with highly-absorbing liquid.[42,43] Nanosecond laser pulses rapidly heat a small volume of liquid, leading to near-instantaneous vaporization and bubble formation. The bubble expands until its internal pressure equilibrates with ambient pressure at its maximum radius, after which it collapses due to compression by the surrounding liquid. The growth and collapse dynamics of these bubbles are influenced by the physical properties of the liquid medium, particularly its viscosity. In this work, we found that higher ink viscosities slow down bubble dynamics. This is a consistent with the fact that in viscous fluids, internal friction resists flow, resulting in slower fluid motion.[44] When the same amount of energy (e.g., from a laser pulse) is applied, a greater proportion is dissipated through viscous forces, leaving less energy available for bubble expansion. Consequently, bubble growth in high-viscosity inks is slower and reaches a smaller maximum radius compared to low-viscosity fluids.[45,46] We also found that higher viscosities require greater energy for jet ejection and lead to longer jet pinch-off times. This is primarily because viscous fluids resist necking flow, allowing the liquid column to sustain elongation for a longer duration before breaking. This behavior is observed in both inkjet and laser-assisted bioprinting. For instance, in alginate inkjet printing, increasing the sodium alginate (NaAlg) concentration from 0.15% to 2% (w/v)—and thus increasing viscosity—results in a fourfold increase in droplet pinch-off time.[47]

The Ohnesorge number (Oh) is a key dimensionless parameter used to evaluate the jetting behavior of fluids. It encapsulates the balance between viscous, inertial, and surface tension forces, and is defined as $Oh = \mu/\sqrt{(\rho\sigma d)}$, where μ is the dynamic viscosity, ρ the fluid density, σ the surface tension, and d the characteristic length scale (typically the nozzle or jet diameter).[48] In this work, the Ohnesorge number ranged from 0.021 for the lowest-viscosity ink (2.8 cP) to 1.31 for the highest-viscosity ink (165 cP). In accordance with our results, Newtonian fluids in the Ohnesorge number range of 0.01 to ~1.5 have been shown to produce stable, satellite-free droplets in laser-assisted flow-focusing systems.[25] The Weber number (We) was also calculated to characterize the ratio of inertial to

surface tension forces, defined as We = $(\rho v^2 d)/\sigma$, where v is the jet velocity. The Weber number is useful for assessing droplet behavior upon impact, such as splashing or penetration into soft substrates (e.g., tissue).[49,50] Across all tested viscosities and laser energies using the mobile LIST printer, the Weber number ranged from 20 to 320—placing it well within the drop spreading regime and avoiding conditions associated with splashing or substrate penetration when targeting soft tissue.[51]

Compared to our previous LIST implementation using a fixed printing head with free-space optics,[28] the present mobile fiber-based setup shows a consistently higher printing threshold energy—by a factor of 1.5—across all tested viscosities (2.8–140 cP) with the same model ink. Two factors likely contribute to this difference. The primary factor is that, in the mobile fiber-based setup, the bubble is generated at the top part of the capillary, which is farther from the opening compared to the free-space optics system, where the bubble forms in the middle of the capillary. The second factor is the focusing lens used in the fixed setup, which produced a smaller spot size compared to the 105 μm fiber output, thereby yielding a higher power density at the focus for the same deposited energy. Nevertheless, both systems achieved printing over a similar viscosity range.

One limitation of the present study is that printing experiments were conducted using a step-by-step movement of the robotic arm rather than continuous motion along predefined paths. This was necessary due to the need for continuous Z-coordinate updates using input from the OCT-based position tracking system. However, this operational mode introduced vibrations, which significantly contributed to drop placement errors. For instance, when the update frequency of the XYZ coordinates was reduced from 5 to 2 Hz, the droplet placement error decreased from 220 ± 113 to 119 ± 57 μm at 3 mm. This suggests that mechanical instability and vibrations in the robotic arm play an important role in accuracy limitations. This issue could potentially be mitigated by using a robotic arm that is less susceptible to vibration, or by employing a separate end-effector dedicated to Z-positioning, thus decoupling vertical adjustments from general motion.

In experiments conducted without Z-position adjustment, the mobile LIST printer operated smoothly at frequencies up to 30 Hz, which corresponds to the maximum repetition rate of our current laser system. Based on the observed pinch-off times, frequencies as high as 800 Hz appear to be theoretically feasible, although this has yet to be experimentally confirmed.

We employed an FDA-approved dye to enhance the model ink's absorption coefficient at 532 nm. While effective for energy absorption, this dye imparts a red coloration to the printed constructs. The dye does not pose biocompatibility concerns,[26–28,34,35] but the coloration may not be entirely washable from some matrices. This may limit the use of this approach in applications that require high optical transparency. One potential solution is to shift to mid-infrared laser sources, where water exhibits a much higher absorption coefficient.[52,53] These wavelengths have already been successfully applied in donor-free LIFT bioprinting,[54,55] suggesting a promising path forward for dye-free LIST.

5. Conclusion

In conclusion, we successfully developed and validated a mobile, laser-assisted DoD printing head integrated with a robotic arm and an optical distance sensor. Printing volumes for model inks with viscosities up to 165 cP were in the nanoliter range. Higher viscosities required increased laser energy and resulted in longer jet pinch-off times. Our results highlight that maintaining a printing head-to-target distance below 3 mm is essential for preserving print quality, and that our dynamic distance compensation effectively mitigates printing quality loss on targets simulating physiological motion. This compact, mobile DoD system can facilitate *in situ* bioprinting applications in dynamic physiological environments.

Acknowledgments

The authors thank Jennyfer Zapata-Farfan and the Meunier lab at Polytechnique Montreal for machining the glass capillaries used in this work. Ahad Mohammadi is a recipient of a PhD scholarship funded by the Hôpital Maisonneuve-Rosemont Foundation. Shakiba Davani is a recipient of a PhD scholarship from the Fonds de recherche en ophtalmologie de l'Université de Montréal.

Funding

Christos Boutopoulos acknowledges financial support from the Canadian Institutes of Health Research (#527176), the Natural Sciences and Engineering Research Council (NSERC) (#RGPIN-2025-07077), the Fonds de la recherche en santé du Québec (FRQS) (#312263), and the Canada Foundation for Innovation (#43112).

Conflict of interest

The authors declare they have no competing interests.

Author contributions

Conceptualization: Ahad Mohammadi, Christos Boutopoulos
Formal analysis: Ahad Mohammadi
Funding acquisition: Christos Boutopoulos

Investigation: Ahad Mohammadi, Shakiba Davani, Christos Boutopoulos
Methodology: Ahad Mohammadi, Shakiba Davani, Christos Boutopoulos
Supervision: Christos Boutopoulos
Visualization: Ahad Mohammadi, Christos Boutopoulos
Writing–original draft: Ahad Mohammadi
Writing–review & editing: Ahad Mohammadi, Shakiba Davani, Christos Boutopoulos

Ethics approval and consent to participate

Not applicable.

Consent for publication

Not applicable.

Availability of data

The data can be obtained from the corresponding author upon reasonable request.

References

1. Leberfinger AN, Dinda S, Wu Y, *et al.* Bioprinting functional tissues. *Acta Biomater.* 2019;95:32-49. doi: 10.1016/j.actbio.2019.01.009.
2. Xu H-Q, Liu J-C, Zhang Z-Y, Xu C-X. A review on cell damage, viability, and functionality during 3D bioprinting. *Mil Med Res.* 2022;9(1):70-82. doi: 10.1186/s40779-022-00429-5.
3. Abuwatfa WH, Pitt WG, Husseini GA. Scaffold-based 3D cell culture models in cancer research. *J Biomed Sci.* 2024;31(1):7-20. doi: 10.1186/s12929-024-00994-y.
4. Lam EHY, Yu F, Zhu S, Wang Z. 3D bioprinting for next-generation personalized medicine. *Int J Mol Sci.* 2023;24(7):6357-6379. doi: 10.3390/ijms24076357.
5. Pathak K, Saikia R, Das A, *et al.* 3D printing in biomedicine: advancing personalized care through additive manufacturing. *Explor Med.* 2023;4(6):1135-1167. doi: 10.37349/emed.2023.00200.
6. Kim M, Kim YJ, Kim YS, *et al.* One-year results of ear reconstruction with 3D printed implants. *Yonsei Med J.* 2024;65(8):456-463. doi: 10.3349/ymj.2023.0444.
7. Singh S, Choudhury D, Yu F, Mironov V, Naing MW. In situ bioprinting—bioprinting from benchside to bedside? *Acta Biomater.* 2020;101:14-25. doi: 10.1016/j.actbio.2019.08.045.
8. MacAdam A, Chaudry E, McTiernan CD, *et al.* Development of in situ bioprinting: a mini review. *Front Bioeng Biotechnol.* 2022;10:940896. doi: 10.3389/fbioe.2022.940896.
9. Li H, Cheng F, Orgill DP, Yao J, Zhang YS. Handheld bioprinting strategies for in situ wound dressing. *Essays Biochem.* 2021;65(3):533-543. doi: 10.1042/EBC20200098.
10. Jain P, Kathuria H, Ramakrishna S, *et al.* In situ bioprinting: process, bioinks, and applications. *ACS Appl Bio Mater.* 2024;7(12):7987-8007. doi: 10.1021/acsabm.3c01303.
11. Kérourédan O, Hakobyan D, Rémy M, *et al.* In situ prevascularization designed by laser-assisted bioprinting: effect on bone regeneration. *Biofabrication.* 2019;11(4):045002. doi: 10.1088/1758-5090/ab2620.
12. Keriquel V, Oliveira H, Rémy M, *et al.* In situ printing of mesenchymal stromal cells by laser-assisted bioprinting for in vivo bone regeneration applications. *Sci Rep.* 2017;7(1):1778-1788. doi: 10.1038/s41598-017-01914-x.
13. Pazhouhnia Z, Beheshtizadeh N, Namini MS, *et al.* Portable hand-held bioprinters promote in situ tissue regeneration. *Bioeng Transl Med.* 2022;7(3):e10307. doi: 10.1002/btm2.10307.
14. Fortunato GM, Bonatti AF, Batoni E, *et al.* Motion compensation system for robotic based in situ bioprinting to balance patient physiological movements. *Bioprinting.* 2022;28:e00248. doi: 10.1016/j.bprint.2022.e00248.
15. Zhao W, Hu C, Xu T. In vivo bioprinting: broadening the therapeutic horizon for tissue injuries. *Bioact Mater.* 2023;25:201-222. doi: 10.1016/j.bioactmat.2023.01.018.
16. Samandari M, Mostafavi A, Quint J, *et al.* In situ bioprinting: intraoperative implementation of regenerative medicine. *Trends Biotechnol.* 2022;40(10):1229-1247. doi: 10.1016/j.tibtech.2022.03.009.
17. Li K, Huang W, Guo H, *et al.* Advancements in robotic arm-based 3D bioprinting for biomedical applications. *Life Med.* 2023;2(6):lnad046. doi: 10.1093/lifemedi/lnad046.
18. Yang Y, Cai Y, Jung Yoon Y, Zhao H, Gupta SK. Sensor-based planning and control for conformal deposition on a deformable surface using an articulated industrial robot. *J Manuf Sci Eng.* 2024;146(1):011005. doi: 10.1115/1.4063560.
19. Li X, Liu B, Pei B, *et al.* Inkjet bioprinting of biomaterials. *Chem Rev.* 2020;120(19):10793-10833. doi: 10.1021/acs.chemrev.0c00008.

20. Serra P, Piqué A. Laser-induced forward transfer: fundamentals and applications. *Adv Mater Technol.* 2019;4(1):1800099. doi: 10.1002/admt.201800099.

21. Morales M, Munoz-Martin D, Marquez A, *et al.* Laser-induced forward transfer techniques and applications. *Adv Laser Mater Process.* 2018:339-379. doi: 10.1016/B978-0-08-101252-9.00013-3.

22. Fernández-Pradas J, Colina M, Serra P, *et al.* Laser-induced forward transfer of biomolecules. *Thin Solid Films.* 2004;453(1-2):27-30. doi: 10.1016/j.tsf.2003.11.154.

23. Elezoglou S, Hatziapostolou A, Giannakopoulos K, *et al.* High-precision depth-controlled laser bioprinting of cells in extracellular matrix for three-dimensional structures. *Int J Bioprint.* 2025;11(3):292-306. doi: 10.36922/IJB025100082.

24. Koch L, Deiwick A, Soriano J, *et al.* Laser bioprinting of human iPSC-derived neural stem cells and neurons: effect on cell survival, multipotency, differentiation, and neuronal activity. *Int J Bioprint.* 2023;9(2):672-684. doi: 10.18063/ijb.v9i2.672.

25. Delrot P, Modestino MA, Gallaire F, *et al.* Inkjet printing of viscous monodisperse microdroplets by laser-induced flow focusing. *Phys Rev Appl.* 2016;6(2):024003. doi: 10.1103/PhysRevApplied.6.024003.

26. Ebrahimi Orimi H, Hosseini Kolkooh SS, Hooker E, *et al.* Drop-on-demand cell bioprinting via laser induced side transfer (LIST). *Sci Rep.* 2020;10(1):9730-9740. doi: 10.1038/s41598-020-66565-x.

27. Roversi K, Ebrahimi Orimi H, Falchetti M, *et al.* Bioprinting of adult dorsal root ganglion (DRG) neurons using laser-induced side transfer (LIST). *Micromachines.* 2021;12(8):865-875. doi: 10.3390/mi12080865.

28. Erfanian M, Mohammadi A, Orimi HE, *et al.* Drop-on-demand bioprinting: a redesigned laser-induced side transfer approach with continuous capillary perfusion. *Int J Bioprint.* 2024;10(3):2832-2845. doi: 10.36922/ijb.2832.

29. Sheely ML. Glycerol viscosity tables. *Ind Eng Chem.* 1932;24(9):1060-1064. doi: 10.1021/ie50273a022.

30. Pope RM, Fry ES. Absorption spectrum (380–700 nm) of pure water. II. Integrating cavity measurements. *Appl Opt.* 1997;36(33):8710-8723. doi: 10.1364/AO.36.008710.

31. Reddy RS, Alahmari KA, Silvian PS, *et al.* Reliability of chest wall mobility and its correlation with lung functions in healthy nonsmokers, healthy smokers, and patients with COPD. *Can Respir J.* 2019;2019:5175949. doi: 10.1155/2019/5175949.

32. Abid A, Duval R, Rezende F, *et al.* A smart vitrector equipped by a fiber-based OCT sensor mitigates intentional attempts at creating iatrogenic retinal breaks during vitrectomy in pigs. *Transl Vis Sci Technol.* 2021;10(13):19. doi: 10.1167/tvst.10.13.19.

33. Abid A, Mittal S, Boutopoulos C. Etching-enabled extreme miniaturization of graded-index fiber-based optical coherence tomography probes. *J Biomed Opt.* 2020;25(3):032006. doi: 10.1117/1.JBO.25.3.032006.

34. Roversi K, Orimi HE, Erfanian M, *et al.* LIST: a newly developed laser-assisted cell bioprinting technology. *Bio Protoc.* 2022;12(19):e4527. doi: 10.21769/BioProtoc.4527.

35. Orimi HE, Hooker E, Narayanswamy S, *et al.* Spatially guided endothelial tubulogenesis by laser-induced side transfer (LIST) bioprinting of HUVECs. *Bioprinting.* 2022;28:e00240. doi: 10.1016/j.bprint.2022.e00240.

36. Thalheim R, Willert A, Mitra D, *et al.* Novel and efficient methodology for drop placement accuracy testing of robot-guided inkjet printing onto 3D objects. *Machines.* 2023;11(5):568-579. doi: 10.3390/machines11050568.

37. Antonopoulou E, Harlen O, Walkley M, *et al.* Jetting behavior in drop-on-demand printing: laboratory experiments and numerical simulations. *Phys Rev Fluids.* 2020;5(4):043603. doi: 10.1103/PhysRevFluids.5.043603.

38. Krainer S, Smit C, Hirn U. The effect of viscosity and surface tension on inkjet printed picoliter dots. *RSC Adv.* 2019;9(54):31708-31719. doi: 10.1039/C9RA04993B.

39. Cimpeanu R, Papageorgiou DT. Three-dimensional high speed drop impact onto solid surfaces at arbitrary angles. *Int J Multiph Flow.* 2018;107:192-207. doi: 10.1016/j.ijmultiphaseflow.2018.06.011.

40. Wijshoff H. The dynamics of the piezo inkjet printhead operation. *Phys Rep.* 2010;491(4-5):77-177. doi: 10.1016/j.physrep.2010.03.003.

41. Zhu Z, Guo SZ, Hirdler T, *et al.* 3D printed functional and biological materials on moving freeform surfaces. *Adv Mater.* 2018;30(23):1707495. doi: 10.1002/adma.201707495.

42. Zaca-Morán R, Amaxal-Cuatetl C, Zaca-Moran P, *et al.* Thermocavitation: a mechanism to pulse fiber lasers. *Opt Express.* 2021;29(15):23439-23446. doi: 10.1364/OE.430319.

43. Schoppink JJ, Alvarez-Chavez JA, Fernandez Rivas D. Laser beam properties and microfluidic confinement control thermocavitation. *Appl Phys Lett.* 2024;124(1):011101. doi: 10.1063/5.0186998.

44. Derby B. Inkjet printing of functional and structural materials: fluid property requirements, feature stability, and resolution. *Annu Rev Mater Res.* 2010;40(1):395-414. doi: 10.1146/annurev-matsci-070909-104502.

45. Chang J, Sun X. Laser-induced forward transfer based laser bioprinting in biomedical applications. *Front Bioeng Biotechnol.* 2023;11:1255782. doi: 10.3389/fbioe.2023.1255782.

46. Wang X, Ning Z, Lv M, *et al.* Machine learning for predicting the bubble-collapse strength as affected by physical conditions. *Results Phys.* 2021;25:104226. doi: 10.1016/j.rinp.2021.104226.

47. Xu C, Zhang M, Huang Y, *et al.* Study of droplet formation process during drop-on-demand inkjetting of living cell-laden bioink. *Langmuir.* 2014;30(30):9130-9138. doi: 10.1021/la501430x.

48. Tai J, Gan HY, Liang YN, *et al.* Control of droplet formation in inkjet printing using Ohnesorge number. *Proc Electron Packag Technol Conf.* 2008:761-766. doi: 10.1109/EPTC.2008.4763524.

49. Qian S, Zhu DZ, Xu H. Splashing generation by water jet impinging on a horizontal plate. *Exp Therm Fluid Sci.* 2022;130:110518. doi: 10.1016/j.expthermflusci.2021.110518.

50. Yarin AL. Drop impact dynamics: splashing, spreading, receding, bouncing. *Annu Rev Fluid Mech.* 2006;38:159-192. doi: 10.1146/annurev.fluid.38.050304.092144.

51. van der Ven DL, Morrone D, Quetzeri-Santiago MA, *et al.* Microfluidic jet impact: spreading, splashing, soft substrate deformation and injection. *J Colloid Interface Sci.* 2023;636:549-558. doi: 10.1016/j.jcis.2023.01.024.

52. Jang HJ, Yu H, Lee S, *et al.* Towards clinical use of a laser-induced microjet system aimed at reliable and safe drug delivery. *J Biomed Opt.* 2014;19(5):058001. doi: 10.1117/1.JBO.19.5.058001.

53. Ishikawa I, Aoki A, Takasaki AA. Potential applications of Erbium:YAG laser in periodontics. *J Periodont Res.* 2004;39(4):275-285. doi: 10.1111/j.1600-0765.2004.00738.x.

54. Cheptsov V, Minaev N, Zhigarkov V, *et al.* Laser bioprinting without donor plate. *Laser Phys Lett.* 2022;19(8):085602. doi: 10.1088/1612-202X/ac7b32.

55. Pushkin AV, Minaev NV, Potemkin FV, *et al.* Bioprinting with 3-μm laser pulses. *Opt Laser Technol.* 2024;172:110482. doi: 10.1016/j.optlastec.2023.110482.

ACCSCIENCE PUBLISHING

International Journal of Bioprinting

RESEARCH ARTICLE

Evaluation of biomechanical properties and early osseointegration of biomimetic bone trabecular Ti6Al4V scaffolds based on Voronoi design

Jinghong Yang[1,2†], Zi Wang[1,3,4†], Lujun Jiang[1,3,4†], Zhong Li[1,3,4*], Linlin Liu[5*], and Juncai Liu[1,3,4*]

[1]Department of Orthopedics, The Affiliated Hospital, Southwest Medical University, Luzhou, Sichuan, China

[2]Department of Orthopaedic Surgery, The First Affiliated Hospital of Chongqing Medical University, Chongqing, China

[3]Stem Cell Immunity and Regeneration Key Laboratory of Luzhou, Southwest Medical University, Luzhou, Sichuan, China

[4]Sichuan Provincial Laboratory of Orthopaedic Engineering, Southwest Medical University, Luzhou, Sichuan, China

[5]School of Integrated Circuits, Chongqing University of Posts and Telecommunications, Chongqing, China

[†]These authors contributed equally to this work.

***Corresponding authors:**
Zhong Li
(lizhong403@swmu.edu.cn)

Linlin Liu
(1102584187@qq.com)

Juncai Liu
(liujuncai011218@163.com)

Citation: Yang J, Wang Z, Jiang L, Li Z, Liu L, Liu J. Evaluation of biomechanical properties and early osseointegration of biomimetic bone trabecular Ti6Al4V scaffolds based on Voronoi design. *Int J Bioprint*. 2025;11(6):311-326. doi: 10.36922/IJB025310311

Received: July 31, 2025
Revised: September 18, 2025
Accepted: September 22, 2025
Published online: September 22, 2025

Copyright: © 2025 Author(s). This is an Open Access article distributed under the terms of the Creative Commons Attribution License, permitting distribution, and reproduction in any medium, provided the original work is properly cited.

Publisher's Note: AccScience Publishing remains neutral with regard to jurisdictional claims in published maps and institutional affiliations.

Abstract

Ti6Al4V scaffolds demonstrate significant translational potential for bone defect reconstruction by virtue of their exceptional biocompatibility and corrosion resistance. However, achieving concurrent osseointegration enhancement and mechanical compatibility with native cancellous bone remains a critical design constraint. A trabecular bone-mimetic porous Ti6Al4V scaffold was fabricated via Voronoi-tessellated computer-aided design and selective laser melting. Precise modulation of pore architecture enabled controlled porosity. The mechanical properties of the scaffold were characterized through compression testing. Early-stage *in vivo* osseointegration was evaluated at weeks 4 and 12 in a rabbit femoral condyle defect model using histomorphometry and micro-computed tomography, with comparisons made against conventional strut-based and G-curved lattice structures. The Voronoi scaffold demonstrated an elastic modulus and yield strength comparable to cancellous bone, thereby mitigating stress-shielding effects. Additionally, according to the results from the biomechanics, computational fluid dynamics, and *in vivo* analyses, the scaffold demonstrated significantly enhanced osteogenic potential and superior bone-implant interface integration compared to the strut and triply periodic minimal surface (TPMS) designs. In conclusion, the Voronoi design provides an effective biomimetic strategy for fabricating porous titanium alloy bone scaffolds with enhanced osteogenic properties, which embody higher potential than conventional struts and TPMS structures in facilitating bone defect repair.

Keywords: Biomechanics; Computational fluid dynamics; Osseointegration; Ti6Al4V scaffolds; Voronoi

1. Introduction

Titanium and its alloys have been widely used in clinical applications for over four decades due to their exceptional biocompatibility and corrosion resistance.[1] In recent years, titanium alloy bone scaffolds have gained significant attention as a promising solution for repairing bone defects that exceed the critical defect threshold. These scaffolds are increasingly recognized as a viable option in orthopedic applications. Titanium alloys exhibit a relatively low Young's modulus (7–30 GPa) compared to other metallic materials, which, although higher than natural bone, results in a significantly reduced stress shielding effect compared to materials such as tantalum and stainless steel. This makes titanium alloys more favorable for bone repair applications. Additionally, titanium implants demonstrate superior compatibility with host bone tissue, reducing bone resorption and implant loosening.[2]

Recent advancements in 3D printing technologies, including selective laser melting (SLM), selective laser sintering, and electron beam melting, have enabled the precise fabrication of porous titanium alloy scaffolds with controllable microstructures.[3–7] By leveraging computer-aided design (CAD) methodologies, researchers can create intricate porous architectures with precisely controlled porosity and interconnectivity.[8] These techniques offer several advantages, such as streamlined construction processes, enhanced feasibility for mechanical evaluations, and rapid prototyping. Consequently, there has been a surge in research efforts by scientists and orthopedic surgeons to develop 3D-printed porous bone scaffolds.

Contemporary advancements in bone tissue engineering have focused on developing porous titanium alloy scaffolds that mimic the hierarchical architecture and multifunctional performance of natural bone. These biomimetic constructs aim to balance often-conflicting requirements, including mechanical load-bearing capacity, osteoconductive porosity, and dynamic biological responsiveness. Critical studies by Gryko et al.[9] using finite element analysis identified 40% porosity as the optimal threshold for maximizing osseointegration rates, highlighting pore architecture as a key factor in bone-scaffold interfacial remodeling. Complementary work by Arjunan et al.[7] systematically quantified how pore morphology in Ti6Al4V scaffolds governs mechanical performance, demonstrating nonlinear correlations between strut geometry and permeability, stiffness, and stress concentration factors.

Emerging Voronoi tessellation-derived scaffolds represent a paradigm shift toward stochastic biomimicry. These structures replicate the anisotropic, non-periodic topology of natural bone trabeculae through Dirichlet spatial segmentation, achieving biomechanical compatibility, enhanced biofluid dynamics, and angiogenic potential.[10] However, while the stochastic nature of Voronoi structures—resulting from the spatial distribution of seed points that generate variations in cell size, shape, and connectivity—mimics the non-periodic architecture of natural trabecular bone, it also introduces unpredictability in stress distribution, leading to localized stress concentrations as high as 2.8× ambient levels, compared to 1.9× in the curved scaffold. This necessitates advanced topology optimization algorithms to mitigate fracture risks at sharp edges. Recent innovations in SLM have enabled the fabrication of Voronoi scaffolds, which maximize osteogenic differentiation while maintaining non-cytotoxicity, as demonstrated by Chen et al.[11]

In contrast, triply periodic minimal surface (TPMS) structures, based on mathematical implicit function generation, leverage mathematical periodicity to achieve mechanical reliability, stress homogenization, and manufacturing precision.[12–15] While TPMS scaffolds demonstrate superior bone-implant contact, their uniform porosity distribution limits vascular infiltration. This dichotomy in biological performance underscores the need for anatomically stratified design strategies: Voronoi's stochastic networks may benefit vascularized defects, whereas the mechanical predictability of TPMS structures makes them well-suited for load-critical applications.[16] Additionally, conventional strut-based scaffolds offer predictable mechanical properties but may be compromised by stress shielding, biofluidic stagnation, and inadequate osteogenic stimulation, which limit the scaffolds' overall performance.[17,18]

In this study, we optimized porous bone scaffolds by evaluating three distinct structures—conventional strut-based, G-curved (TPMS), and Voronoi-trabecular biomimetic architectures—through computational modeling, mechanical testing, and animal experiments. The mechanical properties and early-stage osteogenesis of scaffolds with identical pore sizes (500 μm) and porosities (60%) were systematically assessed. The pore size of 500 μm and porosity of 60% were chosen based on previous studies indicating that this range optimally supports bone ingrowth and vascularization while maintaining mechanical strength.[11]

Mechanical characterization confirmed that all scaffolds met *in vivo* load-bearing requirements. *In vivo* evaluation involved the use of micro-computed tomography (micro-CT) reconstruction and histomorphometric analysis at weeks 4 and 12 in rabbit distal femurs bilaterally implanted with the scaffolds. These

analyses revealed architecture-dependent osteogenesis patterns. Complementary computational fluid dynamics (CFD) simulations quantitatively correlated pore topology with hydrodynamic parameters, elucidating the mechanobiological mechanisms underlying the observed differences in bone ingrowth.

2. Materials and methods

2.1. Design and manufacturing of scaffolds

Three distinct lattice architectures were investigated in this study: (i) a body-centered cubic strut-based configuration (strut), (ii) a TPMS geometry following G-surface topology (curved), and (iii) a biomimetic trabecular bone structure based on the Voronoi algorithm (Voronoi). The modeling workflow was implemented using Unigraphics NX (Siemens PLM Software, Germany) with differential approaches for each architecture.

The body-centered cubic configuration was reproduced following our previously validated modeling methodology,[19] as illustrated in Figure 1A. For the TPMS architecture, the G-surface geometry was mathematically defined using the implicit surface equation (**Equation I**), generating the curvature-dominated structure shown in Figure 1B. The Voronoi structure employed a stochastic generation process: ten seed points were randomly distributed within a $2 \times 2 \times 2$ mm^3 volumetric space, followed by application of the Voronoi tessellation algorithm. Polyhedral edges from the tessellated domains were converted into cylindrical pillars to create the bioinspired porous network depicted in Figure 1C.

$$G: \sin(\omega x)\cos(\omega y) + \sin(\omega y) \cos(\omega z) + \sin(\omega z)\cos(\omega x) = 0 \quad (I)$$

where $\omega = 2\pi/L$, and L is the length of the structural unit.

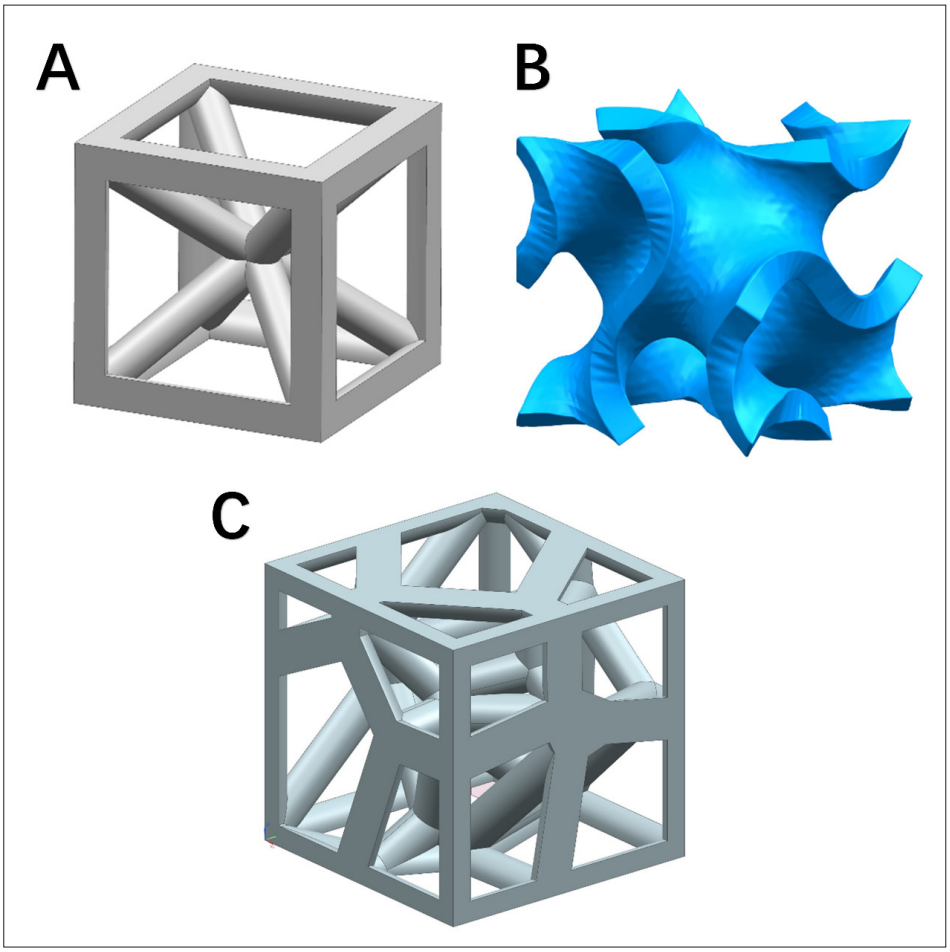

Figure 1. Schematic designs of the three structures: (A) Strut; (B) G Curve; (C) Voronoi.

All scaffolds were fabricated using SLM with the following parameters: laser power of 500 W, spot size of 50 μm, and layer thickness of 20 μm.

2.2. Characterization of the scaffolds

Three-dimensional structural characterization of the porous titanium scaffold, fabricated via SLM, was performed through micro-CT imaging (Figure 2). Following tomographic acquisition, Mimics 21.0 (Materialise, Italy), a medical image processing platform, was used to facilitate comprehensive three-dimensional reconstruction and quantitative morphometric analysis of scaffold architecture and peri-implant osseous tissue.

2.3. Mechanical properties of the scaffolds

Mechanical testing was conducted in accordance with ISO-13314, the international standard for compressive testing of porous and cellular metals. Rectangular scaffolds (n = 5; dimensions: 10 × 10 × 12 mm) were subjected to compressive strength tests using a universal testing machine (E10000 Model; Instron Company, United States) at a compression rate of 1 mm/min (Figure 3A). The elastic modulus (E) and compressive strength (σ) were derived from the material's stress–strain curve. The elastic modulus was determined as the maximum slope in the elastic region, while the yield strength was determined using the 0.2% offset method, a standard technique for metallic materials without a distinct yield point. This method involves constructing a line parallel to the elastic portion of the stress–strain curve but offset by 0.2% strain; the stress value at the intersection of this line and the curve is defined as the yield strength.

2.4. Surgical procedure

Eighteen adult male New Zealand rabbits (2.5–3.0 kg) were obtained from the Laboratory Animal Center of Southwest Medical University for this study. The rabbits were housed

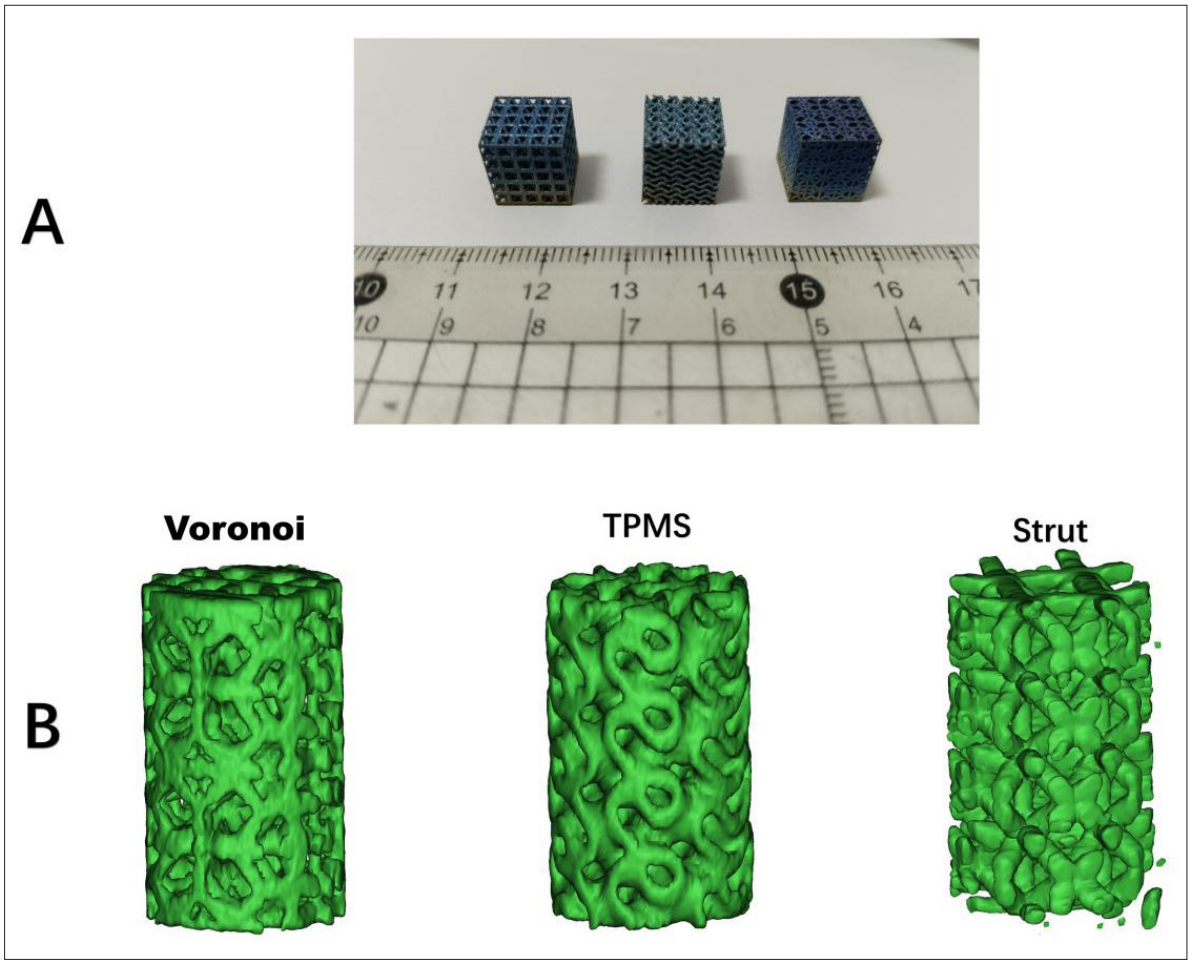

Figure 2. Photograph of the three 3D-printed titanium stents (A), and micro-CT reconstruction of the three porous titanium stents (B). Abbreviations: Micro-CT, micro-computed tomography; TPMS, triply periodic minimal surface.

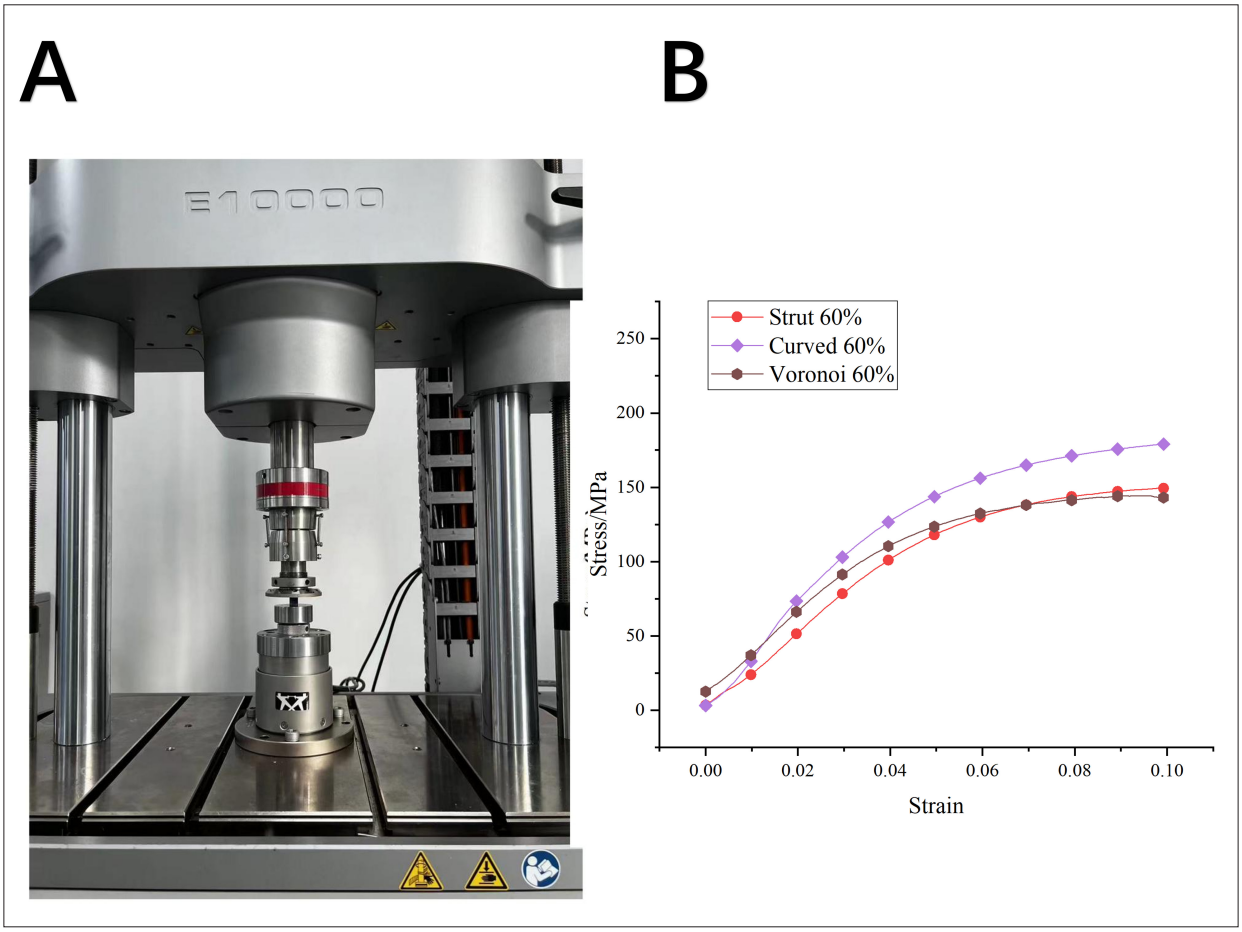

Figure 3. Universal Testing Machine (E10000 Model, Instron Company) (A), and stress–strain curves of the three scaffold specimens (B).

in a controlled environment with a temperature of 24°C and humidity of 60%, with free access to food and water. The experimental protocols involving animals were approved by the Ethics Committee of the Affiliated Hospital of Southwest Medical University to safeguard the welfare of laboratory animals, in compliance with international standards such as the Declaration of Helsinki. The rabbits were randomly assigned to three groups based on the duration of implantation (6 or 12 weeks). In each group, 18 femurs from 18 rabbits were implanted with three types of cylindrical scaffolds, each with distinct structures.

General anesthesia was induced using intravenous 3% sodium pentobarbital (30 mg/kg), supplemented with local anesthesia using 0.5% lidocaine. Following skin preparation and disinfection, a 3 cm longitudinal incision was made at the femoral condyle (Figure 4A). The skin and subcutaneous tissue were incised, the muscles were separated, and the periosteum was cut to expose the femoral condyle. A hole with a diameter of 5 mm and a depth of 8 mm was made in the lateral femoral condyle using a low-speed drill (Figure 4B). To prevent thermal necrosis, the drilling site was continuously irrigated with saline solution. After scaffold implantation (Figure 4C), the wound was closed in layers. Postoperative anti-infective treatment was administered via intramuscular injection of cephalosporin antibiotics for three days.

At 4 and 12 weeks post-implantation, euthanasia was performed via intravenous air injection, followed by harvesting of the femurs. The harvested femurs were rinsed with formalin, dehydrated in ethanol, infiltrated, embedded, and sectioned into 200 μm slices using an EXAKT E300CP hard tissue slicer (Germany). The slices were ground and polished to produce thin sections of approximately 70 μm. Hematoxylin and eosin staining was applied, and the sections were examined under a light microscope (Olympus, Japan) to evaluate the presence of new bone tissue, microvascular structures, or fibrous tissue within the scaffolds.

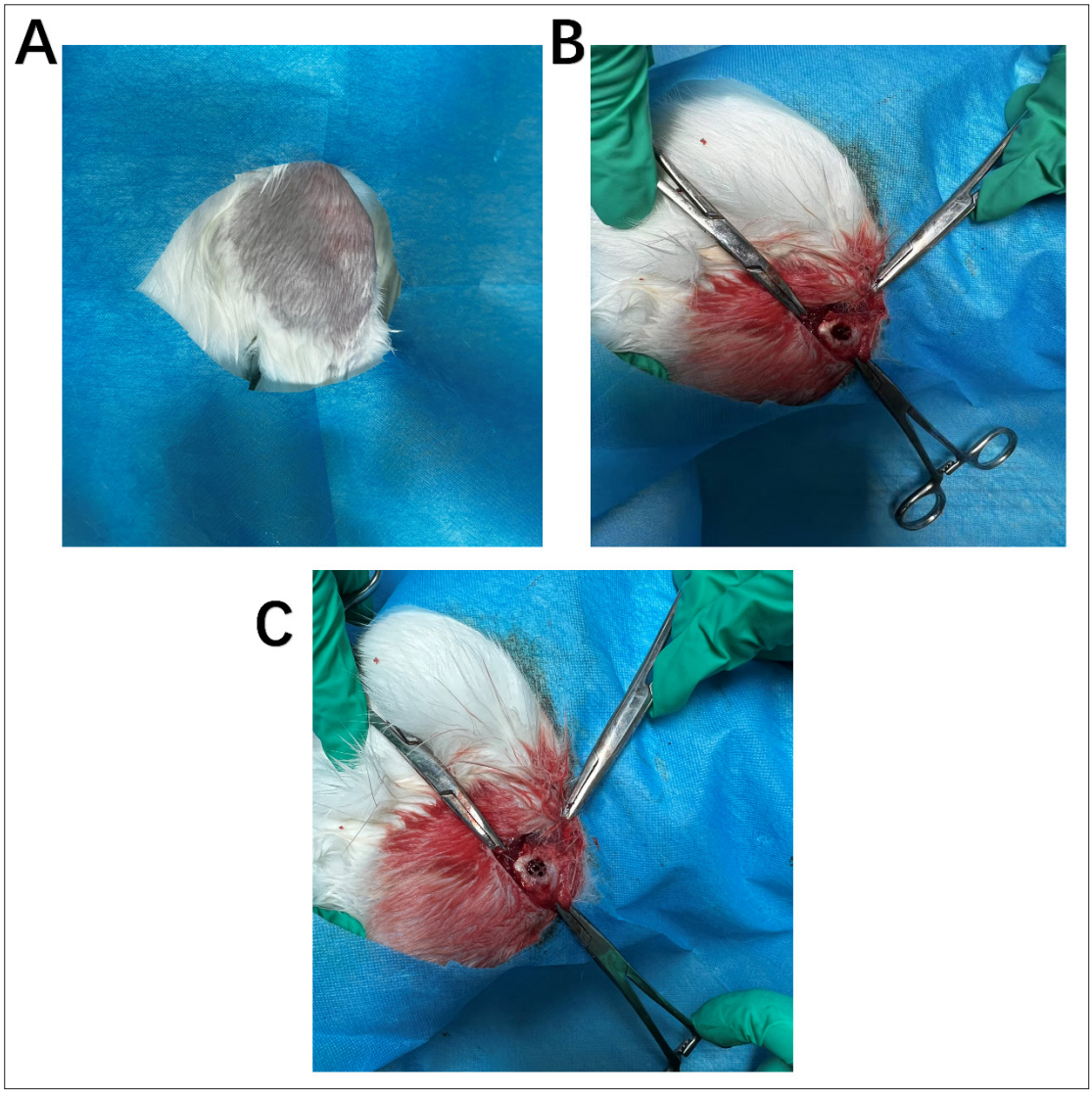

Figure 4. Surgical procedure for scaffold implantation. (A) Peeling and exposing the surgical site. (B) Creating a cylindrical defect—a hole with a diameter of 5 mm and a depth of 8 mm to match the scaffold's size—in the lateral femoral condyle of a rabbit using a low-speed drill. (C) Implanting a titanium scaffold into the femoral condylar osseous defect.

2.5. Micro-computed tomography analysis

To assess new bone formation, micro-CT (Micro-CT100, SCANCO Medical AG, Switzerland) was used to scan the rabbit femurs implanted with porous scaffolds. The scanning parameters were set as follows: X-ray source voltage of 90 kV, a beam current of 200 μA, and a resolution of 17.2 μm. After scanning, the images were reconstructed and segmented into binary forms for further analysis using Mimics 21.0 (Materialise, Belgium). The region of interest was defined as the scaffold's internal volume and the bone tissue ingrowth. Bone volume (BV) and total pore volume (TV) were measured by micro-CT, and the BV/TV ratio was calculated to quantitatively assess bone ingrowth. A higher BV/TV ratio indicates enhanced bone formation within the scaffold.

2.6. Histological evaluation

The femoral condyle was first fixed, then dehydrated with ethanol, and embedded in methyl methacrylate. A 50 μm-thick slice was cut along the longitudinal axis of the cylindrical scaffold using a saw blade. The section was subsequently stained with 1.2% trinitrophenol and 1% acid magenta (Van-Gieson staining). Finally, the stained sample was examined using a fluorescence microscope (Olympus, Japan) for analysis.

2.7. Computational fluid dynamics simulation

CFD was employed to assess permeability, flow velocity, and internal velocity streamlines of various scaffolds. To reduce computational time, the analysis was limited to 2 × 2 unit cells, taking advantage of the structural symmetry. The Navier–Stokes equations[20] were applied under the assumption that the fluid behaves as an incompressible medium.

$$\rho\frac{\theta v}{\theta t} - \mu\nabla^2 V + \rho\left(v \bullet \nabla\right)v + \nabla p = F,\ \nabla.V = 0 \qquad \text{(II)}$$

where ρ, v, and μ represent the density (kg/m³), flow velocity (m/s), and dynamic viscosity (kg/m/s) of the fluid, respectively; ∇ stands for the del operator; p refers to pressure (MPa); and F represents force (N). The permeability κ of the three scaffold designs was computed based on Darcy's law:

$$\kappa = \frac{v.\mu.L}{\Delta P} \qquad \text{(III)}$$

where v denotes the fluid inlet velocity (measured in m/s), L represents the characteristic length of the model (in meters), and ΔP corresponds to the pressure differential across the system (expressed in MPa).

The CFD simulation model was subjected to analysis and computation utilizing Ansys Fluent software (Ansys, United States). During the computational process, specific boundary conditions were assigned: the inlet velocity was established at a value of 0.1 mm/s, the outlet pressure was configured to 0, the fluid density was designated as 1050 kg/m³, and the viscosity was set to 0.0037 kg/(m·s).[21] Additionally, a supplementary fluid domain positioned above the structural configuration was incorporated to mitigate potential boundary effects.

2.8. Finite element analysis

Static structural analysis was carried out on the three scaffold models using the Ansys Static Structural module. The material was modeled as an isotropic linear elastic titanium alloy (Ti6Al4V), with an elastic modulus of 110 GPa and a Poisson's ratio of 0.3. Boundary conditions simulated a porous structural environment: the base was fixed, the side walls were left free, and a compressive force of 10 N was applied normally to the top surface. The resulting stress distributions were analyzed to evaluate pressure variations throughout the scaffold.

2.9. Statistical analysis

The statistical analysis was conducted using the SPSS software (SPSS Inc., Chicago, IL, United States). All data are expressed as the mean ± standard deviation. One-way analysis of variance was employed for data analysis. In every instance, statistical significance was defined as $p < 0.05$.

3. Results

3.1. Mechanical properties of the scaffold

Figure 3B presents the stress–strain curves of three strut specimens, revealing yield strengths comparable to the TPMS structure. Experimental elastic moduli and yield strengths are shown in Table 1. While trabecular bone exhibits an elastic modulus of 0.1–4.5 GPa and yield strengths of 0.56–55.3 MPa in the proximal tibia/femur, all investigated structures demonstrate significantly higher mechanical properties. Their elastic moduli (1.9–4.2 GPa) correspond well with host bone tissue requirements. Consequently, these scaffolds achieve bone-matching stiffness and enhanced yield strength, demonstrating significant potential for bone tissue engineering applications.

3.2. Micro-computed tomography analysis

Titanium scaffolds were implanted in rabbit distal femurs and explanted at weeks 4 and 12 for micro-CT analysis of bone formation. Three-dimensional reconstructions (Figure 5A) demonstrate progressive bone ingrowth within scaffolds over time. Quantitative analysis revealed distinct osseointegration patterns across scaffold types, consistent with the BV/TV ratios (Figure 5B). BV/TV measurements for strut, curved, and Voronoi structures at weeks 4 and 12 are 6.7%/9.3%, 9.1%/11%, and 9.1%/16%, respectively.

3.3. Histological analysis

Animals were sacrificed at 4 and 12 weeks. Harvested samples were fixed in 5% polyformaldehyde, dehydrated through a graded ethanol series (70%–100%), and embedded with poly(methylmethacrylate) (Cool-Set-A, Aorigin, China). Sections (10–20 μm) were prepared using a diamond histological saw (SAT-001, Origin, China) and stained with methylene blue/basic fuchsin (Sigma). Qualitative assessment of bone growth was performed on stained sections (Figure 6), revealing progressive bone

Table 1. Elastic modulus and yield strength of the three types of scaffolds tested

Scaffold type	Elastic modulus, E (GPa)	Yield strength, σ (MPa)
Strut	2.5	120
Curved	2.6	144
Voronoi	2.25	135

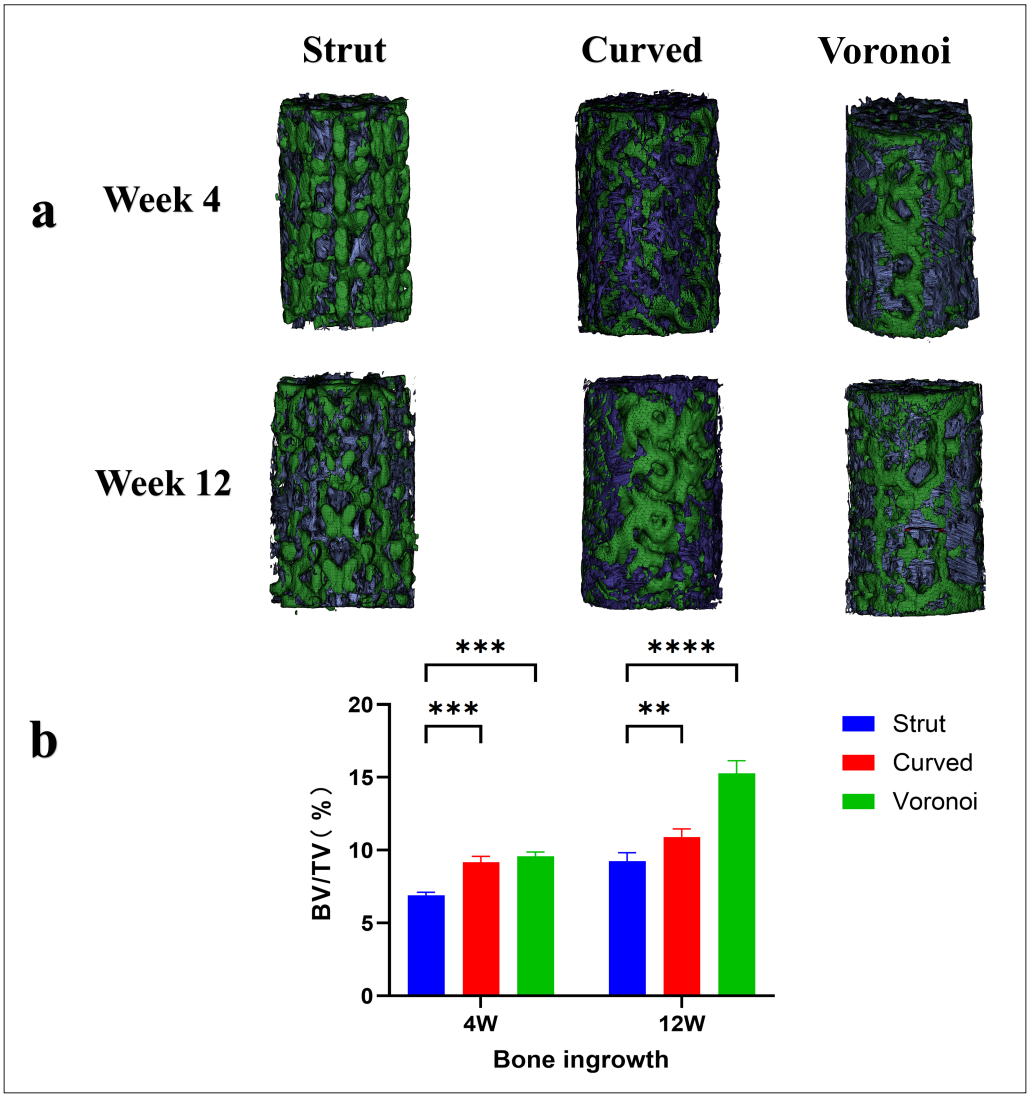

Figure 5. Micro CT image and results. (A) Micro-CT reconstruction of the distal femur of a rabbit at 4 and 12 weeks post-implantation of titanium scaffold. Green color represents the bone scaffold, and blue color represents newly formed bone. (B) BV/TV measurements for implanted scaffolds (**$p < 0.01$, ***$p < 0.001$; ****$p < 0.0001$).

tissue formation within scaffold pores over time. The highest volume of new bone formation was observed in the Voronoi structure, whereas the lowest volume was detected in the strut architecture. These findings align consistently with both the qualitative and quantitative micro-CT analyses. Therefore, histological sectioning results corroborated the experimental data, confirming their validity.

3.4. Computational fluid dynamics analysis

Fluid flow permeability and velocity within scaffolds significantly influence bone tissue regeneration.[22] While interstitial fluid transport delivers essential oxygen and nutrients to cells, excessive permeability impedes cellular adhesion, whereas insufficient permeability compromises nutrient supply.[23]

Figure 7A shows the pressure distribution maps of the stents. The pressure decreases gradually from the highest point at the inlet to the lowest point at the outlet. As shown in the pressure maps (Figure 7A), the pressure decreased gradually from the inlet to the outlet in all three structures. However, the spatial distribution of pressure varied significantly: the strut structure exhibited the most continuous and uniform pressure gradient along its straight channels. In contrast, the TPMS structure showed noticeable localized pressure concentrations at the regions of high curvature, while the Voronoi structure

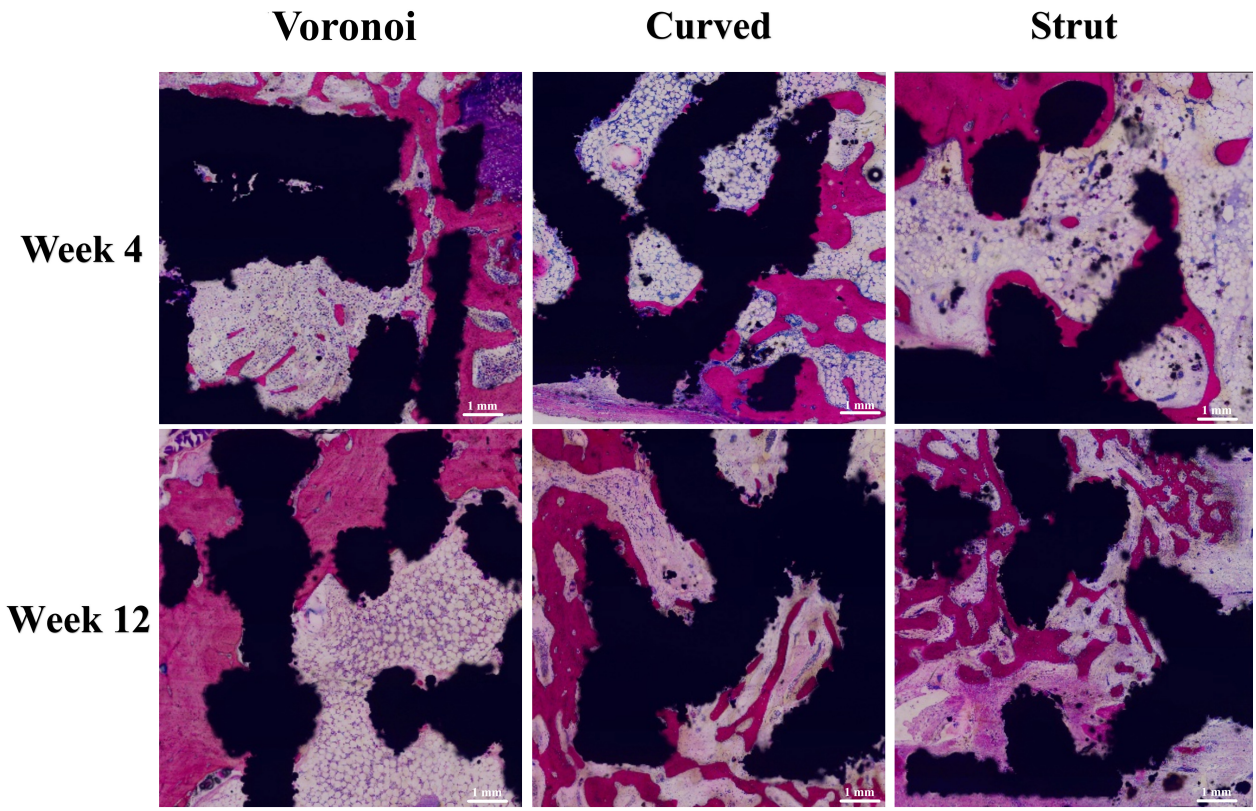

Figure 6. Stained tissue sections of bone specimens at 4 and 12 weeks post-implantation of scaffolds. Red region represents bone tissue, and black region represents scaffolds. Magnification: 10×; scale bar: 1 mm.

demonstrated a more heterogeneous but interconnected pressure distribution, with moderate variations corresponding to its irregular pore morphology.

Figure 7B presents the permeability (κ) of the three scaffold architectures, calculated using **Equation III**. The measured κ values (2.3×10^{-9} to 5.49×10^{-9} m^2) fall within the physiological range reported for proximal tibia (0.467×10^{-9} to 14.8×10^{-9} m^2).[24]

Figure 7C quantifies the pressure differential (ΔP) between the inlet and outlet across the three scaffold architectures. The strut structure shows a relatively small pressure gradient, while the curved structure shows the highest ΔP, and the Voronoi structure displayed an intermediate pressure differential. This pronounced disparity indicates that the strut structure's internal geometry significantly impedes fluid transport, reducing hydrodynamic efficiency and limiting perfusion throughout its internal domains.

Figure 8 presents flow velocity distributions within three scaffold architectures. The Voronoi structure exhibits reduced internal flow velocities relative to comparative designs, which are advantageous for cellular adhesion to scaffold surfaces, thus allowing for enhanced osteogenesis *in vivo*. Conversely, significantly elevated velocities at strut junctions versus pore regions in other structures facilitate cellular infiltration into deeper zones, thereby inhibiting surface adhesion. Consequently, the Voronoi architecture demonstrates superior cellular proliferation compared to its counterparts.

3.5. Results of finite element analysis

Based on the finite element analysis results (Figure 9), the equivalent (von Mises) stress distributions under static structural loading reveal significant mechanical differences among the three scaffold architectures. The strut structure exhibited the maximum von Mises stress of 45.572 MPa, indicating superior stress distribution and mechanical efficiency. The Voronoi structure showed an intermediate peak stress value of 71.714 MPa, reflecting its biomimetic design's ability to mitigate stress concentrations effectively. In contrast, the curved structure endured the highest stress level of 103.71 MPa, suggesting a higher risk of

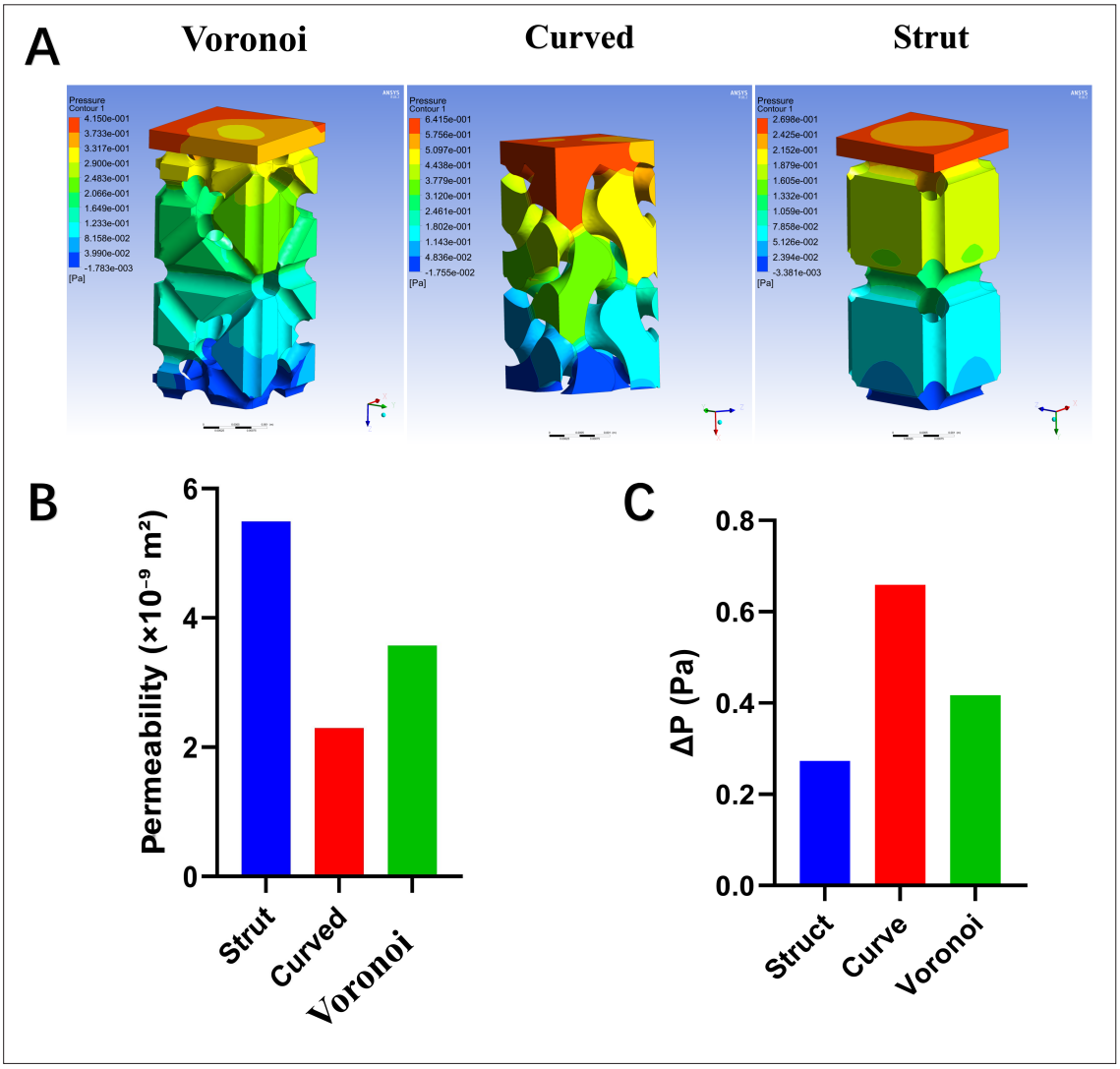

Figure 7. Fluid simulation results across the three types of scaffolds: (A) pressure distribution map; (B) permeability (κ); (C) pressure differential (ΔP).

stress shielding and potential mechanical failure under load. These results highlight the critical influence of pore architecture on mechanical performance, with the Voronoi and strut designs demonstrating more favorable stress profiles for bone scaffold applications compared to the conventional curved design.

4. Discussion

Treating large bone defects has long been a challenge for clinicians, and investigating bone tissue engineering and cancellous bone regeneration remains a hot research topic. Porous scaffolds have recently been recognized as some of the best tools for structural and functional healing of bone defects because of their immediate and lasting stability, along with excellent osteogenic properties.[25,26] Ensuring the immediate stability of bone implants, especially preventing peri-implant bone collapse that can weaken prosthetic stability, is a critical challenge in modern orthopedics. As a result, much effort is directed toward improving osseointegration through structural improvements, surface modifications, and complementary approaches.[27–29]

Our previous work demonstrated the feasibility of fabricating precise titanium scaffolds using SLM and investigated the early osseointegration potential and mechanical properties of conventional porous scaffold structures.[19] Concurrently, extensive research investigates geometry-based architectures in bone scaffolds designed via image-based structure modeling or CAD, predominantly emphasizing mechanical behavior and *in vitro* performance.[11,30,31] Nevertheless, native osseous

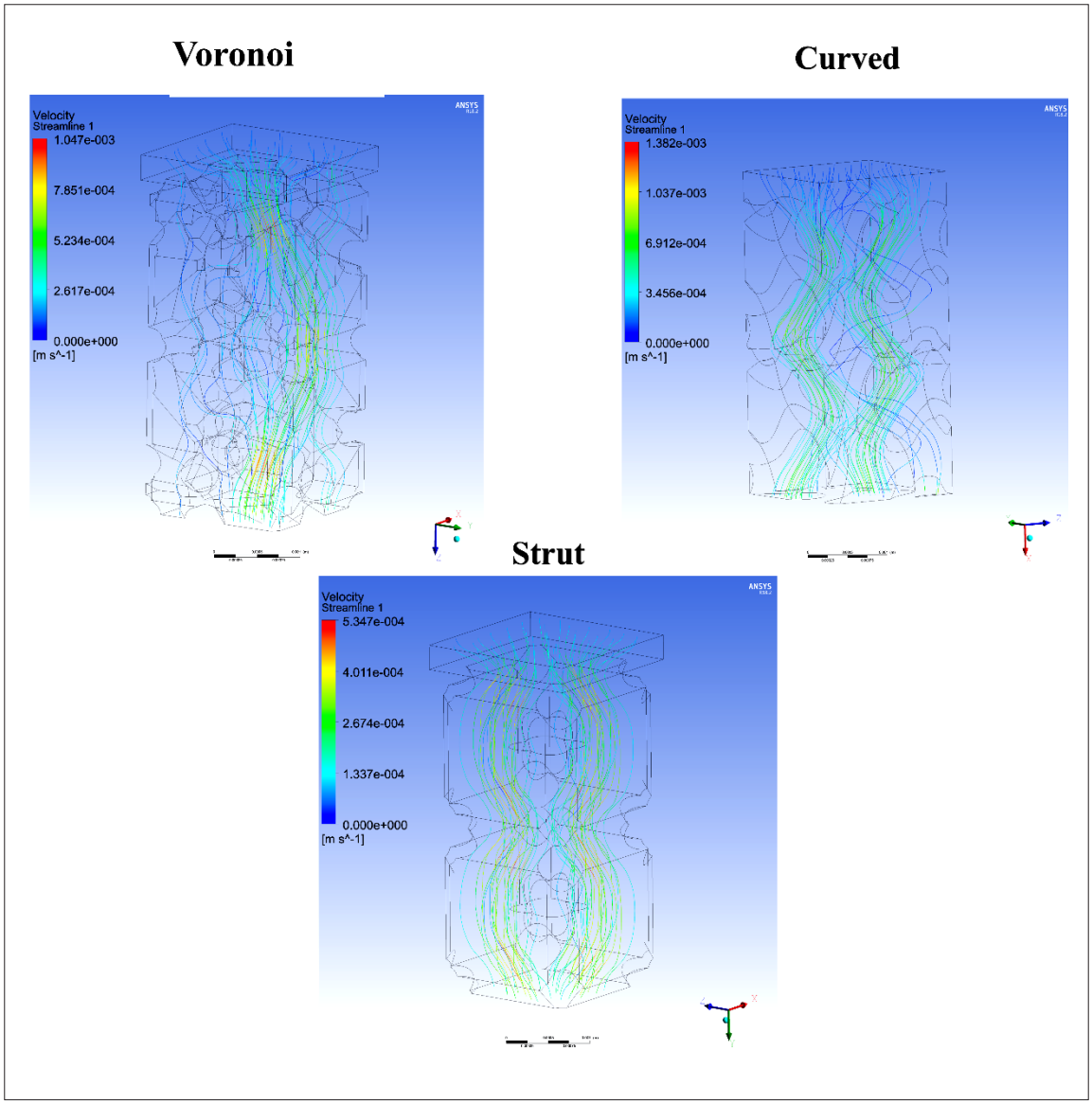

Figure 8. Velocity flow diagrams for the three scaffolds tested.

tissue exhibits intrinsically irregular Voronoi architecture and heterogeneous pore distribution—morphological features conferring biomechanically and osteogenically optimized functionality.[32,33] While CT-derived biomimetic constructs provide anatomical relevance, their clinical translation remains constrained by site-specific anatomical variations in bone microstructure and mechanical requirements. The Voronoi algorithm enables parametric design of biomimetic cancellous bone scaffolds, offering computational tractability and morphological fidelity.[34–36] Since its inception, this approach has been broadly adopted in orthopedic engineering. Voronoi scaffold architecture demonstrates superior mechanical strength and enhanced load transfer efficiency compared to conventional strut-based and gyroid TPMS designs.[37,38] This performance advantage aligns with the physiological load-bearing mechanisms inherent to human skeletal systems.[39]

To assess early osteogenic potential, a systematic comparison was made among three Ti6Al4V scaffold architectures with 60% porosity: Voronoi-based, conventional strut-based, and curved designs. Following implantation of the scaffolds in rabbit femoral condyles, osseointegration dynamics were quantitatively analyzed

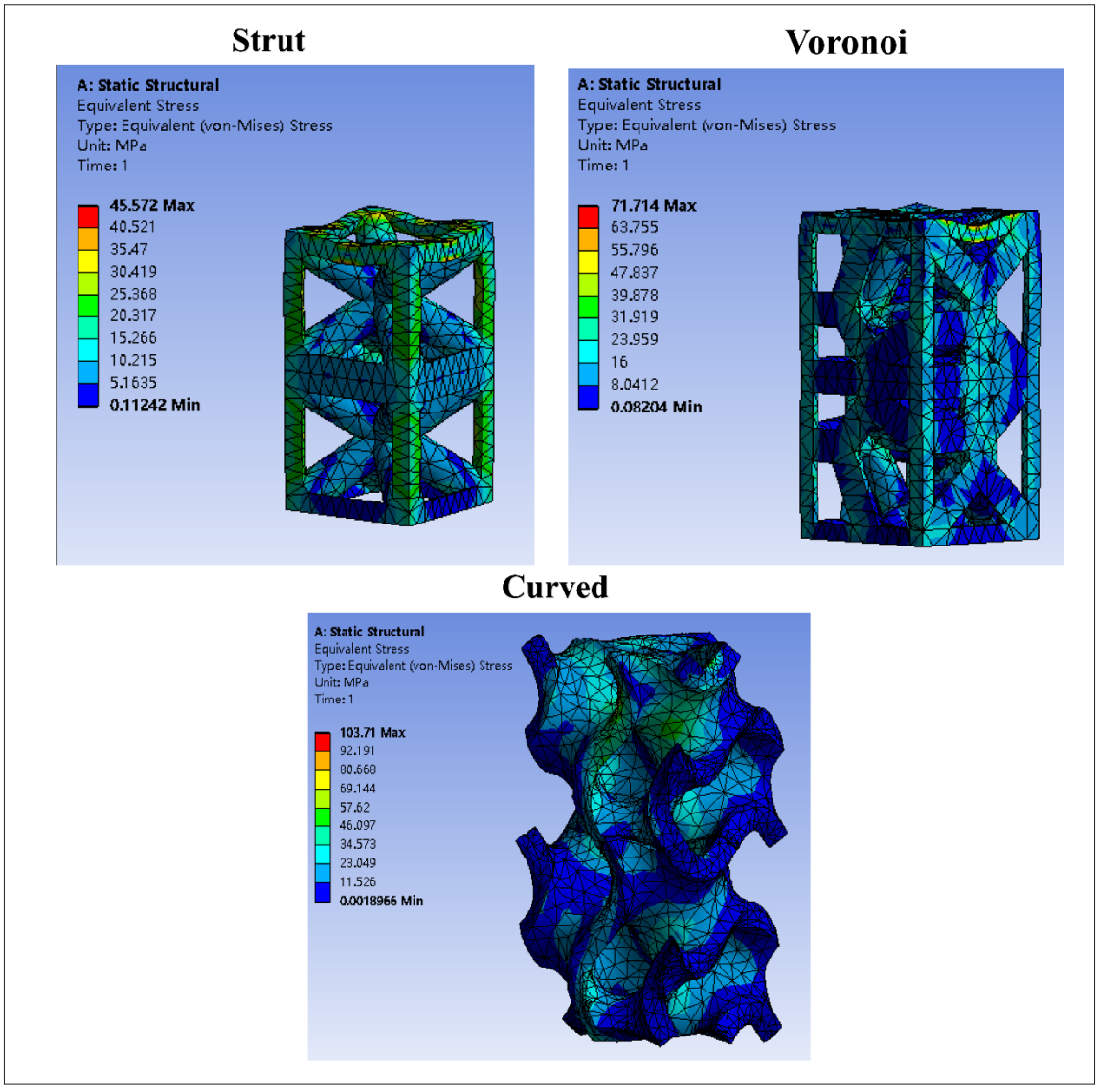

Figure 9. Finite element analysis of the compression test results.

to identify optimal bone-regenerative architectures. CFD simulations were utilized to characterize scaffold permeability, velocity profiles, and flow trajectories. The synergistic integration of *in vivo* experimentation and CFD analysis elucidated structure-dependent osteogenic mechanisms, thereby establishing a novel framework for biomimetic scaffold design.

Considering the influence of materials on osseointegration, Ti6Al4V material, which is biocompatible and promising for a wide range of applications, was used to prepare bone scaffolds in this study, and all the scaffolds were successfully prepared by SLM 3D printing and showed different structural characteristics. Prior to *in vivo* implantation, biomechanical characterization was used to quantify the elastic modulus and yield strength of all scaffold architectures. Scaffold moduli (0.1–4.5 GPa) were found to align with established cancellous bone properties, allowing for mitigation of stress shielding risks through modulus matching. All constructs demonstrated yield strengths exceeding 100 MPa, which significantly surpass documented values for vertebral and femoral cancellous bone, satisfying the mechanical demands of orthopedic implantation.

Quantitative analysis of the histological results confirmed progressive osseous tissue deposition within all scaffold groups during the intervals at weeks 4 and 12. Voronoi constructs demonstrated significantly enhanced osseointegration compared to curved and strut-based designs at both endpoints. These findings were corroborated with micro-CT volumetry data, with BV/TV ratios revealing superior bony ingrowth in Voronoi architectures ($p < 0.01$). Given the precise control over the porosity of the porous scaffolds, the most likely cause of this osteogenic difference is the pore shape. Van Bael et al.[10] found that circular pore structures are more prone to pore plugging than non-circular pore structures based on *in vitro* results. The disparity in pore architecture may influence the transport of nutrients and oxygen within the scaffold, thereby affecting the efficacy of bone regeneration. The suboptimal osteogenic performance of strut-based structures could be attributed to their pore characteristics. In contrast, the Voronoi algorithm-based bionic trabecular configuration demonstrates enhanced osteogenic potential, likely due to its structural resemblance to the native human trabecular bone. We posit this osteogenic superiority originates from biomimetic stochastic morphology: Voronoi-generated trabecular analogs recapitulate cancellous bone's structural heterogeneity, and might facilitate angiogenic–osteogenic coupling while providing osteoconductive topographical cues for cellular adhesion and proliferation.

To elucidate the structural influences on osteogenesis, we utilized CFD simulations to characterize the kinetics of scaffold perfusion and interstitial flow profiles.[40] Following osseous injury, vascular infiltration delivering osteoprogenitor cells and nutrients must permeate the implant architecture to initiate regeneration, where initial osteoblast adhesion dictates the subsequent potential for osseointegration.[41] Consequently, beyond biomechanical competence, fluid mechanics properties constitute a critical determinant of scaffold conductivity. CFD pressure distribution analysis reveals distinct hemodynamic environments across scaffold architectures. The strut configuration exhibits the most moderate pressure gradient (ΔP), while the G-surface-based design demonstrates significantly elevated ΔP. This disparity suggests significant flow impedance in strut architectures, potentially compromising perfusion efficiency.[42] Crucially, this pressure differential directly correlates with fluid shear stress magnitude, a potent mechanical regulator of osteogenic differentiation.[43,44] Consequently, Curved and Voronoi topologies promote substantially enhanced osteogenic efficiency compared to strut structures. Velocity flow diagrams demonstrated reduced intraluminal flow rates in Voronoi designs—a hemodynamic environment conducive to cellular adhesion. Permeability quantification via Darcy's law showed the following hierarchy: strut > Voronoi > curved. We posit that elevated permeability in strut scaffolds enhances mass transport but impedes cellular retention. Conversely, curved architecture promotes cell adhesion at the expense of restricted nutrient exchange.[45] The Voronoi structure approximates the structure of human cancellous bone, achieving an optimal balance between perfusion efficiency and cell retention by balancing the permeability and pressure gradient, which serves as the plausible reason for its superior osteogenic efficacy.[37]

The finite element analysis results provided critical insights into the mechanical behavior of the scaffolds under compressive load, corroborating and explaining the *in vivo* performance. The significantly lower maximum von Mises stress observed in the Voronoi scaffold (45.57 MPa) compared to the strut (103.71 MPa) and curved structures (71.71 MPa) indicates its superior ability to distribute stress more evenly throughout its architecture. This reduced stress concentration is a direct consequence of its biomimetic, stochastic trabecular-like design, which effectively mitigates localized stress peaks that could lead to micro-damage or implant failure over time. More importantly, this mechanical environment is conducive to bone remodeling, as it more closely mimics the physiological stress distribution in natural cancellous bone, thereby reducing the risk of stress-shielding-induced bone resorption. This advantageous stress profile, combined with its optimal permeability and fluid dynamics as revealed by CFD, creates a synergistic mechanobiological microenvironment that promotes enhanced cellular activity and osteogenesis, ultimately explaining the superior BV/TV ratio and osseointegration observed in the Voronoi group.

The current study strongly supports that Voronoi algorithm-based biomimetic bone trabecular scaffolds enhance early osseointegration. Micro-CT (BV/TV) and histological analyses demonstrated superior osteogenic potential, with the Voronoi scaffold inducing significantly greater new bone formation at 4 and 12 weeks post-implantation compared with the curved or traditional pillar structures. This advantage stems from the biomimetic replication of natural trabeculae's random, non-periodic topology, which fosters a microenvironment conducive to cell adhesion, migration, differentiation, and enhanced vascularization/nutrient delivery via optimized fluid dynamics. CFD simulations revealed significantly lower internal ΔP alongside more uniform, reduced flow velocities within the Voronoi scaffold, closely approximating physiological conditions suitable for promoting cell adhesion/retention. Conversely, the pillar

structure exhibited high ΔP and localized high-velocity flows impairing perfusion and cell retention, while the curved structure's low permeability potentially restricted deep nutrient supply. The Voronoi scaffold's intermediate permeability κ suggests an optimal balance for nutrient exchange and cell retention.

While this study demonstrates the promising biomechanical performance and early osseointegration capabilities of Ti6Al4V scaffolds based on the Voronoi designed, several limitations warrant consideration. Firstly, the use of healthy rabbit femoral condyles as experimental models may limit direct extrapolation to complex clinical scenarios involving comorbidities such as osteoporosis or diabetes, where bone regeneration dynamics differ significantly. Secondly, the evaluation period, restricted to 12 weeks post-implantation, provides valuable insights into early-stage tissue response but precludes a comprehensive assessment of long-term structural stability and functional integration. Future studies could explore the integration of topology optimization algorithms with Voronoi tessellation to further refine pore morphology and mechanical stimuli distribution for enhancing biological performance.[46] Long-term animal experiments are also required to investigate specific structural osteogenic mechanisms, aiming to optimize scaffold design for varied clinical applications. Addressing these gaps is essential to translate promising preclinical results into clinically viable solutions for complex bone regeneration challenges.

5. Conclusion

The Voronoi design offers a potent biomimetic strategy for fabricating porous titanium alloy-based bone scaffolds with enhanced osteogenesis properties, which demonstrates superior potential compared to the strut and curved structures in promoting bone defect repair, particularly in situations where rapid osseointegration is crucial. Through future integration of surface functionalization, multi-scale gradients, and patient-specific optimization, bionic scaffolds based on Voronoi design would provide a promising platform for next-generation bone tissue engineering in future.

Acknowledgments

None.

Funding

This study was supported by the Sichuan Science and Technology Program (2024YFHZ0067; awarded to J.L.) and the China Postdoctoral Science Foundation (2023MD744134; awarded to L.L.).

Conflict of interest

All authors report no conflicts of interest relevant to the contents of this paper.

Author contributions

Conceptualization: Jinghong Yang, Zi Wang
Formal analysis: All authors
Investigation: All authors
Methodology: All auhors
Writing–original draft: Jinghong Yang
Writing–review & editing: Linlin Liu, Juncai Liu, Zhong Li
All authors have read and agreed to the published version of the manuscript.

Ethics approval and consent to participate

This study was approved by the Ethics Committee of the Affiliated Hospital of Southwest Medical University and conducted in adherence to the principles set forth in the Declaration of Helsinki.

Consent for publication

Not applicable.

Availability of data and materials

The datasets used and/or analyzed during the current study are available from the corresponding author upon reasonable request.

References

1. Jing Z, Zhang T, Xiu P, et al. Functionalization of 3D-printed titanium alloy orthopedic implants: a literature review. *Biomed Mater*. 2020;15(5):052003. doi: 10.1088/1748-605X/ab9078
2. Li L, Shi J, Zhang K, et al. Early osteointegration evaluation of porous Ti6Al4V scaffolds designed based on triply periodic minimal surface models. *J Orthop Translat*. 2019;19:94-105. doi: 10.1016/j.jot.2019.03.003
3. Revilla-León M, Meyer MJ, Özcan M. Metal additive manufacturing technologies: literature review of current status and prosthodontic applications. *Int J Comput Dent*. 2019;22(1):55-67.
4. Alammar A, Kois JC, Revilla-León M, Att W. Additive Manufacturing Technologies: Current Status and Future Perspectives. *J Prosthodont*. 2022;31(S1):4-12. doi: 10.1111/jopr.13477
5. Liu F, Ran Q, Zhao M, Zhang T, Zhang DZ, Su Z. Additively manufactured continuous cell-size gradient porous scaffolds: pore characteristics, mechanical properties and biological responses in vitro. *Materials (Basel)*. 2020;13(11):2589.

doi: 10.3390/ma13112589

6. Ran Q, Yang W, Hu Y, et al. Osteogenesis of 3D printed porous Ti6Al4V implants with different pore sizes. *J Mech Behav Biomed Mater*. 2018;84:1-11. doi: 10.1016/j.jmbbm.2018.04.010
7. Arjunan A, Demetriou M, Baroutaji A, Wang C. Mechanical performance of highly permeable laser melted Ti6Al4V bone scaffolds. *J Mech Behav Biomed Mater*. 2020;102:103517. doi: 10.1016/j.jmbbm.2019.103517
8. Wang H, Su K, Su L, Liang P, Ji P, Wang C. The effect of 3D-printed Ti(6)Al(4)V scaffolds with various macropore structures on osteointegration and osteogenesis: a biomechanical evaluation. *J Mech Behav Biomed Mater*. 2018;88:488-496. doi: 10.1016/j.jmbbm.2018.08.049
9. Gryko A, Prochor P, Sajewicz E. Finite element analysis of the influence of porosity and pore geometry on mechanical properties of orthopaedic scaffolds. *J Mech Behav Biomed Mater*. 2022;132:105275. doi: 10.1016/j.jmbbm.2022.105275
10. Van Bael S, Chai YC, Truscello S, et al. The effect of pore geometry on the in vitro biological behavior of human periosteum-derived cells seeded on selective laser-melted Ti6Al4V bone scaffolds. *Acta Biomater*. 2012;8(7):2824-34. doi: 10.1016/j.actbio.2012.04.001
11. Chen Z, Yan X, Yin S, et al. Influence of the pore size and porosity of selective laser melted Ti6Al4V ELI porous scaffold on cell proliferation, osteogenesis and bone ingrowth. *Mater Sci Eng C Mater Biol Appl*. 2020;106:110289. doi: 10.1016/j.msec.2019.110289
12. Coburn B, Salary RR. Mechanical characterization of porous bone-like scaffolds with complex microstructures for bone regeneration. *Bioengineering (Basel)*. 2025;12(4):416. doi: 10.3390/bioengineering12040416
13. Kumar PV, Pal S, Birru AK, Jaganathan BG, Muthu N. 3D-printed TPMS-structured hybrid PLA/MgTiO(3) scaffolds: Synergizing bioactivity and antibacterial performance for bone regeneration. *Biomater Adv*. 2025;177:214370. doi: 10.1016/j.bioadv.2025.214370
14. Pazhamannil RV, Alkhedher M. Advances in additive manufacturing for bone tissue engineering: materials, design strategies, and applications. *Biomed Mater*. 2024;20(1). doi: 10.1088/1748-605X/ad9dce
15. Ma J, Li Y, Mi Y, et al. Novel 3D printed TPMS scaffolds: microstructure, characteristics, and applications in bone regeneration. *J Tissue Eng*. 2024;15:20417314241263689. doi: 10.1177/20417314241263689
16. Ye J, Miao B, Xiong Y, et al. 3D printed porous magnesium metal scaffolds with bioactive coating for bone defect repair: enhancing angiogenesis and osteogenesis. *J Nanobiotechnology*. 2025;23(1):160. doi: 10.1186/s12951-025-03222-3
17. Hao W, Yongtao L, Jian J, Hanxing Z. Data-driven inverse design of novel spinodoid bone scaffolds with highly matched mechanical properties in three orthogonal directions. *Mater Des*. 2025;251:113697. doi: 10.1016/j.matdes.2025.113697
18. Amini AR, Laurencin CT, Nukavarapu SP. Bone tissue engineering: recent advances and challenges. *Crit Rev Biomed Eng*. 2012;40(5):363-408. doi: 10.1615/critrevbiomedeng.v40.i5.10
19. Deng F, Liu L, Li Z, Liu J. 3D printed Ti6Al4V bone scaffolds with different pore structure effects on bone ingrowth. *J Biol Eng*. 2021;15(1):4. doi: 10.1186/s13036-021-00255-8
20. Vossenberg P, Higuera GA, van Straten G, van Blitterswijk CA, van Boxtel AJ. Darcian permeability constant as indicator for shear stresses in regular scaffold systems for tissue engineering. *Biomech Model Mechanobiol*. 2009;8(6):499-507. doi: 10.1007/s10237-009-0153-6
21. Sinha R, Le Gac S, Verdonschot N, van den Berg A, Koopman B, Rouwkema J. Endothelial cell alignment as a result of anisotropic strain and flow induced shear stress combinations. *Sci Rep*. 2016;6:29510. doi: 10.1038/srep29510
22. Ali D. Effect of scaffold architecture on cell seeding efficiency: a discrete phase model CFD analysis. *Comput Biol Med*. 2019;109:62-69. doi: 10.1016/j.compbiomed.2019.04.025
23. Melchels FP, Tonnarelli B, Olivares AL, et al. The influence of the scaffold design on the distribution of adhering cells after perfusion cell seeding. *Biomaterials*. 2011;32(11): 2878-2884. doi: 10.1016/j.biomaterials.2011.01.023
24. Beaudoin AJ, Mihalko WM, Krause WR. Finite element modelling of polymethylmethacrylate flow through cancellous bone. *J Biomech*. 1991;24(2):127-136. doi: 10.1016/0021-9290(91)90357-s
25. Sun J, Chen C, Zhang B, Yao C, Zhang Y. Advances in 3D-printed scaffold technologies for bone defect repair: materials, biomechanics, and clinical prospects. *Biomed Eng Online*. 2025;24(1):51. doi: 10.1186/s12938-025-01381-w
26. Zhang L, Yang G, Johnson BN, Jia X. Three-dimensional (3D) printed scaffold and material selection for bone repair. *Acta Biomater*. 2019;84:16-33. doi: 10.1016/j.actbio.2018.11.039
27. Attarilar S, Ebrahimi M, Djavanroodi F, Fu Y, Wang L, Yang J. 3D printing technologies in metallic implants: a thematic review on the techniques and procedures. *Int J Bioprint*. 2021;7(1):306. doi: 10.18063/ijb.v7i1.306

28. Distefano F, Pasta S, Epasto G. Titanium lattice structures produced via additive manufacturing for a bone scaffold: a review. *J Funct Biomater*. 2023;14(3):125. doi: 10.3390/jfb14030125

29. Elhattab K, Hefzy MS, Hanf Z, et al. Biomechanics of additively manufactured metallic scaffolds-a review. *Materials (Basel)*. 2021;14(22):6833. doi: 10.3390/ma14226833

30. Wang C, Xu D, Lin L, et al. Large-pore-size Ti6Al4V scaffolds with different pore structures for vascularized bone regeneration. *Mater Sci Eng C Mater Biol Appl*. 2021;131:112499. doi: 10.1016/j.msec.2021.112499

31. Zhao F, Xiong Y, Ito K, van Rietbergen B, Hofmann S. Porous geometry guided micro-mechanical environment within scaffolds for cell mechanobiology study in bone tissue engineering. *Front Bioeng Biotechnol*. 2021;9:736489. doi: 10.3389/fbioe.2021.736489

32. Fonseca H, Moreira-Gonçalves D, Coriolano HJ, Duarte JA. Bone quality: the determinants of bone strength and fragility. *Sports Med*. 2014;44(1):37-53. doi: 10.1007/s40279-013-0100-7

33. Müller R. Hierarchical microimaging of bone structure and function. *Nat Rev Rheumatol*. 2009;5(7):373-381. doi: 10.1038/nrrheum.2009.107

34. Gómez S, Vlad MD, López J, Fernández E. Design and properties of 3D scaffolds for bone tissue engineering. *Acta Biomater*. 2016;42:341-350. doi: 10.1016/j.actbio.2016.06.032

35. Zhao Z, Li J, Yao D, Wei Y. Mechanical and permeability properties of porous scaffolds developed by a Voronoi tessellation for bone tissue engineering. *J Mater Chem B*. 2022;10(46):9699-9712. doi: 10.1039/d2tb01478e

36. Zou S, Gong H, Gao J. Additively manufactured multilevel voronoi-lattice scaffolds with bonelike mechanical properties. *ACS Biomater Sci Eng*. 2022;8(7):3022-3037. doi: 10.1021/acsbiomaterials.1c01482

37. Mamuti M, Chao L, Tian Z. Analysis of mechanical characteristics and permeability of TPMS and Voronoi porous structure for bone scaffold. *Comput Methods Biomech Biomed Engin*. 2024:1-14. doi: 10.1080/10255842.2024.2358378

38. Zhu L, Liang H, Lv F, et al. Design and compressive fatigue properties of irregular porous scaffolds for orthopedics fabricated using selective laser melting. *ACS Biomater Sci Eng*. 2021;7(4):1663-1672. doi: 10.1021/acsbiomaterials.0c01392

39. Morgan EF, Unnikrisnan GU, Hussein AI. Bone mechanical properties in healthy and diseased states. *Annu Rev Biomed Eng*. 2018;20:119-143. doi: 10.1146/annurev-bioeng-062117-121139

40. Channasanon S, Kaewkong P, Chantaweroad S, et al. Scaffold geometry and computational fluid dynamics simulation supporting osteogenic differentiation in dynamic culture. *Comput Methods Biomech Biomed Engin*. 2024;27(5):587-598. doi: 10.1080/10255842.2023.2195961

41. Prakoso AT, Basri H, Adanta D, et al. The effect of tortuosity on permeability of porous scaffold. *Biomedicines*. 2023;11(2):427. doi: 10.3390/biomedicines11020427

42. Lai R, Jiang J, Huo Y, et al. Design of novel graded bone scaffolds based on triply periodic minimal surfaces with multi-functional pores. *Front Bioeng Biotechnol*. 2025;13:1503582. doi: 10.3389/fbioe.2025.1503582

43. Pei T, Su G, Yang J, et al. Fluid shear stress regulates osteogenic differentiation via annexina6-mediated autophagy in MC3T3-E1 cells. *Int J Mol Sci*. 2022;23(24):15702. doi: 10.3390/ijms232415702

44. Zhao Y, Richardson K, Yang R, et al. Notch signaling and fluid shear stress in regulating osteogenic differentiation. *Front Bioeng Biotechnol*. 2022;10:1007430. doi: 10.3389/fbioe.2022.1007430

45. Ferguson BM, Clark JR, Li Q. Scaffold geometries designed to promote bone ingrowth by enhancing mechanobiological stimulation and biotransportation - a multiobjective optimisation approach. *J Mech Behav Biomed Mater*. 2025;164:106883. doi: 10.1016/j.jmbbm.2024.106883

46. Liu B, Feng J, Chen J, He Y, Fu J. A topology optimisation-based design method for 3D Voronoi porous structures and its application for medical pillows. *Virtual Phys Prototyp*. 2023;18(1):e2285392. doi: 10.1080/17452759.2023.2285392

ACCSCIENCE PUBLISHING

International Journal of Bioprinting

RESEARCH ARTICLE

Integrating machine learning and finite element simulation for interpretable prediction of 3D-printed bone scaffold mechanics

Rixiang Quan, Fengyuan Liu*, and Sergio Cantero Chinchilla*

School of Electrical, Electronic and Mechanical Engineering, University of Bristol, Bristol, United Kingdom

Abstract

An integrated framework combining finite element analysis (FEA) and artificial neural networks (ANN) is presented to enhance the prediction and design of bioprinted scaffolds. By leveraging the strengths of data-driven learning and physics-based simulations, the hybrid approach (ANN + FEA) achieved superior predictive accuracy and generalization compared to standalone approaches. Validation against experimental results demonstrated that a single ANN model yields a relative error of 5.17% when predicting the scaffold's Young's modulus. Incorporating FEA simulation based on ANN-predicted geometry and material properties reduced the relative error to 4.72%, representing an 8.6% improvement. The framework also enables accurate simulation of unseen combinations of printing parameters located far from the experimental data manifold, reducing prediction errors from 14.2% (ANN-only) to 5.7% (hybrid). By integrating predictive modeling, simulation, and data augmentation, this approach offers an efficient pathway for optimizing scaffold designs and accelerating the development of biomaterials with tailored mechanical performance.

Keywords: 3D printing; Artificial neural network; Bone scaffold; Data augmentation; Finite element analysis

***Corresponding authors:**
Fengyuan Liu (fengyuan.liu@bristol.ac.uk)

Sergio Cantero Chinchilla (sergio.canterochinchilla@bristol.ac.uk)

Citation: Quan R, Liu F, Chinchilla SC. Integrating machine learning and finite element simulation for interpretable prediction of 3D-printed bone scaffold mechanics. *Int J Bioprint*. 2025;11(6):327-348. doi: 10.36922/IJB025270257

Received: June 30, 2025
Revised: August 25, 2025
Accepted: September 2, 2025
Published online: September 2, 2025

Copyright: © 2025 Author(s). This is an Open Access article distributed under the terms of the Creative Commons Attribution License, permitting distribution, and reproduction in any medium, provided the original work is properly cited.

Publisher's Note: AccScience Publishing remains neutral with regard to jurisdictional claims in published maps and institutional affiliations.

1. Introduction

Bone tissue engineering involves the development of biological substitutes designed to restore, maintain, or improve tissue function.[1] Central to this field is the design of scaffolds—three-dimensional (3D) structures that mimic the extracellular matrix and provide mechanical and biochemical support for cell adhesion, proliferation, and differentiation.[2] An ideal scaffold should exhibit interconnected porosity to allow for vascularization and nutrient exchange, biodegradability to enable gradual replacement by natural bone, and sufficient mechanical strength to withstand physiological loads during regeneration.[3]

Among various scaffold fabrication strategies, fused deposition modeling (FDM)-based 3D printing has gained significant traction due to its flexibility, cost-effectiveness, and ability to fabricate patient-specific implants with tailored geometry

and porosity.[4] FDM allows layer-by-layer deposition of thermoplastic filaments, enabling rapid prototyping of complex structures with high spatial resolution and reproducibility. Furthermore, it supports a wide range of biomedical polymers, including polycaprolactone (PCL), polyetheretherketone (PEEK), and polylactic acid (PLA).[5]

Polylactic acid has emerged as one of the most widely used materials for scaffold fabrication, owing to its biodegradability, biocompatibility, renewability, and excellent printability.[6] As a widely accepted polymer for biomedical applications, PLA has been extensively adopted in medical devices, resorbable sutures, and implantable scaffolds. Its compatibility with FDM enables the fabrication of complex, patient-specific geometries with tunable porosity and high spatial resolution. However, the mechanical performance of PLA scaffolds is strongly influenced by processing parameters such as nozzle temperature, print speed, layer height, and feed rate.[7] These variables affect both the geometry and stiffness of the printed structure in nonlinear ways. To ensure consistency and performance reliability, especially in customized biomedical applications, predictive models are needed to map processing conditions to scaffold properties.[8]

Traditionally, optimization of these parameters has relied on trial-and-error experimentation, expert knowledge, or statistical methods such as design of experiments and response surface methodology. While informative, these methods are resource-intensive, time-consuming, and poorly suited for high-dimensional design spaces or real-time customization.[9,10] In recent years, machine learning (ML) techniques have emerged as powerful tools for modeling the complex relationships between printing process parameters and scaffold performance.[11] Regression models—including support vector machines, decision trees, random forests, and artificial neural networks (ANN)—have shown great potential in predicting material properties such as tensile strength, Young's modulus, thermal stability, and degradation behavior.[12]

Despite these advances, several limitations remain. First, the direct use of ML to predict mechanical performance, such as Young's modulus or ultimate tensile strength, typically requires a large and diverse dataset obtained through extensive physical experimentation.[13] Such datasets can be difficult and costly to acquire, especially in biomedical contexts where ethical and material constraints apply. Second, many ML models, particularly deep learning approaches, suffer from limited interpretability. These "black-box" models often provide high predictive accuracy without offering insights into the underlying physical mechanisms that govern scaffold performance.[14]

Recent advances have demonstrated the growing potential of integrating finite element analysis (FEA) with ML for optimizing the design and performance prediction of architected materials and scaffolds. For example, Kalina *et al.*[15] proposed the FEANN framework, which embeds physical constraints directly into neural network architectures, allowing for physics-consistent predictions of material responses without explicit constitutive modeling. Their model is trained using automated multiscale data mining and provides efficiency in predicting stress–strain responses of complex hyperelastic materials. However, this framework does not incorporate fabrication parameters or allow for direct design feedback from experimental constraints.[15]

In a similar direction, Peng *et al.*[16] introduced a generative active learning framework (GAD-MALL) that combines 3D convolutional neural networks with FEA to optimize the design of gyroid-based architected implants. Their method excels in high-dimensional, multi-objective optimization, and adapts to clinical constraints such as elastic modulus, yield strength, and printability. The framework achieves notable gains in mechanical performance by exploiting nonuniform gyroid designs and local porosity control, showing excellent agreement between finite element method (FEM) predictions and experimental validation. Nevertheless, this approach focuses on fixed topological families (e.g., triply periodic minimal surfaces) and lacks explicit interpretability or modular prediction steps tied to fabrication conditions.[16]

Another notable line of research by Oladipo *et al.*[17] focuses on optimizing the mechanical performance of re-entrant auxetic metamaterials through a hybrid ML–FEA approach. Their framework integrates experimental characterization of 3D-printed structures, finite element simulation of auxetic deformation under load, and interpretable ML using SHapley Additive exPlanations (SHAP) values to identify dominant geometric features influencing mechanical response. A surrogate model is iteratively corrected using simulation feedback to refine prediction accuracy. This approach offers valuable insight into the structure–response relationship and supports inverse design by highlighting influential geometric descriptors. However, it primarily targets unit cell design within a fixed metamaterial family, and the model relies heavily on empirical geometric encoding rather than direct fabrication parameters. Furthermore, while interpretability is improved through SHAP analysis, the model architecture remains monolithic, limiting modularity and reuse.[17]

Recently, explainable ML approaches have also been introduced for scaffold design to enhance interpretability and provide feature-level insights. For example, Drakoulas

et al.[18] proposed an explainable ML-based framework for bone tissue engineering scaffolds, combining reduced-order modeling with SHAP-value analysis to identify the influence of geometric and material descriptors on mechanical performance. Our modular ANN–FEA framework complements this direction by explicitly integrating filament geometry, material properties, and physics-based simulation to produce interpretable and physically grounded predictions of scaffold stiffness.

Additionally, Dong *et al.*[19] proposed an efficient ML–FEA coupling method to optimize process parameters in laser powder bed fusion for metallic additive manufacturing. Their work addresses the critical challenge of balancing manufacturing-induced thermal effects with final part quality by predicting residual stress and porosity from controllable printing inputs such as laser power and scan speed. The model employs Gaussian process regression and is supported by FEM-based thermal and mechanical simulations, which are used both for training and validation. The study demonstrates significant potential for reducing experimental trial-and-error in metal additive manufacturing (AM) and provides a pathway for process-level optimization. However, this framework is oriented toward process–property prediction at the bulk material level and does not explicitly model the mechanical performance of printed structural architectures (e.g., lattice scaffolds), nor does it incorporate geometric feature learning.[19]

In this study, we introduce a modular hybrid modeling framework (Figure 1) to address the limitations of existing process–performance prediction methods in scaffold fabrication—namely, their dependence on large datasets, limited interpretability, and lack of adaptability. Instead of a monolithic regression model, we decompose the prediction task into three interpretable and physically grounded stages:

(i) ML geometry and material module: Two ANNs (ANN 2 and ANN 3) are used to predict filament geometry (width and height) and the material modulus of PLA, respectively, from the given printing parameters.

(ii) Physics-based module: These predictions are passed into a scaffold-level FEA simulation (Abaqus), which estimates the effective Young's modulus under compressive loading.

(iii) Enhanced ML-based design module: The simulated mechanical outputs are then used to train ANN 1, which predicts optimal printing parameters for desired scaffold stiffness—enabling data augmentation and forward design.

This modular setup mirrors the actual fabrication sequence and ensures that each ANN component aligns with a measurable physical quantity (e.g., scanning electron microscopy [SEM]-derived geometry, tensile-tested modulus). The framework's transparency and adaptability further support generalization under data-scarce or evolving conditions.

The proposed framework offers four key advances over existing approaches. First, it enables modular prediction by decomposing the process–structure–property mapping into interpretable stages, each aligned with physical measurements and simulations. Second, it leverages simulation-guided data augmentation to improve generalization under sparse data conditions, particularly in extrapolative regions of the parameter space. Third, uncertainty-aware modeling is incorporated via ensemble learning and perturbation analysis, allowing confidence-aware predictions for biomedical applications. Finally, the pipeline is designed to be adaptable and extensible, supporting transfer to new materials, scaffold designs, or patient-specific settings by updating only targeted submodules.

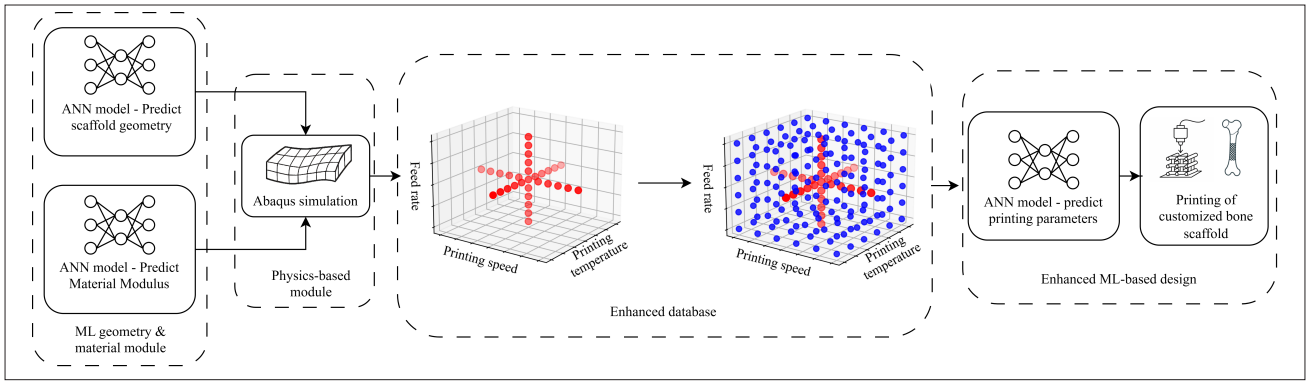

Figure 1. Overview of the proposed framework. Abbreviations: ANN, artificial neural network; ML, machine learning.

The remainder of this paper is organized as follows: **Section 2** details the materials, experimental procedures, and modeling methodology, including the structure of the proposed ANN–FEA framework. **Section 3** presents and discusses the results of model performance and validation. Finally, **Section 4** concludes the study and outlines potential directions for future research.

2. Materials and methods

2.1. Materials and experimental procedures

To quantify how printing parameters affect scaffold geometry—a key determinant of porosity and mechanical properties—detailed measurements of filament dimensions were made using SEM. These experimental data form the foundation for training the geometry-predicting ANN described in **Section 2.3** and are later used to define scaffold models for FEA simulation in **Section 2.4**.

2.1.1. Scaffold design

The scaffolds were designed as grid-like lattice structures, featuring alternating orthogonal filament layers to enhance interconnectivity and mechanical strength. Each scaffold consisted of 20 layers, with filaments in adjacent layers oriented perpendicularly. The nominal pore size, derived from the Computer-Aided Design (CAD) model (Dassault Systèmes, France), was approximately 400 μm, aligning with the optimal range for osteoconduction and vascularization in bone tissue engineering. The designed porosity of the scaffold was approximately 51.1%, calculated based on the ratio of filament volume to total scaffold volume.

Key geometric parameters were held constant across all samples to ensure fabrication consistency: filament diameter (FD) of 0.4 mm, layer thickness (LT) of 0.3 mm, filament gap (FG) of 0.6 mm, and total layer number (LN) of 20. The scaffold dimensions were 10 mm in width and length, and 6 mm in height. Porosity was estimated via a CAD-based volumetric model. The filament layout and key dimensional parameters are illustrated in Figure 2.

2.1.2. Three-dimensional printing of scaffolds

Scaffolds were fabricated using a Prusa MINI+ FDM printer (Prusa Research a.s., Czech Republic) equipped with a 0.4 mm nozzle. PLA "Ecogenius" filaments, purchased from Sigma-Aldrich (Merck Group, USA), were used to produce scaffolds. PLA is a biodegradable, semi-crystalline thermoplastic with a density of 1.24 g/cm^3, a melt flow index of 6.0 g/10 min, an FD of 1.75 mm, a melting point of approximately 144°C, and a Vicat softening temperature of approximately 60°C. Its tensile strength is 65.5 MPa, with a tensile modulus of 3.31 GPa in the machine direction (MD) and 3.86 GPa in the transverse direction (TD).[20] To systematically investigate process–property relationships, three printing parameters were varied:

(i) Nozzle temperature: 180–250°C (five levels: 180; 195; 210; 230; 250°C).

(ii) Printing speed: 100–5100 mm/min (six levels: 100; 300; 900; 1500; 2700; 5100 mm/min).

(iii) Material feed rate: 15–42% (six levels: 15%; 20%; 25%; 30%; 36%; 42%).

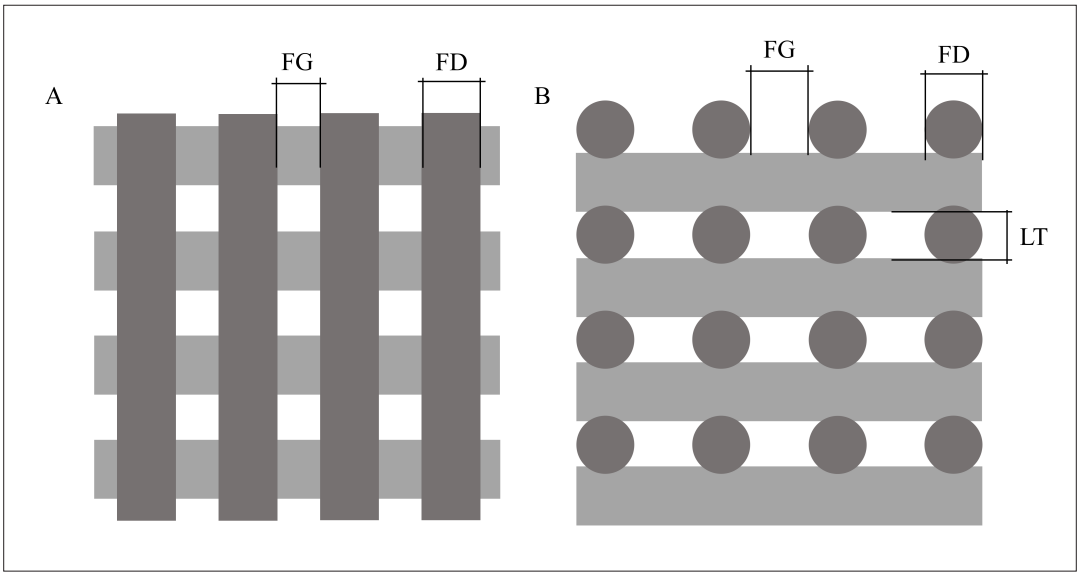

Figure 2. Schematic top view (A) and side view (B) of the printed scaffold structure, illustrating filament gap (FG), filament diameter (FD), and layer thickness (LT).

The selected printing parameters essentially span the typical thermal processing window of PLA, ensuring compatibility with its melting, flow, and solidification behaviors. By covering a broad spectrum of viable printing conditions, these parameters induce substantial variation in filament geometry (e.g., width, height, and inter-layer bonding) and mechanical performance (e.g., Young's modulus and tensile strength).[21] This diversity in output characteristics enables the generation of a rich and discriminative dataset, well-suited for training interpretable and generalizable ML models. From this set, 36 representative parameter sets were selected using stratified sampling, with the goal of covering the printing space evenly across most variable levels.

This resulted in a total of $5 \times 6 \times 6 = 180$ combinations, from which 36 combinations were selected via stratified sampling to cover the design space. Each combination was printed in triplicate, producing 108 scaffolds in total. All other printing parameters that were not the focus of this study (e.g., nozzle size, cooling fan, platform temperature) were kept constant throughout.

2.1.3. Mechanical compressive testing of polylactic acid scaffolds

To evaluate the mechanical performance of the printed scaffolds, uniaxial compression tests were conducted using an INSTRON 3343 universal testing machine (Instron, USA) equipped with a 1 kN load cell. Each scaffold specimen was compressed at a constant crosshead speed of 1 mm/min at room temperature. Force–displacement data were recorded at a sampling rate of 10 Hz.

The compressive Young's modulus was computed from the linear portion of the stress–strain curve, typically within the 5–15% strain range, to exclude the effects of initial seating and nonlinear densification. Stress was calculated based on the projected cross-sectional area, while strain was determined by dividing the crosshead displacement by the initial height of the scaffold.

For each printing parameter combination, three replicate scaffolds were tested. This number was chosen to enable the calculation of mean values and standard deviations, and to quantify fabrication and testing uncertainty, which was subsequently used to validate model predictions.

2.1.4. Mechanical tensile testing of polylactic acid filaments

To assess the intrinsic material properties independent of structural geometry, single-filament tensile tests were carried out. Filament extrusion was initiated at a bed-to-nozzle distance of 0.3 mm, calibrated using standard first-layer gap settings. Filaments were then stretched under uniaxial tension using the same INSTRON system at a crosshead speed of 2 mm/min until failure. The elastic modulus of each filament was extracted from the initial linear elastic region of the stress–strain curve, following the same fitting method used in scaffold compression tests. These filament-level moduli served two purposes: (i) to validate the material modulus predicted by the ANN model, and (ii) to investigate the influence of printing conditions on bulk material behavior. At least three filament specimens were tested per condition.

2.1.5. Scanning electron microscopy

Scanning electron microscopy imaging was performed using a JEOL JSM-IT500 system (JEOL Ltd., Japan) operated at an acceleration voltage of 5.0 kV and a working distance of 14.4 mm. The secondary electron (SE) mode was used to capture both surface and cross-sectional features. Micrographs were acquired under slow scan conditions at magnifications ranging from ×100 to ×1000. Figure 3 shows a representative micrograph, which was used to measure filament width and height, assess layer bonding quality, and identify fabrication defects such as voids or under-extrusion.

Scanning electron microscopy analysis primarily focused on quantifying the geometric structure of individual strands. Cross-sectional images were obtained by fracturing the scaffolds to expose the internal architecture, and the height and width of deposited filaments were measured using ImageJ software (National Institutes of Health, USA).[22] Each filament cross-section was approximated as an ellipse, allowing for a simplified yet representative assessment of strand geometry. These dimensional measurements were subsequently used to validate the ANN-predicted geometry and to calibrate the finite element models.

For each printing parameter combination, three scaffolds were fabricated. Each scaffold was fractured to expose the filament cross-sections, and filament width and height were measured at 20 different locations per scaffold using SEM. For each condition, the reported filament dimensions were obtained by first averaging the 20 measurements for each scaffold, and then averaging the three scaffold-level values to give the final mean.

In addition to geometric evaluation, SEM imaging also provided qualitative insights into interlayer bonding and surface morphology. Process-induced defects such as insufficient fusion, void formation, or surface roughness were identified and used to interpret inconsistencies in mechanical performance and predictive errors within the ANN–FEA framework. The complete experimental

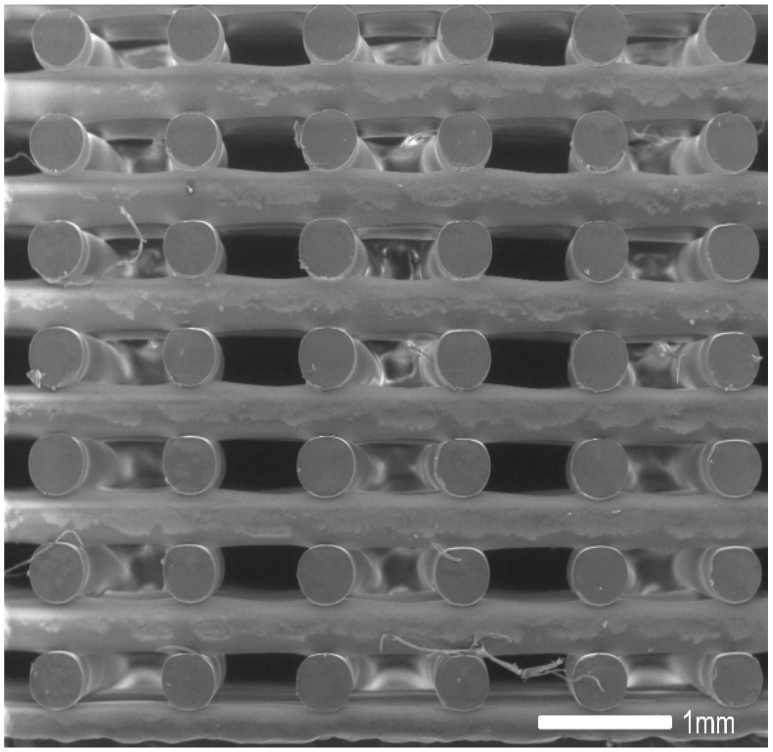

Figure 3. Scanning electron micrograph of the cross-sectional filament layout in a three-dimensional-printed polylactic acid scaffold. Scale bar: 1 mm; magnification: 30×.

workflow, including printing, testing, and image-based analysis, is summarized in Figure 4.

2.1.6. Experimental uncertainty quantification

Repeated tests were conducted for selected printing conditions to evaluate fabrication variability and quantify experimental uncertainty in the measured mechanical and geometric properties. For each selected combination of nozzle temperature, print speed, and feed rate, three scaffolds were fabricated and subjected to the same compression testing protocol. The number of replicates (n = 3) was chosen as a trade-off between statistical robustness and practical throughput, allowing estimation of mean values and standard deviations while managing resource constraints.[23]

The resulting Young's modulus values and filament dimensions (width and height) were analyzed to compute the standard deviation and coefficient of variation for each condition. These metrics characterized the inherent variability arising from machine-level fluctuations and material inconsistencies during the FDM process.[24]

This uncertainty information served a key purpose within the modeling framework: it provided reference bounds for validating ANN and FEA predictions, ensuring that model deviations were interpreted in the context of experimental variability (aleatoric uncertainty).[25]

2.2. Finite element analysis

To complement the geometric dataset and capture intrinsic material variability under different processing conditions, tensile tests were performed on individual PLA filaments. These tests provided ground-truth Young's modulus values for the material-property ANN introduced in **Section 2.3**, ensuring that simulation inputs reflect realistic mechanical properties.

2.2.1. Geometry definition and material properties

Finite element models of the scaffold structures were constructed in Abaqus/Standard to simulate their mechanical response under uniaxial compression. The geometry of each scaffold was defined as a periodic grid-like structure with alternating orthogonal filament layers. Filaments were modeled with approximate elliptical cross-sections, where strand width and height were either experimentally measured (via SEM) or predicted using the ANN model. This elliptical approximation enabled a more

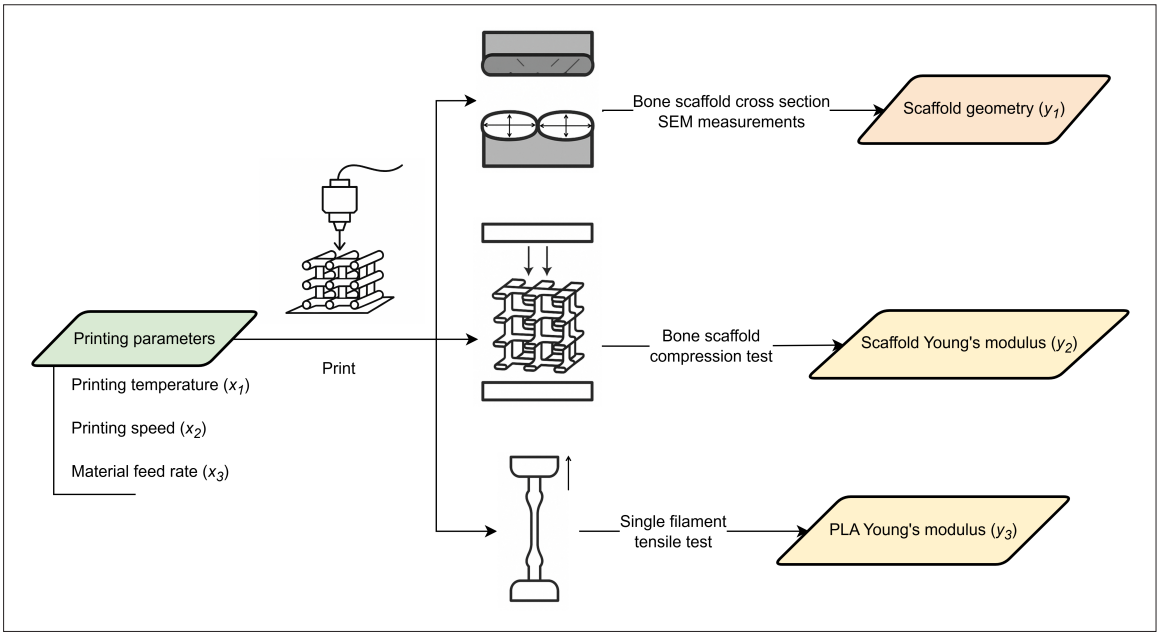

Figure 4. Experimental data collection process, including printing parameters and mechanical property measurement.

realistic representation of printed strand morphology compared to idealized circular or rectangular assumptions.

Each scaffold model comprised multiple filament layers, consistent with the actual printing strategy. The spatial arrangement, filament spacing, and stacking sequence were derived from the original CAD design, ensuring a one-to-one correspondence between the modeled and printed geometries.

Polylactic acid was modeled as a homogeneous, isotropic, and linear elastic material. The Young's modulus was assigned based on ANN-predicted tensile properties of PLA filaments under the same printing parameters used for the corresponding scaffold structure. A constant Poisson's ratio of 0.36 was used throughout.[26]

2.2.2. Mesh convergence study

To ensure the reliability of simulation results and minimize discretization error, a mesh convergence study was conducted on a representative scaffold model.[27] Both linear hexahedral elements (C3D8R) and tetrahedral elements (C3D4) were initially evaluated. Due to the regular scaffold geometry and the dominance of axial loading, C3D8R elements were ultimately selected. These linear hexahedral elements demonstrated higher accuracy in stress prediction and stiffness estimation compared to their tetrahedral counterparts, particularly in structured geometries with predominantly orthogonal filament arrangements. In addition to improved precision, C3D8R elements also offered better numerical stability and reduced element distortion, enabling more efficient simulations without compromising result fidelity.[28]

A series of progressively refined meshes was tested, with element sizes of 0.20, 0.15, 0.10, 0.08, and 0.05 mm. For each mesh level, a fixed compressive load was applied to the scaffold's top surface, and the resulting average vertical displacement was recorded. Mesh convergence was evaluated by tracking the change in displacement across successive mesh refinements. Convergence was considered acceptable when the relative change in top surface displacement between two consecutive mesh levels was less than 5%, a commonly used threshold in similar scaffold and biomedical FEA studies.[29] Based on this criterion, a mesh size of 0.08 mm was selected for subsequent simulations, as it provided a good balance between accuracy and computational efficiency.

2.2.3. Boundary conditions and simulation setup

All simulations were performed under quasi-static, linear elastic conditions using Abaqus/Standard. To replicate the experimental compression tests, the bottom surface of the scaffold model was fully constrained in all translational degrees of freedom. A uniformly distributed vertical 100 N force was applied to the top surface, simulating uniaxial compressive loading. The applied displacement magnitude was selected to remain within the linear elastic regime.

Although inter-filament adhesion in FDM printing is imperfect and influenced by parameters such as cooling rate and filling density, experimental and theoretical studies have shown that, under typical fabrication conditions (e.g., high filling density), interfacial bonding strength becomes relatively stable and has a limited influence on global mechanical performance. Therefore, assuming fully bonded interfaces using tie constraints is a valid simplification when the focus is on comparing stiffness across scaffold geometries.[30] All interfaces between adjacent filaments were modeled using tie constraints to represent fully bonded contact between layers.

The output variables included nodal displacements and maximum stress, from which the effective Young's modulus was derived using the ratio of applied stress to resulting strain. Stress was calculated as the applied force divided by the nominal cross-sectional area, and strain was computed from the displacement normalized by scaffold height.

All simulations were run in batch mode using Python-generated input files, allowing for automatic updates of geometry and material parameters across the design space. This automated setup ensured high-throughput analysis with minimal manual intervention and facilitated direct integration with ANN model predictions.

In FEA simulations of 3D-printed polymer structures, discrepancies between simulated and experimental results can arise from several unmodeled factors. Common sources include imperfect interlayer adhesion and cohesive failure under load, which can reduce effective stiffness compared to an ideal, fully bonded model[31,32]; internal voids and porosity, which act as stress concentrators and reduce the load-bearing cross section[33]; and anisotropic behavior introduced by layer-by-layer deposition, where the build (Z) direction is typically weaker than the in-plane directions.[34,35] Additional differences may occur due to residual thermal stresses or geometric deviations if warpage or shrinkage is not considered.[36]

While some sources of discrepancy between simulation and experiment—such as imperfect layer bonding, anisotropic behavior, or porosity—can exist in 3D-printed materials, these effects are considered minimal in our case for the following reasons. First, the scaffolds are primarily subjected to axial compression, under which layer-to-layer bonding has limited influence on the global mechanical response. Second, the printing path uses continuous filaments arranged in a regular grid, which reduces directional anisotropy. Third, SEM inspection confirmed close agreement with the CAD geometry and revealed no significant internal voids or defects. Therefore, while minor deviations between simulation and experiment are still possible, the FEA model offers a reasonable approximation of scaffold behavior within the bounds of observed experimental variability.

2.2.4. Uncertainty quantification via parameter sensitivity

A perturbation-based analysis was performed to estimate the uncertainty in FEA-predicted Young's modulus due to variability in input parameters. For each simulation case, upper and lower bounds were defined for the key input variables—strand width, strand height, and Young's modulus—based on either experimental standard deviations or ensemble-based ANN predictions.

Instead of systematically perturbing each parameter individually, combinations of minimum and maximum values were applied to generate bounding cases. The corresponding FEA simulations yielded a range of effective stiffness values, representing the potential variation in mechanical performance due to input uncertainty. This approach allowed for a conservative estimate of model output variability without requiring a full factorial or probabilistic analysis.

The resulting modulus range was reported alongside the nominal prediction to provide a confidence interval for each case. These intervals enabled comparison with experimental variability and served to validate the robustness of the simulation framework under realistic fabrication-induced fluctuations.

2.3. Artificial neural network modeling

Based on the experimental measurements in **Sections 2.1** and **2.2**, we trained two ANNs: one to predict filament geometry, and the other to predict intrinsic stiffness from printing parameters. These models form the core of our hybrid framework, enabling forward prediction of structural and material properties required for scaffold-level mechanical simulation.

2.3.1. Model architecture and training

To enable accurate prediction of scaffold-level mechanical performance from printing parameters, two modular ANNs were developed: one to estimate filament geometry (width and height), and the other to predict the intrinsic Young's modulus of the printed PLA material. This decomposition mirrors the physical fabrication sequence and improves interpretability, providing inputs for both validation and downstream FEA.

Each ANN adopts a feedforward structure with three hidden layers containing 256, 128, and 64 neurons, respectively. Layers are activated using rectified linear unit (ReLU) functions, with batch normalization and dropout (rate of 0.2) applied to reduce overfitting. Network weights

were initialized using He-normal initialization to optimize convergence in ReLU-based networks.[37]

Training was performed using the Adaptive Moment Estimation (Adam) optimizer (learning rate: 0.01; batch size: 8), with the mean squared error as the loss function. All input parameters (nozzle temperature, printing speed, and feed rate) and output variables (filament width, filament height, and Young's modulus) were min–max normalized to the [0,1] range. This scaling ensures that all variables contribute proportionally during training and improves the numerical stability of gradient-based optimization.

2.3.2. Data splits and validation process

To rigorously assess the generalization performance of the ANN models while avoiding overfitting and information leakage, we employed a nested cross-validation scheme inspired by He *et al.*[37] Specifically, a five-fold outer cross-validation loop was used to evaluate model performance, with each outer fold holding out eight fixed test samples based on predefined index combinations.

Within each outer training set (28 samples), an inner five-fold cross-validation was performed to tune hyperparameters, including the number of hidden units and the learning rate. This inner loop ensured that model selection was independent of the final test evaluation, a critical requirement for avoiding optimistic bias in performance estimates.

For each outer fold, the ANN model was trained using the optimal hyperparameter set obtained from the inner loop and evaluated on the held-out outer test set. Model development, including weight updates and early stopping, was restricted to the inner training and validation subsets.

Model performance was quantified using the root mean squared error (RMSE) and coefficient of determination (R^2), computed between predicted and experimental values for each target variable (filament width, height, and Young's modulus). The final reported metrics represent the average across all five outer folds, capturing both the accuracy and robustness of the predictive framework.

2.3.3. Hyperparameter optimization

To ensure unbiased model evaluation, hyperparameter tuning was performed within a nested cross-validation framework.[38] For each outer train–test split, a manual grid search was conducted on the inner training folds using five-fold cross-validation to select optimal hyperparameter configurations, thereby preventing information leakage and preserving generalization integrity.[39]

Hyperparameter tuning was conducted using a manual grid search over a constrained search space, including network depth (1–2 layers), number of neurons per layer (5–50), activation functions (ReLU, tanh), optimizers (Adam, Root Mean Square Propagation, Stochastic Gradient Descent), and learning rates (1×10^{-3} to 1×10^{-2}).

Based on average validation performance across inner folds, the best configuration was a shallow feedforward network with a single hidden layer of 10 neurons, which offered a good trade-off between complexity and generalization. This selection is consistent with prior findings that shallow architectures often outperform deeper ones when training data are limited.[39,40] ReLU was chosen as the activation function for its superior gradient flow and convergence efficiency, while a linear output activation was used to retain interpretability in regression tasks.[40] Among optimizers, Adam was selected for its robust and adaptive convergence behavior across diverse tasks.[41]

Additional settings included a learning rate of 0.01, weight decay (L2 regularization) of 1×10^{-4}, mini-batch size of 8, and early stopping with a patience of 30 epochs. These values were selected based on inner-fold validation performance and are supported by empirical studies showing improved generalization with small batch sizes and early stopping in overparameterized settings.[42]

During training, initial models exhibited early signs of overfitting—specifically, validation loss began to increase after 10–15 epochs, despite continued decreases in training loss. While dropout regularization (rate = 0.2) was consistently applied, it was insufficient on its own to prevent this divergence. Hyperparameter optimization, particularly tuning of network width and learning rate, substantially reduced this overfitting behavior and resulted in better alignment between training and validation loss.

Crucially, all hyperparameter optimization was conducted independently within each outer training fold, without access to test data, ensuring that the final test performance metrics reflected true generalization capability under realistic, small-sample experimental conditions.[38]

2.3.4. Uncertainty quantification using deep ensembles

To quantify prediction uncertainty and enhance model robustness, a deep ensemble strategy was implemented. For each train–test split, $M = 10$ independent ANN models were trained using identical architectures and hyperparameters, but with different random weight initializations.[43] The final prediction was reported as the ensemble mean, while the

standard deviation across ensemble members was retained as a confidence measure.

Uncertainty was estimated as the standard deviation of ensemble predictions for each sample, following practices outlined by Rahaman and Thiery,[44] who demonstrated that deep ensembles provide robust uncertainty estimates, especially in data-scarce settings. Wider standard deviations were typically observed in regions of the parameter space with sparse training coverage, such as at extreme values of printing speed or feed rate.

Although the networks shared the same structure and training data, stochastic elements in the training process—including random weight initialization, mini-batch ordering, and the optimizer's inherent randomness—led each model to converge to a different local minimum in the non-convex loss landscape. These variations resulted in non-identical function approximations across the ensemble, particularly under data-scarce conditions. As a result, ensemble variance reflects meaningful epistemic uncertainty—which arises from limited data or model knowledge—rather than numerical noise.[45,46]

Compared to single-model predictions, the ensemble mean produced more stable and accurate results across all splits, while the associated variance served as a reliable indicator of model confidence. These uncertainty estimates were later used to assess the reliability of ANN-predicted geometry and modulus inputs to the FEA simulation pipeline, and to guide targeted data augmentation in low-confidence regions.

2.4. Hybrid artificial neural networks + finite element analysis integration

The ANN-predicted filament geometry and material modulus were used as inputs for finite element simulations of scaffold compression. This final stage of the framework translates predicted sub-structural characteristics into global mechanical properties, directly addressing the paper's objective of process-informed, interpretable scaffold design.

2.4.1. Automated artificial neural network-to-finite element analysis integration pipeline

While single ANN models may suffice for simple regression tasks, they often fail to capture the full process–structure–mechanics linkage. To address this, we propose a modular integration framework that reflects the underlying fabrication logic and enhances interpretability. An automated pipeline is developed to seamlessly link ANN predictions with FEA, enabling efficient simulation of scaffold mechanical properties across a wide range of printing parameters.

Specifically, the pipeline incorporates predicted filament width, height, and Young's modulus from trained neural networks to generate geometry-aware Abaqus input files. This approach addresses a key gap in the existing literature: although many studies attempt to correlate process parameters with mechanical performance, few explicitly resolve the intermediate filament geometry. Our method provides an interpretable bridge from process to geometry to mechanics and delivers a reusable tool for geometry-informed simulation of 3D-printed scaffolds.[46,47]

A Python-based script handles the end-to-end automation, including the insertion of ANN outputs into a predefined .inp file template. Scaffold geometry is defined as a regular grid of elliptical filament cross-sections, with mesh density, material properties, and boundary conditions configured according to the simulation setup described earlier. All geometric and material inputs are dynamically updated based on ANN predictions.

The system supports batch processing of multiple parameter combinations. For each input set, an Abaqus job file is automatically generated, organized into structured output directories, and optionally submitted to a solver queue for parallel execution. Post-processing scripts extract reaction force and displacement data, from which the effective Young's modulus is calculated using standard stress–strain relations. The overall training architecture, including data flow and input/output structure, is illustrated in Figure 5. Building on the experimental data acquisition process shown in Figure 4, this diagram outlines how scaffold geometry and material measurements are used to train neural network models for predictive simulation. Green boxes indicate input parameters; purple indicates ANN models; orange denotes outputs; and pink indicates the FEA simulation module. The three ANN submodels are defined as functions of the printing parameters $x = \{x_1, x_2, x_3,\}$, where:

- $y_1 = f_1(x)$ predicts scaffold Young's modulus based on process conditions;
- $y_2 = f_2(x)$ estimates filament geometry (height and width);
- $y_3 = f_3(x)$ predicts the intrinsic Young's modulus of the PLA material.

A notable example reinforcing the interpretability advantage of such a hybrid framework is provided by Oladipo *et al.*[17] They developed an interpretable ML approach for 3D-printed auxetic metamaterials by integrating experiments, FEA-generated simulations, and ANN modeling. After generating a comprehensive dataset of 8096 geometrically varied honeycomb structures via FEA, they trained a feedforward multilayer perceptron,

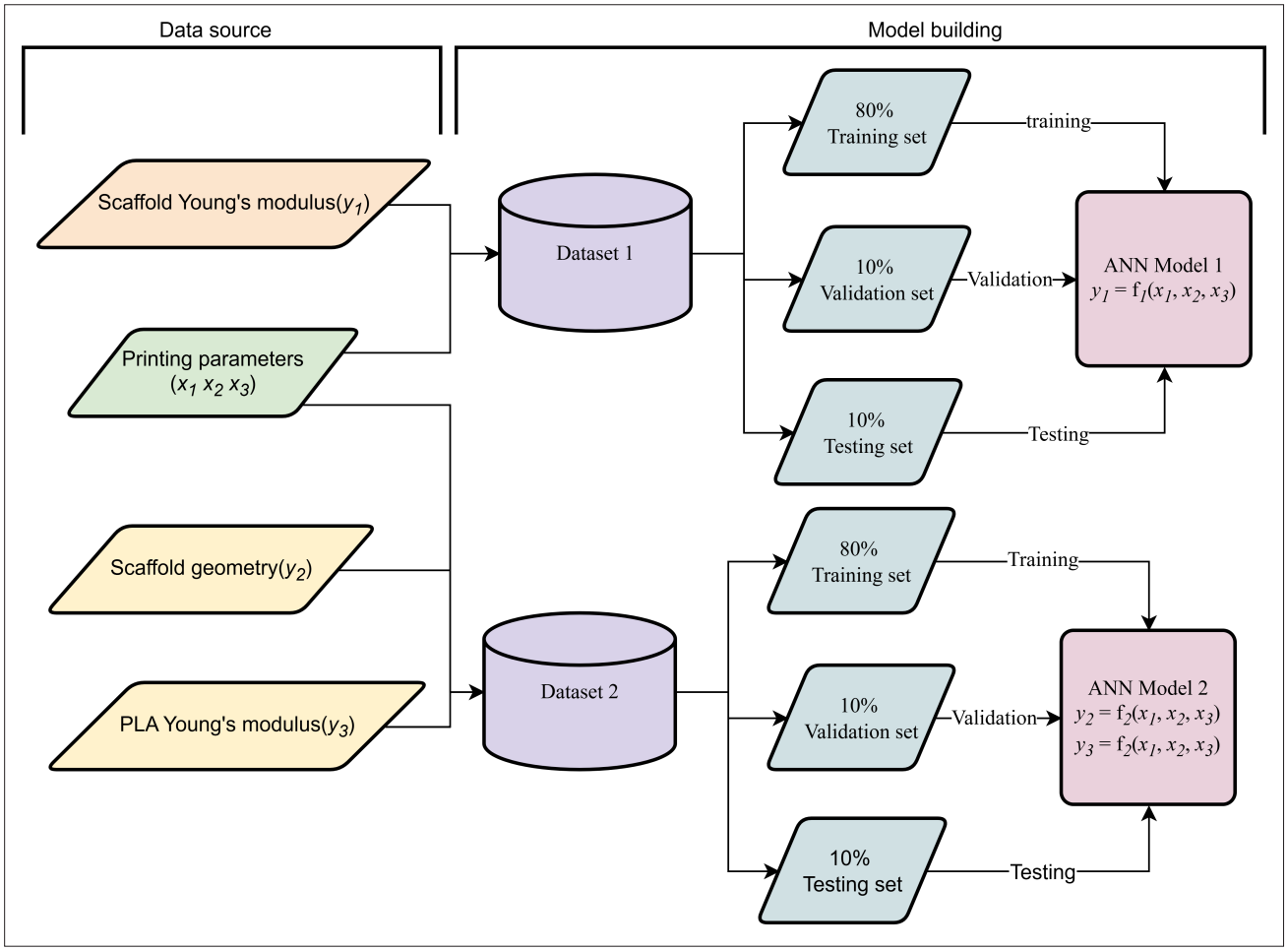

Figure 5. Machine learning model training pipeline, integrating experimental data for predictive modeling.

then applied SHAP analysis to dissect the influence of each geometric parameter on Poisson's ratio predictions. Their findings revealed that slant cell length had the dominant effect, while cell angle and vertical cell length exhibited mixed contributions, and cell thickness had minimal impact. As they conclude, this integrated data-driven framework not only delivered accurate predictive performance but also offered quantitative and interpretable insights into how geometric features influence mechanical response. This study underscores how combining ANN with FEA can elevate both predictive power and transparency in material modeling.[17]

2.4.2. Feedback loop: Augmenting data with simulated results

To address the limitations posed by the small size of the experimental dataset, a data augmentation strategy was implemented by leveraging the integrated ANN–FEA pipeline. Specifically, the ANN models were used to predict geometric and material properties for new combinations of printing parameters, which were then passed into the FEA simulation framework to compute the corresponding effective Young's modulus. These simulated samples formed an extended dataset that approximated additional experimental observations.

This feedback loop enabled the generation of virtual data points in sparsely sampled or previously untested regions of the parameter space, particularly at boundary extremes where physical experimentation may be impractical or resource-intensive. The augmented dataset was subsequently used to retrain or fine-tune the ANN models, improving prediction accuracy and generalization without requiring new physical samples.

While the FEA-based modulus values were not used as direct ground truth for training, they served as a secondary reference to support model evaluation and guide confidence-aware refinement. In addition, uncertainty

estimates from ANN ensembles were cross-checked against the simulation-derived outputs to verify consistency and identify regions with high predictive uncertainty.

Taken together, this hybrid feedback mechanism provides a generalizable solution to data-scarce modelling scenarios where experimental throughput is limited or exhaustive simulation is computationally expensive. The trained ANN models enable near-instantaneous prediction of scaffold geometry and material properties, allowing rapid generation of simulation-ready input files. Compared to manual parameter exploration or full factorial FEA campaigns, this approach substantially reduces iteration time and resource demand, supporting efficient design space augmentation and model refinement. This builds upon the modular training architecture shown in Figure 5, extending it into a full simulation pipeline. The application of trained ANN models to generate FEA input and integrate predictions into scaffold-level simulations is illustrated in Figure 6.

3. Results and discussion

3.1. Predictive performance of artificial neural network submodules

The predictive performance of the ANN models was evaluated using five-fold nested cross-validation, as summarized in Table 1. ANN2, which was trained to predict filament geometry—specifically, height and width—demonstrated strong performance, achieving R^2 values of 0.88 and 0.84, and RMSE values of 0.0181 and 0.0221 mm, respectively. ANN3, which predicts the intrinsic Young's modulus of PLA filaments (from tensile tests), also showed good performance (R^2 = 0.79, RMSE = 0.0259 GPa). These results indicate that geometry and material properties can be accurately inferred from printing parameters when modeled separately.[48]

By contrast, ANN1 was trained in an end-to-end fashion to directly predict scaffold-level modulus from printing parameters. This approach yielded lower predictive accuracy (R^2 = 0.72, RMSE = 0.0338 GPa), likely due to the compounded effects of geometric irregularities, interlayer bonding, and mesostructural variations that affect scaffold mechanics. These complexities make scaffold-level mechanical behavior harder to model without incorporating intermediate structural and material information.[49–51]

Overall, the results support a modular strategy, wherein geometry (ANN2) and material stiffness (ANN3) are predicted separately and then passed to a downstream physics-based FEA simulation. By separating these tasks, each ANN can focus on a narrower, more learnable mapping—improving predictive accuracy, reducing overfitting, enhancing interpretability, and allowing uncertainty to be propagated through the pipeline.[52] This is particularly beneficial in data-scarce settings, where direct end-to-end learning (as in ANN1) risks underfitting or overfitting due to the difficulty of capturing multiscale mechanical interactions.[53]

To better understand how each printing parameter influences the model predictions, we conducted a sensitivity analysis that quantifies the relative contribution of input variables to different outputs. SHAP values, which draw on cooperative game theory, provide a fair, locally accurate, and additive decomposition of a model's prediction, assigning to each input feature its average marginal contribution across all possible combinations.[54,55] In this study, SHAP analysis was performed separately for each ANN submodel: ANN1 (predicting scaffold-level modulus), ANN2 (predicting filament height and width), and ANN3 (predicting filament Young's modulus). In Table 2, SHAP values reveal that printing speed and feed rate are the most influential parameters across all outputs, with feed rate particularly dominating the prediction of

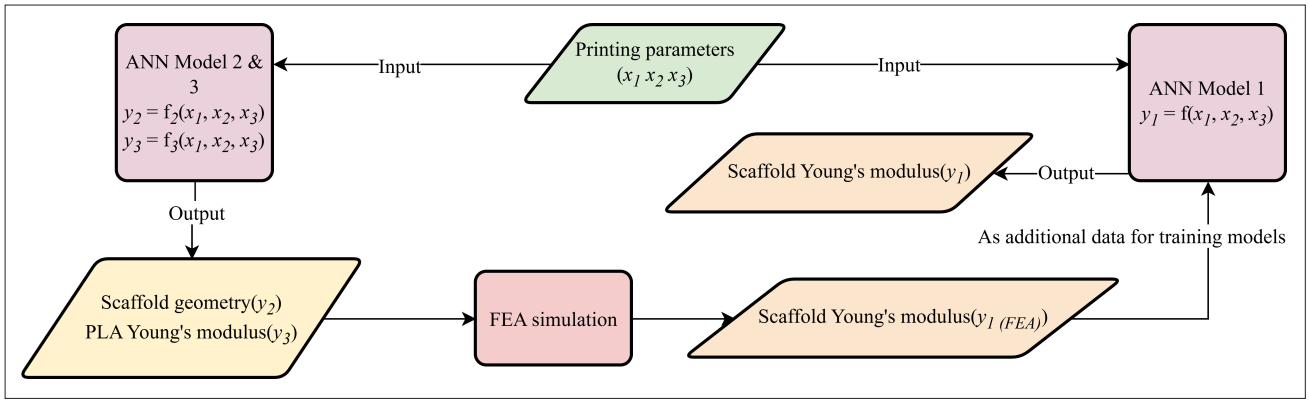

Figure 6. Application of trained models for scaffold property prediction and finite element analysis (FEA) simulation integration. Abbreviations: ANN, artificial neural network; PLA, polylactic acid.

Table 1. Average performance of artificial neural network submodels across five-fold nested cross-validation

Output variable	Predicted by	R^2	RMSE
Height (mm)	ANN2	0.88	0.0181
Width (mm)	ANN2	0.84	0.0221
Filament Young's modulus (tensile test, GPa)	ANN3	0.79	0.0259
Scaffold modulus (compression, GPa)	ANN1	0.72	0.0338

Abbreviation: RMSE, root mean squared error.

filament Young's modulus. Temperature shows relatively minor contributions in all cases.

In addition, a fully dimensionless sensitivity analysis was conducted using a multiple linear regression model applied to FEA-derived outputs (i.e., scaffold stiffness) and their predictors (filament geometry: height and width), all standardized via z-score normalization. By expressing sensitivities in standardized form, one can directly compare the relative influence of each predictor on the FEA model outcome, improving interpretability and comparability across different studies or settings.[56] In Table 3, the estimated coefficients show that feed rate exerts the largest influence across all three outputs, particularly dominating the prediction of scaffold modulus. Temperature has a moderate effect, while printing speed contributes comparatively little.

3.2. Comparison of artificial neural network, finite element analysis, and hybrid artificial neural network–finite element analysis predictions

To evaluate the performance of the proposed two-stage framework, we compared the predicted Young's modulus values from three sources:

(i) ANN: A direct ANN-only model that maps printing parameters (temperature, speed, and feed rate) to scaffold-level Young's modulus. This end-to-end approach does not explicitly model intermediate geometry or material properties and learns purely from experimental data.

(ii) FEA_ANN: A two-stage hybrid model where printing parameters are first input into two ANN submodels to predict filament geometry (width and height) and filament material modulus. These predicted values are then used as inputs to a finite element simulation to compute scaffold modulus.

(iii) FEA: This model uses the same ANN-predicted filament geometry as FEA_ANN but assigns a fixed material modulus of 3500 MPa, based on manufacturer specifications for PLA filament.

(iv) Experiment: Scaffold modulus was measured from compression tests. For each printing condition, three replicate samples were tested, and the mean and standard deviation are reported.

Figure 7 presents the results across three major printing parameters: subfigure (A) corresponds to nozzle temperature, (B) to printing speed, and (C) to feed rate. Shaded regions represent one standard deviation: ensemble-based epistemic uncertainty for ANN and FEA_ANN, and repeatability-based aleatoric uncertainty for experimental data.

To quantify the robustness and statistical variability of ANN predictions, we employed a deep ensemble strategy. Each model was trained 10 times with different random seeds, and the prediction results were aggregated to compute the mean and standard deviation for each test sample. These prediction intervals (mean ± standard deviation) are visualized as error bars in Figure 7. This ensemble-based uncertainty quantification reflects the

Table 2. Average SHapley additive exPlanations values indicating the contribution of printing parameters to each predicted output variable

Input variable	Height	Width	Filament Young's modulus	Scaffold modulus
Printing temperature	2.4×10^{-2}	3.3×10^{-2}	2.8×10^{-2}	1.5×10^{-2}
Printing speed	5.0×10^{-2}	5.7×10^{-2}	4.1×10^{-2}	3.7×10^{-2}
Feed rate	3.8×10^{-2}	5.9×10^{-2}	8.1×10^{-2}	2.1×10^{-2}

Table 3. Standardized regression coefficients from dimensionless sensitivity analysis of printing parameters on each predicted output variable

Input variable	Height	Width	Scaffold modulus
Printing temperature	6.0×10^{-3}	8.0×10^{-3}	1.6×10^{-2}
Printing speed	4.0×10^{-3}	2.0×10^{-3}	8.0×10^{-3}
Feed rate	1.1×10^{-2}	1.3×10^{-2}	3.0×10^{-2}

epistemic uncertainty arising from training stochasticity and provides insight into the stability and generalizability of the model across multiple runs. For the experimental measurements, the error bars likewise represent the mean ± standard deviation obtained from repeated testing, with three scaffold specimens fabricated and tested per printing condition. These experimental bands, therefore, reflect the aleatoric uncertainty associated with fabrication and measurement variability.

The directly predicted modulus from ANN showed good consistency with experimental data, with most values falling within the experimental standard deviation. The modulus values obtained through FEA simulation using ANN-predicted geometry and material properties also aligned reasonably well with experimental results, albeit with slightly higher variance. Notably, the original modulus values computed via direct FEA using measured scaffold geometry and a fixed PLA material modulus of 3500 MPa (as reported by the manufacturer) show systematic overestimation, particularly at higher feed rates and lower print speeds. This is likely because the assigned elastic modulus—by the manufacturer—does not account for local defects or thermal degradation arising from suboptimal printing conditions, such as weak interlayer bonding or residual porosity. These process-induced imperfections can substantially reduce the effective stiffness of the printed material in practice.[30] In contrast, the ANN-informed approach uses material property predictions that reflect the influence of process conditions,

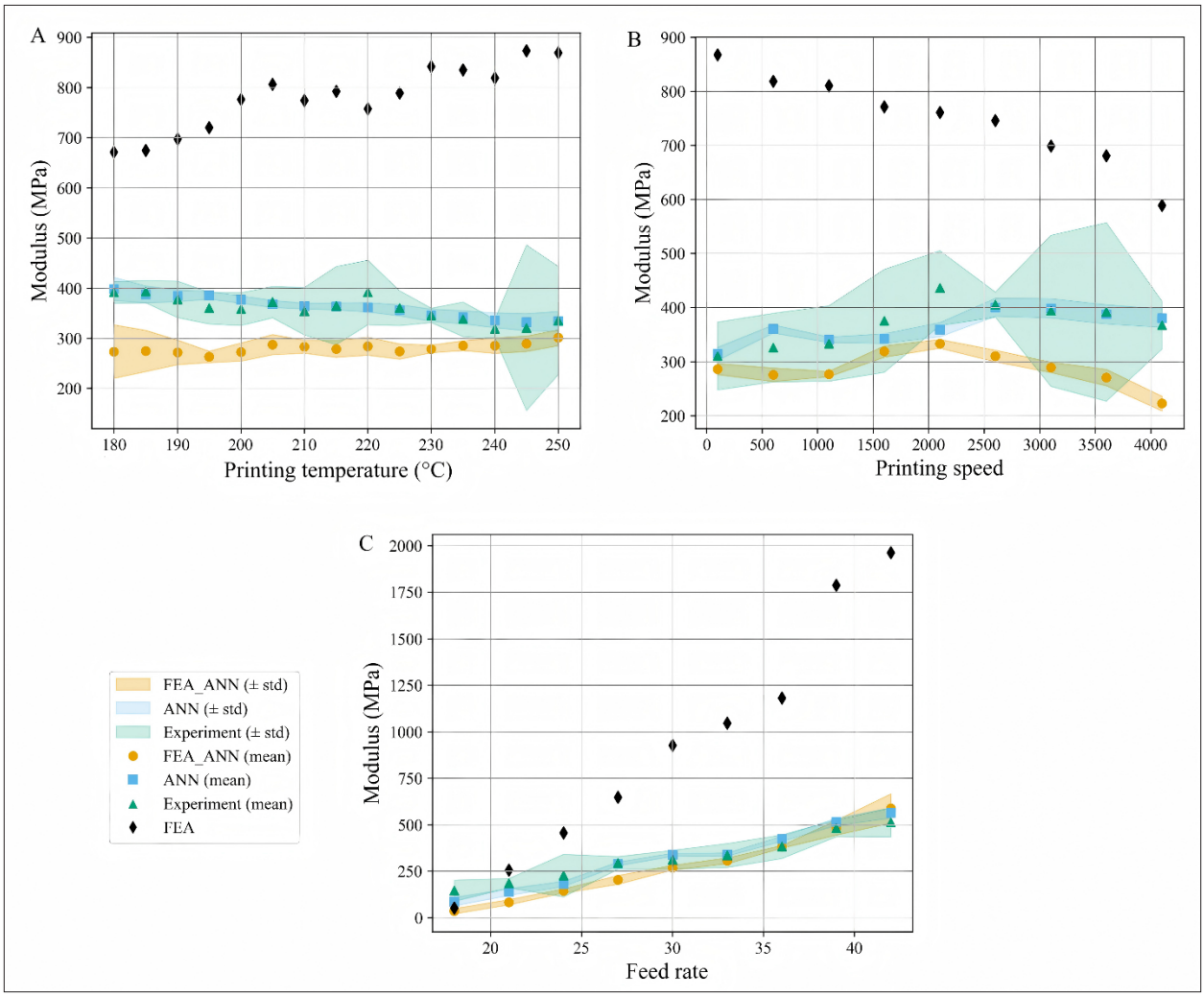

Figure 7. Modulus versus (A) printing temperature, (B) printing speed, and (C) feed rate. Each subplot compares the mean and standard deviation (std) of artificial neural network predictions, finite element analysis (FEA) simulations, and experimental results. Notably, FEA-only results show higher variability, especially under increasing feed rate.

leading to more accurate stiffness estimation when used in FEA simulations.

To quantify uncertainty, we distinguished between two sources: (i) Epistemic uncertainty, which arises from model variability due to limited data, was estimated using a deep ensemble of 10 independently trained models. Prediction error bars in Figure 7 reflect the standard deviation of these ensemble predictions. (ii) Aleatoric uncertainty, caused by fabrication and measurement variability, was captured via three repeated physical tests per printing condition. The resulting experimental standard deviation is shown as green shaded bands, reflecting the repeatability of the physical experiments.

The FEA-predicted scaffold moduli show close agreement with experimental measurements in the elastic regime, as shown in Figure 8. Residual differences are small and fall within the experimental variability, mainly due to minor geometric imperfections or interfacial defects that are not explicitly modeled. This validation confirms that the FEA framework is reliable for generating synthetic samples to support data augmentation.

Uncertainty plays a critical role in evaluating the reliability and generalizability of both data-driven and simulation-based models. In this study, we explicitly address two types of uncertainty:

(i) Aleatoric uncertainty, arising from inherent variability in the fabrication and measurement process, was quantified through repeated experiments. Standard deviations in filament dimensions and scaffold modulus were computed across replicates to capture this stochastic variability.

(ii) Epistemic uncertainty, stemming from limited training data and the model's generalization capacity, was captured via deep ensembles. By training 10 independent ANN models per split with different initializations, the standard deviation across predictions served as an empirical measure of model confidence.

To propagate these uncertainties, we constructed upper and lower bounds for key inputs—geometry and material modulus—based on ensemble variance and experimental statistics. These bounds were passed through the FEA module to generate prediction intervals for the scaffold's Young's modulus.

Notably, larger ensemble variance consistently coincided with input conditions far from the training distribution, such as extreme feed rates or high print speeds. These regions also exhibited larger discrepancies between model predictions and experimental measurements, validating ensemble variance as a useful proxy for model reliability.

This uncertainty-aware hybrid pipeline thus goes beyond point estimates to offer interval-based predictions that better reflect true confidence levels—an essential

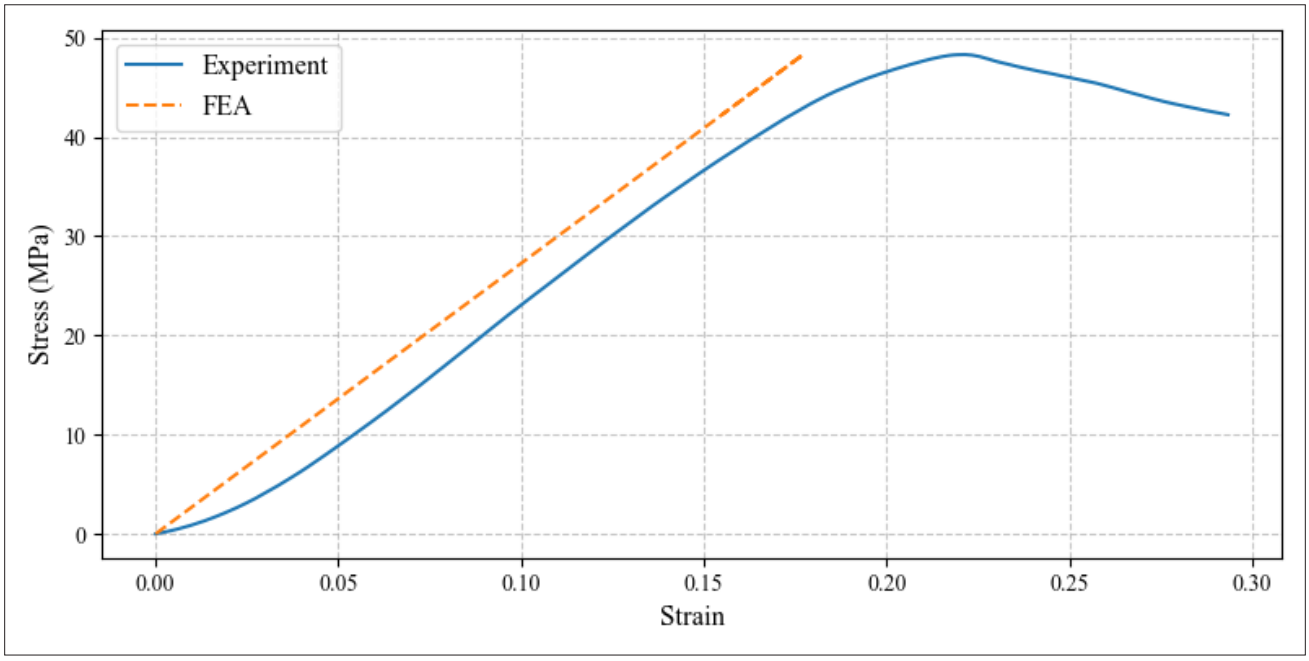

Figure 8. Comparison of experimental and finite element analysis (FEA) stress–strain curves.

feature for biomedical applications, where overconfident errors can carry clinical risk.

While the proposed approach adopts relatively simple ensemble-based and perturbation-based methods to quantify epistemic uncertainty, future work may benefit from integrating more principled uncertainty estimation frameworks. For example, Bayesian deep learning techniques—such as Monte Carlo Dropout or variational inference-based Bayesian neural networks—offer a formal way to capture uncertainty through posterior weight distributions.[57] These methods have been successfully applied in biomedical modeling and are considered strong alternatives to standard ensembles. Similarly, probabilistic FEA frameworks (e.g., stochastic FEA or polynomial chaos expansion) can explicitly propagate parameter uncertainty into mechanical outputs, enabling confidence bounds on predicted stiffness.[58] Incorporating such techniques could enhance the robustness and trustworthiness of hybrid ML–FEA pipelines.

3.3. Extrapolation performance in sparsely sampled regions

This section evaluates the extrapolation capability of the hybrid FEA–ANN model in sparsely sampled regions of the design space, using experimental measurements as the benchmark. Relying solely on physical experiments to explore the full scaffold design space is both time-consuming and costly, making it infeasible to cover every combination of printing parameters. As a result, many parameter combinations remain unseen by a purely data-driven model, which undermines its predictive reliability for new designs. The hybrid ANN–FEA modeling approach is introduced to address this challenge by leveraging physics-based simulations to supplement sparse experimental data. By generating simulation-informed predictions for parameter sets that were never physically tested, the hybrid framework expands the effective dataset and provides better generalization under data scarcity. In essence, FEA acts as a virtual testing ground for rare or extreme conditions, allowing the ANN to maintain accuracy in regions of the design space that would otherwise be beyond its experience.[59]

To demonstrate the benefits of this hybrid strategy, we evaluated the model on 15 scaffold samples with printing parameters deliberately excluded from training. These samples were designed to vary one parameter at a time—temperature, feed rate, or printing speed—while keeping the other two fixed. As summarized in Table 4, the temperature ranges from 190 to 210°C (in 5°C increments), the feed rate varies from 16% to 24% (step size of 2%), and the printing speed ranges from 800 to 1600 mm/min (step size of 200 mm/min). These configurations target boundary or underrepresented regions of the parameter space, allowing for evaluation of the model's extrapolation capability beyond the training distribution.

The Young's modulus was predicted directly by the ANN model and compared with values computed through FEA simulation based on ANN-predicted geometry and material properties. As shown in Table 4, an average relative error of approximately 14.2% was observed for the ANN-only predictions, with errors exceeding 15% in several cases. In contrast, the hybrid FEA+ANN approach achieved significantly improved prediction accuracy, reducing the mean relative error to 5.7%. These results highlight the advantage of incorporating physics-based simulation into the prediction pipeline, particularly when predictions are made beyond the boundaries of the training distribution.[59,60]

These evaluations were performed using the same trained ANN models described in **Section 3.2**; no retraining or fine-tuning was conducted. This setup ensures that the observed improvements in performance are solely attributable to the integration of FEA, rather than any modification of the network. The performance gap can be attributed to several factors. First, the ANN was trained on a relatively sparse dataset, making it difficult to learn accurate mappings in poorly sampled regions. Second, scaffold mechanics are governed by complex, nonlinear interactions among printing parameters (e.g., feed rate affects both deposition volume and cooling behavior), which are difficult to capture with purely data-driven models in extrapolative regimes. Finally, while ANN models interpolate well within the training domain, their reliability declines when predicting outputs for inputs that deviate significantly from those seen during training. These limitations underscore the importance of incorporating physics-based simulations such as FEA to

Table 4. Comparison of artificial neural network model performance with and without simulation-informed data augmentation

Parameter variation	Temperature (°C)	Speed (mm/min)	Feed rate (%)
Varying temperature	190–210 (step = 5)	1200	20
Varying printing speed	200	800–1600 (step = 200)	20
Varying feed rate	200	1200	16–24 (step = 2)

bridge such gaps and maintain predictive fidelity under novel design conditions.[61,62]

To further assess the trend consistency of the prediction models, we visualized the variation in scaffold modulus across three key process parameters: printing speed, feed rate, and nozzle temperature. As shown in Figure 9, subfigures (A), (B), and (C) correspond to the effects of printing temperature, speed, and feed rate, respectively. The predicted modulus from the ANN (blue dashed line) deviates noticeably from experimental trends (orange points), particularly at the extremes of the parameter range. In contrast, the hybrid FEA+ANN predictions (green dashed line) track the experimental data more closely and reproduce expected monotonic relationships, such as the increase in modulus with feed rate and the mild decline with increasing temperature. These findings highlight not only the higher accuracy of the hybrid framework but also its improved ability to generalize physical trends beyond the training data domain.[17,63] This indicates that including simulation-augmented data improves the model's generalization and extrapolation capability.

These results complement the experimental validation in **Section 3.2** and further support the rationale for integrating FEA-based data into the hybrid framework, particularly for exploring regions of the design space beyond the original experiments.

3.4. Data augmentation via simulation and feedback loop

To evaluate the impact of simulation-informed data augmentation on model performance, we trained two versions of the ANN model to predict scaffold Young's

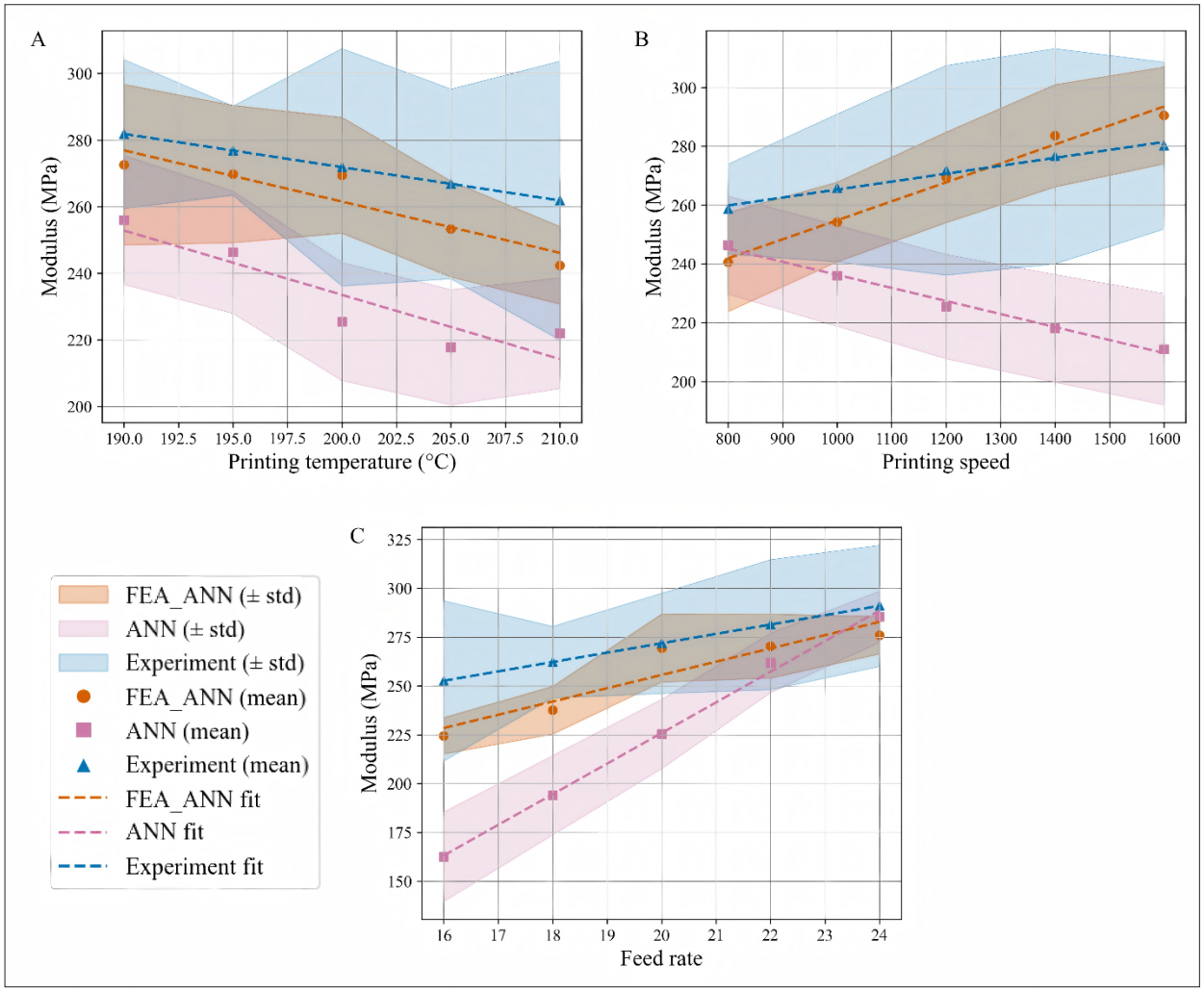

Figure 9. Comparison of predicted and measured Young's modulus under varying (A) printing temperature, (B) printing speed, and (C) feed rate. Dashed lines indicate linear trends for ANN-only (blue), experimental (orange points), and hybrid FEA+ANN predictions (green). The hybrid approach consistently tracks experimental trends more closely. Abbreviations: ANN, artificial neural network; FEA, finite element analysis.

modulus using only printing parameters as input (i.e., ANN3). The first version was trained exclusively on the original experimental dataset. The second version incorporated additional samples to enrich the training distribution. Specifically, 30 new parameter combinations were sampled using Latin Hypercube Sampling (LHS) across the full design space (temperature: 180–250°C; feed rate: 15–42%; printing speed: 100–5100 mm/min). These points were selected to fill underrepresented regions and ensure minimal overlap with existing data. For each LHS-generated point, filament geometry and material properties were predicted using the trained ANN models, and scaffold-level modulus was computed through FEA, resulting in a set of synthetic scaffold samples.

In the present study, we employed a stratified sampling strategy in combination with LHS to achieve uniform initial coverage of the printing parameter space, within the constraints of limited experimental resources. This approach yielded a balanced and interpretable dataset for model training, minimizing sampling bias toward any particular region of the design space. Although effective for the purposes of this study, alternative strategies based on active learning—such as Bayesian optimization or uncertainty-driven sampling—may offer improved data efficiency by adaptively targeting regions with sparse coverage or high predictive uncertainty. While such techniques were not implemented here, they represent a promising direction for future work aimed at accelerating the exploration and optimization of scaffold design spaces.

This combined dataset—consisting of experimental and FEA-augmented samples—was used to train a new ANN model from scratch. As shown in Table 5, both models achieved strong performance on a held-out test set. The ANN trained on experimental data alone yielded a mean absolute error (MAE) of 0.0338 GPa and a relative error of 5.17%. After incorporating simulation-derived data, the MAE was reduced to 0.0283 GPa, and the relative error dropped to 4.72%. These improvements, though modest, indicate that the hybrid ANN–FEA framework can provide valuable generalization benefits by enriching the training distribution, particularly in regions underrepresented in physical experiments.[64,65]

Although the improvement in held-out test performance shown in Table 4 appears modest—reducing the MAE from 0.0338 to 0.0283 GPa—this reflects the fact that the test set is located close to the original experimental data. Given that both training and testing remained within a relatively narrow region of the design space, the benefits of simulation-informed augmentation are partially masked. The true strength of this approach lies in its ability to support extrapolation beyond the training distribution.[66] As demonstrated in **Section 3.3**, for unseen combinations of printing parameters located far from the experimental data manifold, the hybrid ANN–FEA framework achieved substantially lower prediction errors compared to direct ANN models (5.7% vs. 14.2%). This improvement arises because physics-guided data augmentation enriched the training distribution across a wider design space, improving reliability under novel or extreme conditions. These findings suggest that even small test-set improvements may understate the broader generalization gains enabled by simulation-based feedback.

4. Conclusion and future work

This paper presents a modular and interpretable framework that integrates ANN with FEA to predict the mechanical properties of 3D-printed PLA bone scaffolds. By decomposing the prediction process into geometrical, material, and structural levels, the framework supports data-efficient modeling, uncertainty quantification, and enhanced generalization. The key novel contributions are:

(i) Modular prediction pipeline: We proposed a physics-informed, interpretable framework that mirrors real-world scaffold fabrication. It comprises separate ANN submodels for geometry and material property prediction, which feed into a scaffold-scale FEA simulation. This modularity enables validation at each step and simplifies model updating or reuse.

(ii) Simulation-guided data augmentation: We demonstrated how integrating FEA simulations into the training loop augments sparse experimental datasets, enhancing model generalization. In data-scarce regions, the hybrid ANN–FEA approach reduced prediction error from 14.2% (ANN-only) to 5.7% and improved extrapolation performance beyond the training domain.

(iii) Uncertainty-aware modeling: We incorporated deep ensembles and perturbation-based FEA analysis to estimate epistemic and aleatoric uncertainty, offering confidence bounds for predicted scaffold stiffness. This supports risk-aware predictions in biomedical applications.

Table 5. Comparison of artificial neural network model performance with and without simulation-informed data augmentation

Training data	MAE (GPa)	Relative error (%)
Experimental only	0.0338	5.17
Experimental + FEA	0.0283	4.72

Abbreviations: FEA, finite element analysis; MAE, mean absolute error.

(iv) Adaptability and extensibility: The proposed pipeline is reusable and adaptable to new materials, scaffold designs, and clinical requirements. By retraining only relevant ANN submodules, the framework can support multi-material or patient-specific optimization scenarios.

Although the framework demonstrates good predictive performance, it represents a preliminary implementation primarily intended to test feasibility and interpretability under constrained data conditions. This study, therefore, serves as a foundational step toward the development of more generalizable and versatile scaffold design models. Several aspects remain to be expanded in future work. First, this study focuses on short-term mechanical responses of PLA scaffolds under uniaxial compression, without incorporating biological performance factors such as biodegradation, permeability, or cell–scaffold interactions. Second, although the modular structure of the framework supports adaptability, the current implementation has only been applied to a single material system (PLA) and a regular grid architecture. To expand the scope and applicability of the framework, future work is being considered in:

(i) Incorporating advanced material models in the FEA, including poroelastic or viscoelastic constitutive models to represent scaffold behavior under physiological loading and over time.

(ii) Improving data efficiency via active learning strategies—such as Bayesian optimization or uncertainty-guided sampling—to adaptively select new samples in underexplored or high-uncertainty regions, improving efficiency in data acquisition and model refinement.

(iii) Extending to multi-objective optimization by incorporating additional mechanical and biological elements in the objective function.

(iv) Adapting to new materials and architectures through transfer learning techniques: extending the trained models to other biopolymers (e.g., PCL, PEEK) or scaffold topologies (e.g., gyroid, triply periodic minimal surfaces) by leveraging knowledge transfer across related tasks.

(v) Integrating inverse design algorithms: coupling the predictive framework with inverse design methods to enable automated scaffold optimization toward desired mechanical and biological performance.

Acknowledgments

The authors would like to thank Mr. Tom Barnes and Ms. Amy Bland for their technical assistance with 3D printing and mechanical testing at the University of Bristol. We are also grateful to our colleagues Dr. Weiting Xu, Dr. Yi Huang, and Dr. Yan Xu for their constructive discussions and support throughout the development of this research. Special thanks are extended to Dr. Aydin Nassehi, Professor Ben Hicks, and Dr. Qunfen Qi for their academic guidance and inspiration. Rixiang Quan acknowledges the unwavering encouragement and support from his family, especially Qin Yingli, Quan Xin'an, and all those who have supported him along the way.

Funding

This work was supported by the Engineering and Physical Sciences Research Council Impact Acceleration Account 2022–2026 (EP/X525674/1).

Conflict of interest

Fengyuan Liu serves as the Editorial Board Member of the journal but was not involved in the editorial or peer-review process conducted for this paper, either directly or indirectly. The Other authors declare no competing interests.

Author contributions

Conceptualization: Fengyuan Liu, Rixiang Quan, Sergio Cantero Chinchilla
Data interpretation: Sergio Cantero Chinchilla
Formal analysis: Rixiang Quan
Funding acquisition: Fengyuan Liu
Investigation: Rixiang Quan
Methodology: Fengyuan Liu, Rixiang Quan, Sergio Cantero Chinchilla
Supervision: Fengyuan Liu
Writing-original draft: Rixiang Quan
Writing-review & editing: Fengyuan Liu, Sergio Cantero Chinchilla

Ethics approval and consent to participate

Not applicable.

Consent for publication

Not applicable.

Availability of data

The complete implementation of the proposed framework will publicly be available on GitHub (https://github.com/davidquanaa/FEANN-Print), including data processing pipelines, model code, and finite element analysis (FEA) coupling scripts. To support reproducibility and promote

broader adoption, we have prepared a companion software article—to be submitted to SoftwareX—titled: *FEANN-Print: A Coupled ANN and FEA Framework for Enhanced Prediction and Design of 3D-Printed Bone Scaffolds*, which provides comprehensive documentation of the framework's architecture and functionality.

Further disclosure

A portion of this work (title: Machine Learning-Driven Optimization of 3D Printing Parameters for PLA Bone Scaffolds with Enhanced Mechanical Properties) was presented at the 6th CIRP Conference (Dresden, Germany) in June 2024.

References

1. O'Brien FJ. Biomaterials and scaffolds for tissue engineering. *Mater Today.* 2011;14(3):88-95. doi: 10.1016/S1369-7021(11)70058-X
2. Hutmacher DW. Scaffolds in tissue engineering bone and cartilage. *Biomaterials.* 2000;21(24):2529-2543. doi: 10.1016/S0142-9612(00)00121-6
3. Bose S, Roy M, Bandyopadhyay A. Recent advances in bone tissue engineering scaffolds. *Trends Biotechnol.* 2012;30(10):546-554. doi: 10.1016/j.tibtech.2012.07.005
4. Feng Y, Zhu S, Mei D, *et al*. Application of 3D printing technology in bone tissue engineering: a review. *Curr Drug Deliv.* 2021;18:847-861. doi: 10.2174/1567201817999201113100322
5. Xu Y, Zhang F, Zhai W, Cheng S, Li J, Wang Y. Unraveling of advances in 3D-printed polymer-based bone scaffolds. *Polymers (Basel).* 2022;14:566. doi: 10.3390/polym14030566
6. Hussain M, Khan SM, Shafiq M, Abbas N. A review on PLA-based biodegradable materials for biomedical applications. *Giant.* 2024;18(3):100261. doi: 10.1016/j.giant.2024.100261
7. Afonso J, Alves JL, Caldas G, Gouveia BP, Santana L, Belinha J. Influence of 3D printing process parameters on the mechanical properties and mass of PLA parts and predictive models. *Rapid Prototyp J.* 2021;27(3):487-495. doi: 10.1108/RPJ-03-2020-0043
8. Ma S, Tang Q, Liu Y, Feng Q. Prediction of mechanical properties of three-dimensional printed lattice structures through machine learning. *J Comput Inf Sci Eng.* 2022;22(3):031008. doi: 10.1115/1.4053077
9. Sheoran AJ, Kumar H. Fused deposition modeling process parameters optimization and effect on mechanical properties and part quality: review and reflection on present research. *Mater Today Proc.* 2020;21:1659-1672. doi: 10.1016/j.matpr.2019.11.296
10. Goh GD, Sing SL, Yeong WY. A review on machine learning in 3D printing: applications, potential, and challenges. *Artif Intell Rev.* 2021;54(1):63-94. doi: 10.1007/s10462-020-09876-9
11. Goh GD, Sing SL, Lim YF, *et al*. Machine learning for 3D-printed multi-materials tissue-mimicking anatomical models. *Mater Des.* 2021;211:110125. doi: 10.1016/j.matdes.2021.110125
12. Jayasudha M, Elangovan M, Mahdal M, Priyadarshini J. Accurate estimation of tensile strength of 3D-printed parts using machine learning algorithms. *Processes.* 2022;10(6):1158. doi: 10.3390/pr10061158
13. Rodrigues JF, Florea L, de Oliveira MC, Diamond D, Oliveira ON. Big data and machine learning for materials science. *Discover Mater.* 2021;1:1-27. doi: 10.1007/s43939-021-00012-0
14. Oviedo F, Ferres JL, Buonassisi T, Butler KT. Interpretable and explainable machine learning for materials science and chemistry. *Acc Mater Res.* 2022;3(6):597-607. doi: 10.1021/accountsmr.1c00244
15. Kalina KA, Linden L, Brummund J, Kästner M. FE-ANN: an efficient data-driven multiscale approach based on physics-constrained neural networks and automated data mining. *Comput Mech.* 2023;71(5):827-851. doi: 10.1007/s00466-022-02260-0
16. Peng B, Wei Y, Qin Y, *et al*. Machine learning-enabled constrained multi-objective design of architected materials. *Nat Commun.* 2023;14(1):6630. doi: 10.1038/s41467-023-42415-y
17. Oladipo B, Matos H, Krishnan NA, Das SJ. Integrating experiments, finite element analysis, and interpretable machine learning to evaluate the auxetic response of 3D-printed re-entrant metamaterials. *J Mater Res Technol.* 2023;25:1612-1625. doi: 10.1016/j.jmrt.2023.06.038
18. Drakoulas G, Gortsas T, Polyzos E, *et al*. An explainable machine learning-based probabilistic framework for the design of scaffolds in bone tissue engineering. *Biomech Model Mechanobiol.* 2024;23(3):987-1012. doi: 10.1007/s10237-024-01817-7
19. Dong H, Liu F, Ye L, *et al*. Process optimization and mechanical property investigation of Inconel 718 manufactured by selective electron beam melting. *Mater Sci Addit Manuf.* 2022;1(4):23. doi: 10.18063/msam.v1i4.23
20. Rodrigues N, Benning M, Ferreira AM, Dixon L, Dalgarno K. Manufacture and characterisation of porous PLA scaffolds. *Procedia CIRP.* 2016;49:33-38. doi: 10.1016/j.procir.2015.07.025

21. Frunzaverde D, Cojocaru V, Ciubotariu CR, *et al*. The influence of the printing temperature and the filament color on the dimensional accuracy, tensile strength, and friction performance of FFF-printed PLA specimens. *Polymers (Basel)*. 2022;14(10):1978.
doi: 10.3390/polym14101978

22. Lei M, Wei Q, Li M, Zhang J, Yang R, Wang Y. Numerical simulation and experimental study of the effects of process parameters on filament morphology and mechanical properties of FDM 3D-printed PLA/GNPs nanocomposite. *Polymers (Basel)*. 2022; 14(15):3081.
doi: 10.3390/polym14153081

23. Wickramasinghe S, Do T, Tran P. FDM-based 3D printing of polymer and associated composite: a review on mechanical properties, defects, and treatments. *Polymers (Basel)*. 2020;12(7):1529.
doi: 10.3390/polym12071529

24. Heidari-Rarani M, Ezati N, Sadeghi P, Badrossamay M. Optimization of FDM process parameters for tensile properties of polylactic acid specimens using Taguchi design of experiment method. *J Thermoplast Compos Mater*. 2022;35(12):2435-2452.
doi: 10.1177/0892705720964560

25. Chokshi H, Shah DB, Patel KM, Joshi SJ. Experimental investigations of process parameters on mechanical properties for PLA during processing in FDM. *Adv Mater Process Technol*. 2022;8(suppl 2):696-709.
doi: 10.1080/2374068X.2021.1946756

26. Farah S, Anderson DG, Langer R. Physical and mechanical properties of PLA and their functions in widespread applications—a comprehensive review. *Adv Drug Deliv Rev*. 2016;107:367-392.
doi: 10.1016/j.addr.2016.06.012

27. Zienkiewicz OC, Taylor RL, Zhu JZ. Chapter 10: Incompressible problems, mixed methods, and other procedures of solution. In: *The Finite Element Method: Its Basis and Fundamentals*. 7th ed.; 2013:315-359.
doi: 10.1016/B978-1-85617-633-0.00010-1

28. Gomes MS, Carmo GP, Ptak M, Fernandes FA, Alves de Sousa RJ. Accuracy and efficiency of finite element head models: the role of finite element formulation and material laws. *Int J Numer Methods Biomed Eng*. 2024;40(9):e3851.
doi: 10.1002/cnm.3851

29. Zienkiewicz OC, Taylor RL, Zhu JZ. Chapter 16: Adaptive finite element refinement. In: *The Finite Element Method: Its Basis and Fundamentals*. 7th ed.; 2013:545-572.
doi: 10.1016/B978-1-85617-633-0.00016-2

30. Demir M, Seki Y. Interfacial adhesion strength between FDM-printed PLA parts and surface-treated cellulosic-woven fabrics. *Rapid Prototyp J*. 2023;29(6):1166-1174.
doi: 10.1108/RPJ-10-2022-0369

31. Rankouhi B, Javadpour S, Delfanian F, Letcher T. Failure analysis and mechanical characterization of 3D-printed ABS with respect to layer thickness and orientation. *J Fail Anal Prev*. 2016;16(3):467-481.
doi: 10.1007/s11668-016-0113-2

32. Sagias V, Giannakopoulos K, Stergiou C. Mechanical properties of 3D-printed polymer specimens. *Procedia Struct Integr*. 2018;10:85-90.
doi: 10.1016/j.prostr.2018.09.013

33. Xu L, Leguillon D. Dual-notch void model to explain the anisotropic strengths of 3D-printed polymers. *J Eng Mater Technol*. 2020;142(3):031001.
doi: 10.1115/1.4044282

34. Ahn SH, Montero M, Odell D, Roundy S, Wright PK. Anisotropic material properties of fused deposition modeling ABS. *Rapid Prototyp J*. 2002;8(4):248-257.
doi: 10.1108/13552540210441166

35. Chen J, Liu X, Tian Y, *et al*. 3D-printed anisotropic polymer materials for functional applications. *Adv Mater*. 2022;34(5):2102877.
doi: 10.1002/adma.202102877

36. Castelló-Pedrero P, García-Gascón C, García-Manrique J. Multiscale numerical modeling of large-format additive manufacturing processes using carbon fiber reinforced polymer for digital twin applications. *Int J Mater Form*. 2024;17(2):15.
doi: 10.1007/s12289-024-01811-5

37. He K, Zhang X, Ren S, Sun J. Delving deep into rectifiers: surpassing human-level performance on ImageNet classification. In: *Proceedings of the IEEE International Conference on Computer Vision (ICCV);* 2015: 1026-1034.
doi: 10.1109/ICCV.2015.123

38. Varma S, Simon R. Bias in error estimation when using cross-validation for model selection. *BMC Bioinformatics*. 2006;7(1):91.
doi: 10.1186/1471-2105-7-91

39. Banerjee S, Lio P, Jones PB, Cardinal RN. A class-contrastive human-interpretable machine learning approach to predict mortality in severe mental illness. *npj Schizophr*. 2021;7(1):60.
doi: 10.1038/s41537-021-00191-y

40. Schnaubelt M. A comparison of machine learning model validation schemes for non-stationary time series data. Preprint. 2019.

41. Glorot X, Bordes A, Bengio Y. Deep sparse rectifier neural networks. In: JMLR Workshop Conf Proc. 2011;315-323.

42. Vakalopoulou M, Christodoulidis S, Burgos N, Colliot O, Lepetit VJ. Deep Learning: Basics and Convolutional Neural Networks (CNNs); 2023:77-115.
doi: 10.1007/978-1-0716-3195-9_3

43. Cantero-Chinchilla S, Simpson CA, Ballisat A, Croxford AJ, Wilcox PD. Convolutional neural networks for ultrasound corrosion profile time series regression. *NDT E Int*. 2023;133:102756. doi: 10.1016/j.ndteint.2022.102756

44. Rahaman R, Thiery AH. Uncertainty quantification and deep ensembles. *Adv Neural Inf Process Syst*. 2021;34:20063-20075. doi: 10.48550/arXiv.2007.08792

45. Ovadia Y, Fertig E, Ren J, *et al*. Can you trust your model's uncertainty? Evaluating predictive uncertainty under dataset shift. *Adv Neural Inf Process Syst*. 2019;32. doi: 10.48550/arXiv.1906.02530

46. Fort S, Hu H, Lakshminarayanan B. Deep ensembles: a loss landscape perspective. In: International Conference on Learning Representations (ICLR); 2020. doi: 10.48550/arXiv.1912.02757

47. Pepelnjak T, Sevšek L, Movrin D, Milutinović M. Influence of process parameters on the characteristics of additively manufactured parts made from advanced biopolymers. *Polymers (Basel)*. 2023;15(3):716. doi: 10.3390/polym15030716

48. Wang C, Tan XP, Tor SB, Lim CJ. Machine learning in additive manufacturing: state-of-the-art and perspectives. *Addit Manuf*. 2020;36:101538. doi: 10.1016/j.addma.2020.101538

49. Wu H, Sulkis M, Driver J, Saade-Castillo A, Thompson A, Koo JH. Multi-functional ULTEM™ 1010 composite filaments for additive manufacturing using fused filament fabrication (FFF). *Addit Manuf*. 2018;24:298-306. doi: 10.1016/j.addma.2018.10.014

50. Zhao X, Li S, Zhang M, *et al*. Comparison of the microstructures and mechanical properties of Ti–6Al–4V fabricated by selective laser melting and electron beam melting. *Mater Des*. 2016;95:21-31. doi: 10.1016/j.matdes.2015.12.135

51. Dejene ND, Lemu HG. Characterisation and prediction of mechanical properties in laser powder bed fusion-printed parts: a comparative analysis using machine learning. *Mater Tehnol*. 2024;39(1):2419228. doi: 10.1080/10667857.2024.2419228

52. Ibrahimi S, D'Andrea L, Gastaldi D, Rivolta MW, Vena P. Machine learning approaches for the design of biomechanically compatible bone tissue engineering scaffolds. *Comput Methods Appl Mech Eng*. 2024;423:116842. doi: 10.1016/j.cma.2024.116842

53. Rudolph M, Kurz S, Rakitsch J. Hybrid modeling design patterns. *J Math Ind*. 2024;14(1):3. doi: 10.1186/s13362-024-00141-0

54. Lamane H, Mouhir L, Moussadek R, Baghdad B, Kisi O, El Bilali A. Interpreting machine learning models based on SHAP values in predicting suspended sediment concentration. *Int J Sediment Res*. 2025;40(1):91-107. doi: 10.1016/j.ijsrc.2024.10.002

55. Lundberg SM, Lee SI. A unified approach to interpreting model predictions. *Adv Neural Inf Process Syst*. 2017;30. doi: 10.48550/arXiv.1705.07874

56. Rooks NB, Besier TF, Schneider MT. A parameter sensitivity analysis on multiple finite element knee joint models. *Front Bioeng Biotechnol*. 2022;10:841882. doi: 10.3389/fbioe.2022.841882

57. Gal Y, Ghahramani Z. Dropout as a Bayesian Approximation: Representing Model Uncertainty in Deep Learning. In: Proceedings of the 33rd International Conference on Machine Learning (ICML 2016). *Proc Mach Learn Res*. 2016;48:1050-1059. https://proceedings.mlr.press/v48/gal16.html

58. Kendall A, Gal Y. What uncertainties do we need in Bayesian deep learning for computer vision? *Adv Neural Inf Process Syst*. 2017;30:5575-5585.

59. Bock FE, Keller S, Huber N, Klusemann B. Hybrid modelling by machine learning corrections of analytical model predictions towards high-fidelity simulation solutions. *Materials (Basel)*. 2021;14(8):1883. doi: 10.3390/ma14081883

60. Aldakheel F, Elsayed ES, Heider Y, Weeger O. Physics-based machine learning for computational fracture mechanics. *Mach Learn Comput Sci Eng*. 2025;1(1):18. doi: 10.1007/s44379-025-00019-x

61. Napolitano F, Cozzolino E, Papa I, Astarita A, Squillace A. Experimental integrated approach for mechanical characteristic optimization of FDM-printed PLA in an energy-saving perspective. *Int J Adv Manuf Technol*. 2022;121(5):3551-3565. doi: 10.1007/s00170-022-09535-z

62. Yao H, Gao Y, Liu Y. FEA-Net: A physics-guided data-driven model for efficient mechanical response prediction. *Comput Methods Appl Mech Eng*. 2020;363:112892. doi: 10.1016/j.cma.2020.112892

63. Bahraminasab M. Challenges on optimization of 3D-printed bone scaffolds. *BioMed Eng Online*. 2020;19(1):69. doi: 10.1186/s12938-020-00810-2

64. Akbari P, Zamani M, Mostafaei A. Machine learning prediction of mechanical properties in metal additive manufacturing. *Addit Manuf*. 2024;91:104320. doi: 10.1016/j.addma.2024.104320

65. Ng WL, Goh GL, Goh GD, Ten JSJ, Yeong WY. Progress and opportunities for machine learning in materials and processes of additive manufacturing. *Adv Mater*. 2024;36(34):2310006. doi: 10.1002/adma.202310006

66. Mohamed AP, Lee B, Zhang Y, *et al*. Simulation-enhanced data augmentation for machine learning pathloss prediction. In: ICC 2024 - IEEE International Conference on Communications; 2024: 4863-4868.

ACCSCIENCE PUBLISHING

International Journal of Bioprinting

RESEARCH ARTICLE

3D-bioprinted kartogenin-laden hydrogel promotes cartilage regeneration via Smad1/5/9-mediated chondrogenesis of bone marrow stromal cells

Chenhui Yang[1,2,3], Changshun Chen[1,2], Rongjin Cheng[1,2], Fei Yang[1,2], Hefang Xiao[1,2], Bin Geng[1,2], and Yayi Xia[1,2]*

[1]Department of Orthopedics, Lanzhou University Second Hospital, Lanzhou, Gansu, China

[2]Department of Orthopedics I, Orthopedic Clinical Medical Research Center and Intelligent Orthopedic Industry Technology Center of Gansu Province, Lanzhou, Gansu, China

[3]Department of Orthopedics, Tianshui Hand and Foot Surgery Hospital, Tianshui, Gansu, China

Abstract

Cartilage injury and degeneration are common clinical problems that severely affect joint function and quality of life. Due to the limited self-healing capacity of cartilage, there is an urgent need for advanced biomaterials and strategies to promote effective cartilage regeneration. In this study, we present a 3D-bioprinted kartogenin (KGN)-loaded hydrogel with optimized biocompatibility and biomechanical properties for cartilage regeneration. By investigating the molecular mechanisms underlying KGN-induced chondrogenic differentiation of bone marrow stromal cells (BMSCs), we identified the critical role of the Smad1/5/9 signaling pathway through transcriptomic analysis. The hydrogel scaffold demonstrated uniform microstructure, robust mechanical stability, and controlled degradation, supporting BMSC adhesion and proliferation. *In vitro* experiments revealed that KGN activation of Smad1/5/9 significantly enhanced chondrogenic differentiation, evidenced by upregulated cartilage-specific matrix production and morphological changes in BMSCs, while pathway inhibition diminished this effect. Animal experiments using a rat model of cartilage injury demonstrated the hydrogel's biosafety, with no systemic toxicity or adverse inflammation, and its capacity to promote structured neocartilage formation rich in type II collagen. Histological and immunohistochemical analyses further validated the hydrogel's superior repair efficacy compared to controls. These findings highlight the dual functionality of the 3D-printed KGN-loaded hydrogel as a mechanically stable carrier and a bioactive inducer of BMSC chondrogenesis, mediated via Smad1/5/9 signaling, offering a promising strategy for cartilage tissue engineering.

Keywords: 3D bioprinting; Bone marrow stromal cells; Cartilage regeneration; Kartogenin; Smad1/5/9 pathway

***Corresponding author:**
Yayi Xia (xiayy@lzu.edu.cn)

Citation: Yang C, Chen C, Cheng R, *et al.* 3D-bioprinted kartogenin-laden hydrogel promotes cartilage regeneration via Smad1/5/9-mediated chondrogenesis of bone marrow stromal cells. *Int J Bioprint*. 2025;11(6):349-373. doi: 10.36922/IJB025180171

Received: April 28, 2025
Revised: July 29, 2025
Accepted: August 5, 2025
Published Online: August 5, 2025

Copyright: © 2025 Author(s). This is an Open Access article distributed under the terms of the Creative Commons Attribution License, permitting distribution and reproduction in any medium, provided the original work is properly cited.

Publisher's Note: AccScience Publishing remains neutral with regard to jurisdictional claims in published maps and institutional affiliations.

1. Introduction

Cartilage injuries and degenerative joint diseases are common clinical disorders that significantly impact patients' quality of life. Given cartilage's limited intrinsic regenerative capacity, repair remains a significant challenge.[1] Treatment modalities, including pharmacotherapy and surgery, generally alleviate symptoms without fully regenerating the cartilage.[2,3] In recent years, 3D printing technology has emerged as an innovative manufacturing technique with substantial promise in biomedical applications, particularly tissue engineering.[4] This technology enables the precise construction of complex biological structures, offering novel solutions for cartilage tissue engineering by fabricating biomaterials with specific microstructures essential for supporting cell attachment, proliferation, and differentiation.[5,6]

With 3D printing, researchers have developed various hydrogels with excellent biocompatibility that mimic the natural cartilage environment. These hydrogels provide mechanical support and simulate the extracellular matrix (ECM), promoting cell growth and tissue regeneration.[7] Kartogenin (KGN), a small-molecule compound, has been demonstrated to induce bone marrow stromal cells (BMSCs) toward chondrogenic differentiation. Integrating KGN with 3D printing technology presents a new strategy for cartilage engineering.[8] Loading KGN into 3D-printed hydrogels creates a favorable microenvironment for BMSC chondrogenic differentiation, which has demonstrated potential in promoting cartilage regeneration in preliminary studies.[9]

The Smad1/5/9 signaling pathway is a key regulator in the differentiation process, particularly in the osteogenic and chondrogenic differentiation of BMSCs.[10,11] KGN influences this pathway to activate genes associated with cartilage formation.[12,13] Research on the Smad1/5/9 pathway enhances our understanding of BMSC differentiation mechanisms and provides a molecular basis for using these cells in tissue engineering.[14,15] By thoroughly investigating how this pathway regulates BMSC chondrogenic differentiation under the influence of KGN, we can more effectively design and optimize 3D-printed hydrogels to enhance their efficacy and safety in clinical applications.[16]

This study aims to develop a novel 3D-printed hydrogel material with excellent biocompatibility and mechanical properties, capable of effectively loading the small molecule compound KGN and significantly promoting chondrogenic differentiation of BMSCs by activating the Smad1/5/9 signaling pathway. By precisely designing the microstructure of the hydrogel and optimizing the release mechanism of KGN, this study not only validates its ability to promote chondrogenic differentiation of BMSCs *in vitro* but also evaluates its application in cartilage repair through animal models. This study introduces novel biomaterials and therapeutic approaches for managing cartilage lesions, with significant scientific and clinical implications. Especially in the context of limited existing treatment options, the 3D-printed hydrogel loaded with KGN (Hy@KGN) offers a more effective repair strategy for patients with cartilage damage, improving treatment outcomes and quality of life. Overall, the present study not only provides a new solution for chondrogenic differentiation but also lays the foundation for future clinical applications, with broad prospects and translational potential.

2. Materials and methods

2.1. Hydrogel synthesis

To synthesize Hy@KGN, hydroxyethyl methacrylate (HEMA; Sigma-Aldrich, United States of America [USA]) and poly(ethylene glycol) diacrylate (PEGDA; molecular weight [Mw]: 700, Sigma-Aldrich, USA) were dissolved in deionized water (Milli-Q, Merck Millipore, Germany). A solution containing 0.5 g of HEMA and 0.5 g of PEGDA in 5 mL of deionized water was stirred until completely dissolved. Subsequently, 0.05 g of ammonium persulfate (APS; Sigma-Aldrich, USA) and 0.05 mL of N,N,N′,N′-tetramethylethylenediamine (TEMED; Sigma-Aldrich, USA) were added and mixed thoroughly. Next, 0.05, 0.1, or 0.2 g of KGN (HY-16268, MedChemExpress, USA) was dissolved in 1 mL of ethanol and incorporated into the monomer solution, followed by uniform stirring. The mixture was printed into predesigned hydrogel structures using a 3D bioprinter (BioScaffolder 3.1, GeSiM, Germany) under the following parameters: printing temperature of 25°C; pressure of 30 psi; nozzle diameter of 0.203 mm; printing speed of 6 mm/s; and layer height of 0.2 mm.[17] After printing, the hydrogels were cured through chemical crosslinking to obtain the final Hy@KGN hydrogel. The hydrogel formulations are listed in **Table S1, Supporting Information**. The KGN release behavior was evaluated in a simulated body fluid environment. Release tests indicated that the hydrogel prepared with 0.2 g KGN released up to 85% of KGN within the first 2 weeks but exhibited higher cytotoxicity. In contrast, the hydrogel prepared with 0.1 g KGN released approximately 80% of KGN in the first 2 weeks with lower cytotoxicity and then entered a sustained release phase, providing a continuous supply of KGN to promote cartilage repair (Figure S1, Supporting Information). Based on these results, the hydrogel with 0.1 g KGN was selected for subsequent experiments.

2.2. Microstructure characterization

To examine the microstructure of the Hy@KGN hydrogel, scanning electron microscopy (SEM; FEI Quanta 250, Thermo Fisher Scientific, USA) was utilized. Firstly,

the printed hydrogel samples were freeze-dried for 48 h using a freeze dryer (Christ Alpha 1-2 LDplus, Martin Christ, Germany). Following dehydration, specimens were affixed to sample holders and subjected to gold sputter-coating. SEM imaging was performed at four distinct magnification levels to capture detailed structural features, and representative micrographs were recorded.

2.3. Rheological performance testing

To evaluate the viscoelastic behavior of the Hy@KGN hydrogel, a rheological analysis was performed using a rheometer (AR2000, TA Instruments, USA). Disc-shaped samples (diameter: 20 mm; thickness: 1 mm) were prepared for testing. Oscillatory frequency sweeps were carried out at 25°C over a range of 0.1–100 Hz under parallel plate configuration, and both storage modulus (G') and loss modulus (G'') values were recorded.

2.4. Compression performance testing

To measure the compressive properties of the Hy@KGN hydrogel, a compression tester (Instron 5567, Instron, USA) was utilized. Standard cylindrical hydrogel specimens (diameter: 10 mm; height: 10 mm) were prepared. Tests were conducted at room temperature at a compression speed of 1 mm/min. Compressive strength and maximum compressive strain were recorded, and a stress–strain curve was plotted.

2.5. Compression-reloading cycle testing

To evaluate the resilience and fatigue behavior of the Hy@KGN hydrogel, the same compression tester (Instron 5567, Instron, USA) was employed. Standard cylindrical hydrogel specimens (diameter: 10 mm; height: 10 mm) were placed between parallel compression plates of the tester. The tests were carried out at room temperature at a compression speed of 1 mm/min. After setting the maximum compressive strain, the tester initiated compression until the set strain was reached, followed by unloading. Force and displacement data were recorded throughout the process. The compression and unloading cycles were repeated multiple times (typically 10–20) to assess the hydrogel's resilience and fatigue behavior.

2.6. Tensile performance testing

The tensile properties of the Hy@KGN hydrogel were assessed using a tensile tester (Instron 5567, Instron, USA). Specimens were fabricated into standardized dumbbell configurations with dimensions of 75 mm (length), 4 mm (width), and 2 mm (thickness). Experiments were performed at ambient temperature under a constant extension rate of 10 mm/min. Key mechanical parameters, including ultimate tensile strength, fracture elongation, and elastic modulus, were measured, and corresponding stress–strain profiles were generated.

2.7. Water swelling experiment

To determine the water swelling capacity of the 3D-printed hydrogel, a hydration test was conducted. Initially, Hy@KGN hydrogel specimens (approximately 0.1 g in initial mass) were placed in an oven at 60°C until a constant weight was reached. After drying, the samples were immersed in deionized water and weighed hourly after gently removing surface water until equilibrium was reached (at least 30 h). The swelling ratio (SR) was calculated and plotted as:

$$SR = \frac{Wt - W0}{W0} \quad (I)$$

where W_t is the mass at time t and W_0 is the initial dry mass.

2.8. *In vitro* degradation experiment

To evaluate the *in vitro* degradation behavior of the 3D-printed hydrogel, degradation tests were performed. Hy@KGN hydrogel samples were cut into standard sizes (diameter: 10 mm; height: 2 mm) and immersed in phosphate-buffered saline (PBS) buffer (pH 7.4, Gibco, USA) at 37°C on a shaker set to 60 rpm. Samples were removed every 7 days over 8 weeks, dried of surface liquid, and weighed. The degradation rate was calculated and plotted as:

$$\text{Degradation rate} = \frac{W0 - Wt}{W0} \times 100\% \quad (II)$$

2.9. Adhesion strength test

The adhesion strength of the 3D-printed hydrogel in the cartilage repair region was measured using an Instron 5542 tester (Instron, USA). Hydrogel samples (diameter: 10 mm; height: 2 mm) were bonded to rat cartilage tissue (diameter: 10 mm) to create an adhesive interface. The bonded samples were incubated at 37 °C for 24 h to ensure full adhesion. Tensile tests were conducted at a speed of 1 mm/min, and the maximum force (F_{max}) and displacement were recorded. The adhesion strength (σ) was calculated as:

$$\sigma = \frac{Fmax}{A} \quad (III)$$

where A is the bonded area ($A = \pi \times (D/2)^2$; $D = 10$ mm). Each measurement was performed in triplicate to obtain the average adhesion strength.

2.10. Kartogenin release experiment

Release experiments were conducted to determine the release behavior of KGN from Hy@KGN hydrogels. Samples of Hy@KGN (diameter: 10 mm; height: 2 mm) were immersed in PBS buffer (pH 7.4, Gibco, USA) at 37°C on a shaker (60 rpm), with three replicates. Supernatant was collected at 24-h intervals for 14 consecutive days, with partial medium replacement using fresh PBS after each sampling. The KGN concentration in the collected solutions was determined via high-performance liquid chromatography (HPLC; Agilent 1260, Agilent Technologies, USA). The cumulative release was calculated as:

$$\text{Release} = \frac{\text{Ct} \times \text{V}}{m} \quad \text{(IV)}$$

where C_t is the concentration at time t, V is the total volume of the solution, and m is the initial sample mass. Thereafter, a KGN release curve was plotted.

2.11. RNA extraction

To evaluate the effect of KGN on BMSC gene expression, cells were divided into a control group (cultured in alpha minimum essential medium [α-MEM] supplemented with 10% fetal bovine serum [FBS]) and a KGN-treated group (α-MEM supplemented with 10% FBS and 10 μM KGN; Sigma-Aldrich, USA) for 48 h. Post-treatment, cells were harvested, washed with cold PBS, scraped, and centrifuged for RNA extraction.

RNA was extracted utilizing TRIzol reagent (Invitrogen, USA). Cells were thoroughly mixed with TRIzol, allowed to stand for 5 min to ensure complete cell lysis, followed by the addition of 200 μL chloroform (Sigma-Aldrich, USA), vigorous shaking, and phase separation by centrifugation at 12,000 × *g* for 15 min at 4°C. The aqueous phase was mixed with 500 μL isopropanol (Sigma-Aldrich, USA) to precipitate RNAs, then washed twice with 75% ethanol, and dissolved in RNase-free water. RNA concentration and purity were determined using NanoDrop 2000 (Thermo Fisher Scientific, USA), with acceptable A260/A280 ratios between 1.8 and 2.0. RNA integrity was verified using an Agilent 2100 Bioanalyzer (Agilent Technologies, USA), and samples with RNA integrity number (RIN) ≥7.0 were used for further analysis.

2.12. RNA-sequencing analysis

RNA samples were sequenced using the Illumina HiSeq platform. Initially, RNA libraries were prepared using the TruSeq RNA Sample Preparation Kit (Illumina, USA). Once library construction was completed, the quality of the libraries was assessed using the Agilent 2100 Bioanalyzer. Qualified library samples were then sequenced on the Illumina HiSeq 2500 system, generating approximately 50–60 million reads per sample, with a read length of 150 bp. Upon completion of sequencing, raw reads were obtained for subsequent quality control and bioinformatics analysis.

2.13. Data processing and quality control

The raw sequencing data generated by the Illumina HiSeq platform were subjected to quality control and filtering. FastQC was employed to evaluate data quality, and sequences with poor quality or adapter contamination were removed to retain only high-confidence reads for downstream analysis. The reads were then aligned to the reference genome using STAR, utilizing the latest version released by Ensembl. Finally, transcriptome assembly and quantification were performed using StringTie, with gene expression levels reported as FPKM (Fragments Per Kilobase of transcript per Million mapped reads).

2.14. Differentially expressed gene analysis

Differentially expressed gene (DEG) analysis between the control and KGN-treated groups was performed using the DESeq2 or EdgeR package. Genes with $|\log_2\text{FoldChange}| > 1$ and p-values < 0.05 were considered significant DEGs. Volcano plots and heatmaps were generated to visualize the expression patterns and significance of the DEGs.

2.15. Functional enrichment analysis

Enrichment analysis was conducted to evaluate the functional roles of DEGs in terms of biological processes, cellular structures, and molecular activities. The ClusterProfiler tool was employed to perform Gene Ontology (GO) and KEGG pathway analyses, applying a significance threshold of adjusted p-value < 0.05. Particular focus was placed on genes associated with chondrogenic differentiation and the Smad1/5/9 signaling cascade. The top enriched GO terms and KEGG pathways were illustrated using bar plots.

2.16. Weighted gene co-expression network analysis

Weighted gene co-expression network analysis (WGCNA) was constructed to identify gene modules associated with specific phenotypes. Initially, gene expression matrices were loaded using the WGCNA package. Data preprocessing included sample clustering, outlier detection, and normalization. An appropriate soft threshold (power) ensures a scale-free network topology. A weighted gene co-expression network was built by calculating gene similarities, which were then transformed into an adjacency matrix and further into a Topological Overlap Matrix (TOM). Genes were clustered into modules using dynamic tree cutting, and a heatmap illustrating module-trait relationships was created to identify key modules

significantly associated with KGN treatment and explore their biological functions. Genes from these key modules were further analyzed.

2.17. Protein–protein interaction network analysis

Protein–protein interaction (PPI) analysis was conducted to investigate interactions among proteins and identify critical regulatory elements. Interaction data were retrieved from the STRING database (v11.0, https://string-db.org/), using gene sets from selected modules and specifying the relevant species (e.g., human or rat) with a minimum interaction confidence score of 0.4. The interaction networks were constructed and visualized in Cytoscape (v3.7.2). Hub genes were identified using five algorithms integrated via the CytoHubba plugin.

2.18. Cell isolation and culture

Bone marrow stromal cells (BMSCs) were obtained from male Sprague-Dawley rats (6–8 weeks old; Beijing Vital River Laboratory Animal Technology Co., Ltd., China). Bone marrow was collected and cultured in Dulbecco's Modified Eagle Medium (DMEM; Gibco, USA) enriched with 10% FBS and 1% penicillin–streptomycin. Cells were maintained at 37°C in a 5% CO_2 incubator. Morphology and flow cytometry were used to characterize BMSCs.

Articular chondrocytes were isolated from the knees of 4-week-old Sprague-Dawley rats and seeded into 96-well plates at 5000 cells/well in DMEM/F12 medium containing 10% FBS, 100 mg/mL streptomycin, and 100 U/mL penicillin. For NF-κB translocation assays, chondrocytes were stimulated with 10 ng/mL IL-1β.

2.19. Flow cytometry

Flow cytometric analysis was performed using a Fortessa flow cytometer (BD Biosciences, USA) to assess BMSC markers. After PBS washing, cells were incubated with fluorochrome-conjugated antibodies against CD44, CD90, CD105, CD73, CD146, CD45, CD34, and HLA-DR (Miltenyi Biotec, USA), along with corresponding isotype controls. Stained cells were incubated on ice for 30 min, washed with MACS buffer (Miltenyi Biotec, USA), and resuspended in the same buffer for analysis. Cell surface marker expression was analyzed using FlowJo software (TreeStar, USA).

2.20. Cell grouping

Bone marrow stromal cells (BMSCs) and chondrocytes were randomly assigned into the following four experimental groups: the control group (PBS treatment), a hydrogel-only group (3D-printed hydrogel lacking KGN), a KGN group (treated with 10 μM KGN in DMEM), and a Hy@KGN group (cultured with leachate from Hy@KGN hydrogels). All cell groups were seeded into 6-well plates at a density of 5×10^4 cells per well.

2.21. Cell Counting Kit-8 (CCK-8) assay

The cytotoxicity of Hy@KGN on BMSCs was evaluated using the Cell Counting Kit-8 (CCK-8; Dojindo, Japan). BMSCs were seeded in 96-well plates at 1.2×10^4 cells per well across four treatment groups. After 24 h, the medium was removed and replaced with 100 μL of fresh medium containing 10 μL of CCK-8 reagent. Following a 4-h incubation at 37 °C, absorbance at 450 nm was measured using a microplate reader (BioTek, USA). Cell viability was determined by subtracting background values and normalizing to the untreated control.

2.22. Live/dead fluorescence staining

The viability of BMSCs was assessed using the Live/Dead Cell Vitality/Toxicity Assay Kit (Invitrogen, USA). According to the grouping scheme, cells were plated in 24-well plates and incubated for 24 h. Afterward, they were stained in the dark with a solution containing 1 mM calcein-AM and 2 mM ethidium homodimer-1 (EthD-1). Live cells (green) and dead cells (red) were visualized using an inverted fluorescence microscope (IX73, Olympus, Japan). The proportion of viable cells was quantified using ImageJ software.

2.23. Induction of chondrogenic differentiation and staining

For cell culture, BMSCs were seeded directly onto the 3D-printed hydrogel scaffolds in 24-well plates at 6×10^4 cells per well and cultured for 2 days in low-glucose DMEM supplemented with 10% inactivated FBS, 100 U/mL penicillin, and 100 μg/mL streptomycin. From the third day, chondrogenic differentiation was induced using a chondrogenic medium (Cat. A1007101, ThermoFisher, USA) for 3 weeks. After cultivation, the medium was aspirated, and cells were fixed in 10% neutral buffered formalin for 24 h. Samples underwent a graded dehydration process in 50%, 70%, 90%, and 100% ethanol, each for 15 min, followed by two 15-min clearings in xylene. The clarified cells were then embedded in paraffin, sectioned to 5 μm thickness, and rehydrated through 100%, 90%, 70%, and 50% ethanol and distilled water, each for 5 min. The sections were stained with toluidine blue, hematoxylin and eosin (H&E), and Alcian blue. For toluidine blue, sections were stained in 0.1% toluidine blue solution (Sigma-Aldrich, USA) for 10 min and washed three times with distilled water. For H&E staining, sections were stained with hematoxylin for 5 min, rinsed until clear, and then stained with eosin for 3 min. For Alcian blue staining, sections were stained in 1% Alcian blue solution (pH 2.5, Sigma-Aldrich, USA) for 30 min and washed three times. Stained sections were observed and photographed utilizing a microscope (Olympus, Japan).

2.24. Western blot

To detect the expression of proteins associated with chondrogenic differentiation, total proteins were extracted from BMSCs and rat femur tissues using RIPA buffer containing protease inhibitors. Equal amounts of protein were separated via 10% SDS-PAGE and transferred onto PVDF membranes (Millipore, USA). The membranes were blocked with 3% bovine serum albumin (BSA) to minimize non-specific binding, followed by overnight incubation at 4°C with primary antibodies targeting COL2A1 (Cat. no. ab34712, 1:1000, Abcam, USA), ACAN (Cat. no. ab315486, 1:1000, Abcam, USA), SOX9 (Cat. no. ab185966, 1:1000, Abcam, USA), PRG4 (Cat. no. ab28484, 1:1000, Abcam, USA), COX-2 (Cat. no. ab179800, 1:1000, Abcam, USA), matrix metalloproteinase (MMP)-3 (Cat. no. ab52915, 1:1000, Abcam, USA), p65 (Cat. no. ab76302, 1:1000, Abcam, USA), Smad1/5/9 (Cat. no. ab92698, 1:1000, Abcam, USA), phospho-Smad1/5/9 (Cat. no. ab300164, 1:1000, Abcam, USA), and β-actin (A5441, 1:5000, Sigma-Aldrich, USA) as a loading control. Following TBST washing, membranes were incubated with horseradish peroxidase (HRP)-conjugated secondary antibodies and visualized using an enhanced chemiluminescence (ECL) detection kit (Thermo Fisher Scientific, USA). Chemiluminescent signals were captured with an ImageQuant LAS4000mini system (Sweden). Densitometric analysis was conducted using Gel-Pro Analyzer (Media Cybernetics, USA) to quantify protein levels associated with chondrogenesis and Smad pathway activation.

2.25. Reverse transcription quantitative polymerase chain reaction

Reverse transcription quantitative polymerase chain reaction (RT-qPCR) was performed to evaluate the expression of chondrogenesis-related genes. Total RNA was extracted from each group of BMSCs utilizing Trizol reagent (Invitrogen, USA). The purity and concentration of the extracted RNA were determined using NanoDrop 2000 (Thermo Fisher Scientific, USA), and RNA integrity was assessed by 1% agarose gel electrophoresis. Subsequently, 1 μg of total RNA was reverse-transcribed into complementary DNA (cDNA) using the PrimeScript RT kit (Takara, Japan). RT-qPCR reactions were carried out using SYBR Green PCR Master Mix (Applied Biosystems, USA) in a 20 μL total volume, containing 10 μL of master mix, 0.4 μL each of 10 μM forward and reverse primers, 1 μL cDNA, and 8.2 μL nuclease-free water. Amplification was performed on an ABI 7500 Real-Time PCR System (Applied Biosystems, USA) under the following conditions: 95 °C for 10 min, followed by 40 cycles of 95 °C for 15 s and 60 °C for 1 min. All samples were analyzed in triplicate, with β-actin serving as an internal control. Relative gene expression was quantified utilizing the $2^{-\Delta\Delta Ct}$ method. Primer sequences are listed in Table S2, Supporting Information.

2.26. Phalloidin staining

To observe cytoskeletal changes in BMSCs, phalloidin staining was performed. BMSCs were divided into four groups per experimental design and seeded in 6-well plates at a density of 4×10^5 cells per well. After incubation, cells were fixed with 4% paraformaldehyde (PFA; Sigma-Aldrich, USA) for 15 min, then rinsed three times with PBS (5 min each). Permeabilization was performed using 0.1% Triton X-100 for 10 min at room temperature. After additional PBS washes, cells were incubated with phalloidin staining solution (Sigma-Aldrich, USA) at 37 °C for 30 min, followed by three PBS rinses. Cytoskeletal morphology was imaged using a fluorescence microscope (IX73, Olympus, Japan).

2.27. Immunofluorescence staining

NF-κB nuclear translocation in chondrocytes was assessed via immunofluorescence. BMSCs were plated in 6-well plates at 4×10^5 cells/well and treated according to experimental grouping. After 3 h of incubation and stimulation, cells were fixed with 4% PFA for 1 h, washed with PBS, and permeabilized using 0.1% Triton X-100 for 30 min. Non-specific binding was blocked with 1% BSA for 1 h at room temperature. Cells were then incubated with NF-κB p65 primary antibody (1:500; Santa Cruz Biotechnology, USA) for 1 h, followed by three PBS + 0.1% Tween-20 washes and subsequent incubation with FITC-conjugated secondary antibody (Invitrogen, USA) for 1 h. Nuclear staining was performed with DAPI (Sigma-Aldrich, USA) for 5 min. After the final PBS washes, cells were mounted in 50% glycerol and examined using a fluorescence microscope (IX73, Olympus, Japan).

2.28. Establishment of the rat cartilage defect model

Twelve-week-old male Sprague-Dawley rats (400–450 g; Cat. no. 101, Beijing Vital River Laboratory Animal Technology Co., Ltd., China) were housed individually in an specific pathogen-free (SPF) animal laboratory with controlled humidity (60–65%), temperature (22–25°C), and a 12-h light/dark cycle, with free access to food and water. Following a 7-day acclimatization period and baseline health monitoring, all procedures were approved by the Institutional Animal Care and Use Committee (Approval no. D2025-365) and conducted in accordance with institutional animal care guidelines.

Rats were randomly assigned to the following five groups: the PBS control group (injection of PBS into the osteochondral defect area as a baseline comparison), the Hy hydrogel group (implantation of a 3D-printed hydrogel without any drug into the defect area), the KGN

administration group (direct injection of KGN into the defect area), the Hy@KGN group (implantation of a Hy@KGN into the defect area), and the LDN+Hy@KGN group (implantation of Hy@KGN into the defect area and injection of the Smad1/5/9 pathway inhibitor LDN-193189). The dosage of LDN-193189 (Cat. no. S2618, Selleck, China) was 3 mg/kg, and the dosage of KGN (Cat. no. S7658, Selleck, China) was 5 mg/kg.[18–21]

Under 2–4% isoflurane anesthesia, rats were prepped aseptically, and a medial patellar incision exposed the femoral trochlea. A cylindrical full-thickness cartilage defect (1.5 mm diameter × 2 mm depth) was created using a custom drill, and treatment materials were applied according to group allocation. The surgical site was irrigated with sterile saline, closed, and treated with postoperative antibiotics (Baytril, Bayer, Germany). At 6 and 12 weeks post-operation, rats were euthanized using pentobarbital, and distal femurs were harvested for gross evaluation using the International Cartilage Repair Society (ICRS) scoring system.[16,19,22]

Post-surgery, the rats' body weight and behavioral changes were regularly monitored. The rats were weighed weekly using an electronic scale (Sartorius, Germany), and food and water intake were recorded. The activity levels and pain responses of the rats were also observed.

2.29. Biosafety evaluation

To assess the biosafety of the 3D-printed hydrogel, healthy adult Sprague-Dawley rats were selected, and subcutaneous implantation surgery was performed under sterile conditions. Anesthesia was induced using isoflurane (Baxter, USA), and a small incision was made on the dorsal skin of the rats to implant a 1 cm^3 3D-printed hydrogel. The incision was sutured using silk sutures (Ethicon, USA). Rats were randomly divided into three groups: the control group (no experimental procedures performed, serving as baseline), the sham group (underwent all surgical steps but without hydrogel implantation), and the hydrogel implantation group (subcutaneous implantation of Hy@KGN). Each group consisted of 10 rats.

Blood samples were collected weekly from the tail vein, and complete blood counts were conducted using an automated hematology analyzer (Sysmex, Japan). Serum biochemical markers, including ALT, AST, BUN, and creatinine, were assessed using a chemiluminescence immunoassay system (Roche, Switzerland) to monitor liver and kidney function.

At study completion, rats were euthanized, and major organs (heart, liver, spleen, lung, kidney) were harvested, fixed in 4% formaldehyde (Sigma-Aldrich, USA), embedded, sectioned, and stained with H&E. Histopathological examination was performed under an optical microscope (Olympus, Japan) to assess tissue morphology and potential toxicity.

2.30. TUNEL staining

Apoptotic cells were detected using a TUNEL assay kit (Cat. no. C1086, Beyotime, China). Paraffin-embedded tissue sections were processed and stained, and TUNEL-positive cells displaying green fluorescence were visualized under a fluorescence microscope (IX73, Olympus, Japan). Six random fields per section were selected for quantification using ImageJ software.

2.31. ELISA for inflammatory cytokine detection

Serum levels of inflammatory cytokines IL-6 (R6000B), TNF-α (RTA00), and IL-1β (RLB00) were measured using ELISA kits (R&D Systems, USA) to evaluate the systemic inflammatory response. Absorbance was measured using a microplate reader (BioTek, USA), and cytokine concentrations were calculated based on standard curves.

2.32. Histological examination

In this experiment, femurs were initially harvested from exposed joint cavities and fixed in 4% PFA for 48 h. Following fixation, the osteochondral specimens underwent micro-computed tomography (micro-CT) to capture structural details. The specimens were then decalcified in 10% ethylenediaminetetraacetic acid (EDTA) solution for 4 weeks, with daily solution changes. After decalcification, samples were bisected longitudinally through the center of the defect, embedded in paraffin, and sectioned at 5 μm thickness. Sections were deparaffinized, rehydrated, and stained with H&E, Safranin O/Fast Green (SO/FG), Alcian Blue, and Sirius Red. Morphological features of cartilage and subchondral bone were examined under a Leica microscope (Leica Microsystems, Germany), and cartilage repair was graded based on the ICRS visual histological scoring criteria.

2.33. Immunohistochemical analysis

The expression of Bcl-2, collagen I, and collagen II was detected using the streptavidin-biotin peroxidase complex method. Initially, paraffin-embedded sections were processed through standard dewaxing, hydration, and heat-induced antigen retrieval in citrate buffer (pH 6.0). The sections were then blocked with 10% horse serum to prevent non-specific binding and incubated with an endogenous peroxidase blocker for 10 min. Primary antibodies were applied: Bcl-2 (Cat. no. ab196495, 1:250, Abcam, USA), collagen I (Cat. no. ab270993, 1:100, Abcam, USA), and collagen II (Cat. no. ab34712, 1:200, Abcam, USA), and incubated overnight at 4°C. Following PBS washing, HRP-conjugated goat anti-rabbit secondary antibody (Cat. no. ab6721, 1:500, Abcam, USA) was

applied at 37°C for 30 min, followed by streptavidin-biotin incubation and DAB color development. Nuclei were counterstained with hematoxylin. Stained sections were visualized under a light microscope, and ImageJ software was used for quantitative analysis of Bcl-2-positive cells and the area fraction of collagen I/II.

2.34. Micro-computed tomography analysis

Micro-computed tomography (micro-CT) was employed to assess subchondral bone regeneration at defect sites (n = 10 per group) using the SkyScan 1272 system (Bruker, Belgium). Scans were conducted with a voltage of 70 kV, current of 112 μA, 0.2 mm aluminum filter, and 18 μm voxel resolution. 3D reconstructions were generated using CTVol software. Mineralized bone was identified using a threshold of 1400, and key parameters, including bone volume fraction (BV/TV), bone defect volume ratio (BDV/TV), bone mineral density (BMD), and trabecular separation (Tb.Sp), were quantified to evaluate the extent of bone repair.

2.35. Masson's trichrome staining

Masson's trichrome staining was performed to examine collagen deposition in the cartilage repair areas of experimental rats. Corresponding tissue sections were dewaxed, rehydrated, and stained utilizing a Masson's trichrome staining kit (Sigma-Aldrich, USA). This staining method distinguishes collagen fibers (blue), muscle fibers (red), and nuclei (black). Images were captured using a microscope to quantitatively analyze the distribution and density of collagen fibers.

2.36. Statistical analysis

All statistical analyses were carried out using GraphPad Prism 9.5.0 (GraphPad Software, Inc., USA) and R version 4.2.1 (R Foundation for Statistical Computing, Austria). Quantitative data are expressed as mean ± standard deviation. For comparisons between two groups, independent samples t-tests were used after confirming normality with the Shapiro–Wilk test. For comparisons among multiple groups, one-way analysis of variance (ANOVA) was conducted with Tukey's post-hoc test, and normality was also assessed prior to ANOVA. If data did not meet normality assumptions, non-parametric tests (e.g., Kruskal–Wallis test) were applied instead. A p-value < 0.05 was considered statistically significant.

3. Results

3.1. Kartogenin activation of the Smad1/5/9 signaling pathway enhances chondrogenic differentiation of BMSCs

In this study, we successfully isolated and cultured rat BMSCs and conducted a comprehensive characterization. Morphological observations and flow cytometry analysis confirmed that the isolated BMSCs exhibited typical stem cell-like morphology (Figure S2A, Supporting Information). Flow cytometry results indicated high expression levels of markers CD44, CD90, CD105, CD73, and CD146 in BMSCs, while positive expression rates for CD45, CD34, and HLA-DR were below 2% (Figure S2B, Supporting Information). Subsequently, BMSCs were treated with KGN, and gene expression changes before and after treatment were analyzed using RNA-sequencing (RNA-seq), yielding high-quality sequencing data (Figure 1A). Approximately, 50 million 150 bp reads per sample were generated, with data quality control performed using FastQC, revealing that all samples had a Q30 score above 95%. High-quality reads were aligned to the reference genome with an average alignment rate exceeding 90%. Differential expression analysis identified 1223 significantly DEGs, with 569 upregulated and 654 downregulated (Figure 1B and C).

Gene Ontology (GO) and KEGG enrichment analyses revealed that DEGs were involved in biological processes such as cytoskeletal reorganization, ECM binding, cell migration, and proliferation (Figure S3A, Supporting Information). Notably, KEGG pathway analysis revealed marked upregulation in the TGF-β and Wnt signaling pathways, as well as ECM receptor interactions, in the KGN-treated group (Figure S3B and C, Supporting Information). Moreover, expression levels of key genes such as *Acan*, *Bmp2*, *Bmp6*, *Smad1*, *Smad5*, and *Smad9* were significantly increased (Figure 1D). These findings suggest that KGN treatment activates critical signaling pathways associated with chondrogenic differentiation in BMSCs.

Weighted gene co-expression network analysis (WGCNA) further elucidated gene modules associated with KGN treatment. Analysis of the scale-free fit index and the average connectivity identified an appropriate soft-thresholding power. At a soft-thresholding power of 5, the scale-free fit index reached 0.85, and average connectivity remained within a reasonable range (Figure S4A, Supporting Information). The clustering of DEG modules produced a dendrogram that illustrated the clustering relationships among the modules (Figure S4B, Supporting Information). The correlation heatmap revealed that the gene module colored in antiquewhite1 exhibited the highest correlation with the KGN treatment group (r = 0.99, $p < 0.01$) (Figure 1E). Specifically, the antiquewhite1 module included several known regulators of chondrogenic differentiation, such as *Sox9*, *Col2a1*, and *Tgfbr1*, each with correlation coefficients exceeding 0.9 (Figure 1F). KEGG pathway analysis indicated that this module was predominantly

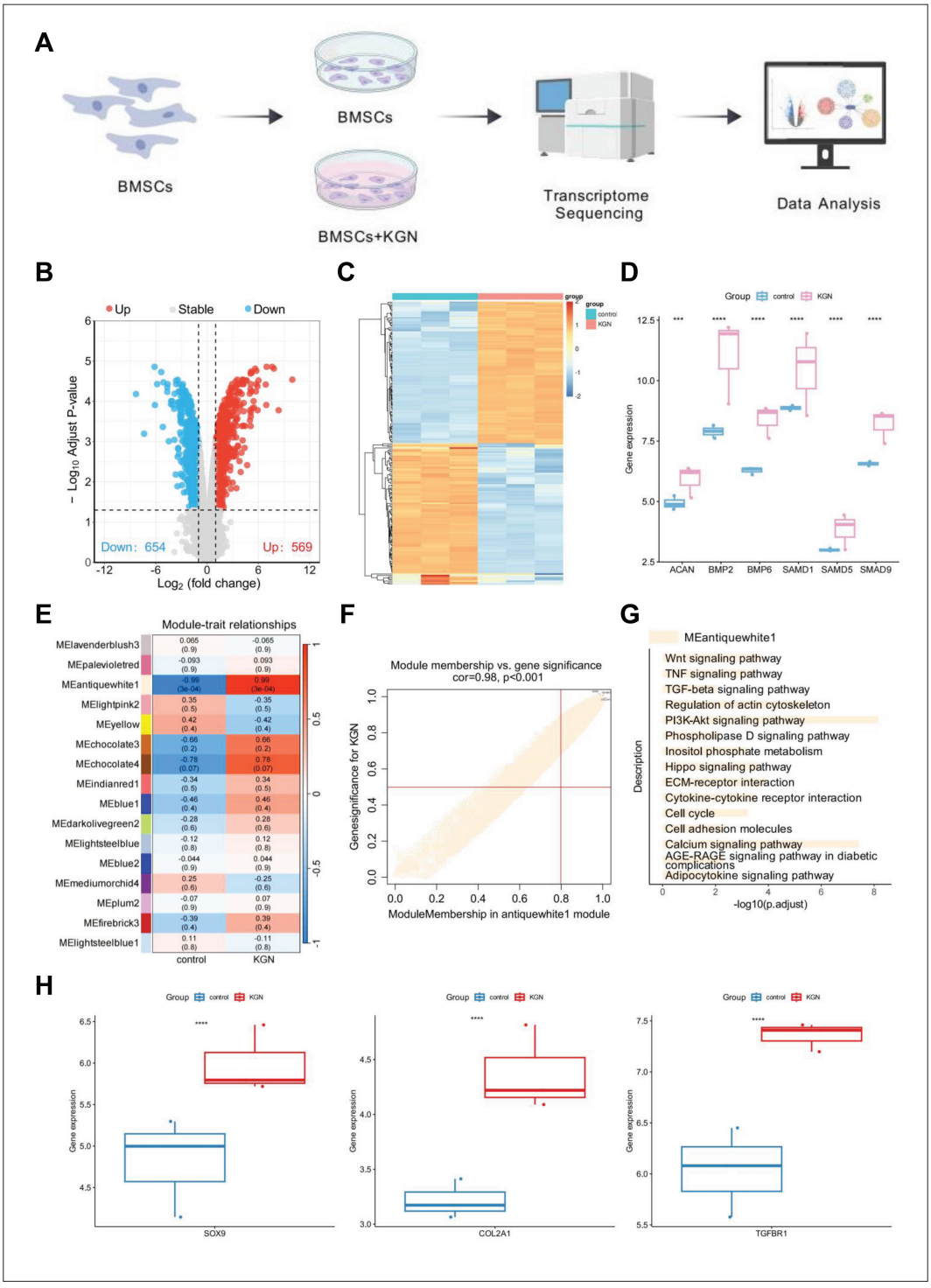

Figure 1. Differential gene expression analysis and screening of chondrogenic differentiation-related genes in BMSCs after KGN treatment. (A) RNA-sequencing analysis workflow. (B) Volcano plot displaying DEGs between the KGN-treated and control groups, with upregulated genes in red and downregulated genes in blue. (C) Heatmap of DEGs between the KGN-treated and control groups. (D) Expression levels of *Acan*, *Bmp2*, *Bmp6*, *Smad1*, *Smad5*, and *Smad9* in the KGN-treated versus control groups. (E) Correlation heatmap between each module and both the control and KGN-treated groups, with each cell displaying the correlation coefficient and *p*-value. (F) Significance analysis of the antiquewhite1 module in the KGN-treated group, with each point representing a gene. (G) KEGG enrichment analysis of the antiquewhite1 module. (H) Box plot of significant chondrogenic differentiation-related genes in the antiquewhite1 module, displaying high expression of *SOX9*, *COL2A1*, and *TGFBR1* in the KGN-treated group. * denotes significance between groups, ***$p < 0.001$, ****$p < 0.0001$. Abbreviations: BMSCs: bone marrow stromal cells; DEGs: differentially expressed genes; KGN: kartogenin.

associated with chondrogenic differentiation, involving pathways like TGF-β, Wnt signaling, and regulation of the actin cytoskeleton (Figure 1G). Expression box plots demonstrated that genes related to chondrogenic differentiation were highly expressed in the KGN treatment group, particularly noting significant increases in *Sox9, Col2a1*, and *Tgfbr1* (Figure 1H).

Furthermore, we constructed a PPI network for the key gene modules in the KGN treatment group using the STRING database to explore core regulatory factors (Figure 2A). Analysis revealed that Smad1, Smad5, and Smad9 had high degrees of connectivity within the network, indicating their pivotal roles in chondrogenic differentiation. The MCODE plugin identified four sub-modules related to chondrogenic differentiation, further confirming the importance of Smad1, Smad5, and Smad9 within these sub-modules (Figure 2B). The network also detailed interactions among other significant chondrogenic differentiation regulatory genes, unveiling their synergistic actions in KGN-induced chondrogenic differentiation (Figure 2C). Using the cytohubba plugin, we identified key nodes within the chondrogenic differentiation network

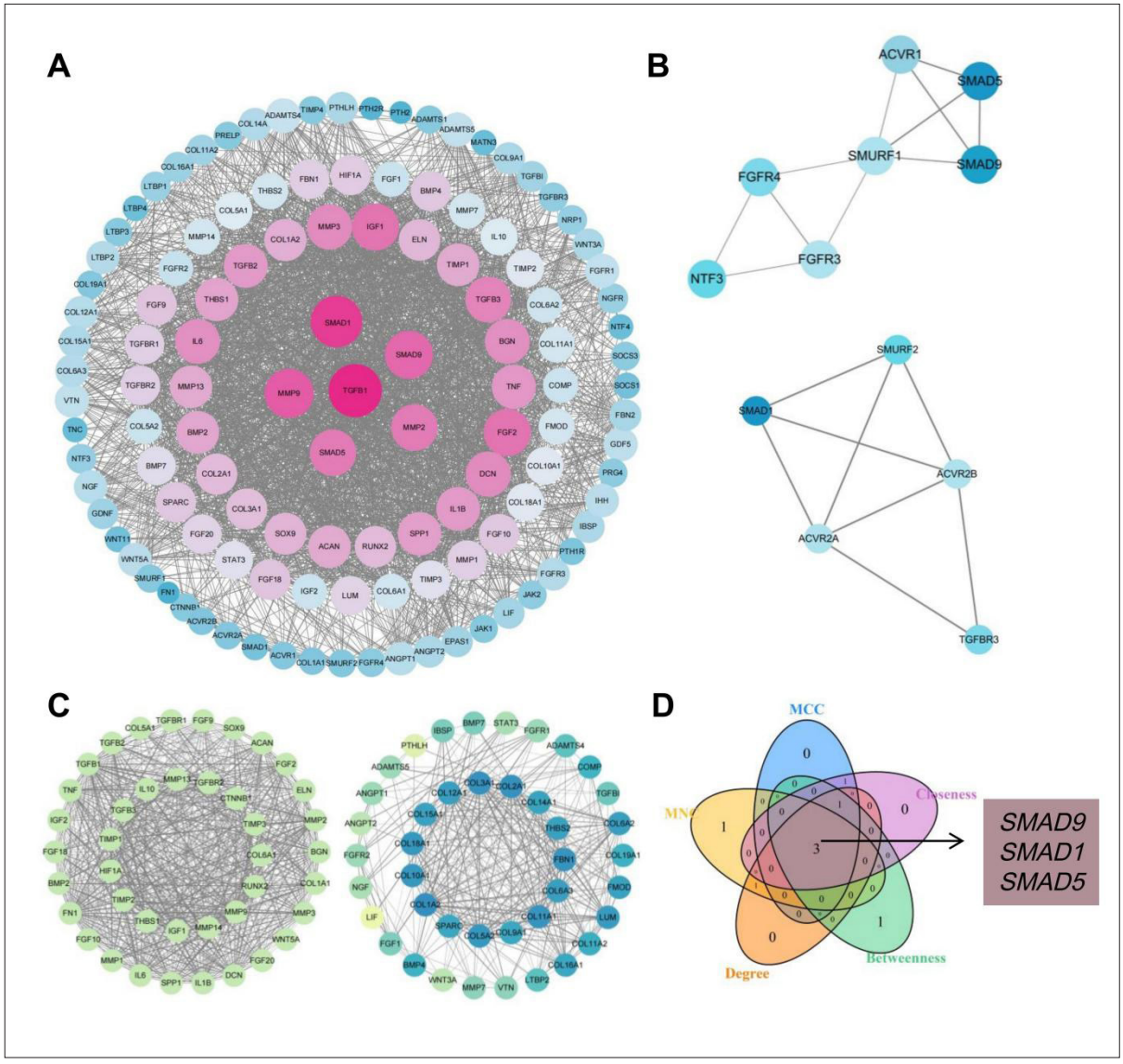

Figure 2. Protein–protein interaction (PPI) network analysis reveals key regulatory factors. (A) PPI network of chondrogenic differentiation-related module genes in the kartogenin (KGN)-treated group, with node degrees represented by a gradient from pink to blue. (B) Interaction relationships of genes, including *Smad1*, *Smad5*, and *Smad9*, in the MCODE module. (C) Interaction relationships of other significant chondrogenic regulatory genes in the MCODE module. (D) Venn diagram displaying three critical chondrogenic differentiation-related genes identified through five cytohubba methods.

Table 1. Cytohubba plugin selects key genes based on five metrics

Metric	Genes				
MCC	MMP9	SMAD9	MMP2	SMAD1	SMAD5
MNC	TGFB1	COL1A1	SMAD9	SMAD1	SMAD5
Degree	TGFB1	MMP9	SMAD9	SMAD1	SMAD5
Betweenness	SMAD9	MMP9	SMAD5	SMAD1	ACAN
Closeness	MMP9	SMAD9	MMP2	SMAD1	SMAD5

Abbreviations: ACAN, aggrecan; COL1A1, collagen type I alpha 1 chain; MCC, maximal clique centrality; MMP, matrix metalloproteinase; MNC, maximum neighborhood component;; SMAD, mothers against decapentaplegic homolog; TGFB1, transforming growth factor beta 1.

(Table 1). By integrating results from five analytical methods, we pinpointed three crucial regulatory factors: Smad9, Smad1, and Smad5 (Figure 2D). These findings further support the central role of Smad1, Smad5, and Smad9 in chondrogenic differentiation.

These results demonstrate that KGN treatment activates the Smad1/5/9 signaling pathway, thereby promoting chondrogenic differentiation in BMSCs.

3.2. Preparation and characterization of Hy@KGN

We successfully synthesized a 3D-printed hydrogel material, Hy@KGN, with excellent biocompatibility and mechanical properties by incorporating the small molecule compound KGN into the hydrogel matrix (Figure 3A). The visible light image of the Hy@KGN hydrogel is presented in Figure 3B. SEM at various magnifications revealed a uniform distribution of micropores within the hydrogel, with pore diameters of 50–100 μm that supported cell adhesion and proliferation (Figure 3C). Additionally, the disc-shaped Hy@KGN hydrogel produced via 3D printing demonstrated good stability with no signs of brittleness, such as cracks or defects, making it suitable for cartilage repair and drug delivery (Figure 3D). Rheological measurements demonstrated that the *G*' of Hy@KGN was 500 Pa, and the *G*" was 200 Pa, indicating desirable elastic and viscoelastic properties (Figure 3E). Compression tests revealed that Hy@KGN hydrogels exhibited a compressive strength of 300 kPa, demonstrating excellent load-bearing performance. Compared to unloaded Hy hydrogels, loading with KGN did not significantly affect the compressive properties (Figure 3F and G). Compression tests using a mechanical testing machine revealed the unloading behavior of the hydrogel, indicating that Hy@KGN possesses excellent fatigue resistance (Figure 3H). Tensile tests revealed that Hy@KGN hydrogels had a tensile strength of 1.5 MPa and 150% elongation at break, indicating superior mechanical properties, with no significant changes compared to unloaded Hy hydrogels (Figures 3I, J and S5). Compared to the hydrogel without the loaded drug (Hy), the KGN-loaded hydrogel did not exhibit significant changes in mechanical properties.

The water absorption and swelling capacities of Hy and Hy@KGN were determined through hydration experiments. The results indicated that the Hy@KGN hydrogel exhibited an impressive SR of 400% within 24 h, demonstrating robust water absorption and swelling properties (Figure 3K). *In vitro* degradation experiments in simulated body fluid demonstrated that Hy@KGN hydrogels had approximately 20% mass loss over 8 weeks, suggesting a moderate degradation rate suitable for long-term tissue repair. Drug loading did not significantly alter the degradation behavior (Figure 3L). Adhesion strength tests indicated that Hy@KGN hydrogels achieved an adhesion strength of 0.8 MPa in cartilage repair regions, with comparable performance to unloaded Hy hydrogels. White-light images confirmed the tight bonding between Hy@KGN hydrogels and rat cartilage tissue (Figure 3M). Compared to the Hy hydrogel, the drug-loaded Hy@KGN hydrogel did not exhibit significant changes in stability or adhesiveness. Moreover, release experiments of KGN in a simulated body fluid environment demonstrated that Hy@KGN released 80% of KGN within the first 2 weeks, followed by a slow-release phase, thus continuously delivering KGN to facilitate cartilage repair (Figure 3N).

3.3. Hy@KGN significantly enhances chondrogenic differentiation of BMSCs and mitigates inflammation

Bone marrow stromal cells (BMSCs) were divided into the following four treatment groups: PBS, Hy hydrogel, KGN, and Hy@KGN hydrogel. Cell viability was assessed via the CCK-8 assay, demonstrating over 90% viability across all groups, suggesting minimal cytotoxicity of the materials (Figure 4A). This finding was further supported by live/lead fluorescence staining, where live cells were stained green and dead cells were stained red, with no significant differences observed among the groups (Figure 4B).

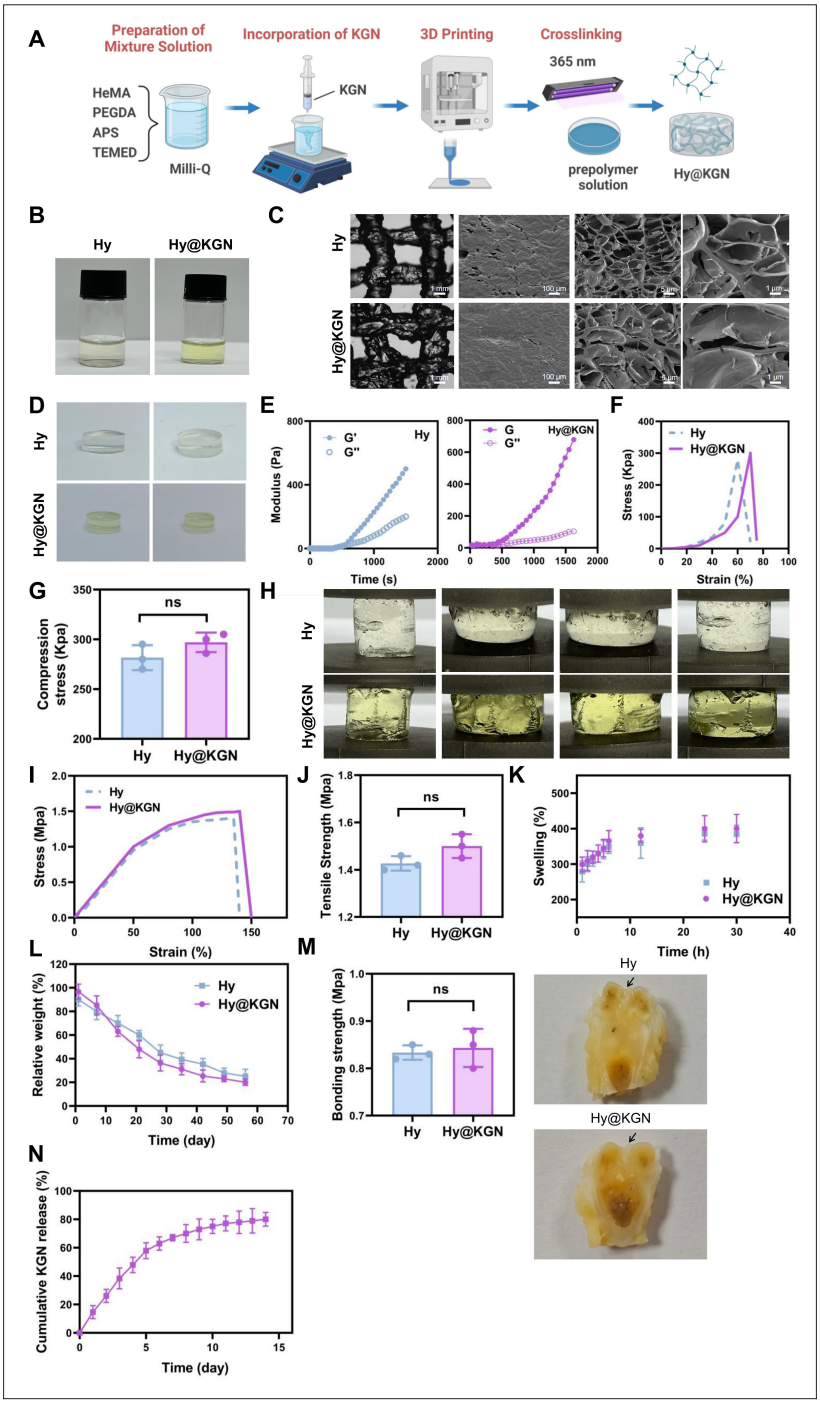

Figure 3. Preparation and characterization of Hy@KGN. (A) Schematic of the preparation process for Hy@KGN. (B) Bright-field images of Hy and Hy@KGN hydrogels. (C) Microstructure of the 3D-printed hydrogel observed under SEM at different magnifications. (D) Bright-field images of disc-shaped Hy and Hy@KGN hydrogels. (E) Rheological measurements of *G*' and *G*" of the 3D-printed hydrogel. (F) Representative compressive stress–strain curves for Hy and Hy@KGN hydrogels. (G) Average compressive strength of Hy and Hy@KGN hydrogels. (H) Compression testing process for Hy and Hy@KGN hydrogels using a mechanical tester. (I) Representative tensile stress–strain curves for Hy and Hy@KGN hydrogels. (J) Average tensile strength of Hy and Hy@KGN hydrogels. (K) SR of Hy and Hy@KGN hydrogels determined through water absorption experiments. (L) *In vitro* degradation behavior of Hy and Hy@KGN hydrogels. (M) Adhesion strength of Hy and Hy@KGN hydrogels in the cartilage repair region, along with bright-field images displaying the bonding interface between Hy@KGN hydrogel and cartilage tissue. (N) KGN release profile of Hy@KGN hydrogel in a simulated body fluid environment; $n = 3$. Scale bars: 1 mm (C). Abbreviations: APS, ammonium persulfate; *G*′, storage modulus; *G*″, loss modulus; HeMA, 2-hydroxyethyl methacrylate; Hy, hydrogel without kartogenin; KGN, Kartogenin; Milli-Q, Ultrapure water; ns, not significant; PEGDA, poly(ethylene glycol) diacrylate; TEMED, N,N,N′,N′-tetramethylethylenediamine.

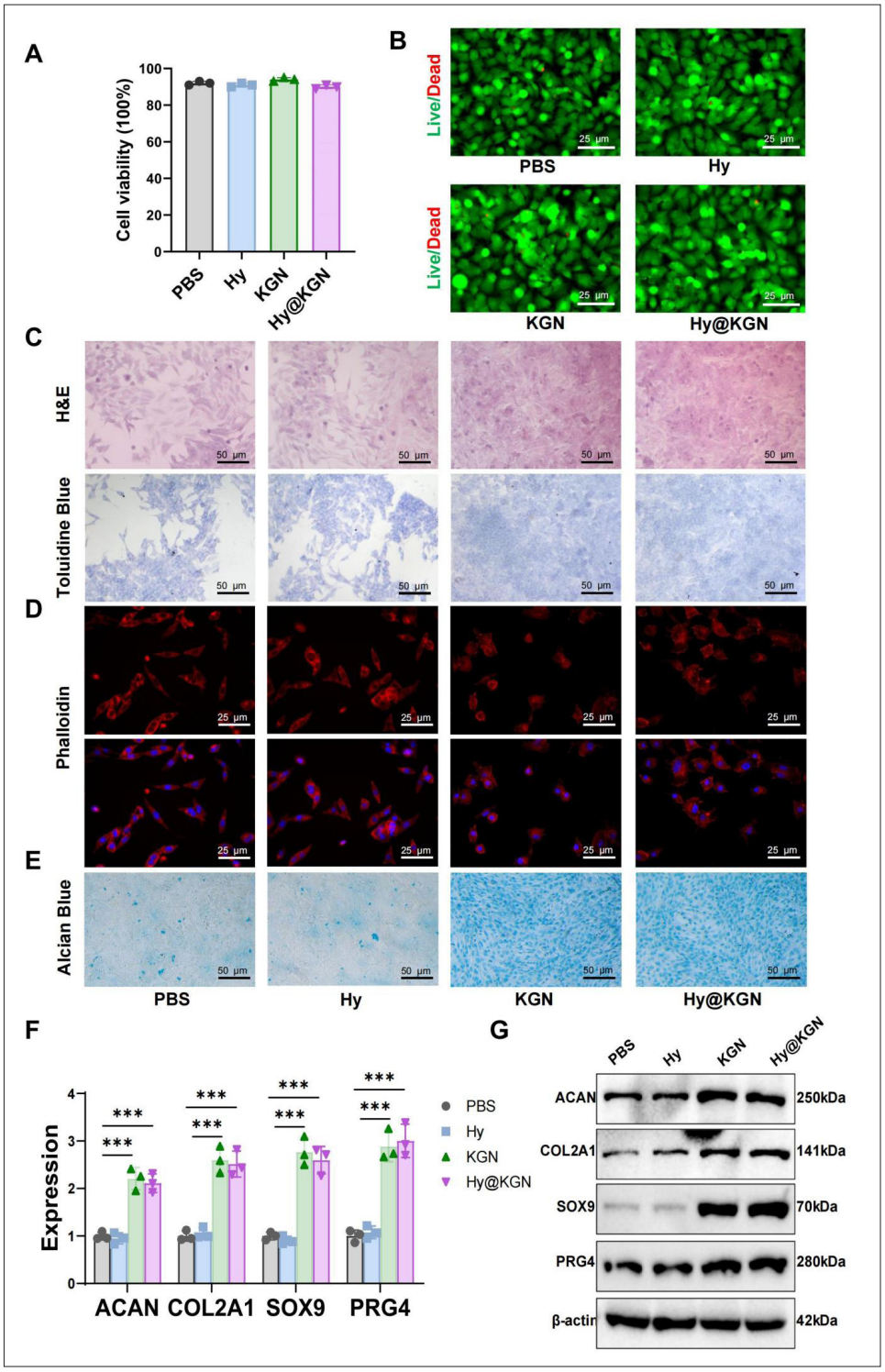

Figure 4. Effects of Hy@KGN hydrogel on chondrogenic differentiation of BMSCs. (A) CCK-8 assay evaluated the cytotoxicity of each treatment on BMSCs. (B) Live/dead fluorescence staining of BMSCs in each treatment group. (C) Toluidine blue and H&E staining of cartilage tissue appearance in BMSCs from different treatment groups. (D) Phalloidin staining to observe morphological changes of BMSCs in different treatment groups. (E) Alcian blue staining to assess chondrogenic differentiation of BMSCs. (F) RT-qPCR analysis of chondrogenesis-related genes: *Col2a1*, *Acan*, *Sox9*, and *Prg4*. (G) Western Blot analysis of chondrogenesis-related protein expression. ***$p < 0.001$, ****$p < 0.0001$. All cell experiments were performed in triplicate. Data were tested for normality using the Shapiro–Wilk test and analyzed using one-way ANOVA with Tukey's HSD post hoc test for group comparisons. Scale bars: 25 μm (A, B, and D), 50 μm (C and E). Abbreviations: BMSCs, bone marrow stromal cells.

To assess the hydrogel's chondrogenic potential, BMSCs were cultured in chondrogenic medium supplemented with 2 μL of hydrogel extract solution (prepared by incubating Hy@KGN hydrogels in culture medium). Using this optimized volume ensured sufficient matrix support while avoiding excessive cell aggregation, balancing bioactivity with nutrient availability. The hydrogel extract enables uniform cell distribution within the medium, prevents clustering, and is easy to handle and mix with the medium. The concentration and volume can be adjusted as needed, providing better control of experimental conditions, with fresh medium changes daily over 21 days. Alcian blue and H&E staining results indicated that the cell morphology in the KGN and Hy@KGN hydrogel groups resembled cartilage tissue, indicating significant differentiation of BMSCs into chondrocytes. In contrast, no notable differences were observed in the PBS and Hy hydrogel groups (Figure 4C). In another experiment, BMSCs were mixed with Hy@KGN hydrogel precursor solution and cultured at 37 °C for 7 days with daily supplementation of rMMP-3 (25 ng/mL). Phalloidin staining results demonstrated that by Day 7, the cell morphology in the KGN and Hy@KGN hydrogel groups transitioned from spindle-shaped to the polygonal shape characteristic of chondrocytes, while the PBS and Hy hydrogel groups displayed no significant morphological changes (Figure 4D).

Additionally, BMSCs were seeded on the surface of hydrogels and cultured with regular medium changes for 7 days. Alcian blue staining confirmed effective chondrogenic differentiation in the KGN and Hy@KGN groups, whereas no notable changes were detected in the PBS and Hy hydrogel groups (Figure 4E). To further validate the induction of chondrogenesis within hydrogels, RT-qPCR and Western blot analyses were conducted. The results revealed marked upregulation of chondrogenic markers, including COL2A1, ACAN, PRG4, and SOX9, in the KGN and Hy@KGN hydrogel groups, with no significant alterations observed in the PBS and Hy hydrogel groups (Figure 4F and G).

In this experiment, the hydrogels used were fabricated by 3D printing technology. The results demonstrate that the 3D-printed KGN-loaded hydrogel scaffolds provided an excellent microenvironment for BMSCs, significantly promoting their chondrogenic differentiation.

Moreover, cartilage injury is often accompanied by an inflammatory response, where inflammatory factors released by M1 macrophages, such as TGF-α and IL-1β, rapidly accumulate in the cartilage microenvironment. These cytokines engage receptors on chondrocytes, triggering the IκBα/NF-κB pathway and promoting NF-κB translocation to the nucleus, thereby initiating cartilage degradation and upregulating MMPs (Figure S6A, Supporting Information). To assess the anti-inflammatory potential of Hy@KGN, chondrocytes were stimulated with IL-1β (10 ng/mL). Immunofluorescence analysis demonstrated that IL-1β induced nuclear translocation of NF-κB (green fluorescence), whereas KGN and Hy@KGN treatments markedly suppressed this effect, indicated by reduced nuclear staining (blue nuclei). In contrast, PBS and Hy hydrogel groups exhibited no inhibition (Figure S6B, Supporting Information). Western blot analysis demonstrated that the KGN and Hy@KGN hydrogel groups reduced the expression of COX-2, MMP-3, and phosphorylated NF-κB (p65) in chondrocytes, while the PBS and Hy hydrogel groups displayed no significant changes (Figure S6C and D, Supporting Information).

3.4. Hy@KGN activates the Smad1/5/9 signaling pathway to promote chondrogenic differentiation of BMSCs

To explore the involvement of a Hy@KGN in promoting chondrogenic differentiation of BMSCs, we divided the BMSCs into four groups: a PBS group, a Smad1/5/9 pathway inhibitor group (treated with LDN-193189), a Hy@KGN hydrogel group, and a group combining the Hy@KGN and the inhibitor (Figure 5A). Western blot analysis was conducted to measure the expression of Smad1/5/9 pathway-related factors in each group. The results demonstrated a significant increase in Smad1/5/9 protein expression in the Hy@KGN hydrogel group, whereas a notable decrease in the expression of these pathway-related factors was observed in both the Hy@KGN + inhibitor group and the LDN-193189 group (Figure 5B).

Alcian blue and H&E staining demonstrated that the inhibitor LDN-193189 significantly reduced the differentiation capability of BMSCs into chondrocytes (Figure 5C and D). Phalloidin staining indicated no significant changes in the morphology of BMSCs treated with LDN-193189 (Figure 5E). When BMSCs were seeded on the hydrogel surface and treated with LDN-193189 in the presence of rMMP-3, Alcian blue staining revealed that the inhibitor significantly reduced the chondrogenic differentiation capability of BMSCs (Figure 5F). To further confirm the chondrogenic differentiation within the hydrogel, we assessed cartilage-related protein expression using RT-qPCR and Western blot, which indicated that LDN-193189 could reverse the upregulation of COL2A1, ACAN, PRG4, and SOX9 promoted by the Hy@KGN hydrogel (Figure 5G and H).

Furthermore, in the inflammatory response of chondrocytes induced by IL-1β (10 ng/mL), immunofluorescence staining demonstrated that LDN-193189 reversed suppression of NF-κB nuclear translocation

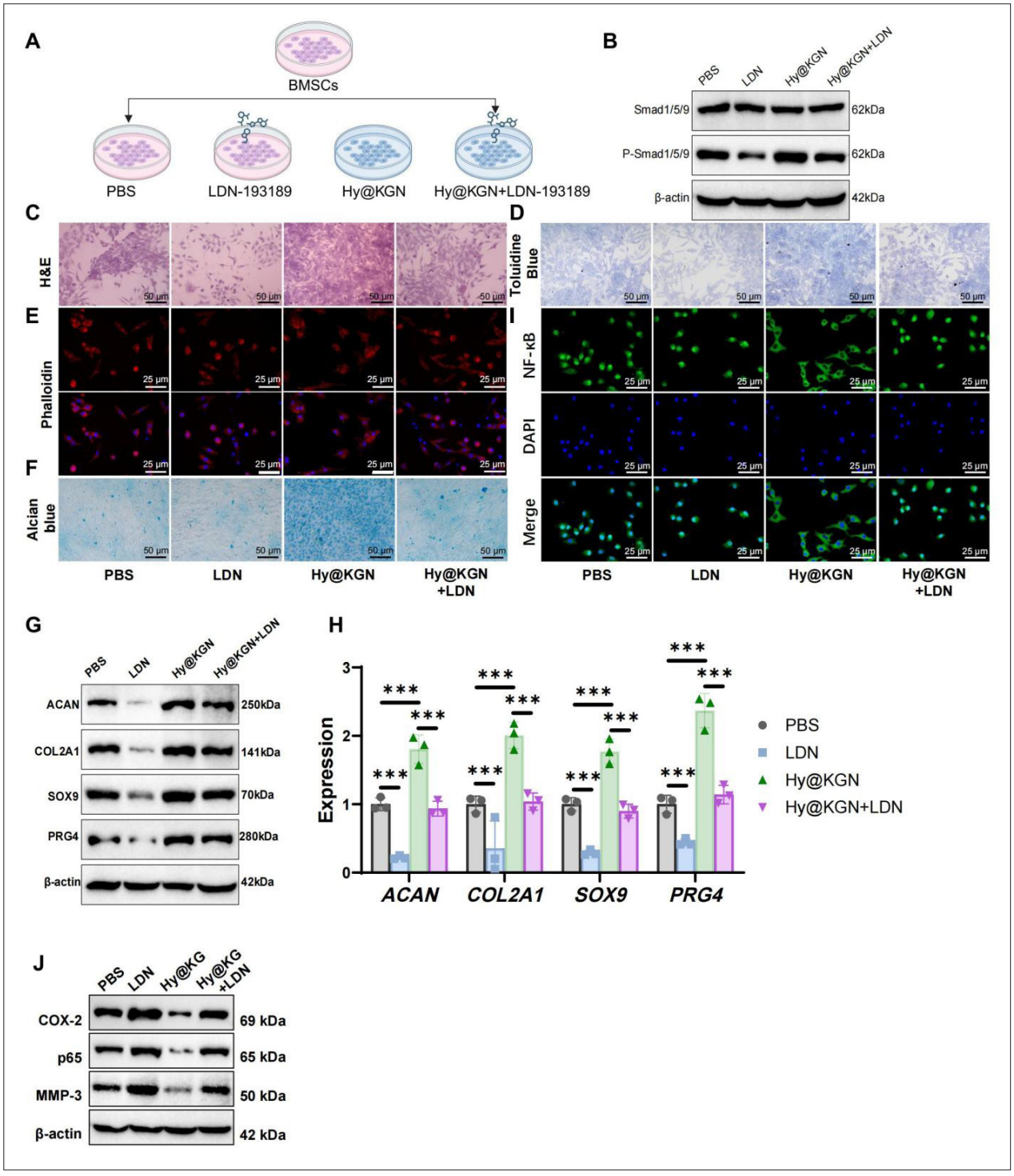

Figure 5. Effects of LDN-193189 inhibitor on chondrogenic differentiation of BMSCs. (A) Schematic of the experimental procedure. (B) Western blot analysis of Smad1/5/9 pathway-related factor expression. (C) H&E staining to assess the chondrogenic differentiation capacity of BMSCs. (D) Toluidine blue staining to assess the chondrogenic differentiation capacity of BMSCs. (E) Phalloidin staining to observe morphological changes in BMSCs. (F) Alcian blue staining to assess the chondrogenic differentiation capacity of BMSCs. (G) Western blot analysis of chondrogenesis-related proteins COL2A1, ACAN, PRG4, and SOX9. (H) RT-qPCR analysis of chondrogenesis-related genes *Col2a1*, *Acan*, *Prg4*, and *Sox9*. (I) Immunofluorescence staining to detect NF-κB nuclear translocation in chondrocytes. (J) Western blot analysis and quantification of COX-2, MMP-3, and phosphorylated NF-κB (p65) expression in chondrocytes. All cell experiments were performed in triplicate; ***$p < 0.001$. Scale bars: 25 μm (E and I); 50 μm (C, D, and F). Abbreviation: BMSCs, bone marrow stromal cells.

observed in the Hy@KGN hydrogel group (Figure 5I). Consistently, Western blot analysis revealed a marked upregulation of COX-2, MMP-3, and phosphorylated NF-κB (p65) following LDN-193189 treatment (Figure 5J). This part of the experiment was based on 3D-printed hydrogel scaffolds. Using a Smad1/5/9 pathway inhibitor, we further validated that the 3D-printed KGN-loaded hydrogel promotes BMSC chondrogenic differentiation by activating the Smad1/5/9 signaling pathway.

3.5. Biocompatibility of Hy@KGN

To verify the *in vivo* biosafety of Hy@KGN hydrogel, we implanted it subcutaneously in healthy rats and monitored their weight and behavior periodically, as illustrated in Figure 6A. Throughout the experiment, all rats demonstrated consistent weight gain without any observed abnormal behaviors or significant weight loss, indicating that the hydrogel implantation had no adverse effects on the physiological activities of the rats (Figure 6B).

Weekly blood samples were collected for complete blood count and biochemical assessments. All hematological parameters remained within physiological limits, indicating no systemic abnormalities (Table 2). Serum biochemical indices, including ALT, AST, BUN, and Cr, displayed no significant deviations from normal reference values throughout the observation period, suggesting that the Hy@KGN hydrogel implantation did not exert any significant toxicity on liver or kidney functions (Figure 6C). Post-experiment, the major organs (liver, kidney, spleen, heart, and lungs) were subjected to H&E staining, which revealed no significant pathological changes or inflammation, with normal tissue architecture and no signs of cellular infiltration or necrosis (Figure 6D).

Furthermore, TUNEL staining indicated low levels of apoptosis at the hydrogel implantation sites, with no significant differences compared to normal tissue (Figure 6E and F). Immunohistochemical (IHC) analysis revealed that the number of Bcl-2–positive cells, characterized by brown-stained cytoplasm, did not differ significantly between the Hy@KGN and control groups (Figure 6G). ELISA results for serum inflammatory markers, such as IL-6 (Figure 6H), TNF-α (Figure 6I), and IL-1β (Figure 6J), exhibited no significant increase, indicating that the implant did not trigger a systemic inflammatory response. These results demonstrate that the Hy@KGN hydrogel possesses excellent biosafety and is suitable for *in vivo* applications.

3.6. Hy@KGN significantly enhances cartilage repair in rats via the Smad 1/5/9 pathway

To assess the potential of this hydrogel for *in vivo* cartilage repair potential of the hydrogel, a full-thickness cartilage defect model was established in Sprague-Dawley rats and divided into the following five groups: PBS control, Hy hydrogel, KGN, Hy@KGN hydrogel, and LDN+Hy@KGN. Each material was implanted into the defect area, with evaluations conducted 6 and 12 weeks post-surgery (the experimental process depicted in Figure 7A). Observations and histological analyses at 6 weeks postoperation (Figure S7A and B, Supporting Information) revealed tissue

Table 2. Complete blood count

Variable	Control ($n = 9$)	Hy ($n = 10$)	KGN@Hy ($n = 10$)
WBC (10^6/4)	3.87 ± 0.72	4.25 ± 1.19	4.01 ± 0.55
RBC (10^6/4)	7.31 ± 0.20	7.38 ± 0.90	7.48 ± 0.32
Hemoglobin (g/dL)	141.59 ± 10.30	141.85 ± 7.85	139.93 ± 8.41
Hematocrit (%)	42.55 ± 4.16	44.58 ± 5.57	43.15 ± 5.03
MCV (fL)	61.08 ± 6.85	60.72 ± 5.81	60.76 ± 2.01
MCH (pg)	19.59 ± 0.22	19.83 ± 0.33	20.35 ± 0.57
MCHC (pg)	324.45 ± 9.32	330.23 ± 11.25	324.55 ± 10.46
Platelet (10^3/4)	1.03 ± 0.19	0.98 ± 0.12	1.04 ± 0.67
RDW-SD (fL)	31.66 ± 1.44	31.72 ± 5.23	31.35 ± 5.11
RDW-CV (%)	13.89 ± 0.98	14.76 ± 2.79	13.20 ± 0.62
Reticulocytes (%)	1.92 ± 0.67	2.15 ± 0.34	1.87 ± 0.43
NRBC (/100 WBC)	0.22 ± 0.15	0.18 ± 0.13	0.83 ± 0.09

Note: Each value represents the mean ± standard deviation. The *p*-values were calculated compared to the control group (*$p < 0.05$). Abbreviations: MCH, mean corpuscular hemoglobin; MCHC, mean corpuscular hemoglobin concentration; MCV, mean corpuscular volume; NRBC, nucleated red blood cell; RBC, red blood cell; RDW-SD, red cell distribution width–standard deviation; RDW-CV, red cell distribution width–coefficient of variation; WBC, white blood cell.

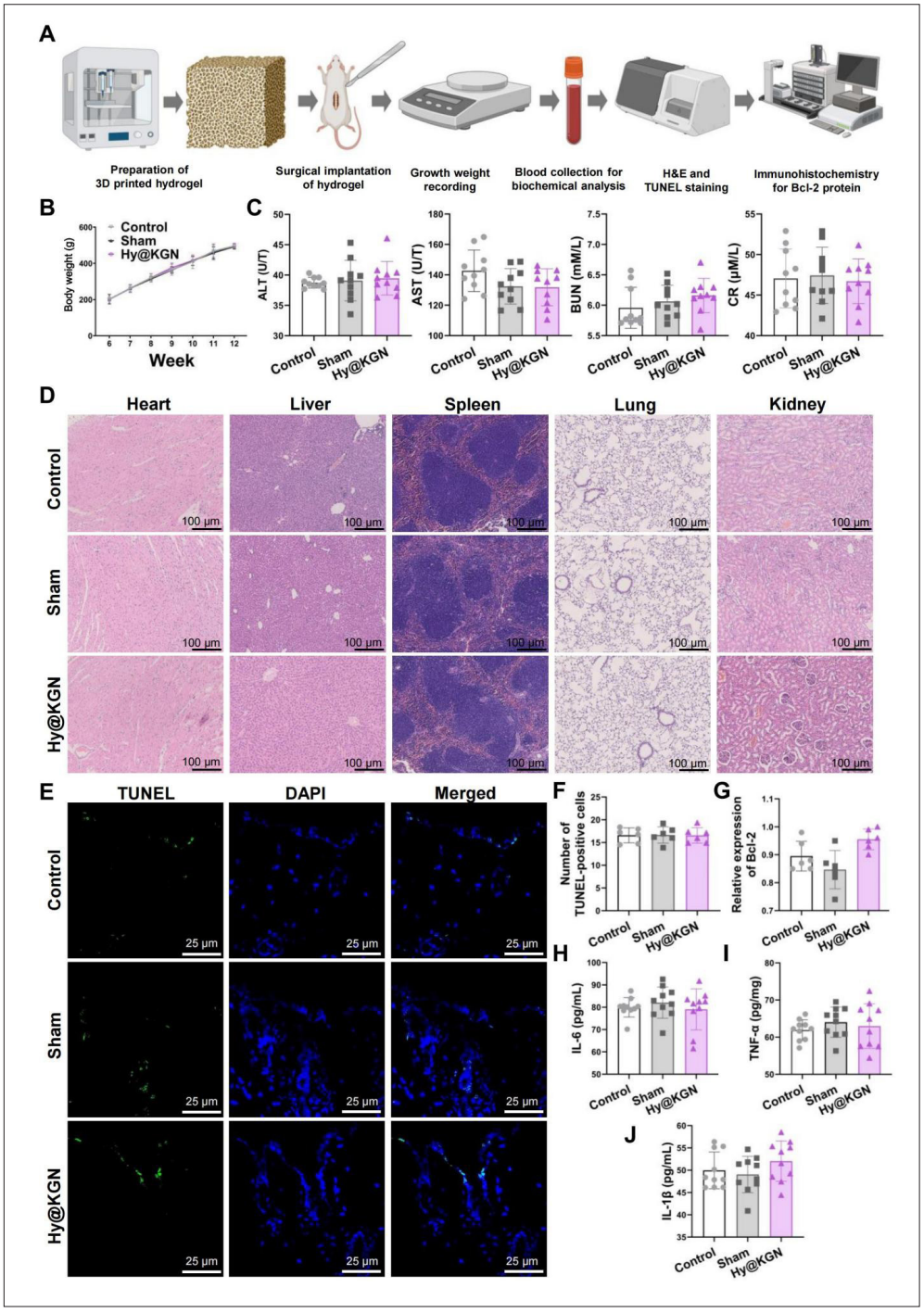

Figure 6. *In vivo* biosafety evaluation of Hy@KGN hydrogel. (A) Technical flowchart illustrating the biosafety assessment procedure. (B) Monitoring of body weight changes in each group of rats (n = 10). (C) Blood biochemical analysis of liver function (ALT, AST) and kidney function (BUN, Cr) levels in rats (n = 10). (D) H&E staining of heart, liver, spleen, lung, and kidney tissues to observe tissue structure and pathology in each group (n = 10). (E) TUNEL staining to detect apoptotic cells in tissues on Day 7 (n = 10). (F) Quantification of TUNEL-positive cells (n = 6). (G) Immunohistochemical staining for Bcl-2 expression in tissues on Day 7 (n = 6). (H–J) ELISA analysis of serum levels of inflammatory factors: IL-6 (H), TNF-α (I), and iNOS (J) (n = 10). All cell experiments were performed in triplicate. Data were tested for normality using the Shapiro–Wilk test and analyzed using one-way ANOVA with Tukey's HSD post hoc test for group comparisons. Scale bars: 100 μm (D); 25 μm (E). Abbreviations: ALT, alanine aminotransferase; AST, aspartate aminotransferase; Bcl-2, B-cell lymphoma-2; BUN, blood urea nitrogen; CR, creatinine; DAPI, 4′,6-diamidino-2-phenylindole; H&E, Hematoxylin and eosin; Hy@KGN, Kartogenin-loaded hydrogel; IL-6, Interleukin-6; IL-1β, Interleukin-1 beta; TNF, tumor necrosis factor; TUNEL, terminal deoxynucleotidyl transferase-mediated dUTP nick-end labeling.;;;; …

regeneration at the defect sites in all groups, although the new cartilage tissue had not yet fully covered the injured areas. The PBS control group displayed the most distinct boundary between the regenerated area and the original cartilage, whereas the Hy@KGN group displayed more seamless integration, likely due to enhanced BMSC survival and chondrogenic differentiation supported by the hydrogel. Consistent with macroscopic observations, the H&E staining revealed disorganized fibrous tissue architecture and lower subchondral bone reconstruction in the PBS and Hy groups. In contrast, the KGN and Hy@KGN groups exhibited more organized repair tissues, indicating accelerated bone reconstruction, though boundaries were still present. SO/FG staining demonstrated the onset of cartilage differentiation, with minimal differentiation in the PBS and LDN+Hy@KGN groups, while the other groups exhibited partial cartilage differentiation, indicating active matrix secretion at this stage, with the Smad 1/5/9 pathway playing a crucial role in the process.

At 12 weeks post-surgery, the defect area displayed a significant increase in the filling rate of repair tissue, with nearly no residual hydrogel visible (Figure S7C, Supporting Information). In the PBS and LDN+Hy@KGN groups, the repair tissue remained recessed relative to the surrounding cartilage and exhibited surface irregularities. In contrast, the KGN and Hy@KGN groups displayed repair tissue that was level with native cartilage and exhibited a smooth, cartilage-like morphology. The Hy group primarily formed fibrous tissue, while the Hy@KGN group featured a more seamless integration between repair and native cartilage compared to the KGN group (Figure S7C, Supporting Information). Repair tissue in the PBS and Hy groups was mainly fibrous, with limited response to SO/FG staining (Figure S7D, Supporting Information). Compared to the PBS and LDN+Hy@KGN groups, the Hy group exhibited improved subchondral bone reconstruction with fewer fissures. The Hy@KGN and KGN groups displayed more substantial cartilage-like new tissue, with the Hy@KGN group presenting more uniform and mature repair cartilage. Notably, SO/FG staining displayed more intense red staining in the Hy@KGN group, indicating a faster cartilage repair rate and higher proteoglycan content than the KGN group. Combined with *in vitro* findings, the 12-week repair outcome likely relates to enhanced BMSC and chondrocyte activity and accelerated matrix synthesis within the defect area, thereby promoting cartilage repair.

Subchondral bone reconstruction was evaluated using micro-CT. At Week 6, all groups exhibited varying degrees of bone defects, with the Hy@KGN and KGN groups displaying the most limited damage (Figure 7B). By Week 12, the subchondral bone in the Hy@KGN group was almost fully reconstructed (Figure 7C). Quantitative evaluation revealed significantly higher BV/TV and BMD values, and reduced BDV/TV and Tb.Sp in the Hy, KGN, and Hy@KGN groups compared to PBS, with the Hy@KGN group exhibiting the most pronounced improvements. However, these effects in the Hy@KGN group were reversed by LDN (Figure 7D–F). The Smad1/5/9 signaling pathway plays a critical role in inducing bone formation; Western blot analysis demonstrated that at both Weeks 6 and 12 post-surgery, the Hy@KGN and KGN groups significantly promoted Smad1/5/9 protein phosphorylation, while phosphorylation levels in the inhibitor group remained low (Figure 7G and H). These findings, supported by H&E, SO/FG staining, and micro-CT data, indicate that the inhibitor group had poorer cartilage repair outcomes, demonstrating that KGN's ability to enhance subchondral bone reconstruction improves over time, with the Hy@KGN hydrogel outperforming KGN alone in this regard.

Additionally, Alcian blue staining at 6 weeks post-surgery indicated significantly higher levels of blue-stained cartilage matrix (hyaluronic acid and acidic glycosaminoglycans) in the KGN and Hy@KGN groups compared to the PBS and Hy groups, with the Hy@KGN group exhibiting the most extensive positive staining. This effect of Hy@KGN was reversed by LDN (Figure 8A and C). Sirius red staining confirmed the presence of collagen types I and II, a finding further supported by IHC results (Figure 8A and D–F). At 12 weeks post-surgery, Alcian blue staining revealed uniform cartilage matrix distribution in all groups except the PBS and LDN+Hy@KGN groups (Figure 8B and C). However, at Week 12, the cartilage matrix in both the KGN and Hy@KGN groups appeared thinner than at Week 6, likely due to ongoing subchondral bone remodeling that led to partial replacement by fibrous or cartilage-like tissue. Notably, the Hy@KGN group exhibited blue staining patterns closely matching those of adjacent native cartilage, indicating more advanced regeneration than the KGN group. IHC and quantitative analysis further confirmed that the Hy@KGN group achieved the most effective cartilage repair, with the highest collagen I and collagen II expression levels in the regenerated cartilage tissue (Figure 8B and D–F). According to the ICRS macroscopic scoring system, repair scores in the Hy, KGN, and Hy@KGN hydrogel groups at Week 6 were higher than in the PBS group, with LDN reversing the repair effects of Hy@KGN hydrogel (Figure 8G). Masson's trichrome staining indicated significantly greater deposition of newly formed collagen at the cartilage defect sites in the Hy@KGN group (Figure 8H and I).

These results demonstrate that the Hy@KGN hydrogel performs well in promoting cartilage regeneration,

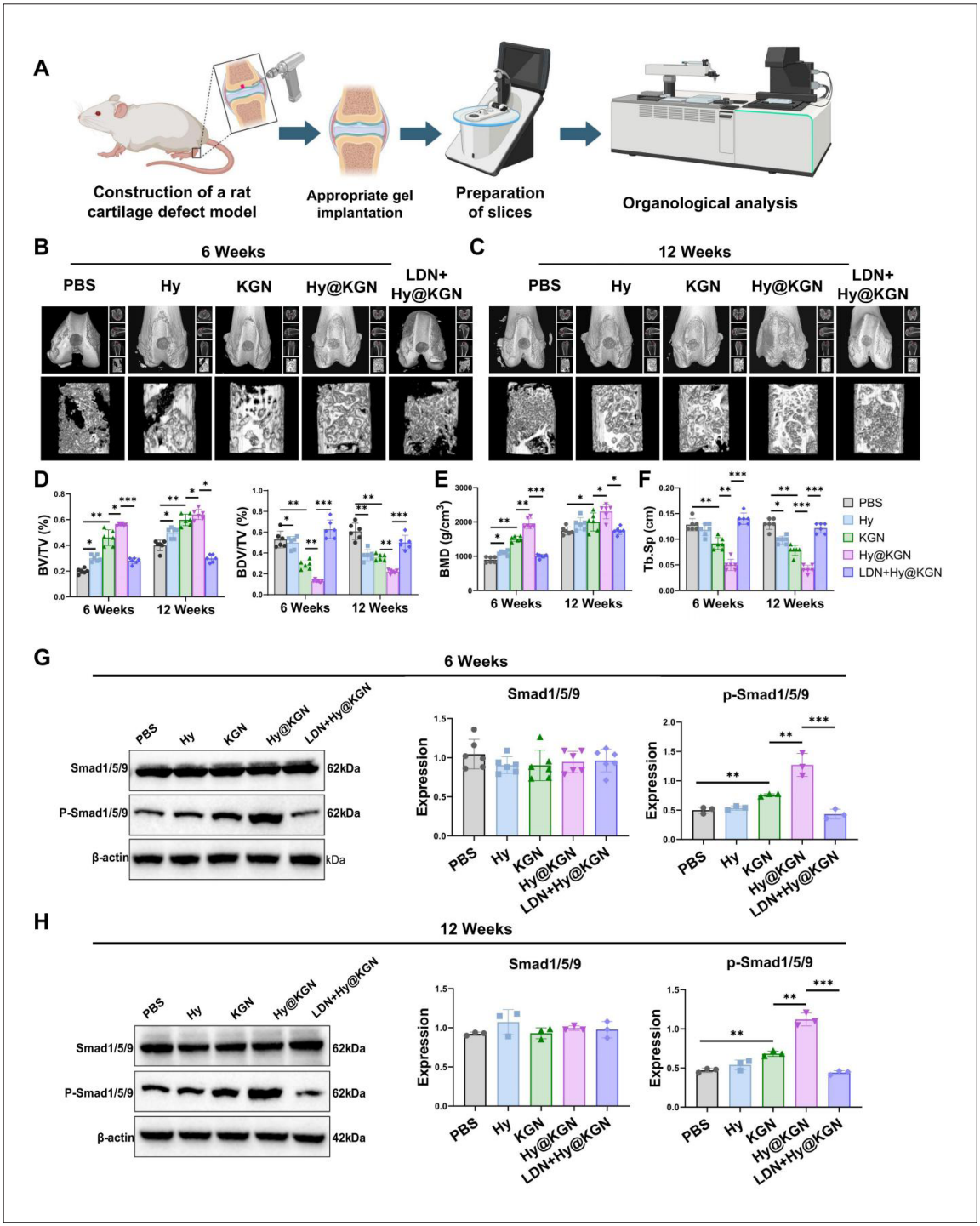

Figure 7. Evaluation of *in vivo* cartilage regeneration potential of Hy@KGN hydrogel. (A) Schematic of the surgical procedure. (B) Micro-CT imaging presents new cartilage formation at 6 weeks post-surgery. (C) Micro-CT imaging presents new cartilage formation at 12 weeks post-surgery; the red dashed line indicates the defect area. (D–F) Quantification of BV/TV and BDV/TV (D), BMD (E), and Tb.Sp (F). (G) Western blot analysis of phosphorylated and non-phosphorylated Smad1/5/9 protein levels at 6 weeks post-surgery in each group. (H) Western blot analysis of phosphorylated and non-phosphorylated Smad1/5/9 protein levels at 12 weeks post-surgery in each group (n = 6 rats per group); * $p < 0.05$, ** $p < 0.01$, *** $p < 0.001$. All cell experiments were performed in triplicate. Data were tested for normality using the Shapiro–Wilk test and analyzed using one-way ANOVA with Tukey's HSD post hoc test for group comparisons. Scale bars: 2 mm (B and C). Abbreviations: β-actin, beta actin; BV/TV, bone volume/tissue volume; BMD, bone mineral density; Hy, hydrogel; Hy@KGN, kartogenin-loaded hydrogel; KGN, kartogenin; LDN, LDN-193189 (BMP pathway inhibitor); PBS, phosphate-buffered saline; P-Smad1/5/9, phosphorylated Smad1/5/9; Smad1/5/9, mothers against decapentaplegic homolog 1/5/9; Tb.Sp, trabecular separation.

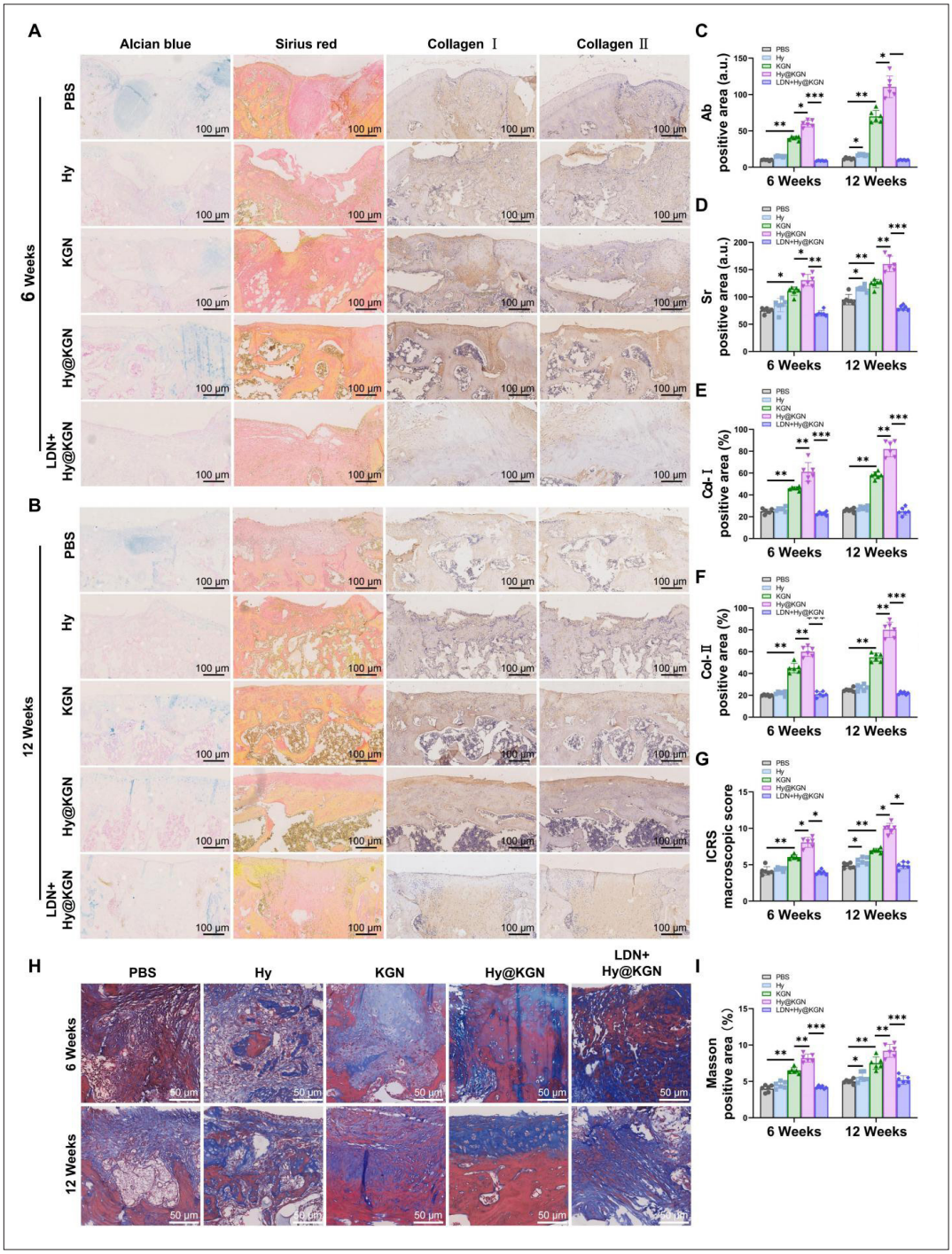

Figure 8. Assessment of cartilage regeneration by Hy@KGN hydrogel in full-thickness cartilage defect model in Sprague-Dawley rats. (A) Alcian blue staining for cartilage proteoglycans, Sirius red staining for collagen fibers, and immunohistochemical staining for collagen types I and II at 6 weeks post-surgery. (B) Alcian blue staining for cartilage proteoglycans, Sirius red staining for collagen fibers, and immunohistochemical staining for collagen types I and II at 12 weeks post-surgery. (C) Quantitative analysis of Alcian blue staining. (D) Quantitative analysis of Sirius red staining. (E) Quantitative analysis of collagen I immunohistochemical staining. (F) Quantitative analysis of collagen II immunohistochemical staining. (G) ICRS macroscopic scoring system for evaluating repair cartilage. (H) Masson's trichrome staining of collagen deposition at 6 and 12 weeks post-surgery across groups. (I) Quantification of collagen deposition across groups. $n = 6$ rats per group; $^{*}p < 0.05$, $^{**}p < 0.01$, $^{***}p < 0.001$. Scale bars: 100 μm (A and B); 50 μm (H). Abbreviations: Alcian blue, Alcian blue staining; Col I, collagen type I; Col II, collagen type II; Hy, hydrogel; Hy@KGN, kartogenin-loaded hydrogel; ICRS, International Cartilage Repair Society; KGN, kartogenin; LDN, LDN-193189 (BMP pathway inhibitor); Odr-1α, osteogenic differentiation-related protein 1 alpha; PBS, phosphate-buffered saline; Sirius red, Sirius red staining.

highlighting its potential as a clinical scaffold material for cartilage repair.

4. Discussion

Cartilage injuries are challenging to treat due to the tissue's limited self-repair capacity. Traditional treatments, such as drug therapy and surgical implants, can alleviate symptoms to some extent but often fall short of achieving ideal repair outcomes.[23] As a result, patients frequently rely on non-curative approaches, including pain management and functional support, which can significantly impact their quality of life over the long term.[24] Recently, 3D printing technology has demonstrated immense potential in biomedical engineering, primarily due to its ability to precisely control material structure and function.[1,3] As a novel delivery vehicle, 3D-printed hydrogel efficiently transports bioactive molecules and provides an environment that mimics the natural ECM, essential for promoting chondrocyte growth and new cartilage formation.[25] This technology addresses the limitations of traditional cartilage repair methods and offers patients a more effective and durable treatment option.[26]

The 3D-printed hydrogel used in this study combines biocompatibility with superior mechanical properties, distinguishing it from conventional cartilage repair materials.[27] Previous research has primarily focused on natural materials, such as collagen and hyaluronic acid, which provide some structural support but often lack the necessary mechanical strength and flexibility for complex cartilage defect applications.[28] In contrast, the synthetic hydrogel in this study, fabricated with precise 3D printing technology, can replicate more intricate biological structures at the microscopic level, a feat challenging to achieve with traditional materials. Additionally, incorporating the small molecule compound KGN through 3D printing introduces an innovative approach by directly modulating stem cell behavior with chemical agents, a relatively rare strategy in prior studies. This approach enhances the efficiency and controllability of stem cell therapy and opens new pathways for future research in regenerative medicine.

In this study, we developed a precise and sustained delivery strategy for KGN by combining 3D bioprinting technology with a HEMA- and PEGDA-based hydrogel formulation, which significantly improved the efficiency of BMSC chondrogenic differentiation. Compared with previously reported dynamic hydrogels crosslinked through host–guest interactions,[29] our delivery system demonstrates higher efficiency and controllability. In addition, compared with the results of BMSC-laden 3D-bioprinted scaffolds reported by Wang *et al.*,[9] our hydrogel demonstrated superior comprehensive performance and more significant cartilage repair outcomes. Moreover, while another study[30] utilized dual-cell living hydrogels, our delivery strategy is more precise and better simulates the natural cartilage microenvironment. Compared with microfluidic-generated hydrogel microspheres,[31] our approach is more suitable for large-scale production and clinical application. Furthermore, compared with studies directly investigating KGN's effect on the osteogenic differentiation of BMMSCs,[32] this study integrates 3D bioprinting technology and systematically elucidates the underlying mechanisms of KGN's action, verifying its efficacy *in vivo* with significantly improved repair effects. Unlike prior studies, we combined RNA-seq, WGCNA, and PPI network analysis to comprehensively reveal the core regulatory role of the Smad1/5/9 signaling axis at both the transcriptomic and protein levels.

Previous studies have demonstrated that the TGF-β pathway promotes chondrocyte proliferation and ECM synthesis by activating the Smad2/3 pathway through its receptors.[33] The Wnt pathway facilitates chondrocyte differentiation through β-catenin accumulation and nuclear translocation.[34] However, in this study, we focused primarily on the Smad1/5/9 pathway for several reasons. Firstly, our RNA-seq differential expression analysis, WGCNA module screening, and PPI network construction consistently indicated that Smad1, Smad5, and Smad9 were significantly upregulated following KGN treatment and occupied core positions within the regulatory networks. This multilevel evidence indicates the critical role of the Smad1/5/9 axis in KGN-induced BMSC chondrogenic differentiation. Secondly, existing studies have demonstrated that activation of the Smad1/5/9 pathway significantly upregulates genes essential for cartilage formation, such as *SOX9* and *COL2A1*, which are vital for chondrocyte maturation and matrix synthesis. Although the Smad2/3 pathway can also contribute to cartilage formation, its effect appears to be relatively modest. Additionally, activation of the Smad1/5/9 pathway can influence the Wnt signaling pathway by regulating downstream gene expression, thereby further promoting chondrocyte differentiation.[33] For these reasons, our study emphasizes the Smad1/5/9 pathway.

The Smad1/5/9 signaling pathway is a crucial intracellular signaling route primarily regulated by activating bone morphogenetic proteins (BMPs). Activation of this pathway begins with BMPs binding to their cell surface receptors, initiating receptor phosphorylation, which subsequently activates downstream Smad1, Smad5, and Smad9 proteins.[35] These phosphorylated Smads subsequently form a complex with the common mediator Smad4, which translocates into the nucleus to regulate the

transcription of downstream target genes.[36] This process is central to various biological functions, particularly in cell differentiation (e.g., BMSC differentiation into osteocytes or chondrocytes), tissue development, and repair, making it a key mechanism in bone and cartilage formation.[37,38]

Our study results demonstrate that KGN significantly activates the Smad1/5/9 signaling pathway, aligning closely with previous findings and further validating the pathway's pivotal role in regulating the chondrogenic differentiation of BMSCs. Activation of this pathway promotes the upregulation of chondrogenic differentiation-related genes and provides critical insights into the molecular mechanisms underlying BMSC differentiation. Unlike other studies using growth factors such as TGF-β to induce differentiation, KGN offers a simpler, more flexible, and efficient approach to cellular differentiation. As a small-molecule compound, KGN can readily penetrate the cell membrane and precisely activate target signaling pathways, thereby avoiding the immune reactions and high costs associated with growth factors. The advantages of this small-molecule induction strategy include lower production and storage costs and increased control and specificity, making it well-suited for large-scale clinical applications and presenting a promising avenue for widespread adoption.

The 3D-printed hydrogel developed in this study demonstrates excellent biocompatibility and mechanical properties. Compared to traditional cartilage repair materials, this novel hydrogel better replicates the physical characteristics of natural cartilage, such as elasticity and resilience, thereby creating an ideal microenvironment for cell adhesion, proliferation, and differentiation. Traditional materials often struggle to balance mechanical strength and elasticity; however, this hydrogel achieves that balance through optimized material composition and 3D printing technology, effectively supporting functional cell growth. Furthermore, water absorption and *in vitro* degradation assessments confirm its suitability for *in vivo* applications, showcasing significant advantages in maintaining structural integrity and enabling controlled degradation post-implantation. These improvements are critical for sustaining long-term cartilage repair effects, reducing the need for secondary surgeries, and enhancing cell-material interactions, providing a solid foundation for future clinical applications.

Through comprehensive *in vitro* and *in vivo* experiments, this study thoroughly evaluated the functionality of the 3D-printed hydrogel. *In vitro* results revealed that KGN significantly promotes chondrogenic differentiation of BMSCs, while *in vivo* experiments confirm the hydrogel's effectiveness in actual cartilage repair. This consistency highlights the reliability of the 3D-printed hydrogel as a cartilage repair material and points to subtle differences that may arise under varying experimental conditions, guiding future research adjustments.

Despite the significant *in vitro* and *in vivo* results demonstrating the potential of the 3D-bioprinted KGN-loaded hydrogel to promote BMSC chondrogenic differentiation and cartilage repair, there are still some limitations. Although we detected a significant increase in phospho-Smad1/5/9 expression by Western blot, we did not perform double IHC staining for phospho-Smad1/5/9 and Smad4 to directly verify the nuclear translocation of the Smad1/5/9–Smad4 complex. This process is crucial for confirming the activation mechanism of the Smad1/5/9 pathway, and future studies should consider double IHC staining to directly visualize this nuclear translocation. Moreover, although we characterized the hydrogel's rheological properties and observed its uniform microporous structure by SEM, we did not experimentally verify how the macroscopic architecture influences its rheological behavior. This verification is crucial for elucidating the relationship between macrostructure and rheological performance. Future studies should include more systematic experiments to address this gap and further optimize the material's properties for biomedical applications. Additionally, the observation of BMSC morphological changes has certain limitations. The cell images presented in Figure 4D were obtained by mixing BMSCs with the Hy@KGN hydrogel precursor solution and then performing phalloidin staining. Although this approach features morphological changes after co-culture with the precursor solution, it does not fully reflect the actual behavior of cells within the 3D hydrogel environment. 3D culture data could more intuitively demonstrate cell distribution, migration, and morphological dynamics within the hydrogel, providing a more comprehensive understanding of cell–material interactions. In future work, we will introduce advanced 3D cell culture techniques and multidimensional imaging methods, such as bioprinting, confocal microscopy, and cell labeling technologies, to directly observe BMSC distribution, migration, and morphological changes within the hydrogel. These improvements will enable a more comprehensive evaluation of Hy@KGN's effects on cell differentiation, providing more reliable evidence for cartilage repair material development. Finally, we did not assess the expression changes of BMP ligands (e.g., BMP2, BMP4, BMP6) directly; therefore, it remains unclear whether Hy@KGN activates the Smad1/5/9 pathway by upregulating these ligands. Although our RNA-seq results indicated upregulation of *Acan*, *Bmp2*, and *Bmp6* (Figure 1D), these findings only indirectly

suggest that BMP ligands may be involved. There is also a lack of direct evidence regarding the activation status of BMP receptors (BMPR1A, BMPR1B, BMPR2). Thus, we could not confirm whether Hy@KGN activates the Smad1/5/9 pathway through receptor phosphorylation or conformational changes. Moreover, since crosstalk exists between the Smad1/5/9 pathway and other pathways, such as Wnt and TGF-β, the absence of upstream receptor activation analysis limits our understanding of potential pathway cross-regulation. Future research should focus on examining whether Hy@KGN regulates BMP ligand expression and BMP receptor activation to clarify whether the pathway is initiated through ligand upregulation or receptor activation. Additionally, exploring crosstalk with other pathways (e.g., Wnt and TGF-β) will help further elucidate the mechanism by which Hy@KGN promotes chondrogenesis. Despite the promising outcomes, challenges remain for the long-term clinical application of 3D-printed hydrogels, including potential issues related to material stability and chronic inflammation. Future research should evaluate the hydrogel's long-term performance *in vivo*, particularly in animal models that mimic more complex clinical scenarios.

This study successfully developed a novel hydrogel by integrating 3D printing technology with the small molecule KGN, demonstrating outstanding efficacy in promoting BMSC chondrogenic differentiation and cartilage repair. These results enhance our understanding of the Smad1/5/9 pathway in chondrogenic differentiation and offer a new material option for treating related clinical conditions. Nonetheless, certain limitations remain, such as the need to further validate long-term biocompatibility and mechanical performance in clinically relevant models. Future studies will aim to optimize the hydrogel's chemical and physical properties and test in models that more closely replicate human physiological conditions.

5. Conclusion

This study successfully synthesized and characterized a Hy@KGN hydrogel, demonstrating its effectiveness in promoting the chondrogenic differentiation of BMSCs. Through a series of *in vitro* experiments, we found that the Hy@KGN hydrogel significantly enhances BMSC proliferation and chondrogenic differentiation while upregulating chondrogenic differentiation-related genes and proteins via activating the Smad1/5/9 signaling pathway.

This research elucidates the molecular mechanism by which the Hy@KGN promotes BMSC chondrogenic differentiation through Smad1/5/9 pathway activation. This finding offers new insights for developing cartilage repair materials. The composite material exhibits excellent biocompatibility and mechanical properties and significantly promotes cartilage regeneration, suggesting strong potential for clinical application. The material holds promise for treating cartilage injuries and degenerative joint diseases, offering patients an effective repair approach. Although substantial results were achieved in *in vitro* experiments, further studies are required to confirm its effectiveness *in vivo*. Additionally, the long-term biosafety and degradation behavior of the Hy@KGN warrants further investigation. The next steps in this research will involve animal model experiments to verify the composite material's efficacy *in vivo* for cartilage repair and to assess its potential side effects and safety profile. With continued technological advancements and deeper research, the Hy@KGN hydrogel is expected to become a valuable tool in cartilage repair, offering new solutions for treating cartilage injuries.

Acknowledgments

None.

Funding

This study was supported by the National Natural Science Foundation of China (81960403, 82060405, and 82360436); Lanzhou Science and Technology Plan Program (2021-RC-102); Natural Science Foundation of Gansu Province (22JR5RA943, 22JR5RA956, and 23JRRA1500); Cuiying Scientific and Technological Innovation Program of Lanzhou University Second Hospital (CY2021-MS-A07).

Conflict of interest

The authors declare no conflict of interest.

Author contributions

Conceptualization: Yayi Xia
Formal analysis: Rongjin Cheng, Fei Yang
Funding: Yayi Xia
Investigation: Chenhui Yang, Changshun Chen, Hefang Xiao, Bin Geng
Methodology: Chenhui Yang, Changshun Chen
Supervision: Yayi Xia
Writing – original draft: Chenhui Yang
Writing – review & editing: Yayi Xia
All authors reviewed and approved the final manuscript.

Ethics approval and consent to participate

All animal experiments were approved by the Institutional Animal Care and Use Committee (IACUC) of Lanzhou University Second Hospital (D2025-365) and conducted

in accordance with local guidelines for the care and use of laboratory animals.

Consent for publication

Not applicable

Availability of data

Data is available from the corresponding author upon reasonable request.

References

1. Xu J, Ji J, Jiao J, *et al*. 3D printing for bone-cartilage interface regeneration. *Front Bioeng Biotechnol*. 2022;10:828921. doi: 10.3389/fbioe.2022.828921
2. Jahani A, Nourbakhsh MS, Ebrahimzadeh MH, Mohammadi M, Yari D, PhD AM. Available 3D-printed biomolecule-loaded alginate-based scaffolds for cartilage tissue engineering applications: a review on current status and future prospective. *Arch Bone Jt Surg*. 2024;12(2):92-101. doi: 10.22038/abjs.2023.73275.3396
3. Liang Q, Ma Y, Yao X, Wei W. Advanced 3D-printing bioinks for articular cartilage repair. *IJB*. 2022;8(3):511. doi: 10.18063/ijb.v8i3.511
4. Deptuła M, Zawrzykraj M, Sawicka J, Banach-Kopeć A, Tylingo R, Pikuła M. Application of 3D-printed hydrogels in wound healing and regenerative medicine. *Biomed Pharmacother*. 2023;167:115416. doi: 10.1016/j.biopha.2023.115416
5. Nabizadeh Z, Nasrollahzadeh M, Daemi H, *et al*. Micro- and nanotechnology in biomedical engineering for cartilage tissue regeneration in osteoarthritis. *Beilstein J Nanotechnol*. 2022;13:363-389. doi: 10.3762/bjnano.13.31
6. Messaoudi O, Henrionnet C, Bourge K, Loeuille D, Gillet P, Pinzano A. Stem cells and extrusion 3D printing for Hyaline cartilage engineering. *Cells*. 2020;10(1):2. doi: 10.3390/cells10010002
7. Wei W, Ma Y, Yao X, *et al*. Advanced hydrogels for the repair of cartilage defects and regeneration. *Bioact Mater*. 2021;6(4):998-1011. doi: 10.1016/j.bioactmat.2020.09.030
8. Zhang W, Chen R, Xu X, *et al*. Construction of biocompatible hydrogel scaffolds with a long-term drug release for facilitating cartilage repair. *Front Pharmacol*. 2022;13:922032. doi: 10.3389/fphar.2022.922032
9. Liu Y, Peng L, Li L, *et al*. 3D-bioprinted BMSC-laden biomimetic multiphasic scaffolds for efficient repair of osteochondral defects in an osteoarthritic rat model. *Biomaterials*. 2021;279:121216. doi: 10.1016/j.biomaterials.2021.121216
10. Chen X, Wang Y, Chen R, Qu N, Zhang B, Xia C. Suppressing PLCγ1 enhances osteogenic and chondrogenic potential of BMSCs. *Biochem Biophys Res Commun*. 2020;532(2):292-299. doi: 10.1016/j.bbrc.2020.08.049
11. Xu Y, Wang Y, Wang A, *et al*. Effect of CD44 on differentiation of human amniotic mesenchymal stem cells into chondrocytes via Smad and ERK signaling pathways. *Mol Med Rep*. 2020;21(4):1777-1786. doi: 10.3892/mmr.2020.11044
12. Hou M, Zhang Y, Zhou X, *et al*. Kartogenin prevents cartilage degradation and alleviates osteoarthritis progression in mice via the miR-146a/NRF2 axis. *Cell Death Dis*. 2021;12(5):503. doi: 10.1038/s41419-021-03765-x
13. Wang J, Zhou J, Zhang N, Zhang X, Li Q. A heterocyclic molecule kartogenin induces collagen synthesis of human dermal fibroblasts by activating the smad4/smad5 pathway. *Biochem Biophys Res Commun*. 2014;450(1):568-574. doi: 10.1016/j.bbrc.2014.06.016
14. de Kroon LMG, Narcisi R, van den Akker GGH, *et al*. SMAD3 and SMAD4 have a more dominant role than SMAD2 in TGFβ-induced chondrogenic differentiation of bone marrow-derived mesenchymal stem cells. *Sci Rep*. 2017;7(1):43164. doi: 10.1038/srep43164
15. Pu P, Wu S, Zhang K, *et al*. Mechanical force induces macrophage-derived exosomal UCHL3 promoting bone marrow mesenchymal stem cell osteogenesis by targeting SMAD1. *J Nanobiotechnol*. 2023;21(1):180. doi: 10.1186/s12951-023-01836-z
16. Zhang S, Hu P, Liu T, *et al*. Kartogenin hydrolysis product 4-aminobiphenyl distributes to cartilage and mediates cartilage regeneration. *Theranostics*. 2019;9(24):7108-7121. doi: 10.7150/thno.38182
17. Dey MK, Devireddy RV. Rheological characterization and printability of sodium alginate–gelatin hydrogel for 3D cultures and bioprinting. *Biomimetics*. 2025;10(1):28. doi: 10.3390/biomimetics10010028
18. Yu PB, Deng DY, Lai CS, *et al*. BMP type I receptor inhibition reduces heterotopic ossification. *Nat Med*. 2008;14(12):1363-1369. doi: 10.1038/nm.1888
19. Tsukamoto S, Mizuta T, Fujimoto M, *et al*. Smad9 is a new type of transcriptional regulator in bone morphogenetic protein signaling. *Sci Rep*. 2014;4:7596. doi: 10.1038/srep07596
20. Yao Y, Wei G, Deng L, Cui W. Visualizable and lubricating hydrogel microspheres via NanoPOSS for cartilage regeneration. *Adv Sci (Weinh)*. 2023;10(15):e2207438. doi: 10.1002/advs.202207438
21. Chen Y, Yan X, Yuan F, *et al*. Kartogenin-conjugated double-network hydrogel combined with stem cell transplantation

and tracing for cartilage repair. *Adv Sci (Weinh)*. 2022;9(35):e2105571.
doi: 10.1002/advs.202105571

22. Xu T, Yu X, Xu K, *et al*. Comparison of the ability of exosomes and ectosomes derived from adipose-derived stromal cells to promote cartilage regeneration in a rat osteochondral defect model. *Stem Cell Res Ther*. 2024;15(1):1.
doi: 10.1186/s13287-024-03632-4

23. Wang M, Wu Y, Li G, *et al*. Articular cartilage repair biomaterials: strategies and applications. *Mater Today Bio*. 2024;24:100948.
doi: 10.1016/j.mtbio.2024.100948

24. Wu Z, Yao H, Sun H, *et al*. Enhanced hyaline cartilage formation and continuous osteochondral regeneration via 3D-Printed heterogeneous hydrogel with multi-crosslinking inks. *Mater Today Bio*. 2024;26:101080.
doi: 10.1016/j.mtbio.2024.101080

25. Mikaeeli Kangarshahi B, Naghib SM, Rabiee N. 3D printing and computer-aided design techniques for drug delivery scaffolds in tissue engineering. *Expert Opin Drug Deliv*. 2024;21(11):1615-1636.
doi: 10.1080/17425247.2024.2409913

26. Hafezi M, Nouri Khorasani S, Zare M, Esmaeely Neisiany R, Davoodi P. Advanced hydrogels for cartilage tissue engineering: recent progress and future directions. *Polymers (Basel)*. 2021;13(23):4199.
doi: 10.3390/polym13234199

27. Antich C, de Vicente J, Jiménez G, *et al*. Bio-inspired hydrogel composed of hyaluronic acid and alginate as a potential bioink for 3D bioprinting of articular cartilage engineering constructs. *Acta Biomater*. 2020;106:114-123.
doi: 10.1016/j.actbio.2020.01.046

28. Murphy CA, Serafin A, Collins MN. Development of 3D printable gelatin methacryloyl/chondroitin sulfate/hyaluronic acid hydrogels as implantable scaffolds. *Polymers (Basel)*. 2024;16(14):1958.
doi: 10.3390/polym16141958

29. Dai W, Zhang L, Yu Y, *et al*. 3D bioprinting of heterogeneous constructs providing tissue-specific microenvironment based on host–guest modulated dynamic hydrogel bioink for osteochondral regeneration. *Adv Funct Mater*. 2022;32(23):2200710.
doi: 10.1002/adfm.202200710

30. Zhang Y, Li D, Liu Y, *et al*. 3D-bioprinted anisotropic bicellular living hydrogels boost osteochondral regeneration via reconstruction of cartilage–bone interface. *Innovation (Camb)*. 2024;5(1):100542.
doi: 10.1016/j.xinn.2023.100542

31. Song C, Wu X, Wei Z, Xu Y, Wang Y, Zhao Y. Dental pulp stem cells-loaded kartogenin-modified hydrogel microspheres with chondrocyte differentiation property for cartilage repair. *Chem Eng J*. 2024;496:153930.
doi: 10.1016/j.cej.2024.153930

32. Yan H, Yu T, Li J, *et al*. Kartogenin improves osteogenesis of bone marrow mesenchymal stem cells via autophagy. *Stem Cells Int*. 2022;2022:1278921.
doi: 10.1155/2022/1278921

33. Li TF. TGF-b signaling in chondrocytes. *Front Biosci*. 2005;10(1-3):681-685.
doi: 10.2741/1563

34. Li J, Dong S. The signaling pathways involved in chondrocyte differentiation and hypertrophic differentiation. *Stem Cells Int*. 2016;2016:2470351.
doi: 10.1155/2016/2470351

35. Huntley R, Jensen E, Gopalakrishnan R, Mansky KC. Bone morphogenetic proteins: their role in regulating osteoclast differentiation. *Bone Rep*. 2019;10:100207.
doi: 10.1016/j.bonr.2019.100207

36. Lu C, Dong X, Yu WP, *et al*. Inorganic phosphate-osteogenic induction medium promotes osteogenic differentiation of valvular interstitial cells via the BMP-2/Smad1/5/9 and RhoA/ROCK-1 signaling pathways. *Am J Transl Res*. 2020;12(7):3329-3345.

37. Wang T, Zhang C, Wu C, *et al*. miR-765 inhibits the osteogenic differentiation of human bone marrow mesenchymal stem cells by targeting BMP6 via regulating the BMP6/Smad1/5/9 signaling pathway. *Stem Cell Res Ther*. 2020;11(1):251.
doi: 10.1186/s13287-020-1579-0

38. Ampuja M, Kallioniemi A. Transcription factors—intricate players of the bone morphogenetic protein signaling pathway. *Genes Chromosomes Cancer*. 2017;57(1):3-11.
doi: 10.1002/gcc.22502

ACCSCIENCE PUBLISHING

International Journal of Bioprinting

RESEARCH ARTICLE

Hyaluronic acid-based self-healing hydrogels with enhanced hydrolytic stability for 3D bioprinting in tissue engineering

Minhyung Kong[1], Hyun Seung Kim[1], Jiwon Hwang[1], Joon Seo Park[1], In Young Lee[1], and Kuen Yong Lee[1,2]*

[1]Department of Bioengineering, Hanyang University, Seoul, Republic of Korea

[2]Institute for Bioengineering and Biopharmaceutical Research, Hanyang University, Seoul, Republic of Korea

(This article belongs to the *Special Issue*: *Future Bioprinting—Celebrating the 10th Anniversary of the International Journal of Bioprinting*)

Abstract

Hyaluronic acid (HA)-based hydrogels have gained significant interest for many biomedical applications because of their biocompatibility and degradability as glycosaminoglycans. However, it is challenging to control their mechanical properties and degradation rates. In this study, we investigated the potential of carbodihydrazide-modified HA (HA-CDH) and oxidized diol-modified HA (odHA) to form hydrogels. We modulated the mechanical stiffness of the HA-CDH/odHA hydrogels by adjusting the degree of CDH substitution and polymer composition in the gels. These hydrogels exhibited improved hydrolytic stability under physiological conditions, which was attributed to the presence of multiple delocalized electron arrangements within the hydrazone bonds. Notably, the enzymatic degradability of these hydrogels was unaffected by the hydrazone bonds. We developed self-healing HA-CDH/odHA hydrogels using free adipic acid dihydrazide and utilized them to fabricate various three-dimensional (3D) structures via 3D printing. We integrated resonance-stabilized hydrazone chemistry with self-healing behavior in HA-based hydrogels, enabling both slow degradation and direct extrusion-based 3D bioprinting of cell-laden constructs without secondary networks or post-crosslinking treatments. Furthermore, we investigated the effect of enhanced mechanical stiffness on *in vitro* cell differentiation and observed significant gene expression levels that were indicative of chondrogenic and osteogenic differentiation within hydrogels with increased stiffness. These findings could help elucidate the effect of the physical properties of natural polysaccharide-based hydrogels on cell phenotype modulation and expand their applications in tissue engineering.

***Keywords*:** 3D bioprinting; Hydrazide-modified hyaluronate; Hydrolytic degradation; Oxidized hyaluronate; Resonance structure; Self-healing

***Corresponding author:**
Kuen Yong Lee
(leeky@hanyang.ac.kr)

Citation: Kong M, Kim HS, Hwang J, Park JS, Lee IY, Lee KY. Hyaluronic acid-based self-healing hydrogels with enhanced hydrolytic stability for 3D bioprinting in tissue engineering. *Int J Bioprint*. 2025;11(6):374-389. doi: 10.36922/IJB025370372

Received: September 9, 2025
Revised: September 25, 2025
Accepted: October 1, 2025
Published online: October 2, 2025

Copyright: © 2025 Author(s). This is an Open Access article distributed under the terms of the Creative Commons Attribution License, permitting distribution, and reproduction in any medium, provided the original work is properly cited.

Publisher's Note: AccScience Publishing remains neutral with regard to jurisdictional claims in published maps and institutional affiliations.

1. Introduction

Hydrogels are defined as three-dimensional (3D) structures that contain crosslinked porous networks.[1] They are composed of hydrophilic polymers, which swell significantly

upon exposure to water or biological fluids.[2] Hydrogels are categorized into natural and synthetic hydrogels based on the origin of their constituent materials.[2,3] Hydrogels are highly biocompatible, and they closely resemble the macromolecular components found in the body. Thus, they are versatile materials with extensive applications in drug delivery and tissue engineering.[3,4] In tissue engineering, hydrogels play a pivotal role as synthetic extracellular matrices that are crucial for generating new tissues.[4,5] Polysaccharide-based hydrogels are typically used for this purpose owing to their biocompatibility and biodegradability.[6] However, the poor mechanical properties of hydrogels prepared using polysaccharides limit their potential applications in various biomedical fields.[7] To address this limitation, numerous strategies have been explored to enhance the mechanical properties of polysaccharide-based hydrogels, including the formation of multiple networks and the development of nanocomposite hydrogels.[8,9]

3D printing has recently emerged as a versatile method for fabricating complex structures, and it is widely used in tissue engineering.[10–12] This technique can be used to produce patient-specific scaffolds with precise shapes using computer-aided design.[13] Common 3D printing techniques include inkjet, extrusion-based, and laser-assisted printing.[14,15] However, conventional hydrogels are often unsuitable for extrusion-based 3D printing, as they may cause nozzle blockage, hinder effective material delivery, and lack the ability to recover their structures after printing.[16,17] Dynamic hydrogels are a new type of hydrogel, different from conventional hydrogels and highly promising for 3D printing. Their reversible crosslinking networks impart self-healing properties, shear-thinning behavior, and adaptability to environmental changes.[18,19] These characteristics enable dynamic hydrogels to recover their structure after extrusion and maintain high shape fidelity without the need for additional post-processing, making them particularly attractive for fabrication of complex, cell-laden structures. However, finding the optimal rheological properties for 3D printing—particularly achieving the right balance of stiffness, viscosity, and recovery speed without the application of external stimuli—remains challenging.[20]

Hyaluronic acid (HA) is a natural polysaccharide with exceptional water retention properties.[21] HA is widely used to prepare hydrogel scaffolds in tissue engineering owing to its excellent biocompatibility and nontoxic degradation products.[22] However, HA hydrogels exhibit rapid degradation rates and poor mechanical characteristics.[23] To overcome these drawbacks, various strategies have been explored to enhance gel stiffness and regulate degradation rates, including the use of dual crosslinking systems.[1,24-26] The formation of hydrazone bonds between HA derivatives introduces self-healing capabilities in resulting hydrogels.[27]

Hydrazone chemistry has been widely employed in hydrogels because of its reversible covalent crosslinking, which imparts dynamic properties such as self-healing, shear-thinning, and injectability. Hydrazone crosslinking can typically be carried out via a reaction between aldehydes and hydrazides, which serves as a dynamic crosslink.[28] These reactions have high reactivity, simple reaction conditions, no toxic reagents or side products, and high yields.[29] Modifying the polymer backbone by incorporating aldehyde or hydrazide groups provides potential crosslinking sites, influencing crosslinking kinetics and bond stability. Faster kinetics result from high concentrations of reactive groups or the use of catalysts like salts, while increased stability is achieved with more stable aromatic hydrazones or lower temperatures. Polymer backbone structure, such as the inherent length or presence of other functional groups, also impacts the reactivity of functional groups and the resulting network density, further controlling mechanical properties and dynamic behavior.[30] However, hydrazone bonds are reversible and prone to hydrolytic instability; this typically leads to rapid hydrogel degradation.[31,32]

In this study, we examined the potential of carbodihydrazide-modified HA (HA-CDH) combined with an aldehyde-containing HA derivative to form hydrogels with enhanced hydrolytic stability, which could be attributed to resonance structure formation within the acylhydrazone bond of the hydrogels (Figure 1). The presence of multiple delocalized electron arrangements within a hydrazone bond contributes to the enhanced stability.[31] We synthesized oxidized diol-modified HA (odHA) as an aldehyde-containing HA derivative because the oxidation of the HA backbone generates an open-chain adduct that is prone to hydrolysis.[33] Initially, a diol group was introduced to the HA side chain, followed by oxidation. This mitigates the significant reduction in the molecular weight of HA during the oxidation process and prevents the rapid degradation of the resulting hydrogels.[34] Additionally, we investigated whether the enzymatic degradation of HA-CDH/odHA hydrogels could be influenced by the resonance structure formation.

Given the significance of self-healing properties in facilitating the construction of 3D structures that encapsulate cells via 3D printing, we enhanced the self-healing capability of HA-CDH/odHA hydrogels using free adipic acid dihydrazide (ADH) through competitive acylhydrazone bond formation (Figure 1). Subsequently, we comprehensively investigated the characteristics of the HA-CDH/odHA/ADH hydrogels. Furthermore, we

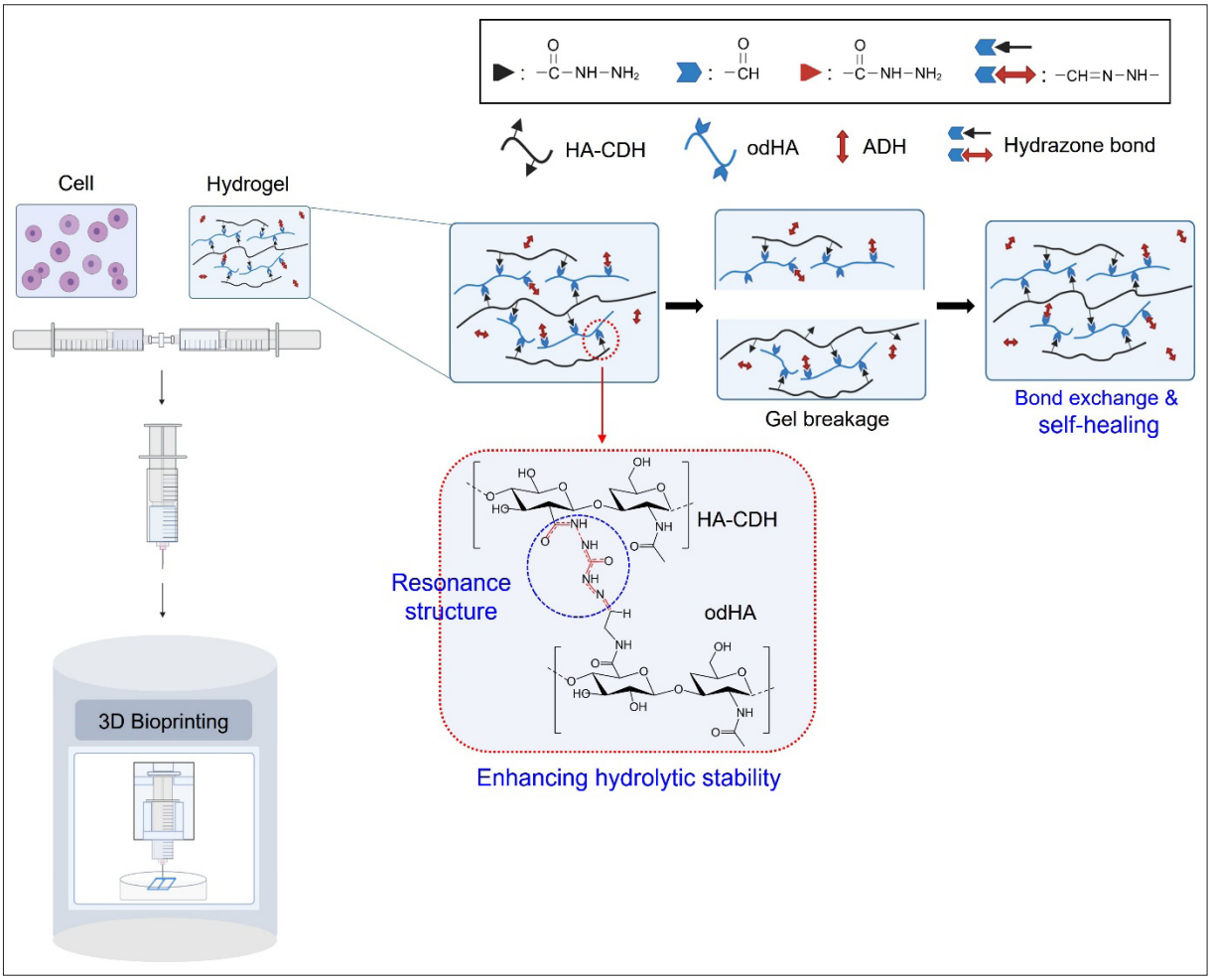

Figure 1. Schematic of 3D bioprinting of self-healing HA-CDH/odHA/ADH hydrogels with enhanced hydrolytic stability. Abbreviations: ADH, adipic acid dihydrazide; HA-CDH, carbodihydrazide-modified hyaluronic acid; odHA, oxidized diol-modified hyaluronic acid.

assessed the impact of the improved degradation and enhanced mechanical properties of the hydrogels on osteogenic and chondrogenic differentiation using *in vitro* experiments.

2. Materials and methods

2.1. Materials

Sodium hyaluronate (MW = 700 kDa) was purchased from Lifecore (Chaska, MN, USA). CDH, 3-amino-1,2-propanediol, and hyaluronidase were purchased from TCI (Tokyo, Japan). 1-Ethyl-3-(dimethylaminopropyl) carbodiimide (EDC) was purchased from Proteochem (Hurricane, UT, USA). *N*-hydroxysulfosuccinimide sodium salt (sulfo-NHS) was purchased from Covachem (Loves Park, IL, USA). Dulbecco's phosphate-buffered saline (DPBS), Dulbecco's modified Eagle's medium nutrient mixture F-12 (DMEM/F-12), minimum essential medium alpha (α-MEM), fetal bovine serum (FBS), and penicillin–streptomycin (PS) were purchased from Gibco (Grand Island, NY, USA). An EZ-Cytox kit was purchased from DoGenBio (Seoul, Korea). Alcian blue was purchased from Vector Laboratories (Newark, CA, USA), and Alizarin Red was purchased from ScienCell (Carlsbad, CA, USA). 2,4,6-Trinitrobenzene sulfonic acid (TNBSA) was purchased from Thermo Fisher Scientific (Waltham, MA, USA). 1-Hydroxybenzotriazole hydrate (HOBt), 2-(*N*-morpholino)ethanesulfonic acid (MES), ADH, and sodium chloride (NaCl) were purchased from Sigma-Aldrich (St. Louis, MO, USA). Sodium dodecyl sulfate (SDS) was purchased from Invitrogen (Waltham, MA, USA). Bovine serum albumin (BSA) was purchased from Amresco (Solon, OH, USA).

2.2. Synthesis of HA derivatives

HA-CDH was synthesized by first dissolving HA (1 g) in deionized water (0.5 wt.%) for 24 h. Then, HOBt (0.3567

g) and CDH (0.2375 g) were added to the HA solution ([HA]:[HOBt]:[CDH] = 1:1:1, molar ratio). EDC was added to the solution after 30 min ([EDC]:[CDH] = 0.1:1, molar ratio), and the pH was adjusted to 6. After 24 h, the reaction solution was dialyzed against 0.1 M NaCl, followed by additional dialysis in deionized water for 24 h (molecular weight cut-off = 3500 g/mol). The molar ratios of HA and CDH were varied ([HA]:[CDH] = 1:2 and 1:3, molar ratio) while maintaining a constant ratio between EDC and CDH ([EDC]:[CDH] = 0.1:1, molar ratio).

ADH-modified HA (HA-ADH) was also synthesized. HA was dissolved in a 0.1 M MES buffer (1 wt.%, pH 6.0), followed by reaction with ADH in the presence of EDC and sulfo-NHS for 24 h ([COOH]:[EDC]:[sulfo-NHS] = 1:0.65:0.65, molar ratio). Ethanol was used to precipitate HA-ADH, followed by lyophilization.[35]

odHA was synthesized by first dissolving HA (1 g) in deionized water (0.5 wt.%) for 24 h. Then, HOBt (0.3567 g) and 3-amino-1,2-propanediol (0.2 g) were added to the HA solution, and the pH was adjusted to 6. EDC (0.1515 g) dissolved in deionized water was added to the HA solution ([NH_2]:[HOBt]:[COOH] = 1:1:1, molar ratio) to synthesize diol-modified HA (dHA). After 24 h, the solution was dialyzed against dilute HCl (pH 3.5) containing 0.1 M NaCl for 48 h, followed by additional dialysis in deionized water for 24 h (molecular weight cut-off = 3500 g/mol) and lyophilization. The lyophilized dHA (1 g) was dissolved in deionized water for 24 h (0.5 wt.%) and partially oxidized with sodium periodate (0.56 g) for 10 min ([HA]/[$NaIO_4$] = 1:0.5, molar ratio). The reactant solution was treated with ethylene glycol (0.736 mL) to stop the oxidation reaction. The solution was dialyzed against deionized water for 48 h (molecular weight cut-off = 3500 g/mol) and lyophilized. All HA derivatives were stored at −20°C.[36]

2.3. Characterization of HA derivatives

The synthesis of the HA derivatives was verified through Fourier-transform infrared (FT-IR) spectroscopy (Nicolet6700, Thermo Fisher Scientific, Waltham, MA, USA). Samples were scanned over a wavenumber range of 600–2000 cm^{-1} (resolution = 4 cm^{-1}; scan rate = 4 mm/s). The TNBSA assay was used to quantify the degree of substitution (DS) of HA-CDH. The reaction buffer was prepared by adding sodium bicarbonate to deionized water and adjusting the pH to 8.5. Samples were dissolved in the reaction buffer (0.5 mL, 1 mg/mL), and a 0.01% TNBSA solution dissolved in the reaction buffer (0.25 mL) was added to the sample solution. Each sample was incubated at 37°C for 2 h, followed by the addition of 10% SDS (0.25 mL, 10%) and 1 N HCl (0.125 mL). The absorbance was measured at 340 nm, and the DS was calculated using BSA as the standard material. The odHA solution was treated with *t*-butyl carbazate, followed by a reaction with $NaCNBH_3$. The degree of aldehyde modification (%) of odHA was determined using ^1H nuclear magnetic resonance (NMR) spectroscopy (D_2O, VNMRS 600 MHz, Varian, Palo Alto, CA, USA).[34,35]

2.4. Determination of molecular weight

The molecular weights of HA derivatives were determined using size-exclusion chromatography with multiangle laser light scattering (SEC-MALLS). A Shimadzu system (Kyoto, Japan) equipped with a PL Aquagel-OH MIXED-H column (7.5 × 300 mm; Tosoh Bioscience, San Francisco, CA, USA), multiangle light scattering photometer, and differential refractometer (DAWN HELEOS || and Optilab Rex, Wyatt Technology, Santa Barbara, CA, USA) were used. Dextran was used as the standard polymer, and DPBS was employed as the mobile phase (flow rate: 0.5 mL/min). The dn/dc value of the HA derivatives was set as 0.167 mL/g.

2.5. Hydrogel fabrication and characterization

HA-CDH was dissolved in DPBS in the presence of free ADH for 24 h, followed by mixing with the odHA solution to form HA-CDH/odHA/ADH hydrogels. The ratio of HA-CDH to odHA was varied. HA-ADH was also used to prepare HA-ADH/odHA/ADH hydrogels. The viscoelastic properties of the hydrogels were determined using a rotational viscometer (Bohlin Gemini 150, Malvern, Worcestershire, UK; 5 Pa, 1 Hz) equipped with a parallel-plate fixture (diameter = 20 mm).

2.6. Hydrolytic stability test

Hydrogel disks (diameter = 10 mm, thickness = 1 mm) were immersed in DPBS and incubated at 37°C for 21 days. The diameter of each disk was determined using ImageJ (National Institutes of Health, USA) at predetermined time points. The changes in the dry weights of the disks were also measured after lyophilization.

2.7. Enzymatic stability test

Hydrogel disks (diameter = 10 mm, thickness = 1 mm) were immersed in DPBS containing hyaluronidase (1 μg/mL) and incubated at 37°C for 3 days. The gel disks were frozen and lyophilized before their dry weights were measured.

2.8. *In vitro* cell culture and cytotoxicity evaluation

ATDC5 cells (RIKEN Cell Bank, Tsukuba, Japan) were cultured in DMEM/F-12 supplemented with 5% FBS and 1% PS (37°C, 5% CO_2 atmosphere). MC3T3-E1 cells (RIKEN Cell Bank, Tsukuba, Japan) were cultured in α-MEM containing 10% FBS and 1% PS (37°C, 5% CO_2 atmosphere).

The *in vitro* cytotoxicity of soluble HA derivatives, sterilized using a 0.22-μm filter, was evaluated using the EZ-Cytox kit. In brief, the cells were seeded in a 96-well plate at a density of 5.0×10^3 cells/well and cultured. After 24 h of incubation, a sample solution (10 μL) was added to each well and incubated for 24 h. Then, the EZ-Cytox solution (10 μL) was added to each well and incubated for 4 h at 37°C. A spectrophotometer (SpectraMax M2e, Molecular Devices, Sunnyvale, CA, USA) was used to measure the absorbance at 450 nm. Cell viability was calculated relative to the absorbance of untreated cells.

2.9. Three-dimensional printing

An extrusion-based 3D printer (Invivo, Seoul, Korea) was used to construct various 3D structures. Hydrogels were placed in a 10 mL syringe and printed through a 25-gauge Teflon® needle (Rokit Healthcare, Seoul, Korea). The motor pressure was set as 300 N, and the infill density was fixed at 80%. The printing speed ranged from 5 to 15 mm/s. The shape fidelity of the 3D-printed cylindrical structures (diameter = 10 mm, height = 4 mm) was calculated by measuring the diameter and height after printing relative to the computer-designed structures. Various 3D structures were designed using Tinkercad (Autodesk, San Francisco, CA, USA) before printing.

The printability of the hydrogel was quantitatively assessed using a lattice structure. Square grids were printed at varying printing speeds, and the printed pore geometries were analyzed using ImageJ software. For each construct, the pore perimeter and area were measured, and the printability parameter (*Pr*) was calculated according to the following equation[37]:

$$Pr = \frac{(\text{Pore perimeter})^2}{16 \times \text{Pore area}}$$

A *Pr* value close to 1 indicates that the printed pore closely approximates an ideal square shape, whereas a value deviating from 1 reflects structural distortion.

2.10. Cell viability within hydrogel after printing

Cells (1×10^6 cells/mL) were mixed with the odHA solution and then mixed with the HA-CDH/ADH solution to form cell-encapsulated HA-CDH/odHA/ADH hydrogels. HA-CDH and odHA solutions were prepared in DPBS. The resulting cell-laden hydrogels were immediately placed in culture plates, covered with fresh medium, and incubated at 37°C in a 5% CO_2 atmosphere. The cell viability within the hydrogels before and after printing was evaluated using a live/dead assay kit (Invitrogen). Ethidium homodimer-1 (20 μL) and calcein AM (5 μL) in DPBS (10 mL) were added to the cell-encapsulating hydrogels. Confocal microscopy was used to obtain images (LSM 900, Carl Zeiss, Germany) at the Biospecimen-Multiomics Digital Bioanalysis Core Facility of Hanyang University.

2.11. *In vitro* histological analysis and gene expression

ATDC5 or MC3T3-E1 cells were encapsulated in the hydrogels at a density of 5×10^6 cells/mL and incubated at 37°C in a 5% CO_2 atmosphere for 14 days. Then, the hydrogels were embedded in a Tissue Tek® O.C.T. compound (Sakura Finetech, Torrance, CA, USA), frozen using liquid nitrogen, and cut to a thickness of 12 μm using a cryostat (Leica Biosystems, Nußloch, Germany). The hydrogel sections were stained with Alcian blue and Alizarin red for ATDC5 and MC3T3-E1 cells, respectively.

The chondrogenic differentiation of ATDC5 cells and osteogenic differentiation of MC3T3-E1 cells were quantified by means of quantitative polymerase chain reaction (PCR) analysis. The hydrogel constructs were homogenized, and RNA was retrieved using an RNAiso Plus kit (Takara, Kusatsu, Japan). The gene expression levels of SRY-box transcription factor 9 (*SOX9*), collagen type 2 (*COL2*), osteopontin (*OPN*), osteocalcin (*OCN*), and collagen type 1 (*COL1*) were quantified through comparison with that of β-actin using an ABI PRISM 7500 Real-Time PCR system (Applied Biosystems, Grand Island, NY, USA) and SensiMax SYBR (Bioline, Memphis, TN, USA).

The following primer sequences were used for ATDC5 (Cosmogenetech, Seoul, Korea): *β-actin*, (*forward*) 5′−CCCTGAACCCTAAGGCCAAC-3′, (*reverse*) 5′-GCATACAGGGACAGCACAGC-3′; *SOX-9*, (*forward*) 5′-AAGTCGGAGAGCCGAGAGCG-3′, (*reverse*) 5′-ACGAAACCG GGGCCACTTGC-3′; *COL2*, (*forward*) 5′-CACACTGGTAAGTGGGGCAAGACCG-3′, 5’-GGATTGTGTT GTTTCAGGGTTCGGG-3′.

The following primer sequences were used for MC3T3-E1 (Cosmogenetech, Seoul, Korea): *β-actin*, (*forward*) 5′-GTATCCTCGGATGTTGCTGCCTTG-3′, (*reverse*) 5′-CGCTGAGCATTGGTCCTCTTGG-3′; *OCN*, (*forward*) 5′-CGCCTACAAACGCATCTACG-3′, (*reverse*) 5′-CAGAGAGAGAGGACAGGGAGGA-3′; *COL1*, (*forward*) 5′-GACATGTTCAGCTTTGTGGACCTC-3′, (*reverse*) 5′-GGGACCCTTAGGCCATTGTGTA-3′.

2.12. Statistical analysis

All data are expressed as mean and standard deviation ($n = 4$). The Student's *t*-test was used to evaluate statistical significance. A *p*-value less than 0.05 was considered statistically significant.

3. Results and discussion

3.1. Synthesis and characterization of HA-CDH and odHA

HA-CDH was synthesized by coupling CDH with HA via carbodiimide chemistry. The hydrazide groups in HA-CDH enabled the formation of hydrazone bonds with the aldehyde group of odHA (Figure 2). The conjugation of CDH to HA was confirmed through FT-IR spectroscopy (Figure S**1**). A new peak was observed at 1710 cm^{-1} (C=O stretching), which corresponded to the formation of hydrazide groups between HA and CDH.[24,38] Various HA-CDH derivatives were synthesized by varying the amount of CDH used in the reaction with HA. The DS of CDH in HA-CDH was determined using the TNBSA assay. The theoretical and actual DS values are listed in Table 1. The conjugation efficiency was >85% for all HA-CDH derivatives used in this study. The number following HA-CDH indicates the theoretical DS. The actual DS of HA-ADH50 was determined using ^{1}H NMR spectroscopy. The peak areas of the acetamido moiety (**1**) and ADH (**3, 4**) of HA-ADH50 (Figure S2) were integrated to calculate the DS, which was found to be 46%.

The presence of aldehyde groups in odHA was confirmed using FT-IR spectroscopy (Figure S1). A clear peak was observed at 1730 cm^{-1} (C=O stretching, aldehyde).[39] The degree of aldehyde modification of odHA was determined to be 20% using ^{1}H NMR spectroscopy. The peak areas of the acetamido (**1**) and *t*-butyl (**2**) moieties of odHA in ^{1}H NMR spectra were integrated to calculate the number of aldehyde groups present (Figure S2). The molecular weight of odHA, as determined by SEC-MALLS, showed no significant decrease compared with that of intact HA. This indicated that the HA backbone was maintained during oxidation. This is in contrast to the oxidation of C2–C3 diols in the pyranose ring of HA, which typically leads to a reduction in the molecular weight. The molecular weights of HA-CDH are listed in Table 2. No significant changes in the molecular weights were observed for most types of HA-CDH, except for HA-CDH30.

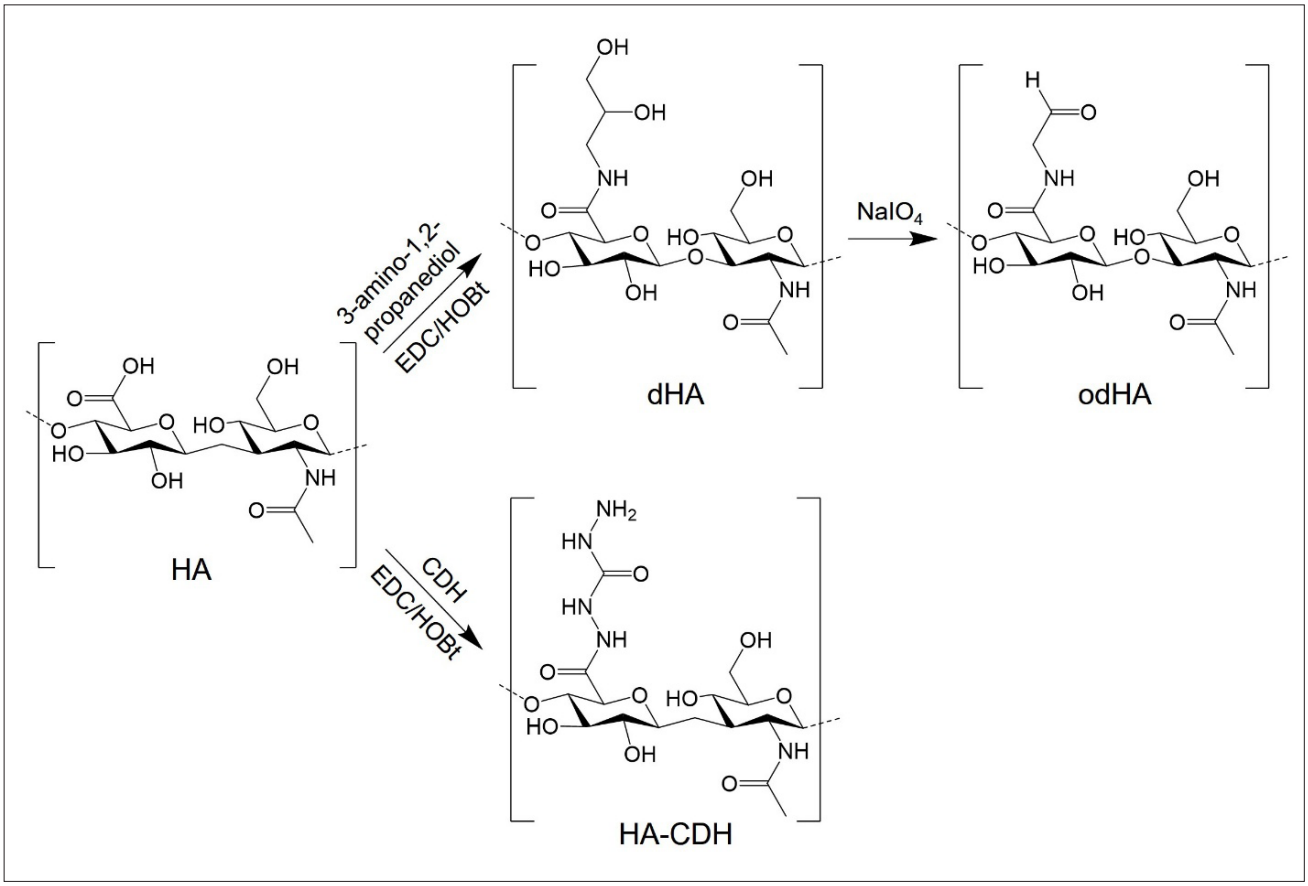

Figure 2. Chemical structures of HA, dHA, odHA, and HA-CDH. Abbreviations: CDH, carbodihydrazide; dHA, diol-modified hyaluronic acid; EDC, 1-ethyl-3-(dimethylaminopropyl) carbodiimide; HA: hyaluronic acid; HA-CDH, carbodihydrazide-modified hyaluronic acid; HOBt, 1-hydroxybenzotriazole hydrate; odHA, oxidized diol-modified hyaluronic acid.

Table 1. Conjugation efficiency and theoretical DS of HA-CDH

Sample[a]	Theoretical DS (%)	Actual DS (%)	Conjugation efficiency (%)
HA-CDH10	10	8.6	86.4
HA-CDH20	20	18.7	93.7
HA-CDH30	30	25.4	84.9

Note: [a]The number after the term 'HA-CDH' indicates the theoretical DS value.

Abbreviations: DS, degree of substitution; HA-CDH, carbodihydrazide-modified hyaluronic acid.

Table 2. Molecular weights of HA derivatives used in this study

Sample	M_w[a] (g/mol)
HA	5.0×10^5
HA-CDH10	5.7×10^5
HA-CDH20	5.7×10^5
HA-CDH30	7.1×10^5
HA-ADH50	5.8×10^5
odHA	4.6×10^5

Note: [a]Weight-average molecular weight determined via SEC-MALLS measurements.

Abbreviations: HA, hyaluronic acid; HA-CDH, carbodihydrazide-modified hyaluronic acid; M_w, molecular weight; odHA, oxidized diol-modified hyaluronic acid; SEC-MALLS, size-exclusion chromatography with multiangle laser light scattering.

The cytotoxicity of the HA-CDH and odHA solutions was evaluated *in vitro* using ATDC5 and MC3T3-E1 cells (Figure S3). The viability of MC3T3-E1 cells was not significantly affected by treatment with the soluble forms of HA-CDH and odHA. However, the number of ATDC5 cells treated with high concentrations of HA-CDH30 was slightly reduced. This suggested that the component polymers of the hydrogels were not cytotoxic. However, high concentrations of certain derivatives, such as HA-CDH30, might have adversely affected specific cell types. Free ADH also did not significantly affect the cytotoxicity.[40]

3.2. Preparation and characterization of hydrogels

The solutions of HA-CDH and odHA in DPBS were thoroughly mixed at room temperature to form hydrogels. An increase in the DS of CDH in HA-CDH enhanced the storage shear modulus (G′) values of the HA-CDH/odHA hydrogels at the same polymer concentration ([HA-CDH] = 1.5 wt.%, [odHA] = 1.0 wt.%). Although the HA-CDH30/odHA hydrogel exhibited the highest value of G′ (Figure 3A), inhomogeneous gel formation was observed. Furthermore, complete dissolution was not achieved when HA-CDH was dissolved in DPBS at 2 wt.%, regardless of the DS. As a result, HA-CDH20 at 1.5 wt.% was selected and used for further experiments because of homogeneous gel-forming capability. The concentration of odHA also influenced gel formation and the resultant viscoelastic properties of the gel. The value of G′ for the HA-CDH20/odHA hydrogels increased with the odHA concentration at [HA-CDH20] = 1.5 wt.% (Figure 3B). However, rapid gelation prevented complete hydrogel formation at [odHA] = 1.5 wt.%. Thus, [odHA] = 1 wt.% was employed for further gel preparation.

Although the hydrazone bond in the HA-CDH20/odHA hydrogel was reversible, it did not exhibit self-healing behavior. To address this, free ADH was added to the hydrogel to induce competitive hydrazone bond formation with the bond between HA-CDH and odHA. The minimum concentration of free ADH required for the self-healing of the HA-CDH20/odHA hydrogel was determined to be 0.1 wt.%, as confirmed by rotational viscometer measurements (data not shown). However, the value of G′ for the HA-CDH20/odHA hydrogel decreased as the ADH concentration in the gel increased (Figure 3C). Therefore, [ADH] = 0.1 wt.% was used to prepare the self-healing HA-CDH20/odHA/ADH hydrogel.

Hydrogels were also prepared using HA-ADH50 as the conventional hydrazone-based dynamic hydrogels, which had a DS similar to that of HA-CDH20. The value of G′ for the HA-CDH20/odHA/ADH hydrogel was considerably higher than that for the HA-ADH50/odHA/ADH hydrogel (Figure 3D). HA-ADH50 was synthesized as previously reported and used to form hydrogels (Figure S4).[34,35] HA-ADH with varying degrees of hydrazide substitution was synthesized and crosslinked with oxidized HA to form self-healing hydrogels, which showed potential for 3D bioprinting. However, these hydrogels exhibited rapid degradation under physiological conditions. To address this limitation, we designed HA-CDH-based hydrogels with improved resistance to degradation.

HA can be chemically tailored by introducing complementary aldehyde and hydrazide moieties, which are crosslinked through hydrazone bond formation. Incorporation of these reactive groups onto the polymer backbone generates sites for covalent bonding, thereby affecting both the rate of crosslinking and the stability of the resulting network. Reaction kinetics are typically

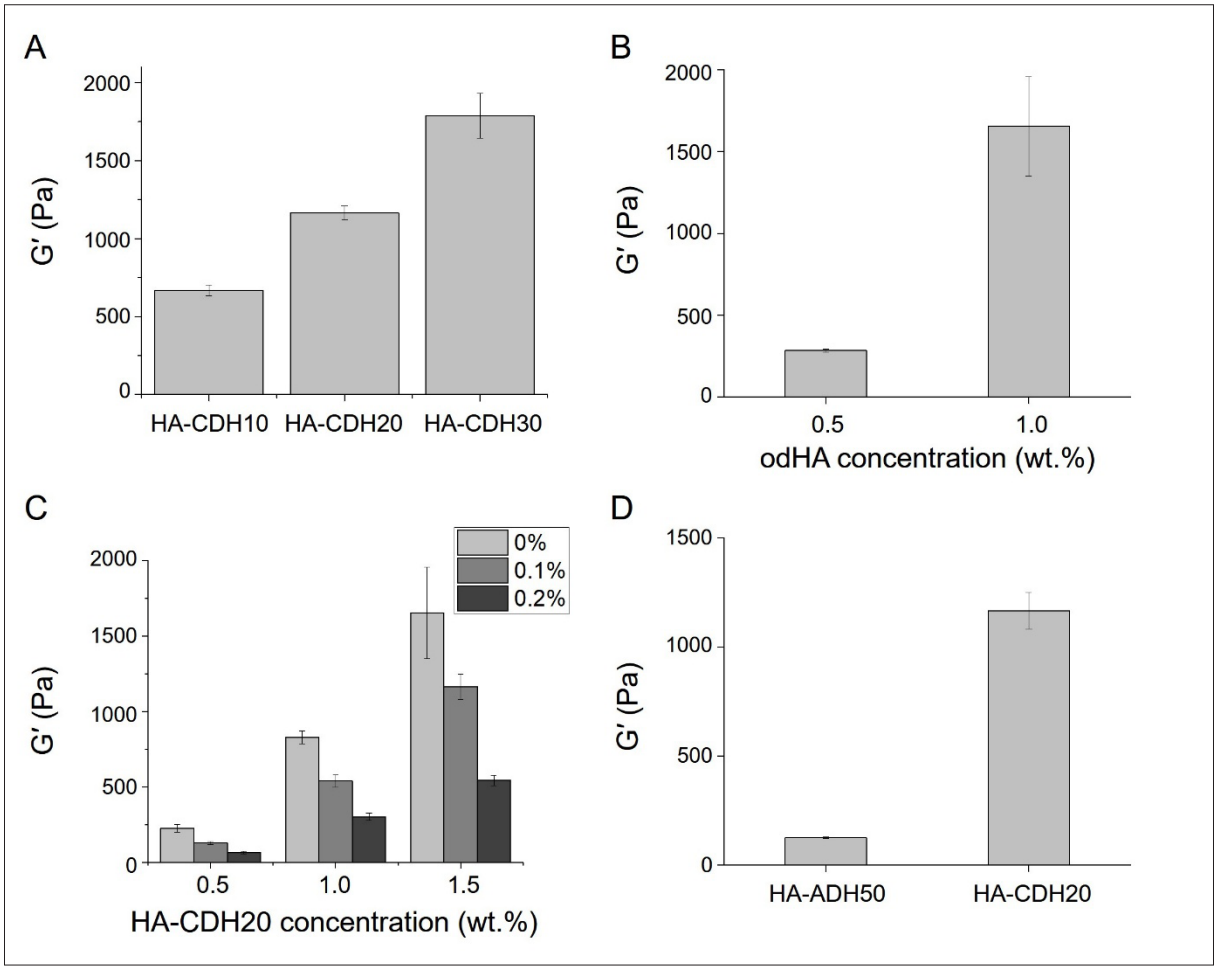

Figure 3. Viscoelastic properties of hydrogels. (A) Storage shear modulus (G′) of HA-CDH/odHA hydrogels prepared using various types of HA-CDH ([HA-CDH] = 1.5 wt.%, [odHA] = 1.0 wt.%). (B) Values of G′for HA-CDH20/odHA hydrogels at different odHA concentrations ([HA-CDH20] = 1.5 wt.%). (C) Values of G′ for HA-CDH20/odHA/ADH hydrogels containing different amounts of HA-CDH20 and ADH ([odHA] = 1.0 wt.%). (D) Values of G′ for hydrogels containing either HA-ADH50 or HA-CDH20 ([HA-ADH50] = 1.5 wt.%, [HA-CDH20] = 1.5 wt.%, [odHA] = 1 wt.%, [ADH] = 0.1 wt.%). Abbreviations: ADH, adipic acid dihydrazide; HA-ADH, adipic acid dihydrazide-modified hyaluronic acid; HA-CDH, carbodihydrazide-modified hyaluronic acid; odHA, oxidized diol-modified hyaluronic acid.

accelerated when the density of functional groups is high or when catalytic agents are present. The structural characteristics of the polymer backbone—including chain length and the presence of other substituents—also influence functional group reactivity, network density, and ultimately the mechanical strength and dynamic behavior of the hydrogel.[30] Moreover, the valency of the crosslinker is another critical factor; for instance, shifting from a divalent to a tetravalent crosslinker has been shown to move the strain-stiffening response into biologically relevant ranges.[41]

3.3. Self-healing properties of hydrogels

The self-healing behavior of the HA-CDH20/odHA/ADH hydrogel was confirmed macroscopically. When the gel was deliberately broken into two pieces and subsequently reattached, the cracks disappeared within 30 min (Figure 4A). This self-healing property was validated using a rotational viscometer. An amplitude sweep was performed to determine the gel flow point (157% strain), which was defined as the intersection point of G′ and G″; this point indicated gel breakage (Figure 4B). During repeated cycles of strain variation from 1% to 500%, G″ became higher than G′ at 500% strain because of gel breakage. However, G′ increased again when strain was reduced to 1%, demonstrating the self-healing properties of the hydrogel (Figure 4C).

Self-healing was achieved through the competitive reaction of free ADH and CDH in HA-CDH, both of which contained the dihydrazide group, with odHA. This resulted in the formation of reversible and dynamic

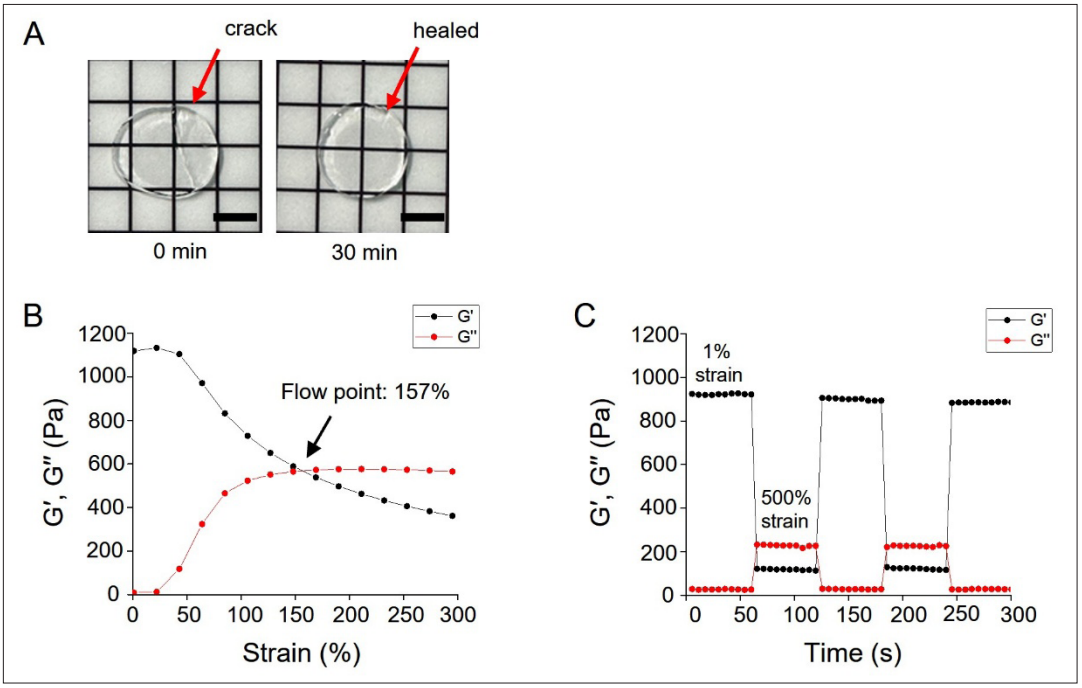

Figure 4. Self-healing properties of hydrogels. (A) Self-healing behavior of HA-CDH20/odHA/ADH hydrogel. The arrows indicate the location of the deliberately induced crack, which self-heals after 30 min (scale bar: 5 mm). (B) Amplitude sweep to determine the flow point of HA-CDH20/odHA/ADH hydrogel and (C) repeated self-healing behavior of the hydrogel ([HA-CDH20] = 1.5 wt.%, [odHA] = 1 wt.%, [ADH] = 0.1 wt.%). Abbreviations: ADH, adipic acid dihydrazide; HA-CDH, carbodihydrazide-modified hyaluronic acid; odHA, oxidized diol-modified hyaluronic acid.

hydrazone bonds. This self-healing property is crucial for the extrusion-based 3D printing of hydrogels as bioinks because it enables the hydrogels to retain their integrated morphology without any additional treatment after printing.[20,42] Without free ADH, the self-healing of HA-CDH/odHA hydrogels was incomplete, with a recovery rate of approximately 75%, making them unsuitable for extrusion-type 3D printing. Importantly, essential requirements for bioinks include shear-thinning behavior, self-healing ability, and rapid recovery of a gel state ($G' > G''$) after extrusion.[43]

3.4. Enhanced hydrolytic stability of hydrogels

The hydrolytic stability of the HA-CDH/odHA/ADH hydrogels was investigated. Hydrogel disks were immersed in DPBS and incubated at 37°C, and the changes in the gel disk diameter were monitored for 21 days. The HA-CDH20/odHA/ADH hydrogel maintained its stability for 21 days. In contrast, the HA-ADH50/odHA/ADH hydrogel rapidly lost its integrity and completely disintegrated within 3 days, even though it contained the same number of aldehyde and hydrazide groups (Figure 5A). The enhanced stability of the HA-CDH20/odHA/ADH hydrogel was attributed to the ability of CDH to form resonance structures when bound to an aldehyde group.[27] Resonance structures were formed when HA-CDH was mixed with odHA, which increased the stability of the hydrogel against hydrolysis (Figure 5B). The presence of multiple delocalized electron arrangements within the hydrazone compound contributed to the enhanced stability. These HA-CDH20/odHA/ADH hydrogels retained their self-healing properties during degradation, indicating preservation of dynamic hydrazone bonds during the process.

In contrast, the HA-ADH50/odHA/ADH hydrogel lacked the resonance structure formation between HA-ADH50 and odHA, leading to rapid disintegration. This was because the hydrocarbon groups in the middle impeded electron movement, thus preventing the formation of resonance structures (Figure S5). The changes in the weights of the hydrogel disks were monitored over time. The HA-ADH50/odHA/ADH hydrogel rapidly lost weight in DPBS at 37°C. In contrast, the HA-CDH/odHA/ADH hydrogel maintained its weight over time (Figure S6).

It should be noted that the HA-CDH20/odHA/ADH hydrogel was degraded by hyaluronidase (Figure 5C). HA was cleaved by hyaluronidase into smaller oligosaccharide fragments,[44] and the HA-CDH20/odHA/ADH hydrogel was similarly degraded by hyaluronidase. This finding clearly indicated that the introduction of CDH into HA contributed solely to the hydrolytic stability of the resultant

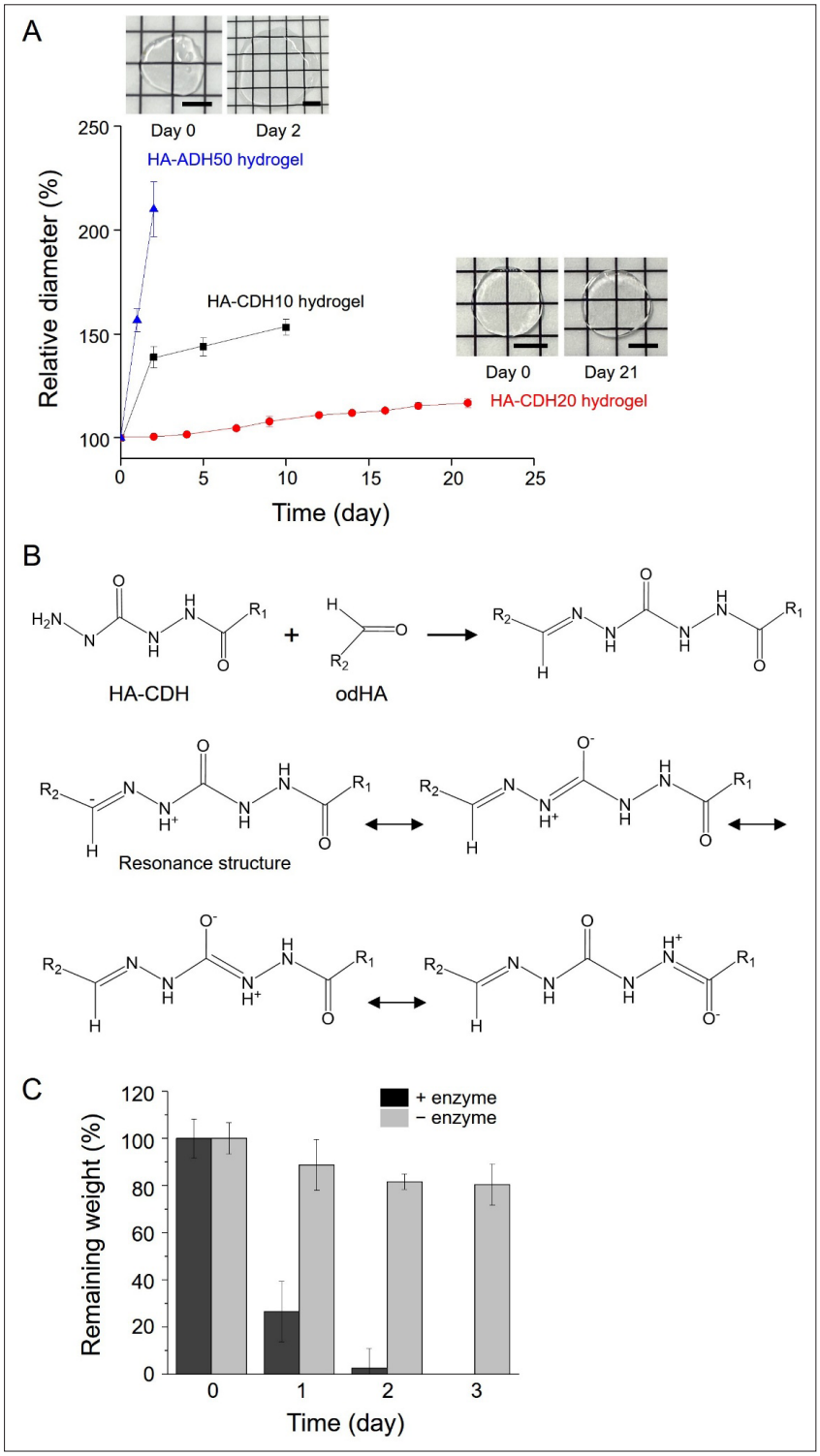

Figure 5. Degradation behavior of hydrogels. (A) Changes in the diameters of various hydrogel disks incubated at 37°C in DPBS over time, as compared with the initial diameters before incubation. Representative images of HA-CDH20/odHA/ADH and HA-ADH50/odHA/ADH hydrogels are included. (B) Possible resonance structures of the hydrazone bond formed between HA-CDH and odHA. (C) Changes in the remaining weights of HA-CDH20/odHA/ADH hydrogels incubated at 37°C in DPBS over time in the presence and absence of hyaluronidase. The remaining dry weight is compared with that before incubation ([HA-CDH20] = 1.5 wt.%, [odHA] = 1 wt.%, [ADH] = 0.1 wt.%, [hyaluronidase] = 1 μg/mL). Abbreviations: ADH, adipic acid dihydrazide; DPBS, Dulbecco's phosphate-buffered saline; HA-ADH, adipic acid dihydrazide-modified hyaluronic acid; HA-CDH, carbodihydrazide-modified hyaluronic acid; odHA, oxidized diol-modified hyaluronic acid.

HA-CDH/odHA/ADH hydrogels and did not interfere with their enzymatic degradability.

It is critical to control the hydrolytic stability of hydrogels because tissue scaffolds must maintain their mechanical integrity to match the rate of tissue regeneration, which varies depending on the tissue type. Conventional self-healing hydrogels are prone to hydrolytic degradation owing to reversible crosslinking. However, HA-CDH prevents the rapid degradation observed in HA-based self-healing hydrogels, which typically employ reversible hydrazone bonds.

3.5. Three-dimensional printing

An extrusion-based 3D printer was used to test the printing capability of the HA-CDH20/odHA/ADH hydrogel. The self-healing capability of the hydrogel allowed for extrusion-based 3D printing because the hydrogel retained its integrated morphology after printing without any additional process. The optimum printing speed was determined by assessing filament diameter, printability, and shape fidelity. As the printing speed increased, the filament diameter significantly decreased. The printed filament maintained an appropriate linear shape at printing speeds of 5 and 10 mm/s. However, the filament occasionally broke along its length at 15 mm/s (Figure 6A).

The printability of the hydrogel was quantitatively evaluated at varying printing speeds. The morphology of the printed lattice pores remained generally consistent across conditions, though minor deviations were noted. At 5 and 10 mm/s, the *Pr* values were close to 1, indicating good preservation of the designed square geometry. In contrast, the *Pr* value decreased slightly at 15 mm/s,

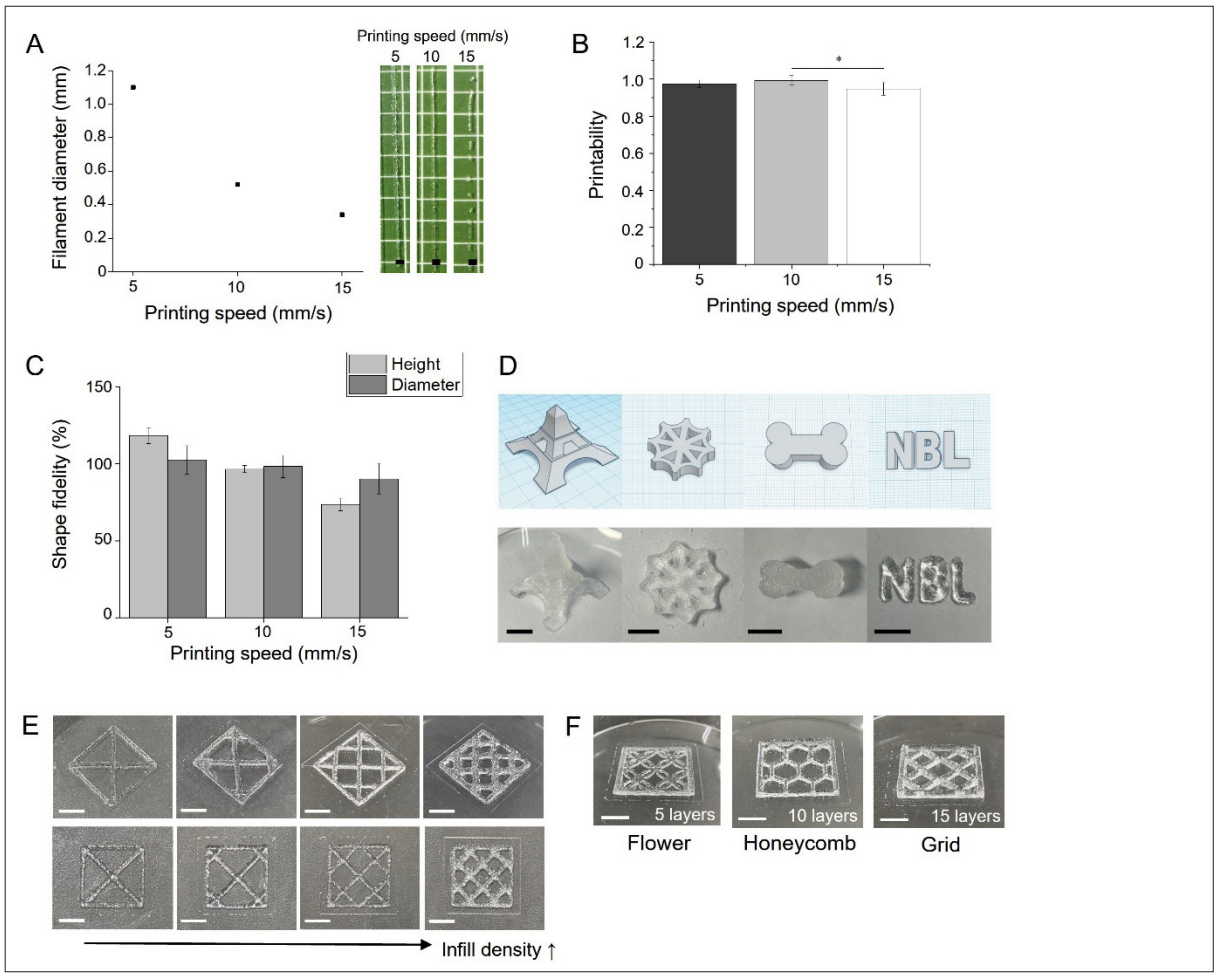

Figure 6. Three-dimensional printing of hydrogels. (A–C) Effects of printing speed on filament diameter (scale bar: 2 mm) (A), printability (B), and shape fidelity (C) for 3D printing using HA-CDH20/odHA/ADH ([HA-CDH20] = 1.5 wt.%, [odHA] = 1 wt.%, [ADH] = 0.1 wt.%; $^*p < 0.05$). (D) Various 3D structures printed using HA-CDH20/odHA/ADH hydrogel (scale bar: 10 mm). (E and F) Changes in infill density (E) and infill pattern (F) of 3D-printed constructs (scale bar: 10 mm). Abbreviations: ADH, adipic acid dihydrazide; HA-CDH, carbodihydrazide-modified hyaluronic acid; odHA, oxidized diol-modified hyaluronic acid.

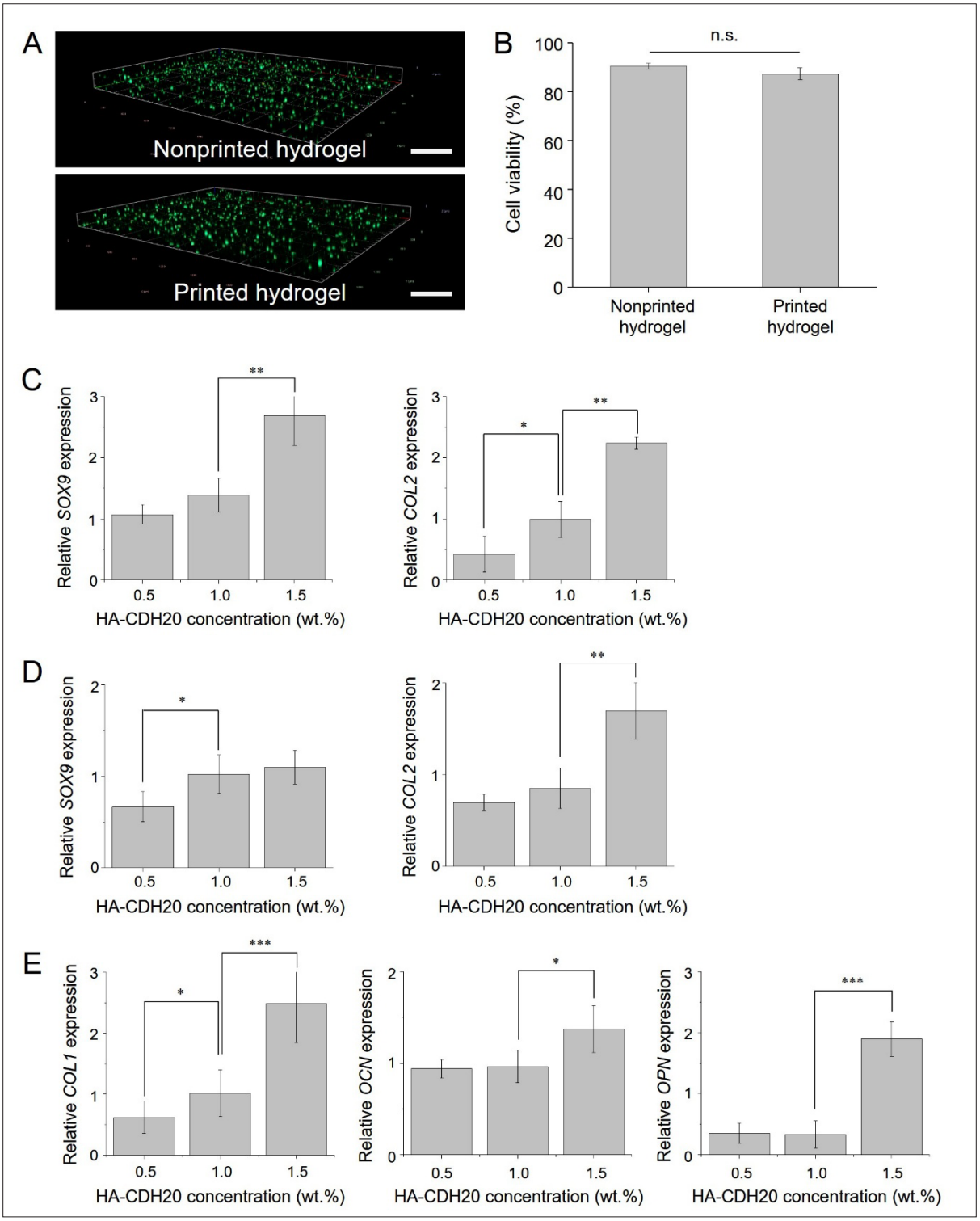

Figure 7. Cell viability and differentiation in hydrogels. (A and B) Confocal microscopy images of HA-CDH20/odHA/ADH hydrogels encapsulating ATDC5 cells after 24 h of culture (A) and their quantitative results (scale bar: 500 μm; n.s.: no statistical significance) (B). (C and D) Quantitative analysis performed on gene expression levels of ATDC5 cells cultured for 7 days (C) and 14 days (D) within HA-CDH20/odHA/ADH hydrogels prepared using various HA-CDH20 concentrations. (E) Quantitative gene expression levels of MC3T3-E1 cells cultured within HA-CDH20/odHA/ADH hydrogels for 14 days (*$p < 0.05$, **$p < 0.01$, ***$p < 0.001$). Abbreviations: ADH, adipic acid dihydrazide; HA-CDH, carbodihydrazide-modified hyaluronic acid; odHA, oxidized diol-modified hyaluronic acid.

reflecting reduced geometric fidelity at higher speeds (Figures 6B and S7).

The shape fidelity was tested by printing a gel disk with a diameter of 10 mm and a height of 4 mm and assessing the accuracy of reproducing these dimensions (Figure 6C). The diameter was close to that of the original design at printing speeds of 5 and 10 mm/s. However, at 5 mm/s, the height increased owing to filament accumulation at a single location. In contrast, the diameter and height of the printed constructs slightly decreased at 15 mm/s. Based on these results, a printing speed of 10 mm/s was selected for further experiments, as it produces lattices with uniform pore geometry, sharp corners, and well-aligned strands.

Various shapes of 3D constructs were designed and printed (Figure 6D). Additionally, adjustable infill density and various infill patterns of 3D-printed constructs were achieved at the optimized printing speed (Figure 6E and F).

3.6. *In vitro* cell differentiation within 3D constructs

Cell viability within the 3D-printed constructs was evaluated. 3D structures encapsulating ATDC5 cells were printed, and their viability was assessed using confocal microscopy (Figure 7A). No significant cytotoxicity was observed within the printed and nonprinted hydrogels 24 h after printing (Figure 7B). This suggested that 3D bioprinting with the HA-CDH20/odHA/ADH hydrogel did not significantly influence cell viability during the printing process and could be a suitable method for fabricating 3D constructs containing cells.

Cellular differentiation is generally affected by matrix stiffness.[45–47] To test the effect of the hydrogel stiffness on chondrogenic and osteogenic differentiation, HA-CDH20/odHA/ADH hydrogels with various HA-CDH20 concentrations ([HA-CDH20] = 0.5–1.5 wt.%) were used to encapsulate either ATDC5 or MC3T3-E1 cells. The chondrogenic differentiation of ATDC5 cells was investigated by quantifying the expression levels of *SOX9* and *COL2* as representative marker genes on days 7 (Figure 7C) and 14 (Figure 7D) after incubation. The osteogenic differentiation of MC3T3-E1 cells was also assessed by quantifying the expression levels of *OCN*, *OPN*, and *COL1* as representative marker genes on day 14 after incubation (Figure 7E). The chondrogenic and osteogenic differentiation of cells were affected by the gel stiffness of the HA-CDH20/odHA/ADH hydrogels induced by varying the HA-CDH20 concentration. The gene expression levels were significantly higher when cells were encapsulated and cultured within HA-CDH20/odHA/ADH hydrogels at [HA-CDH20] = 1.5 wt.% as compared with other groups. This was attributed to the enhanced gel stiffness (Figure 3C). Additionally, the hydrogel sections stained with Alcian blue and Alizarin red supported the pronounced differentiation of ATDC5 or MC3T3-E1 cells cultured within the HA-CDH20/odHA/ADH hydrogels at [HA-CDH20] = 1.5 wt.% (Figure S8).

Matrix stiffness generally controls the cell phenotype, including cell differentiation.[24,45] Thus, hydrogel stiffness significantly influences cell phenotype in tissue engineering approaches. Hydrogel stiffness is typically regulated by controlling the crosslinking density. In this study, the DS of HA-CDH and the concentrations of HA-CDH and odHA in the hydrogels were varied to change the crosslinking density and mechanical stiffness of the resultant gels. Hydrogels should maintain their stiffness and integrity for the required time and ideally match the rate of tissue formation during tissue regeneration. Hydrogel degradation can also be affected by the crosslinking density. However, crosslinking between the hydrazide-modified and aldehyde polymers results in hydrolysable hydrazone bonds in the gel network. The use of CDH in this study significantly reduced the hydrolytic degradation of the HA-CDH/odHA hydrogels owing to the formation of a resonance structure between the crosslinks. This approach of controlling gel stiffness and degradation rate while maintaining self-healing features can be widely utilized for the 3D bioprinting of complex tissue constructs in various tissue engineering applications.

4. Conclusion

In the present study, we demonstrated that: (i) tunable mechanical stiffness can be achieved through controlled CDH substitution and polymer composition; (ii) hydrolytic stability can be significantly enhanced without compromising enzymatic degradability; and (iii) successful fabrication of cell-laden constructs can support both chondrogenic and osteogenic differentiation. HA-based hydrogels with improved mechanical properties and degradation behaviors were successfully synthesized in this study. The combination of HA-CDH and odHA enhanced the hydrolytic stability of the resulting hydrogels, and the addition of free ADH conferred effective self-healing properties to the gels. These hydrogels with tailored DS and polymer concentration could simultaneously achieve slow degradation via CDH-mediated resonance stabilization and robust self-healing properties, which were suitable for extrusion-based 3D printing under optimal conditions. This study also highlighted the influence of enhanced mechanical stiffness on *in vitro* cell differentiation, suggesting the potential of these hydrogels for tissue engineering applications, particularly in cartilage and bone regeneration. These findings address

the limitations associated with the stability and mechanical properties of natural polysaccharide-based hydrogels. In addition, integrating these hydrogels with advanced bioprinting strategies, such as multi-material printing or integration with vascularization approaches, could further accelerate their translational potential in regenerative medicine. Overall, this platform lays the groundwork for the development of next-generation bioinks designed for personalized tissue engineering applications.

Acknowledgments

None.

Funding

This study was supported by the National Research Foundation of Korea (NRF) grant funded by the Korean Government (MSIT) (RS-2024-00355200).

Conflict of interest

The authors declare they have no competing interests.

Author contributions

Conceptualization: Minhyung Kong, Kuen Yong Lee
Investigation: Minhyung Kong, Hyun Seung Kim, In Young Lee
Methodology: Minhyung Kong, Jiwon Hwang, Joon Seo Park
Writing–original draft: Minhyung Kong
Writing–review & editing: Kuen Yong Lee

Ethical approval and consent to participate

Not applicable.

Consent for publication

Not applicable.

Availability of data

Data are available from the corresponding author upon reasonable request.

References

1. Ahmed EM. Hydrogel: preparation, characterization, and applications: a review. *J Adv Res.* 2015;6(2):105-121. doi:10.1016/j.jare.2013.07.006.

2. Zhu T, Mao J, Cheng Y, *et al.* Recent progress of polysaccharide-based hydrogel interfaces for wound healing and tissue engineering. *Adv Mater Interfaces.* 2019;6(17):1900761. doi:10.1002/admi.201900761.

3. Kopecek J. Hydrogel biomaterials: a smart future? *Biomaterials.* 2007;28(34):5185-5192. doi:10.1016/j.biomaterials.2007.07.044.

4. Lee KY, Mooney DJ. Hydrogels for tissue engineering. *Chem Rev.* 2001;101(7):1869-1880. doi:10.1021/cr000108x.

5. Drury JL, Mooney DJ. Hydrogels for tissue engineering: scaffold design variables and applications. *Biomaterials.* 2003;24(24):4337-4351. doi:10.1016/s0142-9612(03)00340-5.

6. Li Z, Lin Z. Recent advances in polysaccharide-based hydrogels for synthesis and applications. *Aggregate.* 2021;2(2):e21. doi:10.1002/agt2.21.

7. Zhang H, Shi LWE, Zhou J. Recent developments of polysaccharide-based double-network hydrogels. *J Polym Sci.* 2022;61(1):7-43. doi:10.1002/pol.20220510.

8. Chen Q, Chen H, Zhu L, Zheng J. Fundamentals of double network hydrogels. *J Mater Chem B.* 2015;3(18):3654-3676. doi:10.1039/c5tb00123d.

9. Gaharwar AK, Peppas NA, Khademhosseini A. Nanocomposite hydrogels for biomedical applications. *Biotechnol Bioeng.* 2014;111(3):441-453. doi:10.1002/bit.25160.

10. Gomes ME, Rodrigues MT, Domingues RMA, Reis, RL. Tissue engineering and regenerative medicine: new trends and directions—a year in review. *Tissue Eng Part B Rev.* 2017;23(3):211-224. doi:10.1089/ten.TEB.2017.0081.

11. Liu C, Xu N, Zong Q, Yu J, Zhang P. Hydrogel prepared by 3D printing technology and its applications in the medical field. *Colloid Interface Sci Commun.* 2021;44:100498. doi:10.1016/j.colcom.2021.100498.

12. Bose S, Vahabzadeh S, Bandyopadhyay A. Bone tissue engineering using 3D printing. *Mater Today.* 2013;16(12):496-504. doi:10.1016/j.mattod.2013.11.017.

13. Li J, Wu C, Chu PK, Gelinsky M. 3D printing of hydrogels: rational design strategies and emerging biomedical applications. *Mater Sci Eng R Rep.* 2020;140:100543. doi:10.1016/j.mser.2020.100543.

14. Mani MP, Sadia M, Jaganathan SK, *et al.* A review on 3D printing in tissue engineering applications. *J Polym Eng.* 2022;42(3):243-265. doi:10.1515/polyeng-2021-0059.

15. Kirchmajer DM, Gorkin Iii R, in het Panhuis M. An overview of the suitability of hydrogel-forming polymers for extrusion-based 3D-printing. *J Mater Chem B.* 2015;3(20):4105-4117. doi:10.1039/c5tb00393h.

16. Xu W, Jambhulkar S, Zhu Y, *et al*. 3D printing for polymer/particle-based processing: a review. *Compos B Eng.* 2021;223:109102. doi:10.1016/j.compositesb.2021.109102.

17. Wei J, Wang J, Su S, *et al*. 3D printing of an extremely tough hydrogel. *RSC Adv.* 2015;5 (99):81324-81329. doi:10.1039/c5ra16362e.

18. Xu C, Dai G, Hong Y. Recent advances in high-strength and elastic hydrogels for 3D printing in biomedical applications. *Acta Biomater.* 2019;95:50-59. doi:10.1016/j.actbio.2019.05.032.

19. Jiang Z, Diggle B, Tan ML, Viktorova J, Bennett CW, Connal LA. Extrusion 3D printing of polymeric materials with advanced properties. *Adv Sci.* 2020;7(17):2001379. doi:10.1002/advs.202001379.

20. Díaz A, Herrada-Manchón H, Nunes J, *et al*. 3D printable dynamic hydrogel: as simple as it gets! *Macromol Rapid Commun.* 2022;43(21):2200449. doi:10.1002/marc.202200449.

21. Zhu Z, Wang Y-M, Yang J, Luo X-S. Hyaluronic acid: a versatile biomaterial in tissue engineering. *Plast Aesthetic Res.* 2017;4(12):219-227. doi:10.20517/2347-9264.2017.71.

22. Nair S, Remya NS, Remya S, Nair PD. A biodegradable in situ injectable hydrogel based on chitosan and oxidized hyaluronic acid for tissue engineering applications. *Carbohydr Polym.* 2011;85(4):838-844. doi:10.1016/j.carbpol.2011.04.004.

23. Jeon O, Song SJ, Lee K-J, *et al*. Mechanical properties and degradation behaviors of hyaluronic acid hydrogels cross-linked at various cross-linking densities. *Carbohydr Polym.* 2007;70(3):251-257. doi:10.1016/j.carbpol.2007.04.002.

24. Kim HS, Kim C, Lee KY. Three-dimensional bioprinting of polysaccharide-based self-healing hydrogels with dual cross-linking. *J Biomed Mater Res A.* 2022;110(4):761-772. doi:10.1002/jbm.a.37325.

25. Ouyang L, Highley CB, Rodell CB, Sun W, Burdick JA. 3D printing of shear-thinning hyaluronic acid hydrogels with secondary cross-linking. *ACS Biomater Sci Eng.* 2016;2(10):1743-1751. doi:10.1021/acsbiomaterials.6b00158.

26. Liu S, Liu X, Ren Y, *et al*. Mussel-inspired dual-cross-linking hyaluronic acid/epsilon-polylysine hydrogel with self-healing and antibacterial properties for wound healing. *ACS Appl Mater Interfaces.* 2020;12(25):27876-27888. doi:10.1021/acsami.0c00782.

27. Kim SW, Kim DY, Roh HH, Kim HS, Lee JW, Lee KY. Three-dimensional bioprinting of cell-laden constructs using polysaccharide-based self-healing hydrogels. *Biomacromolecules.* 2019;20(5):1860-1866. doi:10.1021/acs.biomac.8b01589.

28. Koivusalo L, Karvinen J, Sorsa E, *et al*. Hydrazone crosslinked hyaluronan-based hydrogels for therapeutic delivery of adipose stem cells to treat corneal defects. *Mater Sci Eng C.* 2018;85:68-78. doi:10.1016/j.msec.2017.12.013.

29. Jiang Y, Chen J, Deng C, Suuronen EJ, Zhong Z. Click hydrogels, microgels and nanogels: emerging platforms for drug delivery and tissue engineering. *Biomaterials.* 2014;35(18):4969-4985. doi:10.1016/j.biomaterials.2014.03.001

30. Ramimoghadam D, Eyckens DJ, Evans RA, Moad G, Holmes S, Simons R. Towards sustainable materials: a review of acylhydrazone chemistry for reversible polymers. *Chem Eur J.* 2024;30(49):e202401728. doi:10.1002/chem.202401728.

31. Hozumi T, Kageyama T, Ohta S, Fukuda J, Ito T. Injectable hydrogel with slow degradability composed of gelatin and hyaluronic acid cross-linked by Schiff's base formation. *Biomacromolecules.* 2018;19(2):288-297. doi:10.1021/acs.biomac.7b01133.

32. Oommen OP, Wang S, Kisiel M, Sloff M, Hilborn J, Varghese OP. Smart design of stable extracellular matrix mimetic hydrogel: synthesis, characterization, and in vitro and in vivo evaluation for tissue engineering. *Adv Funct Mater.* 2013;23(10):1273-1280. doi:10.1002/adfm.201201698.

33. Jeon O, Alt DS, Ahmed SM, Alsberg E. The effect of oxidation on the degradation of photocrosslinkable alginate hydrogels. *Biomaterials.* 2012;33(13):3503-3514. doi:10.1016/j.biomaterials.2012.01.041.

34. Kim HS, Kim JS, Hwang J, Lee IY, Lee KY. Decoupling stiffness and toughness of self-healing hydrogels for complex tissue regeneration via 3D bioprinting. *Chem Eng J.* 2024;487:150551. doi:10.1016/j.cej.2024.150551.

35. Mun CU, Kim HS, Kong M, Lee KY. Three-dimensional printing of hyaluronate-based self-healing ferrogel with enhanced stretchability. *Colloids Surf B Biointerfaces.* 2023;221:113004. doi:10.1016/j.colsurfb.2022.113004.

36. Wang S, Oommen OP, Yan H, Varghese OP. Mild and efficient strategy for site-selective aldehyde modification of glycosaminoglycans: tailoring hydrogels with tunable release of growth factor. *Biomacromolecules.* 2013;14(7):2427-2432. doi:10.1021/bm400612h.

37. Kafili G, Tamjid E, Simchi A. The impact of mechanical tuning on the printability of decellularized amniotic membrane bioinks for cell-laden bioprinting of soft tissue constructs. *Sci Rep.* 2024;14(1):29697. doi:10.1038/s41598-024-80973-3.

38. Kim JK, Srinivasan P, Kim JH, *et al*. Structural and antioxidant properties of gamma irradiated hyaluronic acid. *Food Chem.* 2008;109(4):763-770.

doi:10.1016/j.foodchem.2008.01.038.

39. Fan QG, Lewis DM, Tapley KN. Characterization of cellulose aldehyde using Fourier transform infrared spectroscopy. *J Appl Polym Sci.* 2001;82(5):1195-1202. doi:10.1002/app.1953.

40. Roh HH, Kim HS, Kim C, Lee KY. 3D printing of polysaccharide-based self-healing hydrogel reinforced with alginate for secondary cross-linking. *Biomedicines.* 2021;9(9):1224. doi:10.3390/biomedicines9091224.

41. Morgan FLC, Beeren IAO, Moroni L, Baker MB. Designing dynamic hydrogels: The interplay of cross-linker length, valency, and reaction kinetics in hydrazone-based networks. *Chem Mater.* 2025;37(8):2709–2719. doi:10.1021/acs.chemmater.4c02573.

42. Shin W, Chung K. Preparation and characterization of poly(acrylic acid)-based self-healing hydrogel for 3D shape fabrication via extrusion-based 3D printing. *Materials.* 2023;16(5):2085. doi:10.3390/ma16052085.

43. Karvinen J, Kellomäki M. 3D-bioprinting of self-healing hydrogels. *Eur Polym J.* 2024;209:112864. doi:10.1016/j.eurpolymj.2024.112864.

44. Stern R, Jedrzejas MJ. Hyaluronidases: their genomics, structures, and mechanisms of action. *Chem Rev.* 2006;106(3):818-839. doi:10.1021/cr050247k.

45. Lee HJ, Seo Y, Kim HS, Lee JW, Lee KY. Regulation of the viscoelastic properties of hyaluronate-alginate hybrid hydrogel as an injectable for chondrocyte delivery. *ACS Omega* 2020;5(25):15567-15575. doi:10.1021/acsomega.0c01763.

46. Allen JL, Cooke ME, Alliston T. ECM stiffness primes the TGFbeta pathway to promote chondrocyte differentiation. *Mol Biol Cell.* 2012;23(18):3731-3742. doi:10.1091/mbc.E12-03-0172.

47. Arora A, Kothari A, Katti DS. Pericellular plasma clot negates the influence of scaffold stiffness on chondrogenic differentiation. *Acta Biomater.* 2016;46:68-78. doi:10.1016/j.actbio.2016.09.038.

ACCSCIENCE PUBLISHING

International Journal of Bioprinting

RESEARCH ARTICLE

Synergistic bone regeneration by surface-modified 3D-printed PCL/β-TCP scaffolds in various animal defect models

Yulin Jiang[1], Guanghui Xi[1], Chen Zhou[1], Haisong Xu[3]*, Xi Yang[1]*, and Dongxu Ke[1,2]*

[1]Novaprint Therapeutics Suzhou Co., Ltd., Suzhou, Jiangsu, China

[2]Department of Biomedical Engineering, Nanjing University Suzhou Campus, Suzhou, Jiangsu, China

[3]Department of Plastic and Reconstructive Surgery, Shanghai Ninth People's Hospital, School of Medicine, Shanghai Jiao Tong University, Shanghai, China

(This article belongs to the *Special Issue*: *Future Bioprinting—Celebrating the 10th Anniversary of the International Journal of Bioprinting*)

Abstract

The regeneration of large-segmental bone defects remains a significant clinical challenge due to their complex microenvironments. Three-dimensional (3D)-printed polycaprolactone (PCL) scaffolds offer a potential solution but exhibit limited osteoinductive capacity. In this study, 3D-printed PCL/β-tricalcium phosphate (TCP) composite scaffolds were pretreated with NaOH, followed by functionalization with bioactive collagen and β-TCP. These modifications markedly improved the scaffolds' hydrophilicity without compromising mechanical integrity. *In vitro* studies with MC3T3-E1 cells demonstrated that the CS@TCP scaffolds significantly enhanced early osteogenic differentiation compared to C, CS, and CS@COL scaffolds, as indicated by the alkaline phosphatase activity assay. *In vivo* evaluation using three different rabbit cranial defect models revealed superior new bone formation in the partial-thickness cranial defect (PTD) groups compared to the full-thickness cranial defect (FTD) and intact cranial bone onlay (Onlay) groups, potentially due to the increased vascularization and abundant endogenous stem cells in the PTD groups. Despite reduced new bone formation in the Onlay group, its bone integration advantages may be advantageous for cosmetic surgery applications. This study investigated how β-TCP surface modification interacts with clinical application-specific microenvironments to maximize the regenerative potential of 3D-printed scaffolds, providing crucial guidance for scaffold design in effective bone defect repair across various clinical scenarios.

Keywords: 3D-printed scaffolds; *In vitro* proliferation and differentiation; Multiple animal defect models; Surface modification

***Corresponding authors:**
Haisong Xu
(113056@sh9hospital.org.cn)

Xi Yang
(Kathy.Yang@3dnovaprint.com)

Dongxu Ke
(dongxu.ke@wsu.edu)

Citation: Jiang Y, Xi G, Zhou C, Xu H, Yang X, Ke D. Synergistic bone regeneration by surface-modified 3D-printed PCL/β-TCP scaffolds in various animal defect models. *Int J Bioprint*. 2025;11(6):390-406. doi: 10.36922/IJB025380386

Received: September 17, 2025
Revised: October 25, 2025
Accepted: November 3, 2025
Published Online: November 3, 2025

Copyright: © 2025 Author(s). This is an Open Access article distributed under the terms of the Creative Commons Attribution License, permitting distribution and reproduction in any medium, provided the original work is properly cited.

Publisher's Note: AccScience Publishing remains neutral with regard to jurisdictional claims in published maps and institutional affiliations.

1. Introduction

Effective treatment of large-segmental bone defects represents a globally unmet medical need. In the United States (US) alone, approximately 500,000 patients require

surgical intervention for non-healing bone defects annually, while developing countries face higher burdens due to limited access to advanced treatments.[1] Current gold-standard therapies, autografts and allografts, are constrained by donor site morbidity, limited availability, and immunological rejection risks. The economic burden is substantial, with annual healthcare costs exceeding USD 12 billion in the United States for complications related to failed bone defect repairs, emphasizing the urgent need for tissue-engineered solutions capable of addressing this pervasive clinical challenge.[2]

Bone tissue engineering has emerged as a promising alternative for bone defect repair, integrating principles from developmental biology, biomechanics, and materials science to fabricate biomimetic scaffolds that recapitulate the structural hierarchy and functional complexity of native bone tissue.[3,4] Recently, the advent of three-dimensional (3D) printing technologies has revolutionized scaffold fabrication in bone tissue engineering by enabling precise architectural control across multiple length scales.[5] Macroscale optimization of 3D-printed constructs ensures mechanical integrity to withstand physiological loading while maintaining interconnected porosity for new bone ingrowth.[6–8] In addition, microscale modification of 3D-printed scaffolds facilitates cellular attachment, proliferation, and differentiation, promoting new bone formation.

With this powerful tool, many studies have reported 3D-printed biodegradable scaffolds for bone tissue engineering applications. For example, Wang *et al.*[9] developed a hierarchical polycaprolactone (PCL)/β-tricalcium phosphate (TCP) scaffold combining fused deposition modeling (FDM) printed macrofibers and melt electrowriting (MEW) printed microfibers to promote cell infiltration and osteogenesis. While effective, they focused primarily on scaffold structure and composition, without further investigating the regenerative potential of functionalized scaffolds. In another work, Weingärtner *et al.*[10] fabricated 3D-printed PCL scaffolds followed by coating with type I collagen. The biocompatibility of the scaffolds was evaluated by culturing three different cell types on them. Results showed that the collagen coating significantly improved the cell–scaffold interaction. However, their work was primarily focused on *in vitro* cellular responses, without evaluating the performance of the functionalized scaffolds *in vivo*. Taken together, few studies have evaluated the combined effects of the functionalized scaffolds in different clinically relevant bone defect models.

In this study, 3D-printed PCL/β-TCP scaffolds with surface functionalization were constructed to improve osteogenic performance. The surface modification was facilitated using NaOH immersion, followed by collagen coating through vacuum-assisted adsorption, and β-TCP coating by dip-coating deposition. Chemical, physical, and mechanical characterizations confirmed the successful fabrication of bioactive composite scaffolds. Furthermore, the biological performance of the 3D-printed scaffolds was assessed *in vitro* using 3-(4,5-dimethylthiazol-2-yl)-2,5-diphenyltetrazolium bromide (MTT) assay, live/dead staining, alkaline phosphatase (ALP) activity, and alizarin red S (ARS) staining. The results showed that the modified scaffolds significantly promoted cell proliferation and osteogenic differentiation. Finally, the 3D-printed scaffolds were implanted in rabbits' full-thickness cranial defects (FTD), partial-thickness cranial defects (PTD), and onlay placement on intact cranial bone (Onlay), followed by micro-computed tomography (CT), histological, and immunohistochemical analysis to assess *in vivo* osteogenesis and angiogenesis. The implantation demonstrated enhanced new bone formation and angiogenesis in the PTD group. Collectively, this study aims to develop and systematically evaluate multifunctional 3D-printed scaffolds that integrate bioactivity and osteogenic potential, providing comprehensive insights into their translational applicability for effective bone defect repair across diverse clinical scenarios.

2. Materials and methods

2.1. Materials

Polycaprolactone was acquired from Evonik (China), β-TCP powder from DinganTec (China), and collagen from Trauer (China). MC3T3-E1 subclone 14 (CL-0378), basal medium, osteogenic differentiation medium, and ARS solution were supplied by Wuhan Pricella Biotechnology Co., Ltd (China). MTT, live/dead staining kits, ALP assay kits, and 5-bromo-4-chloro-3-indolyl phosphate (BCIP)/nitro blue tetrazolium (NBT) alkaline phosphatase color development kits were provided by Beyotime (China). Hematoxylin and eosin (H&E) staining kits, Goldner's trichrome staining kits, Masson's trichrome staining kits, phosphate-buffered saline (PBS), and paraformaldehyde (PFA) were obtained from Solarbio (China). The primary anti-collagen I (COL) and anti-von Willebrand factor (vWF) antibodies were purchased from Absin (China). All other reagents were purchased from Sigma-Aldrich (USA).

2.2. Scaffold design

A regular triangular pore architecture with a filament diameter of 200 μm and a pore size of 600 μm was selected for the scaffold design based on previous studies.[11] Cuboid scaffolds with dimensions of $4 \times 4 \times 1$ mm^3 were fabricated for cell assays, while larger ones ($5.4 \times 10 \times 10$ mm^3) were used for compressive strength testing. For the animal study, circular plug samples with (dimensions diameter × diameter × height × height) of 15 mm × 10 mm × 1.5 mm

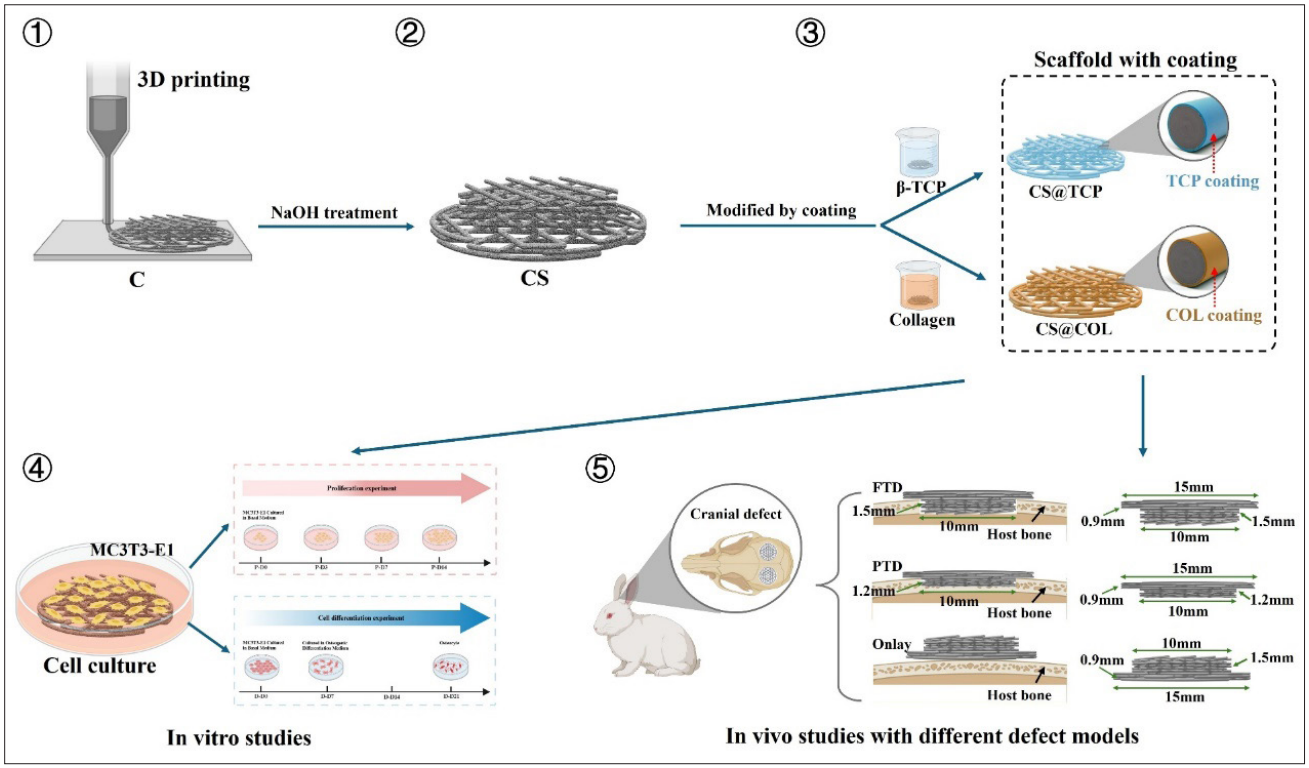

Figure 1. Schematic illustration of the research process of this study. Abbreviations: β-TCP, beta-tricalcium phosphate; C, polycaprolactone/β-tricalcium phosphate; COL, collagen; CS, NaOH-treated polycaprolactone/β-tricalcium phosphate; FTD, full-thickness cranial defect; Onlay, intact cranial bone as an onlay graft; PTD, partial-thickness cranial defect.

× 0.9 mm (FTD), 15 mm × 10 mm × 1.2 mm × 0.9 mm (PTD), and 15 mm × 10 mm × 1.5 mm × 0.9 mm (Onlay) were prepared for different defect models.

2.3. Fabrication of 3D-printed scaffolds

According to the previous study, PCL was added to dichloromethane and mixed at 500 rpm until it was fully dissolved.[12] Then, β-TCP was added to reach a concentration of 20 wt.%. After mixing for 4 h, the solution was poured onto a stainless-steel plate. The dichloromethane was evaporated at 37°C for 24 h, forming thin PCL/β-TCP films. Finally, the films were cut into 5 × 5 mm^2 pieces for printing.

The 3D-printed scaffolds were fabricated using a melt-extrusion-based additive manufacturing system, Organ Printing United System (OPUS, Novaprint Therapeutics, China). The printing parameters were as follows: the syringe temperature was set to 120°C, the extrusion pressure to 750 kPa, the printing speed to 220 mm/min, and the layer thickness to 0.1 mm. Scaffolds were fabricated using tapered steel nozzles with a 200-μm inner diameter, while the printing platform was maintained at 37°C. The printed scaffolds without NaOH treatment were designated as C in the present study.

2.4. Surface modification

The scaffolds were first immersed in 2 mol/L NaOH solution and incubated on a shaker at 37°C for 24 h. After incubation, the solution was removed, and the scaffolds were washed in distilled water using ultrasonication for 5 min. Finally, the scaffolds were dried overnight at 37°C and divided into the following three groups (Figure 1):

- CS group: NaOH-treated and dried scaffolds.
- CS@COL group: NaOH-treated scaffolds immersed in an 8 mg/mL collagen solution and subjected to a 30-min vacuum pressure impregnation, followed by incubation on a shaker at 37°C for 24 h and drying on a Teflon plate at 45°C for 24 h.
- CS@TCP group: NaOH-treated scaffolds immersed in a 1 mg/mL β-TCP suspension and stirred at 500 rpm for 24 h. After treatment, the scaffolds were rinsed three times with distilled water for 5 min each and dried overnight at 37°C.

2.5. Physical, chemical, and mechanical characterizations

The morphology of the scaffolds was observed using scanning electron microscopy (SEM) (S8100, Hitachi,

Japan). The scaffolds were coated with platinum for 180 s and then observed at an accelerating voltage of 3.0 kV. Meanwhile, elemental analyses of the scaffolds were performed using energy dispersive X-ray spectroscopy (EDS).

Next, Fourier transform infrared spectroscopy (FTIR) analysis was conducted to identify the functional groups in the scaffolds. This experiment was performed using an FTIR spectrometer (iS50, Thermo Fisher Scientific, USA) with a wavelength of 4000–400 cm^{-1}.

Optical contact angles were measured using an OCA 15EC goniometer (DataPhysics Instruments, Filderstadt, Germany). A 3 μL deionized water droplet was deposited on the sample surface using a microsyringe. Images of the droplets were captured through a high-resolution camera (EOS 5D, Canon, Japan), and contact angles were analyzed using Surface contact angle (SCA) software (DataPhysics Instruments, Filderstadt, Germany).

The compressive properties of the scaffolds were determined by a compression test using a universal testing system (HY-1080, Shanghai Heng Wing Precision Instrument, China) with a 1000 N load cell. Scaffold samples with dimensions of 5.4 × 10 × 10 mm^3 were compressed at a constant crosshead speed of 5 mm/min, while compressive strengths and compressive modulus were calculated (n = 4).

2.6. Cell proliferation

After ethylene oxide sterilization, four scaffold groups (C, CS, CS@COL, and CS@TCP) were placed into 96-well plates. MC3T3-E1 cells were seeded onto the scaffolds at a density of 1 × 10^5 cells per well and incubated at 37 °C with 5% CO_2 for 3, 7, and 14 days, as illustrated in Figure 4A. The medium was changed every 3 days.

2.7. MTT assay

The samples were treated with 10 μL of 5 mg/mL MTT solution (medium:MTT = 10:1) and incubated at 37°C for 4 h in the dark. After incubation, the supernatant was carefully removed from the wells. Then, 700 μL of dimethyl sulfoxide was added to the samples and shaken on a micro-oscillator for 30 min to ensure complete dissolution. After dissolution, 100 μL of supernatant was transferred into a 96-well plate and the absorbance was measured at 570 nm using a microplate reader (SpectraMax i3x, Molecular device, USA).

2.8. Stability analysis of different coatings

Samples were collected after 0 and 14 days of cell proliferation incubation, followed by fixation in 4% glutaraldehyde for 24 h. Then, the samples were dehydrated through a graded ethanol series (30%, 50%, 70%, 80%, 90%, 95%, and 100%) for 10 min at each step and dried. Finally, the dried samples were coated with platinum for 180 s and then observed at an accelerating voltage of 3.0 kV. Meanwhile, the elemental analyses of the scaffolds were performed using EDS.

2.9. Cell differentiation

MC3T3-E1 cells were seeded onto sterilized scaffolds (C, CS, CS@COL, and CS@TCP) at a density of 1 × 10^5 cells per well. The basic medium was applied for 7 days and then replaced with an osteogenic induction medium for 14 days, as shown in Figure 5A. The osteogenic induction medium was refreshed every 2–3 days.

2.10. Live/dead staining

Cell viability was evaluated using a live-dead staining working solution, which was prepared by mixing calcein acetoxymethyl ester and propidium iodide solutions at a 1:1 ratio. After culture, the culture medium was discarded, and the scaffolds were washed three times with PBS. Following the manufacturer's protocol, 100 μL of the working solution was applied to each well and incubated at 37 °C for 30 min in the dark. Post-incubation, the solution was removed, followed by three washes in PBS. Finally, fluorescent images were captured using an inverted fluorescence microscope (Ts2-FL, Nikon, Japan).

2.11. Alkaline phosphatase staining and activity

At Days 14 and 21 of osteogenic differentiation culture, BCIP/NBT staining was performed to visualize ALP activity. The working solution was prepared by dissolving 10 μL of BCIP and 20 μL of NBT in 3 mL of PBS. A total of 100 μL of the prepared working solution was added to each well and incubated at room temperature for 30 min in the dark. Following incubation, images were acquired using a light microscope (DMi1, Leica, Germany).

Meanwhile, ALP activity was quantitatively analyzed using an enzymatic assay. The scaffolds were lysed with a cell lysis solution and incubated on ice for 10 min. The lysate was collected, and 50 μL of the cell lysate was combined with 50 μL of a chromogenic substrate solution. The reaction was initiated by incubating the mixture at 37 °C for 30 min. To terminate the reaction, 100 μL of a stopping solution was added. The absorbance at 570 nm was measured using the SpectraMax i3x microplate reader. The concentration of *p*-nitrophenol generated was calculated based on the standard curve.

2.12. Alizarin red S staining and quantification

Samples were washed three times with PBS, followed by fixation with 4% PFA for 1 h on Days 14 and 21 of osteogenic differentiation culture. Subsequently, 100 μL of ARS working solution was added to each well,

followed by incubation at room temperature for 30 min in the dark. Afterward, samples were washed gently with deionized water, and images were captured using the DMi1microscope a light microscope. Additionally, 200 µL of 10% cetylpyridinium chloride solution was added to each well, followed by incubation on a shaker at 37°C for 30 min in the dark. Subsequently, 100 µL of the resulting mixture was transferred into a 96-well plate, and the absorbance was measured at 570 nm using the SpectraMax i3x microplate reader.

2.13. *In vivo* studies using different rabbit cranial defect models

In this study, 12 male New Zealand white rabbits aged 6 months were used. Two individual cranial defects were induced in each rabbit, and the defects were divided into the following three different groups (n = 4): FTD, PTD, and Onlay groups, as shown in **Table 1**. Prior to surgery, scaffolds and surgical equipment were sterilized with ethylene oxide, and rabbits were anesthetized with a gaseous mixture of oxygen and isoflurane. After the surgical area was shaved, sanitized, and incised, FTD and 1.2 mm PTD were created by a trephine or surgical drill. Then, the scaffolds were implanted and secured with screws at the defect sites, followed by wound closure by suturing. Additionally, in the Onlay group, the scaffolds were placed on top of the rabbits' intact cranial bone as a graft, as shown in Figure 1. After 12 and 26 weeks, animals were euthanized by carbon dioxide inhalation. The harvested samples were fixed in 10% neutral buffered formalin for at least 3 days before further analysis.

2.14. Micro-computed tomography analysis

A high-resolution micro-CT scanner (Skyscan 1172, Skyscan, Belgium) was used to analyze the new bone formation. Scanning was performed with a voxel size of 20 µm, an X-ray voltage of 80 kV, an electric current of 112 µA, and a rotation step of 0.6°. After scanning, images were reconstructed using the Mimics software (Mimics 21.0, Materialise NV, Belgium). A cylindrical volume of interest with a 10-mm diameter and 1.5-mm height around the defect area was selected for qualitative and quantitative analyses. Bone volume/total volume fraction (BV/TV), trabecular thickness (Tb.Th), bone mineral density (BMD), and trabecular number (Tb.N) were measured for different defect models after implantation for 12 and 26 weeks.

2.15. Histological analysis

Samples were first fixed in 4% PFA for at least 3 days, followed by decalcification in 15% ethylenediaminetetraacetic acid (EDTA) and dehydration through a graded ethanol series. After dehydration, the specimens were embedded in paraffin and sectioned into 5-µm-thick slices using a microtome (RM2016, Leica, Germany). The sections were mounted on glass slides, deparaffinized with xylene, and rehydrated through a descending ethanol series. Subsequently, H&E, Goldner's trichrome, and Masson's trichrome staining were carried out. Images were acquired using the OLYMPUS BX51, Olympus Corporation light microscope.

2.16. Immunohistochemical analysis

Samples were first fixed in 4% PFA and decalcified in 15% EDTA. After decalcification, samples were embedded in

Table 1. Experimental design of the *in vivo* study

Time point	Rabbit ID	Implantation site	
		Right	Left
12 weeks	1	FTD	PTD
	2	FTD	Onlay
	3	PTD	Onlay
	4	PTD	FTD
	5	Onlay	PTD
	6	Onlay	FTD
26 weeks	7	FTD	PTD
	8	FTD	Onlay
	9	PTD	Onlay
	10	PTD	FTD
	11	Onlay	PTD
	12	Onlay	FTD

Abbreviations: FTD, full-thickness cranial defect; Onlay, intact cranial bone as an onlay graft; PTD, partial-thickness cranial defect.

paraffin, followed by sectioning into 5-μm-thick slices using the RM2016 microtome.

Sections were deparaffinized in xylene and rehydrated in a series of graded ethanols and water. Then, antigen retrieval was performed in citrate buffer, followed by quenching of endogenous peroxidase activity with peroxidase block solution at room temperature for 20 min. To prevent nonspecific binding of the secondary antibody, sections were incubated in blocking solution (3% BSA and 0.3% Triton ×100 in PBS) at room temperature for 15 min. Subsequently, sections were incubated overnight at 4 °C with primary antibodies against vWF and COL, followed by 30 min incubation with a biotinylated secondary antibody at room temperature. Finally, images were visualized using the OLYMPUS BX51 light microscope.

2.17. Statistical analysis

Quantitative data were collected from at least three independent experiments per group. Data were expressed as mean ± standard deviation (SD), and one-way analysis of variance (ANOVA) was used to analyze differences between groups. A p-value of less than 0.05 was considered statistically significant ($^*p < 0.05$). Statistical significance was determined using Origin software (Origin 2021, OriginLab Corporation, USA)and GraphPad Prism software (GraphPad 9.5, Graphpad Software Inc., USA)

3. Results

3.1. Microstructure, chemical composition, and compressive strength analysis

An interconnected porous structure was observed in the 3D-printed scaffolds. Compared to the smooth surface of the C scaffold, nanoscale pits appeared on the CS scaffold surface. In addition, a collagen film and nanoscale particles were observed on the surfaces of CS@COL and CS@TCP scaffolds, respectively, as shown in Figure 2A.

No significant differences were observed between the C and CS scaffolds. In contrast, the N peak intensity and content were significantly higher in the CS@COL scaffolds than in the CS group. Moreover, strong Ca and P peaks and increased elemental content were observed in CS@TCP scaffolds compared to CS scaffolds, as shown in Figure 2B. Furthermore, the uniform distribution of C and N elements on the CS@COL scaffolds confirmed the even coverage of the collagen coating, while the uniform Ca distribution on the CS@TCP scaffolds demonstrated the well-distributed β-TCP coating, as shown in Figure 2C.

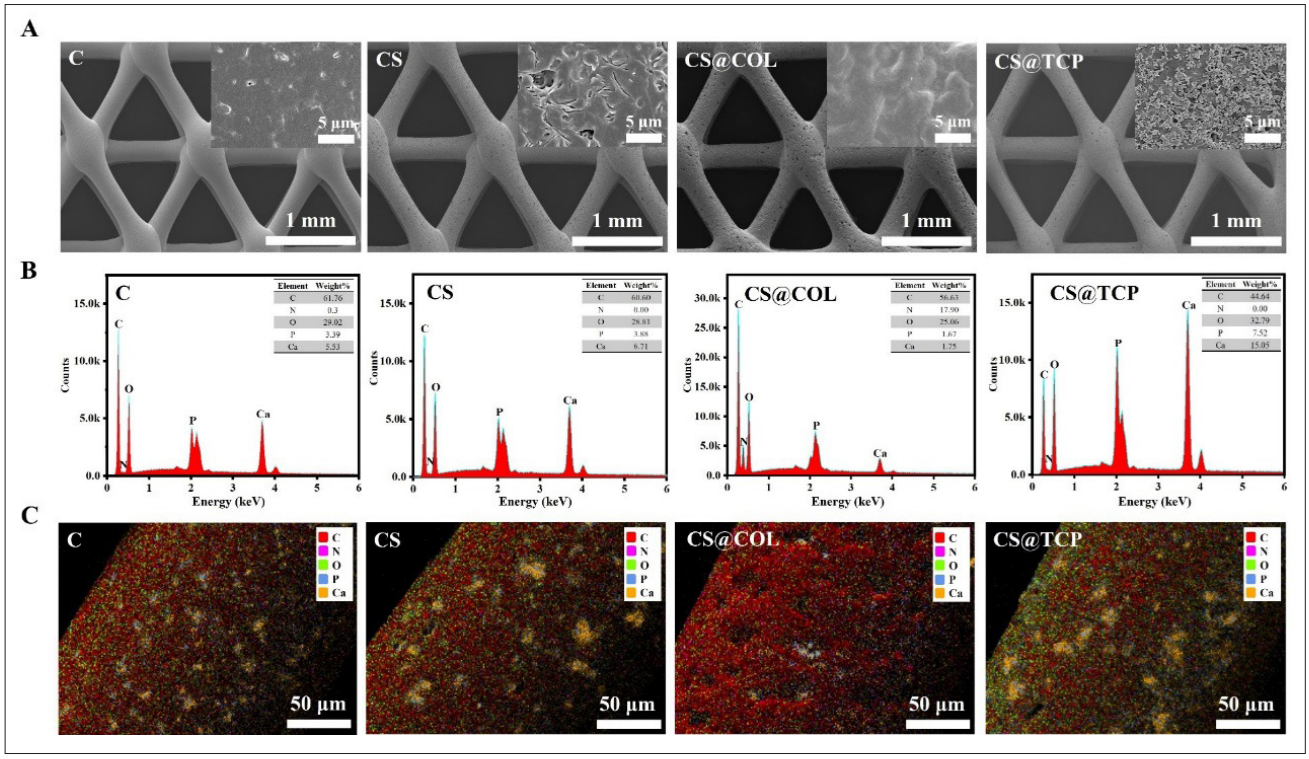

Figure 2. Surface morphology and elemental analysis of different scaffolds. (A) Scanning electron microscopy images. Scale bars: 1 mm, 5 μm (inset); magnifications: ×50, ×10,000 (inset). (B) Energy dispersive X-ray spectroscopy (EDS) spectrum. (C) EDS mapping C, CS, CS@COL, and CS@TCP scaffolds. Scale bars: 50 μm; magnifications: ×500.

The peaks observed at 1720, 2943, and 2864 cm^{-1} in all scaffolds were characteristic bands of PCL, corresponding to the stretching vibration of the carbonyl group (C=O) and the asymmetric stretching vibrations of the CH_2 groups, respectively. Notably, the intensity of the peak at 1043 cm^{-1} significantly increased after the application of β-TCP coating on the CS scaffolds. Additionally, the peaks observed at 3315, 1659, and 1554 cm^{-1} in CS@COL scaffolds corresponded to the amide A (N–H stretching), amide I (C=O stretching), and amide II (N–H bending and C–N stretching) bands, respectively, all of which were typically associated with collagen, as shown in Figure 3A. Furthermore, the contact angles in the C scaffolds were significantly higher than those in the CS, CS@COL, and CS@TCP scaffolds, as presented in Figure 3B. The compressive strength of C (3.48 ± 0.23 MPa) was higher than CS (3.00 ± 0.33 MPa), CS@COL (3.06 ± 0.15 MPa), and CS@TCP (3.10 ± 0.19 MPa) scaffolds; however, no significant differences were observed among them, as presented in Figure 3D. The compressive modulus data showed the same trend, with no significant differences among different groups, as shown in Figure 3E.

3.2. *In vitro* study of cell proliferation

At Day 3, the cell proliferation in C scaffolds was significantly lower than in CS, CS@COL, and CS@TCP scaffolds. At Day 7, the cell proliferation in CS@COL and CS@TCP scaffolds remained significantly higher than that in C scaffolds. At Day 14, only the CS@TCP scaffolds showed a significant increase in proliferation compared to C scaffolds, as shown in Figure 4B. Live/dead staining results showed that cells exhibited better attachment on the CS@TCP and CS@COL scaffold surfaces compared to the C and CS scaffold surfaces, as shown in Figure 4C.

The morphologies of the coatings on Days 0 and 14 were similar, showing no obvious changes, while elemental analysis revealed a slight decrease in Ca content in the TCP-coated scaffolds (from 11.36 ± 0.39 wt.% to 11.10 ± 0.32 wt.%) and a more significant decrease in N content in the COL-coated scaffolds (from 17.81 ± 0.25 wt.% to 12.54 ± 0.36 wt.%), as shown in Figure 4D–G.

3.3. *In vitro* study of cell differentiation

The ALP staining, used to evaluate early osteogenic differentiation, revealed a markedly larger stained area in CS@TCP scaffolds compared to C, CS, and CS@COL

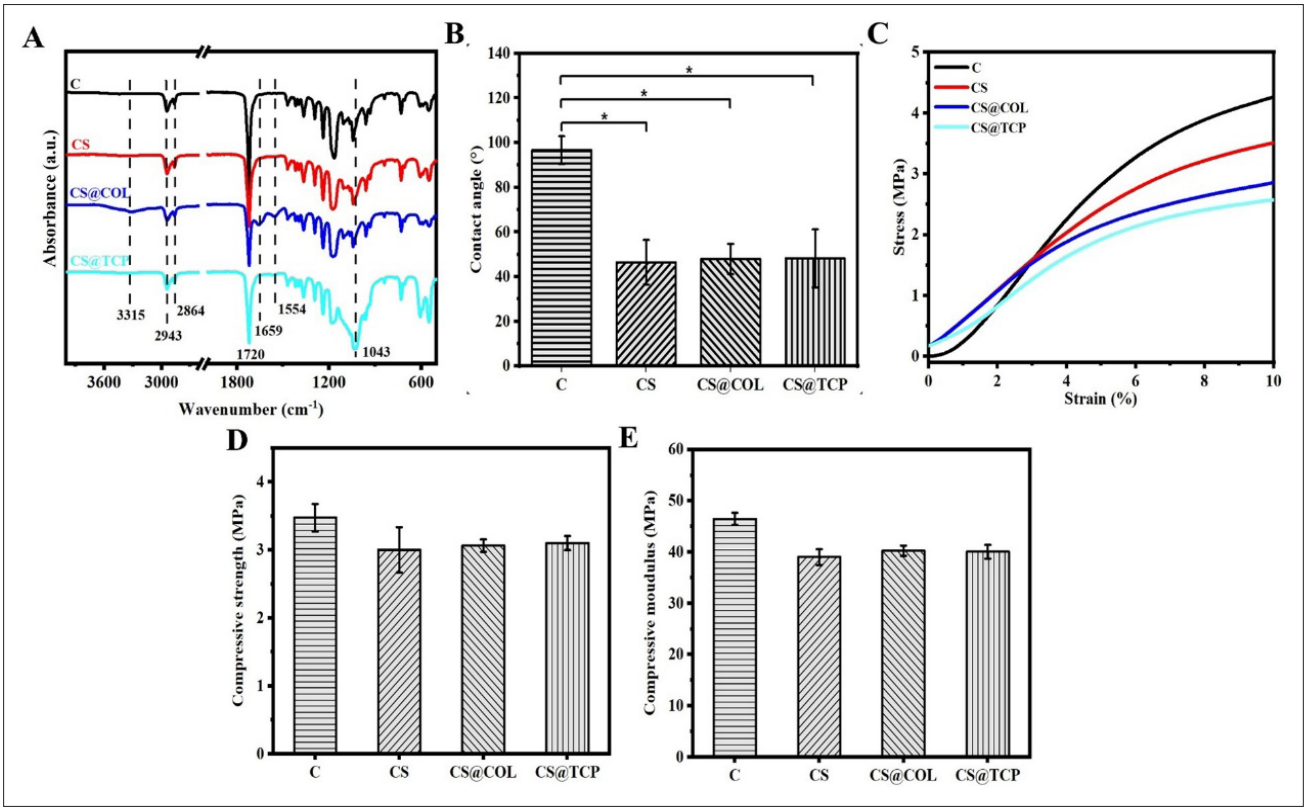

Figure 3. Physical and chemical characterizations for C, CS, CS@COL, and CS@TCP scaffolds. (A) Fourier transform infrared spectroscopy spectra. (B) Contact angle. (C) Stress–strain curves. (D) Compressive strength. (E) Compressive modulus. Notes: Data are expressed as mean ± SD; $n = 4$; *$p < 0.05$.

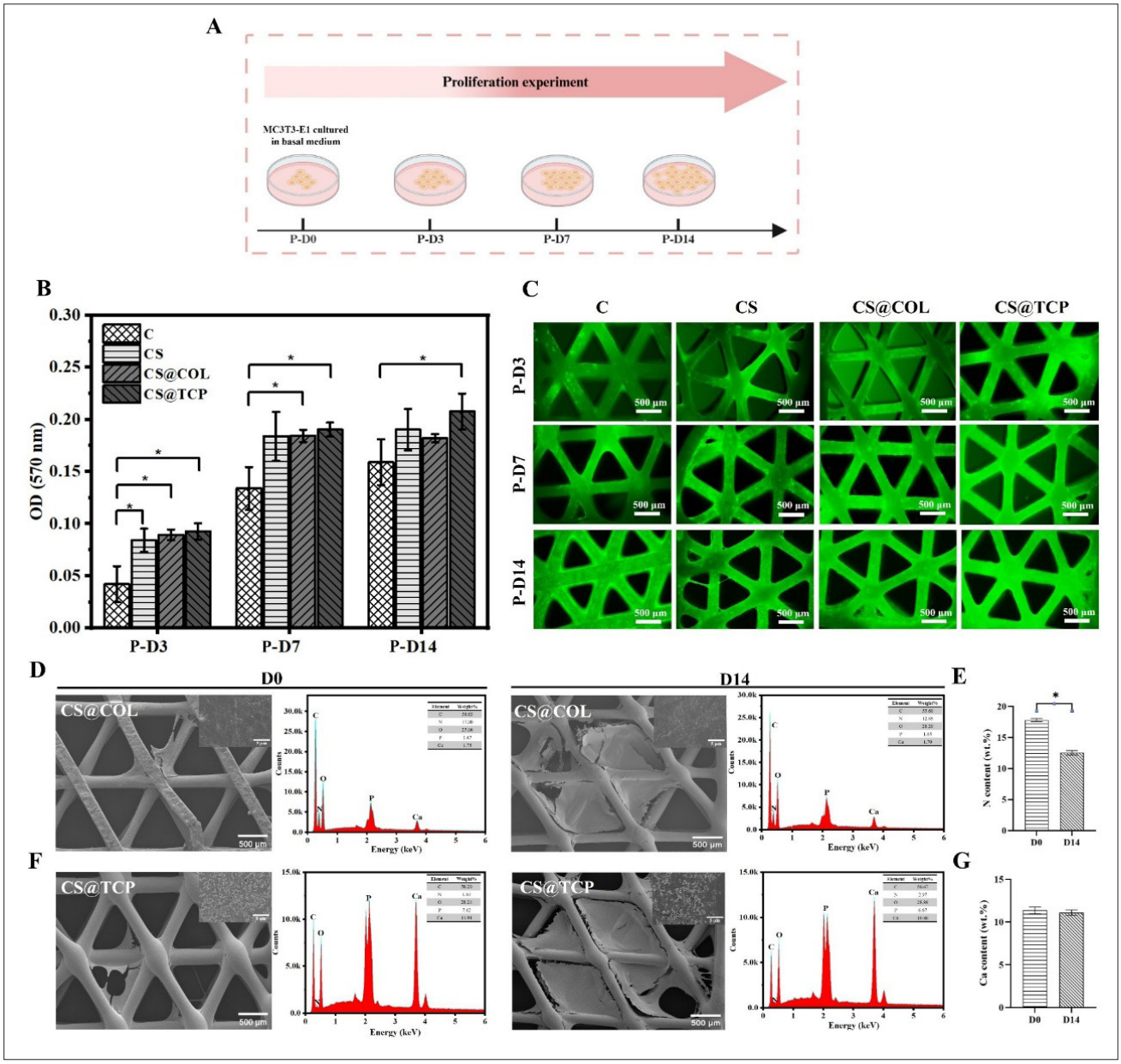

Figure 4. Cell proliferation studies for C, CS, CS@COL, and CS@TCP scaffolds. (A) Cell proliferation culture model. (B) MTT assay. (C) Live/dead staining. Scale bars: 500 μm; magnifications: ×5. (D–G) Scanning electron microscopy images (scale bars: 5 μm (insets); magnifications: ×100, ×10,000 (insets)); and energy dispersive X-ray spectroscopy mapping of scaffold coatings at Days 0 and 14 of cell culture: (D) CS@COL coatings and corresponding (E) N content; (F) CS@TCP coatings and corresponding (G) Ca content. Notes: Data are expressed as mean ± SD; $n = 4$; $^*p < 0.05$. Abbreviations: OD, optical density; P-D, proliferation day.

scaffolds, as illustrated in Figure 5B. At Days 14 and 21, the ALP activity in CS@TCP scaffolds was significantly higher than in C, CS, and CS@COL scaffolds, while CS scaffolds also showed significantly higher activity than C, as illustrated in Figure 5C. In contrast, ARS staining, which reflects late-stage mineral deposition, showed greater calcium deposition in CS@TCP scaffolds compared to the other groups, as shown in Figure 5D. ARS quantification further confirmed significantly higher mineral deposition in CS@TCP scaffolds relative to C and CS@COL groups at Days 14 and 21, as shown in Figure 5E.

3.4. *In vivo* micro-computed tomography evaluation

After 12 and 26 weeks of implantation, the Onlay group exhibited significantly lower values of BV/TV, BMD, and Tb.Th compared with the FTD and PTD groups, as

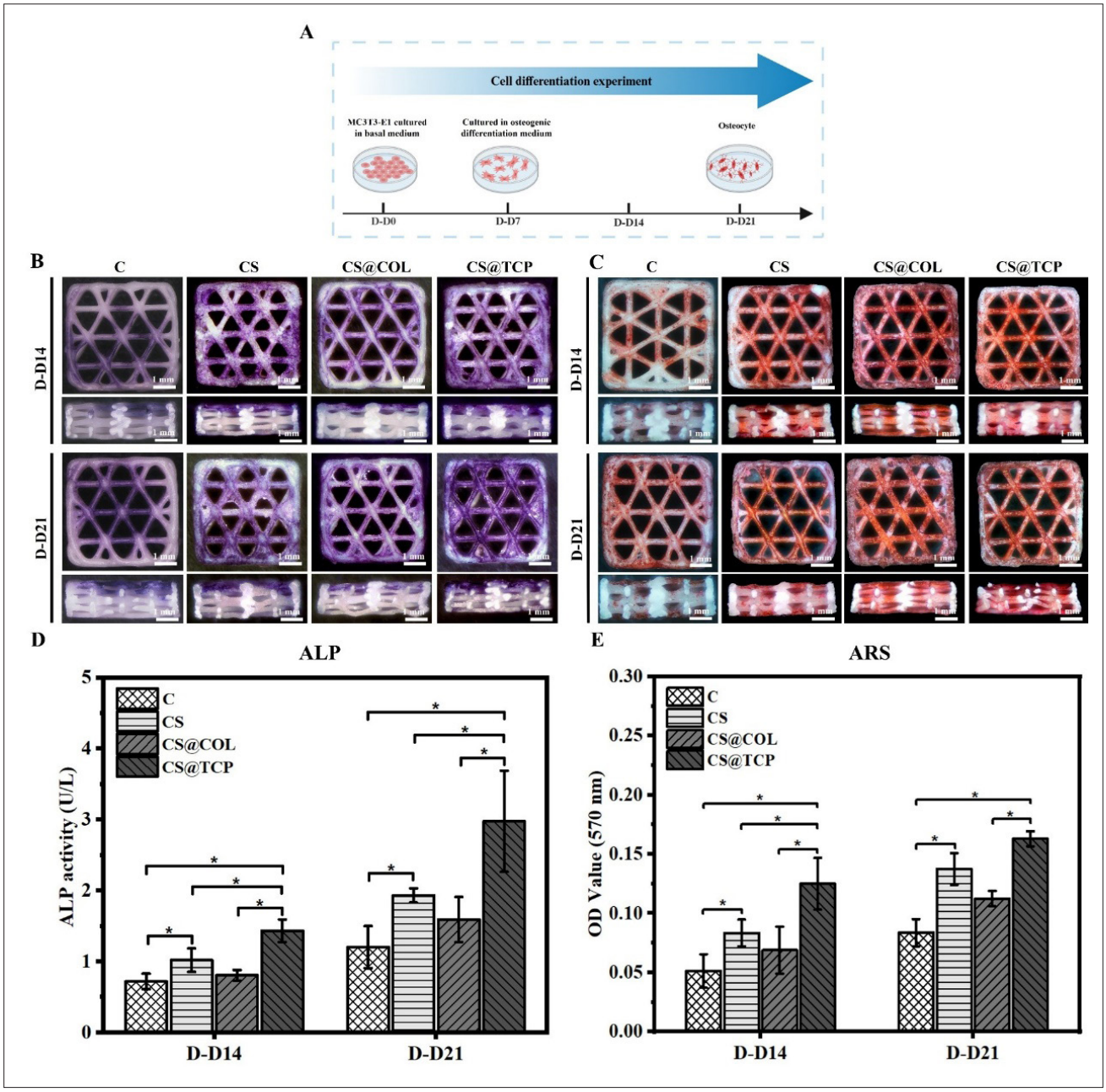

Figure 5. Cell differentiation studies for C, CS, CS@COL, and CS@TCP scaffolds. (A) Cell differentiation model. (B) Alkaline phosphatase (ALP)-stained images. Scale bars: 1 mm; magnifications: ×5. (C) Alizarin red S (ARS)-stained images. Scale bars: 1 mm; magnifications: ×5. (D) Quantitative analysis of ALP staining. (E) Quantitative analysis of ARS staining. Notes: Data are expressed as mean ± SD; $n = 4$; $^*p < 0.05$. Abbreviations: D-D, differentiation day; OD, optical density.

indicated in Figure 6C–F. Notably, the PTD group showed a significantly higher BV/TV than the FTD group at 12 weeks. In contrast, the Tb.N value in the Onlay group was significantly higher than that in the FTD and PTD groups at both 12 and 26 weeks, as shown in Figure 6F.

3.5. Histological analysis

The Onlay group consistently exhibited significantly lower osteoid levels compared to the FTD and PTD groups at 12 and 26 weeks, while the PTD group showed significantly lower osteoid formation than the FTD group at 26 weeks, as shown in Figure 7B. For mineralized bone formation,

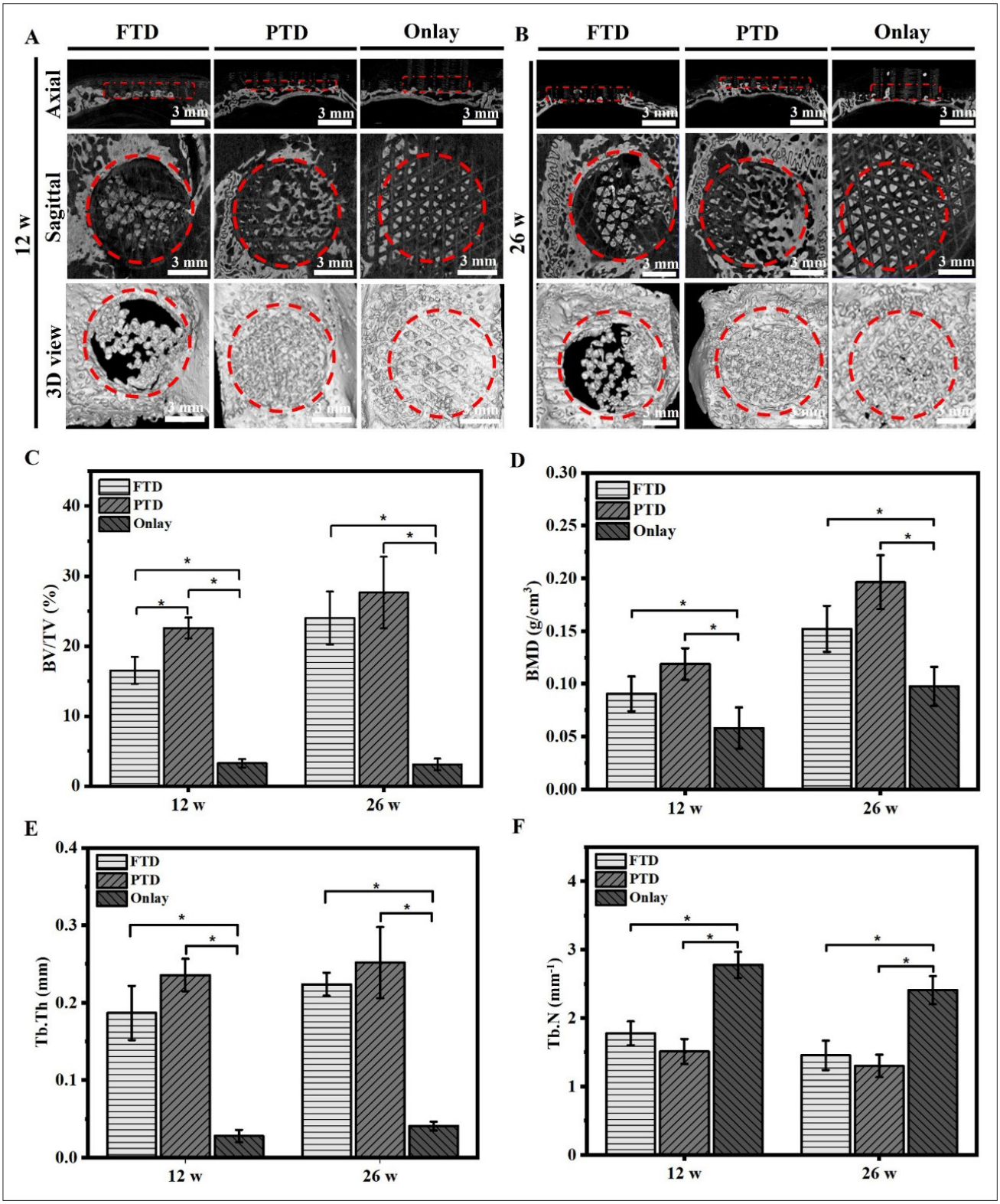

Figure 6. Micro-computed tomography (CT) evaluation of FTD, PTD, and Onlay groups after implantation for 12 and 26 weeks. Micro-CT axial, sagittal, and 3D reconstruction images at (A) 12 weeks and (B) 26 weeks. Scale bars: 3 mm; magnifications: ×1. (C) Bone volume/total volume (BV/TV). (D) Bone mineral density (BMD). (E) Trabecular thickness (Tb.Th). (F) Trabecular number (Tb.N). Notes: Data are expressed as mean ± SD; $n = 4$; $^*p < 0.05$. Abbreviations: FTD, full-thickness cranial defect; Onlay, intact cranial bone as an onlay graft; PTD, partial-thickness cranial defect.

the PTD group demonstrated significantly higher new bone formation than the FTD and Onlay groups at 26 weeks, while the Onlay group showed significantly lower new bone formation than the PTD and FTD groups at both 12 and 26 weeks, as illustrated in Figure 7C. Furthermore, collagen formation in the Onlay group was significantly lower than that in the FTD and PTD groups at both 12 and 26 weeks, as shown in Figure 7D.

3.6. Immunohistochemical analysis

In the PTD and FTD groups, the collagen staining intensity decreased from 12 to 26 weeks; in contrast, the Onlay group exhibited consistently higher collagen deposition compared to the other groups at both 12 and 26 weeks with limited variation, as shown in Figure 8B. A similar pattern was observed for vWF staining, which also declined from 12 to 26 weeks in the PTD and FTD groups. At 12 weeks, vWF staining intensity in the PTD group was significantly lower than that in the FTD group. Notably, the Onlay group consistently exhibited significantly greater vWF immunoreactivity than both the PTD and FTD groups at 12 and 26 weeks (Figure 8D).

4. Discussion

The success of bone tissue engineering primarily depends on the design of a supportive microenvironment, which integrates suitable scaffold architecture, surface chemistry, and bioactive modifications.[13–15] In this study, we developed 3D-printed PCL/β-TCP composite scaffolds

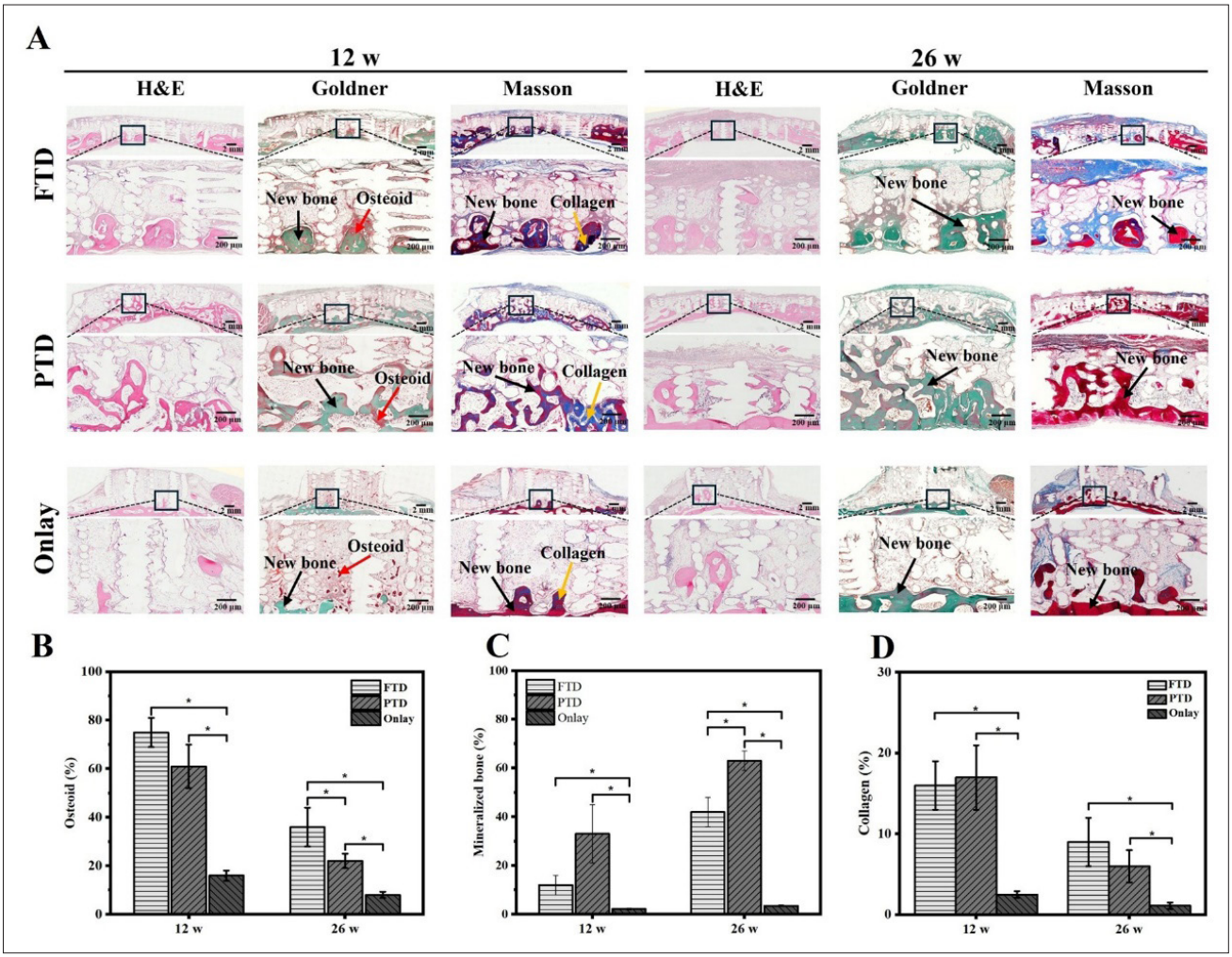

Figure 7. Histological analyses of FTD, PTD, and Onlay groups after implantation for 12 and 26 weeks. (A) Hematoxylin and eosin (H&E), Goldner's trichrome, and Masson's staining. Black arrows indicate new bone, red arrows indicate osteoid, and yellow arrows indicate collagen. Scale bars: 2 mm (top), 200 μm (bottom); magnifications: ×1 (top), ×4 (bottom). (B) Quantification of osteoid. (C) Quantification of mineralized bone. (D) Quantification of collagen. Notes: Data are expressed as mean ± SD; $n = 4$; *$p < 0.05$. Abbreviations: FTD, full-thickness cranial defect; Onlay, intact cranial bone as an onlay graft; PTD, partial-thickness cranial defect.

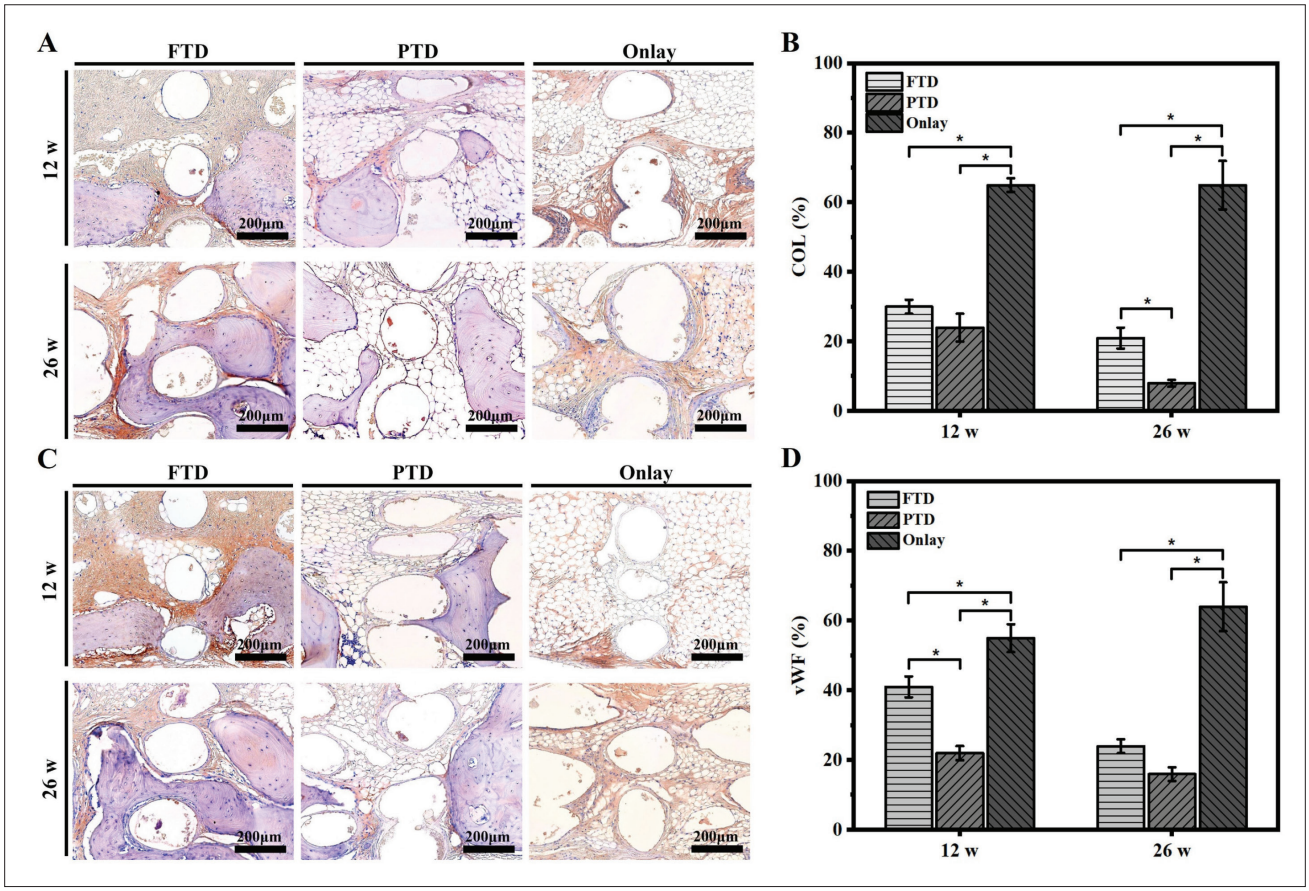

Figure 8. Immunohistochemical analyses of FTD, PTD, and Onlay groups after implantation for 12 and 26 weeks. (A) Collagen (COL)-stained images. Scale bars: 200 μm; magnifications: ×8. (B) Statistical analysis of COL expression. (C) Von Willebrand factor (vWF)-stained images. Scale bars: 200 μm; magnifications: ×8. (D) Statistical analysis of vWF expression. Notes: Data are expressed as mean ± SD; $n = 4$; $^*p < 0.05$. Abbreviations: FTD, full-thickness cranial defect; Onlay, intact cranial bone as an onlay graft; PTD, partial-thickness cranial defect.

with triangular-shaped pores. However, when applied as bone tissue engineering scaffolds, PCL/β-TCP composites still face challenges related to their hydrophobicity and low surface bioactivity.[16–18]

To address these issues, this study employed two different surface modification strategies using NaOH submersion followed by collagen and β-TCP coating, respectively.[19] NaOH modification proved highly effective in enhancing the hydrophilicity, protein adsorption, and cell adhesion properties of the scaffolds while maintaining their overall porous morphology.[20] In this study, a concentration of 2 M NaOH was used on PCL/β-TCP composite scaffolds, resulting in nanoscale pits on surfaces, accompanied by a significant decrease in contact angle. Notably, no obvious changes were detected in the EDS spectra, FTIR spectra, and mechanical properties after NaOH treatment, as illustrated in Figures 2 and 3.

Collagen, a major component of the extracellular matrix, has been widely used to enhance the bioactivity of tissue engineering scaffolds.[21] It has been demonstrated that collagen coating improves cell adhesion, proliferation, and osteogenic differentiation.[22,23] This phenomenon was attributed to the fact that extracellular matrix proteins provide a softer substrate for cell attachment, thereby promoting osteogenic gene expression.[24] β-TCP is a bioactive ceramic whose inorganic composition closely resembles that of natural bone and has been widely used in bone tissue engineering.[25,26] Moreover, β-TCP possesses excellent osteoconductive and osteoinductive properties that support cell attachment, proliferation, and differentiation.[27,28] Given these outstanding characteristics of collagen and β-TCP, the application of collagen and β-TCP has become a hot topic of research in bone graft coating materials.[29,30]

The 3D-printed PCL/β-TCP composite scaffolds were further surface-modified by depositing collagen and

β-TCP, leading to the formation of a collagen film and a nanoporous layer on the scaffold surface, as illustrated in Figure 2A. A notable increase in the N peak in CS@COL, and Ca and P peaks in CS@TCP scaffolds, along with the intensified FTIR bands at 3315, 1659, and 1,554 (amide A, I, and II for collagen), and 1043 cm^{-1} (β-TCP), further confirmed the successful coating of collagen and β-TCP on the scaffold surface, as shown in Figure 3A. Importantly, these surface modifications maintained their excellent hydrophilicity and mechanical properties, as demonstrated in Figure 3B–E.

Surface modification also plays an essential role in dictating cell behavior, as it creates a microenvironment that profoundly influences cell attachment, migration, proliferation, and differentiation.[31] Our *in vitro* results showed that cell proliferation was markedly enhanced in the CS, CS@COL, and CS@TCP scaffolds compared to the C scaffolds throughout the culture period, as illustrated in Figure 4. This may be attributed to the NaOH treatment, which improved the hydrophilicity and surface roughness of the scaffolds, thereby enhancing protein adsorption, facilitating cell attachment, and promoting cell proliferation.[32,33] In addition, our stability analysis revealed that the β-TCP coatings remained largely intact during the 14-day culture period, indicating greater stability compared to COL-coated scaffolds, as shown in Figure 4. For osteogenic differentiation, both ALP activity and ARS staining were significantly elevated in the CS@TCP group compared to the other groups, as shown in Figure 5D and E. It could be caused by the release of Ca^{2+} and PO_4^{3-} ions from β-TCP, which created an osteoinductive microenvironment and promoted early osteogenic activity. This effect may be mediated by stimulating osteogenic-related signaling pathways, such as Wnt/β-catenin and bone morphogenetic protein/Smad, thereby upregulating the expression of ALP, runt-related transcription factor 2, and osteocalcin.[34–38] For *in vivo* characterization, three different defect models were designed to systematically evaluate the osteogenic potential of the CS@TCP scaffolds. The FTD group simulated critical-sized bone defects to assess complete regenerative capability. Meanwhile, the PTD group allowed the investigation of scaffold–bone interface interactions, mimicking clinical inlay applications. The Onlay group mimicked the clinical application of cosmetic surgery, where implants were fixed on the bone surface.

In vivo results showed that both FTD and PTD groups exhibited significantly higher levels of new bone formation compared to the Onlay group, especially for the PTD group at 26 weeks, as presented in Figures 6 and 7. The expression of collagen and vWF in the Onlay group was consistently and significantly higher than that in other groups at both time points. Additionally, the FTD group showed a higher collagen and vWF expression compared to the PTD group, as shown in Figure 8. This may be due to the β-TCP coating on the scaffold surface. When in direct contact with the periosteum, the coating can enhance the recruitment of mesenchymal stem cells (MSCs), promoting efficient graft–host bone integration.[39] The decreasing trend in collagen and vWF expression over time in FTD and PTD groups likely reflects the tissue remodeling process during bone healing.[40] In contrast, the persistently higher expression of collagen and vWF in the Onlay group compared to the other groups at 12 and 26 weeks may reflect the early osteogenic stage rather than active osteogenesis, as shown in Figure 8.[41,42]

The overall reasons for these phenomena are illustrated in Figure 9. In the PTD group, the scaffolds were implanted within partial bone defects, where increased vascular supply and endogenous stem cells could enhance graft–host integration and induce higher levels of new bone formation.[43] This process synergistically interacted with the β-TCP coating on the scaffold surface, promoting MSC recruitment, osteogenic differentiation, and bone regeneration. In contrast, the coating in the FTD group had less contact with the host bone compared to the PTD group, restricting its new bone ingrowth.[44] Furthermore, in the Onlay group, where the scaffold was placed on the periosteum without direct exposure to MSCs or injury-related stimuli, the regenerative microenvironment was less supportive, resulting in limited bone integration only near the graft–bone surfaces.[42,45] Nonetheless, these bone integration effects can still facilitate the major goal of cosmetic surgeries.

In summary, these results highlighted the necessity of aligning scaffold design and surface biofunctionalization with specific clinical contexts to achieve optimal bone regeneration outcomes. Future work should further investigate the interaction between scaffolds and immune/vascular systems, thereby providing a deeper insight into the signaling pathways that regulate osteogenic and angiogenic properties *in vitro* and *in vivo*.

5. Conclusion

Scaffolds for bone tissue engineering aim to restore bone defects through the integration of biomaterials and regenerative microenvironments. This study demonstrated that integrating bioactive coatings with NaOH-pretreated 3D-printed PCL/β-TCP scaffolds effectively enhances scaffold hydrophilicity and bioactivity without compromising compressive properties. The β-TCP coating significantly promoted early osteogenic differentiation *in vitro*, potentially through ion release-mediated stimulation of osteoblast activity. The *in vivo* regenerative outcome

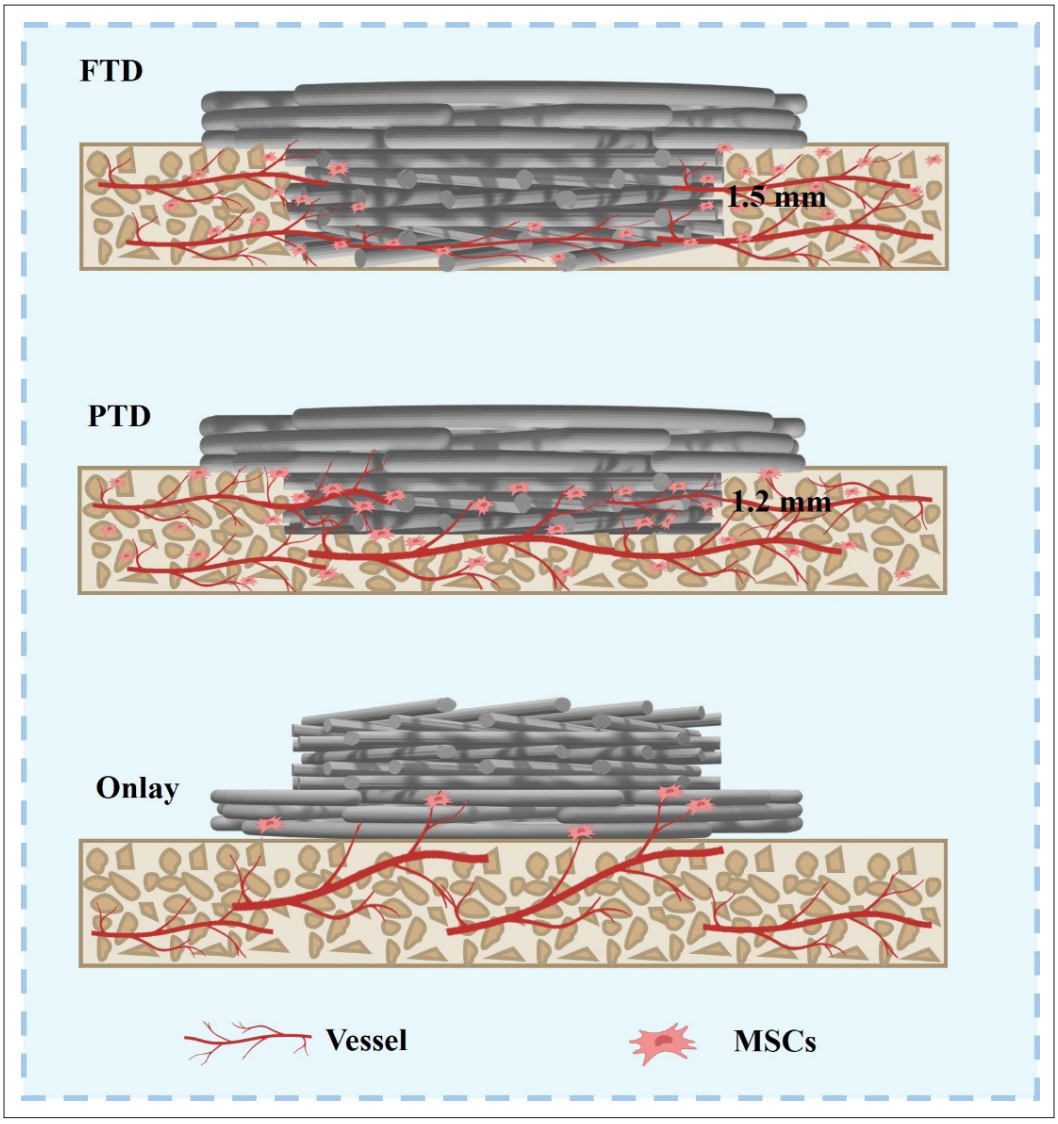

Figure 9. Schematic illustration of three cranial defect models (FTD, PTD, and Onlay) showing differences in scaffold placement and bone repair mechanism. Abbreviations: FTD, full-thickness cranial defect; MSC, mesenchymal stem cell; Onlay, intact cranial bone as an onlay graft; PTD, partial-thickness cranial defect.

was strongly influenced by the microenvironment. The PTD group provided abundant vascular supply and endogenous stem cells, enabling a synergistic interaction with the β-TCP coating and resulting in the highest level of new bone formation. The Onlay group showed new bone formation primarily at the scaffold–host bone interface, which could achieve the goal of excellent bone integration during the application of cosmetic surgeries. Collectively, these findings highlight the importance of tailoring scaffold structure and surface functionalization strategies to specific clinical scenarios, thereby maximizing bone regeneration and facilitating the reliable clinical application of 3D-printed bone scaffolds.

Acknowledgments

None.

Funding

The study was funded by the Natural Science Foundation of Jiangsu Province (BK20210117).

Conflict of interest

Yulin Jiang, Guanghui Xi, Chen Zhou, Xi Yang, and Dongxu Ke are employees of Novaprint Therapeutics

Suzhou Co., Ltd during this study but had no involvement in activities posing a conflict of interest.
The authors declare that they have no known competing financial interests or personal relationships that could have appeared to influence the work reported in this paper.

Author contributions

Conceptualization: Dongxu Ke, Yulin Jiang, Haisong Xu, Xi Yang
Investigation: Yulin Jiang, Guanghui Xi, Haisong Xu
Methodology: Yulin Jiang, Guanghui Xi, Haisong Xu, Chen Zhou
Software: Chen Zhou, Xi Yang
Writing–original draft: Yulin Jiang, Guanghui Xi
Writing–review & editing: Dongxu Ke, Yulin Jiang, Guanghui Xi, Xi Yang, Haisong Xu

Ethics approval and consent to participate

All procedures followed the NIH Guide for the Care and Use of Laboratory Animals and were approved by the Shanghai Jiao Tong University Agricultural Experimental Animal Farm (JDLL-R-20231016).

Consent for publication

Not applicable.

Availability of data

All data that support the findings of this study are included within the article.

References

1. Yelin E, Weinstein S, King T. The burden of musculoskeletal diseases in the United States. *Semin Arthritis Rheum*. 2016;46(3):259-260. doi:10.1016/j.semarthrit.2016.07.013
2. Ong KL, Mowat FS, Chan N, *et al*. Economic burden of revision hip and knee arthroplasty in Medicare enrollees. *Clin Orthop Relat Res*. 2006;446:22-28. doi:10.1097/01.blo.0000214439.95268.59
3. Huang D, Li Z, Li G, *et al*. Biomimetic structural design in 3D-printed scaffolds for bone tissue engineering. *Mater Today Bio*. 2025;32:101664. doi:10.1016/j.mtbio.2025.101664
4. Tsiklin IL, Shabunin AV, Kolsanov AV, Volova LT. In vivo bone tissue engineering strategies: advances and prospects. *Polymers (Basel)*. 2022;14(15):3222. doi:10.3390/polym14153222
5. Wu Y, Ji Y, Lyu Z. 3D printing technology and its combination with nanotechnology in bone tissue engineering. *Biomed Eng Lett*. 2024;14(3):451-464. doi:10.1007/s13534-024-00350-x
6. Wen Y, Xun S, Haoye M, *et al*. 3D printed porous ceramic scaffolds for bone tissue engineering: a review. *Biomater Sci*. 2017;5(9):1690-1698. doi:10.1039/c7bm00315c
7. Meng F, Yin Z, Ren X, Geng Z, Su J. Construction of local drug delivery system on titanium-based implants to improve osseointegration. *Pharmaceutics*. 2022;14(5):1069. doi:10.3390/pharmaceutics14051069
8. Sun S, Liu H, Hu Y, *et al*. Selection and identification of a novel ssDNA aptamer targeting human skeletal muscle. *Bioact Mater*. 2023;20:166-178. doi:10.1016/j.bioactmat.2022.05.016
9. Wang Q, Ye W, Ma Z, *et al*. 3D printed PCL/β-TCP cross-scale scaffold with high-precision fiber for providing cell growth and forming bones in the pores. *Mater Sci Eng C Mater Biol Appl*. 2021;127:112197. doi:10.1016/j.msec.2021.112197
10. Weingärtner L, Latorre SH, Velten D, *et al*. The effect of collagen-I coatings of 3D printed PCL scaffolds for bone replacement on three different cell types. *Appl Sci*. 2021;11(22):11063. doi:10.3390/app112211063
11. Jiang Y, Zhou C, Yang X, Ke D. 3D printed bioactive coated scaffolds boost osteogenesis and angiogenesis via the regulation of scaffold microstructure. *Biofabrication*. 2025;17(3):1-18. doi:10.1088/1758-5090/addc9c
12. Furtado ASA, Cunha MHS, Sousa LMR, *et al*. 3D-printed PCL-based scaffolds with high nanosized synthetic smectic clay content: fabrication, mechanical properties, and biological evaluation for bone tissue engineering. *Int J Nanomedicine*. 2025;20:53-69. doi:10.2147/IJN.S497539
13. Hao S, Wang M, Yin Z, *et al*. Microenvironment-targeted strategy steers advanced bone regeneration. *Materials Today Bio*. 2023;22:100741. doi:10.1016/j.mtbio.2023.100741
14. Zhu G, Zhang T, Chen M, *et al*. Bone physiological microenvironment and healing mechanism: basis for future bone-tissue engineering scaffolds. *Bioact Mater*. 2021;6(11):4110-4140. doi:10.1016/j.bioactmat.2021.03.043
15. Koushik TM, Miller CM, Antunes E. Bone tissue engineering scaffolds: function of multi-material hierarchically structured scaffolds. *Adv Healthc Mater*. 2023;12(9):2202766. doi:10.1002/adhm.202202766
16. Riau AK, Venkatraman SS, Mehta JS. Biomimetic vs. direct approach to deposit hydroxyapatite on the surface of low melting point polymers for tissue engineering. *Nanomaterials*. 2020;10(11):2162. doi:10.3390/nano10112162

17. Shen HY, Xing F, Shang SY, *et al*. Biomimetic mineralized 3D-printed polycaprolactone scaffold induced by self-adaptive nanotopology to accelerate bone regeneration. *ACS Appl Mater Interfaces*. 2024;16(15):18658-18670. doi:10.1021/acsami.4c02636

18. Heo SY, Ko SC, Oh GW, *et al*. Fabrication and characterization of the 3D-printed polycaprolactone/fish bone extract scaffolds for bone tissue regeneration. *J Biomed Mater Res B Appl Biomater*. 2019;107(6):1937-1944. doi:10.1002/jbm.b.34286

19. Tawfick S, De Volder M, Copic D, *et al*. Engineering of micro- and nanostructured surfaces with anisotropic geometries and properties. *Adv Mater*. 2012;24(13): 1628-1674. doi:10.1002/adma.201103796

20. Kocagöz M, Tıhmınlıoğlu F, Aldemir Dikici B. Surface modification *via* alkali treatment and its effect on the physicochemical and biological properties of emulsion templated scaffolds. *Polymer*. 2025;330:128475. doi:10.1016/j.polymer.2025.128475

21. Sherman VR, Yang W, Meyers MA. The materials science of collagen. *J Mech Behav Biomed Mater*. 2015;52:22-50. doi:10.1016/j.jmbbm.2015.05.023

22. Gresita A, Raja I, Petcu E, Hadjiargyrou M. Collagen-coated hyperelastic bone promotes osteoblast adhesion and proliferation. *Materials (Basel)*. 2023;16(21):6996. doi:10.3390/ma16216996

23. Vandrovcová M, Douglas T, Hauk D, *et al*. Influence of collagen and chondroitin sulfate (CS) coatings on poly-(lactide-co-glycolide) (PLGA) on MG 63 osteoblast-like cells. *Physiol Res*. 2011;60(5):797-813. doi:10.33549/physiolres.931994

24. Valdoz JC, Johnson BC, Jacobs DJ, *et al*. The ECM: to scaffold, or not to scaffold, that is the question. *Int J Mol Sci*. 2021;22(23):12690. doi:10.3390/ijms222312690

25. Jeong J, Kim JH, Shim JH, Hwang NS, Heo CY. Bioactive calcium phosphate materials and applications in bone regeneration. *Biomater Res*. 2019;23:4. doi:10.1186/s40824-018-0149-3

26. Boda R, Lázár I, Keczánné-Üveges A, *et al*. β-Tricalcium phosphate-modified aerogel containing PVA/Chitosan hybrid nanospun scaffolds for bone regeneration. *Int J Mol Sci*. 2023;24(8):7562. doi:10.3390/ijms24087562

27. Silva-Barroso AS, Cabral CSD, Ferreira P, Moreira AF, Correia IJ. Lignin-enriched tricalcium phosphate/sodium alginate 3D scaffolds for application in bone tissue regeneration. *Int J Biol Macromol*. 2023;239:124258. doi:10.1016/j.ijbiomac.2023.124258

28. Lu Q, Diao J, Wang Y, *et al*. 3D printed pore morphology mediates bone marrow stem cell behaviors via RhoA/ROCK2 signaling pathway for accelerating bone regeneration. *Bioact Mater*. 2023;26:413-424. doi:10.1016/j.bioactmat.2023.02.025

29. Zheng J, Nozaki K, Hashimoto K, Yamashita K, Wakabayashi N. Exploring the biological impact of β-TCP surface polarization on osteoblast and osteoclast activity. *Int J Mol Sci*. 2024;26(1):141. doi:10.3390/ijms26010141

30. Lu J, Yu H, Chen C. Biological properties of calcium phosphate biomaterials for bone repair: a review. *RSC Adv*. 2018;8(4):2015-2033. doi:10.1039/c7ra11278e

31. Deng W, Yang X, Yu J, Omari-Siaw E, Xu X. Recent advances of physiochemical cues on surfaces for directing cell fates. *Colloids Surf B Biointerfaces*. 2025;250:114550. doi:10.1016/j.colsurfb.2025.114550

32. Gupta D, Singh AK, Kar N, Dravid A, Bellare J. Modelling and optimization of NaOH-etched 3-D printed PCL for enhanced cellular attachment and growth with minimal loss of mechanical strength. *Mater Sci Eng C*. 2019;98:602-611. doi:10.1016/j.msec.2018.12.084

33. Jiang L, Jin S, Geng S, *et al*. Maintenance and restoration effect of the surface hydrophilicity of pure titanium by sodium hydroxide treatment and its effect on the bioactivity of osteoblasts. *Coatings*. 2019;9(4):222. doi:10.3390/coatings9040222

34. Witek L, Shi Y, Smay J. Controlling calcium and phosphate ion release of 3D printed bioactive ceramic scaffolds: an in vitro study. *J Adv Ceram*. 2017;6(2):157-164. doi:10.1007/s40145-017-0228-2

35. Luo F, Yang Y, Li D, *et al*. Low-temperature plasma effect-induced enhancement of osteogenic activity in calcium phosphate ceramics. *Acta Biomater*. 2025;200:667-685. doi:10.1016/j.actbio.2025.04.048

36. González Díaz EC, Shih YRV, Nakasaki M, Liu M, Varghese S. Mineralized biomaterials mediated repair of bone defects through endogenous cells. *Tissue Eng Part A*. 2018;24(13–14):1148-1156. doi:10.1089/ten.tea.2017.0297

37. Weng Y, Jian Y, Huang W, *et al*. Alkaline earth metals for osteogenic scaffolds: from mechanisms to applications. *J Biomed Mater Res B Appl Biomater*. 2023;111(7):1447-1474. doi:10.1002/jbm.b.35246

38. Wang K, Jiang K, Luo C, *et al*. An osteoimmunomodulatory Ca2+/Zn2+-doped scaffold promotes M2 macrophage polarization via the src-mediated chemoking signaling pathway to enhance osteoinduction. *Compos Part B: Eng*. 2024;284:111653. doi:10.1016/j.compositesb.2024.111653

39. Ghiacci G, Graiani G, Ravanetti F, *et al*. "Over-inlay" block graft and differential morphometry: a novel block graft model to study bone regeneration and host-to-graft interfaces in

rats. *J Periodontal Implant Sci*. 2016;46(4):220-233. doi:10.5051/jpis.2016.46.4.220

40. Selvaraj V, Sekaran S, Dhanasekaran A, Warrier S. Type 1 collagen: synthesis, structure and key functions in bone mineralization. *Differentiation*. 2024;136:100757. doi:10.1016/j.diff.2024.100757

41. Pilliar RM, Lee JM, Maniatopoulos C. Observations on the effect of movement on bone ingrowth into porous-surfaced implants. *Clin Orthop Relat Res*. 1986;7(208):108-113.

42. Sosakul T, Tuchpramuk P, Suvannapruk W, *et al*. Evaluation of tissue ingrowth and reaction of a porous polyethylene block as an onlay bone graft in rabbit posterior mandible. *J Periodontal Implant Sci*. 2020;50(2):106-120. doi:10.5051/jpis.2020.50.2.106

43. Canto FRT, Garcia SB, Issa JPM, *et al*. Influence of decortication of the recipient graft bed on graft integration and tissue neoformation in the graft-recipient bed interface. *Eur Spine J*. 2008;17(5):706-714. doi:10.1007/s00586-008-0642-9

44. Wu S, Luo S, Cen Z, *et al*. All-in-one porous membrane enables full protection in guided bone regeneration. *Nat Commun*. 2024;15(1):119. doi:10.1038/s41467-023-43476-9

45. Ku JK, Lee KG, Ghim MS, *et al*. Onlay-graft of 3D printed Kagome-structure PCL scaffold incorporated with rhBMP-2 based on hyaluronic acid hydrogel. *Biomed Mater*. 2021;16(5):055004. doi:10.1088/1748-605X/ac0f47

ACCSCIENCE PUBLISHING

International Journal of Bioprinting

RESEARCH ARTICLE

Three-dimensional-printed collagen scaffold with limbal stem cells derived from adipose-derived mesenchymal stem cells for the treatment of limbal stem cell deficiency

Martha Stokking[1†], Marta Cadenas-Martín[1†], Ana I. Martín-González[1], Alba Fernández-Ferrer[1], Francisco Arnalich-Montiel[2], and Maria P. De Miguel[1*]

[1]Cell Engineering Laboratory, La Paz University Hospital Health Research Institute (IdiPAZ), Madrid, Spain

[2]Ophthalmology Department, Ramón y Cajal Institute for Biohealth Research (IRYCIS), Ramón y Cajal University Hospital, Madrid, Spain

[†]These authors contributed equally to this work.

***Corresponding author:**
Maria P. De Miguel
(mmiguelgonzalez@salud.madrid.org)

Citation: Stokking M, Cadenas-Martin M, Martín-González AI, Fernández-Ferrer A, Arnalich-Montiel F, De Miguel MP. Three-dimensional-printed collagen scaffold with limbal stem cells derived from adipose-derived mesenchymal stem cells for the treatment of limbal stem cell deficiency. *Int J Bioprint*. 2025;11(6):407-429. doi: 10.36922/IJB025290293

Received: July 18, 2025
1st revised: August 27, 2025
2nd revised: September 5, 2025
Accepted: September 8, 2025
Published online: September 8, 2025

Copyright: © 2025 Author(s). This is an Open Access article distributed under the terms of the Creative Commons Attribution License, permitting distribution, and reproduction in any medium, provided the original work is properly cited.

Publisher's Note: AccScience Publishing remains neutral with regard to jurisdictional claims in published maps and institutional affiliations.

Abstract

When limbal stem cell deficiency (LSCD) is partial, the standard treatment involves covering the corneal surface with amniotic membrane (AM), which supports the proliferation of the remaining limbal stem cells (LSCs). In cases of complete LSCD, the most common treatment is cultured limbal epithelial transplantation (CLET), although there is a risk of rejection. Studies have shown that mesenchymal stem cell transplantation is equally safe and effective as CLET. Recent research has demonstrated successful differentiation of adipose-derived adult mesenchymal stem cells (ADSCs) into LSCs. Combining AM transplantation with LSCs improves treatment efficacy. However, a limitation of AM use is donor variability and the associated risk of immune rejection. We propose the use of 3D-printed collagen as a scaffold seeded with LSCs derived from ADSCs for the treatment of LSCD in a rat model. The 3D-printed collagen scaffolds exhibited good transparency. *In vitro* differentiation of ADSCs into LSCs showed morphological changes that were more pronounced and occurred more rapidly on 3D-printed collagen. Among the tested substrates, 3D-printed collagen was the most efficient for differentiation, yielding the highest expression of LSC-specific markers (p63α and BMI-1) and the corneal epithelial marker (SSEA-4). LSCs differentiated in either AM or 3D-printed collagen I scaffolds were transplanted into a rat model of LSCD and compared with the standard, cell-free AM treatment. In all treatment groups, the induced epithelial wound was closed; however, integration of the 3D-printed collagen scaffold was statistically superior to that of AM. However, markers for different corneal structures (PAS, BMI-1, p63α, and cytokeratins 12 and 13) indicated that the generated epithelium was conjunctival rather than corneal, suggesting that the contribution of ADSC-derived LSCs was insufficient for complete corneal re-epithelization.

Keywords: Amniotic membrane; Bioprinting; Cornea; Limbal stem cell deficiency; Mesenchymal stem cells; Regenerative medicine; Tissue engineering; Vision loss

1. Introduction

The cornea is a transparent, avascular structure located at the front of the eye. Histologically, it is composed of the following three main cellular layers: epithelium, stroma, and endothelium. The most superficial layer is the epithelium, a stratified layer that accounts for approximately 10% of the total corneal thickness. It serves as a protective barrier against mechanical injury and external biological agents. The corneal stroma comprises about 90% of the total thickness and is composed primarily of an organized extracellular matrix rich in collagen and proteoglycans. This layer provides the cornea with strength, morphology, and transparency.[1] The endothelium is a single layer of cells whose primary function is to regulate corneal hydration through a pump-leak mechanism, thereby maintaining corneal transparency.[2] Each of these layers can be selectively replaced through either full-thickness (penetrating) or lamellar keratoplasty techniques, depending on the depth and extent of the corneal pathology.[3] However, these keratoplasty techniques typically involve only the central portion of the cornea and, therefore, do not address limbal stem cell deficiency (LSCD), which affects the peripheral cornea and requires a distinct therapeutic approach.

Damage to the corneal epithelium is usually repaired through self-regeneration, driven by a specialized population of corneal epithelial stem cells located at the limbus, known as limbal stem cells (LSCs).[4] These LSCs typically undergo asymmetric division, producing one daughter cell that remains in the niche to preserve the stem cell pool and another that becomes a transient amplifying cell (TAC). TACs proliferate rapidly and differentiate into the various functional cells of the corneal epithelium, collectively known as corneal epithelial cells.[5] Epithelial repair follows a coordinated centripetal and upward growth pattern.[6]

The differentiation and maturation of the corneal epithelium are linked to the expression of cytokeratin 12 (CK-12), a type of intermediate filament essential for epithelial integrity,[7] which is expressed in all cell layers of the differentiated and stratified epithelium.[8] Stage-specific embryonic antigen-4 (SSEA-4) is a well-established marker for human embryonic stem cells. High levels of SSEA-4 expression have been observed in differentiated corneal epithelial cells as well as in the limbal epithelium.[9]

Unlike the corneal epithelium, no definitive marker has yet been established for LSCs, although several candidates have been proposed. One such candidate is the transcription factor p63α, which is expressed in progenitor cells within the basal layer of the limbal epithelium. Another relevant factor is BMI-1, a transcription factor associated with stem cell self-renewal, which has been identified in the human limbus.[10] Cytokeratin 19 (CK-19) has also emerged as a potential marker.[11]

Destruction or dysfunction of LSCs or their niche leads to LSCD.[12] In this condition, the loss of LSCs impairs the regenerative capacity of the corneal epithelium, allowing the conjunctival epithelium—a non-keratinized stratified squamous epithelium containing mucin (MUC)-secreting goblet cells—to invade the corneal surface. This process, known as conjunctivalization, compromises corneal transparency and promotes neovascularization. As a result, LSCD can lead to chronic ocular surface inflammation, persistent pain, and severe vision loss or blindness in advanced cases. Characteristic markers of the invading conjunctival epithelium include MUC and cytokeratin 13 (CK-13), the latter being expressed in all conjunctival epithelial cells.[13]

When LSCD is partial, one of the most commonly employed treatments is the application of amniotic membrane (AM) to cover the corneal surface. AM serves as a biological bandage that protects the damaged area from mechanical stress, promotes epithelial healing, reduces inflammation and pain, and facilitates the proliferation of the remaining LSCs.

In cases of total LSCD, if the disease is unilateral, several autologous approaches are available, such as conjunctival limbal autograft, which involves transplanting two relatively large limbal-conjunctival grafts from the healthy contralateral eye to the affected eye. An alternative, cultured limbal epithelial transplantation (CLET), requires only a small limbal biopsy, which is expanded *in vitro* and then transplanted to the damaged eye.[14] In bilateral LSCD, where no autologous donor tissue is available, treatment options include allogeneic CLET or keratolimbal allograft. These approaches require systemic immunosuppression, which increases the risk of patient morbidity.[15]

The rising number of bilateral LSCD cases has led to an increased reliance on allogeneic LSCs, which inherently carry the risk of immune rejection and necessitate long-term immunosuppressive therapy. To overcome these limitations, numerous research groups have explored the use of autologous stem cells of extraocular origin as an alternative source for ocular surface regeneration.

The use of mesenchymal stem cells (MSCs) has gained significant momentum in recent years.[15] Among these, bone marrow-derived MSCs have been extensively studied for ocular surface regeneration, showing promising results. However, adipose-derived stem cells (ADSCs) offer key practical advantages as follows: they are more readily accessible, cost-effective, and less invasive to obtain, which has led to their increasing popularity in translational

research.[16] At the clinical level, Calonge *et al.*[17] provided compelling evidence that MSC transplantation is as safe and effective as CLET for the treatment of LSCD.

More recently, our group and collaborators have shown that ADSCs can be successfully differentiated into LSC-like phenotypes, expressing key LSC markers.[18,19] Notably, using an LSC-specific induction medium, ADSCs achieved structural epithelial regeneration, further supporting their potential as an autologous cell source for ocular surface reconstruction.[16,19]

With respect to the cell carrier, the most widely used scaffold in clinical practice is the AM.[20] AM is a biologically active, avascular tissue. This collagen-rich matrix mimics the biochemical properties of the corneal and scleral stroma, facilitating cell migration, differentiation, and inhibition of apoptosis.[21] AM's biocompatibility and low immunogenicity make it practical and convenient for clinical use. However, in cases of total LSCD, AM transplantation alone is insufficient to restore a functional epithelium.[22] Combining AM with LSCs has shown improved therapeutic outcomes,[6] and more recently, AM seeded with MSCs has demonstrated the ability to restore a corneal epithelial phenotype in LSCD models.[16,19,23]

Despite its advantages, AM has several limitations, including donor variability, which can increase the risk of immunologic rejection in allogeneic settings. In addition, its scarcity and the complexity of procurement, processing, and storage contribute to significant costs and limit its widespread availability. Due to these limitations, alternative scaffolds are being actively investigated to support, or even stimulate, corneal epithelial regeneration prior to implantation on the damaged ocular surface. Among the biomaterials explored are fibrin, chitosan, and silk fibroin—materials that are biocompatible, mechanically resilient, and easy to handle. However, their clinical application may be hindered by immune rejection or suboptimal biomechanical properties, such as excessive rigidity, fragility, or insufficient tensile strength.[24]

Collagen-based scaffolds have emerged as a highly promising option due to their structural similarity to native corneal stroma and excellent biocompatibility. In parallel, advances in three-dimensional (3D) bioprinting have enabled the creation of complex, cell-compatible constructs using bioinks—formulations that combine living cells with biological materials.[25] The use of 3D-printing techniques to replicate complex patterns found in biological tissues is an emerging field in tissue engineering. Among these, extrusion-based bioprinting is particularly prominent due to its versatility and its ability to use a wide range of bioinks with varying viscosities. This technique uses pneumatic or mechanical forces for continuous layer-by-layer deposition. While pneumatic systems provide better control over bioink viscosities, they may cause cell membrane disruption due to pressure fluctuations. Conversely, mechanical systems offer precise control but introduce higher shear stress, which can affect cell viability. Optimizing critical parameters such as shear stress, nozzle diameter, and material crosslinking is essential for balancing cell viability with shape fidelity.[26] The combination of high speed and the ability to utilize highly viscous bioinks makes extrusion-based bioprinting particularly suitable for fabricating anatomically compliant constructs. Jetting-based bioprinting, in contrast, employs a drop-on-demand mechanism to deposit bioink droplets at pre-defined positions, enabling precise cell placement and enhanced cell–cell interactions. This technique includes several modalities, such as inkjet-based, electrohydrodynamic jet-based, laser-induced forward transfer-based bioprinting, and others. However, the jetting itself is governed by the surface tension and viscosity of the bioink, which restricts printability and limits the fabrication of large, anatomically complex constructs. Vat photopolymerization-based bioprinting stands out for its high resolution, making it ideal for fabricating intricate surface topographies. This technique utilizes selective light irradiation to induce localized curing of liquid biomaterials contained within a vat. Variants such as stereolithography, digital light processing, two-photon polymerization, and volumetric printing further expand its capabilities (for a comprehensive review, see Ng *et al.*[27]).

In this study, we propose the use of mechanically driven extrusion-based 3D-printed scaffolds, as this printing method allows for the use of highly concentrated and viscous collagen bioinks in continuous deposition layers, enabling control over the construct's shape. In addition, the constructs were colonized with adipose-derived stem cell–derived limbal stem cells (ADSC-LSCs) for the treatment of total LSCD in a rat model, as a step toward the development of fully autologous, bioengineered ocular surface reconstruction strategies.

2. Materials and methods

2.1. Scaffolds

2.1.1. Preparation of human amniotic membrane

A total of 64 cm^2 of human AM unsuitable for transplantation was obtained from a 37-year-old human donor via the Barcelona Blood and Tissue Bank. The sample was anonymized by the Barcelona Biobank, as stipulated by the Organic Law on Data Protection, and was accompanied by a serological analysis report showing negative for human immunodeficiency virus (HIV), hepatitis A virus (HAV), hepatitis B virus (HBV), hepatitis

C virus (HCV), human T-cell lymphotropic virus (HTLV), dengue virus, and syphilis. The sample was washed four times for 15 min with PBS to remove the glycerol in which it had been preserved, scraped on both sides to remove the epithelium, and cut into 6 mm diameter circles.

2.1.2. Three-dimensional bioprinting

Sheets of rat collagen I were obtained by 3D printing at the Cell Engineering Laboratory of the La Paz Health University Hospital Research Institute (IdiPAZ).[28] For the 3D printing, the Regemat® V1 mechanical extrusion printer (Regemat®, Spain) was used together with Regemat 3D Designer software (Regemat®, Spain), which enabled adjustment of the object geometry and configuration of printing parameters. A nozzle diameter of 580 μm was selected. Collagen bioink (Cellink®, Sweden) was neutralized to pH 7 and printed at a concentration of 8 mg/mL, with 9 μg/mL of proteoglycans (glycosaminoglycans) derived from goat cornea (R&D Systems, USA). The 3D-printed scaffolds were designed as flat cylindrical shapes with a diameter of 6 mm using an STL format. To obtain a thickness of approximately 100 μm, two layers were printed in a diagonal pattern oriented at 90° relative to each other. The printed cylinders underwent two post-printing curation steps: first, a gelation step involving incubation in a carbon dioxide (CO_2) cell culture incubator at 37°C for a minimum of 2 h (longer periods showed no added benefit); and second, a controlled dehydration step, in which the gelled samples were incubated in a 40% humidity-controlled chamber at 37°C for 1 week. This final step could be performed in a humidity-controlled environmental chamber (Thermo Fisher Scientific, USA) or chemically, by adding the saturated potassium carbonate (Sigma, USA) in a sealed glass desiccator (Sigma, USA). These curation steps ensured transparency and tensile strength rheological characteristics similar to AM (see Section 3). As the cornea is avascular, no vascularization strategies were employed.

2.1.3. Macroscopic characterization of the scaffolds

Optical coherence tomography was performed on both the AM and 3D-printed scaffolds to determine their thickness. In addition, graft transparency was assessed, following standard ophthalmological procedures, by placing AM and 3D-printed constructs on a black background and a back-lit chart composed of parallel black lines over a white background, in order to compare light transmittance and refraction, as described in previous studies.[29] This assessment was conducted by an ophthalmologist (FA-M) in a blinded fashion. Tensile strength was evaluated subjectively by the same ophthalmologist, also in a blinded manner, by placing sutures on two sides of the AM or 3D-printed scaffolds.

2.2. Mesenchymal stem cell isolation and culture

The cells used in this study were obtained through the isolation of human tissues via procedures approved by the Institutional Review Board of IdiPAZ (protocol code PI308) and deposited in the La Paz University Hospital Biobank. Ophthalmic cells were obtained under the approval of the Institutional Review Board of the Ramón y Cajal University Hospital (protocol code 305/11), or from commercial cell lines (ATCC, USA). All adipose tissue donations were collected with prior written informed consent from the donors, in line with the World Medical Association Declaration of Helsinki (2000) and the Organic Law on Data Protection, which guarantees donor anonymity. Each sample was subjected to serological analysis prior to processing to rule out active infection by HIV, HAV, HBV, HCV, HTLV, dengue virus, and syphilis, in compliance with the official state guidelines for the use of human cells and tissues for experimental purposes (Royal Decree 09/2014; July 4, 2014). No test for SARS-CoV-2 was performed, as all donations predated the COVID-19 pandemic.

Human adipose-derived mesenchymal stem cells (hADSCs) were extracted from the lipoaspirates of six female donors aged 37–55, with body mass indexes ranging from 26.4 to 31.8 kg/m^2, who had undergone elective liposuction. All donors were healthy and were not receiving any drug therapy, except for one who was being treated with fluoxetine for depression. The protocol already established by Zuk *et al.*[30] was followed, as previous studies by our laboratory demonstrated its effectiveness in isolating multipotent hADSCs capable of differentiating into multiple cell lineages. All cells were maintained in culture until reaching sub-confluence (80–90%) in their corresponding medium at 37°C with 5% CO_2, with medium changes three times per week. Subsequently, the cells were cryopreserved in liquid nitrogen using complete medium supplemented with 10% dimethyl sulfoxide (DMSO; EMSURE®, Abbott Laboratories, USA) for subsequent use in the various experiments.

2.3. Human adipose-derived mesenchymal stem cell differentiation into limbal stem cells

The hADSCs were differentiated into LSCs according to a previously published protocol.[18] Briefly, hADSC-derived limbal cells were differentiated for 7 days in an ectodermal induction medium of Dulbecco's Modified Eagle Medium (DMEM; Gibco, USA) with: GlutaMax (2 mM; Gibco, USA); sodium pyruvate (1 mM; Gibco™, USA); 15% fetal bovine serum (FBS; Gibco™); 1% penicillin/streptomycin (P/S) (Gibco™); 10 μM SB505124 (a transforming growth factor beta-pathway inhibitor; Merck KGaA, Germany); 10 μM IWP2 (a Wnt pathway inhibitor, Merck KGaA); and 50 ng/mL fibroblast growth factor 2 (ORF Genetics,

Iceland).[31] The second differentiation step lasted 10 days and used a corneal epithelial cell differentiation medium based on that of Casaroli-Marano *et al.*[32] named SHEM. This medium consisted of DMEM/Ham F12 (1:2) supplemented with: GlutaMax (2 mM); sodium pyruvate (1 mM; Gibco™); 2% FBS (Gibco™); 1% P/S (Gibco™); 5 μg/mL insulin (Humalog®, USA); 10 ng/mL human epidermal growth factor (Peprotech, USA); 0.18 mM adenine (Merck KGaA); 0.4 μg/mL hydrocortisone (Merck KGaA); 2 nM 3,30,5-triiodo-L-thyronine (T3) (Merck KGaA); 0.5% DMSO (EMSURE®); supplemented with 4 nM pigment epithelium-derived factor (PEDF; Peprotech); and 20 ng/mL keratinocyte growth factor (KGF; Peprotech).

Three different substrates were used: standard culture plastic, AM, and 3D-printed collagen I, each coated with 0.75 μg/cm^2 of vitronectin (Gibco™) to improve cell adhesion and differentiation efficiency.

2.4. Morphometric analysis of differentiation and kinetics

Differentiation kinetics were analyzed to morphological changes in the cells. The performance of the three different substrates during differentiation was evaluated by measuring the length and number of hADSCs before differentiation, 7 days after the first differentiation step, and 9 days after the second differentiation step. Measurements were taken using ImageJ software (version 1.51a, NIH, USA) from microscopic images of the cell cultures, following the method described by Cadenas-Martín *et al.*[18]

2.5. Immunofluorescence

Given that no specific marker exists for LSCs, while several are associated with the corneal limbal niche, we evaluated the differentiation efficiency of ADSC-LSCs cultured on plastic, 3D-printed collagen, and AM (all coated with vitronectin), by detecting the colocalization of nuclear p63α (1:100; 4892, Cell Signaling Technology Inc., USA) and BMI-1 (1:60; sc-390443, Santa Cruz Biotechnology, USA) markers, along with the cytoplasmic embryonic stem cell marker SSEA-4 (1:50/1:100; MAB1435, R&D Systems). For positive controls, the HaCat cell line was used for p63α and BMI-1, and the NTERA cell line for SSEA-4. For negative controls, the primary antibodies were omitted.

Quantitative data on marker positivity were obtained by calculating the ratio of positive to negative cells in 30 random fields at 630× magnification using a confocal microscope (DMI 4000 B, Leica, Germany).

2.6. *In vivo* studies

The animal studies complied with European Union regulations on vertebrate animal experimentation and were carried out in accordance with the 3Rs principle (replacement, reduction, and refinement), as stipulated in Royal Decree 53/2013 of February 1, 2013, on the protection of animals used for scientific purposes, and in accordance with the guidelines of the Association for Research in Vision and Ophthalmology. All procedures were performed by certified personnel authorized to conduct animal experimentation and approved by the Animal Welfare Committee of IdiPAZ, under the Regional Ministry of Environment, Agriculture, and the Interior of the Community of Madrid (code PROEX: 347.1/21). Animals were housed at the Experimental Surgery Service animal facility of IdiPAZ, Madrid (Registration Number: 280790001941).

2.6.1. Animal model and surgical procedures

Twenty-four female Sprague Dawley rats weighing 220–380 g were used to test the biosafety and efficacy of hADSC-LSCs on AM and 3D-printed collagen to repair corneal epithelium damage following LSC obliteration. The rats were randomly assigned to three groups (n=8 per group): control group with cell-free AM; experimental group 1 with 1×10^5 LSCs on AM; and experimental group 2 with 1×10^5 LSCs on 3D-printed collagen.

In the surgical procedure, a 4-min chemical burn was induced on the cornea of the right eye using heptanol, under anesthesia, according to a previously published protocol.[16] This was followed by mechanical removal of the remaining corneal epithelium and limbal region using an AlgerBrush II BR-2 1 mm (Eickemeyer, Germany). All rats received a retro-orbital injection of 40 mg/mL triamcinolone acetonide (Kenacort®, Bristol Myers Squibb Company, USA) for local immunosuppression. Subsequently, the animals were transplanted with one of the following: cell-free AM, AM with ADSC-LSCs, or 3D-printed collagen with ADSC-LSCs. A drop of fibrin glue (Tisseel, Baxter International Inc., USA) was applied beneath the scaffold to promote adhesion. Then, a 5.5 mm diameter ACLAR® (chlorotrifluoroethylene, OcuScience®, USA) contact lens was placed over the graft to prevent graft detachment and reduce pain. To prevent infection, Tobradex (Novartis, Switzerland) was applied, and the eyelid was closed with tarsorrhaphy using two 5/0 Vicryl stitches (Ethicon Inc., USA) to prevent self-inflicted trauma. Postoperative care included: tramadol (25 mg/kg; Grünenthal GmbH, Germany) subcutaneously once daily for 1 week, and one drop of Tobradex (Novartis) every 12 h. The animals were monitored for 10 days, until full reepithelialization was observed.

Out of the 24 rats used in the study, only half (n = 12) were suitable for final analysis. Eight rats died before the end of the study due to complications related to analgesia, not the surgical procedure. Four rats were excluded due to tissue processing issues—corneal epithelium was either

folded, absent, or the scaffold (AM or 3D-printed collagen) was missing from the paraffin block. Therefore, the final analysis included: three rats treated with cell-free-AM, five rats treated with LSC-AM, and four rats treated with LSC-3D-printed collagen.

2.6.2. Macroscopic study

The progression of re-epithelization was assessed using fluorescein staining (Bausch&Lomb, USA) and ultraviolet lamp photography of the treated eyes at the end of the 10-day experimental period.

2.6.3. Histopathology

Ten days after surgery, the rats were euthanized. The eyes were enucleated—right eyes (treated) and left eyes (untreated) in the case of negative controls. Corneas were fixed in 10% buffered formalin (VWR, USA), embedded in paraffin blocks, and sectioned at a thickness of 7 µm using a Leica RM2255 microtome. Sections were stained with hematoxylin-eosin or periodic acid–Schiff (PAS) stain and observed under an Olympus BX41 light microscope (Japan).

2.6.4. Immunohistochemistry

Immunohistochemical staining was performed using diaminobenzidine (SK-4103-100, Vector Laboratories, USA) to detect various markers of corneal epithelia, limbal, or conjunctival cells. The following primary antibodies were used: basal limbal epithelial markers—anti-p63α (1:100; 4892, Cell Signaling Technology Inc.) and anti-BMI-1 (1:100; sc-390443, Santa Cruz Biotechnology); stratum basale of the limbal epithelium—anti-CK-19 (1:200; PA5-95304, Invitrogen, USA); corneal epithelial markers—anti-stage-specific embryonic antigen-4 (SSEA4; 1:50; MAB1435, R&D Systems) and anti-CK-12 (1:250; MA5-42505, Invitrogen); conjunctival epithelium—CK-13 (1:200; sc-57003, Santa Cruz Biotechnology); and conjunctival epithelial mucus goblet cell markers—MUC-4 (1:500; MA5-42811, Invitrogen), and MUC-5 (1:500; WH0004586M7, Sigma-Aldrich).

2.7. Statistical analysis

The chi-square test (χ^2) was used to assess whether differences in scaffold integration were statistically significant.

For quantification of p63α expression following immunohistochemical staining, labeled cells were counted using ImageJ image-processing software. The percentage of p63α-positive cells was calculated in both limbal regions and in three randomly chosen corneal fields. Epithelial stratification was also considered by dividing the epithelium into layers and calculating marker distribution accordingly.

Normality of the data was assessed using the Shapiro–Wilk test. For normally distributed data, Student's *t*-test for independent samples was used (assuming equal variances. If variances were unequal, Welch's correction was applied. For non-normally distributed data, the Mann–Whitney *U* test was used. All statistical analyses were performed using GraphPad Prism 8.0 (Dotmatics, USA). A p-value < 0.05 was considered statistically significant.

3. Results

3.1. Macroscopic characterization and scaffold transparency

The 3D prints exhibited a perfect cylindrical shape and a 6 mm diameter as planned (Figure 1). Their thickness, measured by optical coherence tomography, was 110.6 ± 20.7 µm, comparable to that of the AM, which measured 113.2 ± 20 µm (Figure 1A). Each printed layer contributed approximately 50 µm of thickness, enabling reproducible and customizable scaffold thickness by adjusting the number of printed layers. Regarding transparency measurements, macroscopic images showed that the 3D-printed collagen scaffolds exhibited better transparency than AM in both light transmission and refraction, as assessed on a black background and a back-lit chart composed of parallel black lines (Figure 1B).

3.2. Differentiation kinetics of limbal stem cells on soft substrates

The results of hADSC differentiation into LSCs on 3D-printed collagen are shown in Figure 2. The results for plastic and AM substrates were previously published by Cadenas-Martín *et al.*[18] hADSCs seeded on the different substrates (plastic, AM, and 3D-printed collagen) significantly increased in average length during the first differentiation step toward ectoderm. However, in the second step, cells on all substrates significantly decreased in length, adopting the rounded morphology characteristic of LSCs (Figure 2A and C). Differences were also observed in cell numbers: on plastic and 3D-printed collagen, the cell count decreased during the second step (Figure 2B), whereas it increased on AM.

To compare the different substrates, the data were grouped into bar graphs. As shown in Figure 3A, cells seeded on culture plastic before differentiation were significantly more elongated than those on 3D-printed collagen and AM. However, although hADSCs seeded on 3D-printed collagen and AM reached similar lengths to those on plastic during the first differentiation step, they became significantly rounder by the end of the process. Specifically, cell length reduced to 50 µm on plastic, while it decreased to around 30 µm on 3D-printed collagen and AM (Figure 3A).

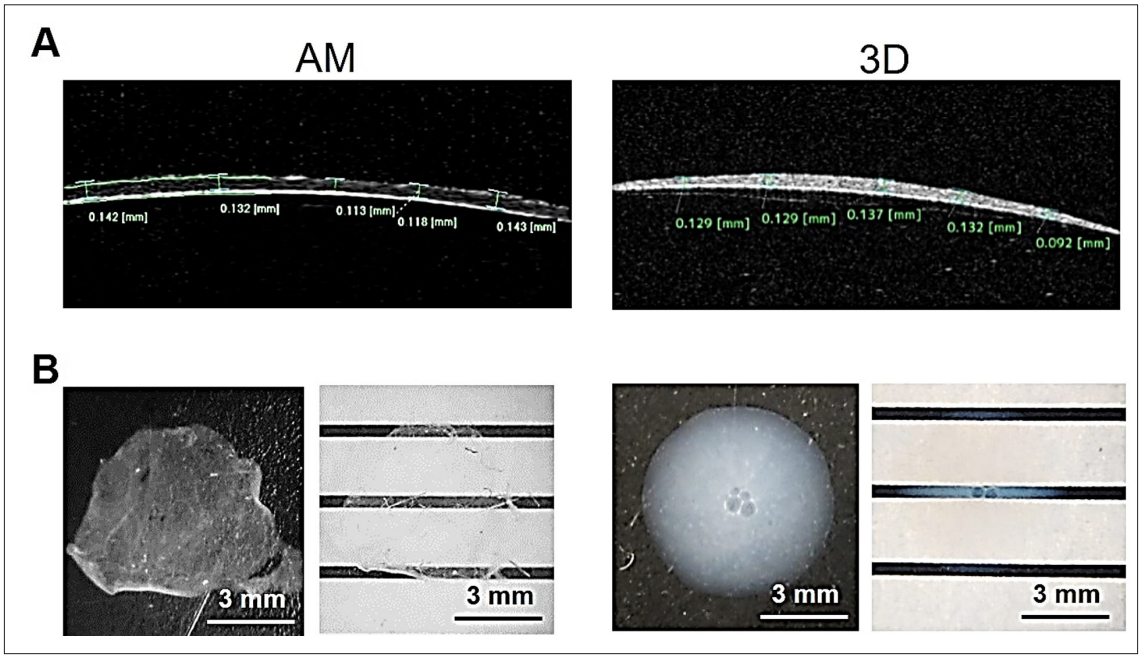

Figure 1. Macroscopic comparison between amniotic membrane (AM) and three-dimensional (3D) printed collagen scaffold. (A) Optical coherence tomography images showing thickness measurements in μm (in green). (B) Photographs illustrating light transmittance and refraction on a black and back-lit graphic background. Scale bar = 3 mm; magnification = 2×.

Figure 3B shows that hADSCs seeded on culture plastic proliferated significantly more than those on AM during the first step, although similar cell numbers were observed across all substrates after complete differentiation.

In summary, targeted differentiation into LSCs led to cell elongation during the first step and rounding during the second step on all substrates, with the shortening being more pronounced on 3D-printed collagen and AM than on plastic. Moreover, derivation of LSCs from hADSCs on 3D-printed collagen and AM showed faster kinetics, as cells acquired the rounded phenotype characteristic of LSCs within just 9 days of the second differentiation step.

3.3. Expression of limbal stem cell markers in human adipose-derived mesenchymal stem cell–derived cells on three-dimensional printed collagen

To assess the differentiation of hADSCs, the expression of LSC-specific markers was evaluated by immunofluorescence. After 10 days in the second differentiation step on 3D-printed collagen coated with vitronectin, 59% of the cells were double-positive for p63α and BMI-1 (Figure 4). When the culture period was extended to 11 days, the percentage of double-positive cells decreased slightly to 52% (Figure 4). Notably, at 13 days, this percentage dropped drastically to only 4% (Figure 4), suggesting that the LSCs actively differentiated toward corneal epithelial cells over time.

In agreement with these findings, 90.7% of cells on 3D-printed collagen were positive for the corneal epithelial marker SSEA-4 after 10 days in the second differentiation step (Figure 5). After 11 days, SSEA-4 positivity decreased to 36.8% (Figure 5), reinforcing the conclusion that 10 days of the second differentiation step represents the optimal time point for transplantation.

3.4. Re-epithelization outcomes in *in vivo* macroscopic study

Twelve rats were included and analyzed in the *in vivo* study: n = 3 for the cell-free AM group; n = 5 for the AM with ADSC-derived LSC group; and n = 4 for the 3D-printed collagen with ADSC-derived LSC group. Surface reepithelialization was evaluated using fluorescein staining after 10 days. In the cell-free AM group, one rat showed complete re-epithelization (absence of fluorescein; Figure 6A) while the remaining two showed nearly complete coverage (Figure 6B and C). In the AM + LSC group, three eyes were completely re-epithelialized (Figure 6D, F, and H), and two showed partial healing (Figure 6E and G). In the 3D-printed collagen + LSC group, three eyes were fully re-epithelized (Figure 6J, K, and L), and one remained partially re-epithelized (Figure 6I).

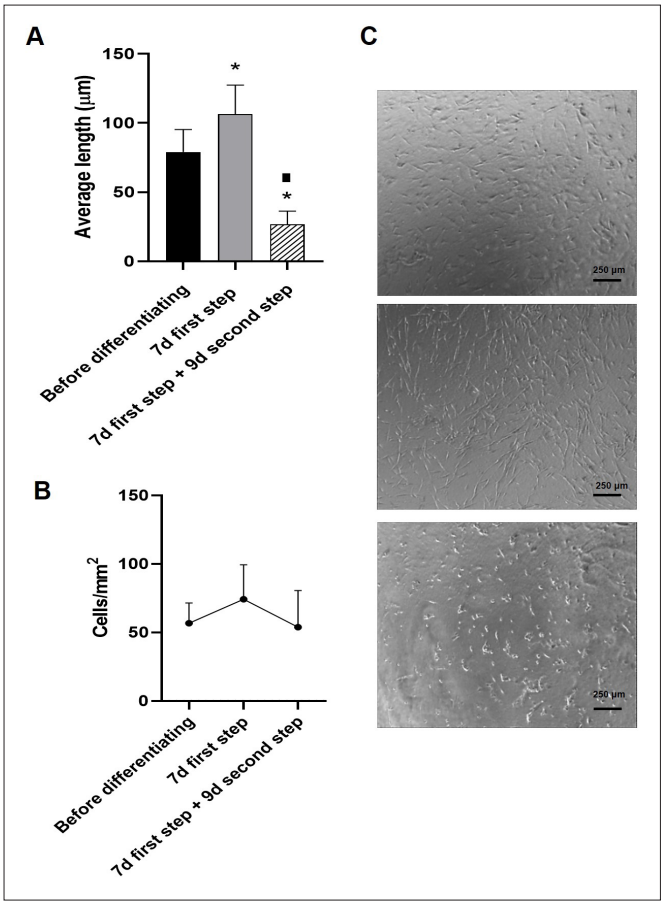

Figure 2. Differentiation kinetics, morphology, and cell numbers during differentiation of adipose-derived stem cells into limbal stem cells on three-dimensional printed collagen. (A) Average cell length (μm), (B) cell number per mm^2, and (C) phase contrast images before differentiation (top), after the first step (middle), and after the second step (bottom). Notes: Error bars indicate standard deviation. * indicates a statistically significant difference compared to human adipose-derived mesenchymal stem cells (hADSCs) before differentiation. ▪ indicates a statistically significant difference compared to hADSCs in the first differentiation step (* and ▪ = $p \leq 0.05$). Scale bar = 250 μm; magnification = 40×.

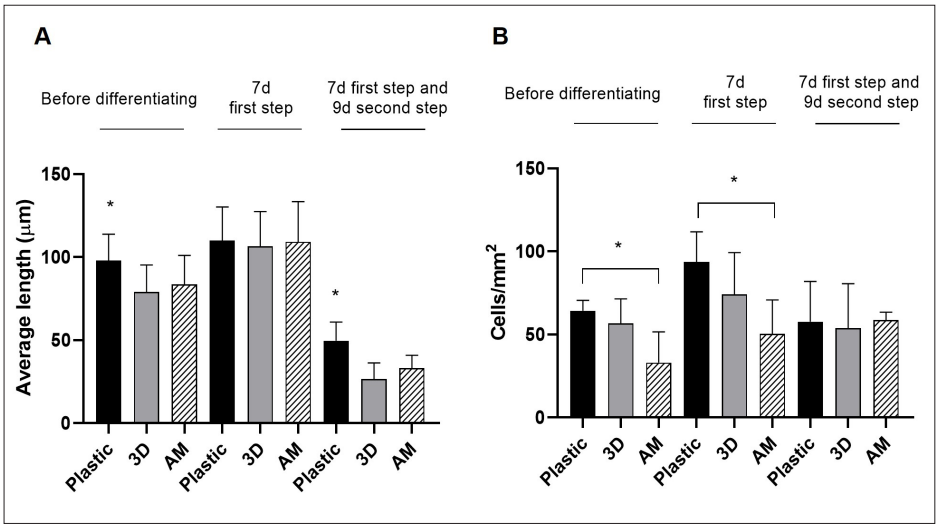

Figure 3. Comparison of morphometric analysis on the different substrates before and after each differentiation step. (A) Average cell length on plastic, three-dimensional printed collagen (3D), and amniotic membrane (AM). (B) Number of cells/mm^2 on plastic, 3D, and AM. Note: *$p \leq 0.05$.

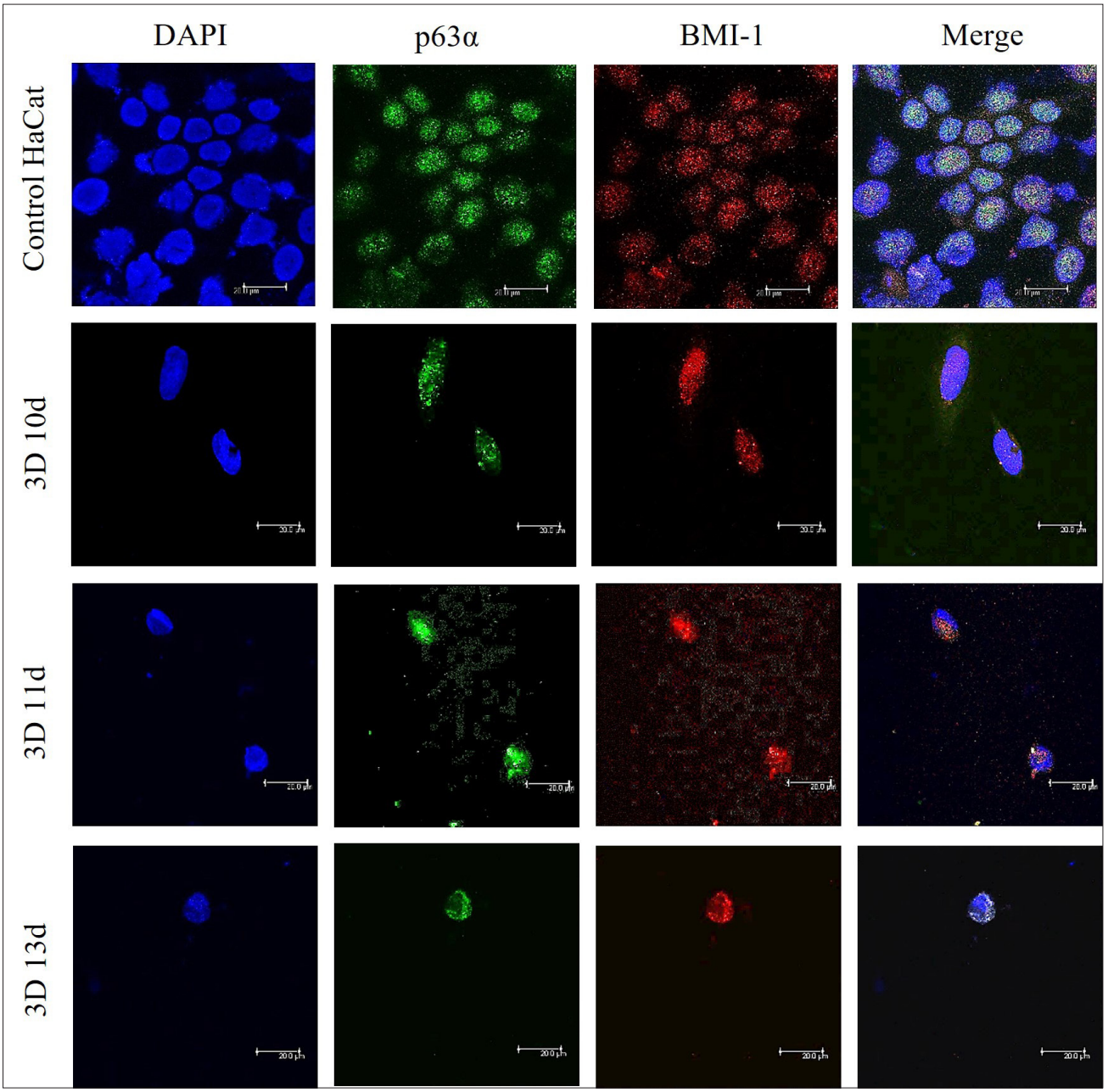

Figure 4. Confocal microscopy images showing double immunofluorescence for p63α/BMI-1 in human adipose-derived mesenchymal stem cell-derived limbal stem cells on three-dimensional printed collagen at different time points during the second differentiation step (10, 11, or 13 days). p63α appears in green, BMI-1 in red, and nuclei in blue (4',6-diamidino-2-phenylindole [DAPI]). HaCat cells grown to confluency were used as the positive control. Scale bar = 20 μm; magnification = 630×.

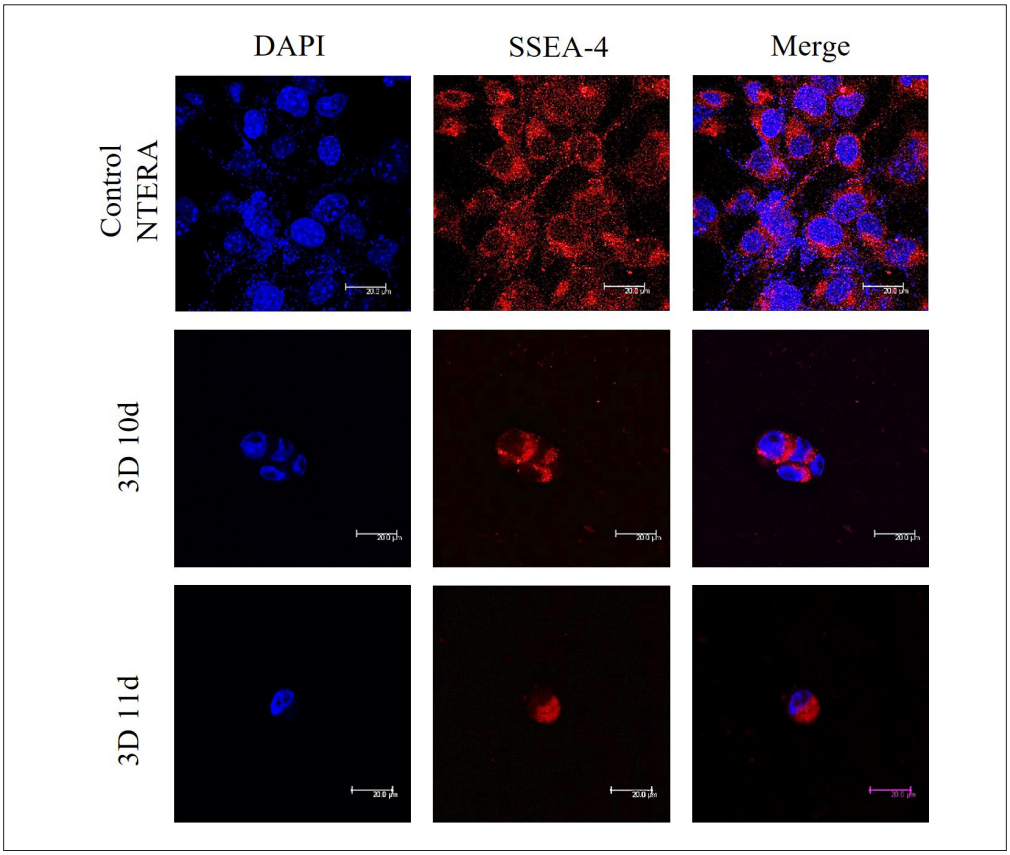

Figure 5. Confocal microscopy images of anti-stage-specific embryonic antigen-4 (SSEA4) immunofluorescence in three-dimensional (3D)-printed scaffolds with human adipose-derived mesenchymal stem cell-derived limbal stem cells after 10 or 11 days of the second differentiation step. SSEA4 is shown in red, and nuclei in blue (4',6-diamidino-2-phenylindole [DAPI]). NTERA cells grown to confluence served as the positive control. Scale bar = 20 μm; magnification = 630×.

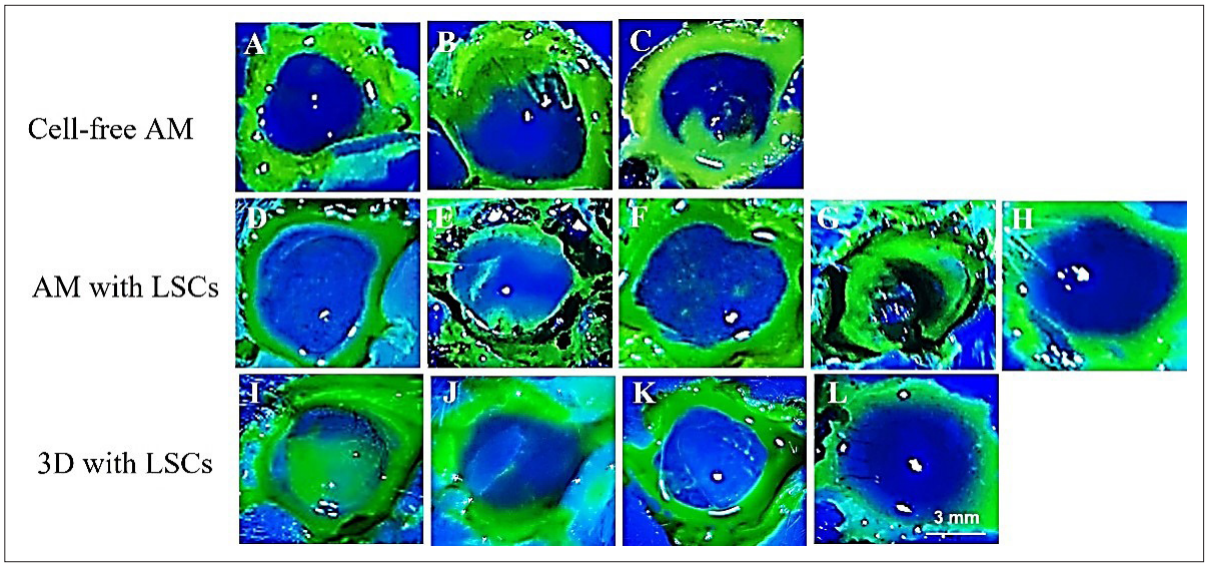

Figure 6. Macroscopic fluorescein staining images of rat eyes after amniotic membrane (AM) or three-dimensional (3D)-printed collagen transplantation. Areas of re-epithelization appear as an absence of fluorescein staining (blue), whereas persistent defects retain fluorescein (green). Scale bar = 3 mm; magnification = 10×. Abbreviation: LSC, limbal stem cells.

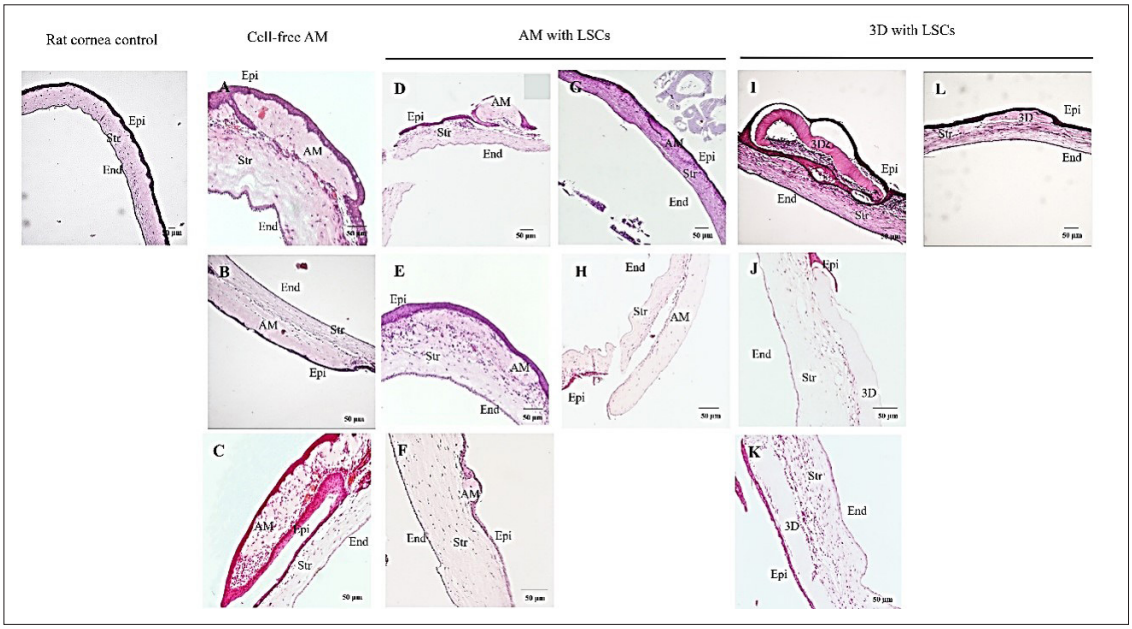

Figure 7. Hematoxylin-eosin-stained images of rat corneas after epithelial damage and scaffold transplantation. (A–C) Cell-free AM, (D–H) AM with LSCs, and (I–L) 3D with LSCs. Scale bar = 50 μm; magnification = (Control, G, L) 50×; (B–D, F, H–K) 100×, (A and E) 200×. Abbreviations: AM, amniotic membrane; End, corneal endothelium; Epi, corneal epithelium; LSCs, limbal stem cells; Str, corneal stroma; 3D, 3D-printed collagen.

In most cases, re-epithelization was nearly complete by day 10. A longer observation period would likely have resulted in full epithelial closure in all experimental groups.

3.5. Biocompatibility and superior integration of three-dimensional printed collagen scaffolds compared to amniotic membrane

Hematoxylin-eosin staining was performed on paraffin-embedded tissue sections to visualize the 3D-printed collagen and AM scaffolds (Figure 7). In the cell-free AM group, the scaffold was observed in all cases, but integration was evident in only one (Figure 7B). In the remaining rats, the cell-free AM was surrounded by epithelium, resulting in a regenerated epithelial layer and either partial or complete scaffold extrusion (Figure 7A and C).

In the AM with the LSC group, the AM was not integrated in two rats (Figure 7H) or was nearly completely surrounded by epithelium beneath it, suggesting impending extrusion (Figure 7D). However, in the remaining three rats, AM-LSC scaffolds were integrated with epithelial growth over the scaffold (Figure 7E, F, and G).

In the 3D-printed collagen with the LSC group, scaffolds were integrated in three out of four cases (Figure 7J, 7K, and 7L). In the remaining case, the scaffold was not integrated, and epithelial growth was observed surrounding it (Figure 7I).

With respect to scaffold biocompatibility, epithelial closure of the induced wound occurred in all groups, whether over or under the scaffold. The 3D-printed collagen with the ADSC-LSC group showed the highest integration rate (75%), followed by AM with ADSC-LSCs (60%) and cell-free AM (33%). A statistically significant difference was observed between the 3D-printed collagen with cells and the cell-free AM groups, suggesting that both the 3D-printed scaffold and the hADSC-derived LSCs actively contribute to scaffold integration (Table 1).

Table 1. Integration and epithelial growth rates (% of cases) after transplantation

Group	Number of rats	Rats with integrated scaffold (*n*)	Integration rate (%)	Epithelial growth (% of cases, underneath if not integrated)
Cell-free AM	3	1	33	100
AM with LSCs	5	3	60	100
3D with LSCs	4	3	75*	100

Note: * indicates statistical significance compared to cell-free AM at $p \leq 0.05$.

Abbreviations: AM, amniotic membrane; LSCs, limbal stem cells; 3D, 3D-printed collagen

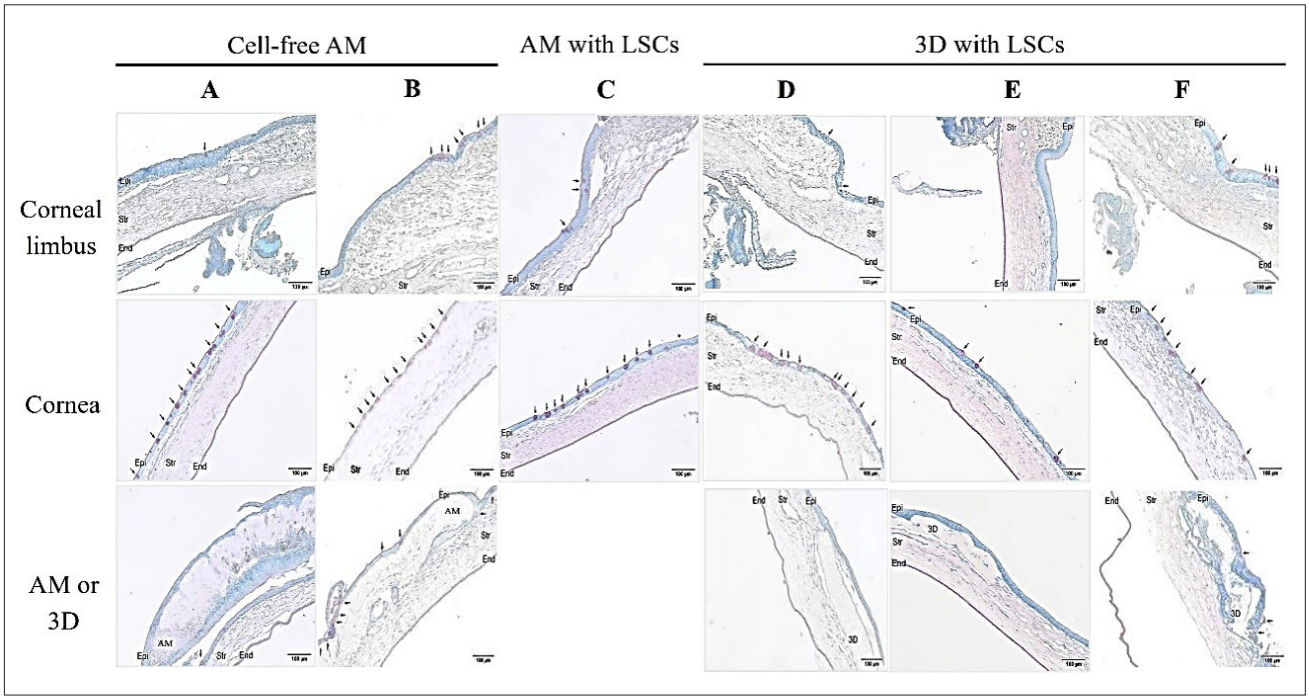

Figure 8. Periodic acid–Schiff staining of the corneal limbus, cornea, and scaffolds (AM or 3D), if present, in rats treated with (A–B) cell-free AM, (C) AM with ADSC-LSCs, and (D–F) 3D-printed collagen with ADSC-LSCs. Mucus goblet cells are stained pink (arrows). Scale bar = 100 μm; magnification = 100×. Abbreviations: ADSC-LSCs, adipose-derived mesenchymal stem cell–derived limbal stem cells; AM, Amniotic membrane; End, endothelium; Epi, epithelium; LSCs, limbal stem cells; Str, stroma; 3D, 3D-printed collagen.

3.6. Mucus conjunctival cells in the corneal epithelium revealed by periodic acid–Schiff staining

Periodic acid-Schiff staining demonstrated the presence of conjunctival mucus goblet cells in the corneal epithelium of all treatment groups, with variations depending on the treatment received. In the rats treated with cell-free AM, mucus cells were observed in both the sclerocorneal limbus and the corneal epithelium. Several PAS-positive cells were visible in the limbus and in the regenerated epithelium beneath the detached AM (Figure 8A and B). In one case, an increased number of mucus cells in the corneal epithelium near the limbus, although the central corneal region was absent and could not be assessed (not shown).

In the AM with the ADSC-LSC group, PAS-positive mucus cells were observed in the limbal regions of two animals, with additional labeled cells detected near one limbal area. Abundant MUC-positive cells in the corneal epithelium were identified in only one rat (Figure 8C). The AM scaffold was not present in any of the PAS-stained sections from this treatment group.

Rats treated with 3D-printed collagen with ADSC-LSCs showed PAS-positive cells in the corneal epithelium, while the limbus was largely negative. In one case, the epithelium preserved over the printed collagen scaffold lacked labeled mucus cells, although positive cells were observed in both limbal regions and the corneal epithelium (Figure 8D). In another case, mucus cells were found only in the corneal epithelium (Figure 8E). In the final case, both limbal regions and the corneal epithelium contained goblet cells, with some positive cells also present in the epithelium overlying the 3D-printed scaffold (Figure 8F).

3.7. Immunochemical evidence of regenerated conjunctival epithelium across all groups

3.7.1. Distribution of p63α-positive cells in limbal and corneal epithelia of control and treated corneas

Immunodetection of the p63α marker was positive (p63+) in all cases, with labeled cell nuclei in the limbal basal layer of both healthy rat corneas and all treated eyes. Interestingly, in both the undamaged negative control and all damaged and treated rats, $p63^+$ cells were detected not only in the basal layer of the limbal epithelium, as expected, but also throughout the basal layer of the corneal epithelium. In the human corneas used as positive controls, p63α was also detected in the basal layer of the corneal epithelium, although it was not detected in the limbal regions due to tissue loss after antigenic unmasking. Notably, all three treatments showed a higher number of $p63^+$ cells compared to the undamaged control rat, especially in the limbal region, which appeared considerably thinner in the control compared to the damaged and treated corneas. This suggests active limbal regeneration (Figure 9).

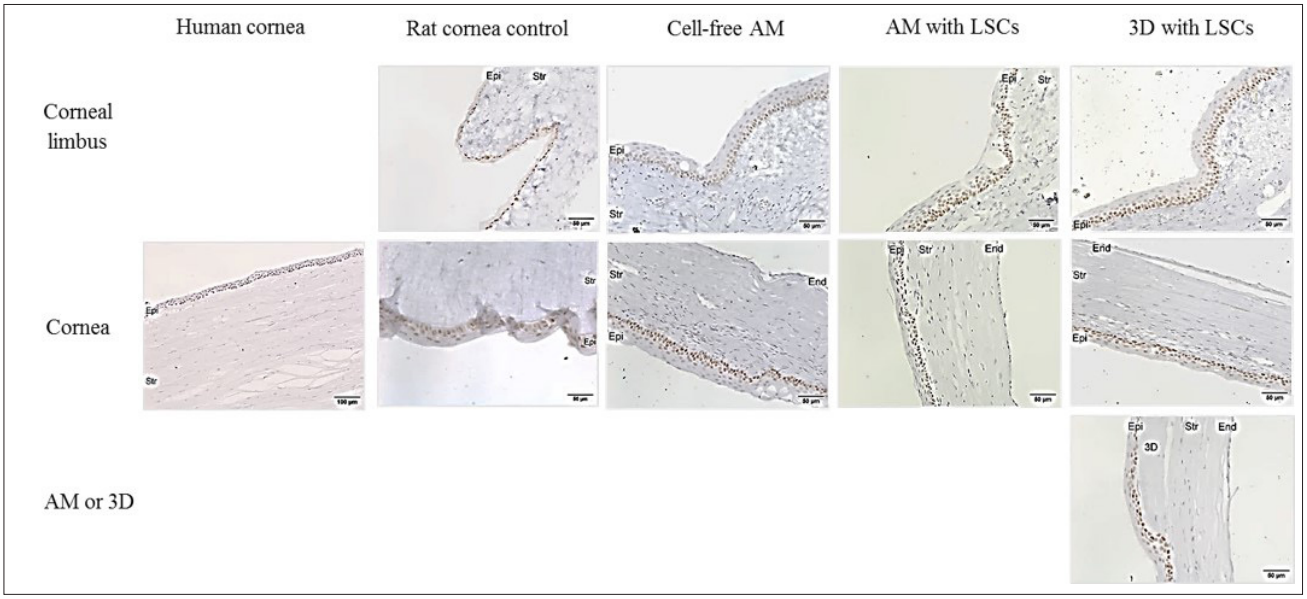

Figure 9. Positive labeling for p63α in the limbal and corneal epithelia of control and treated corneas. Positive cell nuclei appear brown. Scale bars = 100 μm (human cornea), 50 μm (rat corneas); magnifications = 100× (human cornea); 200× the rest, endothelium; Epi, epithelium; LSCs, limbal stem cells; Str, stroma; 3D, 3D-printed collagen scaffold.

To quantify the differences in the proportion of p63⁺-labeled cells between the control rat cornea and the various treatment groups, a general cell count was performed to calculate the percentage of positive cells in both limbal and corneal regions (Figures 10 and 11). No statistically significant differences were observed between the treatments and the healthy control, although individual variability was noted among rats within the same treatment group (data not shown). In the limbal epithelium, the proportion of p63α⁺ cells was 74% in the control, 64% in the cell-free AM, 66% in the AM with ADSC-LSC group, and 76% in the 3D-printed collagen with ADSC-LSC group (Figure 10A). However, differences in p63α labeling across epithelial layers may have masked overall results. Therefore, the distribution of p63⁺ cells across the different epithelial layers was also quantified, revealing significant differences between the control and the treatment groups. In the basal layer of the limbal epithelium, p63⁺ cells accounted for 93% in control samples, 92% in the cell-free AM group, 87% in the AM with ADSC-LSC group, and 95% in the 3D-printed collagen with ADSC-LSC group, though these differences were not statistically significant (Figure 10A). In the first suprabasal layer, statistically significant increases in p63⁺ cells were observed in all treatment groups compared to the control: 37% in the control, 79% in the cell-free AM group, 81% in the AM with LSC group, and 89% in the 3D-printed collagen with LSC group. In the second layer, p63α⁺ cells were absent in the healthy control but remained detectable in the treated groups, with significant differences: 66% in the cell-free AM group, 75% in the AM with ADSC-LSC group, and 70% in the 3D-printed collagen with ADSC-LSC group. In the third layer, similar results were observed but at lower proportions: 28% in the cell-free AM group, 38% in the AM with LSC group, and 44% in the 3D-printed collagen group, all significantly different from the control, which showed no p63α⁺ cells in that layer. These findings suggest that epithelial damage followed by any of the treatments promotes the expansion of p63α+ cells into the more superficial layers of the corneal epithelium. From the fourth layer onward, p63α⁺ cells were absent in all groups (Figure 10B).

In the corneal epithelium, statistically significant differences were observed between the healthy control and the damaged, treated groups. The control cornea exhibited 92% p63⁺ cells, compared to 63% in the cell-free AM group, 64% in the AM with LSC group, and 68% in the 3D-printed collagen with LSC group (Figure 11A). A statistically significant difference was noted between the cell-free AM group and 3D-printed collagen with LSCs, but not between the AM with and without cells, suggesting that the increased p63α presence may be attributed to the biomaterial rather than the cells. Layer-wise analysis in the corneal epithelium revealed no significant differences in the basal layer. In the first suprabasal layer, the percentages were 98% in the control, 64% in the cell-free AM group, 79% in the AM with LSC group, and 78% in the 3D-printed collagen with LSC group. Significant differences were observed between the control and the AM without cells. In the second layer, p63⁺ cell proportions dropped more sharply in the cell-free AM group (16%) compared to

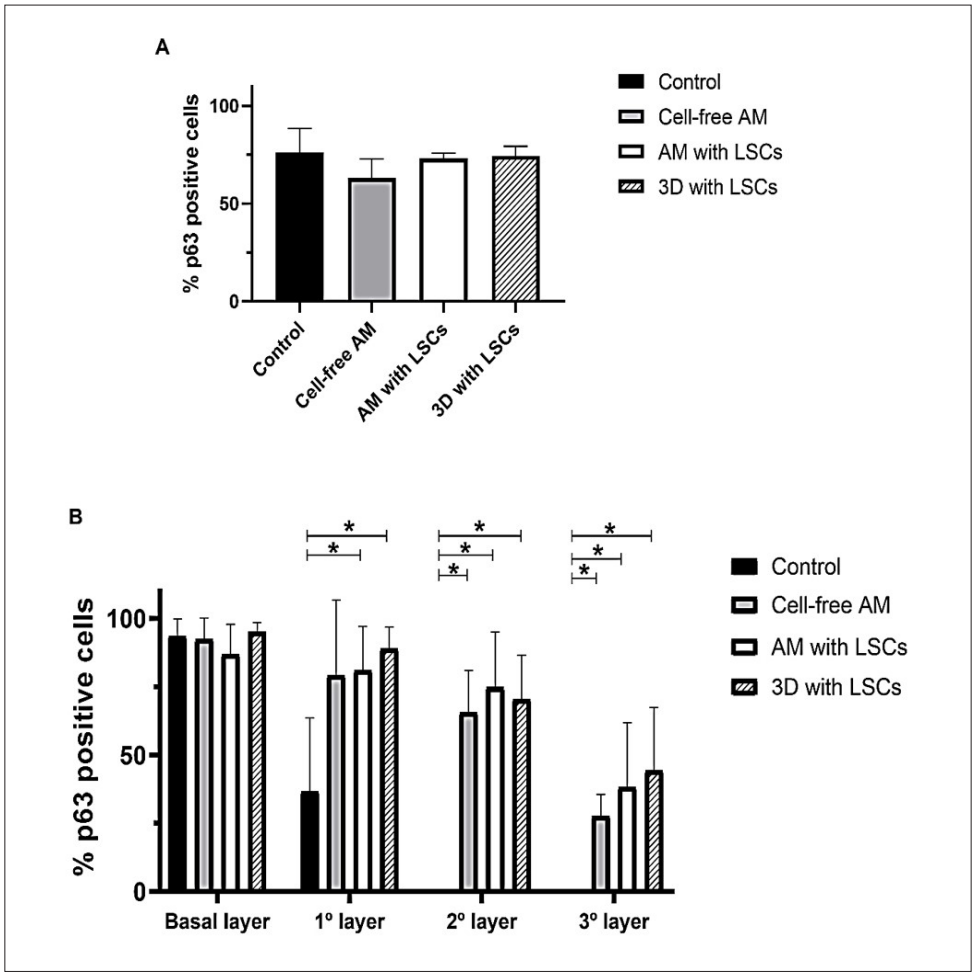

Figure 10. p63+ cell counts in the limbal epithelium. (A) Values across the entire epithelium, showing no significant differences between controls and treatments. (B) Proportion of p63+ cells per epithelial layer. Statistically significant differences (*) at $p \leq 0.05$ are observed between treatments within the same layer. Abbreviations: AM, amniotic membrane; LSCs, limbal stem cells; 3D, 3D-printed collagen scaffold.

the control (88%), AM with LSCs (54%), and 3D-printed collagen with LSCs (58%). In the third layer, an overall reduction was noted: 9% in the control, 6% in the cell-free AM group, 7% in the AM with LSC group, and 23% in the 3D-printed collagen with LSC group. Significant differences were found between the 3D-printed collagen group and both AM groups, regardless of cell inclusion (Figure 11B).

3.7.2. Limbal cell marker BMI-1-positive cells on the three-dimensional scaffold

The positive control tissues—human prostate and healthy rat cornea—showed limbal cell marker BMI-1$^+$ cells, located in the epithelium of the prostatic c-glands and in the stratum basale of the limbal and corneal epithelia, respectively (Figure 12A and B). In contrast, no positivity was generally detected in the treated eyes. BMI-1 labeling was observed in only one rat from the 3D-printed collagen with hADSC-derived LSC group, where several BMI-1$^+$ cells were found around the printed scaffold (Figure 12C). This suggests that these labeled cells may correspond to the transplanted human cells in this particular section.

3.7.3. Absence of cytokeratin 12 in the regenerated epithelium

Detection of CK-12 in the positive controls (human cornea and untreated healthy rat cornea) confirmed its established role as a specific marker of corneal epithelium. CK-12 strongly labeled the entire surface of the healthy corneal epithelium and clearly marked the transition zone at the sclerocorneal limbus, where conjunctival epithelium (negative for CK-12) begins. In contrast, no CK-12 labeling was observed in any of the rats subjected to epithelial damage and subsequent treatment. This result confirms that the regenerated epithelium was not of corneal origin and that the ADSC-LSCs did not differentiate into corneal epithelium (Figure 13).

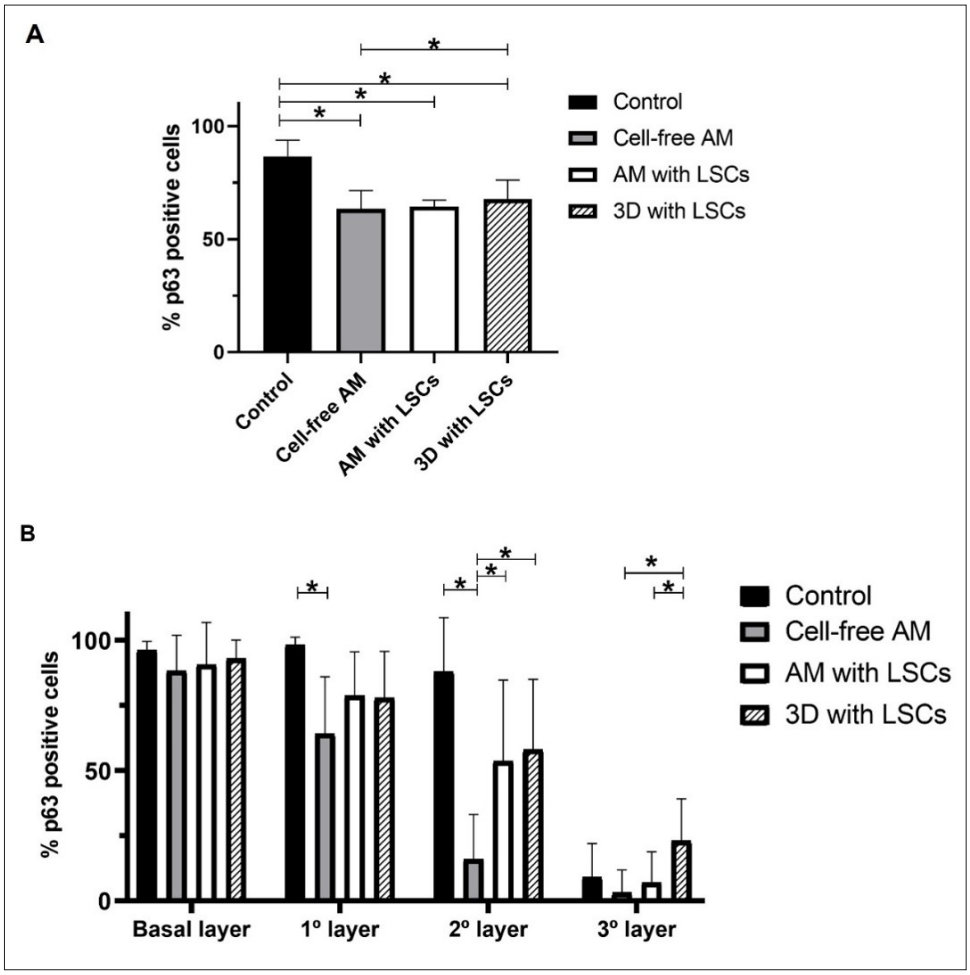

Figure 11. p63⁺ cell counts in the corneal epithelium. (A) Quantification of p63⁺ in the corneal epithelium. Significant differences (*) at $p \leq 0.05$ were observed between the healthy control and all treated groups, as well as between 3D-printed collagen with cells and cell-free AM. (B) Proportion of p63α⁺ cells per corneal epithelial layer. Statistically significant differences (*) at $p \leq 0.05$ are shown between treatments within the same layer. Abbreviations: AM, amniotic membrane; LSCs, limbal stem cells; 3D, 3D-printed collagen scaffold.

3.7.4. Non-specific cytokeratin 13 labeling in corneal and conjunctival epithelium

Although CK-13 is generally considered a marker for conjunctival epithelium, both the control human cornea and healthy rat cornea showed CK-13⁺ cytoplasmic labeling in the corneal and limbal epithelia as well. In the healthy rat cornea, labeled conjunctival epithelium was also distinguishable (Figure 14). In treated samples, CK-13 labeling was observed in the conjunctival, limbal, and corneal epithelia of all rats, with no clear differences between treatment groups. Positive labeling was also detected in epithelial layers located above and below both the AM and 3D-printed collagen scaffolds when present (Figure 14). Hence, CK-13 did not provide further insight into the nature of the regenerated epithelium.

Other epithelial markers, including SSEA-4 (corneal), MUC-4 and MUC-5 (conjunctival), and CK-19 (limbal), were not conclusive in determining cell identity (results not shown).

4. Discussion

In this study, hADSCs were differentiated into LSCs within a 3D-printed collagen I scaffold for transplantation into a rat model of total LSCD. The aim was to evaluate its biocompatibility and regenerative capacity in comparison with standard AM transplantation. We achieved successful *in vitro* differentiation of hADSCs into LSCs, as confirmed by the expression of specific markers, and observed superior *in vivo* scaffold integration compared to AM. However, analysis of structural markers revealed that the regenerated epithelium was conjunctival rather than corneal, indicating that the contribution of ADSC-LSCs was insufficient for complete corneal re-epithelization. *In vitro*, it was observed that during ectodermal induction, the cells initially elongated and then, with SHEM

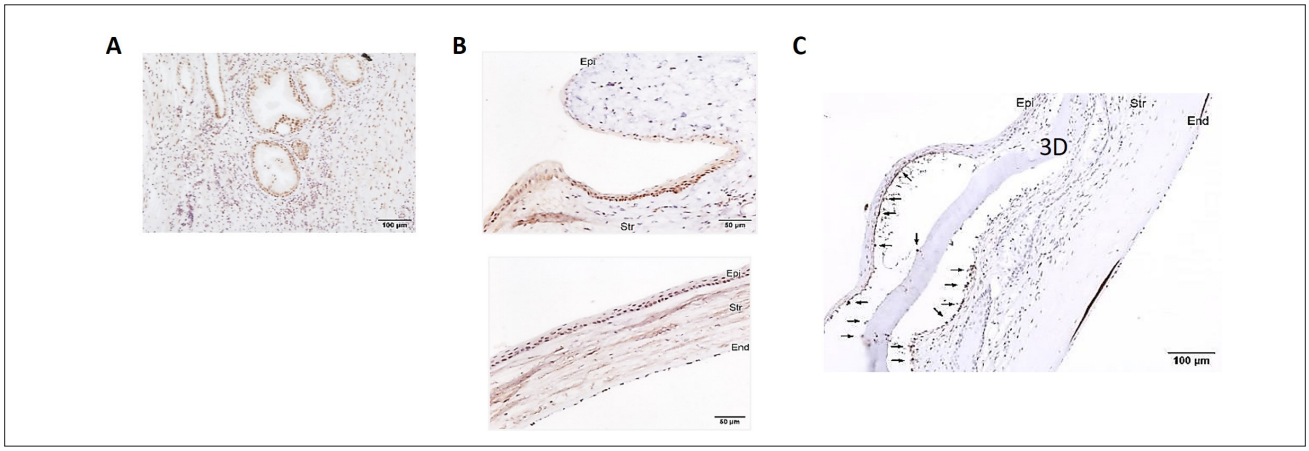

Figure 12. Results of anti-BMI-1 immunohistochemistry. Positive brown nuclear labeling is seen (A) in the epithelium of human prostate glands, and (B) in the stratum basale of the limbal and corneal epithelium of a healthy rat cornea. (C) Detail of the three-dimensional (3D)-printed collagen scaffold with ADSC-LSCs, showing BMI-1$^+$ cells around the scaffold (arrows). An empty space artifact is visible, caused by differential dehydration of the printed collagen relative to the corneal stroma during processing. Scale bars = 50 µm (B), 100 µm (A, C); Magnifications = 200× (B),100× (A, C). Abbreviations: ADSC-LSCs, adipose-derived mesenchymal stem cell–derived limbal stem cells; End, endothelium; Epi, epithelium; Str, stroma.

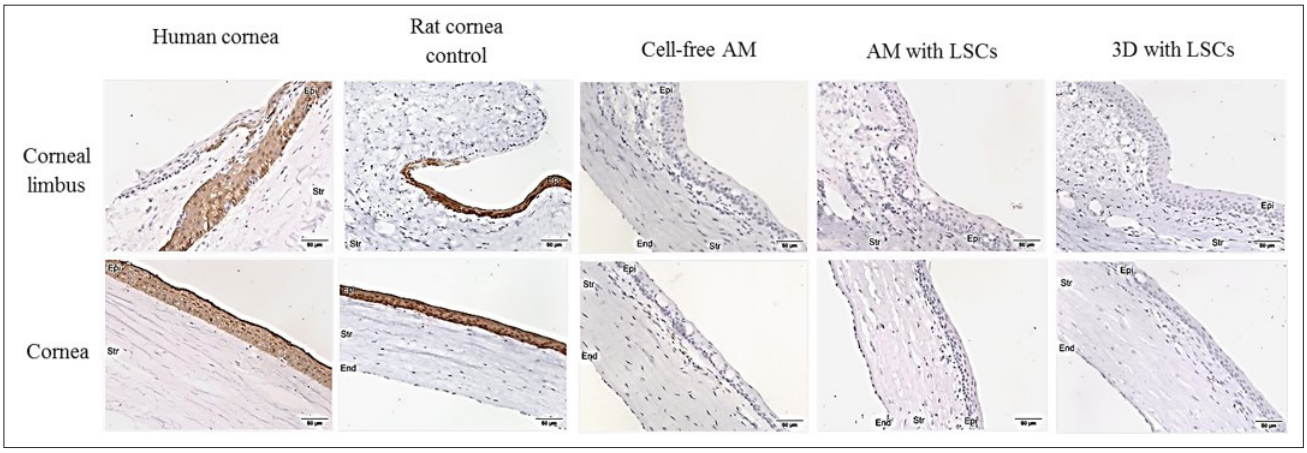

Figure 13. Results of anti-cytokeratin 12 immunohistochemistry. Positive brown cytoplasmic labeling is present only in corneal epithelial cells. Scale bar = 50 µm; Magnification = 200×. Abbreviations: AM, amniotic membrane; End, endothelium; Epi, epithelium; LSCs, limbal stem cells; Str, Stroma; 3D, 3D-printed collagen.

medium supplemented with PEDF and KGF, they became statistically significantly more rounded, similarly to those on AM.[18] Directed differentiation on 3D-printed collagen and AM soft scaffolds showed faster kinetics than on plastic. Only nine days of culture were required in the second differentiation step to acquire the rounded morphology with a high nucleus-to-cytoplasm ratio characteristic of LSCs, compared to the 13 days needed on plastic culture surfaces.

When comparing the average cell length, hADSCs seeded on 3D-printed collagen and AM were significantly shorter both before differentiation and after differentiation than those seeded on culture plastic. This may be due to the fact that soft substrates lead to decreased maturation of focal adhesions, lower stress fiber content, and reduced nuclear stretch—conditions that promote the development of LSCs. Indeed, MSCs cultured on soft substrates have been shown to acquire a relaxed state caused by low cell contractility and stiffness, which correlates with increased reprogramming efficiency and, therefore, earlier colony formation compared to cells seeded on stiff substrates.[33] This explains the improved differentiation efficiency observed on 3D-printed collagen and AM.

Regarding cell count, hADSCs actively replicated during ectodermal induction on all substrates. Subsequently, in the case of 3D-printed collagen and plastic, cell numbers decreased to their initial levels.[18] This initial increase may have been due to the composition of the induction medium, which contains a higher proportion of FBS (15%) than the SHEM medium (2%).[31] The subsequent decrease in cell number

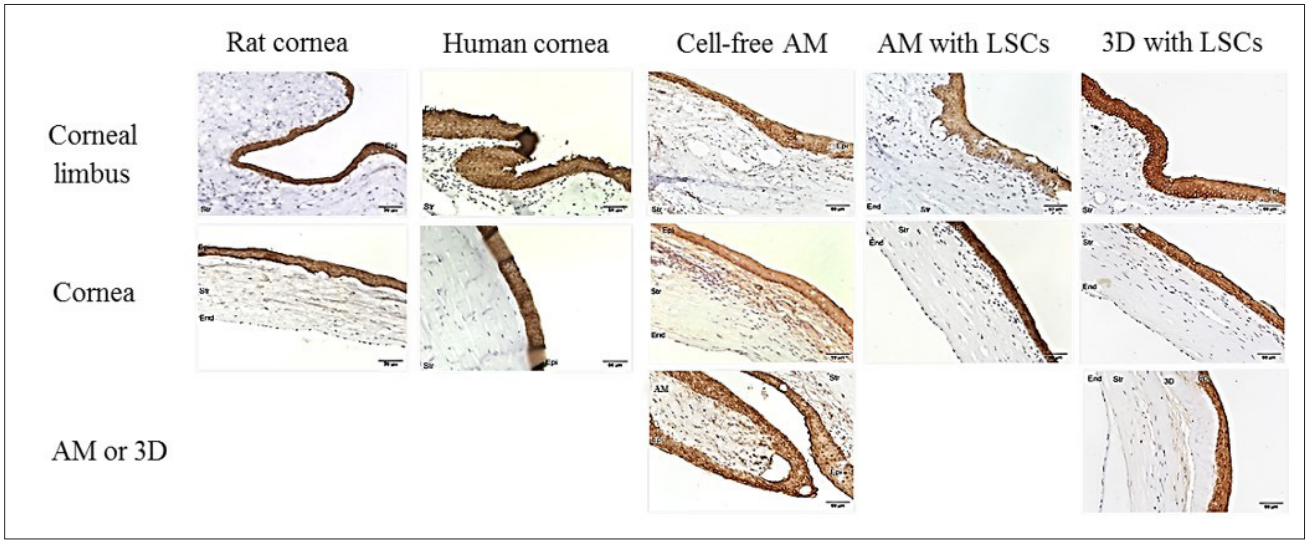

Figure 14. Results of anti-cytokeratin 13 immunohistochemistry. Positive brown cytoplasmic labeling is present in both corneal and limbal epithelial cells. Scale bar = 50 μm; magnification = 200×. Abbreviations: AM, amniotic membrane; End, endothelium; Epi, epithelium; LSCs, limbal stem cells; Str, stroma; 3D, 3D-printed collagen.

during the second stage of differentiation could be attributed to the differentiation process itself and the acquisition of a slower cell cycle, which is a known characteristic of stem cells.[1]

The only widely accepted marker of limbal cells is p63α,[14] but it is not present in all limbal niche cells. Therefore, we also evaluated the expression of potential differentiation markers such as BMI-1 and SSEA-4, given the lack of a consensus panel of markers for LSCs. LSCs have been shown to co-express BMI-1 and p63α under conditions of normal homeostasis, identifying human limbal holoclones.[10] In contrast, SSEA-4 has been described as a marker for stem cells but also for differentiated corneal epithelial cells.[9] One study reports 12% of hADSCs as positive for SSEA-4,[34] while another claims no expression.[35] Compared to the results on AM and plastic published in Cadenas-Martín *et al.*[18], hADSC-derived LSCs cultured for 10 days in SHEM medium supplemented with PEDF and KGF (second differentiation stage) showed 53.3% double-positive cells for p63α/BMI-1 on plastic, increasing to 59% on 3D-printed collagen. When culture for one additional day, the percentage of double-positive cells decreased to 43.4% on plastic and 52% on 3D-printed collagen. Interestingly, while this percentage remained relatively stable on plastic in extended cultures (41.4% at 13 days), it dropped drastically on 3D-printed collagen to only 4%, suggesting active differentiation of LSCs into corneal epithelial cells in the 3D scaffold. On AM, the percentage of p63α/BMI-1-positive cells at 13 days was 34.1%. These findings indicate that, despite reaching a similar number of cells across all substrates, differentiation efficiency and kinetics were higher on the 3D-printed collagen scaffold than on AM or culture plastic.

This is consistent with results obtained for the corneal epithelium marker SSEA-4, which showed 52.9% positivity on plastic,[18] compared to 90.7% on 3D-printed collagen at day 10 of the second differentiation step. As previously mentioned, this high percentage may reflect either a population of more differentiated corneal epithelial cells or residual undifferentiated hADSCs. Nonetheless, the presence of undifferentiated hADSCs within the LSC population could be beneficial, as they express epithelial markers such as ABCG2, p63α, CK12, and CK76, making them a suitable cell source for LSCD treatment.[36] These results suggest that 10 days of the second differentiation step represents the optimal time point for transplantation. Among the substrates tested, 3D-printed collagen proved to be the most efficient for differentiation, yielding the highest percentage of hADSC-derived LSCs expressing the specific markers used. Moreover, the use of ADSC-derived LSCs not only eliminates the need for a corneal donor but also avoids donor-dependent variation in the expression of epithelial and LSC markers.[37]

In vivo, biocompatibility and re-epithelization were achieved in all treatment groups, including AM with or without LSCs (controls) and 3D-printed collagen with LSCs. Hematoxylin staining confirmed 100% re-epithelization above and/or below the scaffolds, with wound closure observed in all cases. The 3D-printed collagen with the LSC group showed the highest statistically significant integration rate (75%), demonstrating superior biocompatibility and safety. Significant differences were observed between the 3D-printed collagen with cells and the cell-free AM groups,

suggesting that hADSC-derived LSCs actively contribute to scaffold integration.

To ascertain whether the nature of the epithelium was corneal or conjunctival, the following putative specific markers were studied: for the corneal limbus (p63α,[12] BMI-1,[10] CK-19,[11] and SSEA-4[9]); for the corneal epithelium (CK-12[7] and SSEA-4[9]); and for the conjunctival epithelium (MUC-4, MUC-5, and CK-13[13]). Surprisingly, in healthy eye controls, the presence of several of these markers did not match previously published data. Positive p63α labeling was observed in the stratum basale of both the limbal and corneal epithelium in healthy human and rat corneas, and in the stratum basale and several suprabasal layers of the limbal and corneal epithelium in all treated rats. However, Di Iorio *et al.*[38], using the 4A4 pan-p63 monoclonal antibody from BD Biosciences, which detects all p63 isoforms and allows differentiation between them by Western blot, found that the p63α isoform was restricted to the basal layer of the limbal epithelium in healthy corneas. In damaged corneas, their results aligned with ours, showing p63α expression extending throughout the corneal stratum basale and into several suprabasal layers of both the limbal and corneal epithelium. Collin *et al.*,[39] who used the same antibody as in our study (anti-p63α from Cell Signaling), reported identical findings to ours, with p63α expression observed throughout the basal epithelium of the corneal surface. The difference in p63α detection in the stratum basale of the healthy corneal epithelium between the two studies may be attributed to discrepancies in antibody specificity. The anti-p63α antibody used in our study detects two isoforms of p63α: the full-length TAp63α, which contains an amino-terminal transactivation domain, and the truncated ΔNp63α, which lacks this domain. In the human corneal epithelium, ΔNp63α is the predominant isoform and is crucial for the differentiation of TACs,[12] while TAp63α, which is highly expressed in the limbal epithelium, is involved in maintaining less differentiated limbal cells.[40] In addition, TAp63α is required for the initiation of epithelial stratification, while ΔNp63α is essential for maintaining epithelial differentiation.[41] According to Verma *et al.*,[42] the corneal epithelial cells generated by LSCs distribute across the corneal surface depending on their degree of maturation. When the cornea is damaged, limbal cells, positive for ΔNp63α, proliferate and migrate along the stratum basale of the corneal epithelium, maintaining ΔNp63α expression.[12] This could explain our findings, in which ΔNp63α is likely being detected in the stratum basale epithelium of control corneas, while both TAp63α and/or ΔNp63α are detected in damaged corneas.

Quantitatively, a greater number of suprabasal layers in both the limbal and corneal epithelia was observed in all treated rats compared to the healthy control corneas. Despite showing a higher proportion of p63α$^+$ cells in the corneal epithelium, the healthy corneas had a statistically lower number of epithelial layers, which may reflect the proliferation-inducing effect of the treatments. Among the treatments, the cell-free AM group showed the lowest proportion of p63α$^+$ cells in both the limbus and cornea, although this group exhibited high variability. This may be due to inconsistent membrane orientation during surgery; the epithelial side of the AM could not always be placed facing the damaged corneal surface, as recently emphasized by Bisevac *et al.*[20] Nevertheless, the AM treatments (with or without cells) showed no significant differences, except in the upper layers of the corneal epithelium in the AM-LSC-treated group, suggesting that the presence of LSCs enhances tissue regeneration, albeit modestly. Importantly, the statistically significant difference in the group treated with the 3D-printed collagen with cells indicates that the primary contributing factor is the biomaterial used as the scaffold.

Regarding BMI-1, although positive controls showed its presence in the basal layer of the peripheral corneal and limbal epithelium, in the treated corneas, BMI-1$^+$ cells were observed around the 3D print in only one rat, suggesting that the transplanted LSCs remained attached to the 3D scaffold. Previous studies indicate that in humans, BMI-1 is expressed during the embryonic period in corneal cells that are also p63$^+$, and that after birth, BMI-1 becomes restricted to the corneal limbus,[10] with expression being lost as LSCs proliferate and migrate to repair damage.[42] This differs in murine models, where BMI-1 expression appears to be age-dependent. BMI-1 expression has been detected in the basal and suprabasal layers from before epithelial stratification until eight weeks of age, after which only isolated colonies of small BMI-1$^+$ cells are observed, which eventually disappear.[43] This supports the interpretation that the BMI-1$^+$ cells detected around the 3D print were transplanted LSCs. On the other hand, the absence of positive BMI-1 labeling in the rest of the epithelium indicates that either most of the transplanted cells did not remain in place, were not present in the sections analyzed, or had differentiated *in situ*. Increasing the number of LSCs seeded on the scaffolds or enhancing their attachment may improve outcomes. Despite this, the presence of BMI-1$^+$ cells on the 3D print suggests that it is superior to AM in supporting the survival of transplanted human LSCs until the end of the *in vivo* study.

Immunodetection of cytokeratin 12 confirmed that the regenerated epithelium on the corneal surface in our study is not corneal epithelium. CK-12 is a recognized marker of corneal epithelium,[7] and was detected in the positive controls, clearly labeling the entire surface of the healthy corneal epithelium and allowing identification of the transition point between the corneal and conjunctival epithelia (negative for CK-12) in the sclerocorneal limbus. No CK-12 was detected in the damaged and treated corneas, suggesting that the regenerated epithelium is not corneal in nature.

Cytokeratin 13 is a recognized marker for conjunctival epithelium,[44] typically found in the suprabasal stratum of the limbal epithelium and in all layers of the conjunctiva, while being absent in the corneal epithelium.[45] However, in our study, both the control human and healthy rat corneas showed CK-13 labeling in the corneal and limbal epithelia. Treated rats also showed CK-13$^+$ labeling in all layers of the regenerated corneal epithelium; hence, this marker does not further clarify the nature of the regenerated tissue.

Consistent with these findings, PAS staining highlighted the presence of mucus-secreting cells typical of conjunctival epithelium in the regenerated corneal surface across all treatments, supporting the conclusion that the regenerated epithelium is conjunctival. Some variation in the number of mucus-secreting cells was observed between treatments with and without LSCs, with a greater number of labeled cells found in the acellular group. This may indicate the presence of a lower-quality epithelium with reduced transparency (although conjunctival in all cases) in the standard bare AM treatment, supporting the further development of cell therapies using cultured LSCs for corneal surface reconstruction.

Many researchers have studied the use of MSCs to address LSCD or corneal epithelial damage.[46] The ability of these cells to differentiate into LSCs makes them ideal, especially for the treatment of bilateral LSCD, where an autologous extraocular source is needed. ADSCs cultured with LSC-specific medium improved anti-inflammatory and anti-angiogenic paracrine profile, in addition to improving wound healing in the rat LSCD model through a paracrine mechanism,[16] as in this study. Overall, our study supports the favorable effect of hADSC-derived LSCs on corneal epithelial regeneration, with an improved reparative response observed in cell-based treatments. Both groups of rats treated with AM with cells and 3D-printed collagen with cells had a higher proportion of p63α progenitor cells (and in the case of 3D-printed collagen, also BMI-1), and a lower number of mucus cells, which would support enhanced corneal transparency. Furthermore, among the cell-based treatments, the 3D collagen I print appeared to generate a more favorable response, supporting the viability of transplanted LSCs during re-epithelization and promoting increased proliferation of p63$^+$ cells.

Regarding carriers, AM is the most commonly used carrier for ocular surface reconstruction,[47] as its composition—rich in type I and III collagens—mimics, to some extent, the extracellular matrix composition of the limbal niche. In addition, it possesses anti-inflammatory, antimicrobial, and anti-angiogenic properties. However, the success rate of reepithelialization seems to depend on the integrity of the membrane and the amount of growth factors it releases; thus, the results obtained vary depending on how the membrane is handled and on donor-specific characteristics. AM use also presents several drawbacks, such as batch-to-batch variability, limited availability, potential risk of infectious disease transmission, and low transparency.[48] In our case, we used type I collagen, as it is one of the most widely used biomaterials for tissue engineering applications due to its biocompatibility and low immunogenicity.[49] Moreover, it is the main component of the cornea and has long been considered a suitable substrate as an epithelial cell carrier,[24] potentially helping to address shortages of donor corneas and AM and offering a more affordable alternative treatment. In fact, *in vivo* studies have already demonstrated that bovine dermis-derived type I collagen implants, even without 3D printing, integrate and promote reepithelialization in anterior lamellar keratoplasty models in rabbits.[50] Simpson *et al.*[51] used an inflammation-suppressing phosphorylcholine coating on a collagen analogue peptide implant conjugated to polyethylene glycol, which enhanced the corneal regenerative response by accelerating nerve regeneration and corneal sensory recovery. This suggests further improvements may be possible by incorporating supplements into our collagen I print to enhance the quality of regeneration.

In a recent collaborative study, Edel *et al.*[19] used an *in vivo* LSCD model and generated induced pluripotent stem cells (iPSCs) from bone marrow mesenchymal stem cells, which were subsequently differentiated into LSCs (iPSC-LSCs). Differentiation was performed in two stages: the first lasted 4 days and used the same supplements as Cadenas-Martin *et al.*[18] but in E6 medium without FBS; the second stage lasted another 11 days and used commercial CnT30 epithelial differentiation medium to obtain LSCs. These cells were seeded on fibrin gel patches coated with laminin or collagen IV instead of vitronectin. The cells were positive for p63α, CK-3, and CK-12, and by day 30, they showed structural regeneration of the epithelium.[19]

5. Conclusion

Our results suggest that, similar to AM and fibrin, 3D-printed collagen may serve as an alternative carrier for corneal epithelial reconstruction. Furthermore, it offers advantages: collagen does not degrade as quickly as fibrin, integrates better than AM, and could mimic the 3D topography of the Palisades of Vogt, where LSCs are located,[52] thus improving biocompatibility. Moreover, its thickness can be customized to facilitate handling,[53] allowing for the development of a substitute with greater transparency, stability,[54] and adaptation to patient-specific requirements.

Acknowledgments

The authors would like to thank the La Paz Biobank and the Image and Immunohistochemistry and Cell Culture platforms for the use of their facilities and technical assistance. They also thank Francisco Navarro, Paula Linzoaín, and Elsa Umiri for their technical support. The authors further acknowledge Morote Traducciones for the English editing.

Funding

The authors received grants from: the Ministry of Science and Innovation, Strategic Health Action, Instituto de Salud Carlos III (ISCIII), Proyectos de I+D+I en Salud (grant number PI23/00207) and co-funded by the European Union; as well as the Foundation for Biomedical Research of La Paz University Hospital (Luis Álvarez Projects; grant number 07/252898.9/24). The study was also supported by StemVision and Carl Zeiss AG. M. Cadenas-Martín and M. Stokking were financed by the European Social Fund (PI_SEPE_MPDM PROGRAMA INVESTIGO 1785344099 and PI_SEPE_PROGRAMA INVESTIGO 26-23, respectively).





Conflict of interest

The authors declare that the research was conducted in the absence of any commercial or financial relationships that could be construed as a potential conflict of interest.

Author contribution

Conceptualization: Maria P. De Miguel

Formal analysis: Marta Cadenas-Martín, Martha Stokking, Ana I. Martín-González, Alba Fernández-Ferrer, Francisco Arnalich-Montiel, Maria P. De Miguel

Funding acquisition: Maria P. De Miguel, Francisco Arnalich-Montiel

Investigation: Marta Cadenas-Martín, Martha Stokking, Ana I. Martín-González, Alba Fernández-Ferrer, Francisco Arnalich-Montiel, Maria P. De Miguel

Methodology: Marta Cadenas-Martín, Martha Stokking, Ana I. Martín-González, Alba Fernández-Ferrer, Francisco Arnalich-Montiel, Maria P. De Miguel

Project administration: Maria P. De Miguel

Resources: Maria P. De Miguel, Francisco Arnalich-Montiel

Supervision: Maria P. De Miguel

Validation: Marta Cadenas-Martín, Martha Stokking, Ana I. Martín-González, Alba Fernández-Ferrer, Francisco Arnalich-Montiel, Maria P. De Miguel

Writing-original draft preparation: Marta Cadenas-Martín, Martha Stokking, Ana I. Martín-González, Alba Fernández-Ferrer, Francisco Arnalich-Montiel, Maria P. De Miguel

Writing-review and editing: Marta Cadenas-Martín, Martha Stokking, Ana I. Martín-González, Alba Fernández-Ferrer, Francisco Arnalich-Montiel, Maria P. De Miguel

Ethics approval and consent to participate

The study was conducted in accordance with the guidelines of the Declaration of Helsinki, and was approved by the Institutional Review Boards of La Paz Hospital (protocol code PI308, 2/4/2004) and Ramon y Cajal Hospital (protocol code 305/11, 10/1/2011). Informed consent was obtained from the tissue donors involved in the study.

Consent for publication

Informed consent for publication was obtained from all subjects involved in the study.

Availability of data

Data obtained from this study can be requested from the corresponding author upon reasonable request.

References

1. De Miguel MP, Casaroli-Marano RP, Nieto-Nicolau N, *et al*. Frontiers in regenerative medicine for cornea and ocular surface. In: *Frontiers in Stem Cell and Regenerative Medicine Research*. Vol 1. Bentham Science Publishers; 2015:92-138. doi: 10.2174/978160805994211501006

2. Zavala J, López Jaime GR, Rodríguez Barrientos CA, Valdez-Garcia J. Corneal endothelium: developmental strategies for regeneration. *Eye (Basingstoke)*. 2013;27(5):579-588. doi: 10.1038/eye.2013.15

3. Akanda ZZ, Naeem A, Russell E, Belrose J, Si FF, Hodge WG. Graft rejection rate and graft failure rate of penetrating keratoplasty (PKP) vs lamellar procedures: a systematic review. *PLoS One*. 2015;10(3):e0119934. doi: 10.1371/journal.pone.0119934

4. Popova P, Malalana F, Biddolph S, *et al*. Interspecies comparative morphological evaluation of the corneal epithelial stem cell niche: a pilot observational study. *J Vet Sci*. 2022;23(4):e62. doi: 10.4142/JVS.22009

5. Fernández A, Moreno J, Prósper F, García M, Echeveste J. *Regeneration of the ocular surface: stem cells and reconstructive techni-ques*. *An Sist Sunit Navar*. 2008; 31(1): 53-69. doi: 10.4321/s1137-66272008000100005

6. Nuzzi A, Pozzo Giuffrida F, Luccarelli S, Nucci P. Corneal epithelial regeneration: old and new perspectives. *Int J Mol Sci*. 2022;23(21):13114. doi: 10.3390/ijms232113114

7. Tanifuji-Terai N, Terai K, Hayashi Y, Chikama TI, Kao WWY. Expression of keratin 12 and maturation of corneal epithelium during development and postnatal growth. *Invest Ophthalmol Vis Sci*. 2006;47(2):545-551. doi: 10.1167/iovs.05-1182

8. Kayama M, Kurokawa MS, Ueno H, Suzuki N. Recent advances in corneal regeneration and possible application of embryonic stem cell-derived corneal epithelial cells. *Clin Ophthalmol*. 2007;1(4):373-382.

9. Truong TT, Huynh K, Nakatsu MN, Deng SX. SSEA4 Is a potential negative marker for the enrichment of human corneal epithelial stem/progenitor cells. *Invest Ophthalmol Vis Sci*. 2011;52(9):6315-6320. doi: 10.1167/iovs.11-7518

10. Barbaro V, Testa A, Di Iorio E, Mavilio F, Pellegrini G, De Luca M. C/EBPδ regulates cell cycle and self-renewal of human limbal stem cells. *J Cell Biol*. 2007;177(6):1037-1049. doi: 10.1083/jcb.200703003

11. Polisetti N, Sharaf L, Schlötzer-Schrehardt U, Schlunck G, Reinhard T. Efficient isolation and functional characterization of niche cells from human corneal limbus. *Int J Mol Sci*. 2022;23(5):2750. doi: 10.3390/ijms23052750

12. Novelli F, Ganini C, Melino G, *et al*. p63 in corneal and epidermal differentiation. *Biochem Biophys Res Commun*. 2022;610:15-22. doi: 10.1016/j.bbrc.2022.04.022

13. Ramos T, Scott D, Ahmad S. An update on ocular surface epithelial stem cells: cornea and conjunctiva. *Stem Cells Int*. 2015;2015:601731. doi: 10.1155/2015/601731

14. Pellegrini G, Rama P, Matuska S, *et al*. Biological parameters determining the clinical outcome of autologous cultures of limbal stem cells. *Regenerative Med*. 2013;8(5):553-567. doi: 10.2217/rme.13.43

15. Galindo S, Herreras JM, López-Paniagua M, *et al*. Therapeutic effect of human adipose tissue-derived mesenchymal stem cells in experimental corneal failure due to limbal stem cell niche damage. *Stem Cells*. 2017;35(10): 2160-2174. doi: 10.1002/stem.2672

16. Nieto-Nicolau N, Martínez-Conesa EM, Fuentes-Julián S, *et al*. Priming human adipose-derived mesenchymal stem cells for corneal surface regeneration. *J Cell Mol Med*. 2021;25(11):5124-5137. doi: 10.1111/jcmm.16501

17. Calonge M, Pérez I, Galindo S, *et al*. A proof-of-concept clinical trial using mesenchymal stem cells for the treatment of corneal epithelial stem cell deficiency. *Transl Res*. 2019;206:18-40. doi: 10.1016/j.trsl.2018.11.003

18. Cadenas-Martin M, Arnalich-Montiel F, Miguel MPD. Derivation of limbal stem cells from human adult mesenchymal stem cells for the treatment of limbal stem cell deficiency. *Int J Mol Sci*. 2023;24(3):2350. doi: 10.3390/ijms24032350

19. Edel MJ, Casellas HS, Osete JR, *et al*. An optimized method to produce human-induced pluripotent stem cell-derived limbal stem cells easily adaptable for clinical use. *Stem Cells Dev*. 2025;34(3-4):49-60. doi: 10.1089/scd.2024.0172

20. Bisevac J, Moe MC, Drolsum L, Kristianslund O, Petrovski G, Noer A. A novel technique of amniotic membrane preparation mimicking limbal epithelial crypts enhances the number of progenitor cells upon expansion. *Cells*. 2023;12(5):738. doi: 10.3390/cells12050738

21. Malhotra C, Jain AK. Human amniotic membrane transplantation: different modalities of its use in ophthalmology. *World J Transplant*. 2014;4(2):111. doi: 10.5500/wjt.v4.i2.111

22. Paolin A, Cogliati E, Trojan D, *et al*. Amniotic membranes in ophthalmology: long term data on transplantation outcomes. *Cell Tissue Bank*. 2016;17(1):51-58. doi: 10.1007/s10561-015-9520-y

23. Harkin DG, Foyn L, Bray LJ, Sutherland AJ, Li FJ, Cronin BG. Concise reviews: can mesenchymal stromal cells differentiate into corneal cells? A systematic review of published data. *Stem Cells*. 2015;33(3):785-791. doi: 10.1002/stem.1895

24. Nguyen KN, Bobba S, Richardson A, *et al*. Native and synthetic scaffolds for limbal epithelial stem cell transplantation. *Acta Biomater*. 2018;65:21-35. doi: 10.1016/j.actbio.2017.10.037

25. Tan G, Ioannou N, Mathew E, Tagalakis AD, Lamprou DA, Yu-Wai-Man C. 3D printing in ophthalmology: from

medical implants to personalised medicine. *Int J Pharm*. 2022;625:122094.
doi: 10.1016/j.ijpharm.2022.122094

26. Boularaoui S, Al Hussein G, Khan KA, Christoforou N, Stefanini C. An overview of extrusion-based bioprinting with a focus on induced shear stress and its effect on cell viability. *Bioprinting*. 2020;20:e00093.
doi: 10.1016/j.bprint.2020.e00093

27. Ng WL, Vyas C, Huang B, Yeong WY, Bartolo P. Advanced bioprinting strategies for fabrication of biomimetic tissues and organs. *Int J Extreme Manuf*. 2025; 7(6):062006.
doi: 10.1088/2631-7990/adeee0

28. De Miguel MP. European Patent Application No. 22382119.0. Published online 2022.

29. He Z, Forest F, Bernard A, *et al*. Cutting and decellularization of multiple corneal stromal lamellae for the bioengineering of endothelial grafts. *Invest Ophthalmol Vis Sci*. 2016;57(15):6639-6651.
doi: 10.1167/iovs.16-20256

30. Zuk PA, Zhu M, Ashjian P, *et al*. Human adipose tissue is a source of multipotent stem cells. *Mol Biol Cell*. 2002;13(12):4279-4295.
doi: 10.1091/mbc.E02-02-0105

31. Mikhailova A, Ilmarinen T, Uusitalo H, Skottman H. Small-molecule induction promotes corneal epithelial cell differentiation from human induced pluripotent stem cells. *Stem Cell Reports*. 2014;2(2):219-231.
doi: 10.1016/j.stemcr.2013.12.014

32. Casaroli-Marano RP, Martínez-Conesa EM, Nieto-Nicolau N, Arnalich-Montiel F, Fuentes-Julian S, De Miguel MP. Adipose derived stem cells (ADS) for ocular surface regeneration. *Invest Ophthalmol Vis Sci*. 2014; 55(13):5183.

33. Gerardo H, Lima A, Carvalho J, *et al*. Soft culture substrates favor stem-like cellular phenotype and facilitate reprogramming of human mesenchymal stem/stromal cells (hMSCs) through mechanotransduction. *Sci Rep*. 2019;9(1):9086.
doi: 10.1038/s41598-019-45352-3

34. Maddox JR, Ludlow KD, Li F, Niyibizi C. Breast and abdominal adipose multipotent mesenchymal stromal cells and stage-specific embryonic antigen 4 expression. *Cells Tissues Organs*. 2012;196(2):107-116.
doi: 10.1159/000331332

35. Guasti L, Prasongchean W, Kleftouris G, *et al*. High plasticity of pediatric adipose tissue-derived stem cells: too much for selective skeletogenic differentiation? *Stem Cells Transl Med*. 2012;1(5):384-395.
doi: 10.5966/sctm.2012-0009

36. Martínez-Conesa EM, Espel E, Reina M, Casaroli-Marano RP. Characterization of ocular surface epithelial and progenitor cell markers in human adipose stromal cells derived from lipoaspirates. *Invest Ophthalmol Vis Sci*. 2012;53(1):513-520.
doi: 10.1167/iovs.11-7550

37. Ahearne M, Masterton S. Donor dependent limbal derived stem cell response to fluidic shear stress. *Invest Ophthalmol Vis Sci*. 2024;65(7):4462-4462.

38. Di Iorio E, Barbaro V, Ruzza A, Ponzin D, Pellegrini G, De Luca M. *Isoforms of Np63 and the Migration of Ocular Limbal Cells in Human Corneal Regeneration*; 2005.
www.pnas.orgcgidoi10.1073pnas.0503437102

39. Collin J, Queen R, Zerti D, *et al*. A single cell atlas of human cornea that defines its development, limbal progenitor cells and their interactions with the immune cells. *Ocul Surf*. 2021;21:279-298.
doi: 10.1016/j.jtos.2021.03.010

40. Wang DY, Cheng CC, Kao MH, Hsueh YJ, Ma DHK, Chen JK. Regulation of limbal keratinocyte proliferation and differentiation by TAp63 and ΔNp63 transcription factors. *Invest Ophthalmol Vis Sci*. 2005;46(9):3102-3108.
doi: 10.1167/iovs.05-0051

41. Koster MI, Kim S, Mills AA, DeMayo FJ, Roop DR. p63 is the molecular switch for initiation of an epithelial stratification program. *Genes Dev*. 2004;18(2):126-131.
doi: 10.1101/gad.1165104

42. Verma S, Lin X, Coulson-Thomas VJ. The potential reversible transition between stem cells and transient-amplifying cells: the limbal epithelial stem cell perspective. *Cells*. 2024;13(9):748.
doi: 10.3390/cells13090748

43. Kalha S, Shrestha B, Sanz Navarro M, Jones KB, Klein OD, Michon F. Bmi1+ progenitor cell dynamics in murine cornea during homeostasis and wound healing. *Stem Cells*. 2018;36(4):562-573.
doi: 10.1002/stem.2767

44. Liang Q, Le Q, Wang L, *et al*. Cytokeratin 13 is a new biomarker for the diagnosis of limbal stem cell deficiency. *Cornea*. 2022;41(7):867-873.
doi: 10.1097/ICO.0000000000002903

45. Ramirez-Miranda A, Nakatsu MN, Zarei-Ghanavati S, Nguyen CV, Deng SX. Keratin 13 is a more specific marker of conjunctival epithelium than keratin 19. Mol Vis. 2011;17:1652-1661.
http://www.molvis.org/molvis/v17/a183

46. De Miguel MP, Cadenas-Martin M, Stokking M, Martin-Gonzalez AI. Biomedical application of MSCs in corneal regeneration and repair. *Int J Mol Sci*. 2025;26(2):695.
doi: 10.3390/ijms26020695

47. Dietrich-Ntoukas T, Hofmann-Rummelt C, Kruse FE, Schlötzer-Schrehardt U. *Comparative* analysis of the basement membrane composition of the human limbus epithelium and amniotic membrane epithelium. Cornea. 2012;31(5):564-569.
doi: 10.1097/ICO.0b013e3182254b78

48. Yazdanpanah G, Haq Z, Kang K, Jabbehdari S, Rosenblatt Ml, Djalilian AR. Strategies for reconstructing the limbal stem cell niche. *Ocular Surf*. 2019;17(2):230-240. doi: 10.1016/j.jtos.2019.01.002

49. Dong C, Lv Y. Application of collagen scaffold in tissue engineering: Recent advances and new perspectives. *Polymers (Basel)*. 2016;8(2):42. doi: 10.3390/polym8020042

50. Wang X, Majumdar S, Soiberman U, *et al*. Multifunctional synthetic Bowman's membrane-stromal biomimetic for corneal reconstruction. *Biomaterials*. 2020;241:119880. doi: 10.1016/j.biomaterials.2020.119880

51. Simpson FC, McTiernan CD, Islam MM, *et al*. Collagen analogs with phosphorylcholine are inflammation-suppressing scaffolds for corneal regeneration from alkali burns in mini-pigs. *Commun Biol*. 2021;4(1):608. doi: 10.1038/s42003-021-02108-y

52. Levis HJ, Daniels JT. Recreating the human limbal epithelial stem cell niche with bioengineered limbal crypts. *Curr Eye Res*. 2016;41(9):1153-1160. doi: 10.3109/02713683.2015.1095932

53. Zhang B, Xue Q, Li J, *et al*. 3D bioprinting for artificial cornea: challenges and perspectives. *Med Eng Phys*. 2019;71:68-78. doi: 10.1016/j.medengphy.2019.05.002

54. Bonnet C, Gonzalez S, Deng SX. Limbal stem cell therapy. *Curr Opin Ophthalmol*. 2024;35(4):309-314. doi: 10.1097/ICU.0000000000001061

ACCSCIENCE PUBLISHING

International Journal of Bioprinting

RESEARCH ARTICLE

Development and evaluation of dual-controlled release antibiotic-loaded bone scaffolds

Peijie Zhao[1,2,3,4], Liangguo Si[1,2], Huan He[1,3], Huanhuan Sun[1,2], Zhipeng Yang[1,2], Mei Tian[1,3], Haiqiang Ma[1,2], Xu Ma[1,2], Huanxiang Guan[1,2], Yaodong Wang[1,2], and Zewen Qiao[2]*

[1]Ningxia Medical University, Yinchuan, Ningxia, China

[2]Department of Hand Foot Ankle Surgical Ward, General Hospital of Ningxia Medical University, Yinchuan, Ningxia, China

[3]Ningxia Key Laboratory of Clinical and Pathogenic Microbiology, Institute of Medical Sciences, General Hospital of Ningxia Medical University, Yinchuan, Ningxia, China

[4]Institute of Clinical Pharmacology, Department of Pharmacy, General Hospital of Ningxia Medical University, Yinchuan, Ningxia, China

Abstract

The treatment of infectious bone defects is a major challenge in orthopedics, with infection control and defect repair as the two primary treatment goals. The development of 3D-printed bone scaffolds capable of sustained and stable antibiotic release is an effective strategy for treating such defects. Specifically, the antibiotic loading method and the concentration of released antibiotics significantly affect infection control and bone repair outcomes. In this study, double antibiotic microspheres were prepared via the double emulsion-solvent evaporation method. Moxifloxacin and rifampicin (RM) were encapsulated by poly(lactic-co-glycolic acid) (PLGA), forming RM–PLGA. Subsequently, different concentrations of RM–PLGA and basic fibroblast growth factor (bFGF) were loaded onto a 3D-printed triply periodic minimal surface (TPMS) titanium scaffold (TiS) with a graded porosity design, enabling stable dual-controlled antibiotic release and enhanced release stability. In vitro results revealed that RM–PLGA/bFGFgelatin methacrylate [GelMA])@TiS exhibited strong antimicrobial properties, cytocompatibility, and the capacity for osteoblast differentiation and extracellular mineralization. In vivo, RM–PLGA/bFGF(GelMA)@TiS was effective in inhibiting infections induced by *Staphylococcus aureus* while promoting osteogenesis and angiogenesis. These results suggest that RM–PLGA-2/bFGF(GelMA)@TiS can stably release antibiotics to achieve the therapeutic goals of infection control and induction of both osteogenesis and angiogenesis.

Keywords: 3D printing; Antimicrobial; Basic fibroblast growth factor; Bone regeneration; Infectious bone defect; Moxifloxacin; Poly(lactic-co-glycolic acid) RM–PLGA; Rifampicin

Corresponding author:
Zewen Qiao
(13995307859@163.com)

Citation: Zhao P, Si L, He H, *et al.* Development and evaluation of dual-controlled release antibiotic-loaded bone scaffolds. *Int J Bioprint.* 2025;11(6):430-450. doi: 10.36922/IJB025330325

Received: August 11, 2025
Revised: August 26, 2025
Accepted: September 3, 2025
Published online: September 9, 2025

Copyright: © 2025 Author(s). This is an Open Access article distributed under the terms of the Creative Commons Attribution License, permitting distribution and reproduction in any medium, provided the original work is properly cited.

Publisher's Note: AccScience Publishing remains neutral with regard to jurisdictional claims in published maps and institutional affiliations.

1. Introduction

Infectious bone defects (IBDs) are a difficult-to-treat condition often encountered in orthopedic clinical practice.[1] Common causes include high-energy trauma and

complications following endoprosthetic procedures. Fractures caused by high-energy trauma are often classified as Gustilo type III. Such fractures are accompanied by bone loss, soft tissue damage, extensive periosteal stripping, and severe contamination, with IBDs eventually developing in approximately 5%–30% of cases. With the popularization of endoprosthetic surgery in orthopedics, infections following internal fixation or joint replacement have occurred at steady incidence rates of 2%–5% and ultimately resulted in IBDs. The coexistence and progressive worsening of bone infections and defects pose a significant challenge to treatment.[2,3] Infection control prior to defect repair is currently the primary treatment of IBDs. Specific clinical methods include debridement and autologous bone grafting, bone transport, and the Masquelet technique. Although these techniques can achieve clinical therapeutic effects, they suffer from common drawbacks, such as multiple surgeries, prolonged disease duration, high cost, and multiple complications. The design of 3D artificial anti-infective bone scaffolds capable of repairing infected bone defects has garnered considerable research interest and is considered a promising solution for the future treatment of IBDs.[4–6]

Bone formation and bone healing are essential functions of bone scaffolds. Reconstruction of the vascular network is a critical stage in the process of bone defect repair.[7] A good vascular network can provide sufficient oxygen and nutrients for bone tissue repair, promote the proliferation and differentiation of osteocytes, and accelerate bone defect healing.[8,9] Gelatin methacrylate (GelMA) hydrogel is a gelatin derivative that supports cell attachment and proliferation and possesses good biocompatibility.[10,11] Chu *et al.*[12] prepared GelMA scaffolds loaded with basic fibroblast growth factor (bFGF) and confirmed that bFGF is a multifunctional heparin-binding protein that promotes mitosis and chemotaxis in mesenchymal cells, thereby enhancing neovascularization. Currently, 3D-printed bone scaffolds not only address individualized treatment needs through their physical form but also meet the therapeutic requirements for various diseases through scaffold functionalization. For instance, scaffolds loaded with antitumor drugs for treating bone defects after tumor resection can be surface-functionalized to promote cartilage repair, while added bacteriostatic material or antibiotics can effectively prevent or treat bone infection.[13–15] Bacteriostatic materials form a local microenvironment detrimental to bacterial growth, thereby inhibiting bacterial proliferation and spread while reducing infection risk. In contrast, antibiotics can act directly on bacteria to destroy their cell walls or inhibit their protein synthesis, ultimately achieving bactericidal effects. Therefore, bone scaffolds capable of continuous and stable antibiotic release are crucial for the treatment of IBDs.

IBDs are chronic bone infections highly prone to recurrence, with approximately 70% of cases caused by *Staphylococcus aureus* (SA).[16] It has been determined that SA causes persistent and highly recurrent bone infections through two main routes: (i) SA adheres to the surface of the endoprosthesis or ischemic tissue and forms bacterial biofilms that resist antibiotics and the host immune response, enabling the bacteria to survive, thereby promoting further bacterial proliferation and spread; (ii) SA evades the bactericidal effects of antibiotics by internalizing into osteocytes and alters cellular functions, thereby disrupting bone homeostasis and causing bone loss.[17–19] With advances in understanding bone infections and their causative organisms, current clinical treatment parallels the principles of cancer treatment—specifically, early aggressive physical resection and localized administration of sustained high-dose antimicrobial chemotherapy.[20] Although methods such as 3D printing and chemical grafting enable the addition of antibiotics or certain antimicrobial materials into 3D bone scaffolds, previous research on antimicrobial bone scaffolds has reported several issues[21,22]: (i) while adding antimicrobial materials to the surfaces of 3D scaffolds provides preventive effects against infection, their effectiveness against pre-existing infections remains uncertain; (ii) when antibiotics are mixed with other materials for scaffold preparation using 3D printing, the printing process may render some antibiotics ineffective, or release due to scaffold degradation may alter the release rate and antibiotics concentration; (iii) achieving sufficient and sustained antibiotic release is difficult when antibiotics are coated or assembled on scaffold surfaces.

In this study, we aimed to resolve the issue of unstable antibiotic release from bone scaffolds. Two broad-spectrum antibiotics with high bioavailability in bone, namely moxifloxacin (Mox) and rifampin (Rif), were encapsulated in poly(lactic-co-glycolic acid) (PLGA) using the double emulsion-solvent evaporation method[23] for the preparation of Rif-Mox PLGA (RM–PLGA) microspheres.[24,25] Subsequently, the microspheres were diluted to various concentrations in GelMA hydrogel and loaded into a scaffold with a TPMS structure and graded porosity design. Among these, the gyroid (G) unit is one of the structures of the TMPS scaffold, characterized by a pore volume fraction that increases from 55% in the inner layer to 90% in the outer layer, with smaller pores inside and progressively larger pores toward the surface. The dual-controlled-release function enabled by the scaffold structure and microsphere degradation provided an initial high-concentration antibiotic release, followed by sustained

release at therapeutic levels. bFGF, a pro-angiogenic factor, was also incorporated into the bone scaffold to provide dual functionality: bone infection treatment during the early stage and bone defect repair in later stages. The performance of the scaffolds was examined by *in vivo* and *in vitro* experiments.

2. Materials and methods

2.1. Materials

The following materials were used: PLGA (Jinan Daigang Biomaterial, China), bFGF (MedChemExpress, China), Mox (Aladdin, China), Rif (Yuanye Biotechnology, China), GelMA (Engineering For Life, China), and MC3T3-E1 Subclone 14 (iCell Bioscience, China).

2.2. Sample preparation

2.2.1. Preparation and testing of RM–PLGA microspheres

The RM–PLGA microspheres were prepared using the double emulsion-solvent evaporation method (refer to **S1 [in the Supplementary file]** for the detailed experimental steps). Briefly, 10 mg of dried microspheres was mixed with 5 mL of phosphate-buffered saline (PBS). The mixture was ultrasonicated for 2 h, left to stand for 24 h, and centrifuged for 10 min. Subsequently, the supernatant was collected, diluted 20-fold, and analyzed for Mox and Rif contents using an ultraviolet (UV) spectrophotometer. Drug loading and encapsulation efficiency were calculated as follows[26]:

$$\text{Drug loading} = \frac{\text{Mass of Mox in microspheres}}{\text{Total mass of loaded PLGA microspheres}} \times 100\% \quad \text{(I)}$$

$$\text{Encapsulation efficiency} = \frac{\text{mass of Mox in microspheres}}{\text{total mass of Mox in the system}} \times 100\% \quad \text{(II)}$$

The dried microspheres were directly coated onto a conductive film and sputter-coated with gold under vacuum conditions. Scaffold morphology was observed using a scanning electron microscope (SEM; S-3400N, Hitachi Co., Ltd., Japan) at 10.0 kV, and particle size was measured.

2.2.2. Hydrogel preparation and concentration selection

Different amounts of GelMA (5, 10, and 15 g) were separately placed in light-protected centrifuge tubes containing 0.05 g of an initiator. Hydrogels with concentrations of 5%, 10%, and 15% (w/v) were prepared by heating the mixtures in a 60–70 °C water bath for 30 min in the dark until complete dissolution. The hydrogels were separately co-cultured with MC3T3 cells for 24 h and subsequently subjected to the Cell Counting Kit-8 (CCK-8) cell proliferation assay (Figure S1). Absorbance measurements at 450 nm on a microplate reader indicated that the 10% (w/v) hydrogel demonstrated the best performance. Therefore, this concentration was selected for subsequent experiments.

2.2.3. bFGF concentration selection

Lyophilized bFGF powder (10 μg) was dissolved in 1 mL of sterile water to prepare a 10 μg/mL bFGF stock solution. Thereafter, 1.5 μL bFGF stock solution was added to 300 μL of PBS to prepare a 50 ng/mL bFGF solution. Using the same method, 3, 4.5, and 6 μL of the bFGF stock solution were separately added to 300 μL PBS for the preparation of 100, 150, and 200 ng/mL bFGF solutions, respectively. The bFGF solutions with different concentrations were separately co-cultured with MC3T3 cells for 24 h, after which the CCK-8 cell proliferation assay was performed (Figure S2). Microplate reader measurements revealed that the 100 ng/mL bFGF group exhibited the highest absorbance at 450 nm. Therefore, this concentration was used for subsequent experiments.

2.2.4. Preparation and grouping of composite scaffolds

Scaffolds with a TPMS G-unit structure were prepared by selective laser melting (SLM) using Ti-6Al-4V powder as the starting material. The TiSs were washed with anhydrous ethanol and deionized water, sterilized by autoclaving, and dried. A TiS was placed in a flat-bottom container, and 1 mL of bFGF (100 ng/mL) hydrogel was added. The mixture was shaken to ensure thorough integration of the hydrogel with the TiS, then photocured using a 405 nm UV flashlight to obtain the semi-finished scaffold. After 24 h, 20 mg of RM–PLGA microspheres were added to the uncured hydrogel and thoroughly mixed. The mixture was placed into the semi-finished scaffold obtained the previous day, and the hydrogel was photocured using a 405 nm UV flashlight to obtain the 3D-printed anti-infective bone scaffold loaded with 20 mg RM–PLGA and bFGF. Preliminary experiments identified that antibiotic microspheres <10 mg exhibited no significant antibacterial effects. Composite scaffolds with concentrations of 10 and 30 mg/mL were prepared using the same method. For the powder group, the composite scaffold was loaded with 10 mg of Mox and Rif each. The experimental groups included the RM–PLGA-1/bFGF(GelMA)@TiS, RM–PLGA-2/bFGF(GelMA)@TiS, RM–PLGA-3/bFGF(GelMA)@TiS, RM-Powder/bFGF(GelMA)@TiS, and TiS groups.

2.3. Sustained drug release performance evaluation

2.3.1. Sustained antibiotic release

Titanium bone scaffold and 1 mL of PBS were placed in a dialysis bag and sealed. The bag was placed in a Polyethylene (PE) tube containing 5 mL PBS and incubated with shaking. Liquid samples were obtained at different time points, and the amount of Mox and Rif in the released solution was determined using a UV spectrophotometer (refer to **S2 [in the Supplementary File]** for the detailed experimental procedure). The amount of antibiotics released was calculated as follows[27]:

$$\text{Amount released} = \frac{m1}{m2} \times 100\% \quad \text{(III)}$$

where m1 is the amount of Mox and Rif released by the microspheres in the buffer solution, and m2 is the total amount of Mox and Rif in the microspheres.

2.3.2. bFGF release

Titanium bone scaffold was immersed in 1 mL buffer solution and incubated at 37 °C. The supernatant was collected at predetermined time points (days 1, 3, 5, 7, 14, 21, and 28) and replenished with an equivalent amount of buffer. The amount of bFGF released in the buffer was measured using the bFGF ELISA kit (refer to **S3 [in the Supplementary File]** for the detailed experimental procedure). Optical density (OD) in each well was measured at 450 nm using a microplate reader.

2.4. Characterization and morphological analysis of composite scaffolds

A dried RM–PLGA-2/bFGF(GelMA)@TiS scaffold was directly coated onto a conductive film and sputter-coated with gold under vacuum conditions. SEM was used to observe the morphology of the scaffold, and the elemental composition of the material was analyzed using energy-dispersive X-ray spectroscopy (EDS; Oxford, England).

2.5. Evaluation of *in vitro* biological performance

MC3T3-E1 Subclone 14 cells were rapidly thawed and transferred to an incubator for culture. Sterilized composite scaffolds of the various groups were placed in 12-well plates. To each well, 100 μL cell suspension (1×10^5/mL) was added to inoculate the surface of each scaffold, and culture medium was subsequently added to cover the entire scaffold. Scaffolds of the various groups that had been co-cultured with cells were fixed with glutaraldehyde for 24 h. After dehydration and gold sputter-coating, the scaffolds were examined using SEM to observe cell adhesion. Live/dead cell staining was performed on days 1 and 3 of culture. The influence of the various scaffolds on cell viability was observed under a fluorescence microscope (Leica, Germany). On days 1, 3, 5, and 7 of culture, the CCK-8 assay was performed, and absorbance (OD) at 450 nm was measured with a microplate reader to assess the influence of the scaffolds on cytotoxicity and cell proliferation.

Titanium bone scaffold was placed in the lower chamber of a Transwell plate, and 100 μL of the cell suspension (1×10^5/mL) was inoculated into the upper chamber. After co-culture for 24 h, the cells were fixed with 4% paraformaldehyde for 10 min, incubated in the dark at room temperature for 30 min with a staining solution—prepared by diluting Actin-Tracker Green in PBS containing 5% bovine serum albumin and 0.1% Triton X-100 at a ratio of 1:100—and incubated for additional 5 min in the dark following the addition of 1 μg/mL DAPI staining solution. Upon the completion of staining, the membrane from the chamber was placed on a glass slide and examined under a fluorescence microscope to observe the cytoskeleton morphology.

2.6. Influence of scaffolds on osteogenic differentiation of cells

A scaffold was placed in the lower chamber of a Transwell plate, and 100 μL of the cell suspension (1×10^5/mL) was inoculated into the upper chamber. After 24 h of culture, the complete medium was replaced with an osteogenic induction medium, and the medium was changed every 3 days. On day 7 of co-culture, the cells were fixed with 4% paraformaldehyde for 10 min and stained with Sirius Red staining solution for 2 h. Subsequently, the membrane was transferred onto a glass slide and examined under a microscope to observe the staining. Upon completion of microscopic examination, the membrane was rinsed three times with 0.1 M acetic acid, dissolved in an eluent consisting of 0.2 M NaOH and methanol, and transferred to a 96-well plate. OD at 540 nm was measured using a microplate reader. Cells induced for 7 and 12 days were fixed with 4% paraformaldehyde for 10 min, stained with an alkaline phosphatase (ALP) assay kit, and observed under a microscope. OD at 405 nm was measured using a microplate reader. Cells induced for 21 and 28 days were fixed with 4% paraformaldehyde for 10 min. After aspirating the paraformaldehyde, an appropriate amount of Alizarin Red S working solution was added to each well for 30 min of staining, and the stained cells were examined under a microscope. Upon completion of microscopic examination, the membrane was placed in a clean container, and 10% cetylpyridinium chloride solution was added to each well to dissolve the Alizarin Red S precipitate. OD at 620 nm was measured using a microplate reader.

2.7. *In vitro* antimicrobial performance

The frozen SA bacterial suspension (EGFP-labeled) was removed from storage, rapidly thawed, and cultured on tryptic soy agar (TSA) plates. Pure SA was obtained after the TSA plates had been placed in a constant-temperature incubator at 37 °C for 24 h. Approximately 100 μL of the bacterial suspension (1.0×10^8 CFU/mL) was applied evenly onto each TSA plate using a cell spreader. For each experimental group, the scaffold was placed in the center of the plate. No scaffolds were placed for the blank group. All plates were incubated for 24 h and subsequently removed for observation of the zone of inhibition around each scaffold.

Coverslips were placed in 12-well plates, and 1 mL of bacteria (1.0×10^8 CFU/mL) was inoculated onto each coverslip. Subsequently, the composite scaffolds were placed in the wells. After 24 h, the scaffolds were removed, fixed with 4% paraformaldehyde, dried for 12 h, stained with 0.5% crystal violet solution at room temperature for 10 min, and examined under a microscope for observation of bacterial biofilms on the scaffolds. Each biofilm was dissolved in 33% acetic acid solution, and the OD at 575 nm was measured with a microplate reader.

Scaffolds co-cultured with cells for 24 h were fixed with glutaraldehyde for 24 h, dehydrated, gold-plated, and placed under an SEM for observation of the biofilms. Coverslips were placed in 12-well plates, and 1 mL of bacteria suspension (1.0×10^6 CFU/mL) was inoculated into each well. After the scaffolds had been placed in the wells, the plates were cultured in a constant-temperature incubator at 37°C for 24 h. Subsequently, the scaffolds were removed, incubated with SYTO 9/propidium iodide (PI) staining solution (diluted 10-fold with PBS) at room temperature in the dark for 10 min, and placed under a fluorescence microscope for observation of live/dead bacterial cell staining.

2.8. Establishment of infection model

The animal ethics committee (Experimental Animals Use and Management Committee of Ningxia Medical University) approved the experimental animals and experimental procedures adopted in this study (approval no. IACUC-H2025003). A model of subcutaneous infection was established with Sprague-Dawley rats. All experimental animals used were obtained from the Laboratory Animal Center of Ningxia Medical University and were managed and disposed of in accordance with the Guide for the Care and Use of Laboratory Animals issued by the National Research Council. A total of 60 Sprague-Dawley rats (aged 8 weeks; weighing 280–360 g each) were selected and randomly divided into five groups of 12 rats each. The animals were fed according to standard protocols, and all experiments were compliant with the animal ethics review standards of Ningxia Medical University. We used 1% isoflurane inhalation for anesthesia. A skin wound of approximately 18 mm in length was made on the back of the left thigh of each Sprague-Dawley rat using a sterile scalpel. Subsequently, scaffolds of the RM–PLGA-1/bFGF(GelMA)@TiS, RM–PLGA-2/bFGF(GelMA)@TiS, RM–PLGA-3/bFGF(GelMA)@TiS, RM-Powder/bFGF(GelMA)@TiS, and TiS groups were separately placed beneath the incised skin of the animals, and the incisions were sutured. Approximately 1 mL of bacteria (1.0×10^6 CFU/mL) was injected into the vicinity of the scaffold to establish a Sprague-Dawley rat model of infection. The condition of the wound skin, weight changes, and dietary habits of the rats were observed after the operation.

At 2 weeks post-operation, the rats were subjected to X-ray imaging and *in vivo* small-animal imaging (refer to **S4 [in the Supplementary File]** for the detailed procedure). Soft tissues were obtained from the modeling area for the preparation of sections for hematoxylin and eosin (H&E) and Masson's trichrome staining, plate toxicity assays at 10- and 100-fold dilutions, Western blotting (**S5 [in the Supplementary File]**), and reverse transcription-quantitative polymerase chain reaction detection (**S6 [in the Supplementary File]; Table S1**). The heart, lung, kidney, liver, and spleen tissues of the rats were collected and subjected to H&E staining for evaluation of the potential *in vivo* toxicity of the scaffolds. The influence of the scaffolds on angiogenesis was further investigated by immunofluorescence staining of tissue sections for CD31 and TNF-α.

2.9. Statistical analysis

All values were expressed as mean ± standard deviation. One-way analysis of variance was performed to analyze significant differences between the two groups. Differences were considered statistically significant when $p < 0.05$. The significance of differences was denoted as follows: $^*p < 0.05$; $^{**}p < 0.01$; $^{***}p < 0.001$; $^{****}p < 0.0001$; ns: not significant.

3. Results

3.1. Preparation and characterization of RM–PLGA-2/bFGF(GelMA)@TiS

In this study, the double emulsion-solvent evaporation method was adopted for the preparation of PLGA antibiotic microspheres (Figure 1A) encapsulating Mox (Figure 1C) and Rif (Figure 1B). The external phase solution was prepared using petroleum ether, liquid paraffin, and Span 85 (Figure 1D). PLGA used for the preparation of microspheres is a white, transparent, and odorless particulate material that can be dissolved in acetonitrile and isopropanol by sonication (Figure 1E). Mox is a

white fine powder, and Rif is an orange fine powder; both of which were soluble in the internal phase solution (Figure 1F). After freeze-drying at −80°C, the Mox- and Rif-loaded PLGA microspheres appeared as a loose dark orange powder (Figure 1G). Gelatin appeared as a loose, colorless, and odorless white mass-like structure (Figure 1H). SEM results (Figure 2A) indicated that the spherical surfaces of the Rif/Mox–PLGA microspheres were smooth. The average diameter of the microspheres was 23.23 μm (Figure 2B). The drug loadings of Mox and Rif in the Rif/Mox–PLGA microspheres were 4.15% ± 0.58% and 5.17% ± 0.69%, respectively. The encapsulation efficiencies were 40.63% ± 4.82% and 51.2% ± 9.37%, respectively. The TiSs had a diameter of 15 mm and a height of 2 mm. In this study, SLM was adopted to prepare TPMS scaffolds with a G-unit structure. The scaffolds exhibited a radially increasing porosity gradient from the inner to the outer layer, with pore sizes in the range of 420–630 μm. Porosity was 55% in the inner layer and 90% in the outer periphery. The prepared scaffolds had a diameter of 15 mm and a height of 2 mm, characterized as flat, circular structures with a hard texture (Figure 1I). SEM revealed that the RM–PLGA microspheres and bFGF were uniformly distributed within the GelMA hydrogel and filled the scaffold pores. Results of EDS analysis (Figure 2G) revealed the presence of titanium (Ti), carbon (C), oxygen (O), nitrogen (N), chlorine (Cl), potassium (K), sodium (Na), phosphorus (P), and fluorine (F) on the surface of RM–PLGA-2/bFGF(GelMA)@TiS, which confirmed successful incorporation of hydrogel-loaded RM–PLGA and bFGF into TiS.[28] Figure 2C displays the physical appearances of RM–PLGA-1/bFGF(GelMA)@TiS, RM–PLGA-2/bFGF(GelMA)@TiS, RM–PLGA-3/bFGF(GelMA)@TiS, RM–Powder/bFGF(GelMA)@TiS, and TiS. Figure 2D presents the release profiles of the four bFGF-loaded groups. The sudden release of bFGF was not observed during the first 24 h. For the RM-Powder/bFGF(GelMA)@TiS group, the bFGF release rate at all subsequent time points was higher than that of all other experimental groups. A possible explanation is that the rapid release of the Mox and Rif powders indirectly influenced the release of bFGF from the gaps. The loading of 10 mg RM–PLGA microspheres in the RM–PLGA-1/bFGF(GelMA)@TiS group provided more gaps that facilitated the release of bFGF. In contrast, the loading of 30 mg RM–PLGA microspheres in the RM–PLGA-3/bFGF(GelMA)@TiS group retarded bFGF release.[29] Figure 2E and F presents the release profiles of Mox and Rif. Both antibiotics exhibited rapid release in powder form. In the RM-Powder/bFGF(GelMA)@TiS group, by day 15, 80% of Mox and 83.7% of Rif had been released. By day 20, the total release rate of the two antibiotics was approximately 85%, and the total release rate remained basically the same in subsequent periods. However, in the three groups that added RM–PLGA, the total release of the two antibiotics for each group was only about 59% by day 15 and approached 83% by day 30. Among them, the group with 10 and 30 mg of RM–PLGA microspheres achieved this release level first, while the group with 20 mg of RM–PLGA microspheres reached it last.

3.2. Evaluation of *in vitro* biocompatibility of RM–PLGA-2/bFGF(GelMA)@TiS

The *in vitro* biological performance of RM–PLGA-2/bFGF(GelMA)@TiS was evaluated by determining cell adhesion, cell viability, and the influence of the scaffolds on cytotoxicity and proliferation.

Figure 3A and B presents the adhesion and cell count of MC3T3 cells on the scaffold surfaces detected by SEM. The MC3T3 cells exhibited a short spindle shape, with their pseudopodia extended and adhering to the struts of scaffolds. Certain hydrogels developed cracks upon drying, with typically long spindle-shaped bone marrow stromal cells (MC3T3) adhered to the surface. Cells in all four experimental groups were dispersed and interconnected, forming cellular films. In particular, cells in the RM–PLGA-2/bFGF(GelMA)@TiS group exhibited more complex interconnections, resulting in the formation of a dense cellular film covering the scaffold surface.[30] Differences in the number of cells between groups were not statistically significant, and only a few cells of the control group exhibited atrophy with no obvious pseudopodia. Figure 3E displays the CCK-8 assay results. On day 1, the OD of the RM–PLGA-2/bFGF(GelMA)@TiS group was significantly different from that of the control group but did not differ significantly from those of the other three experimental groups. The changes in the OD values remained consistent over time.

Results of live/dead cell staining indicated the presence of a large number of green-stained viable cells and only a handful of red-stained dead cells in all four experimental groups on days 1 and 3 (Figure 3C). Differences among the four groups were not statistically significant (Figure 3D). In contrast, the number of viable cells in the control group was significantly smaller than that of the other four groups. Figure 3F and G present the results and quantification of nuclear and cytoskeletal staining. It can be observed that the four experimental groups had similar numbers of blue-stained nuclei that were surrounded by elongated, interconnected red-stained cytoskeletons. Compared with the control group, the experimental groups had cytoskeletons that were broader and wider, with cells surrounded by pseudopodial protrusions. These observations demonstrated that all four scaffold groups with added bFGF possessed good biocompatibility.

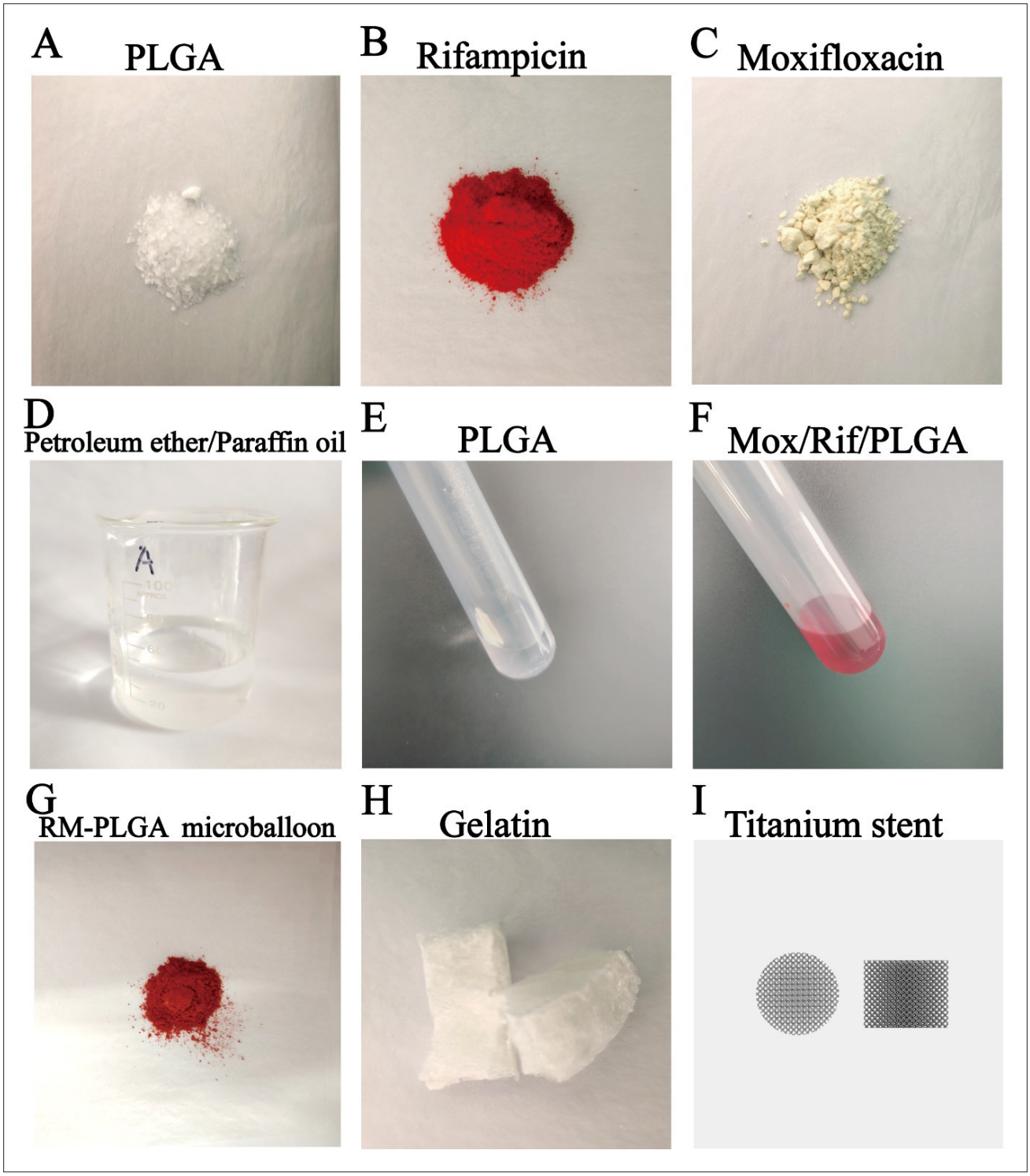

Figure 1. Preparation of RM–PLGA copolymer microspheres. (A) Physical sample of PLGA. (B) Physical sample of Rif. (C) Physical sample of Mox. (D) Mox dissolved in petroleum ether and liquid paraffin. (E) PLGA dissolved in acetonitrile and isopropanol. (F) Mox and rifampicin added to the PLGA solution. (G) Mox/Rif microspheres. (H) Gelatin. (I) Titanium bone scaffold. Abbreviations: PLGA, poly(lactic-co-glycolic acid); RM: rifampicin/moxifloxacin; Mox, moxifloxacin; Rif, rifampicin.

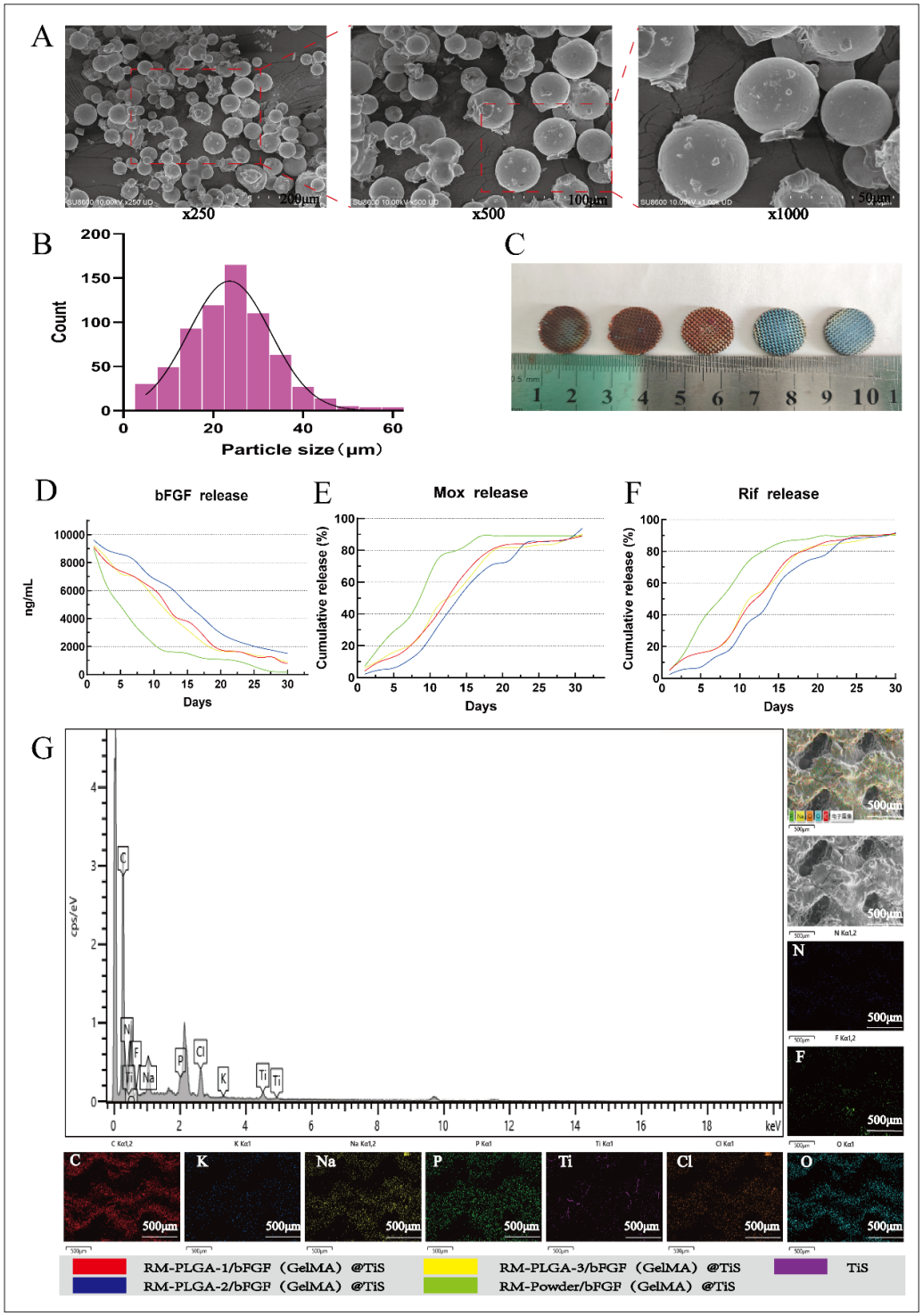

Figure 2. Basic tests of RM–PLGA microspheres and titanium bone scaffolds. (A) Scanning electron microscope image of the RM–PLGA microspheres. (B) Particle size distribution graph of the RM–PLGA microspheres. (C) Grouping of the scaffolds (from left to right): RM–PLGA-1/bFGF (GelMA)@TiS, RM–PLGA-2/bFGF (GelMA)@TiS, RM–PLGA-3/bFGF (GelMA)@TiS, RM-powder/bFGF (GelMA)@TiS, and the TiS group. (D) Release graph of the four groups loaded with bFGF. (E) Release graph of the four groups with different forms of moxifloxacin loading. (F) Release graph of the four groups with different forms of rifampicin loading. (G) Energy spectral scan of the RM–PLGA-2/bFGF (GelMA)@TiS scaffold. Scale bars: 200 μm (A), 100 μm (A), 50 μm (A), 500 μm (G). Abbreviations: PLGA, poly(lactic-co-glycolic acid) copolymer; RM, rifampicin–moxifloxacin; bFGF, basic fibroblast growth factor; GelMA, methylacrylate-modified gelatin.

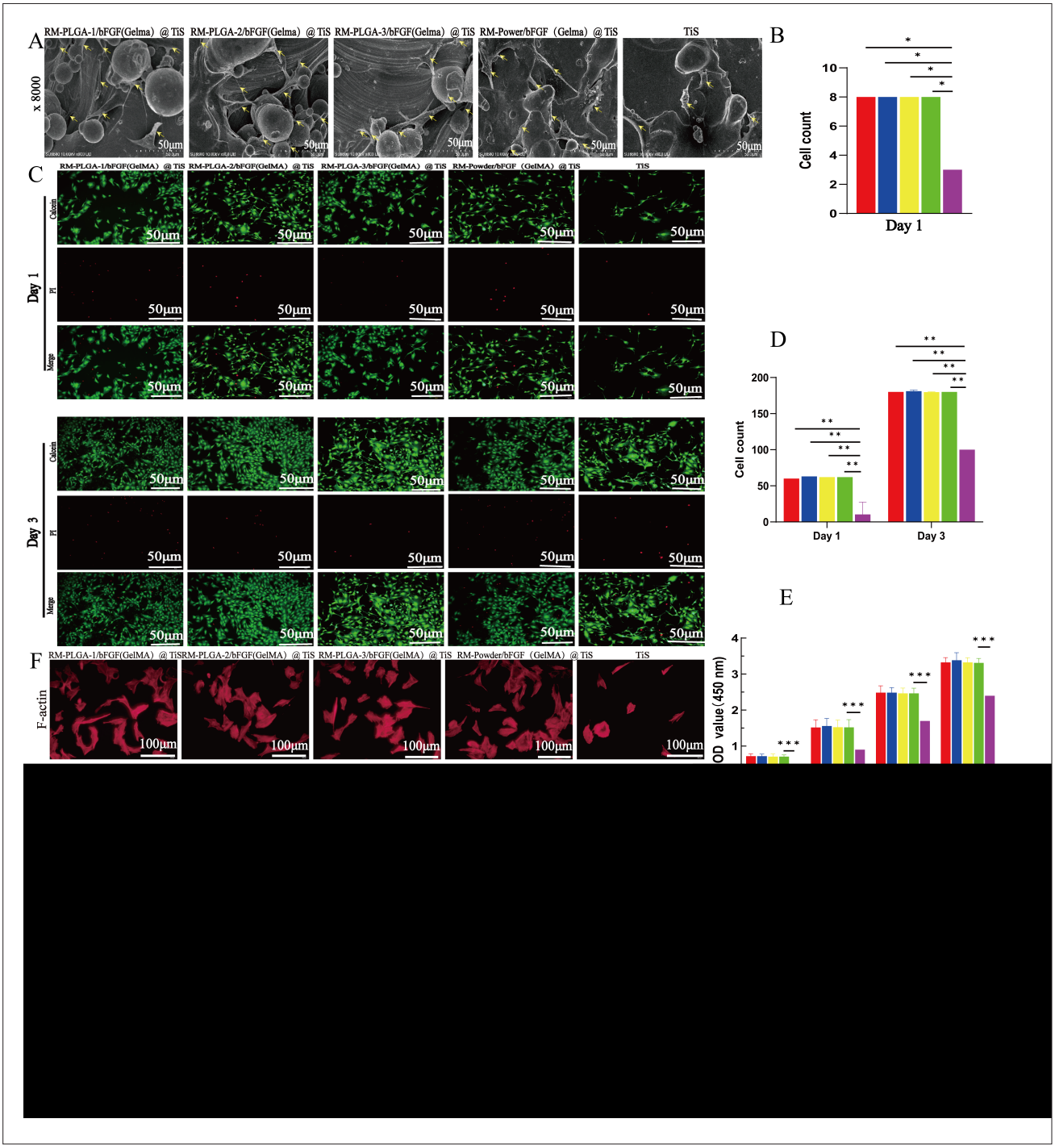

Figure 3. In vitro biological performance evaluation of the titanium bone scaffold. (A) Scanning electron microscope image of the co-culture of the composite scaffold and cells. (B) Number of cells adhered to the scaffold. (C) Live and dead cell staining images on days 1 and 3. (D) Live and dead cell statistics on days 1 and 3. (E) CCK-8 test results. (F) Cell morphology staining (blue represents the cell nucleus, red represents the cell skeleton). (G) Cell morphology quantification. *$p < 0.05$, **$p < 0.01$, ***$p < 0.001$, ****$p < 0.0001$; $n = 3$. Scale bars: 50 μm (A), 50 μm (C), 100 μm (F). Magnification: ×8000 (A). Abbreviations: PLGA, poly(lactic-co-glycolic acid) copolymer; RM, rifampicin–moxifloxacin; bFGF, basic fibroblast growth factor; GelMA, methylacrylate-modified gelatin.

3.3. Influence of RM–PLGA-2/bFGF(GelMA)@TiS on osteogenic differentiation of cells

The influence of RM–PLGA-2/bFGF(GelMA)@TiS on osteogenic differentiation of cells was determined by performing collagen fiber staining, ALP staining and quantification, and qualitative and quantitative analysis of calcium nodules.

Figure 4A presents the results of Sirius red staining. A light pink color was observed in MC3T3 cells that had undergone 7 days of osteogenic induction. Microscopic examination revealed that the collagen fibers of the four experimental groups exhibited a pink color, whereas the control group presented faintly colored collagen fibers (red) and muscle fibers (yellow). By day 12, the red color of the film at the bottom of the well plates was significantly more intense compared with day 7, and dense clustering of red COL-1 with irregular shapes and uneven sizes was observed under the microscope. Significant differences existed between the four experimental groups and the control group. The degradation solution was light red on day 7 and darker red on day 12. Similar results were obtained for the OD of the degradation solution at 540 nm (Figure 4B).

ALP is a well-recognized marker of early osteogenesis and can be used to assess osteogenic differentiation in early-stage osteoblasts.[31] After 7 days of incubation with the induction solution, light blue ALP was observed in all four experimental groups, with no statistically significant differences between the groups. The TiS control group displayed a significant reduction in ALP compared to the four experimental groups, with the difference being statistically significant. At day 12 of culture, the MC3T3 cells became denser, and the color of ALP was more intense (Figure 4C). Similar results were obtained for the OD of the degradation solution at 405 nm (Figure 4D).

Figure 4E displays the results of Alizarin red S staining. After 21 days of osteogenic induction of MC3T3 cells, red mineralized nodules were scattered at the bottom of the well plates, and cell films formed by MC3T3 were visible in certain areas. In contrast, the control group merely exhibited sporadic mineralized nodules. On day 28 of induction, all four experimental groups had mineralized nodules of different sizes and irregular shapes that were densely distributed and interconnected with each other to form mass-like structures, with no significant difference between groups. The number of mineralized nodules in the control group was significantly different from those of the four experimental groups. Figure 4F presents the OD of the degradation solution at 620 nm.

Collectively, these findings demonstrated that all four scaffold groups with added bFGF provided good osteogenic differentiation and mineralization effects.

3.4. *In vitro* antimicrobial performance of RM–PLGA-2/bFGF(GelMA)@TiS

The SEM results demonstrated that normal SA had a regular spherical morphology and were aggregated into clusters.[32] Treatment with Mox and Rif led to the disintegration of SA, with the residue intertwining to form a filamentous mesh-like structure. In the RM–PLGA-2/bFGF(GelMA)@TiS group, the filamentous mesh-like necrotic material filled the entire field of view under the microscope, with only individual SA cells remaining intact. The number of intact SA increased progressively across the RM–PLGA-1/bFGF(GelMA)@TiS, RM–PLGA-3/bFGF(GelMA)@TiS, and RM-powder/bFGF(GelMA)@TiS groups. In contrast, the control group presented entirely intact and spherical SA (Figure 5A). Results of crystal violet staining of bacterial biofilms (Figure 5B) revealed a massive accumulation of dark purple biofilm in the RM–PLGA-2/bFGF(GelMA)@TiS group. The biofilms of the other three experimental groups were purple, whereas no stained biofilms were observed in the control group. Figure 5C illustrates the results of semi-quantitative analysis of the biofilms.

An *in vitro* antimicrobial assay was performed to evaluate the antimicrobial properties of RM–PLGA-2/bFGF(GelMA)@TiS. Figure 5D presents the inhibition zones of the various groups. There was an absence of inhibition zones around the scaffolds of the TiS group. Scaffolds of the RM–PLGA-1/bFGF(GelMA)@TiS, RM–PLGA-2/bFGF(GelMA)@TiS, RM–PLGA-3/bFGF(GelMA)@TiS, and RM-powder/bFGF(GelMA)@TiS groups exhibited inhibition zones of varying sizes, with the RM–PLGA-2/bFGF(GelMA)@TiS group reporting the largest inhibition zone diameter.

Results of live/dead bacterial cell staining (Figure 5E) indicated that massive numbers of red-stained dead bacteria were observed in all antibiotic-dosing groups. In contrast, green-stained viable bacteria were barely present. In contrast, the blank control group displayed large numbers of green-stained viable bacteria and only a handful of red-stained dead bacteria. Figure 5F illustrates the relative quantitative analysis of live and dead bacteria.

These findings demonstrated that the newly developed RM–PLGA-2/bFGF(GelMA)@TiS composite scaffold provided remarkable *in vitro* antimicrobial performance.

3.5. *In vivo* antimicrobial performance of RM–PLGA-2/bFGF(GelMA)@TiS

Results of the plate-coating experiment for the measurement of toxicity to soft tissue (Figure 6A) demonstrated varying

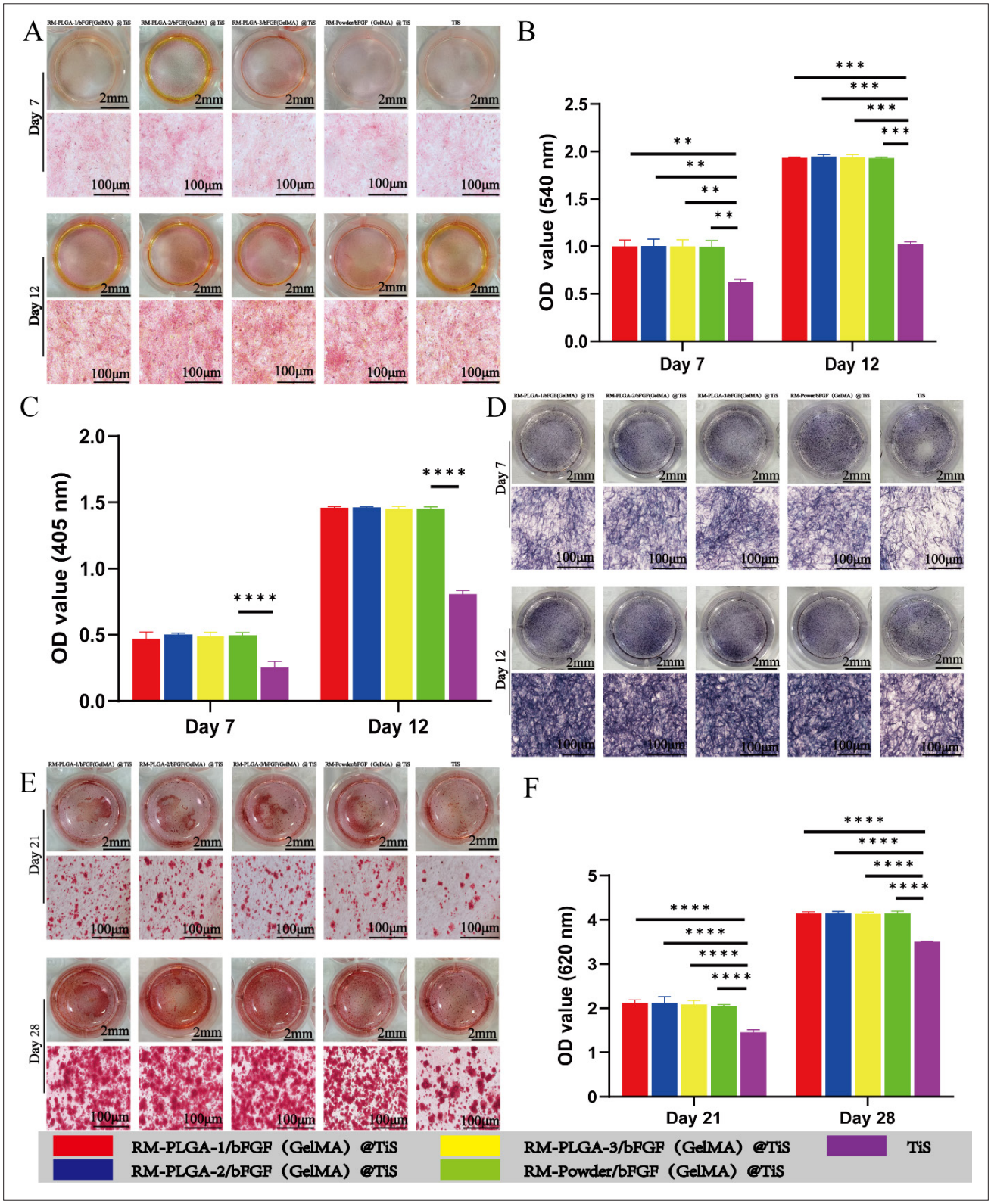

Figure 4. The effect of titanium bone scaffold on osteogenic differentiation of cells. (A) Result of Sirius Red staining. (B) Result of collagen secretion. (C) Quantitative ALP detection. (D) ALP staining result. (E) Result of Alizarin Red staining. (F) Quantitative detection of calcium nodules. $^{**}p < 0.01$, $^{***}p < 0.001$, $^{****}p < 0.0001$; $n = 3$. Scale bars: 100 μm (A), 100 μm (D), 100 μm (E). Abbreviations: PLGA, poly(lactic-co-glycolic acid) copolymer; RM, rifampicin–moxifloxacin; bFGF, basic fibroblast growth factor; GelMA, methylacrylate-modified gelatin.

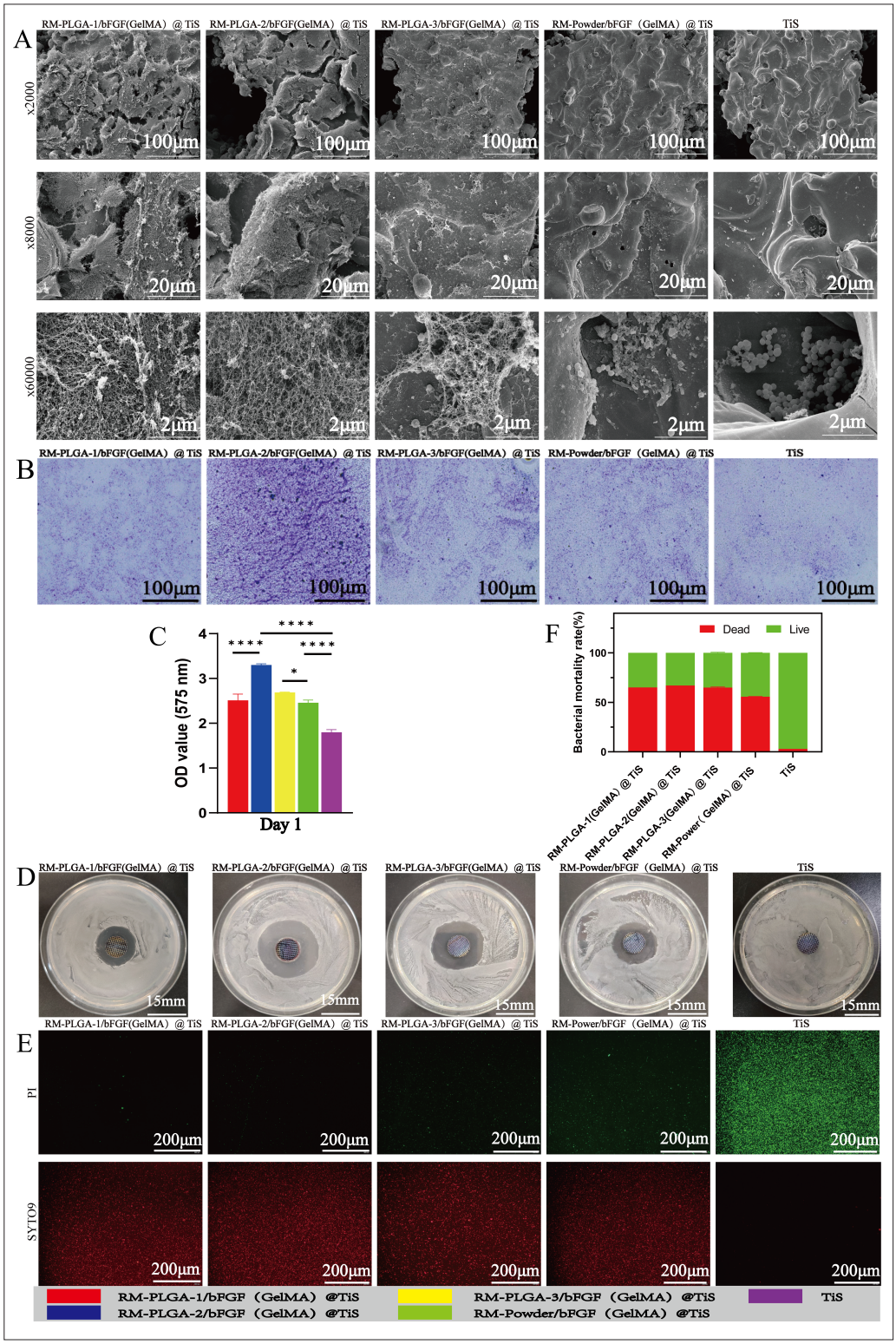

Figure 5. In vitro antibacterial performance of the titanium bone scaffold. (A) Scanning electron microscope image of the composite scaffold co-cultured with bacteria. (B) Crystal violet staining of the bacterial biofilm. (C) Quantitative analysis of crystal violet staining. (D) Inhibition zones of different scaffold groups. (E) Live/dead bacterial staining results. (F) Quantitative analysis of live/dead bacteria. *$p < 0.05$, ****$p < 0.0001$; $n = 3$. Scale bars: 100 μm (A), 100 μm (B), 15 mm (C), 200 μm (E). Magnification: ×2000 (A). Abbreviations: PLGA, poly(lactic-co-glycolic acid) copolymer; RM, rifampicin–moxifloxacin; bFGF, basic fibroblast growth factor; GelMA, methylacrylate-modified gelatin.

degrees of bacterial growth on TSA plates with 10- and 100-fold diluted cultures. The RM–PLGA-2/bFGF(GelMA)@TiS group merely exhibited minimal bacterial growth, whereas SA covered the TSA plates of the control group. The bacterial counts of the remaining three experimental groups were between those of the two aforementioned groups. Statistical analysis (Figure 6B and C) indicated a significant difference in the bacterial count between the control and RM–PLGA-2/bFGF(GelMA)@TiS groups.

Figure 6D presents the results of *in vivo* bacterial bioluminescence imaging[33,34] for monitoring antimicrobial performance. The intensity of bioluminescence emitted by the experimental strain in the *in vivo* imaging system (IVIS) provides a direct indication of the bacterial load. After the subcutaneous implantation of the different scaffolds and inoculation of bioluminescent bacteria, the subcutaneous antimicrobial performance of the scaffold materials could be monitored in real-time using IVIS. On day 0, the intensities and diffusion ranges of bacterial bioluminescence did not differ significantly among the experimental groups. On day 7, the RM–PLGA-1/bFGF(GelMA)@TiS, RM–PLGA-2/bFGF(GelMA)@TiS, RM–PLGA-3/bFGF(GelMA)@TiS, and RM-Powder/bFGF(GelMA)@TiS groups exhibited varying degrees of reduction in bioluminescence intensity and diffusion range. In particular, the RM–PLGA-2/bFGF(GelMA)@TiS group exhibited the most pronounced decrease, which was different from the other three experimental groups and significantly different from that of the blank control group. On day 14, fluorescence signals were essentially unobservable in the RM–PLGA-2/bFGF(GelMA)@TiS group, which was different from the other three experimental groups and significantly different from that of the blank control group. Figure 6E illustrates the statistical analysis of fluorescence data.

3.6. *In vivo* repair performance of RM–PLGA-2/bFGF(GelMA)@TiS

Figure 7A presents the results of the X-ray examination at 2 weeks postoperation, displaying implanted scaffolds that were well-positioned without loosening or detachment. The expression of the osteogenic proteins RUNX2 and OPN (Figure 7C and D) was detected by Western blotting (Figure 7B). Results indicated that protein expression was more abundant in the RM–PLGA-2/bFGF(GelMA)@TiS group, which was different from the other three experimental groups and significantly different from that of the control group. Results of qPCR (Figure 7E and F) were consistent with Western blotting. H&E staining was also performed on the heart, liver, spleen, lung, and kidney tissues of rats to further exclude potential biotoxicity associated with the implanted scaffolds.[35] The results (Figure 7G) indicated that the various tissues had intact morphology. Compared with the control group, no obvious signs of organ damage were observed in the experimental groups, effectively eliminating the possibility that implanted scaffolds could cause toxic reactions.

Figure 8A presents the results of H&E and Giemsa staining. The H&E staining results of the control group featured significant neutrophil infiltration in the soft tissues and a severe inflammatory response.[36] In the RM–PLGA-1/bFGF(GelMA)@TiS, RM–PLGA-3/bFGF(GelMA)@TiS, and RM-Powder/bFGF(GelMA)@TiS groups, the number of neutrophils in the soft tissues was significantly reduced, and inflammation was significantly alleviated compared to the control group. The RM–PLGA-2/bFGF(GelMA)@TiS group had the lowest neutrophil count, with the difference being significant compared with the control group. Results of Giemsa staining revealed a large number of blue collagen fibers and pale red muscle fibers in the RM–PLGA-2/bFGF(GelMA)@TiS group. The RM–PLGA-1/bFGF(GelMA)@TiS, RM–PLGA-3/bFGF(GelMA)@TiS, and RM-powder/bFGF(GelMA)@TiS groups displayed fewer collagen fibers and muscle fibers.[37] However, the control group merely exhibited sporadic collagen fibers, which were significantly different from the other groups. These results suggested that the RM–PLGA-2/bFGF(GelMA)@TiS group possessed good abilities for attenuating inflammation and promoting tissue repair and regeneration.

Figure 8B–D presents the results of TNF-α and CD31 immunofluorescence staining and relative fluorescence intensity analysis. TNF-α, an inflammatory cytokine produced during the inflammatory phase, activates the production of neutrophils and lymphocytes and plays an important role in the inflammatory process. Therefore, it is commonly employed as an indicator for evaluating inflammation.[38] CD31, a transmembrane protein expressed during early angiogenesis, is also used to assess endothelial differentiation and angiogenesis during wound healing.[39] The TNF-α protein, CD31, and cell nuclei, respectively, exhibited red, green, and blue fluorescence. Our results indicated that the TNF-α fluorescence intensity of RM–PLGA-2/bFGF(GelMA)@TiS was significantly lower than that of the other groups. This may be attributed to reduced TNF-α expression caused by the sustained release of RM–PLGA. The RM–PLGA-2/bFGF(GelMA)@TiS group also had the highest CD31 protein expression, which may be ascribed to the promotion of endothelial differentiation and angiogenesis by bFGF in an environment exhibiting strong anti-infective effects.

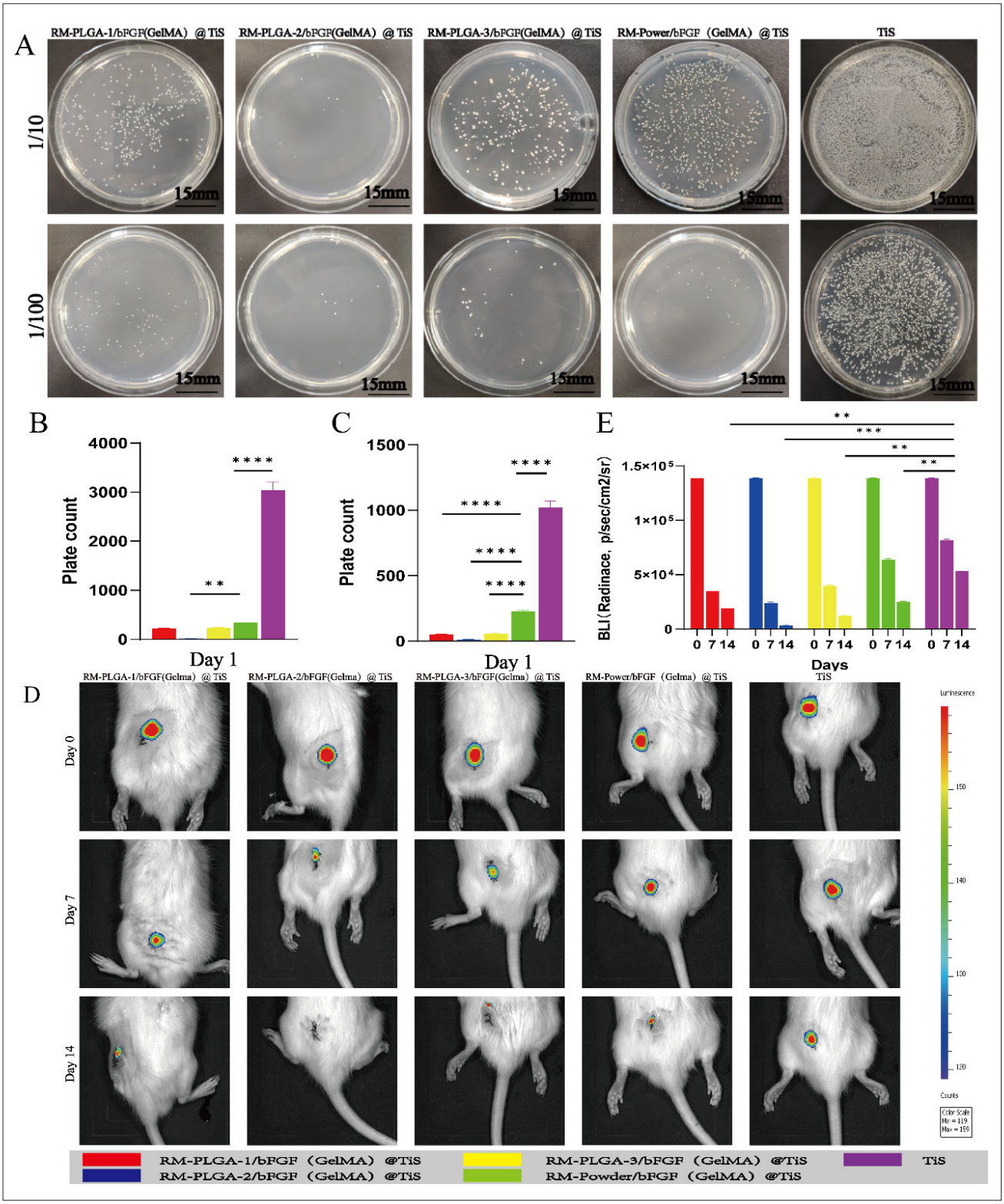

Figure 6. Relevant tests on titanium bone scaffold implantation in SD rats. (A-C) Results of plate toxicity tests (A) and their corresponding quantitative analyses at 10-fold (B) and 100-fold dilutions (C). (D and E) In vivo bacterial bioluminescence imaging (D) and corresponding fluorescence intensity (E). $^{**}p < 0.01$, $^{***}p < 0.001$, $^{****}p < 0.0001$; $n = 3$. Scale bar: 15 mm (A). Abbreviations: BLI, bioluminescence imaging; PLGA, poly(lactic-co-glycolic acid) copolymer; RM, rifampicin–moxifloxacin; bFGF, basic fibroblast growth factor; GelMA, methylacrylate-modified gelatin.

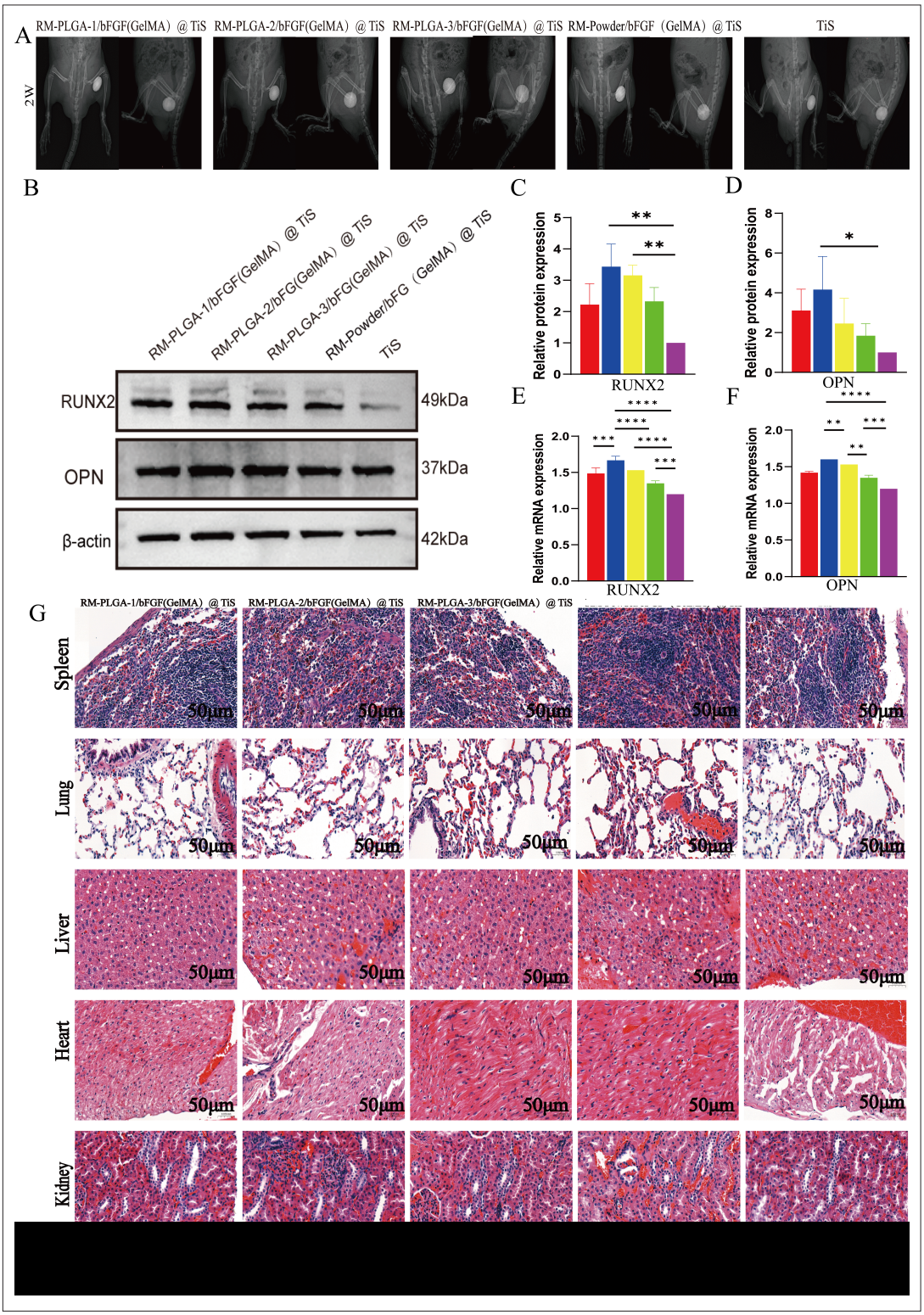

Figure 7. Relevant tests of titanium bone stent implantation in SD rats. (A) X-ray results 2 weeks after surgery. (B–D) Western-blot detection of osteogenesis-related markers (B) and corresponding quantitative analysis of RUNX2 (C) and OPN (D). (E, F) qPCR results of RUNX2 (E) and OPN (F). (G) H&E staining results of the hearts, livers, spleens, lungs, and kidneys of each group of rats. *$p < 0.05$, **$p < 0.01$, ***$p < 0.001$, ****$p < 0.0001$; $n = 3$. Scale bars: 50 μm (G). Abbreviations: PLGA, poly(lactic-co-glycolic acid) copolymer; RM, rifampicin–moxifloxacin; bFGF, basic fibroblast growth factor; GelMA, methylacrylate-modified gelatin.

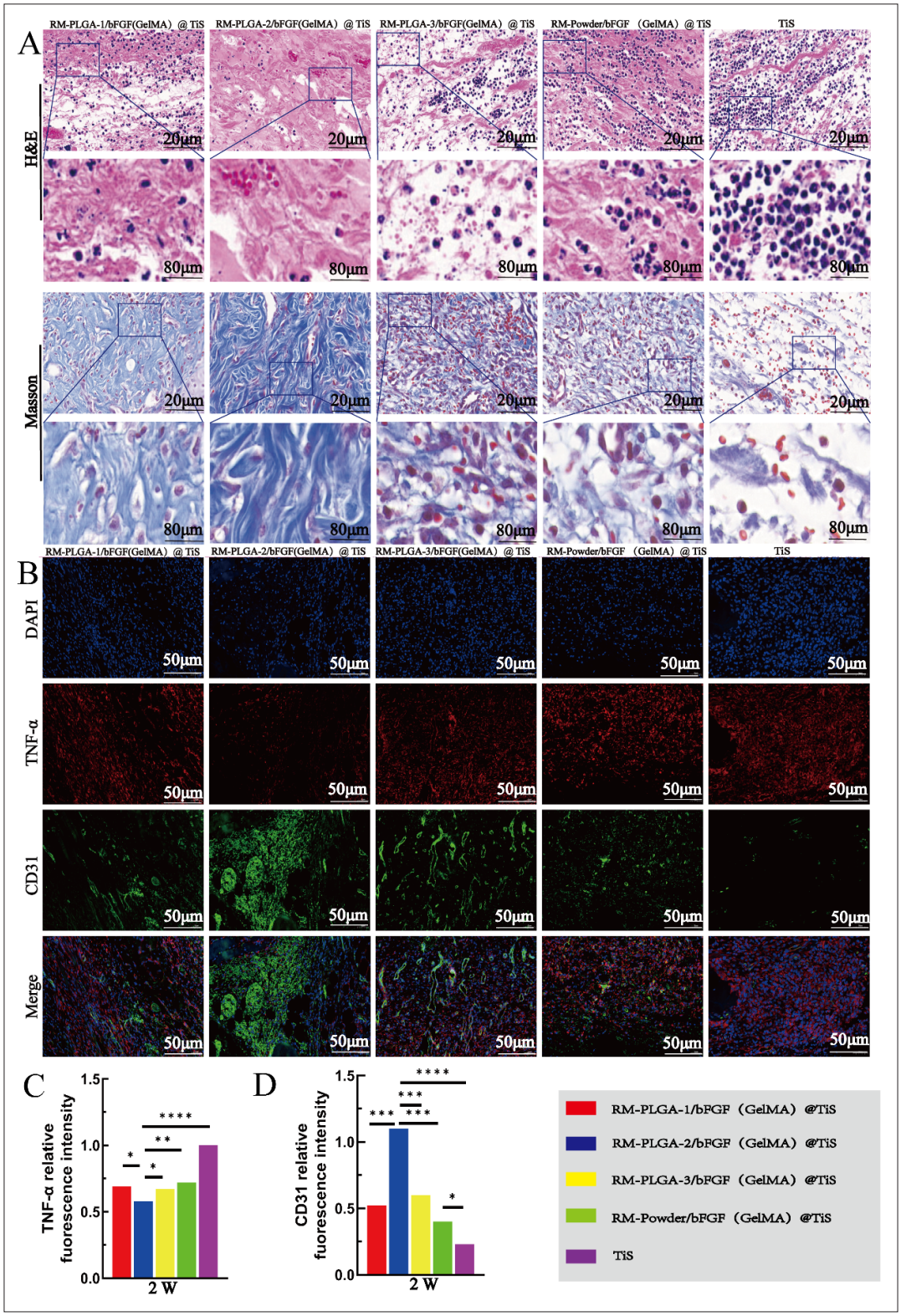

Figure 8. In vivo related detections of the SD rat model. (A) Results of H&E staining and Giemsa staining. (B–D) Immunofluorescence staining (B) and corresponding relative fluorescence intensities of TNF-α (C) and CD31 (D). *$p < 0.05$, **$p < 0.01$, ***$p < 0.001$, ****$p < 0.0001$; $n = 3$. Scale bars: 20 μm (A), 80 μm (A), 50 μm (B). Abbreviations: *PLGA*, poly(lactic-co-glycolic acid) copolymer; RM, rifampicin–moxifloxacin; bFGF, basic fibroblast growth factor; GelMA, methylacrylate-modified gelatin.

4. Discussion

Infection control and defect repair are two major factors in the treatment of IBDs. The development of 3D-printed bone scaffolds capable of sustained and stable release of antibiotics and osteogenic factors is an effective strategy for the treatment of IBDs; the antibiotic loading method and concentration of antibiotics released significantly affect infection control and bone repair effects. Scaffolds with high porosity enable better loading of antibiotics and osteogenic factors. In recent years, many researchers have focused on developing bionic scaffolds with multilayer, graded structures that mimic natural human bone. For instance, Beeren *et al.*[40] developed an extrusion-based functional graded additive manufacturing device and fabricated a novel bone scaffold by combining extrusion-based 3D printing with foam template methods, enabling the creation of specific pore structures. Compared with scaffolds with random pore structures, those with aligned pore architectures have demonstrated higher compression modulus, greater cell infiltration, and better mineralization capacity. An advantage of the SLM method for preparing 3D scaffolds is the precise printing of pore size. Koushik *et al.*[41] suggested that the ideal pore size of osteoblasts should be greater than 100 μm; a pore size of 100–300 μm favors the induction of endochondral ossification; and a pore size greater than 300 μm facilitates waste removal and nutrient supply. The TiSs designed in this study had a pore size of 420–630 μm, which contributed to a larger surface area of newly formed bone within the pores and also supported the localized and controlled release of various bioactive molecules. In this study, the necessity of incorporating bFGF and RM–PLGA into the scaffolds was thoroughly considered.

Basic fibroblast growth factor (bFGF) is a hydrophilic material frequently used in tissue engineering studies related to bone regeneration. Chen *et al.*[42] introduced bFGF into 3D-printed hydrogel scaffolds, thereby enhancing the osteoinductive properties of the hydrogel and validating the potential of bioscaffolds for *in vivo* drug delivery. Additionally, Chen *et al.*[42] demonstrated that Mox, a fourth-generation quinolone, has high bioavailability and cellular penetration in bone, enabling it to enter osteocytes and eliminate latent SA therein. Lin *et al.*[43] found that despite the inability of Rif alone to treat osteomyelitis, its combination with other antibiotics can significantly reduce Rif resistance and enhance the treatment of IBDs. Wang *et al.*[44] confirmed that the synthetic polymers PGA, PLLA, and PLGA possess the advantages of low rejection rate, good biocompatibility, and controllable degradation rate. The hardness of these materials also varies with changes in molecular structure and molecular weight, highlighting the therapeutic potential of these polymers as carriers for sustained antibiotic release. Jackson[45] used PLGA for the encapsulation of vancomycin (Van). This enabled sustained and stable antibiotic release, which provided a more pronounced therapeutic effect compared with the direct use of antibiotic powder. However, repairing the defects after infection control is a major challenge; coating Van with PLGA alone is insufficient to fully address this issue.

In this study, we incorporated an RM–PLGA- and bFGF-loaded hydrogel into TiS for the preparation of a multifunctional composite scaffold capable of the graded release of RM–PLGA microspheres and bFGF, with the aim of promoting bone repair and angiogenesis in the implantation area. We established 10, 20, and 30 mg RM–PLGA microsphere groups to verify the influence of the concentration of antibiotics released on infection control and bone repair effects. An antibiotic powder group was also established to verify the influence of the antibiotic loading method on infection control and bone repair effects. During the first 24 h, no immediate release of bFGF was observed in any of the experimental groups. In subsequent time points, the release rate of bFGF in the powder group was faster than that in the RM–PLGA group. This was considered to be due to the faster release rate of Mox and Rif powders, which indirectly affected the release of bFGF from the voids. RM–PLGA-1/bFGF(GelMA)@TiS had 10mg of RM–PLGA microspheres loaded, providing more gaps for bFGF release, while RM–PLGA-3/bFGF(GelMA)@TiS had 30mg of RM–PLGA microspheres loaded, which slowed down the release rate of bFGF. The release curves of the four groups loaded with bFGF showed that no sudden release of bFGF was observed within the first 24 h. In each subsequent time point, the release rate of bFGF in the RM-powder/bFGF(GelMA)@TiS group was faster than that in the other experimental groups. This was likely due to the faster release rate of Mox and Rif powders, which indirectly affected the release of bFGF from the pores. RM–PLGA-1/bFGF(GelMA)@TiS was loaded with 10 mg RM–PLGA microspheres, providing more pores for bFGF release, while RM–PLGA-3/bFGF(GelMA)@TiS was loaded with 30 mg RM–PLGA microspheres, which slowed down the release rate of bFGF. The effects of the experimental groups with three different amounts of RM–PLGA *in vitro* and *in vivo* were better than those of the powder groups, indicating that sustained and sufficient antibiotic activity is necessary to create an environment conducive to optimal bFGF function. The *in vitro* biocompatibility of the scaffolds was evaluated through experiments that assessed cell adhesion, cell viability, and the cytotoxic and proliferation-promoting effects of the scaffolds. Compared with the blank control group, the four experimental groups with added bFGF displayed a significant increase in cell proliferation, demonstrating

that bFGF effectively induced osteoblast growth. An investigation of the influence on osteogenic differentiation of cells revealed that the four experimental groups with added bFGF exhibited a significant increase in collagen fibers, ALP, and Alizarin Red S staining compared to the blank control group, suggesting that bFGF effectively promoted cell differentiation and tissue mineralization. Measurement of *in vitro* antimicrobial performance indicated that, despite differences in antibiotic release concentrations and antibiotic loading methods, all four experimental groups exhibited obvious bacterial fragmentation and death compared to the blank control group. However, antimicrobial performance during the early stage was not significantly different among the groups. A combined analysis of the *in vivo* antimicrobial performance after modeling and both the *in vitro* and *in vivo* imaging data revealed that antibiotic-loaded PLGA demonstrated stronger antimicrobial effects than the direct use of antibiotic powder when the duration of antimicrobial treatment exceeded seven days. Therefore, for antibiotics loaded onto PLGA, a high concentration does not necessarily lead to better sustained antimicrobial effects. For concentration-dependent antibiotics, antimicrobial activity is closely related to drug concentration, and the peak plasma concentration primarily determines bactericidal effects. However, the maximum bactericidal effect can be achieved once the blood drug concentration exceeds the minimum inhibitory concentration. Further increases in concentration will not significantly enhance the bactericidal effect; instead, excessive antibiotic concentrations may induce local side effects, such as irritation. Results of H&E and Masson's trichrome staining revealed that the RM–PLGA-2/bFGF(GelMA)@TiS group had the lowest neutrophil count and the largest amount of neovasculature and collagen fibers, which may be attributed to the sustained antimicrobial effects of RM–PLGA, thereby providing a favorable environment for bone regeneration and the induction of osteogenesis and angiogenesis by bFGF. The synergistic effects of antibiotics and bFGF further promoted bone repair and angiogenesis.

RUNX2, a key osteogenic factor, is a transcription factor expressed in osteoblasts that is essential for skeletal development. OPN not only promotes osteoblast function and bone mineralization but also plays a crucial role in enhancing bone turnover. We found that the expression of RUNX2 and OPN was upregulated in the RM–PLGA-2/bFGF(GelMA)@TiS group, suggesting that the composite scaffold promoted new bone formation through the regulation of osteogenic factors. qPCR results of the RM–PLGA-2/bFGF(GelMA)@TiS group provided further support for the findings described above. An increase in CD31 immunofluorescence indicates increased formation of new capillaries, while TNF-α expression reflects the severity of inflammation. The RM–PLGA-2/bFGF(GelMA)@TiS group presented significantly higher CD31 expression and significantly lower TNF-α expression compared to the other groups, suggesting that RM–PLGA-2/bFGF(GelMA)@TiS exerted excellent anti-infective and pro-angiogenic effects *in vivo*.

Notably, the surface curvature at any point of a TPMS-structured scaffold is zero. This allows stress to be uniformly distributed, thereby avoiding damage caused by stress concentration.[46] TPMS-structured scaffolds also possess high specific strength and high specific energy absorption; *i.e.*, under conditions of identical weight, they are capable of withstanding greater loads and absorbing more energy. Such scaffolds can thus provide better stress support, which will promote bone regeneration and repair in IBDs. For the RM–PLGA- and bFGF-loaded dual-controlled-release anti-infective bone scaffolds developed in this study, both the *in vivo* and *in vitro* experiments have confirmed that the antibiotic loading method and concentration of antibiotics released significantly influence infection control and bone repair effects. However, further experimental verification is warranted to determine the influence of the graded pore size design on the IBD treatment result.

A key limitation of this study is the lack of a comparative analysis evaluating how different porosity ratios affect the loading efficiency of RM–PLGA and bFGF, particularly in relation to antibacterial activity and bone regeneration. Additionally, the relatively small sample size may limit the generalizability of the findings. Future studies should include larger and more diverse cohorts to validate these results.

5. Conclusion

In this study, we prepared 3D-printed dual-controlled-release composite scaffolds loaded with bFGF and RM–PLGA microspheres for treating IBDs. The composite scaffolds were systematically evaluated *in vitro* for surface morphology, antimicrobial capacity, cytocompatibility, mineralization ability, and osteogenic differentiation potential. Results indicated that RM–PLGA/bFGF(GelMA)@TiS loaded with 20 mg RM–PLGA microspheres exhibited optimal mineralization capability, antimicrobial capacity, and osteogenic activity. The *in vivo* experimental results revealed that RM–PLGA/bFGF(GelMA)@TiS loaded with 20 mg RM–PLGA microspheres effectively inhibited bone infection induced by SA. These findings highlight the immense potential of the composite scaffolds for clinical application in treating IBDs.

Acknowledgments

None.

Funding

This research was supported by the National Natural Science Foundation of China (Grant No. 82460431) and the Ningxia Natural Science Foundation (Grant No. 2023AACO2064).

Conflict of interest

The authors declare that there are no conflicts of interest.

Author contributions

Conceptualization: Peijie Zhao, Zewen Qiao
Formal analysis: Peijie Zhao, Zhipeng Yang,Yaodong Wang
Investigation: Peijie Zhao, Mei Tian, Huan He,Liangguo Si
Methodology: Peijie Zhao, Huanhuan Sun,Xu Ma
Writing–original draft: Peijie Zhao, Zewen Qiao, Huanhuan Sun,Haiqiang Ma
Writing–review & editing: Peijie Zhao, Zewen Qiao, Huanxiang Guan

Ethics approval and consent to participate

The animal ethics committee of Ningxia Medical University approved the experimental procedures involving the Sprague-Dawley rats used in this study. All experimental animals used were obtained from the Laboratory Animal Center of Ningxia Medical University (Approval of Animal Ethical and Welfare No. IACUC-H2025003).

Consent for publication

Not applicable.

Availability of data

Data is available from the corresponding author upon reasonable request.

References

1. Zhang S, Lian Z, Chen X, *et al*. Preparation and properties of chitosan quaternary ammonium salt/α-calcium sulfate hemihydrate/β-tricalcium phosphate composite bone cement. *Colloids Surf B Biointerfaces*. 2025;253:114738. doi: 10.1016/j.colsurfb.2025.114738
2. Zhang P, Liu X, Guo P, *et al*. Effect of cyclic mechanical loading on immunoinflammatory microenvironment in biofabricating hydroxyapatite scaffold for bone regeneration. *Bioact Mater*. 2021;6(10):3097-3108. doi: 10.1016/j.bioactmat.2021.02.024
3. Li J, Jiang B, Yang L, *et al*. Dual-functional titanium implants via polydopamine-mediated lithium and copper co-incorporation: synergistic enhancement of osseointegration and antibacterial efficacy. *Front Bioeng Biotechnol*. 2025;13:1593545. doi: 10.3389/fbioe.2025.1593545
4. Farazin A, Mahjoubi S. Dual-functional hydroxyapatite scaffolds for bone regeneration and precision drug delivery. *J Mech Behav Biomed Mater*. 2024;157:106661. doi: 10.1016/j.jmbbm.2024.106661
5. Buchholz T, Siverino C, Moriarty TF, *et al*. Antibiotic-loaded polymer-calcium phosphate scaffold for treating orthopedic device-related infection in a rabbit segmental bone defect model. *J Biomed Mater Res A*. 2025; 113(5):e.37917. doi: 10.1002/jbm.a.37917
6. Ceccarelli G, Perciballi B, Russo A, *et al*. Chronic suppressive antibiotic treatment for *Staphylococcal* bone and joint implant-related infections. *Antibiotics*. 2023;12(5):937. doi: 10.3390/antibiotics12050937
7. Hu K, Olsen BR. Osteoblast-derived VEGF regulates osteoblast differentiation and bone formation during bone repair. *J Clin Investig*. 2016;126(2):509-526. doi: 10.1172/jci82585
8. Eelen G, Treps L, Li X, Carmeliet P. Basic and therapeutic aspects of angiogenesis updated. *Circ Res*. 2020;127(2):310-329. doi: 10.1161/circresaha.120.316851
9. Chen Z, Yang Y, Liu B, Li X, Tian Y. Application of 3D-printed porous prosthesis for the reconstruction of infectious bone defect with concomitant severe soft tissue lesion: a case series of 13 cases. *BMC Musculoskelet Disord*. 2024;25(1):1090. doi: 10.1186/s12891-024-08248-6
10. Wang J, Liu M, Yang C, *et al*. Photocrosslinked gelatin methacryloyl/hyaluronic acid methacryloyl composite hydrogels loaded with bone morphogenetic protein 2-black phosphorus nanosheets for bone regeneration. *J Biomater Sci Polym Ed*. 2025:1-23. doi: 10.1080/09205063.2025.2489846
11. Pramanik S, Alhomrani M, Alamri AS, *et al*. Unveiling the versatility of gelatin methacryloyl hydrogels: a comprehensive journey into biomedical applications. *Biomed Mater*. 2024;19(4):042008. doi: 10.1088/1748-605x/ad4df7
12. Chu C, Qiu J, Zhao Q, *et al*. Injectable dual drug-loaded thermosensitive liposome-hydrogel composite scaffold for vascularised and innervated bone regeneration. *Colloids Surf B Biointerfaces*. 2024;245:114203. doi: 10.1016/j.colsurfb.2024.114203
13. Seifert LB, Aigner A, Abazi S, *et al*. A 3D printed hydroxyapatite implant for temporal hollowing reconstruction: a patient-

specific approach. *Craniomaxillofac Trauma Reconstr*. 2025;18(2):28.
doi: 10.3390/cmtr18020028

14. Cidonio G, Glinka M, Kim YH, *et al*. Nanoclay-based 3D printed scaffolds promote vascular ingrowth ex vivo and generate bone mineral tissue in vitro and in vivo. *Biofabrication*. 2020;12(3):035010.
doi: 10.1088/1758-5090/ab8753

15. Li J, Yang Y, Sun Z, *et al*. Integrated evaluation of biomechanical and biological properties of the biomimetic structural bone scaffold: biomechanics, simulation analysis, and osteogenesis. *Mater Today Bio*. 2023;24:100934.
doi: 10.1016/j.mtbio.2023.100934

16. Chi G, Ren H, Lin B, Huang K. Subtrochanteric femoral fracture with postoperative chronic osteomyelitis treated successfully by 1-stage operation: a case report. *Ann Transl Med*. 2021;9(6):514.
doi: 10.21037/atm-21-413

17. Graczyk S, Pasławski R, Grzeczka A, *et al*. Antimicrobial and antiproliferative coatings for stents in veterinary medicine—state of the art and perspectives. *Materials*. 2023;16(21):6834.
doi: 10.3390/ma16216834

18. Barua N, Huang L, Li C, *et al*. Comparative study of two-dimensional (2D) vs. three-dimensional (3D) organotypic kertatinocyte-fibroblast skin models for *Staphylococcus aureus* (MRSA) infection. *Int J Mol Sci*. 2021;23(1):299.
doi: 10.3390/ijms23010299

19. Pinho MG, Foster SJ. Cell growth and division of *Staphylococcus aureus*. *Annu Rev Microbiol*. 2024;78(1):293-310.
doi: 10.1146/annurev-micro-041222-125931

20. Zhang H, Wang Y, Qiang H, *et al*. Exploring the frontiers: the potential and challenges of bioactive scaffolds in osteosarcoma treatment and bone regeneration. *Mater Today Bio*. 2024;29:101276.
doi: 10.1016/j.mtbio.2024.101276

21. Hackemann VCJ, Hagel S, Jandt KD, Rödel J, Löffler B, Tuchscherr L. The controversial effect of antibiotics on methicillin-sensitive *S. aureus*: a comparative in vitro study. *Int J Mol Sci*. 2023;24(22):16308.
doi: 10.3390/ijms242216308

22. Ayre WN, Birchall JC, Evans SL, Denyer SP. A novel liposomal drug delivery system for PMMA bone cements. *J Biomed Mater Res B Appl Biomater*. 2015;104(8):1510-1524.
doi: 10.1002/jbm.b.33488

23. Qiao Z, Yuan Z, Zhang W, Wei D, Hu N. Preparation, in vitro release and antibacterial activity evaluation of rifampicin and moxifloxacin-loaded poly(D,L-lactide-co-glycolide) microspheres. *Artif Cells Nanomed Biotechnol*. 2019;47(1):790-798.
doi: 10.1080/21691401.2019.1581792

24. Liang D, Frank S, Schwendeman SP. Aqueous remote loading of model cationic peptides in uncapped poly(lactide-co-glycolide) microspheres for long-term controlled release. *Drug Deliv Transl Res*. 2023;14(3):696-704.
doi: 10.1007/s13346-023-01424-6

25. Li S, Shi X, Xu B, *et al*. In vitro drug release and antibacterial activity evaluation of silk fibroin coated vancomycin hydrochloride loaded poly (lactic-co-glycolic acid) (PLGA) sustained release microspheres. *J Biomater Appl*. 2022;36(9):1676-1688.
doi: 10.1177/08853282211064098

26. Vishwa B, Moin A, Gowda DV, *et al*. Pulmonary targeting of inhalable moxifloxacin microspheres for effective management of tuberculosis. *Pharmaceutics*. 2021;13(1):79.
doi: 10.3390/pharmaceutics13010079

27. Lin Y, Liu L, He J, Shen J, Ren Q. Rapid release of high-valent silver ions from water-soluble porphyrin complexes to enhance the direct killing of methicillin-resistant *Staphylococcus aureus*. *Acta Biomater*. 2024;192:419-430.
doi: 10.1016/j.actbio.2024.12.004

28. Chung JH, Baek N, Lim H, *et al*. Inner surface modification of polyurethane ureteral stents using plasma-enhanced chemical vapor deposition to improve the resistance to encrustation in a pig model. *Investig Clin Urol*. 2023;64(2):175.
doi: 10.4111/icu.20220393

29. Vishwakarma A, Sinha N. Determination of the optimum architecture of additively manufactured magnetic bioactive glass scaffolds for bone tissue engineering and drug-delivery applications. *ACS Appl Bio Mater*. 2024;7(10):6847-6864.
doi: 10.1021/acsabm.4c00995

30. Panagakis P, Zygogiannis K, Fanourgiakis I, Kalatzis D, Stathopoulos K. The role of the periosteum in bone formation from adolescence to old age. *Cureus*. 2025;17(1):e76774.
doi: 10.7759/cureus.76774

31. Fiume E, Tulyaganov DU, Akbarov A, *et al*. Biological evaluation of a new sodium-potassium silico-phosphate glass for bone regeneration: in vitro and in vivo studies. *Materials*. 2021;14(16):4546.
doi: 10.3390/ma14164546

32. Sevinc-Sasmaz C, Erci F, Torlak E, Yöntem M. Characterization of silver nanoparticles synthesized using *Hypericum perforatum* L. and their effects on *Staphylococcus aureus*. *Microsc Res Tech*. 2025;88(8):2321-2332.
doi: 10.1002/jemt.24862

33. Wang Y, Hu Y, Pan K, *et al*. In-vivo imaging revealed antigen-directed gingival B10 infiltration in experimental periodontitis. *Biochim Biophys Acta Mol Basis Dis*. 2020;1867(1):165991.
doi: 10.1016/j.bbadis.2020.165991

34. DeMourdant T, Rajkovic CJ, Tracz JA, *et al*. A novel rodent model of chronic spinal implant-associated infection. *Spine J*. 2023;23(9):1389-1399.

doi: 10.1016/j.spinee.2023.05.014

35. Subramanian AK, Sreenivasagan S, Mohanraj KG, Kumar RS. Assessment of toxicity of green synthesized silver nanoparticle-coated titanium mini-implants with uncoated mini-implants: comparison in an animal model study. *J Contemp Dent Pract*. 2024;24(12):944-950. doi: 10.5005/jp-journals-10024-3577

36. Sifi A, Adi-Bessalem S, Laraba-Djebari F. Role of angiotensin II and angiotensin type-1 receptor in scorpion venom-induced cardiac and aortic tissue inflammation. *Exp Mol Pathol*. 2016;102(1):32-40. doi: 10.1016/j.yexmp.2016.11.006

37. Yamamoto J, Deguchi H, Sumiyoshi T, *et al*. Accumulation and phagocytosis of fluorescently visualized macrophages against *Edwardsiella piscicida* infection in established mpeg1.1-transgenic Japanese Medaka *Oryzias latipes*. *Mar Biotechnol*. 2024;26(4):658-671. doi: 10.1007/s10126-024-10333-9

38. Ratnaningtyas NI, Husen F. Therapeutic potential of *Coprinus comatus* nanogels: antiarthritic and anti-inflammatory effects in rheumatoid arthritis models. *Vet World*. 2025;18(13):582-597. doi: 10.14202/vetworld.2025.582-597

39. Correia MR, Han SW, Escalante T, Moreira V. The role of the cyclooxygenase-2 pathway in tissue ischemia and revascularization following skeletal muscle injury induced by bothropic snake venom. *Microvasc Res*. 2024; 157:104760. doi: 10.1016/j.mvr.2024.104760

40. Beeren IAO, Dijkstra PJ, Lourenço AFH, *et al*. Installation of click-type functional groups enable the creation of an additive manufactured construct for the osteochondral interface. *Biofabrication*. 2022;15(1):014106. doi: 10.1088/1758-5090/aca3d4

41. Koushik TM, Miller CM, Antunes E. Graded hydroxyapatite triply periodic minimal surface structures for bone tissue engineering applications. *Adv Healthc Mater*. 2025:e2402953. doi: 10.1002/adhm.202402953

42. Chen XJ, Wu X, Lin HH, Liu ZX, Liu S. Effects of methacrylic anhydride gelatin hydrogel loaded with silver and recombinant human basic fibroblast growth factor on deep partial-thickness burn wounds in rabbits. *Zhonghua Shao Shang Yu Chuang Mian Xiu Fu Za Zhi*. 2022;38(7):640-649. doi: 10.3760/cma.j.cn501120-20210726-00260

43. Lin H, Gao Z, Shan T, *et al*. A review on the promising antibacterial agents in bone cement–from past to current insights. *J Orthop Surg Res*. 2024;19(1):673. doi: 10.1186/s13018-024-05143-7

44. Wang L, Wang P, Liu Y, *et al*. The effect of different factors on poly(lactic-co-glycolic acid) nanoparticle properties and drug release behaviors when co-loaded with hydrophilic and hydrophobic drugs. *Polymers*. 2024;16(7):865. doi: 10.3390/polym16070865

45. Jackson J. Triple encapsulation and controlled release of vancomycin, rifampicin and silver from poly (methyl methacrylate) or poly (lactic-co-glycolic acid) nanofibers. *Bioengineering*. 2024;11(6):529. doi: 10.3390/bioengineering11060529

46. Li Y, Xu W, Su Q, Wang Q. Microstructure and properties of TI–AL coating on titanium alloy surface assisted by electromagnetic field. *ACS Omega*. 2024;9(46):46176-46191. doi: 10.1021/acsomega.4c06757

ACCSCIENCE PUBLISHING

International Journal of Bioprinting

RESEARCH ARTICLE

Optimal structural characteristics of bone tissue engineering scaffolds from bionics and PSO-BP-NSGA III integrated algorithm

Yuxi Liu[1,2†*], Aihua Li[3†], Hong Sun[1], Shuge Li[1], and Song Chen[4]

[1] School of Smart Health, Chongqing Polytechnic University of Electronic Technology, Chongqing, China

[2] College of Mechanical and Vehicle Engineering, Chongqing University, Chongqing, China

[3] Department of Gastroenterology, Chongqing University Cancer Hospital, School of Medicine, Chongqing University, Chongqing 400030, China

[4] College of Mechanical Engineering, Chongqing University of Technology, Chongqing, China

Abstract

The repair of large segmental bone defects has always been a significant challenge in clinical practice, with stress shielding being one of the key issues. Here, tree-like fractal biomimetic scaffolds were created based on the morphological similarity between natural trees and bone trabeculae. To optimize the balance between high yield strength and low elastic modulus of the scaffold, an integrated particle swarm optimization-backpropagation-non-dominated sorting genetic algorithm III (PSO-BP-NSGA III) was employed. The scaffolds were fabricated using selective laser melting three-dimensional printing with Ti6Al4V, and their mechanical performance was experimentally evaluated and compared with the algorithm's predictions. The tree-like fractal scaffold exhibited a radial gradient in porosity, similar to that of natural bone. The second-order fractal scaffold achieved an effective synergy between yield strength and Young's modulus, demonstrating high yield strength and low Young's modulus. Additionally, it showed a favorable fluid flow gradient and permeability, with a comprehensive permeability of 3.13×10^{-8} m^2. The relative errors between the test and predicted values of yield strength and Young's modulus were 0.83% and 7.93% respectively, indicating that the PSO-BP-NSGA III integrated algorithm has good predictive ability. These findings establish a validated bionic design framework that integrates advanced optimization algorithms to guide the development of bone tissue engineering scaffolds.

***Keywords*:** Integrated algorithm; Multi-objective optimization; Stress shielding; Tree-like fractal scaffold; Young's modulus

†These authors contributed equally to this work.

***Corresponding author:**
Yuxi Liu (liuyuxi@cqcet.edu.cn)

Citation: Liu Y, Li A, Sun H, Li S, Chen S. Optimal structural characteristics of bone tissue engineering scaffolds from bionics and PSO-BP-NSGA III integrated algorithm. *Int J Bioprint*. 2025;11(6):451-471. doi: 10.36922/IJB025380381

Received: September 15, 2025
Revised: October 19, 2025
Accepted: October 25, 2025
Published Online: October 27, 2025

Copyright: © 2025 Author(s). This is an Open Access article distributed under the terms of the Creative Commons Attribution License, permitting distribution, and reproduction in any medium, provided the original work is properly cited.

Publisher's Note: AccScience Publishing remains neutral with regard to jurisdictional claims in published maps and institutional affiliations.

1. Introduction

Large segmental bone defects have long been a significant challenge in clinical practice,[1] often leading to complications such as nonunion and implant failure.[2] Stress shielding is one of the primary reasons for the failure of bone implants, usually due to the implant's stiffness exceeding that of the adjacent bone, leading to bone resorption around the

prosthesis.[3,4] According to clinical research, more than 15% of patients require revision surgery after total hip replacement, of which approximately 33% are directly related to implant loosening caused by stress shielding.[5] To address this challenge, there is an urgent need to conduct in-depth research on the balance between the structure, function, and mechanical properties of bone implants.

In recent years, as the core carrier of bone tissue engineering, the design and optimization of porous bone scaffolds have mainly focused on mechanical properties, biological activity, and manufacturing accuracy.[6] In terms of biomimetic structural innovation, the three-period minimal surface (TPMS) has emerged as a research hotspot due to its continuous curvature, high specific surface area, and bone trabecular-like characteristics.[7,8] For example, the I-WP type TPMS scaffold can achieve a gradient distribution of porosity ranging from 68.01% to 96.48%.[9] The Voronoi structure scaffold has a wall shear stress ratio of 34.68%, which is closer to the fluid environment of natural bone trabeculae.[10] The application of multi-objective optimization algorithms has promoted the precise regulation of scaffold performance.[11,12] The application of machine learning (ML) and genetic algorithms can effectively improve the reverse design accuracy of porous scaffolds.[13] In addition, the innovative application of ML and optimization algorithms in bone tissue helps to enhance the osteoinductive capacity of scaffolds,[14] optimize the mechanobiological properties of scaffolds,[15] and achieve a leap from limited results to infinite theoretical results.[16] The breakthrough of additive manufacturing (AM) technology has provided the possibility for the realization of complex structures.[17] New-type scaffolds based on AM can meet the mechanical requirements of cancellous bone,[18] enhance compressive strength[19] and biomineralization ability,[20] and guide the transformation of the immune microenvironment toward promoting bone regeneration.[21] Furthermore, the radial gradient porosity prepared via three-dimensional (3D) printing closely resembles the hierarchical structure of human bones.[22]

The material and mechanical properties of porous scaffolds are key factors that determine their clinical effectiveness and directly affect stability and regeneration efficiency.[23] With the popularization of 3D printing technology and breakthroughs in materials science, the mechanical design of porous scaffolds has evolved from a single "modulus matching" to "structure–function collaborative optimization."[24] TPMS magnesium alloy scaffolds help to enhance early cell adhesion and proliferation capabilities,[25] and the Si–OH groups in Ti_3SiC_2 ceramic scaffolds are beneficial for promoting the mineralization rate of apatite.[26] The structural optimization of bone scaffolds can effectively reduce the risk of stress shielding and improve the permeability of the scaffold,[27] and the porosity and specific surface area of the scaffold directly affect the ability of bone regeneration.[28] The strut-type bionic scaffold with a negative Poisson's ratio is also an effective means of reducing the stress-shielding effect of implants.[29] Permeability refers to the ability of fluid to transmit within porous media, which is a core performance index of bone scaffolds. It directly affects nutrient diffusion and vascular network formation, thereby determining the efficiency of bone regeneration.[30] There is an inherent contradiction between the high permeability and mechanical strength of porous scaffolds: increasing porosity enhances permeability but reduces scaffold strength.[31] Therefore, while improving the permeability of the scaffold, its mechanical strength must also be taken into account. In existing studies, the primary methods to enhance permeability include the optimal design of porous scaffold structures[32–34] and the development of novel porous materials.[35]

Reducing the stiffness of porous bone implants while maintaining sufficient strength to withstand loads during daily activities is a key challenge in their design. Currently, research on bone implants mainly attempts to reduce stress shielding through methods such as pore optimization,[8,18] material development,[25,26] and structural bionics,[13,27] but the effects are limited. Moreover, research on the synergy between the structure, function, and mechanical properties of porous scaffolds is severely insufficient. Based on this, this study aims to reduce stress shielding in porous scaffolds and achieve a balance between their structure, modulus, and strength. A combined approach of computer-integrated algorithms, mechanical experiments, finite element (FE) calculations, and computational fluid dynamics (CFD) simulation calculations was adopted to perform multi-objective optimization on the structural parameters of tree-like fractal scaffolds. Firstly, based on the morphological similarity between natural trees and bone trabeculae, biomimetic design of tree-like fractal scaffolds and theoretical analysis were completed. Secondly, through 3D printing preparation, mechanical testing, FE analysis, and CFD permeability simulation, a fractal structure model with excellent mechanical properties and permeability was determined, and the feasibility and accuracy of the FE calculation were verified. Then, through orthogonal design and FE calculation, a dataset for multi-objective optimization calculation was obtained. The integrated particle swarm optimization-backpropagation-non-dominated sorting genetic algorithm III (PSO-BP-NSGA III) algorithm was used to complete the multi-objective optimization of the tree-like fractal scaffold, and the Pareto optimal solution set was obtained. Finally,

the scaffold structure parameters corresponding to the optimal solution were selected, and the porous scaffold was prepared and mechanically tested. The feasibility and correlation of the multi-objective optimization algorithm were verified by comparing the obtained results. This research provides theoretical and practical guidance for the structure design optimization and stress shielding reduction of novel porous bone scaffolds.

2. Materials and methods

The study's workflow is illustrated in Figure 1.

2.1. Design and analysis of the tree-like fractal scaffold

In response to the personalized needs of porous bone scaffolds for the repair of large segmental bone defects in clinical practice, this study focuses on the structural design and characteristic optimization of tree-like fractal biomimetic bone scaffolds. The goal is for their structure and performance to be optimized to closely resemble those of natural bone, while minimizing stress shielding. A systematic study was conducted on the synergistic effects among their structure, function, and mechanical properties.

The schematic diagram of the design process for the bionic scaffold with a radial gradient tree-like fractal structure is shown in Figure 2. The human bone has a radially gradient porous structure (Figure 2A).[36] The inner part is cancellous bone with high porosity (50–90%) to reduce weight and facilitate nutrient transport, while the outer part is cortical bone with low porosity, which can bear loads.[37] Based on the similarity between the branching structure of natural trees and the morphology of bone trabeculae,[38] four different tree-like fractal curves were designed, respectively, as shown in Figure 2B. By enabling tree-like fractal structures to grow radially and to array circumferentially, a porous structure with radial porosity gradients was designed (Figure 2C). Clinically, according to the specific bone defect site of the patient and the corresponding porosity distribution, a unique porous scaffold can be designed by optimizing the fractal curves. Firstly, according to the size of the bone defect site, the outer diameter D, inner diameter d, and height H of the implant (Figure 2D) were determined. Secondly, based on the radial distribution of porosity at the site of the bone defect, fractal curves were designed and fractal parameters were determined to complete the structural design of a concentric ring-shaped bone matrix (Figure 2E) and a radial tree-like trabecular network (Figure 2F). Then, the bone matrix and trabecular layers were alternately stacked along the axial direction to form a porous scaffold (Figure 2G). The axial structure of the second-order fractal biomimetic bone scaffold is shown in Figure 2H. Finally, a crisscross structure was used to connect and fix the bone matrix and trabecular layers (Figure 2I). To calculate the radial distribution of porosity of the scaffolds, the biomimetic scaffold was divided into regions a, b, c, d,

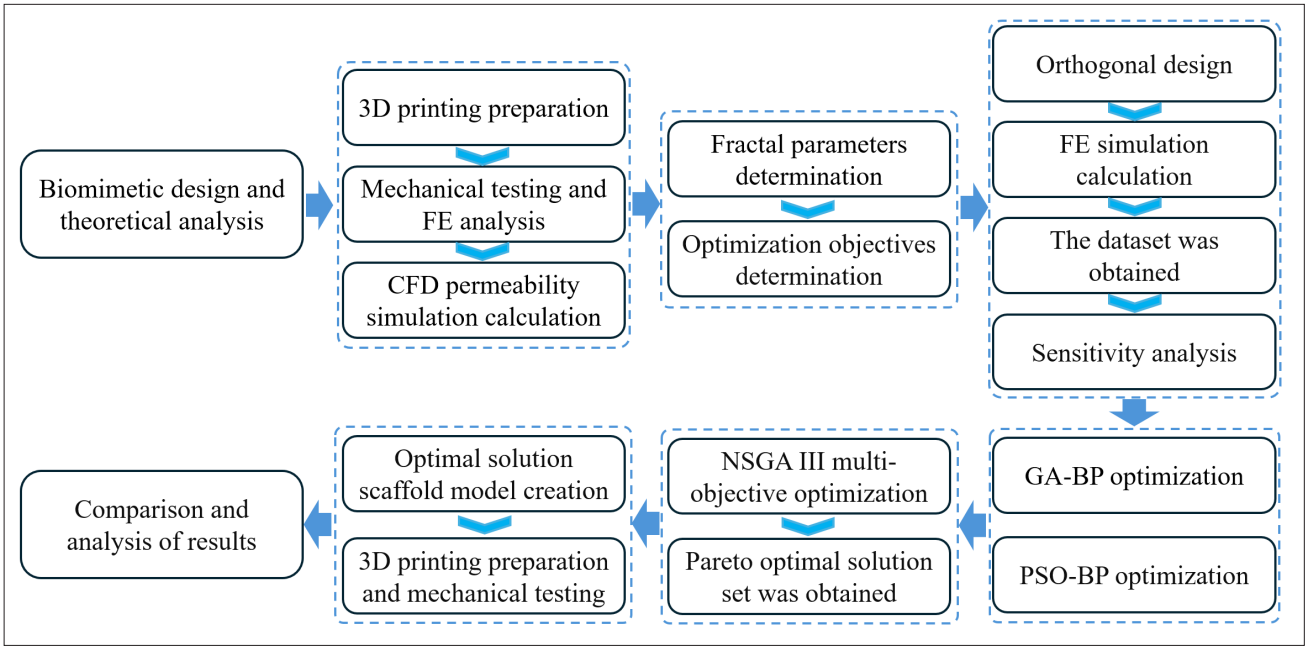

Figure 1. Workflow diagram. Abbreviations: 3D, three-dimensional; BP, backpropagation; CFD, computed fluid dynamics; FE, finite element; GA, genetic algorithm; NS, non-dominated sorting; PSO, particle swarm optimization.

and e along the radial direction with the centers of adjacent concentric rings as boundaries (Figure 2J).

The fractal parameters directly determine the pore size and the distribution of porosity in the tree-like fractal scaffold. The theoretical porosity calculation for the tree-like fractal scaffold was established in this study. The length ratio γ and diameter ratio μ of the j-th and (j-1)-th order trabeculae were calculated using **Equation (1)**:

$$\gamma = \frac{l_j}{l_{j-1}}, \mu = \frac{d_j}{d_{j-1}}, j = 1,2,3,\cdots,n \quad (1)$$

where N is the order of the tree-like fractal bone trabeculae; l_j and l_{j-1} are the lengths of the j-th and (j-1)-th order bone trabeculae, and d_j and d_{j-1} are their corresponding diameters.

The volume V_m of concentric ring bone matrix was calculated using **Equation (2)**:

$$V_m = \sum_{i=1}^{N} V_{mi} = \sum_{i=1}^{N} 2\pi R_i \cdot r_i^2, i = 1, 2, 3, ..., N \quad (2)$$

where R_i is the distance from the center line of the i-th bone matrix ring (counting from the inside to the outside)

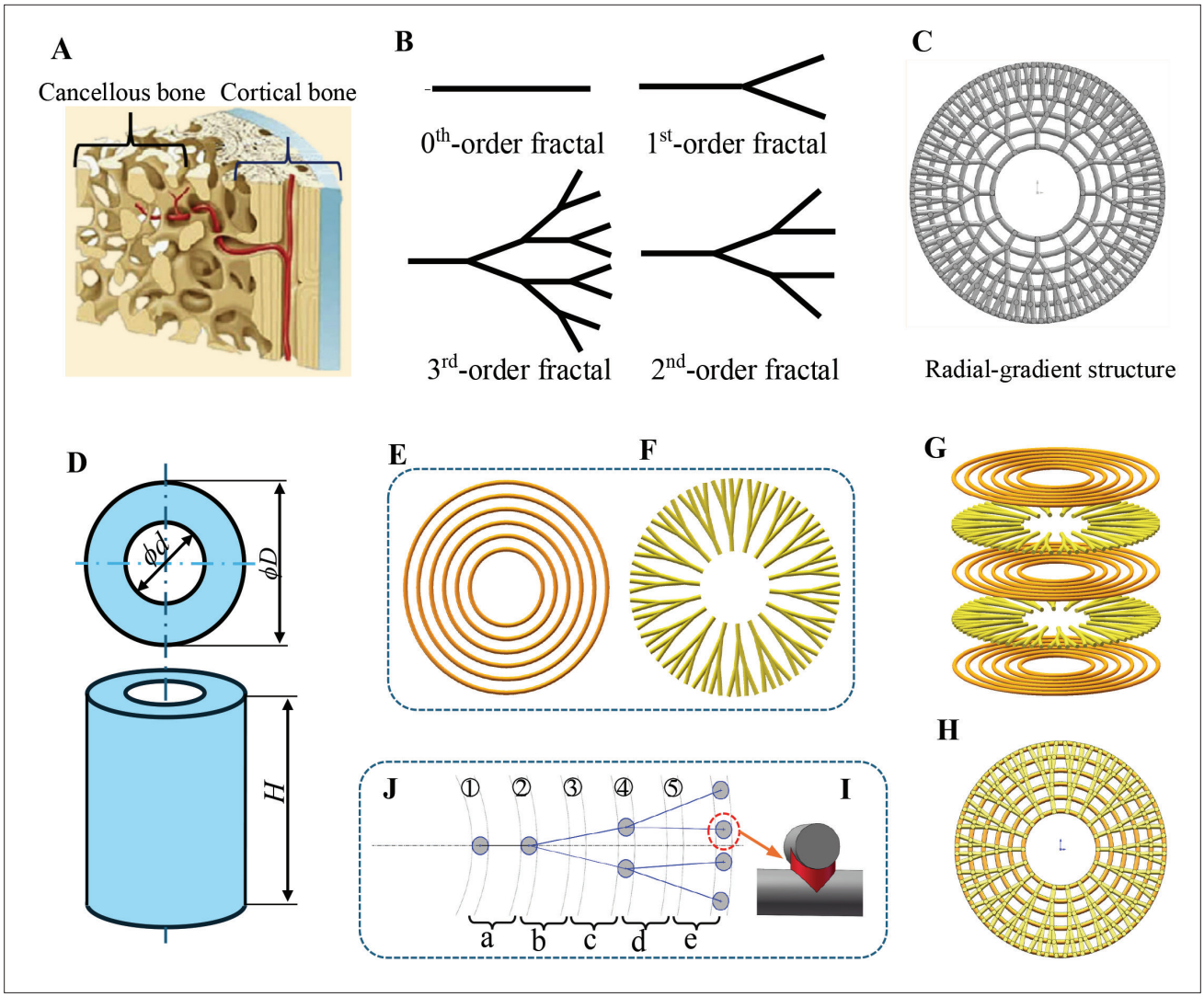

Figure 2. Schematic illustrations for designing tree-like fractal scaffolds. (A) Microstructure of human bone, (B) tree-like fractal curves with 0th-order, 1st-order, 2nd-order, and 3rd-order fractal, (C) radial-gradient structure from cancellous bone to cortical bone, (D) the geometric dimensions of the bone scaffold, (E) concentric ring-shaped bone matrix layer, (F) radial bone trabecular layer, (G) the bottom-up stacking of bone matrix layer and bone trabecular layer, (H) axial view of biomimetic scaffold, (I) 2nd-order tree like fractal structure and radial region division, and (J) the crisscross connection structure between bone matrix and trabeculae.

to the center of the bionic bone, and r_i is the radius of the i-th bone matrix ring.

The calculation for the volume V_{bc} of a bone trabecular network with a circular cross-section is as follows in **Equation (3)**:

$$V_{bc} = \sum_{j=0}^{n} V_{jbc} = \sum_{j=0}^{n} m_j \pi \left(\frac{d_j}{2}\right)^2 l_j = \frac{\pi}{4} d_0^2 l_0 \frac{1-(m\gamma\mu)^{n+1}}{1-m\gamma\mu} \quad (3)$$

where, m_j, d_j, and l_j are the number of bifurcations, diameter, and length of the j-th order trabecular, respectively.

The overall porosity k of the biomimetic scaffold can be determined using **Equations (2)** and **(3)**. The calculation is as follows in **Equation (4)**:

$$k = 1 - NV_{bc} - V_m \quad (4)$$

where k is the porosity of the scaffold.

2.2. Optimization problem

The stress-shielding effect is a key challenge for bone implants. Traditional dense metal implants have an elastic modulus significantly higher than that of natural bone tissue, leading to excessive physiological load on the prosthesis and complications such as bone resorption and prosthesis loosening. Natural bone tissue exhibits high strength and low modulus.[2,39] Therefore, maintaining sufficient strength to withstand loads during daily activities while reducing the modulus of bone implants is a key issue in the design of porous bone scaffolds. Based on this, this study aims to reduce stress shielding in porous scaffolds and achieve a synergy between their modulus and strength. The optimization goal is to minimize the effective Young's modulus and maximize the yield strength of porous scaffolds, and to conduct multi-objective optimization of the structural dimensions of a tree-like fractal bionic scaffold. Firstly, using the biomimetic scaffold design process (Figure 2), feasible design spaces were extracted based on the defect-site structure and biological constraints, and porous scaffolds with different fractal parameters were then designed. The scaffolds were fabricated using the selective laser melting (SLM) process, and their mechanical and biological properties were analyzed. Secondly, the fractal structure with favorable mechanical and biological properties was selected as the research object, and the porous scaffolds with different geometric parameters were created. Then, based on FE mechanics calculations, the effective Young's modulus (E_e) and yield strength (Y_s) of the porous scaffold were obtained, and a dataset was obtained. The optimal design set was selected from the target space according to the multi-objective optimization results. Finally, based on the tree-like fractal scaffold obtained through the multi-objective optimization, the correlation of the multi-objective optimization design was verified through experimental testing. In this article, E_e is referred to as the "effective Young's modulus" or "Young's modulus" of the scaffold, which can be used interchangeably with "stiffness."

The definition of the problem of minimizing the effective Young's modulus and maximizing the yield strength of porous bone scaffolds with predefined fractal parameters is shown in **Equation (5)**.

$$\begin{aligned} &\text{Maximize:} \quad E_e \\ &\text{Minimize:} \quad Y_e \\ &\text{Subject to:} \\ &\qquad \theta: \ [20^\circ, 30^\circ] \\ &\qquad d_h: \ [0.3, 0.7] \\ &\qquad N: \ [3, \ 6] \\ &\qquad d_j: \ [0.3, 0.7] \end{aligned} \quad (5)$$

where θ is the fractal angle of the tree-like fractal structure; d_h is the diameter of the annular bone matrix in mm; N is the number of concentric rings of the annular bone matrix; and d_j is the diameter of radial bone trabeculae in mm.

2.3. Optimization methods

2.3.1. Orthogonal design and sensitivity calculation

The orthogonal test method is a statistical method that scientifically arranges multi-factor experiments through orthogonal arrays. It enables efficient analysis of multiple factors and multiple levels with a small number of representative experiments, and its core advantage lies in significantly reducing the number of experiments through a test design characterized by "uniform dispersion and neat comparability."[40] To avoid difficulties in fitting caused by differences in the dimensions of dependent variables, all data must undergo normalization processing, and the formula is show in **Equation (6)**:

$$X_i = -1 + 2 \times \frac{x_i - x_{min}}{x_{max} - x_{min}} \quad (6)$$

where X_i is the normalized index value of the i-th test, x_i is the index value of test i, and x_{max} and x_{min} are the maximum and minimum index values among all tests in the orthogonal array, respectively.

Based on the design process of the tree-like fractal scaffold and the experimental analysis of its mechanical properties, the specific structural parameters of the porous bone scaffold to be optimized were determined.

Orthogonal design experiments were conducted using four parameters: fractal angle θ, diameter of the annular bone matrix ring d_h, number of concentric bone matrix rings m, and radial trabecular diameter d_j. Three levels were determined for each factor, as shown in Table 1.

To reduce the number of experiments and computational complexity, an L9(4^3) orthogonal table was established based on the four-factor, three-level design requirements using the orthogonal experimental design method. A total of nine experiments were conducted.[41] Then, based on the nine different structural parameters listed in the orthogonal table, corresponding porous scaffold models with tree-like fractal structures were established.

To compare and analyze the influence of structural parameters of tree-like fractal porous scaffolds on optimization objectives, the response values of each experiment were obtained based on the porous scaffold model. Using the variance-based sensitivity analysis method, the sensitivity index for each design variable to the response was measured. The calculation method for the sensitivity of the i-th optimization variable to the j-th optimization objective, denoted as $S_j(X_i)$, is shown in **Equation (7)**[42]:

$$S_j(X_i) = \frac{V[E(Y_j/X_i)]}{V(Y_j)} \tag{7}$$

where Y_j is the j-th optimization objective, X_i is the i-th optimization parameter, $E(Y_j/X_i)$ is the average value of Y_j when X_i is fixed, $V[E(Y_j/X_i)]$ is the variance of $E(Y_j/X_i)$, and $V(Y_j)$ is the variance of the Y_j.

2.3.2. Multi-objective optimization algorithm

Based on the structural parameters of the porous tree-like fractal scaffold obtained by the orthogonal experimental design method, the corresponding porous scaffold models were established, and a dataset for multi-objective optimization calculation was obtained through FE simulation calculation. Then, the PSO-BP-NSGAIII integrated algorithm was used to optimize the optimal eigenvalue parameters of the tree-like fractal scaffold. Specifically, the GA and PSO algorithms were adopted to optimize the weights and thresholds of the BP neural network, and the NSGA III was employed to perform multi-objective optimization on the optimal structural eigenvalues of the tree-like fractal porous scaffold.

The BP neural network is a multi-layer feedforward network trained by the error BP algorithm.[43] The main approach of the GA optimization is to perform crossover and mutation on thresholds and weights, followed by fitness calculation and selection of optimal ones. Since the initial weights and thresholds of the BP neural network are random arrays, they affect the prediction correlation of the entire network. Thus, its weight and threshold must be optimized. The GA was utilized to optimize the BP neural network, and the Levenberg–Marquardt algorithm was employed for local optimization to obtain the global optimal solution.[44] PSO is a method for searching for optimal solutions. The initial weights and thresholds of the BP neural network were defined as particles in the particle swarm, and all particles form a group. The basic idea of the PSO algorithm is to find the optimal solution through cooperation and information sharing among individuals in the group.[45]

The calculations of particle velocity and position are shown in **Equations (8)** and **(9)**:

$$V_{i(n+1)} = \omega V_{i(n)} + C_1 * rand * (gbest - X_{i(n)}) + C_2 * rand * (zbest - X_{i(n)}) \tag{8}$$

where $V_{i(n+1)}$ is the velocity of the i-th particle in the $(n+1)$-th iteration; C_1 is the global learning factor; C_2 is the individual learning factor; ω is the iteration weight; *rand* is a random number of [0,1]; *gbest* is the globally optimal X value, and *zbest* is the individually optimal X value.

$$X_{i(n+1)} = X_{i(n)} + V_{i(n+1)} \tag{9}$$

where $X_{i(n+1)}$ represents the specific position of the i-th particle in the $(n+1)$-th iteration.

Table 1. Levels of factors used in the orthogonal design experiments

Factors \ Levels	Level 1	Level 2	Level 3
Fractal angle θ (°)	20	25	30
Diameter of the annular bone matrix d_h (mm)	0.4	0.5	0.6
Number of concentric rings of bone matrix N	4	5	6
Radial trabecular diameter d_j (mm)	0.4	0.5	0.6

The NSGA-III can perform multi-objective fitness comparisons, which distinguishes it from the GA. NSGA III replaces congestion calculation with the reference point method for optimization based on the NSGA II algorithm, avoiding getting stuck in local optima.[46] Therefore, the NSGA III algorithm was applied to the multi-objective optimization in this study.

2.4. Finite element analysis for scaffold Young's modulus

The effective Young's modulus of the porous scaffold was calculated using the Abaqus software (version 2021, Dassault Corp., USA), and its boundary conditions are shown in Figure 3. Both the upper and lower steel plates were treated as rigid bodies; the lower plate was fixed. The compressive strain was sufficiently small to ensure that the stress and strain of the entire scaffold remain within the elastic region. The upper steel plate was uniformly loaded along the Z-axis at a speed of 0.5 mm/min, with a loading displacement of 5% of the specimen height, which is consistent with the compression test. Friction hard contact was used between the porous scaffold and the rigid plate, and the penalty coefficient was set to 0.2.[24] Due to the central-axis symmetry of the porous bone scaffold, 1/4 of the model was used for the compression analysis. The mesh type adopted was quadratic tetrahedral elements of type C3D10. Through mesh independence calculation and size optimization, the final mesh size was determined to be 0.07 mm. In this FE analysis, the bone scaffold material was Ti6Al4V. Its material parameters were as follows: elastic modulus of 113.8 GPa, Poisson's ratio of 0.32, density of 4430 kg/m^3, and yield strength of 970 MPa.[47] The material parameters of the upper and lower steel plates were: Poisson's ratio of 0.29, elastic modulus of 193 GPa, and a density of 7930 kg/m^3.

According to the FE method, the reaction force was calculated and converted into stress. The effective Young's modulus calculation formula for the scaffold is as follows in **Equation (10)** [24]:

$$Ee = \frac{RF/A_{\text{ave}}}{\varepsilon} = \frac{RF/[(1-k)A_{\text{c}}]}{\Delta L/L_0} \quad (10)$$

where A_{ave} is the average cross-sectional area of the scaffold perpendicular to the compression direction, A_c is the total cross-sectional area perpendicular to the compression direction (excluding pores), ε_0 is the compressive strain, k is the porosity of the scaffold, and ΔL and L_0 are the length change and initial length of the scaffold in the compression direction, respectively.

2.5. Computed fluid dynamics analysis for scaffold permeability

In addition to bearing loads, the porous structure of bone scaffolds plays an essential role in nutrient transport in damaged areas. To evaluate the mass-diffusion capacity of the scaffold, permeability is defined as an intrinsic property of the scaffold that determines the liquid flow rate through it. In this study, the permeability of porous scaffolds was calculated using CFD software (version 2022 R1, ANSYS, USA). Due to the symmetrical structure of the porous scaffold, a 1/4 model of the scaffold was selected for simulation calculation. The CFD simulation model and boundary conditions for the tree-like fractal scaffold are shown in Figure 4. To ensure consistency with the actual service conditions, the parameters of human body fluids were used to simulate the real surrounding flow environment of the porous scaffold in the human body.[36] The specific fluid parameters were as follows: viscosity in

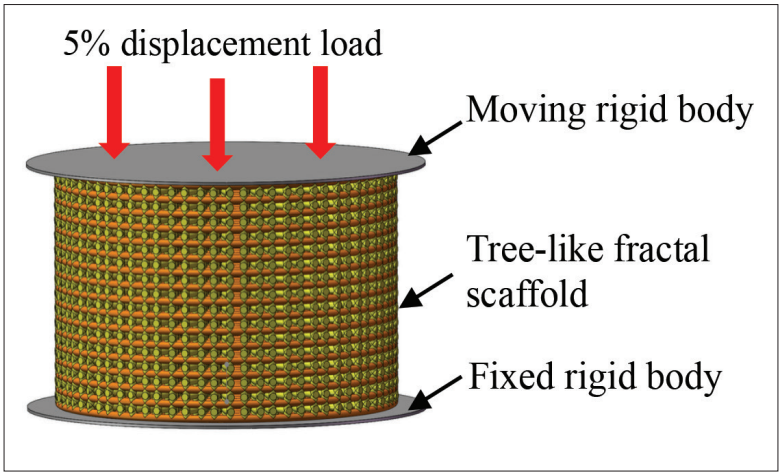

Figure 3. Schematic diagram of finite element compression calculation.

the fluid region μ = 0.0035 Pa·s, inlet flow velocity v_i = 0.01 m/s, outlet pressure P_{outer} = 0 Pa, and no sliding on the support wall. By simulating the steady-state fluid flow inside the scaffold, the pressure drop ΔP between the inlet and outlet of the scaffold was calculated using **Equation (11)**, and the permeability was calculated using Darcy's law (**Equation [12]**)[47]:

$$\Delta P = P_{inner} - P_{outer} \quad (11)$$

$$k = \frac{\mu \cdot v_i \cdot L}{\Delta P} \quad (12)$$

where k is the permeability of the scaffold (m^2), μ is the viscosity of human body fluids (Pa·s), v_i is the inlet velocity of the fluid (m/s), L is the characteristic length of the fluid model in the direction of fluid flow (m), ΔP is pressure difference, and P_{inner} and P_{outer} are the pressures at the inlet and outlet of the scaffold (Pa), respectively (Figure 4).

2.6. Fabrication of biomimetic scaffolds

Ti6Al4V exhibits excellent biocompatibility and is widely used in bone implants.[47,48] Therefore, Ti6Al4V was selected for the preparation of tree-like fractal porous scaffolds. The Ti6Al4V metal powder is spherical in morphology, with a particle size of 15–45 μm and a Hall flowability of 45S. The scaffolds were fabricated using the 3D printing equipment BLT-S210 (Xi'an Bright Laser Technologies, China). Computer-aided design models of the porous scaffolds were modeled in SolidWorks 2023 and then converted to STL file format. The main process parameters for SLM 3D printing were a laser power of 120 W, a hatch spacing of 70 μm, a layer thickness of 30 μm, a scan speed

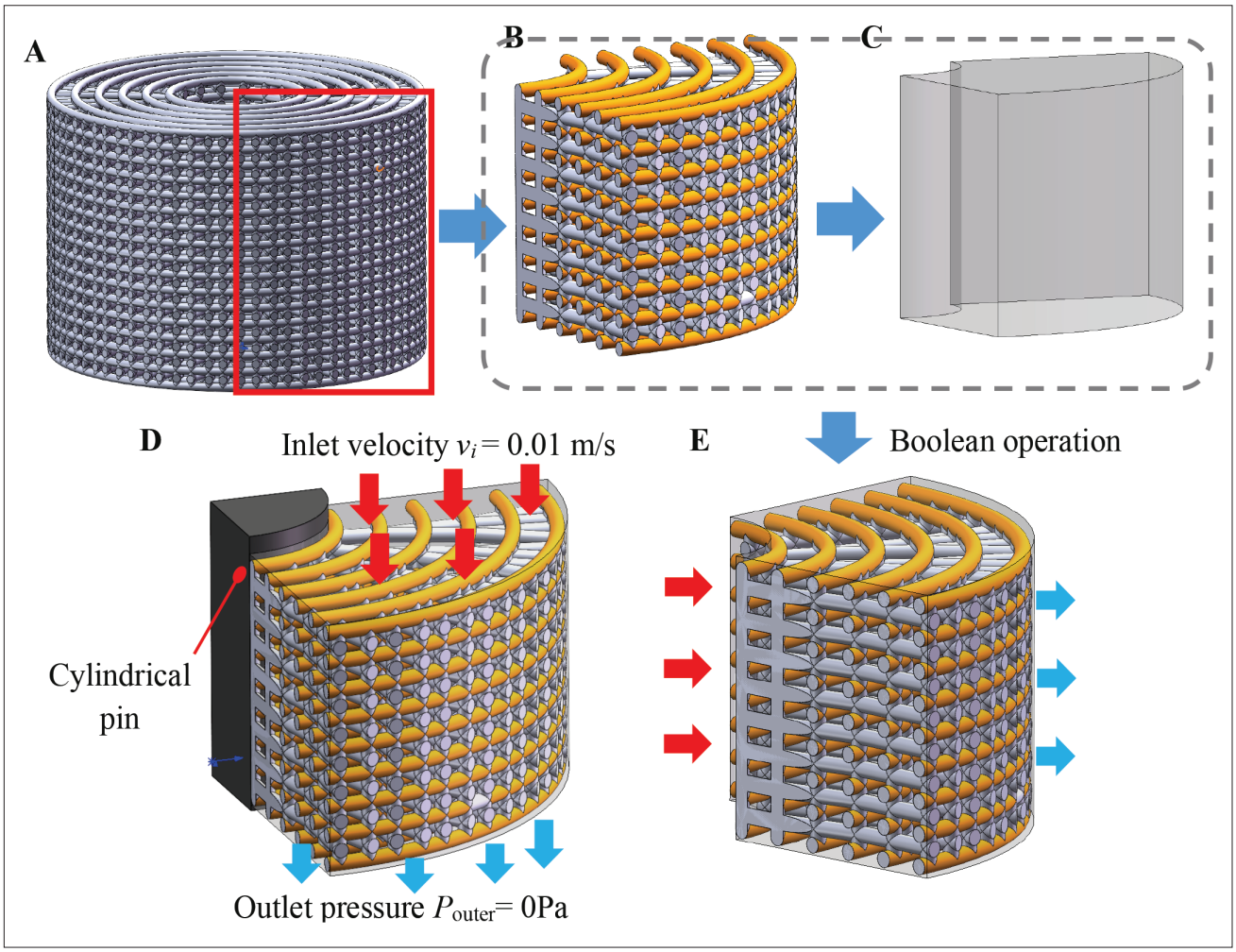

Figure 4. Schematic diagram of the computed fluid dynamics (CFD) fluid simulation. (A) The tree-like fractal scaffold model, (B) the 1/4 model, (B) the fluid domain model, (D) the CFD calculation model for axial permeability, and (E) the CFD calculation model for radial permeability (v_i is inlet velocity, P_{outer} is outlet pressure).

of 800 mm/s, and a laser spot size of 60 μm. The rotation angle between adjacent layers during printing was 67°, and the entire preparation process was performed under full argon conditions. After SLM 3D printing was completed, a wire cutting machine was used to cut the sample from the substrate. To ensure the mechanical properties of the sample, thermal stress treatment was performed to eliminate residual stress. The process was as follows: an annealing treatment was carried out at 650°C for 120 min, and heating was conducted at a rate of 10°C/min from 25 to 650°C. Furthermore, to remove the unmelted Ti6Al4V powder from the sample surfaces, anhydrous ethanol was used for ultrasonic cleaning. To minimize the impact of the preparation process on the accuracy of sample preparation, all scaffolds were fabricated using the same material and process. The tree-like fractal porous biomimetic scaffold prepared by SLM is shown in Figure 5, with geometric dimensions D = 24 mm, d = 8 mm, and h = 16.5 mm.

2.7. Mechanical properties testing

Mechanical property testing was conducted to compare and analyze the influence of fractal parameters on the mechanical properties of tree-like fractal biomimetic scaffolds. Additionally, to evaluate the correctness of FE calculations, the FE calculation results were compared with the test results. The test equipment used was a DF13.105T universal testing machine (Sinotest Equipment, China), and the testing standard referred to ISO 13314–2011.[49] The sample was placed at the center of the workbench and the upper plate downward to compress the sample, with no restrictions on the lateral expansion, as shown in Figure 6A. Loading rate of 0.5 mm/min, and the compression test was stopped when the sample fractured. During the compression process, the variation history of force with displacement was recorded, and the stress–strain curve was obtained. Then, the Young's modulus (E_e), yield strength (Y_s), and compressive strength (σ_c) of tree-like fractal scaffolds were obtained. E_e was determined by the slope of the straight line within the elastic region of the stress–strain curve, Y_s was determined by the intersection of the stress–strain curve at a 0.2% offset line parallel to the elastic line, and the σ_c was obtained through the first peak stress in the curve (Figure 6B).[50]

Due to the different structures of the four fractal scaffolds, their masses also varied. For a more scientific comparative analysis, we performed normalization on the masses of the four fractal scaffolds. The normalization calculation process is as follows in **Equations (13)–(15)**:

$$V_{total} = \pi \cdot \left(\frac{D}{2}\right)^2 \cdot h - \pi \cdot \left(\frac{d}{2}\right)^2 \cdot h \tag{13}$$

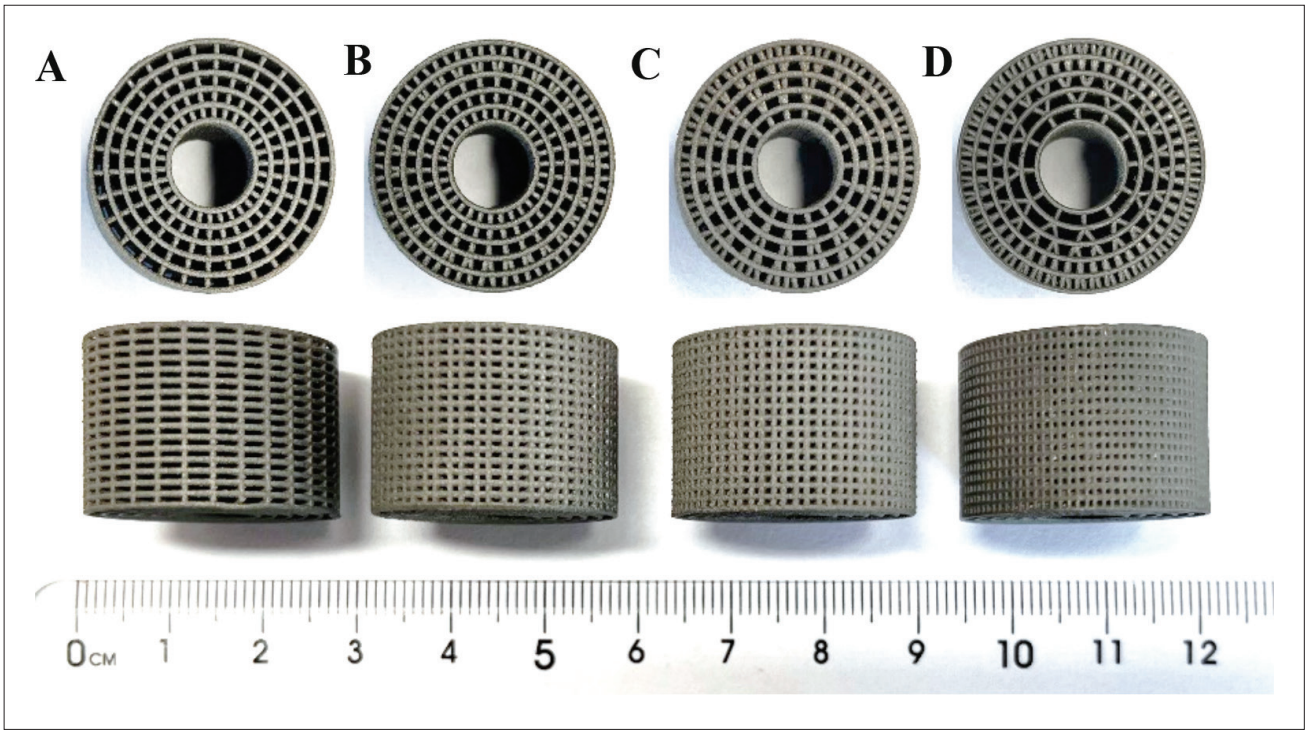

Figure 5. Tree-like fractal scaffolds fabricated using selective laser melting three-dimensional printing. (A) 0th-order scaffold, (B) 1st-order scaffold, (C) 2nd-order scaffold, and (D) 3rd-order scaffold.

where D is the outer diameter of the cylinder (mm), d is the inner diameter of the cylinder (mm), and h is the initial height of the sample (mm)

$$\rho_t = \frac{m}{V_{\text{total}}} \tag{14}$$

where m is the mass of the fractal scaffold (g).

$$\rho_r = \frac{\rho_t}{\rho_m} \tag{15}$$

where ρ_m is the density of Ti6Al4V material and ρ_m = 0.00443 g/mm^3.

Lastly, each stress data point on the original stress–strain curve was divided by the relative density (ρ_r) of the corresponding specimen.

3. Results and discussion

3.1. Effects of fractal parameters on porosity

The distribution of porosity along the radial direction is shown in Figure 7. In Figure 7, a, b, c, d, and e correspond to the local regions of the porous scaffold (Figure 2J) and the porosity within those regions, respectively. In the 0th-order fractal model, the radial porosity distribution showed that the internal region had lower porosity, while the external region had a larger one (Figure 7A), which is opposite to the radial porosity distribution of natural bone. The porosity of the 1st-order fractal scaffold along the radial direction showed a distribution in which the middle region had the largest porosity, while the inner and outer regions had the smallest porosities (Figure 7B). The porosity of 2nd-order and 3rd-order fractal scaffolds exhibited approximately linear distributions along the radial direction (Figure 7C,D), with a gradually decreasing gradient from the inner to the outer region, which is similar to that of natural bone.[51] In the 2nd-order fractal model, the porosities of the inner and outer regions were 74% and 67%, respectively. In the 3rd-order fractal model, the porosities of the inner and outer regions were 77% and 63%, respectively. The larger porosity in the inner region is similar to that of cancellous bone. In comparison, the smaller porosity in the outer region is similar to that of cortical bone (Figure 2A).

The above findings indicate that, through a tree-like fractal design, bionic bone scaffolds with a radial porosity gradient can be obtained by adjusting fractal parameters. In clinical applications, porous scaffolds can be designed with porosity matching the gradient distribution of the patient's bone defect site by optimizing fractal parameters, thereby better satisfying the personalized requirements of patients for implants.

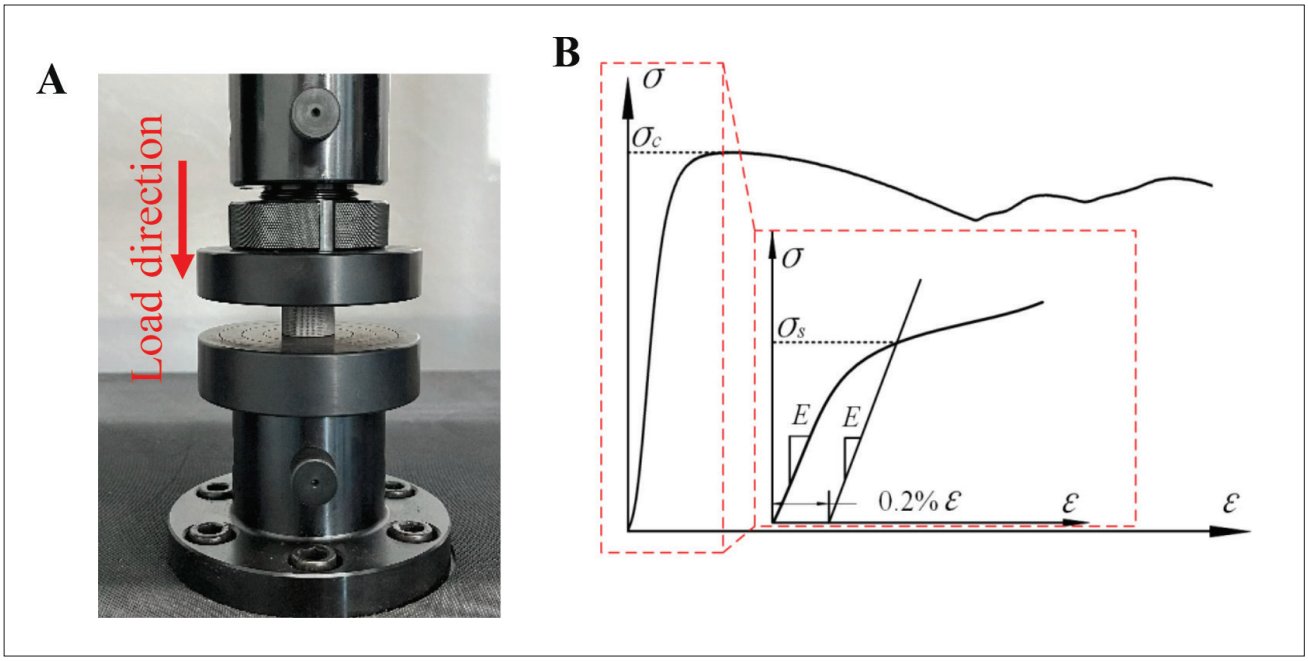

Figure 6. Mechanical properties testing and parameters calculation. (A) Compression testing, and (B) schematic of elastic modulus and strength.

3.2. Effects of fractal parameters on mechanical properties

To comparatively analyze the influence of fractal parameters on the mechanical properties of the scaffolds, quasi-static compression experiments were conducted on samples with different fractal parameters. A total of 20 samples were tested (five per type). Considering the differences in mechanical response and for the convenience of comparative analysis, only the mean stress–strain curves were plotted, as shown in Figure 8A. In the inception phase, the curve showed an elastic response until the yield point was reached. A small nonlinear phase appeared before the linear elastic phase, which is due to the establishment of complete contact between the plate and the sample. According to the measurement method for elastic modulus and yield strength in **Section 2.7** (Figure 6B) and the normalized stress–strain response curves (Figure 8A), the normalized yield strength and Young's modulus of the four groups of specimens were obtained as shown in Figure 7B and C. It is shown that under the condition of the same structural size parameters, the normalized yield strength of the 2nd-order fractal structure was the largest. Among the models with fractal structures, the 3rd-order fractal structure had the smallest normalized Young's modulus (13.602 GPa), followed by the 2nd-order fractal structure with a normalized Young's modulus of 15.424 GPa. However, the normalized yield strength of the 2nd-order fractal structure was significantly higher than that of the 3rd-order fractal structure. The comprehensive analysis of the test results shows that the 2nd-order tree-like fractal scaffold exhibited high yield strength and low Young's modulus, similar to the mechanical properties of natural bone, and can effectively reduce the risk of stress shielding. Furthermore, the comparison between the FE simulation results and the test results (Figure 8C) shows that the normalized Young's modulus calculated by the FE simulation was larger than the test results, with only a small difference. For example, the Young's modulus calculated by the FE of the 2nd-order fractal scaffold was 6.9% larger than the average of the test results. The Young's modulus calculation results for the four scaffolds showed small fluctuations and no significant differences, indicating the reliability of the FE simulation.

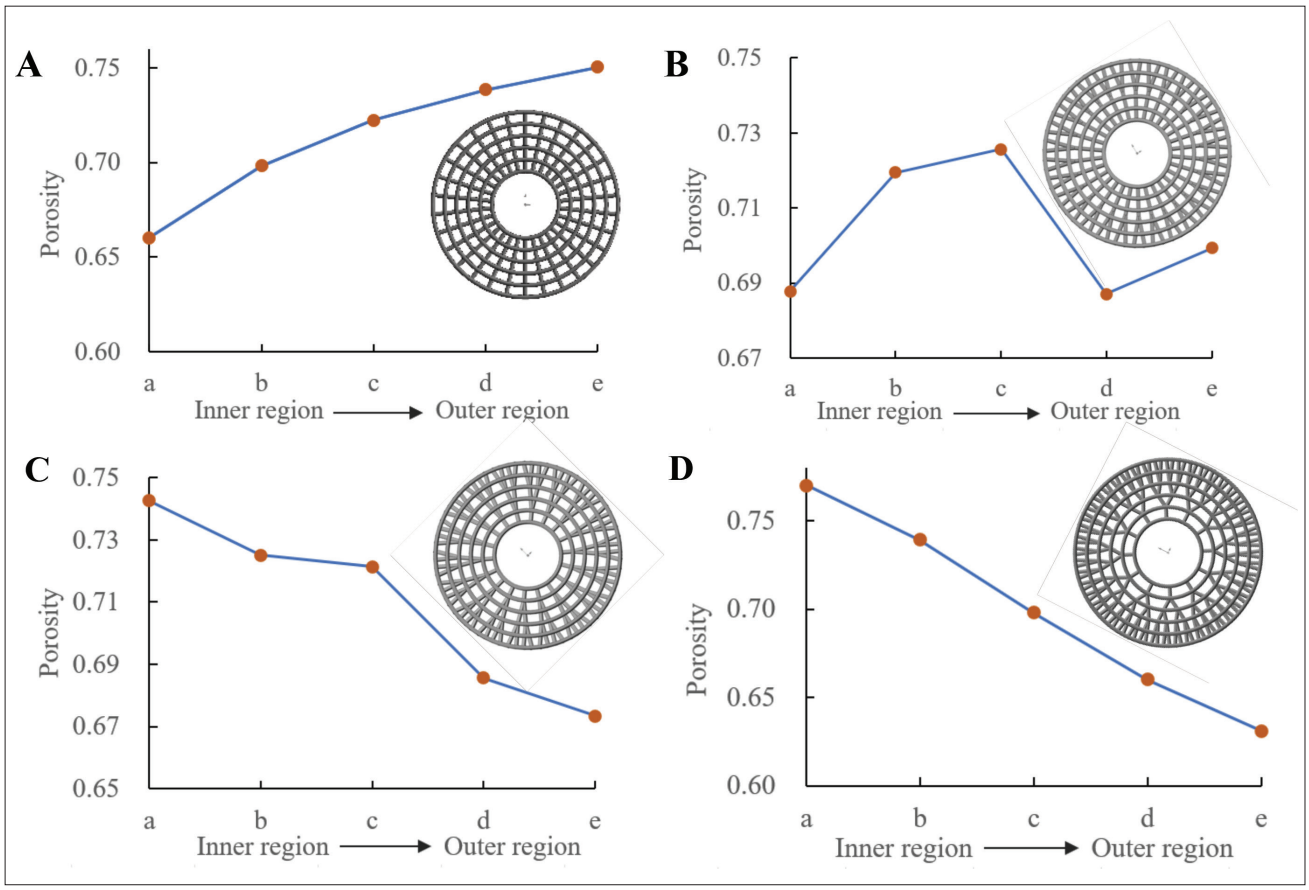

Figure 7. Radial distribution of porosity in porous scaffolds. (A) 0th-order fractal, (B) 1st-order fractal, (C) 2nd-order fractal, and (D) 3rd-order fractal.

The above findings indicate that tree-like fractal scaffolds exhibited high strength and low Young's modulus, characteristics consistent with those of natural bone, and can effectively reduce the risk of stress shielding. In addition, fractal parameters directly affect the mechanical properties of tree-like fractal scaffolds. Under the condition of equal strain, there were significant differences in the compressive stress of samples with different fractal structures. By optimizing fractal parameters, bone implants with different mechanical properties can be designed, making the Young's modulus and yield strength of bone implants closer to that of native bone.

3.3. Effects of fractal parameters on permeability

The CFD simulation results of the four porous scaffolds with different fractal parameters are shown in Figures 9 and 10. According to Darcy's law, the axial and radial permeabilities of the four models are shown in Figure 11. From the contour maps of the flow velocity distribution (Figures 9 and 10), it is evident that the distribution shows significant differences. The axial permeabilities of the 2nd-order and 3rd-order fractal scaffolds exhibited a strong fluid flow gradient from the inside to the outside, indicating that fractal parameters significantly affect the flow velocity distribution. Among the four different fractal structures, the 2nd-order tree-like structure had the maximum axial and radial permeability, while the 1st-order fractal structure had the minimum axial and radial permeability (Figure 11). Furthermore, the total permeabilities of the four fractal models from the 0th-order to the 3rd-order were as follows: 1.81×10^{-8} m^2, 1.31×10^{-8} m^2, 3.13×10^{-8} m^2, and 2.56×10^{-8} m^2. The 2nd-order fractal scaffold had the optimal comprehensive permeability, followed by the 3rd-order fractal model. The comprehensive permeability of the 2nd-order was 22.2% higher than that of the 3rd-order, thereby effectively improving cell diffusion.[24] According to the porosity distribution in **Section 3.1**, the porosities of the 2nd-order and 3rd-order fractal structures showed

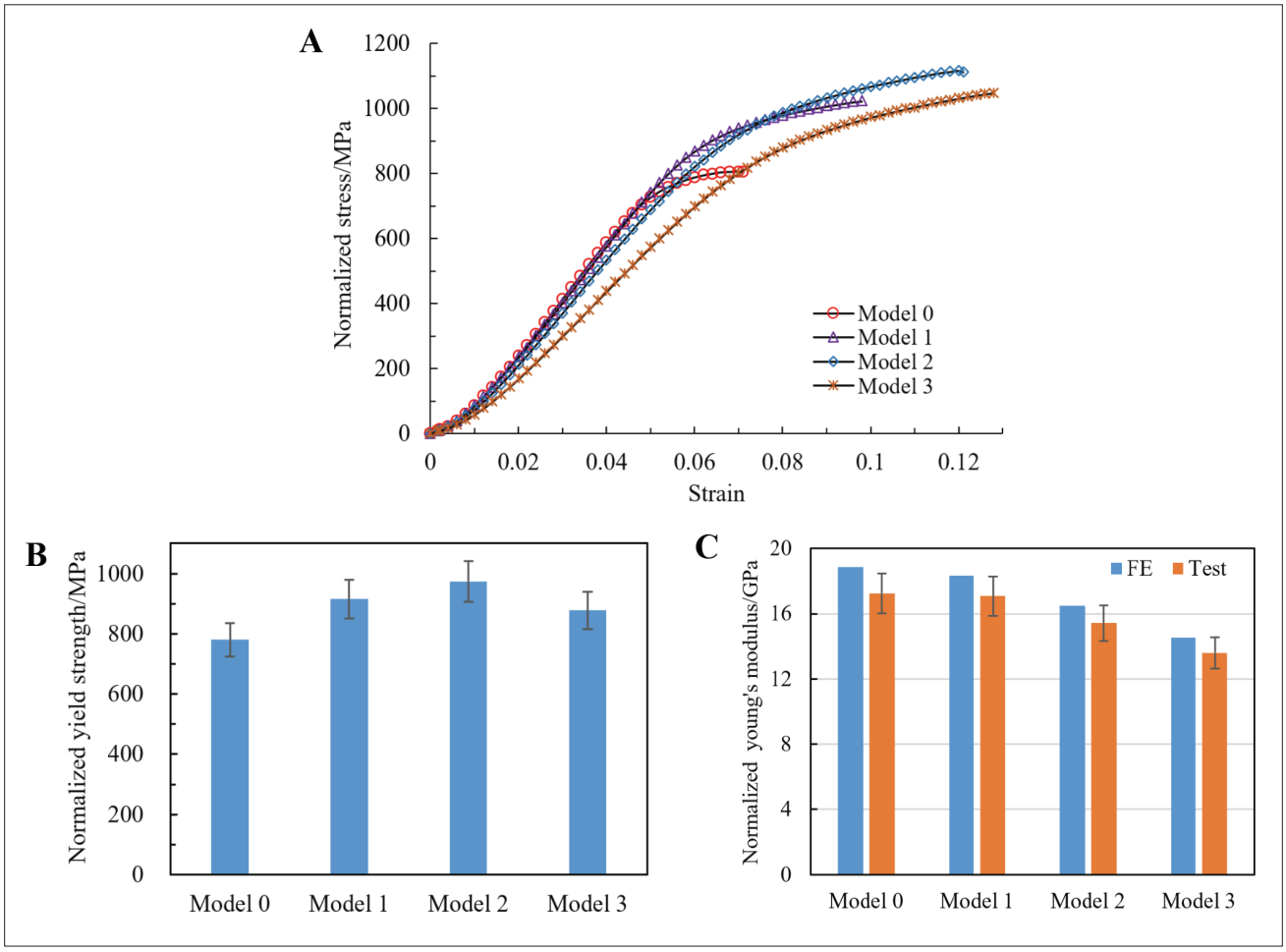

Figure 8. Mechanical properties test results. (A) Mean stress–strain curves of fractal scaffolds, (B) the yield strength of the scaffold, and (C) the Young's modulus of the scaffold. Note: Model 0, Model 1, Model 2, and Model 3 in the figure correspond to the 0th-order to 3rd-order fractal models, respectively. Abbreviation: FE, finite element.

a uniform gradient change from the inside to the outside. Therefore, the greater internal porosity can significantly improve the scaffold's permeability and offset the impact of reduced edge porosity, thereby enabling the radial-gradient porous scaffold to exhibit better permeability.

These findings indicate that 2nd-order fractal scaffolds exhibit good fluid-flow gradients and optimal overall permeability. The fractal parameters directly affect the distribution of flow velocity and permeability. In practical applications, by adjusting the fractal parameters, porous scaffolds with different permeability can be designed to better promote the bone regeneration process.

3.4. Orthogonal design calculation and sensitivity analysis

According to the experimental and FE calculation results in **Section 3.2**, the design of porous scaffolds with high yield strength and low elastic modulus can be achieved by optimizing the fractal parameters. The 2nd-order fractal scaffold exhibited good permeability (**Section 3.3**), and the Young's modulus of the 2nd-order fractal structure was approximately equal to that of the 3rd-order fractal structure. Since the 2nd-order fractal structure is simpler than the 3rd-order fractal structure, the 2nd-order fractal structure was selected as the research object for multi-objective optimization. Based on the L9(4^3) orthogonal design, nine tree-like fractal porous scaffold models with different structural parameters were created. The Young's modulus and yield strength corresponding to each porous scaffold were obtained through FE calculations. Each set of calculated data was entered into the corresponding positions to complete the design calculation of the orthogonal table, as shown in Table 2. The orthogonal design results in Table 2 were used as the dataset for subsequent neural network training.

The sensitivity indices of the four design variables to the response values were calculated using the variance-

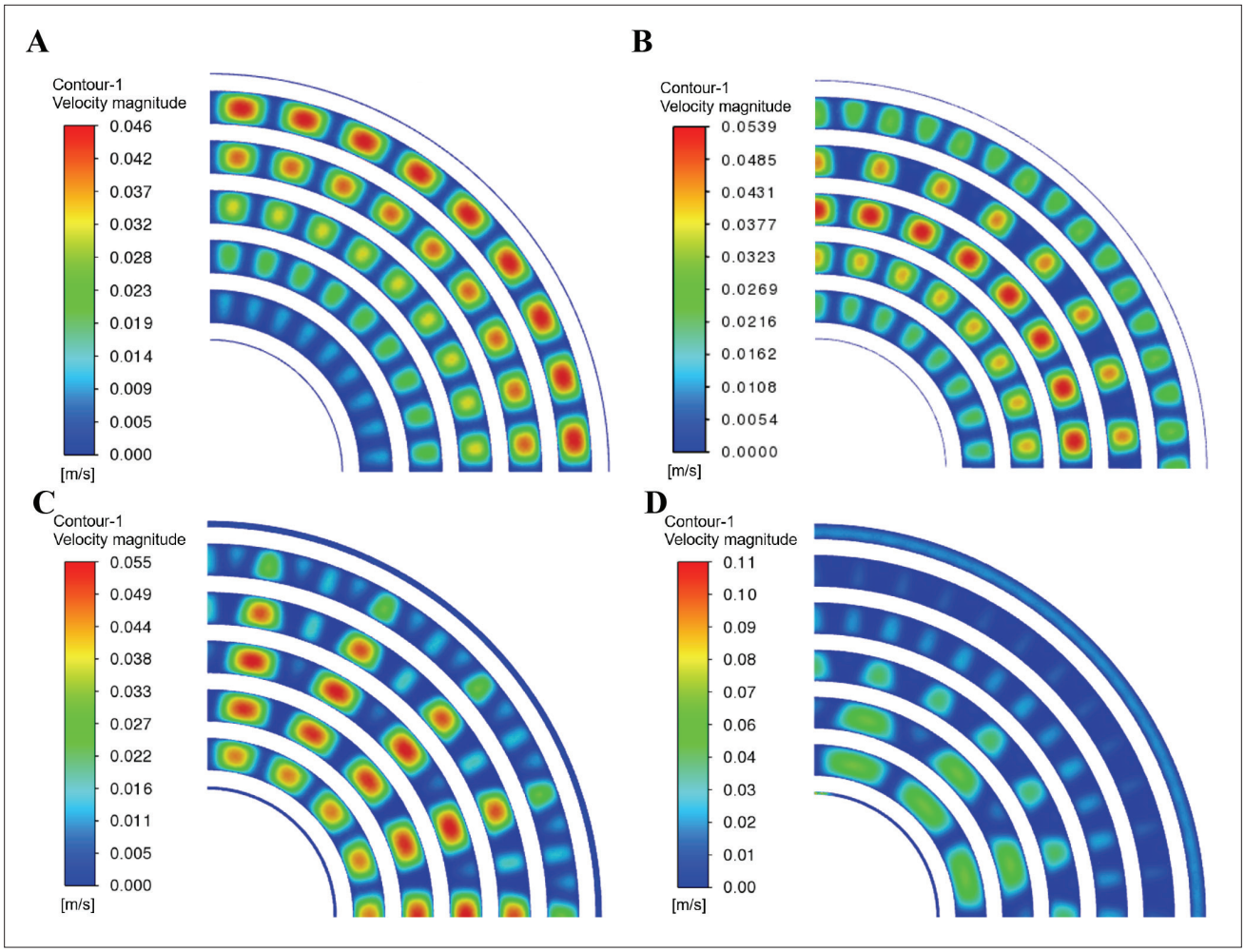

Figure 9. Cloud chart of axial flow velocity distribution. (A) 0th-order model, (B) 1st-order model, (C) 2nd-order model, and (D) 3rd-order model.

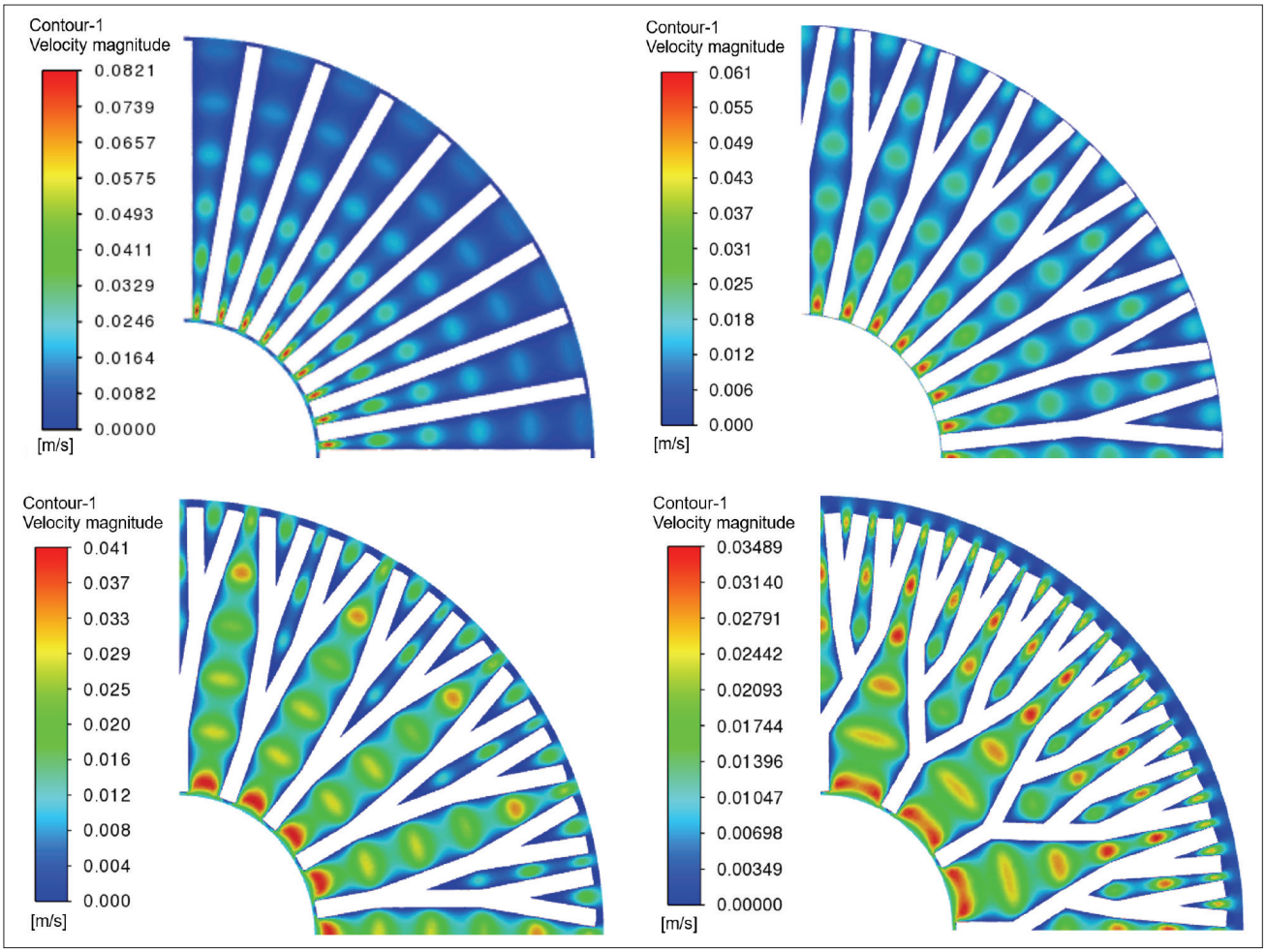

Figure 10. Cloud chart of radial flow velocity distribution. (A) 0th-order model, (B) 1st-order model, (C) 2nd-order model, and (D) 3rd-order model.

based sensitivity analysis method, as shown in Table 3. The sensitivity index of the fractal angle θ to the Young's modulus of the scaffold was 0.108, and its sensitivity index to the yield strength was 0.098. The sensitivity index of the annular bone matrix diameter d_h to Young's modulus was 0.465, and its sensitivity index to yield strength was 0.536, which is the most significant sensitivity index among the four design variables. Furthermore, both the number of concentric rings of the bone matrix N and the radial trabecular diameter d_j significantly impacted the sensitivity index of the scaffold. The four design variables selected in this study had varying degrees of influence on the scaffold's Young's modulus and yield strength. Therefore, it was reasonable to use Table 2 as the dataset for subsequent neural network training.

3.5. Algorithm optimization of the backpropagation neural network

Random initial thresholds and weights in the BP neural network negatively affected fitting correlation. Therefore, the GA was used to optimize the initial thresholds, while PSO was used to optimize the initial weights. The GA-BP neural network was subsequently used for training, and the PSO-BP neural network was used to perform multi-objective fitting on the dataset (Table 2). Root-mean-square errors (RMSEs) for multi-objective prediction were obtained, as shown in Figure 12. For GA-BP, when predicting Young's modulus, the RMSE of the training and test sets were 0.857 and 4.671, respectively (Figure 12A). When predicting yield strength, the RMSEs for the training and test sets were 9.889 and 48.729, respectively (Figure 12B). For PSO-BP, when predicting Young's modulus, the RMSEs of the training and test sets were 0.112 and 3.068, respectively (Figure 12C). When predicting yield strength, the RMSEs for the training and test sets were 1.119 and 32.314, respectively (Figure 12D). When PSO-BP and GA-BP were used to predict Young's modulus, the differences in RMSE between the training and test sets were relatively small. However, in the prediction of yield strength, the RMSE of both the training set and

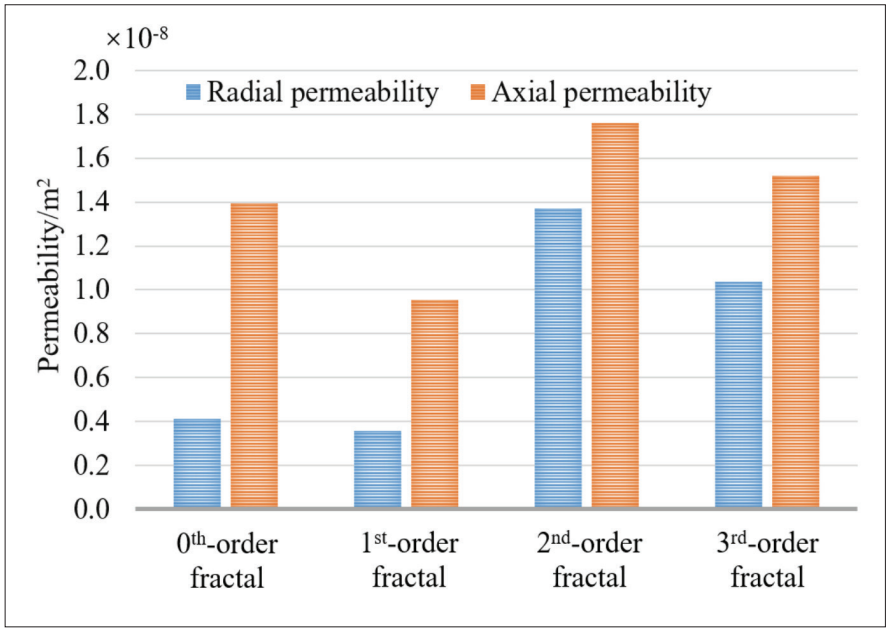

Figure 11. Axial and radial permeability of tree-like fractal porous scaffold.

Table 2. Orthogonal table corresponding to the nine tree-like fractal scaffolds

Number	Fractal angle θ (°)	Diameter of the annular bone matrix d_h (mm)	Number of concentric rings of bone matrix	Radial trabecular diameter d_j (mm)	Young's modulus E_e (GPa)	Yield strength Y_s (MPa)
1	20	0.4	4	0.4	7.439	82.894
2	20	0.5	6	0.5	18.216	190.386
3	20	0.6	5	0.6	17.119	185.603
4	25	0.4	6	0.6	14.095	126.843
5	25	0.5	5	0.4	12.555	132.859
6	25	0.6	4	0.5	12.035	124.034
7	30	0.4	5	0.5	10.661	111.981
8	30	0.5	4	0.6	18.395	152.903
9	30	0.6	6	0.4	18.716	177.534

Table 3. Sensitivity index of various variables

Name	Fractal angle θ (°)	Diameter of the annular bone matrix d_h (mm)	Number of concentric rings of bone matrix	Radial trabecular diameter d_j (mm)
Young's modulus, E_e (GPa)	0.108	0.465	0.255	0.173
Yield strength, Y_s (MPa)	0.098	0.536	0.285	0.081

test set fitted by PSO-BP were significantly smaller than those fitted by GA-BP. This indicates that the PSO-BP fit is considerably better than that of GA-BP.

The comparison of prediction correlation between GA-BP and PSO-BP is shown in Figure 13. The correlation coefficient for the training set relationship in GA-BP was 0.99797, while that for PSO-BP was 1, which is slightly higher than that for GA-BP. Both the PSO-BP and the GA-BP achieved a correlation coefficient of 1 in both the test and validation sets. The comprehensive fitting correlation coefficient of GA-BP was 0.783, while that of PSO-BP was close to 1, indicating that PSO-BP has a higher comprehensive fitting correlation coefficient.

The results comparison in Figures 12 and 13 shows that the RMSEs of both the training and test sets fitted by the PSO-BP were significantly smaller than those fitted by the GA-BP, indicating that the PSO-BP neural network has a better fitting effect. The training set fitting correlation

coefficient of the PSO-BP was slightly higher than that of the GA-BP, while the comprehensive fitting correlation coefficient of the PSO-BP (0.9998) was 27.72% higher than that of the GA-BP (0.78278). These results indicate that the prediction correlation coefficient of the BP neural network optimized by PSO is higher. Therefore, the PSO-BP neural network was selected to model the relationships among Young's modulus, yield strength, and the structural parameters of the tree-like fractal scaffold.

3.6. Multi-objective optimization and result verification

Based on the fitting results of the PSO-BP, the NSGA III was adopted to optimize the minimum value of the scaffold's Young's modulus and the maximum value of the yield strength. Based on the Pareto chart obtained from the multi-objective optimization, the optimal solution was determined by selecting the point with a smaller Young's modulus and a larger yield strength as the comprehensive optimal point, as shown in Figure 14. When the yield strength increased to 58.09 MPa, the decreasing amplitude of the minimum Young's modulus showed a significant weakening. Therefore, the point with a yield strength of 58.09 MPa and a Young's modulus of 5.965 GPa was selected as the optimal point (Figure 14). The structural dimension parameters of the tree-like fractal scaffold corresponding to this optimal point were obtained: fractal angle θ = 20.004° (rounded to 20°), diameter of the annular bone matrix d_h = 0.415 mm (rounded to 0.42 mm), number of rings of annular bone matrix N =4.17 (rounded

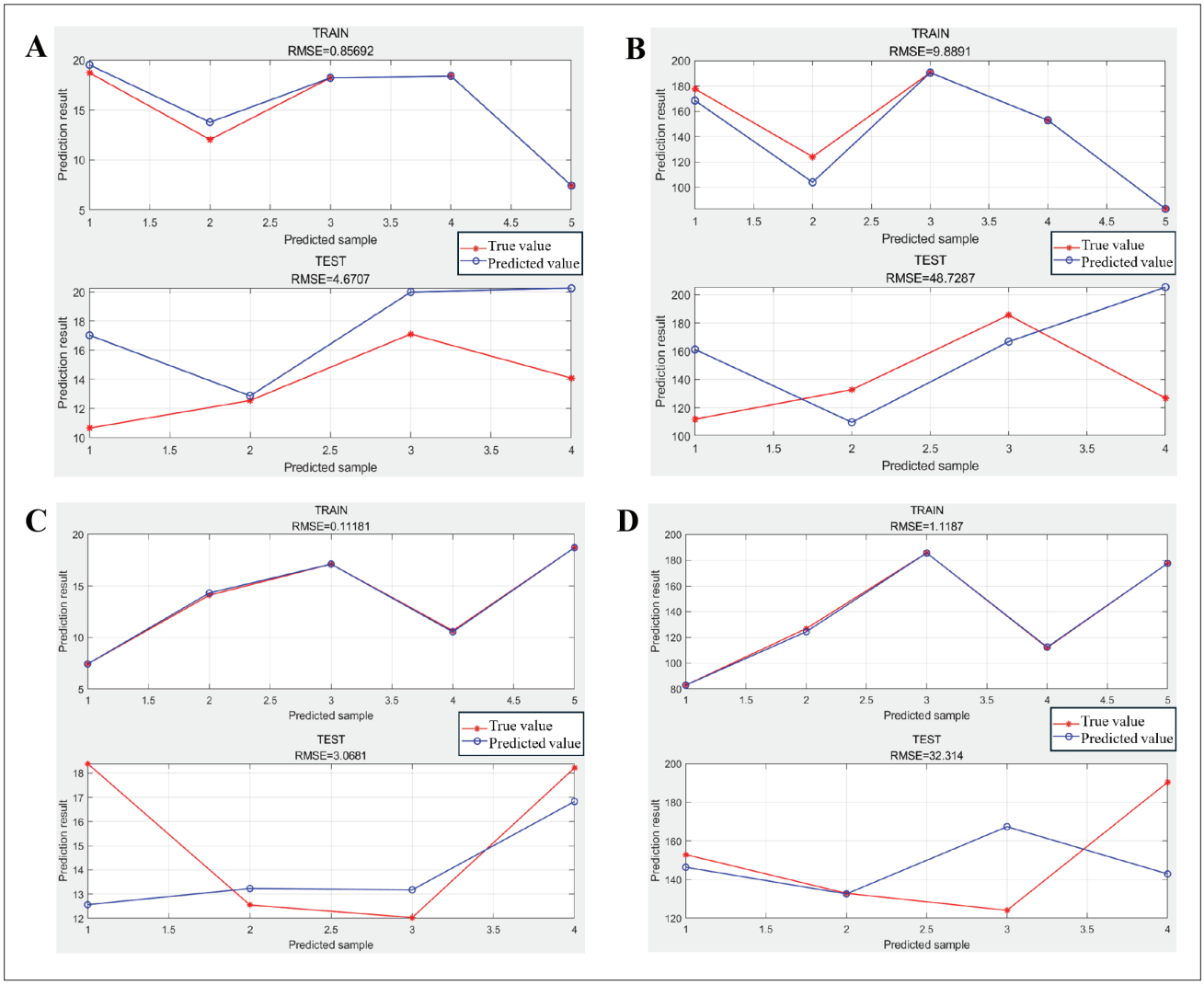

Figure 12. Root-mean-square error (RMSE) of neural network target prediction. (A) RMSE of genetic algorithm-back propagation (GA-BP) for Young's modulus prediction, (B) RMSE of GA-BP for yield strength prediction, (C) RMSE of particle swarm optimization (PSO)-BP for Young's modulus prediction, and (D) RMSE of PSO-BP for yield strength prediction.

to four), and radial trabecular diameter d_j = 0.3 mm. Based on the obtained key structural parameters of the 2nd-order tree-like fractal scaffold, an optimized 2nd-order tree-like scaffold model was established and fabricated using SLM 3D printing. Subsequently, mechanical experiments were conducted to verify the feasibility and correlation of the multi-objective optimization. The average stress–strain curve and performance parameters of the 2nd-order tree-like fractal scaffold after multi-objective optimization are shown in Figure 15.

The test value and predicted value of the Young's modulus of the optimized 2nd-order fractal scaffold were 5.965 and 6.438 GPa, respectively. The predicted and tested yield strengths were 58.09 and 58.576 MPa, respectively (Figure 15B). The difference between the tested value and the predicted value of Young's modulus was only 0.473 GPa; the tested value was 7.93% larger than the predicted value. The difference between the test value and the predicted value of yield strength was only 0.486 MPa, and the test value was 0.83% greater than the predicted value. It can be concluded that the PSO-BP-NSGA III integrated algorithm has strong reliability and predictive ability for tree-like fractal scaffolds.

4. Conclusion

This study aimed to achieve a synergistic effect among structure, modulus, and strength of porous scaffolds and to reduce stress shielding. A novel method for the design and optimization of porous bone scaffolds based on bionics and PSO-BP-NSGA III integrated algorithm was proposed.

The tree-like fractal biomimetic scaffold exhibited a radial porosity gradient similar to that of natural bone. The porosity of the 2nd-order and 3rd-order fractal scaffolds showed approximately linear distributions along the radial direction, with a radial gradient in porosity that gradually decreased from the inside to the outside.

The tree-like fractal scaffold can achieve effective synergy of high strength and low Young's modulus. The yield strength and Young's modulus of the porous scaffold can be effectively adjusted by optimizing the fractal order. Test and FE results showed that the 2nd-order fractal scaffold exhibited a significantly high yield strength and a low Young's modulus.

The 2nd-order fractal scaffold exhibited a favorable fluid flow gradient and good permeability. Among the four different fractal structures, the 2nd-order fractal structure showed the optimal axial and radial permeability, with a comprehensive permeability of 3.13×10^{-8} m^2, which was 22.2% higher than that of the 3rd-order fractal scaffold.

The PSO-BP showed a higher correlation with Young's modulus and yield strength for tree-like fractal scaffolds. In terms of target prediction RMSE, the RMSEs of both the training and test sets were significantly smaller for PSO-

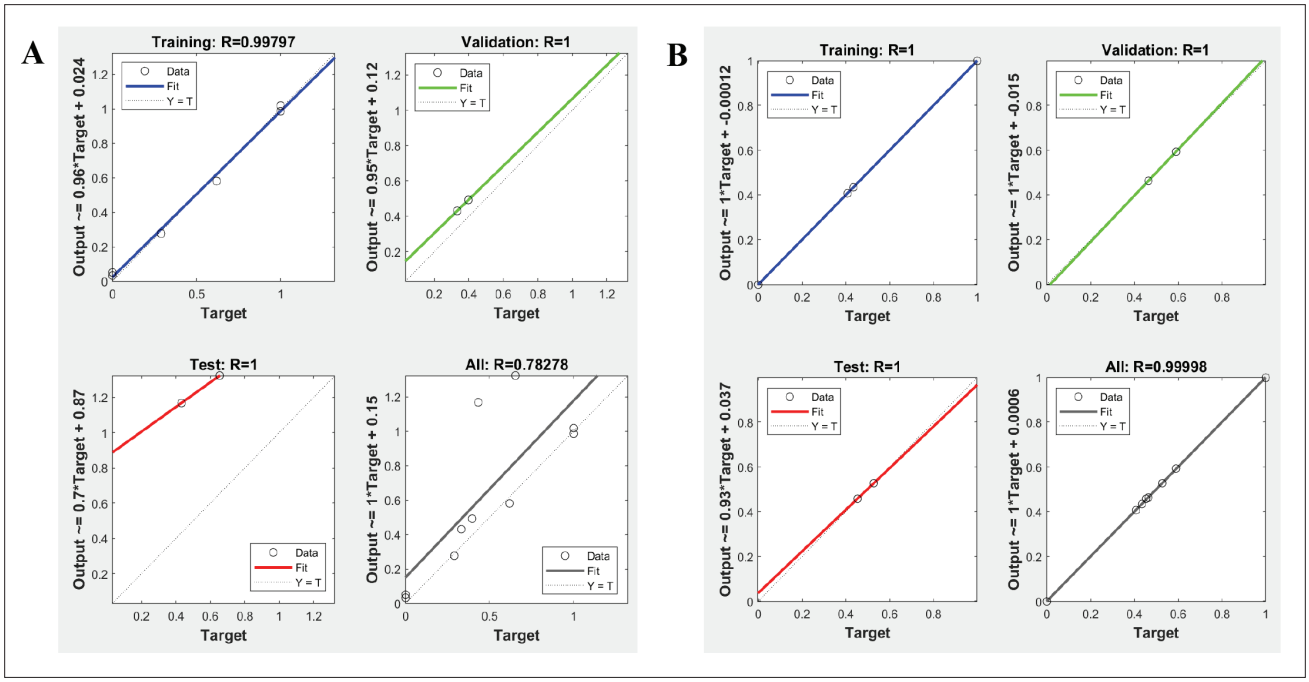

Figure 13. Prediction correlation of genetic algorithm-backpropagation (GA-BP) and particle swarm optimization (PSO)-BP. (A) Prediction correlation coefficient of GA-BP, and (B) prediction correlation coefficient of PSO-BP.

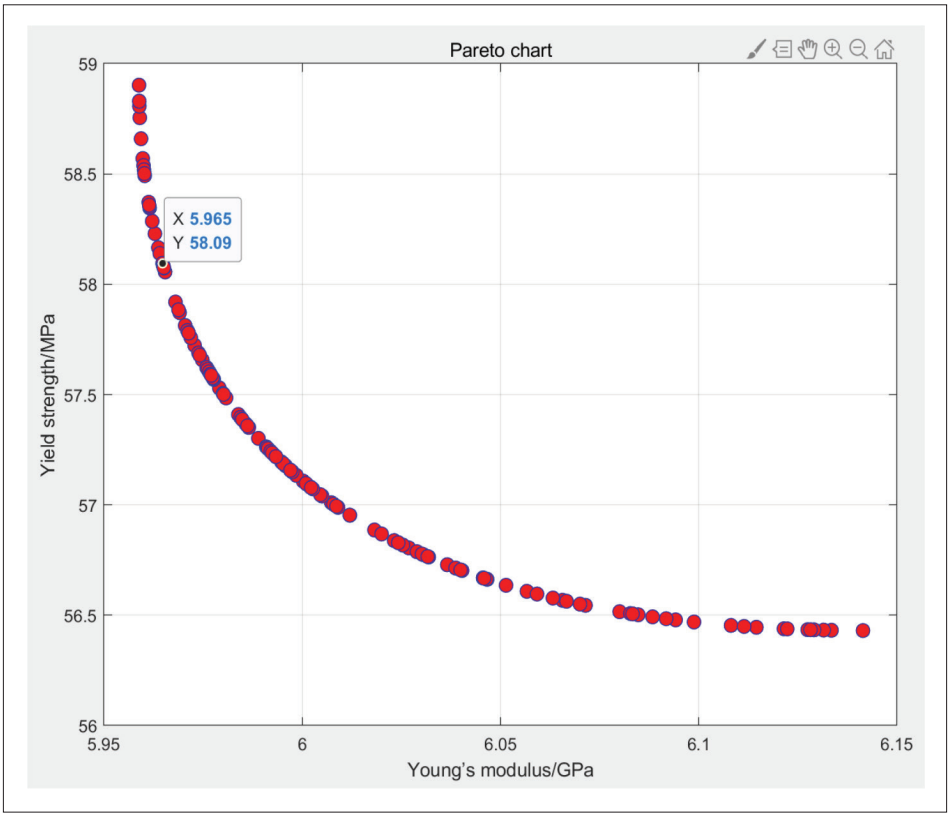

Figure 14. Pareto optimal solution set diagram.

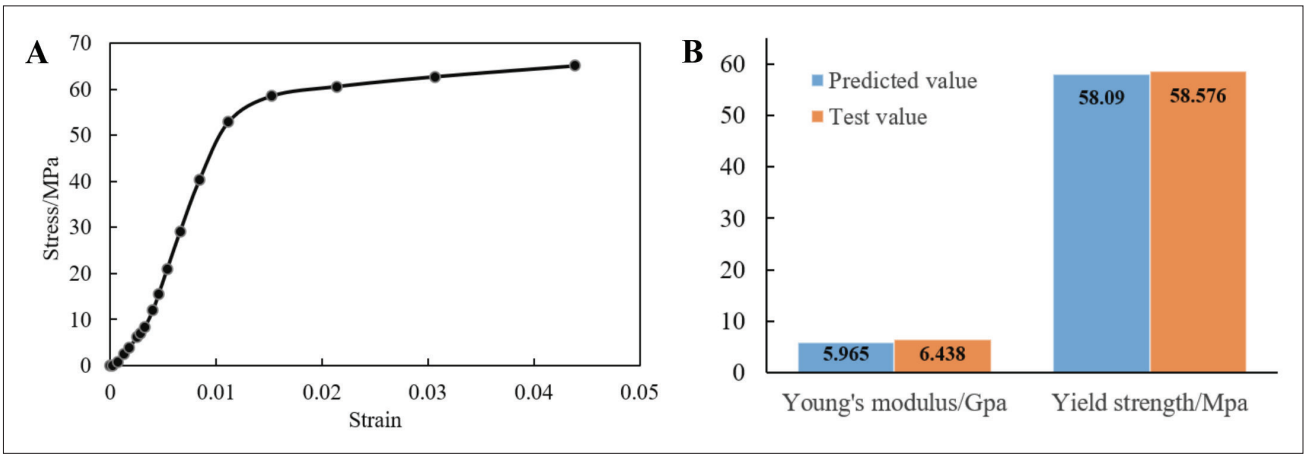

Figure 15. The mechanical properties of a 2nd-order tree-like fractal scaffold after multi-objective optimization. (A) Average stress–strain curve, and (B) yield strength and Young's modulus.

BP than for GA-BP. In terms of the prediction correlation coefficient, the comprehensive fitting correlation coefficient of the PSO-BP was close to 1, indicating a high overall fit.

The PSO-BP-NSGA Ⅲ integrated algorithm demonstrated high reliability and correlation in the multi-objective optimization of tree-like porous scaffolds. The tested value of Young's modulus was 7.93% larger than the predicted value. The measured yield strength was 0.83% higher than the predicted value, and the correlation between the prediction and the measured value was 99.17%.

Acknowledgments

None

Funding

This work was supported by the Natural Science Foundation of Chongqing Municipality (Grant no.: CSTB2023NSCQ-MSX0255), the Key Project of Science and Technology Research Program of Chongqing Education Commission (Grant no.: KJZD-K202203104), and the Science and Technology Research Program of Chongqing Education Commission (Grant no.: KJQN202403112).

Conflict of interest

The authors declare that there is no conflict of interest.

Author contributions

Conceptualization: Yuxi Liu, Aihua Li
Formal analysis: Hong Sun, Shuge Li
Investigation: Yuxi Liu, Aihua Li, Hong Sun
Methodology: Aihua Li, Yuxi Liu, Song Chen
Validation: Shuge Li, Aihua Li
Writing–original draft: Yuxi Liu, Aihua Li, Hong Sun
Writing–review & editing: Song Chen, Shuge Li, Hong Sun, Aihua Li

Ethics approval and consent to participate

Not applicable.

Consent for publication

Not applicable.

Availability of data

The data that support the findings of this study are available from the corresponding author upon reasonable request.

References

1. Luo L, Zheng W, Li J, *et al.* 3D-printed titanium trabecular scaffolds with sustained release of hypoxia-induced exosomes for dual-mimetic bone regeneration. *Adv Sci.* 2025;12(23):2500599.
doi: 10.1002/advs.202500599

2. Qin Y, Jing Z, Zou D, *et al.* A metamaterial scaffold beyond modulus limits: enhanced osteogenesis and angiogenesis of critical bone defects. *Nat Commun.* 2025;16:2180.
doi: 10.1038/s41467-025-57609-9

3. Jin Y, Li J, Fan H, Du J, He Y. Biomechanics and mechanobiology of additively manufactured porous load-bearing bone implants. *Small.* 2025;21(20):2409955.
doi: 10.1002/smll.202409955

4. Ahmed H, Shakshak M, Trompeter A. A review of the Masquelet technique in the treatment of lower limb critical-size bone defects. *Ann R Coll Surg Engl.* 2025;107(6): 383-389.
doi: 10.1308/rcsann.2023.0022

5. Naghavi SA, Tamaddon M, Garcia-Souto P, *et al.* A novel hybrid design and modelling of a customised graded Ti-6Al-4V porous hip implant to reduce stress-shielding: An experimental and numerical analysis. *Front Bioeng Biotechnol.* 2023;11:1092361.
doi: 10.3389/fbioe.2023.1092361

6. Li Z, Chen Z, Chen X, Zhao R. Design and evaluation of TPMS-inspired 3D-printed scaffolds for bone tissue engineering: enabling tailored mechanical and mass transport properties. *Compos Struct.* 2024;327:117638.
doi: 10.1016/j.compstruct.2023.117638

7. D'Andrea L, Gabrieli R, Milano L, *et al.* Elastic and failure characterization of hydroxyapatite TPMS scaffolds using a combined approach of ultrasound, compression tests and micro-CT based numerical models. *Acta Mater.* 2025;287:120776.
doi: 10.1016/j.actamat.2025.120776

8. Liu H, Chen H, Sun B, *et al.* Enhancing angiogenesis and osseointegration through a double gyroid Ti6Al4V scaffold with triply periodic minimal surface. *Bio-Des Manuf.* 2025;8(1):36-54.
doi: 10.1631/bdm.2400114

9. Men Y, Tang S, Chen W, Liu F, Zhang C. Design and performance study of bone trabecular scaffolds based on triply periodic minimal surface method. *J Biomed Eng.* 2024;41(3):584-594.
doi: 10.7507/1001-5515.202310005

10. Deng T, Li M, Gong S, *et al.* Voronoi as the optimal approach for strut-based bone scaffold design. *Int J Mech Sci.* 2025;295:110124.
doi: 10.1016/j.ijmecsci.2025.110124

11. Wu C, Wan B, Xu Y, *et al.* Dynamic optimisation for graded tissue scaffolds using machine learning techniques. *Comput Methods Appl Mech Eng.* 2024;425:116911.
doi: 10.1016/j.cma.2024.116911

12. Ibrahimi S, D'Andrea L, Gastaldi D, Rivolta MW, Vena P. Machine learning approaches for the design of biomechanically compatible bone tissue engineering scaffolds. *Comput Methods Appl Mech Eng.* 2024; 423:116842.
doi: 10.1016/j.cma.2024.116842

13. Liu W, Zhang Y, Lyu Y, Bosiakov S, Liu Y. Inverse design of anisotropic bone scaffold based on machine learning and regenerative genetic algorithm. *Front Bioeng Biotechnol.* 2023;11:1241151.
doi: 10.3389/fbioe.2023.1241151

14. Boccaccio A, Uva AE, Fiorentino M, Mori G, Monno G. Geometry design optimization of functionally graded scaffolds for bone tissue engineering: a mechanobiological approach. *PLoS One.* 2016;11(1):e0146935.

doi: 10.1371/journal.pone.0146935

15. Wu C, Wan B, Entezari A, Fang J, Xu Y, Li Q. Machine learning-based design for additive manufacturing in biomedical engineering. *Int J Mech Sci.* 2024;266:108828. doi: 10.1016/j.ijmecsci.2023.108828
16. Zhang J, Zhao J, Rong Q, Yu W, Li X, Misra RD. Machine learning guided prediction of mechanical properties of TPMS structures based on finite element simulation for biomedical titanium. *Mater Technol.* 2022;37(1):1-8. doi: 10.1080/10667857.2021.1999558
17. Liu G, Zhang X, Chen X, *et al*. Additive manufacturing of structural materials. *Mater Sci Eng R Rep.* 2021;145: 100596. doi: 10.1016/j.mser.2020.100596
18. Bie H, Chen H, Shan L, *et al*. 3D printing and performance study of porous artificial bone based on HA-ZrO2-PVA composites. *Materials (Basel).* 2023;16(3):1107. doi: 10.3390/ma16031107
19. Xu Q, Wang S, Bai Y, *et al*. Porous Ti3SiC2 ceramics with improved osteogenic functions via biomineralization as load-bearing bone implants. *J Mater Sci Technol.* 2024;195:248-259. doi: 10.1016/j.jmst.2024.01.025
20. Guo W, Li P, Wei Y, *et al*. Long ionic substitution through bredigite doping for microstructure and performance adjustment in DLP 3D-printed TPMS porous HA bone scaffolds. *Virtual Phys Prototyp.* 2024;19(1):e2423840. doi: 10.1080/17452759.2024.2423840
21. Li S, Yang H, Qu X, *et al*. Multiscale architecture design of 3D printed biodegradable Zn-based porous scaffolds for immunomodulatory osteogenesis. *Nat Commun.* 2024;15:3131. doi: 10.1038/s41467-024-47189-5
22. Min S, Wang C, Liu B, Lu D, Jin ZM. The biological properties of 3D-printed degradable magnesium alloy WE43 porous scaffolds via the oxidative heat strategy. *Int J Bioprint.* 2023;9(3):686. doi: 10.18063/ijb.686
23. Erica L, Giulia R, Stefania P, Silvia B, Alessandro F, Paolo C. Mechanical interaction between additive-manufactured metal lattice structures and bone in compression: implications for stress shielding of orthopaedic implants. *J Mech Behav Biomed Mater.* 2021;121:104608. doi: 10.1016/j.jmbbm.2021.104608
24. Foroughi AH, Razavi MJ. Multi-objective shape optimization of bone scaffolds: enhancement of mechanical properties and permeability. *Acta Biomater.* 2022;146:317-340. doi: 10.1016/j.actbio.2022.04.051
25. Li K, Liao R, Zheng Q, *et al*. Design exploration of staggered hybrid minimal surface magnesium alloy bone scaffolds. *Int J Mech Sci.* 2024;284:1109566. doi: 10.1016/j.ijmecsci.2024.109566
26. Wang Y, Qin X, Lv N, *et al*. Microstructure optimization for design of porous tantalum scaffolds based on mechanical properties and permeability. *Materials (Basel).* 2023;16:7568. doi: 10.3390/ma16247568
27. Paul R, Rana M, Gupta A, Banerjee T, Karmakar SK, Chowdhury AR. Design of biomimetic porous scaffolds for bone tissue engineering. *Transp Porous Media.* 2024;151:1453-1473. doi: 10.1007/s11242-024-02082-z
28. Liu Y, Cao Q, Yong S, *et al*. Optimal structural characteristics of osteoinductivity in bioceramics derived from a novel high-throughput screening plus machine learning approach. *Biomaterials.* 2025;321:123348. doi: 10.1016/j.biomaterials.2025.123348
29. Sorrentino A, Bianchi G, Radi E, Castagnetti D. Towards new strut-based auxetic meta-biomaterials for trabecular bone scaffolds. *Int J Eng Sci.* 2025;215:104316. doi: 10.1016/j.ijengsci.2025.104316
30. Xu Y, Zhang S, Ding W, *et al*. Additively-manufactured gradient porous bio-scaffolds: permeability, cytocompatibility and mechanical properties. *Compos Struct.* 2024;336:118021. doi: 10.1016/j.compstruct.2024.118021
31. Ma H, Men Y, Tang S, Hao P, Zhang C. Simulation analysis of strength and permeability of crystalline porous scaffolds. *Med Biomech.* 2024;39(2):222-228. doi: 10.16156/j.1004-7220.2024.02.005
32. Xu B, Lee K, Li W, *et al*. A comparative study on cylindrical and spherical models in fabrication of bone tissue engineering scaffolds: finite element simulation and experiments. *Mater Des.* 2021;211:110150. doi: 10.1016/j.matdes.2021.110150
33. Santos J, Pires T, Gouveia BP, *et al*. On the permeability of TPMS scaffolds. *J Mech Behav Biomed Mater.* 2023;142:105848. doi: 10.1016/j.jmbbm.2020.103932
34. Mamuti M, Chao L, Tian Z. Analysis of mechanical characteristics and permeability of TPMS and Voronoi porous structure for bone scaffold. *Comput Methods Biomech Biomed Engin.* 2025;28(14):2111-2124. doi: 10.1080/10255842.2024.2358378
35. Zhang X, Fang G, Leeflang S, Zadpoor AA, Zhou J. Topological design, permeability and mechanical behavior of additively manufactured functionally graded porous metallic biomaterials. *Acta Biomater.* 2019;84:437-452. doi: 10.1016/j.actbio.2018.12.013
36. Lv Y, Wang B, Liu G, *et al*. Design of bone-like continuous gradient porous scaffold based on triply periodic minimal surfaces. *J Mater Res Technol.* 2022;21:3650-3665. doi: 10.1016/j.jmrt.2022.10.160
37. Maconachie T, Leary M, Lozanovski B, *et al*. SLM lattice structures: properties, performance, applications and challenges. *Mater Des.* 2019;183:108137.

doi: 10.1016/j.matdes.2019.108137

38. Liu Y, Li A, Du B, He X. Design and properties research of radial gradient controllable biomimetic bone scaffold based on tree-liked fractal structure. *Chem Eng J.* 2024;499:156168. doi: 10.1016/j.cej.2024.156168

39. Chmielewska A, Dean D. The role of stiffness-matching in avoiding stress shielding-induced bone loss and stress concentration-induced skeletal reconstruction device failure. *Acta Biomater.* 2024;173:51-65. doi: 10.1016/j.actbio.2023.11.011

40. Li Z, Qian G, Shen Z, *et al*. Effects of operating parameters for low-grade heat driven thermo-electrochemical cells based on orthogonal experiments. *Appl Therm Eng.* 2024;243:122664. doi: 10.1016/j.applthermaleng.2024.122664

41. Tang L, Lai C, Tan L. Heat dissipation performance analysis and structure optimization of cooling channels for motors and controllers. *J Chongqing Univ Technol (Nat Sci).* 2023;37(2):104-112. doi: 10.3969/j.issn.1674-8425(z).2023.02.012

42. Chen S, Xu P, Liu Y. Design and multi-objective optimization of hairpin motor cooling system based on orthogonal design method and composite algorithm. *Appl Therm Eng.* 2025;259:124971. doi: 10.1016/j.applthermaleng.2024.124971

43. Zhang H, Hui JM. A back propagation neural network-based method for intelligent decision-making. *Complexity.* 2021;2021(1):610797. doi: 10.1155/2021/6610797

44. Biswas MAR, Robinson MD, Fumo N. Prediction of residential building energy consumption: a neural network approach. *Energy.* 2016;117:84-92. doi: 10.1016/j.energy.2016.10.066

45. Zhu C, Zhu J, Liu Y. Comparison of GA-BP and PSO-BP neural network models with initial BP model for rainfall-induced landslides risk assessment in regional scale: a case study in Sichuan, China. *Nat Hazards.* 2020;100(1):173-204. doi: 10.1007/s11069-019-03806-x

46. Papasani A, Devarakonda N. A novel feature selection algorithm using decomposition-based multi-objective guided honey badger algorithm (MO-GHBA) and NSGA-III. *Kuwait J Sci.* 2023;50(2):53-64. doi: 10.1016/j.kjs.2023.02.009

47. Qin Y, Wang Q, Shi C, Liu B, Ma S, Zhang M. Structural design and performance study of primitive triply periodic minimal surfaces Ti6Al4V biomimetic scaffold. *Sci Rep.* 2022;12(1):12759. doi: 10.1038/s41598-022-17066-6

48. Koju N, Niraula S, Fotovvati B. Additively manufactured porous Ti6Al4V for bone implants: a review. *Metals (Basel).* 2022;12(4):687. doi: 10.3390/met12040687

49. International Organization for Standardization. *ISO 13314: Compression Test for Porous and Cellular Metals*. Geneva: ISO; 2011.

50. Zhu J, Zou S, Mu Y, Wang J, Jin Y. Additively manufactured scaffolds with optimized thickness based on triply periodic minimal surface. *Materials (Basel).* 2022;15:7084. doi: 10.3390/ma15207084

51. Qu H, Han Z, Chen Z, *et al*. Fractal design boosts extrusion-based 3D printing of bone-mimicking radial-gradient scaffolds. *Research (Wash D C).* 2021;2021:9892689. doi: 10.34133/2021/9892689

ACCSCIENCE PUBLISHING

International Journal of Bioprinting

RESEARCH ARTICLE

Mixed ultrashort peptide bioinks for improved 3D bioprinting of self-healing trachea-like constructs

Alexander U. Valle-Pérez[1,2‡], Dana Alhattab[1,3], Rui Ge[1,2], Eter Othman[1], Panayiotis Bilalis[1], Abdulelah Alrashoudi[1], Antonio Cárdenas-Calvario[1], Alan Eduardo Avila Ramírez[1], Zainab N. Khan[1], Manola Moretti[1,2], Christian Baumgartner[4], and Charlotte A. E. Hauser[1,2,4*]

[1]Laboratory for Nanomedicine, Division of Biological and Environmental Science and Engineering, King Abdullah University of Science and Technology, Thuwal, Makkah Province, Saudi Arabia

[2]Computational Bioscience Research Center, Computer, Electrical and Mathematical Sciences and Engineering Division, King Abdullah University of Science and Technology, Thuwal, Makkah Province, Saudi Arabia

[3]Bio-ontology research group, Computer, Electrical and Mathematical Sciences and Engineering Division, King Abdullah University of Science and Technology, Thuwal, Makkah Province, Saudi Arabia

[4]Institute of Health Care Engineering with European Testing Center of Medical Devices, Faculty of Computer Science and Biomedical Engineering, Graz University of Technology, Graz, Styria, Austria

‡Current author affiliation: Marine Biology Research Division, Scripps Institution of Oceanography, University of California San Diego, San Diego, California, United States

***Corresponding author:**
Charlotte A. E. Hauser
(charlotte.hauser-funke@tugraz.at)

Citation: Valle-Pérez AU, Alhattab D, Ge R, *et al*. Mixed ultrashort peptide bioinks for improved 3D bioprinting of self-healing trachea-like constructs. *Int J Bioprint*. 2025;11(6):472-498. doi: 10.36922/IJB025320317

Received: August 7, 2025
Revised: September 16, 2025
Accepted: September 24, 2025
Published online: September 26, 2025

Copyright: © 2025 Author(s). This is an Open Access article distributed under the terms of the Creative Commons Attribution License, permitting distribution and reproduction in any medium, provided the original work is properly cited.

Publisher's Note: AccScience Publishing remains neutral with regard to jurisdictional claims in published maps and institutional affiliations.

Abstract

Concerns related to the trachea frequently arise from obstructive conditions and occlusions, such as tracheal stenosis, tracheomalacia, traumatic disruptions, and papillary thyroid carcinoma. These medical challenges underscore the need for new biomaterials to support tissue engineering for tissue regeneration. The advent of three-dimensional (3D) bioprinting technology has emerged as a pivotal advancement, facilitating the fabrication of patient-specific, biocompatible, cell-laden constructs. This technological advancement enables the controlled promotion of cell growth and tissue development, thereby offering a promising avenue for tissue regeneration. In this study, we developed mixed ultrashort peptide bioinks for the 3D bioprinting of a trachea-like construct that exhibits self-healing and elastic properties. We employed a stiffness prediction map (SPM) as an empirical tool to predict the physical characteristics and stiffness behavior of the mixed bioinks, thereby facilitating the optimization of the 3D bioprinting process. The SPM enabled the fine-tuning of these bioinks by identifying peptide mixtures that successfully mimic the natural stiffness of the perichondral niche microenvironment. These mixed bioinks successfully promoted mesenchymal stromal cell differentiation towards chondrocyte formation, thereby facilitating the biofabrication of elastic 3D-printed structures for trachea regeneration. Our bioinks exhibited remarkable printing resolution and mechanical properties while supporting cell growth and chondrogenesis. The bioprinted trachea-like model, cultured for up to 100 days, showed excellent mechanical properties, resulting a stable elastic biomaterial. This

study is the first to combine SPM with 3D bioprinting for the fabrication of a trachea-like model, supporting the development of advanced self-healing biomaterials for trachea tissue regeneration.

***Keywords*:** 3D bioprinting; Chondrocytes; Mesenchymal stromal cells; Self-healing biomaterials; Stiffness prediction map; Trachea-like model; Ultrashort peptide bioinks

1. Introduction

Advances in the development of biomaterials are desired to improve the reconstruction of physiologically relevant tissues and cellular grafts for tissue engineering and healthcare purposes.[1–3] The optimal biomaterials are biomimetic and can be used as models to simulate human tissue behavior, study cell growth and differentiation, investigate diseases, and potentially generate patient-specific non-immunogenic tissues for personalized medicine approaches. They also offer an alternative to *in vivo* animal models deployed in various tests, such as in drug screening assays.[4–8]

Three-dimensional (3D) bioprinting is an evolving technology that can be used to produce biomaterials replicating functional and biomimetic tissues and cellular grafts, advancing biomedical applications and healthcare. The technology has the potential to overcome donor shortages.[9] Conventional 3D printing falls into three main strategies: material extrusion, jetting, and vat polymerization.[10] On the other hand, 3D bioprinting technologies include cellular systems and are classified into nine main approaches: fused deposition modeling, stereolithography, inkjet, extrusion-based, laser-assisted, vat polymerization, magnetic, acoustic, and bioplotting.[10] Examples of 3D bioprinted constructs include organoids, human-scale mandible bone, ear-shaped cartilage, skeletal muscle, bone tissue, blood vessels, implanted vascular grafts, nose structures, trachea-like constructs, skin tissues, mouse brain structures, and full-size models of the human heart.[1,3,4,11–19]

In recent years, the use of computer-driven methods in bioprinting has led to significant progress.[9] Examples are the optimization of flow rates for peptide hydrogel-based 3D bioprinting, the integration of 3D bioprinting with multi-algorithm to identify microenvironment characteristics, the improvement of bioink formulation, and the tracking and classification of bioprinted organoids.[20–23] In addition, statistical procedures, such as response surface methodology (RSM), have been employed to optimize printing parameters in the bioprinting process. Applying RSM enables the construction of a dynamic printability window, which has recently been used for preparing polysaccharide-blended inks, optimizing printing speed and pressure conditions for silk–fibroin–gelatin-based constructs, developing *in situ* printability maps, and, more recently, statistically optimizing cell–hydrogel interactions in the area of green microbiology.[24–27]

Bioinks can be of natural or synthetic origin, which in turn determines the scaffold's biocompatibility, printability, and viscoelastic properties.[28,29] Natural-based bioinks include collagen, gelatin, chitosan, fibrin, silk, and alginate, while synthetic bioinks include polyethylene glycol (PEG), poly-N,N-dimethyl acrylamide (PDMA), acrylonitrile butadiene styrene, polylactic acid, polyvinyl alcohol (PVA), polyvinylpyrrolidone, polylactic-co-glycolic acid, and polycaprolactone (PCL).[10,30] Bioinks can also be mixtures of synthetic or natural and synthetic materials, resulting in the formation of multi-component hybrid bioinks, such as PLA–hydroxyapatite, PCL–alginate, PEG–gelatin, PCL–PEG, methacrylated hyaluronic acid–gelatin methacryloyl (GelMA), nanohydroxyapatite–PEG methacrylate, and PEG diacrylate–alginate, which could enhance biocompatibility and mechanical properties while affecting bioink printability.[30–33]

Peptide-based hydrogels are another class of promising bioinks for bioprinting due to their facile design, offering highly biocompatible and mechanically stable bioinks suitable as cellular scaffolds with a broad range of viscoelastic properties.[34] Peptide bioinks possess distinctive properties that integrate both natural and synthetic characteristics, rendering them particularly advantageous when compared with the other mentioned bioinks. Rationally designed ultrashort peptide compounds consisting of 3–7, preferably non-aromatic, amino acids are of particular interest due to their short sequence.[34,35] Through self-assembly, they form nano-fibrous networks and scaffolds, in the form of hydrogels, in aqueous solutions.[35,36] These thoroughly characterized self-assembling peptides exhibit a characteristic amphiphilic motif—consisting of a long hydrophobic tail of hydrophobic amino acids—and a short hydrophilic head group—mostly comprising a single hydrophilic amino acid. The peptide hydrogels' tunability makes them suitable

for 3D cell culture and tissue engineering, as they can span a broad range of viscoelastic properties, including hydrogel scaffold stiffness or softness, which in turn directly affects the material's storage and loss modulus, stress relaxation, and resistance to deformation under stress.[34] Previous studies have shown that peptide compounds containing lysine as a hydrophilic head group are excellent peptide bioinks, demonstrating the immediate solidification of cell-laden constructs under physiological salt conditions using extrusion-based 3D bioprinting, avoiding harsh situations such as UV exposure, reactive chemical additives, and elevated temperature conditions.[15,16,37]

Peptide hydrogels can also be used as biocontainment systems for clinical applications.[38] Peptide bioinks have been utilized in diverse applications, including 3D bioprinting of spheroids with induced pluripotent stem cells, printing brain models to study Parkinson's disease, modeling tissue to study leukemia, investigating colorectal cancer organoid development, printing ear models, and bioprinting large-scale constructs, as well as developing gel electrolytes, instant glues and hydrogel-based adhesives for environmental and biomedical applications.[12,15,16,39–46] This versatility has fueled growing interest in the use of multi-component bioinks for 3D bioprinting. Such bioinks can be formulated as mixtures from different ultrashort-peptide bioinks, forming peptide hybrid bioinks. For example, when combining the properties of various peptide bioinks that have different functional moieties, a previous study has formulated optimized mixed peptide bioinks as biofunctionalized peptide scaffolds to fabricate bioprinted colorectal organoids.[47]

Despite the progress made in bioprinting, several challenges still need to be addressed to produce fully functional tissues and cellular grafts.[48,49] These challenges include optimizing bioinks to promote more sophisticated bioprinting strategies without compromising cellular viability, ensuring the biocompatibility and structural stability of biomaterials, and better addressing biomimicry and functionality. Additionally, integrating vascularization into bioprinted structures, ensuring scalability, and replicating the complexity of organ architecture in bioprinted structures remain significant challenges.[14,48] More recently, there has been a growing interest in the 3D printing of smart and intelligent biomaterials, capable of reacting to both external and intrinsic stimuli for sustainability and healthcare applications.[50] Bioinks play a crucial role in forming the 3D structure with living cells, which can produce their own extracellular matrix (ECM) components during growth and development. To advance 3D bioprinted cellular grafts for further cell development, it is essential to establish a bioprinting strategy that combines all important factors, such as bioink materials, cellular components, and an optimal bioprinting strategy. Therefore, ongoing research is focusing on advanced bioprinting processes using optimized biomaterials with scalable, functional, biocompatible, and biomimetic characteristics to mimic tissues and cellular grafts.

There is a need to develop alternative tracheal replacements using tissue engineering technologies to advance the treatment and rehabilitation of patients with tracheal pathology.[51] Therefore, 3D printing and bioprinting technologies have been applied to engineer materials (e.g., polymers of synthetic origin) and biomaterials (e.g., biomimetic and biocompatible living materials) for tracheal tissue engineering, such as constructing artificial organs for the trachea. Although synthetic materials may exhibit strong structural robustness, they often have lower cell biocompatibility and a higher chance of inducing immune rejection. Conversely, biomaterials may exhibit high biocompatibility and low immune response, but have insufficient mechanical properties.

Remarkable progress has been made in the 3D printing of trachea-like constructs. For example, the 3D bioprinting of trachea-mimetic cellular construct with clinically relevant size has been performed through a two-step printing strategy and a bioink that consists of PCL-based thermoplastic polymer; the long segmental tracheal replacement has been conducted using PCL and collagen bioink mixture; the development of biomimetic trachea through a modular ring strategy with poly(sebacoyl diglyceride) and PCL bioink mixture; the dual-nozzle extrusion bioprinting of cartilage-vascularized fibrous tissue-integrated trachea with photo-cross-linkable GelMA and chondroitin sulfate methacrylate bioink mixtures; and the bioprinting of patient-matched trachea with PCL and HyStem®-HP hydrogel bioinks hydrogel bioinks.[13,52–55] Alternative non-printing strategies include the use of fully synthetic polymers and the bioengineering of tracheal prostheses with autologous chondrocytes and decellularized trachea scaffolds.[56,57] Nevertheless, there are still bottlenecks that limit the translation of bioengineered tracheostomies for medical applications. These limitations include insufficient material mechanics (e.g., material weakening over time and longitudinal rigidity), lack of biomimetic properties (e.g., low cell density, mucous accumulation, and lack of epithelial lining), adverse immune response (e.g., inflammation and fibrosis), biomaterial infection (e.g., contamination during cultivation), and low functionality (e.g., uniform geometries and transmural pressures).[58–62]

This study employed the stiffness prediction map (SPM) to formulate mixed ultrashort peptide bioinks for extrusion-based robotic 3D bioprinting. The approach

allows the selection of peptide scaffolds with initial stiffness supportive of stromal cell differentiation into chondrocytes, enabling the development of customizable bioinks suitable for 3D bioprinting. SPM enhanced the ability to assess the rheological properties of mixed ultrashort peptide hydrogels, allowing robust evaluation of materials' stiffness and accelerating mesenchymal stromal cell (MSC) differentiation into chondrocytes. Through SPM, we identified and developed three mixed ultrashort-peptide bioinks that, in addition to being highly biocompatible, exhibited diverging viscoelastic properties compared to bioinks made from single peptides. Additionally, the mixed bioinks promoted the formation of chondrogenic cell nodules in 3D bioprinted constructs cultured for 28 days, as evidenced by changes in gene expression and morphology. Based on these results, we selected the optimal-performing bioink in terms of printability and cell-scaffold interaction to bioprint a trachea-like model. The resulting construct exhibited accelerated self-healing (due to the presence of cells and their subsequent enrichment of the hydrogel scaffold with ECM components), structural stability, and remarkable elastic properties, highlighting it as a promising self-healing biomaterial for tracheal tissue regeneration. This study introduced a statistical cutting-edge approach to optimizing mixed peptide bioinks for 3D bioprinting, enabling automated production of stable and self-healing cellular constructs for long-term culture.

2. Materials and methods

2.1. Peptide synthesis

N- and C-terminus protected peptides Ac–Ile–Ile–Cha–Lys–NH_2 (IIZK) and Ac–Ile–Ile–Phe–Lys–NH_2 (IIFK) were synthesized through solid-phase peptide synthesis using a CS136X synthesizer (CSBio, USA). After synthesis, the peptides were removed from the resin using a mixture of 95% trifluoroacetic acid, 2.5% tri-isopropyl silane, and 2.5% water at room temperature for 2 h. The peptide was then precipitated by adding cold diethyl ether to the peptide solution and kept overnight at 4°C. The precipitated peptide was separated from the supernatant by centrifugation at 5000 rpm for 5 min using Eppendorf 5810R (Eppendorf, Germany). Finally, the peptide was purified using reverse-phase high-performance liquid chromatography with a C-18 column (2–98% acetonitrile in 15 min) at a flow rate of 20 mL/min and collected at a yield of over 60%.

2.2. G-code design and slicing

The 3D models were configured with computer-aided design in SolidWorks® version 2024 (Dassault Systèmes, USA), optimized with Slic3r version 1.3.0 (https://slic3r.org/), and translated into G-codes using the Repetier-Host software 2.3.2 (Hot-World GmbH & Co. KG, Germany).

2.3. Cell culture

Human bone marrow MSCs were cultured with Minimum Essential Medium (MEM)-α and supplemented with 10% mesenchymal stem cells (MSC-qualified) fetal bovine serum (FBS), 1% penicillin/streptomycin, and 1% GlutaMAX (Thermo Fisher Scientific, USA). The cells were thawed, cultured, and subsequently incubated at 37°C with 5% CO_2, and were sub-cultured when reaching 95% confluency using 0.25% trypsin.

2.4. Bioink preparation

Peptide powders were weighed at different peptide ratios (see Table 1) with a Mettler Toledo analytical balance (XPR204DUE, Switzerland). Initially, the measured first peptide type was added to a 2 mL glass vial, followed by the addition of the second peptide type to the same vial. The glass vial was sealed with a cap, and the mixed peptide powder was gently vortexed for 30 s. A class II biological safety cabinet was sterilized by decontaminating surrounding surfaces with 70% ethanol and UV irradiation for 30 min to ensure sterile working conditions. Subsequently, the mixed peptide-powder-containing glass vial cap was removed in the biosafety cabinet, and the UV light was applied for 1 h to prevent external contamination. Then, 900 µL of Gibco™ cell culture grade distilled water (Thermo Fisher Scientific, USA) was added to the vial, and the mixture was vortexed for 30 s to obtain a homogeneous solution, followed by sonication for 15 min to remove air bubbles. The resulting bioinks were used for subsequent 3D bioprinting experiments.

2.5. 3D bioprinting

Bioprinting experiments were conducted using a robotic 3D bioprinter (Dobot Magician, Dobot, China) composed of a four-degrees-of-freedom robotic arm, a custom-designed dual-coaxial nozzle, microfluidic pumps, and a stirring hot plate (RCT basic, IKA, Germany). The robotic arm was interfaced with Repetier-Host. The printing files were designed using SolidWorks and sliced into G-code through the Slic3r and Repetier-Host software. The used dual-coaxial nozzle was fabricated according to the literature.[12] The commercial microfluidic pumps were controlled simultaneously using the automated pulse mode with square waves.[63] According to the viscosity and surface tension results, flow rates were identified to extrude the formulated mixed ultrashortpeptide bioinks with minimal clogging and clumping during the extrusion-based bioprinting process. The optimized pumping flows were 40–45 µL/min (peptide solution), 15–20 µL/min (5× phosphate-buffered saline [PBS]), and 15 µL/min (1× PBS with cells) for each of the pumps, respectively. It is essential to highlight that the interaction between PBS and peptide solution within the nozzle forms the gel

Table 1. State-of-the-art peptide-based trachea engineering and bioinks formulation

Peptide-based trachea-like construct	Mixed peptide bioink	Ratio	Concentration (mg/mL)			Molarity (mM)			Reference
			IIZK	IIFK	IZZK	IIZK	IIFK	IZZK	
Extrusion-based bioprinting of a 3.0-cm-high, 2.2-cm-diameter, self-healing, elastic human trachea-like model that is cultured for up to 100 days with hBM-MSCs and MSC-derived chondrocytes. The 3D-printed structures exhibit excellent printability, high resolution, low clogging, and strong structural rigidity.	Bioink 1	3:1	7.1	2.4	–	12.5	4.3	–	This work
Extrusion-based bioprinting of a 1.36-cm-high, self-healing, small-diameter trachea-like model that is cultured for up to 28 days with hBM-MSCs and MSC-derived chondrocytes. The 3D-printed structures exhibit excellent printability, high resolution, low clogging, and strong structural rigidity.	Bioink 2	1:1	4.1	4.1	–	7.2	7.2	–	This work
Extrusion-based bioprinting of a 1.39-cm-high, self-healing, small-diameter trachea-like model that is cultured for up to 28 days with hBM-MSCs and MSC-derived chondrocytes. The 3D-printed structures exhibit excellent printability, high resolution, and minimal clogging, but with reduced structural stability.	Bioink 3	1:3	2.4	7.1	–	4.2	12.6	–	This work
Extrusion-based bioprinting of 1-cm-high, small-diameter cylinders that are cultured for up to 24 and 30 days with HDFn and hBM-MSC cells, respectively. The 3D-printed constructs exhibit sagging issues, resulting in low printability.	Single peptide IIFK	–	13.0	–	–	23.5	–	–	[12]
Extrusion-based bioprinting of 3.8-cm-high, small-diameter cylinders that are cultured for up to 24 and 30 days with HDFn and hBM-MSCs, respectively. The 3D-printed constructs exhibit superb printability, although potential clogging issues arose due to bioink overgelation.	Single peptide IIZK	–	–	13.0	–	–	23.1	–	[12]
Extrusion-based bioprinting of a 4-cm-high, small-diameter cylinder that is cultured for up to 30 days with hBM-MSC-derived chondrocytes. The 3D-printed constructs exhibit superb printability, although potential clogging issues arose due to bioink overgelation.	Single peptide IZZK	–	–	–	13.0	–	–	22.88	[12]
Extrusion-based bioprinting of a 1-cm-high, 1-cm-diameter cylinder that was cultured for up to 14 days with hBM-MSCs and MSC-derived chondrocytes. The 3D-printed constructs exhibit superb printability, although potential clogging issues arose due to bioink overgelation.	Single peptide IIZK	–	13.0	–	–	–	23.1	–	[73]
Extrusion-based bioprinting of a 3.8-cm-high, small-diameter cylinder that was cultured for up to 14 days with hBM-MSCs and MSC-derived chondrocytes. The 3D-printed constructs exhibit superb printability, although potential clogging issues arose due to bioink overgelation.	Single peptide IZZK	–	–	–	13.0	–	–	22.88	[73]

Abbreviations: hBM-MSC, human bone marrow-derived mesenchymal stromal cell; HDFn, human dermal fibroblast cells.

material for extrusion-based bioprinting. The cells were concentrated in 500 µL of FBS, MSC-qualified, and slowly pushed throughout the tubbing. Transparent square cover slides were thoroughly washed in 70% ethanol and left under UV irradiation for 30 min. The bioprinting process was performed inside a class II biological safety cabinet. Tweezers were sterilized using MLS-3781L autoclave (Panasonic, Japan) at 121°C for 15 min.

2.6. Printability and shape fidelity assessment

The mixed ultrashort peptide bioinks were 3D-printed into trachea-like structures. The ImageJ software version 1.54p (https://imagej.net/ij/) was used to calculate the width and height of the samples. Photographs were taken from the

side and from the top, with a calibration ruler included in the frame to calibrate pixel dimensions against actual measurements.

2.7. Chondrogenic differentiation

Bioprinted constructs were incubated at 37°C, supplemented with 5% CO_2 and MEM-α for 7 days. Afterward, chondrogenic media (PT-3925) and tumor growth factor (TGF)-β3 (PT-4121) were mixed and added (until completely covering the structures), and the cultures were maintained for 28 days with medium exchanged every 2 days. The chondrogenic media consisted of 1 mL dextrose (PT-4130G), 2 mL ascorbate (PT-4131G), 2 mL insulin–transferrin–selenium with supplements (PT-4113G), 2 mL pyruvate (PT-4114G), 2 mL proline (PT-4115G), 200 µL gentamicin sulfate–amphotericin (GA-1000; PT-4505G), and 4 mL *L*-glutamine (PT-4140G). The lyophilized TGF-β3 was prepared by adding 200 µL of sterile 4 mM hydrochloric acid (supplemented with 1 mg/mL bovine serum albumin) to 2 µg TGF-β3, and aliquots were stored at −80°C. All of these reagents and media were purchased from Lonza (Switzerland).

2.8. RNA extraction and quantification

Total RNA was extracted using Trizol (15596026, Thermo Fisher Scientific, USA) and Qiagen RNeasy Mini kit (74104, Qiagen, USA). The 3D bioprinted samples were digested by adding 2 mL of TRIzol reagent, mixed through pipetting, and stored at −80°C until further processing. The samples were dissolved at room temperature for 5 min, and 200 µL of chloroform per mL of TRIzol was added to each sample. They were vortexed for 20 s and centrifuged (Centrifuge 5424 R, Eppendorf, Germany) at 10,000 g for 18 min at 4°C. The aqueous phase was carefully removed and transferred to sterile RNAse-free microtubes, and an equal amount of RNA-free EtOH was added. The samples were inverted three times, loaded into the RNeasy columns, and centrifuged for 30 s at 8000 g. The flow-through was discarded. Then, 700 µL of RW1 buffer was added to the columns and centrifuged for 30 s at 8000 g. The columns were transferred to new collection tubes, and 500 µL of RPE buffer was added. The samples were centrifuged for 30 s at 8000 g. Again, 500 µL of RPE buffer was added, and samples were centrifuged for 2 min at 8000 g. The flow-through was discarded. The columns were centrifuged for 1 min at 8000 g. Columns were transferred to new collection tubes, and 35 µL of RNase-free water was added directly to the membrane. Samples were left at room temperature for 1–2 min and then centrifuged at 8000 g to elute the RNA. The RNA samples were quantified by measuring 2 µL from each sample using the Nanodrop 2000 spectrophotometer instrument (Thermo Fisher Scientific, USA) and were immediately stored at −80°C. The RNaseZap cleaner (AM9780, Invitrogen, USA) was used during the entire experiment.

2.9. Complementary DNA synthesis

The RNA was reverse-transcribed into complementary DNA (cDNA). First, the extracted RNA samples were normalized (**Equation I**). Subsequently, the SuperScript™ VILO™ Master Mix (11755-050, Thermo Fisher Scientific, USA) was used for cDNA synthesis. A 20 µL total reaction volume was prepared by adding 4 µL Master Mix and 5µL normalized RNA, then filling to 20 µL with nuclease-free water. The samples were placed in a thermomixer (Eppendorf ThermoMixer® C, Germany) with incubation cycles: 25°C for 10 min, 42°C for 90 min, and 85°C for 5 min. The cDNA was diluted at a 1:5 ratio by mixing 20 µL of cDNA with 80 µL of nuclease-free water. Aliquots were stored at −20°C.

$$Normalized\ RNA\ volume = \frac{800\ ng}{Extracted\ RNA\ in\ ng\ per\ \mu L} \quad \text{(I)}$$

2.10. Quantitative polymerase chain reaction for gene expression analysis

The quantitative polymerase chain reaction (qPCR) was performed using the TaqMan gene expression assay (Table 2) and TaqMan Fast Advanced master mix (4444557, Thermo Fisher Scientific, USA). Briefly, a total volume of 150 µL solution, composed of 100 µL master mix, 10 µL TaqMan probe, and 40 µL nuclease-free water, was added to each well and mixed. Subsequently, 2.5 µL of the diluted cDNA was added per well. The reverse transcription-qPCR was performed using the QuantStudio 3, 0.1 mL instrument (Thermo Fisher Scientific, USA) with thermal cycling parameters: 50°C for 2 min, 95°C for 2 min, and 40 cycles of 95°C for 1 s and 60°C for 20 s.

2.11. Viscoelastic characterization

The viscoelastic properties of the peptide hydrogels, including mechanical stiffness, viscosity, and thixotropy, were analyzed using the Ares-G2 Rheometer (TA Instruments, USA) equipped with an advanced Peltier system (APS). The stiffness of the peptide hydrogels was measured using an 8-mm parallel plate with a gap of 1.5 mm between plates. The peptide concentrations were prepared according to the SPM's experimental design. The peptide hydrogel concentrations were prepared by mixing 135 µL of peptide solution with 15 µL of PBS in a 9-mm internal diameter Sigmacote-coated glass ring. The rings were kept overnight inside Petri dishes at room temperature,

Table 2. TaqMan probes for gene expression

Gene	Catalog number of TaqMan probe	Catalog number
Collagen I (*COLI*)	Hs00164004_m1	4331182
Collagen II (*COLII*)	Hs00264051_m1	4331182
Collagen X (*COLX*)	Hs00166657_m1	4331182
Aggrecan (*ACAN*)	Hs00202971_m1	4331182
SOX9	Hs00165814_m1	4331182
SOX5	Hs00374709_m1	4331182
RUNX2	Hs01047973_m1	4331182
ALPL	Hs01029144_m1	4331182
CEBPB	Hs00942496_s1	4331182
PPARG	Hs01115513_m1	4331182
GAPDH	Hs99999905_m1	4448490

surrounded by water and tightly sealed to avoid dehydration. The viscoelastic properties were analyzed through three successive tests: time-sweep, frequency-sweep, and amplitude-sweep. The time-sweep test was first performed for 5 min with an angular frequency and a strain of 1 rad/s and 0.1%, respectively. The frequency-sweep test was subsequently performed on the sample with a range of angular frequency of 0.1–100 rad/s and the same strain of 0.1%. The amplitude-sweep test was performed by applying a gradual strain increase from 0.01 to 100% at 1 rad/s angular frequency. The interpolation from the oscillation strain curves was performed using the trace interpolation tool in the OriginPro software (OriginLab, USA). The thixotropic properties of the mixed ultrashort-peptide bioinks were measured using an angular frequency of 1 rad/s and a sampling rate of 1 pts/s. An initial strain of 0.1% was applied to the peptide hydrogel for 5 min. Then, the peptide hydrogel was exposed to different strains ranging from 100% (1 min) to 0.1% (10 min) with 11 oscillation cycles. The total duration of the thixotropy test for each sample was 3600 s.

2.12. Measurement of self-healing properties

The self-healing capabilities of the 3D bioprinted structures were analyzed using the Ares-G2 Rheometer equipped with APS and an 8 mm parallel plate. The 3Dbioprinted structures were placed on top of the parallel plate, and the self-healing properties of the mixed ultrashort peptide bioinks were measured with an angular frequency of 1 rad/s and a sampling rate of 1 pts/s. An initial strain of 0.1% was applied to the peptide hydrogel for 5 min. Then, the peptide hydrogel was exposed to different strains ranging from 100% (1 min) to 0.1% (10 min) with 11 oscillation cycles. The total duration of the thixotropy test for each sample was 3600 s.

2.13. Design of experiments and response surface methodology

The Minitab version 21.4.1 software (Minitab, USA) was used to derive an initial model representation for the interaction between the IIZK and IIFK peptides and their measured responses regarding stiffness. First, experiments were designed according to the RSM. A central composite design for two continuous factors (IIZK and IIFK) was selected here. The design consisted of one center point, four cube points, and four axial points, resulting in a total of nine points to build the matrix using a face-centered design with an α of 1 (Figure S1). The design levels considered the lowest and highest values of 2 and 8 mg/mL, respectively. This concentration range was selected based on the printability window for extrusion-based bioprinting with the IIZK and IIFK bioinks reported in previous studies to prevent clogging during the bioprinting process.[12] The performance of four RSM models was evaluated, considering their R^2, adjusted R^2, predicted R^2, and standard deviation to select the optimal mathematical model for fitting the data (Tables S2 and S3; Figures S2–S5). The top-performing model was chosen for fitting the experimental data; the design of experiments (DOE) and analysis of variance (ANOVA) from the top-performing model are shown in detail in Tables S4 and S5. For each of the nine mesh points according to the design matrix (Figure S1), 20 samples were prepared and measured (n=20), resulting in 188 experimental rheology measurements. The data distribution of the rheology measurements was visualized in Figure S6. Following experimental measurements, data preprocessing was carried out to identify potential outliers using boxplot visualization, corroborated by Z-score and mean absolute deviation (MAD) methodologies. The MAD threshold values for outlier detection were calculated (Table S6) according to Equations II and III.[64]

After identification, outliers were removed from the dataset and substituted with new measurements. Subsequently, the processed dataset was fed into Minitab to derive an RSM-based mathematical modeling equation that represents the proposed 3D representation of the DOE (Equation IV) according to the experimental data and DOE from the top-performing model (Tables S2, S3, & S7). The data distribution, residuals, and adjustment to the modeling equations can be found in the supplementary information (Figures S2–S6; and Tables S2–S7). Further information on the RSM methodology can be found in the literature that applied RSM to model the mixing of different materials in the formulation of bioinks.[27,65,66] Lastly, the 3D representation of the SPM was plotted and visualized in MATLAB version R2024b (MathWorks, USA).

$$\textit{Outliers maximum threshold value} = \textit{median}\ (X) + (\alpha \times MAD) \quad \text{(II)}$$

$$\textit{Outliers maximum threshold value} = \textit{median}\ (X) + (\alpha \times MAD) \quad \text{(III)}$$

where X was the n original observations, set to 3 according to the literature.

$$\gamma = (\pm \delta_0) \pm \delta_1\alpha \pm \delta_2\beta \pm \delta_3\alpha^2 \pm \delta_4\beta^2 \pm \delta_5\ (\alpha \times \beta) + \varepsilon \quad \text{(IV)}$$

where γ represents the storage modulus (response in Pa), δ (0–5) represents the obtained constants from the statistical equation from the fit of the experimental data, α represents peptide 1 (factor 1 in mg/mL), β represents peptide 2 (factor 2 in mg/mL), and ε represents the total error from the model

2.14. Measurements of the bioinks' viscoelastic properties

The viscoelastic properties of the bioinks were analyzed using the Ares-G2 Rheometer equipped with APS. Viscosity measurements were conducted at 25°C using a 25 mm parallel plate geometry and a 0.5 mm gap between plates. The bioinks were prepared by mixing IIZK and IIFK at a 1:1, 1:3, or 3:1 ratio to a final concentration of 10 mg/mL. Viscosity was assessed in both solution and gel states. For gel measurements, 225 µL of bioink solution was placed on the Peltier plate, followed by the addition of 25 µL 10× PBS, and allowed to react for 10 min before performing a shear rate sweep (0.01–50/s). For solution measurements, 250 µL of bioink solution was placed on the Peltier plate and directly measured.

2.15. Gelation tests

Gelation tests were performed following established protocols for peptide hydrogel formation.[12] Peptide powder was dissolved in 900 µL of Mili-Q water and vortexed until fully dissolved, and solubility was recorded. To induce gelation, 100 µL of 10× PBS (without Ca^{2+} and Mg^{2+}) was added to the solution. The vial was left at room temperature, and gel formation was monitored visually to determine gelation time.

2.16. Thermomechanical characterization

Thermogravimetric analysis (TGA) was performed on dried samples (10 mg initial weight) using a TGA 5500 (TA Instruments, USA). Samples were heated in platinum pans from 25 to 700°C at 10°C/min under a N_2 atmosphere. Weight loss curves were plotted, and first derivatives were calculated. Subsequently, differential data were smoothed using the Savitzky–Golay method. All data plotting, derivative calculations, and signal processing were performed in the OriginPro 2022b software.

2.17. Measurement of surface tension

A force tensiometer (Kruss K100 MK2, KRÜSS GmbH, Germany) was used to measure the surface and interfacial tension of samples. A custom glass probe was prepared by cutting the glass to the desired size of 15×25×1 mm. The tensiometer was stabilized at room temperature prior to use. For each measurement, 3 mL of peptide solution (10 mg/mL) was placed in a 10 mL beaker, and the probe was gently placed on the surface of the liquid. Detection parameters were set to a speed of 10 mm/min, sensitivity of 0.005 g, and immersion depth of 1 mm.

2.18. Phase contrast and epifluorescence microscopy

Kinetic imaging experiments were performed using the DMI3000 B phase contrast microscope (Leica, Germany) on days 5, 10, 15, and 28. Photographs and videos of the full-sized trachea-like ring were recorded using the EVOS M7000 epifluorescence microscope (Invitrogen, USA).

2.19. Assessment of cell viability

The viability of the bioprinted trachea-like structures was assessed using the live/dead cell viability cytotoxicity kit (L3224, Thermo Fisher Scientific, USA). Calcein acetoxymethyl ester was used to detect live cells, while ethidium homodimer-I was used for dead cells. Media was discarded, and the structures were subsequently washed three times with 1× PBS. Staining solution, consisting of 3 µL calcein, 6 µL ethidium homodimer, and 3 mL 1× PBS, was prepared and added until the structure was submerged. The samples were covered with aluminum foil and left in an incubator for 1 h. After incubation, the staining solution was discarded, and 3 mL of 1× PBS was added. The entire procedure was carried out under dark conditions to avoid

photobleaching. The structure viability was assessed after 15, 24, and 100 days.

2.20. Cytoskeleton staining

Cells were previously fixed using methanol-free formaldehyde. The media were removed for fixation, and constructs were washed three times with 1× PBS. Then, 1 mL of 16% (w/v) formaldehyde solution was diluted with 3 mL of 1× PBS, resulting in 4% formaldehyde. The construct was incubated at room temperature for 1 h, followed by three washes with 1× PBS, then covered with parafilm, and stored at 4°C. Next, a blocking buffer—consisting of 1.25 mL FBS, 25 µL TWEEN 20, and 5 mg sodium azide—and a cytoskeletal buffer—composed of 125 µL Triton 100, 15.2 mg $MgCl_2$, and 2.6 g sucrose—were prepared and filled to 25 mL using 1× PBS. For staining, both solutions were placed on ice for 10 min. Construct media were removed, and cold cytoskeletal buffer was added and incubated for 5 min. Then, the construct was washed twice with 1× PBS. Subsequently, the blocking solution was added, and the sample was left incubating at room temperature for 1 h. The primary antibody solution, consisting of actin-phalloidin, was diluted by mixing 10 µL of the antibody in 4 mL of 1× PBS. Samples were immersed in the primary antibody solution and incubated for 1 h at room temperature while covered with aluminum foil. Then, the solution was removed, and the construct was washed with 1× PBS, followed by adding 4 µL of 4',6-diamidino-2-phenylindole (Thermo Fisher Scientific, USA) for every mL of the final volume, and then incubating for 5 min at room temperature with minimal light exposure.

2.21. Confocal imaging

The bioprinted constructs were imaged using a laser scanning confocal microscope (LSM 880 with Airyscan, ZEISS, Germany). Z-stack and 2D images were collected throughout the experiment using a pinhole size of 1.25 airy units. Images were postprocessed using the ZEN (black edition) software (ZEISS, Germany).

2.22. Scanning electron microscopy imaging of cell-laden bioprinted scaffolds

Peptide scaffolds were fixed with 25% electron microscopy-grade glutaraldehyde. The media was removed, and the construct was washed three times with 1× PBS. Then, 1 mL of 25% glutaraldehyde was diluted in 9 mL of 1× PBS to a final concentration of 2.5% glutaraldehyde solution. The solution was added to the sample and incubated in the fume hood for 1 h, followed by washing with 1× PBS. Then, 2 mL of 4% osmium tetroxide solution (Polysciences, USA) was mixed with 8 mL of 1× PBS to a final osmium tetroxide concentration of 1%. The diluted osmium solution was added to the structure and incubated for 1 h under dark conditions. Then, the osmium solution was discarded, and the samples were washed three times with dH_2O for periods of 15 min each. Subsequently, the samples were dehydrated by gradually increasing ethanol concentrations (20, 40, 60, and 80% in 2 mL dH_2O for 5 min periods each). The sample was finally dehydrated in 2 mL of 100% ethanol for 2 h. For 3D bioprinted samples, dehydrated gels were mounted on 12-mm-outer-diameter PELCO Tabs™ (Ted Pella, Inc., USA) and dried using the Critical Point Dryer CPD300 (Leica, Germany). Immediately after CPD drying, the samples were sputter-coated with a 5 nm Pt layer using the K575X Sputter Coater (Quorum Technologies, UK) under 20 mA for 40 s. Scanning electron microscopy (SEM) images were acquired using the Teneo SEM (FEI Company, USA) with an accelerating voltage of 3kV and a current of 13 pA for cell imaging.

2.23. Scanning electron microscopy imaging of peptide fibers

Peptide bioinks were prepared at a concentration of 10 mg/mL. Then, 9 µL of peptide solution was mixed with 1 µL of 10× PBS on a silicon wafer. The bioinks were left at room temperature for 2 h in sealed containers and subsequently dehydrated through an ethanol gradient (20, 40, 60, and 80%, 5 min each). The bioinks were finally left in a 100% ethanol solution for 2 h. Subsequently, the dehydrated bioinks were dried using the Automegasamdri-916B series C critical point dryer (Tousimis, USA). The samples were mounted on an SEM stub using silver paste and sputter-coated with a 5-nm-thick iridium layer. SEM images were acquired using the Teneo EM with an accelerating voltage of 5kV and a current of 50 pA.

2.24. Atomic force microscopy

Atomic force microscopy (AFM) topography data were collected on three mixtures of the peptides at IIZK-to-IIFK ratios of 3:1, 1:1, and 1:3, with final concentrations of 9.39, 8.12, and 9.39 mg/mL, respectively. The peptides were dissolved in Milli-Q water, and 10 µL of the solution was cast on a freshly cleaved mica sheet and dried immediately with an N_2 stream. The samples were immediately measured using a JPK Nanowizard III (Bruker, USA) and a calibrated AFM probe (AC240TS, Olympus, Japan) with a nominal resonance frequency of 65 kHz and a spring constant of 0.2 N/m. Several images were acquired through a scan size of 2×2 µm and a 1024×1024 lines per pixel resolution. The topography scans were then processed by applying a three-point surface flattening and assigning the lowest value to zero. A mask was applied to the fibers to isolate them for 1D height analysis.

2.25. Raman spectroscopy

Raman spectra were acquired using a confocal Raman spectrometer (WiTEC Alpha 300R, Oxford Instruments, UK) with a backscattering configuration, a laser wavelength

of 532 nm, and a power of 12 mW at the source. In this context, the mixed ultrashort peptide bioinks were prepared at the following IIZK-to-IIFK ratios: 3:1, 1:1, and 1:3, with a final concentration of 10 mg/mL. The peptide hydrogels were immediately measured under the micro-Raman spectrometer, acquiring several spectra at different locations for each sample, with an integration time of 3 s per 10 accumulations. The acquired spectra were then averaged, cropped to the Amide I range from 1500 to 1800 cm^{-1}, baseline subtracted by endpoints weighing, and fitted with the most intense peak by a Voigt function in the 1660–1678 cm^{-1} range, which is specific for beta-sheet secondary structures. In this way, the fitting procedure was constrained to identify the Raman shift at which the strongest peak signal occurred.

2.26. Molecular dynamics simulations of peptide assembly

In this study, molecular dynamics (MD) simulations were employed to explore the self-assembly process of mixtures of IIZK and IIFK peptide molecules in an aqueous environment, focusing on fiber formation at the atomic level. Utilizing GROMACS 2018 (https://www.gromacs.org/index.html), the simulations leveraged the optimized potentials for liquid simulations force field to model interactions.[67,68] For the specific residue cyclohexylalanine (Z), we generated topology parameters using the LigParGen webserver (https://zarbi.chem.yale.edu/ligpargen/).[69] Water molecules were represented using the simple point charge extended model, and a 2-fs timestep was adopted for integrating motion equations. The simulations were configured with cubic boxes, applying periodic boundary conditions. The particle mesh Ewald method was used for long-range electrostatic interactions, while a cutoff of 1.4 nm was set for short-range non-bonded interactions.[70] The MD simulation process comprised three stages: energy minimization, equilibration, and production MD. Initially, energy minimization relaxed the peptide structures, ensuring a realistic starting point. Equilibration occurred in two phases, with the first phase number volume temperature (NVT ensemble) stabilizing temperature and the second number pressure temperature (NPT ensemble) stabilizing pressure. The production phase employed a Berendsen Barostat and a V-Rescale thermostat, maintaining a standard pressure of 100 kPa and temperature of 26.85°C over a total simulation duration of 100 ns (**Tables S8–S12**).[71,72] These simulations ran on 512 Intel Haswell cores (USA) at 2.3 GHz. For each peptide, three configurations were examined: assemblies of 4 or 5, 10, and 60 peptides. Peptides were evenly distributed within the simulation box, surrounded by water. More details regarding peptide concentration and number of peptides are reported in the Supplementary material (**Table S8**).

2.27. Statistical analysis

The TGA thermochemical characterization, viscosity, and surface tension results were performed in duplicate. 3D bioprinting experiments were performed in triplicate. The gene expression, thixotropic, and self-healing experiments were performed in duplicate. The rheological measurements for the SPM strategy consisted of 188 measurements. Subsequent statistical analyses for SPM (i.e., data distribution, experimental fitting and statistical modeling, DOE, ANOVA, residual plots, Pareto charts, and RSM) were performed using the Minitab software. For multiple comparisons, the Tukey test was used to determine the statistical significance of the population mean, with an alpha value of $p<0.05$, as determined by the OriginPro software (version 2024b). For outlier identification, the Z-score, MAD, and threshold limits were calculated as previously described in the DOE and RSM section. The derivative weight of the TGA data was calculated using the OriginPro software. Longitudinal and orthogonal profiles were applied for AFM image analysis. The dimensions of the 3D bioprinted trachea were analyzed using the ImageJ software. The SPM model was plotted and visualized using the MATLAB software.

3. Results and discussion

3.1. Stiffness prediction map for improved scaffold design of 3D bioprinted trachea-like constructs

To formulate mixed ultrashort peptide bioinks for 3D bioprinting of an elastic and self-healing trachea-like model, two ultrashort peptides, IIZK and IIFK, were selected due to their characteristic properties. We have previously reported on peptides IIZK and IIFK, demonstrating high mechanical strength with fast gelation kinetics for IIZK and a three-fold lower mechanical strength with slower gelation kinetics for IIFK, thereby rendering them suitable for stem cell growth and proliferation.[12] In that study, both peptides were used at a cost-effective low bioink concentration, printing over 3 cm large-scale structures containing human adult stem cells, which were differentiated into chondrocytes. In the present study, peptides IIZK and IIFK were used in combination with RSM to analyze numerous data from rheology measurements to predict stiffness conditions using SPM (Figure S1). The SPM supported the identification of mixture conditions between the two peptides, predicting the formulation of mixed peptide bioinks suitable for 3D bioprinting. Further details on the SPM's modeling and its application to identify specific stiffness regions to formulate peptide-based bioinks are available in the supplementary information (Figures S2–S8, Tables S2–S7). Using the mixed peptide bioinks, it was observed that printing was possible at significantly lower concentrations, using 27.77–37.54% less peptides, compared to when using single peptide bioinks. A mixed

peptide bioink was able to bioprint large-scale trachea-like structures with human-size diameter (Tables 1 & S1). The mixed peptide bioinks were then investigated for bioprinting cell-laden trachea-like constructs that contained either undifferentiated MSCs or chondrocytes differentiated from MSCs. All constructs demonstrated structural stability, elasticity, and self-healing properties. The overall process is schematically shown in Figure 1.

The importance of appropriately selecting the stiffness of the embedding material (bioink/scaffold) for stem cell differentiation—and its effects on cell compatibility, as well as its role in regulating cell development, interaction, and behavior—has been well documented.[74–77] We observed that IIZK showed higher stiffness than IIFK and that the stiffness of the individual bioinks increased with higher peptide concentrations (Figure S9). For the mixed ultrashort peptide bioinks composed of both IIZK and IIFK peptides, a proportional increase of IIZK remarkably enhanced the stiffness of the bioinks (Figures 2 & S8), suggesting that both peptides can simultaneously contribute to bioink stiffness without hindering individual fiber formation. This finding is consistent with prior studies showing that IIZK promotes a more robust fiber assembly than IIFK, primarily due to the characteristic residue cyclohexylalanine (Z).[12]

Due to the interactions between the two peptides, which significantly influence the stiffness of the resulting mixed peptide bioink (Figure S8), under certain mixing conditions, peptide IIFK can behave similarly to IIZK in terms of scaffold stiffness. This can be observed when mixing 2 mg/mL of IIZK with 8 mg/mL of IIFK, resulting in a stiffness of 29.3 kPa, comparable to the 28.4 kPa observed when the ratio was reversed (8 mg/mL IIZK with 2 mg/mL IIFK; Figure S6). In contrast, at lower peptide concentrations, the outcome differed: mixing 5 mg/mL IIZK with 2 mg/mL IIFK resulted in 17.1 kPa, whereas 2 mg/mL IIZK with 5 mg/mL IIFK resulted in 30.8 kPa. Here, the resulting scaffold stiffness is not the same even when containing the same overall amount of material (Figure S6). As shown in Figure 2D**,** a higher proportion of IIFK in the mixture resulted in a stiffness value comparable to pure IIZK. This tunable stiffness behavior aligns with our MD simulation results, where interchangeable peptide effects were observed and attributed to increased intramolecular bonding. Specifically, IIFK formed a higher number of intramolecular bonds during assembly, resembling mixtures with more IIZK (Figure S10). Taken together, these findings highlight that the combination of IIFK and IIZK produces a non-linear effect on the resulting storage modulus. Importantly, IIFK has a stronger influence on scaffold stiffness than IIZK (Figure S8). This emphasizes the importance of understanding the combined effects of different peptides when formulating peptide bioinks and suggests that modeling the interactions between these two peptides requires the consideration of non-linear components (e.g., curvatures by quadratic, polynomial, exponential, and logarithmic relationships).

At higher peptide concentrations, the mixed ultrashort-peptide bioinks showed increased stiffness. However, when IIFK was added to IIZK, the stiffness increase followed a non-linear behavior (Tables S2 & S3). This was supported by statistical analysis using the Pareto chart of standardized effects (Figure S8), demonstrating that the squared term of the model, $IIFK^2$, significantly contributed to the stiffness model, whereas $IIZK^2$ did not (Figure 2D). Therefore, when formulating mixed ultrashort peptide bioinks, it is crucial to consider the interaction between peptides, as they can lead to non-linear relationships.

RSM was used to analyze rheology measurements and develop an SPM for the selection of optimal bioink formulations with specific stiffness suitable for extrusion-based bioprinting of MSCs (Figure 2A). Additional details of the SPM's DOEs and ANOVA results are provided in Tables S4 and S5. To construct the peptide stiffness map for ultrashort peptide scaffolds, 188 rheological measurements were collected. The dataset was then pre-processed to identify outliers. An initial boxplot visualization test revealed six outliers (Figure 2B). Subsequently, the *Z*-score with a threshold of 2.5 and MAD identified one additional outlier (Figure 2C**,** Table S6). Comparison of the boxplot, *Z*-score (Figure 2D**)**, and MAD approaches confirmed the consistent detection of seven outliers, which were removed and replaced with new measurements. The SPM approach, incorporating IIZK and IIFK to model mixed ultrashort-peptide bioinks, is depicted in Figure 2D. Overall, this approach demonstrated high accuracy in predicting the stiffness map based on the proposed RSM equation, as shown by the strong agreement between experimental and predicted measurements (Table S7), and successfully identified several ultrashort peptide bioink formulations with specific stiffness values (Figures 2D & S7).

3.2. Identification, formulation, and characterization of mixed ultrashort peptide bioinks

In this study, IIZK and IIFK, differing by an exchange of only one single amino acid Z for F in the peptide sequence, were selected as model peptides for the SPM approach (Figure 3A). In a previous study, these peptides had demonstrated biocompatibility and characteristic stiffness properties, with IIZK being stiffer and IIFK being softer.[12] We assumed that, when using these two peptides to formulate bioink mixtures, it would potentially improve the stiffness tunability, which is important for cell

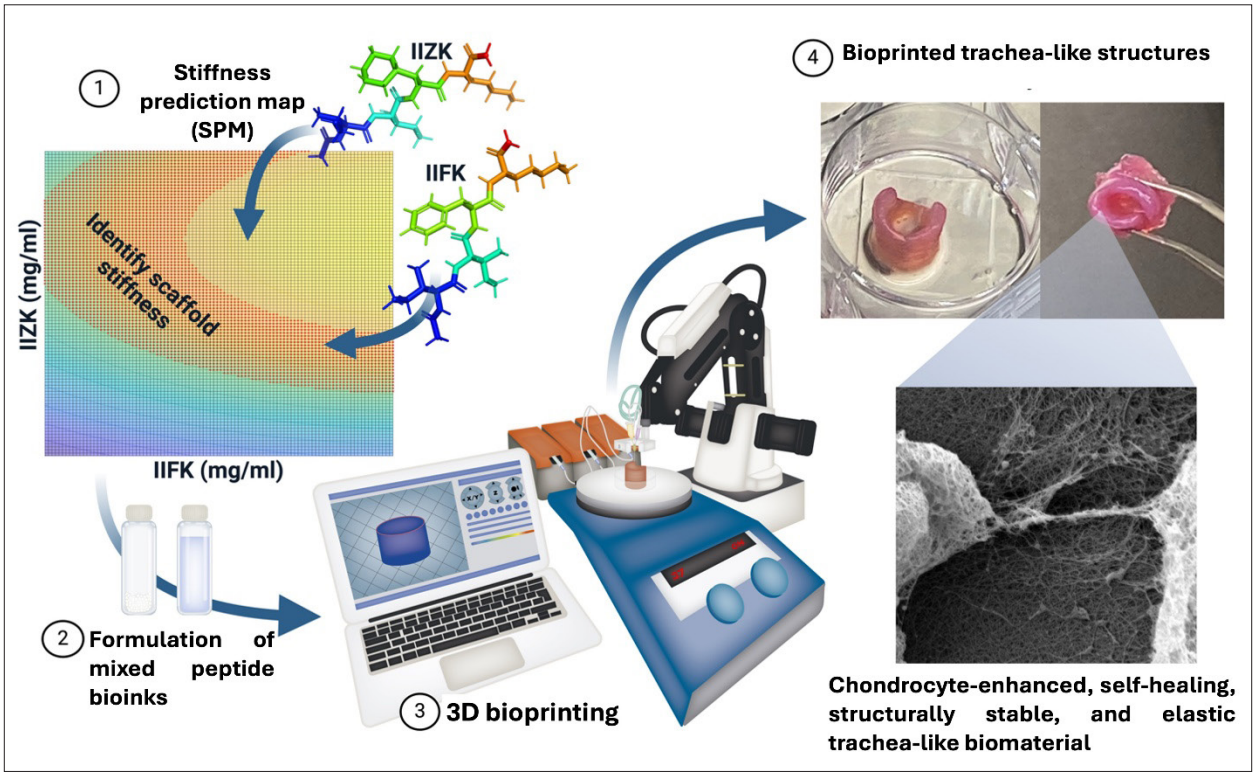

Figure 1. Schematic overview of the stiffness prediction map strategy supporting the formulation of optimized mixed ultrashort peptide bioinks for robotic extrusion-based 3D bioprinting of self-healing and elastic trachea-like constructs. Created with BioRender.com.

differentiation. Therefore, the SPM strategy was applied to formulate mixed ultrashort peptide bioinks with tailored stiffness to support chondrogenic differentiation, aiming to enable bioprinting of elastic and structurally stable constructs for tracheal regeneration. The stiffness range was selected based on the scaffold stiffness of the perichondral space, which has been reported as an ideal graft for repairing severe laryngotracheal stenosis due to its high pliability, chondrogenic capacity, mucosalization, and resistance to infection. Additionally, studies have shown that a stiffness of 30 kPa induced the formation of chondrogenic nodules and collagen type II production.[78–80] Therefore, the SPM was used to identify three potential mixed peptide compositions within a stiffness range of 24–34 kPa, closely resembling the chondrocyte stiffness microenvironment (Figure 3B & 3C, Table S13). Using peptides IIZK and IIFK as the underlying scaffold sequences, three mixed ultrashort peptide bioinks were identified and prepared for chondrogenic differentiation.

The SPM correctly predicted the experimental stiffness values of these bioinks to the actual measurements (Table S7), and they were congruent with the theoretical model accuracy (Table S3). Additional factors could further enhance prediction capabilities, such as considering the effects of temperature and pH on the gelation of peptide hydrogels. Stiffness variation in viscoelastic samples can arise due to several reasons, including the material of the rheometer geometries (e.g., stainless steel), instrument inertia, momentum diffusion artifacts, viscoelastic wave propagation (viscous or elastic), surface tension artifacts in rotational geometries, and secondary flows caused by purely elastic instabilities that violate the assumption of homogeneous shear deformation.[81] Therefore, there has been an interest in automated preparation of homogeneous bioinks in 3D bioprinting, which could further improve rheology-based data acquisition of viscoelastic samples.[82]

The selected bioinks exhibited different viscosities and surface tensions (Figure 3D & 3E). These properties have been highlighted as important parameters for the successful 3D bioprinting of bioinks.[83] In this study, the 3:1 IIZK:IIFK mixed peptide bioink exhibited a viscosity similar to that of the 1:3 IIZK:IIFK composition in suspension, suggesting that the 3:1 ratio would be less prone to clogging during extrusion-based bioprinting. Furthermore, both bioinks exhibited surface tensions of approximately 5 mN/m, which reduced bioink adhesion and supported smoother

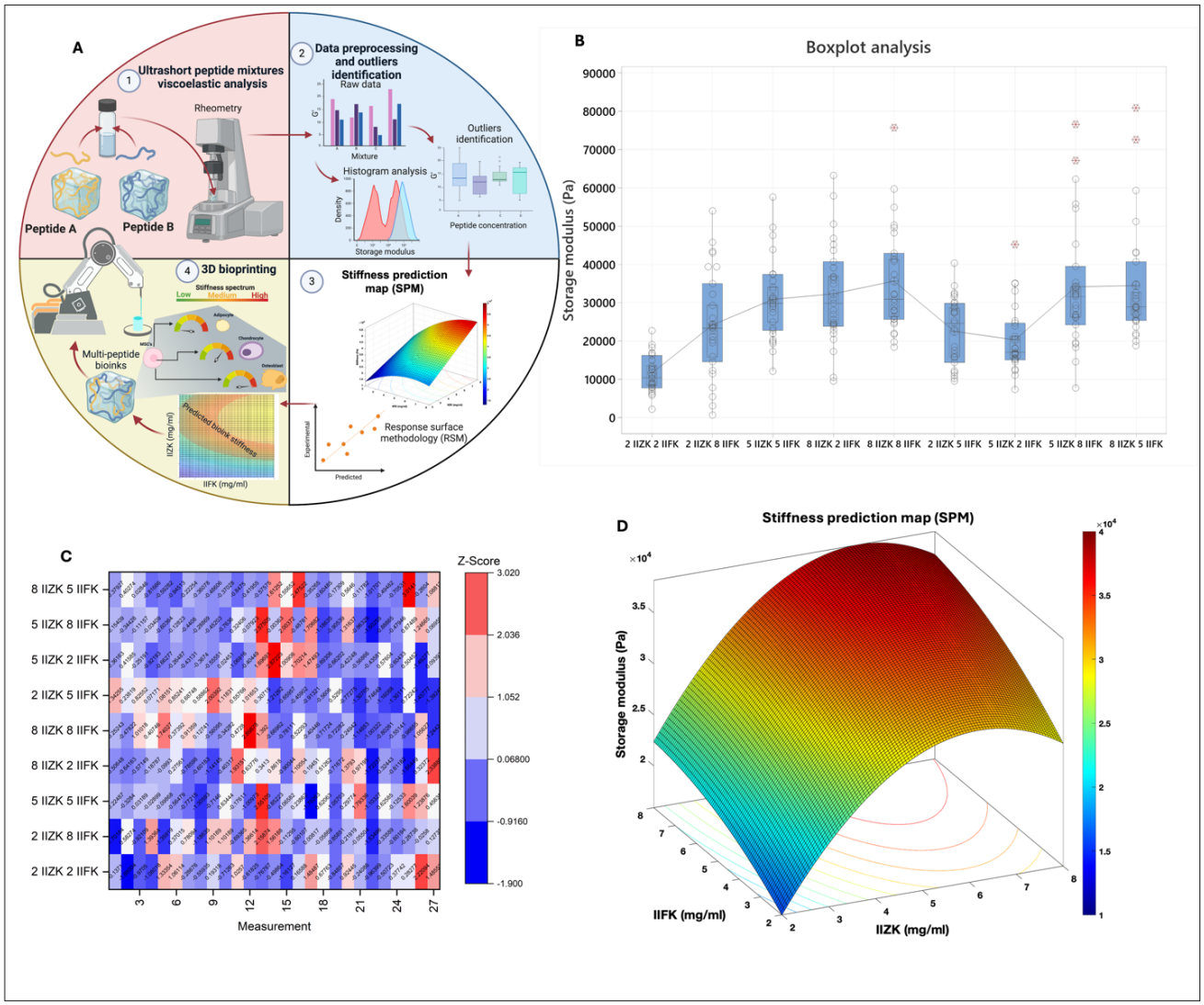

Figure 2. Stiffness prediction mapping of peptide bioinks for precise control of the 3D microenvironment stiffness. (A) Schematic representation describing the four steps in the SPM strategy for the development of mixed ultrashort peptide bioinks for extrusion-based 3D bioprinting. (B) Visualization of outliers through boxplot plotting. (C) Identification of outliers according to their *Z*-scores. (D) Stiffness prediction map to identify, predict, and formulate the stiffness of mixed ultrashort peptide bioinks. Figure 2A created with BioRender.com.

extrusion through the microfluidic tubing, ensuring compatibility with the extrusion-based bioprinter. In general, it was observed that bioinks containing higher amounts of IIFK resulted in higher viscosity, while those containing higher amounts of IIZK reduced the viscosity.

The mixed peptide bioinks formed stable fiber assemblies, with the number of intermolecular hydrogen bonds varying according to peptide ratios (Figures 3F & S9–S11, Tables S8–S12). SEM imaging confirmed the formation of fibers in all cases (Figure 3G). Our simulation results suggest that both IIZK and IIFK, when mixed, can form intra- and intermolecular bonds during peptide assembly (Figures S10 & S11). Furthermore, a higher amount of IIFK resulted in hydrogen bond numbers comparable to those of IIZK (Tables S9 & S10), while IIFK formed fewer random coil and more β-turn secondary structures during assembly (Tables S11 & S12). This suggests that IIFK, within mixed ultrashort peptide bioinks, can mimic the assembly behavior of IIZK, enabling high biocompatibility while retaining solid structural properties after bioprinting. This is interesting because IIFK-bioprinted structures have been reported to exhibit lower structural stability and resolution than IIZK-printed structures.[50] Meanwhile,

IIFK is known for excellent cytocompatibility during stem cell proliferation.[12] Therefore, it would be possible to retain both properties in the form of mixed ultrashort-peptide bioinks for extrusion-based bioprinting. Such cooperative assembly is commonly seen in ultrashort-peptide bioinks, where peptides of different properties can assemble into higher-order structures.[47] Moreover, this dual-peptide gelation highlights how molecular pairing tunes the stiffness–softness balance of the resulting bioinks (Tables S9 & S10). AFM topographical analysis of the peptide mixtures revealed a predominant nanofiber diameter of approximately 8.5 nm across all observed fibers (Figure 3H).

AFM topographical analysis of the peptide mixtures revealed different height profiles depending on peptide combinations: 3:1 IIZK:IIFK fibers had an average diameter of 6.54±0.92 nm, 1:1 IIZK:IIFK fibers averaged 7.06±0.49 nm, and 1:3 IIZK:IIFK fibers averaged 7.46±0.45 nm (Figures 3H, S12A–S12C, S13A–S13C, & S14A–S14C). In most cases, the supramolecular handedness of the fibers was not readily discernible, and no consistent helical pitch could be resolved, as can be observed from the sample longitudinal profiles provided in Figures S12D, S12E, S13D, S13E, S14D, and S14E. By contrast, in our previous investigations involving IIZK and IIFK, AFM topography demonstrated distinct helical pitches, with IIFK consistently forming left-handed nanofibers and IIZK forming right-handed ones. In this study, the nanofiber diameters were consistently smaller than those previously reported, which may reflect slower assembly kinetics of the two peptides.

Regarding the fibers of the peptide mixtures, the absence of discrete left-handed and right-handed supramolecular assemblies suggests that the IIZK and IIFK peptides co-assemble along the same nanofiber rather than forming distinct fibers. However, due to the inherent resolution limitations of the AFM technique and convolution effects between the AFM probe and the nanofiber surface, it is currently not possible to unambiguously resolve the precise arrangement of the peptide constituents within individual nanofibers. Additionally, Raman spectral analysis of the Amide I region revealed a predominant sharp peak in the range of 1660 cm^{-1}, typical of well-ordered amyloid-like nanofibers with β-turn secondary structure, a kinked structural variant of β-sheets. The slight differences in the values of the Raman peak shift were not significant and can be attributed to the instrument's resolution (Figure 3I). The solubility and gelation properties of the mixed ultrashort-peptide bioinks are provided in Table S13.

TGA was performed on mixed ultrashort peptide and single peptide bioinks to evaluate their composition under thermal changes. In Figure S15, a 5% reduction in weight was observed when heating from room temperature to 200°C, attributed to the evaporation of residual solvent and the release of H_2O within the crystalline arrangements, confirming the absence of adsorbed water or solvent molecules across all peptides.[65,84] Subsequently, a further 15% loss was observed when heating from 200 to 250°C in all samples, associated with progressive deamination, decarboxylation, and depolymerization resulting from peptide bond breakage.[85,86] A further 65% loss occurred between 300 and 340°C due to primary decomposition, followed by secondary decomposition from 380 to 650°C, ultimately leading to complete degradation with only residual weight remaining. Additionally, we can observe that the highest rates of decomposition occurred at 230 and 325°C across all samples. The physico-chemical analysis of the peptide mixtures showed that they remained stable up to 332°C (Figure S15). One of the primary advantages of utilizing mixed peptide bioinks lies in their ability to adapt to the desired mechanical stiffness needed for prospective applications. Consequently, in TGA, consistent degradation trends in terms of weight loss versus temperature are discernible for the ultrashort peptides IIZK and IIFK. According to our results (Figure S15), we can conclude that there are no significant changes from a thermomechanical perspective, indicating the stable performance of all mixed bioinks. This stability is crucial for applications where biofabrication is pertinent, allowing for the adjustment of other properties, such as biological and chemical, without interfering with thermal modifications.

3.3. 3D bioprinting of trachea-like constructs containing mesenchymal stromal cells

Our robotic 3D bioprinting system has been extensively used with single peptide bioinks to fabricate various cell-laden tissue constructs.[12,15,16,87] As reported earlier, depending on the individual cellular graft of choice, the 3D bioprinting system must be adapted to guarantee a continuous gel deposition by considering the speed of the robotic arm, selecting the suitable nozzle, adjusting the microfluidic pumps, and choosing the correct viscosities of the bioinks. For the bioprinting of trachea-like constructs using mixed peptide bioinks, we adopted a constant flow rate and pulse mode for the automated extrusion of cells, buffer, and peptide solution (Figures 4A & S16, Video S1).

On days 14 and 28, after differentiation of MSCs, no cytotoxicity was observed for the newly generated chondrocytes within the scaffolds (Figure 4G & 4H, see also the cytocompatibility of the non-mixed individual peptide bioinks in Figure S17). The constructs exhibited excellent resolution, formed multiple layers through gel-thread deposition, and showed visibly refined details without

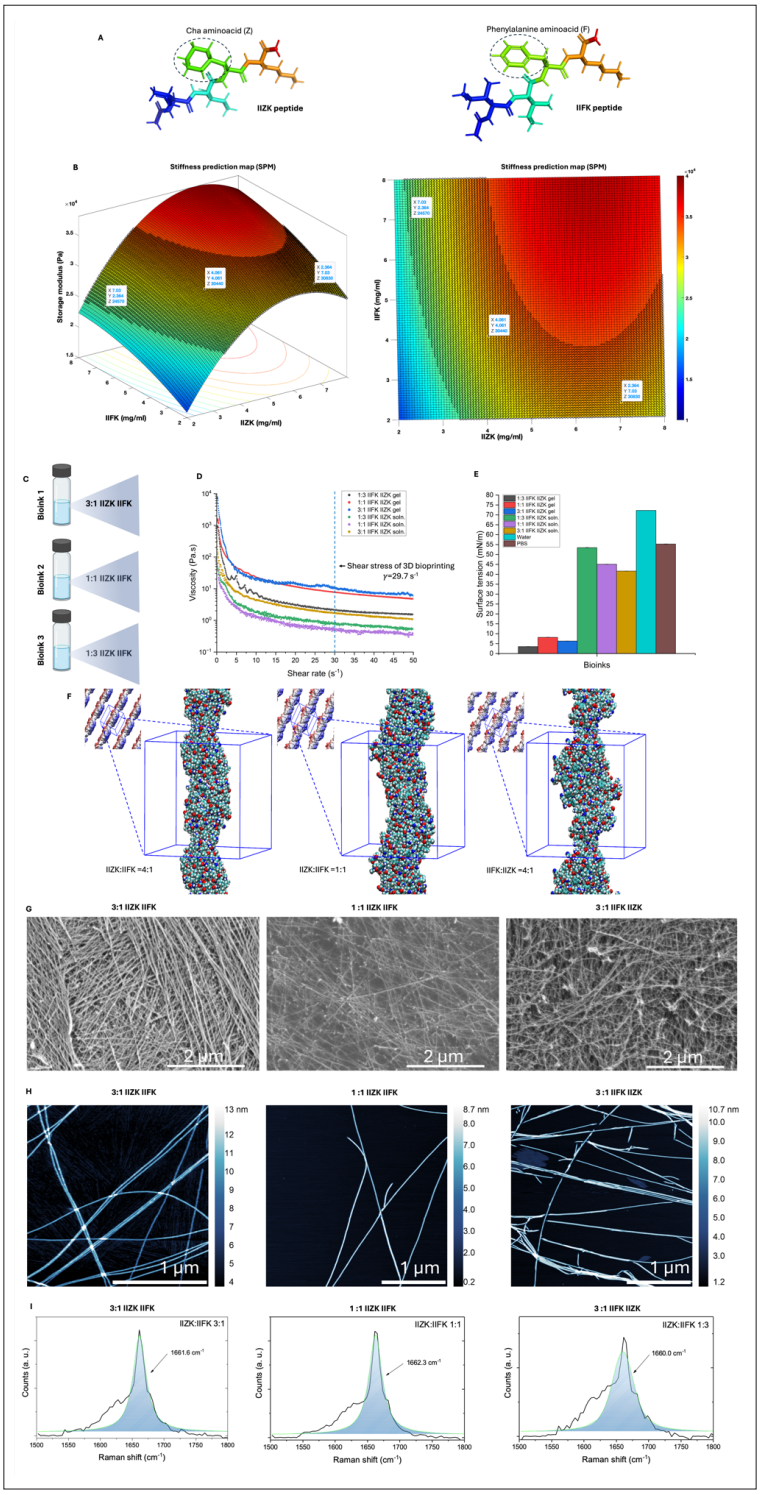

Figure 3. Characteristics of IIZK–IIFK peptide mixtures. (A) Structure of peptides IIZK and IIFK. (B) Application of the stiffness prediction map to formulate three bioinks with initial stiffness between 24 and 31 kPa, where the red marks identify the stiffness range. (C) Formulated bioinks and their (D) viscosities and (E) surface tensions. (F) Molecular docking simulations for assembling the mixed ultrashort peptide bioinks for 3D bioprinting. (G) Scanning electron microscopy images (scale bars: 2 µm; magnifications: 25, 000x), (H) atomic force microscopy topography (scale bar: 1 µm; Figure H left, magnification is about 15,000 based on displayed image size of 3x3 cm; Figures H center and right, magnification is about 10,000 based on displayed image size of 3x3 cm), and (I) Raman spectra of the Amide I region of mixed peptide bioink fibers with different ratios: 3:1 IIZK:IIFK (left), 1:1 IIZK:IIFK (center), and 3:1 IIFK:IIZK (right). In Panel I, dark lines indicate the raw data, blue areas/lines represent the central peak in the Amide I region, and the values indicate the prevalent peak value in cm^{-1}.

collapsing under their weight or after the addition of media (Figure 4C–4F, Table S1). Among the tested formulations, it was observed that the 3:1 IIZK:IIFK (7.03 and 2.36 mg/mL, respectively) mixed peptide bioink showed the best results for layer deposition and printing resolution, with minimal clogging and clumping during the printing process (Figure 4B & 4C, Video S1). Bioinks with higher IIZK contents exhibited viable, spherical chondrocytes that were better preserved than those from single peptide bioink formulations (Figure S17), while those with higher IIFK contents resulted in lower-resolution constructs (Table S1). Interestingly, a higher proportion of IIZK decreased solubility, whereas IIFK improved it (Table S13), with opposite effects observed for gelation speed. These results are congruent with previous reports showing that IIFK-based bioinks gel more slowly than IIZK-based bioinks at 10 mg/mL.[12] Nonetheless, all mixed formulations were easily printable and formed stable, multilayered structures using 3.60–4.88 mg less peptides than previously reported for bioprinting large-scale constructs.[12,73] This

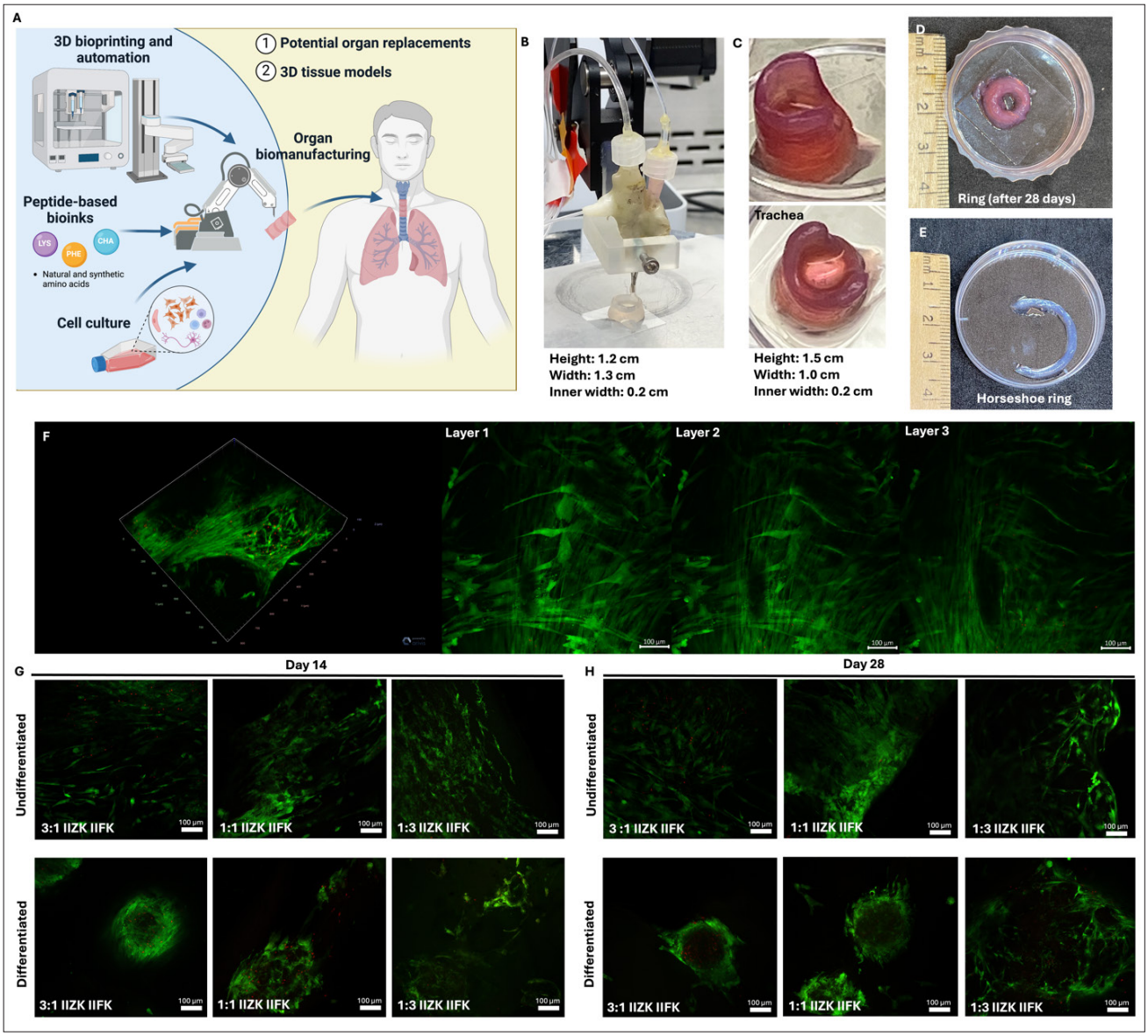

Figure 4. Bioink biocompatibility. (A) Schematic overview of the biofabrication procedure generating cell-laden trachea-like structures. (B) Picture of the robotic bioprinter during printing. (C) The trachea-like construct cultures in media. (D) Bioprinted ring structures. (E) "C-shaped" half-cylinder structures. (F) Confocal microscopy images of the bioprinted cell-containing trachea-like constructs after 28 days in culture media (scale bars: 100 µm; magnifications: 20×). Cytocompatibility results of the 3D bioprinted structures at (G) day 14 and (H) day 28 with and without mesenchymal stromal cell differentiation across different IIZK:IIFK ratios (scale bars: 100 µm; magnifications: 20×). Figure 4A created with BioRender.com.

reduction in peptide concentration represents a significant improvement, potentially reducing synthesis costs and promoting overall process sustainability.[88] The viscoelastic properties of these bioinks further underscore their use in the extrusion-based bioprinting of 3D structures (Figure S18). Overall, these findings demonstrate that mixed ultrashort peptide bioinks are highly extrudable, compatible with the robotic 3D bioprinting process, and hold strong potential for upscaling and automated printing of large-scale tissue and organ constructs.

3.4. Chondrogenesis and cartilage formation through mesenchymal stromal cell differentiation

Using different mixed peptide bioink formulations, the bioprinted ring structures exhibited distinct morphological features during stem cell differentiation (Figure 5). The presence of dense segments of chondrogenic nodules indicated the presence of several chondrocytes surrounded by a pericellular matrix.[89,90] The formation of chondrogenic nodules was mainly observed in Figures 5A and 5C. This is similar to previous observations where, at higher concentrations, both IIZK and IIFK promote a chondrogenic-like microenvironment. It has been highlighted that stiff to moderately stiff scaffold matrices promote chondrocyte spreading, while softer matrices induce a spherical chondrocyte shape.[91] This is consistent with the observed chondrocyte morphogenesis in this study, where bioinks containing more IIFK exhibited more spheroid chondrocytes (Figure 5A), while those with more IIZK showed dense dark areas due to cell spreading (Figures 5B & 5C).

Gene expression analysis revealed that the 3:1 IIZK:IIFK and the 3:1 IIFK:IIZK (i.e., 1:3 IIZK: IIFK) mixed peptide bioinks showed high expressions of collagen type X, collagen type 2, collagen type 1, *SOX9*, and *RUNX2* (Figure 5G). On the contrary, the *ALPL* gene expression was highest for the 1:1 IIZK:IIFK mixed peptide bioink, with almost no chondrogenic gene expression. The expression of the *SOX5* gene was also observed with the 3:1 IIZK:IIFK mixed peptide bioink. These findings indicate that 1:1 IIZK:IIFK mixed peptide bioink yielded a peptide hydrogel network that was not suitable for chondrogenesis (Figure 3F–3H), potentially due to differences in the amount of differentiated cells, their morphology, and the formation of chondrogenic nodules that successfully condensed into mature cartilage nodules.[92–94] This observation is further supported by the morphogenesis of chondrocytes with this formulation (Figure 5B & 5E). In contrast, the abundance of collagen type II and type X promoted chondrocytes and chondrogenic nodules (Figure 5A–5C), resulting in dense segments distributed throughout the bioprinted trachea-like constructs containing differentiated MSCs.

It has been reported that the expression of collagen type I is found in early chondrocytes, followed by the enrichment of collagen type II for the structural strength of the ECM, and then the essential roles of SOX5 and SOX9 in directing MSC differentiation into chondrocytes for cartilage formation. Lastly, the presence of collagen type X indicates abundant ECM production and hypertrophic chondrocyte formation, highlighting the protein as an essential component for tissue integration and function.[73,95] Furthermore, the viscoelastic properties of the IIZK/IIFK bioinks appeared to further promote chondrogenic nodule formation (Figure S17). Our results parallel previous findings with GelMA-based hydrogels,[96] where chondrocytes showed similar morphology, and gene expression analysis confirmed the production of collagen types I, II, and X (Figure 5G). Specifically, the bioprinted trachea-like constructs printed with 3:1 IIZK:IIFK and 3:1 IIFK:IIZK ratios resulted in higher gene expression of collagen type X, followed by collagen types II and I, consistent with the composition of hyaline cartilage. Collagen type I forms fibers with high tensile strength and is commonly present in articular and meniscal cartilages, as well as bone, dermis, tendon, ligaments, and cornea.[97,98]

Interestingly, previous studies using single IIZK peptide bioinks in 3D bioprinting reported high collagen type II expression but low collagen type I, collagen type X, SOX-9, and aggrecan expressions.[12,73] In contrast, in the present study, the bioink that contained high levels of IIZK induced the expression of all these genes, with particularly high collagen type X expression. The presence of collagen X suggests successful cartilage formation through hypertrophic chondrocytes and serves as a pre-indicator of endochondral ossification.[99,100] It provides strong inter- and intramolecular interactions among network-forming short-chain collagens.[97] It has been found in scaffold-free endotracheal structures transplanted in rabbits, native tracheal cartilage,[98,101,102] deep zone articular cartilage, articular chondrocytes, auricular and nasal cartilages, and during the development of mid-diaphysis. Importantly, its presence does not necessarily imply mineralization.[98] While collagen type X contributes to the structural stability of bioprinted trachea constructs due to its high stiffness properties, it is not sufficient for successful trachea regeneration and may predispose to tracheal stenosis after transplantation.[102] Therefore, the balanced expression of collagens, such as collagen type II, is essential for successful trachea regeneration. This type of biomaterial could also be useful for articular cartilage repair due to its high expression of collagen type X.

3.5. Self-healing properties

Next, we analyzed the self-healing properties of the mixed- and individual-peptide bioinks in the presence or absence

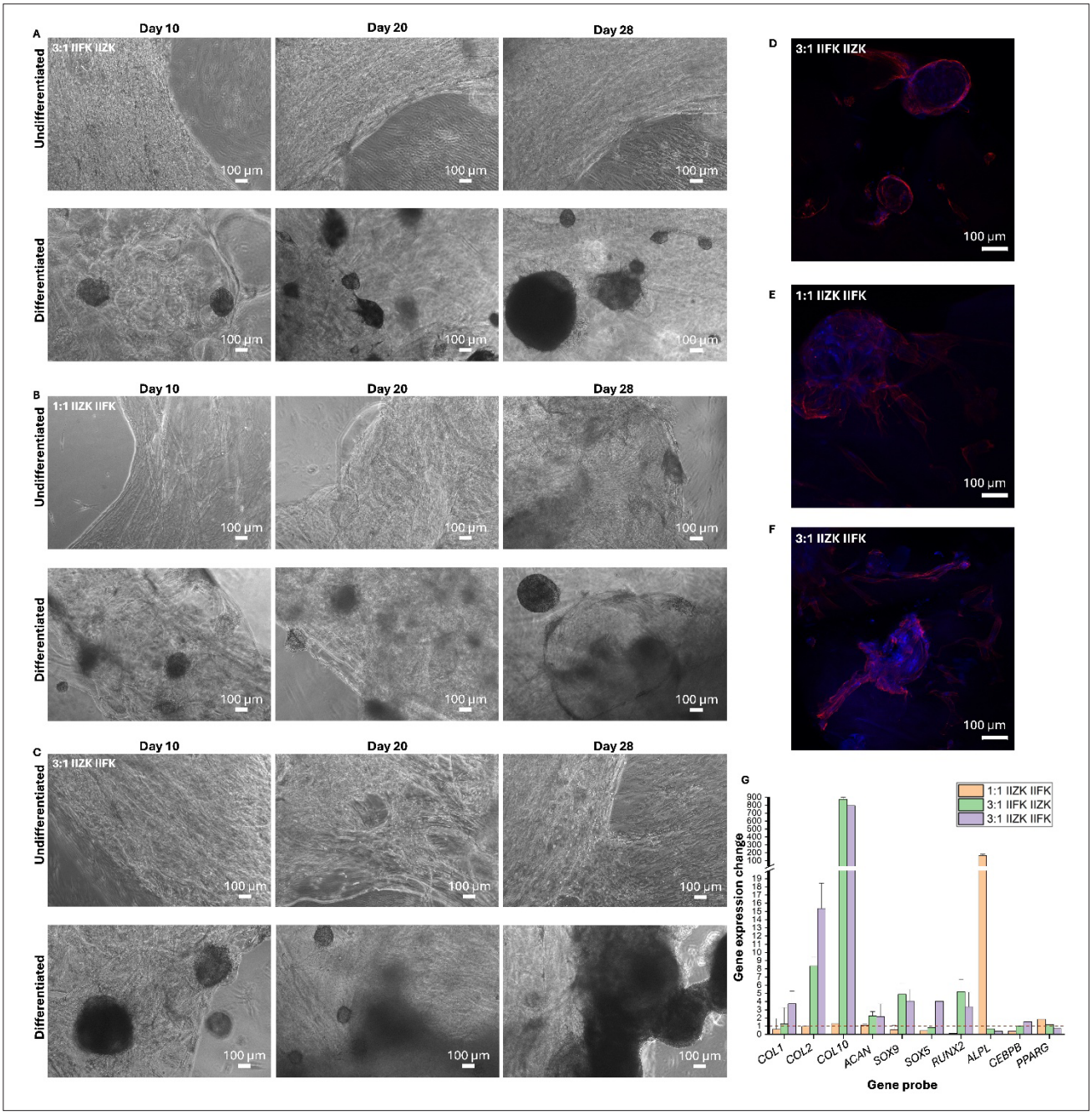

Figure 5. Analysis of the differentiation capacity of 3D bioprinted mesenchymal stromal cells (MSCs) using different mixed ultrashort peptide bioink formulations. Undifferentiated and differentiated MSCs embedded in the (A) 3:1 IIFK:IIZK, (B) 1:1 IIZK:IIFK, and (C) 3:1 IIZK:IIFK mixed peptide bioinks (scale bars: 100 µm; magnifications: 40×). (D–F) Fluorescence microscopy images of MSCs showing cytoskeleton staining on day 14 across different peptide ratios using actin-phalloidin and 4',6-diamidino-2-phenylindole (DAPI) (scale bars: 100 µm; magnifications: 20×). (G) Gene expression analysis of differentiated MSCs on day 14 across formulations.

of cells, including undifferentiated MSCs and MSC-derived chondrocytes (Figures 6A, S17, S19, & S20). The circular structures of printed bioinks had full contact with the rheometer probe (Figure 6B–6D). The acellular scaffolds, i.e., bioinks without any cells, exhibited a self-healing capacity between 81.42 and 99.06% (Figure 6N). When the samples were 3D bioprinted with undifferentiated MSCs and incubated for 28 days, their stiffness decreased compared to acellular scaffolds (Figure 6E, 6H, 6K), likely due to cellular reorganization on the 3D scaffolds.

Among the mixed formulations, the self-healing properties of the 3:1 IIZK:IIFK bioink were higher in the presence of chondrocyte-enriched ECM compared to those with undifferentiated MSCs after an incubation of 28 days and a healing time of 60 min (Figure 6N), with a healing efficiency of 94.62%, along with the expression of collagen and the presence of chondrocytes. In comparison, the 3:1 IIFK:IIZK bioink reached 61.65% healing efficiency, while the 1:1 IIZK:IIFK bioink only achieved 29.33%. Conversely, the self-healing capabilities were slower for bioinks containing MSCs, with healing efficiencies between 70.24 and 71.88% (Figure 6F, 6I, 6L, & 6N). Notably, the mixed ultrashort peptide bioinks consistently outperformed individual peptide formulations in terms of self-healing properties (Figures 6N–6P, S19, & S20).

The self-healing properties of our mixed peptide bioinks were found to be faster and more stable than several reported thixotropic polymer-based and nanocomposite hydrogels, such as PDMA hydrogels, telechelic difunctional PEG mixed with glycol chitosan hydrogels, and nanofibrillated cellulose mixed with PVA hydrogels. Overall, the mixed ultrashort peptide bioinks exhibited remarkable self-healing properties comparable to those of PVA functionalized with methyl viologen cellulose nanocrystals, which exhibit near-instantaneous self-recovery.[103] Remarkably, the 3:1 IIZK:IIFK bioink containing chondrocytes demonstrated the most profound and stable self-healing properties in comparison to the other formulations tested in this study.

3.6. Changes in viscoelastic behavior during long-term 3D cell culture

Our findings demonstrate that the 3:1 IIZK:IIFK bioink performed remarkably well in terms of printability, cytocompatibility, chondrogenic differentiation, and healing efficiency. These observations, including excellent resolution and structural stability of the bioprinted constructs, support the bioink's superior performance in the bioprinting process of trachea-like structures (Figure 7A & 7B, Table S1). By day 14, confocal microscopy imaging revealed connecting actin filaments within the bioprinted trachea-like structures, with few dead cells (Figure 7C). Furthermore, the presence of undifferentiated MSCs was observed within the bioprinted trachea-like structure, particularly at the sides (Figure 7E). The fibers of the bioprinted scaffold exhibited anisotropic alignment to form the scaffolding 3D structure (Figure 7F). Following 28 days of differentiation, the bioprinted trachea-like structure exhibited the formation of a dense region (Figure 7G) and high elasticity (Figure 7K, Videos S2 & S3), a finding that is consistent with earlier observations. SEM imaging revealed the presence of chondrocytes within this region, accompanied by the formation of filopodia bridges (Figure 7H–7J). An explicit change in the rigidity of the trachea-like structures was evident following a 100-day incubation period (Figure 7L). The bioprinted trachea-like structures, containing MSC-derived chondrocytes, demonstrated a 2.7-fold increase in structural stiffness, while the trachea constructs containing undifferentiated MSCs exhibited a 26.8% decrease in stiffness. The 3D trachea-like constructs were bioprinted in human-size dimensions and then cultured for a period of up to 100 days (Figure 7M–7O, Video S4).

The observed elasticity of the bioprinted trachea-like structures (Figure 7K, Videos S2 & S3) is attributable to the presence of collagen type II, which comprises 90–95% of the collagen in the ECM, especially in hyaline, auricular, epiglottal, nasal, articular, and meniscal cartilages.[98] Collagen type II is a marker of musculoskeletal maturity and comprises, together with glycosaminoglycans, a dominant part of the chondrocytes' microenvironment.[80,104] It forms mixed fibrils with collagen type IX and collagen type XI, promoting tissue elasticity and the formation of hyaline fibrous cartilage. It is also known to form 400-nm-thick crossbanded fibrils with a banding pattern, which constitutes the fibrous cartilage matrix.[97]

The arrangement of collagen fibers in the bioprinted trachea-like structures (Figure 7I & 7J) exhibited a high degree of similarity with previously described cases.[105] The gene expression, the morphology of chondrocytes, and the SEM images all indicated the successful establishment of a collagen type II matrix within the structures. The presence of collagen type II has been shown to reinforce the ECM matrix, thereby enhancing the elasticity of the 3D structures (Figure 7K). However, culturing the trachea-like structures with MSCs for 100 days did not increase biomaterial stiffness. Instead, the storage modulus remained statistically consistent with the initial material stiffness, suggesting that bone marrow-derived MSCs remodeled the scaffold toward a softer tissue. In contrast, when the bioprinted trachea-like structures containing MSC-derived chondrocytes were cultured for a longer period, there was a significant increase in the stiffness of the structure between day 28 and day 100 ($p<0.001$;

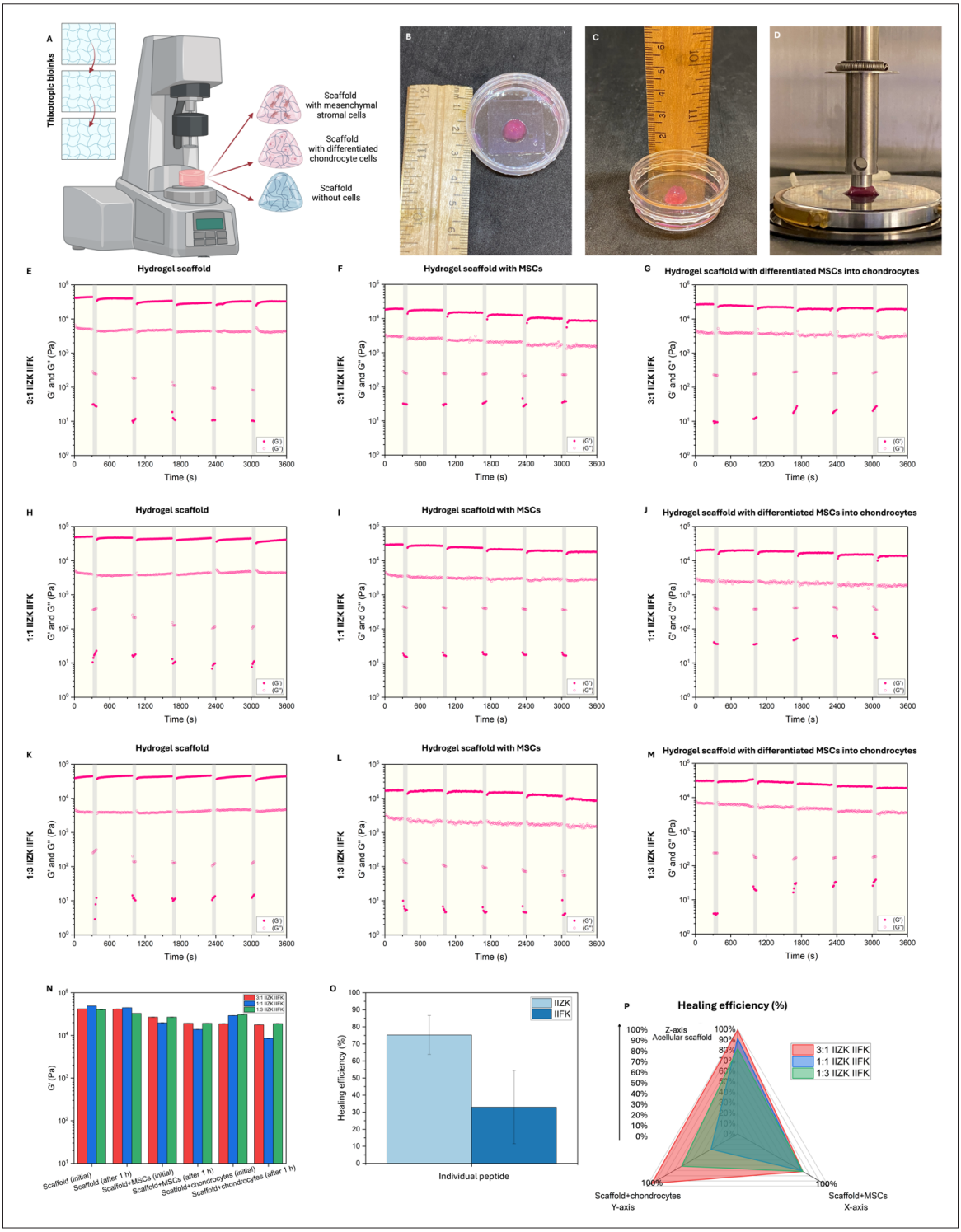

Figure 6. Studies on the self-healing capabilities of 3D bioprinted scaffold structures in the presence and absence of mesenchymal stromal cells (MSCs) and MSC-derived chondrocytes on day 28. (A) A schematic representation. (B & C) Images of 3D bioprinted circular structures. (D) Rheological analyses of the viscoelastic behavior of the bioprinted scaffold structures. (E–M) Mixed ultrashort peptide bioinks' self-healing tests (E, H, K) without cells, (F, I, L) in the presence of MSCs, and (G, J, M) in the presence of MSC-derived chondrocytes. (N) Initial and final storage modulus of the bioinks in the presence and absence of undifferentiated MSCs or MSC-derived chondrocytes after inducing self-healing cycles for 1 h. (O & P) Self-healing efficiencies of (O) individual IIZK or IIFK peptide bioinks and (P) mixed ultrashort peptide bioinks. Experiments were performed with alternate step–strain relaxation at 25°C. Figure 6A created with BioRender.com.

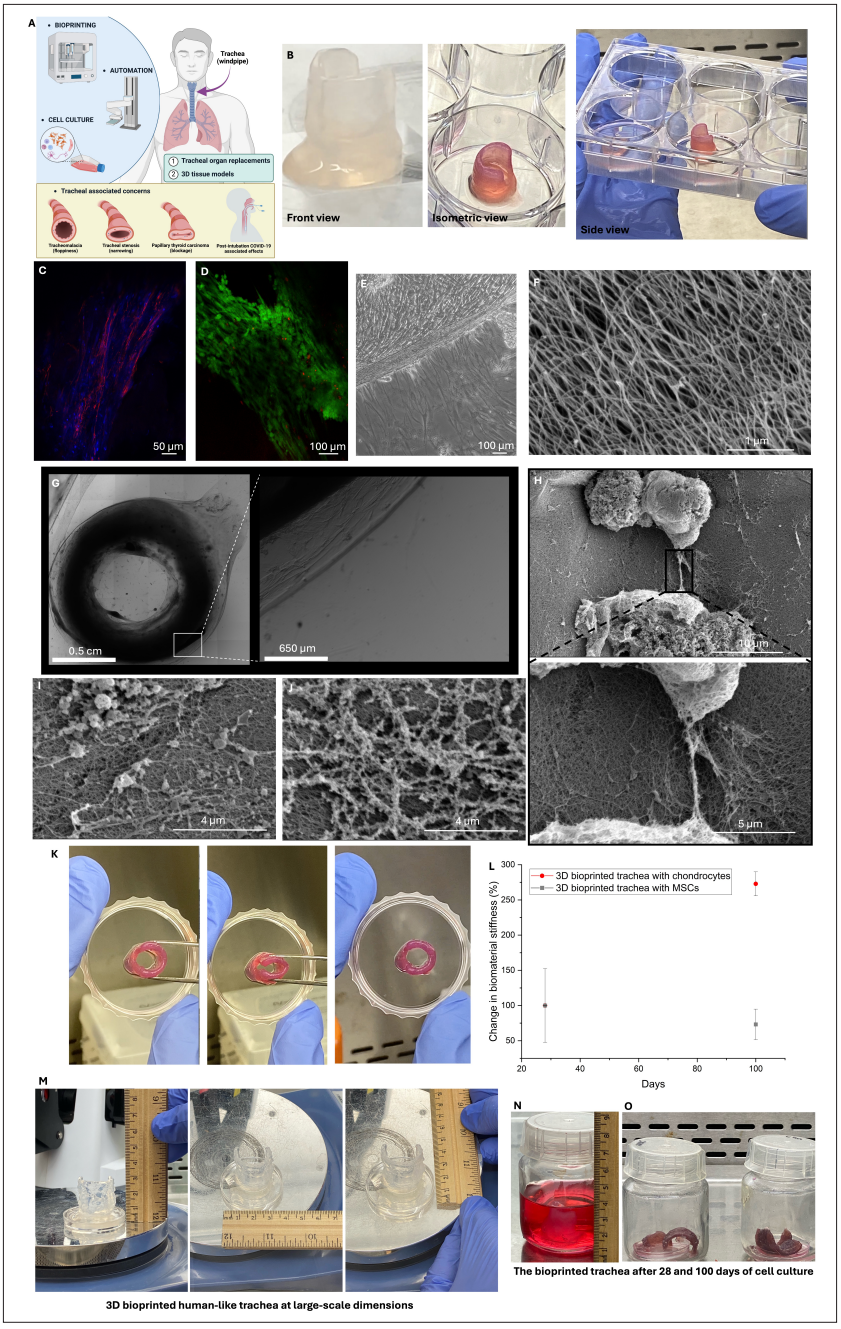

Figure 7. 3D bioprinted trachea-like structures fabricated from 3:1 IIZK:IIFK mixed peptide bioinks. (A) An overview of the bioprinting process and the main structural concerns associated with the trachea. (B) A 3D bioprinted trachea-like construct that is 2 cm in height (left), generated through extrusion-based bioprinting. The same construct after 5 days (middle) and 28 days (right) of incubation with cell media. (C) Confocal microscopy of the cytoskeleton (scale bar: 50 µm; magnification: 20×). (D) Live/dead staining of the inner tracheal-like ring (scale bar: 100 µm; magnification: 20×). (E) Phase-contrast microscopy (PCM) image of the outer, tracheal-like ring (scale bar: 100 µm; magnification: 40×). (F) Scanning electron microscopy (SEM) images of the fibers derived from the mixed ultrashort peptide bioink scaffold (scale bar: 1 µm; magnification: 50,000×). (G) PCM images of the bioprinted trachea-like construct on day 28 (scale bar (right): 650 µm; magnification: 20x (right). (H) SEM images show the differentiation of MSCs into chondrocytes and their interaction with the scaffold through filopodia (scale bars: 10 µm [top], 5 µm[bottom]; magnification : 5,000x [top], 12,000 x [bottom]). (I & J) After 28 days, extracellular matrix components were secreted within the fibrous scaffold biomaterial (scale bars: 4 µm; magnifications: 20,000×). (K) Elasticity and structural stability of the bioprinted trachea-like construct on day 28 after stem cell differentiation into chondrocytes. (L) Changes in the biomaterial stiffness after long-term incubation. (M) Extrusion-based 3D bioprinting of a peptide-based human-like tracheal construct with cells at clinically relevant dimensions. (N & O) The biomaterial was subjected to chondrogenic differentiation and cultured for (N) 28 days and (O) up to 100 days. Videos are additionally provided in **Videos S2 & S3**. Figure 7A created with BioRender.com.

Figure 7L). This increase can be attained through the adaptation of the scaffold into a more cartilage-like tissue.

Our findings align with earlier observations on the formation of chondrogenic nodules and their associated gene expression profiles (Figure 5), as well as with the high elasticity exhibited by the bioprinted trachea-like model. This discrepancy in the changes of stiffness may be attributable to the distinct interactions and organization of MSC-derived chondrocytes with the mixed peptide scaffold (Figure 7H) and the ECM components they secrete (Figure 7I & 7J), compared with those secreted by MSCs. These results emphasize the function of cell type in ECM deposition within bioprinted structures. In comparison to undifferentiated MSCs, trachea-like structures containing chondrocytes exhibited a significantly higher storage modulus ($p<0.001$).

The present study employed 3D bioprinting and an SPM to predict scaffold stiffness, with the objective of fabricating trachea-like constructs for healthcare applications. The stiffness map was instrumental in the formulation of three distinct bioinks with pre-tuned stiffness designed to facilitate stromal cell differentiation. These bioinks demonstrated adequate mechanical and physicochemical properties for bioprinting and exhibited compatibility with living tissues, rendering them optimal for chondrogenic nodule formation. The differentiation of MSCs into chondrocytes was facilitated by each bioink, as evidenced by both morphological observations and gene expression analysis (Figure 5). Notably, two bioinks successfully induced the production of collagen type II and type X.

The 3D bioprinted trachea-like constructs exhibited structural stability, elasticity, and self-healing properties, as well as enhanced viscoelastic properties through the deposition of ECM components, visualized through SEM. In addition, the presence of collagen was shown through gene expression analysis. In the future, histochemical analysis of the printed structures could visually facilitate the localization of deposited collagens and glycosaminoglycans. Our findings suggest a new strategy for the bioprinting of tracheal-like structures for trachea regeneration.

4. Conclusion

The trachea can face various issues, such as structural deformities, blockages, and other health conditions arising from intubation (e.g., due to SARS-CoV-2 post-intubation effects), as well as aging-related degeneration. Advanced biomaterial is needed for trachea engineering to address these serious issues. Our research focuses on developing 3D bioprinted, elastic, self-healing trachea-like models using mixed ultrashort peptide bioinks. This involves using the RSM to develop an SPM to formulate mixed ultrashort peptide bioinks that enhance MSC differentiation into chondrocytes through the bioink scaffold stiffness architectures. To our knowledge, this is the first report of utilizing the SPM strategy with robotic-assisted extrusion-based 3D bioprinting for developing trachea-like models. The resulting bioinks demonstrated excellent printing resolution, mechanical solid properties, and biocompatibility, promoting hyaline and hypertrophic cartilage formation while exhibiting superior self-healing properties compared to single peptide bioinks. Furthermore, our bioinks also promoted the expression of collagen type X, suggesting potential utility in bone formation studies. After being cultured for up to 100 days, the trachea-like structures further enhanced their mechanical properties, making them suitable for trachea regeneration. This research advances the engineering of trachea-like structures using mixed ultrashort peptide bioinks to develop tracheal models. Future work should include the evaluation of the long-term changes in viscoelasticity through rheology measurements (e.g., evaluation of mixed bioinks' dynamic fiber formation), protein-level validation through Western blotting of key chondrogenic markers (e.g., collagen type II alpha-1, SOX9, and runt-related transcription factor 2), and histochemical staining (e.g., Alcian blue and Safranin O) to complement our current gene expression and morphological evidence. Additional studies will explore AI-driven modeling for the formulation of multi-peptide (≥3) bioinks and integrate epithelial cells into the trachea-like models to investigate the formation of tracheal mucosa. Finally, *in vivo* studies in rabbits or other animal models will be essential to assess the functionality and potential immunogenicity of the trachea-like constructs.

Acknowledgments

We thank the KAUST Core Labs for their support. We thank Prof. Gabriel Wittum, KAUST, for his feedback on statistical and mathematical modeling. We thank Prof. Abdalla Awidi from The University of Jordan/Cell Therapy Center, Amman, Jordan, for his kind gift of human bone marrow-derived MSCs. We thank the bioprinting group members, particularly Ms. Kowther Kahin and Ms. Zainab Khan, for the development of the robotic 3D bioprinting system, including the dual-coaxial nozzle. We thank Mauricio Aguilar Aguila Isaias for his help with the schematic representation of the 3D robotic arm bioprinter (**Figure 1**). We thank Montserrat del Socorro Valle Perez for the design of the graphical abstract.

Funding

This research was funded by King Abdullah University of Science and Technology (KAUST) to Charlotte A. E.

Hauser (grant number: Faculty (CH) baseline funding) and Graz University of Technology (TU Graz) for additional funding.

Conflict of interest

Charlotte A. E. Hauser serves as the Editorial Board Member of the journal, but did not in any way involve in the editorial and peer-review process conducted for this paper, directly or indirectly. Other authors declare they have no competing interests.

Author contributions

Conceptualization: Charlotte A. E. Hauser
Formal analysis: Alexander U. Valle-Pérez
Investigation: Alexander U. Valle-Pérez, Dana Alhattab, Rui Ge, Eter Othman, Panayiotis Bilalis, Abdulelah Alrashoudi, Antonio Cárdenas-Calvario, Alan Eduardo Avila Ramírez, Zainab N. Khan, Manola Moretti
Methodology: Alexander U. Valle-Pérez, Panayiotis Bilalis, Zainab N. Khan, Dana Alhattab, Manola Moretti
Writing–original draft: Alexander U. Valle-Pérez, Dana Alhattab, Rui Ge, Manola Moretti
Writing–review & editing: Charlotte A.E. Hauser, Christian Baumgartner

Ethics approval and consent to participate

Not applicable.

Consent for publication

Not applicable.

Availability of data

Data is available from the corresponding author upon reasonable request.

References

1. Murphy SV, Atala A. 3D bioprinting of tissues and organs. *Nat Biotechnol*. 2014;32(8):773-785. doi: 10.1038/nbt.2958
2. Gaharwar AK, Singh I, Khademhosseini A. Engineered biomaterials for in situ tissue regeneration. *Nat Rev Mater*. 2020;5(9):686-705. doi: 10.1038/s41578-020-0209-x
3. Kang HW, Lee SJ, Ko IK, Kengla C, Yoo JJ, Atala A. A 3D bioprinting system to produce human-scale tissue constructs with structural integrity. *Nat Biotechnol*. 2016;34(3): 312-319. doi: 10.1038/nbt.3413
4. Melchels FPW, Domingos MAN, Klein TJ, Malda J, Bartolo PJ, Hutmacher DW. Additive manufacturing of tissues and organs. *Prog Polym Sci*. 2012;37(8):1079-1104. doi: 10.1016/j.progpolymsci.2011.11.007
5. Jorgensen AM, Yoo JJ, Atala A. Solid organ bioprinting: strategies to achieve organ function. *Chem Rev*. 2020;120(19):11093-11127. doi: 10.1021/acs.chemrev.0c00145
6. Low LA, Mummery C, Berridge BR, Austin CP, Tagle DA. Organs-on-chips: into the next decade. *Nat Rev Drug Discov*. 2021;20(5):345-361. doi: 10.1038/s41573-020-0079-3
7. Ingber DE. Human organs-on-chips for disease modelling, drug development and personalized medicine. *Nat Rev Genet*. 2022;23(8):467-491. doi: 10.1038/s41576-022-00466-9
8. Dey M, Ozbolat IT. 3D bioprinting of cells, tissues and organs. *Sci Rep*. 2020;10(1):14023, s41598-020-70086-y. doi: 10.1038/s41598-020-70086-y
9. Shin J, Lee Y, Li Z, Hu J, Park SS, Kim K. Optimized 3D bioprinting technology based on machine learning: A review of recent trends and advances. *Micromachines*. 2022;13(3):363. doi: 10.3390/mi13030363
10. Vanaei S, Parizi MS, Vanaei S, Salemizadehparizi F, Vanaei HR. An overview on materials and techniques in 3D bioprinting toward biomedical application. *Eng Regen*. 2021;2:1-18. doi: 10.1016/j.engreg.2020.12.001
11. Wang Y, Wang J, Ji Z, *et al*. Application of bioprinting in ophthalmology. *Int J Bioprint*. 2022;8(2):552. doi: 10.18063/ijb.v8i2.552
12. Susapto HH, Alhattab D, Abdelrahman S, *et al*. Ultrashort peptide bioinks support automated printing of large-scale constructs assuring long-term survival of printed tissue constructs. *Nano Lett*. 2021;21(7):2719-2729. doi: 10.1021/acs.nanolett.0c04426
13. Huo Y, Xu Y, Wu X, *et al*. Functional trachea reconstruction using 3D-bioprinted native-like tissue architecture based on designable tissue-specific bioinks. *Adv Sci*. 2022;9(29):2202181. doi: 10.1002/advs.202202181
14. Murphy SV, De Coppi P, Atala A. Opportunities and challenges of translational 3D bioprinting. *Nat Biomed Eng*. 2019;4(4):370-380. doi: 10.1038/s41551-019-0471-7
15. Abdelrahman S, Alsanie WF, Khan ZN, *et al*. A Parkinson's disease model composed of 3D bioprinted dopaminergic neurons within a biomimetic peptide scaffold. *Biofabrication*. 2022;14(4):044103. doi: 10.1088/1758-5090/ac7eec
16. Khan ZN, Albalawi HI, Valle-Pérez AU, *et al*. From 3D printed molds to bioprinted scaffolds: A hybrid material

extrusion and vat polymerization bioprinting approach for soft matter constructs. *Mater Sci Addit Manuf*. 2022;1(1):7. doi: 10.18063/msam.v1i1.7

17. Mirdamadi E, Tashman JW, Shiwarski DJ, Palchesko RN, Feinberg AW. Fresh 3D bioprinting a full-size model of the human heart. *ACS Biomater Sci Eng*. 2020;6(11):6453-6459. doi: 10.1021/acsbiomaterials.0c01133

18. Jiang X, Zuo X, Wang H, Zhu P, Kang YJ. Fabrication of vascular grafts using poly(ε-caprolactone) and collagen-encapsuled ADSCs for interposition implantation of abdominal aorta in rhesus monkeys. *ACS Biomater Sci Eng*. 2024;10(5):3120-3135. doi: 10.1021/acsbiomaterials.3c01209

19. He C, Yan J, Fu Y, Guo J, Shi Y, Guo J. Organoid bioprinting strategy and application in biomedicine: a review. *IJB*. 2023;9(6):0112. doi: 10.36922/ijb.0112

20. Hammad NS, Khan ZN, Valle-Pérez AU, Hauser C. A predictive machine learning model to optimize flow rates on an integrated microfluidic pumping system for peptide-based 3D bioprinting. In: Gray BL, Rapp BE, eds. *Microfluidics, BioMEMS, and Medical Microsystems XXI*. SPIE; 2023:3. doi: 10.1117/12.2650440

21. Tang M, Jiang S, Huang X, *et al*. Integration of 3D bioprinting and multi-algorithm machine learning identified glioma susceptibilities and microenvironment characteristics. *Cell Discov*. 2024;10(1):39. doi: 10.1038/s41421-024-00650-7

22. Freeman S, Calabro S, Williams R, Jin S, Ye K. Bioink formulation and machine learning-empowered bioprinting optimization. *Front Bioeng Biotechnol*. 2022;10:913579. doi: 10.3389/fbioe.2022.913579

23. Tebon PJ, Wang B, Markowitz AL, *et al*. Drug screening at single-organoid resolution via bioprinting and interferometry. *Nat Commun*. 2023;14(1):3168. doi: 10.1038/s41467-023-38832-8

24. Trucco D, Sharma A, Manferdini C, *et al*. Modeling and fabrication of silk fibroin–gelatin-based constructs using extrusion-based three-dimensional bioprinting. *ACS Biomater Sci Eng*. 2021;7(7):3306-3320. doi: 10.1021/acsbiomaterials.1c00410

25. Perin F, Spessot E, Famà A, *et al*. Modeling a dynamic printability window on polysaccharide blend inks for extrusion bioprinting. *ACS Biomater Sci Eng*. 2023;9(3):1320-1331. doi: 10.1021/acsbiomaterials.2c01143

26. Zanderigo G, Bracco F, Semeraro Q, Colosimo BM. In-situ printability maps (IPM): a new approach for in-situ printability assessment with application to extrusion-based bioprinting. *Bioprinting*. 2023;36:e00320. doi: 10.1016/j.bprint.2023.e00320

27. Harris CG, Semprini L, Rochefort WE, Fogg KC. Statistical optimization of cell–hydrogel interactions for green microbiology – a tutorial review. *RSC Sustain*. 2024;2(12):3750-3768. doi: 10.1039/D4SU00400K

28. Chung JHY, Naficy S, Yue Z, *et al*. Bio-ink properties and printability for extrusion printing living cells. *Biomater Sci*. 2013;1(7):763. doi: 10.1039/c3bm00012e

29. Hölzl K, Lin S, Tytgat L, Van Vlierberghe S, Gu L, Ovsianikov A. Bioink properties before, during and after 3D bioprinting. *Biofabrication*. 2016;8(3):032002. doi: 10.1088/1758-5090/8/3/032002

30. Khoeini R, Nosrati H, Akbarzadeh A, *et al*. Natural and synthetic bioinks for 3D bioprinting. *Adv NanoBiomed Res*. 2021;1(8):2000097. doi: 10.1002/anbr.202000097

31. Kumar S, Tharayil A, Thomas S. 3D bioprinting of nature-inspired hydrogel inks based on synthetic polymers. *ACS Appl Polym Mater*. 2021;3(8):3685-3701. doi: 10.1021/acsapm.1c00567

32. Cui X, Li J, Hartanto Y, *et al*. Advances in extrusion 3d bioprinting: a focus on multicomponent hydrogel-based bioinks. *Adv Healthc Mater*. 2020;9(15):1901648. doi: 10.1002/adhm.201901648

33. Ashammakhi N, Ahadian S, Xu C, *et al*. Bioinks and bioprinting technologies to make heterogeneous and biomimetic tissue constructs. *Mater Today Bio*. 2019;1:100008. doi: 10.1016/j.mtbio.2019.100008

34. Pérez-Pedroza R, Ávila-Ramírez A, Khan Z, Moretti M, Hauser CAE. Supramolecular biopolymers for tissue engineering. *Adv Polym Technol*. 2021;2021:1-23. doi: 10.1155/2021/8815006

35. Mishra A, Loo Y, Deng R, *et al*. Ultrasmall natural peptides self-assemble to strong temperature-resistant helical fibers in scaffolds suitable for tissue engineering. *Nano Today*. 2011;6(3):232-239. doi: 10.1016/j.nantod.2011.05.001

36. Hauser CAE, Deng R, Mishra A, *et al*. Natural tri- to hexapeptides self-assemble in water to amyloid β-type fiber aggregates by unexpected α-helical intermediate structures. *Proc Natl Acad Sci U S A*. 2011;108(4):1361-1366. doi: 10.1073/pnas.1014796108

37. Khan Z, Kahin K, Rauf S, *et al*. Optimization of a 3D bioprinting process using ultrashort peptide bioinks. *IJB*. 2018;5(1):173. doi: 10.18063/ijb.v5i1.173

38. Pantoja Angles A, Valle-Pérez AU, Hauser C, Mahfouz MM. Microbial biocontainment systems for clinical, agricultural, and industrial applications. *Front Bioeng Biotechnol*. 2022;10:830200. doi: 10.3389/fbioe.2022.830200

39. Li Q, Qi G, Liu X, *et al*. Universal peptide hydrogel for scalable physiological formation and bioprinting of 3d

spheroids from human induced pluripotent stem cells. *Adv Funct Mater*. 2021;31(41):2104046.
doi: 10.1002/adfm.202104046

40. Loo Y, Hauser CAE. Bioprinting synthetic self-assembling peptide hydrogels for biomedical applications. *Biomed Mater*. 2015;11(1):014103.
doi: 10.1088/1748-6041/11/1/014103

41. Alhattab DM, Isaioglou I, Alshehri S, *et al*. Fabrication of a three-dimensional bone marrow niche-like acute myeloid leukemia disease model by an automated and controlled process using a robotic multicellular bioprinting system. *Biomater Res*. 2023;27(1):111.
doi: 10.1186/s40824-023-00457-9

42. Bilalis P, Alrashoudi AA, Susapto HH, *et al*. Dipeptide-based photoreactive instant glue for environmental and biomedical applications. *ACS Appl Mater Interfaces*. 2023;15(40):46710-46720.
doi: 10.1021/acsami.3c10726

43. Perez-Pedroza R, Moretti M, Hauser CAE. Fabrication and characterization of colorectal cancer organoids from SW1222 cell line in ultrashort self-assembling peptide matrix. *JoVE*. 2024;(207):66060.
doi: 10.3791/66060

44. Wang Y, Liu X, Ge R, *et al*. Peptide gel electrolytes for stabilized Zn metal anodes. *ACS Nano*. 2024;18(1): 164-177.
doi: 10.1021/acsnano.3c04414

45. Moretti M, Hountondji M, Ge R, *et al*. Selectively positioned catechol moiety supports ultrashort self-assembling peptide hydrogel adhesion for coral restoration. *Langmuir*. 2023;39(49):17903-17920.
doi: 10.1021/acs.langmuir.3c02553

46. Xu J, Pérez-Pedroza R, Moretti M, *et al*. 3D bioprinting of colon organoids in ultrashort self-assembling and decorated peptide matrices. *IJB*. 2024;0(0):3033.
doi: 10.36922/ijb.3033

47. Sarkar B, Nguyen PK, Gao W, Dondapati A, Siddiqui Z, Kumar VA. Angiogenic self-assembling peptide scaffolds for functional tissue regeneration. *Biomacromolecules*. 2018;19(9):3597-3611.
doi: 10.1021/acs.biomac.8b01137

48. Ng WL, Chua CK, Shen YF. Print me an organ! Why we are not there yet. *Prog Polym Sci*. 2019;97:101145.
doi: 10.1016/j.progpolymsci.2019.101145

49. Tang D. Biofabrication of bone tissue: approaches, challenges and translation for bone regeneration. 2016;83:363-382.
doi: 10.1016/j.biomaterials.2016.01.024

50. de León EHP, Valle-Pérez AU, Khan ZN, Hauser CAE. Intelligent and smart biomaterials for sustainable 3D printing applications. *Curr Opin Biomed Eng*. 2023;26:100450.
doi: 10.1016/j.cobme.2023.100450

51. Crowley C, Birchall M, Seifalian AM. Trachea transplantation: from laboratory to patient: trachea transplantation. *J Tissue Eng Regen Med*. 2015;9(4):357-367.
doi: 10.1002/term.1847

52. Park JH, Ahn M, Park SH, *et al*. 3D bioprinting of a trachea-mimetic cellular construct of a clinically relevant size. *Biomaterials*. 2021;279:121246.
doi: 10.1016/j.biomaterials.2021.121246

53. She Y, Fan Z, Wang L, *et al*. 3D printed biomimetic PCL scaffold as framework interspersed with collagen for long segment tracheal replacement. *Front Cell Dev Biol*. 2021;9:629796.
doi: 10.3389/fcell.2021.629796

54. Xu Y, Guo Y, Li Y, *et al*. Biomimetic trachea regeneration using a modular ring strategy based on poly(sebacoyl diglyceride)/polycaprolactone for segmental trachea defect repair. *Adv Funct Mater*. 2020;30(42):2004276.
doi: 10.1002/adfm.202004276

55. Ke D, Yi H, Est-Witte S, *et al*. Bioprinted trachea constructs with patient-matched design, mechanical and biological properties. *Biofabrication*. 2019;12(1):015022.
doi: 10.1088/1758-5090/ab5354

56. Nomoto M, Nomoto Y, Tada Y, *et al*. Bioengineered trachea using autologous chondrocytes for regeneration of tracheal cartilage in a rabbit model. *Laryngoscope*. 2013;123(9):2195-2201.
doi: 10.1002/lary.23784

57. Tan ZH, Dharmadhikari S, Liu L, *et al*. Regeneration of tracheal neotissue in partially decellularized scaffolds. *NPJ Regen Med*. 2023;8(1):35.
doi: 10.1038/s41536-023-00312-4

58. Weber JF, Rehmani SS, Baig MZ, Jadoon Y, Bhora FY. Successes and failures in tracheal bioengineering: lessons learned. *Ann Thorac Surg*. 2021;112(4):1089-1094.
doi: 10.1016/j.athoracsur.2020.10.021

59. Wei S, Zhang Y, Luo F, Duan K, Li M, Lv G. Tissue-engineered tracheal implants: Advancements, challenges, and clinical considerations. *Bioeng Transl Med*. 2024;9(4):e10671.
doi: 10.1002/btm2.10671

60. Mammana M, Bonis A, Verzeletti V, Dell'Amore A, Rea F. Tracheal tissue engineering: principles and state of the art. *Bioengineering*. 2024;11(2):198.
doi: 10.3390/bioengineering11020198

61. Fux T, Österholm C, Themudo R, Simonson O, Grinnemo KH, Corbascio M. Synthetic tracheal grafts seeded with bone marrow cells fail to generate functional tracheae: first long-term follow-up study. *J Thorac Cardiovasc Surg*. 2020;159(6):2525-2537.e23.
doi: 10.1016/j.jtcvs.2019.09.185

62. Dharmadhikari S, Liu L, Shontz K, *et al*. Deconstructing tissue engineered trachea: assessing the role of synthetic scaffolds, segmental replacement and cell seeding on graft performance. *Acta Biomater*. 2020;102:181-191.

doi: 10.1016/j.actbio.2019.11.008

63. Khan Z, Kahin K, Hauser C. Time-dependent pulsing of microfluidic pumps to enhance 3D bioprinting of peptide bioinks. In: Gray BL, Becker H, eds. *Microfluidics, BioMEMS, and Medical Microsystems XIX*. SPIE; 2021:5. doi: 10.1117/12.2578830

64. Yang J, Rahardja S, Fränti P. Outlier detection: how to threshold outlier scores? In: *Proceedings of the International Conference on Artificial Intelligence, Information Processing and Cloud Computing*. ACM; 2019:1-6. doi: 10.1145/3371425.3371427

65. Avila-Ramírez A, Valle-Perez AU, Susapto HH, *et al*. Ecologically friendly biofunctional ink for reconstruction of rigid living systems under wet conditions. *Int J Bioprint*. 2021;7(4):398. doi: 10.18063/ijb.v7i4.398.

66. Khuri AI, Mukhopadhyay S. Response surface methodology. *WIREs Comput Stat*. 2010;2(2):128-149. doi: 10.1002/wics.73

67. Jorgensen WL, Tirado-Rives J. Potential energy functions for atomic-level simulations of water and organic and biomolecular systems. *Proc Natl Acad Sci U S A*. 2005;102(19):6665-6670. doi: 10.1073/pnas.0408037102

68. Abraham MJ, Murtola T, Schulz R, *et al*. GROMACS: High performance molecular simulations through multi-level parallelism from laptops to supercomputers. *SoftwareX*. 2015;1-2:19-25. doi: 10.1016/j.softx.2015.06.001

69. Dodda LS, Cabeza de Vaca I, Tirado-Rives J, Jorgensen WL. LigParGen web server: an automatic OPLS-AA parameter generator for organic ligands. *Nucleic Acids Res*. 2017;45(W1):W331-W336. doi: 10.1093/nar/gkx312

70. Darden T, York D, Pedersen L. Particle mesh Ewald: An $N \cdot \log(N)$ method for Ewald sums in large systems. *J Chem Phys*. 1993;98(12):10089-10092. doi: 10.1063/1.464397

71. Berendsen HJC, Postma JPM, Van Gunsteren WF, DiNola A, Haak JR. Molecular dynamics with coupling to an external bath. *J Chem Phys*. 1984;81(8):3684-3690. doi: 10.1063/1.448118

72. Bussi G, Donadio D, Parrinello M. Canonical sampling through velocity rescaling. *J Chem Phys*. 2007;126(1):014101. doi: 10.1063/1.2408420

73. Alhattab D, Khan Z, Alshehri S, H. Susapto H, A. E. Hauser C. 3D bioprinting of ultrashort self-assembling peptides to engineer scaffolds with different matrix stiffness for chondrogenesis. *Int J Bioprint*. 2023;9(4):719. doi: 10.18063/ijb.719

74. Chaudhuri O, Cooper-White J, Janmey PA, Mooney DJ, Shenoy VB. Effects of extracellular matrix viscoelasticity on cellular behaviour. *Nature*. 2020;584(7822):535-546. doi: 10.1038/s41586-020-2612-2

75. Chaudhuri O, Koshy ST, Branco Da Cunha C, *et al*. Extracellular matrix stiffness and composition jointly regulate the induction of malignant phenotypes in mammary epithelium. *Nat Mater*. 2014;13(10):970-978. doi: 10.1038/nmat4009

76. Wen JH, Vincent LG, Fuhrmann A, *et al*. Interplay of matrix stiffness and protein tethering in stem cell differentiation. *Nat Mater*. 2014;13(10):979-987. doi: 10.1038/nmat4051

77. Kumar S. Stiffness does matter. *Nat Mater*. 2014;13(10):918-920. doi: 10.1038/nmat4094

78. Foyt DA, Taheem DK, Ferreira SA, *et al*. Hypoxia impacts human MSC response to substrate stiffness during chondrogenic differentiation. *Acta Biomater*. 2019;89:73-83. doi: 10.1016/j.actbio.2019.03.002

79. Hartig G, Esclamado R, Telian S. Comparison of the chondrogenic potential of free and vascularized perichondrium in the airway. *Ann Otol Rhinol Laryngol*. 1994;103(1):9-15. doi: 10.1177/000348949410300102

80. Bachmann B, Spitz S, Schädl B, *et al*. Stiffness matters: fine-tuned hydrogel elasticity alters chondrogenic redifferentiation. *Front Bioeng Biotechnol*. 2020;8:373. doi: 10.3389/fbioe.2020.00373

81. Spagnolie SE, ed. *Complex Fluids in Biological Systems: Experiment, Theory, and Computation*. New York: Springer; 2015. doi: 10.1007/978-1-4939-2065-5

82. Wu D, Pang S, Röhrs V, *et al*. Man vs. machine: automated bioink mixing device improves reliability and reproducibility of bioprinting results compared to human operators. *IJB*. 2024;10(2):1974. doi: 10.36922/ijb.1974

83. Ning L, Gil CJ, Hwang B, *et al*. Biomechanical factors in three-dimensional tissue bioprinting. *Appl Phys Rev*. 2020;7(4):041319. doi: 10.1063/5.0023206

84. Giri RS, Mandal B. Boc-Val-Val-OMe (Aβ39–40) and Boc-Ile-Ala-OMe (Aβ41–42) crystallize in a parallel β-sheet arrangement but generate a different morphology. *CrystEngComm*. 2018;20(31):4441-4448. doi: 10.1039/C8CE00097B

85. Dandurand J, Samouillan V, Lacoste-Ferre MH, Lacabanne C, B.Bochicchio, Pepe A. Conformational and thermal characterization of a synthetic peptidic fragment inspired from human tropoelastin: signature of the amyloid fibers. *Pathol Biol*. 2014;62(2):100-107. doi: 10.1016/j.patbio.2014.02.001

86. Qian Y, Engel MH, Macko SA, Carpenter S, Deming JW. Kinetics of peptide hydrolysis and amino acid decomposition at high temperature. *Geochim Cosmochim Acta*. 1993;57(14):3281-3293.
doi: 10.1016/0016-7037(93)90540-D

87. Kahin K, Khan Z, Albagami M, *et al*. Development of a robotic 3D bioprinting and microfluidic pumping system for tissue and organ engineering. In: Gray BL, Becker H, eds. *Microfluidics, BioMEMS, and Medical Microsystems XVII*. SPIE; 2019:25.
doi: 10.1117/12.2507237

88. Isidro-Llobet A, Kenworthy MN, Mukherjee S, *et al*. Sustainability challenges in peptide synthesis and purification: from R&D to production. *J Org Chem*. 2019;84(8):4615-4628.
doi: 10.1021/acs.joc.8b03001

89. Lotz MK, Otsuki S, Grogan SP, Sah R, Terkeltaub R, D'Lima D. Cartilage cell clusters. *Arthritis Rheum*. 2010;62(8):2206-2218.
doi: 10.1002/art.27528

90. Matta C, Mobasheri A. Regulation of chondrogenesis by protein kinase C: emerging new roles in calcium signalling. *Cell Signal*. 2014;26(5):979-1000.
doi: 10.1016/j.cellsig.2014.01.011

91. Zhang Q, Yu Y, Zhao H. The effect of matrix stiffness on biomechanical properties of chondrocytes. *ABBS*. 2016;48(10):958-965.
doi: 10.1093/abbs/gmw087

92. Malko AV, Villagomez M, Aubin JE, Opas M. Both chondroinduction and proliferation account for growth of cartilage nodules in mouse limb bud cultures. *Stem Cell Rev Rep*. 2013;9(2):121-131.
doi: 10.1007/s12015-013-9434-7

93. Sarem M, Otto O, Tanaka S, Shastri VP. Cell number in mesenchymal stem cell aggregates dictates cell stiffness and chondrogenesis. *Stem Cell Res Ther*. 2019;10(1):10.
doi: 10.1186/s13287-018-1103-y

94. Rolfe RA, Shea CA, Murphy P. Geometric analysis of chondrogenic self-organisation of embryonic limb bud cells in micromass culture. *Cell Tissue Res*. 2022;388(1): 49-62.
doi: 10.1007/s00441-021-03564-y

95. Lefebvre V, Behringer RR, De Crombrugghe B. L-Sox5, Sox6 and Sox9 control essential steps of the chondrocyte differentiation pathway. *Osteoarthritis Cartilage*. 2001;9 Suppl A:S69-S75.
doi: 10.1053/joca.2001.0447

96. De Moor L, Fernandez S, Vercruysse C, *et al*. Hybrid bioprinting of chondrogenically induced human mesenchymal stem cell spheroids. *Front Bioeng Biotechnol*. 2020;8:484.
doi: 10.3389/fbioe.2020.00484

97. Von Der Mark K. Structure, biosynthesis and gene regulation of collagens in cartilage and bone. In: *Dynamics of Bone and Cartilage Metabolism*. Erlangen, Germany: Elsevier; 2006:3-40.
doi: 10.1016/B978-012088562-6/50002-9

98. Naumann A, Dennis JE, Awadallah A, *et al*. Immunochemical and Mechanical Characterization of Cartilage Subtypes in Rabbit. 2002;50(8):1049-1058.
doi: 10.1177/002215540205000807

99. Department of Oral and Maxillofacial Surgery, Special Dental Care and Orthodontics, Erasmus MC, 3000 DR Rotterdam, the Netherlands, Knuth C, Andres Sastre E, *et al*. Collagen type X is essential for successful mesenchymal stem cell-mediated cartilage formation and subsequent endochondral ossification. *eCM*. 2019;38: 106-122.
doi: 10.22203/eCM.v038a09

100. He Y, Siebuhr AS, Brandt-Hansen NU, *et al*. Type X collagen levels are elevated in serum from human osteoarthritis patients and associated with biomarkers of cartilage degradation and inflammation. *BMC Musculoskelet Disord*. 2014;15(1):309.
doi: 10.1186/1471-2474-15-309

101. Sasano Y, Takahashi I, Mizoguchi I, Kagayama M, Takita H, Kuboki Y. Type X collagen is not localized in hypertrophic or calcified cartilage in the developing rat trachea. *Anat Embryol*. 1998;197(5):399-403.
doi: 10.1007/s004290050151

102. Weidenbecher M, Tucker HM, Gilpin DA, Dennis JE. Tissue-engineered trachea for airway reconstruction. *Laryngoscope*. 2009;119(11):2118-2123.
doi: 10.1002/lary.20700

103. Taylor DL, In Het Panhuis M. Self-healing hydrogels. *Adv Mater*. 2016;28(41):9060-9093.
doi: 10.1002/adma.201601613

104. Sophia Fox AJ, Bedi A, Rodeo SA. The basic science of articular cartilage: structure, composition, and function. *Sports Health*. 2009;1(6):461-468.
doi: 10.1177/1941738109350438

105. Villegas DF, Donahue TLH. Collagen morphology in human meniscal attachments: a SEM study. *Connect Tissue Res*. 2010;51(5):327-336.
doi: 10.3109/03008200903349639

ACCSCIENCE PUBLISHING

International Journal of Bioprinting

RESEARCH ARTICLE

Enhancing osteogenesis using 3D-printed porous tantalum scaffolds: A biomechanical, *in vivo*, and *in vitro* study

Mengxiao Tantai[1,2,3†], Yi Zhang[1,2,3†], Chengbin Wang[2,3], Tongwei Du[4], Sihao Yu[1,2,3], Zhihai Zhang[1,2,3], Hui Ma[3], Junliang Song[3], Dong Qu[5], Gangning Feng[1,2,3*], and Zhidong Lu[1,2,3*]

[1]Department of Spinal Surgery, General Hospital of Ningxia Medical University, Yinchuan, Ningxia, China

[2]Institute of Osteoarthropathy, Institute of Medical Sciences, General Hospital of Ningxia Medical University, Yinchuan, Ningxia, China

[3]The First Clinical Medical School, Ningxia Medical University, Yinchuan, Ningxia, China

[4]State Key Laboratory for Manufacturing System Engineering, School of Mechanical Engineering, Xi'an Jiaotong University, Xi'an, Shaanxi, China

[5]School of Metallurgical Engineering, Xi'an University of Architecture and Technology, Xi'an, Shaanxi, China

[†]These authors contributed equally to this work.

***Corresponding authors:**
Zhidong Lu
(15709600520@163.com)

Gangning Feng
(2867734776@qq.com)

Citation: Tantai M, Zhang Y, Wang C, *et al.* Enhancing osteogenesis using 3D-printed porous tantalum scaffolds: A biomechanical, *in vivo*, and *in vitro* study. *Int J Bioprint.* 2025;11(6):499-514. doi: 10.36922/IJB025390395

Received: September 23, 2025
Revised: October 4, 2024
Accepted: October 11, 2025
Published online: October 14, 2025

Copyright: © 2025 Author(s). This is an Open Access article distributed under the terms of the Creative Commons Attribution License, permitting distribution, and reproduction in any medium, provided the original work is properly cited.

Publisher's Note: AccScience Publishing remains neutral with regard to jurisdictional claims in published maps and institutional affiliations.

Abstract

Complex bone defects continue to pose significant challenges in the field of orthopedics, where restoring structural integrity and promoting osteointegration are essential for successful repair outcomes. Three-dimensional (3D) printing offers a robust approach for fabricating patient-specific scaffolds with precise architectural and functional control. In this study, we designed and fabricated porous scaffolds composed of tantalum and titanium alloys, both with identical porosity, utilizing 3D printing technology. We systematically compared their mechanical properties, *in vitro* osteogenic potential, and *in vivo* bone integration within a defect model. The porous tantalum (PTa) scaffolds demonstrated exceptional biocompatibility, enhanced cell adhesion, and significantly promoted the osteogenic differentiation of mesenchymal stem cells, as well as extracellular matrix mineralization. *In vivo*, the PTa scaffolds not only expedited bone repair but also improved osteoconductive ingrowth compared to their titanium counterparts. Multi-omics analyses further elucidated potential biological mechanisms underlying the superior performance of PTa. These findings underscore the potential of 3D-printed PTa as a promising scaffold material for the clinical repair of bone defects.

Keywords: Biomaterials; Bone regeneration; Multi-omics analysis; Osteogenic differentiation; Porous tantalum

1. Introduction

Bone defects currently represent a prevalent clinical challenge in orthopedic practice. Critical-sized bone defects, resulting from trauma, infection, or bone tumors, frequently

exceed the regenerative capacity of autologous bone grafts, making repair difficult. These defects have emerged as a significant global health concern, adversely impacting patients' quality of life. As a result, biomaterials research has focused on developing innovative bone substitutes.[1] Traditionally, autologous bone grafting has been considered the "gold standard" for bone regeneration. Nevertheless, its clinical utility is constrained by the limited availability of donor tissue and the invasive nature of harvesting.[2]

In recent years, metal-based implant materials have become a key focus due to their potential in bone defect repair. With excellent mechanical performance and favorable biological properties, these materials have been widely applied in the biomedical field. Among them, tantalum, titanium, and their alloys are commonly used in clinical orthopedic practice due to their superior strength and biocompatibility.[3] However, titanium alloys exhibit relatively low bioactivity and limited osteoconductivity. Their high elastic modulus may also lead to stress shielding and localized stress concentration, increasing the risk of implant loosening, fracture, and periprosthetic bone loss.[4]

Tantalum has emerged as a promising alternative due to its remarkable properties. It is characterized by exceptional corrosion resistance and superior biocompatibility, rendering it highly suitable for implant applications.[5] Porous tantalum (PTa), an innovative biomaterial, has shown considerable promise in bone tissue engineering. Its high porosity and interconnected pore structure not only enhance mechanical adaptability but also facilitate osseointegration, promoting new bone formation and long-term implant stability.[6] Furthermore, its low elastic modulus and high surface friction coefficient contribute to the effective reduction of stress shielding, minimization of marginal bone loss, and improvement of initial implant stability.[7]

PTa has been increasingly applied in orthopedic procedures such as hip and knee joint reconstruction,[8] and has also demonstrated encouraging outcomes in dental implants.[9] Compared with conventional titanium, PTa significantly promotes the proliferation and differentiation of primary osteoblasts, particularly in elderly patients, thereby supporting more stable bone integration.[10]

Despite these advancements, the molecular mechanisms by which PTa promotes bone regeneration remain insufficiently understood, with few studies employing multi-omics approaches. To our knowledge, this is the first study to systematically integrate transcriptomic and proteomic analyses to investigate these mechanisms. Structurally identical PTa and porous titanium alloy (PTi6Al4V) scaffolds were fabricated using a uniform process and characterized mechanically. *In vitro*, we compared rabbit bone marrow-derived mesenchymal stem cell (BMSC) adhesion, proliferation, and osteogenic differentiation on both scaffolds. *In vivo*, we assessed bone ingrowth post-implantation. Multi-omics analysis of peri-implant bone tissue revealed distinct biological pathways associated with each material, offering new insights into the molecular basis of PTa-enhanced osteogenesis.

2. Materials and methods

2.1. Materials

The porous cylindrical scaffolds, measuring 70 mm × 70 mm, were designed with a porosity of 75% and pore sizes ranging from 300 to 600 μm. These scaffolds were modeled using SolidWorks (Dassault Systèmes, France), employing a diamond lattice unit cell structure to delineate the internal geometry. The 3D modeling files can be found in Supplementary Material S1. Following initial modeling, the designs were optimized and repaired with Materialise Magics 24.0 (Materialise N.V., Belgium) to ensure suitability for three-dimensional (3D) printing. The raw materials utilized included highly spherical metal powders with particle sizes between 15 and 53 μm, specifically radio frequency plasma-spheroidized tantalum powder and plasma rotating electrode-atomized Ti6Al4V powder. The particle size distribution was assessed using a laser diffraction particle size analyzer. The scaffolds were fabricated by Ningxia Orient Additive Manufacturing Technology Co., Ltd., utilizing an FS271M laser powder bed fusion system (Farsoon Technologies Co., Ltd., China). To mitigate oxidation, all fabrication processes were conducted in an argon atmosphere, with the oxygen concentrations maintained below 100 ppm. A 67° layer rotation scanning strategy was implemented during printing to reduce residual stress accumulation between adjacent layers.

Optimized processing parameters were employed to produce high-density porous scaffolds. For tantalum scaffolds, the parameters included a laser power of 340 ± 5 W, a scanning speed of 530 ± 5 mm/s, a hatch spacing of 100 μm, and a layer thickness of 30 μm. For titanium alloy (Ti6Al4V) scaffolds, the parameters included a laser power of 280 ± 5 W, a scanning speed of 650 mm/s, a hatch spacing of 90 μm, and a layer thickness of 40 μm. Upon completion of fabrication, the scaffolds were detached from the build platform using wire electrical discharge machining. Residual and partially sintered powders were removed via sandblasting, followed by ultrasonic cleaning in ethanol. Finally, post-fabrication annealing was conducted to alleviate residual thermal stresses induced during the laser powder bed fusion process. The tantulum scaffolds were vacuum-annealed at 1200°C for 2 h, while

the Ti6Al4V scaffolds underwent annealing at 800°C for the same duration under identical atmospheric conditions.

Cylindrical scaffolds measured 7 mm in both diameter and height, while disc-shaped scaffolds measured 15 mm in diameter and 1 mm in height. Surface morphology and microstructure were examined using scanning electron microscopy (SEM), and energy-dispersive spectroscopy was used to qualitatively analyze surface elemental composition.

2.2. Static mechanical testing

To assess the mechanical properties of the scaffolds both before and after implantation, as well as to monitor their temporal changes, uniaxial compression tests were performed using a universal testing machine (CMT4000, MTS SYSTEMS Co., Ltd., China). These tests were conducted on scaffold samples prior to implantation and again after a two-month *in vivo* period. Load–displacement data were recorded and subsequently converted into stress–strain curves, from which the elastic modulus and yield strength were derived. Three samples from each group were tested.

2.3. *In vitro* evaluation of bone marrow-derived mesenchymal stem cell–scaffold interactions

Disc-shaped samples (φ15 mm × 1 mm) were used for *in vitro* co-culture experiments. Rabbit BMSCs (2×10^4 cells per well) were seeded onto the surfaces of both scaffolds in 12-well plates. Cell proliferation was assessed on days 1, 3, and 5 using the Cell Counting Kit-8 (CCK-8; Biyuntian, China). Scaffold cytotoxicity was evaluated on day 1 using a live/dead cell staining kit (C2015S, Biyuntian, China). Cell adhesion to the scaffold surfaces was examined using SEM, as well as phalloidin and 4',6-diamidino-2-phenylindole (DAPI) fluorescence staining (Biyuntian, China). These analyses were performed to comprehensively assess the biocompatibility of the two scaffold types.

2.4. Alkaline phosphatase activity and mineralized nodule staining

A total of 1×10^5 BMSCs were seeded onto the surfaces of both scaffolds in six-well plates. After 24 h of culture, the medium was replaced with osteogenic induction medium (OriCell, China), which was refreshed every three days. Alkaline phosphatase (ALP) activity was measured on days 3, 5, and 7 using an ALP assay kit (C3206, Biyuntian, China). On days 14 and 21, osteogenic mineralization was evaluated using alizarin Red S staining (ARS; OriCell, China) to assess the osteogenic differentiation capacity of BMSCs on the scaffolds.

2.5. Real-time quantitative polymerase chain reaction

To evaluate the expression of osteogenic-related genes in co-cultured cells, 1×10^5 BMSCs were seeded onto the surfaces of both scaffolds in 12-well plates. Total RNA was extracted at days 3, 7, and 14 of induction using the FreeZol reagent kit (R711-01/02, Vazyme, China). Complementary DNA (cDNA) was synthesized using a reverse transcription kit (R233-01, Vazyme, China). Quantitative real-time polymerase chain reaction (qRT-PCR) was conducted using a real-time PCR system under the following cycling conditions: 95°C for 30 s, followed by 45 cycles of 95°C for 5 s and 60°C for 34 s. Relative messenger RNA (mRNA) expression levels of osteogenic genes—*Bmp2*, *Col1a1*, *Runx2*, *Ocn*, and *Ogn*—were calculated using the $2^{-\Delta\Delta Ct}$ method. All primers were synthesized by Wuhan JinKaiRui Bioengineering Co., Ltd. (China), and their sequences are listed in Table 1.

2.6. Western blot

To evaluate the expression of proteins related to the bone morphogenetic protein 2 (BMP2)–Smad signaling pathway, BMSCs were co-cultured with PTi and PTa scaffolds for seven days. Total protein was extracted using a protein extraction kit and quantified using a bicinchoninic acid (BCA) assay (both from keyGEN BioTECH, China). Equal amounts of protein were separated via 10% sodium dodecyl sulfate (SDS)-polyacrylamide gel electrophoresis (Epizyme, China) and transferred onto methanol-activated polyvinylidene fluoride membranes. Membranes were blocked with 5% skim milk for 2 h at room temperature, followed by overnight incubation at 4°C with primary antibodies against BMP-2, SMAD1, phosphorylated (p)-

Table 1. Primers used for quantitative real-time polymerase chain reaction analysis

Gene	Forward primer sequence (5'–3')	Reverse primer sequence (5'–3')
Gapdh	TGAAGGTCGGAGTGAACGGAT	CGTTCTCAGCCTTGACCGTG
Runx2	TCGCCTCACAAACAACCACAG	CTGGTAGTGACCTGCGGAGATT
Bmp2	GGTGGAACGACTGGATTGTG	CGGAATCTTAGAGTTCACGGAGT
Ocn	CTCACTCTTGTCGCCCTGCT	CTCTTGGACACGAAGGCTGAG
Ogn	GCAGATCATTTGGAAGAAGCCA	CACATAGCAAGCAAGTGGGC
Col1a1	CAAGAACGGAGATGACGGAGAA	CATCCAAACCACTGAAACCTCTGT

SMAD1/5/9, Runt-related transcription factor 2 (RUNX2), and glyceraldehyde 3-phosphate dehydrogenase (GAPDH; Abcam, United States of America). After three 10-minute washes with Tris-buffered saline with Tween-20, membranes were incubated with horseradish peroxidase-conjugated secondary antibodies (1:5000; Affinity, China) for 2 h at room temperature. Protein bands were visualized using an automated fluorescence detection system.

2.7. Rabbit femoral defect model and scaffold implantation

All animal experiments complied with the relevant laws and regulations governing animal research in China and were approved by the Ethics Committee of Ningxia Medical University (approval number IACUC-NYLAC-2024-049). A total of 54 male New Zealand White rabbits (6–8 weeks old, 3.1 ± 0.5 kg) were randomly assigned to four groups: blank (periosteum exposed without treatment), defect (bone defect created without scaffold implantation), PTi scaffold, and PTa scaffold groups.

Following anesthesia, a 2.5 cm longitudinal incision was made along the axis of the distal femur (Animal modeling hollow drills can be found in Supplementary Material S2). A cylindrical bone defect (8 mm in diameter) was created using an orthopedic hollow drill, and sterilized PTi or PTa scaffolds were implanted accordingly. After implantation, the site was rinsed with hydrogen peroxide and saline, disinfected with iodine tincture, and closed in layers with sutures. A pressure dressing with sterile gauze was applied. All procedures were conducted in a standardized surgical environment at the Animal Center of Ningxia Medical University. X-ray imaging was performed at four and eight weeks post-implantation to evaluate implant stability.

2.8. Histological staining: hematoxylin and eosin, Masson's trichrome, and toluidine blue

At four and eight weeks post-implantation, rabbits in each group were euthanized, and the scaffolds, along with surrounding tissues, were harvested. The specimens were fixed in 4% paraformaldehyde, followed by dehydration through a graded ethanol series. After paraffin embedding, hard tissue sections were prepared. These sections were subsequently stained with hematoxylin and eosin (H&E), Masson's trichrome, and toluidine blue, then examined under a light microscope.

2.9. Transcriptomic analysis

At four weeks post-implantation, the experimental rabbits were euthanized, and bone tissue surrounding the implanted scaffolds was harvested and immediately flash-frozen in liquid nitrogen. The samples were ground into a fine powder, and total RNA was extracted using an RNA purification kit (TaKaRa Biomedicals, Japan). RNA purity and integrity were assessed using a NanoDrop 2000 spectrophotometer (Thermo Fisher Scientific, United States of America) and an Agilent 2100 Bioanalyzer (United States of America) or LabChip GX system (PerkinElmer, United States of America). Following quality assessment, cDNA libraries were constructed and evaluated using a Qsep400 high-throughput analyzer (Bioptic, China). Libraries that passed quality control were subjected to paired-end 150 base pair (PE150) sequencing on a high-throughput sequencing platform.[11,12]

2.10. Proteomic analysis

The method for bone tissue sample collection was consistent with that used in the transcriptomic analysis. Tissues were lysed in buffer containing 1% SDS and 1% protease inhibitor, followed by ultrasonic disruption. Protein concentrations were measured using a BCA protein assay kit. Equal amounts of protein from each group were enzymatically digested with trypsin using the filter-aided sample preparation method.

The resulting peptides were dissolved in mobile phase A (0.1% formic acid and 2% acetonitrile in water) and separated using a NanoElute ultra-high-performance liquid chromatography system (Bruker Daltonics, Germany). Peptides were subsequently ionized via a CaptiveSpray ion source and analyzed using a timsTOF Pro mass spectrometer (Bruker Daltonics, Germany). Data were acquired in data-independent acquisition mode using parallel accumulation–serial fragmentation.[13,14]

2.11. Bioinformatics analysis

We performed bioinformatics analyses on both RNA-sequencing and proteomics datasets. Differential expression analysis of the transcriptomic data was conducted using the DESeq R package (version 1.10.1) to identify differentially expressed genes (DEGs), while proteomic data were analyzed to identify differentially expressed proteins (DEPs). The screening criteria for DEGs were a false discovery rate <0.05 and fold change (FC) ≥1.5. For DEPs, the criteria were $p < 0.05$ and FC ≥ 1.2. Principal component analysis (PCA) was used to assess sample clustering within each group. Venn diagrams and volcano plots were employed to visualize upregulated and downregulated DEGs and DEPs. Gene Ontology (GO) and Kyoto Encyclopedia of Genes and Genomes (KEGG) enrichment analyses of DEGs were performed using the ClusterProfiler package (v3.8.1).[15] Finally, osteogenesis-related DEGs and DEPs were screened, and the top 50 candidates were subjected to protein–protein interaction (PPI) network analysis.

2.12. Statistical analysis

All data are expressed as mean ± standard deviation. Statistical analyses were performed using GraphPad Prism 8.0 (GraphPad Software, United States of America). For comparisons between two groups, unpaired two-tailed Student's *t*-tests were conducted. For comparisons among multiple groups, one-way analysis of variance followed by Tukey's post hoc test was used. A p-value <0.05 was considered statistically significant.

3. Results

3.1. Comprehensive characterization of porous tantalum and porous titanium alloy scaffolds

A comprehensive characterization of the fabricated PTi6Al4V (PTi) and PTa scaffolds—including their design architecture, microstructural morphology, elemental composition, and mechanical properties—is presented in Figure 1.

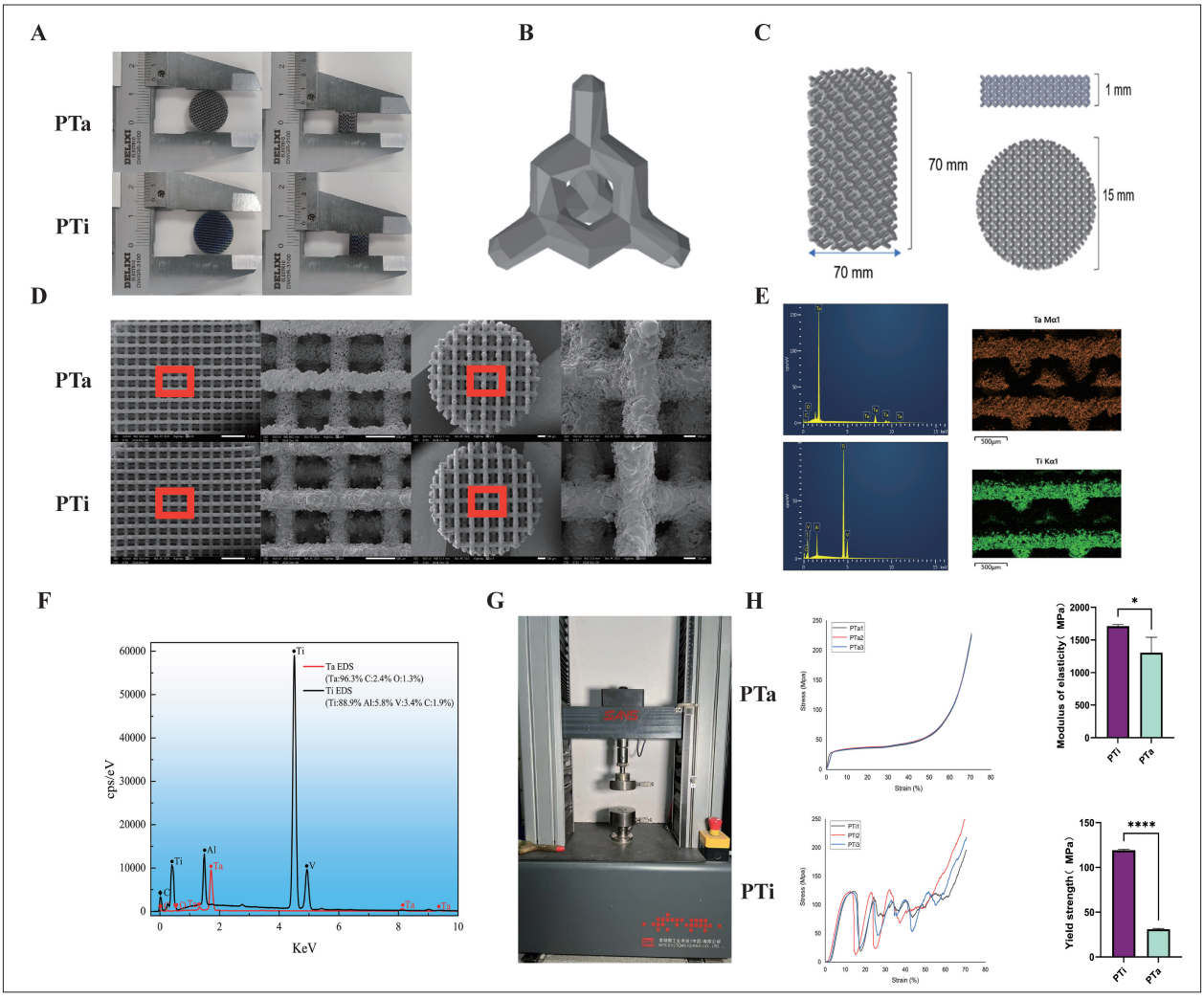

Figure 1. Design and characterization of PTa and porous titanium alloy (PTi6Al4V) scaffolds. (A) Photographs of the fabricated PTa and PTi scaffolds. (B) Illustration of the diamond lattice unit cell structure employed in the scaffold design. (C) Schematic showing the design parameters of cylindrical and disc-shaped scaffolds. (D) Scanning electron microscopy images showing the surface morphology and microstructural features of both scaffold types, with PTa exhibiting a rougher surface topology than PTi. Magnifications = 10×, 50×; scale bars: 2 μm, 500 μm. (E and F) EDS results showing the surface elemental composition: PTa scaffolds were primarily composed of tantalum (Ta; 96.3%), whereas PTi scaffolds contained titanium (Ti; 88.9%), aluminum (Al; 5.8%), and vanadium (V; 3.4%). Magnification = 50×; scale bar: 500 μm. (G and H) Stress–strain curves obtained from compression testing of both scaffold types, with the calculated elastic modulus and yield strength indicating that PTa has a lower modulus (1.3 ± 0.2 GPa) and significantly lower yield strength (30 ± 0.8 MPa) compared to PTi (1.7 ± 0.04 GPa and 119 ± 1 MPa, respectively), though more closely matching that of human cancellous bone. Abbreviations: C, carbon; O, oxygen; PTa, porous tantalum; EDS, energy-dispersive spectroscopy.

Photographs of the PTi and PTa scaffolds are shown in Figure 1A, and the diamond lattice unit cell structure employed for both scaffold types is illustrated in Figure 1B. The geometric dimensions of the cylindrical and disc-shaped scaffolds are detailed in Figure 1C.

SEM images (Figure 1D) revealed that both PTi and PTa scaffolds possessed a consistent 3D porous structure. At higher magnification, the surface of the PTa scaffold appeared notably rougher than that of PTi, which may facilitate enhanced cell adhesion. Energy-dispersive spectroscopy analysis (Figure 1E and 1F) confirmed that PTa scaffolds were primarily composed of tantalum, whereas PTi scaffolds contained titanium (88.9%), aluminum (5.8%), and vanadium (3.4%).

Stress–strain curves for both scaffold types are depicted in Figure 1G–1H. The elastic modulus of the PTa scaffold was slightly lower (1.3 ± 0.2 GPa) than that of the PTi scaffold (1.7 ± 0.04 GPa). Force-displacement curves for both types of brackets can be found in Supplementary Material S3. Notably, although the PTa scaffold exhibited a significantly lower yield strength (30 ± 0.8 MPa) compared to the PTi scaffold (119 ± 1 MPa), its mechanical strength is closer to that of human cancellous bone, potentially offering improved biomechanical compatibility in bone tissue regeneration applications.

3.2. *In vitro* evaluation of rabbit bone marrow-derived mesenchymal stem cell co-cultured with porous tantalum and porous titanium alloy scaffolds

To comprehensively evaluate the *in vitro* biocompatibility and osteogenic potential of PTa and PTi scaffolds, a series of experiments was conducted to assess BMSC viability, proliferation, adhesion, and osteogenic differentiation (Figure 2).

Live/dead staining was used to assess the viability of BMSCs co-cultured with PTa and PTi scaffolds. Fluorescence microscopy revealed a predominance of green fluorescence in the control, PTi, and PTa groups, indicating high cell viability across all groups. Only minimal red fluorescence was observed, suggesting that both scaffold types exhibited negligible cytotoxicity (Figure 2A). Cell proliferation was evaluated using the CCK-8 assay. Compared to the control group, BMSCs cultured on the PTa scaffold showed significantly increased proliferation at days 1 and 3 relative to those on the PTi scaffold. By day 5, no significant difference in proliferation was observed between the PTa and PTi groups, indicating a similar long-term proliferative capacity (Figure 2B).

SEM imaging on day 1 revealed the morphology and adhesion of BMSCs on the surfaces of both scaffolds. Cells exhibited good spreading and attachment on both materials (Figure 2C). Furthermore, confocal microscopy following phalloidin (for F-actin) and DAPI (for nuclei) staining demonstrated a higher density of adherent cells on the PTa scaffold compared to the PTi scaffold, suggesting superior initial cell attachment on PTa (Figure 2D).

3.3. Evaluation of osteogenic differentiation potential

Rabbit BMSCs were co-cultured with PTi and PTa scaffolds and subjected to osteogenic induction for three, five, and seven days. ALP staining and corresponding quantitative analysis were performed at each time point (Figure 2E). The results demonstrated that ALP activity in the PTa group was consistently higher than that in the PTi group across all time points, indicating that PTa scaffolds promoted enhanced early osteogenic differentiation. To determine late-stage osteogenesis, ARS staining was conducted on days 14 and 21 to evaluate mineralized nodule formation (Figure 2F). The PTa group exhibited a significantly greater number of mineralized nodules than the PTi group at both time points, suggesting a superior osteogenic mineralization capacity of the PTa scaffolds.

3.4. Expression of osteogenesis-related genes

The relative mRNA expression levels of osteogenic markers—*Bmp2*, *Col1a1*, *Runx2*, *Ocn*, and *Ogn*—were evaluated on days 3, 7, and 14 of BMSC co-culture with PTa and PTi scaffolds. GAPDH served as the internal control, and expression levels in the control group were normalized to 1.00. The $2^{-\Delta\Delta Ct}$ method was used to calculate the relative expression of target genes in the PTi and PTa groups. On day 3, *Bmp2*, *Col1a1*, and *Runx2* expression levels were significantly upregulated in the PTa group compared to the PTi group, while OCN and OGN showed no significant differences. On day 7, the PTa group exhibited significantly higher expression of all five osteogenic genes. By day 14, the expression levels of all genes showed no significant differences between the two groups (Figure 2G). These findings suggest that the PTa scaffold may promote the early expression of osteogenesis-related genes, potentially contributing to its enhanced osteoinductive capacity during the initial stages of bone regeneration.

3.5. Evaluation of BMP-2/SMAD1/RUNX2 signaling pathway activation

After 7 days of co-culture of BMSCs with PTa and PTi scaffolds, the expression levels of BMP-2, SMAD1, p-SMAD1/5/9, and RUNX2 proteins were evaluated using Western blotting. Band intensities were quantified with ImageJ software (National Institutes of Health, United States of America), and the p-SMAD1/5/9 to SMAD1 ratio was calculated for each group. All experiments were performed in triplicate, and the resulting data were statistically analyzed. The results demonstrated that the

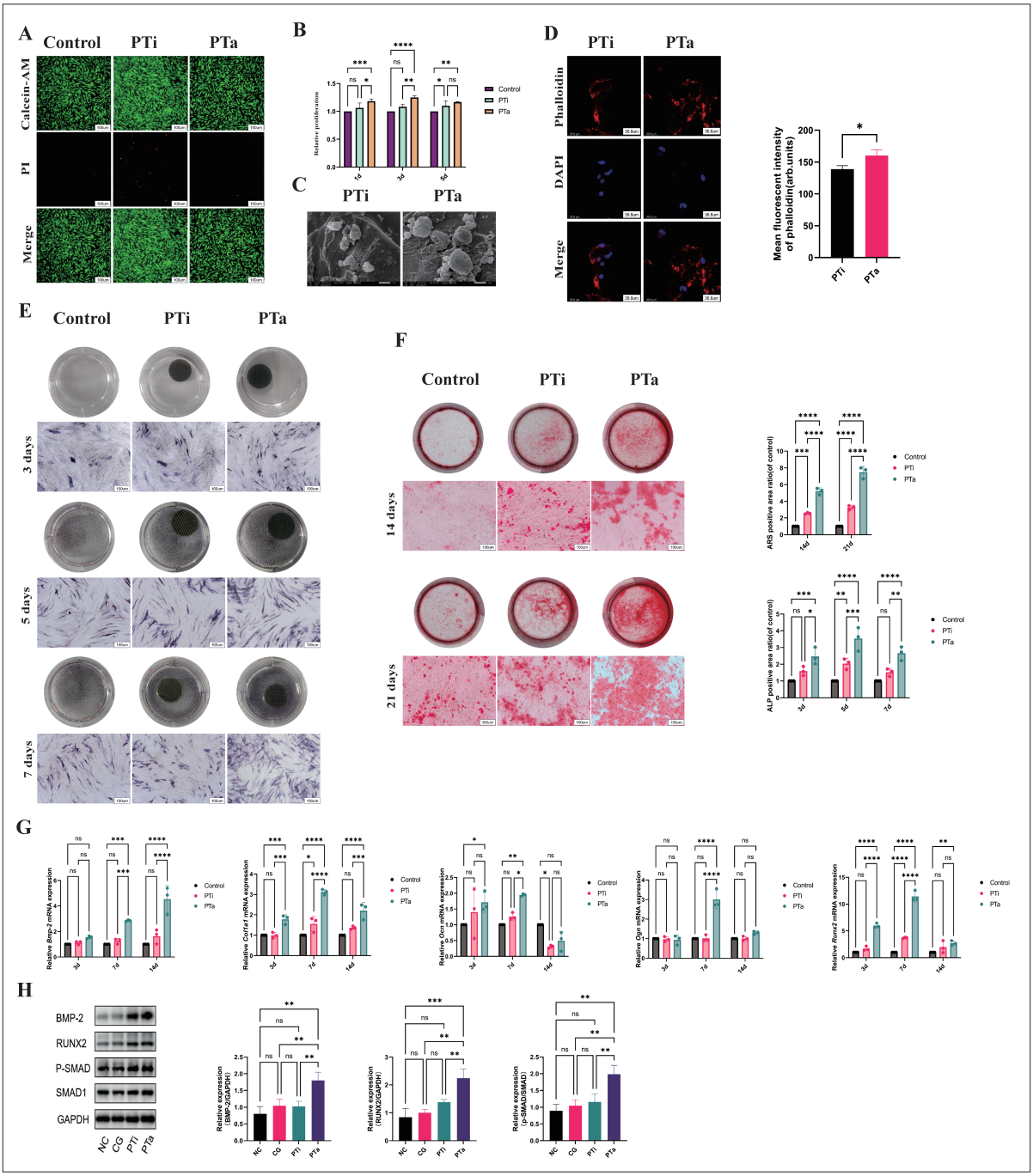

Figure 2. *In vitro* cellular responses of rabbit BMSCs co-cultured with porous tantalum (PTa) and porous titanium alloy (Pti) scaffolds. (A) Live/dead staining of BMSCs after 1 day of co-culture with PTa and PTi scaffolds, indicating high cell viability. (B) Cell Counting Kit-8 assay showing the relative proliferation of BMSCs on days 1, 3, and 5. (C) Scanning electron microscopy images showing BMSC adhesion and morphology on the scaffold surfaces after one day. Magnification = 8000×; scale bar: 2 μm. (D) Confocal microscopy images showing F-actin (phalloidin; red) and nuclei (DAPI; blue) staining to evaluate cytoskeletal organization and cell attachment. Magnification = 600×; scale bar: 36.8 μm. (E) ALP staining and semi-quantitative analysis on days 3, 5, and 7 post-osteogenic induction to assess early osteogenic differentiation. Magnification = 10×; scale bar: 100 μm. (F) ARS staining and quantification of mineralized matrix formation on days 14 and 21. Magnification = 10×; scale bar: 100 μm. (G) mRNA expression levels of osteogenic genes (*Bmp2*, *Col1a1*, *Runx2*, *Ocn*, and *Ogn*) on days 3, 7, and 14, normalized to *Gapdh*. (H) Western blot analysis of BMP-2, SMAD1, phosphorylated SMAD1/5/9 (p-SMAD1/5/9), and RUNX2 proteins at day 7, indicating activation of the BMP-2/SMAD1/RUNX2 signaling pathway. Abbreviations: AM, acetoxymethyl; arb., arbitrary; CG, defect control group; d, days; GAPDH, glyceraldehyde 3-phosphate dehydrogenase; NC, normal control group; ns, not significant; PI, propidium iodide; BMSCs, bone marrow-derived mesenchymal stem cells; DAPI, 4',6-diamidino-2-phenylindole; ALP, alkaline phosphatase; ARS, Alizarin red S; mRNA, relative messenger RNA; BMP-2, bone morphogenetic protein 2; RUNX2, runt-related transcription factor.

expression levels of BMP-2, SMAD1, p-SMAD1/5/9, and RUNX2 were significantly upregulated in the PTa group compared to the PTi group (Figure 2H), indicating that PTa scaffolds more effectively activate the BMP-2/SMAD1/RUNX2 signaling pathway. This enhanced signaling activity may underlie the superior osteoinductive potential observed in the PTa group.

3.6. Postoperative recovery and histological evaluation of bone regeneration

A thorough assessment of *in vivo* bone regeneration, including postoperative recovery, implant fixation, and histological analysis, was performed to evaluate the osteogenic efficacy of PTa and PTi scaffolds (Figure 3).

All rabbits regained consciousness within 2 h following surgery. The local incisions healed well, without signs of inflammation, infection, or wound dehiscence. X-ray imaging at four and eight weeks postoperatively confirmed that the implants remained properly fixed at the defect sites (Figure 3A).

To assess bone regeneration at the microscopic level, histological staining was performed at four and eight weeks after implantation. H&E, Masson's trichrome, and toluidine blue staining revealed substantial new bone formation within the defect regions in both PTa and PTi scaffold groups (Figure 3B–3G). Notably, the PTa group demonstrated more pronounced new bone tissue formation and superior bone ingrowth compared to the PTi group, indicating a stronger osteogenic capacity associated with the PTa scaffolds.

3.7. Comparative transcriptomic analysis of porous tantalum and porous titanium alloy scaffold-induced bone regeneration

Comprehensive lists of all identified proteins and genes from the proteomic and RNA-seq analyses are available in Supplementary File 2. To further elucidate the osteogenic mechanisms associated with PTa and PTi scaffolds, RNA sequencing was conducted on bone tissue samples collected one month after implantation(Figure 4). The

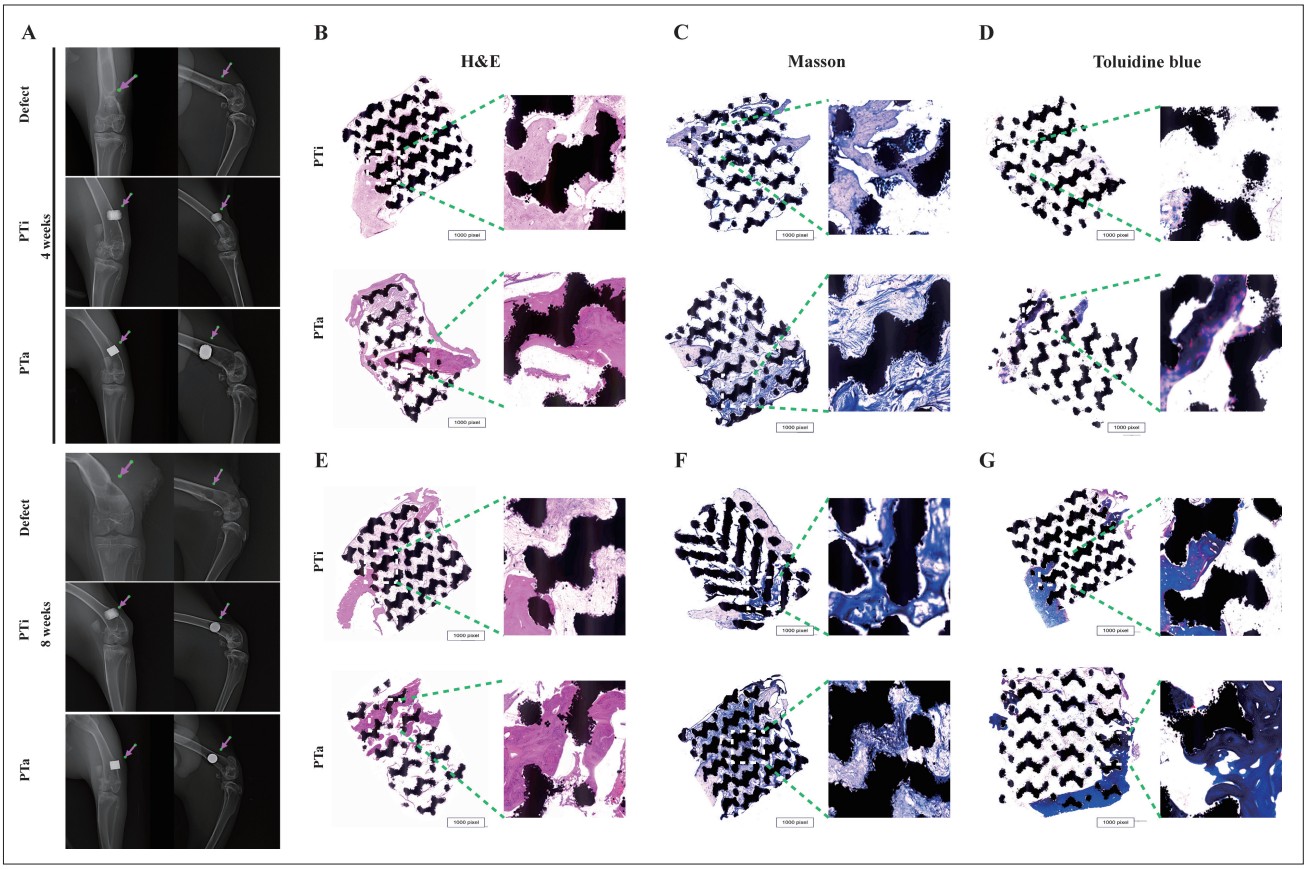

Figure 3. *In vivo* histological evaluation of bone regeneration induced by porous tantalum (PTa) and porous titanium alloy (PTi) scaffolds. (A) Representative X-ray images at four and eight weeks post-implantation in the rabbit femoral defect model, showing stable scaffold fixation. Histological staining at four weeks, including (B) hematoxylin and eosin (H&E), (C) Masson's trichrome, and (D) toluidine blue, reveals new bone formation in both groups. Histological staining at eight weeks using (E) H&E, (F) Masson's trichrome, and (G) toluidine blue demonstrates more extensive bone ingrowth into the PTa scaffold compared to the PTi scaffold.

study encompassed four groups: a normal control group (NC, representing healthy bone), a defect group (CG, comprising newly regenerated bone at the defect site), and two scaffold groups (PTa and PTi, representing new bone formation surrounding each respective scaffold). Each group consisted of six biological replicates.

Principal component analysis (Figure 4A) demonstrated a distinct separation among the groups, signifying unique transcriptomic profiles. The Venn diagram (Figure 4B) depicts both the overlap and distinctiveness of DEGs across the comparisons. Pearson correlation analysis (Figure 4C) corroborated strong intra-group consistency and pronounced inter-group differences. Volcano plots and hierarchical clustering heatmaps (Figure 4D and 4E) further underscored significant variations in gene expression patterns. A total of 2459 DEGs were identified between the PTa and PTi groups, with an FC of ≥ 1.5 and a false discovery rate of < 0.05. These DEGs underwent GO and KEGG enrichment analyses (Figure 4F–4I). GO analysis revealed enrichment in processes such as integrin-mediated signaling, glycolysis, and phagocytosis. Notably, genes upregulated in the PTi group were linked to neutrophil chemotaxis, innate immunity, and adaptive immune responses. KEGG analysis indicated significant enrichment in the mitogen-activated protein kinase signaling pathway, osteoclast differentiation, and chemokine signaling pathways.

To elucidate the principal regulators implicated in PTa-mediated osteogenesis, a PPI network analysis was subsequently performed on both transcriptome-derived DEGs and proteome-identified DEPs associated with osteogenesis (Figure 6). This analysis identified several hub genes, including *Col1a1*, *Spp1*, *Col3a1*, *Mmp9*, and *Acan*, which are intricately linked to collagen synthesis, osteoblast adhesion and mineralization, bone remodeling, and angiogenesis (Figure 6E and 6G). These results imply that PTa may facilitate bone regeneration through the coordinated regulation of extracellular matrix production, cellular adhesion, and remodeling pathways.

To enhance the validation and complementarity of the transcriptomic findings at the protein level, a proteomic analysis was subsequently performed to investigate differential protein expression patterns and the associated biological processes between the PTa and PTi scaffolds.

3.8. Comparative proteomic analysis of porous tantalum and porous titanium alloy scaffold-induced bone regeneration

Proteomic analysis was conducted utilizing the same sample cohorts as employed in the RNA-sequencing investigation. PCA (Figure 5A) demonstrated distinct clustering among the four groups, indicative of divergent proteomic profiles. Pearson correlation analysis (Figure 5B) confirmed strong intra-group consistency. A bar chart (Figure 5C) illustrates the number of DEPs identified between the groups. Heatmaps and volcano plots (Figure 5D and 5E) further revealed distinct protein expression patterns across the groups. Subsequent GO and KEGG enrichment analyses were performed on the DEPs (Figure 5F–5I). GO analysis indicated that the DEPs between the PTa and PTi groups were predominantly associated with biological regulation, primary metabolic processes, anatomical structure development, and signal transduction. KEGG pathway analysis demonstrated significant enrichment of these DEPs in pathways related to phagosomes, lysosomes, nuclear factor kappa-light-chain-enhancer of activated B cell signaling, nucleotide oligomerization domain-like receptor signaling, and the catabolism of branched-chain amino acids (valine, leucine, and isoleucine).

In the PTi group, upregulated proteins were significantly enriched in pathways related to immune responses and cell proliferation, including the erythroblastic oncogene B signaling pathway, B cell receptor signaling pathway, and phosphoinositide 3-kinase–protein kinase B signaling pathway. A PPI network analysis of osteogenesis-associated DEPs (Figure 6A and 6C) identified several key regulators potentially involved in PTa-induced bone regeneration, such as Ras-related C3 botulinum toxin substrate 2 (RAC2), caveolin-1 (CAV1), annexin A1 (ANXA1), Ras homolog gene family, member B (RHOB), and integrin subunit alpha 1 (ITGA1). These findings suggest that the superior osteogenic potential of PTa scaffolds may be attributed to enhanced cell adhesion, signal transduction, chromatin remodeling, and cytoskeletal reorganization.

4. Discussion

This study elucidates, through comprehensive *in vitro* and *in vivo* experiments, that PTa scaffolds facilitate bone regeneration by providing mechanical support and modulating various biological processes. By employing integrated transcriptomic and proteomic analyses of peri-implant bone tissue within a rabbit model, we gained new insights into the molecular mechanisms underpinning PTa-induced osseointegration. While prior studies have investigated the biological performance of PTa scaffolds, most have focused on individual pathways or cellular behaviors.[16–18] Few studies have applied integrated multi-omics approaches. Our findings suggest that PTa scaffolds promote bone regeneration through advantageous physical properties combined with the activation of specific molecular pathways, which may act synergistically to enhance osseointegration and new bone formation.

To our knowledge, this study represents the first systematic investigation of the *in vivo* osteogenic

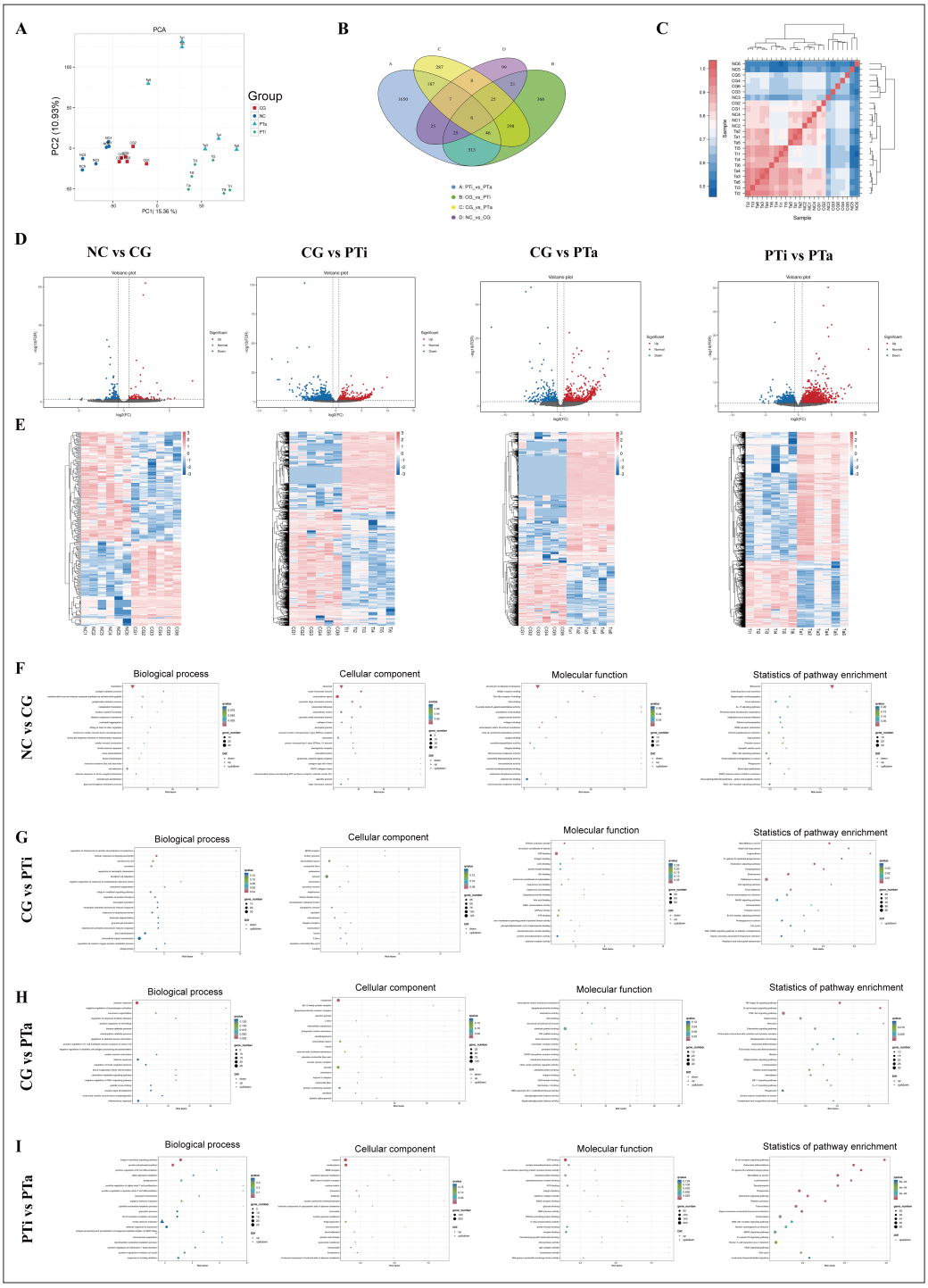

Figure 4. Transcriptomic profiling and comparative analysis of bone tissue surrounding porous tantalum (PTa) and porous titanium alloy (PTi) scaffolds. (A) Principal component analysis (PCA) reveals distinct clustering of samples from the normal control (NC), defect control (CG), PTi, and PTa groups, indicating divergent transcriptomic signatures. (B) Venn diagram illustrating the overlap and uniqueness of differentially expressed genes (DEGs) among the groups. (C) Pearson correlation heatmap showing strong intra-group consistency and clear inter-group distinctions. (D) Volcano plot and (E) hierarchical clustering heatmap highlighting DEGs between the PTa and PTi groups. (F) Gene Ontology (GO) and Kyoto Encyclopedia of Genes and Genomes (KEGG) enrichment analyses of DEGs between the NC and CG groups, identifying biological processes associated with bone defect response. (G) GO and KEGG enrichment analyses comparing the CG and PTi groups, revealing enrichment of immune and inflammatory pathways in PTi. (H) GO and KEGG enrichment analyses comparing the CG and PTa groups, indicating enhanced osteogenic and metabolic pathways in PTa. (I) GO and KEGG enrichment of DEGs between the PTi and PTa groups, showing key differences in osteogenesis, immune modulation, and cell signaling processes.

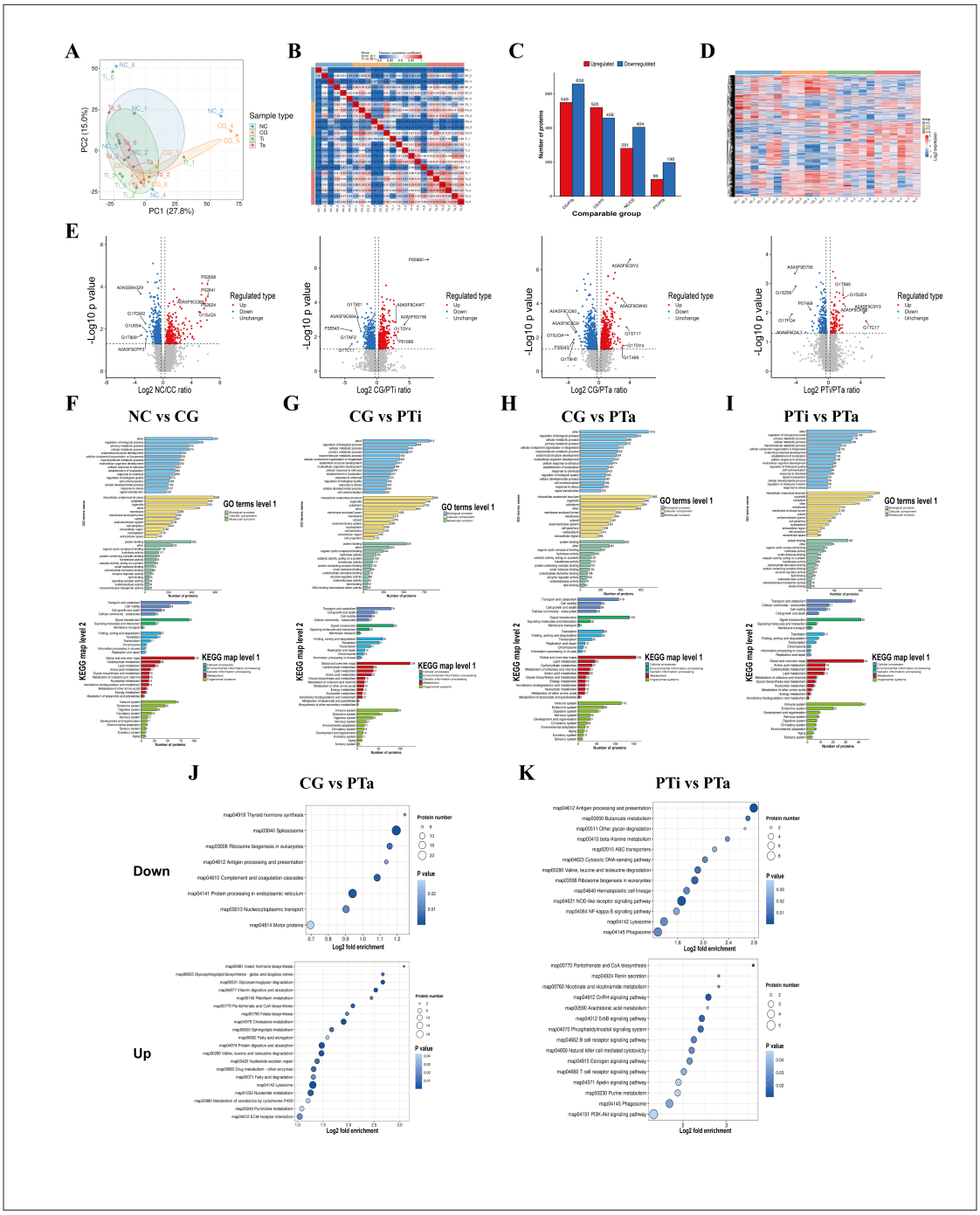

Figure 5. Proteomic profiling and comparative analysis of peri-implant bone tissues in different scaffold groups. (A) Principal component analysis (PCA) revealed distinct clustering among normal control (NC), defect control (CG), porous titanium alloy (PTi), and porous tantalum (PTa) groups, indicating divergent proteomic profiles. Pearson correlation coefficient (B) heatmaps and (C) bar chart confirm high intra-group consistency and distinct inter-group variation. (D) Hierarchical clustering heatmap of differentially expressed proteins (DEPs) across all groups. (E) Volcano plots highlighting significantly upregulated and downregulated proteins between groups. (F) Gene Ontology (GO) and Kyoto Encyclopedia of Genes and Genomes (KEGG) enrichment analyses of DEPs between NC and CG groups revealed biological processes related to bone defect responses. (G) GO and KEGG analyses comparing the CG and PTi groups demonstrate enrichment in immune-related pathways. (H) GO and KEGG analyses of CG vs. PTa groups indicate activation of osteogenic, metabolic, and angiogenic pathways. (I) Comparative GO and KEGG analysis between PTi and PTa groups reveals distinct molecular mechanisms underlying bone regeneration. (J) Bubble plots of the top 20 upregulated and downregulated KEGG pathways in PTa vs. CG, showing osteogenesis- and repair-associated signaling activation. (K) Bubble plots of the top 20 upregulated and downregulated KEGG pathways in PTa vs. PTi, emphasizing enhanced bone formation and immune modulation in PTa.

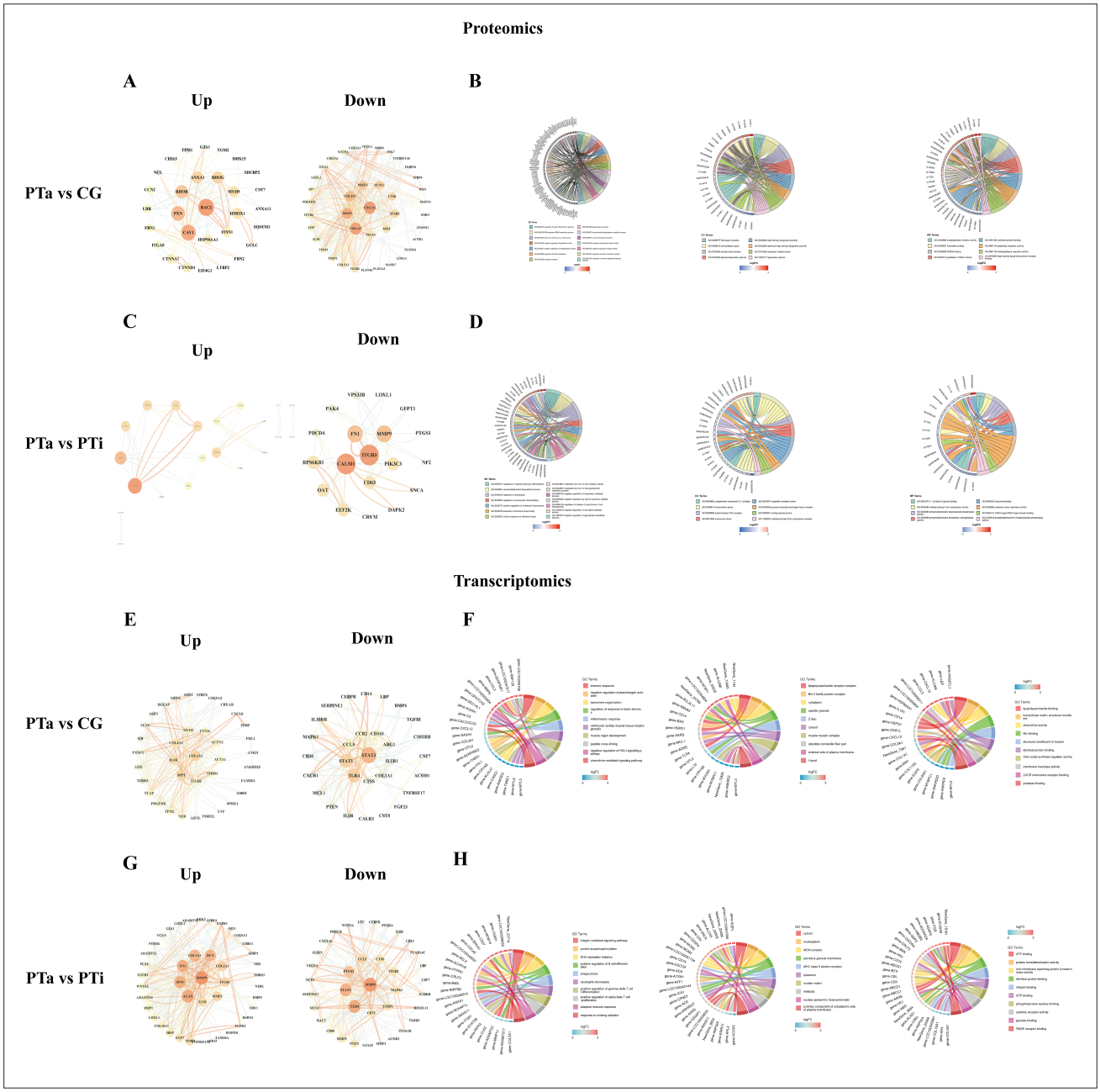

Figure 6. Protein–protein interaction (PPI) networks and Gene Ontology (GO) enrichment chord plots of differentially expressed proteins (DEPs) and genes (DEGs). (A) PPI network of the top 50 upregulated and downregulated osteogenesis-related DEPs between the porous tantalum (PTa) and defect control (CG) groups. (B) GO enrichment chord diagram displaying biological processes associated with DEPs between the PTa and CG groups. (C) PPI network of the top 50 upregulated and downregulated osteogenesis-related DEPs between PTa and porous titanium alloy (PTi) groups. (D) GO enrichment chord diagram illustrating the relationship between DEPs and enriched biological functions in the PTa vs. PTi comparison. (E) PPI network of the top 50 upregulated and downregulated osteogenesis-related DEGs between the PTa and CG groups. (F) GO enrichment chord diagram showing biological processes linked to DEGs in the PTa vs. CG comparison. (G) PPI network of the top 50 upregulated and downregulated osteogenesis-related DEGs between the PTa and PTi groups. (H) GO enrichment chord diagram visualizing functional associations of DEGs between PTa and PTi groups.

mechanisms of PTa and PTi scaffolds utilizing integrated transcriptomic and proteomic analyses. We also performed a direct comparison of the biological responses elicited by these two materials. Given the complexity of the physiological environment and the multifactorial nature of bone regeneration, the clinical translation of PTa scaffolds remains a long-term objective.[19] Nevertheless, our findings provide significant evidence supporting the potential application of PTa in bone tissue engineering.

Extensive and complex bone defects remain a major challenge in orthopedic treatment.[20] Although autologous bone grafting is regarded as the gold standard, its application is limited by the scarcity of donor tissue and complications associated with graft harvesting.[21] Metal-based implants have emerged as promising alternatives for the reconstruction of large bone defects. Materials such as stainless steel and titanium alloys are widely used in clinical settings due to their favorable mechanical properties.[22,23] However, their relatively high elastic modulus may lead to stress shielding, which can result in bone resorption and impaired osseointegration over time.[24]

The introduction of PTa represents a significant advancement in the development of metallic biomaterials. Compared with traditional metallic implants, such as titanium alloys, PTa demonstrates enhanced corrosion resistance, higher friction coefficients, and superior wear resistance.[25] Moreover, the elastic modulus and mechanical strength of PTa are closely aligned with those of cancellous bone, which helps reduce stress shielding while offering sufficient biomechanical support.[26] Nevertheless, the high melting point and density of tantalum have historically presented substantial challenges in its processing and clinical application. The rapid progress in additive manufacturing has facilitated the emergence of 3D-printed PTa as a next-generation implant material. This technology allows for precise and customizable fabrication of intricate implant geometries with high resolution and integration. When combined with computed tomography (CT)-based 3D modeling, 3D-printed PTa holds significant promise for applications in the treatment of complex bone defects.[27]

In addition, to address the mechanical and functional requirements of bone repair, various strategies have been developed for modifying the surface properties of metallic alloys. A prevalent method involves applying tantalum coatings to titanium scaffolds to improve their bioactivity and osseointegration potential.[28] Studies have also shown that incorporating PTa scaffolds with drug delivery systems and targeted therapeutic strategies can mitigate the inherent limitations of the material's mechanical and physicochemical properties, thereby facilitating multifunctional enhancements.[29] Nonetheless, the biological mechanisms through which PTa promotes osteogenesis are not yet fully elucidated and require further investigation.

In this study, PTa and PTi scaffolds with identical specifications were fabricated. Mechanical testing indicated that PTi exhibited a significantly higher elastic modulus and yield strength compared to PTa; however, the elastic modulus of PTa more closely approximated that of human cancellous bone. Moreover, PTa still provided sufficient mechanical strength to support bone tissue. Its highly porous and interconnected architecture facilitates cell adhesion and bone tissue ingrowth, rendering PTa a promising candidate for load-bearing bone integration applications.[27] Subsequent *in vitro* experiments assessed the biocompatibility of PTa by evaluating cytotoxicity, cell adhesion, and proliferation of rabbit BMSCs co-cultured with PTa scaffolds. The results confirmed the excellent biocompatibility of PTa. It is worth noting that, in both the SEM and Phalloidin staining experiments, PTa and PTi scaffolds were used as direct comparators, without including a separate tissue culture plastic control. This design choice was deliberate. The two scaffolds share identical structural parameters but differ in material composition, allowing for a direct evaluation of how the intrinsic physicochemical properties of tantalum versus titanium influence cellular behavior. By contrast, cells grown on smooth tissue culture plastic exhibit fundamentally different adhesion and morphology due to the distinct surface characteristics, which would confound interpretation in the context of scaffold comparison. The osteogenic differentiation potential was further evaluated using ALP activity and ARS, which demonstrated that PTa significantly enhanced the osteogenic differentiation of BMSCs compared to PTi. These findings are consistent with previous reports.[30,31]

Gene expression analysis utilizing RT-qPCR demonstrated that PTa scaffolds significantly upregulated the mRNA expression levels of osteogenic markers, including *Bmp2*, *Col1a1*, *Runx2*, *Ocn*, and *Ogn*, particularly during the initial phases of differentiation. This indicates a superior osteoinductive capacity of PTa compared to PTi. These findings were corroborated by western blot analysis of the BMP-2/SMAD1/RUNX2 signaling pathway, which confirmed enhanced osteogenic signaling in the PTa group. To further validate the *in vivo* efficacy of the scaffolds, PTa and PTi were implanted into rabbit femoral bone defect models. Histological analyses, including H&E, Masson's trichrome, and toluidine blue staining, conducted at four and eight weeks post-implantation, revealed more substantial new bone formation and improved osseointegration in the PTa group relative to the PTi group.

To further elucidate the biological mechanisms underlying PTa-mediated bone regeneration, we conducted integrated transcriptomic (RNA-sequencing) and proteomic (liquid chromatography coupled with tandem mass spectrometry) analyses on peri-implant bone tissues collected one month after surgery. The multi-omics data indicated that PTa promotes bone formation via pathways related to collagen biosynthesis, osteoblast adhesion and mineralization, bone remodeling, angiogenesis, histone acetylation, cytoskeletal dynamics, and cellular metabolism. To pinpoint key molecular regulators involved in PTa-induced osteogenesis, we constructed PPI networks based on both transcriptomic and proteomic osteogenesis-related DEGs and DEPs. Core hub genes (e.g., *Col1a1*, *Spp1*, *Col3a1*, *Mmp9*, Acan) and proteins (e.g., RAC2, CAV1, ANXA1, RHOB, ITGA1) were identified at the transcriptomic and proteomic levels, respectively. These molecules are implicated in essential processes, including extracellular matrix organization, cell adhesion, cytoskeletal remodeling, and intracellular signaling—highlighting their potential roles in mediating the superior osteogenic performance of PTa scaffolds.

While our findings highlight the clinical potential of PTa scaffolds for bone defect repair, additional research is necessary to validate their efficacy in more complex scenarios, such as irregular defect models and patient-specific implants designed using CT-based methodologies. Furthermore, given that PTa is a relatively recent addition to the field of biomaterials, its long-term *in vivo* stability and clinical performance warrant continued investigation.

Overall, this study provides new insights into the osteogenic mechanisms associated with PTa scaffolds. Utilizing integrated multi-omics analysis, we identified specific molecular pathways that contribute to PTa-mediated bone regeneration. These findings not only inform the functional optimization of PTa scaffolds but also lay a scientific foundation for their future clinical translation in addressing complex bone defects.

5. Conclusion

This study highlights the promising role of 3D-printed PTa, which demonstrates a remarkable capacity to enhance bone differentiation and ingrowth via multiple biological pathways, rendering it a highly suitable scaffold material for the treatment of complex bone defects.

Acknowledgments

None.

Funding

This work was supported by the Key R&D Project of the Ningxia Hui Autonomous Region (Project No. 2021BEG02037), the University-level Fund of Ningxia Medical University (Grant No. XT2024028) and Ningxia Natural Science Foundation (Grant No. 2025 AAC030863).

Conflict of interest

The authors declare no conflicts of interest.

Author contributions

Conceptualization: Mengxiao Tantai
Data curation: Sihao Yu, Zhihai Zhang, and Hui Ma
Formal analysis: Chengbin Wang and Tongwei Du
Funding acquisition: Zhidong Lu
Project administration: Gangning Feng
Resources: Junliang Song and Dong Qu
Visualization: Yi Zhang
Writing: Mengxiao Tantai

Ethics approval and consent to participate

The animal experiments complied with all relevant laws and regulations governing animal research in China and were approved by the Ethics Committee of Ningxia Medical University (approval number IACUC-NYLAC-2024-049).

Consent for publication

Not applicable.

Availability of data

The data generated or analyzed during this study are available from the corresponding author upon reasonable request.

References

1. Zura R, Xiong Z, Einhorn T, *et al*. Epidemiology of fracture nonunion in 18 human bones. *JAMA Surg*. 2016;151(11):e162775.
doi: 10.1001/jamasurg.2016.2775

2. Miron RJ. Advanced functional materials. *Periodontology 2000*. 2024;94(1):143-160.
doi: 10.1111/prd.12517

3. Zadpoor AA. Current trends in metallic orthopedic biomaterials: from additive manufacturing to bio-functionalization, infection prevention, and beyond. *IJMS*. 2018;19(9):2684.
doi: 10.3390/ijms19092684

4. Arabnejad S, Johnston B, Tanzer M, Pasini D. Fully porous 3D printed titanium femoral stem to reduce stress-

shielding following total hip arthroplasty. *J Orthop Res*. 2017;35(8):1774-1783.
doi: 10.1002/jor.23445

5. Wauthle R, Van Der Stok J, Amin Yavari S, *et al*. Additively manufactured porous tantalum implants. *Acta Biomater*. 2015;14:217-225.
doi: 10.1016/j.actbio.2014.12.003

6. Melancon D, Bagheri ZS, Johnston RB, Liu L, Tanzer M, Pasini D. Mechanical characterization of structurally porous biomaterials built via additive manufacturing: experiments, predictive models, and design maps for load-bearing bone replacement implants. *Acta Biomater*. 2017;63:350-368.
doi: 10.1016/j.actbio.2017.09.013

7. Levine BR, Sporer S, Poggie RA, Della Valle CJ, Jacobs JJ. Experimental and clinical performance of porous tantalum in orthopedic surgery. *Biomaterials*. 2006;27(27):4671-4681.
doi: 10.1016/j.biomaterials.2006.04.041

8. Mao S, Liu Y, Wang F, *et al*. Design and biomechanical analysis of patientspecific porous tantalum prostheses for knee joint revision surgery. *IJB*. 2024;9(4):735.
doi: 10.18063/ijb.735

9. Liu Y, Bao C, Wismeijer D, Wu G. The physicochemical/biological properties of porous tantalum and the potential surface modification techniques to improve its clinical application in dental implantology. *Mater Sci Eng C*. 2015;49:323-329.
doi: 10.1016/j.msec.2015.01.007

10. Sagomonyants KB, Hakim-Zargar M, Jhaveri A, Aronow MS, Gronowicz G. Porous tantalum stimulates the proliferation and osteogenesis of osteoblasts from elderly female patients. *J Orthop Res*. 2011;29(4):609-616.
doi: 10.1002/jor.21251

11. Pertea M, Pertea GM, Antonescu CM, Chang TC, Mendell JT, Salzberg SL. StringTie enables improved reconstruction of a transcriptome from RNA-seq reads. *Nat Biotechnol*. 2015;33(3):290-295.
doi: 10.1038/nbt.3122

12. Love MI, Huber W, Anders S. Moderated estimation of fold change and dispersion for RNA-seq data with DESeq2. *Genome Biol*. 2014;15(12):550.
doi: 10.1186/s13059-014-0550-8

13. Wiśniewski JR, Zougman A, Nagaraj N, Mann M. Universal sample preparation method for proteome analysis. *Nat Methods*. 2009;6(5):359-362.
doi: 10.1038/nmeth.1322

14. Schwanhäusser B, Busse D, Li N, *et al*. Global quantification of mammalian gene expression control. *Nature*. 2011;473(7347):337-342.
doi: 10.1038/nature10098

15. Kanehisa M, Goto S, Sato Y, Furumichi M, Tanabe M. KEGG for integration and interpretation of large-scale molecular data sets. *Nucleic Acids Res*. 2012;40(D1):D109-D114.
doi: 10.1093/nar/gkr988

16. Dou X, Wei X, Liu G, *et al*. Effect of porous tantalum on promoting the osteogenic differentiation of bone marrow mesenchymal stem cells in vitro through the MAPK/ERK signal pathway. *J Orthop Transl*. 2019;19:81-93.
doi: 10.1016/j.jot.2019.03.006

17. Qian H, Lei T, Hua L, *et al*. Fabrication, bacteriostasis and osteointegration properties researches of the additively-manufactured porous tantalum scaffolds loading vancomycin. *Bioact Mater*. 2023;24:450-462.
doi: 10.1016/j.bioactmat.2022.12.013

18. Luo C, Wang C, Wu X, *et al*. Influence of porous tantalum scaffold pore size on osteogenesis and osteointegration: a comprehensive study based on 3D-printing technology. *Mater Sci Eng C*. 2021;129:112382.
doi: 10.1016/j.msec.2021.112382

19. Fan L, Chen S, Yang M, Liu Y, Liu J. Metallic materials for bone repair. *Adv Healthc Mater*. 2024;13(3):2302132.
doi: 10.1002/adhm.202302132

20. Li JJ, Ebied M, Xu J, Zreiqat H. Current approaches to bone tissue engineering: the interface between biology and engineering. *Adv Healthc Mater*. 2018;7(6):1701061.
doi: 10.1002/adhm.201701061

21. Dimitriou R, Jones E, McGonagle D, Giannoudis PV. Bone regeneration: current concepts and future directions. *BMC Med*. 2011;9(1):66.
doi: 10.1186/1741-7015-9-66

22. Bekmurzayeva A, Duncanson WJ, Azevedo HS, Kanayeva D. Surface modification of stainless steel for biomedical applications: revisiting a century-old material. *Mater Sci Eng C*. 2018;93:1073-1089.
doi: 10.1016/j.msec.2018.08.049

23. Kaur M, Singh K. Review on titanium and titanium based alloys as biomaterials for orthopaedic applications. *Mater Sci Eng C*. 2019;102:844-862.
doi: 10.1016/j.msec.2019.04.064

24. Zhang Y, Sun B, Zhao L, Yang G. Design and manufacturing of a novel trabecular tibial implant. *Materials*. 2023;16(13):4720.
doi: 10.3390/ma16134720

25. Qian H, Lei T, Lei P, Hu Y. Additively manufactured tantalum implants for repairing bone defects: a systematic review. *Tissue Eng B Rev*. 2021;27(2):166-180.
doi: 10.1089/ten.teb.2020.0134

26. Liu B, Ma Z, Li J, *et al*. Experimental study of a 3D printed permanent implantable porous Ta-coated bone plate for fracture fixation. *Bioact Mater*. 2022;10:269-280.
doi: 10.1016/j.bioactmat.2021.09.009

27. Jin J, Wang D, Qian H, *et al*. Precision pore structure optimization of additive manufacturing porous tantalum scaffolds for bone regeneration: a proof-of-concept study. *Biomaterials*. 2025;313:122756.

doi: 10.1016/j.biomaterials.2024.122756

28. Balla VK, Banerjee S, Bose S, Bandyopadhyay A. Direct laser processing of a tantalum coating on titanium for bone replacement structures. *Acta Biomater*. 2010;6(6):2329-2334. doi: 10.1016/j.actbio.2009.11.021

29. Sautet P, Parratte S, Mékidèche T, *et al*. Antibiotic-loaded tantalum may serve as an antimicrobial delivery agent. *Bone Joint J*. 2019;101-B(7):848-851. doi: 10.1302/0301-620X.101B7.BJJ-2018-1206.R1

30. Wang X, Liu W, Jiang C, *et al*. Research progress on the osteogenic properties of tantalum in the field of medical implant materials. *J Mater Res Technol*. 2024;30:1706-1715. doi: 10.1016/j.jmrt.2024.03.200

31. Zhou Z, Liu D. Mesenchymal stem cell-seeded porous tantalum-based biomaterial: a promising choice for promoting bone regeneration. *Colloids Surf B Biointerfaces*. 2022;215:112491. doi: 10.1016/j.colsurfb.2022.112491

ACCSCIENCE PUBLISHING

International Journal of Bioprinting

RESEARCH ARTICLE

Design and performance of 3D-printed cross-scale metamaterial porous structures for orthopedic implants

Guoqing Zhang[1]*, Junxin Li[2], Congcong Shangguan[3], Juanjuan Xie[1], Yongsheng Zhou[1], Aibing Huang[4], and Yuchao Bai[5]

[1]Department of Mechanical Design and Manufacturing, School of Mechanical and Electrical Engineering, Zhoukou Normal University, Zhoukou, Henan, China

[2]Contract Section, State owned Assets Management Office, Zhoukou Normal University, Zhoukou, Henan, China

[3]Veterinary Laboratory, Shangzhou District Animal Health Supervision Institute, Shangluo, Shaanxi, China

[4]Department of Orthopedics, Taizhou People's Hospital Affiliated to Nanjing Medical University, Taizhou, Jiangsu, China

[5]Department of Mechanical Engineering, School of Robotics and Advanced Manufacture, Harbin Institute of Technology, Shenzhen, Guangdong, China

(This article belongs to the *Special Issue*: *Additive Manufacturing of Functional Biomaterials-Series2*)

Abstract

The rising prevalence of orthopedic conditions in aging populations has created a growing demand for advanced implants with enhanced biocompatibility, mechanical performance, and tissue integration. To meet these demands, it is necessary to investigate the metamaterial properties of cross-scale porous structures, including both macroscale architecture and microscale texture. Accordingly, we employed parametric modeling to design porous structures; analyzed blood flow distribution through various multi-level porous designs using mold flow simulation; evaluated their compressive properties through finite element analysis; assessed biocompatibility via animal experiments; and obtained tissue ingrowth data using micro-computed tomography. The results indicated that when fluid flowed through cross-scale porous structures, the overall pressure was low, and the Kelvin cell structure exhibited favorable flow field characteristics under low pressure. When the structures were pressurized, texturization methods involving material removal resulted in larger displacements, while those involving material addition led to smaller displacements. The Kelvin cell structure exhibited extensive tissue ingrowth with a dense tissue pattern internally, and the amount of ingrowth decreased from the inside to the outside. Increasing the roughness of porous structures via material removal increased the surface-to-volume ratio to a certain extent but did not promote tissue ingrowth. In contrast, increasing roughness by material addition favored tissue ingrowth, laying a foundation for the design of cross-scale metamaterial implants.

Keywords: 3D printing; Biocompatibility; Mechanical properties; Metamaterial; Porous structure

***Corresponding author:**
Guoqing Zhang
(zhangguoqing1202@sohu.com)

Citation: Zhang G, Li J, Shangguan C, *et al.* Design and performance of 3D-printed cross-scale metamaterial porous structures for orthopedic implants. *Int J Bioprint*. 2025;11(6):515-530. doi: 10.36922/IJB025390401

Received: September 27, 2025
Revised: October 4, 2025
Accepted: October 11, 2025
Published online: October 14, 2025

Copyright: © 2025 Author(s). This is an Open Access article distributed under the terms of the Creative Commons Attribution License, permitting distribution, and reproduction in any medium, provided the original work is properly cited.

Publisher's Note: AccScience Publishing remains neutral with regard to jurisdictional claims in published maps and institutional affiliations.

1. Introduction

Aging is positively correlated with the incidence of orthopedic diseases. Currently, the population aged 60 and above in China has reached 264 million, with over 190 million aged 65 and above. Osteoporosis, fractures, osteoarthritis, dental cavities, and other bone diseases pose a significant threat to the health of the Chinese population.[1] In response to the growing demand for bone disease treatment, prosthetic replacement and repair of the affected area have emerged as effective solutions. Studies have shown that designing implants with personalized bio-fixed structures (partially or fully porous) can significantly improve biocompatibility, reduce weight, and minimize the risk of "stress shielding".[2,3] Novel multi-level porous structures have been widely applied in fields such as aeronautics, astronautics, and military technology due to their advantages, such as low relative density, high specific strength, high specific surface area, lightweight properties, sound and heat insulation, and good permeability. Therefore, studying the metamaterial properties of multi-level porous structures is crucial for the development of customized, integrated, lightweight, and cost-effective orthopedic implants with ultra-high mechanical and biomedical performance.

The advent of additive manufacturing (3D printing) technology has made it feasible to fabricate novel multi-level porous structures. 3D printing involves slicing a 3D model using specialized software to obtain sectional data, which is then input into a rapid prototyping device to manufacture solid parts by stacking the materials layer by layer. Owing to the layer-by-layer approach, 3D printing technology enables the production of components with virtually any geometric shape, offering advantages such as single-piece processing, small-batch production, complex geometries, and high-density finished parts.[4,5] Selective laser melting (SLM), a prominent 3D printing technology, is based on the laser melting of metal powders.[6]

Wang[7] evaluated the biocompatibility of titanium alloy samples produced by different 3D printing processes. *In vitro* cell experiments indicated no significant impact on the growth and osteogenic differentiation abilities of canine bone marrow mesenchymal stem cells (BMMSCs) in titanium alloy samples fabricated by both electron beam melting and SLM. Yang *et al.*[8] designed five titanium alloy scaffolds with different shapes and found that, during 3D printing, cell configuration and cell parameters significantly influenced the mechanical and permeability properties of triply periodic minimal surface unit cells. Wang[9] documented that artificial bone trabecular structures with uneven pore sizes were more conducive to the adhesion, proliferation, and differentiation of mouse pre-osteoblasts on titanium scaffolds than microporous structures with uniform pore sizes or dense solid structures, providing better osseointegration performance from a theoretical standpoint. Wang *et al.*[10] examined 3D printing-assisted internal fixation for complex tibial plateau fractures and found that it could shorten surgery duration, reduce intraoperative bleeding and fluoroscopy frequency, and improve patients' knee joint function, while effectively repositioning the articular surface. Zhang *et al.*[11] investigated the genotoxicity, hemolysis, *in vitro* cytotoxicity, post-implantation local reaction, intradermal reaction, skin sensitization, acute systemic toxicity, and subchronic toxicity of 3D-printed porous tantalum, with all experimental results meeting the requirements of GB/T 16886. Liang *et al.*[12] noted that porous structures can maintain cell morphology and facilitate the adhesion and proliferation of osteoblasts. This was not only conducive to the transport of nutrients and metabolites but also provided substantial physical space for the ingrowth of blood vessels and nerves, thereby enhancing the ingrowth and long-term stability of bone tissue. Liu *et al.*[13] demonstrated that the mechanical properties of 3D-printed porous Ti6Al4V titanium alloy scaffolds were influenced by their porous architecture, with initial strength well-suited to physiological demands. Furthermore, the materials exhibited excellent cellular biocompatibility. The 3D mesh structure in the porous scaffolds provided space for cell growth, enhanced the proliferative capacity of BMMSCs, and accelerated the growth of bone tissue into the micropores of titanium scaffolds. Lei *et al.*[14] used 3D printing technology to customize and manufacture structurally optimized porous pedicle screws, which enhanced bone regeneration and integration at the defect site, thereby improving the biological fixation of the implant *in vivo*. Tamaddon *et al.*[15] fabricated a porous titanium scaffold with 72% porosity using 3D printing technology and seeded sheep BMMSCs onto the surface for *in vitro* culture. The results indicated that the cells exhibited good adhesion on the scaffold surface. Zaharin *et al.*[16] examined the effects of cubic and helical micropores (300–600 μm in size) on the properties of porous titanium alloys. The results suggested that cubic structures were more suitable for implants, while all samples with helical structures remained viable candidates. Zadpoor[17] noted that alterations in the surface curvature of scaffolds can influence cell adhesion rates, cell migration, and morphology. Additionally, the growth rate of cells on concave surfaces was significantly higher than on convex and planar surfaces. Meanwhile, Kumar *et al.*[18] found that porous gradient scaffolds offered an ideal combination of porosity and mechanical properties for bone defect sites.

To date, extensive research has been conducted on the mechanical and biological properties of 3D-printed porous structures, which has partly improved the feasibility of their use in implants. However, significant potential remains for improving the metamaterial properties of these structures. Accordingly, the present study investigates the metamaterial properties and enhancement strategies for various cross-scale porous structures.

2. Materials and methods

2.1. Design methods

The design of metamaterial porous structures based on 3D printing should meet the following constraints[19–21]: (i) biocompatibility constraints – the pore size of porous scaffolds should range from 100 to 1000 μm, and the porosity should be between 50% and 90%. A higher surface-to-volume ratio is preferred. (ii) Manufacturing constraints: Sharp corners and thin walls should be larger than the diameter of the laser spot, and the minimum pore size should be greater than the diameter of the laser spot.

2.1.1. Design of different porous structures

Cylindrical porous scaffolds (n=3, ∅5×8 mm) were utilized for *in vivo* experiments. For ease of comparative analysis, the cylindrical porous structures were designed using the same parameters. The basic unit parameters of porous structures were as follows: unit radius = 0.7 mm, unit height = 1.3 mm, and strut diameter = 0.16 mm. The porous structures were designed using Rhinoceros (version 6.0, Robert McNeel & Associates, United States of America), a parametric modeling software, and the design results are shown in Figure 1. Table 1 lists the parameters of the designed porous structures. It can be observed from Table 1 that, under identical parameters, the Kelvin cell structure achieved a higher porosity.

2.1.2. Different texturization designs for the Kelvin cell structure

The surface morphology of porous structures can influence the biological functions of implants. Studies have shown that rougher surfaces with larger surface areas are favorable for cell adhesion.[22] For this reason, the Kelvin Cell porous structure, demonstrating relatively good overall performance, was selected for applying different forms of texturization in order to compare their effects on biological properties. Using secondary programming in Rhinoceros, four types of millimeter-scale surface textures were implemented on the Kelvin cell structure to explore how different surface morphologies affect biocompatibility. Cylindrical porous scaffolds (n=3, ∅5×8 mm) were used. For ease of comparative analysis, the structures were designed with identical parameters. The basic unit parameters were as follows: unit radius =

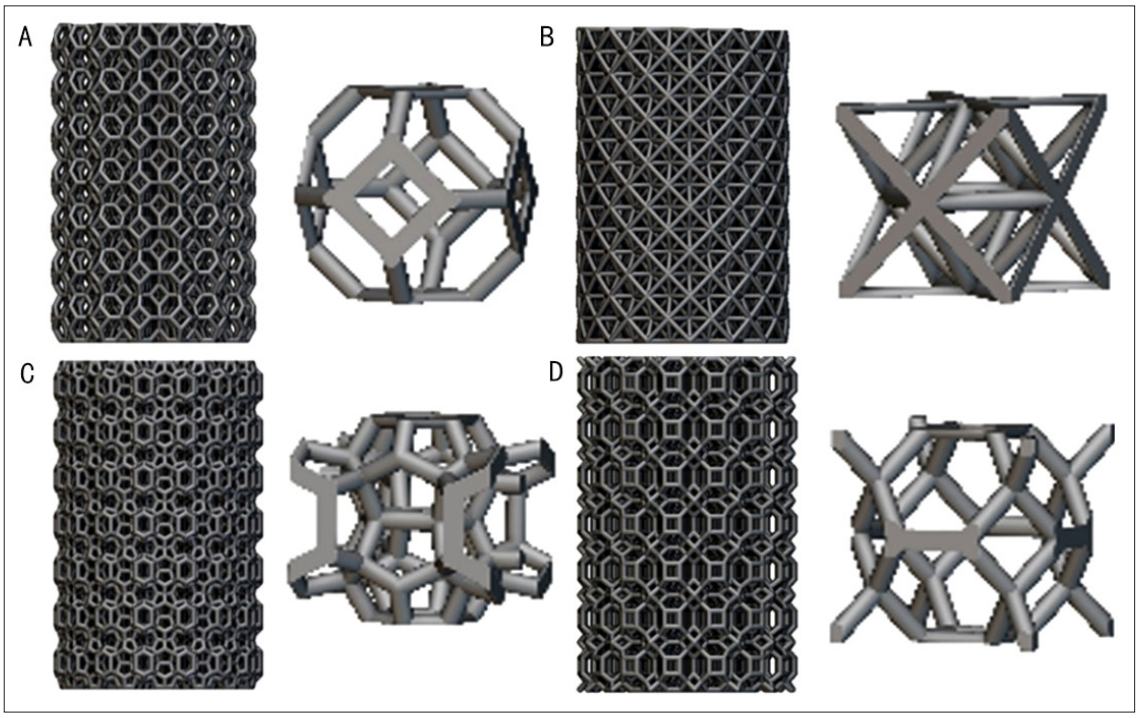

Figure 1. Design of multi-level porous structures with different geometries: (A) Kelvin cell; (B) Octet; (C) Weaire–Phelan; (D) Truncated octahedron.

Table 1. Structural parameters of different porous structures

Porous structure type	Porosity (%)	Average pore size (mm)	Surface area to volume ratio
Octet	74.08	0.28	4.75
Kelvin cell	83.89	0.39	3.28
Weaire–Phelan	68.16	0.25	5.46
Truncated octahedron	78.57	0.33	3.95

0.7 mm, unit height = 1.3 mm, strut diameter = 0.16 mm, roughness peak = 0.07 mm, roughness frequency = 8000, and the number of seeds = 100. The design outcomes are shown in Figure 2.

Table 2 lists the structural parameters of the textured porous structures. Comparison revealed that surface roughness, simplex noise deboss, and Voronoi deboss structures, where surface roughness involved material removal, had slightly higher porosity. In contrast, the Voronoi Emboss structure, where material was added, had slightly lower porosity. Comparing the Kelvin cell structures in Tables 1 and 2, it was found that the porosity increased with material removal and decreased with material addition. The surface-to-volume ratios of surface roughness, simplex noise deboss, and Voronoi emboss structures increased substantially, while the morphology of the Voronoi deboss structure remained largely unchanged. An increase in surface-to-volume ratio may improve biocompatibility to a certain extent.

2.1.3 Kelvin cell structures subjected to Voronoi emboss texturization with different roughness peaks

To investigate the effects of different roughness peaks on biocompatibility, we texturized the Kelvin cell structure using the same parameters outlined in **Section 2.1.2**, but with roughness peaks set at 0.06 mm and 0.08 mm, respectively. The results are presented in Figure 3. Based on the relevant parameters in Table 3, it was found that as the roughness peak increased, both porosity and average pore size decreased, while the surface-to-volume ratio increased.

2.2. Materials and manufacturing methods

The porous structures were fabricated using Ti6Al4V alloy metal powder supplied by Zhejiang Yatong Advanced Materials Co., Ltd., China. The powder composition met the requirements of ASTM F136 and GB/T 13810-2007, as detailed in Table 4. The powder was prepared via gas atomization and had a spherical morphology, with an apparent density (ρ_s) of 2.43 g/cm^3 and a flowability of 36.3 s/50 g. The particle size distribution was narrow, with D90=57.99 μm and D50=35.67 μm.

The molding process was carried out using GYD150 SLM equipment from Shenzhen Sunshine Laser & Electronics Technology Co., Ltd., China. Argon was used as the protective gas, with oxygen content controlled below 0.03%. The process parameters were as follows: laser power = 180W, scanning speed = 500 mm/s, scanning interval = 80 μm, layer thickness = 25 μm, scanning strategy = X–Y interlayer alternating scanning. At least three samples were fabricated for each group.

2.3. Bone defect repair in the distal femur of rabbits via scaffold implantation

To assess the biocompatibility of the porous structures, an *in vivo* animal experiment was carried out at the Veterinary Laboratory of the Animal Health Surveillance Office in Shangzhou district, Shangluo city, Shaanxi province, China. The study was approved by the relevant Ethics Committee. A total of 24 3-month-old rabbits (weighing about 2.5–3.0 kg) were used for the implantation experiment.

Prior to implantation, the materials were first cleaned using an ultrasonic cleaner (Hangzhou BOKE Ultrasonic Equipment Co., Ltd., China), followed by sterilization in an autoclave (160°C for 40 min; Hangzhou Corfied Experimental Instrument Co., Ltd., China). After general anesthesia was administered using xylazine hydrochloride (0.1 mL/kg), a cylindrical bone defect (∅ 5×8 mm) was drilled into the distal femur of each rabbit using an electric drill. A scaffold was randomly implanted into each defect area, and the incision was sutured. The surgical procedure is illustrated in Figure 4. Postoperatively, the rabbits received penicillin for 3 days and were housed individually. After 4 weeks of implantation, the rabbits were euthanized via intravenous injection of an overdose of 3% pentobarbital sodium. The femoral condyles containing the scaffolds were fixed in 10% formalin for subsequent evaluation. 2D cross-sectional images were obtained using a Micro-CT SKYSCAN 1276 scanner (Bruker, Germany).

2.4. Analysis methods

The flow field distribution of blood through different multi-level porous structures was analyzed using Autodesk Simulation CFD 2021 software (Autodesk Software, Inc., United States of America). Animal experiments

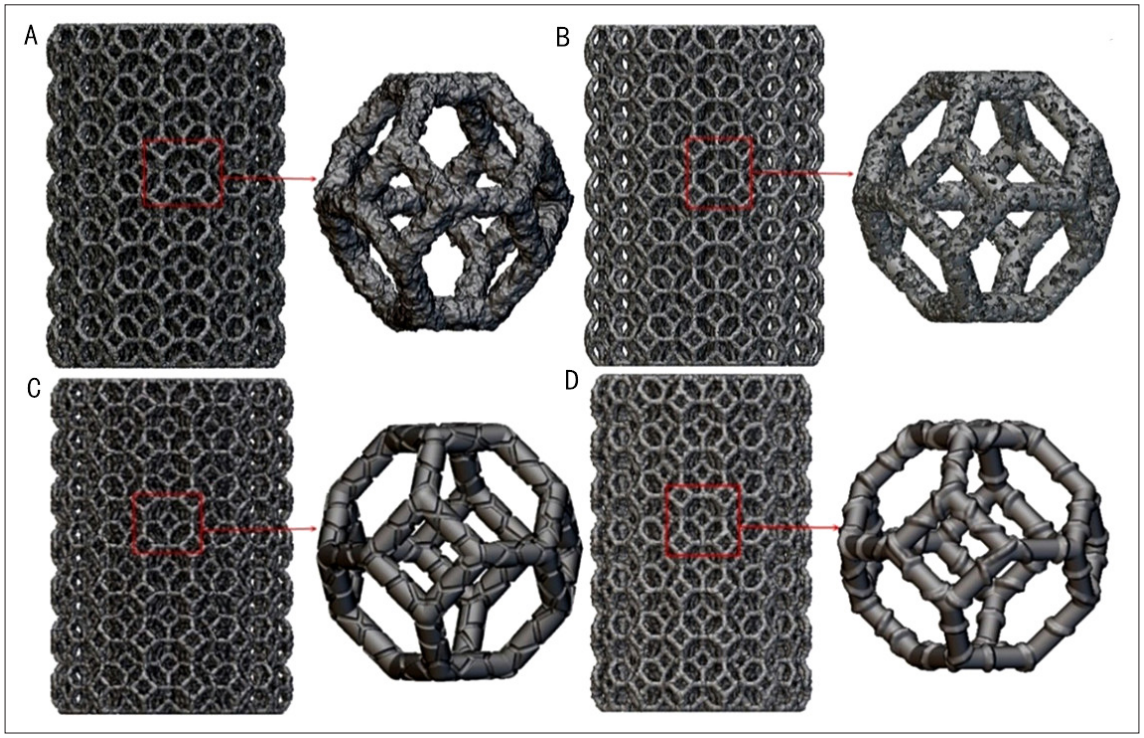

Figure 2. Surfaces of porous structures with different texturizations: (A) Surface roughness; (B) Simplex noise deboss; (C) Voronoi deboss; (D) Voronoi emboss.

Table 2. Structural parameters of different texturizations applied to the Kelvin cell porous structures

Porous structure type	Porosity (%)	Average pore size (mm)	Surface area to volume ratio
Surface roughness	86.89	0.39	3.43
Simplex noise deboss	84.13	0.36	3.66
Voronoi deboss	88.27	0.40	3.29
Voronoi emboss	80.68	0.34	3.59

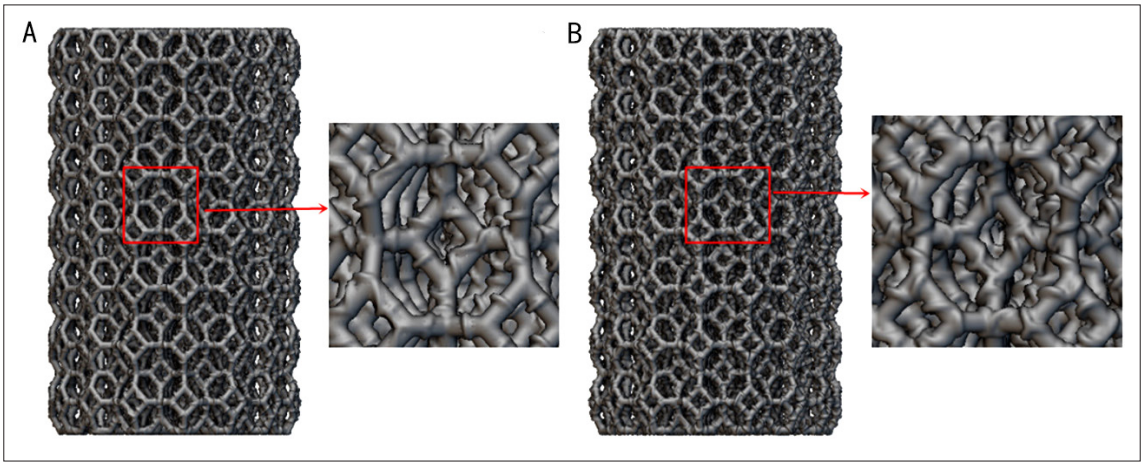

Figure 3. Voronoi emboss textured Kelvin cell structures with different roughness peaks: (A) 0.06 mm; (B) 0.08 mm.

Table 3. Parameters of Kelvin cell structures with Voronoi emboss texturization at different roughness peaks

Porous structure type	Porosity (%)	Average pore size (mm)	Surface area to volume ratio
Voronoi deboss (0.06 mm)	81.72	0.35	3.54
Voronoi deboss (0.08mm)	79.50	0.32	3.70

Table 4. Comparison of powder material manufactured via selective laser melting and the American Society for Testing and Materials (ASTM F136) standard

Element	ti6al4v powder	ASTM f75 standard
Al	5.5–6.75%	5.5–6.5%
V	3.5–4.5%	3.5–4.5%
Fe	0.3%	<0.3%
C	0.08%	<0.08%
N	0.05%	<0.05%
H	0.015%	<0.012%
O	<0.12%	<0.13%
Ti	Balance	Balance

Abbreviations: Al, aluminum; C, carbon; Fe, ferrum; H, hydrogen; O, oxygen; Ti, titanium; V, vanadium.

were conducted to evaluate the biocompatibility of the various porous structures. Four types of surface texturization were applied to the porous structures via secondary programming in Rhinoceros 6.0 (Robert McNeel & Associates, United States of America). The surface morphology of the 3D-printed bone grating plates was observed with a high-definition VGA electron microscope (BOCHENG, China). The effects of different surface texturization methods on biocompatibility were further evaluated through animal experiments. A micro-computed tomography (Micro-CT) SKYSCAN 1276 scanner (Bruker, Germany) was used to obtain tissue ingrowth data within the porous structures and to observe tissue development. The Micro-CT parameters were: pixel resolution = 4032×4032; animal bed resolution = 8 μm; filter = gold + aluminum. For finite element stress analysis, the porous structures in STL format were converted into implicit models using nTop 4.24 software (nTop Software Inc., United States of America). The analysis settings were: units = mm; material = Ti-6Al-4V; mesh type = triangular; mesh size = 0.1 mm; mesh growth rate = 2; boundary conditions = lower end of porous structure fully fixed, 20 N pressure applied at the top.

3. Results

3.1. Mold flow simulation analysis for the porous structures

The presence of "vortex flow" can both dissipate flow energy and increase resistance to fluid entering the center of the scaffold. Moreover, self-circulating flow near the wall forms a barrier between the high-speed, nutrient-rich fluid and the cells on the material surface, which hinders the exchange of metabolic substances.[23] Therefore, further investigation into the flow field distribution of blood within porous structures is necessary to objectively assess the biocompatibility of different porous structures.

3.1.1. Establishment of fluid model

For simulation purposes, the porous structures were designed in a square shape and reduced to a single-layer model. To generate the fluid medium and prevent fluid loss from the sides, 0.15 mm-thick walls were added to the front,

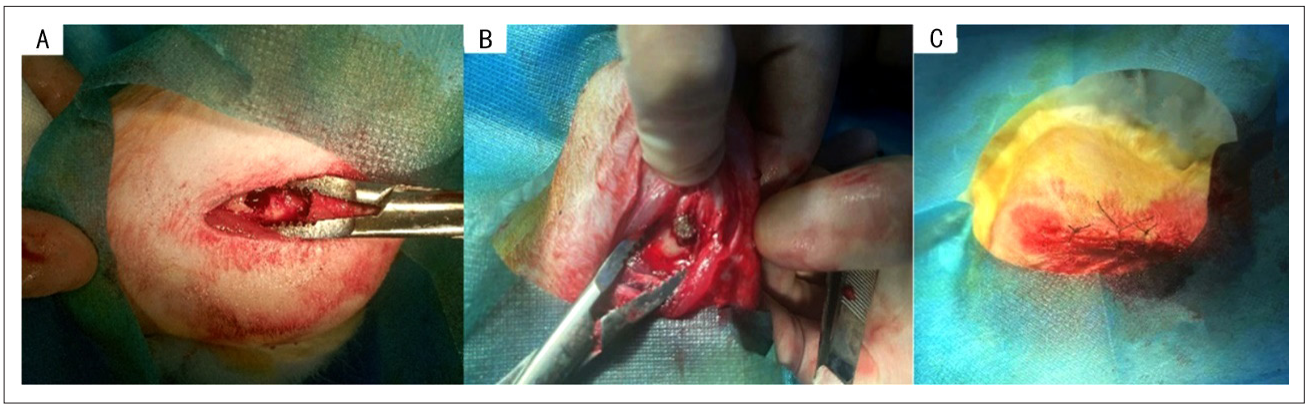

Figure 4. Stent implantation in rabbits: (A) Drilling; (B) Scaffold implantation; (C) Suturing.

back, left, and right of the porous structure to improve the accuracy of the simulation results. The designed porous structure was then split along the centerline with Rhinoceros software to obtain a fluid model cross-section.

The resulting porous structure was imported into Autodesk Simulation CFD software. First, the edges were merged, and then the "Create Surface" command was applied to close the fluid inlet and outlet. The fluid region was generated with the following boundary conditions: "Velocity-inlet" at the inlet, "Pressure-outlet" at the outlet, and "Wall" on all other surfaces, as illustrated in Figure 5. The wall material was defined as TC4, and blood was modeled as an incompressible fluid with a viscosity of 0.033 Pa·s and a density of 1050 kg/m^3. Based on normal human blood flow velocities—125 mm/s for females and 140 mm/s for males—the inlet velocity was set to 140 mm/s, while the outlet pressure was set to 0 Pa. Automatic mesh division was applied.

3.1.2. Flow field analysis

Following the mold flow simulation, the flow field was cut along the direction of blood flow to observe the internal flow distribution, as shown in Figure 6. From Figure 6, it can be observed that when blood entered and exited the octet structure, it encountered a basic unit composed of eight struts. The fluid passed through three of these struts, demonstrating faster flow between them and slower flow at the intersections of the eight struts. This may be due to a vacuum region forming at the strut intersections of the octet structure, making blood entry more difficult.

In contrast, the metamaterial Kelvin Cell structure, featuring a central square formed by four struts, enabled fluid to pass directly through the square, displaying fast central flow that gradually diffused outward. The truncated octahedron and Weaire–Phelan structures, with small squares at the top and bottom and internal pores, allowed fluid to flow through the squares, similarly exhibiting faster central flow and slower peripheral flow. In terms of flow field distribution, the Kelvin Cell structure demonstrated superior characteristics.

The contact area between blood through the porous structure and the strut surfaces is one of the indicators for evaluating biocompatibility. According to the distribution principle of "vortex flow," when liquid encounters an obstacle during motion, it disintegrates and forms a group of mass points rotating around a common axis. Thus, it is necessary to observe the "vortex flow" distribution perpendicular to the blood flow direction. From Figure 7, it can be observed that the octet structure exhibited the strongest vortex intensity, with the center of the vortex located at the strut intersection. The intensity increased outward from the intersection, approaching nearly 0 m/s at the unit's edge. This may be attributed to the closed regions formed at the strut intersections of the octet structure, which are not conducive to blood circulation. In contrast, the Kelvin cell structure demonstrated the weakest vortex intensity, with the vortex spreading outward from the square strut edges and gradually diminishing to nearly 0 m/s at the unit's boundary. The truncated octahedron and Weaire–Phelan structures showed similar vortex distributions, with the vortex flow patterns spreading outward from the small square struts and intensity also diminishing toward the boundaries. In terms of both vortex distribution and intensity, the Kelvin cell structure showed more favorable flow field characteristics.

When fluid flows through the porous structure, higher flow speed and lower pressure are generally more favorable for the exchange of metabolites. Hence, it is important to assess both flow speed and pressure at the inlet of the porous structure to comprehensively evaluate its performance. By measuring the flow speed at the outlet of the porous structure simulation model, we found that the flow speeds were: 139.893 mm/s for the octet structure, 139.824 mm/s for the Kelvin cell, 139.897 mm/s for the truncated octahedron, and 139.769 mm/s for the Weaire–Phelan

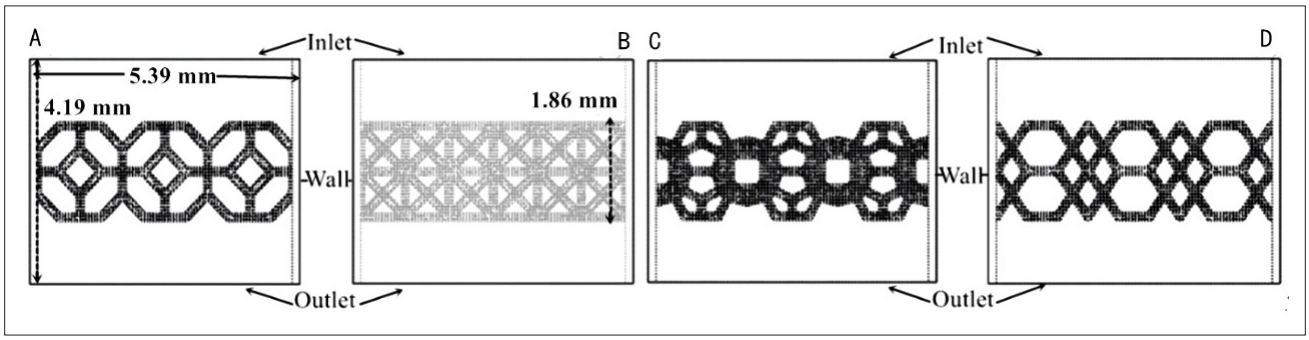

Figure 5. Construction of the fluid model: (A) Kelvin cell; (B) Octet; (C) Truncated octahedron; (D) Weaire–Phelan.

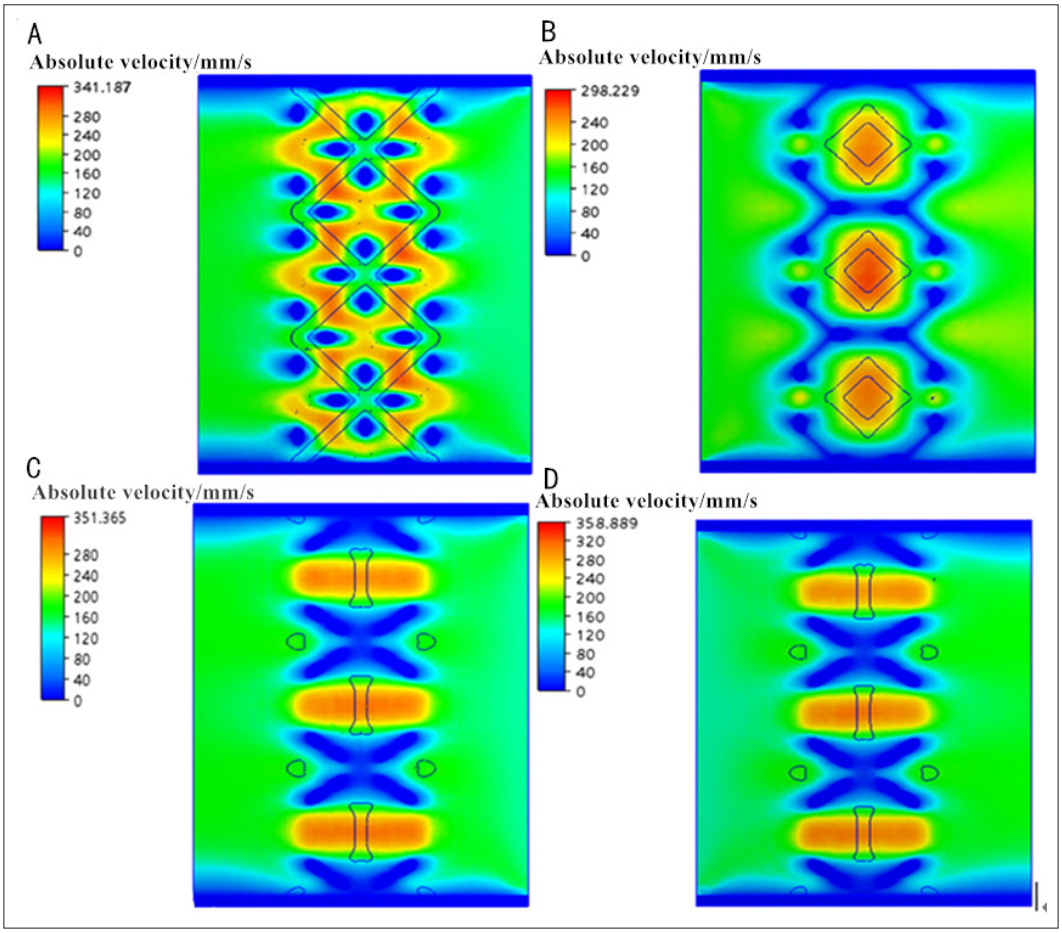

Figure 6. Blood flow analysis of porous structures: (A) Octet; (B) Kelvin cell; (C) Truncated octahedron; (D) Weaire–Phelan.

structure. There was no significant difference between the flow speeds of conventional and metamaterial structures, possibly due to the use of a single-layer structure and the relatively low blood flow speed in the human body. By measuring the pressure at the inlet of the porous structure simulation model, we found: 27,255.1 Pa for octet, 12,241.3 Pa for Kelvin cell, 15,834.9 Pa for truncated octahedron, and 15,977.0 Pa for Weaire–Phelan. Comparison revealed that metamaterial porous structures exhibited lower inlet pressures overall, and the Kelvin cell structure achieved higher flow speeds under lower pressures, demonstrating the best performance among the structures tested.

3.2 Compressive properties simulation analysis of the porous structures

3.2.1. Compression simulation analysis of Kelvin cell porous structures with different texturization methods

Whether the application of surface texturization compromises the mechanical performance of metamaterial porous structures is crucial for the success of implant design. Thus, finite element simulation was used to analyze the fracture behavior of these porous structures and assess their mechanical performance.

Figure 8 shows the finite element analysis results for the textured Kelvin cell structures. From the displacement contour maps (Figures 8A, B, C, and D), it can be observed that under a pressure of 20 N, the displacement of the porous structures was generally small and increased from bottom to top, which is consistent with the typical displacement distribution in loaded components. In descending order, the displacements were: 1.97×10^{-3} mm for Voronoi deboss, 1.38×10^{-3} mm for surface roughness, 1.27×10^{-3} mm for simplex noise deboss, and 9.24×10^{-4} mm for Voronoi emboss. Maximum displacement was inversely proportional to porosity. Texturization methods involving material removal (Voronoi deboss, surface roughness, and simplex noise deboss) resulted in larger displacements, while Voronoi emboss, a material addition method, produced smaller displacements. From the stress contour maps (Figures 8A, B, C, and D), it was observed that stress

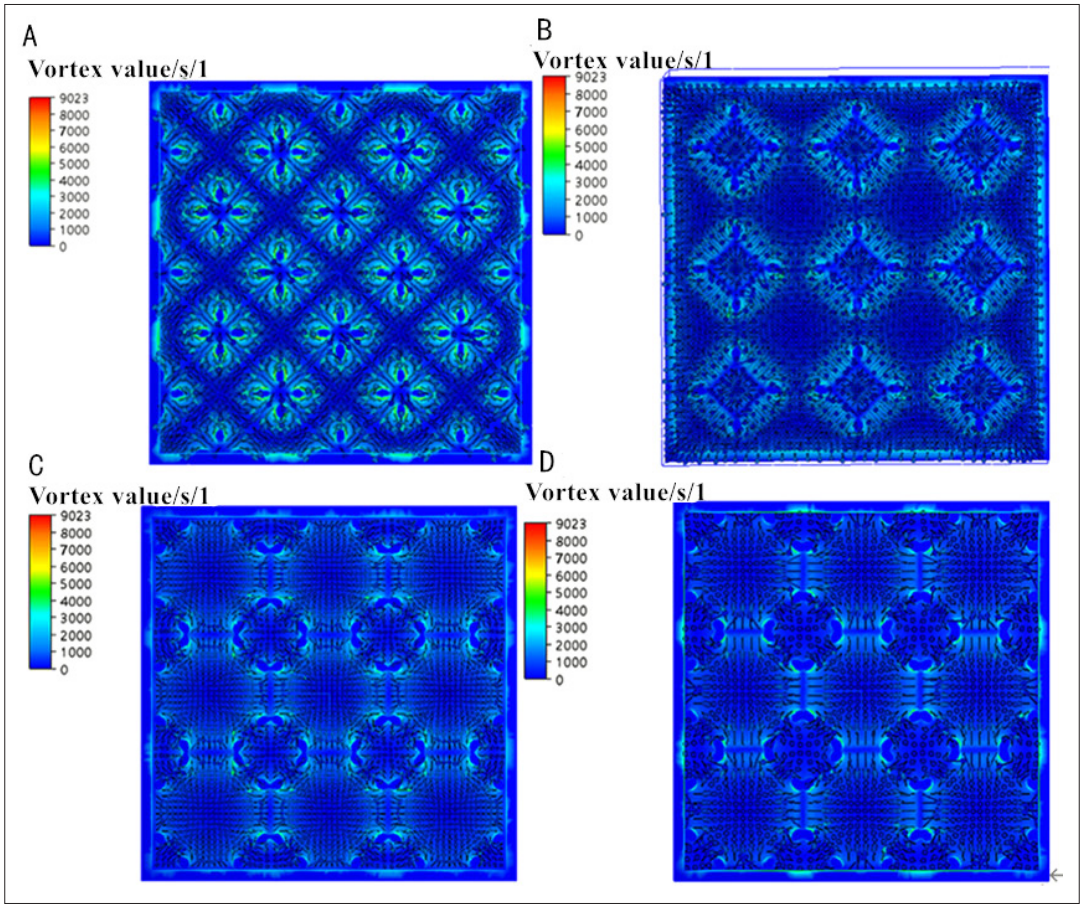

Figure 7. Vortex distribution perpendicular to the blood flow direction in porous structures: (A) Octet; (B) Kelvin cell; (C) Truncated octahedron; (D) Weaire–Phelan.

accumulated along the longitudinal direction in different levels of the porous structures, though the distribution was relatively uniform in both the longitudinal and transverse directions. This may be attributed to the ability of the second-level structure to relieve some of the stress through deformation when subjected to longitudinal pressure. The maximum stress values were: 5.9775×10^{3} MPa for simplex noise deboss, 1.05053×10^{2} MPa for Voronoi deboss, 1.07689×10^{2} MPa for surface roughness, and 8.61795×10^{1} MPa for Voronoi emboss. Based on these results, Voronoi Emboss texturization demonstrated better mechanical performance, especially in cases where high porosity is not the primary requirement.

3.2.2. Simulation analysis for Kelvin cell porous structures with Voronoi emboss texturization at different roughness peaks

As previously analyzed, the Kelvin cell structure with Voronoi emboss texturization and a roughness peak of 0.07 mm showed good mechanical performance. To further explore the impact of different roughness peaks on the compressive properties of the Kelvin cell structure, additional simulations were conducted using the parameters described in **Section 2.4**, and the porous structures were analyzed using nTop 4.24 software.

The results are shown in Figure 9. As the roughness peak increased, both stress concentration and displacement of the porous structures under compression decreased. This indicated that the Kelvin Cell structure subjected to Voronoi emboss texturization exhibited improved mechanical performance with a higher roughness peak. However, increasing the roughness peak may lead to reduced porosity and potentially compromise biocompatibility. This trade-off will be further analyzed in future work.

3.3. Analysis of the 3D printing effect of the porous structures

Based on previous findings on the support addition and placement methods for SLM-formed parts,[24] the designed porous structures with varying geometries and subjected to different texturization methods were imported into

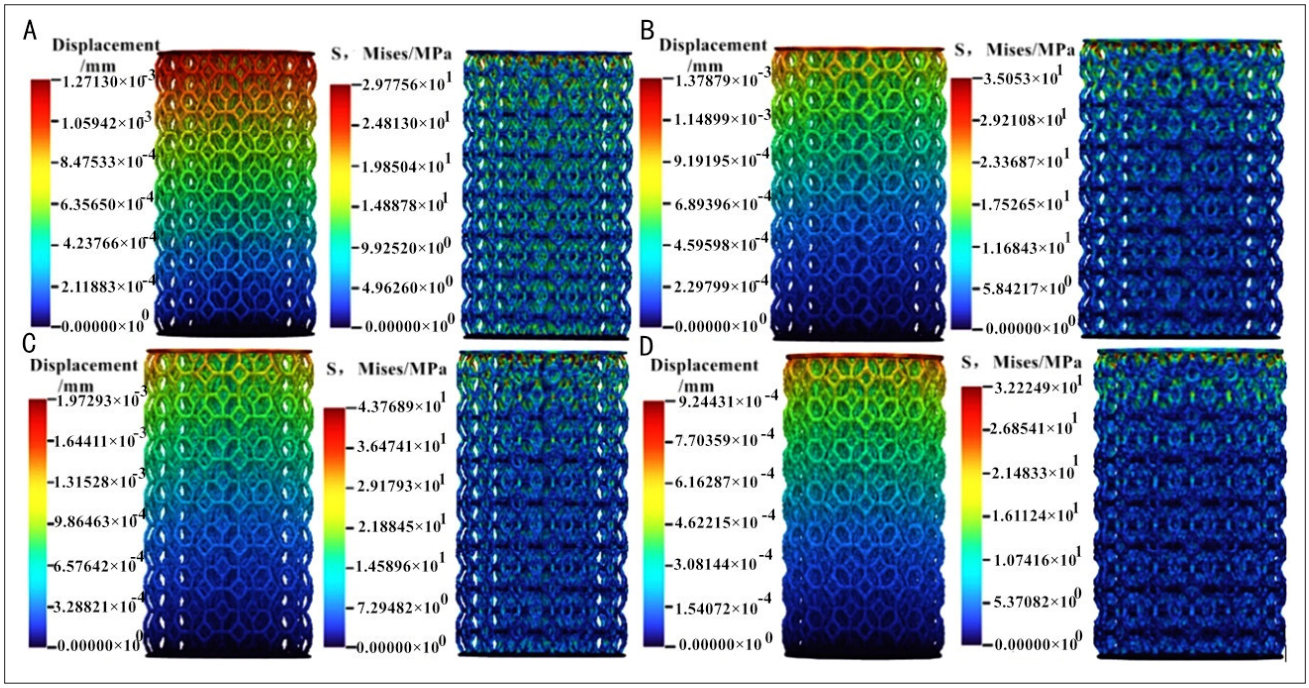

Figure 8. Finite element analysis results for differently textured Kelvin cell porous structures: (A) Simplex noise deboss; (B) Surface roughness; (C) Voronoi deboss; (D) Voronoi emboss.

Materialise Magics 22 software. They were placed vertically in contact with the substrate for slicing, layering, and data processing, and subsequently imported into a metal 3D printer for fabrication.

3.3.1. Analysis of the forming effects of porous structures with different structures

The porous scaffolds printed using the metal 3D printer are shown in Figure 10. Observations of Figure 10 reveal that the porous scaffolds exhibited a bright surface, a clear grid structure, a good metallic texture, minimal slag, and no visible warping or deformation. The intersection between the struts of the porous structure was well-formed, without noticeable collapse visible to the naked eye, indicating that the 3D-printed porous scaffold demonstrated good forming quality and surface integrity. Microscopic examination of the porous structure revealed clear melt tracks and good pore connectivity. Some powder adherence was observed at the pore locations, particularly at the intersection of the struts, though this did not affect subsequent usage.

3.3.2. Analysis of the forming effects of Kelvin cell structures subjected to different texturization methods

Upon examining the 3D-printed texturized porous structure shown in Figure 11, it was found that it had a

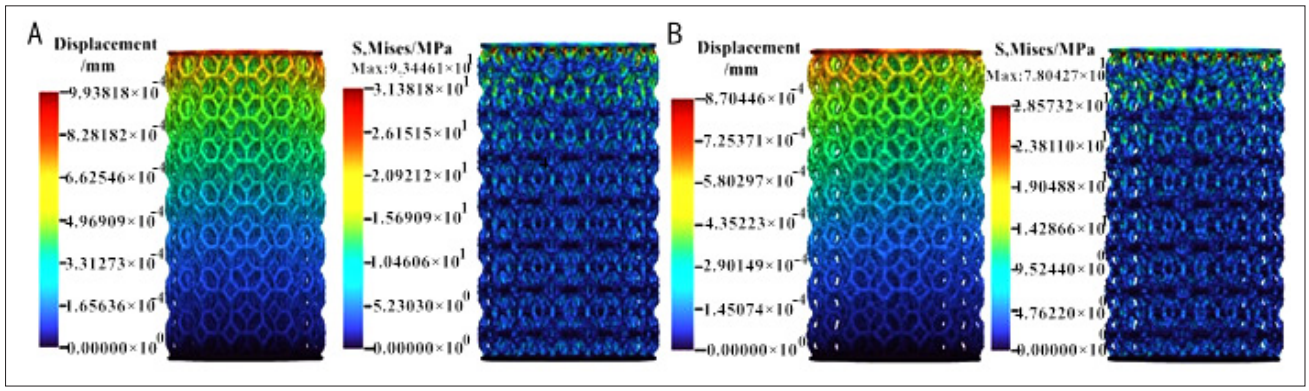

Figure 9. Simulation analysis of Voronoi emboss texturization with different roughness peaks on Kelvin cell porous structures: (A) 0.06 mm; (B) 0.08 mm.

bright surface, clear strut geometry, good metallic texture, no visible warping or deformation, well-formed strut intersections, and no noticeable collapse visible to the naked eye. These observations indicate that the 3D-printed porous structures demonstrated good forming quality and surface finish. Microscopic analysis showed clear melt tracks in the pore structures. However, compared with the surface morphology before texturization, a noticeable increase in slag accumulation and surface roughness was observed after texturization, possibly due to grooves or protrusions introduced by the texturing process. The Voronoi deboss structure, characterized by groove-like surface roughness along the struts, exhibited some strut fractures, although these did not affect its usability. The other texturized porous structures maintained good connectivity.

3.4. Biocompatibility study of the porous structures

3.4.1. Analysis of the repair effect of porous structures with different structures for the bone defects in the distal femur of the rabbits

The scanning data were saved as .bmp format and imported into Mimics Research 20.0 software (Materialise, Belgium) for 3D reconstruction of the porous structures. First, threshold segmentation was conducted using the same threshold values for all four scaffold types (min: −984, max: −929), followed by region growth and 3D reconstruction. As shown in the 3D reconstruction images (Figure 12), bone tissue had grown into the interior of the porous structures within 4 weeks, indicating good biocompatibility of the TC4 material. The Kelvin cell structure exhibited more tissue ingrowth with a denser tissue pattern, with the amount of ingrowth decreasing from the interior to the exterior. This suggests that gradient porosity is beneficial for tissue ingrowth. The slightly reduced ingrowth performance on the exterior of the Kelvin cell structure may be due to its relatively large external pores. With further design optimization, it would be possible to maintain good initial ingrowth while providing sufficient space for continued tissue development. The octet structure exhibited a similar gradient ingrowth pattern, but the internal ingrowth was less dense, possibly due to pore blockage after initial tissue growth. The external pores exhibited good tissue integration, likely due to their smaller pore size. The Weaire–Phelan structure showed complete tissue ingrowth, filling all pores, possibly due to its small pore size. However, excessively small pores of the Weaire–Phelan architecture may hinder material exchange and affect osteogenesis. The truncated octahedron structure demonstrated an ingrowth pattern similar to the Kelvin cell structure, with considerable tissue growth, although the internal ingrowth was slightly less dense, possible due to blockage of smaller pores in the center of the structure. Overall, the Kelvin cell structure exhibited the best tissue ingrowth performance.

3.4.3. Analysis of the repair effect of Kelvin cell structures subjected to different texturization methods on bone defects in the distal femur of rabbits

The data for the Kelvin cell structures with different texturization methods were saved as .bmp format, imported into Mimics Research 20.0 software, and subjected to the same 3D reconstruction process described in **Section 3.4.2**. Observations from Figure 13 revealed that all four types of texturized Kelvin cell structures exhibited good tissue ingrowth. However, compared with the non-

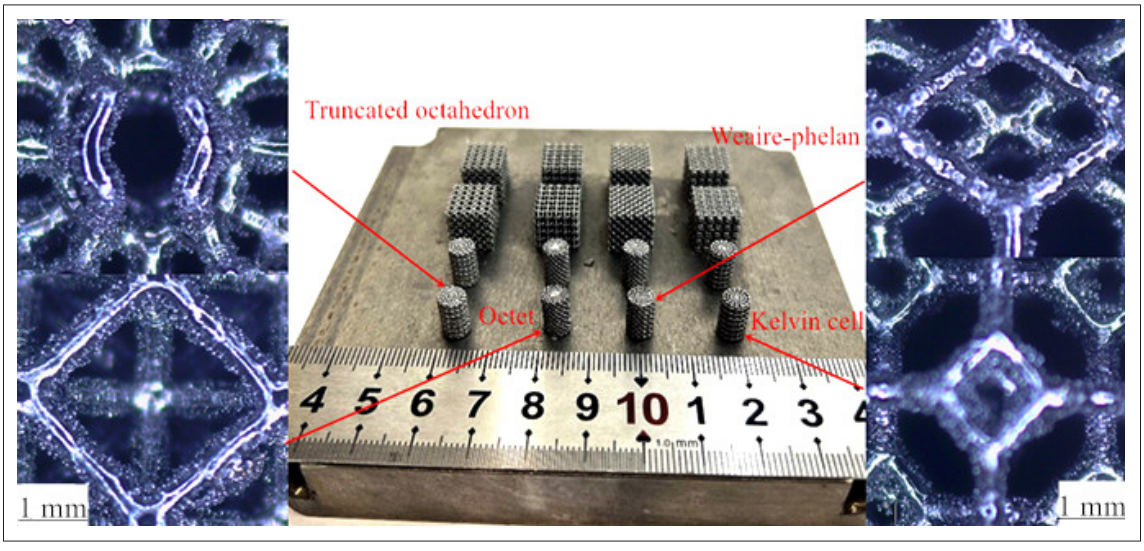

Figure 10. 3D-printed porous structures with different geometries.

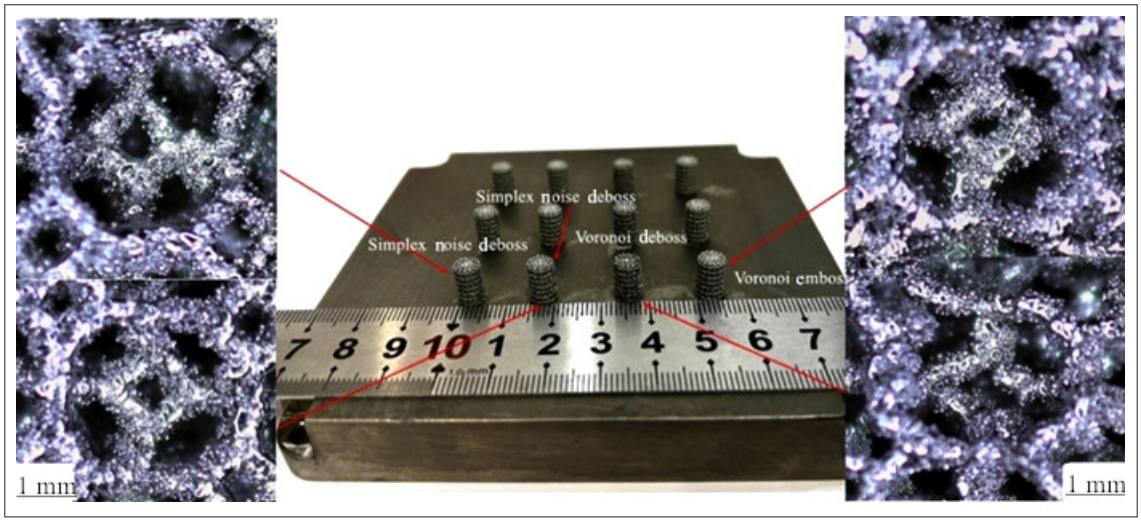

Figure 11. Different texturized porous structures fabricated via 3D printing.

texturized structures, the surface roughness, simplex noise deboss, and Voronoi deboss structures did not significantly promote tissue ingrowth, and in some cases, even showed reduced ingrowth than non-texturized ones. This suggests that increasing surface roughness via material removal slightly increased the surface-to-volume ratio of the porous structure, but was not favorable for tissue integration, thus failing to improve biocompatibility effectively. In contrast, the Voronoi emboss structure showed a gradual decrease in tissue ingrowth from the interior to the exterior. Compared with the non-texturized structures, the Voronoi Emboss structure exhibited significantly improved tissue ingrowth, indicating that increasing surface roughness and surface-to-volume ratio via material addition was more beneficial for tissue ingrowth and could effectively improve biocompatibility. Therefore, in future designs of bio-fixed medical devices, a surface protrusion approach could be considered to enhance the biocompatibility of implants.

3.4.4. Analysis of the repair effect of Kelvin cell structures with Voronoi emboss texturization at different roughness peaks on bone defects in the distal femur of rabbits

By examining Figure 14 and comparing it with Figure 13D, it can be concluded that as the roughness peak increased, bone tissue density at the center of the scaffold also increased. This may be attributed to the gradual decrease in pore size. In terms of tissue adhesion on the scaffold's exterior, a slight increase was observed with increasing roughness peak, possibly resulting from the increased surface-to-volume ratio. Overall, increasing the roughness peak through a convex structure can improve biocompatibility. However, it also reduces pore size, thereby limiting the space available for tissue ingrowth. Therefore, both factors should be considered comprehensively during the actual design process.

4. Discussion

The fluid properties of porous structures directly influence the material exchange efficiency of medical implants. Traditional octet structures, which used eight struts as their basic units, exhibited faster blood flow between three struts and slower flow at the intersections of 8 struts. This fluctuation in local flow speed tends to induce energy loss and is unfavorable for stable material exchange. Metamaterial porous structures perform better in this regard. The Kelvin cell structure demonstrated the characteristic of "fast flow in the center, diffusing to the surrounding area." The truncated octahedron and Weaire–Phelan structures exhibited a pattern of "fast flow in the center and slow flow in the surrounding area", which reduced flow speed fluctuations and lowered the overall pressure on the metamaterial, thereby decreasing circulation resistance. The Kelvin cell structure achieved higher flow speed under low pressure and offers the best fluid transmission efficiency, making it an ideal choice for bone implants, tissue scaffolds, and similar applications.

Texturization processes significantly affected the mechanical safety of the Kelvin cell structure. The Voronoi deboss, surface roughness, and simplex noise deboss structures utilized material removal methods, resulting in greater surface displacements. In contrast, the Voronoi emboss structure applied a material addition method, leading to smaller displacements. In terms of stress distribution, the simplex noise deboss structure

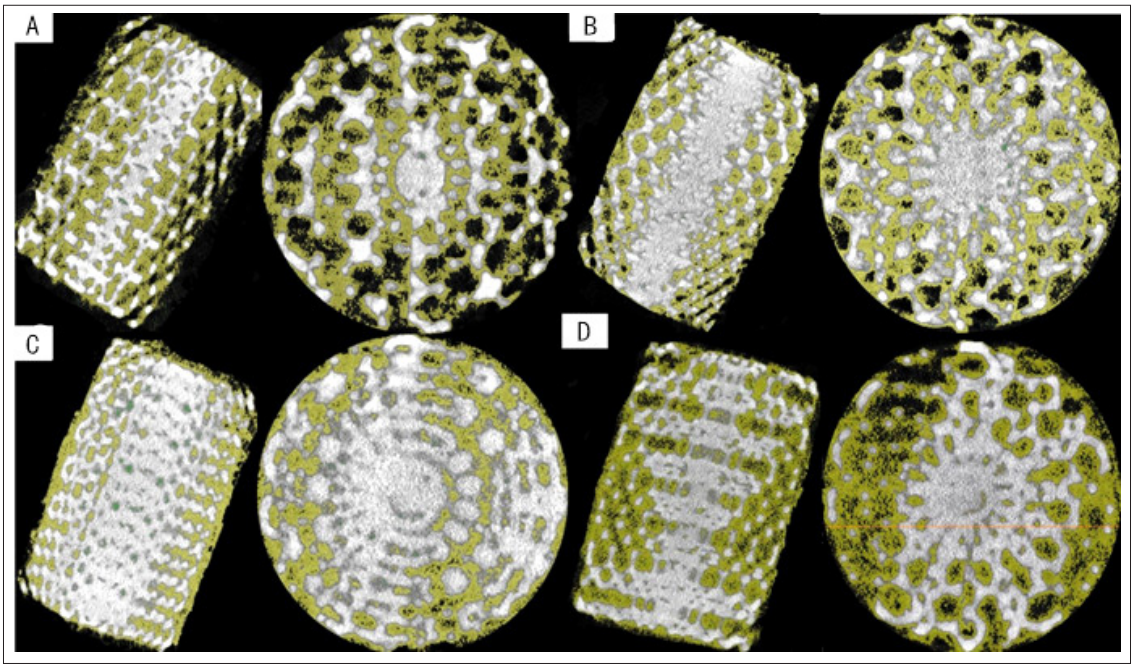

Figure 12. Repair effect of bone defects in the distal femur of rabbits: (A) Kelvin cell; (B) Octet; (C) Weaire–Phelan; (D) Truncated octahedron.

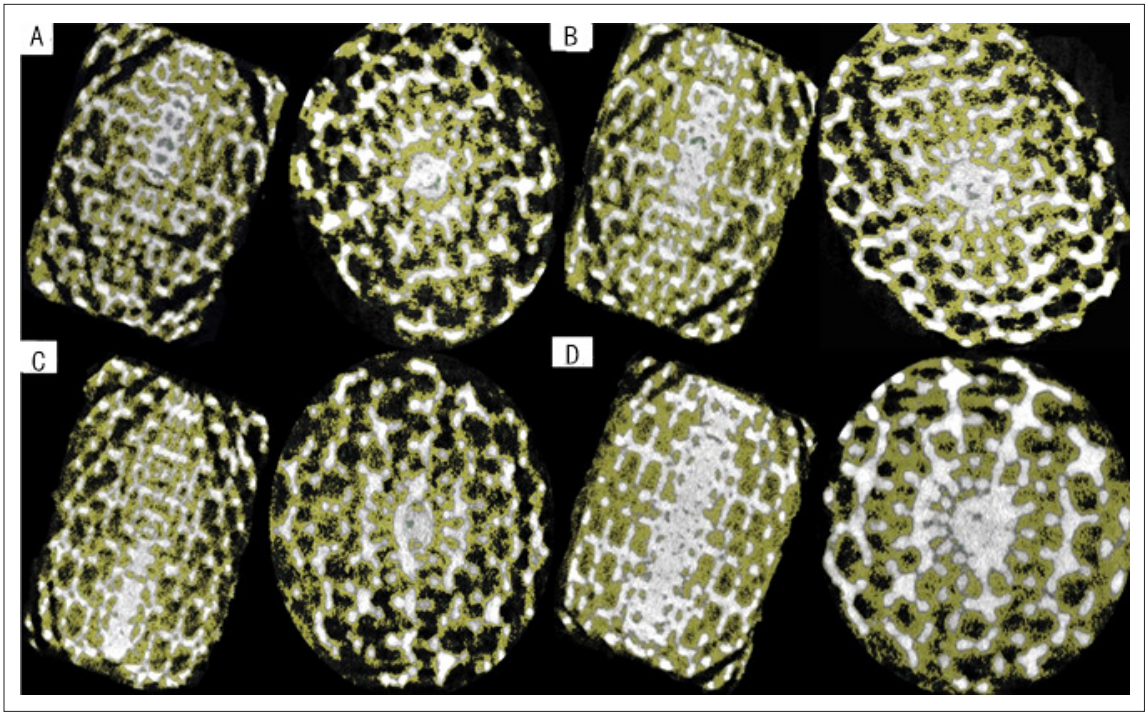

Figure 13. Tissue ingrowth in different textured porous structures: (A) Surface roughness; (B) Simplex noise deboss; (C) Voronoi deboss; (D) Voronoi emboss.

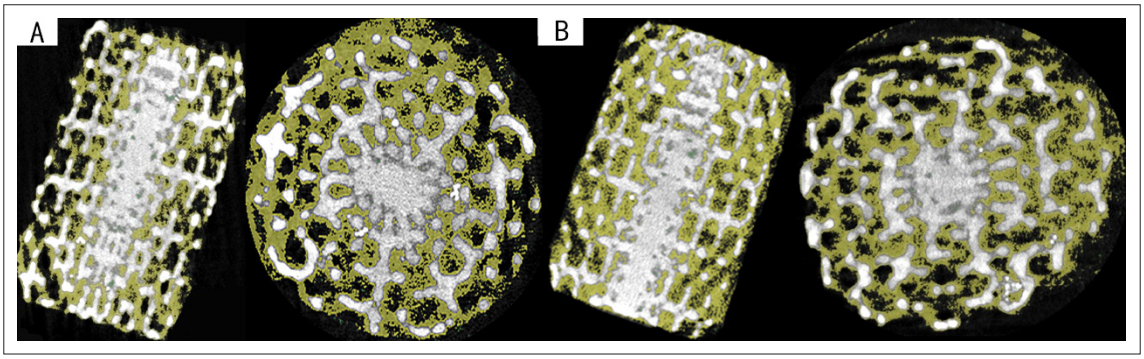

Figure 14. Repair effect of Kelvin cell porous structures with different roughness peaks: (A) 0.06 mm; (B) 0.08 mm.

experienced the highest stress concentration due to its irregular texture, which increases the risk of cracking. The Voronoi deboss and surface roughness structures showed moderate stress concentrations, while the Voronoi emboss structure demonstrated the least stress concentration, with a maximum stress of only 8.61795×10^{1} MPa, meeting mechanical safety requirements. Therefore, in implant design, material addition methods should be prioritized, or material removal parameters should be optimized to minimize structural risks.

The tissue growth effect varied among the different porous structures, with the Kelvin cell structure showing a slightly better performance. These were influenced by factors such as pore gradient, porosity, and potential pore blockage. Texturization introduced a trade-off in biocompatibility. Material removal methods can enhance roughness and increase the surface-to-volume ratio but may compromise pore connectivity, hindering tissue ingrowth. In contrast, material addition methods also enhance roughness but better support tissue integration. Surface protrusions can effectively increase roughness peaks and improve biocompatibility. However, it is important to note that increasing the roughness peak may compress pore space and reduce porosity, thereby limiting deep cellular proliferation. In future work, a quantitative model describing the relationship among roughness, porosity, and tissue ingrowth should be developed to guide collaborative optimization.

5. Conclusion

In the selection of scaffold-type porous structures for medical implants, the Kelvin cell structure demonstrated the best overall performance. It not only achieved high flow velocity and low circulation resistance under low-pressure conditions through its flow field characteristic of "rapid central flow and peripheral diffusion," but also exhibited slightly superior cell growth performance. Therefore, it is an ideal choice for applications such as bone implants and tissue scaffolds. The traditional octahedral structure has limited applicability due to significant local flow velocity fluctuations and high energy loss. Although the truncated octahedron and Weaire–Phelan structures help mitigate flow velocity fluctuations, their fluid transport efficiency remains lower than that of the Kelvin Cell structure.

To ensure the mechanical safety and biocompatibility of Kelvin cell structures, implant design should prioritize material addition processes (such as Voronoi emboss) to reduce the risk of stress concentration and minimize surface displacement. If material removal processes such as Voronoi deboss, surface roughness, or simplex noise deboss are used, parameter optimization (such as controlling removal depth and optimizing texture regularity) is necessary to reduce the risks of cracking and pore connectivity damage, while balancing roughness improvement with structural integrity.

This study presents a preliminary exploration of the fluid characteristics, mechanical safety, and tissue growth effects of porous structures. However, it does not include cell growth experiments, implant site applicability analysis, or histological staining. Future research should include dynamic mechanical testing to evaluate impact resistance, provide biocompatibility direct evidence through cell growth experiments, and clarify the application scope of the structures based on the physiological needs of different implantation sites. Additionally, a quantitative model of "roughness–porosity –tissue growth" should be established to enable multi-parameter collaborative optimization, laying the groundwork for the development of high-performance 3D-printed medical implants.

Acknowledgments

The manufacturing and observation of the femoral prosthesis described in this article were carried out at the Key Laboratory of Special Processing, Zhoukou city.

Funding

The study was funded by the National Natural Science Foundation of China (grant no. 52575470), Natural Science Foundation Project of Henan Province (grant no. 252300421971) and the Zhoukou Science and Technology Plan Project (grant no. ZKSKJGG 100084).

Conflict of interest

The authors declare no conflicts of interest.

Ethics approval and consent to participate

The *in vivo* animal experiment was approved by the Agricultural and Rural Affairs Bureauof Shangzhou District Ethical Review Report (2025922)

Author contributions

Conceptualization: Guoqing Zhang
Formal analysis: Guoqing Zhang, Yongsheng Zhou, Juanjuan Xie
Funding acquisition: Guoqing Zhang
Investigation: Guoqing Zhang, Junxin Li, Congcong Shangguan, Yuchao Bai
Methodology: Guoqing Zhang
Writing–original draft: Guoqing Zhang, Yongsheng Zhou
Writing–review & editing: Guoqing Zhang, Aibing Huang

Consent for publication

Not applicable.

Availability of data

The datasets generated and/or analyzed during the current study are not publicly available due to confidentiality requirements but are available from the corresponding author upon reasonable request.

References

1. Chinese Osteoporosis and Mineral Diseases Society. Guidelines for the diagnosis and treatment of primary osteoporosis(2022). *Chin J Gen Pract*. 2023;26(14):1671-1691. doi: 10.12114/j.issn.1007-9572.2023.0121.
2. Wu Y, Wang Y, Liu M, *et al*. Design, manufacturing, and application of porous implants based on 3D printing technology. *Chin J Med Devices*. 2024;48(01):15-19. doi: CNKI: SUN:ZYLZ.0.2024-01-004.
3. Salaha ZFM, Ammarullah MI, Abdullah NNAA, *et al*. Biomechanical effects of the porous structure of gyroid and voronoi hip implants: a finite element analysis using an experimentally validated model. *Materials*. 2023;16(9):3298. doi: 10.3390/ma16093298
4. Jandyal A, Chaturvedi I, Wazir I, Raina A, Haq MIU. 3D printing–a review of processes, materials and applications in industry 4.0. *Sustain Oper Comput*. 2022;3:33-42. doi: 10.1016/j.susoc.2021.09.004
5. Leschok M, Cheibas I, Piccioni V, *et al*. 3D printing facades: design, fabrication, and assessment methods. *Autom Constr*. 2023;152:104918. doi: 10.1016/j.autcon.2023.104918
6. Li, K, Ji C, Bai S, Jiang B, Pan F. Selective laser melting of magnesium alloys: necessity, formability, performance, optimization and applications. *J Mater Sci Technol*. 2023;154:65-93. doi: 10.1016/j.jmst.2022.12.053
7. Wang H. *Comparative Study on the Application of Personalized Titanium Alloy Prostheses and Allogeneic Mandibular Bones for Mandibular Defect Repair in Beagle Dogs*. Beijing: Chinese People's Liberation Army Medical College; 2017.
8. Yang J, Li Y, Shi X, *et al*. Design and analysis of three-dimensional printing of a porous titanium scaffold. *BMC Musculoskelet Dis*. 2021;22(1):654. doi: 10.1186/s12891-021-04520-1
9. Wang Y. *Experimental Study on Biomechanical Properties and Biocompatibility of 3D Printed Artificial Trabecular Prosthesis*. Zhengzhou University; 2021.
10. Wang S, Gao K, Xu Z, *et al*. 3D printing-assisted traditional steel plate internal fixation for complex tibial plateau fractures. *Chin J Tissue Eng Res*. 2022;26(18):2823-2827. doi: 10.12307/2022.688.
11. Zhang P, Jiang B, Zhang L, *et al*. Biocompatibility evaluation of 3D printed porous tantalum. *Med Equip*. 2022; 35(09):44-49. doi: CNKI: SUN: YLZB.0. 2022-09-014.
12. Liang H, Li R, Liu G, *et al*. Research and clinical application status of porous structure design for medical orthopedic implants. *J Clin Rehabil Tissue Eng Res*. 2017;21(15):2410-2417. doi: CNKI: SUN:XDKF.0.2017-15-023.
13. Liu C, Wang C, Liu H, *et al*. Mechanical properties and biocompatibility of 3D printed Ti6Al4V titanium alloy scaffolds. *Chin J Nonferrous Metal*. 2018; 28(04):758-765. doi: 10.19476/j.ysxb.1004.0609.2018.04.14
14. Lei H, Zhou Z, Liu J, *et al*. Structural optimization of 3D-printed porous titanium implants promotes bone regeneration for enhanced biological fixation. *ACS Appl Mater Interfaces*. 2025;17(12):18059-18073. doi: 10.1021/acsami.4c22401
15. Tamaddon M, Samizadeh S, Wang L, Blunn G, Liu C. Intrinsic osteoinductivity of porous titanium scaffold for bone tissue engineering. *Int J Biomater*. 2017;2017(1):5093063. doi: 10.1155/2017/5093063

16. Zaharin HA, Abdul Rani AM, Azam FI, *et al*. Effect of unit cell type and pore size on porosity and mechanical behavior of additively manufactured Ti6Al4V scaffolds. *Materials*. 2018;11(12):2402.
doi: 10.3390/ma11122402

17. Zadpoor AA. Bone tissue regeneration: the role of scaffold geometry. *Biomater Sci*. 2015;3(2):231-245.
doi: 10.1039/c4bm00291a

18. Kumar A, Nune KC, Murr LE, Misra RDK. Biocompatibility and mechanical behaviour of three-dimensional scaffolds for biomedical devices: process–structure–property paradigm. *Int Mater Rev*. 2016;61(1):20-45.
doi: 10.1080/09506608.2015.1128310

19. Tu C. *Study on the Biocompatibility of 3D Printed Porous Composite Scaffolds*. Huazhong University of Science and Technology; 2016.

20. Zhao Y, Li H, Guo Y, *et al*. Preparation and biocompatibility study of mPEG-PDLLA/nHAP/TTCP porous bone scaffolds. *J Armed Police Med Coll (Med Ed)*. 2016;25(12):954-958.
doi: 10.16548/j.2095-3720.2016.12.002.

21. Jodati H, Yılmaz B, Evis Z. A review of bioceramic porous scaffolds for hard tissue applications: effects of structural features. *Ceram Int*. 2020;46(10):15725-15739.
doi: 10.1016/j.ceramint.2020.03.192

22. Zheng H. *Research on the Surface Topological Structure Regulation of Degradable Polymer Microspheres and its Effects on Cell Adhesion and Function*. Zhejiang University; 2018.

23. Lai Y. *Basic Research on the Application of Micro-groove Topography and Nano-antibacterial Coating to the Surface of Gingival-crossing Part of Dental Implants*. Fujian Medical University; 2014.

24. Zhang G, Yang Y, Zhang Z, *et al*. Optimization design of support structure for laser selective melting forming parts. *China Laser*. 2016;43(12):59-66.
doi: 10.3788/CJL201643.1202002

ACCSCIENCE PUBLISHING

International Journal of Bioprinting

RESEARCH ARTICLE

Personalized 3D-printed TDM/ZrO_2 scaffolds laden with iPSC-derived SOX9$^+$ sclerotomal progenitors for functional osteochondral regeneration

Yuqing Dong[1,2], Zhijun Zhang[3], Fengxiao Zhao[1], Weihua Guo[1,4*], Jingfei Xiong[5], Zhonghan Li[5], and Yuming Zhao[2*]

[1]State Key Laboratory of Oral Diseases and National Clinical Research Center for Oral Diseases, Department of Pediatrics, West China Hospital of Stomatology, Sichuan University, Chengdu, Sichuan, China

[2]Department of Pediatric Dentistry, National Engineering Laboratory for Digital and Material Technology of Stomatology, National Center of Stomatology, National Clinical Research Center for Oral Diseases, Peking University School and Hospital of Stomatology, Beijing, China

[3]Department of Stomatology, School of Clinical Medical, Chengdu Medical College, Chengdu, Sichuan, China

[4]Yunnan Key Laboratory of Stomatology, The Affiliated Hospital of Stomatology, School of Stomatology, Kunming Medical University, Kunming, Yunnan, China

[5]Key Laboratory of Bio-Resource and Eco-Environment of Ministry of Education, Center of Growth Metabolism and Aging, College of Life Sciences, Sichuan University, Chengdu, Sichuan, China

***Corresponding authors:**
Weihua Guo
(guoweihua943019@163.com)

Yuming Zhao
(yumingzhao70@sina.com)

Citation: Dong Y, Zhang Z, Zhao F, *et al.* Personalized 3D-printed TDM/ZrO_2 scaffolds laden with iPSC-derived SOX9$^+$ sclerotomal progenitors for functional osteochondral regeneration. *Int J Bioprint*. 2025;11(6):531-550. doi: 10.36922/IJB025330333

Received: August 13, 2025
1st revised: September 25, 2025
2nd revised: October 9, 2025
Accepted: October 15, 2025
Published online: October 23, 2025

Copyright: © 2025 Author(s). This is an Open Access article distributed under the terms of the Creative Commons Attribution License, permitting distribution, and reproduction in any medium, provided the original work is properly cited.

Publisher's Note: AccScience Publishing remains neutral with regard to jurisdictional claims in published maps and institutional affiliations.

Abstract

Osteochondral defects resulting from trauma or degenerative diseases are challenging to treat due to the complex hierarchical structure and limited self-healing capacity of articular cartilage. Recent advancements have identified SOX9-positive (SOX9$^+$) sclerotomal progenitors (scl-progenitors), derived from human pluripotent stem cells, as a promising cell source capable of mimicking endochondral ossification and promoting osteochondral regeneration. A personalized three-dimensional (3D)-bioprinted scaffold was developed using treated dentin matrix (TDM)—a decellularized matrix rich in low-crystallinity hydroxyapatite, type I collagen, and osteoinductive factors—as the core bioactive material. To enhance mechanical strength and printability, the TDM was combined with methacrylated gelatin and zirconia nanoparticles. SOX9$^+$ scl-progenitors were encapsulated within the hydrogel matrix and printed using extrusion-based 3D bioprinting to fabricate cell-laden scaffolds with tunable biomechanical and biological properties. The engineered constructs supported robust cell viability, proliferation, and differentiation toward osteochondral lineages *in vitro*. *In vivo* implantation in a nude rat knee osteochondral defect model demonstrated excellent biocompatibility and significant regeneration of both cartilage and subchondral bone tissue. This study presents a translatable and customizable platform integrating stem cell technology, natural biomaterials, and 3D bioprinting for osteochondral tissue engineering. The bioengineered construct offers substantial advantages for personalized osteochondral defect repair over conventional approaches.

***Keywords*:** Osteochondral regeneration; SOX9-positive sclerotomal progenitors; Three-dimensional bioprinting; Tissue engineering; Treated dentin matrix

1. Introduction

Articular cartilage injury represents a pivotal pathological event in the initiation and progression of osteoarthritis.[1] Recent epidemiological studies report that the prevalence of osteoarthritis among individuals over 40 years old in China reaches 46.3%, with a notable trend toward earlier onset in younger populations.[2] Osteochondral tissue is composed of articular cartilage and the underlying subchondral bone, bridged by a layer of calcified cartilage that ensures mechanical integrity and facilitates load transfer across the joint interface.[3] Repairing osteochondral defects remains a formidable clinical challenge due to the distinct biochemical compositions and mechanical properties of its constituent layers, as well as the inherently limited regenerative capacity of cartilage.[4] An epidemiological survey from 2020 indicates that 7.6% of the global population suffers from osteoarthritis, with an increasing number of cases among younger individuals due to inappropriate exercise and repetitive joint overuse.[5] Prolonged mechanical overloading and chronic trauma, often exacerbating joint degeneration, severely impair mobility and quality of life.[2,6] As life expectancy increases and sports-related injuries become more frequent, the demand for effective osteochondral repair strategies continues to grow.

Although current clinical options, such as autologous chondrocyte implantation, remain the gold standard for focal cartilage repair,[7] the limited availability and low proliferative potential of chondrocytes pose significant challenges, as they rapidly lose their functional phenotype in culture and may cause additional donor site damage.[8] Moreover, cartilage lesions are often accompanied by subchondral bone involvement, further complicating the regenerative process and accelerating disease progression.[9,10] Therefore, identifying more effective and feasible osteochondral repair strategies has become a key focus of the current research.

Recent studies have demonstrated the potential of using human pluripotent stem cells (hPSCs) to generate cell types capable of mimicking the natural developmental sequence of osteochondral tissue.[11] Among them, SOX9-positive ($SOX9^+$) sclerotomal progenitors (scl-progenitors) have emerged as a particularly compelling cell population due to their ability to mimic critical stages of endochondral ossification, including mesenchymal condensation, chondrocyte hypertrophy, vascular invasion, and bone marrow cavity formation.[12] These progenitors are derived from hPSCs using a stepwise protocol that faithfully recapitulates embryonic development, yielding over 99% purity across multiple cell lines. Notably, they can be efficiently expanded *in vitro* and directed toward cartilage or bone fates, forming polarized, growth plate-like structures that contribute to cartilage repair *in vivo* without exhibiting undesired hypertrophy or ossification. Compared to mesenchymal stem cells (MSCs) or primary chondrocytes, $SOX9^+$ scl-progenitors display a juvenile-like phenotype, enhanced proliferative potential, and greater resistance to inflammatory cytokines, making them particularly suitable for regenerative applications in aging or osteoarthritic tissues.

However, a limitation in translating these biological advances into clinical practice is the lack of customizable, biomimetic scaffolds capable of integrating mechanical and biological cues for tissue regeneration. As osteochondral defects often vary in size, shape, and location, personalized solutions are essential. In this context, three-dimensional (3D) bioprinting has emerged as a transformative technology that enables the precise fabrication of structurally complex scaffolds tailored to patient-specific anatomy and tissue requirements. To address this, we developed a hybrid osteochondral scaffold by combining treated dentin matrix (TDM)—a natural, bioactive, and mechanically resilient material[13]—with methacrylated gelatin (GelMA) and zirconia (ZrO_2) nanoparticles.

As a decellularized extracellular matrix, TDM retains low-crystallinity hydroxyapatite and a variety of bioactive molecules, including transforming growth factor-β (TGF-β) and bone morphogenetic proteins (BMPs).[14] These components have been shown to efficiently induce MSC differentiation toward both osteogenic and chondrogenic lineages, enhancing tissue regeneration.[15] Numerous *in vitro* and *in vivo* studies have demonstrated that TDM can promote proliferation and lineage-specific differentiation of MSCs into bone- and dentin-forming cells.[16,17] Mechanically, TDM exhibits elastic properties similar to those of calcified cartilage and subchondral bone, along with low immunogenicity and good processability, making it an attractive material for osteochondral scaffold design.[18] Our previous studies demonstrated that TDM exhibits excellent printability when processed into particles less than 40 μm in diameter and combined with suitable excipients.[19] The resulting TDM-based 3D-printed scaffolds provided a favorable microenvironment for cell attachment, proliferation, and differentiation.

Although TDM has been widely explored for osteogenesis and odontogenesis, dentin protein extracts enriched in TGF-β and BMP members have been shown to promote cartilage-like matrix deposition. In line with these findings, we observed that TDM-containing scaffolds released TGF-β3 and BMP-2 at concentrations comparable

to those used in chondrogenic induction media for induced pluripotent stem cell (iPSC)-derived SOX9$^+$ progenitors. This observation provides the rationale for testing TDM as a bioactive component to support chondrogenesis in the present study.

This study aims to develop an effective scaffold for the simultaneous regeneration of articular cartilage and subchondral bone. To achieve this, we used GelMA to enhance the printability and structural stability of TDM, yielding scaffolds with high water content and an interconnected porous network.[20] To reinforce the scaffold further, ZrO_2 was incorporated as a structural additive. ZrO_2 effectively fills the scaffold pores, converting the otherwise brittle and fragile hydrogel network into a mechanically robust, drug-resistant framework that can withstand repetitive mechanical loading and exhibits high resistance to volumetric expansion.[21,22]

Additionally, we employed 3D bioprinting to fabricate a personalized osteochondral scaffold by incorporating iPSC-derived SOX9$^+$ scl-progenitors into TDM/ZrO_2 hydrogel matrices. The resulting bioengineered construct not only offers tunable mechanical properties but also serves as a biologically active platform for supporting stem cell viability, proliferation, and differentiation. We systematically characterized the physical and chemical properties of the scaffolds *in vitro*, and further evaluated their biological performance and regenerative capacity *in vivo* using an osteochondral defect model (Figure 1). This strategy represents a synergistic integration of developmental biology, stem cell engineering, and advanced manufacturing, offering a promising avenue for personalized osteochondral repair.

2. Materials and methods

2.1. Materials

GelMA (degree of substitution: 60%) was purchased from EFL, China. Enzyme-linked immunosorbent assay (ELISA) kits (JL17935-48T, JL25973-48T, JL21985-48T, JL17851-48T) were obtained from J&L Biological, China. Insulin–transferrin–selenium supplement, sodium pyruvate, and Rho-associated protein kinase inhibitors were purchased from Beyotime Biotechnology, China. Basic Dulbecco's Modified Eagle Medium, penicillin–streptomycin, and type II collagenase were purchased from Hyclone, United States. SOX9$^+$ scl-progenitors were obtained from Professor Zhonghan Li, School of Life Sciences, Sichuan University, as described in our previous study.[12]

The experimental animals (nude rats [n=36], male, 6–8 weeks, 200–250 g) were purchased from Ensiweier Biotechnology Co., Ltd., China. All animals were housed under specific pathogen-free conditions with a 12 h light/dark cycle, a temperature of 22 ± 2°C, and a relative humidity of 55 ± 10%. All experimental procedures were approved by the Institutional Animal Care and Use Committee of West China Hospital (ethics approval number: WCHSIRB-D-2023-309) and complied with the National Institutes of Health guidelines for the care and use of laboratory animals.

2.2. Preparation of bioprinting inks

The TDM used in this experiment was prepared according to the method established in a previous study.[23] The samples were then freeze-dried for 8 h and ground into powder passing through a 40 μm sieve.

A 10% (w/v) GelMA-60 solution was prepared by dissolving GelMA in phosphate-buffered saline (PBS) solution at 60°C under continuous stirring, followed by sterilization through a 0.22 μm filter. The bioinks were prepared by mixing the GelMA solution with ZrO_2 nanoparticles (particle size <100 nm) and TDM powder at ratios specified in Table 1.

Mixtures were homogenized using a magnetic stirrer for 30 min at room temperature until uniformly dispersed. Printing was performed using a 3D bioplotter (EnvisionTEC 3D-Bioplotter, Germany) equipped with a low-temperature print head (25°C). The extrusion pressure was set at 2.5 bar, and the printing speed was 8 mm/min. Immediately after printing, constructs were photocrosslinked under a 405 nm UV lamp for 30 s.

2.3. Scaffold characterization

2.3.1. Scanning electron microscopy

Printed scaffolds were freeze-dried for 24 h, cut into cross-sections, and sputter-coated with gold (10 nm thickness) using a Quorum SC7620 ion sputter coater (manufacturer, country). Samples were observed using a Zeiss Sigma 500 scanning electron microscope (Carl Zeiss, Germany) under high vacuum (1×10^{-5} mbar) at an accelerating voltage of 20 kV. Pore morphology and distribution were recorded at various magnifications.

Table 1. Composition of methacrylated gelatin-based bioinks

Groups	Reagent
0 % TDM	0.05 g ZrO2; 1 mL 10 % GelMA-60
30 % TDM	0.05 g ZrO2;1 mL 10 % GelMA-60
50 % TDM	0.05 g ZrO2; 1 mL 10 % GelMA-60
70 % TDM	0.05 g ZrO2; 1 mL 10 % GelMA-60

Abbreviations: GelMA, methacrylated gelatin; TDM, treated dentin matrix; ZrO_2, zirconia.

2.3.2. Fourier transform infrared spectroscopy

Scaffolds were ground into powder (<200 μm) and analyzed using a Bruker EQUINOX 55 Fourier transform infrared (FTIR) spectrometer (Bruker, Germany) in attenuated total reflectance mode. Spectra were recorded in the range of 400–4000 cm^{-1} at a resolution of 4 cm^{-1} with 32 scans per sample.

2.3.3. X-ray diffraction

The treatment method for the scaffolds was similar to that described in **Section 2.3.2**. The crystal phase analysis of the scaffold was performed using an X-ray diffractometer (manufacturer, country). The scanning angle range was selected from 5–85°, and detection was carried out at a scanning rate of 5°/min. Jade software (developer, country) was used to analyze and process the X-ray diffraction data, and phase characterization was based on the principle of the three strongest peaks.

2.3.4. Mechanical test

A Shimadzu universal testing machine (manufacturer, country) was used to conduct compression and tensile tests on the scaffolds. Cylindrical (diameter = 0.8 cm, height = 1 cm) and rectangular (0.4×1×3 cm) specimens were tested (n = 4) per group. The stroke was set to 0.8 cm (the height limit of the instrument was 0.2 cm), and the descending speed was 0.1 mm/s (n=4).

2.3.5. Degradation test

Quadruplicate scaffold samples were placed in a 12-well plate containing 1 mL of PBS, and the test was performed in a 37°C constant-temperature shaker at 1, 7, 14, 21, and 28 days. The scaffolds were freeze-dried and weighed on days 21 and 28, and the mass loss of the scaffold samples was quantified. The remaining mass of the scaffold after freeze-drying for different time points was calculated to evaluate its degradation rate. The scaffold material degradation rate (Q_d) was calculated using the following formula (**Equation (1)**):

$$Q_d = \frac{(W_0 - W_d)}{W_0} \times 100\% \quad (1)$$

where W_0 is the initial mass of the scaffold and W_d is the remaining mass of the scaffold after freeze-drying (n=4).

2.3.6. Swelling test

Quadruplicate scaffolds were freeze-dried, soaked in PBS at 37°C, and weighed at six time points: 1, 2, 4, 8, 12, and 24 h. The swelling ratio (SR) can be calculated as follows (**Equation (2)**):

$$SR = \frac{(W_S - W_d)}{W_d} \times 100\% \quad (2)$$

where W_s and W_d represent the weights of the scaffolds before and after freeze-drying, respectively, indicating the mass change of the scaffold after water absorption (n = 4).

2.3.7. Enzyme-linked immunosorbent assay

Scaffolds were incubated in PBS at 37°C. At weeks 1, 2, 3, and 4, extracts were collected after centrifugation at 5000 rpm for 5 min. Proteins released from the scaffolds were quantified using ELISA kits following the manufacturer's protocol. Each group was tested in quadruplicate[24] (n = 6).

2.4. *In vitro* studies

2.4.1. Culture and induction of differentiation of $SOX9^+$ sclerotomal progenitors

After obtaining human fibroblasts for genetic reprogramming, a cell line was established by inserting the fluorescent reporter gene tdTomato downstream of *SOX9* to enable cell screening and polymerase chain reaction (PCR)-based detection of related gene expression. Sclerotome-like cells were obtained following genetic reprogramming and induction of differentiation. Owing to their high expression of *SOX9*, these cells were designated as $SOX9^+$ scl-progenitors in this study. The detailed cell culture and induction protocols have been described in our previous study.[12]

2.4.2. Cytocompatibility testing of scaffolds

Scaffolds were placed in 24-well plates, and cells were seeded onto the scaffold surfaces at a density of 5×10^3 cells per well. Subsequently, the scaffolds were transferred to transwell inserts, and the culture medium was added to fully submerge them, allowing co-culture under standard conditions. After 1, 3, 5, and 7 days of co-culture, the medium was removed, and 500 μL of Cell Counting Kit-8 reagent (manufacturer, country) was added to each well to ensure complete immersion of the scaffolds. The plates were incubated at 37°C in the dark for 1 h. Following incubation, the supernatants were transferred to 96-well plates, and absorbance was measured at 450 nm using a microplate reader (manufacturer, country).

Live/dead staining was performed using the same co-culture method. After the designated incubation period, the scaffolds were inverted and placed at the bottom of confocal dishes, and imaging was performed using confocal microscopy to assess cell viability and distribution (n=4).

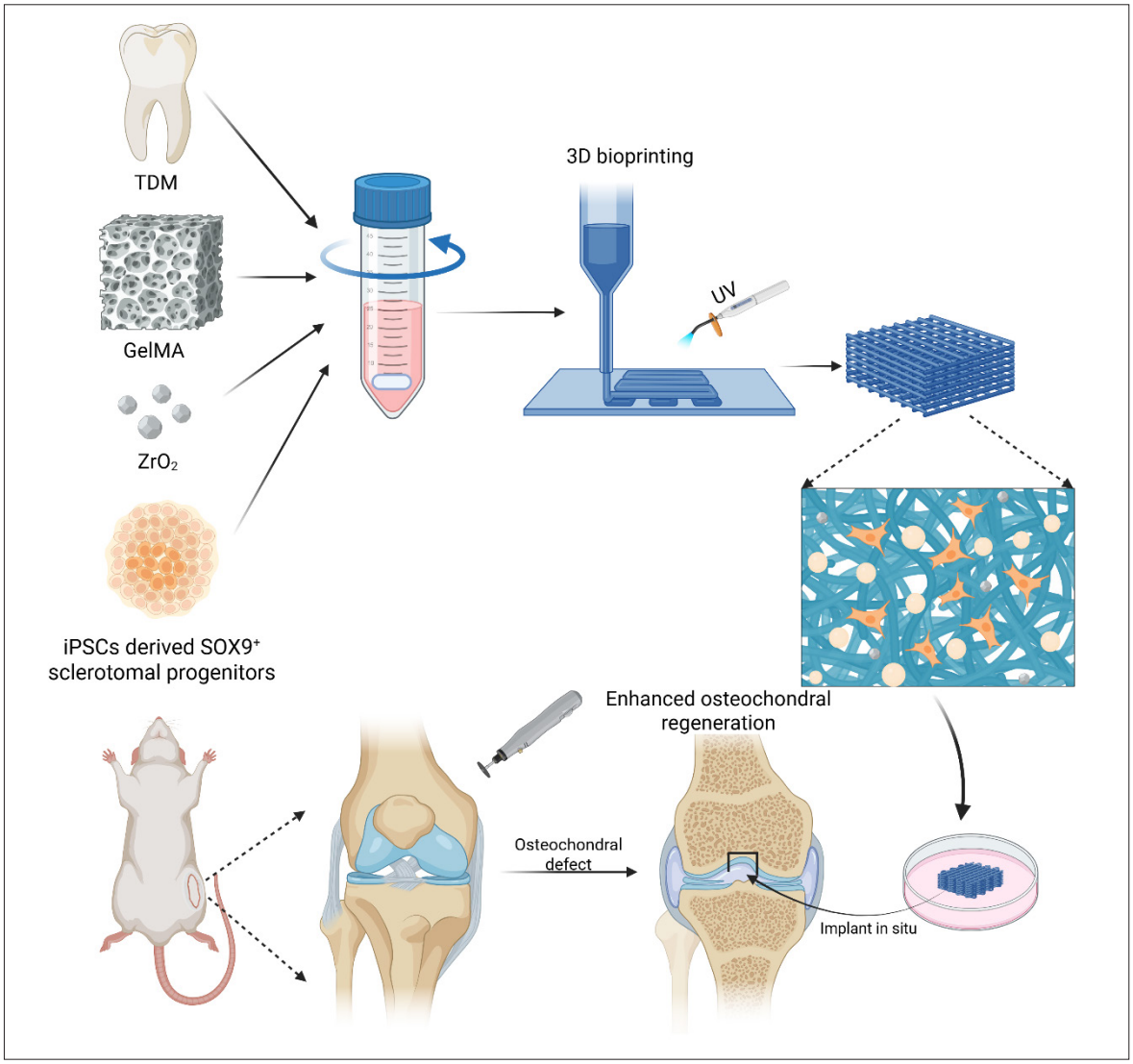

Figure 1. Schematic diagram of TDM/ZrO_2 hydrogel scaffold for osteochondral defect regeneration. Abbreviations: 3D, three-dimensional; GelMA, methacrylated gelatin; iPSC, induced pluripotent stem cell; Scl, sclerotomal; TDM, treated dentin matrix; UV, ultraviolet; ZrO_2, zirconia.

2.4.3 Effect of scaffold material on gene expression in iPSC-derived SOX9⁺ scl-progenitors

The iPSC-derived SOX9⁺ scl-progenitors were co-cultured with the scaffolds for seven days, and RNA and protein were extracted for quantitative reverse transcription PCR and Western blot analysis, respectively. Real-time quantitative PCR was performed using a LightCycler PCR System (Roche, Switzerland) with SYBR qPCR Master Mix (manufacturer, country). The cycle threshold (Ct) values were recorded after each reaction and analyzed using the $2^{-\Delta\Delta Ct}$ method with β-actin as the loading control. Primer sequences are provided in Table S1. All experiments were performed in triplicate (n=6).

2.5. *In vivo* studies

2.5.1. Implantation in situ

A nude rat knee joint defect model was established to evaluate the scaffold performance *in vivo*. The cell-loaded bioink was prepared from a cell suspension concentration of 1 × 10^8 cells/mL, with temperature maintained at 30 ± 2°C, printing speed set at 8 mm/s, and air pressure at 1.5–2 bar. Cylindrical scaffolds (diameter: 2 mm; height: 1.5 mm) were printed according to the defect model, photocrosslinked, and preconditioned in complete Dulbecco's Modified Eagle Medium before implantation. A cylindrical defect (diameter: 2.0 mm; depth: 1.5 mm)

was created in the femoral intercondylar fossa of the rat knee using a dental handpiece-mounted trephine under continuous sterile saline irrigation.[25] The printed scaffolds were then implanted into the prepared defects of the nude rat knees and observed *in vivo* for 6 and 12 weeks (n=4).

2.5.2. Micro-computed tomography imaging evaluation and histological staining

The samples were stacked and placed into a 48-mm-diameter sample tube compatible with micro-computed tomography (micro-CT) for scanning. The scanning parameters were as follows: (i) voltage: 55 kVp; (ii) current: 145 pA; (iii) filter: Al 0.5 mm; (iv) exposure time: 250 ms; (v) scan resolution: 500 projections per 180°; and (vi) scan precision: 8 μm. The scanning data were used for 3D reconstruction using evaluation software (software, developer, country). Quantitative analysis of the subchondral bone volume fraction (BV/TV), bone mineral density (BMD), and trabecular bone number (Tb.N) was performed to assess the increase in subchondral bone.

2.5.3 Histological and morphological evaluation of regenerated osteochondral tissue

Samples were demineralized in a 10% ethylenediaminetetraacetic acid solution for 4 weeks. After dehydration and embedding in paraffin, demineralized samples were cut into 5-mm-thick sections. The sections were then subjected to hematoxylin and eosin staining and Safranin O staining to differentiate between newly formed cartilage and bone tissue. Additionally, immunohistochemical staining was performed to confirm the presence of type II collagen (COLII) in the newly formed cartilage tissue.

2.6 Statistical analysis

Data are presented as mean ± standard deviation. Differences between groups were analyzed using t-test and one-way analysis of variance, and $p < 0.05$ was considered statistically significant (software, developer, country).

3. Results

3.1. Scaffold morphological characterization

3.1.1. Scaffold microstructure

A bioplotter 3D printing system was employed to fabricate TDM/ZrO_2 hydrogel composite scaffolds. The incorporation of TDM particles enhanced print fidelity, resulting in more uniform and continuous filament extrusion. The printed constructs exhibited a milky-white and opaque appearance (Figure 2A), consistent with successful TDM integration. Compared to conventional hydroxyapatite-based scaffolds, the surfaces of the TDM/ZrO_2 scaffolds appeared notably rougher due to the irregular morphology of the TDM particles, which increased the effective surface area and was expected to facilitate cell attachment and adhesion (Figure S1). Demineralized TDM exhibited an extensive dentinal tubule network, facilitating the sustained release of embedded bioactive molecules into the surrounding matrix. This not only mitigated the partial occupation of GelMA domains by TDM particles but also contributed to the formation of a favorable biochemical microenvironment that promotes lineage-specific differentiation of stem cells involved in osteochondral regeneration.[26]

Internally, the scaffold architecture exhibited interconnected porous networks, which are critical for the diffusion of nutrients and oxygen, as well as the removal of metabolic waste products, thereby supporting cellular viability and activity. In the 0% TDM group, the absence of TDM led to significant structural collapse upon dehydration, with sparsely distributed ZrO_2 particles occupying the remaining voids (Figure 2B). In contrast, scaffolds with 30, 50, and 70% of TDM retained their macroscopic morphology following freeze-drying, suggesting improved dimensional stability and structural integrity. Side-view imaging demonstrated a clear layer-by-layer deposition pattern, characteristic of extrusion-based bioprinting (Figure 2C). Additionally, cross-sectional analysis revealed a loosely porous internal structure (Figure 2D), providing sufficient space for cell infiltration and proliferation and offering structural support for cell-laden bioprinting applications.

3.1.2. Physicochemical characterization of treated dentin matrix/zirconia hydrogel scaffolds

FTIR spectroscopy analysis confirmed that the major components of TDM closely resembled those of hydroxyapatite, containing characteristic organic functional groups such as carbonate and phosphate. Evidence of hydrogen-bonding interactions between GelMA and TDM was observed. In particular, the enhanced absorption peak at 1114 cm^{-1}, attributed to C–OH stretching vibrations and/or aliphatic C–N stretching, indicated the successful chemical integration of TDM into the composite scaffold (Figure 2E). The FTIR spectra of the 30, 50, and 70% TDM scaffolds exhibited similar peak patterns, with variations primarily in peak intensity and width corresponding to differences in TDM content. As the TDM concentration increased, the area of the characteristic peaks also increased, further supporting the dose-dependent integration of TDM into the scaffold matrix.

X-ray diffraction analysis provided additional insights into the phase composition of the scaffolds. In addition to the primary elements of hydroxyapatite (calcium, phosphorus, and carbon), the spectra also revealed the

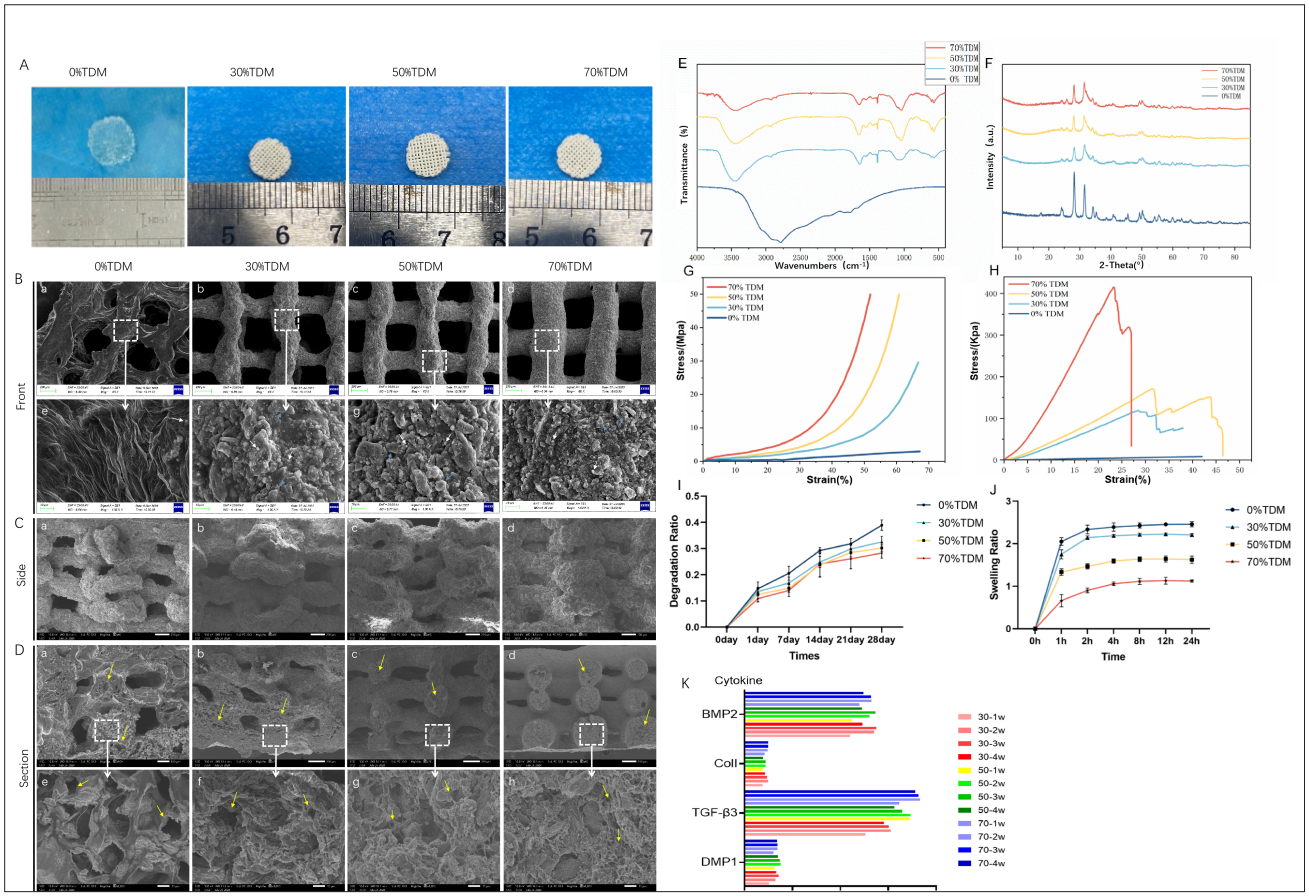

Figure 2. Morphological, structural, and mechanical characterization of 3D-printed TDM/ZrO_2 composite scaffolds. (A) 3D-printed composite scaffold used for various characterizations. (B) SEM images of the front views of 3D-printed scaffolds with different concentrations of TDM (scale bar: 200 μM; magnification: 60×). (C) SEM images of the TDM/ZrO_2 hydrogel scaffolds in side view (scale bar: 200 μM; magnification: 60×). (D) SEM images of the TDM/ZrO_2 hydrogel scaffolds in cross-sectional view, with yellow arrows indicating internal voids in the scaffold (scale bar: 100 μM; magnification: 200×). (E) Fourier transform infrared spectra of the scaffold material. (F) X-ray diffraction spectra of the scaffold material. (G, H) Stress–strain curves obtained from static compression and tensile tests and extrapolated Young's modulus. (I) Degradation ratio of 3D-printed scaffolds. (J) Swelling isotherms of 3D printed scaffolds. (K) Osteogenesis-associated protein released from scaffolds (n=4). Abbreviations: 3D, three-dimensional; SEM, scanning electron microscopy; TDM, treated dentin matrix; ZrO_2, zirconia.

presence of oxygen, magnesium, and sodium, along with trace amounts of nitrogen and sulfur, indicating the retention of both organic and mineral components from natural dentin. In the 0% TDM group, the diffraction pattern corresponded closely to the standard reference for ZrO_2 (PDF#88-1449), confirming its dominant phase composition. In contrast, scaffolds containing TDM exhibited diffraction peaks aligned with the hydroxyapatite reference pattern (PDF#73-0293), confirming the presence of both hydroxyapatite and ZrO_2 as the main crystalline phases. Notably, the broader full-width at half maximum of the TDM-related peaks suggested lower crystallinity in TDM compared to synthetic hydroxyapatite. Moreover, the gradual increase in the hydroxyapatite peak area across the 30, 50, and 70% TDM groups further supports the dose-dependent incorporation of TDM within the scaffold structure (Figure 2F).

3.1.3. Mechanical properties of three-dimensional printed scaffolds

The mechanical performance of the TDM/ZrO_2 scaffolds was evaluated under both compressive and tensile loading conditions. As the TDM content within the GelMA hydrogel matrix increased, the compressive strength of the scaffolds also increased. At 50% strain, the compressive strengths of the 30, 50, and 70% TDM groups reached 7.4, 22.5, and 48.2 MPa, respectively, with corresponding elastic moduli of 0.32, 0.65, and 0.89 MPa. These values fall within the range of native human cartilage and osteochondral composite structures (0.5–3 MPa and

5—54 MPa, respectively),[27] suggesting that the scaffolds exhibit mechanical properties physiologically relevant to native tissue. In contrast, the 0% TDM group exhibited a significantly lower compressive modulus of only 0.12 MPa (Figure 2G).

Tensile testing further confirmed the mechanical enhancement conferred by TDM incorporation. The tensile strengths of the 30, 50, and 70% TDM groups were 120, 150, and 342 kPa, respectively, compared to only 0.035 kPa in the 0% TDM group, which lacked the reinforcing TDM phase (Figure 2H). Collectively, both the compressive and tensile moduli were significantly improved in the gradient scaffolds relative to the pure hydrogel control, contributing to enhanced shape fidelity and defect conformity following *in vivo* implantation. This mechanical robustness provides a supportive and protective microenvironment for the proliferation and differentiation of the encapsulated seed cells during the early stages of tissue regeneration.

3.1.4. Degradation and swelling properties

The shape and structure of the scaffolds remained relatively stable during the first 2 weeks, showing no apparent structural damage or mass loss. After 21 days of incubation, the scaffolds maintained a relatively intact morphology. After 28 days of incubation, the 3D network structure gradually disintegrated and collapsed, accompanied by a significant increase in mass loss; however, the remaining mass still exceeded 70% of the initial weight. Beyond this point, the degradation profile reached a plateau, with only a gradual and slow decline in mass (Figure 2I). The 0% TDM group exhibited faster degradation and higher mass loss, attributed to the absence of mechanical reinforcement provided by TDM particles. As the TDM content increased, the degradation rate progressively decreased.

Both GelMA hydrogel and TDM particles possessed a porous structure and intrinsic water absorption capacity, which facilitate cell migration and nutrient transport, thereby supporting the survival of seeded cells within the printed scaffold. The freeze-dried scaffolds exhibited rapid water uptake and swelling behavior, with the mass reaching its peak at 6 h and gradually attaining swelling equilibrium at approximately 8 h (Figure 2J). As the TDM content increased, the SR of the scaffold decreased, as the GelMA network became progressively occupied by a greater number of TDM particles, which hindered the penetration and retention of water molecules.

3.1.5. Sustained release of osteogenic and chondrogenic factors from the scaffold

Owing to the porous structure of the scaffold and the encapsulation characteristics of the hydrogel, the scaffold continuously released osteogenic and chondrogenic proteins such as BMP2, TGF-β3, COL I, and DMP1, reaching a peak within 2–3 weeks. To more intuitively display the release profiles of these factors, a histogram was used. As the TDM content increased, the amount of released proteins also increased. Among them, TGF-β3 exhibited the highest concentration, reaching 363 ng/mL (Figure 2K). Compared with a previous study, in which TDM-related protein release primarily occurred within 1 week of culture,[24] the release of scaffold-related proteins in this study peaked at 2–3 weeks, demonstrating a significant sustained-release effect.

3.2. Biocompatibility of the scaffolds

The findings revealed that live cells were distributed in a grid-like arrangement along the scaffold morphology, whereas dead cells were scattered throughout the scaffolds (Figure 3A). To investigate the effect of the scaffold materials on cell viability, Cell Counting Kit-8 assays and live/dead staining were performed at various time points *in vitro*. Live/dead staining yielded consistent results, with only a few red fluorescent cells observed across all groups on days 5 and 7, showing no notable deviation from the control group (Figure 3B). The cell proliferation trends were similar between the scaffold co-culture and control groups. Over time, cells in all five groups continued to proliferate, leading to a gradual increase in the optical density values (Figure 3C). No significant differences were observed between the groups on corresponding days; however, significant differences were observed within each group ($p < 0.0001$). Notably, the optical density value of the control group on day 7 was comparable to that on day 5, possibly due to a slightly higher initial cell seeding density. By day 7 of culture, cells in the wells had reached over 90% confluency, indicating contact inhibition. These findings suggest that the TDM/ZrO_2 hydrogel scaffold material is non-toxic and does not hinder cell proliferation. Although the TDM/ZrO_2 hydrogel scaffold did not affect cell proliferation, it exhibited excellent biocompatibility, providing a solid foundation for subsequent *in vivo* experiments.

$SOX9^+$ precursor cells generally exhibited a spindle-shaped morphology within the scaffold, extending pseudopodia and displaying an elongated growth pattern (**Figure 3D**). The porous internal structure of the scaffold provided a favorable microenvironment for cell attachment and growth. After three days of *in vitro* culture of the cell-loaded printed scaffold, $SOX9^+$ precursor cells migrated outward from the scaffold surface (Figure 3E). The scaffolds in all groups demonstrated good biocompatibility with no evidence of significant cytotoxicity.

3.3. *In vitro* effects on cell biological behavior of treated dentin matrix/zirconia hydrogel scaffold

After co-culturing $SOX9^+$ scl-progenitors with TDM/ZrO_2 hydrogel scaffolds for seven days, the mRNA

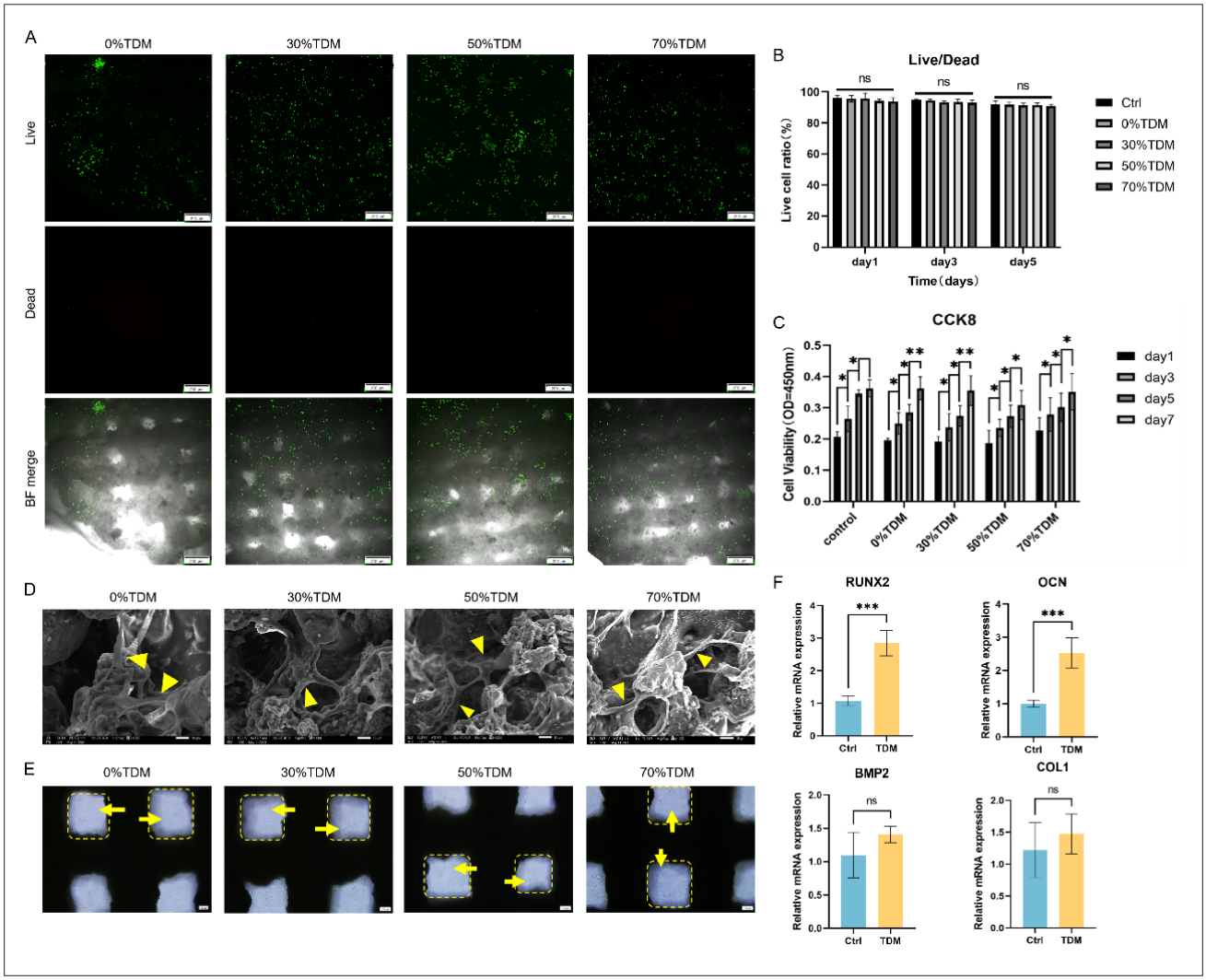

Figure 3. Biocompatibility and cell-scaffold interaction of the 3D-printed composite scaffold. (**A**) Viability of cells co-cultured with 3D-printed scaffolds for 4 days, assessed by Live/Dead staining (scale bar: 200 μm; magnification: 10×). (**B**) SEM image of a printed construct, with yellow arrows indicating cells extending pseudopodia on the scaffold surface (scale bar: 10 μm; magnification: 2000×). (**C**) Quantitative analysis of cell migration from the TDM/ZrO_2-GelMA scaffold over time. *, **, and *** indicate statistically significant differences at $p < 0.05$, $p < 0.01$, and $p < 0.001$, respectively. "ns" denotes no statistical significance. (**D**) SEM image of cellular growth within the scaffold, with a yellow arrow indicating a cell embedded in the internal structure (scale bar: 10 μm; magnification: 2000×). (**E**) Bright-field image showing cell migration, with a yellow arrow indicating a cell crawling out from the cell-laden printed scaffold (scale bar: 100 μm; magnification: 20×). (**F**) Gene expression levels of osteogenic and chondrogenic markers after 7 days of co-culture with the scaffolds.

expression levels of *OCN* and *RUNX2* were significantly higher than those of the control group, whereas the mRNA expression levels of *BMP2* and *COL1A1* showed no significant difference. The protein expression levels of OCN, RUNX2, and BMP2 were also increased (Figure 3F). RUNX2 is an important marker of late-stage chondrogenesis, and its upregulation can further promote the expression of the osteogenesis-related gene *OCN*. OCN is involved in bone formation and development, and is expressed in the early stages of osteogenesis.[28,29] These findings suggest that the TDM/ZrO2 hydrogel scaffold can promote the osteogenic and chondrogenic differentiation of SOX9⁺ scl-progenitors.

3.4. Transcriptomic changes in SOX9⁺ scl-progenitors following co-culture with the 50% TDM/ZrO_2 hydrogel scaffold

Comprehensive transcriptomic analysis of SOX9⁺ scl-progenitors cultured under standard conditions (control) and SOX9⁺ scl-progenitors co-cultured with the 50% TDM/ZrO_2 hydrogel scaffold was performed to characterize RNA expression profiles. As shown in Figure 4A, 162 genes were upregulated and 141 genes were downregulated

in the TDM group compared with the control group. Differentially expressed genes were analyzed using Gene Ontology, a bioinformatics approach encompassing three main categories (Figure 5B). Notably, the analysis revealed that genes related to extracellular matrix organization ($p < 0.001$) and encapsulating structure formation ($p < 0.005$) were significantly upregulated, indicating alterations in organelle-associated processes, particularly those involving membrane-bound organelles (Figure 4C).

Kyoto Encyclopedia of Genes and Genomes (KEGG) pathway enrichment analysis was conducted to identify potential signaling pathways through which TDM may regulate bone tissue regeneration. The calcium signaling pathway, known to modulate osteoblastic differentiation and bone formation,[30] was significantly upregulated. Notably, the hypoxia-inducible factor 1 signaling pathway, which plays a critical role in maintaining bone homeostasis and regulating glycolytic metabolism in chondrocytes, was also significantly enriched among the differentially expressed genes,[31,32] indicating its potential involvement in scaffold-induced cellular responses (Figure 4D).

To further validate the transcriptomic results and assess gene expression during the chondrogenic and osteogenic differentiation of SOX9$^+$ scl-progenitors, quantitative reverse transcription PCR was performed after seven days of co-culture. The TDM group exhibited significantly increased expression of *VEGFA*, *SOX9*, *GLUT1*, *COL2A1*, and *CDC6*, whereas *MMP7* and *KLF15* were downregulated (Figure 4E).

Western blot analysis revealed consistent trends, except that SOX9 protein expression showed no significant difference (Figure 4F), which may be attributed to the duration of the culture period. Similarly, the cell spheroids demonstrated robust glycosaminoglycan deposition, sustained chondrogenic differentiation, and abundant expression of COL2A1 (Figure S4).

These findings suggest that the TDM/ZrO_2 hydrogel scaffold promotes cell proliferation and angiogenesis while suppressing the expression of matrix metalloproteinases (MMPs), which are associated with osteoarthritis and articular cartilage degeneration.[33] Furthermore, it enhances the osteogenic and chondrogenic differentiation of SOX9$^+$ scl-progenitors, thereby supporting osteochondral tissue regeneration.

3.5. Calcification and hypertrophy following subcutaneous implantation

Under 3D culture conditions, SOX9$^+$ scl-progenitors spontaneously aggregated into compact spheroids with well-defined spherical shapes and smooth surfaces. Microscopic observation revealed that the spheroids exhibited a densely packed structure with strong cell–cell adhesion. The cell surfaces exhibited abundant microvilli-like protrusions, indicating high cellular activity and enhanced intercellular interactions, which collectively provided a favorable microenvironment for subsequent differentiation and tissue regeneration (Figure S3). After subcutaneous implantation of TDM/ZrO_2 hydrogel-encapsulated cell spheroids (Figure 5A), cells in all four groups exhibited robust chondrogenic differentiation by week 4, with no evidence of calcification or hypertrophy.

Higher magnification images revealed cells residing within cartilage lacunae, whereas darkly stained granules at the edges represented the printed material (Figure 5B). By week 8, Alcian blue staining showed that the cell nuclei were light blue, and the cytoplasm contained abundant glycosaminoglycans (Figure 5C). In the 0% TDM group, cells did not exhibit calcification or hypertrophy, whereas in the 30, 50, and 70% TDM groups, significant calcification and hypertrophy were observed. At this stage, the cells secreted more cartilage matrix, adopted a moderately cuboidal morphology, and were noticeably larger than the surrounding cells. Furthermore, Alizarin red staining demonstrated distinct calcified nodules within the cell spheroids, with some cells differentiating toward the osteogenic lineage (Figure 5D). Importantly, at both week 4 and week 8, no teratoma formation or tumorigenic cells were detected in any of the subcutaneous implants.

Fluorescein isothiocyanate labeling confirmed the presence of type X collagen (ColX)-positive chondrocytes, indicating chondrocyte hypertrophy, which is a hallmark of chondrocyte maturation. In the 30, 50, and 70% TDM groups, ColX expression overlapped with the calcified regions identified by Alizarin red staining (Figure 5E). These ColX-positive cells exhibited an enlarged cellular volume compared with surrounding cells and produced higher levels of ColX, while the production of COL2A1 decreased, indicating the initiation of osteogenic differentiation.[34–36]

3.6. *In vivo* osteochondral regeneration by SOX9$^+$ cell scaffolds

The results of hematoxylin and eosin staining of organs harvested from nude rats at weeks 6 and 12 are provided in the Supplementary file. No significant abnormalities were observed in any group (Figure S5). Based on the gross images (Figure S6), a significant concavity remained at the defect site at week 6, with the blank control group exhibiting the most pronounced depression. In contrast, the 70% TDM group exhibited a relatively smoother surface at the defect site. The micro-CT reconstructed model of the nude rat knee joint provided a more intuitive visualization of the bone tissue defect repair process. By week 12, the defect sites in the scaffold-implanted groups

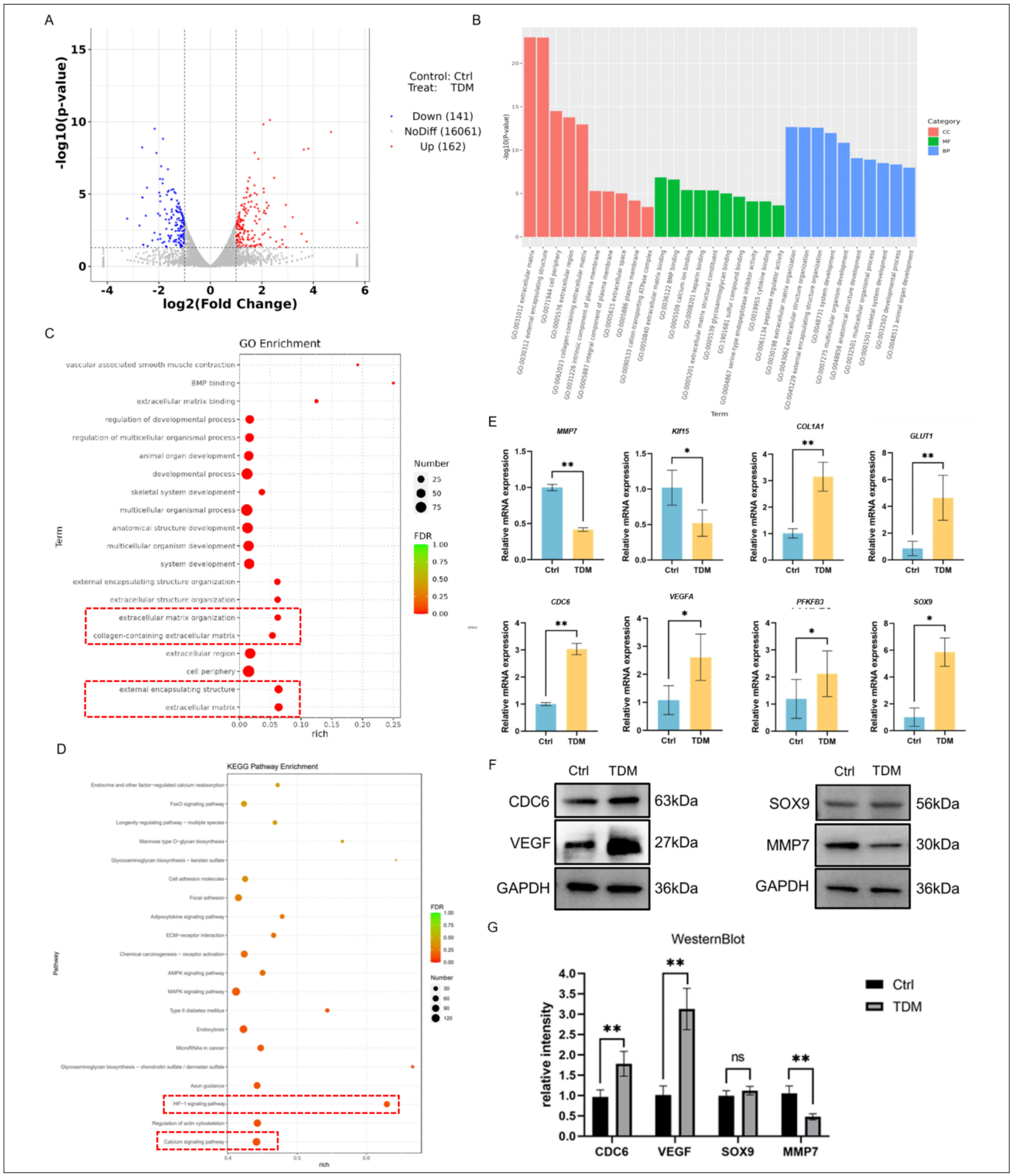

Figure 4. Transcriptome profiling and validation of differentially expressed genes in TDM-treated sclerotomal progenitors. (A) Significantly upregulated and downregulated genes in the TDM versus the control groups. (B) Differentially expressed genes classified by GO. (C) GO enrichment of upregulated genes in the TDM groups compared with the control group. (D) KEGG pathway enrichment of differentially expressed genes, depicting up- and downregulated RNAs. (E) mRNA expression of selected differentially expressed genes of SOX9^{+} sclerotomal progenitors. (F) Protein expression of selected differentially expressed genes. (G) Quantitative analysis of Western blot results. * and ** indicate statistically significant differences at $p < 0.05$ and $p < 0.01$, respectively. "ns" denotes no statistical significance. Abbreviations: Ctrl, control; GO, gene oncology; KEGG: Kyoto Encyclopedia of Genes and Genomes; TDM, treated dentin matrix.

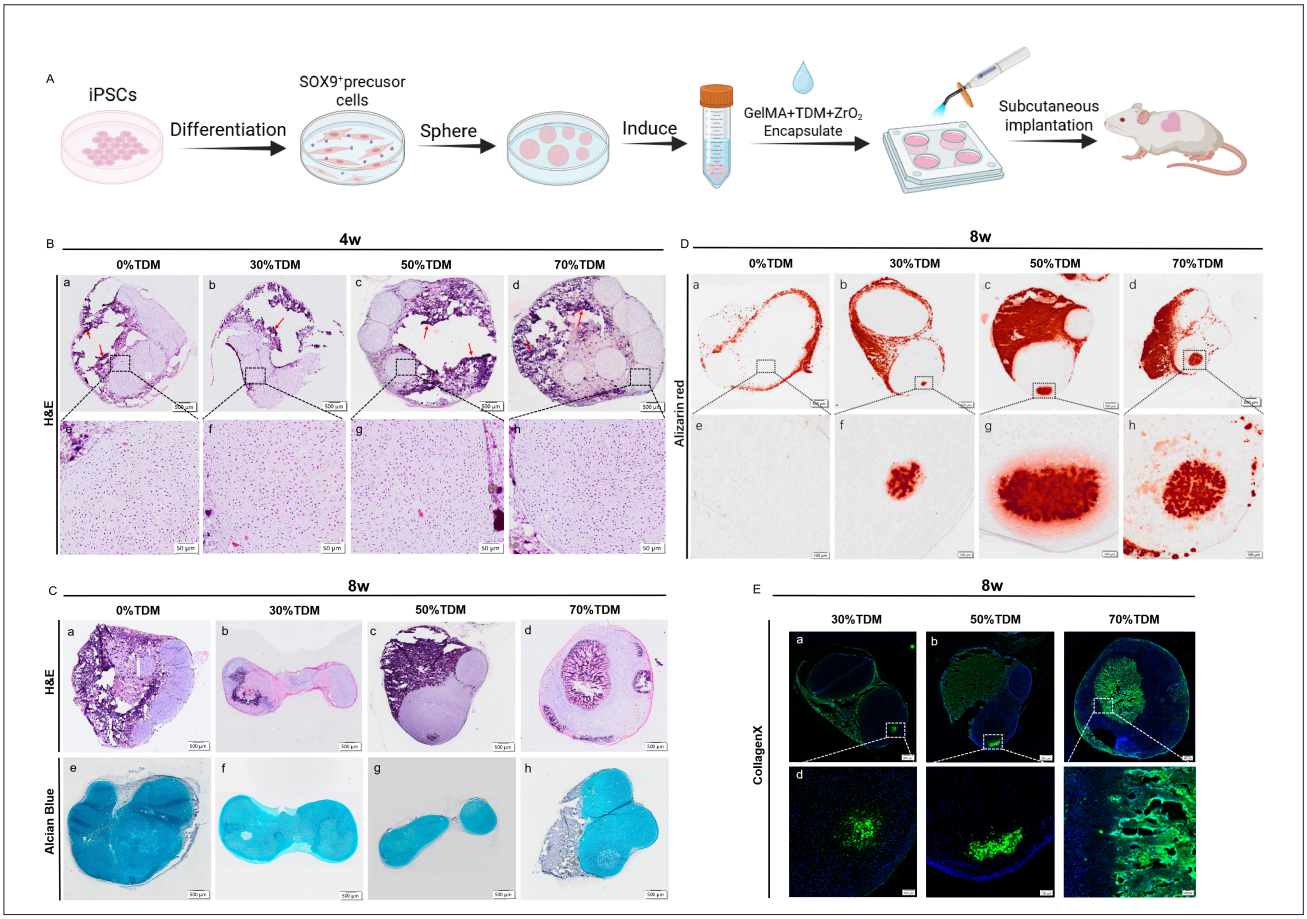

Figure 5. In vivo implantation of SOX9+ sclerotomal progenitor spheroids in 3D-printed scaffolds and subsequent evaluation of tissue formation and osteochondral differentiation. (A) Schematic diagram of subcutaneous implantation of SOX9⁺ sclerotomal progenitor spheroids encapsulated in three-dimensional-printed scaffolds. (B) H&E staining at week 4 after subcutaneous implantation, with red arrows indicating the 3D-printed scaffolds (scale bar: 500 μM; magnification: 10×). (C–E) Histological and immunofluorescence analysis at week 8: (C) H&E and Alcian blue staining (scale bar: 500 μM; magnification: 10×), (D) Alizanin red staining (scale bar: 500 μM; magnification: 10×), and (E) type X collagen immunofluorescence staining (scale bar: 500 μM; magnification: 10×). Abbreviations: GelMA, methacrylated gelatin; H&E, hematoxylin and eosin; iPSC, induced pluripotent stem cell; TDM, treated dentin matrix; ZrO_2, zirconia.

were no longer easily distinguishable from the surrounding tissue. An increase in TDM content within the scaffold correlated with a more pronounced repair of the defect site (Figure 6A). A semi-transparent, cartilage-like layer covered the center of the trochlear region, with faint reddish hard tissue visible beneath (Figure 6B). However, a distinct concavity persisted in the blank control group.

Micro-CT analysis quantified the BMD (g/cm^3), BV/TV (%), and Tb.N (mm^{-1}) in samples collected at weeks 6 and 12, with the corresponding statistical results shown in Figure 6. The blank control group at week 6 exhibited the lowest BMD and Tb.N values, with statistically significant differences compared with other groups (Figure 6C). However, the difference between the blank control and 0% TDM groups was not statistically significant. This may be attributed to the fact that SOX9⁺ scl-progenitors primarily contribute to cartilage repair, whereas bone repair predominantly relies on TDM within the scaffold material. As the TDM content increased, BMD showed a gradual increase, with the TDM scaffold-implanted group exhibiting an average of approximately 70% in both BMD and Tb.N. On average, bone tissue repair was significantly improved, and BV/TV was significantly increased (Figure 6D). Although the average Tb.N in the 30% TDM group was higher than that in the 0% TDM group, the difference was not statistically significant (Figure 6E), suggesting that TDM concentration plays a crucial role in bone mass recovery.

Macroscopic cartilage repair in each group was further evaluated using the cartilage injury grading system proposed by the International Cartilage Repair Society.[37] The scoring results are shown in Figure 6F. At week 6,

although the 0% TDM group had a higher average score than the control group, the difference was not statistically significant. However, by week 12, a statistically significant difference was observed between the two groups (Figure 6F). TDM groups exhibited significantly higher scores than the control group. Notably, the 70% TDM group achieved average scores of 10.9 and 13.67 at weeks 6 and 12, respectively, while the 50% TDM group reached a score of 11.1 at week 12, corresponding to Grade II (nearly normal) in the cartilage injury grading system.

These findings indicate that the TDM/ZrO_2 hydrogel scaffold loaded with SOX9$^+$ scl-progenitors possesses strong therapeutic potential for osteochondral defect repair. The synergistic interaction between TDM and SOX9$^+$ scl-progenitors significantly enhanced the repair process, leading to superior tissue regeneration compared with scaffolds lacking TDM-loaded cells.

3.7. Histological assessment of scaffold-mediated osteochondral repair

Safranin-fast green staining results indicated that no significant subchondral bone repair was observed in either the control or 0% TDM group at week 6. The control group exhibited extensive fibrous proliferation, whereas the 0% TDM group displayed a notable depression at the defect site (Figure 6G). As the quality of the scaffold material improved, degradation resulted in gaps within the tissue; however, the 30, 50, and 70% TDM groups demonstrated substantial cartilage repair, active subchondral bone trabecular proliferation, and smooth joint surfaces.

After 12 weeks, the control group still exhibited pronounced surface defects, while the 0% TDM group retained a greater amount of cartilage-like tissue. The 30% TDM group exhibited less cartilage tissue than the 0% TDM group but greater subchondral bone repair, whereas the 50% TDM group exhibited more cartilage tissue than the 0% TDM group. The 50% TDM and 70% TDM groups, containing higher levels of TDM, induced hypertrophy and maturation of SOX9$^+$ precursor cells, leaving only a layer of collagen fibers on the surface of the newly formed bone (Figure 6H). COL2A1 expression was most pronounced in the 0 and 30% TDM groups (Figure S7). In contrast, COLII expression in the 50% TDM and 70% TDM groups was relatively lower, although still higher than that in the control group. This may be attributed to the increased TDM content, particularly its hydroxyapatite component, which accelerates cartilage hypertrophy and calcification, thereby promoting enhanced osteogenic differentiation. Implantation of the cell-loaded scaffold did not cause any significant systemic effects in the nude rats (Figure S5).

4. Discussion

Articular cartilage is composed of a three-layer gradient structure, comprising hyaline cartilage, calcified cartilage, and subchondral bone.[38,39] Collagen fibers run perpendicular to the joint surface, traverse the calcified layer, and anchor into the subchondral bone.[40,41] This osteochondral interface, consisting of the tidemark, calcified cartilage, and subchondral bone plate, functions as a structurally and biologically complex composite that is essential for load transmission and joint integrity.[42,43]

Osteochondral injuries can be classified as partial-thickness cartilage lesions, full-thickness defects, and injuries involving the subchondral bone.[44] A hallmark of osteochondral defects is the damage to the subchondral bone plate.[9] Associated pathological features, such as sclerosis, osteophyte formation, and bone remodeling, are common in conditions such as osteoarthritis and can significantly affect treatment outcomes.[10] Existing clinical strategies, including arthroscopic debridement, microfracture, and abrasion arthroplasty, often lead to the formation of fibrous cartilage, which lacks the mechanical and biochemical properties of native hyaline cartilage.[7] Autologous chondrocyte implantation, considered the current gold standard, is hindered by limited cell availability, donor site morbidity, and the need for additional surgery.[45] Therefore, there is a pressing need for regenerative strategies that can promote both chondrogenesis and osteogenesis within a single construct.

In this context, the selection of appropriate seed cells is vital for successful osteochondral regeneration. Among common candidates, MSCs are widely used but often exhibit undesired ossification and vascularization *in vivo*.[46] Embryonic stem cells possess strong regenerative capacity but face ethical and safety concerns. In contrast, iPSCs combine embryonic stem cell-like pluripotency with improved accessibility and immunocompatibility.[47,48]

In this study, we employed genetic reprogramming to induce high levels of SOX9 expression, a master transcription factor for chondrogenesis, in iPSCs. The resulting SOX9$^+$ scl-progenitors exhibited downregulated expression of pluripotency markers (*OCT4* and *NANOG*) and upregulated expression of differentiation markers (*SOX9* and *TWIST1*), indicating a stable commitment to the chondrogenic or osteogenic lineage. These cells were sorted via tdTomato fluorescence labeling and flow cytometry to obtain a high-purity population (>99.6%). Notably, SOX9 serves as a central integrator of chondrogenic signaling pathways and regulates key processes in cartilage formation and maintenance.[49,50]

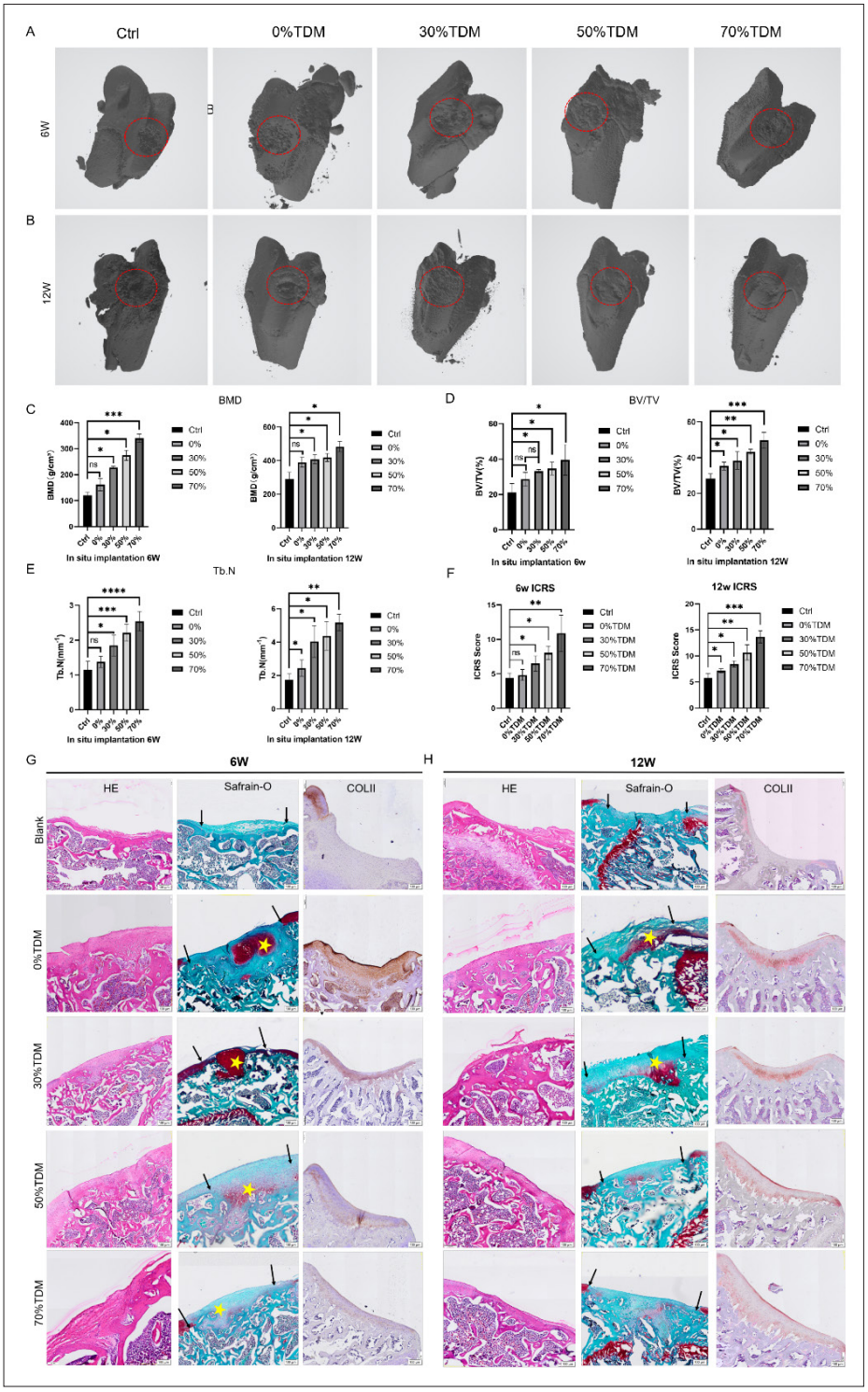

Figure 6. In vivo evaluation of osteochondral defect repair using 3D-printed scaffolds with varying TDM concentrations. (A, B) Micro-computed tomography reconstructed images at (A) week 6 and (B) week 12. (C) BMD at the defect site. (D) BV/TV. (E) Tb.N (n=3). (F) Cartilage damage assessed using the ICRS score. (G, H) H&E staining, Safranin O staining, and COLII immunohistochemistry of knee joint implantation at (G) week 6 and (H) week 12. Groups included blank, 0, 30, 50, and 70% TDM scaffold implantation. Arrows indicate scaffold placement, and stars indicate red-stained cartilage tissue (scale bar: 200 μM; magnification: 10×). *, **, and *** indicate statistically significant differences at $p < 0.05$, $p < 0.01$, and $p < 0.001$, respectively. "ns" denotes no statistical significance. Abbreviations: BMD, bone mineral density; BV/TV, bone volume fraction; COLII, type II collagen; Ctrl, control; H&E, hematoxylin and eosin; ICRS: International Cartilage Research Society; Tb.N, trabecular bone number; TDM, treated dentin matrix.

The need for personalized, mechanically robust, and biologically active scaffolds to match these cell sources has driven the development of 3D-printed biomaterial systems. Tissue engineering approaches offer promising potential, enabling the fabrication of customized, biomimetic scaffolds with precise architectures tailored to individual anatomical and functional needs.[51,52] Within this framework, TDM has emerged as a promising scaffold component. As a natural decellularized extracellular matrix, TDM retains bioactive molecules such as low-crystallinity hydroxyapatite, collagen type I, TGF-β, and BMP-2. These components have been shown to enhance the proliferation and osteogenic or odontogenic differentiation of various types of stem cells. Our previous studies demonstrated that TDM/polycaprolactone scaffolds exhibit superior mechanical properties compared with HA/polycaprolactone scaffolds, with an elastic modulus similar to that of demineralized dentin. Moreover, TDM scaffolds maintained their structural integrity over six months *in vivo*, with only a minor reduction in mechanical strength, whereas the HA group showed a marked decline.[19]

Importantly, TDM exhibits concentration-dependent biological effects: low concentrations favor cell proliferation, whereas higher concentrations promote osteogenic differentiation.[13] This dual functionality allows for the precise tuning of scaffold bioactivity according to regenerative needs. The incorporation of TDM into GelMA hydrogels significantly improves the mechanical strength of the scaffold, while the addition of nano-ZrO_2 helps to fill internal pores, thereby enhancing durability, drug resistance, and structural stability under cyclic mechanical stress.[53] Microscopic characterization confirmed the high porosity of the scaffold, which supports cell adhesion and infiltration, and *in vitro* biocompatibility assays demonstrated that the scaffold did not impair cell proliferation. Additionally, *in vivo* toxicity assessments showed no evidence of organ damage or systemic toxicity, confirming the biosafety of ZrO_2 at the applied dose and implantation method.[54]

Previous studies have emphasized that the compressive modulus of native articular cartilage varies substantially depending on the anatomical site, tissue depth, and testing methodology. Eschweiler *et al.*[55] reported aggregate moduli ranging from 0.5 to 0.9 MPa in healthy human cartilage, while more recent studies have extended this range up to 3.0 MPa, highlighting inter-study variability.[56] As a composite tissue, the osteochondral unit exhibits higher stiffness, with compressive moduli of approximately 5–54 MPa depending on site-specific and methodological differences.[57] These gradients reflect the hierarchical structure of the cartilage—from the softer superficial zone to the stiffer deep zone and subchondral bone—which collectively provide both shock absorption and load-bearing capacity. Within this context, the compressive moduli achieved by our scaffolds (0.32–0.89 MPa) are consistent with the native cartilage range, while the compressive strengths (7.4–48.2 MPa) overlap with those of the osteochondral unit. This dual-level correspondence suggests that the TDM/ZrO_2 scaffolds not only mimic the mechanical behavior of cartilage but also approximate the structural robustness of osteochondral composites, thereby offering the mechanical resilience necessary for load-bearing joint environments.

In this study, spheroids of SOX9$^+$ scl-progenitors were encapsulated within TDM/ZrO_2 hydrogel bioinks and implanted subcutaneously in immunodeficient mice. This *in vivo* model facilitated the evaluation of the biological behavior and regenerative potential of the combined cell–scaffold system. Transcriptome sequencing validated our hypothesis: the TDM/ZrO_2 scaffold significantly enhanced the osteochondral repair capacity of SOX9$^+$ scl-progenitors. Among the 303 differentially expressed genes, a marked downregulation of *MMP* family members was observed, particularly *MMP7*, a key enzyme involved in the degradation of COLII and the pathogenesis of osteoarthritis.[58] Conversely, *CDC6*—a gene involved in DNA replication and cell cycle progression—was significantly upregulated, indicating active cell proliferation.[59,60] The expression of *VEGFA* was also elevated, suggesting enhanced angiogenic potential, which is critical for effective bone tissue regeneration.[61,62]

After co-culturing SOX9$^+$ scl-progenitors with TDM/ZrO_2 hydrogel scaffolds for seven days, the mRNA expression levels of *OCN* and *RUNX2* were significantly higher than those of the control group, whereas the mRNA expression levels of *BMP2* and *COL1A1* demonstrated no significant difference. *BMP2* has been reported to promote SOX9-driven chondrogenesis and cartilage tissue formation, although it can also induce ossification under certain conditions.[63,64] Several studies have reported that *RUNX2* is closely associated with chondrocyte hypertrophy and osteogenic differentiation, and its upregulation may reflect a shift toward hypertrophy and endochondral ossification rather than stable cartilage formation.[65,66]

Notably, we observed an inconsistency between *SOX9* mRNA upregulation and the lack of significant changes in SOX9 protein expression, consistent with previous studies in stem cell differentiation contexts, where transcriptional activation of *SOX9* does not immediately translate into detectable protein accumulation.[67] Possible explanations include post-transcriptional regulation by microRNAs,

translational delays, or rapid protein turnover.[68] In addition, the culture duration in our study may not have been sufficient for protein levels to reach a detectable threshold. While our findings highlight the importance of *SOX9* in regulating chondrogenic differentiation, we acknowledge that the mRNA–protein discrepancy warrants further investigation. Future studies should focus on time-course analyses and mechanistic validation to better elucidate the regulatory dynamics of *SOX9* expression.

Our RNA sequencing results revealed significant enrichment of the hypoxia-inducible factor 1 signaling pathway, which is consistent with its known role in regulating chondrocyte survival and matrix metabolism under hypoxic conditions.[69] While this finding is intriguing, it remains to be clarified whether the observed activation is specifically elicited by the bioactive components of TDM or reflects the hypoxic microenvironment characteristic of dense 3D cell-laden scaffolds.

These transcriptomic findings were further supported by the *in vivo* implantation analysis. The cell-laden scaffolds showed no signs of systemic toxicity; histological analysis revealed no morphological abnormalities in the spleen, liver, or kidney; and blood biochemical parameters remained within normal ranges. Moreover, histological staining demonstrated hyaline cartilage regeneration in groups with lower TDM content (0 and 30%), whereas higher TDM levels (50 and 70%) favored osteogenic differentiation, likely due to the hydroxyapatite-rich composition of TDM. Safranin O/fast green staining confirmed the presence of cartilage, bone, and fibrous tissue within the repair site, reflecting distinct stages of endochondral ossification.

In a fully developed joint, the zonal architecture comprises fibrous, proliferative, mature, and hypertrophic layers, which are critical for mechanical and biological functions. During endochondral ossification, *SOX9* expression sharply declines in the hypertrophic zone, marking the transition toward bone formation. Thus, the precise modulation of TDM content may offer a strategy to recreate this native zonal structure and direct tissue-specific differentiation. The presence of COLII in the regenerated cartilage indicates the production of hyaline cartilage, reflecting the functional integrity of the cartilage tissue.[10] Safranin O/fast green staining effectively distinguished cartilage, bone, and fibrous tissue. In the control group, the defect was predominantly filled with dense fibrous tissue. Conversely, the 0 and 30% TDM groups exhibited repair of cartilage-like tissues. In the 50 and 70% TDM groups, where the primary component of TDM is hydroxyapatite, cell differentiation and maturation were enhanced.[70] Consequently, the defect was primarily repaired by bone and fibrous tissues, which accounts for the discrepancies observed in the staining results among the samples and sections. Our findings suggest that by adjusting the scaffold composition and integrating iPSC-derived SOX9$^+$ scl-progenitors, it is possible to guide the regeneration of functional osteochondral tissue.

Previous studies have established that iPSC-derived SOX9$^+$ scl-progenitors are not restricted to a single lineage fate, but instead display bipotent differentiation potential that mirrors the endochondral ossification process.[12] These cells can first generate cartilaginous templates and subsequently contribute to bone formation, mimicking the developmental programs of skeletal tissue morphogenesis. In the context of our osteochondral scaffold system, such lineage flexibility provides a developmental rationale for their capacity to support both chondral and subchondral bone regeneration within the defect site.

A limitation of the present study is the absence of a gradient-based or zone-specific scaffold design that more closely mimics the native cartilage-to-bone transition. Gradient or multiphasic scaffolds have been widely recognized as advantageous for osteochondral repair, as they enable smooth compositional and mechanical transitions that promote interface integration and zonal tissue formation.[71] Recent studies have demonstrated that gradient or multiphasic scaffolds fabricated via 3D printing can better replicate the osteochondral interface, thereby enhancing integration and zonal tissue formation.[72,73] In contrast to these gradient strategies, our current design served as a simplified proof-of-concept model to validate the feasibility of the TDM/ZrO_2 bioink with SOX9$^+$ progenitors. Future studies should focus on implementing layer-by-layer or continuous gradient printing (e.g., varying TDM/ZrO_2 ratios, graded crosslinking, and zonal growth factor delivery) to recreate the osteochondral gradient and evaluate both interface mechanics and long-term functional outcomes.

Advances in biomaterial design and nanotechnology will continue to improve scaffold efficacy and drive innovations in iPSC-based osteochondral tissue engineering. Additionally, a deeper understanding of the signaling mechanisms that regulate the differentiation of iPSC-derived SOX9$^+$ scl-progenitors remains a key objective in translating these findings into clinical application.

5. Conclusion

This study presents a customizable 3D-bioprinted scaffold system that leverages the developmental potential of iPSC-derived SOX9$^+$ scl-progenitors and the biological

and mechanical advantages of TDM/ZrO_2 composites. The scaffolds exhibited excellent mechanical properties, biocompatibility, and bioactivity, while the $SOX9^+$ scl-progenitors demonstrated stable chondrogenic potential and favorable *in vivo* outcomes. Future work should focus on fine-tuning TDM concentrations to engineer layered osteochondral structures, as well as elucidating the molecular signaling mechanisms governing SOX9-mediated lineage commitment. These advancements will help facilitate the translation of this approach toward clinically applicable regenerative therapies for joint cartilage and subchondral bone defects.

Acknowledgments

We appreciate the technical assistance provided by the laboratory staff for the experimental procedures

Funding

This work was supported by grants from the National Nature Science Foundation of China (82270958), the Major Science and Technology Projects in Yunnan Province(202302AA310038), and West China Hospital of Stomatology, Sichuan University Interdisciplinary innovation projects with research and development projects (RD-03-202106).

Conflict of interest

The authors declare that they have no affiliations with or involvement in any organization or entity with any financial interest in the subject matter or materials discussed in this manuscript.

Author contributions

Conceptualization: Weihua Guo, Yuqing Dong
Data curation: Jingfei Xiong, Fengxiao Zhao
Formal analysis: Yuqing Dong, Weihua Guo
Investigation: Jingfei Xiong, Fengxiao Zhao
Project administration: Weihua Guo, Zhonghan Li
Resources: Zhijun Zhang
Writing–original draft: All authors
Writing–review & editing: Yuqing Dong, Yuming Zhao
All authors have read and approved the final manuscript.

Ethics approval and consent to participate

All experimental procedures were approved by the Institutional Animal Care and Use Committee of West China Hospital (ethics approval number: WCHSIRB-D-2023-309) and complied with the National Institutes of Health guidelines for the care and use of laboratory animals.

Consent for publication

Not applicable.

Availability of data

All data associated with this study are presented in the paper.

References

1. Everhart JS, Abouljoud MM, Flanigan DC. Role of full-thickness cartilage defects in knee osteoarthritis (OA) incidence and progression: data from the OA initiative. *J Orthop Res*. 2019;37(1):77-83.
doi: 10.1002/jor.24140

2. Lee WY-w, Bin W. Cartilage repair by mesenchymal stem cells: clinical trial update and perspectives. *J Orthop Transl*. 2017;9:76-88.
doi: 10.1016/j.jot.2017.03.005

3. Shi W, Sun M, Hu X, *et al*. Structurally and functionally optimized silk-fibroin gelatin scaffold using 3D printing. *Adv Mater*. 2017;29(29).
doi: 10.1002/adma.201701089

4. Levingstone TJ, Moran C, Almeida HV, Kelly DJ, O'Brien FJ. Layer-specific stem cell differentiation in trilayered tissue engineering biomaterials: towards development of a single-stage cell-based approach for osteochondral defect repair. *Mater Today Bio*. 2021;12.
doi: 10.1016/j.mtbio.2021.100173

5. Minnig MCC, Golightly YM, Nelson AE. Epidemiology of osteoarthritis_ literature update 2022–2023. *Curr Opin Rheumatol*. 2024;36(2):108-112.
doi: 10.1097/BOR.0000000000000985

6. Tang H, Zhu W, Cao L, *et al*. miR-210-3p protects against osteoarthritis through inhibiting subchondral angiogenesis by targeting the expression of TGFBR1 and ID4. *Front Immunol*. 2022;13.
doi: 10.3389/fimmu.2022.982278

7. Jiang L, Zhou X, Xu K, *et al*. miR-7_EGFR_MEGF9 axis regulates cartilage degradation in osteoarthritis via PI3K_AKT_mTOR signaling pathway. *Bioengineered*. 2021;12(1):8622-8634.
doi: 10.1080/21655979.2021.1988362

8. Costa E, Gonzalez-Garcia C, Gomez Ribelles JL, Salmeron-Sanchez M. Maintenance of chondrocyte phenotype during expansion on PLLA microtopographies. *J Tissue Eng*. 2018;9:2041731418789829.
doi: 10.1177/2041731418789829

9. Kovács B, Vajda E, Nagy EE. Regulatory effects and interactions of the Wnt and OPG-RANKL-RANK signaling at the bone-cartilage interface in osteoarthritis. *Int J Mol Sci*. 2019;20(18).
doi: 10.3390/ijms20184653

10. Hsieh Y-H, Shen B-Y, Wang Y-H, Lin B, Lee H-M, Hsieh M-F. Healing of osteochondral defects implanted with biomimetic scaffolds of poly(ε-caprolactone)_hydroxyapatite and glycidyl-methacrylate-modified hyaluronic acid in a Minipig. *Int J Mol Sci*. 2018;19(4);1125. doi: 10.3390/ijms19041125

11. Liao Y, Kang F, Xiong J, *et al*. MSX1(+)PDGFRA(low) limb mesenchyme-like cells as an efficient stem cell source for human cartilage regeneration. *Stem Cell Reports*. 2024;19(3):399-413. doi: 10.1016/j.stemcr.2024.02.001

12. Xiong J, Ma R, Xie K, *et al*. Recapitulation of endochondral ossification by hPSC-derived SOX9+ sclerotomal progenitors. *Nat Commun*. 2025;16(1):2781. doi: 10.1038/s41467-025-58122-9

13. Chen G Chen J, Yang B, *et al*. Combination of aligned PLGA gelatin electrospun sheets, native dental pulp extracellular matrix and treated dentin matrix as substrates for tooth root regeneration. *Biomaterials*. 2015;52:56-70. doi: 10.1016/j.biomaterials.2015.02.011

14. Grawish ME, Grawish LM, Grawish HM, *et al*. Demineralized dentin matrix for dental and alveolar bone tissues regeneration: an innovative scope review. *Tissue Eng Regen Med*. 2022;19(4):687-701. doi: 10.1007/s13770-022-00438-4

15. Li M, Yang S, Song J, *et al*. Different grinding speeds affect induced regeneration capacity of human treated dentin. *J Biomed Mater Res*. 2021;110(4):755-767. doi: 10.1002/jbm.b.34954

16. Wen B, Dai Y, Han X, *et al*. Biomineralization-inspired mineralized hydrogel promotes the__repair and regeneration of dentin_bone hard tissue. *NPJ Regen Med*. 2023;8(1):253-262. doi: 10.1038/s41536-023-00286-3

17. Wen B, Huang Y, Qiu T, *et al*. Reparative dentin formation by dentin matrix proteins and small extracellular vesicles. *J Endod*. 2021;47(2):253-262. doi: 10.1016/j.joen.2020.11.017

18. Chen J, Cui C, Qiao X, *et al*. Treated dentin matrix paste as a novel pulp capping agent for dentin regeneration. *J Tissue Eng Regen Med*. 2017;11(12):3428-3436. doi: 10.1002/term.2256

19. Huang Y, Zhang Z, Bi F, *et al*. Personalized 3D-printed scaffolds with multiple bioactivities for bioroot. *Adv Healthc Mater*. 2023;12(28):2300625. doi: 10.1002/adhm.202300625

20. Rehman SRU, Augustine R, Zahid AA, Ahmen R, Tariq M, Hasan A. Reduced graphene oxide incorporated GelMA hydrogel promotes angiogenesis for wound healing applications. *Int J Nanomedicine*. 2019;14:9603-9617. doi: 10.2147/IJN.S218120

21. Sennerby L, Dasmah A, Larsson B, Iverhed M. Bone tissue responses to surface-modified zirconia implants: a histomorphometric and removal torque study in the rabbit. *Clin Implant Dent Relat Res*. 2005;7(Suppl 1):S13-S20. doi: 10.1111/j.1708-8208.2005.tb00070.x

22. Zhang J, Huang D, Liu S, *et al*. Zirconia toughened hydroxyapatite biocomposite formed by a DLP 3D printing process for potential bone tissue engineering. *Mater Sci Eng*. 2019;105:110054. doi: 10.1016/j.msec.2019.110054

23. Li R, Guo W, Yang B, *et al*. Human treated dentin matrix as a natural scaffold for complete human dentin tissue regeneration. *Biomaterials*. 2011;32(20):4525-4538. doi: 10.1016/j.biomaterials.2011.03.008

24. Lan T, Bi F, Xu Y, *et al*. PPAR-γ activation promotes xenogenic bioroot regenerationby attenuating the xenograft induced-oxidative stress. *Int J Oral Sci*. 2023;15(1):10. doi: 10.1038/s41368-023-00217-4

25. Chu CR, Szczodry M, Bruno S. Animal models for cartilage regeneration and repair. *Tissue Eng Part B Rev*. 2010;16(1):105-115. doi: 10.1089/ten.TEB.2009.0452

26. Tang H, Bi F, Chen G, *et al*. 3D-bioprinted recombination structure of Hertwig's epithelial root sheath cells and dental papilla cells for alveolar bone regeneration. *Int J Bioprint*. 2022;8(3):512. doi: 10.18063/ijb.v8i3.512

27. Ebrahimi M, Ojanen S, Mohammadi A, *et al*. Elastic, viscoelastic and fibril-reinforced poroelastic material properties of healthy and osteoarthritic human tibial cartilage. *Ann Biomed Eng*. 2019;47(4):953-966. doi: 10.1007/s10439-019-02213-4

28. Li J, Wang P, Xie Z, *et al*. TRAF4 positively regulates the osteogenic differentiation of mesenchymal stem cells by acting as an E3 ubiquitin ligase to degrade Smurf2. *Cell Death Differ*. 2019;26(12):2652-2666. doi: 10.1038/s41418-019-0328-3

29. Kim H, Park S, Kim K, Ku S, Seo J, Roh S. *Enterococcus faecium* L-15 cell-free extract improves the chondrogenic differentiation of human dental pulp stem cells. *Int J Mol Sci*. 2019;20(3):624. doi: 10.3390/ijms20030624

30. Wang T, Chen Y, Zhu X, *et al*. IFT80 and TRPA1 cooperatively regulate bone formation by calcium signaling in response to mechanical stimuli. *Metabolism*. 2025;166:156159. doi: 10.1016/j.metabol.2025.156159

31. Menendez M T TC, Wade K, *et al*. siRNA screening identifies the host hexokinase 2 (HK2) gene as an__important hypoxia-inducible transcription factor 1 (HIF-1) target gene in toxoplasma gondii-infected cells. *mBio*. 2015;6(3):e00462. doi: 10.1128/mBio.00462-15

32. Wang Z-Y, Yiu L, Li S-P, *et al*. Hypoxia inducible factor 1α promotes interleukin-1 receptor antagonist expression during hepatic ischemia-reperfusion injury. *World J Gastroenterol*. 2022;28(38):5573-5588.
doi: 10.3748/wjg.v28.i38.5573

33. Zayed M, Newby S, Misk N, Donnell R, Dhar M. Xenogenic implantation of equine synovial fluid-derived mesenchymal stem cells leads to articular cartilage regeneration. *Stem Cells Int*. 2018;2018:1073705.
doi: 10.1155/2018/1073705

34. Zheng ZY, Jiang T, Huang ZF, *et al*. Fatty acids derived from apoptotic chondrocytes fuel macrophages FAO through MSR1 for facilitating BMSCs osteogenic differentiation. *Redox Biol*. 2022;53:102326.
doi: 10.1016/j.redox.2022.102326

35. Liu ES, Raimann A, Chae BT, Martins JS, Baccarini M, Demay MB. c-Raf promotes angiogenesis during normal growth plate maturation. *Development*. 2016;143(2): 348-355.
doi: 10.1242/dev.127142

36. Zhou X, von der Mark K, Henry S, Norton W, Adams H, de Crombrugghe B. Chondrocytes transdifferentiate into osteoblasts in endochondral bone during development, postnatal growth and fracture healing in mice. *PLoS Genet*. 2014;10(12):e1004820.
doi: 10.1371/journal.pgen.1004820

37. van den Borne MPJ, Raijmakers NJH, Vanlauwe J, *et al*. International Cartilage Repair Society (ICRS) and Oswestry macroscopic cartilage evaluation scores validated for use in Autologous Chondrocyte Implantation (ACI) and microfracture1. *Osteoarthritis Cartilage*. 2007;15(12):1397-1402.
doi: 10.1016/j.joca.2007.05.005

38. Alberton P, Dugonitsch HC, Hartmann B, *et al*. Aggrecan hypomorphism compromisesarticular cartilage biomechanical propertiesand is associated with increased incidenceof spontaneous osteoarthritis. *Int J Mol Sci*. 2019;20(5):1008.
doi: 10.3390/ijms20051008

39. Chen S, Fu P, Wu H, Pei M. Meniscus, articular cartilage, and nucleus pulposus a comparative review of cartilage-like tissues in anatomy, development, and function. *Cell Tissue Res*. 2017;370(1):53-70.
doi: 10.1007/s00441-017-2613-0

40. Gannon AR, Nagel T, Bell AP, Avery NC, Kelly DJ. Postnatal changes to the mechanical properties of articular cartilage are driven by the evolution of its collagen network. *Eur Cells Mater*. 2015;29:105-123.
doi: 10.22203/eCM.v029a09

41. Richardson SM, Kalamegam G, Pushparaj PN, *et al*. Mesenchymal stem cells in regenerative medicine: focus on articular cartilage and intervertebral disc regeneration. *Methods*. 2016;99:69-81.
doi: 10.1016/j.ymeth.2015.09.015

42. Deng C, Zhu H, Li J, *et al*. Bioactive scaffolds for regeneration of cartilage and subchondral bone interface. *Theranostics*. 2018;8(7):1940-1955.
doi: 10.7150/thno.23674

43. Chen L, Yao F, Wang T, *et al*. Horizontal fissuring at the osteochondral interface: a novel and unique pathological feature in patients with obesity-related osteoarthritis. *Ann Rheum Dis*. 2020;79(6):811-818.
doi: 10.1136/annrheumdis-2020-216942

44. Slattery C, Kweon CY. Classifications in brief: outerbridge classification of chondral lesions. *Clin Orthop Relat Res*. 2018;476(10):2101-2104.
doi: 10.1007/s11999.0000000000000255

45. Pereira RC, Martinelli D, Cancedda R, Gentili C, Poggi A. Human articular chondrocytes regulate immune response by affecting directly T cell proliferation and indirectly inhibiting monocyte differentiation to professional antigen-presenting cells. *Front Immunol*. 2016;7:415.
doi: 10.3389/fimmu.2016.00415

46. Freeman FE, Kelly DJ. Tuning alginate bioink stifness and composition for controlled growth factor delivery and to spatially direct MSC fate within bioprinted tissues. *Sci Rep*. 2017;7(1):17042.
doi: 10.1038/s41598-017-17286-1

47. Aboul-Soud MAM, Alzahrani AJ, Mahmoud A. Induced pluripotent stem cells (iPSCs)—roles in regenerative therapies, disease modelling and drug screening. *Cells*. 2021;10(9):2319.
doi: 10.3390/cells10092319

48. Yamashita A, Morioka M, Yahara Y, *et al*. Generation of scaffoldless hyaline car tilaginous tissue from human iPSCs. *Stem Cell Reports*. 2015;4(3)404-418.
doi: 10.1016/j.stemcr.2015.01.016

49. Song H, Park K-H. Regulation and function of SOX9 during cartilage development and regeneration. *Semin Cancer Biol*. 2020;67(Pt 1):12-23.
doi: 10.1016/j.semcancer.2020.04.008

50. Jang Y, Jung H, Nam Y, *et al*. Centrifugal gravity-induced BMP4 induces chondrogenic differentiation of adiposederived stem cells via SOX9 upregulation. *Stem Cell Res Ther*. 2016;7(1):184.
doi: 10.1186/s13287-016-0445-6

51. Yan B Zhang Z, Wang X, *et al*. PLGA-PTMC-cultured bone mesenchymal stem cell scaffold enhances cartilage regeneration in tissue-engineered tracheal transplantation. *Artif Organs*. 2016;41(5):461-469.
doi: 10.1111/aor.12805

52. Wanjare M, Hou L, Nakayama KH, *et al*. Anisotropic microfibrous scaffolds enhance the organization and function of cardiomyocytes derived from induced pluripotent stem cells. *Biomater Sci*. 2017;5(8):1567-1578. doi: 10.1039/c7bm00323d

53. Schunck A, Kronz A, Fischer C, Buchhorn GH. Release of zirconia nanoparticles at the metal stem–bone cement interface in implant loosening of total hip replacements. *Acta Biomater*. 2016;31:412-424. doi: 10.1016/j.actbio.2015.11.044

54. Yang Y, Bao H, Chai Q, *et al*. Toxicity, biodistribution and oxidative damage caused by zirconia nanoparticles after intravenous injection. *Int J Nanomedicine*. 2019;14:5175-5186. doi: 10.2147/IJN.S197565

55. Eschweiler J, Horn N, Rath B, *et al*. The biomechanics of cartilage–an overview. *Life (Basel)*. 2021;11(4):302. doi: 10.3390/life11040302

56. Zhang M, Lu Q, Miller AH, Barnthouse NC, Wang J. Dynamic epigenetic mechanisms regulate age-dependent SOX9 expression in mouse articular cartilage. *Int J Biochem Cell Biol*. 2016;72:125-134. doi: 10.1016/j.biocel.2016.01.013

57. Korhonen RK, Laasanen MS, Töyräs J, *et al*. Comparison of the equilibrium response of articular cartilage in unconfined compression, confined compression and indentation. *J Biomech*. 2002;35(7):903-909. doi: 10.1016/s0021-9290(02)00052-0

58. Lehtola T, Nummenmaa E, Tuure L, *et al*. Dexamethasone attenuates the expression of MMP-13 in chondrocytes through MKP-1. *Int J Mol Sci*. 2022;23(7):3880. doi: 10.3390/ijms23073880

59. Chen C, Zhao W, Lu X, *et al*. AUP1 regulates lipid metabolism and induces lipidaccumulation to accelerate the progression of renal clearcell carcinoma. *Cancer Sci*. 2022;113(8):2600-2615. doi: 10.1111/cas.15445

60. Barkley LR, Hong HK, Kingsbury SR, James M, Stoeber K, Williams GH. Cdc6 is a rate-limiting factor for proliferative capacity during HL60 cell differentiation. *Exp Cell Res*. 2007;313(17):3789-3799. doi: 10.1016/j.yexcr.2007.07.004

61. Tu J, Wan C, Zhang F, *et al*. Genetic correction of Werner syndrome gene reveals impaired pro-angiogenic function and HGF insufficiency in mesenchymal stem cells. *Aging Cell*. 2020;19(5):e.13116. doi: 10.1111/acel.13116

62. Li Z, Yan G, Diao Q, *et al*. Transplantation of human endometrial perivascular cells with elevated CYR61 expression induces angiogenesis and promotes repair of a full-thickness uterine injury in rat. *Stem Cell Res Ther*. 2019;10(1):179. doi: 10.1186/s13287-019-1272-3

63. Gouttenoire J, Bougault C, Aubert-Foucher E, *et al*. BMP-2 and TGF-beta1 differentially control expression of type II procollagen and alpha 10 and alpha 11 integrins in mouse chondrocytes. *Eur J Cell Biol*. 2010;89(4):307-314. doi: 10.1016/j.ejcb.2009.10.018

64. Zhou N, Li Q, Lin X, *et al*. BMP2 induces chondrogenic differentiation, osteogenic differentiation and endochondral ossification in stem cells. *Cell Tissue Res*. 2016;366(1):101-111. doi: 10.1007/s00441-016-2403-0

65. Caron MJ, Welting TJ, Surtel DA, *et al*. BMP-2 and BMP-7: differential regulation of chondrogenic differentiation. *Osteoarthritis Cartilage*. 2012;20(1):S151. doi: 10.1016/j.joca.2012.02.220

66. Legendre F, Ollitrault D, Gomez-Leduc T, *et al*. Enhanced chondrogenesis of bone marrow-derived stem cells by using a combinatory cell therapy strategy with BMP-2/TGF-β1, hypoxia, and COL1A1/HtrA1 siRNAs. *Sci Rep*. 2017;7(1):3406. doi: 10.1038/s41598-017-03579-y

67. Chavez RD, Coricor G, Perez J, Seo HS, Serra R. SOX9 protein is stabilized by TGF-beta and regulates PAPSS2 mRNA expression in chondrocytes. *Osteoarthritis Cartilage*. 2017;25(2):332-340. doi: 10.1016/j.joca.2016.10.007

68. Tew SR, Clegg PD. Analysis of post transcriptional regulation of SOX9 mRNA during in vitro chondrogenesis. *Tissue Eng Part A*. 2011;17(13-14):1801-1807. doi: 10.1089/ten.TEA.2010.0579

69. Stegen S, Laperre K, Eelen G, *et al*. HIF-1alpha metabolically controls collagen synthesis and modification in chondrocytes. *Nature*. 2019;565(7740):511-515. doi: 10.1038/s41586-019-0874-3

70. Guo W, Gong K, Shi H, *et al*. Dental follicle cells and treated dentin matrix scaffold for tissue engineering the tooth root. *Biomaterials*. 2012;33(5):1291-1302. doi: 10.1016/j.biomaterials.2011.09.068

71. Idaszek J, Costantini M, Karlsen TA, *et al*. 3D bioprinting of hydrogel constructs with cell and material gradients for the regeneration of full-thickness chondral defect using a microfluidic printing head. *Biofabrication*. 2019;11(4):044101. doi: 10.1088/1758-5090/ab2622

72. Zhang B, Huang J, Narayan RJ. Gradient scaffolds for osteochondral tissue engineering and regeneration. *J Mater Chem B*. 2020;8(36):8149-8170. doi: 10.1039/d0tb00688b

73. Corrado F, Di Maio L, Palmero P, *et al*. Vat photo-polymerization 3D printing of gradient scaffolds for osteochondral tissue regeneration. *Acta Biomater*. 2025;200:67-86. doi: 10.1016/j.actbio.2025.05.042

Our Journals

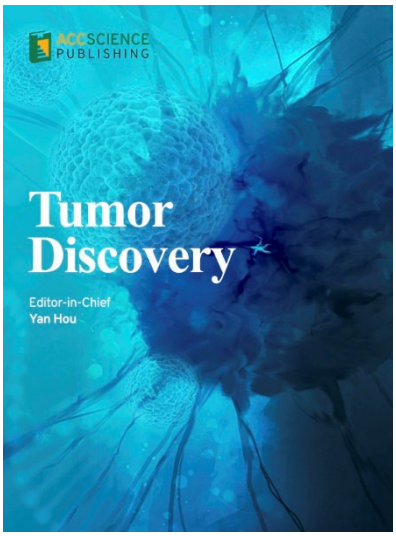

Tumor Discovery is a peer-reviewed and open-access journal that aims to present new cancer research with strong emphasis on fundamental and translational studies. *Tumor Discovery* covers topics, including but not limited to the following:

- Etiology and pathogenesis of cancer
- Mechanisms and molecular pathways underlying cancer initiation and progression
- Tumor metastasis
- Tumor evolution and heterogeneity
- Tumor microenvironment and tumor-host interactions
- Cancer genetics and genomics
- Cancer characterization using omics approaches
- Discovery and validation of cancer biomarker
- Discovery of new therapeutic targets
- New approaches of diagnostic and treatment modalities
- Statistical methods in cancer research

Global Translational Medicine is a quarterly journal that focuses on medicine, biological sciences, and biomaterials engineering. The goal of *Global Translational Medicine* is to provide a platform to researchers for showcasing their latest research works in translational medicine so as to advance the field towards the betterment of human health. Despite the advancement of omics and new technologies, the process of transforming these technologies and scientific research results into effective therapies and putting them into clinical use still has a long way to go. *Global Translational Medicine* provides a platform to fill the gaps in preclinical and inter-disciplinary research, to promote clinical translation of scientific research results, and to contribute to the conception of new and improved preventive measures as well as diagnostic and therapeutic techniques of diseases.

Global Translational Medicine covers the following themes: cardiovascular disease, metabolism/diabetes/obesity, neuroscience/neurology, cancer, biomaterials and their applications in medicine, proteomics/metabolomics, pharmacogenomics, biomarkers, bioinformatics and data mining, animal and clinical research, and medical methods arising from interdisciplinary crossover.

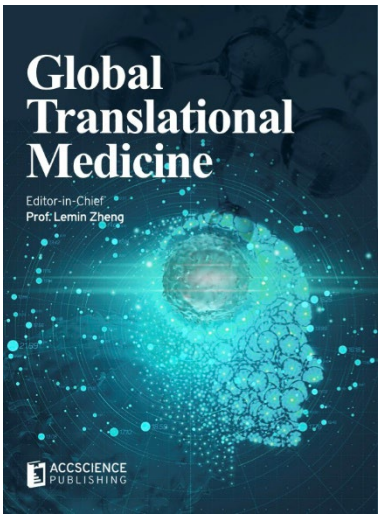

Start a new journal

Write to us via email if you are interested to start a new journal with AccScience Publishing. Please attach your CV, professional profile page and a brief pitch proposal in your email. We shall inform you of our decision whether we are interested to collaborate in starting a new journal.

Contact: info@accscience.com

https://accscience.com/journal/IJB



Contact
www.accscience.com
9 Raffles Place, Republic Plaza 1 #06-00 Singapore 048619
Email: editorial@accscience.com
Phone: +65 8182 1586